Contents

Préface

La semaine de l'Astronomie Française 2008 s'est tenue du 30 juin au 4 Juillet à l'Université Paris Diderot, dans son nouvel environnement de Paris-Tolbiac. Les séances plénières du Mardi et Mercredi se sont déroulées dans le grand auditorium de la Bibliothèque François Mitterand. Pour l'anniversaire des 30 ans de la SF2A, l'ambiance de fête et la bonne humeur ont rassemblé près de 450 participants. Cette semaine a réuni en parallèle les ateliers des programmes nationaux, groupements de recherche et actions spécifiques (PNP, PNST, PCHE, PCMI, PNPS, PNG et PNC, GRAAPH, ASHRA, AS–GAIA, AS–OV), ainsi qu'une session spéciale sur l'Enseignement de l'Astronomie. Plusieurs de ces programmes ont tenu des sessions communes.

Pendant les deux journées en session plénière, chaque Programme a présenté un exposé de revue. Les présentations d'intérêt général nous ont permis de découvrir les réformes de l'INSU par Dominique Lequéau, la prospective en cours de la communauté européenne pour les 10 ans à venir avec Astronet, par Jean-Marie Hameury, ainsi que l'état de la prospective de l'ESA, du CNES et de l'INSU. Michael Rowan-Robinson a présenté la Société invitée du Royaume-Uni, la Royal Astronomical Society, qui participait aussi à un atelier en commun avec les PNC et PNG, sur l'infra-rouge extra-galactique. 2009 étant l'année mondiale de l'Astronomie, Anny-Chantal Levasseur-Regourd nous a présenté les diverses actions qui allaient ponctuer et animer cette année de grande communication vers le public.

Enfin, un des moments forts de la session plénière a été l'intervention des anciens présidents de la SF2A au cours de ces dernières années, à commencer par Raymond Michard, qui a évoqué pour nous des souvenirs émouvants. Ont successivement pu placer quelques anecdotes Jean-Paul Zahn, Catherine Cesarsky, Sylvie Vauclair, Suzy Collin, Françoise Combes, Fabienne Casoli et Didier Barret. Alors que la séance était sur sa fin, André Brahic a joué les prolongations avec humour et bagoût.

Les lauréats du prix jeune chercheur, Guilaine Lagache, et du prix jeune enseignant–chercheur, Olivier Mousis, nous ont présenté leurs travaux de façon vivante et passionnante. Ces prix ont été remis par Jean-Loup Puget et François Vernotte et parrainés par la société HP et la SF2A. Nous remercions chaleureusement HP et son représentant, Philippe Devins, pour l'intérêt qu'ils portent à notre discipline, rendant ainsi possible la remise de ce prix. Roland Lehoucq a reçu pour la première fois le Prix SF2A/A Ciel Ouvert (ACO) de la communication scientifique en Astronomie, en présence de Bruno Monflier, Président d'ACO. Enfin, EDP-Sciences en partenariat avec la SF2A ont attribué les prix des meilleurs posters dans chaque Session.

Nous avons également tenu la traditionnelle conférence de presse, qui a vu la présentation de plusieurs "premières" scientifiques.

Pour l'ensemble de la manifestation, l'Université Paris Diderot nous a généreusement accueillis dans ses locaux. Nous remercions vivement pour leur aide financière le MEN, CNRS, le CNES, l'Observatoire de Paris, l'IAP, l'IAS, le CEA/SAp, le CESR, les Observatoires de Marseille Provence, Grenoble, Besançon, Strasbourg, et Toulouse. Sans leur soutien, l'organisation de cette grande manifestation n'aurait pas été possible.

Nous tenons à remercier chaleureusement les membres du Comité Local d'Organisation qui ont fait de cette semaine une réussite: Stéphane Basa, Corinne Charbonnel, Suzy Collin, Françoise Combes, Dolorès Granat, Mohammad Heydari, Alain Lecavelier, Jacqueline Plançy, Réza Samadi, Stéphane Thomas, et Olivier Tiret. Enfin que soient remerciés le bureau et le conseil de la SF2A, qui ont activement participé au pilotage de cette manifestation.

Didier Barret et Denis Burgarella
Ancien et nouveau Présidents de la SF2A

Foreword

The 2008 annual meeting of the French Astronomical Society ("La semaine de l'Astrophysique Française") was held in Paris, at the Université Paris Diderot, from June 30 to July 4. For this 30th anniversary, a new site was inaugurated at Tolbiac, the parallel sessions in the university campus, and the plenary sessions, at the Grand Auditorum of the National Library François Mitterand. It was organized in parallel with the National Program workshops, "groupements de recherche" and "actions spécifiques", which support astronomy research activities in France (there are currently 11 National Programs). Several of these programs held common sessions.

During the two days of the plenary sessions, each Program presented a review talk. For the general interest, Dominique Lequéau presented the future of INSU/CNRS and Jean-Marie Hameury the current prospective, being worked out by the consortium Astronet, for the European countries, as their first common decadal survey. Were also presented the curent prospectives of ESA, CNES and INSU. Michael Rowan-Robinson presented the invited UK Society, the Royal Astronomical Society, which participated also to a common workshop with PNC and PNG, on the extra-galactic infrared sky. 2009 being the international year of Astronomy, Anny-Chantal Levasseur-Regourd presented the various actions which will ponctuate and animate this year of great public outreach.

One of the great moments of the plenary session was the intervention of the previous SF2A presidents, invited for its birthday. Raymond Michard began by describing the beginning of the Society, with touching souvenirs. Then successively Jean-Paul Zahn, Catherine Cesarsky, Sylvie Vauclair, Suzy Collin, Françoise Combes, Fabienne Casoli and Didier Barret presented some anecdotes. When the session was finishing, André Brahic played the prolongations with good humour and vivacity.

Nearly 450 astronomers gathered during the "Week", which fully played its role in animating the scientific community, including very exciting information on the latest scientific achievements and debates on future projects. This annual meeting allows us to initiate collaborations, and exchange results in a friendly and stimulating atmosphere.

The 2008 SF2A/HP prizes were awarded to Guilaine Lagache and Olivier Mousis. The prizes were presented by Jean-Loup Puget and François Vernotte and sponsored by the HP company and the SF2A. We warmly thank HP and its representative, Philippe Devins, for their continuing interest in our science, which allows us to award this prize to a young researcher every year. Roland Lehoucq received for the first time the prize SF2A/A Ciel Ouvert (ACO) of the scientific communication in Astronomy, in presence of Bruno Monflier, President of ACO. In addition, EDP-Sciences and SF2A attributed the prizes of the best posters in each Session.

We sincerely thank the MEN, CNRS, le CNES, l'Observatoire de Paris, l'IAP, l'IAS, le CEA/SAp, le CESR, and the Observatories of Marseille Provence, Grenoble, Besançon, Strasbourg, Toulouse, for their financial support, and the Université Paris Diderot for hosting most of the meeting. Without them, the organisation of this major meeting would not have been possible.

We wish to thank the members of the Local Organizing Committee, Stéphane Basa, Corinne Charbonnel, Suzy Collin, Françoise Combes, Dolorès Granat, Mohammad Heydari, Alain Lecavelier, Jacqueline Plançy, Réza Samadi, Stéphane Thomas, et Olivier Tiret, whose outstanding contributions made the event the great success it was. Finally the SF2A board and council should be thanked for contributing actively to the 2008 annual meeting of the French Astronomical Society.

Didier Barret et Denis Burgarella
Previous and present Presidents of SF2A

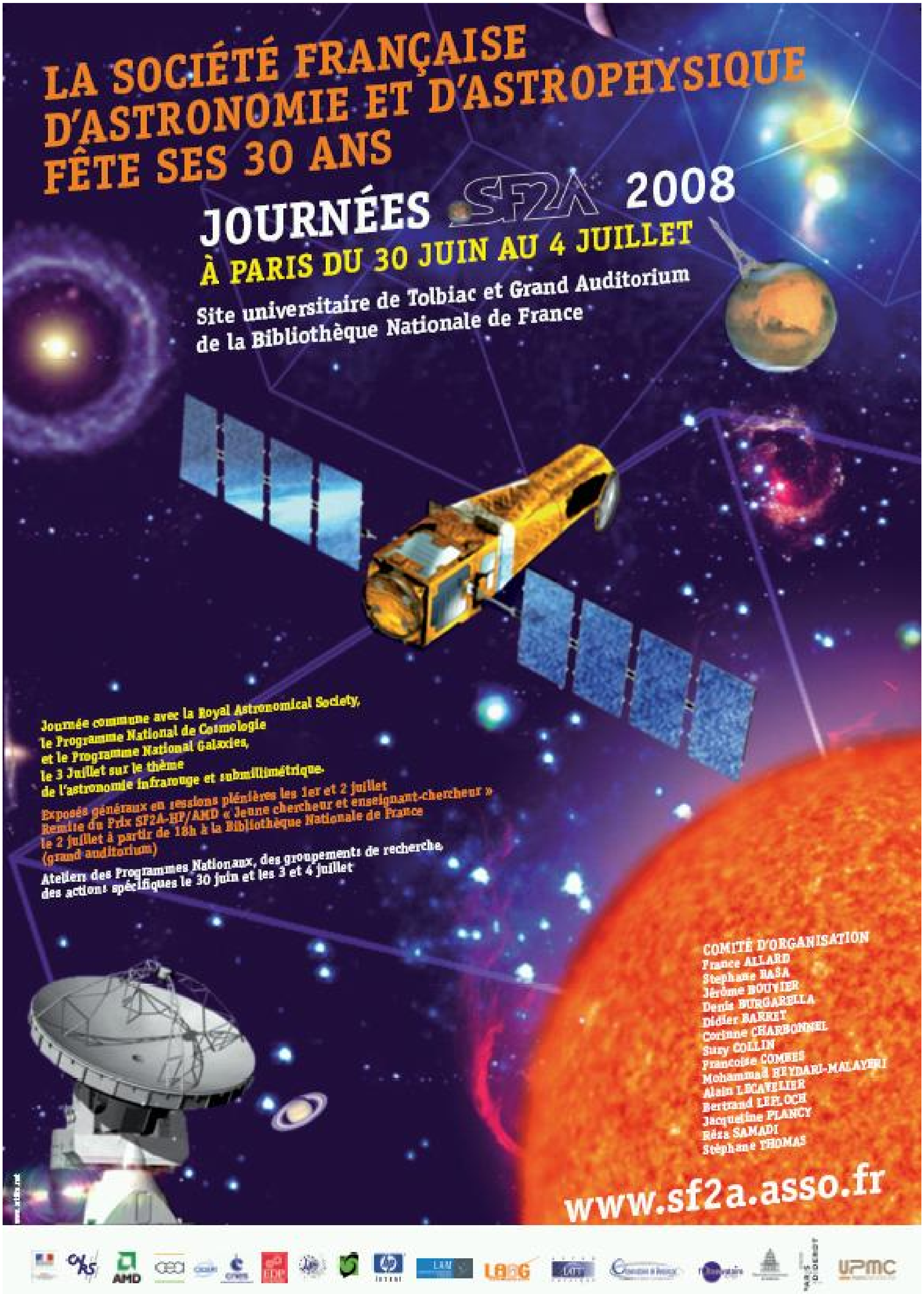
LA SOCIÉTÉ FRANÇAISE
D'ASTRONOMIE ET D'ASTROPHYSIQUE
FÊTE SES 30 ANS
JOURNÉES SF2A 2008
À PARIS DU 30 JUIN AU 4 JUILLET
Site universitaire de Tolbiac et Grand Auditorium
de la Bibliothèque Nationale de France
Journée commune avec la Royal Astronomical Society,
le Programme National de Cosmologie
et le Programme National Galaxies,
le 3 Juillet sur le thème
de l'astronomie infrarouge et submillimétrique.
Exposés généraux en sessions plénières les 1er et 2 juillet
Remise du Prix SF2A-HP/AMD « Jeune chercheur et enseignant-chercheur »
le 2 juillet à partir de 18h à la Bibliothèque Nationale de France
(grand auditorium)
Ateliers des Programmes Nationaux, des groupements de recherche,
des actions spécifiques le 30 juin et les 3 et 4 juillet
COMITÉ D'ORGANISATION
France ALLARD
Stéphane BASA
Jérôme BOUVIER
Denis BURGARELLA
Didier BARRET
Corinne CHARBONNEL
Suzy COLLIN
Françoise COMBES
Mohammad HEYDARI-MALAYERI
Alain LECAVELIER
Bertrand LEFLOCH
Jacqueline PLANCY
Réza SAMADI
Stéphane THOMAS
www.sf2a.asso.fr
AMD
UPMC

Participant list

Fabio Acero (fabio.acero@cea.fr)
Christophe Adami (christophe.adami@oamp.fr)
France Allard (fallard@ens-lyon.fr)
Denis Allard (allard@apc.univ-paris7.fr)
Danielle Alloin (danielle.alloin@cea.fr)
Frédéric Arenou (frederic.arenou@obspm.fr)
Jean-eudes Arlot (arlot@imcce.fr)
Luc Arnold (luc.arnold@oamp.fr)
Hakim Atek (atek@iap.fr)
Raphael Attie (attie@mps.mpg.de)
Frederic Auchere (frederic.auchere@ias.u-psud.fr)
Jean-charles Augereau (augereau@obs.ujf-grenoble.fr)
Guillaume Aulanier (guillaume.aulanier@obspm.fr)
Nicolas Aunai (nicolas.aunai@cetp.ipsl.fr)
Ossama Azagrouze (oazagrouze@yahoo.fr)
Sunghye Baek (sunghye.baek@obspm.fr)
Balkowski (chantal.balkowski@obspm.fr)
Chantal Balkowski (chantal.balkowski@obspm.fr)
Cécile Barbachoux (cecile.barbachoux@obspm.fr)
Didier Barret (didier.barret@cesr.fr)
Matteo Barsuglia (barsu@apc.univ-paris7.fr)
Stephane Basa (stephane.basa@oamp.fr)
Yvonne Becherini (Yvonne.Becherini@apc.univ-paris7.fr)
Arnaud Beck (arnaud.beck@obspm.fr)
Kévin Belkacem (kevin.belkacem@obspm.fr)
Arnaud Bellétoile (belletoile@lpsc.in2p3.fr)
Zahir Bellil (bellil@iap.fr)
Renaud Belmont (belmont@cesr.Fr)
George Bendo (g.bendo@imperial.ac.uk)
Aurélien Benoit-lévy (benoitle@csnsm.in2p3.fr)
Jerome Berthier (berthier@imcce.fr)
Benjamin Bertincourt (Benjamin.Bertincourt@ias.u-psud.fr)
Bruno Bézard (Bruno.Bezard@obspm.fr)
Olivier Bienaymé (bienayme@astro.u-strasbg.fr)
Lionel Bigot (lbigot@oca.eu)
Pierre Binétruy (binetruy@apc.univ-paris7.fr)
Guillaume Blanc (blanc@apc.univ-paris7.fr)
Elisabeth Blanc (elisabeth.blanc@cea.fr)
Oscar Blanch Bigas (blanch@lpnhe.in2p3.fr)
Anthony Boccaletti (anthony.boccaletti@obspm.fr)
Michel Boer (Michel.Boer@oamp.fr)
Isabelle Boisse (iboisse@iap.fr)
Samuel Boissier (samuel.boissier@oamp.fr)
Jérémie Boissier (boissier@iram.fr)
Catherine Boisson (catherine.boisson@obspm.fr)
Véronique Bommier (V.Bommier@obspm.fr)
Carla Bonifazi (bonifazi@lpnhe.in2p3.fr)
Daniel Bonneau (daniel.bonneau@obs-azur.fr)
Mickaël Bonnefoy (mbonnefo@obs.ujf-grenoble.fr)
Xavier Bonnin (xavier.bonnin@obspm.fr)
Alessandro Boselli (alessandro.boselli@oamp.fr)
Zeljka Bosnjak (bosnjak@iap.fr)

Francois Bouchy (bouchy@iap.fr)
Florian Boudol (boudol@apc.univ-paris7.fr)
François Boulanger (francois.boulanger@ias.u-psud.fr)
Géraldine Bourda (Geraldine.Bourda@obs.u-bordeaux1.fr)
Laurent Bourgès (Laurent.Bourges@obspm.fr)
Martin Boutelier (martin.boutelier@cesr.fr)
Timothé Boutelier (timothe.boutelier@obs.ujf-grenoble.fr)
Jerome Bouvier (jbouvier@obs.ujf-grenoble.fr)
Carine Briand (carine.briand@obspm.fr)
Danielle Briot (danielle.briot@obspm.fr)
Allan Sacha Brun (sacha.brun@cea.fr)
Veronique Buat (veronique.buat@oamp.fr)
Eric Buchlin (eric.buchlin@ias.fr)
Denis Burgarella (denis.burgarella@oamp.fr)
Nicolas Busca (ngbusca@apc.univ-paris7.fr)
Jose Busto (busto@cppm.in2p3.fr)
Sylvie Cabrit (sylvie.cabrit@obspm.fr)
Laurent Cambresy (cambresy@astro.u-strasbg.fr)
Nicole Capitaine (nicole.capitaine@obspm.fr)
Anabela Cardoso Goncalves (anabela.goncalves@astro.u-strasbg.fr)
Jean-marc Casandjian (casandjian@cea.fr)
Fabienne Casoli (fabienne.casoli@free.fr)
Fabien Casse (fcasse@apc.univ-paris7.fr)
Thibault Cavalié (Thibault.Cavalie@obs.u-bordeaux1.fr)
Cécile Cavet (cecile.cavet@obspm.fr)
Marie-noëlle Célérier (marie-noelle.celerier@obspm.fr)
Benoît Cerutti (benoit.cerutti@obs.ujf-grenoble.fr)
Henda Chaabouni (henda.chaabouni@u-cergy.fr)
Gérard Chanteur (gerard.chanteur@cetp.ipsl.fr)
Edwige Chapillon (edwige.chapillon@obs.u-bordeaux1.fr)
Corinne Charbonnel (Corinne.Charbonnel@obs.unige.ch)
Aldée Charbonnier (aldee@lpnhe.in2p3.fr)
Patrick Charlot (charlot@obs.u-bordeaux1.fr)
Stephane Charlot (charlot@iap.fr)
Eric Chassande-mottin (ecm@apc.univ-paris7.fr)
Bertrand Chauvineau (chauvineau@obs-azur.fr)
Mourad Chehrouri (Mourad.Chehrouri@u-cergy.fr)
Alain Chelli (Alain.Chelli@obj.ujf-grenoble.fr)
Laurent Chemin (laurent.chemin@obspm.fr)
Olivier Chesneau (Olivier.Chesneau@obs-azur.fr)
Igor Chilingarian (Igor.Chilingarian@obspm.fr)
Bruno Christophe (bruno.christophe@onera.fr)
Andrea Ciardi (andrea.ciardi@obspm.fr)
Benjamin Clément (benjamin.clement@oamp.fr)
Suzy Collin-zahn (suzy.collin@obspm.fr)
Arnaud Collioud (collioud@obs.u-bordeaux1.fr)
Pierre Colom (pierre.colom@obspm.fr)
Francoise Combes (francoise.combes@obspm.fr)
Mathieu Compiegne (compiegne@cita.utoronto.ca)
Thierry Contini (contini@ast.obs-mip.fr)
Yannick Copin (y.copin@ipnl.in2p3.fr)
Stéphane Corbel (stephane.corbel@cea.fr)
Mickaël Coriat (mickael.coriat@cea.fr)
Alberto Cornia (alberto.cornia@onera.fr)

Emmanuel Correia (Emmanuel.Correia@obspm.fr)
Vincent Coudé Du Foresto (vincent.foresto@obspm.fr)
Jerome Courtin (jerome.courtin@obspm.fr)
Stephanie Courty (scourty@uclan.ac.uk)
Athéna Coustenis (athena.coustenis@obspm.fr)
Paschal Coyle (coyle@cppm.in2p3.fr)
Audrey Crespin (audrey.crespin@wanadoo.fr)
Françoise Crifo (francoise.crifo@obspm.fr)
Jacques Crovisier (jacques.crovisier@obspm.fr)
Timea Csengeri (timea.csengeri@cea.fr)
Jean-charles Cuillandre (jcc@cfht.hawaii.edu)
Frédéric Daigne (daigne@iap.fr)
Richard Dallier (richard.dallier@subatech.in2p3.fr)
Iannis Dandouras (Iannis.Dandouras@cesr.fr)
Emmanuel Dartois (emmanuel.dartois@ias.u-psud.fr)
Xavier Daudigeos (xavier.daudigeos@obspm.fr)
Mathieu De Naurois (denauroi@in2p3.fr)
Emma De Ona Wilhelmi (emma@apc.univ-paris7.fr)
Estelle Déau (estelle.deau@cea.fr)
Guillaume Decerprit (decerprit@apc.univ-paris7.fr)
Typhaine Déchelette (typhaine.dechelette@gmail.com)
Anne Decourchelle (anne.decourchelle@cea.fr)
Thibaut Decressin (decressin@astro.uni-bonn.de)
Bernard Degrange (degrange@llr.in2p3.fr)
Sébastien Deheuvels (sebastien.deheuvels@obspm.fr)
Marco Delbo (delbo@oca.eu)
Florent Deleflie (florent.Deleflie@obs-azur.fr)
Rodney Delgado (rodney.delgado@obspm.fr)
Olivier Deligny (deligny@ipno.in2p3.fr)
Céline Delle Luche (celine.delleluche@obspm.fr)
Audrey Delsanti (Audrey.Delsanti@obspm.fr)
Audrey Delsanti (Audrey.Delsanti@obspm.fr)
Nicolas Delsate (nicolas.delsate@math.fundp.ac.be)
Jean-michel Désert (desert@iap.fr)
Josselin Desmars (desmars@imcce.fr)
Paola Di Matteo (paola.dimatteo@obspm.fr)
Sami Dib (sami.dib@cea.fr)
Noël Dimarcq (noel.dimarcq@obspm.fr)
Arache Djannati-ataï (djannati@apc.univ-paris7.fr)
Armando Domiciano De Souza (Armando.Domiciano@obs-azur.fr)
Damien Dornic (dornic@cppm.in2p3.fr)
Robert Droulans (Robert.Droulans@cesr.fr)
Marie-lise Dubernet (marie-lise.dubernet@obspm.fr)
Yohan Dubois (ydubois@cea.fr)
Florent Dubois (duboisf@lapp.in2p3.fr)
Guillaume Dubus (gdubus@obs.ujf-grenoble.fr)
Pierre-alain Duc (paduc@cea.fr)
Vincent Duez (vincent.duez@cea.fr)
Julien Dufey (julien.dufey@fundp.ac.be)
Florence Durret (durret@iap.fr)
Daniel Egret (daniel.egret@obspm.fr)
David Elbaz (delbaz@cea.fr)
Eric Emsellem (emsellem@obs.univ-lyon1.fr)
Nicolas Epchtein (epchtein@unice.fr)

Cyril Escolano (cyril.escolano@oamp.fr)
Pierre Exertier (Pierre.Exertier@obs-azur.fr)
Maurizio Falanga (mfalanga@cea.fr)
Edith Falgarone (edith@lra.ens.fr)
Emeric Falize (Emeric.Falize@obspm.fr)
Nicole Feautrier (Nicole.Feautrier@obspm.fr)
Roger Ferlet (ferlet@iap.fr)
Gilles Ferrand (gilles.ferrand@cesr.fr)
Philippe Ferrando (philippe.ferrando@cea.fr)
Katia Ferrière (ferriere@obs-mip.fr)
Clement Filliard (filliarc@yahoo.fr)
Jean-hugues Fillion (jean-hugues.fillion@upmc.fr)
Nicolas Fiolet (fiolet@iap.fr)
Patrick Fleury (patrick.fleury@llr.polytechnique.fr)
Hector Flores (hector.flores@obspm.fr)
Cedric Foellmi (cedric.foellmi@obs.ujf-grenoble.fr)
Dominique Fontaine (dominique.fontaine@cetp.ipsl.fr)
Jordi Fontdecaba (jordi.fontdecaba@obs-azur.fr)
Eric Fossat (eric.fossat@unice.fr)
Renaud Foy (foy@obs.univ-lyon1.fr)
Didier Fraix-burnet (fraix@obs.ujf-grenoble.fr)
Federico Fraschetti (federico.fraschetti@cea.fr)
Michael Friedjung (fried@iap.fr)
Julien Frouard (frouard@imcce.fr)
Maud Galametz (maud.galametz@cea.fr)
Raphaël Galicher (raphael.galicher@obspm.fr)
Sébastien Galtier (sebastien.galtier@ias.fr)
Thomas Gastine (tgastine@ast.obs-mip.fr)
Patrick Gaulme (Patrick.Gaulme@obspm.fr)
Jean Gay (jean_gay_astro@yahoo.fr)
Bruce Gendre (bruce.gendre@oamp.fr)
Françoise Genova (genova@astro.u-strasbg.fr)
Eric Gerard (eric.gerard@obspm.fr)
Lucie Gérard (lucie.gerard@apc.univ-paris7.fr)
Martin Giard (martin.giard@cesr.fr)
Julien Girard (girard@astroscu.unam.mx)
Magda Evgenia Gkini (magda.gkini@obspm.fr)
Jean-françois Glicenstein (glicens@cea.fr)
Marie-line Gobinddass (gobinddass@ipgp.jussieu.fr)
Marie Godard (marie.godard@ias.u-psud.fr)
Benjamin Godard (godard@lra.ens.fr)
Bertrand Goldman (goldman@mpia.de)
Andrea Goldwurm (andrea.goldwurm@cea.fr)
Anne-marie Gontier (anne-marie.gontier@obspm.fr)
Manuel Gonzalez Garcia (Manuel.Gonzalez@obspm.fr)
René Goosmann (goosmann@astro.cas.cz)
Philippe Gorodetzky (philippe.gorodetzky@cern.ch)
Mariejo Goupil (mariejo.goupil@obspm.fr)
Eric Gourgoulhon (eric.gourgoulhon@obspm.fr)
Roland Grappin (roland.grappin@obspm.fr)
Catherine Grec (catherine.grec@unice.fr)
Isabelle Grenier (isabelle.grenier@cea.fr)
Nicolas Grosso (grosso@astro.u-strasbg.fr)
Sandrine Guerlet (sandrine.guerlet@obspm.fr)

Jean Guibert (jean.Guibert@obspm.fr)
Pierre Guillard (pierre.guillard@ias.u-psud.fr)
Juan GutiÉrrez-soto (juan.gutierrez@obspm.fr)
Jean-marie Hameury (jean-marie.hameury@cnrs-dir.fr)
Hammer (francois.hammer@obspm.fr)
Misha Haywood (Misha.Haywood@obspm.fr)
Guillaume Hébrard (hebrard@iap.fr)
Patrick Hennebelle (patrick.hennebelle@ens.fr)
Pierre Henri (pierre.henri@obspm.fr)
Franck Hersant (Franck.Hersant@obs.u-bordeaux1.fr)
Emilie Herwats (emilie.herwats@obs.ujf-grenoble.fr)
Emilie Herwats (emilie.herwats@obs.ujf-grenoble.fr)
D. Hestroffer (hestro@imcce.fr)
Mohammad Heydari-malayeri (m.heydari@obspm.fr)
Anne-laure Huat (anne-laure.huat@obspm.fr)
Marc Huertas-company (marc.huertas@obspm.fr)
Stéphane Ilic (stephane.ilic@ias.u-psud.fr)
Karine Issautier (karine.issautier@obspm.fr)
Rob Ivison (rji@roe.ac.uk)
Agnieszka Jacholkowska (Agnieszka.Jacholkowska@cern.ch)
Stephane Jacquemoud (jacquemoud@ipgp.jussieu.fr)
Laurène Jouve (ljouve@cea.fr)
Sihem Kalli (k.sihem@gmail.com)
Samer Kanaan (Samer.Kanaan@obs-azur.fr)
Pierre Kervella (pierre.kervella@obspm.fr)
Karl-ludwig Klein (ludwig.klein@obspm.fr)
Laurent Koechlin (laurent.koechlin@ast.obs-mip.fr)
Nukri Komin (Nukri.Komin@cea.fr)
Kumiko Kotera (kotera@iap.fr)
Jean Kovalevsky (jean.kovalevsky@obs-azur.fr)
Lucas Labadie (labadie@mpia.de)
Johann Labasque (labasque@iap.fr)
Sylvestre Lacour (sylvestre.lacour@obs.ujf-grenoble.fr)
Guilaine Lagache (guilaine.lagache@ias.u-psud.fr)
Maurice Laloum (Maurice.Laloum@lpnhe.in2p3.fr)
Sebastien Lambert (sebastien.lambert@obspm.fr)
Laurent Lamy (laurent.lamy@obspm.fr)
Philippe Laurent (plaurent@cea.fr)
Thibaut Le Bertre (thibaut.lebertre@obspm.fr)
Gaétan Le Chat (gaetan.lechat@obspm.fr)
Franck Le Petit (Franck.LePetit@obspm.fr)
Christophe Le Poncin-lafitte (christophe.leponcin-lafitte@obspm.fr)
Pierre Le Sidaner (pierre.lesidaner@obspm.fr)
Alexandre Le Tiec (letiec@iap.fr)
Loic Le Tiran (loic.le-tiran@obspm.fr)
Agnes Lebre (lebre@graal.univ-montp2.fr)
Alain Lecavelier Des Etangs (lecaveli@iap.fr)
Laure Lefevre (laure.lefevre@obspm.fr)
Bertrand Lefloch (lefloch@obs.ujf-grenoble.fr)
Matthew Lehnert (matthew.lehnert@obspm.fr)
John Leibacher (john.leibacher@ias.u-psud.fr)
Anica Lekic (lekic@lpma.jussieu.fr)
Jean Louis Lemaire (jean-louis.lemaire@obspm.fr)
Bertrand Lemasle (bertrand.lemasle@etud.u-picardie.fr)

Martin Lemoine (lemoine@iap.fr)
Pierre Lena (pierre.lena@obspm.fr)
Pierre Lepetit (popedodi@wanadoo.fr)
Nicolas Leroy (leroy@llr.in2p3.fr)
Pierre Lesaffre (pierre.lesaffre]lra.ens.fr)
Jean-francois Lestrade (jean-francois.lestrade@obspm.fr)
Geoffroy Lesur (g.lesur@damtp.cam.ac.uk)
Anny-chantal Levasseur-regourd (aclr@aerov.jussieu.fr)
Agnès Levy (agnes.levy@onera.fr)
Yannick Libert (yannick.libert@obspm.fr)
François Lignieres (ligniere@ast.obs-mip.fr)
Constantino Listowski (listowski@mpia.de)
Guillaume Loisel (guillaume.loisel@cea.fr)
Bérénice Loupias (berenice.loupias@polytechnique.edu)
Hans Ludwig (Hans.Ludwig@obspm.fr)
Suzanne Madden (suzanne.madden@cea.fr)
Milan Maksimovic (milan.maksimovic@obspm.fr)
Vincent Marandon (marandon@apc.univ-paris7.fr)
Ulysse Marboeuf (marboeuf@obs-besancon.fr)
Delphine Marcillac (delphine.marcillac@ias.u-psud.fr)
Alexandre Marcowith (Alexandre.Marcowith@lpta.in2p3.fr)
Jérôme Margueron (jmargue@ipno.in2p3.fr)
Christian Marinoni (marinoni@cpt.univ-mrs.fr)
Accolla Mario (mario.accolla@u-cergy)
Christophe Martayan (martayan@oma.be)
Claire Martin-zaidi (claire.martin-zaidi@obs.ujf-grenoble.fr)
Jean-louis Masnou (jean-louis.masnou@courrier.univ-paris1.fr)
Sophie Masson (sophie.masson@obspm.fr)
Elie Matar (elie.matar@u-cergy.fr)
Stéphane Mathis (stephane.mathis@cea.fr)
Fabio Mattana (fabio.mattana@apc.univ-paris7.fr)
Nicolas Mauron (mauron@graal.univ-montp2.fr)
Anaelle Maury (anaelle.maury@cea.fr)
Christian Mazelle (Christian.Mazelle@cesr.fr)
Héloïse Méheut (hmeheut@apc.univ-paris7.fr)
Anne-laure Melchior (Anne-Laure.Melchior@obspm.fr)
Yannick Mellier (mellier@iap.fr)
Eric Michel (eric.michel@obspm.fr)
Leo Michel-dansac (leo@oac.uncor.edu)
Francois Mignard (francois.mignard@oca.eu)
Vincent Minier (vincent.minier@cea.fr)
Marc-antoine Miville-deschenes (mamd@ias.u-psud.fr)
Xavier Moisson (xavier.moisson@astrium.eads.net)
Hakima Mokrane (hakima.mokrane@u-cergy.fr)
Michel Moncuquet (michel.moncuquet@obspm.fr)
Estelle Moraux (emoraux@obs.ujf-grenoble.fr)
Guy Moreels (guy.moreels@obs-besancon.fr)
Christophe Morisset (morisset@astroscu.unam.mx)
Benoît Mosser (benoit.mosser@obspm.fr)
Fabrice Mottez (fabrice.mottez@obspm.fr)
Martine Mouchet (martine.mouchet@apc.univ-paris7.fr)
Audrey Moudens (audrey.moudens@univ-rennes1.fr)
Denis Mourard (denis.mourard@obs-azur.fr)
Serge Mouret (mouret@imcce.fr)

Olivier Mousis (olivier.mousis@obs-besancon.fr)
Melitta Naumann-godo (naumann-godo@llr.in2p3.fr)
Coralie Neiner (coralie.neiner@obspm.fr)
Nicole Nesvadba (nicole.nesvadba@obspm.fr)
Stefan Noll (stefan.noll@oamp.fr)
Pasquier Noterdaeme (noterdaeme@iap.fr)
Benoît Noyelles (Benoit.Noyelles@imcce.fr)
Anaïs Oberto (oberto@astro.u-strasbg.fr)
Micaela Oertel (micaela.oertel@obspm.fr)
Johan Olofsson (olofsson@obs.ujf-grenoble.fr)
Rhita-maria Ouazzani (rhita-maria.ouazzani@obspm.fr)
Laurent Pagani (laurent.pagani@obspm.fr)
Manfred Pakull (pakull@astro.u-strasbg.fr)
Ana Palacios (palacios@univ-montp2.fr)
Frédéric Paletou (fpaletou@ast.obs-mip.fr)
Laurent Pallier (laurent.pallier@obspm.fr)
Etienne Parizot (parizot@apc.univ-paris7.fr)
Michel Parrot (mparrot@cnrs-orleans.fr)
Thierry Passot (passot@oca.eu)
Kevin Payet (payet@lpsc.in2p3.fr)
Sebastien Peirani (peirani@iap.fr)
Sophie Pelisson (sophiepelisson@orange.fr)
Pascal Petit (petit@ast.obs-mip.fr)
Gérard Petit (gpetit@bipm.org)
Patrick Petitjean (petitjean@iap.fr)
Jérôme Pétri (jerome.petri@cetp.ipsl.fr)
Romain Petrov (Romain.Petrov@unice.fr)
Pierre-olivier Petrucci (pierre-olivier.petrucci@obs.ujf-grenoble.fr)
Jérôme Pety (pety@iram.fr)
Monique Pick (monique.pick@obspm.fr)
Jean-louis Pinçon (jlpincon@cnrs-orleans.fr)
Christophe Pinte (pinte@astro.ex.ac.uk)
Rui Pinto (rui.pinto@obspm.fr)
Sophie Pireaux (sophie.pireaux@oma.be)
Santiago Pita (santiago.pita@apc.univ-paris7.fr)
Eric Plagnol (eric.plagnol@APC.univ-paris7.fr)
Nicolas Ponthieu (nicolas.ponthieu@ias.u-psud.fr)
Gabriele Ponti (ponti@iasfbo.inaf.it)
Delphine Porquet (porquet@astro.u-strasbg.fr)
François Poulet (francois.poulet@ias.u-psud.fr)
Nikos Prantzos (prantzos@iap.fr)
Lionel Prat (lionel.prat@cea.fr)
Dominique Proust (dominique.proust@obspm.fr)
Michael Punch (punch@in2p3.fr)
Yan Qu (yan.qu@obspm.fr)
Julien Queyrel (jqueyrel@ast.obs-mip.fr)
Daniel Reese (D.Reese@sheffield.ac.uk)
Céline Reylé (celine@obs-besancon.fr)
Noël Robichon (noel.robichon@obspm.fr)
Annie Robin (annie.robin@obs-besancon.fr)
Brigitte Rocca-volmerange (rocca@iap.fr)
Myriam Rodrigues (myriam.rodrigues@obspm.fr)
Jerome Rodriguez (jrodriguez@cea.fr)
Sébastien Rodriguez (sebastien.rodriguez@cea.fr)

Françoise Roques (francoise.roques@obspm.fr)
Thierry Roudier (thierry.roudier@ast.obs-mip.fr)
Evelyne Roueff (evelyne.roueff@obspm.fr)
Benjamin Rouillé D'orfeuil (rouille@apc.univ-paris7.fr)
Gérard Rousset (gerard.rousset@obspm.fr)
Frédéric Royer (frederic.royer@obspm.fr)
Delphine Russeil (delphine.russeil@oamp.fr)
Sylvie Sahal-brÉchot (sylvie.sahal-brechot@obspm.fr)
Julien Salmon (julien.salmon@cea.fr)
Philippe Salome (salome@iram.fr)
Réza Samadi (reza.samadi@obspm.fr)
Philippe Savoini (philippe.Savoini@cetp.ipsl.fr)
François-xavier Schmider (schmider@unice.fr)
Brigitte Schmieder (brigitte.schmieder@obspm.fr)
Benoit Semelin (benoit.semelin@obspm.fr)
Lucia Seoane (lucia.seoane@obspm.fr)
Mathieu Servillat (mathieu.servillat@cesr.fr)
Hélène Sol (helene.sol@obspm.fr)
Caroline Soubiran (soubiran@obs.u-bordeaux1.fr)
Jean Souchay (Jean.Souchay@obspm.fr)
Monique Spite (monique.spite@obspm.fr)
Chantal Stehle (chantal.stehle@obspm.fr)
Tiina Suomijarvi (tiina@ipno.in2p3.fr)
Giulia Superina (superina@llr.in2p3.fr)
Nicolas Taburet (nicolas.taburet@ias.u-psud.fr)
Michel Tagger (michel.tagger@cnrs-orleans.fr)
Michel Tallon (mtallon@obs.univ-lyon1.fr)
Paolo Tanga (tanga@oca.eu)
François Taris (francois.taris@obspm.fr)
Eric Tatulli (Eric.Tatulli@obs.ujf-grenoble.fr)
Sonia Giovanna Temporin (sonia.temporin@cea.fr)
Pierre Teyssandier (Pierre.Teyssandier@obspm.fr)
Gilles Theureau (theureau@cnrs-orleans.fr)
Frédéric Thévenin (thevenin@obs-nice.fr)
Wing-fai Thi (wfdt2004@roe.ac.uk)
Caroline Thomas (caroline.thomas@univ-fcomte.fr)
Gérard Thuillier (gerard.thuillier@aerov.jussieu.fr)
William Thuillot (thuillot@imcce.fr)
Olivier Tiret (olivier.tiret@obspm.fr)
Guillaume Trap (trap@apc.univ-paris7.fr)
Gérard Tristram (tristram@in2p3.fr)
Sylvaine Turck-chieze (cturck@cea.fr)
Catherine Turon (catherine.turon@obspm.fr)
Frédéric Vachier (fv@imcce.fr)
Farrokh Vakili (Farrokh.Vakili@unice.fr)
David Valls-gabaud (david.valls-gabaud@obspm.fr)
Jean-claude Valtier (valtier@obs-nice.fr)
Veronique Van Elewyck (elewyck@apc.univ-paris7.fr)
Peggy Varniere (varniere@apc.univ-paris7.fr)
Nicolas Vasset (nicolas.vasset@gmail.com)
Isabelle Vauglin (vauglinàobs.univ-lyon1.fr)
Christian Veillet (veillet@cfht.hawaii.edu)
Lionel Veltz (lveltz@aip.de)
Louis Venter (louis.venter@obspm.fr)

Susanna Vergani (susilandia@gmail.com)
Francois Vernotte (francois.vernotte@obs-besancon.fr)
Jacques Vetois (jacques.vetois@obspm.fr)
Yves-paul Viala (yves.viala@obspm.fr)
Alain Vienne (alain.vienne@univ-lille1.fr)
Arthur Vigan (arthur.vigan@oamp.fr)
Nicole Vilmer (nicole.vilmer@obspm.fr)
Sandrine Vinatier (sandrine.vinatier@obspm.fr)
Frédéric Vincent (frederic.vincent@obspm.fr)
Patrick Vonlanthen (Patrick.Vonlanthen@graal.univ-montp2.fr)
Michael Weiler (michael.weiler@obspm.fr)
Klaus Werner (werner@subatech.in2p3.fr)
Herve Wozniak (herve.wozniak@obs.univ-lyon1.fr)
Jean-paul Zahn (jean-paul.zahn@obspm.fr)
Wassila Zerhouni (wassila.zerhouni@obspm.fr)
Ioannis Zouganelis (ioannis.zouganelis@obspm.fr)

ASGAIA

Preparation to GAIA

SF2A 2008
C. Charbonnel, F. Combes and R. Samadi (eds)

3D HYDRODYNAMICAL SIMULATIONS OF STELLAR SURFACES : APPLICATIONS TO *GAIA*

Bigot, L. & Thévenin, F.[1]

Abstract.
We use 3D time-dependent hydrodynamical simulations to model the photospheres of late type stars in a very realistic way. We apply these simulations to study the 3D line formation in the spectral domain of the spectrometer on board in the space mission *Gaia*.

1 Introduction

The *Gaia* space mission (Perryman et al. 2001) will provide an unprecedented opportunity to map the actual chemical composition of million of stars throughout the Milky Way. Knowing the distances thanks to the astrometric instrument, the photometer on board will provide the fundamental stellar parameters such as the effective temperature, gravity and average metallicity. The Radial Velocity Spectrometer (RVS) will allow a determination of the chemical abundances by observing individual spectral lines (Katz et al. 2004, Wilkinson et al. 2005). Collecting these stellar abundances, it will be then possible to map of the chemical composition of our Galaxy for million of stars (up to V=12-13), i.e. to a scale never reached before. The knowledge of this chemical composition of the Galaxy from the disk to the halo will provide information on its formation and history. Regarding the importance of the mission and its goals, it is mandatory to have the best models to extract the physical parameters of the observed stars. It is worth mentioning that these abundances are *not* observed but *interpret* through models. The model atmospheres must therefore be as realistic as possible. The convection plays an essential role in the line forming process and deeply influences the shape, shift and asymmetry of lines in late type stars which will represent most of the stars that will be observed by *Gaia*. To date, most of the abundance determinations are done in 1D hydro*static* models in LTE or NLTE. These models have difficulties to fit the shape of the observed lines and more important they require the use of adjustable parameters such as the micro and macro turbulence which are used to mimic the effects of the convection. This is an important source of uncertainties in the diagnostic. This problem can be avoided by using 3D radiative hydrodynamical (RHD) models that naturally account for turbulent motions. Another important aspect of the 3D RHD simulations is that they can correct the convective shifts (few hundreds m/s) of the lines which has to be subtracted to the global lineshifts when determining the stellar radial velocities. A realistic modelling of stellar atmospheres is therefore crucial for a better interpretation of future data.

In this paper, we present preliminary work which consists in using state-of-the-art 3D RHD simulations to calculate synthetic line profiles in the wavelength region of *Gaia*/RVS. We first focus on the Ca II triplet and then discuss the use of these models to derive accurate radial velocities, corrected from convective lineshifts.

2 The 3D modelling of the stellar atmospheres

Realistic modelling of the solar and stellar surfaces has been developed since the early eighties by Nordlund and coworkers (Nordlund 1982, Stein & Nordlund 1989, Nordlund & Dravins 1990, Stein & Nordlund 1998, Asplund et al. 2000). They found great success in reproducing observed constraints such as granulation topology, spectral lines, helioseismic data. In the present work, we use a code that solves the equations for mass, momentum and internal energy in a conservative form, for fully 3D compressible flow on a staggered mesh (Nordlund &

[1] Université Nice Sophia Antipolis, Observatoire de la Côte d'Azur, BP 4229, 06304, Nice cedex 4

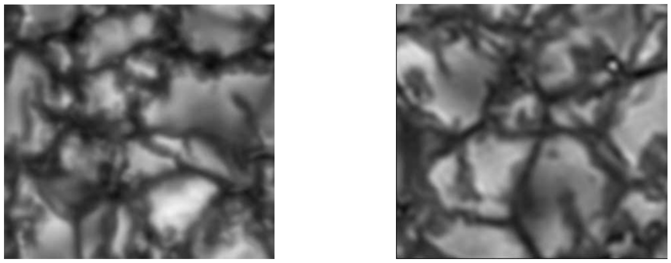

Fig. 1. Comparison between synthetic disk-center emergent intensity (left panel) and the observed equivalent (Right panel) made at the Solar Swedish Telescope (SST). Each panel represents an area of 6000 × 6000 kms. (Left) Synthetic image obtained by a 3D RHD simulation (Bigot, unpublished) with a grid resolution of $512^2 \times 384$ (11.6 kms horizontal). The synthetic image is smoothed by an Airy function that mimics the PSF of the SST. (Right) G-band (4305 Å) image obtained at the SST using adaptative optics and speckle reconstruction. This image (unpublished) is kindly provided by J. Hirzberger. Data of the same observations may be found in Wiehr et al. (2004) and Hirzberger & Wiehr (2005). The resolution is 0.041"(30kms).

Galsgaard 1995). The code uses 6th order finite differences and 5th order interpolation. The time advance is done by a 3rd order Runge-Kutta scheme. Horizontal boundary conditions are periodic whereas top and bottom boundary conditions are transmitting. We use ghost zones at the top and the bottom of the domain in order to use the same spatial derivative scheme at the boundaries and in the interior. The code is stabilized by numerical diffusion of the Von Neumann and Richtmyer type in the momentum and energy equations. The Uppsala's equation-of-states and opacities are used (Gustafsson et al. 1975 + updates). The radiative transfer is solved by using wavelength binning technique (Nordlund 1982).
Each model is defined by the entropy at the bottom of the simulation domain, the gravity and the chemical composition. We note that the effective temperature is not an input in our model but rather an output fluctuating around a mean value. For each stellar model, the time sequence spans several hours, enough to cover several convective turn-overs. An illustration of the realism of the 3D RHD simulation is shown in Fig. 1.

In order to calculate synthetic spectra, we extract from the 3D RHD simulation a run of about 1 hour, with snapshots stored every 10 min. For each of them, the radiative line transfer was solved with long characteristics using a Feautrier scheme. Pure LTE (no scattering) is assumed. We use the most recent quantum mechanical calculations of hydrogen collisions with neutral species (Barklem & O'Mara 1997, Barklem et al. 1998) to account for Van der Waals broadening. This is a great improvement compared with the traditional Unsöld recipe since we no longer need an enhancement factor. The disk-center or disk-integrated intensities are computed for each grid point at the surface. The 2D time-dependent surface intensity profiles are then spatially and temporally averaged before comparison with observations.

3 Applications to *Gaia*/RVS

There are several advantages to use 3D RHD simulations in stellar abundance and radial velocity determinations. These simulations lead to a very good fit of the observed lines in shape, depth, shifts and asymmetry as shown by Asplund and coworkers in a series of papers (e.g. Asplund et al. 2000, 2004) and by Bigot & Thévenin (2006) for the RVS spectral domain. Moreover, on the contrary to hydrostatic models, the 3D hydrodynamical ones naturally account for turbulent motions and therefore do not need the use of the traditional micro and macro turbulence. These adjustable quantities, which are unavoidable in 1D hydrostatic models, lead to some uncertainties in the diagnostic of stellar parameter determinations, in particular for abundance determinations.

Another important advantage is the possibility to calculate the convective shifts of the spectral lines. These shifts are of the order of a few hundreds m/s to a few km/s for late type stars. Since the RVS aims at determining the stellar radial velocities ($V_{\rm rad}$) of the Galaxy, it is particularly important to use these simulations to subtract the doppler shifts coming from the hydrodynamic motions *inside* the star. The precision expected for *Gaia*/RVS will be of the order of 1km/s (up to V=15 depending on spectral type).

In the following sections we apply these 3D hydrodynamical simulations to two cases of interest for *Gaia*/RVS which are the fit of the Ca II triplet and the convective shift correction for radial velocity determination.

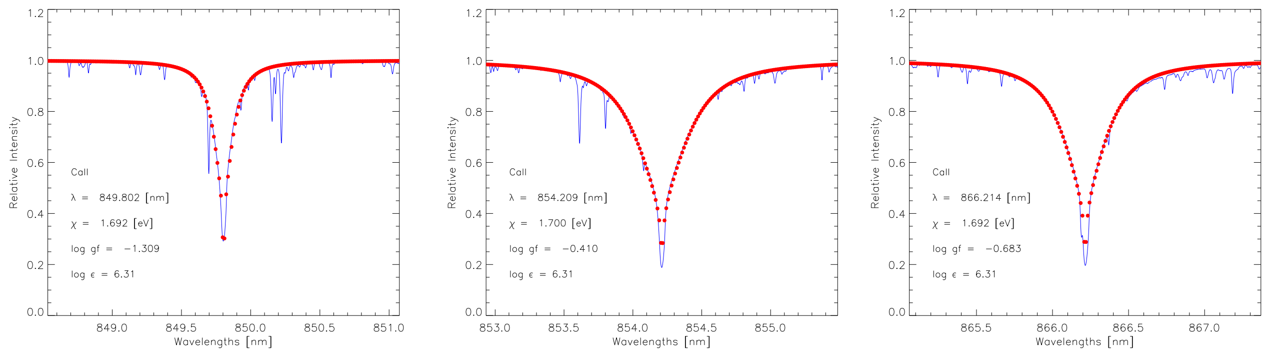

Fig. 2. Fits of the synthetic (•) disk-center Ca II triplet with solar spectrum (full line). The central depression is not well fitted since the line cores are formed in non-LTE conditions.

3.1 The calcium II triplet

The RVS spectral domain has been chosen mainly for the presence of the calcium II triplet (λ = 849.802, 854.209, 866.214 nm). This strong triplet will be visible in most stars, even in metal poor stars. We then pay a special attention to the calculation of synthetic profiles for these three lines (Bigot & Thévenin, 2008). In this work, we decided to fit the solar Ca II triplet by fixing the abundance of calcium ([Ca/H]=6.31) and by adjusting the oscillator strengths (log gf) whose values provided by database such as VALD (Kupka et al. 1999) are often badly known. The fit of these three lines is shown in Fig. 2. For such simulations we used a grid resolution of $253^2 \times 163$. The synthetic profiles were convolved with a Gaussian function representing the instrumental profile of the solar FTS ($\lambda/\delta\lambda \approx 500000$). The calculated profiles are shifted to take into account the gravitational redshift (633 m/s). Since the core of these lines is formed in the chromosphere and might suffer from NLTE effects, we only fit the wings of the Ca II triplet. The derived values (-1.309, -0.410, -0.683) are very close to quantuum mechanical calculation of Meléndez et al. (2007) : -1.356 , -0.405, -0.668, respectively. This good agreement, without adjustable parameters, is in favor of the realism of our simulations.

3.2 The convective shift corrections

The primary goal of the RVS is to determine the radial velocities of stars. In order to have an accurate $V_{\rm rad}$, one must correct the contribution of the convective shift. The amplitude of these lineshifts depends on the location of the formation of the line and on the star itself. We calculate a series of line profiles for different stars : α Cen B (K dwarf), sun and α Cen A (G dwarfs), Procyon (F star) and the metal poor star HD 84937. For this work, we used in all cases a grid resolution of $128^2 \times 96$. An investigation of convective shifts for late type stars was first made by Dravins & Nordlund (1990) but with a much lower resolution than ours. We focus for this exercise on the Ca II triplet and Fe I lines. The latter were selected to be non blended lines and to cover the spectral domain of the RVS (Bigot & Thévenin 2006).

As seen in Fig. 3ab the Fe I lines are blueshifted. This is due to the fact that they are formed deeply into the atmosphere where most of the light is emitted from the bright ascending granules. This is the case of most of the Fe I lines of our sample, with some exceptions like Fe I 868.86 nm. The convective shifts for Fe I lines range from a few hundreds m/s for α Cen B up to about 1 km/s for Procyon. The amplitude of the shift increases when going from K dwarfs to earlier type star such as Procyon, as a consequence of the more vigourous convective motions : $V_{\rm rms} = 1.4$ km/s for α Cen B and 4.1 km/s for Procyon.

As seen in Fig. 3c the Ca II triplet lines are redshifted. This is a consequence of the fact that these lines are formed well above the photosphere ($\tau < 0.1$). This is an overshoot region where the granulation is reversed: The largest fluctuations of temperature correspond to the descending flows (see e.g. Cheung et al. 2004 for a numerical investigation of this property.). The amplitude of the convective shift is larger than for Fe I lines.

4 Conclusion

The 3D RHD simulations are very helpful for the stellar abundance and radial velocity determinations. The main advantage lies in the fact that these simulations reproduce the stellar surfaces with a great realism. Since

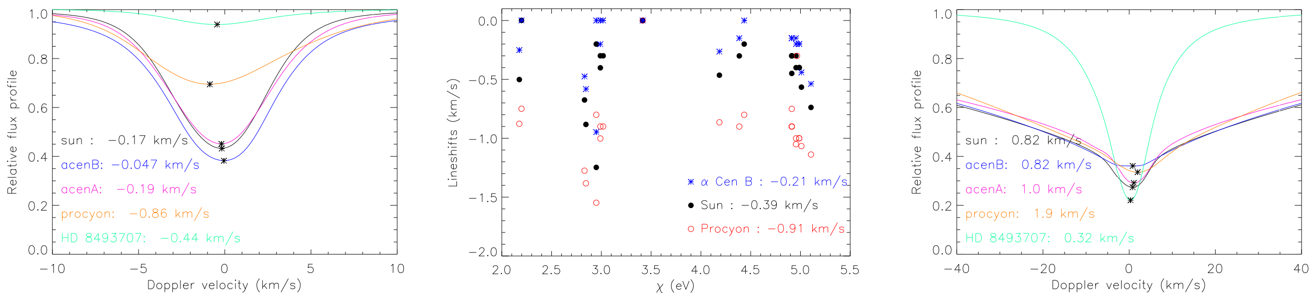

Fig. 3. (Left) Flux profiles of the Fe I at 851.407 nm for different stars. The lineshifts are indicated in each case. (Middle) Convective blueshifts of some Fe I lines of interest for the RVS (Bigot & Thévenin, 2006) as function of the excitation potential for three different stars: α Cen B, the Sun and Procyon. The convective shift increases as the star is hotter. (Right) The same as left panel but for the Ca II line at 854.209 nm. In that case, the convection leads to a redshift.

all the dynamics is naturally taken into account, they do not need to use adjustable free parameters that generally pollute the diagnostics in stellar physics. We have shown that these simulations can be useful for *Gaia*/RVS to get accurate line profiles and even more important for the RVS they allow corrections of the convective shifts to the determination of radial velocities. The amplitude of these lineshifts for late type stars can be of the order of the accuracy expected for the radial velocities, i.e. ~ 1 km/s. In a future work, we will explore these corrections to more stars throughout the HR diagram.

Acknowledgments

We thank Å. Nordlund for providing his code. L. Bigot thanks the organizers of the session "Action Spécifique Gaia" for the invitation to present this work during the "Journées de la SF2A 2008".

References

Asplund, M., Nordlund, Å, Trampedach, R., Allende Prieto, C., & Stein, R. F. 2000, A&A, 359, 729
Asplund, M., Grevesse, N., Sauval, A. J., Allende Prieto, C., & Kiselman, D. 2004, A&A, 417, 751
Barklem, P. S., & O'Mara, B. J. 1997, MNRAS, 290, 102
Barklem, P. S., O'Mara, B. J., & Ross, J. E. 1998, MNRAS, 296, 1057
Bigot, L., & Thévenin, F. 2006, MNRAS, 372, 609
Bigot, L., & Thévenin, F. 2008, *Journal of Physics Conference Series*, in press
Cheung, M. C. M., Schessler, M., & Moreno-Insertis, F. 2004, A&A, 461, 1163
Dravins, D., & Nordlund, Å. 1990, A&A, 228, 184
Dravins, D., & Nordlund, Å. 1990, A&A, 228, 203
Gustafsson, B. et al. 1975, A&A, 42, 407
Hirzberger, J., & Wiehr, E. 2005, A&A, 438, 1059
Katz, D., Munari, U., Cropper, M., Zwitter, T., Thévenin, F., David, M., Viala, Y., et al. 2004, MNRAS, 354, 1223
Kupka, F., Piskunov, N., Ryabchikova, T. A., Stempels, H. C., & Weiss, W. W. 1999, A&AS, 138, 119
Meléndez, M., Bautista, M. A., & Badnell, N. R. 2007, A&A, 469, 1203
Nordlund, Å. 1982, A&A, 107, 1
Nordlund, Å., & Dravins, D. 1990, 228, 155
Nordlund, Å., & Galsgaard, K. 1995, http://www.astro.ku.dk/ kg
Perryman, M. A. C., de Boer, K. S., Gilmore, G., Hög, E., Lattanzi, M. G., et al. 2001, A&A, 369, 339
Stein, R.F., & Nordlund, Å. 1989, ApJ, 342, L95-98
Stein, R.F., & Nordlund, Å. 1998, ApJ, 499, 914
Wiehr, E., Bovelet, B., & Hirzberger, J. 2004, A&A, 422, L63
Wilkinson, M. I., Vallenari, A., Turon, C., Munari, et al. 2005, 359, 1306.

SF2A 2008
C. Charbonnel, F. Combes and R. Samadi (eds)

MULTI-STEP VLBI OBSERVATIONS OF WEAK EXTRAGALACTIC RADIO SOURCES TO ALIGN THE ICRF AND THE FUTURE GAIA FRAME

Bourda, G.[1], Charlot, P.[1], Porcas, R.[2] and Garrington, S.[3]

Abstract. The space astrometry mission Gaia will construct a dense optical QSO-based celestial reference frame. For consistency between optical and radio positions, it will be important to align the Gaia frame and the International Celestial Reference Frame (ICRF) with the highest accuracy. Currently, it is found that only 10% of the ICRF sources (70 sources) are suitable to establish this link, either because they are not bright enough at optical wavelengths or because they have significant extended radio emission which precludes reaching the highest astrometric accuracy. In order to improve the situation, we have initiated a VLBI survey dedicated to finding additional suitable radio sources for aligning the two frames. The sample consists of about 450 sources, typically 20 times weaker than the current ICRF sources, which have been selected by cross-correlating optical and radio catalogues. This paper presents the observing strategy to detect, image, and measure accurate positions for these sources. It also provides results about the VLBI detectability of the sources, as derived from initial observations with the European VLBI Network in June and October 2007. Based on these observations, an excellent detection rate of 89% is found, which is very promising for the continuation of this project.

1 Context

The International Celestial Reference Frame (ICRF) is the realization at radio wavelengths of the International Celestial Reference System (ICRS; Arias et al. 1995), through Very Long Baseline Interferometry (VLBI) measurements of extragalactic radio source positions (Ma et al. 1998; Fey et al. 2004). It was adopted by the International Astronomical Union (IAU) as the fundamental celestial reference frame during the IAU 23^{rd} General Assembly at Kyoto, in 1997. The ICRF currently consists of a catalogue with the VLBI coordinates of 717 extragalactic radio sources (from which 212 are defining sources), with sub-milliarcsecond accuracy.

The European space astrometry mission Gaia, to be launched by 2011, will survey about (i) one billion stars in our Galaxy and throughout the Local Group, and (ii) 500 000 Quasi Stellar Objects (QSOs), down to an apparent optical magnitude V of 20 (Perryman et al. 2001). Optical positions with Gaia will be determined with an unprecedented accuracy, ranging from a few tens of microarcseconds (μas) at magnitude 15–18 to about 200 μas at magnitude 20. Unlike Hipparcos, Gaia will permit the realization of the extragalactic reference frame directly at optical bands, based on the QSOs that have the most accurate positions (i.e. those with $V \leq 18$ (Mignard 2003); it is expected to detect at least 10 000 of such QSOs (Mignard 2002)). A preliminary Gaia catalogue is expected to be available by 2015 with the final version released by 2020.

In the future, aligning the ICRF and the Gaia frame will be crucial for ensuring consistency between the measured radio and optical positions. This alignment, to be determined with the highest accuracy, requires several hundreds of common sources, with a uniform sky coverage and very accurate radio and optical positions. Obtaining such accurate positions implies that the link sources must have (i) an apparent optical magnitude V brighter than 18 (for the highest Gaia astrometric accuracy), and (ii) no extended VLBI structures (for the highest VLBI astrometric accuracy). In a previous study, we investigated the current status of this alignment based on the present list of ICRF sources (Bourda et al. 2008). We showed that although about 30% of the ICRF sources have an optical counterpart with $V \leq 18$, only one third of these are compact enough on VLBI

[1] Laboratoire d'Astrophysique de Bordeaux, Université de Bordeaux, CNRS UMR 5804, BP89, 33271 Floirac Cedex, France
[2] Max-Planck-Institute for Radio Astronomy, P.O. Box 2024, 53010 Bonn, Germany
[3] Jodrell Bank Observatory, The University of Manchester, Macclesfield, Cheshire, SK11 9DL, UK

scales for the highest astrometric accuracy. Overall only 10% of the current ICRF sources (70 sources) are available today for the alignment with the future Gaia frame. This highlights the need to identify additional suitable radio sources, which is the purpose of the project described here.

2 Strategy to identify new VLBI radio sources for the ICRF–Gaia alignment

Searching for additional radio sources suitable for aligning accurately the ICRF and the Gaia frame could rely on the VLBA Calibrator Survey (VCS; Petrov et al. 2008 and references therein), a catalogue of more than 3000 extragalactic radio sources observed with the VLBA (Very Long Baseline Array). This investigation is currently underway. Another possibility is to search for new VLBI sources, which implies going to weaker radio sources that have a flux density typically below 100 mJy. This can now be envisioned owing to the recent increase in the VLBI network sensitivity (i.e. recording now possible at 1Gb/s) and by using a network with big antennas like the EVN (European VLBI Network). A sample of about 450 radio sources that mostly have never been observed with VLBI (i.e. not part of the ICRF or VCS) has been selected for this purpose by cross-identifying the NRAO VLA Sky Survey (NVSS; Condon et al. 1998), a deep radio survey (complete to the 2.5 mJy level) that covers the entire sky north of $-40°$, with the Véron-Cetty & Véron (2006) optical catalogue of QSOs. This sample is based on the following criteria: $V \leq 18$ (for an accurate position with Gaia), $\delta \geq -10°$ (for possible observing with northern VLBI arrays), and NVSS flux density ≥ 20 mJy (for possible VLBI detection). The observing strategy to identify the appropriate link sources in the sample includes three successive steps: (1) to determine the VLBI detectability of these weak radio sources, mostly not observed before with VLBI; (2) to image the sources detected in the previous step, in order to reveal their VLBI structure; and (3) to determine an accurate astrometric position for the most point–like sources of the sample.

3 VLBI results

Initial VLBI observations for this project were carried out in June and October 2007 (during two 48–hours experiments), with a network of 4 or 5 VLBI antennas from the EVN. The purpose of these two experiments was to determine the VLBI detectability of the 447 weak radio sources in our sample based on snapshot observations. Our results indicate excellent detection rates of 97% at X band and 89% at S band. Overall, 398 sources were detected at both frequencies. The overall mean correlated flux densities were determined for each source and band by the mean over all scans and baselines detected. At X band, 432 sources were detected and the mean correlated fluxes range from 1 mJy to 190 mJy, with a median value of 26 mJy. At S band, 399 sources were detected and the mean correlated fluxes range from 8 mJy to 481 mJy, with a median value of 46 mJy. A comparison between the X-band flux density distribution for our sources, those from the VCS and the ICRF shows that the sources of our sample are indeed much weaker. On average, they are 27 times weaker than the ICRF sources and 8 times weaker than the VCS sources. The spectral index α ($S \propto \nu^{\alpha}$, S being the source flux density and ν the frequency) was determined for the 398 radio sources detected at both frequencies; the sources with a compact core are expected to have $\alpha > -0.5$. The median value of α in our sample is -0.34 and about 70% of the sources have $\alpha > -0.5$, hence indicating that they must have a dominating core component, which is very promising for the future stages of this project. The next step will be targeted at imaging the 398 sources that we have detected at both frequencies, by using the global VLBI network (EVN+VLBA), in order to identify the most point–like sources and therefore the most suitable ones for the ICRF–Gaia link.

References

Arias, E. F., Charlot, P., Feissel, M., & Lestrade, J.-F. 1995, A&A, 303, 604

Bourda, G., Charlot, P., & Le Campion, J.-F. 2008, A&A (in press)

Condon, J. J., Cotton, W. D., Greisen, E. W., Yin, Q. F., Perley, R., et al. 1998, AJ, 115, 1693

Fey, A. L., Ma, C., Arias, E. F., Charlot, P., Feissel-Vernier, M., et al. 2004, AJ, 127, 3587

Ma, C., Arias, E. F., Eubanks, T. M., Fey, A. L., Gontier, A.-M., et al. 1998, AJ, 116, 516

Mignard, F. 2002, In: Gaia: A European space project, O. Bienaymé & C. Turon (eds.), EAS Publications series, 2, 327

Mignard, F. 2003, In: IAU XXV, Joint Discussion 16, R. Gaume, D. McCarthy & J. Souchay (eds.), 133

Perryman, M. A. C., de Boer, K. S., Gilmore, G., Hog, E., Lattanzi, M. G., et al. 2001, A&A, 369, 339

Petrov, L., Kovalev, Y., Fomalont, E., & Gordon, D. 2005, AJ, 129, 1163

Véron-Cetty, M.-P., & Véron, P. 2006, A&A, 455, 773

SF2A 2008
C. Charbonnel, F. Combes and R. Samadi (eds)

THE FUTURE OF OPTICAL REFERENCE SYSTEMS

Charlot, P.[1]

Abstract. Optical reference frames have been traditionally limited in astrometric accuracy compared to radio reference frames which have long reached a sub-milliarcsecond accuracy. The next decade holds promises for big changes in this area with the launch of the Gaia space astrometric mission which unlike Hipparcos will be able to observe several hundred thousands of extragalactic objects with an astrometric accuracy of a few tens of microarcseconds. After reviewing the current status of optical and radio reference frames, this paper draws prospects for building the Gaia optical frame and its alignment with the current International Celestial Reference Frame (ICRF) which is based on radio-interferometric measurements.

1 Introduction

The extragalactic reference system is defined based on the positions of active galactic nuclei (AGN), a class of objects located at the center of distant active galaxies and characterized by extremely compact and bright emission on milliarcsecond (mas) scales. These sources show various observational properties over the whole electromagnetic spectrum, ranging from radio to γ-ray energies, most of which are explained by unified theories of active galactic nuclei. According to the standard representation (Urry & Padovani 1995), illustrated in Fig. 1a, the key elements of a radio-loud active galactic nucleus are a central supermassive black hole, an accretion disk, a broad-line region (fast-moving gas clouds) surrounded by a dusty torus region, an extended narrow-line region (slow-moving gas clouds), and a pair of relativistically out-flowing jets emitting synchrotron radiation which originate within a few tens of Schwarzschild radii from the black hole.

The inner compact radio structure (usually called the source core) detected by Very Long Baseline Interferometry (VLBI) arrays, originates at the base of the jet where the optical depth is approximately unity. Orientation has a major influence on the observed AGN properties since relativistic beaming strongly amplifies kinematics and brightness for jets that are pointed towards us while it attenuates these for jets that are pointed away from us. As a result, most sources show a one-sided morphology with a dominant core component on VLBI scales (Figs. 1b & c) due to sensitivity limitations and selection effects. The most suitable sources for defining a celestial reference frame are those that are the most compact on these scales. Due to their cosmological distances, such extragalactic sources show no transverse motion and therefore define a quasi-inertial system in a kinematical way, i.e. the system is non-rotating with respect to a local inertial frame.

2 The current IAU fundamental frame

The official IAU reference frame in use since 1 January 1998 is the International Celestial Reference Frame (ICRF), which is currently based on the VLBI positions of 717 extragalactic radio sources (Fig. 2). Of these, 608 sources are from the original ICRF (Ma et al. 1998), built from geodetic/astrometric VLBI data obtained between 1979 and 1995. The ICRF source categorization comprised 212 well-observed *defining* sources (which served to orient the axes of the frame), 294 less-observed *candidate* sources, and 102 *other* sources showing coordinate instabilities. The accuracy in the individual ICRF source positions has a floor of 250 microarcseconds (μas), while the axes of the frame are stable to about 20 μas in orientation (Fig. 2). Since then the position of the non-defining sources has been improved and the frame has been extended by 109 *new* sources in ICRF-Ext.1 and ICRF-Ext.2 using additional data acquired in the period 1995–2002 (Fey et al. 2004a).

[1] Laboratoire d'Astrophysique de Bordeaux, Université de Bordeaux, CNRS, 2 rue de l'Observatoire, BP 89, 33271 Floirac Cedex, France

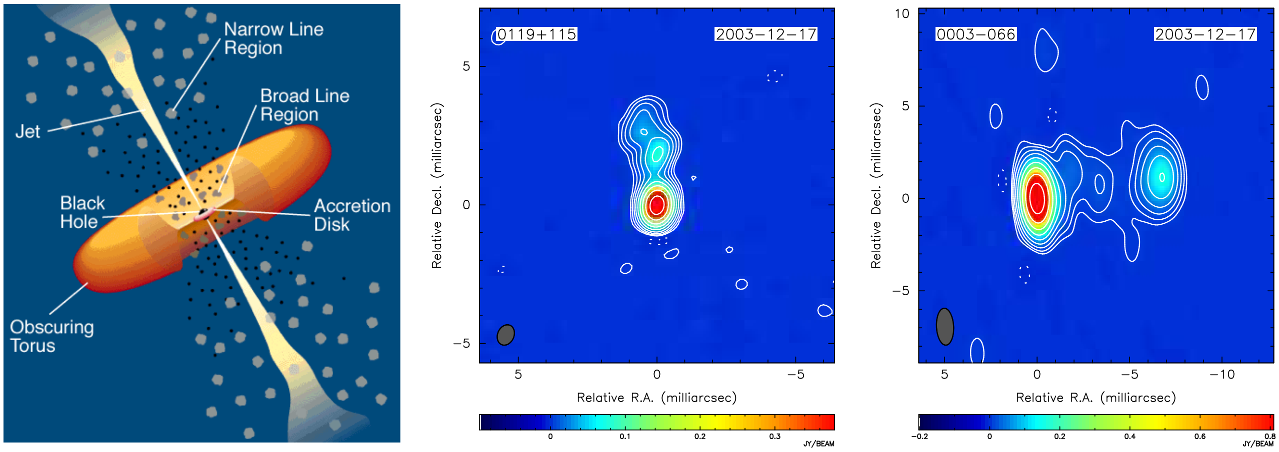

Fig. 1. *Left panel:* Schematic view of the key elements of an active galactic nucleus (credit: C. M. Urry & P. Padovani). *Middle/right panels:* VLBI images at 8.6 GHz for two ICRF sources (0003−066 and 0119+215) observed on 2003/12/17.

Continued VLBI observation of the ICRF sources is essential to maintain the viability and integrity of the frame on the long term because the intensity and VLBI morphology of extragalactic objects evolve in impredictable ways. Densification of the frame through the identification and observation of new high-quality sources is equally important to facilitate routine differential phase-referenced astrometry, e.g. for spacecraft navigation, and to control any local deformations of the frame which might be caused by tropospheric propagation effects or apparent source motions due to variable intrinsic VLBI structure. The VLBA Calibrator Survey (VCS) provides single-epoch VLBI images and astrometric positions at the milliarcsecond level for approximately 3500 additional sources (Petrov et al. 2008 and references therein). This survey forms the basis for the ICRF densification north of $-45°$ declination. Increasing the density of sources further south has been more difficult because of the limited number of VLBI antennas in the southern hemisphere. Dedicated programs have now been initiated (Fey et al. 2004b, 2006), which should improve the situation, but progress is slower than for the northern sky.

At the IAU XXVI$^{\text{th}}$ General Assembly in Prague (August 2006), the community decided to engage in the realization of the successor of the ICRF, to be presented at the next IAU General Assembly in 2009. The motivation for generating this new celestial frame is to benefit from recent improvements in VLBI modeling (e.g. for the troposphere) and to take advantage of the wealth of VLBI data that have been acquired since the time the ICRF was built. A specific issue to be addressed is whether and how to incorporate the VCS sources in this new realization. Another major issue is the revision of the source categorization, in particular the choice of the defining sources. Such a revision is necessary because some of the original ICRF defining sources were found to have extended structures (Fey & Charlot 2000) or position instabilities (e.g. MacMillan 2006), and are therefore improper for defining the celestial frame with the highest accuracy.

3 Towards the Gaia optical frame

The most comprehensive optical catalog available to date is the Large Quasar Astrometric Catalog (LQAC) recently compiled by Souchay et al. (2008). This catalog comprises 113666 objects, an increase of 25% compared to the previous compilation by Véron-Cetty & Véron (2006) which reported only about 85000 objects. The construction of the LQAC was guided by the aim of reporting the most accurate position for every identified quasar, as available through 11 major optical catalogs from which the LQAC was derived. Among these, the largest contributing catalog was the DR5 release of the Sloan Digital Sky Survey which comprises about 75000 quasars (Schneider et al. 2007). In addition to source position estimates, the LQAC also provides redshift and photometric information when available as well as estimates of absolute magnitudes. It is anticipated that the LQAC will be updated on an annual basis by adding newly-discovered quasars with the goal of obtaining the most complete and the most precise optical catalog of quasars by the time Gaia is launched in 2011.

The Gaia space astrometric mission will survey all stars and quasars down to an apparent magnitude of 20 (Perryman 2002). Position accuracies will range from a few tens of microarcseconds at magnitude 15–18 to about 200 μas at magnitude 20. Based on current estimates from local surveys, it is expected that 500 000 such

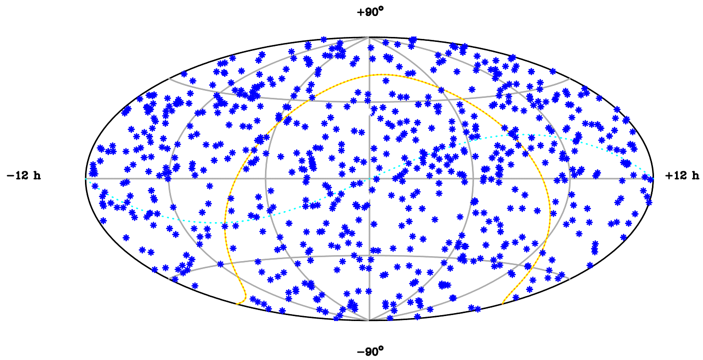

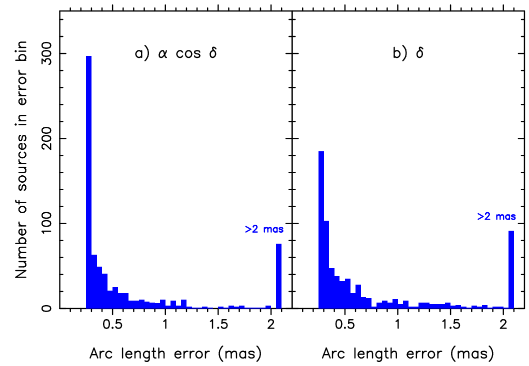

Fig. 2. *Left panel:* Distribution of the current 717 ICRF sources on an Aitoff equal-area projection of the celestial sphere. *Right panel:* Histogram of source position errors in *(a)* right ascension and *(b)* declination.

quasars should be detected; unlike Hipparcos, Gaia will thus be able to construct a dense optical reference frame *directly* in the visible wavebands. Initial simulations showed that the residual spin of the Gaia reference frame could be determined to 0.5 μas/yr with a *clean sample* of 10 000 defining sources (Mignard 2002). In practice, the ultimate accuracy of the frame may be limited by random instability of the sources which may show extended and variable structure on these spatial scales, similar to that observed at radio wavelengths (Fey & Charlot 2000). Despite this limitation, the Gaia reference frame should surpass the current ICRF, both in accuracy and in source density. Hence, it is likely that the realization of the fundamental celestial frame will be brought back to visible wavebands in about 10 years when the Gaia catalog is published, although the VLBI reference frame should remain for specific applications such as the monitoring of the Earth's rotation.

4 Issues in realizing the Gaia frame

Prior to acquiring data, simulations will be essential in order to determine how to best use the thousands of quasars that will be detected by Gaia for realizing the celestial frame. In particular, it will important to study the impact of the lack of sources in the galactic plane and more generally the effect of the distribution of the sources on the quality of the frame. Another important parameter to decide on is the magnitude limit of the sources to consider for inclusion in the clean sample that will define the Gaia frame. Should this magnitude be strictly limited to a value of 18 as originally anticipated (Mignard 2002) or should this criterion be relaxed in order include more sources at the expense of coordinate accuracy? In this respect, the actual magnitude distribution in the LQAC should be quite useful to determine the best compromise between having more sources of lesser astrometric quality or less sources of higher astrometric quality. One should also note that these objects may vary in magnitude, especially the blazar-type objects (a class of objects with jets oriented close to the line of sight) which can show changes of several magnitudes over short time scales (see Fig. 2b). Such variability needs to be investigated as it may affect the choice of the Gaia-defining sources and the quality of the frame.

During the construction process for the Gaia frame, an essential element will be its alignment with the current ICRF in order to maintain consistency with the International Celestial Reference System (Arias et al. 1995) when the transition from radio to optical wavelengths is made. Such alignement, to be obtained with the highest accuracy, requires a large number of sources common to the two frames. A study by Bourda et al. (2008a) revealed that only 10% of the current ICRF sources may be used for this purpose when considering the source magnitude and their VLBI position accuracy and compactness. This prompted the development of new VLBI observing program, targeted to weaker sources, in order to identify further high-quality sources for this alignment (Bourda et al. 2008b). Also to be investigated in this framework is the registration between the VLBI and Gaia positions since the spatial location of the radio and optical emission may differ due to opacities in the quasar jets. Kovalev et al. (2008) showed that on average the optical-radio *core shifts* in a sample of 29 ICRF objects are at the level of 100 μas, which is significant considering the expected accuracy of the Gaia catalog and that foreseen for the ICRF by 2015–2020. Such effects would thus have to be accounted for when aligning the two frames. On the other hand, the differences between the optical and radio positions may provide a direct measurement of such core shifts, which would be of high interest for probing AGN jet properties.

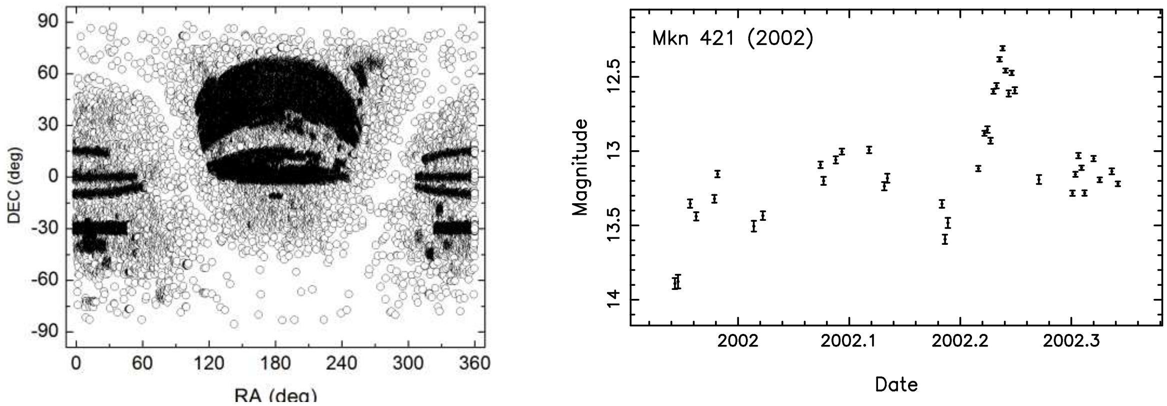

Fig. 3. *Left panel:* Distribution in equatorial coordinates of the 113666 quasars in the Large Quasar Astrometric Catalogue (reproduced from Souchay et al. 2008). *Right panel:* Optical variability of the BL Lac object Mkn 421 (corresponding to the ICRF source 1101+384) on scales of a few months in 2002.

5 Conclusion

The Gaia space astrometric mission will realize for the first time a highly-accurate extragalactic reference frame directly at optical wavelengths. This future frame will surpass the current radio-based ICRF both in accuracy (a few tens of microarcseconds in the individual source positions) and in the number of objects (500 000 sources). Simulations are necessary in order to determine the best strategy for constructing the frame (number of defining sources, sky distribution, magnitude limit) and assess the impact of limiting factors such as photometric variability. Particular attention should be paid to the alignment of the future Gaia frame with the current ICRF in order to maintain continuity in the International Celestial Reference System. Ultimately, comparisons of radio and optical positions may bring new insights into the physical properties of AGN jets.

References

Arias, E. F., Charlot, P., Feissel, M., & Lestrade, J.-F. 1995, A&A, 303, 604

Bourda, G., Charlot, P., & Le Campion, J.-F. 2008a, A&A, 490, 403

Bourda, G., Charlot, P., Porcas, R., & Garrington, S. T. 2008, in Proceedings of the Fifth International VLBI Service for Geodesy and Astrometry General Meeting, St. Petersburg, Russia, March 3–6, 2008 (in press)

Fey, A. L., & Charlot, P. 2000, ApJS, 128, 17

Fey, A. L., Ma, C., Arias, E. F., Charlot, P., Feissel-Vernier, M., Gontier, A.-M., Jacobs, C. S., Li, J., & MacMillan, D. S. 2004a, AJ, 127, 3587

Fey, A. L., Ojha, R., Jauncey, D. L., Johnston, K. J., Reynolds, J. E., Lovell, J., Tzioumis, A. K., Quick, J. F. H., Nicolson, G. D., Ellingsen, S. P., McCulloch, P. M., & Koyama, Y. 2004b, AJ, 127, 1791

Fey, A. L., Ojha, R., Quick, J. F. H., Nicolson, G. D., Lovell, J., Reynolds, J. E., Ellingsen, S. P., McCulloch, P. M., Johnston, K. J., Jauncey, D. L., & Tzioumis, A. K. 2006, AJ, 132, 1944

Kovalev, Y. Y., Lobanov, A. P., Pushkarev, A. B. & Zensus, J. A. 2008, A&A, 483, 759

Ma, C., Arias, E. F., Eubanks, T. M., Fey, A. L., Gontier, A.-M., Jacobs, C. S., Sovers, O. J., Archinal, B. A., & Charlot, P. 1998, AJ, 116, 516

MacMillan, D. S. 2006, in International VLBI Service for Geodesy and Astrometry 2006 General Meeting Proceedings, ed. D. Behrend & K. D. Baver, NASA/CP-2006-214140, 274

Mignard, F. 2002, in Gaia: A European Space Project, ed. O. Bienaymé & C. Turon, EAS Publ. Ser., 2, 327

Perryman, M. A. C., in Gaia: A European Space Project, ed. O. Bienaymé & C. Turon, EAS Publ. Ser., 2, 3

Petrov, L., Kovalev, Y. Y., Fomalont, E. B., & Gordon, D. 2008, AJ, 136, 580

Schneider, D. P., Hall, P. B., Richards, G. T. et al. 2007, AJ, 134, 102

Souchay, J., Andrei, A. H., Barache, et al. 2008, in Proceedings of the Fifth International VLBI Service for Geodesy and Astrometry General Meeting, St. Petersburg, Russia, March 3–6, 2008 (in press)

Urry, C. M, & Padovani, P. 1995, PASP, 107, 803

Véron-Cetty, M.-P., & Véron, P. 2006, A&A, 455, 773

SF2A 2008
C. Charbonnel, F. Combes and R. Samadi (eds)

RADIAL VELOCITY STANDARDS FOR THE GAIA-RVS

Crifo, F.[1], Jasniewicz, G.[2], Soubiran, C.[3], Veltz, L.[4], Hestroffer, D.[5], Katz, D.[1], Siebert, A.[6] and Udry, S.[7]

Abstract. The ESA GAIA mission (launch expected end 2011) , besides the 5 astrometric parameters and photometry for some 10^9 objects, will also produce radial velocities and short spectra for a few 10^8 stars, with a 1 to 15 km/s accuracy.

The calibration of radial velocities in the integral-field spectrograph will rely on a set of some 1000 bright RV-stable stars already observed with a much higher accuracy from the ground, on a few bright enough asteroids, and a set of some 10^5 stable stars selected later from the RVS measurements themselves. We present here a status report on the ongoing effort to construct the basic list with ground-based observations.

1 The RVS and the need for ground-based standards

The Radial Velocity Spectrometer (RVS) onboard GAIA is designed mainly for measuring radial velocities of the brightest GAIA targets. It is a slitless spectrograph, without onboard calibration device. It covers the spectral range (847 - 874) nm. The brightest stars ($V \leq 10$) will be observed with a resolution of 11500; and the fainter ones with a resolution of about 4000.

The RVS is a self-calibrating instrument relying on a set of about 1000 bright, stable objects with well-known RVs. This sample must be well-distributed over the sky to set the RV zero-point and is included in the iterative reduction process. As these objects will be regularly observed by GAIA (some 40 observations each, over the 5 years of mission), they will also allow a permanent check of the state and performances of the instrument.

2 Star selection

Bright asteroids and single stars with a good observational history are selected and re-observed before the start of the mission to insure a stability at the level of 300m/s until the end of mission (2017). Selection criteria for stars have been already given with some details (see Crifo et al, 2007) (HIP stars; $V \geq 6; G_{RVS} \leq 10$; F5-K; M dwarfs; not variable, not double or multiple; no disturbing neighbour in the selection window, i.e. within 80 arcsec; already well observed).

The stars are selected within the 3 following published lists: Nidever et al. (2002); Nordström et al. (2004; mostly CORAVEL data); Famaey et al. (2005; CORAVEL data). A provisional list of about 1400 stars is now defined, and used for the observations.

[1] GEPI (UMR 811 du CNRS; Université Paris 7), Observatoire de Paris, 92195 MEUDON Cedex, France
[2] UMR CNRS/UM2 GRAAL, CC 72, Université Montpellier2, 34095 MONTPELLIER Cedex 05, France
[3] Université Bordeaux 1, CNRS, LAB, F-33270 FLOIRAC, France
[4] Astrophysikalisches Institut Potsdam, POTSDAM, Germany
[5] IMCCE (UMR 8028 du CNRS),Observatoire de Paris, 77 av. Denfert-Rocherau, 75014 PARIS, France
[6] Observatoire de Strasbourg (Université Louis Pasteur et CNRS), 11 rue de l'Université, 67000 STRASBOURG, France
[7] Observatoire de Genève, 51 Ch. des Maillettes, 1290 SAUVERNY, Switzerland

3 On-going ground-based observations

Each candidate is re-observed at least once before launch to eliminate evident variables. Supplementary observations are made, depending on the observational history of the star, and for follow-up during the mission. The observing programme is running on the echelle spectrographs SOPHIE (OHP), NARVAL (TBL, Pic du Midi), and CORALIE (Swiss Euler telescope, La Silla), for a total of about 9 nights per semester. The observations started in 2006. The new data are stored in an on-purpose database, presently hosted at AIP-Potsdam.

NARVAL is the only spectrograph covering totally the RVS spectral interval, and these spectra will therefore also be used for comparing the velocities obtained either over the full spectral range, or only over the RVS range.

Figure 1 shows for asteroids the difference (O-C) between data and calculated predictions, as a function of the S/N ratio during the observation, for SOPHIE and previous ELODIE. Figure 2 shows for stars the comparison between the Sophie data and and previous data as published by Famaey (Coravel), Nordström (Coravel) or Nidever: the larger dispersion for Famaey and Nordström is due to lower Coravel accuracy.

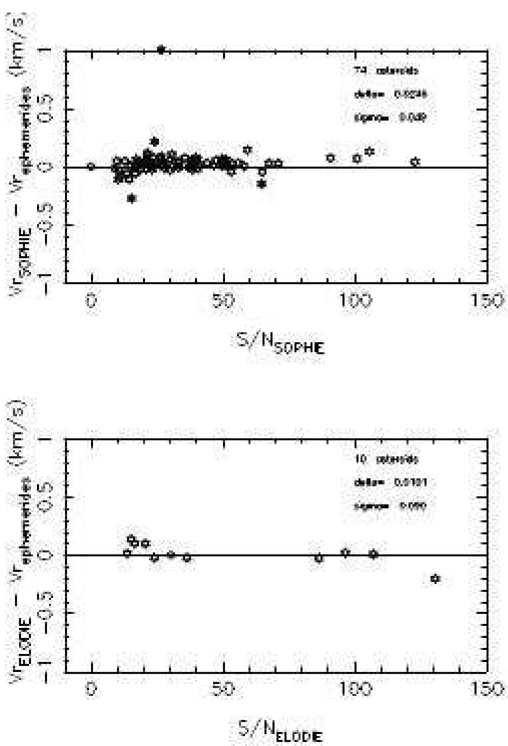

Fig. 1. Asteroids: O-C vs S/N, Sophie & Elodie

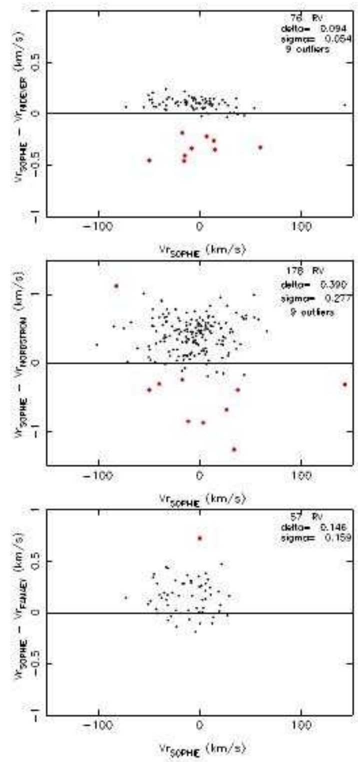

Fig. 2. Stars: Sophie vs Nidever, Nordström and Famaey

4 Conclusion

Good RV standards for the RVS, stable over a long period, must be used to control the accuracy of the RVS instrument zero point. Such a sample can be defined using bright, well-known stars and asteroids, and an important observational effort is underway to verify the stability of about 1000 such objects over the full sky.

References

Crifo, F., Jasniewicz, G., Soubiran, C., Hestroffer, D., Siebert, A., Guerrier, A., Katz, D., Thévenin, F., & Turon, C. 2007, 2007sf2a.conf..459C

Famaey, B., Jorissen, A., Luri, X., et al. 2005, A&A, 430, 165

Nidever, D. L., Marcy, G. W., Butler, R.P., et al. 2002, ApJS, 141, 503

Nordström, B., Mayor, M., Andersen, J., et al. 2004, A&A, 418, 989

SF2A 2008
C. Charbonnel, F. Combes and R. Samadi (eds)

THE THIN AND THICK GALACTIC DISKS: MIGRATION AND LINEAGE

Haywood M.[1]

Abstract. Our understanding of the local constraints of the chemical evolution of the Galaxy have significantly changed in the recent years. This includes new results on the link between the two disks and on the two main constraints of galactic chemical evolution - the distribution of metallicities and the age-metallicity relation - and their new interpretation when radial migration of stars is properly taken into account. I discuss most recent advances on these three points.

It is argued that the so-called G dwarf problem cannot constrain infall because, starting with an initial metallicity of -0.2 dex, the thin disk could not have formed stars with 1/3 of solar abundance. Given this initial metal content, the problem is not to explain why there are so few metal-poor stars, but more likely to explain why there are so few metal-rich ones, for which infall could bring a correct answer. As a consequence of the conclusive link that relates the thin and thick disks, the picture that emerge is that the thick disk appears to have been the main episode of chemical enrichment in the Galaxy. The Gaia perspective is evoked.

1 Introduction

Our understanding of local constraints (within 100 pc of the Sun) of the chemical evolution of the Galaxy have significantly changed in the recent years. This is due to both new accurate spectroscopic data and from the in depth analysis of the Hipparcos catalogue and complementary data (Nordström et al., 2004), giving access to the full 3D space velocities of solar neighbourhood stars. Several recent studies (Haywood (2008), Roškar et al. (2008), Schoenrich & Binney (2008)) have pointed out the importance of analysing both kinematic and chemical data in order to interpret key features, leading to a new understanding to the main constraints of the disk galactic chemical evolution. This includes new results on the link between the two disks, and the two main constraints of galactic chemical evolution, the age-metallicity relation and the distribution of metallicities. I review most recent advances on these three subjects.

2 Linking the thick and thin disks

2.1 Radial migration & the homogeneity of chemical species in the disk

Empirical evidences that radial mixing is effective have been found in solar neighbourhood data (Haywood, 2008). The study of the metallicity and orbital characteristics of thin disk stars sampled locally shows that the low and high metallicity tails of the thin disk are populated by objects which origins are in the outer and inner disk, and brought to the solar radius by radial migration. One possible mechanism giving rise to this mixing has been identified in Sellwood & Binney (2002), and its impact on the local kinematics and chemistry has been studied thoroughly by Schoenrich & Binney (2008). Signatures of this mixing is detected on the kinematic and orbital behaviour of thin disk stars, which show systematic trends as a function of metallicity. Metal-poor stars of the thin disk have guiding centres larger than the mean of solar neighbourhood stars (Fig. 1b), corresponding to a V space velocity systematically higher than the LSR (Fig. 1a). Metal-rich stars have a symmetrical behaviour (Fig. 1c). This is best interpreted as corresponding to the inward and outward shift of stars that migrate from the outer and inner disk.

[1] GEPI, Observatoire de Paris, F-92195 Meudon Cedex,France

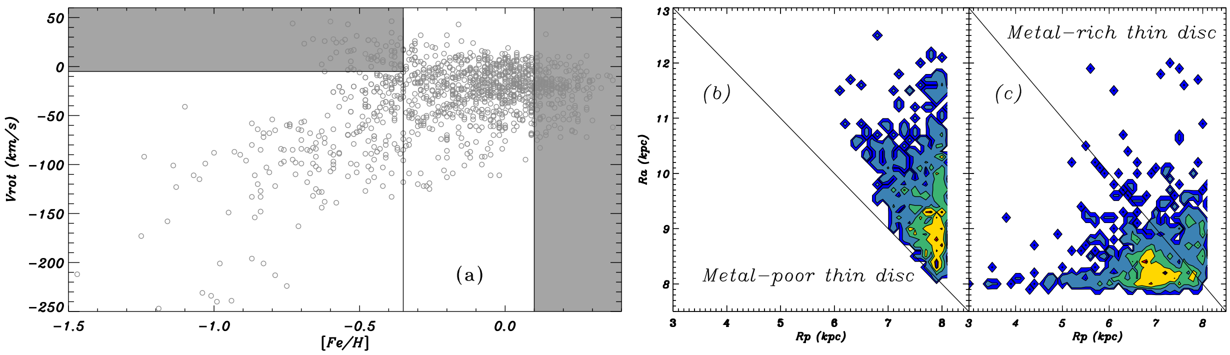

Fig. 1. (a) V_{rot}-[Fe/H] plot for a sample of stars with accurate metallicities. (b) and (c) are the density distribution in the (pericentre, apocentre) space for stars as selected by the 2 boxes of plot (a) in the GCS catalogue.

Evidences are now accumulating that chemical evolution proceeds essentially from homogeneous ISM at all times in the disk, as testified by meteoritic presolar grains (Nittler, 2005), spectroscopic measurements through the ISM (Cartledge et al. 2006), and abundance ratios. Allowing for the effect of radial mixing as being responsible for most of the dispersion measured on stellar metallicities, implies that thin disk stars born at the solar galactocentric radius have a rather restricted range of metallicites - within [-0.2 to +0.2] dex.

It means that although the ISM is well mixed at a given radius, giving rise to similar relative abundance ratios of chemical species at all radii, the absolute level of enrichment (the metallicity) is mainly a function of galactic radius, much less a function of time. Radial migration of stars gave rise to some mixing in the disk, and thereby increased the dispersion in metallicity, while the relative ratios, being a slow function of metallicity, have remained relatively homogeneous. Together with the small age-dependence of the metallicity at the solar neighbourhood, the widening of the metallicity interval due to radial mixing and present measurements of the radial metallicity gradient suggest that the radial variation of metallicity is 3 to 4 times more important than its local temporal evolution.

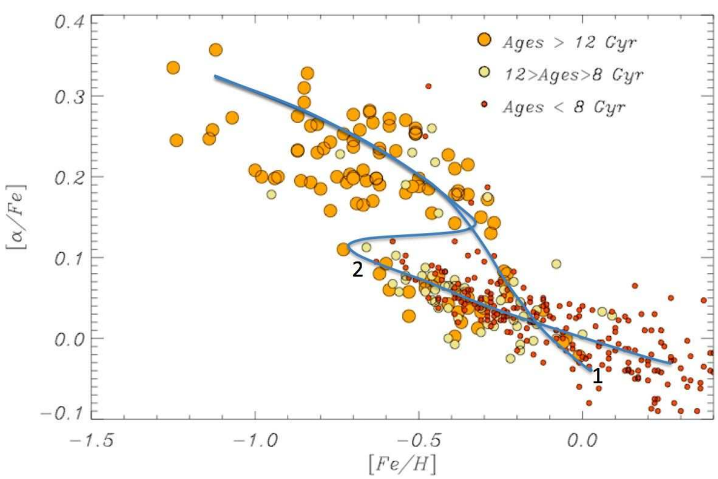

Fig. 2. Linking the thick and thin disks through α-element abundances. It has been suggested that the hiatus in metallicity could have resulted from an infall episode of gas that would have diluted metals in the ISM at the end of the thick disk formation (2). Orbital parameters of solar neighbourhood stars suggest on the contrary that the thin disk outside the metallicity interval [-0.2, +0.2] dex are objects brought to the solar radius by radial migration. It suggests that the local thin disk at solar metallicities could be the continuation and the end point of a sequence (1) starting near [Fe/H]=-1.2 dex, or lower. Samples from Reddy et al., 2003, 2006 and Gilli et al. (2006)

2.2 The parenthood between the two disks

The accurate abundance patterns now available on local stars give the best indication so far of a continuity, or parenthood, between the thin and thick disks. The hiatus in metallicity (see Fig. 2) between thick disk stars (at [Fe/H]=-0.2 dex, [α/Fe]=0.18 dex) and thin disk stars (at [Fe/H]=-0.7 dex, [α/Fe]=0.1 dex) interpreted as the signature of an infall episode in standard chemical evolution (curve (2) on Fig. 2) is in fact best understood by taking into account the kinematic behaviour of the stars. The thin disk metal-poor stars, responsible for the hiatus, have a mean rotational component and a corresponding guiding centre greater than the mean disk population (Haywood, 2008). This is best interpreted has testifying the outer disk origin of these stars (Haywood, 2008b, Schoenrich & Binney, 2008). If this interpretation is correct, these stars are outliers to the local thin disk chemical evolution, and the hiatus is not resulting from the local chemical evolution, but is a consequence of the radial redistribution of stars in the disk due to migration. The local evolution can then be seen to proceed continuously from high [α/Fe] and low metallicities to low [α/Fe] and solar metallicities (curve 1 on Fig. 2). In the ([α/Fe],[Fe/H]) plane, the thick disk seem to develop a sequence, while stars endemic of the thin disk at solar galactocentric radius are almost restricted a point (nearly centred on the sun), at the end of, but possibly separated from, the thick disk sequence.

2.3 Inconsistencies in the description of the thick disk

Chemical data of stars kinematically labeled as thick disk in the solar vicinity seem to confirm a high degree of homogeneity, as is apparent in different studies (see in particular Fuhrmann 2008, Nissen & Schuster 2008), pointing to a well-defined population. What poses a problem however is its kinematic definition. Fig. 3 shows an histogram of V space velocity values from the work of Soubiran & Girard (2005). Stars flagged as thick disk members according to probability membership based on mean kinematic properties are given as the smaller histogram. One of these properties is the rotational lag, which in the case of the thick disk is standardly assumed to be 40-50 km/s. The plot shows that the thick disk selected in Soubiran & Girard (2005) is more likely to rotate with a mean lag of 80 km/s. Similar values are found on all kinematically defined thick disk samples from solar neighbourhood stars. Notice that this is near to the value found by Arifyanto & Fuchs (2006), making it unclear if thick disk parameters are polluted by an unknown stream or if Arifyanto & Fuchs (2006) have been pointing to the 'correct' thick disk. More generally, it must be clarified how the several streams that have been found on solar neighbourhood stars (Helmi et al. (2006), Arifyanto & Fuchs (2006)) are linked to the thick disk or even if they could be part of the thick disk.

The thick disk age in the solar neighbourhood is not better known. For example, Bernkopf & Fuhrmann (2006) advocates that the thick disk stars form a coeval population formed in a single burst of star formation 12 Gyrs. Enlarged samples however seems to indicate a substantial evolution, as demonstrated in Bensby et al. (2004), Haywood (2006) and below. Obviously this point needs to be clarified, and echoes the more general challenge of identifying stars that truly make up this population.

3 Age-metallicity relations in the thick and thin disks

3.1 How to correlate age and metallicity: biases in action

Depending on the selection that is made to choose local stars, samples will include various amount of migrants from the outer or inner disk, or stars of the thick disk, and will therefore represent the local evolution accordingly. This is illustrated in Fig. 4, which shows the sample of Edvardsson et al. (1993) overplotted on our age-metallicity distribution from Haywood (2008). The sample of Edvardsson et al. (1993) was designed to be representative of the range of local metallicities, but has been often used to estimate the age-metallicity relation. The ages of the two samples were derived using the same procedure described in Haywood (2008). The sample of Edvardsson et al. is known to have provided the basis for claims of a real correlation between age and metallicity (Pont & Eyer, 2004). The age-metallicity relation evidenced in these studies stems from three different effects. The first one is the inclusion of thick disk objects. Non-differentiating the thick and thin disk stretches the relation across the two populations (down to -0.8 dex) and artificially creates a correlation that is mostly nonexistent within the thin disk. The inclusion of thin disk stars without taking account their radial origin also extends the metallicity range outside its normal interval by including metal-poor stars from

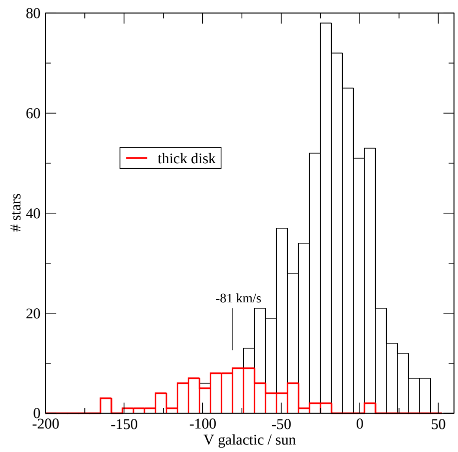

Fig. 3. Histogram of velocities in the direction of galactic rotation for the sample of Soubiran & Girard (2005). The histogram with mean at -81 km/s is representing stars flagged as thick disk using kinematic membership probability in their catalogue.

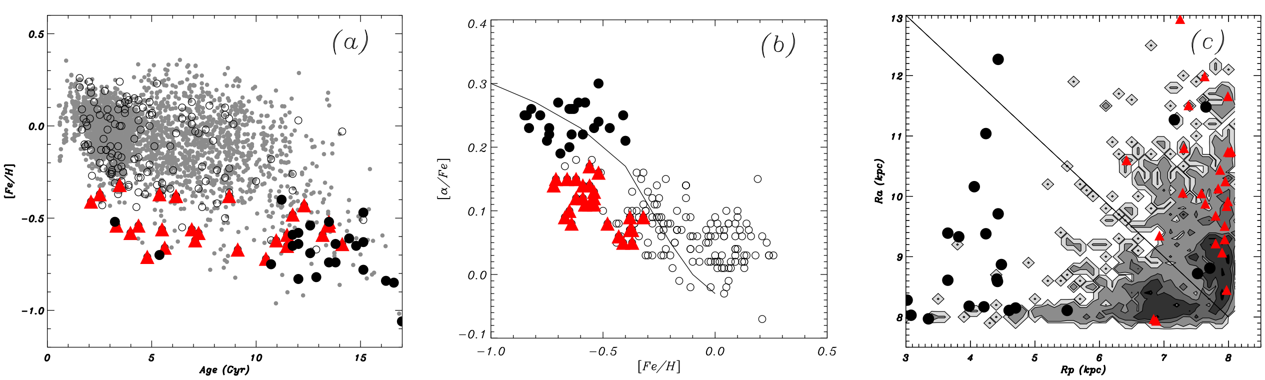

Fig. 4. (a) Stars from Edvardsson et al. (1993), overlayed to our age-metallicity distribution (small grey dots). Triangles are thin disk stars with V>-5 km/s, [Fe/H]<-0.3 dex and [α/Fe]<0.18 dex. Large black dots are thick disk object with the condition that [α/Fe]>0.18 dex. The age-metallicity distribution of the sample of Edvardsson et al. (1993) is heavily weighted towards metal-poor stars, due to the fact that it is biased against old solar metallicity or metal-rich stars, and contains both thin disk stars from the outer disk and thick disk objects, which have not contributed to the thin disk local evolution. The apparent correlation between age and metallicity that has been obtained from this sample (Pont & Eyer, 2004) is essentially due to the combination of these 3 effects. (b) Position of these two groups in the ([α/Fe],[Fe/H]) diagram, and on the (Rp, Ra) distribution.

the outer disk. Finally, Edvardsson et al. (1993) acknowledge that their selection excluded old metal-rich star, also contributing to enhance the correlation.

3.2 The thick disk as the main episode of galactic chemical enrichment

Figure 5 illustrates the different pace at which metal enrichment occurred in the galactic thin and thick disks. Metallicity has changed by about 0.3 dex in 8-10 Gyrs in the thin disk, or a factor of 2 of increase in Z. This is to compare with a factor 10 increase in 3-4 Gyr in the thick disk, and implies that most chemical enrichment in the solar neighbourhood have preceded the thin disk. Evidences are becoming more acute for a thick disk playing a central role in the building of the Milky Way. Most recently, Nissen & Schuster (2008) presented new data on solar vicinity stars at lower metallicities ([Fe/H]<-0.6 dex), showing that two distinct components (accreted and dissipative) that make up the halo. One is clearly the continuity of the thick disk at lower metallicities, possibly making a single dissipative component of the Galaxy, the other shows distinct lower abundances of α elements with a pattern that resembles closely the one observed on dwarf spheroidals. On the contrary, if stars of the thick disk are of external origin, we are left with a gap of about 1.2 dex between the metallicity of the halo and that of the old thin disk. It would also imply that the Milky Way would have been relatively exceptional in the sense of having negligible star formation activity for several Gyrs when the universe was having its most intense phase of star formation.

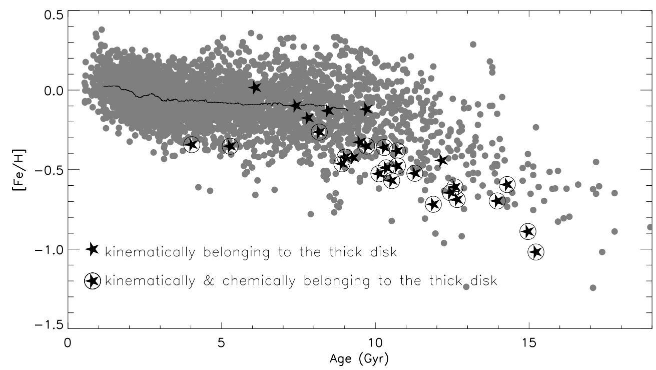

Fig. 5. Age-metallicity distribution for stars in the solar vicinity. Continuous curve is the mean metallicity of thin disk stars as a function of age. Star symbols are objects kinematically known has belonging to the thick disk (see Haywood (2006)). Symbols within circles have the additional condition that [α/Fe]>0.18 dex. The age of these objects has been derived taking into account their α-element content, which explains why they have systematically lower ages than stars of the same metallicities.

4 The new 'G dwarf problem', or the lack of metal-rich stars born at solar galactocentric radius

Contrary to what is stated in Prantzos (2008), Haywood (2006) didn't argue that the solar neigbourhood behaved like a closed box, but that its metallicity distribution, if the thick disk contribution is taken into account, is similar to a close box distribution. It does only imply that the argument that infall-must-have-occurred-because-the-MDF-is-not-closed-box is fake, but does not imply that infall did not occur. Given the difficulties that classical modelling have to go beyond the unfruitful dilemma infall *vs* closed-box model, it is encouraging that new models (Brook et al. (2007), Schoenrich & Binney (2008), Roškar et al (2008)) combining dynamical and chemical evolution have had more success to account for local distributions as resulting from a mix of both kind of processes.

How does radial mixing affects the local metallicity distribution ? Radial mixing has the effect of enlarging the range of observed metallicities at the solar radius, amounting to an approximate 10% of the stars, either metal-poor or metal-rich. As mentioned above, stars that are truly endemic of the solar galactocentric radius, have a range of metallicities of -0.2 <[Fe/H]< 0.2 dex in the thin disk, while the thick disk have [Fe/H]<-0.2 dex. How does it impact on the interpretation of the local metallicity distribution ? The 'G-dwarf' problem, in its classical form, concerns the lack of stars with 1/3 of metals of the peak population (which is at [Fe/H]$\approx$0), or [Fe/H]$\approx$-0.45 dex. Clearly, *there are no such stars stemming from the local evolution (at solar galactocentric radius) in the thin disk*, because at this metallicity, stars all reside in the thick disk. Since the metallicity was already -0.2 dex at the end of the thick disk phase, there is no point questioning why the thin disk has not formed stars more metal-poor than this limit, and there is no *metal-poor* G-dwarf problem in the thin disk, while there may be one in the thick disk. Unfortunately, there is no statistically meaningful sample of thick disk stars in the solar vicinity to test this prediction.

In 1974 B. Tinsley already pointed out the problem posed by the slow enrichment rate in the galactic thin disk: "Although disk-population stars of all ages have considerable dispersion in Z, the mean value is only a very slowly increasing function of birth epoch". Considering an initial gas disk with surface density at the solar galactocentric radius of 40 $M_{\odot}.pc^{-2}$, mean initial metallicity -0.2 dex, mean star formation rate $4M_{\odot}.pc^{-2}.Gyr^{-1}$, yield 2% and return gas fraction of 30%, it is expected that the present metallicity in the disk at the solar radius, would be about +0.5 dex, when at most 0.2 dex is observed. Arguably all these quantities are very uncertain, but still, there may be a 'G-dwarf metal-rich problem', to which infall would be solution, as already noted by Tinsley. In other words, infall is not necessary to explain the absence of metal-poor dwarfs in the thin disk, but may be required to explain why so few metal rich stars have formed at the solar radius.

5 Gaia prospect

The vast majority of the stars Gaia will observe are disk stars. Accurate age determinations should be achievable within 2 kpc for a typical G type main sequence star and 3 kpc for an old subgiant. The age-scale itself should also benefit from a drastic improvement in stellar physics that are expected from the availability of numerous fine calibrators that will map the entirety of the HR diagram, both from Gaia itself and present or forthcoming asteroseismology studies and complementary data. It is therefore expected that several millions of stars with accurate age determination will be available for the kind of studies that are achievable today only on a few hundreds of objects in the solar vicinity (within 50-100 pc). It implies that, complemented with high resolution, high SN spectroscopic data, a detailed map of the interface between the thick and thin disc populations should be obtainable, not only in the solar neighbourhood but also radially on several kpc. Moreover, the continuity that is lacking between local and in situ samples of the thick disk should help to characterize the properties of this population. Concerning the thin disk, particularly important will be the availability of radially distributed samples to understand the intricacy of chemical and dynamical processes as outlined here. Realistic simulations of the thin disk evolution including radial redistribution of stars and gas are just coming out in recent studies (see Roškar et al. 2008, Schoenrich & Binney 2008), and give us insights of what this complexity could be.

References

Arifyanto M. I. & Fuchs B., 2006, A&A, 449, 533
Bensby T., Feltzing S., Lundström I., 2004, A&A, 421, 969
Bernkopf, J. & Fuhrmann, K., 2006, MNRAS 369, 673
Brook, C. et al., 2007, ApJ 658, 60
Cartledge et al., 2006,641, 327
Edvardsson B., et al., 1993, A&A, 275, 101
Fuhrmann K., 2008, MNRAS 384, 174
Gilli, G., et al, A&A 449, 723
Haywood, M., 2006, MNRAS, 371, 1760
Haywood, M., 2008, MNRAS 388, 1175
Helmi, A. et al., 2006, MNRAS 365, 1309
Nissen, P.E. & Schuster, W.J., 2008, astro-ph, 0807.3831
Nordström B., Mayor, M., Andersen, J., et al., 2004, A&A, 418, 989
Nittler, L. R., 2005, ApJ 618, 281
Pont F., Eyer L., 2004, MNRAS, 351, 487
Prantzos, N., 2008, astro-ph 0809.2507
Reddy B. E., Tomkin J., Lambert D. L., Allende Prieto C., 2003, MNRAS, 340, 304
Reddy B. E., Lambert D. L., Allende Prieto C., 2006, MNRAS, 367, 1329
Roškar, R. et al., 2008, ApJ 684, 79
Schoenrich, R. & Binney, J., 2008, astro-ph
Sellwood J. A. & Binney J. J., 2002, MNRAS, 336, 785
Soubiran C. & Girard P., 2005, A&A, 438, 139
Tinsley B. M., 1974, ApJ, 192, 629

SF2A 2008
C. Charbonnel, F. Combes and R. Samadi (eds)

GROUND-BASED OBSERVATIONS OF SOLAR SYSTEM BODIES IN COMPLEMENT TO GAIA.

Hestroffer, D.[1], Thuillot, W.[1], Mouret, S.[1,2], Colas, F.[1], Tanga, P.[3], Mignard, F.[3], Delbò, M.[3] and Carry, B.[4]

Abstract. The ESA cornerstone mission Gaia, to be launched during end-2011, will observe $\approx 250,000$ small bodies. These are mostly main belt asteroids, but also Near-Earth objects, Trojans, and a few comets, or planetary satellites. The scientific harvest that Gaia will provide – given the high astrometric accuracy (at sub-milli-arcsec level), valuable photometric measurements (at milli-mag level), and moderate imaging (about 2,000 objects will be resolved) – will have a major impact on our knowledge of this population in terms of composition, formation and evolution (Mignard et al. 2007). There are nevertheless some intrinsic limitations in particular due to the unavoidable limited duration of the mission (5 years), the peculiar observing strategy that is not optimised to the observation of solar system objects, and last, the limited imaging possibilities. We can thus identify two kind of complementary data and ground-based observations, whether they are part of the Gaia Data Processing and Analysis Consortium (DPAC), or not, but provide a strong leverage to the Gaia science.

We discuss different aspects of additional observations from ground (yet not exclusively) either in preparation to the Gaia mission, in alert during the mission, or after the mission as additional complementary information. Observations of a set of well defined and selected targets, with different telescopes and instrumentation, will increase the scientific output in three particular and important topics: mass of asteroids, their bulk density and possible link to their taxonomy, and non-gravitational forces.

1 Gaia an ESA cornerstone astrometric mission

Gaia is the next space mission from the European Space Agency dedicated to astrometry. It is much more ambitious compared to its precursor Hipparcos, considering either the number of targets, the astrometric and photometric precision reached, or last the potential scientific outputs. For instance Gaia will enable the determination of asteroids taxonomy, spin state, and – for a smaller set – sizes, and masses. Nevertheless, the limiting magnitude and scanning law as well as the modest imaging resolution power, make that not all category of objects can be observed optimally. It is then interesting to complement such space data with dedicated ground-based observations. Such observations can be made on alert during the Gaia mission, but also either before or after the mission completion. Ground-based observations of asteroids and small bodies can be used a) for practical reasons during the data reduction itself, b) as supplementary data over larger time span, or c) as complementary data because out of the accessibility of the Gaia instruments.

2 Ground-based complements

Here we focus on a few points of interest:

1. Observations in alert will enable to trigger ground-based observations in short time (but not less than ≈ 24 hours) to ensure a good threading of the object, avoid its loss (and potential hazard), and complete

[1] IMCCE, Observatoire de Paris, UPMC, USTL, CNRS, 77 av. Denfert-Rochereau 75014 Paris, France – mailto:hestro@imcce.fr
[2] Univ. of Helsinki observatory, Helsinki, Finland
[3] OCA, CNRS, Le Mont Gros 06000 Nice, France
[4] ESO, Vitacura, Chile. LESIA, Observatoire de Paris, UMR CNRS/INSU 8109, place J. Janssen, 92195 Meudon, France

the Gaia observations limited at $V \leq 20$ Tanga et al. (2008). These are delicate observations due to the possible low solar elongation, and the large parallax of the satellite located at the Sun-Earth L2 Lagrangian point;

2. High angular-resolution observations for selected asteroids will provide precise size and shape estimate and, once combined to good mass knowledge, their bulk density. Because there are no particular bias toward the binary asteroid population, and many taxonomic classes will be sampled, we will test for a possible link between asteroids' taxonomy and their interior (see Table 1). Additionally, these observations will be useful to calibrate the size determination from the Gaia imaging itself, and to calibrate the photocenter correction modelling to apply during the astrometric reduction;

3. Astrometric observations before and after Gaia of about more than 50 target asteroids will increase the number of derived asteroids masses (Mouret 2007) adding more than 25 bodies to the list of approx. 150 from Gaia observations alone. Moreover, astrometry and radiometric size measurements of several selected NEOs will enable the detection of the Yarkovsky effect and possibly give an indication on their thermal inertia. These additional information will also enable us to better understand and model possible bias in the global adjustment of the complex model to the Gaia observations, avoiding hence a degradation of the general quality of any global parameter estimation (test of General Relativity, link of the dynamical reference frame to the optical ICRF, etc.);

4. Last, the availability of the Gaia stellar catalogue – together with better orbits of asteroids – will enable a much better prediction of stellar occultations, and their path on the surface of the Earth (see Fig. 1).

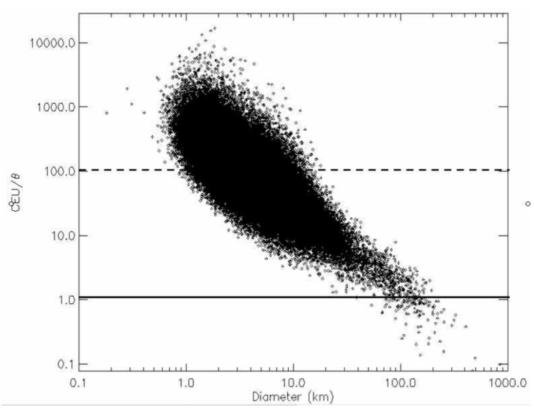

Fig. 1 Asteroids accessible to stellar occultations, as a function of their prediction precision and size. This is given by the ratio of the asteroids ephemeris uncertainty (CEU) to angular diameter θ as a function of the asteroid size. Good predictions are provided when $\mathrm{CEU}/\theta \leq 1$ thus an increase of one dex on the CEU precision would yield an increase of two dex in the number of potential asteroids, and also enable to sample smaller bodies (diameter $\gtrsim 10$ km). Compared to what can be achieved today with the Tycho catalogue, Gaia will yield a much larger number of interesting events; which in turn will be observed with a larger number of chords and not for only one snapshot, and consequently provide a completely scaled 3-dimensional view of the whole body.

Table 1. Taxonomic type sampling of asteroids with expected known masses (and apparent diameter ≥ 80 mas) observable at the VLT during forecoming ESO observations periods (covering 2 years).

Type	A	B	C	K	L	Q	R	S	T	X
P83	–	1	6	1	–	1	–	10	–	5
P84	1	–	7	–	–	–	–	4	–	4
P85	–	1	5	1	1	–	1	9	1	2
P86	–	1	5	1	–	–	–	6	–	3
Total	1	3	23	3	1	1	1	29	1	14

References

Mignard F., Cellino A., Muinonen K., et al., Dec. 2007, Earth Moon and Planets, 101, 97

Mouret S., 2007, Investigations on the dynamics of minor planets with Gaia, Ph.D. thesis, Observatoire de Paris

Tanga P., Hestroffer D., Delbò M., et al., 2008, Planetary and Space Science, In press

SF2A 2008
C. Charbonnel, F. Combes and R. Samadi (eds)

ASTROMETRY WITH Gaia IN PERSPECTIVE

Mignard, F.[1]

Abstract. The astrometric accuracy of Gaia is placed in perspective by showing its expected performances in relation with the slow and unsteady historical progress, specifically in two areas: (i) the realisation of the reference frame, (ii) the measurement of trigonometric parallaxes. It appears clearly that both Hipparcos and Gaia are truly epoch-making steps in this age-old quest for accurate star position. No earlier generation of astrometrists has witnessed such a dramatic improvement over so short a period of time.

1 Introduction

With Gaia expected for a launch in less than four years, astrometry will benefit from a new decisive boost into the highest achievable accuracy, recurring just two decades after a similar outstanding landmark with Hipparcos. This will be the (provisionally) final result of a long quest that can be traced back to the origin of position astronomy.

As it stands today, Gaia is a powerful astronomical space project dedicated to high precision astrometry, photometry and spectroscopy. Starting in about 2012, Gaia will survey the whole sky and detect any sufficiently point-like sources brighter than the 20th magnitude with repeated observations over the 5-year mission. The astrometric precision of 25μas at 15 magnitude will improve on Hipparcos by nearly two orders of magnitude providing position, proper motions and parallaxes. These observations consist primarily of 1D accurate determination of the image location at the transit time on a frame rigidly attached to the payload together with an estimate of the source brightness. A global adjustment of these elementary observations produces the final astrometric solution with the five astrometric parameters for all the well-behaved stars. This rigid sphere is made inertial through the observations of distant, extragalactic, and non-moving quasars in the visible range.

For astrometry Gaia will be in 2020 the current best astrometric catalogue and the crowning of centuries of painstaking effort by generations of astronomers and instrumentalists to achieve the highest accuracy in pinpointing the stars. In this few pages I attempt to place Gaia in perspective by illustrating the major stages in the construction of reference frames and the measurement of stellar distances.

2 High precision astrometry

It is impossible to trace back the very moment when humankind started recording the position of heavenly bodies, and in the word *recording* we include organized oral transmission as a true mean to hand down a knowledge to posterity. It cannot be doubted however that the daily motion of the celestial sphere, the regular return of the sun in the morning were a shared knowledge within the small groups of humans. Very little is recorded before the apparition of true writing, although several megalithic monuments bear witness of the narrow relationship between the Neolithic man and the cosmos when distinction between science and myths or religion simply did not exist. Whatever the goal of these observations, the monuments can be viewed, at least partly, as astronomical observatories using long baselines to make accurate records of astronomical events from the alignments between markers. In short these early men were the forerunners of astrometry, that branch of astronomy dealing with the determination of the positions, distances and motions of celestial bodies.

This is one the oldest fields of scientific investigations, known for centuries as positional astronomy with social importance for astrology or timekeeping. Until the mid-19th century an astronomer was primarily a man

[1] OCA/Cassiopée, BP404, Nice Cedex

able to describe the celestial sphere and its diurnal rotation to make predictions for the returns of the seasons, the planet wandering or the occurrence of eclipses. As positions and motions are not absolute concepts they can only be described with respect to some reference using a system of coordinates that can be constructed with much freedom.

Astrometry as it is understood today dates back at least to Hipparchus, who compiled in the 2nd century BC the first catalogue of stars visible to him and invented the stellar brightness scale basically still in use today. Hipparchus catalogue has come down to us through Ptolemy who published it in the 2nd century as part of his Almagest. (This sequence of events is, and by far, not shared by every historian, but seems to me very probable). This Hipparchus/Ptolemy Catalogue remained the standard star catalogue in the Western and Muslim worlds for over a thousand years, copied and updated by adding the effect of precession to the longitudes, until new observations by Ulugh Begh in Samarkand (early 15th century) and later by Tycho Brahe (late 16th century) led to the production of truly new catalogues of the stars accessible to the unaided eye.

Modern position astronomy, or in short astrometry, was founded by W.F. Bessel (see a short biography in Fricke, 1985) with his Fundamenta astronomiae, in which he gave the mean position of 3222 stars observed between 1750 and 1762 by James Bradley at Greenwich. Bessel is also credited and best remembered for the first real measurement of a stellar distance carried out on 61 Cyg in 1838, by which he opened up a totally new window on the scale of the Universe. Apart from the fundamental function of providing astronomers with a

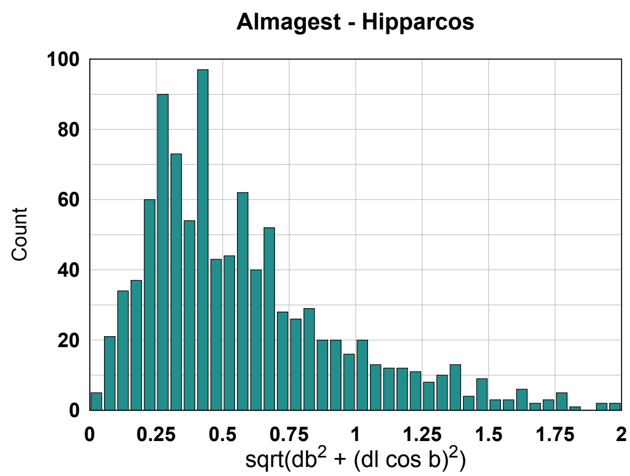

Fig. 1. Accuracy of the Almagest star catalogue (in degrees). The histogram is based on a comparison of the positionws provided by Ptolemy to those computed with the Hipparcos Catalogue. The date for the precession has been adjusted to give a zero mean in the residuals in longitude.

reference frame to relate their observations, astrometry is also fundamental for fields like celestial mechanics, stellar dynamics and galactic astronomy. In observational astronomy, astrometric techniques help identify stellar objects by their unique motions or predict the orbit of spacecrafts. Astrometry is also involved in creating the cosmic distance ladder because it is used to establish trigonometric reference distances for stars in the Milky Way, that is to say it sets the first rung of the ladder needed to determine the distances of the more distant sources belonging to the next rung. On a more mundane side, astrometry is still instrumental for keeping time, in that the UTC timescale used worldwide in science or for civilian activities is basically the atomic time synchronized to Earth's rotation by means of exact astrometric observations.

Since the early times star catalogues have never ceased to be used to chart the sky and to serve as reference maps to refer the motions of celestial bodies or the positions of fainter stars. As everywhere in science, refinements in the instruments and in computational techniques have been the main source of improvement of the astrometric accuracy from about one half of a degree at the time of Hipparchus to about $0\overset{''}{.}05$ for the best ground based measurements of the early 1980s. The improvement in the realisation of the reference frame with fundamental catalogues is clearly visible in the list of Table 1.

Over the last two decades new astrometric techniques like radio interferometry on the ground or global astrometry in space in the visible has brought a considerable improvement with positional accuracy at the

$0''.001$ level. This enormous improvement in few years contrasts with the slow and steady progress which has been the rule for centuries and in the 20th century diverted young astronomers from starting a career in astrometry as they were lured by the nearly monthly breakthroughs in astrophysics.

3 Global space astrometry

The possibility to achieve global astrometry with a spinning satellite doing one dimensional measurements is not a trivial thing and has been the subject of animated discussions, and even challenged, before Hipparcos. The genesis from the initial proposal by P. Lacroute in 1967 to the Hipparcos selection is detailed in Turon & Arenou (2008) with first hand information. The principle which leads to absolute astrometry and nearly absolute parallaxes is still very subtle and deserves attention, all the more as it remains the Gaia baseline.

Table 1. List of the precision astrometry catalogues.

Year	Name	Number of stars	Comment
1790	Maskelyne	36	zodiacal stars, one epoch
1818	Bradley/Bessel	3000	no PM, nearly fundamental for one epoch
1830	Bessel	36	with PM, + precession
1878	FK1	539	Start of the FK series
1898	Newcomb	1297	Start of the GC series
1907	FK2	925	
1937	FK3	873	1st IAU supported international RF
1963	FK4	1535	$\sigma_{1950} \sim 0''.07$- $0''.15$, $\sigma_{2000} \sim 0''.15$-$0''.30$
1988	FK5	1535	$\sigma_{2000} \sim 0''.05$ - $0''.10$
1997	Hipparcos	100,000	Quasi fundamental catalogue
1998	ICRF	212([1])	First extragalactic primary reference frame

[1] This is the number of defining sources. The full ICRF has now more than 700 sources.

If one knows how the spacecraft rotates, meaning it rigid body attitude is available at any time, then from a local observation of point-source images onto the focal plane and a good time recording, it is clear that the position of each source can be recovered in the same reference frame in which the spacecraft attitude is given. Conversely with an on-board stellar catalogue and a star tracker rigidly connected to the spacecraft, one could know the attitude with great accuracy. In the case of Hipparcos or Gaia neither of the two is initially available (the Input Catalogue of Hipparcos was just a list of program stars, not an astrometric catalogue matching the observing accuracy). There is apparently a vicious loop since ultimately one wishes to determine the position of the stars and to know the spacecraft attitude. In practice this works thanks to the circle closure.

Consider the simpler case of a satellite rotating around a fixed spin axis and stars distributed on the perpendicular great circle, just in one dimension. After one revolution a star transits again in the telescope field of view, and between the two epochs one knows that the satellite has exactly rotated by 360 degrees (within a small amount related to the star proper motion). Since the time is recorded, one knows also the mean rotation rate averaged out over one revolution. But we have many stars at different longitudes on this circle, and each of them produces an average rate at a different time. One sees that it is therefore possible to reconstruct precisely the rotation of the satellite from purely geometrical and kinematical arguments. If one knows from a dynamical modeling that the rotation is smooth and that it can be modeled with few parameters, it becomes easy to fit these parameters. Within a single convention about the origin, one ends up also with the positions of the individual stars on the circle together with their proper motions. With Hipparcos and Gaia one has also the basic angle which tells us that a known rotation has taken place between an observation in the preceding and following field.

Finally the angular distance between pairs of stars will be quickly known if the star density is such that several stars are simultaneously measurable in both fields of view. Even in the simplified 1D celestial *circle* one sees that as soon as the number of arcs is large enough, there is only one way to place the stars, keeping at the end just one degree of freedom for the global rotation (or two if the stars have a proper motion).

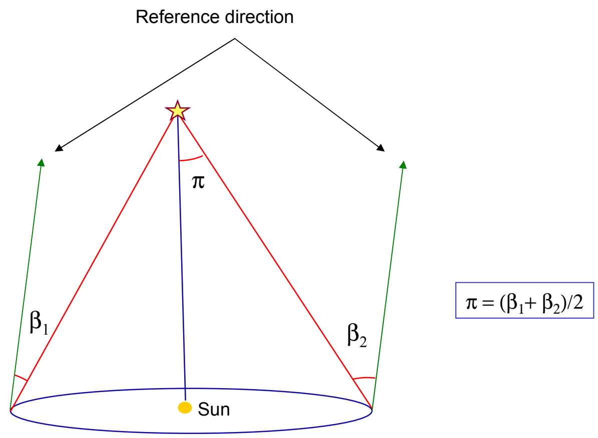

Fig. 2. Principle of measurement of absolute parallaxes. The star parallactic motion is monitored against an absolute reference frame or an absolute direction that can be accessed over the different observations. No other distant star is involved in the process and this should permit to obtain the true parallax of the star. This needs some form of global astrometry to maintain a consistent reference frame over the set of observations.

The same principle extends to the real celestial sphere, although there are several complications arising from the time change of the basic angle. Therefore the attitude reconstruction plays a very important and critical role in the reduction of a space astrometry mission aiming to carry out global astrometry. It is through the attitude reconstruction that the observations from the two fields of view become properly linked. It is therefore not helpful if one field of view contains many more stars than the other. To accommodate this for the Hipparcos mission, an Input Catalogue was created such that the stars were more or less evenly distributed over the sky. For Gaia a dedicated subset of stars will be used to solve for the attitude and the instrument parameters. Then the attitude solution will be used to find the astrometric parameters of the remaining stars.

4 Absolute and relative parallaxes

In many astronomy textbooks the principle of measuring stellar parallaxes is nicely presented, although there is little effort done to draw attention on the difference between relative and absolute parallaxes.

The parallactic effect is the difference in the direction of a distant celestial object as seen from two different viewpoints, that is to say the difference between two unit vectors. In classical astronomy the usual viewpoint was an observing place on the Earth, and the reference point was taken as the centre of the sun or, better, the barycentre of the solar system. Because of the annual motion, the parallactic vector is not constant during the year and the elliptical apparent displacement of the star cannot be incorporated into a linear proper motion. Quite naturally, one adopts as the standard direction of the star that defined in the barycentric frame. The annual parallax, usually referred to as the parallax, is the angle subtended at a star by one astronomical unit and is formally equivalent to the distance to the star. In principle a determination of this angle can be obtained by triangulation as illustrated in Fig. 2 which sketches the variation in the absolute direction of a nearby star. The possibility to do such a measurement implies that a reference direction can be materialised and transported in some way through the different observations while the Earth moves about the Sun. Given the size of the parallax, even for the nearest star, this is very hard to achieve. Typical measurements of this kind were carried out in the early days of the parallax search and later in the XIXth century successfully. The reference direction was either the local vertical (search of Bradley for example) or the spin axis of the Earth (measurement of stellar declination). This was the method used with success by T. Henderson at the Cape from which he determined

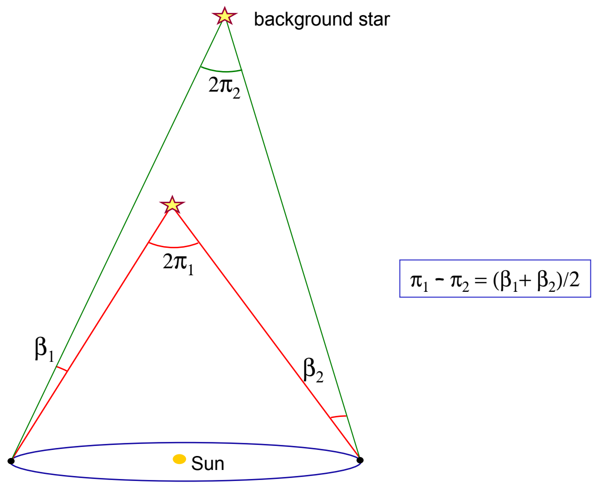

Fig. 3. Principle of measurements of relative parallaxes by referring the parallactic motion of a nearby star to a distant background star. This technique has been first described by Galileo in the Dialogo and considered as more promising than the absolute method. By nature it involves small field astrometry and requires an assumption about the distance of the background stars.

the parallax of α centauri in 1839 and later by others with meridian circles or zenithal telescope.

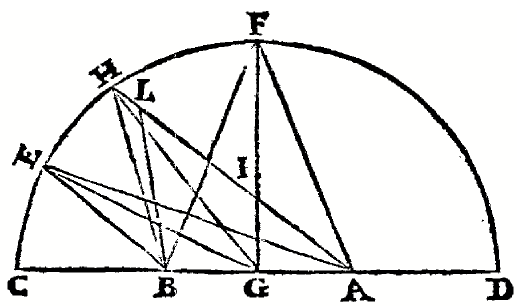

Fig. 4. Original drawing in the Dialogo (Third day) where Galileo describes the alteration in star elevation due to the motion of the Earth about the Sun. A and B are two points diametrically opposite on the ecliptic from where stars E, H or F (the latter at the ecliptic pole) are observed at six months interval. Galileo stresses that the change of directions should be visible in the direction of rising or setting of the star and that landscape features, like a remote hill, could be used as the arms of a gigantic quadrant.

In the Dialogues Galileo is probably the first to investigate rather deeply the consequences of the annual motion of the Earth on the position of the fixed stars. The qualitative features (i.e. the reflex stellar displacement) have been known for long, but Galileo set himself the objective of ascertaining the observable changes and how to actually do the measurements (Figs. 4- 5).

It took in practice more than 150 years between the first attempts to detect the parallactic motion and its undisputable first measurement by W.F. Bessel in 1838 on the star 61 Cygni. He was shortly followed in publication by F. Struve for Vega and T. Henderson in α Centauri. Work on measuring parallaxes proceeded very slowly with about 20 parallaxes available 10 years later and around 100 at the turn of the century. The number of known parallaxes varies greatly from one author to another since some quote the number found in the early compilation, while other attempt to tell how many *reliable* parallaxes are available at a particular time (Table 2). In the early days, for each star all the published parallaxes are listed and not necessarily discussed.

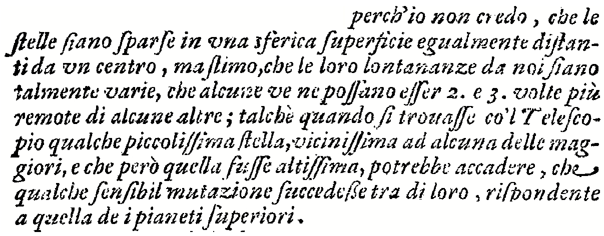
perch'io non credo, che le
ſtelle ſiano ſparſe in vna sferica ſuperficie egualmente diſtan-
ti da vn centro, ma ſtimo, che le loro lontananze da noi ſiano
talmente varie, che alcune ve ne poſſano eſſer 2. e 3. volte più
remote di alcune altre; talchè quando ſi trouaſſe co'l Teleſco-
pio qualche piccoliſſima ſtella, viciniſſima ad alcuna delle mag-
giori, e che però quella fuſſe altiſſima, potrebbe accadere, che
qualche ſenſibil mutazione ſuccedeſſe tra di loro, riſpondente
a quella de i pianeti ſuperiori.

Fig. 5. Original text in the Dialogo (Third day) where Galileo describes the relative parallaxes with reference to the geocentric motion of the planets. The text reads: *I do not believe that the stars are spread over a spherical surface at equal distances from one center; I suppose their distances from us to vary so much that some are 2 or 3 times as remote as the others. Thus if some tiny star were found by the telescope quite close to some of the larger ones, and if that one were therefore very remote it might happen that some sensible alteration would take place among them corresponding to those of the outer planets.* Translation of S. Drake, Univ. of California Press.

Several technics are involved with relative or absolute measurements and very often with scatter larger than the quoted individual precision, when available. In the modern era, the Catalogue entries are based on critical examination of the available values and lead to an adopted value with an estimated accuracy. For example the 4th General Catalogue of Trigonometric Parallaxes contains 15430 determinations of parallaxes for 7888 stars.

Table 2. Progress in the number of available stellar parallaxes.

Year	Number	Comment
1840	3	Published parallaxes
1850	20	Catalogue of Peters
1888	40	Catalogue of Oudemans
1910	100	of which 52 photog. parall. from Kateyn
1912	250	Catalogue of Bigourdan
1917	500	Catalogue of Walkey
1924	1870	Catalogue of Schlesinger
1930	2000	From here it may include spectroscopic parallaxes
1952	5800	Yale Parallax Catalog (Jenkins)
1965	7000	Yale Parallax Catalog (Jenkins)
1993	8000	Yale Parallax Catalog (van Altena et al.)
1997	110,000	Hipparcos

References

van Altena, W. F., Lee, J. T. & Hoffleit, E. D., 1995, The General Catalogue of Trigonometric Stellar Parallaxes, 4th ed., New Haven, Yale Univ. Obs.

Fricke, W., 1985, Friedrich Wilhelm Bessel, Astrophysics and Space Science, 110, 11-19.

Turon, C. & Arenou, F., 2008, The Hipparcos Catalogue: 10th anniversary and its legacy, in Proc. of IAU Symposium No. 248, W.J. Jin, I. Platais & M. A. C. Perryman, eds.

SF2A 2008
C. Charbonnel, F. Combes and R. Samadi (eds)

THE GALACTIC BULGE AS SEEN IN OPTICAL SURVEYS

Reylé, C.[1], Marshall, D. J.[2], Schultheis, M.[1] and Robin, A. C.[1]

Abstract. The bulge is a region of the Galaxy of tremendous interest for understanding galaxy formation. However measuring photometry and kinematics in it raises several inherent issues, such as severe crowding and high extinction in the visible. Using the Besançon Galaxy model and a 3D extinction map, we estimate the stellar density as a function of longitude, latitude and apparent magnitude and we deduce the possibility of reaching and measuring bulge stars with Gaia. We also present an ongoing analysis of the bulge using the Canada-France-Hawaii Telescope.

1 Introduction

Observing towards the bulge gives measures for a large number of individual stars that are the tracers of the Galactic formation and evolution. A detailed study of the bulge is necessary to understand its structure, dynamics and formation. The bulge of the Milky Way is the only one where the parameters in the six dimensions of phase space can be determined, as well as elemental abundances, on a star by star basis. Its detailed observation is thus very useful to test different scenarii of galactic bulges formation.

The bulge has been explored by a few ground based surveys, for example DENIS, 2MASS and microlensing surveys (OGLE, MACHO, DUO, EROS-2 and MOA) in the visible and the infrared, and from space by Spitzer in the mid infrared. The interstellar matter distributed in the plane is a major obstacle to the observation of the stars in the direction of the bulge and the Galactic center, particularly in the visible.

Gaia will give unprecedented view of the Galaxy, but it is often stated that, due to the wavelength coverage of instruments, it will be hardly usable for bulge studies. However, estimations of what Gaia will effectively see in the bulge is worthwhile to do before launch. We have investigated this question using a population synthesis model and a realistic 3D map of the extinction in the inner Galaxy. Studies of the bulge from ground before Gaia are also possible. We present an on-going survey of the bulge undertaken with Megacam aimed at producing good photometry and proper motions for a substancial number of clump stars.

2 Interstellar extinction

Extinction is so clumpy in the Galactic plane that it determines for a great part the number density of stars, more than any other large scale galactic structure. Thus, it is possible to extract information about the distribution of the extinction from photometry and star counts. Marshall et al. (2006) have shown that the 3D extinction distribution can be inferred from the stellar colour distributions in the 2MASS survey. Using stellar colours in $J - K_S$ as extinction indicators and assuming that most of the Galaxy model prediction deviations on small scales from observed colours arises from the variation of extinction along the line of sight, they built a 3D extinction map of the galactic plane. The resulting 3D extinction map furnishes an accurate description of the large scale structure of the disc of dust.

[1] Observatoire de Besançon, Institut UTINAM, Université de France-Comté, BP 1615, 25010 Besançon Cedex, France
[2] Département de Physique et Centre Observatoire du Mont Mégantic, Université Laval, Québec, G1K 7P4, Canada

3 The bulge density law from DENIS and 2MASS

The DENIS survey has produced specific observations in the direction of the bulge. Picaud & Robin (2004) used these data in 94 low extinction windows with $|l| < 10°$ and $|b| < 4°$ and the Besancon population synthesis model to determine shape parameters of the bulge as well as constraints on its age and luminosity function.

Using the 3D extinction map described above and the Galaxy model thus constrained, it is possible to perform a realistic comparison of the number of stars from the Galactic model with the number of observed stars in the 2MASS data (Fig. 1). The comparison points to significant discrepancies. In particular the bulge as defined by Picaud & Robin (2004) discrepants from the data at $4 < |b| < 10$, probably because the bulge shape was determined from a more restricted area in latitudes A better adjustement of all 11 parameters characterizing the bulge over the whole 2MASS data set towards the bulge is ongoing.

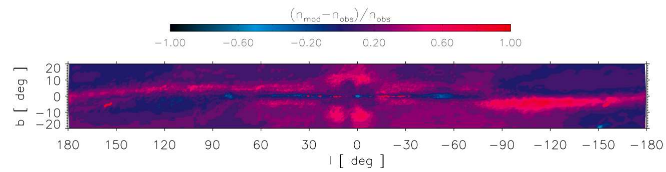

Fig. 1. Comparison between predicted star counts from the Galaxy model and 2MASS data. The colours code the relative difference $(n_{mod} - n_{obs})/n_{obs}$, n_{mod} and n_{obs} being star counts per square degree to magnitude K_S=12 for the model and the data respectively. It varies from a factor of two excess in modeled star counts (in red) to a factor of two deficiency in modeled star counts (in dark blue). Regions where the Galaxy model overestimates or underestimates de density of stars clearly appear.

4 The bulge with MegaCam

We started a photometric and astrometric survey of the bulge with MegaCam at CFHT. We observed 22 fields covering $-5° < l < +5°$, $-1° < b < +1°$, in the r', i', and z' bands. The observations are made at two epochs, separated by 3 years and have just been completed.

This survey provides unprecedented observations of the red clump very close to the Galactic plane. It will bring constraints on the luminosity function of the bulge. Moreover, a detailed extinction map with a very high spatial resolution can be obtained, using theoretical isochrones, such as the map obtained with Spitzer data (Schultheis et al., submitted). Proper motions will also be measured. We expect to get a precision of 1 mas yr^{-1}, corresponding to a velocity of 18 km s^{-1} at the bulge distance. 6 of the fields have also Giraffe observations (PI Babusiaux). In these fields we will get the 3 components of the velocity, as well as metallicity, allowing us to investigate the kinematics/metallicity relation.

Fig. 2 shows the colour-magnitude diagram for one field, in different parts of the CCDs mosaic. It shows how patchy and variable the extinction is. The red clump is clearly visible in some parts of the image, whereas it is not detected in other more extinguished parts.

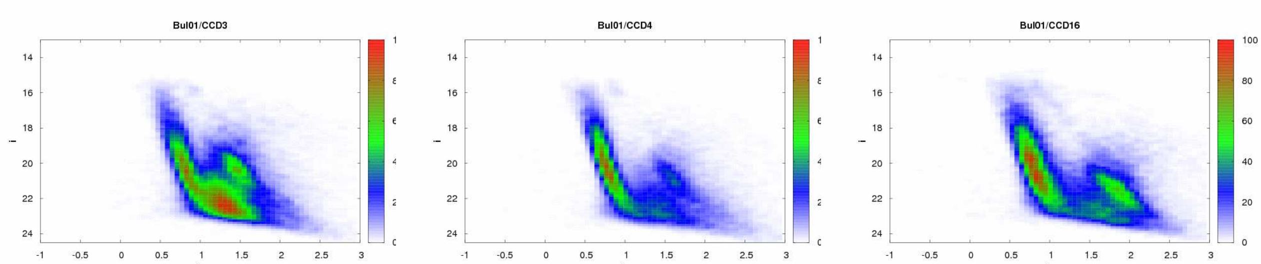

Fig. 2. i' versus $i' - z'$ diagram in 3 CCDs of one of the bulge fields.

5 The bulge with Gaia

Gaia will provide accurate positional, radial velocity, and photometry measurements for 1 billion of stars, that is about 1% of the Milky Way stellar content. Each star will be observed about one hundred times during the time of the mission, allowing the determination of proper motions. It comprises an astrometric instrument, photometers (GRP and GBP) and a spectrometer (RVS). The limit magnitude is G=20[1], except for the RVS (G=17). Detection problems may occur for these low spatial resolution instruments if the observed field is crowded. The estimated crowding limit is 600 000 stars deg^{-2} on the astrometric fields and photometers, and 40 000 stars deg^{-2} on the spectrometer.

Observations of bulge stars will strongly depend on the extinction and on the crowding. If the extinction is too high, the number of stars will be low (no crowding) but conversely the bulge stars would be out of reach, as they would be too faint. If the extinction is low (like in Baade's window), bulge giants on the red clump are bright enough to be reached, but the crowding will limit the number and/or the quality of their measurements. Of course the number of stars in the bulge also strongly depends on latitudes and longitudes.

We use the Galaxy model together with the Marshall et al. (2006) extinction map to address the following question: is there a combination of parameters (extinction, latitude) in the galactic bulge where the extinction is large enough to avoid crowding and not too high to allow bulge star measurements with Gaia instruments? The results of the simulations are shown in Fig. 3 for the astrometric fields and in Fig. 4 for the spectrometer. The left panel shows the density of bulge stars at the limiting G magnitude of the instrument, as a function of longitude and latitude. The blue contour depicts the density at which crowding occurs. The green contour shows a iso-density of 100 bulge stars deg^{-1}, value at which we consider that the number of bulge stars starts to be significant. The right panel shows the absolute magnitude M_V of the intrinsically faintest bulge stars reached at the limiting G magnitude.

In the astrometric fields, a large part of the bulge will be visible, mainly in the Northern hemisphere, where extinction is higher. That corresponds to a number of 23 million bulge stars over an area of 220 deg^2. Even still, in the Southern hemisphere bulge stars brighter than the limiting magnitude G=20 will be detected. Turn-off stars ($M_V \sim 4$) and even main sequence stars are observable at high latitudes. At lower latitudes, including regions very close to the Galactic plane, the absolute magnitude of the bulge stars is $M_V \sim 1$ to 2, and these stars are mainly clump giants. In the spectrometer (Fig. 4) where the crowding is a much more dramatic issue, there are unextended regions where the extinction is high enough to make the crowding low but still not too strong to mask competely bulge stars. About 30 000 bulge stars over 9.7 deg^2 are predicted to be observed, in regions around $b = 1$ to $2°$. They are clump giants.

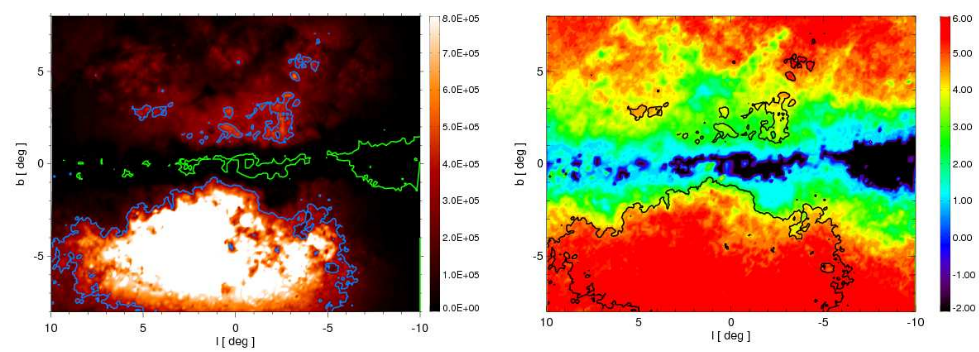

Fig. 3. Left: Density of the bulge in the Gaia astrometric fields at the limiting magnitude G=20, as a function of latitude and longitude. The bleu contour shows the iso-density of 600 000 stars deg^{-2}, which is the crowding limit in the astrometric fields. The green contour shows the iso-density of 100 stars deg^{-2}. Right: Absolute magnitude M_V of bulge stars just reached at the limiting magnitude G=20.

There will be opportunities for Gaia to access reliable measurements in the Galactic bulge, photometry and astrometry, parallaxes, and proper motions, in nearly all the bulge regions.These regions strongly depend on the

[1] G is the photometric band used by the GAIA sky mappers. It is close to the V magnitude for stars with $V - I = 0$

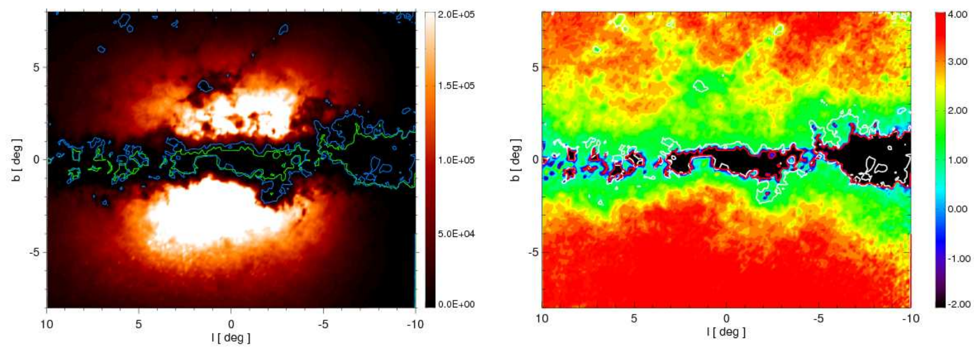

Fig. 4. Same as Fig. 3 for the RVS (limiting magnitude G=17 and crowding limit of 30 000 stars deg^{-2}).

assumed extinction. However, if the extinction maps do not suffer from systematics, there should be accessible windows well spread in longitude quite close to the dust lane in the Galactic plane. Observable bulge stars will also be spread in depth well inside the bulge. At low latitudes in the dense dust lane, most of the bulge stars will be too faint (due to extinction) to be reached. However in a few fields close to the Galactic plane in windows of lower extinction, stars in the giant clump should be observed. In any event, the position of the fields given here should be taken with caution because of the extreme sensitivity of the computation to the extinction which is not known to better than about 2 magnitudes in the most obscured regions. Putting together observations of the different instruments including RVS, Gaia should produce a detailed survey of bulge giants in terms of photometry as well as kinematics. Detailed analysis of these data sets should allow us to put strong constraints on the bulge structure and history.

6 Conclusion

Thanks to new photometric and astrometric surveys, the bulge structure can be revealed, bringing important constraints on the galaxy formation and evolution scenarii. We presented here several studies using such data set. Other available data are worthwhile to be analysed, such as the 49 OGLE-II fields for which proper motions have been measured Sumi et al. (2004). A preliminary analysis of these data with the Galaxy model shows that the bulge rotation can be constrained with these data.

Furthermore, radial velocities and metallicities data are available in the bulge directions (Ibata & Gilmore 1995; Minniti et al. 1996; Tiede & Terndrup 1999; Rich et al. 2007).The analysis of these data will allow us to refine the kinematical parameters of the bulge, as well as bulge metallicity. Finally, we showed that Gaia should give a detailed survey of bulge stars, down to the main sequence, in terms of photometry but also kinematics, including regions very close to the Galactic plane..

References

Ibata, R. A. & Gilmore, G. F. 1995, MNRAS, 275, 605

Marshall, D.J., Robin, A.C., Reylé, C., Schultheis, M., Picaud, S. 2006, A&A 453, 635

Minniti, D., Liebert, J., Olszewski, E. W., & White, S. D. M. 1996, AJ, 112, 590

Picaud, S., & Robin, A. C. 2004, A&A, 428, 891

Rich, R. M., Reitzel, D. B., Howard, C. D., & Zhao, H. 2007, ApJ, 658, L29

Robin, A.C., Reylé, C., Derrière, S., & Picaud S. 2003, A&A, 409, 523. Erratum 2004, A&A, 416, 157

Sumi, T., et al. 2004, MNRAS, 348, 1439

Tiede, G. P., & Terndrup, D. M. 1999, AJ, 118, 895

SF2A 2008
C. Charbonnel, F. Combes and R. Samadi (eds)

A LIBRARY OF SYNTHETIC GALAXY SPECTRA FOR GAIA

Rocca-Volmerange, B.[1], Tsalmantza, P.[2] and Kontizas, M.[3]

Abstract. An extended library of synthetic spectra of galaxies is built for training and testing the classification system (SVM) of GAIA. The final aim is to derive astrophysical parameters for all the unresolved galaxies observed by the satellite with the low resolution prism spectrometer. Predictions of the evolutionary code PÉGASE give the basic templates by spectral types and their corresponding astrophysical parameters (star formation rates, initial mass function, metallicity, ages and others). The new library is a largely extended sample from basic templates, tested for classification. In the future, a peculiar attention will be focused on a selection of the main astrophysical parameters. Moreover we keep in mind ambitious objectives to make coherent the interpretation of low resolution data with high resolution spectra obtained with the RVS.

1 Introduction

Gaia will obtain observations of several million of unresolved galaxies over the whole sky, down to the 20th magnitude. This is an exceptional opportunity to access to statistical samples of galaxy data with a rare accuracy, every source being observed up to 70 times by Gaia. The main objectives are to use the low resolution spectroscopic observations to classify and determine the main astrophysical parameters of all the unresolved galaxies. The method rests on a set of galaxy templates by spectral types produced by the spectrophotometric evolutionary code PÉGASE (http://www2.iap.fr/pegase). The comparison of the model predictions with observed data is done with the SDSS colour-colour diagrams. The model templates are extended to the complete coverage of observations by varying the main physical parameters. The final part is to simulate Gaia observations and to train classification and parametrization algorithms.

1.1 The new extended library

The new library (Tsalmantza et al. 2008) corresponds to 28885 synthetic spectra at redshift zero covering four Hubble type of galaxies respecting resolution and wavelength domains of the low resolution prism spectrometer. It is an improved version of the synthetic library (Tsalmantza et al. 2007). The first improvements are to add scenarios of starburst galaxies to cover the blue part of the SDSS colour-colour diagrams. The second improvement is to shorten the time-scales of star formation rates for elliptical galaxies to fit the reddest part of the diagrams. The comparison of model predictions with SDSS data in the g-r/r-i diagram is shown on Fig.1. The new library is also found in good agreement with LEDA (Paturel et al. 1997) photometric observations.

Tzalmantza et al. (2008) also presents a detailed comparison of synthetic spectra of the new library with flux calibrated spectra of the Kennicutt's atlas (Kennicutt, 1992) for similar types. Normalization, conversion to rest frame and spectra rebinning were done for such a comparison.

1.2 Classification and Parametrization

The Support Vector Machines (SVMs) are trained and tested on an extremely large number of synthetic spectra derived from the new library for three G-band magnitude values G=15, G=18.5, G=20. Extinction by our

[1] Institut d'Astrophysique de Paris, 98bis Bd Arago, F-75014 Paris, France
[2] Max-Planck-Institut für Astronomie, Königstuhl 17, 69117 Heidelberg, Germany
[3] Department of Astrophysics Astronomy & Mechanics, Faculty of Physics, University of Athens, GR-15783, Athens, Greece

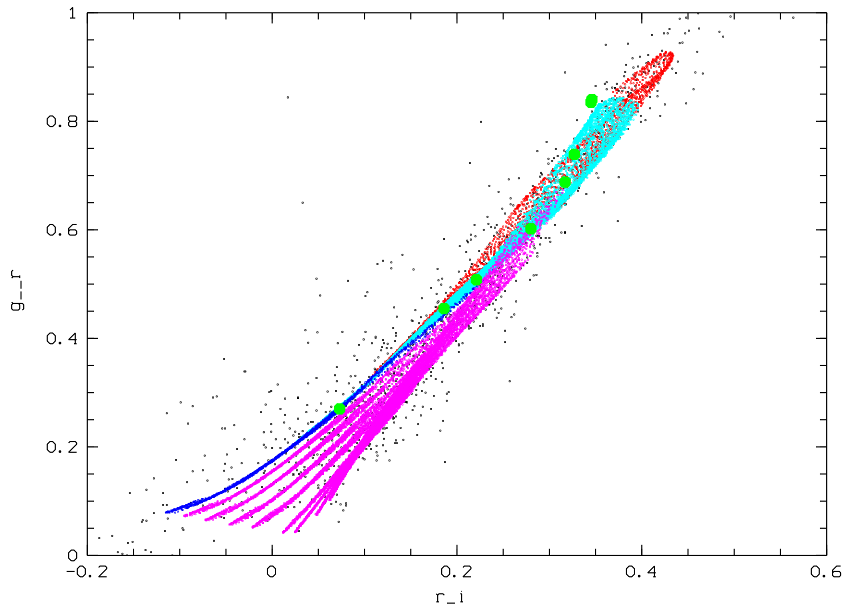

Fig. 1. Model predictions for the four galaxy types: irregular(blue), starburst(magenta), spirals(light blue) and early type galaxies (red). Observations (black dots) are from the SDSS data sample. Examples of the classical PÉGASE models for various types are also shown (green dots).

Galaxy, various noises (Poisson, CCD readout) are taken into account. Regression tests by galaxy types allow to test the classification of SVMs. Regression of redshifts are also performed by comparing predicted versus true z values for the test set. The first results of classification and parametrisation of the second library are very satisfying.

1.3 Conclusion

The new library gives a satisfying comparison to observations of colours and spectra at low resolution. The training of SVMs with the extended library gives good results for galaxy types, redshift and Galaxy reddening. Improvements are required for the extraction of the astrophysical parameters. Synthetic models might suffer any degeneracy for the extremely extended training library. The best solution will be in the future to extract only a few number of the main physical parameters, representative of the morphology and evolution by type at all redshifts. Moreover a new exploration is in progress by building the high-resolution spectra library for the RVS instrument which will allow to coherently link the interpretation of resolved observations of nearby galaxies with the unresolved galaxy samples at higher redshifts.

References

Fioc, M., & Rocca-Volmerange, B. 1997, A&A, 326, 950

Kennicutt, R.C. Jr 1992, ApJS, 79, 255

Paturel, G., Andernach, H., Bottinelli, L., et al. 1997, A&AS, 124, 109

Tsalmantza, P., Kontizas, M., Bailer-Jones, C.A.L.,Rocca-Volmerange, B., et al. 2007, A&A, 470, 761

Tsalmantza, P., Kontizas, M. & Rocca-Volmerange et al. 2008, submitted

SF2A 2008
C. Charbonnel, F. Combes and R. Samadi (eds)

GROUND-BASED OBSERVATIONS FOR GAIA (GBOG)

Soubiran, C.[1], Allende Prieto, C.[2], Altmann, M.[3], Bragaglia, A.[4], Clementini, G.[4], Frémat, Y.[5], Heiter, U.[6], Joliet, E.[7], Pancino, E.[4], Sartoretti, P.[8], Smart, R.[9] and Thuillot, W.[10]

Abstract. This contribution gives an overview of the ground-based observing efforts organized to collect the auxiliary data mandatory for the calibrations and tests of the Gaia data processing.

1 Introduction

Gaia is an ambitious space astrometry mission of ESA the main objective of which is to map the sky in astrometry down to V=20 mag with unprecedented accuracy. Additionally, photometry of all objects and spectroscopy down to V=17 will be obtained. The final catalogue will include distances, motions and astrophysical parameters of one billion stars, a fundamental dataset for unravelling the structure, formation and evolution of our Milky Way. The challenging task of the data processing is under the responsibility of 320 scientists from 15 countries organised in the DPAC consortium: a major project for the European astronomical community (Mignard et al. 2008).

The Gaia data processing requires reference data in photometry and spectroscopy in order to tie the instrumental system to physical units. The GBOG Working Group is responsible for the coordination of the joint ground-based observing efforts to collect the auxiliary data mandatory for Gaia's calibrations.

2 The major on-going observations

- For the spectrophotometric calibration of the RP-BP and G bands, it is planned to collect the absolute fluxes of 250 spectrophotometric standard stars at 1% accuracy within 330-1050 nm. The targets will be monitored for variability. The facilities used are : REM/ROSS+REMIR, TNG/DOLORES, San Pedro Martir 1.5m/LARUCA, CAHA 2.2-m/CAFOS, Loiano 1.52m/BFOSC, ESO-NTT/EFOSC2 (Large Programme).

- For the radial velocity calibration, it is planned to qualify 1000 reference stars to fix the zero point of radial velocities and to validate a method of calibration with asteroids. This implies to gather ~3500 RV measurements (Crifo et al. 2008). The observing programmes, supported by PNG and PNPS, are conducted on OHP/SOPHIE and TBL/NARVAL for the Northern part. An agreement was obtained with Geneva Observatory for the Southern part on the Swiss 1.2-m Leonard Euler telescope / CORALIE, with support from AS-Gaia.

[1] Laboratoire d'Astrophysique de Bordeaux
[2] MSSL, University College London
[3] Zentrum für Astronomie der Universitt Heidelberg
[4] INAF - Osservatorio Astronomico di Bologna
[5] Observatoire Royal de Belgique
[6] Uppsala Astronomical Observatory
[7] ESAC/ESA European Space Astronomy Centre
[8] Observatoire de Paris Meudon
[9] INAF - Osservatorio Astronomico di Torino
[10] IMCCE, Observatoire de Paris

- The calibration of the classification / parametrization algorithms needs to establish a grid of reference stars for astrophysical parameter determination across the HR diagram. The corresponding spectra at high and low resolution will also be used to correct synthetic spectra. A part of the programme is made on TBL/NARVAL with support of PNPS, while a Large Programme is to be submitted on ESO-NTT/EFOSC2.
- Calibration fields are built at the Ecliptic Poles for the in-orbit test of the data processing. It is requested to assemble astrometry, photometry and spectroscopy in 1 sq. deg around each ecliptic pole. The imaging part is done on CFHT/Megaprime and ESO-MPI 2.2m/WFI, while some spectroscopy is planned on VLT/FLAMES.

3 Other on-going or foreseen observing programmes for Gaia

- Benchmark stars for critical tests of stellar atmosphere models (ESO 3.6m/HARPS, TNG/SARG)
- Library of solar analogs for Solar System studies (VLT/UVES)
- Primary standards for the flux calibration of RVS spectra 847-874 nm (La Palma 2.5m INT/IDS)
- Time-series photometry of specific classes of variable stars (network already in place)
- Spectroscopy of asteroids (TNG/DOLORES)
- ICRF link with the European VLBI Network (Bourda et al. 2008)
- Optical tracking of the satellite (network to be organised)

4 General considerations

New observations are needed because no pre-existing dataset fulfills the Gaia requirements in terms of homogenity, precision, sky coverage, magnitude range and spectral interval.

Most of the observations must be done right now because the calibration data must be ready when the data processing will start in 2012.

All data and resulting libraries will be made available to the astronomical community and will offer excellent possibilities for various research programmes.

The GBOG observing programmes are mostly long term ones : follow-up observations will continue during the mission to ensure the stability (photometric or spectroscopic) of the sources. It implies that facilities will be needed until 2017.

The GBOG observing programmes face the problem of being in competition, for the allocation of telescope time, with programmes that are more directly scientifically related.

The GBOG observing programmes have already started with a good support of national facilities but there are still some difficulties covering the southern hemisphere.

The GBOG WG is mandated to coordinate observing programmes required to support the Gaia mission. Follow-up ground based observations resulting from Gaia science alerts are not included under this mandate.

References

Bourda, G., Charlot, P., Porcas, R.; Garrington, S. 2008, in SF2A-2008: Proceedings of the Annual meeting of the French Society of Astronomy and Astrophysics held in Paris, France, July 2-6, 2008, Eds.: C. Charbonnel, F. Combes and R. Samadi

Crifo, F., Jasniewicz, G., Soubiran, C., Hestroffer, D., Katz, D., Siebert, A., Veltz, L., Udry, S. 2008, in SF2A-2008: Proceedings of the Annual meeting of the French Society of Astronomy and Astrophysics held in Paris, France, July 2-6, 2008, Eds.: C. Charbonnel, F. Combes and R. Samadi

Mignard, F., Bailer-Jones, C., Bastian, U., Drimmel, R. et al. 2008, in "A Giant Step: from Milli- to Micro-arcsecond Astrometry", Proceedings of the International Astronomical Union, IAU Symposium, Volume 248, p. 224-230

SF2A 2008
C. Charbonnel, F. Combes and R. Samadi (eds)

ACTIVITIES OF THE ICRS PRODUCT CENTRE (SYRTE, PARIS OBSERVATORY)

Souchay, J.[1], Bouquillon, S.[1], Barache, C.[1], Gontier, A.-M.[1], Lambert, S. B.[1], Le Poncin-Lafitte, C.[1], Taris, F.[1], Arias, E.F.[2], Fienga, A.[3] and Andrei, A.H.[4]

Abstract.
We present the various activities of the International Celestial Reference System Product Center (ICRS-PC) hosted jointly at Paris Observatory and US Naval Observatory (Washington) in the frame of the IERS (International Earth Rotation and Reference System Service)

1 Introduction

At its 23rd General Assembly in August 1997, the International Astronomical Union (IAU) decided that starting from 1 January 1998, the IAU celestial reference system shall be the International Celestial Reference System (ICRS), in replacement of the FK5 (Fricke et al. 1988). The ICRS is accessible by means of coordinates of reference extragalactic radio sources (Arias et al. 1995), the International Celestial Reference Frame (ICRF). The ICRS complies with the conditions specified by the 1991 IAU Recommendations. Its origin is located at the barycenter of the solar system through appropriate modelling of VLBI observations in the framework of General Relativity. Its pole is in the direction defined by the conventional IAU models for precession (Lieske et al. 1977) and nutation (Wahr 1981). Its origin of right ascensions was implicitly defined by fixing the right ascension of 3C 273B (see Arias et al. (1995) for more details).

2 The activities of the ICRS Product Centre

In the following we present the various activities of the ICRS Product Centre of the IERS which is hosted both by the SYRTE at Paris Observatory and by the US Naval Observatory (Washington DC). It has two directors, one from each institution, presently R. Gaume(USNO) and J. Souchay (SYRTE), and the sharing of tasks is shared among the two institutions. They can be listed as in the following (for full bibliography, see IERS Annual report 2006, 2007).

2.1 Reference system and frame

• **Maintenance and extension of the ICRF**

We publish extensions to the ICRF consistent to the currently adopted ICRF, e.g. without changes in the positions of the 212 defining sources representing the core sources of the ICRF (Ma et al. 1998). Moreover we compare on a regular basis the VLBI catalogues of quasars obtained by different networks.

• **Investigation of future VLBI realizations of the ICRS**

Fundamental revisions to the ICRF will occur only when improvements in the quantity of data, together with modeling and data analysis strategies are sufficient to justify a complete reconstruction of the standard frame. The responsability for this decision lies with the appropriate IAU and IVS groups of experts, of which four reserchers of the ICRS PC at the SYRTE are members.

[1] SYRTE, Observatoire de Paris, 61, av. de l'observatoire, 75014 Paris
[2] BIPM
[3] Observatoire de Besançn
[4] Observatorio Nacional/MCT, Rio de Janeiro // Observatorio do Valongo;UFRJ, Rio de Janeiro

• **Investigation of future non VLBI realizations of the ICRS**
Future astrometric satellite missions such as J-MAPS, SIM and GAIA, may provide fundamental reference frames more accurate than the current VLBI-based ICRF. Members of the ICRS Product Centre have direct ties to these programs, and are in a unique position to study these prospective reference frames.

2.2 Extragalactic radio-sources

• **Monitoring of structure to assess astrometric quality**
The task of imaging the sources (essentially quasars) from VLBI observations and evaluating their astrometric quality is shared between the USNO and Bordeaux observatory.
• **Maintenance of the time stability of the ICRF** Members of the SYRTE adress the time stability of the celestial reference frames and the effect on geodetic products. To do so they provide the time variation of the sources astrometric coordiantes (Lambert & Gontier 2008)

2.3 Link of other reference frames to the ICRS

• **Maintenance of the link to Hipparcos catalogue**
The location of Hipparcos axes is an object of particular attention, as well as the effect of Hipparcos proper motion uncertainties On example is the UCAC program which provides a link at the level of 1 mas.
• **Maintenance of the link to the solar dynamical reference frame through millisecond pulsar analysis**
Pulsar timing ia a very accurate way to positioning of the ecliptic with respect to the ICRF. Efforts have been recently developed in the frame of a PPF (Plan Pluri Formation) lead by A. Fienga (Besançon Observatory), in association with the Nancay radiotelescope where plusars are observed in a very regular basis, the SYRTE and the IMCCE (Paris Observatory).
• **Maintenance of the link to the solar system dynamical reference frame through observations of asteroids and planets**
Following the asteroids trajectories with respect to quasars enables one to get direct link between the dynamical system and the ICRF. Studies are done recently in order to make statistics of the close approaches between these two classes of objects and to observe these close approaches with middle size telescopes.
• **Maintenance of the link to the solar system dynamical reference frame through Lunar Laser Ranging analysis** The SYRTE has a long history of analysis of the Lunar Laser Ranging (LLR) observations done at CERGA (Grasse). When combiend with VLBI technique, the LLR technique is one of the most efficients ways to determine the orientation of the planetary reference frame relative to the ICRF. The ICRS PC gather the various data coming from LLR measurements.

3 Discussion and conclusion

Recent studies in the frame of the ICRS Product Centre at the SYRTE-USNO have begun in the scope of the GAIA mission. One of them is the preparation of a Large Quasar Astrometric Catalogue (Souchay et al. 2008), which contains 113 663 objects. It could serve as a kind of input catalogue for GAIA, to make statistics and to cross-identify the objects with the 200 000 quasars or more which will be observed by the astrometric space mission. Another study is the follow-up of the WMAP satellite which is located at the L_2 Lagrange point, as GAIA. Applying the same methods will allow a very accuarte astrometric determination of GAIA

References

Arias, E. F., Charlot P., Feissel M., & Lestrade J.-F. 1995 Astron. Astrophys., 303, p. 604
Fricke, W., Schwan, H., & Lederle, T. 1988: FK5, Part I. Verff. Astron. Rechen Inst., Heidelberg.
IERS Annual report 2006 or 2007, Verlag des Bundesamts fur Kartographieund Geodasie (BKG), Frankfurt, Main
Lieske, J. H., Lederle, T., Fricke, W., and Morando, B.,Astron. Astrophys., 58, pp. 1-16.
Ma, C., & Arias, E.F., Eubanks, M., et al. 1998, AJ116,516
Wahr, J.M., Geophys. J.R. Astron. Soc., 64, 705

SF2A 2008
C. Charbonnel, F. Combes and R. Samadi (eds)

ASTROMETRY WITH GROUND BASED OPTICAL TELESCOPES

Taris, F.[1], Bouquillon, S.[1], Souchay, J.[1], Andrei, A.H.[2] and Albert-Aguilar, A.[1]

Abstract. Astrometry with ground based optical telescopes is a newly developed theme in the SYRTE department of the Paris observatory. It recovers some activities like: - the observation of the WMAP probe with optical telescopes for the future astrometric monitoring of GAIA, - the realization of an ecliptic catalog of quasars (using the CFHT images), - the link between radio and optical positions of quasars. In the case of WMAP we will detail more particularly the observations made with the ESO 2.2 m telescope and with the 105 cm telescope of the Pic du Midi. Our goal is to be able to obtain the position of GAIA on its orbit with an uncertainty of 150m in position and 2.5 mm/s in velocity. For that purpose, the telescope of the Pic du Midi could be used as a main observing station when GAIA will be launch. We will give the firsts results obtain for the astrometric reduction of the images of WMAP obtain with these two telescopes. We also present the CFHT-LS project. We will use the images of the Very Wide survey to realize an astrometric catalog of quasars. The goal of this project is to obtain the position of quasars with an uncertainty around 10mas up to the 25th magnitude. It will permit to densify the GAIA catalog.

1 Introduction

In the domain of astrometry, SYRTE is involved in the realization of the International Celestial Reference Frame (ICRF) which is necessary to know with optimal precision the location of all the bodies in the Universe. One of the tasks consists in establishing the coordinates of quasars as accurately as possible. These quasars are assumed to provide fixed (quasi-inertial) directions in space, which make it possible to determine the coordinates of moving objects: stars in galactic rotation, planets and asteroids rotating around the sun etc... Because of the increasing number of sources in the catalogues of quasars, it is necessary to make their intercomparison as well as the analysis of the extremely accurate observation data obtained by very long baseline interferometry (VLBI) in the radio domain, or by CCD images in the focal plan of large telescopes at optical wavelengths. Another research theme is the link between the International Celestial Reference System and the dynamical system represented by the trajectories of the mobile bodies in the solar system. At SYRTE, the analysis of lunar laser ranging data, of pulsar chronometry, and the use of optical observations lead to the determination of this link.

2 Astrometry with optical telescopes at SYRTE-OP

Since january 2007 a team of SYRTE-OP is particularly involved in the field of astrometry with ground based optical telescopes. Some points of interest are currently under development: - The realization of an ecliptic catalogue of quasars, - the link between the dynamical reference system and the ICRF through the observation of asteroids, - the link between radio and optical positions of quasars and their photometric vs astrometric variability, - the observation of WMAP to prepare the GAIA mission. The two next subsections show the telescopes and softwares used to obtain images and analyse them.

[1] Observatoire de Paris, SYRTE, CNRS UMR 8630, 61 av. de l'observatoire, F75014, Paris, France
[2] Observatorio Nacional/MCT, Observatorio do Valongo/UFRJ, Brasil

2.1 The telescopes

Up to now three ground based optical telescopes have been used to obtain images both for quasars and WMAP. The larger one is the 3.6m optical/infrared telescope TCFH (Telescope Canada France Hawaii). The observatory is located atop the summit of Mauna Kea, a 4200 meter dormant volcano, located on the island of Hawaii (USA). The MEGACAM camera, a set of 36 CCD, was used together with the telescope (see 4.1). The second one is the 2.2m Telescope of the European Southern Observatory at La Silla (Chile). It has been in operation since 1984. The telescope is a Ritchey-Chretien design mounted on an equatorial fork mount. The telescope is at a geographical location of 70d44'4"543 W 29d15'15"433 S and an altitude of 2335 metres. It was used with the Wide Field Imager (WFI), a focal reducer-type camera at the Cassegrain focus and with a field of view of 34'x33'. The last and small one is the 1.05m Telescope of the Pic du Midi (France). It is located in the south-west of France by 42d56'10".9N, 00d08'32".6E and 2877m in altitude. In 1963 that telescope was used in collaboration with the Na tional Aeronautics and Space Administration (NASA) to prepare the Apollo missions for moon landing.

2.2 Tools for reduction/analysis of observations

Softwares used to reduce and analyse images can be devided in two sets. The home made softwares have been built for astrometric reduction, linking of independant CCD of a large camera (MEGACAM, WFI...), quasars identification, differential astrometry. The automatization of these softwares is scheduled for large catalogue realization. The other set is made of known softwares (IRAF or TERAPIX suite, see 4.3). Sextractor, Scamp, Swarp were used to obtain a file with the postion of the detected object on the CCD and to control that the equatorial coordinates obtain by the home made softwares were consistent.

3 WMAP for GAIA

3.1 Preparing the GAIA mission

The requirements, due to astrometric reasons, about the position and velocity of the spacecraft on its orbit are very stringent. It has been shown (Perryman 2005, Mignard 2005) that the uncertainty must be, at most, 150m (20mas) and 2.5 mm/s (1mas/h) respectively. The classic Doppler and ranging techniques can only deliver 6 km and 8 mm/s. To achieve that high level of requirements the only usable technique is the Ground Based Optical Tracking (GBOT). GAIA's location roundabout the L2 Lagrange point is approximately 1.5 million km from the Earth, facing roughly opposite of the sun. It's visual magnitude would be approximately 18 (this value can be off by a hugge amounts). In order to prepare the GBOT of GAIA, the Wilkinson Microwave Anisotropy Probe (WMAP) has been choosen. That probe is also located around the L2 Lagrange point and its magnitude (roughly 19) is very near from the expected magnitude of GAIA. WMAP is then a reasonable model for the brightness and observability of GAIA. The precise astrometric position of WMAP has been provided by Dale Fink, Navigator of WMAP Spacecraft Control Team at NASA.

3.2 ESO 2.2m + WFI

Sebastien Bouquillon (SYRTE-OP), Ricky Smart (INAF/OATo, Torino) and Alexandre Andrei (Observatorio Nacional, Rio de Janeiro) have used the 2.2m telescope of the European Southern Observatory at La Silla, Chile, to take several images of NASA's WMAP satellite in its orbit. Sextractor (Terapix) or Daophot (IRAF) have been used to obtain the (x,y) positions of the sources on the CCD. The standard deviation of the difference between the computed and the observed positions gives the best available information about the standard deviation of WMAP. Results obtained with three independant softwares are given here:

	Home made	TERAPIX	IRAF
Right asc.	70.1mas	70.5mas	69.7mas
Dec.	80.8mas	77.0mas	72.2mas

3.3 T105 Pic du Midi (France)

The astrometric reduction has been done with the same three independant softwares that for the ESO CCD. A plate solution was determined with a second order polynomial in x and y leading to the following residuals:

Time of observ.	sigma(alpha)	sigma(delta)
23h05m33s	64mas	48mas
23h09m00s	65mas	61mas
23h12m25s	65mas	57mas

The results obtain were compared with the theoretical ephemeride supplied by Dale Fink. Moreover the brightness of WMAP has been calibrated with respect to the UCAC2 reference stars (UCAC2 stars are not photometric standards). The results are as follows:

Time of observ.	diff(alpha)	diff(delta)	mag(+/-1sigma)
23h05m33s	21.104"	3.234"	18.620(+/-0.249)
23h09m00s	21.297"	3.141"	18.661(+/-0.257)
23h12m25s	21.530"	3.231"	18.757(+/-0.251)

The difference between the observed position and the ephemeride is relatively large but quite constant. This can be due to the ephemeride itself (constant offset), to the inaccuracy of the position of the telescope (10m), to the time synchronisation of the Pic du Midi (0.1s) or to other effect...

The fluctuation of the magnitude can be explained by the ambient condtions (extremely difficult conditions with light diffusion through clouds, moon's age of 11 and bad seeing). The rapid changes in object brightness due to varying illumination of spacecraft must also be taken into account.

4 The CFHT-LS

Canada and France have joined a large fraction of their dark and grey telescope time for a large project, the Canada-France-Hawaii Telescope Legacy Survey (CFHTLS). More than 450 nights over 5 years will be devoted to the survey using the wide field imager MegaPrime equipped with MegaCam. The three main entities serving the Canadian and French communities are 1) the CFHT for the data acquisition, pre-processing and calibration, 2) the Canadian Astronomy Data Centre (CADC) for all activities related to the archiving and release of the various data products to the communities, and 3) Terapix (based in Paris) for the data ressampling and stacking, fine astrometric calibration, and source catalogs generation.

4.1 TCFH-MEGAPRIME/MEGACAM

The telescope itself has been described above (see 2.1). MegaPrime is the wide-field optical imaging facility at CFHT. The wide-field imager, MegaCam (built by CEA, France), consists of 36 2048 x 4612 pixel CCDs (a total of 340 megapixels), covering a full 1 degree x 1 degree field-of-view with a resolution of 0.187 arcsecond per pixel to properly sample the 0.7 arcsecond median seeing offered by the CFHT at Mauna Kea. The new prime focus upper end includes an image stabilization unit and a guide/autofocus unit with two independent guide CCD detectors.

4.2 CADC

The Canadian Astronomy Data Centre (CADC) serves the Canadian and French communities for all activities related to the archiving and release of the various data products.

4.3 Terapix

TERAPIX (Traitement Elementaire, Reduction et Analyse des PIXels de megacam) is an astronomical data reduction centre dedicated to the processing of extremely large data flows from digital sky surveys. TERAPIX is located at IAP (Institut d'Astrophysique de Paris). Its primary tasks are: - to develop image processing and pipeline software for MegaCam; - to develop and provide tools for handling of large CCD images; - to operate the final reduction pipeline to produce calibrated images and catalogues of MegaCam images over the next 5 years; - to provide technical assistance and computing facilities for MegaCam and WIRCam users.

4.4 The three surveys

The Canadian and French scientific agencies have decided to set up the CFHTLS observational program. It consists of three observational programs: - The CFHT-LS "very wide": 1300 square degrees over the ecliptic area and focussed on the Trans-Neptunian and Kuiper Belt observations. - The CFHT-LS "wide": covering 170 square degrees over three large fields located at high galactic latitude, in "dust-free" areas of the sky. The wide survey will be focussed on large-scale structure of the Universe, cosmological weak lensing, clusters of galaxies, quasars as well as stellar proper motions in the Galaxy. - The CFHT-LS "deep": covering four uncorrelated 1 square degree patches (i.e., one MegaCam field) in "dust-free" areas of the sky. The deep survey will be optimised for the detection of light-curve measurements of Type Ia supernovae and the study of very high redshift galaxies.

5 Observations with TCFH

Six of the QSO quasars densest (on average 25 QSOs up to R=21) SDSS DR5 regions were selected for two band optimum photometry observation using MEGACAM to obtain the largest at this date, statistically significant and coherent sample of the magnitude, size, and astrophysics of the host galaxies of the quasars. The DR5 regions guarantee a high number of galaxy and stellar comparison objects. In parallel it furnishes ugriz magnitudes for all and spectral information for many ones. Two fields in the ecliptic plane complied the density threshold and will additionally enable one to obtain a direct comparison between the ICRF and the dynamical system represented by field asteroids. Bright cusps on the GAIA QSOs PSF will give rise to astrometric jitter. This program will give practical templates and constraints for the definition of the QSO Initial Catalogue for GAIA. The detailed luminosity profile of the host galaxy so obtained can be combined to the DR5 data in order to contribut e to the understanding of their morphology, star formation history and dust distribution. The observations of the semester 08A obtained at TCFH are up to now under investigation.

Other observations in the public domain will be used to transfer the astrometric precision of the GAIA catalogue to faint objetcs, up to the 25th magnitude, in the ecliptic fields, with the help of the CFHT-LS VW survey. In return it will permit us to densify the GAIA catalogue.

6 Conclusion

Since january 2007 a team of SYRTE-OP is particularly involved in the field of astrometry with ground based optical telescopes

In the frame of the GBOT-GAIA, first observations of WMAP have been done with the 2.2m ESO and 1.05m Pic du Midi telescopes. For that late telescope we propose to use it as a main observing station when GAIA will be launched. Preliminary results show that it is possible to obtain the postion of WMAP with the uncertainty of the UCAC2 stars. Hence when the GAIA early-catalogue will be accessible to the GBOT community the uncertainty about the GAIA position could be better than 20 mas. It will permit to reach the very stringent requirements of the GAIA mission.

Observations of the CFHTLS will be used to transfert the astrometric precision of the GAIA catalog for faint objects, up to the 25th magnitude, in the ecliptic fields, with the help of the Very Wide survey. In return it will permit us to densify the GAIA catalog.

References

Perryman, M. 2005, GAIA-CA-TN-ESA-MP-012-2

Mignard, F. 2005, GAIA-FM-023

Andrei, A. H., et al. 2008, these proceedings

SF2A 2008
C. Charbonnel, F. Combes and R. Samadi (eds)

GAIA IN THE EUROPEAN CONTEXT

Turon, C.[1]

Abstract. The ESA Gaia mission is placed in the context of the European and worldwide astronomy: What are its main characteristics? What is its place within the ESA Cosmic Vision? What is its place within the Astronet roadmap context? Which actions should be supported or started for taking full benefit of this ambitious mission?

1 Introduction

In the early 90's, the unprecedented success of Hipparcos (see for example Lindegren et al. 1994; Perryman et al. 1995; Perryman et al. 1997) showed how powerful space was for astrometry and what a powerful tool for astrophysics was high accuracy astrometry, and first ideas on how a future astrometry mission could be enhanced with respect to Hipparcos were already discussed. These were including much higher astrometric accuracy, a much larger number of objects observed systematically down to a fainter magnitude, and the possibility to have the radial velocity and an astrophysical characterisation of the observed objects obtained on-board, in parallel with the astrometric measurements. Within the frame of ESA's *Horizon 2000 Plus* long-term scientific programme, a proposal was made for a new mission, Gaia, able to reach 10 μarcsecond accuracy on positions, trigonometric parallaxes and annual proper motions for some 50 millions stars down to magnitude 15, along with multi-colour multi-epoch photometry of each object (Lindegren & Perryman 1996). The mission finally included in the ESA Science programme in October 2000 is still much more ambitious (Perryman et al. 2001), with the goal to produce a stereoscopic and kinematic census of about one billion stars, down to magnitude 20, throughout our Galaxy, and into the Local Group.

2 The Gaia mission

Gaia, planned to be launched by the end of 2011, is a unique mission thanks to several of its principles: unprecedented astrometric accuracy; three complementary instruments on board, providing parallel astrometric, photometric and spectroscopic observations, i.e. a complete characterisation of the billion objects which will be observed; a largely uniform scanning of the sky surveying all stellar populations over the whole part of the Galaxy observable at optical wavelengths; an on-board systematic detection of all objects down to magnitude 20 (Solar System objects, stars, galaxies, QSOs); a regular sampling over the five years of mission, leading to about 80 observations per object, which will allow photometric and spectroscopic variability analysis and orbit determination for double and multiple stars, giant planets and Solar System objects; global absolute astrometry with extreme accuracy, providing absolute parallaxes for stars of all spectral types, evolutionary status and populations, and absolute proper motions for stars up to the brightest parts of the nearest galaxies of the Local Group. The only parts of the Galaxy which will be poorly observed by Gaia are zones with very heavy extinction in the bulge or some parts of the disc.

The comparison with the Hipparcos performance (Perryman et al. 1997; van Leeuwen & Fantino 2005) gives a flavour of the giant step which will be achieved with Gaia (Perryman et al. 2001): number of stars (1 billion versus 118 000), limiting magnitude (20 versus 12.4), astrometric accuracy (best expected accuracy of 8 μarcsecond for stars brighter than 13 versus 0.2 mas for stars brighter than 5; 0.2 mas accuracy at magnitude 20), astrophysical characterisation (multi-colour photometry down to magnitude 20 and spectra

[1] Observatoire de Paris, GEPI, CNRS UMR 8111, 92195 Meudon, France

down to magnitude 16.5 versus 2 colours down to 12.4), observing programme (on-board systematic detection down to magnitude 20 versus preliminary ground-based star selection). In addition, the sixth dimension in the space parameter, the radial velocity, will be measured on-board for stars brighter than 16.5, in parallel with astrometric and photometric observations. Some 10 million stars will have their distances known to 1%, 100 million to 10% (to be compared with 21 000 with Hipparcos); the photometric accuracy of each of the $\sim$ 80 observations of a star brighter than V=15 will be of a few milli-magnitudes in several colours; the radial velocity of stars brighter than 15 will be measured to better than 1 $km.s^{-1}$; for stars brighter than G=16, the effective temperature will be obtained to better than 5%, their gravity ($\log g$) to 0.2-0.3, their metallicity to 0.2-0.4.

Thanks to this variety of observations, Gaia will contribute to many domains in astronomy: complete census of a large proportion of the Galaxy; characterisation of all stellar populations, both in the Galaxy itself and in the brightest parts of the nearest galaxies of the Local Group; dynamical and chemical evolution of the Galaxy; dynamics of the Galaxy and the Local Group, with a much better knowledge of the distribution of the dark matter at small and large scales; distance scale determination, using various distance candles, and impact on H_0; determination of the PPN parameter γ; stellar structure and evolution; stellar variability; complete census, orbital improvement, and taxonomy of Solar System objects; etc. Finally, it will provide a systematic selection of many specific objects (very metal poor stars, stellar groups and streams, variable stars, double stars or stars with planets, etc.etc.); the distinction between foreground Galactic stars and bright stars in dwarf spheroidal neighbours; the systematic detection of relativistic effects; etc.

3 Gaia within the international and European context

International context

Europe has been a pioneer in developing and launching a satellite entirely dedicated to high accuracy astrometric measurements. The dramatic success of Hipparcos (more than 5000 papers are using its data by mid-2008, among which nearly 2000 refereed) stimulated numerous proposals for similar missions in several countries (Russia, USA, Germany, Japan, Europe). At the moment, only a few are still considered or in development:

- JASMINE (Japan Astrometry Satellite Mission for INfrared Exploration, not totally funded) would be the ideal complement to Gaia as it will operate in the 0.9 μm z band. Thereby it will be able to observe deeply in the Galactic centre, the bulge and parts of the disc (not possible with Gaia because of heavy extinction and crowding) with astrometric accuracies similar to Gaia (Gouda et al. 2008). A nano-size satellite (5-cm telescope, 14 kg), Nano-JASMINE, is also being developed in Japan (Kobayashi et al. 2008).

- SIM PlanetQuest (Space Interferometry Mission, NASA-JPL) is a project for an optical interferometer. The goal is to measure the position, trigonometric parallax and proper motion of stars with an accuracy of 4 μas down to magnitude 20 (Shao, 2008). A SIM-Light mission is under consideration.

- J-MAPS micro-satellite to be launched by 2011 (15-cm telescope), aim at re-observing all Hipparcos stars (as well as virtually all other stars down to around 14th magnitude) with an accuracy of 1 mas down to 12th magnitude and with reduced accuracy down to 15th magnitude (USNO, Dorland & Gaume 2007).

Gaia in the ESA context

In the last ten years, there has been a festival of Solar System missions launched in the frame of the ESA Science Programme: Soho (Solar observations, with NASA, 1995), Cassini-Huygens (to Saturn and Titan, NASA-ESA, 1997), Cluster (magnetosphere observations, 2000), Mars Express (to Mars, 2003), Smart (to the Moon, 2003), Double-Star (magnetosphere observations, Chinese satellite with ESA collaboration, 2003), Rosetta (to comet Churyumov-Gerasimenko, 2004), Venus Express (to Venus, 2005). The next launches are Chandrayaan-1 (to the Moon, an Indian satellite with ESA collaboration) and Bepi-Colombo (to Mercury, with JAXA, 2013).

The astronomy missions in operation are Hubble (NASA-ESA, 1990), XMM-Newton (observations in X-rays, 1999), and Integral (observations in γ-rays, with Russia, 2002). In addition, ESA is involved in two collaborative missions: AKARI (observations in the IR, JAXA, 2006), and Corot (stellar seismology, exo-planets, CNES, 2006). Herschel (far-IR and sub-mm observations to observe star and galaxy formation) and Planck (map of the Cosmic Microwave Background anisotropies) will be launched in 2009. Gaia is then the only astronomy mission to be launched before JWST (NASA-ESA, 2013).

Four major questions were identified in the **ESA Cosmic Vision 2015-2025** (Bignami el al., 2005): What are the conditions for planet formation and the emergence of life? How does the Solar System work? What are the fundamental physical laws of the Universe? How did the Universe originate and what is it made of? With its unique capability of surveying all stellar populations, over the whole Galaxy, Gaia will be a major contributor to the first steps of the first and last questions:

- From gas and dust to stars and planets. What are exoplanets and which stars have them?
  Gaia will provide unprecedented and complete information on stars of all spectral types, even the rarest, and all evolutionary stages, even the fastest: luminosities, motions, ages, duplicity and chemical characterisation. This will give a detailed picture of which stars form and have been formed where, in each of the component of the Galaxy. Gaia will also make a systematic census of giant planets, delivering insights into the frequency of giant planets as a function of the characteristics of their host stars and their locations in the Galaxy. This will give unique information about the conditions which favour the formation of planets. In addition, since the presence and location of one or several giant planets may severely affect the formation of smaller planets in a system, GAIA will provide important information on the likelihood of finding Earth-like planets orbiting their stars in the habitable zone.
- The Universe taking shape.
  Gaia will bring major inputs to the understanding of the formation and history of our own Galaxy by combining positional, kinematics and chemical information: tests of hierarchical structure formation theories and star formation history; detection of disrupted star clusters and satellite debris; firm establishment of the relations between ages, metallicity and kinematics; determination of the dynamical interactions between the bar and the bulge, the disc and the halo, the disc and the warp; etc. It will also provide insights in the distribution of invisible mass, both in our Galaxy and in the Local Group, with an improved determination of galaxy orbits. Finally, the Galaxy will be described in such exquisite detail that it will be possible to use it as a template for the interpretation of observations of external galaxies.

Gaia and ASTRONET Science Vision

ASTRONET was created to develop a comprehensive strategic plan for European astronomy covering the ambitions of all of astronomy, ground and space, and to establish the most effective approach towards answering the highest priority scientific question. The first step was the development of a *Science Vision* identifying the key astronomical questions which may be answered in the next twenty years by a combination of observations, simulations, laboratory experiments, interpretation and theory (de Zeeuw et al. 2007). Four key questions were identified where significant advances and breakthroughs can be expected in the coming two decades: Do we understand the extremes of the Universe? How do galaxies form and evolve? What is the origin and evolution of stars and planets? How do we (and the Solar System) fit in? The recommendations distinguish essential facilities, without which a certain scientific goal simply cannot be achieved, and complementary ones, which would go a long way towards answering the question, but may have their main scientific driver elsewhere.

In this frame, Gaia was considered as an *essential* facility for two main questions:

- How do galaxies form and evolve? Obtain a complete history of our Galaxy early formation and subsequent evolution.
- What is the origin and evolution of stars and planets? Understand the formation and mass distributions of single, binary or multiple stellar systems and stellar clusters. Unveil the mysteries of stellar structure and evolution, also probing stellar interiors. Explore the diversity of exo-planets, in relation with the characteristics of their host stars.

Gaia was also considered as a *complementary* facility for

- How do we fit in? Dynamical history and the composition of trans-Neptunian objects, asteroids and comets.

4 Gaia in 2012

Gaia will provide a huge quantity of unique data which, in addition to being used for themselves, will help the interpretation of many other data: by making our Galaxy a template for the interpretation of external galaxies observed by JWST, VLT, ELT, XEUS, etc; by providing an unprecedented luminosity calibration for all stellar types from all stellar populations, further observed by the VLT, ELT, JWST, etc; by providing the 3^{rd} dimension and 3-D kinematics to stellar formation areas observed by Herschel, Planck, and Alma; by providing an extremely accurate determination of the PNN parameter γ to be compared with the future results of LISA.

With a systematic census down to magnitude 20 and a complete characterisation of all observed objects, Gaia will be a fantastic tool to select well defined samples in targeted populations, to be further observed with other instruments. Powerful high spectral resolution spectrographs on JWST, VLT, ELT, etc. could be used to study in detail the chemical abundances of statistically significant samples selected from Gaia data: halo stars in a well defined volume; thin and thick disk samples at different distances from the Galactic plane and at different Galacto-radius; stars in streams; stars of a given metallicity; stars in a very rapid evolutionary phase. Gaia will also be able to make systematic statistics of planetary formation versus stellar type, and identify nearby systems with planets, to be further observed in more detail with JWST, ELT, SIM, Darwin, TPF, etc. Last example, Gaia will systematically observe a huge number of asteroids, further targets for observations over longer periods of time, in order to cover larger parts of their orbits.

It is then essential to get prepared for, and in some cases to start in anticipation, these ground-based observations, which will make the difference in the exploitation of Gaia data: spectroscopic observations of exoplanets detected by their astrometric motion; detailed element abundances for unbiased stellar samples; follow-up observations of variable stars, orbital systems, asteroids; etc. The other aspect is to consider spectroscopic and radial velocity observations in complement to those of Gaia for stars fainter than V=16.5, for example for halo streams, spiral arms, substructures in the disc or bulge, kinematics in the Local Group, etc.

5 Conclusion

Gaia is planned for launch by the end of 2011, the publication of the final catalogue for 2020. However, some intermediate publications may be expected, especially for photometric and spectroscopic data. To take full advantage of the investment made in the preparatory work on Gaia, and take a leading position in the exploitation of these unique data, thoughts and work have to be devoted *from now on* on several aspects: the development of new statistical methods to use such a mass of data, the improvement of theories and modelling of the Galaxy dynamical and chemical behaviour, the choice of the best methods to use Gaia data for the definition of the optical reference system, the definition - and organisation - of the most adapted follow-up and complementary ground-based or space observations. Finally, in addition to the future use of already existing instrument, it would be extremely valuable to define a multi-object wide-field spectrograph, able to observe simultaneously a few thousands stars, well suited for follow-up and complementary observations of Gaia selected samples. This is supported by the recommendations of the ASTRONET Infrastructure Roadmap (Bode et al. 2008) and by ESA-ESO Working Group Report on Galactic science (Turon et al. 2008). The French - and European - community put a major effort in the preparation of the Gaia data processing. Let us be in the best position to use these data in the many domains where it will provide a complete renewal of the observational basis.

References

ASTRONET Science Vision 2007, *A Science Vision for European Astronomy*, de Zeeuw P.T. & Molster, F.J. (eds)
Bignami, G.F., Cargill, P.J., Schutz, B., & Turon, C., 2005, Cosmic Vision, ESA BR 247, A. Wilson ed.
ASTRONET Infrastructure Roadmap 2008, Bode, M. & Cruz, M. (eds)
Dorland, B.N. & Gaume, R.A. 2007, AIAA Space 2007 Conf., 18-20 sept. 2007, AIAA 2007-9927
Gouda, N., Kobayashi, Y., Yamada, Y., et al. 2008, IAU Symp., 248, 248
Kobayashi, Y., Gouda, N., Yano, T., et al. 2008, IAU Symp., 248, 270
Lindegren, L., Kovalevsky, J., Høg, E., Turon, C. & Perryman, M.A.C. 1994, ESA Bull., 77, 42
Lindegren, L., & Perryman, M.A.C. 1996, A&A Suppl., 116, 579
Perryman, M.A.C., Lindegren, L., Kovalevsky, J., et al. 1995, A&A, 304, 69
Perryman, M.A.C., Lindegren, L., Kovalevsky, J., et al. 1997, A&A, 323, L49
Perryman, M.A.C., de Boer, K.S., Gilmore, G., et al. 2001, A&A, 369, 339
Shao, M. 2008, IAU Symp., 248, 231
Turon, C., Primas, F., Binney, J., et al. 2008, ESA-ESO Working Group Report on Galactic science
van Leeuwen, F., & Fantino, E. 2005, A&A, 439, 791

SF2A 2008
C. Charbonnel, F. Combes and R. Samadi (eds)

GALACTIC KINEMATICS FROM RAVE TO GAIA-RVS DATA

Veltz, L.[1], Bienaymé, O.[2], Steinmetz, M.[1], Zwitter, T.[3], Watson, F. G.[4], Binney, J.[5], Bland-Hawthorn, J.[6], Campbell, R..[1], Freeman, K. C.[7], Gibson, B.[8], Gilmore, G.[9], Grebel, E. K.[10], Helmi, A.[11], Munari, U.[12], Navarro, J. F.[13], Parker, Q. A.[14], Seabroke, G.[15], Siebert, A.[2], Siviero, A.[12,1], Williams, M.[1] and Wyse, R. F. G.[16]

Abstract. RAVE data has provided new results on Galactic kinematics like the kinematical decomposition of the Galactic disk. This decomposition permits to identify the different components of the disk and to characterize them in terms of scale height and scale length. With the data provided by Gaia and in particular the RVS, we will have a completly renewed view of the Galaxy. The precision of the RVS will permit to undertake a precise analysis of the kinematics of the Galactic disks. This knowledge will provide significant clues to constrain the scenarios of the Galactic disk formation.

1 Introduction

The hierarchical formation scenario is a great success in describing the formation of the large-scale structure of the universe. But, the detailed mechanisms of formation of individual galaxies are still an open question. Some answers to this question rely on the knowledge of the position, the kinematics and chemical composition of the stars of the Milky Way. Therefore, in 2000, ESA has approved the Gaia mission that will provide the 6-D (position-velocity) information for 50 millions stars in the Galaxy. The expected launch of the Gaia satellite is planned for 2011. As a precursor in the spectroscopic area, an international cooperation called "RAdial Velocity Experiment" (RAVE) has started in 2003 a survey of one million stars in the southern sky hemisphere (Steinmetz 2003). There has been already two data releases. The first release contains about 25 000 radial velocity measurements (Steinmetz et al. 2006). The second data release contains about 25 000 radial velocity measurements more and 20 000 stars for which the stellar parameters ($[M/H]$, $\log g$, $T_{\rm eff}$) have been determined (Zwitter et al. 2008). The spectroscopic acquisition techniques differ between RAVE and the Gaia Radial Velocity Spectrometer (RVS), although they have almost the same resolution and wavelength range.

[1] Astrophysical Institute Potsdam, An der Sternwarte 16, 14482 Postdam, Germany
[2] Observatoire Astronomique de Strasbourg, 11 rue de l'Universit, 67000 Strasbourg, France
[3] University of Ljubljana, Department of Physics, Jadranska 19, 1000 Ljubljana, Slovenia
[4] Anglo-Australian Observatory, Coonabarabran, NSW 2357, Australia
[5] Rudolf Peierls Centre for Theoretical Physics, 1 Keble Road, Oxford, UK
[6] School of Physics, University of Sydney, NSW 2006, Australia
[7] Research School of Astronomy & Astrophysics, Mount Stromlo Observatory, Cotter Road, Weston ACT 2611, Australia
[8] Centre for Astrophysics, University of Central Lancashire, Preston, UK
[9] Institute of Astronomy, University of Cambridge, Madingley Road, Cambridge, UK
[10] Astronomisches Rechen-Institut, Zentrum für Astronomie der Universität Heidelberg, Mönchhofstrae 12-14, 69120 Heidelberg, Germany
[11] Kapteyn Astronomical Institute, University of Groningen, P.O. Box 800, 9700 AV Groningen, Netherlands
[12] Osservatorio Astronomico di Padova - INAF, Sede di Asiago, 36012 Asiago, Italy
[13] Department of Physics and Astronomy, University of Victoria, P.O.Box 3055, Victoria, Canada
[14] Department of Physics, Macquarie University, NSW 2109, Australia
[15] Planetary & Space Sciences Research Institute, The Open University, Milton Keynes, UK
[16] Department of Physics and Astronomy, Johns Hopkins University, 3400 N. Charles Street, Baltimore, USA

The RAVE spectra are obtained with the multi-fiber spectrograph 6dF (Watson et al. 2000) on the UK Schmidt telescope at the Anglo-Australian Observatory. Each field is observed during five exposures of 600 seconds. The RVS is an integral field instrument on board of the Gaia satellite that will not use fibers (Katz et al. 2004). The observation will be done in a time delay integration scan mode. Each spectrum will be exposed for 4 seconds.

The 6dF spectrograph and RVS are medium resolution instruments with $R = 7500$ and 11500, respectively. The spectra have a near infrared wavelength range between [8470 - 8740] Å for Gaia-RVS and [8410 - 8795] Å for RAVE. This wavelength range and resolution have three main advantages (Munari 1999, 2003). They present the lowest possible contamination by telluric absorptions that will facilitate the pre- and post- Gaia mission observations from the ground. According to the Galaxy model, the largest number of stars that will be observed by Gaia will have an energy distribution that peaks in this wavelength range due to their spectral type or the interstellar extinction. In this wavelength range, the presence of the CaII triplet lines for cool stars, the Paschen lines for hot stars and metallic lines will be useful to determine accurately radial velocity and chemical abundances.

2 A model of Galactic kinematics

In order to analyze the spectroscopic data in combination with the photometric information and proper motion, we have developed a self-consistant model of the Galactic disk. The disk is describe as sum of 20 isothermal stellar components with a vertical velocity dispersion σ_{zz} ranging from 10 to 70 km.s^{-1}. The distribution function of each component is built from three elementary functions describing the vertical density ρ_i, the kinematic distribution f_i (3D-gaussians) and the luminosity function ϕ_{ik}.

We define $\mathcal{N}(z, V_R, V_\phi, V_z; M)$ to be the density of stars in the Galactic position-velocity-absolute magnitude space:

$$\mathcal{N} = \sum_{ik} \rho_i(z) f_i(V_R, V_\phi, V_z) \phi_{ik}(M), \tag{2.1}$$

where the index i differentiates the stellar components and the index k the absolute magnitudes used to model the luminosity function.

We insert this model in the generalized equation of stellar statistics giving:

$$A(m, \mu_l, \mu_b, V_r) = \int N(z, V_R, V_\phi, V_z; M)\, z^2\, \omega\, dz. \tag{2.2}$$

To determine $A(m)$, the apparent magnitude count, together with the marginal distributions of the proper motion μ_l and μ_b and the distributions of radial velocities for any direction and apparent magnitudes.

Assuming the stationarity of the density distribution, the consistency between the vertical velocity $\sigma_{zz,i}$ and density $\rho_i(z)$ distributions for each stellar component i is ensured by the following expression:

$$\rho_i(z) = \exp\left(-\Phi(z)/\sigma_{zz,i}^2\right) \tag{2.3}$$

where $\Phi(z)$ is the vertical gravitational potential at the solar Galactic position.

For the vertical gravitational potential, we use the recent determination obtained by Bienaymé et al. (2006). The vertical potential is defined at the solar position by:

$$\Phi(z) = 4\pi G \left(\Sigma_0 \left(\sqrt{z^2 + D^2} - D\right) + \rho_{\rm eff}\, z^2\right)$$

with $\Sigma_0 = 48\,\mathrm{M}_\odot\,\mathrm{pc}^{-2}$, $D = 800\,\mathrm{pc}$ and $\rho_{\rm eff} = 0.07\,\mathrm{M}_\odot\,\mathrm{pc}^{-3}$.

The kinematical model is given by shifted 3D gaussian velocity ellipsoids. For simplicity, we assume that the $\sigma_{RR}/\sigma_{\phi\phi}$ ratio is the same for all the stellar components. The velocity ellipsoids are inclined along the Galactic meridian plane. The main axis of velocity ellipsoids are set parallel to confocal hyperboloids as in Stäckel potentials. The focus is set to z_{hyp}=6 kpc on the main axis giving them realistic orientations (see Bienaymé 1999).

The luminosity function of each stellar component is modeled with n different kinds of stars according to their absolute magnitude:

$$\phi_i(M) = \sum_{k=1,n} \phi_{ik}(M) = \frac{1}{\sqrt{2\pi}\sigma_M} \sum_{k=1,n} c_{ik}\, e^{-\frac{1}{2}\left(\frac{M-M_k}{\sigma_M}\right)^2}$$

where c_{ik} is the density for each type of star (index k) of each stellar component (index i).

3 Results

We have have adjusted the density of each stellar component to a sample of stars extracted from the 2MASS catalogue for the photometric data, the UCAC2 catalogue for proper motion and RAVE for the radial velocity. These stars are selected in color with J-K = [0.5-0.7]. In this color interval, we have defined 4 types of stars: Stars with a mean absolute magnitude $M_{\rm K} = -1.61$ are identified to be the red clump giants ($k = 1$), with $M_{\rm K} = -0.89$ and $M_{\rm K} = -0.17$ are first ascent giants stars ($k = 2-3$) and with $M_{\rm K} = 4.15$ for dwarfs ($k = 4$). We neglected sub-giant populations with an absolute magnitude $M_{\rm K}$ between 0.2 and 2. We adopt $\sigma_M = 0.25$ for each kind of stars on the luminosity function.

Adjusting the Galactic kinematical model to star counts, proper motions and radial velocities histograms, we obtained a kinematical decomposition of the Galactic disk (Fig. 1 left). The kinematical decomposition exhibits three main structures. We propose to identify the first one with vertical velocity dispersion σ_W = [10-25] km s^{-1} with the thin disk, the second with σ_W = [30-45] km s^{-1} with the thick disk. The decomposition shows a clear separation between the thin and thick components. For the third component with σ_W = [60-70] km s^{-1}, the kinematical information is missing. This component could be a 'hot' kinematically thick disk or the halo.

From the kinematical decomposition, the scale height of the thin and thick disk could be determined independently by fitting an exponential on the density $\rho(z)$ (Fig. 1 right). We find a scale height for stellar components with σ_W = [10-25] km s^{-1} (thin disk) of 225±10 pc, for stellar components with σ_W = [30-45] km s^{-1} (thick disk) of 1048±36 pc and the density ratio of thick to thin disk stars to be 8.7% at z=0 pc. Our values are in agreement with previous determinations like the ones of Cabrera-Lavers et al. (2005) who have obtained a scale height of 267±13 pc and 1062±52 pc for the thin and thick disks respectively.

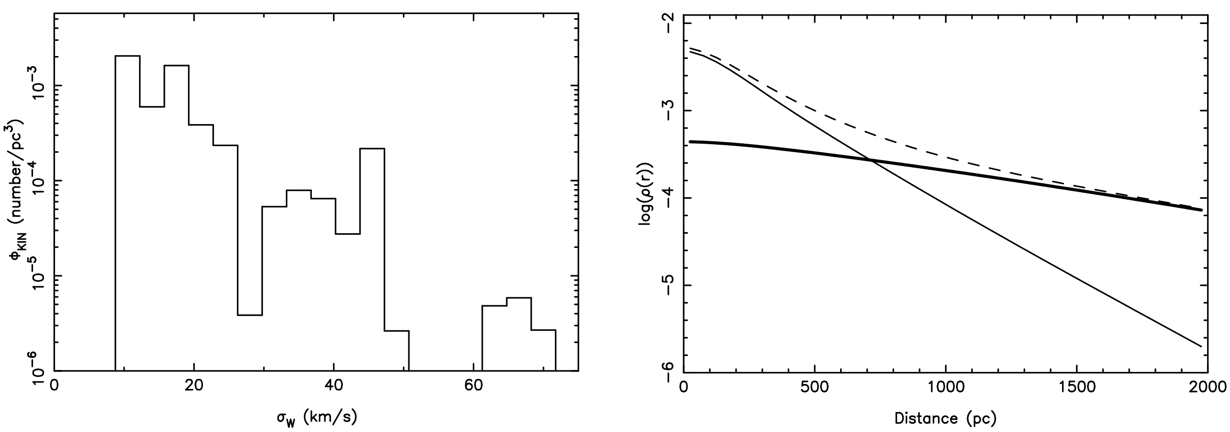

Fig. 1. Left: Kinematical decomposition of the Galactic disk. **Right:** The logarithm of the vertical stellar density $\rho(z)$ towards the the North Galactic Pole (dashed line) and its thin and thick disk decomposition (respectively thin and thick lines).

From our model, the solar motion relative to the LSR and the asymmetric drift were also determined. We obtained a value of $u_\odot$=8.5±0.3 km s^{-1}, $w_\odot$=11.1±1.0 km s^{-1} and a thick disk lag is $V_{\rm lag}$ = 33±2 km s^{-1} relative to the LSR. $v_\odot$ was fixed to = 5.2 km s^{-1}, otherwise we could not measure the asymmetric drift.

By looking at latitude $|b| > 20°$, we measure a radial scale length of 2.5±0.4 kpc for the thin disk and 3.5±1.0 kpc for the thick disk. There is no consensus on the values of the scale length of the values of the scale length of the thin and thick disk, but our values are in relative agreement, for example, with Ojha (2001) who finds 2.8±0.3 kpc for the thin disk and $3.7^{0.8}_{-0.5}$ kpc for the thick disk.

4 Conclusions

The fact that the decomposition of the Galactic disk reveals the kinematical separation of the thin and the thick disk puts some constraints on the scenarios of the Galactic disk formation. The thick disk could not have been created by a continuous 'heating' mechanism like the diffusion due to molecular clouds or spiral arms.

The scientific use of the RAVE data has already permitted us to obtain a lot of results on Galactic structure and kinematics: constrains on the local Galactic escape speed (Smith et al. 2007), absence of the Sgr stream near the Sun (Seabroke et al. 2008), scale height of the thin and thick disk (Veltz et al. 2008), vertical tilt of the ellipsoid (Siebert et al. 2008). With the accuracy and number of stars that will be observed by Gaia, the future is very promising for the analysis of the structure and kinematics of the disk. All these new informations will help to improve our understanding of the formation and evolution not only of the Milky Way but also the galaxies in general.

Acknowledgments

Funding for RAVE has been provided by the Anglo-Australian Observatory, by the Astrophysical Institute Potsdam, by the Australian Research Council, by the German Research Foundation, by the National Institute for Astrophysics at Padova, by The Johns Hopkins University, by the Netherlands Research School for Astronomy, by the Natural Sciences and Engineering Research Council of Canada, by the Slovenian Research Agency, by the Swiss National Science Foundation, by the National Science Foundation of the USA, by the Netherlands Organisation for Scientific Research, by the Particle Physics and Astronomy Research Council of the UK, by Opticon, by Strasbourg Observatory, and by the Universities of Basel, Cambridge, and Groningen.
The RAVE web site is at http://www.rave-survey.org.

References

Bienaymé, O. 1999, A&A, 341,86

Bienaymé, O., Soubiran, C., Mishenina, T. V., Kovtyukh, V. V. & Siebert, A. 2006, A&A, 446, 933

Cabrera-Lavers, A., Garzn, F., & Hammersley, P. L. 2005, A&A, 433, 173

Katz, D., Munari, U., Cropper, et al. 2004, MNRAS, 354, 1223

Munari, U. 1999, Baltic Astronomy, 8, 73

Munari, U. 2003, editor, ASPC: "GAIA Spectroscopy: Science and Technology", 298

Ojha, D. K. 2001, MNRAS, 322, 426

Seabroke, G. M., Gilmore, G., Siebert, A., et al. 2008, MNRAS, 384, 11

Siebert, A., Bienaymé, O., Binney, J., et al. 2008, arXiv0809.0615

Smith, M. C., Ruchti, G. R., Helmi, A., Wyse, R. F. G., & Fulbright, J. P., et al. 2007, MNRAS, 379, 755

Steinmetz, M 2003, ASPC: "Gaia Spectroscopy: Science and Technology", 298, 381

Steinmetz, M., Zwitter, T., Siebert, A., et al. 2006, AJ, 132, 1645

Veltz, L., Bienaymé, O.; Freeman, K. C., et al. 2008, A&A, 480, 753

Watson, F. G., Parker, Q. A., Bogatu, G., et al. 2000, Proc. SPIE, 4008, 123

Zwitter, T., Siebert, A., Munari, U., et al. 2008, AJ, 136, 421

SF2A 2008
C. Charbonnel, F. Combes and R. Samadi (eds)

RADIAL VELOCITIES WITH THE GAIA RVS SPECTROMETER

Viala, Y.P.[1], Blomme, R.[2], Damerdji, Y.[3], Delle Luche, C.[1], Frémat, Y.[2], Gosset, E.[3], Jonckheere, A.[2], Katz, D.[1], Martayan, C.[2], Morel, T.[3], Poels, J.[3] and Royer, F.[1]

Abstract. Four different method are used to derive radial velocities from spectra observed by the Gaia Radial Velocity Spectrometer (RVS). They are briefly presented here together with very preliminary results.

1 Introduction

The main aim of the Gaia Radial Velocity Spectrometer (RVS) is to determine the radial velocities of nearly 100 to 200 millions of stars, with an expected accuracy of 1 km/s up to magnitude $V = 13$ and 15 km/s down to $V = 16$. These data will be a very useful tool for kinematics and dynamics studies of our Galaxy.
The Gaia data will be processed and analyzed by an international consortium (DPAC) including ESA and european institutes participating to the mission (Mignard & Drimmel 2007). Within DPAC nine coordination units CU have in charge a specific scientific or management problem. The processing of spectroscopic data provided by the RVS is devoted to CU6. The aim of this paper is to briefly present the work done within the development unit (DU) "Single transit analysis (STA)" in charge of analysing the data obtained during a unique transit of an object through the RVS field of view.

2 Radial velocity determination of single stars during a single transit

Deriving radial velocities of the observed object is an important task of DU STA. We restrict here to radial velocity determination of single stars. Four different algorithms have been developped using Java programming language : i) Cross-correlation between the object spectrum and a template spectrum in direct space, ii) Cross-correlation between the object spectrum and a template spectrum in Fourier space, iii)Cross-correlation between the object spectrum and a template spectrum in Fourier space using the Chelli's method (Chelli 2000), iv) Method of minimum distance between the object spectrum and a series of templates. A detailed escription of these methods can be found in (Viala et al. 2007).
For a given set of astrophysical parameters/magnitude, Monte-Carlo simulations (provided by CU2) led to 1000 spectra differing only by noise realisation but all shifted by 20 km/s. Radial velocities from the series of spectra were derived by the 4 algorithms. As an example, figure 1 shows histograms of the radial velocities for solar type stars of magnitude 8.6, 10.6 and 12.6. The mean value of the distribution slighly differ from 20 km/s : this small bias is due to different slopes of the continuum between the object and the template spectrum. The dispersion of the distribution gives the error on the radial velocity determination. Preliminary error derivations are listed in table 1 for several spectral types.

3 Conclusion

For a single transit and for the three methods discussed, radial velocities can be determined with an fairly good accuracy in the range 1 to 8 km/s down to magnitude $G_{RVS} \leq 14$ for F-G-K spectral types. Accuracies and magnitude limit are much less good for hotter stars (Spectral types O, B and A). Tests have not yet been done for cool M stars. Tentative determination of the projected rotational velocities, using the three algorithms developped within DU STA is planned for a near future.

[1] Observatoire de Paris, GEPI, 92195 Meudon Cedex
[2] Observatoire Royal de Belgique, Avenue circulaire 3, B 1180 Uccle(Bruxelles)
[3] Institut d'Astrophysique et de Geophysique, Universite de Liege, Allee du 6 aout, B-4000 Liege

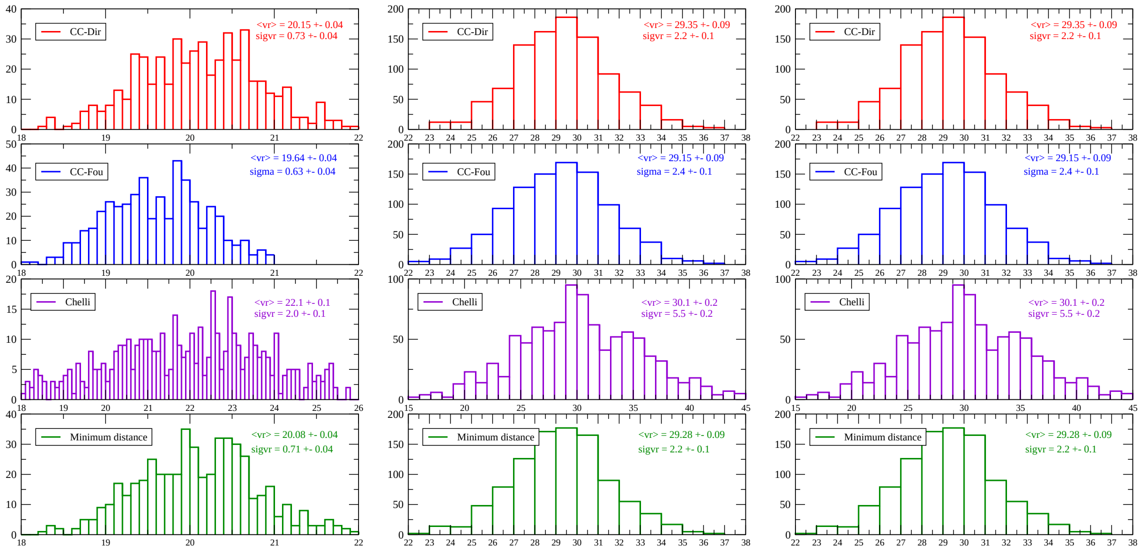

Fig. 1. Histograms derived radial velocities by the 4 algorithms for a G5V star of RVS magnitude 8.6, 10.6 and 12.6

Table 1. Errors from Monte Carlo simulations on radial velocity derivation for single stars of various spectral types

Sp. type	T_{eff}	logg	Fe/H	RVS magnitude	error on vrad in km/s			
					CCDir	CCFou	Chelli	MinDist
K5V	4000 K	4.0	0.0	8.7	0.63	0.63	1.8	0.62
				12.7	7.1	7.5	22.2	7.4
G5V	5500 K	4.0	0.0	8.6	0.73	0.63	2.0	0.71
				12.6	7.9	8.1	26.6	8.1
F5V	7500 K	4.0	0.0	8.2	0.87	0.85	3.7	0.86
				12.2	8.6	8.8	46.2	8.5
A5V	10000 K	4.0	0.0	7.5	0.94	0.92	5.9	0.96
				11.5	11.1	12.9	46.2	10.6
B2V	20000 K	4.0	0.0	6.8	3.0	3.1	15.5	2.4
				10.8	31.9	33.7	315	24.8
B0V	30000 K	4.0	0.0	6.4	2.7	2.8	17.0	2.3
				9.9	33.5	18.3	204	28.9
O6V	39000 K	4.0	0.0	6.4	4.1	0.5	14.5	53.0

References

Chelli, A. 2000, AA, 358, L59

Mignard, F., & Drimmel, R. 2007, ESA Note, GAIA-CD-SP-DPAC-FM-030-2

Viala, Y., Blomme, R., Dammerdji, Y., et al. 2007, ESA Note, GAIA-C6-SP-OPM-YV-004-1

Viala, Y., Blomme, R., Dammerdji, Y., et al. 2008, ESA Note, GAIA-C6-SP-OPM-YV-002-3

SF2A 2008
C. Charbonnel, F. Combes and R. Samadi (eds)

SIMULATING CHARGE TRANSFER INEFFICIENCY EFFECTS ON FUTURE GAIA DATA

Weiler, M.[1] and Babusiaux, C.[1]

Abstract. Gaia is an ESA cornerstone mission to perform high-accuracy astrometry as well as photometry of about 10^9 objects in the sky down to 20^{mag}. For the brightest objects also spectrocopic observations will be obtained. To reach the accuracy aimed for, the data calibration has to correct for Charge Transfer Inefficiency effects in the CCDs, resulting from particle irradiation in space. This work presents first attempts to simulate the influence of such effects upon the expected data Gaia will provide - an essential step towards the development of calibration procedures.

1 Introduction

The Gaia spacecraft will scan the whole sky continuously during five years. All non-extended astronomical sources brighter than 20^{mag} will be automatically detected and the CCD data within a window allocated to the source will be sent to ground. The CCDs will be operated in Time Delay and Integration mode (TDI), shifting the electrical charges produced by the light of the source with the same velocity towards the read-out register as with which the source moves over the focal plane due to the scanning. From the windows allocated to a source on different CCDs, the position of the center of the Point-Spread-Function (PSF), the brightness of the source, and, using the spectroscopic instrument, the position of spectral lines will be determined (Lindegren et al. 2008).

2 What is Charge Transfer Inefficiency?

In the space environment, the CCDs will be subject to particle irradiation, mainly by protons of solar origin. The particles can cause displacements of atoms from their regular position within the CCD semiconductor lattice. Such vacancy defects result in localized electronic energy levels between the valence band and the conduction band. Electrons from the conduction band can enter these energy levels and getting thus excluded from the charge transfer until a re-emission to the conduction band. The defects are therefore called ”traps”, while the full effect is called Charge Transfer Inefficiency (CTI). It leads to a ”smearing” of the PSF, complicating the data analysis.
Since electron release time scales can reach up to hundreds of seconds, sources that have passed over the CCD before a particular other source can influence the CTI effects. Traps may still be filled by electrons from the preceding source, or electrons captured from the source before are released into the PSF of the following source.

3 How are Charge Transfer Inefficiency Effects Modeled?

The current modeling approach, a certain number of electrons inside a CCD pixel access a certain number of traps and fill these traps completely, while the remaining number of traps inside the pixel remains empty. It is assumed that the electrons are captured instantaneously by the traps (i.e. the capture time constant is much smaller than the residence time inside one pixel), and that the electrons are re-emitted according to a sum of five exponentials. Each exponential represents a particular type of trap, characterized by its release time constant. Such different types of traps could be realized by complexes of two or more vacancy defects in the lattice, or by

[1] Observatoire de Paris-Meudon, GEPI, 92195 Meudon, France

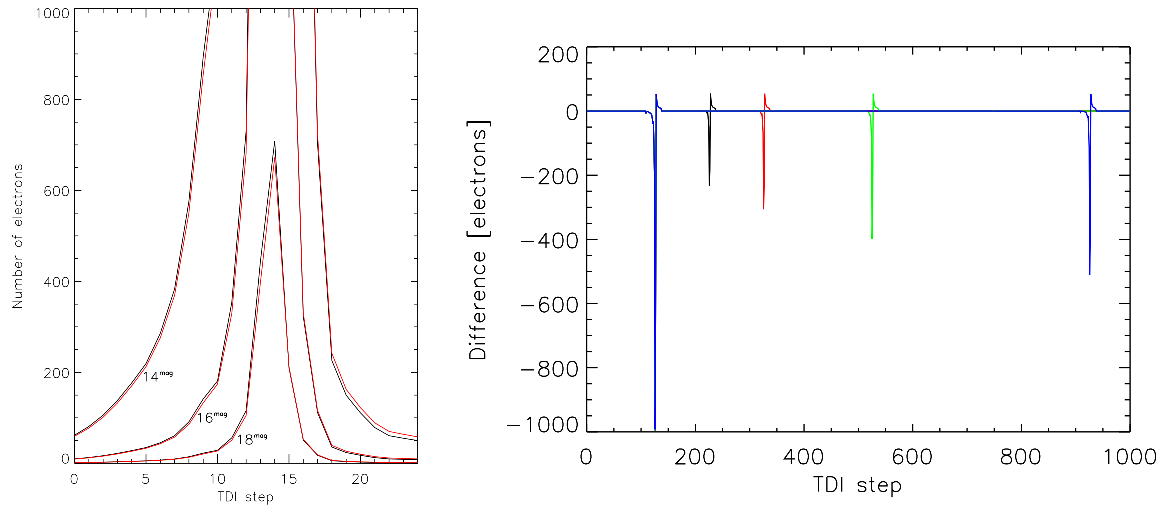

Fig. 1. Left: Cut through the central part of the PSF of stars with three different magnitudes. Black lines: without CTI effects, red lines: with CTI effects. **Right:** Difference in electrons between simulations with and without CTI effects for two consecutive stars. The different colours represent the results for different separations of the stars. In both images pixels were read out in the order of increasing numbers of TDI steps.

complexes of vacancy defects and dopants. The model keeps track of the amounts of electrons that have passed through a CCD pixel before, and thus allows to compute the fraction of empty traps and the release probability of electrons from filled traps at any TDI step. The model is included in the Gaia Instrument and Basic Image Simulator, GIBIS, that allows to simulate Gaia data, taking the physical properties of the sources as well as the optical, electronic, and mechanical properties of the Gaia spacecraft and instruments into account (Babusiaux 2005).

4 Simulation Results

First results of the modeling of CTI effects for simple source configurations are presented in Fig. 1. The left shows the central row of the PSF of stars of three different magnitudes with and without CTI effects. One can see a loss of electrons on the leading edge of the PSF and the center due to electron capture, and an excess of electrons on the trailing edge due to re-emission. The right shows the difference in electrons between a simulation without and with CTI effects for two consecutive stars of the same brightness (14^{mag}). In all cases one sees again the typical loss of electrons on the leading edge of the PSF and an excess of electrons on the trailing edge. For the trailing star, the charge loss is reduced compared to the leading star since traps are filled by electrons captured from the leading star. The larger the distance between the leading and the trailing star is, the less effective is the reduction of CTI effects for the trailing star.

5 Outlook

For more effective simulations of CTI effects, more realistic models are currently developed. These models will release strong assumptions such as the instantaneous capture of electrons. Furthermore, new models aim for faster computations in order to simulate the CCD read-out over longer times. For a more accurate modeling of the CTI effects, better constrained trap parameters (number, release time constants) are required.

References

Babusiaux, C. 2005, ESASP 576, 417

Lindegren, L., et al. 2008, IAU Symposium, Vol. 248, 217-223

ASHRA

High Angular Resolution

SF2A 2008
C. Charbonnel, F. Combes and R. Samadi (eds)

THE 2D APODIZATION OF RECTANGULAR TELESCOPE APERTURE USING MICHELSON INTERFEROMETER AND MONOCHROMATIC LIGHT

Azagrouze, O.[1], El Azhari, Y.[1] and Habib, A.[1]

Abstract. In this laboratory experiment study, we present a two dimensional apodization approach for rectangular apertures by using an interferometric assembly. We used a He-Ne Laser source to simulate a star and two cascaded classical Michelson interferometers in order to perform the apodization in two perpendicular directions. The goal is to study the performences of the assembly and fined out the optimal configuration leading to the best apodization.

1 Introduction

The development of methods for direct detection of exoplanets is one of the most popular subjects in astronomy. The apodization, possibly associated with coronography, occupies a prominent place among the current methods of observation. The interest of the apodized apertures in the imaging of exoplanets was reported for the first time by Nienson & Papaliolios (2001) in their proposal of apodized square aperture. The basic idea is to use a telescope with a variable aperture transmission to reduce sharply the wings of the diffraction point spread function (PSF). The technique reported in this document is based on the proposal of Aime et al. (2002) where they suggest using a Michelson interferometer or Mach-Zehnder interferometer. The first experiments using a Michelson interferometer were conducted by Soummer (2002) and El Azhari et al. (2005). Recently, the result of using a Mach-Zehnder was proposed by Carlotti et al. (2008). In this work, we will present an interefrometric apodization approach. Our aim is to study the performences of the cascaded classical Michelson interferometers assembly and fined out the optimal configuration leading to the best square apodization.

2 Experimental assembly and results

The experimental assembly is presented in figure 1, the lens L_2 allows us to light up the interferometer (MI_1) with a plane wave and forms an image of the telescope pupil (P) on the mirror M_2 of (MI_1). The lens L_3 allows us to obtain an image (P_2) of the plane (P_1). The lens L_4 allows us to light up the interferometer (MI_2) by a plane wave and it forms an image of the mirror M'_2 on the mirror M_2. The lens L_5 forms the final image of the telescope pupil (P) at the plane (P_4) and forms the image of the telescope focal plane (P_1) at the plane (P_3). The resulting PSF in the plane P_3 is:

$$\psi(X,Y) = \frac{4}{\pi^2}\frac{\cos(\pi X)}{1-4X^2}\frac{\cos(\pi Y)}{1-4Y^2}$$

Figures 2 and 3 show a typical example of tow dimensional cosine and one dimensional cos^2 apodization for rectangular aperture.

[1] UFR: APHE, Universite Cadi Ayyad, Faculté des Sciences Semlalia, Av. Prince My Abdellah, BP 2390 Marrakech, Morocco
E-mail: oazagrouze@yahoo.fr

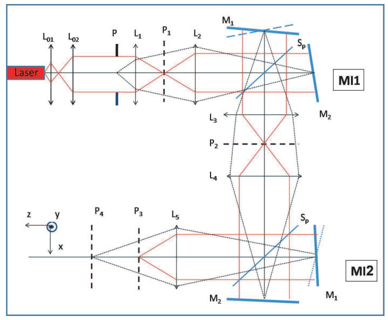

Fig. 1. Experimental assembly of two dimensional apodization. Michelson interferometers (MI1) and (MI2) are represented by mirrors M_1 and M_2 and beamspliters S_p. The lens L_1 represents the telescope of focal plane P_1 and a rectangular pupil (P). The afocal system formed by the lenses L_{01} and L_{02} allows us to obtain a large parallel light beam of the He-Ne laser ($\lambda = 632.8$ nm).

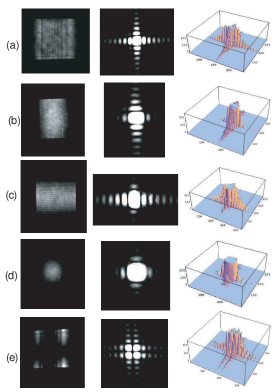

Fig. 2. Tow dimensional cosine apodization: The left column shows the pupil plane and the middle column shows the focal plane and the right column the 3D repartition of intensity in the focal plane. (a): case of the unapodized pupil. (b): case of the cosine apodized pupil along X axis. (c): case of the cosine apodized pupil along Y axis. (d): case of the 2D apodized pupil by CosX*CosY transmittance function. (e): case of the anti-apodized pupil.

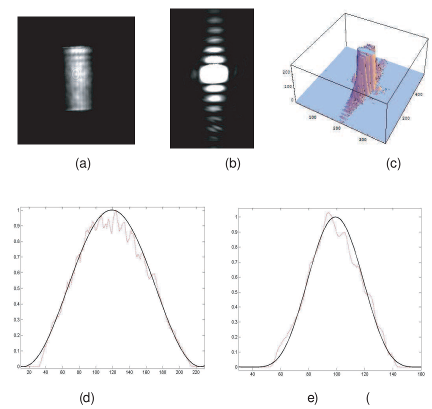

Fig. 3. One dimensional $\cos^2$ apodization along X axis: (a) the pupil plane. (b) the focal plane. (c) the 3D distribution of intensity in the pupil plane at the focal plane.(d) cut of the apodized pupil in the case of the cosine apodization. (e) cut of the apodized pupil in the case of the $\cos^2$ apodization.

3 Conclusions

This experimental work will be followed by another study on the effect of non-monochromaticity of light on apodization interference. Indeed, the interference phenomena and the transmission function depend on wave length. These results could be very useful in high angular resolution applications.

References

Aime, C. Soummer, R. Ferrari, A. 2001, A&A 379,697

Carlotti, A., Ricort, G., Aime, C., El Azhari, Y., & Soummer, R. 2008, A&A, 477, 329

El Azhari, Y., Azagrouze, O., Martin, F., Soummer, R., & Aime, C. 2006, IAU Colloq. 200: Direct Imaging of Exoplanets: Science & Techniques, 445

Nisenson, P., & Papaliolios, C. 2001, ApJ, 548, L201

Soummer, R. 2002 PhD, Université de Nice Sophia Antipolis

SF2A 2008
C. Charbonnel, F. Combes and R. Samadi (eds)

PRECISE CANOPUS ANGULAR DIAMETER MEASUREMENT FROM AMBER/VLTI, PHOTOSPHERIC STRUCTURES SUSPECTED

Bendjoya, Ph.[1], Domiciano de Souza, A. [1], Vakili, F.[1], Millour, F.[2] and Petrov, R.G.[1]

Abstract. Direct measurements of fundamental parameters and photospheric structures of post-main-sequence intermediate-mass stars are required for a deeper understanding of their evolution. Based on near-IR long-baseline interferometry we aim to resolve the stellar surface of the F0 supergiant star Canopus, and to precisely measure its angular diameter and related physical parameters. We used the AMBER/VLTI instrument to record interferometric data on Canopus: visibilities and closure phases in the H and K bands with a spectral resolution of 35. The available baselines ($\simeq 60 - 110$ m) and the high quality of the AMBER/VLTI observations allowed us to measure fringe visibilities as far as in the third visibility lobe. We determined an angular diameter of $\theta = 6.93 \pm 0.15$ mas by adopting a linearly limb-darkened disk model. From this angular diameter and Hipparcos distance we derived a stellar radius $R = 71.4 \pm 4.0 R_{\odot}$. In addition to providing the most precise angular diameter obtained to date, the AMBER interferometric data point towards additional photospheric structures on Canopus beyond the limb-darkened model alone. A promising explanation for such surface structures is the presence of convection cells. We checked such a hypothesis using first order star-cell models and concluded that the observations are compatible with the presence of surface convective structures. This direct detection of convective cells on Canopus from interferometry can provide strong constraints to radiation-hydrodynamics models of photospheres of F-type supergiants.

1 Introduction

The evolved star Canopus (α Carinae, HD45348) is a F0 supergiant (F0Ib) star, the second brightest star (V $= -0.72$) in the night sky, just after Sirius. To constrain evolutionary models it is quite important to have precise measurements of fundamental stellar parameters, such as the effective temperature, luminosity, radius. The most precise angular diameter θ measurements can be obtained by modern long baseline interferometers. In this work we present precise measurements of the angular diameter (and other derived physical parameters) of Canopus obtained with the AMBER beam-combiner instrument (Petrov et al. 2007), installed at the ESO-VLTI (Glindemann et al. 2004) located at Cerro Paranal in Chile. This work is based on observations performed at the European Southern Observatory, Chile under ESO Program 078.D-0295(A). A detailed description of the results is given by Domiciano de Souza et al. (2008).

2 Observations and data reduction

The AMBER observations were performed at spectral resolution $R = \lambda/\Delta\lambda \simeq 35$ in the H and K bands, using three Auxiliary Telescopes (ATs) placed on the VLTI stations A0, K0, and G1. A relatively complete uv-plane coverage was obtained on Canopus and the calibrator star (HD79917) thanks to observations performed over 3 nights (2007 April 6, 7, 8) spanning $\simeq 2$ h each night and several projected baselines ranging from $\simeq 60$ m to $\simeq 110$ m. The data was reduced using the standard routines of the AMBER Data Reduction Software (called amdlib) version 2.1[1]. Tatulli et al. (2007) describe the principles of the AMBER-DRS routines allowing the conversion of raw-data frames into individual complex visibilities. Depending on the night and on the wavelength λ, the relative uncertainties on the visibilities were estimated as $\sigma_V(\lambda)/V(\lambda) \leq 0.1$ in the H band and $\sigma_V(\lambda)/V(\lambda) \leq 0.07$ in the K band.

[1] Lab. H. Fizeau, CNRS UMR 6525, Univ. de Nice-Sophia Antipolis, Observatoire de la Côte d'Azur, 06108 Nice, France
[2] Max-Planck-Institut für Radioastronomie, Auf dem Hügel 69, 53121 Bonn, Germany
[1]Available at http://www.jmmc.fr/data_processing_amber.htm

3 Model fitting and physical parameters

The visibilities measured on Canopus are shown in Fig. 1. To determine the angular diameter of Canopus we fitted a linearly limb-darkened disk (LLD) model[2] to both H and K band observed visibilities. The free parameters of the model are the LLD angular diameter θ, and the H and K band LLD coefficients ϵ_H and ϵ_K.

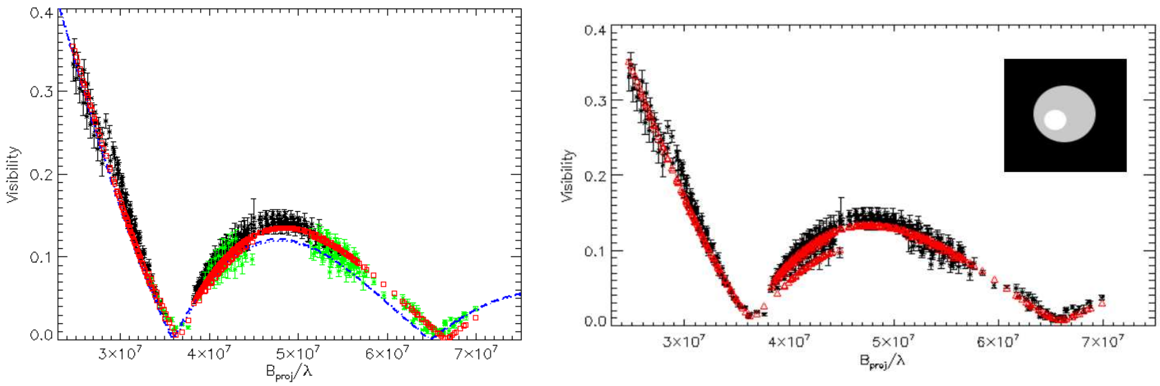

Fig. 1. *Left:* AMBER/VLTI visibility amplitudes and uncertainties in the H (green) and K bands (black). The model visibilities (red squares) were calculated with a linear limb-darkened (LLD) disk model fitted to the data. We also show the theoretical visibilities (dots for H and dashes for K) expected for Canopus from a LLD disk with parameters determined by Claret (2000). Clearly, these LLD models do not account for the observations, especially after the first minimum. *Right:* Visibility of the model with a spot of angular diameter of 36% of the star angular diameter and a flux of 3% plotted as red triangles over the observed visibility in black. In the upper right corner an illustration of such a model. A more satisfactory fit is obtained with models including photospheric structures.

The parameters derived from a Levenberg-Marquardt (L-M) least-squares fit are fit are: $\theta = 6.93 \pm 0.15$ mas, $\epsilon_H = 0.04 \pm 0.01$, and $\epsilon_K = -0.07 \pm 0.01$. From the Hipparcos distance $d = 95.9 \pm 4.9$ pc (Perryman et al. 1997) we derive a linear radius $R/R_\odot = 71.4 \pm 4.0$ for Canopus. Depending on bolometric fluxes existing in the literature, the measured θ provides two estimates of the effective temperature: $T_{\rm eff} = 7284 \pm 107$ K and $T_{\rm eff} = 7582 \pm 252$ K.

The reduced χ^2 of the fit is $\chi^2_{\rm red} = 7.0$, suggesting that the LLD disk cannot completely explain the observations. One promising explanation for the failure of the LLD disk model is the presence of convective photospheric cells introducing fine scale structures in the intensity maps that are detectable by stellar interferometry. We have attempted to explain the interferometric observations of Canopus by adopting simple exploratory models where the granular cells are mimicked by circles of uniform brightness added to a larger uniform disk representing the stellar photosphere itself with a total flux arbitrarily fixed at 1. These models provide better fits to the visibilities than the LLD model. For example, by fitting a single cell added to the stellar surface we obtain $\chi^2_{\rm red} = 4.0$ for $\theta_{\rm cell} = 36\%\theta$ and a total cell flux of 0.035 (Fig. 1 right).

References

Claret, A. 2000, A&A, 363, 1081

Domiciano de Souza, A., Bendjoya, P., Vakili, F., Millour, F., & Petrov, R.G. 2008, A&A, 489, L5

Glindemann, A., Albertsen, M., Andolfato, L. et al. 2004, Proceedings SPIE, 5491, 447

Perryman, M. A. C., Lindegren, L., Kovalevsky, J., et al., *The Hipparcos Catalogue*, 1997, A&A, 323, 49

Petrov, R. G., Malbet, F., Weigelt, G. et al. 2007, A & A, 464, 1

[2] $I(\mu)/I(1) = 1 - \epsilon(1 - \mu)$, where I is the specific intensity, and μ is the cos of the angle between the line of sight and the emergent intensity.

SF2A 2008
C. Charbonnel, F. Combes and R. Samadi (eds)

SEE COAST, A SPECTRO-POLARIMETRIC IMAGING MISSION TO CHARACTERIZE EXOPLANETS

Boccaletti, A.[1], Schneider, J.[2], Tinetti, G.[3], Mawet, D.[4], Baudoz, P.[1] and Galicher, R.[1]

Abstract. SEE COAST is a space mission concept submitted to Cosmic Vision in 2007. It is designed for the characterization of giant gazeous planets and possibly Super Earths both in spectroscopy and polarimetry at visible wavelengths (0.4-1.2μm). The SEE COAST concept relies on a series of high contrast imaging techniques like coronagraphy, wavefront control and differential imaging. The strategy of the mission is presented and the instrumental concept briefly introduced.

1 The context

With the ever-growing number of exoplanets discovered with high precision spectrographs and at a lower extent using the transit technique a large number of projects to directly detect these objects have emerged recently. From the ground, current 8-m class telescopes equipped with AO facilities have already started to image some planetary mass objects in some favorable conditions, namely, for very young systems with large separations (>100 AU) and small mass ratios ; ; ; ; ; ; . But the identification of such planets is quite marginal (7 objects) and raise the problem of their formation which is pointing to a stellar formation process rather than a planetary one. In a few years from now (2010-2011), the same telescopes will benefit from extreme AO systems with advanced coronagaphic devices and differential imaging techniques, like SPHERE at the VLT and GPI on Gemini . These instruments will be specialized for the search and spectro-polarimetric characterization of young and/or massive planets in the solar neighborhood achieving contrast of 10^6 to 10^7. In some particular cases Jupiter mass planets could become detectable if physically close to their host very nearby stars (0.5-1 AU) to increase the reflected light contribution. As for the space, JWST by 2015 will probably reach the realm of mature massive planets (1-5 Gyr) and will be able to characterize some of them on 5 to 10 AU orbits ; in the 2-15μm spectral range. On the longer term (2018-2020), Extremely Large Telescopes are foreseen and again high contrast imaging instruments are being studied now to reach higher contrast (10^8 -10^9). We expect spectral characterization of giant gas planets to be feasible in the near IR and polarimetric characterization in the visible. Ideally, a few Super Earths would become detectable and possibly roughly characterized.

At the moment, future projects like TPF or DARWIN are prospective and the need for a clear roadmap has been expressed worldwide. This exercise has been done twice in the US, with the Exoplanet Task Force and the Exoplanet Forum . Similarly in Europe, a team has been appointed by ESA and one by the community. The objective is to trace a roadmap towards the ultimate goal that is the spectroscopy of terrestrial planets in the habitable zone. Reports will become public in 2009.

Several techniques are being proposed in this context. A clear distinction can be made between indirect detection techniques which are able to derive statistics and/or geometrical parameters (mass, radius, orbital parameters). On the other hand, the ambition of direct imaging is to perform a deeper characterization of the planetary atmosphere. It is now mostly admitted that the spectral characterization of Earth-like planets would require previous mission(s) to identify the targets .

[1] Observatoire de Paris, LESIA, CNRS UMR 8109, 92195 Meudon, France
[2] Observatoire de Paris, LUTH, CNRS UMR 8109, 92195 Meudon, France
[3] University College London, Gower Street, London WC1E 6BT, UK
[4] JPL, 4800 Oak Grove Drive, Pasadena, California 91109, US

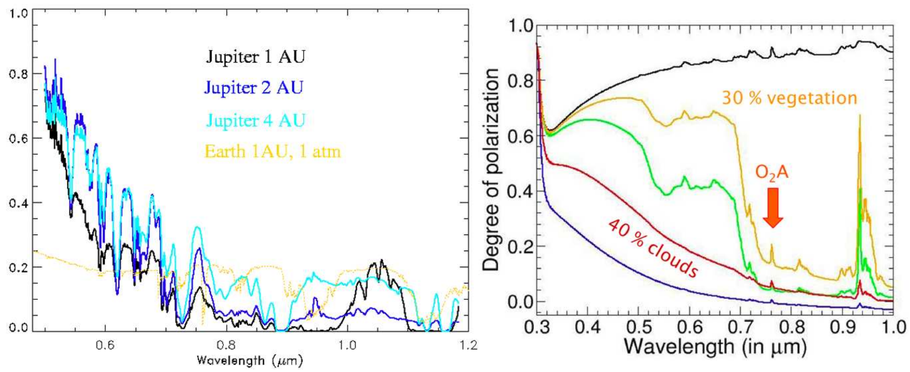

Fig. 1. Spectra for giant gazeous planets (left) and degree of polarization for telluric planets (right) from Stam (2008).

2 Philosophy and strategy

The detection of the first exoplanetary systems has shown a diversity of mass and orbital distributions and has indicated that the Solar System is not representative of planetary systems in general. Diversity and Open-mindedness must thus be the keywords for future exoplanet exploration. Importantly, a consensus is now emerging that habitable planets are not restricted to just Earth-size bodies: Super-Earths with masses up to a tens of Earth's mass may well be habitable. Super-Earths are defined as planets for which terrestrial concepts apply: ocean/continents, planet tectonics, volcanism, habitability.

As described in the previous section, current and committed projects from ground and space are not capable of studying these Super Earths, except for the ELTs which presumably will obtain some rough characterization in the near IR. As we know that these worlds are numerous and many detections are still to come from Radial Velocity surveys, we consider that a mission optimized to study this class of objects is at the moment a valuable program rather than an identification mission for finding Earth-mass planets. In the framework of exoplanet exploration, a space telescope operated in the visible would be very much complementary to what is foreseen on ground-based projects. Therefore, this approach has the advantage to provide scientific data to characterize planets and explore their diversity without the need of a previous mission to find these targets.

This is precisely the purpose of the SEE COAST (Super Earth Explorer - Coronagraphic Off-Axis Space Telescope) proposal to the ESA Cosmic Vision in 2007. Several mission concepts for direct detection were proposed in this frame but none were selected. A new call for proposal will be issued in a couple of years and in the meantime we are intended to progress on the concept definition of SEE COAST.

3 Science case

Our main objective is the spectroscopic and polarimetric characterization of mature jovian planets and Super Earths in order to explore the planetary diversity at lower masses. These classes of objects represent an intermediate topic in between the capabilities of ground based instruments and future long term missions like DARWIN. Therefore, a mission like SEE COAST could be operated in parallel to ELTs on the ground with the objective to contribute to the characterization of the lowest mass gaseous planets and the most massive telluric ones.

Several physical parameters are of interest in the SEE COAST program:

Mass: Msin i is obtained from RV data. Several observations along the orbit will constrain the inclination angle and hence the mass.

Atmosphere: visible spectrum is rich and provides spectral features of water, oxygen, methane and CO_2 (at $1.25\mu m$, Fig. 1). In addition, the Rayleigh scattering gives the column density of clear atmosphere above clouds or solid surface. Also, the polarization of reflected light has wavelength dependence and is a tracer of clouds coverage and haze (Fig. 1).

Surface: oceans and continents have a different temperatures and albedos (a factor of 5). The planetary flux and polarization signals are thus modulated by the planetary rotation ; . The period of this rotation gives the duration of the day for these planets and is important to constraint planetary formation mechanisms as the

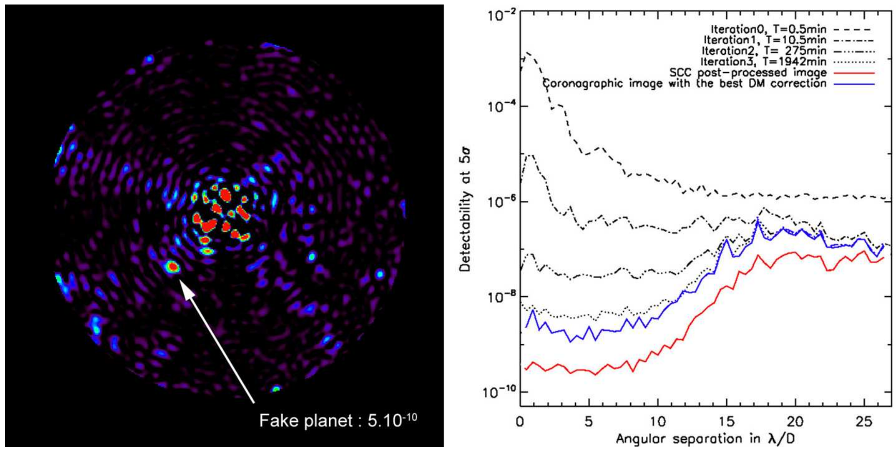

Fig. 2. Laboratory experiment of a multi-sage phase mask obtained at the Observatoire de Paris (left) and simulation of detectability with WF control in a 1.5 m space coronagraph (right).

presence of a magnetic field.

Biosignatures: One can search for spectral signatures of 1) organic materials, and 2) by-products of photosynthesis. On Earth, a strong increase of the albedo due to the vegetation is seen at $0.72\mu m$; , but the red-edge can be at different wavelengths on other planets. Photosynthesis produces O_2 (at $0.76\mu m$), and its derivative O_3 (at $9.6\mu m$) but conversely their presence is not a direct proof of biological activity and hence the abiotic production of these species must be investigated.

4 Mission concept

Based on astrophysical requirements the technical aspects of a mission to detect and characterize exoplanets down to close-by Super-Earths can be derived. The philosophy is a simple and compact telescope and spacecraft to reduce cost and development time, the complexity and requirements for achieving high contrast being relayed to the focal instrument. Here, a 1.5-2 m class off-axis telescope is needed to reach a reasonable amount of targets (giant planets and close-by super-Earths) providing high contrast can be obtained at 2 or 3 λ/D. The focal instrument should provide spectroscopy as well as polarimetric measurements in a narrow field of view (3×3") between 0.4 and 1.25 μm. The optical implementation of such a concept deserve a thorough study but Integral Field Unit are promising. For that, the heritage of SPHERE and EPICS will be a major advantage for the technical aspects and instrumental modelling.

In the previous SEE COAST study we identified 3 main critical aspects or sub-systems, namely: 1/ the wavefront errors (WFE), 2/ the system to suppress the starlight (coronagraph), and 3/ the system to perform calibration and hence further improvement of the contrast. WFE requirements can be obtained with good optical quality at the primary mirror but we also investigated the performance of a dedicated focal plane wavefront sensing (Fig. 2). Implementation of deformable mirrors in space are also being studied around the world. The coronagraphic device should provide high contrast (10^6 - 10^7), high throughput (>50%) and smooth chromaticity. In that context, several concepts are being prototyped (Fig. 2). Finally, further starlight rejection can be obtained with appropriate calibration technique either using spectral or polarimetric signatures of planets with respect to stars. Preliminary performance of SEE COAST was addressed with simulations for the Cosmic Vision proposal. Two examples of simulated spectra for a Jovian planet and a Super Earth are shown in Fig. 3. More details of the SEE COAST project can be found in Schneider et al. (2008).

References

Arnold, L., Gillet, S., Lardière, O. et al. 2002, A&A 392, 231

Baudoz, P., Boccaletti, A,; Riaud, P. et al. 2006, PASP 118, 765

Baudoz, P., Boccaletti, A. & Rouan, D. 2007, Proc. of the conference "In the Spirit of Bernard Lyot", 25

Beuzit, J.-L., Feldt, M., Dohlen, K. et al. 2006, The Messenger 125, 29

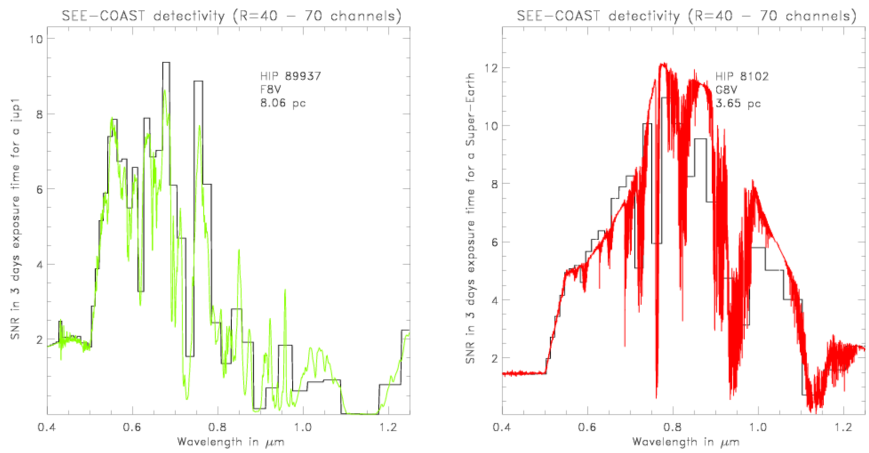

Fig. 3. Instrumental simulations were made for Cosmic Vision to assess the capabilities of SEE COAST. Two examples are shown for illustration here for a mature Jovian planet (left) and a Super Earth of 2.5 Earth radii (right).

Boccaletti, A., Baudoz, P., Baudrand, J. et al. 2005, Advances in Space Research 36, 1099

Chauvin, G., Lagrange, A.-M., Dumas, C. et al. 2004, A&A 425, L29

Chauvin, G., Lagrange, A.-M., Zuckerman, B. et al. 2005, A&A 438, 29

Ford, E., Seager, S. & Turner, M. 2001, Nature, 412, 885

Galicher, R., Baudoz, P. & Rousset, G. 2008, A&A 488, 9

Gardner, J. P., Mather, J. C., Clampin, M. et al. 2006, Space Science Review 123, 485

Gilmozzi, R. & Spyromilio, J. 2007, The Messenger 127, 11

Itoh, Y., Hayashi, M., Tamura, M. 2005, ApJ 620, 984

Lafrenière, D., Jayawardhana, R., van Kerkwijk, M. 2008, arXiv:0809.1424

Lawson, P.R., Traub, W.A. & Unwin, S.C. 2008, Exoplanet Forum Report (draft), JPL publication

Luhman, K.L., Wilson, J.C., Brandner, W. et al. 2006 ApJ 649 894

Luhman, K.L., Patten, B.M., Marengo, M. et al. 2007 ApJ, 654 570

Lunine, J.I., Fischer, D., Hammel, H., et al. 2008, Report of the Exoplanet Task Force to the Astronomy and Astrophysics Advisory Committee, arXiv0808.2754

Macintosh, B., Graham, J., Palmer, D. et al. 2006, SPIE 6272, 18

Neuhäuser, R., Guenther, E.W., Wuchterl, G. et al. 2005, A&A 435, 13

Vérinaud, C., Hubin, N., Kasper, M. et al. 2006, SPIE 6272, 19

Stam, D.M. 2008, A&A 482, 989

Schneider, J. Boccaletti, A., Baudoz, P. et al. 2008, proposal to Cosmic Vision to appear in Experimental Astronomy

Woolf, N.J., Smith, P.S., Traub, W.A. et al. 2002, ApJ 574, 430

SF2A 2008
C. Charbonnel, F. Combes and R. Samadi (eds)

MAXIMUM LIKELIHOOD-BASED METHOD FOR ANGULAR DIFFERENTIAL IMAGING

Cornia, A.[1,2], Mugnier, L.[1], Sauvage, J.-F.[1], Fusco, T.[1], Rousset, G.[2] and Védrenne, N.[1]

Abstract. In the context of the SPHERE planet finder project, we further develop a recently proposed method, based on detection theory, for the efficient detection of planets using angular differential imaging. The proposed method uses the fact that with the SPHERE instrument the field rotates during the night. The method starts with the appropriate combination of images recorded at different times into so-called pseudo-data. It then uses jointly all these pseudo-data in a Maximum-Likelihood (ML) framework to detect the position and amplitude of potential companions of the observed star, taking into account the mixture of photon and detector noises. The method is validated on simulated data.

1 Introduction

The European project SPHERE (Beuzit *et al.* 2008) is the planet searcher of VLT (ESO), based on direct imaging in the near-IR. The goal of SPHERE is to detect warm Jupiters, orbiting sun-like stars at 10 pc from the Sun. To do so, one needs to use an extreme adaptive optics system (XAO) to compensate the atmospheric turbulence which spreads the light of the star, and a high-performance coronagraph to remove the star's photons in order to reduce the noise. But these two techniques alone are not sufficient, because the contrast between the star and the planet at 1.6 μm is close to 10^6. In order to reach the ultimate detection performance needed to detect a warm Jupiter, it is mandatory to combine the abovementioned optical devices to an *a posteriori* processing of all data.

The main problematic is to disentangle the potential companion's signal from the quasi static speckles, which are due to residual aberrations and constitute a major "noise" source. These speckles present the same characteristic angular size as the diffraction element, λ/D, and the same size as the companion's signal. With no more information, it is impossible to discriminate between the speckles and the companion. In order to do so, the SPHERE instrument includes the ability to perform spectral and angular differential imaging.

Spectral differential imaging consists in acquiring simultaneous images of the system star-companion at different wavelengths. The spectral signatures of the exoplanet's atmosphere ensures that the planet's response will significantly vary in the images, while the star response and therefore the speckles remain the same.

Angular differential imaging relies on the fact that, if the pupil is stabilized, the field rotates naturally as the speckle in principle should remain fixed.

If both temporal and spectral channels are available, as is the case with the SPHERE instrument, then one may first combine each pair of simultaneous spectral images into one image so as to enhance the planet's signal, and then use the resulting image series as temporal channels for angular imaging. In this paper, we investigate the joint processing of such temporal series of images.

At least two approaches are possible for this problem:

- jointly estimate the coronagraphic response of the star, and the companion's position and amplitude (or flux). This approach has been adopted by Smith *et al.* (2007);
- numerically remove the star signal, and only estimate the planet (Mugnier *et al.* 2007).

[1] ONERA/DOTA, B.P. 72, 92322 Châtillon cedex, France
[2] LESIA, Observatoire de Paris, 5 place Jules Janssen, 92195 Meudon, France

In the framework of the SPHERE project, the static aberrations are likely to evolve during observing time, and the estimation of the star signal should therefore be done several times during night. We therefore choose the second option, which consists in cancelling the star image numerically.

This suppression is done by a pairwise subtraction of sufficiently separated images. Let $\boldsymbol{i}_t$ the raw images, the new data are the images differences $\Delta(\boldsymbol{r},k) = \boldsymbol{i}_{k_1(k)}(\boldsymbol{r}) - \boldsymbol{i}_{k_2(k)}(\boldsymbol{r})$, where $k_1(k)$ and $k_2(k)$ are indices chosen so as to preserve the planet's signal in the difference. The estimation of the companion's position and amplitude is done on these new data, through a Maximum Likelihood approach.

2 Maximum-Likelihood estimation for position and amplitude of the companion

In the new data consisting of the $k_{\max}$ differential images denoted by $\Delta(\boldsymbol{r},k)$, and assuming that a planet is indeed present, the data model at each pixel $\boldsymbol{r}$ of image k is the following:

$$\Delta(\boldsymbol{r},k) = a \cdot \boldsymbol{p}(\boldsymbol{r},k;\boldsymbol{r}_0) + \boldsymbol{n}(\boldsymbol{r},k), \tag{2.1}$$

where a is the planet's amplitude and $\boldsymbol{r}_0$ is the initial planet's position, $\boldsymbol{p}(\boldsymbol{r},k;\boldsymbol{r}_0)$ is the known pattern of the planet in this data for an assumed $\boldsymbol{r}_0$ (which is the difference of two PSF's), and $\boldsymbol{n}(\boldsymbol{r},k)$ denotes the noise.

The maximum likelihood approach consists in searching for $(\hat{\boldsymbol{r}}_0, \hat{a})$ that maximize the likelihood $L(\boldsymbol{r}_0, a)$. In the following we assume that the noise is non-homogeneous, Gaussian and white, with variance $\sigma^2(\boldsymbol{r},k)$. This assumption is reasonable and allows us to take into account both the photon and the detector noises, as done in AO-corrected image restoration (Mugnier *et al.* 2004).

We can define a criterion J to be maximized, which is linked to the likelihood L this way:

$$J \triangleq -a^2 \sum_{k,\boldsymbol{r}} \frac{p^2(\boldsymbol{r},k;\boldsymbol{r}_0)}{\sigma^2(\boldsymbol{r},k)} + 2a \sum_{k,\boldsymbol{r}} \frac{p(\boldsymbol{r},k;\boldsymbol{r}_0)\Delta(\boldsymbol{r},k)}{\sigma^2(\boldsymbol{r},k)} = -\sum_{k,\boldsymbol{r}} \frac{|\Delta(\boldsymbol{r},k) - a\,p(\boldsymbol{r},k;\boldsymbol{r}_0)|^2}{2\sigma^2(\boldsymbol{r},k)} + \text{const} = 2\ln L(\boldsymbol{r}_0,a) + \text{const} \tag{2.2}$$

The optimal value $\hat{a}(\boldsymbol{r}_0)$ of a for each given $\boldsymbol{r}_0$ is computable analytically; we can also take into account the fact that the flux always has to be positive:

$$\hat{a}(\boldsymbol{r}_0) = \max\left(\frac{\sum_{k,\boldsymbol{r}} p(\boldsymbol{r},k;\boldsymbol{r}_0)\Delta(\boldsymbol{r},k)/\sigma^2(\boldsymbol{r},k)}{\sum_{k,\boldsymbol{r}} p^2(\boldsymbol{r},k;\boldsymbol{r}_0)/\sigma^2(\boldsymbol{r},k)}, 0\right). \tag{2.3}$$

The numerator of this expression can be seen as a scalar product (correlation) between the planet's patterns and the images, with weights given by the noise variance. And the denominator is simply a normalization constant.

If we insert this optimal value for the amplitude into metric J, we obtain an expression of the latter that depends, explicitly at least, only on the sought planet position:

$$J'(\boldsymbol{r}_0) \triangleq J(\boldsymbol{r}_0, \hat{a}(\boldsymbol{r}_0)) = \begin{cases} \frac{\left(\sum_{k,\boldsymbol{r}} p(\boldsymbol{r},k;\boldsymbol{r}_0)\Delta(\boldsymbol{r},k)/\sigma^2(\boldsymbol{r},k)\right)^2}{\sum_{k,\boldsymbol{r}} p^2(\boldsymbol{r},k;\boldsymbol{r}_0)/\sigma^2(\boldsymbol{r},k)} & \text{if } \hat{a}(\boldsymbol{r}_0) > 0 \\ 0 & \text{if } \hat{a}(\boldsymbol{r}_0) \leq 0. \end{cases} \tag{2.4}$$

This criterion J' can be computed for each possible initial planet position on a grid, which can be chosen as the original pixel grid of the images, or as a finer grid if it is useful. The most likely initial planet's position is then $\hat{\boldsymbol{r}}_0 = \arg\max J'(\boldsymbol{r}_0)$, and the most likely amplitude is $\hat{a}(\hat{\boldsymbol{r}}_0)$ as computed with Eq. (2.3).

3 Detection criterion

Once the likelihood and amplitude maps are computed, the main problem is to decide which peaks are true companions and which ones are not. One way to do so is to additionally compute the standard deviation of the estimated amplitude, $\sigma(\hat{a}(\boldsymbol{r}_0))$, for each possible planet position $\boldsymbol{r}_0$, *i.e.* to compute how the noise propagates from the images to our amplitude estimator. A possible detection criterion, which can be linked to the probability of false alarm, is then to decide that all positions where the signal-to-noise ratio (SNR) of the estimated amplitude, defined as:

$$\text{SNR}(a) = \hat{a}(\boldsymbol{r}_0)/\sigma(\hat{a}(\boldsymbol{r}_0)), \tag{3.1}$$

is greater than some threshold are true detections.

The variance of the estimated flux for a given position $\boldsymbol{r}_0$ is computed by means of Eq. (2.3) using the fact that the noise in our images $\Delta(k, \boldsymbol{r})$ is white, both temporally and spatially; after some maths we obtain:

$$\sigma^2(\hat{a}(\boldsymbol{r}_0)) = \left(\sum_{\boldsymbol{r},k} \frac{p^2(\boldsymbol{r}, k; \boldsymbol{r}_0)}{\sigma^2(\boldsymbol{r}, k)} \right)^{-1} . \tag{3.2}$$

4 Validation by simulation

4.1 Simulation conditions

The conditions of simulation are representative of the SPHERE/IRDIS instrument on the VLT: an 8 m telescope, a seeing of 0.8″, a wind speed of 12.5 m/s; a SAXO-like AO system: 41×41 actuators, a 40×40 sub-aperture Hartmann-Shack wavefront sensor, a sampling frequency of 1200 Hz; residual static aberrations with a standard deviation of $\sigma_{\phi_u} = 35$ nm upstream of the coronagraph and $\sigma_{\phi_d} = 100$ nm downstream of the coronagraph. We have assumed a pupil-stabilized mode, with residual aberrations kept constant during the simulated run.

A hundred 256×256 images are simulated at an imaging wavelength of $\lambda = 1.593\ \mu$m with Poisson (photon) noise. The image of the star is computed by means of the analytical expression for the long-exposure AO-corrected coronagraphic image of a star (Sauvage 2007).

We have simulated seven planets which lie aligned at distances multiple of $4\lambda/D$ from the central star. The long-exposure AO-corrected images of the planets are computed using the static aberrations and the residual phase structure function, assuming that the planets do not "see" the coronagraph.

The star flux is $2.67 \cdot 10^7$ ph/s, the planet flux is 28.5 ph/s, which yields a ratio of $9.36 \cdot 10^5$. Depending on the simulation, the total exposure time is either 1h or 2h.

4.2 Impact of the proposed positivity constraint and of the noise variance map

Fig. 1 shows the improvements brought by the positivity constraint and a non-homogeneous noise variance map: a part of the peaks due to false detections are eliminated by the former, and the remaining are dimmed by the latter.

In order to better quantify the improvement brought by positivity and by the use of an inhomogeneous noise variance map, Fig. 2 shows the SNR of the estimated amplitude (defined by Equation (3.1)) thresholded to value of 4, in the difficult case of a one hour total observation time. In the two cases where a homogeneous noise is assumed in the processing, the noise variance has been taken equal to the spatial average of the empirical variance of each pixel in time.

For the case where both the positivity and the inhomogeneous noise variance map are used, all the true planets are detected and no false alarm is present with the displayed threshold. The corresponding detection map is the boxed one of Fig. 2. For the three other cases, whatever the chosen threshold, in this simulation there are either false alarms (for low threshold values) or undetected planets (for high threshold values).

4.3 Impact of the exposure time

As expected, for two hours of total exposure time instead of one, there are less false detections for low thresholds and all planets are detected even for higher threshold values. A more detailed discussion with figures can be found in Mugnier *et al.* (2008).

5 Perspectives

Further simulations are to be run to exploit the two spectral channels too, and to test the robustness of the method for slowly varying aberrations.

References

Beuzit, J.-L., Feldt, M., Dohlen, K., Mouillet, D., Puget, P., & Wildi, F. 2008, in *Adaptive Optics Systems*, 7015, Proc. Soc. Photo-Opt. Instrum. Eng.

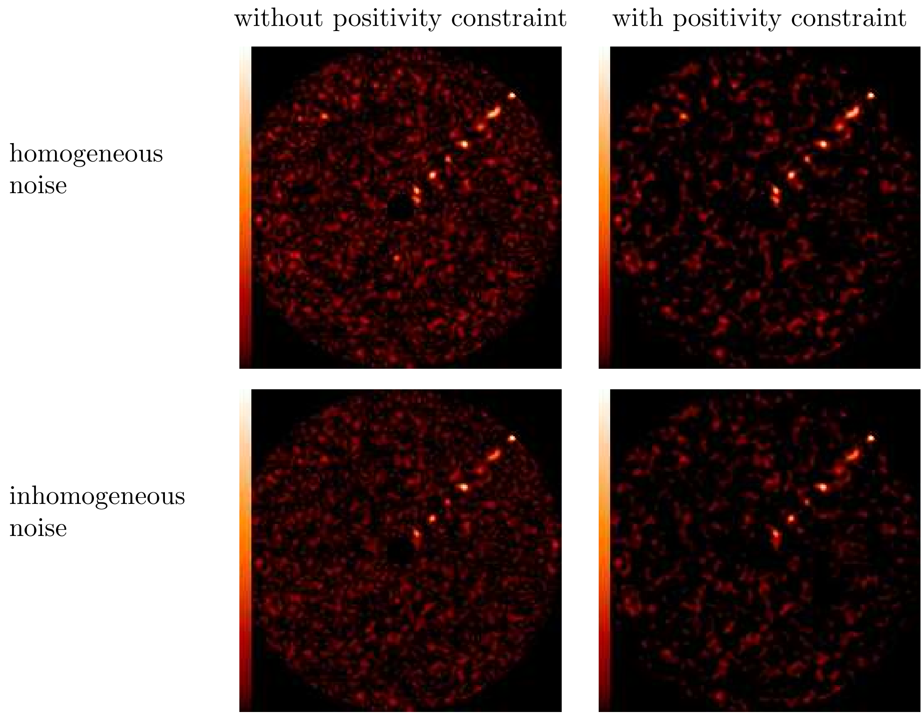

Fig. 1. Likelihood maps with 100 images and an exposure time of 1 h. Top row: homogeneous noise. Bottom row: inhomogeneous noise. Left column: without positivity constraint. Right column: with positivity constraint.

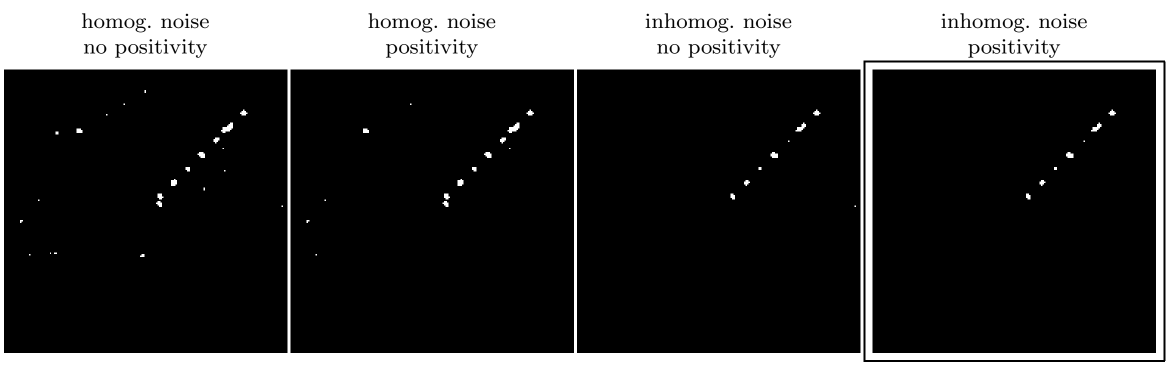

Fig. 2. Detection maps obtained by thresholding the maps of the SNR of the estimated flux of Fig. 1 at the value of 4.

Mugnier, L., Sauvage, J.-F., Fusco, T., & Rousset, G. 2007, in *Adaptive Optics: Analysis and Methods*, OSA, June 18–20, 2007, Vancouver (Canada)

Mugnier, L., Fusco, T., & Conan, J.-M. 2004, *J. Opt. Soc. Am. A*, 21, 1841–1854

Sauvage, J.-F. 2007, PhD thesis, Université Paris VII, December 2007

Mugnier, L., Cornia, A., Sauvage, J.-F., Védrenne, N., Fusco, T., & Rousset., G. 2008, in *Astronomical telescopes 2008 SPIE Symposium*, Adaptive Optics Systems Conference, N. Hubin, C. E. Max, and P. L. Wizinowich editors, 7015, June 2008, Marseille (France)

SF2A 2008
C. Charbonnel, F. Combes and R. Samadi (eds)

MODEL AND SETUP OF THE PROTOTYPE OF THE POLYCHROMATIC LASER GUIDE STAR AT OBSERVATOIRE DE HAUTE-PROVENCE

Foy, R.[1], [2], Blanc, P.-E.[2], Fusco, T.[3], Laloge, A.[2], Le Van Suu, A.[2], Perruchot, S.[2], Petit, A.[4], Richaud, P.[2], Tallon, M.[1], Thiébaut, E.[1] and Boër, M.[2]

Abstract. We discuss our Polychromatic Laser Guide Star (PLGS) end-to-end model and describe the the status of demonstrator at OHP. PLGS aims at measuring the tilt from the LGS without any NGS. Two dye pulsed laser chains locked at 589 and 569nm are required. Beams will deliver 34 W each, so that 22 W will be deposited into the mesosphere. These lasers are being settled in the building of the OHP 1.52m telescope. Beams will propagate from there to the launch device attached to the 1.52 m telescope through a train of mirrors with constant incident angles. The coudé focus of the 1.52m telescope will be equipped with an adaptive optics device, closely derived from the ONERA's BOA one. The Strehl ratio at 330nm is expected to be 30-40% for $r_0 = 8 - 10$cm. The full demonstrator is planned to run in 2010.

1 Introduction

Diffraction limited long exposure images at large telescopes is possible thanks to adaptive optics (AO) if there is at least one source of reference bright enough within the isoplanatic patch of the source of interest, in order to measure the wavefront phase. If there is no such a source, the phase reference can be provided by a laser guide star (Foy & Labeyrie, 1985) (LGS), generally relying on the mesospheric NaI D_2 line. But with a LGS the wavefront tilt remains undetermined, because the location of the laser spot in the mesosphere is not known (Pilkington, 1987; Séchaud, 1988).

At large telescopes equipped with LGSs the tilt is measured from a natural guide star (NGS), whereas higher orders of the wavefront are measured from the LGS. It results in limited sky coverage performances, dramatically at visible wavelengths. Nevertheless, AO at visible wavelengths is still in its infancy, although it has been proved it works (Fugate et al, 1994; Madec et al, 1997). With or without LGS, coronographic observations of the environment of cool stars, or of AGN seems to be very promising targets such devices. Interesting reviews of other programmes of AO + LGS at visible wavelengths are given in the SPIE-7015 conference (Max et al, 2008; Ammons et al, 2008; Gavel et al, 2008; Bouchez et al, 2008; Britton et al, 2008).

A number of different solutions have been proposed to overcome the tilt problem, e.g. Esposito et al (2000), Foy et al (2000), Belenkii et al (1999), Belenkii (2000) & Schöck et al (2000). Currently the only ongoing R& D programme to measure the tilt from the LGS alone is the *Polychromatic LGS (PLGS)* (Foy et al, 1995). It is the *Étoile Laser Polychromatique pour l'Optique Adaptative ELP-OA* project, which we are conducting at Observatoire de Haute-Provence (*OHP*). The overall goal of ELP-OA is the experimental validation that the measurement of the wavefront tilt *without NGS* is possible at an astronomical telescope.

The PLGS concept relies on the chromatism of the air refraction index n, mostly in the ultraviolet. Therefore the tilt θ of the wavefront slightly varies with λ. Foy et al (1995) have shown that: $\theta_{\lambda_3} = \Delta\theta_{\lambda_1,\lambda_2}(n_{\lambda_3} - 1)/\Delta n_{\lambda_1,\lambda_2}$. Thus the tilt at λ_3 can be derived from $\Delta\theta_{\lambda_1,\lambda_2}$ between λ_1 and λ_2 . The larger is the wavelength difference $\Delta\lambda$ and the shorter is the shortest λ, the higher is $\Delta\theta$ and accordingly the sensitivity.

[1] Université de Lyon, F-69000 Lyon, France; Université de Lyon 1, F-69622 Villeurbanne, France; Centre de Recherche Astrophysique de Lyon, Observatoire de Lyon, 9 avenue Charles André, F-69561 Saint-Genis Laval cedex, France; CNRS, UMR 5574; Ecole Normale Supérieure de Lyon, F-69007 Lyon, France

[2] Observatoire de Haute-Provence, F-04870 Saint-Michel l'Observatoire; CNRS, USR 2207, France

[3] ONERA, BP. 52, 29 avenue de la Division Leclerc, F-92320 Chatillon cedex, France

[4] DEN/DANS/DPC, Commissariat l'nergie Atomique Saclay, 91191 Gif-sur-Yvette cedex, France

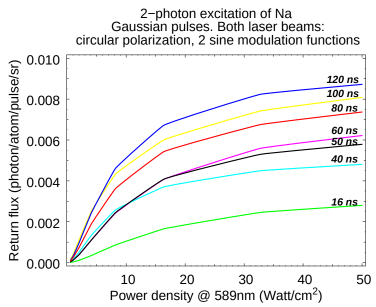

Fig. 1. Curve of growth of the return flux at 330 nm from the resonant two-photon excitation of the $4D_{5/2}$ energy level of sodium, for different pulse durations. BEACON code of CEA (Bellanger et al, 2004).

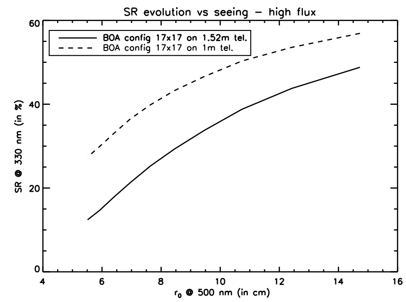

Fig. 2. Expected performances of a 17^2 actuators adaptive optics device at an 1.52m telescope at 330 nm, for two aperture diameters. Case of a bright reference source.

The process to create the polychromatic LGS is the excitation of the $4D_{5/2}$ energy level of sodium atoms in the mesosphere, via the $3P_{3/2}$ level with two laser beams locked at 589 nm and 569 nm respectively. From the $4D_{5/2}$ level, valence electrons decay down to the ground level radiating within spectral lines spanning the 0.330 μm to 2.34 μm interval. Choosing $\lambda_1 = 0.33$ μm and $\lambda_2 = 2.34$ μm leads to $\theta/\Delta\theta = 18$. Thus one needs either 18^2 times more photons, or a spot size 18 times smaller than with a NGS to get the same error in θ if measured with a center of gravity algorithm. The feasibility study of ELP-OA is summarized in Foy et al. (2007).

2 Atomic physics modeling

The PLGS relies on the two-photon incoherent resonant excitation of Na atoms in the mesosphere: $3S_{1/2} \rightarrow 3P_{3/2} \rightarrow 4D_{5/2}$. It provides a spectrum ranging from 330 nm to 2.34μm. We investigated the direct one-photon excitation (Foy et al, 1995) $3S_{1/2} \rightarrow 4P_{3/2}$ at 330 nm: it fails to provide us with enough return flux because the cross section σ_{330} is too low and because the number of velocity classes is much higher than that of the transitions $3S_{1/2} \rightarrow 3P_{3/2} \rightarrow 4D_{5/2}$. High return fluxes modeled by Pique et al (2006) are overoptimistic because they have $\sigma_{330} = 4.0 \times 10^{-14}\mathrm{m}^2$ instead of $1.1 \times 10^{-14}\mathrm{m}^2$ (see e.g. Siegman (1983)), and their rate equation model for a phase modulated laser does not fit with Morris (1994) and Bellanger et al. (2004) models which relies on optical Bloch equations.

Laser parameters have to be optimized to maximize the return flux at 330 nm f_{330}. Figure 1 shows f_{330} as a function of the laser power density d_P at 589 nm. One could conclude that at given d_P the longer is the pulse duration τ, the higher is f_{330}. But d_P being kept constant, increasing τ requires to increase the average power $\overline{P}$ in the same ratio, or to decrease the repetition rate F_R. But these parameters cannot be varied easily because of technological constraints, from NdYAGs and dye lasers. At given $\overline{P}$ and F_R, increasing τ increases F_R but decreases d_p which decreases f_{330}. The balance between these two effects depends on the local slope of the $f_{330} = f(d_p)$ relationship and hence on the spatial energy distribution of the laser beam at the mesosphere.

3 End-to-end model

We have developed a code to simulate the whole ELP process, from the pupil of the launch device lightened by the two lasers up to the measurement of the Strehl ratio $\mathcal{S}$ due to the only tilt at the focus of the master telescope. Our previous, analytical, code (Schöck et al, 2002) was not coupled with the laser-sodium interaction code BEACON. A Kolmogorov phase screen is applied to the pupil function. The power spectrum of the resulting phase map provides us with the spatial d_p map in the mesosphere. It is converted into a photon flux map by interpolating the density power in Fig. 1. The image of this flux map is convolved with the point spread function (PSF) at the output of the master telescope. It is generated from another area of the same Kolmogorov phase screen used for the projector. It includes also an AO device. It is simply modeled by subtracting from the phase screen itself its smoothed map in order to fit an input value $\mathcal{S}$.

The detector is assumed to be an EMCCD, so that the readout noise can be neglected (Basden et al, 2003).

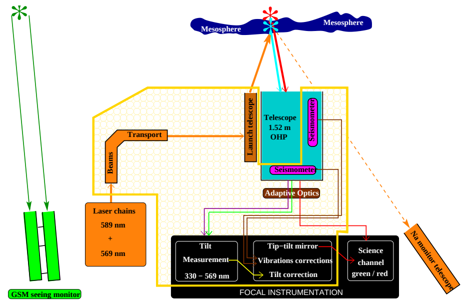

Fig. 3. Layout of the ELP-OA experiment at OHP. In addition to the equipment installed at the master 1.52 m telescope, there will be a seeing monitor and a monitor of the sodium density in the mesosphere installed at another telescope on the OHP site

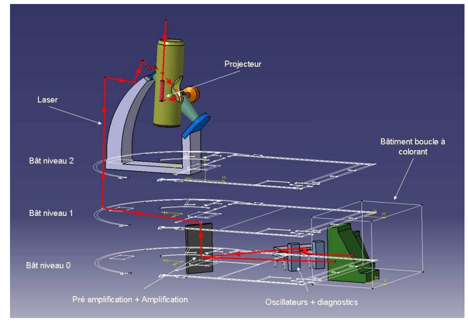

Fig. 4. Layout of the optical path of laser beams from the clean room to the projector through the master telescope mount. All incidence angles are constant.

We do not use a center of gravity algorithm to measure $\Delta\theta$. Indeed in this case the accuracy is ultimately limited by the seeing disc size. We use of the smallest features in the image, following the Cramér-Rao criterion, e.g. the speckle pattern of the laser spot. Phase restoration from the images themselves has now proven to work (Rondeau et al, 2007) up to $D/r_0 \approx 75$. But since it is an iterative algorithm it can be barely used on line. Instead, we use cross correlations, either between the images at the two λs (e.g. at 330 nm and at 569 nm), or between these images and a model. Consequently, the larger is the projector pupil p, the smaller are the spot pattern features in the mesosphere. The master telescope has to resolve this pattern at the longer wavelength used to measure $\Delta\theta$. At an 1.52 m telescope $p < 0.44$ m with IR lines, or $p < 1.5$ m with 569 nm line.

4 Layout of the ELP-OA experiment

Work is in progress to setup the ELP-OA demonstrator at the 1.52 m telescope at OHP. Figure 3 shows the layout of the experimental setup. Phase modulated pulsed dye laser are similar to those which we have used at the LLNL (Foy et al, 2000) and at CEA/Pierrelatte (Schöck et al, 2000) for our previous experiment to check experimentally on the sky the efficiency of the two-photons excitation of sodium atoms in the mesosphere. Pump lasers will be NdYAGs. The laser clean room is being equipped at the ground level of the 1.52 m telescope building. Dye pumps will be installed in an extension of the building, for easier operation and also for safety. The two beams are carried up to the projector telescope through a train of mirrors (Fig. 4). The master telescope has an English equatorial mount. They enter the master telescope English mount through the North tip of its hour angle axis. Then laser beams propagate until the cross of the two telescope axis and through the flat M3 mirror, which has to be drilled. All along their path in the telescope, beams are confined within the M2 central obscuration. In this way, all reflexion angles of the mirror train are constant, which avoid changes in the coating efficiency and of the polarization.

M3 and M4 and possibly M2 mirrors will be coated for improved reflectivity at 330 and 569 nm.

An adapted version of the ONERA's BOA device (Madec et al, 1997) will be implemented at the coudé focus. Modifications are required to improve the throughput at 330nm. The deformable mirror will be an ALPAO's 17^2 actuators one, the Shack-Hartmann wavefront sensor with an EMCCD camera being lent by LAOG. The wavefront sensor will be fed by the backscattered D_2 line. Modeled performances are shown in Fig. 2.

Since θ is derived from $\Delta\theta$, it is insensitive to telescope vibrations. The rms amplitude of resonance vibrations at the OHP 1.52 m telescope is ≈66 mas (Tokovinin, 2000), which is close to the Airy disc FWHM at 550 nm. They will be measured with two pendular seismometers (Tokovinin, 2000) mated to telescope axises.

In parallel to the main ELP-OA setup, two devices will run, to fully characterize the observing conditions. The seeing parameters r_0, τ_0 and the atmospheric transparency will be measured with a Generalized Seeing Monitor (G.S.M.), on loan from Nice University thanks to A. Ziad and J. Borgnino. The GSM will be operated close to the 1.52 m telescope, as far as possible every night to get quantitative measurements of these parameters over the year, which are lacking. For a few runs, a second GSM will be installed inside the dome and it will operated simultaneously with the outer one, in order to get a quantitative estimate of dome seeing. From these campaigns, we hope to be able to improve the telescope environment in terms of image quality.

The second device will be a monitor of the Na column density in the mesosphere at the 1.20 m OHP telescope. Since they are located a few hundred meters away from the 1.52 m telescope, we will get information about the sodium density vertical profile and therefore on the sodium layer average altitude. We will compare our results with measurements at the Grard Mgie Station of aeronomy located 100 m North of the 1.52 m telescope.

5 Conclusion

Models allow us to predict tilt Strehl ratios of ≈30 to 40% at 550 nm.

The current status of the setup of ELP-OA is the following. Power water supplies have been increased to match the ELP-OA requirement. The clean room is being installed at the ground level of the building. Negotiations for loans of the laser chains and of AO components are almost completed. We plan to start the installation of these systems by the end of 2008. First launch of laser beams are planned for the end of 2009, and the whole ELP-OA experiment is plan to start first tip-tilt measurement by the end of 2010.

6 Acknowledgments

We thank the staff of Observatoire de Haute-Provence. This project is funded by ANR (contract NT05-4_41579), CNRS/INSU/CSA, DGA (contract 06-34046) and PACA Region (contract 2006_20307).

References

Ammons, S.M., Johnson, L., Laag, E.A., Kupke, R., & Gavel, D. T. 2008, SPIE, 7015, 0C-1

Basden, A., Haniff, C., & Mackay, C. 2003, Mon. Not. R. Astron. Soc, 345, 985

Belenkii, M., Karis, S. J., II, J. M. B., & Fugate, R. Q. 1999, Optics L., 24, 637

Belenkii, M. S. 2000, Applied Optics, 39, 6097

Bellanger, V., Courcelle, A., & Petit, A. 2004, Computer Physics Communications, 162, 143

Biraben, F. 2006, private communication

Bouchez, A. H., Dekany, R. G., Angione, J. R., et al. 2008, in SPIE, Vol. 7015, Adaptive Optics Systems

Britton, M., Velur, V., Law, N., Choi, P., & Penprase, B. E. 2008, in SPIE, Vol. 7015, Adaptive Optics Systems

Esposito, S., Ragazzoni, R., Riccardi, A., et al. 2000, ExpA, 10, 135

Foy, R., Éric, P., Eysseric, J., et al. 2007, in Astronomical Adaptive Optics Systems and Applications III. Ed. Tyson, Robert K.; Lloyd-Hart, Michael. Proceedings of the SPIE, Volume 6691, 66910R, Vol. 6691

Foy, R. & Labeyrie, A. 1985, AA, 152, L29

Foy, R., Migus, A., Biraben, F., et al. 1995, Astron. Astrophys. Suppl. Ser., 111, 569

Foy, R., Tallon, M., Tallon-Bosc, I., et al. 2000, J. Opt. Soc. Am. A, 17, 2236

Fugate, R. Q., Ellerbroek, B., Higgings, C., et al. 1994, J. Opt. Soc. Am. A, 11, 310

Gavel, D., Ammons, M., Bauman, B., et al. 2008, in SPIE, Vol. 7015, Adaptive Optics Systems

Madec, P.-Y., Rabaud, D., Fleury, B., et al. 1997, La Lettre de l'OHP, 16, 2

Max, C., McGrath, E., Gavel, D., et al. 2008, in SPIE, Vol. 7015, Adaptive Optics Systems

Morris, J. 1994, J. Opt. Soc. Am. A, 11, 832

Pilkington, J. 1987, Nature, 330, 116

Pique, J.-P., Moldovan, I. C., & Fesquet, V. 2006, Journal of the Optical Society of America A, 23, 2817

Rondeau, X., Thibaut, E., Tallon, M., & Foy, R. 2007, Journal of the Optical Society of America A, 24

Schöck, M., Foy, R., Pique, J.-P., et al. 2000, in SPIE, Vol. 4007, Adaptive Optical Systems Technology, ed. P. L. Wizinowich, 296–307

Schöck, M., Foy, R., Tallon, M., Noethe, L., & Pique, J.-P. 2002, MNRAS, 337, 910

Séchaud, M., Hubin, N., Brixon, L., et al. 1988, in Very Large Telescopes and their Instrumentation, ed. M.-H. Ulrich, ESO/NOAO Conferences No. 30, ESO, Garching, Germany, 705–714

Siegman, A. E. 1983, Am. J. Phys., 51, 1110

Tokovinin, A. 2000, MNRAS, 316, 637

SF2A 2008
C. Charbonnel, F. Combes and R. Samadi (eds)

INTERFEROMETRY AT THE LBT

Labadie, L.[1], Herbst, T. M.[1] and Rix, H.-W.[1]

Abstract. The Large Binocular Telescope, resulting from a US/Germany/Italy partnership, is designed to be a multi-purpose observatory with single-dish and interferometric capabilities in the optical, near and mid infrared. The LBT is partially operational for science observations, and the interferometric instruments LINC-NIRVANA and LBTI will become available in 2010. I will summarize the current status of the LBT, focusing more particularly on the Fizeau interferometric wide-field imager LINC-Nirvana.

1 Introduction

The Large Binocular Telescope (LBT) installed on Mount Graham, Arizona, is a unique facility supporting two 8.4-m primary mirrors jointly moved by an alt-azimuth mount (see Fig. 1). The LBT will offer, at time of full operation, eight "single-eye" instruments and two interferometers. For comparison, The Paranal Observatory runs thirteen instruments including the three interferometers AMBER, MIDI and PRIMA, this last one being presently commissioned. The LBT is a gregorian telescope, which means that the primary focus lies between the primary and the secondary mirror. This offers the opportunity to exploit the prime focus for wide-field imaging over several arcminutes. The telescope appears as a compact ensemble of circa $25\,\mathrm{m}^3$ and is installed under a cubic dome that opens horizontally a further 20 m in observing mode (see white arrows in Fig 1). The two interferometers, LINC-Nirvana and LBTI, are installed on the interferometric platform between the two primaries, and therefore bounded to the telescope structure. This solution certainly means that LBTI and LINC-Nirvana will have to support additional flexure during operation, unlike traditional interferometers installed at the Coudé focus. However, this configuration will allow us to perform Fizeau interferometry with LINC-Nirvana for the first time on large telescopes, and in addition is very favorable to nulling interferometry performed by the LBTI since it reduces the number of warm reflections and consequent background contamination. The LINC-Nirvana instrument is currently under integration at the MPIA of Heidelberg. In its coherent combination configuration, LINC-Nirvana will offer the equivalent of a 23-m telescope, which is among the largest telescopes in the world and naturally appearing as a pre-ELT facility. To exploit the full potential of the telescope, adaptive optics is installed to allow reaching diffraction-limited images. At LBT, the secondary mirror is adaptive to correct for the ground layer turbulence.

2 Overview of LBT instrumentation

Eight single-aperture instruments equip the LBT. These are the two LUCIFER near-infrared spectro-imagers, the two prime focus cameras LBC-Blue and LBC-Red operating in the visible and in binocular mode, the two MODS and the two PEPSI spectrographs, one on each eye of the telescope.

LUCIFER : This is the *LBT Near Infrared Spectroscopic Utility with Camera and Integral Field Unit for Extragalactic Research* (Mandel et al. 2006), the near-infrared instrument built by a German consortium. LUCIFER operates in the 0.9 - 2.5 m spectral range and provides imaging and spectroscopic capabilities in seeing and diffraction limited modes. LUCIFER can reach a spectral resolution up to R$\sim$30000 and covers a field-of-view of 30"$\times$30" in the diffraction-limited mode.

LBC : The LBT is equipped with two prime focus camera covering the visible range thanks to several broad-band and narrow-band visible filters. The mosaic of CCD detectors gives access to a large field-of-view of 27

[1] Max-Planck Institut für Astronomie; Königstuhl, 17, 69117 – Heidelberg – Germany

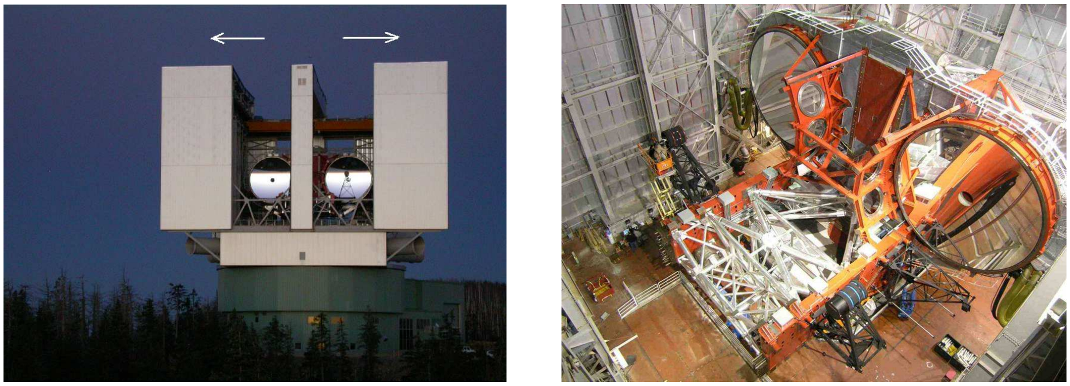

Fig. 1. *Left*: general view of the LBT dome on Mount Graham, Arizona. The enclosure has a cubic shape. On this image, only the blue prime focus camera is installed on the left eye. The *Right*: the binocular telescope inside the dome. The two 8.4-m mirrors are 14.4-m center-to-center and supported by an alt-azimuth mount.

arcmin square with 0.23” pixel scale. The two camera are in operation at the moment at LBT delivering science data.

MODS and PEPSI : MODS 1 and 2 – blue and red – are the two visible imagers and medium-resolution spectrographs placed directly at the F/15 focus of the telescope. The accessible field-of-view is 6’×6’ with 125 mas pixel scale. PEPSI is a fiber-feed high-resolution Echelle spectrograph – up to R$\sim$300000 – designed to use the two apertures in spectropolarimetric mode.

3 Interferometric capabilities at the LBT

3.1 Nulling interferometry with LBTI

The two primary mirrors are located 14.4 meters apart center-to-center, which is a moderate baseline compared to classical long-baseline interferometers like MIDI or Keck. However, this is particularly adapted for nulling interferometry since a short baseline will minimize the leakage from the cancelled star. The LBT-Interferometer – LBTI – is the nulling interferometry instrument devoted to the search for exo-zodiacal dust around solar-type stars (Hinz et al. 2004). In addition to the various noises from astrophysical origin, the thermal background is a strong limitation for the detection of exo-zodiacal light. With only three warm reflexions prior to entering the cryostat, LBTI is able to keep this level of instrumental contamination at a very low level. Combined to the relatively short baseline, the detection capabilities of the LBTI are clearly improved in comparison to the Keck nuller (see Table 1).

Wavelength (μm)	ratio ρ=EZE/star at LBT	ratio ρ=EZE/star at Keck
8 μm	0.14	0.012
10 μm	0.45	0.031
10 μm	1.07	0.067

Table 1. expected ratios between the exo-zodiacal emission (EZE) and stellar leakage expected in the N band at the LBT and Keck interferometer. The short-baseline configuration of the LBT is very advantageous because of its broad null across the stellar disk.

3.2 Fizeau interferometry with LINC-Nirvana

LINC-Nirvana is a Fizeau interferometer that coherently combines on the detector the images from each aperture. If the condition of homotheticity between the input and output pupils is respected (Angel et al. 1998), every point-like source produces a interferometric fringe pattern at the spatial frequency B/λ modulated by the 8.4-m PSF, where B=22.8 m and λ is the wavelength. This combination scheme permits to access a wide

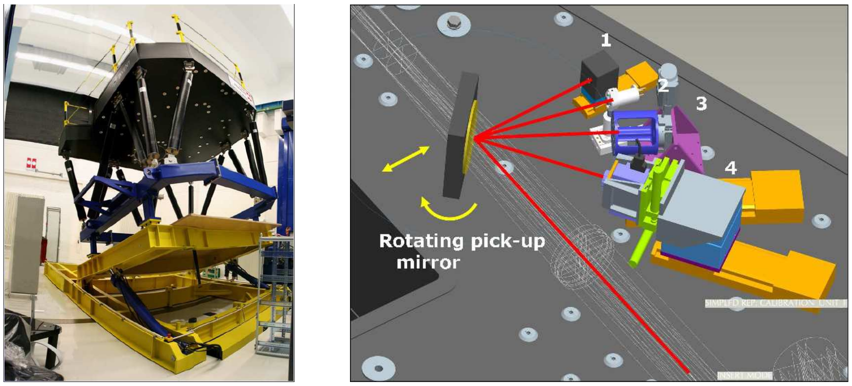

Fig. 2. *Left*: The LINC-Nirvana bench tilted to simulate the behavior on the telescope. *Right*: Design of the calibration unit with the pick-up mirror that feeds the instrument with the sources 1, 2, 3 and 4 alternatively.

field-of-view at high angular resolution, unlike other classical pupil-plane interferometers. LINC-Nirvana operates as a true imager delivering the angular resolution of a 23-m telescope over a 10"×10" field-of-view. The angular resolution is, respectively, 10, 15 and 20 mas in the J, H and K bands. As for any large telescope, diffraction-limited observations require a performing adaptive optics system to compensate for the atmospheric turbulence. Conventional adaptive optics systems are able to correct the wavefront corrugations with a good Strehl ratio only over a small field-of-view of a few arcseconds. This is a limiting factor for science programs that aim at studying large scale structures. The alternative is to implement multi-conjugated adaptive optics (MCAO), which makes use of several guide stars, and possibly several deformable mirrors, to analyze the atmospheric turbulence over a larger field-of-view. Several approaches are possible for implementing MCAO (Ground Layer AO, Layer-Oriented AO etc...) and a starting point on this technique can be found in Beckers (1993) or Ragazzoni et al. (2002). This technique is obviously more complex than single AO systems, but in the case of LINC-Nirvana using MCAO is clearly mandatory to obtain a good fringe contrast over a larger field-of-view. The MCAO system on LINC-Nirvana is based on eight pyramid wavefront sensors operating in the visible (Ragazzoni et al. 2003). The correction of the ground layer turbulence can be achieved over a 6 arcminutes field-of-view by coupling the wavefront sensor to the deformable secondary mirror. The internal 2 arcminutes field-of-view that is used for interferometry is also corrected for higher atmospheric turbulence at 4 and 10 km, by conjugating the deformable mirror to the appropriate altitude. Such an adaptive optics system for wide-field correction will clearly be a major step towards large telescope operation. Meanwhile, the technique was demonstrated on-sky recently with the first spectacular K-band images from MAD at the VLT which delivered a high Strehl correction over a 2'×2' field-of-view (ESO press release).

3.3 Status of LINC-Nirvana

LINC-Nirvana is currently under integration at the MPIA. The optical bench can be tilted as a whole in order to reproduce the configuration at the telescope (see Fig. 2). This will permit to investigate the impact of flexure on the optical alignment and the stability of the fringes. This is also an essential aspect to estimate the operability of the fringe tracking system, which is responsible for detecting and correcting the effects of flexure on the PSF overlap.

The MCAO has been delivered for integration at the MPIA and is currently undergoing functional tests. Other key sub-systems are following a test phase prior to integration on the bench. This concerns the piston mirror unit that corrects for the residual optical path difference (OPD) in conjunction with the FFTS[1], the cryostat and the infrared detector and the calibration unit. Concerning this last sub-system, we have developed a design that can ensure a good stability for the reference sources (see Fig. 2). The purpose of the calibration unit is to give absolute references to the piston mirror for the zero-OPD position, to check for simultaneous zero-OPD on-axis and off-axis for pupil homotheticity, to provide reference sources for the MCAO unit and flat-fielding for

[1]FFTS: Fringe and Flexure Tracking System

the detector (Labadie et al. 2008). Tests are in progress, in particular for the zero-OPD unit which represents the most critical part in terms of calibration of systematic errors due to telescope flexure.

3.4 Scientific programs with LINC-Nirvana and installation schedule

LINC-Nirvana, as a high-resolution and wide-field imager, will permit to study a large variety of science cases in the field of galactic and extragalactic astronomy. They are:

- YSOs environment, circumstellar disks, outflows, formation of binary stars.
- Stellar clusters and compact HII regions.
- Astrometry for extrasolar planets.
- Solar systems minor bodies.
- The Galactic Center.
- Host galaxies at z$\sim$1-2.

The main constraints for these different science cases are on the availability of reference stars for the MCAO, the quality of the PSF and the astrometric and photometric capabilities of the instrument.

The integration phase at the LBT has started in 2005 with the installation of LBC-Red and will go on until the installation of the interferometric *strategic* instruments. The two prime focus cameras are in place and performing science observations. LUCIFER 1 has passed the acceptance test and is currently being commissioned on Mount Graham. The two interferometers LBTI and LINC-Nirvana are following the integration phase and are expected to be on sky on 2010.

References

Mandel, H. G., Appenzeller, I., Seifert, W. et al. 2006, Proc. of SPIE, vol. 6269, 62693F

Hinz, P. M, Connors, T., McMahon, T. et al. 2004, Proc. of SPIE, vol. 5491, 787

Angel, J. R. P., Hill, J. M., Strittmatter, P. A. et al. 1998, Proc. of SPIE, vol. 3350, 881

Beckers, J. M. 1993, ARA&A, 31, 13

Ragazzoni, R., Herbst, T. M., Gässler, W. et al. 2003, Proc. of SPIE, vol. 4839, 536

Ragazzoni, R., Diolaiti, E., Farinato, J. et al 2002, A&A, 396, 731

Labadie, L., de Bonis, F., Egner, S. et al. 2008, Proc. of SPIE, vol. 7013, 701334

ESO press release 19/07 (30/03/2007) at www.eso.org/public/outreach/pressrel/pr-2007/pr-19-07.html

SF2A 2008
C. Charbonnel, F. Combes and R. Samadi (eds)

WAVEFRONT RECONSTRUCTION WITH ELONGATED SODIUM LASER GUIDE STARS

Tallon, M.[1], Tallon-Bosc, I.[1], Béchet, C.[1] and Thiébaut, E.[1]

Abstract. When forming a sodium laser guide star (LGS), the lightened volume in this layer can be seen as a cylindrical source ∼1m in diameter and ∼10 km in length. Because of the parallax, the LGS looks significantly elongated when observed from the edge of the pupil of an Extremely Large Telescope. This effect prompts the lasers to be launched from behind the secondary instead of from around the telescope, but still degrades significantly the accuracy of wavefront sensing for adaptive optics. Further, the measurement uncertainties are no more uniform across the pupil and correlations are introduced. From numerical simulations, we analyze the benefit of taking into account these structured correlations and the effect of priors in wavefront reconstruction algorithms. We found that priors are effective for a single LGS launched behind the secondary. When combining the measurements from several LGSs in a Ground Layer adaptive optics system, we found that taking into account the noise covariances and launching from the edge yields the best reconstruction. Further, in this configuration, we can discard the worse measurements along the elongated direction and reduce the field of view (thus use a smaller detector) without any significant loss of accuracy.

1 Introduction

Extremely Large Telescopes (ELT) all rely on adaptive optics systems using several laser guide stars (LGS). But since the atmospheric sodium atoms are concentrated at ∼90 km in altitude, in a ∼ 10km thick layer (Papen et al. 1996), a LGS is seen as a significantly elongated spot from the edge of an ELT (Fig. 1).

The elongation of the spots at the focus of the subapertures of a Shack-Hartmann wavefront sensor significantly reduces the accuracy on the measurement of the centroid displacements. Furthermore, much larger detectors are necessary to image the enlarged spots. New centroiding algorithms like the matched filter (Gilles & Ellerbroek 2006) have been devised to cope with the increase of reading noise, but the magnitude of photon noise – proportional to the size of the spots (Rousset 1999) – is much higher.

Our aim is here to assess the effect of the spot elongation on the reconstructed wavefront. Since the elongations vary in amplitude and orientation (Fig. 1), the noise is no more uniform across the pupil and correlations appear between x and y coordinates of the measured gradients of the wavefront. We show that introducing Kolmogorov (or von Kármán) priors and taking into account the actual noise correlations dramatically improve the quality of the reconstruction, compared to ignoring them. From numerical simulations, we compare the wavefront reconstruction capability of different methods and show that unexpected better results can be obtained when the LGSs are launched from the edge of the telescope pupil, although all the current ELT projects expect to minimize the problem by launching the LGS from the center, behind the secondary. Furthermore, we show that truncating the spots with smaller detectors does not degrade significantly the results.

2 Reconstruction methods and assumptions

In the following, we will compare four reconstruction methods, introducing priors or not, and taking into account actual noise correlations or not. All of them start with the same model of data:

$$\boldsymbol{d} = \mathbf{S} \cdot \boldsymbol{w} + \boldsymbol{n}, \tag{2.1}$$

[1] Université de Lyon, Lyon, F-69003, France ; Université Lyon 1, Observatoire de Lyon, 9 avenue Charles André, Saint-Genis Laval, F-69230, France ; CNRS, UMR 5574, Centre de Recherche Astrophysique de Lyon ; Ecole Normale Supérieure de Lyon, Lyon, F-69007, France

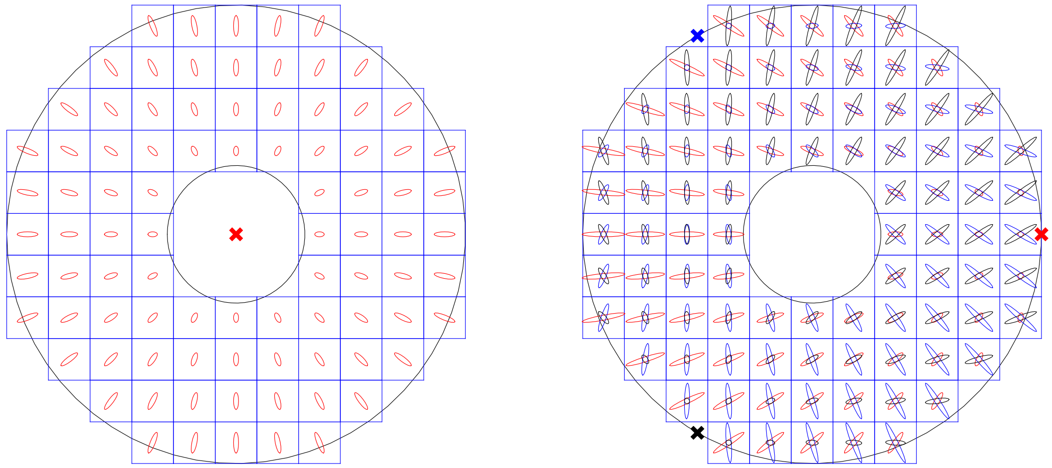

Fig. 1. Layout of the elongated spots for centered LGSs (left) and for three LGSs launched at 120° from the edge of the pupil (right). The diameter of the pupil is 42m with 30% central obstruction. In the two cases, $h_0 = 90$ km, the FWHM of the Sodium layer is 10 km, and the minimal FWHM of the spots is $1.2''$ (spot size with no elongation). This configuration with 11×11 subapertures is chosen to be illustrative, but 100×100 subapertures are used for the simulations. Here, the field of view of the 3.8m subapertures is $10''$, and the squares represent both the subapertures and their field-of-view limits. Launching from the center minimizes the elongation and produces radially elongated spots: this is the chosen configuration for the Thirty Meter Telescope (TMT) (Gilles & Ellerbroek 2006).

where the vector of data, $\boldsymbol{d}$, is obtained from the vector of wavefront samples on a suitable grid, $\boldsymbol{w}$, using a linear model $\mathbf{S}$ of the wavefront sensor. Vector $\boldsymbol{n}$ stands for an additive zero-mean noise independent from the data. We will assume a Shack-Hartmann wavefront sensor with Fried's geometry for $\mathbf{S}$ (Fried 1977).

We consider four different methods to invert Eq. (2.1), corresponding to the following equations:

$$\left(\mathbf{S}^{\mathrm{T}} \cdot \mathbf{S}\right) \cdot \boldsymbol{w} = \mathbf{S}^{\mathrm{T}} \cdot \boldsymbol{d}, \qquad \text{for pure least squares,} \tag{2.2}$$

$$\left(\mathbf{S}^{\mathrm{T}} \cdot \mathbf{C}_{\boldsymbol{n}}^{-1} \cdot \mathbf{S}\right) \cdot \boldsymbol{w} = \mathbf{S}^{\mathrm{T}} \cdot \mathbf{C}_{\boldsymbol{n}}^{-1} \cdot \boldsymbol{d}, \qquad \text{for weighted least squares,} \tag{2.3}$$

$$\left(\mathbf{S}^{\mathrm{T}} \cdot \mathbf{C}_{\boldsymbol{n}}^{-1} \cdot \mathbf{S} + \mathbf{C}_{\boldsymbol{w}}^{-1}\right) \cdot \boldsymbol{w} = \mathbf{S}^{\mathrm{T}} \cdot \mathbf{C}_{\boldsymbol{n}}^{-1} \cdot \boldsymbol{d}, \qquad \text{for maximum } a\ priori \text{ (MAP),} \tag{2.4}$$

$$\left(\mathbf{S}^{\mathrm{T}} \cdot \mathbf{S} + \sigma_n^2 \mathbf{C}_{\boldsymbol{w}}^{-1}\right) \cdot \boldsymbol{w} = \mathbf{S}^{\mathrm{T}} \cdot \boldsymbol{d}, \qquad \text{for MAP with uniform noise.} \tag{2.5}$$

Equations (2.2) and (2.5) assume uniform Gaussian noise. The equations are written in the form $\mathbf{A} \cdot \boldsymbol{x} = \boldsymbol{y}$ where we are looking for $\boldsymbol{x}$. Indeed, we solve them with the conjugate gradient method (Barrett et al. 1994). This yields the "minimum norm" solution (*i.e.* the method is equivalent to use the pseudo-inverse of $\mathbf{A}$) when $\mathbf{A}$ is not invertible. Also, the conjugate gradient method does not need to compute the inverse of $\mathbf{A}$ which is a huge matrix in our ELT case ($\sim 2\ 10^4 \times 10^4$ for our 100×100 subapertures wavefront sensor). For computing efficiency, we use the Fractal Iterative Method (Tallon et al. 2007), a preconditioned conjugate gradient method using a so-called fractal operator and an optimal diagonal preconditioner.

In our simulations, we introduce some simplifications to only focus on the effect of the spot elongations. We assume that the LGSs can measure tip/tilts and that all the turbulence is in the pupil plane. Thus the results are not affected by any focus anisoplanatism or tip/tilt indetermination. We also assume a Gaussian distribution of the vertical density profile of the sodium atoms, centered at altitude 90 km, and spots with elongated Gaussian shapes at the focus of the 100×100 subapertures of the Shack-Hartmann wavefront sensor. The actual noise covariance matrix $\mathbf{C}_{\boldsymbol{n}}$ is determined by assuming that the noise is proportional to the size of the spot (Rousset 1999). Seeing is set to $0.7''$ at 589 nm (i.e. $r_0 = 17.4$ cm at 589 nm), corresponding approximately to median conditions at Paranal observatory, with an outer scale $L_0 = 22$m.

3 Simulation results

From the same simulated data, the aim is to compare the errors of the wavefront reconstructions obtained with the different reconstruction algorithms listed in Sec. 2.

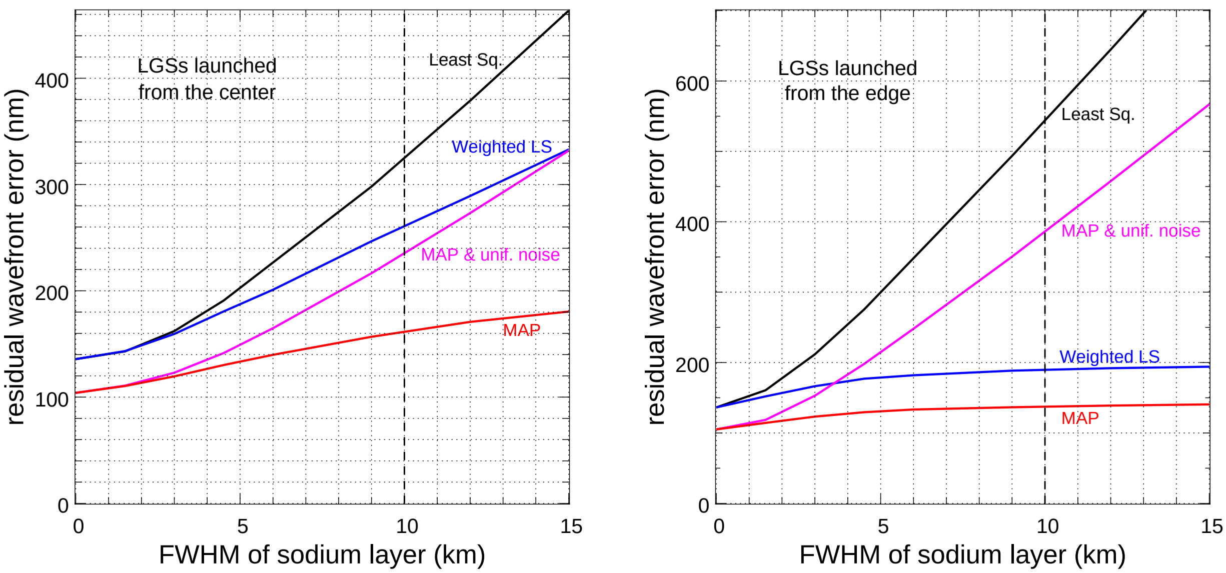

Fig. 2. Comparison of the wavefront errors obtained with the different reconstruction methods, depending on the amount of elongation. On the left, one LGS launched from the center. The same curves are obtained when combining three LGSs three times fainter (noise variance three times higher). On the right, three LGSs launched from the edge. Corresponding configurations are shown on Fig. 1. Noise covariance matrix is only used for *Weighted LS* (Eq. 2.3) and *MAP* (Eq. 2.4), while priors are only used for *MAP* and *MAP+uniform noise* (Eq. 2.5). The dashed vertical line corresponds to the typical mean FWHM of sodium density profile.

Results for a single LGS launched from the center of the pupil are shown in Fig. 2 (left) as a function of the amount of elongation (FWHM of the sodium layer is varied from 0 to 15 km). Noise has been fixed to 1 rad^2/subaperture where no elongation, with a spot size of 1.2$''$ FWHM. This phase error at 589 nm corresponds to $\sim$ 0.046$''$rms of jitter, or $\sim$94 nm rms of wavefront error, measured as the rms path difference between the edges of the subapertures. The signal to noise ratio per subaperture is $\sim$ 5.5.

If we consider the FWHM for the mean sodium profile (10 km), we can see a significant difference between the worse method (*Least Squares*) where the elongation increases the wavefront error by a factor of 2.4, and the best method (*MAP*) where this factor is only 1.6. For such an elongation, *MAP* gives a wavefront error half as big as *Least Squares*. When no elongation, we can see that using priors (MAP methods) allows the variance of the error to be reduced by almost a factor of two as already found by Béchet et al. (2007). The curves show that the usefulness of the priors increases with the elongation. We interpret this behavior by an increasing error on the radial modes because of the radial elongation: priors allow reducing this error by using covariances with the other modes that are less affected by the elongation.

If we equally split the light of this single LGS into 3 LGSs launched from the center, the variance of the noise will be three times higher, *i.e.* 3 rad^2/subaperture at 589 nm. Since the three LGSs will give three times the same radially elongated spots (Fig. 1, left), the combination of the three independent measurements will give again the same results (Fig. 2, left). We expect that launching these fainter LGSs from the edge (Fig. 1, right) will improve the reconstruction since each subaperture will see three spots elongated in different directions. This is shown on Fig. 2 (right). The use of the noise covariances is now critical. Indeed, not to take into account the noise covariances makes the residual wavefront errors to be much higher (*Least Squares* and *MAP with uniform noise* methods). The noise covariance matrix allows the reconstruction to properly weight the measurements in each subaperture in order to take into account mainly the measurements in the most accurate directions (*i.e.* the directions perpendicular to the elongations). We can notice that *MAP* method with any elongation gives a better reconstruction than using least squares (weighted or not) without elongation.

Further, when the actual noise covariances are used, Fig. 2 shows an asymptotic behavior as the sodium profile FWHM increases, indicating that as soon as the elongation is significant, the relative weight of the corresponding measurement is so small that it has no more influence. Yet increasing the elongation does no more degrade the situation. In such a regime, we could then set to zero the weights on these measurements

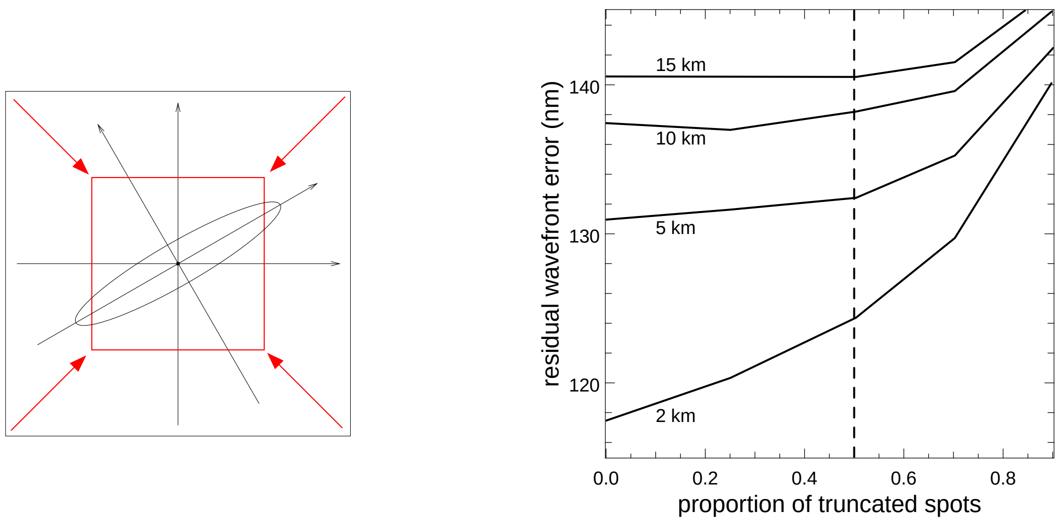

Fig. 3. Reducing the field-of-view truncates the most elongated spots (left) and prevent the measurement of its displacement along the elongation. Simulations (right) show that the quality of the reconstruction is not significantly degraded if 50% of the spots are truncated. The increase for higher proportions is due to the loss of photons.

without significant loss of accuracy. This also means that we should not even need these measurements, so that we could reduce the size of the detectors even if the spots are truncated (Fig. 3, left). We consider in this simulation that a spot is truncated if it is cut at more than 1% of its maximum. Figure 3 shows that the quality of the reconstruction is not significantly degraded if 50% of the spots are truncated.

4 Conclusion

This work shows that, even if priors are helpful, using the actual noise covariances in the reconstruction algorithm is critical. When combining several LGSs launched from the edge of the pupil, the effect of the elongation is then mitigated, even if we use detectors as small as those used when launching from the center, so truncating 50% of the spots.

This activity is supported by the European Community (Framework Program 6, ELT Design Study, contract No 011863). The algorithms and the simulations presented in this article have been implemented in Yorick, a free data processing language written by D. Munro (http://sourceforge.net/projects/yorick/).

References

Barrett, R., Berry, M., Chan, T. F., et al. 1994, Templates for the Solution of Linear Systems: Building Blocks for Iterative Methods (SIAM, Philadelphia PA)

Béchet, C., Tallon, M., & Thiébaut, E. 2007, in Signal Recovery and Synthesis, ed. B. L. Ellerbroek & J. C. Christou, OSA topical meetings (Optical Society of America, Washington, USA), paper JTuA4

Fried, D. L. 1977, J. Opt. Soc. Am., 67, 370

Gilles, L. & Ellerbroek, B. 2006, Appl. Opt., 45, 6568

Papen, G. C., Gardner, C. S., & Yu, J. 1996, in Adaptive optics, O.S.A. topical meeting (Optical Society of America, Washington, USA), 96–99

Rousset, G. 1999, in Adaptive Optics in Astronomy, ed. F. Roddier (Cambridge University Press), 91–130

Tallon, M., Thiébaut, E., & Béchet, C. 2007, in Adaptive Optics: Analysis and Methods, ed. B. L. Ellerbroek & J. C. Christou, OSA topical meetings (Optical Society of America, Washington, USA), paper PMA2

SF2A 2008
C. Charbonnel, F. Combes and R. Samadi (eds)

EXOPLANET CHARACTERIZATION WITH LONG SLIT SPECTROSCOPY IN HIGH CONTRAST IMAGING

Vigan, A.[1], Moutou, C.[1] and Langlois, M.[1]

Abstract. Extrasolar planets observation and characterization with high contrast imaging instruments will be a very important subject for observational astronomy in the coming decade. Dedicated new instruments are being developed in order to achieve this goal with very high performance. In particular, full spectroscopic characterization of low temperature planetary companions is an extremely important milestone. We present a new data analysis method for long slit spectroscopy (LSS) with coronagraphy which allows characterization of planetary companions with low effective temperature. In a speckle-limited regime, the method allows an accurate estimation and subtraction of the scattered starlight, in order to extract a clean spectrum of the planetary companion. This method was developed in the context of SPHERE (Dohlen et al. 2006), a second generation instrument for the VLT, that will offer several observing modes for detection and characterization of exoplanets in the near-infrared. Using this method we are able to achieve a contrast reduction of 0.5 to 2.0 magnitudes compared to the coronagraphic observations on simulated images, leading to the possible characterization of planetary companions with effective temperatures of 600 K and 900 K orbiting respectively around M0 and G0 stars at 10 pc, and for angular separations of 1.0″.

1 Data analysis

The main limitation in high-contrast coronagraphic images are the speckles induced by atmospheric phase residuals and instrumental aberrations. To remove the scattered starlight and retrieve a clean planetary spectrum we have developed a data analysis method for long slit spectroscopy which uses the fact that the speckle pattern size and position is wavelength dependant (Sparks & Ford 2002), whereas the planet position remains fixed with wavelength (Fig. 1). A detailed description of the method is available in Vigan et al. (2008).

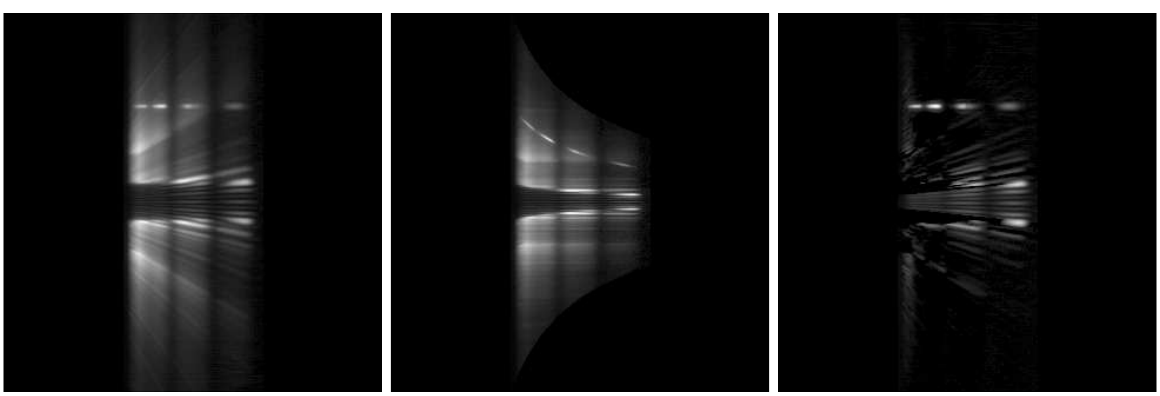

Fig. 1. Illustration of our data analysis method. **Left:** the coronagraphic star spectrum with one companions at 1″. **Middle:** same spectrum after spatially rescaling each column according to its corresponding wavelength. **Right:** final spectrum after removing the star contribution and rescaling the columns back to their original size.

[1] Laboratoire d'Astrophysique de Marseille, Technopôle Marseille Étoile, 38, rue Frédéric Joliot Curie 13013 Marseille, France
e-mail: `arthur.vigan@oamp.fr`

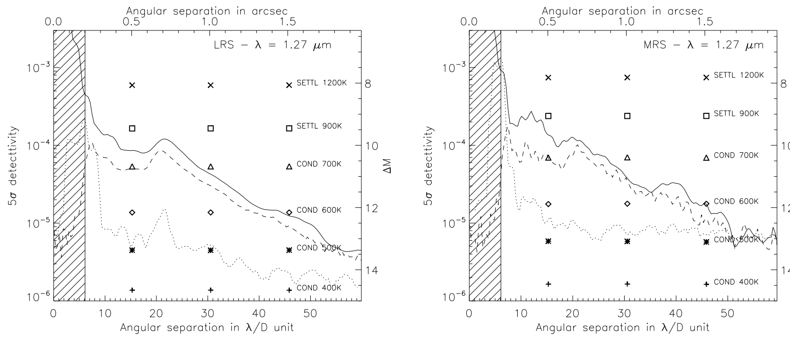

Fig. 2. Detection limit as a function of angular separation for an M0 star at 10 pc in low (left) and medium (right) resolution at $\lambda = 1.27$ μm, and for an exposure time of 1 hour. *Plain line*: non-coronagraphic PSF. *Dashed line*: coronagraphic PSF. *Dotted line*: detection limit after data analysis. *Hatched area*: coronagraph mask.

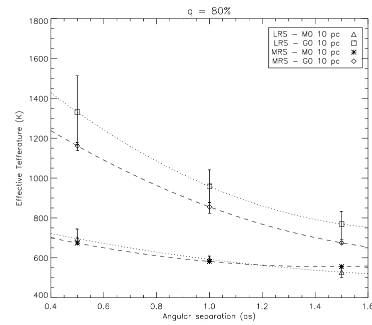

Fig. 3. Effective temperature at which a value of $q = 80\%$ is reached for M0 and G0 stars at 10 pc, as a function of angular separation, in low and medium resolution.

2 Performances

The performance of the data analysis method is evaluated in two ways: the contrast reduction and the quality of the spectrum extraction.

2.1 Contrast reduction

Our data analysis method offers an improvement of the detection limit by 1.0 to 2.5 magnitudes (Fig. 2) in J and H band. In K band the results are slightly decreased because the contrast is already very favorable. Considering COND-2003 models (Allard et al. 2003), our method would allow proper characterization a 600 K companion orbiting at $1.0''$ around an M0 star at 10 pc, in both low ($R = 35$) and medium ($R = 400$) resolution. This performance is equivalent to the detection mode of SPHERE (Boccaletti et al. 2008).

2.2 Extraction quality

We defined a quality factor, q, which measures the correlation and discrepancy between input and output spectra of the companion. Analysis with COND-2003 atmosphere models shows that error on $T_{\rm eff}$ determination of the companion is less than 100 K for $q > 80\%$. Figure 3 shows the effective temperature at which a value of $q = 80\%$ is reached in different cases. We see that the performance is comparable in low and medium resolution for both M0 and G0 stars at 10 pc. The performance depends on angular separation, especially for bright stars.

References

Dohlen, K. 2006, SPIE Proc., 6269

Sparks, W. B. & Ford, H. C. 2002, ApJ, 578, 543

Vigan, A. 2008, ArXive e-prints, 808, arXiv:0808.3817

Allard, F. 2003, IAU Symposium, 211, Brown Dwarfs

Boccaletti, A. 2008, ArXiv e-prints, 807, arXiv:0807.0697

ASOV

Virtual Observatories

SF2A 2008
C. Charbonnel, F. Combes and R. Samadi (eds)

EVOLUTIONS OF THE VIRTUAL OBSERVATORY

Genova, F.[1]

Abstract. The paper describes the status of the astronomical Virtual Observatory, and introduces the new European projects of the Seventh Framework Programme, EuroVO-AIDA (Astronomical Infrastructure for Data Access) and EuroPlaNet Research Infrastructure. The role of the *Action Spécifique Observatoires Virtuels France* is also discussed.

1 Introduction

The objective of the Virtual Observatory (VO) is to provide seamless and transparent query of on-line data and services, with tools, in particular for data visualisation, processing and analysis. The VO also offers data centers a framework of standards and tools to "publish" their data and services in the VO.

The VO concept has emerged in 1999/2000, and the first projects have been funded in 2001, among which the European Phase A project, *Astrophysical Virtual Observatory* (AVO) . The VO is now in transition to operations, and it appears in the AstroNet European Roadmap as one essential infrastructure of astronomy.

At European level, the VO development is coordinated by the Euro-VO project, a best effort alliance of 8 partners (France, Germany, Italy, the Netherlands, Spain, the United Kingdom, and the two European Agencies, ESA and ESO). Building on the expertise gained during Phase A, Euro-VO is organised in three interacting parts: the *Euro-VO Data Centre Alliance* (DCA), led by the *Centre de Données astronomiques de Strasbourg* (CDS), a network of data centres which populate the system with data, metadata and services; the *Euro-VO Technology Centre* (VOTC), led by AstroGrid (the UK VO project), a distributed organisation which coordinates a set of research and development projects on the advancement of VO technology, systems and tools; and the *Euro-VO Facility Centre* (VOFC), led by ESA and ESO, which provides a registry of resources as well as community support for VO take-up and dissemination.

The following sections follow the Euro-VO structure: Section 2 describes the status of the construction of VO technical infrastructure, Section 3 deals with data centres in the VO and with the Euro-VO DCA Coordination Action, and Section 4 with interaction with users. Finally, Section 5 describes the new European VO project in astronomy (Euro-VO Astronomical Infrastructure for Data Access - EuroVO-AIDA) and the emergence of an international coordination in the field of planetary studies (the International Planetary Data Alliance and the EuroPlaNet projects of the Sixth and Seventh Framework Programmes). The conclusion summarizes open questions on the evolution of the *Action Spcifique Observatoires Virtuels France.*

2 Building the VO technical infrastructure

National VO projects are all different. For instance, in France, the *Action Spécifique Observatoires Virtuels France* (ASOV) coordinates French participation in the VO development, with a small amount of "triggering" money from INSU and CNES. The work force is coming from the commitment of research laboratories. In other countries VO projects also pay for human resources engaged in the VO development.

The astronomical VO aims at building *a single VO* to access all astronomical data available world-wide, and it was realized early that internationally agreed interoperability standards were the key, which would allow VO tools to communicate with all VO-enabled data and services for data discovery, retrieval and analysis. The first structure which tackled the development of interoperability standards was a Working Group formed by the

[1] Observatoire Astronomique, UMR 7550, CNRS/UdS, 11 rue de l'Université, 67000 Strasbourg, France

OPTICON European network in 2000, led by CDS, which included from the beginning membership from USA and Canada. It was shortly superseded by the *International Virtual Observatory Alliance* (IVOA), founded in 2002 by the three projects which had then started (AVO for Europe, the USA *National Virtual Observatory* and AstroGrid). The IVOA is an alliance of the national and continental VO projects, with presently (mid-2008) 16 members including France and Euro-VO. It coordinates the definition of the VO interoperability standards, and has created Working Groups and Interest Groups to tackle the different aspects (Fig. 1).

Fig. 1. Summary of IVOA activities, showing in particular the list of IVOA Working Groups and Interest Groups (copy of a web page from the IVOA web site).

At the European level, the VOTC is as explained earlier a distributed entity. One component of VOTC is the VO-TECH Design Study (2005-2008), led by AstroGrid, with three British Universities (Edinburgh, Cambridge, Leicester), CDS, ESO and INAF as partners. The ESA-VO project is also an important contributor.

In France, the CDS has been involved in the development of VO interoperability standards from the beginning (e.g. VOTable, Ochsenbein et al. 2002), and at present many French groups participate actively in IVOA activities. Mid-2008, several Working Groups and Interest Groups (Applications, Data Model, Semantics, Theory, VOTable) have French leadership, and French teams are significantly contributing to many standards.

The development of standards for Theory is one interesting recent evolution of IVOA. The main objectives are to give access to simulation services or to simulation results, and to be able to compare simulation results with observations. French teams have been among the pioneers in this domain (Wozniak 2004), and Theory was one of the first Working Groups created by ASOV in 2004. The IVOA also formed a Theory Interest Group in 2004, with the goal of ensuring that theoretical data and services are taken into account in the IVOA standards process. A significant effort has been devoted to the assessment and definition of standards for the theoretical VO, with support in particular of the *Euro-VO Data Center Alliance* project, which is described in the next section. EuroVO-DCA has a specific work package led by the *Max Planck Institut fur extraterrestrische Physik*, with a strong French and Italian participation. In France teams from the LUTH, the CRAL and the OSUB are actively involved, respectively in Paris, Lyon and Besançon Observatories. They assess the standards on very different types of services: the HORIZON project, microphysics code (e.g. photoionized or photodissociation regions), and the Besançon model of stellar population synthesis of the Galaxy. Several services are available on-line, for instance, the GalMer simulations of the Horizon project (di Matteo et al. 2007), which implement several of the IVOA standards, or the Besançon model (Debray et al. 2006).

3 Data centres in the VO

Data centres are the essential building blocks of the VO. They provide different types of services, such as data archives, added-value services, tools, software suites, theory results and services. They are very different in size, and work in different contexts, from observation archives maintained by large Agencies to small teams in scientific laboratories. They however all share the same keywords: providing a service to users, caring for quality, and having at least some kind of medium term sustainability. The ASOV has performed a first census of French data centres in the VO context in 2005 (more than 40 answers), which has been updated in 2006, and effectively shows a wide diversity.

At European level, actions towards data centres are currently tackled by the *Euro-VO Data Centre Alliance* project. EuroVO-DCA is a Coordination Action of the eInfrastructure *Communication Network Development* programme, which started in September 2006 for 28 months, and is supported at the level of 1.5 MEuro by the European Commission. It is led by CNRS and gathers the 8 Euro-VO partners. The main objective is to help European data centres to publish their data and services in the VO. It also has work packages dealing more specifically with Theory, as explained above, and with connections with the computational Grid, plus one devoted to support to data centres from other European countries. Detailed information about the project activities is available from the project TWiki page at http://cds.u-strasbg.fr/twikiDCA/bin/view/EuroVODCA/WebHome. The project does not fund the data centres themselves, but organises support actions.

Among the actions organised by the EuroVO-DCA project:

- a census of the European data centres, which has produced more than 65 answers showing as expected a wide diversity;

- two workshops on *how to publish data in the VO*, organised respectively by ESAC in Villafranca in June 2007 and by ESO in Garching in June 2008, aimed at data providers;

- several workshops aiming at improving liaison and information exchange between the VO teams and the community. The first one, *Astronomical Spectroscopy & the Virtual Observatory* (Villafranca, March 2007), dealt with a domain of interest for several of the Euro-VO partners. Two other Workshops were organised back-to-back in Garching in April 2008, in domains of specific interest to EuroVO-DCA: *Theory in the Virtual Observatory* and *Grid and the Virtual Observatory*. Some more details about these workshops will be given in the next section.

4 Liaison with the science community

The 2007 *Astronomical Spectroscopy & the Virtual Observatory* Workshop has been a remarkable success, with more than 130 participants, a significant fraction of them not previously involved in the VO. ASOV has a Working Group in the domain and has been in contact for a long time with the national community on this topic. There has been an active French participation in the Organising Committee, review papers, and discussions during the workshop.

The workshop showed a high level of community expectations. One major requirement is that the "VO layer" must be transparent when seen from the users, which reinforces one of the main VO objectives. The community understands that there is a need for underlying technical work on standards and was ready to give its requirements, but insisted on the fact that standards were needed NOW. It was confirmed that some data producers do not wish to share their data, often by fear of not being cited, or that the data be misused. The only action that the VO can take in these matters is to provide detailed information on data characterisation and provenance, and hope that widespread VO take-up will ease these concerns.

The two 2008 Garching Workshops on Theory and the Grid have also been been excellent occasions for information dissemination and debate. The *Theory in the Virtual Observatory* Workshop has permitted presentation and discussion of different types of models, and nurtured the preparation of IVOA standards. The *Grid and the Virtual Observatory* workshop has allowed a good contact between VO and European and national grid projects.

5 VO projects in FP7

5.1 Euro-VO Astronomical Infrastructure for Data Access

The *Euro-VO Astronomical Infrastructure for Data Access* project has been selected in 2007 in the first Infrastructure Call of the Seventh Framework Programme, in the *Scientific Digital Repositories* framework. Like EuroVO-DCA, EuroVO-AIDA is coordinated by CNRS and gathers the 8 Euro-VO partners. The project will get a support of 2.7 Meuros from the European Commission for 30 months, beginning in February 2008. Its aim is to lead the transition of Euro-VO into an operational phase, and it covers all aspects of Euro-VO (DCA, VOFC and VOTC).

EuroVO-AIDA is an *Integrated Infrastructure Initiative* (I3) with Networking, Service and Joint Research Activities. In terms of the different parts of Euro-VO:

- Support to users (VOFC): Several Workshops will be organised, two "Community Workshops" on specific topics (the first one at ESAC in December 2008 on *Multiwavelength astronomy*), and one "Hands-on" Workshop in March 2008; two Announcement of Opportunities for allowing science teams to get support from VO teams to perform science programmes will also be organised (in June 2008 - this one is closed - and June 2009); on-line tutorials will be provided, as well as tools for science usage of the VO.

- Support to data centres (DCA): an additional workshop on *how to publish data in the VO* will be organised at ESAC in June 2009; "service activities" will provide a registry of resources, tools for data and service providers, and on-line tutorials.

- Technological activities (VOTC) will cover continuous development and adjustments of interoperability standards and assessment of the usage of new technologies (such as the Web 2.0) in the VO context.

An additional, new topic for Euro-VO is outreach, which is tackled by a specific work package of EuroVO-AIDA.

5.2 EuroPlaNet: From IDIS towards a European Planetary VO

The planetary science community has recently launched the International Planetary Data Alliance (IPDA), an international structure focused on the development of standards for data archiving and promotion of interoperability among planetary science data archive systems, with the aim to share scientific results returned from exploration of the solar system. IPDA was invited to the last IVOA Interoperability meeting (Trieste, May 2008). This activity has been actively prepared at the national level for several years by the ASOV *Planetology* Working Group.

The FP6 EuroPlaNet Coordination Action (2005-2008), coordinated by CNRS, included a network devoted to *Integrated & Distributed Information Service* (N7 - IDIS). IDIS provides two general services (a directory of scientists and an inventory of resources). It has focussed its activities on documenting science cases produced by EuroPlaNet Discipline Working Groups in different sub-topics of planetary sciences. It is organised into four thematic nodes, with a significant participation of French laboratories:

- Planetary surfaces and interiors (DLR/IPR Berlin)

- Planetary atmospheres (CNRS/IPSL Paris)

- Space plasmas (CNRS/CESR Toulouse and IWF Graz)

- Small bodies and dust (INAF/IFSI Frascati)

with also a technical node located at FMI (Helsinki).

A new project, *EuroPlaNet Research Infrastructure* (EuroPlaNet RI), also coordinated by CNRS, has been proposed as an I3 in the first 2008 Infrastructure Call. It has been selected for the negociation phase with the European Commission for a total budget of 6 Meuros, and is expected to start its four year term in January 2009. The French participation in EuroPlaNet RI is enlarged with the contribution of Paris Observatory, especially the VO Data Centre. EuroPlaNet RI contains among others an IDIS Service Activity, which will provide web access to a host of data sources from space, ground-based, laboratory work and numerical simulations, and to modeling and advanced data analysis tools. A companion Joint Research Activity aims at expanding and integrating web services offered by IDIS to prepare a future planetary VO. The share of IDIS JRA and SA, amounts to 1.14 Meuros within the total budget of EuroPlaNet RI.

6 Conclusion

The future of the VO is to be a seamless but important part of the research infrastructure of astronomy, as well stated in the AstroNet Roadmap. The AstroNet census of future infrastructures shows that future large projects actually plan to provide their data in the VO.

In France, the present activities of the VO teams are well described in the Web site of the 2007 ASOV annual meeting. Services and tools are incrementally made available. ASOV has been created to coordinate French participation in the VO development, and with the advent of the VO operational phase one important issue is to find if and how it is possible to help the French community to use the VO capacities at best. The community is encouraged to participate in all European activities, and gets financial support to attend the Workshops. Are there complementary actions to be taken at the national level? Suggestions are welcome, in particular from the National Programmes.

The author is grateful to Gérard Chanteur for providing her with up-to-date information about EuroPlaNet, and to Igor Chilingarian and Franck Le Petit for their input about theory services.

References

Debray, B., Robin, A. C., Reylé, C., & Schultheis, M. 2006, ADASS XV, Asp. Conf. Ser., 351, 224

di Matteo, P., Combes, F., Chilingarian, I., Melchior, A.Ł., & Semelin, B. 2007, SF2A 2007, 322

Ochsenbein, F. et al. 2002, Toward an International Virtual Observatory, ESO Astrophysics Symposia, ed. P. J. Quinn & K. M. Górski (Springer-Verlag, Berlin/Heidelberg), 118

Wozniak, H. 2004, SF2A 2004 (EdP-Sciences Conference Series), 585

SF2A 2008
C. Charbonnel, F. Combes and R. Samadi (eds)

V.O. PARIS DATA CENTRE PORTAL

Le Sidaner, P.[1], Normand, J.[1], Shih, A.[1], Berthier, J.[1], Bertin, E.[2], Boisson, C.[1], Borsenberger, J.[1], Chilingarian, I.[1], de Batz, B.[1], Desert, J.M.[2], Dubernet, M.-L.[1], Guibert, J.[1], Haigron, R.[1], Jegouzo, I.[1], Le Petit, F.[1], Neiner, C.[1], Prugniel, P.[1], Roy, F.[1], Royer, F.[1], Savalle, R.[1], Schneider, J.[1], Simon, G.[1], Tajahmady, F.[1], Thuillot, W.[1], Vachier, F.[1] and Vetois, J.[1]

Abstract. This is a presentation of the new VO-Paris Portal which provides a direct web access to data available in the Paris Obervatory and partners institutions, through VO Protocols. Our portal allows access to services over the data like image mosaicing, source extraction or astrometry evaluation.

1 Introduction

VO-Paris Data Centre http://vo-web.obspm.fr/ is a federation which was set up by Paris Observatory and partners (IPSL, IAP, CEA). The evolution towards a data centre was a key for the development of a data and services Portal. We present here a prototype of this portal based on protocols and formats of the Virtual Observatory http://voparis-srv.obspm.fr/portal/.

2 VO-Paris Data Centre Portal

VO-Paris promotes a large amount of data through the VO. To increase the visibility of all those resources and to provide useful access, we have developed a portal based on web 2.0 technologies. To access the portal, the end user needs only a browser (no third party application is required). This portal uses VO protocols to query images, spectra and tabular data. It provides a simple query form and allows to launch codes for computation over the available data. All the information associated to the various services comes directly from IVOA registries. All the data displayed on the screen are result of XSLT transformation of VOTable documents.

3 Data and services available through the Portal

3.1 Spectra

VO Access is already available for spectra databases: Fuse, HIG, Giraffe and BeSS (Be Stars Spectra) through SSA (Simple Spectral Access) protocol. HESS database will soon be available.

A client is also available for 3D Spectroscopy, compatible with Euro-3D format. Using the new VO standard PLASTIC, this client allows communication with Aladin and VOSpec which are used for spectrum visualization. Two databases already deliver this kind of spectra through SSA: Giraffe and Aspid.

3.2 Images

VOPSAT (Virtual Observatory Paris Southern ATlas) provides access to surveys ESO-R and SRCJ (B band) available through SIA using different modes. A special effort has been put on astrometric accuracy. The southern part of POSS-E will be soon accessible and DENIS will follow with all the available strips.

[1] Paris Observatory, Paris, France
[2] Institut d'Astrophysique de Paris, Paris, France

Fig. 1. visualization of access and result interface

3.3 *Tabular data*

The Extrasolar Planets Encyclopaedia is the first catalogue providing access to exoplanet information using the VO Cone Search protocol. A TAP (Table Access Protocol) prototype is available for that database.

3.4 *Solar system services*

IMCCE allows VO access to ephemerids, databases of physicals parameters of the Solar System small bodies and comets. The SkyBot service is queryable from our portal.

3.5 *Access to numerical simulations*

Paris Observatory develops numerical simulation services using advantage of VO technologies and standards. About twenty researchers offer simulation codes and databases of theoretical results :
http://vo.obspm.fr/simulation/index.html.
These programs deal with : Physics and chemistry of interstellar medium, physics of active nucleus galaxies, MHD on solar wind, stellar population synthesis, 3D radiative transfer, numerical relativity... Our Services Portal can be extended to launch simulation codes through a user-friendly interface. Some simple functionalities can be added: session variables, access to VOSpace to store results ...

4 Portal of services

The available services dedicated to images are: SExtractor, image mosaicing (using SWarp) and Astrocheck (quality of astrometry). When a service is launched, calculation is submitted to the cluster via the batch queue. The use of the Grid is currently being studied.

5 Conclusion

This portal is an important tool to promote data and to allow online calculation. Thanks to web 2.0 technologies, all the added values services can be used directly via a web browser.

References

Le Sidaner P., Dubernet M.-L., Simon, G. et al., 2007, SF2A-2007: Proceedings of SF2A, p.71

Simon G., Dubernet M.-L., Le Sidaner P., et al., 2006, ASP Conference Series, v.351, p.394

Savalle R., Normand J., Le Petit F. et al. 2008, ASP Conference Series, v.394, p.305

SF2A 2008
C. Charbonnel, F. Combes and R. Samadi (eds)

A SKY BROWSER IN ALADIN

Oberto, A.[1], Boch, T.[1], Bonnarel, F.[1], Bot, C.[1], Fernique, P.[1] and Genova, F.[1]

Abstract. We present a new feature in progress in ALADIN software : an interactive sky browser. The aim is to give a way to browse the sky as easily as outreach softwares can do, but geared for astronomers. The user can visualize a wide field and move seamlessly on the whole sky. This navigation mode will be available for some ALADIN archive surveys, the needed images are automatically downloaded by the ALADIN client. The images for such a view have been preprocessed using the HEALPix scheme, providing a multiresolution pixelization. Usual ALADIN features (overlay of catalogs or images) remain available in this visualization mode.

1 Introduction

ALADIN is an interactive software sky atlas developed and maintained by the Centre de Données astronomiques de Strasbourg (CDS; Genova et al.). It allows the user to visualize digitized astronomical images, superimpose entries from astronomical catalogs or databases. In the context of the Virtual Observatory, ALADIN takes full advantage of the recent development for exploring distributed datasets, visualizing multi-wavelength data and providing liaison with other communities. In this paper, we focus on a new feature in progress, such as a wide view, built on the HEALPix scheme (Hierarchical Equal Area isoLatitude Pixelization; Górski et al., 2005)).

2 Building the view

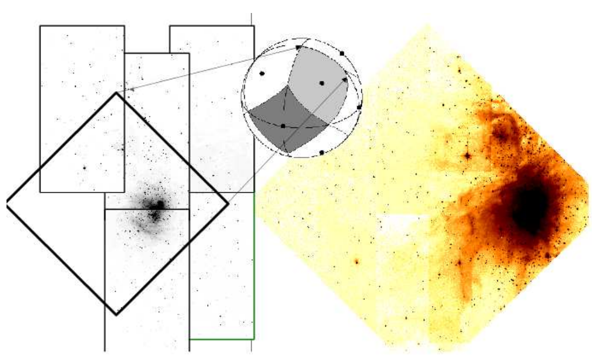

Fig. 1. Building a file following the HEALPix grid from common 2MASS images.

First, we select images from a survey in the wide field to build. Secondly, we copy (nearest pixel method) each pixel from these images on a FITS file which has exactly the same cover as a HEALPix pixel (in a rhombus shape). Figure 1 shows an example of the creation of one file with a wide field of view (Orion in 2MASS Ks).

As soon as the user wants to zoom (or unzoom) we can use the HEALPix pixelization scheme to know immediately the new file to show. As shown in Figure 2, we can see the HEALPix refinable quadrilateral mesh on the sphere, geometrically constructed, self-similar.

[1] CDS, Observatoire Astronomique de Strasbourg, France

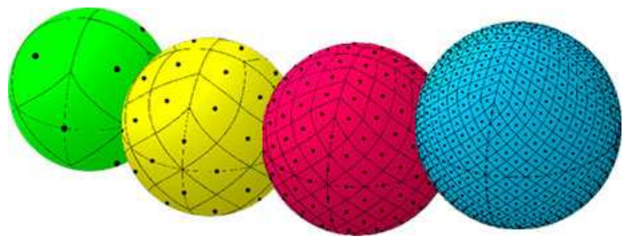

Fig. 2. The HEALPix grid is hierarchically subdivided.

3 Navigation mode

We store such as files for the whole survey in the ALADIN server. Then, the ALADIN client just loads the files covering the best the requested field of view. The user can easily move the view on the sky thanks to a panning feature, and then browse the sky seamlessly.

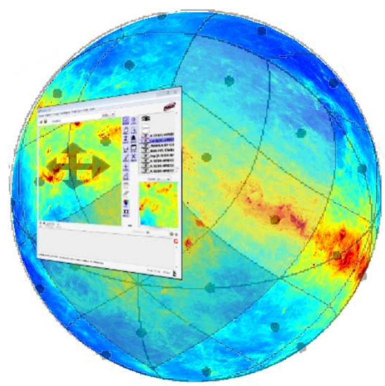

Fig. 3. Representation of the navigation in the ALADIN software.

As usual, you can superimpose catalogs, or other images from other wavelengths.

References

Bonnarel, F., Fernique, P., Bienaymé O., et al. 2000, A&AS, 143, 33

Górski, K.M., Hivon, E., Banday, A.J. 2005, ApJ, 622, 759

ENS

Teaching Session

THE NEW "TEACHING" SECTION ON THE SOCIÉTÉ FRANÇAISE D'ASTRONOMIE ET D'ASTROPHYSIQUE (SF2A) WEBSITE

Delsanti, A.[1], Roques, F.[1], Braine, J.[2] and Mosser, B.[1]

Abstract. We present the recently (spring 2008) created "Teaching" section of the *Société Française d'Astronomie et d'Astrophysique* (SF2A) website. This section was created to foster interactions between the researchers who deliver astronomy and astrophysics courses of various kinds (academic courses, e-formations, practical work, conferences, etc) to students at all levels, from the general public to PhD students in France. In particular, thanks to contributions from numerous institutes, the site now contains a directory of astronomy classes for the general public, *Licence*, master and e-learning. It will soon list astronomy courses for primary, middle and high school teachers, as well as for PhD students (*Ecoles Doctorales* and post-master teaching). This teaching directory will be regularly updated and refined in order to provide an accurate picture of the Astronomy teaching landscape in France.

1 Purpose of the "Teaching" section on the SF2A website

Astronomy and Astrophysics classes are taught countrywide at several levels, from educating primary, middle and high school teachers to PhD students in Astronomy, through *licence* and master students in science and now the general public. This teaching is delivered under various forms: undergraduate and graduate general or optional academic courses, observational and practical work, workshops, e-formations (where the class content is electronic and available on the web, with the teacher interacting from a distance), etc.

This very diverse offer is supported by scientific researchers from numerous universities and research institutions in France. Astronomy is a very attractive subject to students and can be taught by itself or as an application from mathematics, physics, computer science courses or engineering techniques. Given the current indisposition of young people for scientific careers, this widely appreciated discipline ought to be used to attract more students toward a scientific academic education.

We decided to create the "Teaching" section on the SF2A website to fulfill two main objectives:

1. highlight the existing teaching effort in astronomy countrywide and foster interactions between the researchers (and their home institution or university) who are involved in astronomy teaching at all levels
2. offer an up-to-date, as exhaustive as possible, directory of the teaching in astronomy in France. This directory is mainly dedicated to (with no particular order):
   - students looking for Astronomy and Astrophysics academic education opportunities
   - primary, middle and high school teachers looking for an astronomy education adjusted to their level of scientific knowledge (to re-invest it in class or simply out of personal curiosity)
   - scientific researcher in search for teaching opportunities in a particular institution
   - public outreach presenter in search of an astronomy degree
   - any person who is interested in developing a knowledge in astronomy (several attractive offers are now available for the general public, see for instance Roques et al. proceedings SF2A 2008)

The SF2A website, whose mission is to help the development and diffusion of astronomy in France, is the ideal location to host such "Teaching" information pages.

[1] Observatoire de Paris - Site de Meudon, LESIA, 5 place Jules Janssen, 92195 Meudon cedex - France
[2] Laboratoire d'Astrophysique de Bordeaux, UMR 5804 2 rue de l'Observatoire, BP 89, 33270 Floirac

Fig. 1. A screen capture of the directory for the *Licence* level. Address : http://www.sf2a.asso.fr, tab *"Enseignement"*

2 Content

2.1 The Astronomy courses directory

The first version of the directory was created in June 2008. It was based on a SF2A mailing list survey. Numerous responses were collected and about 80 entries were published on-line. This draws the first lines of what should be a more complete picture of the Astronomy teaching landscape. The directory is divided into the following sections:

- Astronomy courses at the "Licence" level (*Enseignement au niveau Licence (L1, L2 et L3))*
- Astronomy courses at the Master level (*Enseignement au niveau Master (M1, M2 recherche et M2 pro))*
- *Diplômes d'Université* in Astronomy
- e-learning (homeschooling in Astronomy): *les formations à distance*

Every entry lists the following (see Fig. 1): the institute name, the course's title, the pedagogic director name and email, the (academic) level, the university credits delivered (if any), the type (talk, practical work, etc) and length (in hours) of the course and the address of the related website (if any).

More sections are foreseen and should be completed by the end of 2008 :

- Graduate schools in Astronomy and Astrophysics (*Ecoles Doctorales*) and post-master teaching
- Astronomy teaching dedicated to primary, middle and high school teachers

2.2 Other material

In this "Teaching" section, several documents will be posted and made available to the community: call for contributions and program of the "Teaching" session at the *Journées de la SF2A*, reports on this session with presentations available as PDF files, any think-piece or document of interest for the teaching community.

3 How to contribute

This live information is reliable and accurate only if the web-pages and the directory are regularly updated. This is where all researchers involved in any Astronomy or Astrophysics teaching should play a role and send to the SF2A website “Teaching” section manager (see email contact information on the web-page) the current information on their courses and the astronomy degrees delivered.

A call for new, updated or to-be-removed contributions to the “Teaching in Astronomy” directory will be sent the beginning of every April (e.g. when students are looking for education opportunities for the next academic year) and beginning of every October (e.g. when classes and other activities have actually started). Volunteer email contributions are accepted year-round.

With this managing, we expect to have a quite complete picture of the Astronomy teaching in France by researchers in science by May 2009. It will then be kept as up-to-date as possible.
In the future, we expect that an on-line form available to all teachers at anytime will be created, in the same spirit as the SF2A professionals in Astronomy directory currently in service. This on-line form will guarantee an even more efficient update of the directory of the Astronomy teaching in France.

GRAAPH

Gravitation and Reference Systems

SF2A 2008
C. Charbonnel, F. Combes and R. Samadi (eds)

GRAVITY ADVANCED PACKAGE, AN ACCELEROMETER PACKAGE FOR LAPLACE OR TANDEM MISSIONS

Christophe, B.[1], Foulon, B.[1], Levy, A.[1], Anderson, J.D.[2], Sumner, T.J.[3], Bertolami, O.[4], Gil, P.[4], Paramos, J.[4], Progrebenko, S.V.[5], Gurtvis, L.[5], Reynaud, S.[6], Courty, J-M.[6], Asmar, S.W.[7], Métris, G.[8], Bério, P.[8], Bingham, R.[9], Kent, B.[9], Olsen, O.[10], Andersen, P.H.[10], Dittus, H.[11], Lämmerzahl, K.[11], Theil, S.[11], Rievers, B.[11] and Bremer, S.[11]

Abstract. The Einsteinian theory of gravitation, General Relativity (GR), is well verified at scales ranging up to the size of planetary orbits but it is challenged by larger-scale observations. In the Solar System, several anomalies have also been detected in the trajectories of some spacecraft: a small anomalous Doppler acceleration has been detected on Pioneer 10 and 11, and several spacecrafts have an unpredicted increment of velocity after their Earth flyby. Therefore, it is extremely interesting to test the gravity laws at interplanetary scales in the solar system.

In the frame of Cosmic Vision selection, the Fundamental Physic Advisory Group of ESA suggested to use an accelerometer, as presented in Odyssey mission proposal, on the future interplanetary mission, Laplace or Tandem mission, pre-selected by ESA, in order to achieve this scientific objective.

For such objective, an accelerometer without bias is mandatory in order to discriminate between conventional forces applied on the spacecraft and gravity forces, in the low-frequency domain. The Gravity Advanced Package takes advantage of mature technology developed at ONERA for ultra-sensitive accelerometry and a bias rejection system is added in order to obtain the performance in the expected bandwidth.

1 Introduction

The Einsteinian theory of gravitation, General Relativity (GR), is well verified at scales ranging up to the size of planetary orbits but it is challenged by larger-scale observations. Gravitational anomalies are indeed observed in the rotation curves of galaxies and also in the relation between red-shifts and luminosities of supernovae. These anomalies (deviations between observed and expected behaviors) are interpreted as revealing the presence of dark components in the content of the Universe, but the observed anomalies can as well be consequences of modifications of GR at galactic or cosmic scales. Given the immense challenge posed by these large scale behaviors, it is important to explore any possible option. It is in particular extremely interesting to test the gravity laws at the largest possible distances, that is practically speaking at interplanetary scales in the solar system.

Odyssey (Christophe 2008) was submitted by large international teams to ESA in response to the Cosmic Vision 2007 call, with the aim of testing gravity laws in the deep solar system, beyond the orbit of Saturn.

[1] ONERA/DMPH, 29, av. Division Leclerc, F-92322 Chatillon
[2] Global Aerospace, USA
[3] Imperial College, London, UK
[4] Instituto Superior Técnico, Lisboa, Portugal
[5] Joint Institute for VLBI in Europe, The Netherlands
[6] Laboratoire Kastler Brossel, ENS, UPMC, CNRS, Paris, France
[7] NASA, JPL, Pasadena CA, USA
[8] Geoscience Azur, Université Nice-Sophia Antipolis, Observatoire de la Côte dAzur, Grasse, France
[9] Rutherford Appleton Laboratory, Didcot, UK
[10] University of Oslo, FFI, Norway
[11] ZARM, University of Bremen, Germany

Though the proposal was not selected as dedicated mission, its scientific objectives were supported by the Fundamental Physics Advisory Group and a recommendation issued by ESA for embarking an accelerometer similar to that designed for Odyssey on-board one of the planetary missions selected LAPLACE or TANDEM.

The two missions have their main objectives devoted respectively to the systems of Jupiter and Saturn. They will explore heliocentric distances up to 5 AU and 9 AU respectively. Their trajectories will take benefit of several gravity assists at Earth and other planets. Embarking an accelerometer on-board one of these planetary missions would allow one to meet some of the objectives of the Odyssey project without waiting for a dedicated mission: the solar system gravity test and the flyby investigation.

2 Scientific Objectives

2.1 The solar system gravity test

Such a test has been performed by Pioneer 10/11 probes during the extended missions decided by NASA after their primary planetary objectives had been met. This largest scaled test of gravity ever performed has failed to reproduce the expected variation of the gravity force with distance due to the presence of a small anomalous Doppler acceleration (time derivative of the Doppler velocity). This deviation from the predictions of GR can be interpreted as an unexpected Sunward acceleration with a nearly constant magnitude of 0.87 ± 0.13 nm/s^2 for probes beyond the orbit of Saturn. This signal has become known as the "Pioneer Anomaly" (Anderson et al. 2002) and has been confirmed by independent analysis of the Doppler data (Levy et al. 2008). Although the most obvious explanation would be a systematic effect, the extensive analysis performed by J. Anderson et al at JPL did not support any of the numerous mechanisms which were considered (Anderson et al. 2002). Investigations have been initiated for confronting the Pioneer data with other gravity tests in the solar system as well as analyzing the potential significance of the anomaly for fundamental physics, solar system physics or astrophysics (Jaekel & Reynaud 2006; Brownstein & Moffat 2006; Bertolami & Paramos 2004).

Modern planetary probes are navigated with radio-metric tracking (Doppler and range measurements) as the main tool for producing precise orbit determination and prediction. The accelerometer of the Gravity Advanced Package provides the navigators with a direct measurement of non-gravitational forces, thereby eliminating the uncertainties in the models currently used to deal with these forces, and then leading to a better accuracy and reliability in orbit reconstruction. It represents a major improvement with respect to the navigation in the solar system and solve interpretation ambiguity on the nature of the results in an immediate manner. It also allows one to perform measurements at earlier phases of the mission, when the solar effects are still much larger than the looked for accelerations.

In the GAP experience, the resolution havs been fixed at a value of 0.05 nm/s^2 that is 5% of the recorded Pioneer anomaly.

2.2 The flyby investigation

In most recent missions using Earth gravity assistance (EGA), NASA (Antreasian & Guinn 1998) and ESA (Morley & Budnik 2006) navigation teams have noticed that the spacecraft possesses after the fly-by a velocity larger than calculated from the precisely measured initial conditions and the known properties of the Earth gravity field. The anomalous additional velocities ΔV corresponding to this "flyby anomaly" reach values up to 13 mm/s for the first EGA of the NEAR probe. The various systematic effects which could spoil the effect (the gravity field of the Earth, atmospheric drag, charging and Earth tides, etc) have to be studied in a careful manner, but are thought (Lammerzahl et al. 2008) to result in uncertainties well below the measured ΔV. Very recently, an empirical formula has been proposed which relates the anomaly to a planet-dependent constant and to the incoming and outgoing geocentric latitudes of the asymptotic spacecraft motion (Anderson et al. 2008). This formula can now be used to predict the magnitude of the anomaly. Another important objective is to compare gravity assists at Earth and other planets in order to correlate their constants with the physical properties of the planets.

With the accelerometer on board, the non gravitational acceleration will be measured during the whole fly-by, including the typical DSN black-out period. It will enable an unambiguous characterization of the nature of the fly-by anomalies, and either confirm the presence of the anomaly or solve the discrepancy, then leading to a significant improvement of our capabilities in trajectory prediction and navigation. The velocity increment ΔV will be measured by the radio-tracking system before and after the fly-by with a precision of 10 μm/s, which is less than 1% of the typical anomalous ΔV registered in the presently available analysis.

3 μSTAR accelerometer description

The Gravity Advanced Package is light-weight, small, and has low power consumption (3kg, 3l, 3W, including the bias compensation mechanism and the interfaces). Its core is an accelerometer benefiting from the Onera design heritage that was successfully used in many recent space experiments CHAMP, GRACE and GOCE (Touboul et al. 2004). The main challenges are the development of the bias calibration system and the integration of the package in the spacecraft.

3.1 Accelerometer Sensor

Three axis electrostatic accelerometers developed at ONERA are based on the electrostatic levitation of the instrument inertial mass with almost no mechanical contact with the instrument frame. Measurements of the electrostatic forces and torques, which result from the six servo-loops necessary to maintain the mass motionless with respect to the sensor cage, provide the six outputs of the accelerometer. The relative motion of the proof-mass (6 degrees of freedom) is in fact finely measured by capacitive sensors with respect to the sensor silica core selected for its very high geometric stability. Whatever is along the orbit the charged particles radiation, the electrical potential of the mass is maintained at a constant level to linearize the actuators. The control of the proof-mass is performed by low consumption analogue functions. The outputs of the accelerometer, which are the applied voltages on the electrodes to control the proof-mass, are sent to an Interface Control Unit.

The bias rejection system is similar to rotating stage existing on the shelf, but optimized in order to reduce the mass and the consumption. This system consists of a flip mechanism to create a $\pm 180°$ rotation of the accelerometer sensitive axes with respect to the satellite ones at regularly spaced times. As a consequence, the resulting modulation of the measured accelerations projected on the instrument sensitive axes allows to distinguish the applied acceleration on the satellite from the accelerometer bias, the latter staying at DC while the first is transposed at the modulation frequency.

3.2 Instrument Performance

The total error budget of the instrument package includes the following main limitation sources:

Accelerometer noise: Taking advantage of the previous instrument development and models, the instrument characteristics can be evaluated on the basis of the selected configuration for the sensor core and the electronics functions. Over one day, the integrated noise, along one sensitive axis considering a thermal stability of $1°\mathrm{C/Hz}^{1/2}$ at 0.01 mHz is 0.01 nm/s^2 rms. In this configuration, the accelerometer full range is 20 μm/s^2.

Misalignment of accelerometer axes: The misalignments of the accelerometer axes with respect to the ones of the spacecraft, given by the star tracker lead to errors proportional to the maximal non-gravitational acceleration applied on the spacecraft. Considering a one ton spacecraft, with a 30 m^2 surface of solar panel, the impact of misalignment is less than 0.01 nm/s^2 at 2 AU, with a requirement of misalignment less than 0.2 mrad.

Error of bias rejection: The error of the bias evaluation and rejection comes from the non perfect rotation of the instrument with respect to the considered one in the processing, the post-processing limitation, the evolution of the bias and non-gravitational acceleration during the processing period and the effect of the external acceleration signals at harmonics of the flip frequency. The total error due to the bias rejection system and the post-processing should be less than 0.02 nm/s^2.

Coupling with spacecraft angular motion: As the sensitive centre of the accelerometer (centre of gravity of the proof-mass) will not be perfectly co-localized with the centre of gravity of the spacecraft, a coupling term with the angular motion of the spacecraft will perturb the linear acceleration measurement. This term could be corrected according to the knowledge of the relative position of the accelerometer with respect to the centre of gravity of the spacecraft and to the estimate of the angular motion of the spacecraft from the star tracker quaternions. Requirement on the residue of this term evaluation has been considered to be 0.04 nm/s^2. Considering a decentring of the accelerometer of 0.5 m, known with 1 cm accuracy, a star tracker accuracy of 10 arcs, the attitude control of the spacecraft should be better than 0.15° from DC to 0.1 mHz.

Spacecraft self-gravity: All the masses around the accelerometer will attract the proof-mass and creates a parasitic acceleration, the satellite self-gravity: this acceleration cannot be rejected by the rejection system as its direction is linked to the spacecraft and not to the accelerometer. This contributor shall be less than 0.01 nm/s^2. If too large, it can be estimated according to the satellite design but nevertheless has to be limited either by a good symmetric architecture or by a good knowledge of the steady mass repartition of the components around the accelerometer in order to reduce the estimation residue.

A supplementary 0.01 nm/s^2 error is added for all other error sources, not detailed here above.

4 Conclusions

It has to be emphasized that the presence of the accelerometer on-board not only enables fundamental physics objectives to be met, but also constitutes an invaluable complement to the planetary mission in terms of navigation as well as knowledge of the gravity field and environment of the visited planets and moons. After a more detailed study with specialists of these scientific questions, this can be used to increase the scientific return for some solar system physics objectives. First, the accurate measurements of the surface forces during the cruise phase can be translated into an improved knowledge of solar system environment. The same conclusion holds for measurements in the vicinity of the planet or its moons. Then the improved reconstruction of the orbits around the planet, thanks to the presence of an accurate accelerometer on board, should result in a determination of the gravity field of the planet or its moons (like in Earth gravity mission CHAMP (Touboul et al. 1998), with potentially new information of major interest for the study of these bodies.

References

Anderson,J.D., Laing, P.A., Lau, E.L., Liu, A.S., Nieto, M.M., & Turyshev, S.G. 2002, Phys. Rev., D65, 082004

Anderson, J.D. Campbell, J.K., Ekelund, J.E., Ellis,J., & Jordan, J.F. 2008, Phys. Rev. Lett., 100, 091102

Antreasian P.G., & Guinn, J.R. 1998, in Astrodynamics Specialist Conference (AIAA, Washington) p.4287

Bertolami, O. & Paramos, J. 2004, Class. Quantum Grav., 21, 3309

Bertolami, O., & Vieira, P., 2006, Class. Quantum Grav., 23, 4625

Bertolami, O., Paramos, J., Turyshev, S.G. 2008, in Lasers, Clocks, and Dragfree: Exploration of Relativistic Gravity in Space, eds. H. Dittus, C. Lämmerzahl, S. G. Turyshev, Astrophysics and Space Science Library 349 (Springer-Verlag, Berlin) p. 27

J. Brownstein, R., & Moffat, J.W., 2006, Class. Quantum Grav., 23, 3427

Christophe, B. and the Solar System Odyssey team 2008, Experimental Astronomy, DOI 10.1007/s10686-008-9084-y [arXiv:0711.2007]

Jaekel, M.T., & Reynaud, S. 2006, Class. Quantum Grav. 23 777 [arXiv:gr-qc/0510068]

Lämmerzahl, C., Preuss, O., & Dittus, H. 2008, in Lasers, Clocks, and Dragfree: Exploration of Relativistic Gravity in Space, eds. H. Dittus, C. Lämmerzahl, S. G. Turyshev, Astrophysics and Space Science Library 349 (Springer-Verlag, Berlin) p. 75 [arXiv:gr-qc/0604052]

Levy, A., Bério, P., Métris, G., & Courty, J.-M. 2008, SF2A Conference, in this proceedings

Morley, T., & Budnik,F. 2006, International Symposium on Space Technologies and Science,25,593

Touboul, P., Foulon, B., & Le Clerc, G.M. 1998, in Proceedings of 49th International Astronautical Congress, AIAA

Touboul, P., Foulon, B., Rodrigues, M., & Marque, J.-P. 2004, Aerospace Science and Technology,8,431

SF2A 2008
C. Charbonnel, F. Combes and R. Samadi (eds)

THE BORDEAUX VLBI IMAGE DATABASE

Collioud, A.[1] and Charlot, P.[1]

Abstract.
As part of its contribution to the International VLBI Service for Geodesy and Astrometry (IVS) and the maintenance and improvement of the current International Celestial Reference Frame (ICRF), the Laboratoire d'Astrophysique de Bordeaux produces VLBI images of extragalactic radio sources, structure correction maps and structure indices in order to characterize the astrometric suitability of the ICRF sources. All such products are available online through the Bordeaux VLBI Image Database (BVID) which include more than 1000 VLBI images at 8.4 GHz and 2.3 GHz for more than 250 different sources, as well as more than 5000 structure correction maps and structure indices. The amount of data is constantly increasing with the processing of new VLBI experiments and new BVID features are being developed. The Bordeaux VLBI Image Database is accessible through the following web address: http://www.obs.u-bordeaux1.fr/m2a/BVID/.

1 Introduction

The VLBI (Very Long Baseline Interferometry) group at the Laboratoire d'Astrophysique de Bordeaux (LAB) collaborates to the International VLBI Service for Geodesy and Astrometry (IVS) (Charlot et al. 2006). In this framework, one of its contribution consists in producing VLBI images of the extragalactic radio sources that comprise the International Celestial Reference Frame (ICRF).

Such images are essential for maintaining and improving the frame since the ICRF sources typically exhibit extended structures on milliarcsecond scales (Fey & Charlot 1997, 2000), setting limits on the accuracy of astrometric source positions if not accounted for. In practice, source structure modeling requires imaging the sources on a regular basis (up to six times a year) with a VLBI network of 15 to 20 radiotelescopes in order to monitor the structural evolution and positional stability of the reference frame sources.

The Bordeaux VLBI image database (BVID) provides the national and international scientific community with data related to radio source structures and its application to VLBI astrometry. Additionally, it is also useful for astrophysical studies, e.g. for investigating superluminal motions in extragalactic radio sources.

Section 2 describes the products available online trough the BVID web page. Future improvements and extensions of the BVID are presented in Section 3.

2 Current BVID content

The Bordeaux VLBI Image Database comprises more than 1000 VLBI images at 8.4 GHz and 2.3 GHz for more than 250 different reference frame sources (Fig. 1).

In addition to revealing source structures, these images are used to derive structure correction maps. Such maps show the magnitude of intrinsic source structure effects in VLBI bandwidth synthesis delay measurements (the basic quantity in astrometric VLBI) as a function of interferometer resolution. These form the basis for calculating structure indices which characterize the astrometric suitability of the observed sources (Fig. 2) as devised by Fey & Charlot (1997, 2000). *Structure correction maps and structure indices are BVID specificities* compared to other VLBI image databases such as the Radio Reference Frame Image Database (http://rorf.usno.navy.mil/RRFID).

Overall, there are more than 5000 structure correction maps and structure indices available in the BVID, and as many visibility maps. The latter show normalized visibilities as a function of interferometer resolution, similar to the structure correction maps, and are useful e.g. for scheduling purposes (Fig. 1).

[1] Laboratoire d'Astrophysique de Bordeaux, Université de Bordeaux, CNRS, 2 rue de l'Observatoire, BP 89, 33271 Floirac Cedex

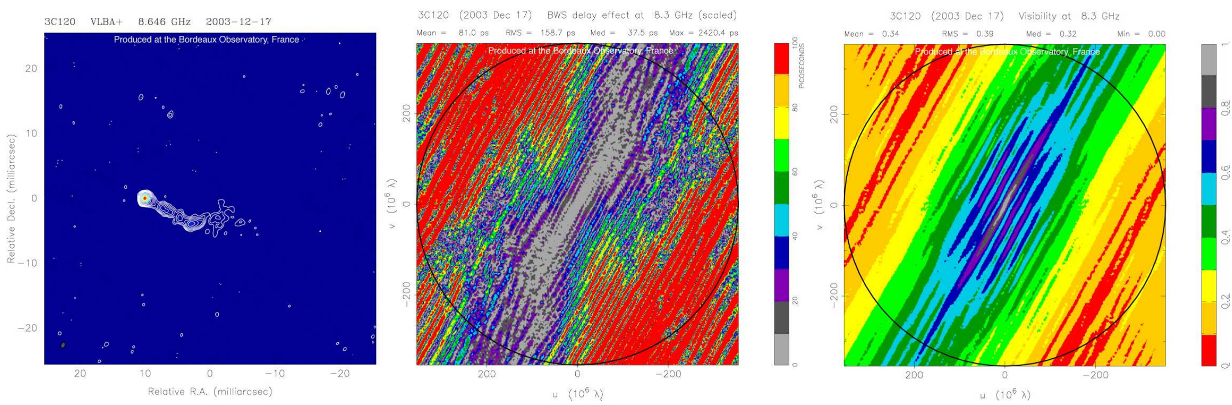

Fig. 1. BVID content for the source 3C120 observed at 8.4 GHz (X-band) in December 2003. From left to right: VLBI image, structure correction map and visibility map. The structure index is 4 since the source is very extended.

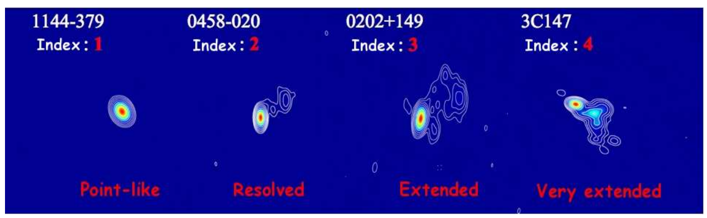

Fig. 2. Illustration of possible values of the structure index according to the complexity of the structure.

The BVID is accessible via a web interface (http://www.obs.u-bordeaux1.fr/m2a/BVID) and is remotely queryable. It may be searched through several criteria: source name, source coordinates or observing date. Thumbnails for the most recent images are also available to facilitate visualization.

3 Future evolution

Maintenance, extension and future development of the BVID will be accomplished through the following:

- Regular addition of data as new VLBI experiments are processed. About 600 VLBI images are expected to be added each year along with structure correction maps, structure indices and visibility maps.
- Addition of structure correction maps and structure indices derived from VLBI observations at higher frequencies (24 et 43 GHz).
- Further development of the database capabilities, the related tools and the web interface.
- Integration of the BVID into the Virtual Observatory in order to facilitate data access.

4 Acknowledgements

The authors would like to thank Arnaud Caillo from the Observatoire Aquitain des Sciences de l'Univers (OASU–UMS2567) for the conception and development of the BVID.

References

Charlot, P., Bellanger, A., Bourda, G., Camargo, J. I. B., Collioud, A., & Baudry, A. 2006, SF2A Proceedings 2006, Eds. D. Barret, F. Casoli, T. Contini, G. Lagache, A. Lecavelier and L. Pagani, p. 53

Fey, A., & Charlot, P. 1997, ApJS, 111, 95

Fey, A., & Charlot, P. 2000, ApJS, 128, 17

LONG TIME SERIES OF THE LOW WAVELENGTHS OF THE EARTH'S GRAVITY FIELD, FROM SLR-ONLY DATA: 1992-2008

Deleflie, F.[1] and Exertier, P.[1]

Abstract. We use SLR data tracked by the ILRS network to derive long time series of the low wavelenghts of the Earths gravity field. The work is based on post-fit residuals analyses, performed with the computation of orbit of geodetic satellites (LA-1 and LA-2 in particular). Osculating orbital arcs are propagated over short periods of time and adjusted on tracking data. Normal matrices are deduced from that adjustment, and then mixed. We give here a time series of the J_2 and J_3 coefficients, where variations, to be analyzed by geophysicists, can be linked to mass transfer inside the Earth: post-glacial rebound, 18.6 year tide, El Niño Southern Oscillation events.

1 Introduction

As an official Analysis Center (AC) of ILRS, GRGS (Groupe de Recherche en Géodésie Spatiale) provides every week station positions, site velocities, Earth Orientation Parameters (EOP), deduced from a post-fit analysis of LAGEOS-1 and LAGEOS-2 orbits, adjusted on SLR data tracked by SLR stations. This is the prime objective of the International Laser Ranging System (ILRS) (Pearlman et al., 2002). In parallel, the group is currently developing an operational service providing time series of the low wavelenghts of the Earth's gravity field based on SLR data: even if methodological developments are still required to ensure the best decorrelation of the different parameters, the level of residuals is good enough, since many years, to enlighten in time series temporal variations linked to mass transfer within the terrestrial system.

In fact, SLR geodetic satellites are still extremely used to determine the very-long wavelengths part of Earth gravity field models, even since the launch of the GRACE mission in 2002. One of the first impressive results was given by (Yoder et al. 1983), enlightening the effects induced by the post glacial rebound on the orbit of LAGEOS-1. In 2008, geodetic satellites still give an unique information on some parameters of geophysical interest, such as time variations of the Earth's oblateness, which can be now determined over a very long period of time (about 30 years, in 2008). This long term history of the SLR measurements makes it possible for geodesists to determine the changes over time in polar ice sheets and sea level change. It is the part of astronomy for Earth's Sciences.

2 Post-fit analysis of Satellite Laser Ranging (SLR) Data

Five geodetic satellites were used in this study to derive time series of spherical harmonics coefficients: LAGEOS-1 and LAGEOS-2, but also ETALON-1, AJISAI, STARLETTE.

Figure 1 (resp. Figure 2) shows the estimated variations of $C_{2,0} = -J_2$ (resp. of $C_{3,0} = -J_3$) for each 10-day interval over the period 1992-2008, on the basis of a weighting procedure (ie the Helmert's method) using the SLR data avaiable during each orbital arc, propagated every week. Each figure contains as well a running average of the time series, in order to enlighten secular, tidal and seasonal variations of the coefficients.

[1] Géosciences Azur - Terre Océan Espace - GRGS, Université Nice Sophia-Antipolis, Observatoire de la Côte d'Azur, CNRS, IRD, Université Pierre et Marie Curie ; Avenue Copernic, 06130 Grasse, France

More than two coefficients of the geopotential have in fact to be routinely determined, to ensure the accuracy of the two first coefficients. Since we focuse only on the main temporal variations of the gravity field, they are not shown here.

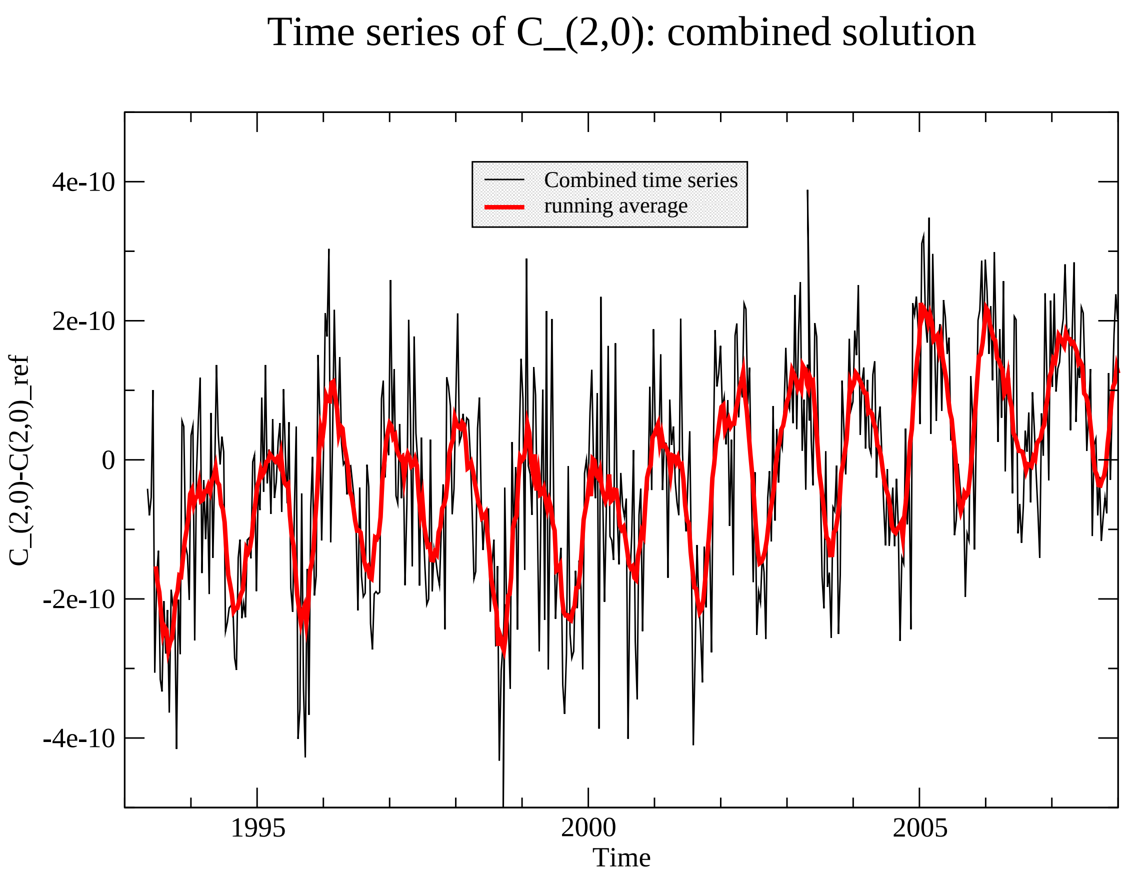

Fig. 1. Times series for the $C_{2,0} = -J_2$ coefficient.

3 A first analysis

The $C_{2,0} = -J_2$ and $C_{3,0} = -J_3$ time series contain a broad spectrum of signals.

Concerning J_2, the secular trend and annual variations appear to be the strongest. A large interannual variation is related to the strong El Niño Southern Oscillation event during the period 1996-2002, and was studied by many authors (in particular (Cazenave & Nerem 2002), (Cox & Chao 2002), and, in the framework of mean orbital motion (Deleflie et al. 2003)).

As far as the J_3 time series is concerned, a secular and an annual part should have been expected as well, but, it seems not to be the case. In particular, the strong variations during the 1998 El Niño Southern Oscillation event suggest that most of the signal induced on J_3 corresponds to a mass redistribution linked to such events. A detailed study devoted to a possible correlation will be the subject of a forthcoming paper. Nevertheless, such a correlation seems to be visible with naked eye between the $C_{3,0} = -J_3$ time series, and the Sea Level Anomaly shown Figure 3. Moreover, on the basis of the $C_{3,0} = -J_3$ time series, it is not reasonable to try to

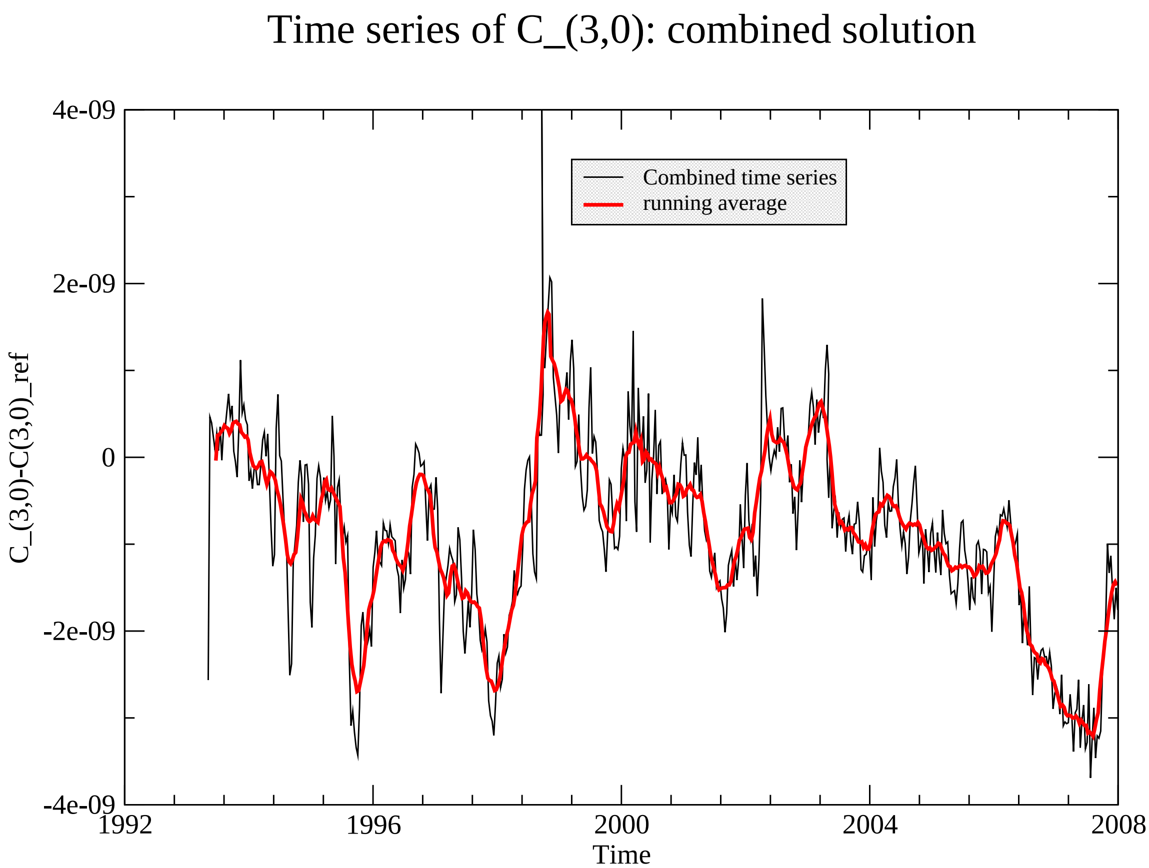

Fig. 2. Times series for the $C_{3,0} = -J_3$ coefficient.

determine a coefficient $\dot{J}_3$, standing for a secular variation of J_3.

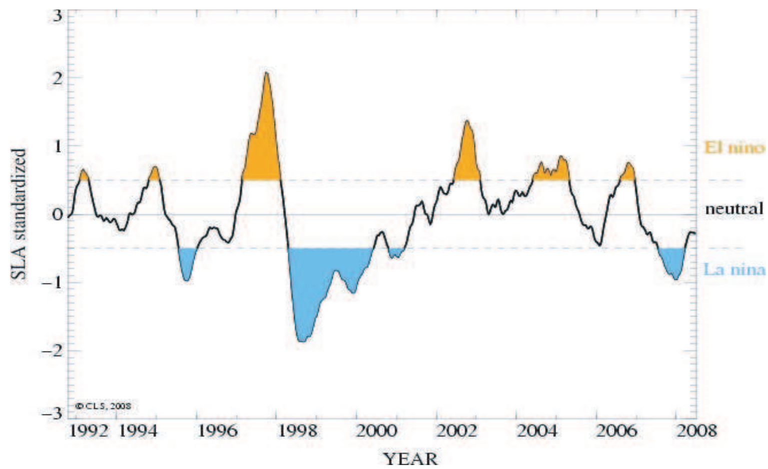

Fig. 3. El Niño and La Nina Southern Oscillation events, deduced from sea level anomaly (SLA), from 1992 to 2008. From http://www.aviso.oceanobs.com/

4 Conclusion

As a conclusion, SLR geodetic satellites still gives an information on temporal variations of the gravity field with a high level of quality, and it is likely to continue over the next years. These variations, as well as those of the main tesseral coefficients, should be used as a constraint in geophysical models.

These time series have to be analyzed in terms of mass transfer within the system Earth, even over a longer period of time. Such an analysis will aim at carefully determining, over 30 years, the 18.6 year tide, the 9.3 year tide, and other periods, such as an interannual cycle suggested by (Cheng & Tapley 2002) which started in 2002, and the secular variation. What happens for odd coefficients will be very challenging, even more than for even coefficients, whose variations are well known.

We should reinforce the role played by the SLR technique among other ones to permanently observe the Earth and its space environment. Because of the limitations in coverage due to weather conditions and anisotropy of the laser network, it is not possible to compare the SLR technique to GNSS, for example. But, they are complementary, for the determination of terrestrial reference frames as well as for the deterination of the gravity field.

References

Cazenave, A., & R.S. Nerem 2002, Redistributing Earth's mass, Science, 297, 783-784

Cox C.M., & Chao, B.F. 2002, Detection of a large-scale mass redistribution in the terrestrial system since 1998, Science, 297, 831-833

Deleflie, F., Exertier, P., Métris, G., Berio, P., Laurain, O. , Lemoine, J.-M., & Biancale, R. 2003, Why the 18.6 year tide cannot explain the change of sign observed in J2dot?, Adv. Geosci., 1, 103-108

Cheng, M., & Tapley, B.D. 2004, Variations in the Earth's oblateness during the past 28 years, J. Geophys. Res., 109, B09402, doi:10.1029/2004JB003028

Pearlman, M.R., Degnan, J.J., & Bosworth, J.M. 2002, The International Laser Ranging Service, Advances in Space Research, Vol. 30, No. 2, pp. 135-143, DOI:10.1016/S0273-1177(02)00277-6.

Yoder, C.F., Williams, J. G., Dickey, J. O., et al. 1983, Secular variations of Earth's gravitational harmonic J_2 coefficient from Lageos and non tidal acceleration of Earth rotation, Nature, 303, 757

SF2A 2008
C. Charbonnel, F. Combes and R. Samadi (eds)

HIGH AREA-TO-MASS RATIOS GEOSTATIONARY SPACE DEBRIS : STABILITY AND SECONDARY RESONANCES (MEGNO AND FREQUENCY ANALYSIS)

Delsate, N.[1], Valk, S.[1], Carletti, T.[1] and Lemaître, A.[1]

Abstract. Recently a new unexpected population of 10 cm size space debris near the geostationary orbit (GEO) has been discovered. These objects with high area-to mass ratios sometimes present highly eccentric orbits (Schildknecht et al., 2004, 2005). Recent numerical and analytical investigations (Anselmo & Pardini, 2005; Liou & Weaver, 2005) prove that this newly discovered population consists of near geosynchronous objects with high area-to-mass ratios. The large area-to-mass ratios space debris have a dynamical behavior dominated by the solar radiation pressure and the resonance with C_{22} spherical harmonic. In this paper we develop further the analysis done by Valk et al. (2008) by using a frequency analysis to study both the stability and the resonances of such particular orbits.

1 Introduction

As the GEO region is indisputably all-important for both commercial and scientific missions, ESA has recently initiated an optical search for fragments in the geostationary ring in order to improve the knowledge about the debris population and to understand their future evolution (Schildknecht et al. 2005). These observations have been performed, on behalf of ESA, by the Astronomical Institute of the University of Bern (AIUB) by using the 1 meter telescope located in Tenerife (Canary Islands). The recent observational discoveries in high altitude Earth's orbit (for the most part in geosynchronous orbits) stimulated the revisit of direct radiation pressure models. In particular, numerical investigations were recently performed in order to assess the time evolution of objects subject to such extreme situations (Anselmo & Pardini 2005; Liou & Weaver 2004). In this framework, short-term as well as long-term evolutions of geosynchronous space debris were studied in detail. These objects sometimes present highly eccentric orbits with eccentricities as high as 0.55 (Schildknecht et al. 2004, 2005). In addition, these authors and others, such as Chao (2006) and later Valk et al. (2007) presented some detailed analytical results concerning the short- and long-term evolution of high area-to-mass ratios geosynchronous space debris subjected to direct solar radiation pressure. More specifically, these latter authors mainly focused their attention on the long-term variation of both the eccentricity and the inclination vector. Recently, Valk et al. (2008) presented investigations of the long-term stability (intrinsic stability of such uncommon orbits) of high area-to-mass ratios space debris subjected to the direct solar radiation pressure, by means of the `MEGNO` criterion, moreover a relevant class of additional resonances (w.r.t the main resonance due to C_{22} spherical harmonic) appearing in the phase space were emphasized. In this paper, we improve such results based on the `MEGNO` indicator, by performing a preliminary frequency analysis of these additional resonances. The paper is organised as follows, first we summarize the Valk et al. (2008) paper. Secondly, we sketch the main ideas of the FMA (Frequency Map Analysis) theory and we lastly conclude by presenting our results based on the frequency analysis results.

2 Short review of the state of the art

In a recent paper (Valk et al. 2008) we studied the global dynamics of high area-to-mass ratios geosynchronous space debris, applying a recent technique developed by Cincotta et al. (2000), Mean Exponential Growth factor

[1] University of Namur, Département de Mathématique, Unité de Systèmes Dynamiques, 8, Rempart de la Vierge, B-5000, Namur, Belgium

of Nearby Orbits (MEGNO), which provides an efficient tool to investigate both regular and chaotic components of the phase space. For the purpose of this study, we considered the modeling of a space debris subjected to the influence of the Earth gravity field (includes the central body attraction, the second degree and order harmonics J_2, C_{22} and S_{22}), as well as the combined attractions of the Sun and the Moon. The perturbing effects of the direct solar radiation pressure were also taken into account for a high area-to-mass ratio fixed to $A/m = 10$ m^2/kg. The GEO objects exhibit a resonance due to the C_{22} harmonic, thus the main dynamics of a large set of GEO object can be described by the double pendulum. In this paper we improve the main results of the Valk et al. (2008) reported in Figure 1. The interested reader could find there more details in Valk et al. (2008).

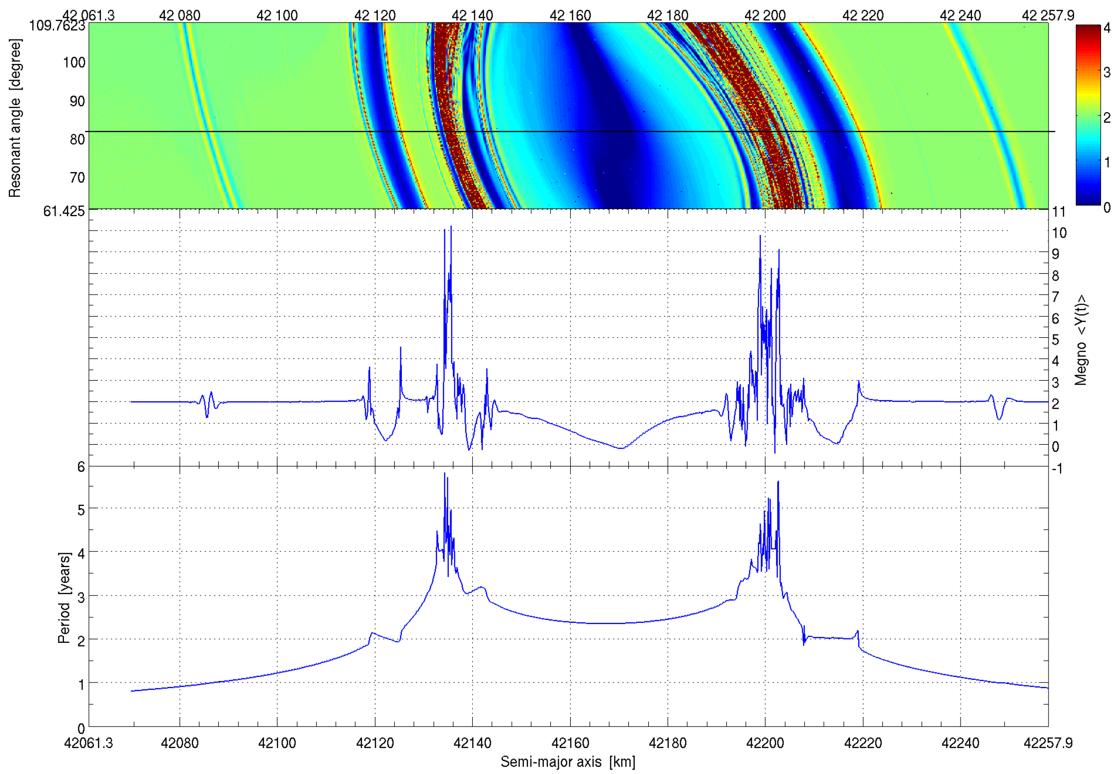

Fig. 1. Blow-up of the phase space around 1:1 resonance due to C_{22} [Graphics and caption from Valk et al. (2008)]. For a resonant angle section (horizontal black solid line), evolution of the MEGNO (middle panel) and the fundamental period of σ with respect to the initial semi-major axis a_0 (bottom panel).

3 Extended numerical analysis: Frequency Map Analysis

We now introduce a second original approach to study the stability of the high area-to-mass ratio space debris. We use a powerful frequency analysis FMA (Laskar 1990, 1993, 1995), previously introduce and used to study, for example, the chaotic motion of the solar system (Laskar 1990). To the best of our knowledge the present study provides the first application of FMA to the geodesy.

Let us briefly sketch the main idea of the FMA. Let $f(t)$ be a quasiperiodic regular function of the time t, with values in a complex domain, whose Fourier coefficient a_k have decreasing amplitudes with k. The FMA is a efficient numerical method allowing to obtain an approximation $f'(t)$ of the given signal with a given number (N) of harmonics, from the numerical knowledge of $f(t)$ over a finite time span $[-T, T]$ (Laskar 1990, 1995)

$$f(t) = \sum_{k=1}^{\infty} a_k e^{i\nu_k t} \qquad\qquad f'(t) = \sum_{k=1}^{N} a'_k e^{i\nu'_k t}$$

For our results, we use the FMA software (Laskar 1990). For the same resonant angle section (Fig. 1) but within a simpler model (only J_2, C_{22} and radiation pressure with circular sun, over a time span of 500 years) we calculate the first fundamental period of resonant angle (Fig. 2 bottom). To improve the direct analysis of the frequency curve ($\nu_1(a)$), we calculate (Laskar 1993) the numerical second derivative ($\delta\delta\nu_1(a) = \nu_1(a) - 2\nu_1(a-h) + \nu_1(a-2h)$) of the frequency of the resonant angle (Fig. 2 middle pannel). We can also calculate the diffusion of the main frequency with respect to the time (Laskar 1993). This is obtained by computing a first value $\nu_1^{(1)}$ of the main frequency of the resonant angle over a time span T_1 (for example to $-T$ untill 0) and a second value $\nu_1^{(2)}$ of this main frequency of the same signal but over a time span T_2 (for example to 0 untill T). Then we estimate the diffusion rate (Fig. 2 top) by computing a numerical indicator of diffusion of frequency $\log|1-\nu_1^{(2)}/\nu_1^{(1)}|$.

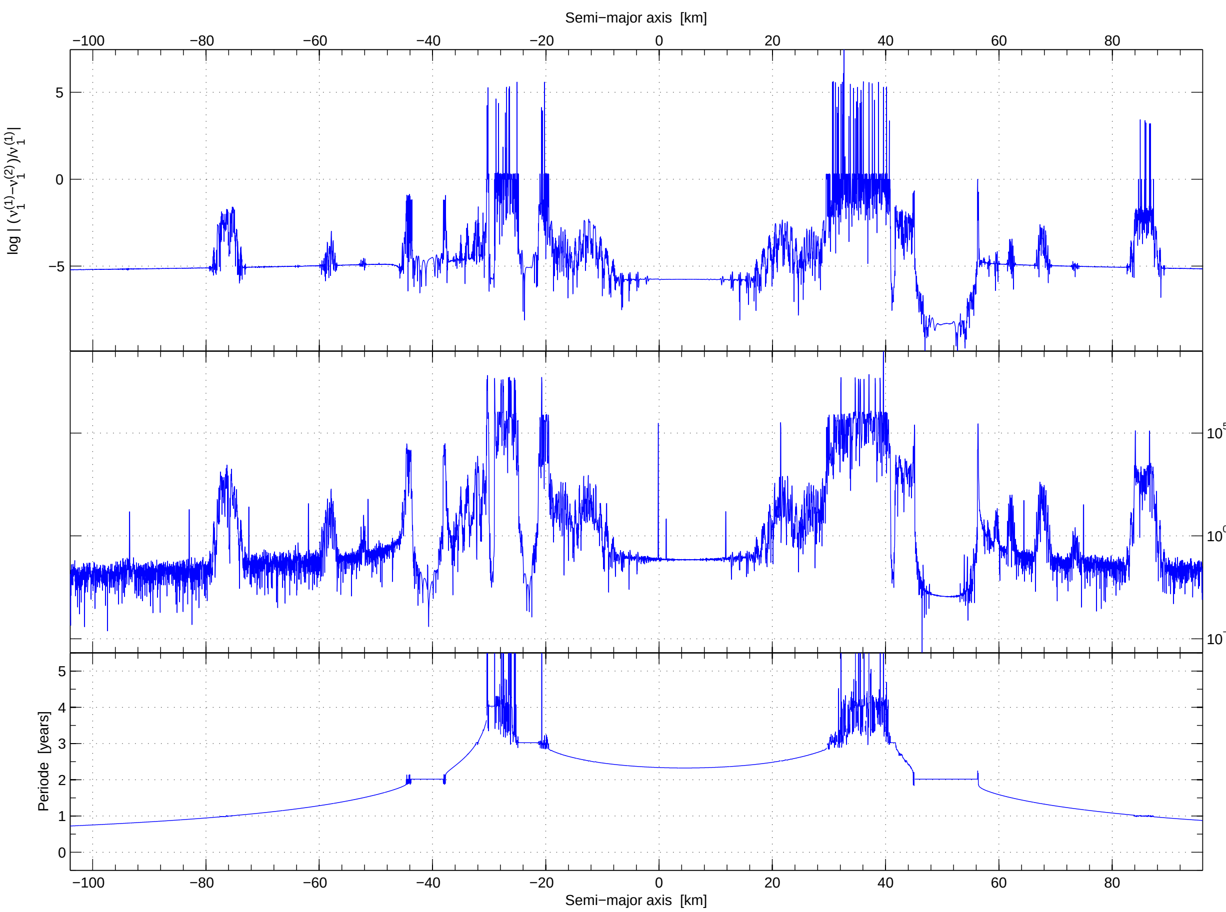

Fig. 2. The same resonant angle section in Fig. 1 but with a simpler model. Evolution of the fundamental period (bottom panel), second derivative (middle panel) and diffusion indicator (top panel), with respect to the initial semi-major axis a_0.

We can observe the same structure on both plots for derivative and for diffusion indicator. But the former exhibits less noise. One can easily recognize the main additional resonances when the period is equal to 2 years (between 42 and 58 km above the "eye" of the resonance due to C_{22} and between -36 and -44 km below the "eye" of the resonance). One can also observe an additional resonance when the period is equal to 1 year (between 84 and 86 km above the "eye" of the resonance due to C_{22} and near to -76 km below the "eye" of the resonance). Our analysis suggest that other additional resonances can be observed. A first one when the period is equal to 3 years (at $\pm 42km$ above the "eye" and $\pm -32km$ below the main resonance); a second resonance when the period is equal to 4 years (at $-30km$ below the main resonance) and a third one when the period is equal to 3/2 years and equal to 4/3 years. We can also observe a secondary resonance (inside the main "eye" of the resonance due to C_{22}) when the period of the resonant angle is equal to 3 years, clsoe to the separatrix (at $-20km$ to $-24km$ above the main resonance) and a weak evidence of secondary resonance (in the main "eye" of the resonance due to C_{22}) when the period of the resonant angle is equal to 2.5 years (at $-16km$ below and $24km$ above the main resonance).

4 Conclusions

In this paper, using numerical estimato, we brought to the fore a relevant class of additional resonances in the GEO for space debris with high area-to-mass ratio. Some of these resonances correspond to commensurabilities between the primary resonant angle and the ecliptic longitude of the Sun were also underlined in Valk et al. (2008). A set of these resonances have been discovered using the `MEGNO` indicator. Because of its better resolution, a larger set of resonances has been discovered by using the FMA (corresponding to periods equal to 4/3 and 3/2 years).

An analytical analysis of these additional resonances will be investigated in a forthcoming publication. Moreover a whole atlas, as in Valk et al. (2008), has been created using frequency analysis confirming the existence of a large number of additional resonances that wasn't discovered using the `MEGNO` indicator.

References

Anselmo L., & Pardini C. 2005, in Danesy, D. (Ed.), Proceedings of the Fourth European Conference on Space Debris, ESA SP-587, ESA Publications Division, Noordwijk, The Netherlands, pp. 279-284

Chao, C.C. 2006, AIAA Paper No. AIAA-2006-6514. In: Proceedings of the 2006 AIAA/AAS Astrodynamics Specialist Conference, Keystone, Colorado

Cincotta, P.M, & Simó, C. 2000, A&A Suppl. 147, 205

Laskar, J. 1990, Icarus, 88, 266

Laskar, J. 1993, Physica D, 67, 257

Laskar, J. 1995, in Proceedings of 3DHAM95 NATO Advanced Institute 533, S'Agaro, June 1995, pp. 134-150.

Liou, J.-C, & Weaver, J.K. 2004, The Orbital Quarterly News, Vol. 8 issue 3, The NASA Orbital Debris Program Office.

Schildknecht T., Musci, R., Ploner, M., Beutler G., Flury, W., Kuusela, J., Leon Cruz, J., de Fatima Dominguez Palmero, L. 2004, Advances in Space Research, 34, 901

Schildknecht, T., Musci, R. Flury, W., Kuusela, J. de Leon, J., & de Fatima Dominguez Palmero, L. 2005, in Danesy, D. (Ed), Proceedings of the Fourth European Conference on Space Debris, ESA SP-587. ESA Publications Divison, Noordwijk, The Netherlands, pp. 113-118.

Valk, S., Lemaître, A., & Anselmo, L. 2007, Advances in Space Research, doi:10.1016/j.asr.2007.10.025.

Valk, S., Delsate, N., Lemaître, A, & Carletti, T. 2008, Advances in Space Research, submitted for publication.

SF2A 2008
C. Charbonnel, F. Combes and R. Samadi (eds)

PLANETARY PERTURBATIONS ON THE ROTATION OF MERCURY

Dufey, J.[1], Noyelles, B.[1, 2], Rambaux, N.[1,2] and Lemaître, A.[1]

Abstract. The space missions MESSENGER and BepiColombo require precise short-term studies of Mercury's rotation. In this scope, we perform analytically and numerically by Hamiltonian approach a synthetic 2-dimensional representation of its rotation, using complete ephemerides of the orbital motions of the planets of the Solar System. This representation allows us to derive the librations in longitude and latitude of the resonant arguments. We point out that the contributions of Venus and Jupiter cannot be neglected in the study of the librations in longitude. We also show that the librations in latitude are much smaller, with an amplitude of about 0.2 arcsec, whereas the librations in longitude have an amplitude of about 40 arcsec. Moreover, we mention the possibility of a resonance involving the free libration in longitude and the orbital motion of Jupiter. All these results are compared to those given by SONYR model, which integrates simultaneously the orbital motions of the planets and the rotation of Mercury, and therefore gives the full spin-orbit coupling motion of Mercury.

1 Introduction

Over the last decade, there has been a renewed interest in Mercury with the space missions BepiColombo and MESSENGER, along with radar measurements revealing a molten core (Margot et al. (2007)). To have a better understanding of the observations and the measurements, an analytical model as accurate as possible is necessary.
In the first section, we study the libration in longitude of Mercury. After stating our basic hypotheses, we use a Hamiltonian formalism to analyse the different planetary contributions on the libration in longitude. The results are compared with the numerical model SONYR and with a study of Peale et al. (2007).
In the second section, to analyse the libration in latitude, we use a more complete model of the rotation. Using a similar approach to the study of the libration in longitude, we analyse the planetary perturbations acting on the ecliptic obliquity and the angle representing the 1:1 commensurability between the rotational and orbital nodes.

2 Libration in longitude

In this section, we study the libration in longitude in the planar problem of the rotation of Mercury. In other words, we consider that the inclinations of all the planets are equal to zero. As a result, all the planets move in the same plane (the ecliptic J2000).
Before explaining this problem in more details, let us mention that we choose Mercury's equatorial radius as length unit, Mercury's mass as mass unit and the year of the Earth as time unit.

2.1 Basic hypotheses

Here are the hypotheses for this first model:

1. Mercury is a triaxial body. The development of the gravitational potential in spherical harmonics is limited at the second order. The values chosen for the coefficients are $J_2 = 6 \times 10^{-5}$ and $C_{22} = 10^{-5}$ (Anderson et al. 1987).

[1] University of Namur, Rempart de la Vierge 8, 5000 Namur, Belgium
[2] IMCCE, Observatoire de Paris - Universit Pierre et Marie Curie-Paris 6 - USTL, CNRS UMR 8028, Paris, France

2. Mercury is a two-layer body: a solid mantle and a spherical liquid core. There is no magnetic or viscous interaction between the mantle and the core. Consequently, in this short-term study, the rotation of Mercury is actually the rotation of the mantle.

3. The third axis of inertia and the direction of the angular momentum coincide.

4. Mercury is in a 3:2 spin-orbit resonance.

5. The orbit of Mercury is perturbated by the other planets. As ephemerides, we use a VSOP (Variations Séculaires des Orbites Planétaires) theory given by Simon in a private communication (Fienga and Simon (2004)).

6. All the planets move in the same plane. The orbital inclinations of the planets (with respect to the ecliptic J2000) are set to 0.

2.2 Hamiltonian formalism

Let us first define the angle σ_1, representing the 3:2 spin-orbit resonance: $\sigma_1 = g - \frac{3}{2}l_o - \varpi$, with g the spin angle, l_o the mean anomaly and ϖ the longitude of the perihelion. This angle actually represents the libration in longitude of the planet, in other words, it is the deviation from the exact 3:2 spin-orbit resonance.
With the basic hypotheses, the Hamiltonian of the problem consists of three parts (see papers of D'Hoedt and Lemaitre (2004) and Dufey et al. (2008) for a more detailed explanation of the Hamiltonian):

$$H = H_{2B} + T + V_G, \tag{2.1}$$

where H_{2B} is the Hamiltonian of the 2-body problem, $T = \frac{\Lambda_1^2}{2C_m}$ is the rotational kinetic energy, with Λ_1 the moment associated to the resonant angle σ_1, and $V_G = V_G(l_o, \varpi, e, a, \sigma_1, \Lambda_o, \Lambda_1)$ is the gravitational potential, with e the eccentricity, a the semi-major axis and Λ_o the moment associated to l_o.
It is possible to compute the fundamental period of σ_1:

$$T_{\sigma_1} = 11.21 \text{ years}, \tag{2.2}$$

with $C = 0.34$ and C_m/C=0.5.

2.3 Introduction of planetary perturbations

The planetary perturbations are introduced through the orbital elements a, e, l_o and ϖ, using the Poisson series of the planetary theory given by Simon.
Numerical tests allowed us to conclude that the Sun, Jupiter, Venus, the Earth and Saturn have the largest influence on the rotation. Consequently, we have five new variables in our Hamiltonian: $\lambda_M, \lambda_J, \lambda_V, \lambda_E, \lambda_S$, respectively the longitudes of Mercury, Jupiter, Venus, the barycenter Earth-Moon and Saturn. We only include the periodic contributions in the perturbations, not the Poisson terms. On a time scale of 100 years they are at least 100 times smaller than the periodic contributions.

2.4 The libration in longitude

There will be two steps in order to compute the libration in longitude (See Dufey et al. (2008) and references therein):

- First we use a Lie averaging process to average the Hamiltonian over all the angular variables (the short periodic terms). We then compute the generators of this transformation.

- We use the first-order generator (containing only short periodic terms) to compute the evolution of σ_1.

To confirm the results of the analytical method, we compare them with the results of the SONYR (Spin-Orbit N-bodY Relativstic) model, which is a dynamical model that integrates numerically the orbital motions in the Solar system and includes the coupled spin-orbit motion of the terrestrial planets and of the Moon (see Bois and Vokrouhlicky (1995) and Rambaux and Bois (2004) for references for SONYR).

Effect of	Period (years)	Amplitude	Relative amplitude
Sun (l_o)	0.2408	40.69	1
Jupiter (λ_J)	11.86	13.27	0.3261
Sun ($2l_o$)	0.1204	4.530	0.1114
Venus ($2l_o - 5\lambda_V$)	5.663	4.350	0.1069
Jupiter ($2\lambda_J$)	5.931	1.673	0.0411
Saturn ($2\lambda_S$)	14.73	1.233	0.0303
Earth ($l_o - 4\lambda_E$)	6.575	0.7038	0.0176

Table 1. The main planetary contributions on the resonant angle σ_1.

After this integration, a frequency analysis is used to find the contributions on the libration in longitude. The comparison of the methods is very satisfactory (see Dufey et al. (2008) for the detailed comparison). Table 1 states the result of our method.

The 88-day contribution is the largest, followed by Jupiter's contribution (11.86 years), which is around 33% of the 88-day forced librations. Then Venus' contribution (5.67 year-period) is around 10% and Saturn's (14.73 years) and the Earth's (6.58 years) are around 3% and 2%.

Compared to the results in the paper of Peale et al. (2007), we underline the contributions of the 11.86 year-period, and the contributions of Saturn and the Earth.

Let us mention that the fundamental period is proportional to $\sqrt{\frac{C_m}{B-A}}$ (A and B being the smallest moments of inertia). With the value given by Margot et al. (2007) ($\frac{B-A}{C_m} = 2.03 \times 10^{-4}$) the fundamental period would be $T_{\sigma_1} = 11.21$ years, which is much closer to Jupiter's orbital period. Consequently, the effect of Jupiter on the libration in longitude would be much larger.

3 Libration in latitude

The hypotheses for the 3-dimensional problem are

1. Mercury is a triaxial body.
2. It consists of a solid mantle and a spherical liquid core.
3. The third axis of inertia and the angular momentum coincide.
4. Mercury is in a 3:2 spin-orbit resonance <u>and there is a 1:1 commensurabitlity between the orbital and rotational nodes</u>, i.e. both nodes precess at the same rate.
5. The orbit of Mercury is perturbated by the other planets.
6. <u>The orbital inclinations of the planets are different from zero</u>.

We define a new resonant angle $\sigma_3 = -h + \omega_o$, where h is the argument of the rotational node and ω_o is the argument of the ascending (orbital) node. The angle σ_3 represents the 1:1 commensurability between the rotational and orbital nodes.

Due to the precession of the orbital node, the equilibrium of the ecliptic obliquity is now $K_{\text{eq}} = i_o + 1.2$ arcmin. We compute the evolution of σ_3 and of the ecliptic obliquity K using an approach similar to the previous section. Table 2 summarizes our results. The main observation here is that the amplitudes of the oscillations are very small, under 0.2 arcsec for σ_3 and under 1 mas for the obliquity K. Such amplitudes should be under the observational accuracy of the space misssions.

We also note that the great inequality ($2\lambda_J$-$5\lambda_S$) is the largest of the planetary contributions (aside from the orbital motion of Mercury around the Sun). Jupiter, Venus, Saturn and the Earth also have contributions, but much smaller in this case.

Effect of	Period (years)	Amplitude (as)
Sun (l_o)	0.2408	0.1524
Great ineq.($2\lambda_J - 5\lambda_S$)	883.3	0.0545
Sun ($2l_o$)	0.1204	0.0538
Sun ($3l_o$)	0.0803	0.0420
Jupiter ($2\lambda_J$)	5.931	0.0169
Venus ($2l_o - 5\lambda_V$)	5.663	0.0067
Jupiter ($1\lambda_J$)	11.86	0.0066
Saturn ($2\lambda_S$)	14.72	0.0052
Earth ($l_o - 4\lambda_E$)	6.575	0.0021

Effect of	Period (years)	Amplitude (mas)
Sun ($2l_o$)	0.1204	9.187
Sun ($3l_o$)	0.0803	5.607
Sun (l_o)	0.2408	4.415
Great ineq.($2\lambda_J - 5\lambda_S$)	883.3	4.045
Jupiter ($2\lambda_J$)	5.931	1.738
Jupiter ($1\lambda_J$)	11.86	1.340
Venus ($2l_o - 5\lambda_V$)	5.663	0.608
Saturn ($2\lambda_S$)	14.72	0.461
Earth ($l_o - 4\lambda_E$)	6.575	0.216

Table 2. Left table: main planetary contributions on the resonant angle σ_3. Right table: main planetary contributions on the ecliptic obliquity K.

4 Conclusion

Using a Hamiltonian approach, we are able to analyse the main planetary perturbations acting on the librations in longitude and latitude.

For the libration in longitude, in addition to the 40 arcsec coming from the 88-day orbital motion, we point out that Jupiter's signature (11.86 year-period) is about 13 arcsec, Venus' (5.67 years) is about 4 arcsec and Saturn's and the Earth's (14.72 and 6.58 years) are about 1 arcsec. We also observe that in the case of a close resonance between the orbital period of Jupiter and the fundamental period of the 3:2 resonant angle, Jupiter's contribution would be much larger.

Concerning the libration in latitude, we studied the ecliptic obliquity and the angle describing the 1:1 commensurability in nodes. The amplitude of the oscillations are really small (less than 0.2 arcsec for the resonant angle and less than 1 mas for the obliquity) and the largest planetary contribution (aside from the orbital motion of Mercury) is the great inequality between Jupiter and Saturn. We also detect the signatures of the other planets alone (Jupiter, Venus, Saturn and the Earth), but they are very faint.

References

Anderson, J.D., Colombo, G., Esposito, P.B., Lau, E.L., & Trager, T.B. 1987, Icarus, 71, 337

Bois, E. & Vokrouhlicky, D. 1995, A&A, 300, 559-567.

D'Hoedt, S. & Lemaitre, A. 2004, Celestial Mechanics and Dynamical Astronomy, 89, 267

Dufey, J., Lemaitre, A., & Rambaux, N. 2008, Celestial Mechanics and Dynamical Astronomy, 101, 141

Fienga, A., & Simon, J.-L., 2004, A&A, 429, 361

Margot, J.L., Peale, S.J., Jurgens, R.F., Slade, M.A., & Holin, I.V. 2007, Science, 316, 710

Peale, S.J., Yseboodt, M., & Margot, J.-L. 2007, Icarus, 187, 365

Rambaux, N., & Bois, E. 2004, A&A, 413, 381

COMPARISON OF FAST LYAPUNOV CHAOS INDICATORS FOR CELESTIAL MECHANICS

Frouard, J.[1,2], Fouchard, M.[1,2] and Vienne, A.[1,2]

Abstract. For a long time, the estimation of the Lyapunov Characteristic Exponents (LCEs) had been used in Celestial Mechanics to caracterize the chaoticity of orbits. With the aim of gaining speed and accuracy in detecting this chaoticity, several indicators based on the theory of Lyapunov exponents have been developped. Here we present a comparison in terms of precision, CPU speed, and practicability of several of these indicators ; the FLI (Froeschlé *et al*, 1997) , MEGNO (Cincotta & Simó, 2000), and the GALI (Skokos *et al*, 2007). The GALI3 (using three tangent vectors) is the version of the GALI used here. While the FLI and MEGNO have been commonly used, the GALI has not yet been applied to Celestial Mechanics. However, this indicator has its own qualities and specificities. The final aim of the comparison of these indicators is the production of stability maps in the case of irregular satellites of giant planets, the examples and applications are shown in this sense.

1 Introduction

The three indicators presented here are variants of the Lyapunov Characteristic Exponent (LCE) which is defined by :

$$\sigma = \lim_{t\to\infty} (\frac{1}{t}) \ln \frac{\|\overrightarrow{w}(t)\|}{\|\overrightarrow{w}(0)\|} \tag{1.1}$$

with the use of a tangent vector obtained from the variational equation : $\dot{\overrightarrow{w}} = \frac{\partial \overrightarrow{F}}{\partial \overrightarrow{X}} \overrightarrow{w}$

2 Behaviour of the indicators in different situations

We compare the indicators with several criterions such as the contrast obtained for differentiating chaotic orbits, the integration and CPU times. The location in the orbital elements of the examples on Fig. 1 et Fig. 2 are chosen to be representative of different regimes undergone by a Jovian satellite in the restricted circular and planar three-body problem (Sun + Jupiter + satellite). The first example represent a part of the system dominated by chaotic and resonant orbits, while the second contains quasi-periodic, resonant and unstable orbits. In the figures, the final values over different integration times of the FLI and the MEGNO is shown, in addition with the inverse of the time τ_{GALI3} needed by the GALI3 to attain a particular treshold.

3 Discussions

We are making different objective tests to the methods, concerning mainly contrast between orbits and CPU time which are important for creating maps. Firstly, and as it is already thought, we found that the strong points of the FLI is its simplicity of use and its rapid computation. The FLI and MEGNO seems equivalent (Fig. 1 and 2), although it appears that the MEGNO can show structures and resonances faster in integration time than the FLI, but with more CPU time. Despite its slower speed, the MEGNO is perfectly adapted for the studies of resonant orbits thanks to its quasi-fixed value for stable orbits. Indeed, the value of the FLI and

[1] IMCCE, Observatoire de Paris, UMR 8028, 75014 Paris, France
[2] Université de Lille 1, LAL-IMCCE, UMR 8028, 59000 Lille, France

GALI3 for stable orbits depend (although faintly) on the location of the orbits (Fig. 2). Concerning the CPU time vs integration time, the MEGNO and GALI3 are slower by at least a factor 3 than the FLI, but in this case the GALI method is fundamentally different in its use : using in fact the time for indicator, it allows to deal with chaotic orbits very fast, making it more efficient for regions where chaos is largely extended. This fact can be for example interesting for the studies of orbits which escape rapidly from a giant planet's Hill radius. Conversely, the CPU time increase drastically for the case of stable orbits, although this can be overcome by adding more tangent vectors to the computation of the GALI, thus using a more convergent indicator. We must add that this indicator cannot be computed up to a certain threshold (i.e. integration time) corresponding to the numerical limit.

To continue the comparison, we are adding more tests as objective as possible, in particular comparing the detection of resonances by the different methods in function of time.

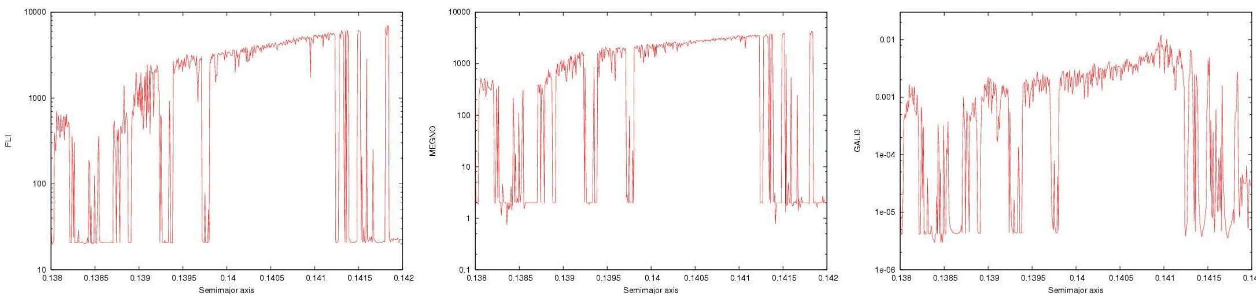

Fig. 1. Final values of the indicators for an integration time of 100,000 years (or treshold value of 10^{-16} for the GALI3), varying the semi-major axis in [0.138-0.142 UA] with e(0)=0.68 and f(0)=w(0)=0. FLI (**Left**), MEGNO (**Center**) and $\frac{1}{\tau_{GALI3}}$ (**Right**). The CPU time is respectively 3.5h, 10.5h and 7.25h.

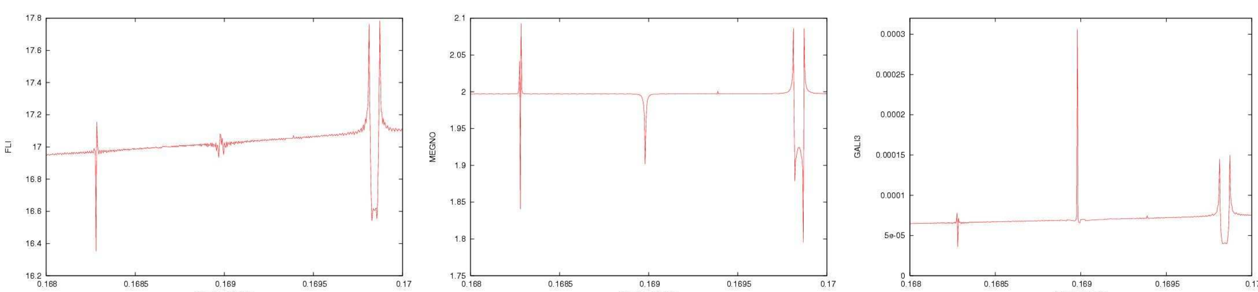

Fig. 2. Final values of the indicators for an integration time of 10,000 years (or treshold value of 10^{-11} for the GALI3), varying the semi-major axis in [0.168-0.17 UA] with e(0)=f(0)=w(0)=0. FLI (**Left**), MEGNO (**Center**) and $\frac{1}{\tau_{GALI3}}$ (**Right**). The CPU time is respectively 0.25h, 1h and 1.5h.

References

Froeschlé, C., Gonczi, R., & Lega, E. 1997, Planetary & Space Science, 45, 881

Cincotta, P.M., & Simó, C. 2000, Astronomy & Astrophysics Supplement, 147, 205

Skokos, C., Bountis, T.C., & Antonopoulos, C. 2007, Physica D, 231, 1, 30

SF2A 2008
C. Charbonnel, F. Combes and R. Samadi (eds)

EARTH'S INTERIOR WITH VLBI: PUSHING THE LIMITS

Lambert, S. B.[1] and Gontier, A.-M.[2]

Abstract. This paper reports on some recent Earth-related studies within the VLBI group of the SYRTE department at the Paris Observatory. Especially, we focus on the determination of some outer core properties through VLBI estimates of the Earth's nutation.

1 Earth's interior and Earth's rotation

The Earth's rotation is irregular, in response to various external and internal excitations. The atmosphere and the hydrosphere, by exchanging angular momentum with the lithosphere, induce variations in position of the rotation pole at seasonal, interannual and diurnal time scales, the latter being the result of the diurnal solar heating of the atmosphere and of the ocean tides. Effects of continental water, snow, and ice sheets, although significant at seasonal time scales, are totally negligible in the diurnal band. Besides, gravitational forces arise from celestial bodies. Combined with the internal structure and rheology of our planet, they determine the shapes of the mantle, and of the fluid-solid interfaces at the core-mantle boundary (CMB) and inner core boundary (ICB).

In presence of a mantle, a fluid outer core and a solid inner core, the dynamic of the system is described by the angular momentum conservation equations (see, e.g., Mathews et al. 1991)

$$\frac{d\vec{H}}{dt} + \vec{\omega} \times \vec{H} = \vec{\Gamma}, \quad \frac{d\vec{H}_{\rm f}}{dt} + \vec{\omega} \times \vec{H}_{\rm f} = \vec{\Gamma}_{\rm f}, \quad \frac{d\vec{H}_{\rm s}}{dt} + \vec{\omega} \times \vec{H}_{\rm s} = \vec{\Gamma}_{\rm s}, \tag{1.1}$$

where $\vec{H}$, $\vec{H}_{\rm f}$, and $\vec{H}_{\rm s}$ are the angular momentum of the Earth rotating at $\vec{\omega}$, the outer and inner cores, respectively, and $\vec{\Gamma}$, $\vec{\Gamma}_{\rm f}$, and $\vec{\Gamma}_{\rm s}$ are torques (including gravitational, interaction, and electromagnetic couplings). Such a 3-layer Earth admits normal rotational modes. The well-known Chandler wobble occurs with a period around 433 days in the terrestrial frame and is associated with the ellipticity of the Earth system (basically the mantle ellipticity plus an oceanic bulge contribution). Two normal modes associated with the free nutations of the outer and inner cores (free core nutation, or FCN, and free inner core nutation, FICN) affect the motion of the Earth's figure axis in space at diurnal frequencies. Finally, a fourth eigenmode is associated with the free motion of the inner core with respect to the mantle and is known as inner core wobble (ICW). The ratio of the nutational amplitude $\tilde{\eta}$ of the whole, 3-layer Earth, solution of (1.1), to its rigid counterpart is expressed in the frequency domain as

$$\frac{\tilde{\eta}(\sigma)}{\tilde{\eta}_{\rm R}(\sigma)} = \left[1 + \sigma' \left(\frac{\tilde{N}_{\rm CW}}{\sigma - \tilde{\sigma}_{\rm CW}} + \frac{\tilde{N}_{\rm FCN}}{\sigma - \tilde{\sigma}_{\rm FCN}} + \frac{\tilde{N}_{\rm FICN}}{\sigma - \tilde{\sigma}_{\rm FICN}} + \frac{\tilde{N}_{\rm ICW}}{\sigma - \tilde{\sigma}_{\rm ICW}} \right)\right], \tag{1.2}$$

where $\sigma' = \sigma + \Omega$, e is the Earth flattening, and the $\tilde{N}$ are functions of the frequency and of a limited number of geophysical parameters. The full expression of this transfer function can be found in Mathews et al. (1991; 2002) wherein (1.1) is solved in the same line as the 2-layer Earth of Sasao et al. (1980). One gets

$$\tilde{\sigma}'_{\rm FCN} = -\Omega \left(1 + \frac{A_{\rm f}}{A_{\rm m}}\right) \left(e_{\rm f} - \tilde{\beta} + \tilde{K}_{\rm CMB} + \frac{A_{\rm s}}{A_{\rm f}} \tilde{K}_{\rm ICB}\right), \quad \tilde{\sigma}'_{\rm FICN} = -\Omega \left(1 + \frac{A_{\rm s}}{A_{\rm m}}\right) \left(\alpha_2 e_{\rm s} + \tilde{\nu} - \tilde{K}_{\rm ICB}\right), \tag{1.3}$$

[1] Observatoire de Paris, SYRTE, CNRS UMR8630, 61 av. de l'Observatoire, F-75014, Paris
[2] Observatoire de Paris, SYRTE, CNRS UMR8630, 61 av. de l'Observatoire, F-75014, Paris

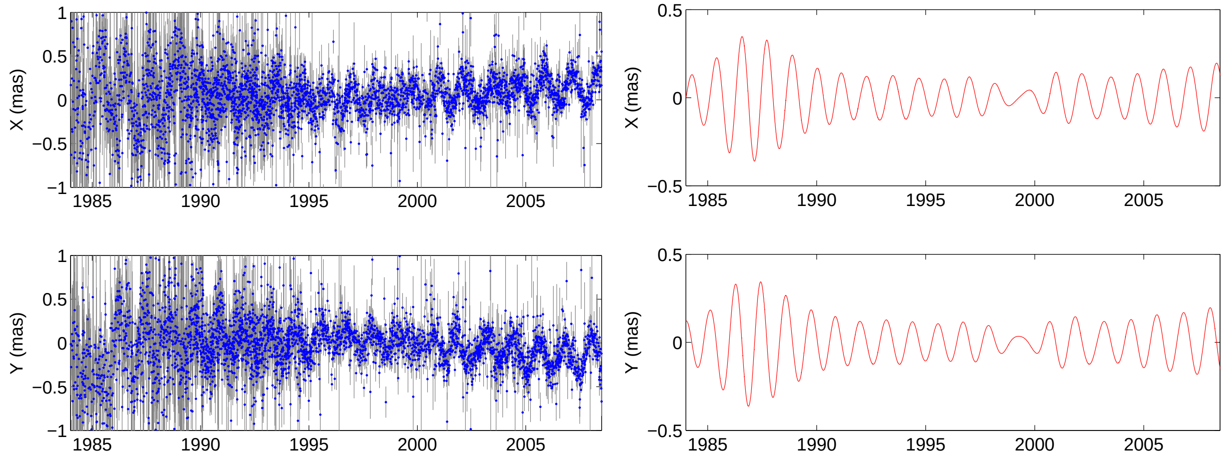

Fig. 1. Left: nutation offsets to Mathews et al. (2002)'s model as computed at the IVS OPAR VLBI analysis center. Right: FCN mode extracted by least-squares fit.

where e_f and e_s are the outer and inner core flattenings, $\tilde{\beta}$ and $\tilde{\nu}$ the compliances expressing the deformability of the CMB and the ICB under the centrifugal forces due to the outer and inner core wobbles, respectively. $\tilde{K}_\mathrm{CMB}$ and $\tilde{K}_\mathrm{ICB}$ are related to the electromagnetic torque at the relevant interface (see Buffett et al. 1992).

One can see from (1.2) that the normal modes amplify the response to an excitation occuring at frequencies close to the resonant frequencies. Thus, tidal forces that excite the Earth at diurnal frequencies would have their response enhanced by the FCN and the FICN modes. Comparison of observed nutations (which traduce the response of the real Earth to the tidal potential) against theoretical response of an hypothetical rigid Earth having the same moments of inertia would therefore lead to determine some Earth's interior properties. Especially, one can fit the resonant frequencies onto the observations and deduce constraints on geophysical parameters that appear in their respective theoretical expressions.

2 VLBI observations for geosciences

Very long baseline interferometry (VLBI) measures differential arrival times of radio signals emitted by extragalactic radio sources (e.g., quasars, BL Lac, AGN) on several antennas separated by thousands kilometers. On a typical 24-hr geodetic VLBI session, a network of 6–12 antennas observes about 80 sources. After correlation of the signals and some analyses, one gets the orientation of the network with respect to the polyhedra realized by the observed sources. Regular observations since ∼1984 (on the basis of one session every 3–4 days) had produced more than 5 million delays that are exploitable for precise geodesy. The improvement of the network geometry (from 4 antennas in the 1980's to 6–12 antennas nowadays) and receiver reliability makes the geodetic VLBI products reach an accuracy (repeatability) of about 6 mm (alternatively 0.2 milliarc second on the Earth orientation, or 20 ps). Geodetic VLBI observing program has long been set up by the NASA and the US Navy. Since 1998, the International VLBI Service for Geodesy and Astrometry (IVS) realizes most of that work through its coordinating center at NASA/GSFC and several analysis centers. It is important to figure out that VLBI is currently the only technique providing dense and accurate estimates of the Earth's nutation, and thereby constitutes a powerful technique for Earth's interior exploration along with local measurements of deformations or gravity variations and seismology. Note also that VLBI is the only technique that observes the free motion of the Earth associated with the FCN (see Section 5 of this paper).

Since 2007, the IVS analysis center located at the department SYRTE of the Paris Observatory (Gontier et al. 2006) and known as IVS OPAR, makes operational analysis of all geodetic VLBI sessions. We especially take care of reference frame effects to improve the reliability of Earth orientation parameters time series. The data sets used in this paper are made available at http://ivsopar.obspm.fr.

3 Estimates of the FCN resonant frequency and damping factor

Several studies have estimated geophysical parameters from VLBI data (Mathews et al. 2002; Vondrák et al. 2005; Lambert & Dehant 2007; Lambert et al. 2008; Koot et al. 2008). Among the interesting results that emerge from these papers, one can retain an estimate of $\tilde{\sigma}'_{\rm FCN}$ (Mathews et al.: 430.21 ± 0.6d; Lambert et al.: 430.31 ± 0.2d) that departs by about 4% from the theoretical value obtained using the seismology-based Earth model of Dziewonski & Anderson (1981) that assumes the CMB in hydrostatic equilibrium. The departure is attributed to an extra outer core flattening, that is confirmed by tomographic and gravimetric observations and explained by convection in the lower mantle (Defraigne et al. 1996).

The imaginary part of the FCN frequency is a damping factor $Q_{\rm FCN}$, such that ${\rm Im}\tilde{\sigma}'_{\rm FCN} = {\rm Re}\tilde{\sigma}'_{\rm FCN}/2Q_{\rm FCN}$, related to the viscous electromagnetic coupling at the CMB and the ICB. Though Mathews et al. yielded $Q_{\rm FCN} = 20\,000$ using VLBI data until 2002, an extra six years of data in Lambert et al. brings out a lower estimate $Q_{\rm FCN} = 19\,000$ where only the FCN frequency is estimated. Recently, one of the author (SBL) re-estimated the FCN frequency among other geophysical parameters and found a $Q_{\rm FCN}$ around $13\,000$, consistently with estimates from superconducting gravimeter data (Rosat et al. 2008). Such a result has been confirmed by Koot et al. These results bring possible new constraints on the value of the electromagnetic field at the CMB that will not be discussed here.

4 Celestial reference frame effects in geophysical results

Global analysis of a large number of sessions permit an estimate of both the Earth orientation parameters and the radio source coordinates. (Incidentally, on the terrestrial side, the positions and velocities of the observing sites are also estimated.) Time evolution of source coordinates due to various intrinsic phenomenon like plasma jets make the use of older coordinate determinations unreliable for precise geodetic analysis. However, estimating all sources' coordinates needs no-net rotation (NNR) constraints to ensure that the global set of quasars does not rotate with respect to the far universe. In practice, the NNR condition is applied to the coordinates of a certain number of 'defining' sources. This core ensemble has been verified to be non rotating by exhaustive tests. The current International Celestial Reference Frame (ICRF, Ma et al. 1998) proposes such a set of 212 defining sources, selected on the basis of VLBI observation until 1995. Since then, this set has become unstable and more reliable sets can be found (e.g., Feissel-Vernier 2003).

The sensitivity of VLBI products to celestial frame realization is still an open question. We give a brief review of various related studies in Lambert & Gontier (2008) where we also propose new sets of defining sources that provide celestial reference frames more reliable than the ICRF. In Lambert et al., we showed that the way of handling source coordinates during the analysis as well as the choice of the defining sources could produce substantial differences on Earth orientation parameter estimates. These differences result in uncertainties in estimates of the resonant frequencies that reach 0.2 day for the FCN and 300 days for the FICN. A spurious rotation of the celestial frame results in biases in the nutation angles, that reduces to zero when the system is perfectly non rotating. Effects on precession, rate and main periodic terms remain small, with no consequences on further geophysical analyses.

5 Outer core nutation excitation mechanisms

The signature of the FCN mode on the Earth's figure axis, observed from a space-fixed frame of reference, is a retrograde motion (opposite the Earth's rotation) that reaches an amplitude of $\sim$200 mas, variable in time, and with a variable phase. This signal clearly shows up in VLBI residuals. The apparent period oscillates between 430 and 460 days (Vondrák et al. 2005) and is most likely driven by diurnal atmospheric pressure variations (Gegout et al. 1998). Lambert (2006), under the assumption of a white noise excitation, showed that about a half of the observed amplitude could be explained using atmospheric general circulation models (GCMs), and that it is not possible to conclude whether the remaining half is due to another mechanism or to the poor quality of the diurnal atmospheric pressure data in the diurnal band.

Here, we propose to use a different approach based on a numerical resolution of the dynamical equations describing the Earth's nutation. We basically force the system (1.1) by the atmospheric data obtained from two distinct GCMs (US National Center for Environmental Prediction/National Center for Atmospheric Research reanalysis project, referred to hereunder as NCEP, and European Center for Medium range Weather Forecast,

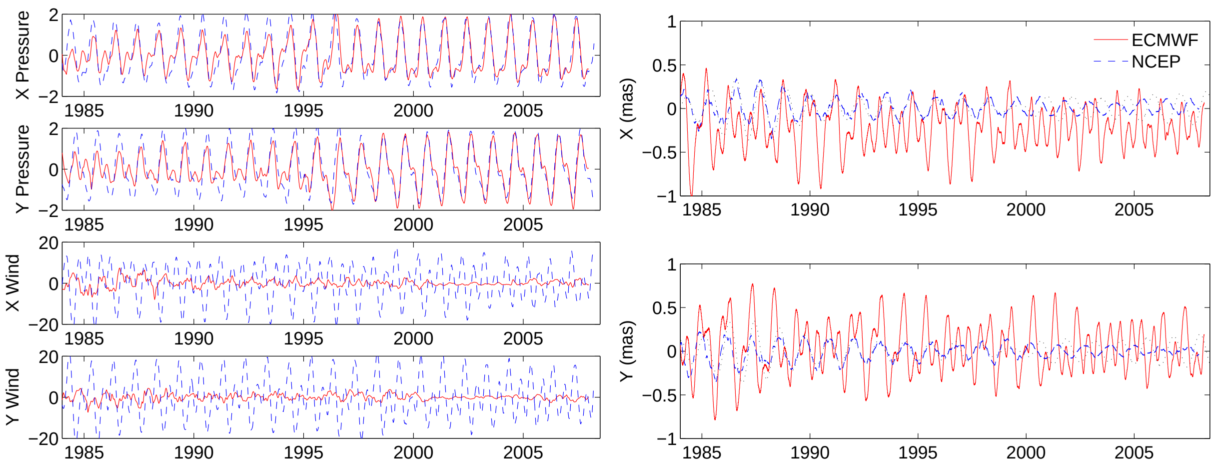

Fig. 2. Left: X and Y components of the modulation of the diurnal term in the atmospheric angular momentum from ECMWF (solid) and NCEP (dashed) in units of 10^{23} kg m^2/s. Right: predicted FCN mode.

referred to as ECMWF). This approach does not reduce the atmospheric signal to a white noise but takes any possible spectral signature into account. Moreover, we also consider wind data, in addition to surface pressure data, that were not studied in the work of 2006. Figure 2 displays the (mainly annual) modulation of the diurnal atmospheric angular momentum cycle. One can see significant discrepancies between NCEP and ECMWF, both in amplitude and phase, especially on the wind term. The right plot displays the predicted FCN mode, that must be compared to the VLBI reported in dotted line. It appears that the NCEP data (wind + pressure) fairly explains the VLBI-observed mode, including the decrase of the amplitude before 2000, but fails in explaning the amplitude at the very end. NCEP winds explain about 60% of the signal. However, ECMWF data lead to completely different results, far away from the observation. Although the pressure alone give a predicted mode that is very close the NCEP-predicted one, the wind part, which is smaller but noisier (with higher derivatives) produces a strong, unrealistic FCN mode. We thus conclude that the NCEP GCM is more reliable for study of diurnal atmospheric effects on the Earth's rotation. It is important to note that this does not disqualify the ECMWF data at all: one must understand that GCMs does not aim to produce diurnal data, since meteorological centers are mainly interested in 2- to 10-day forecasts.

References

Buffett, B.A., Mathews, P.M., & Herring, T.A. 2002, J. Geophys. Res.,107(B4), 10.1029/2000JB000056
Defraigne, P., Dehant, V., & Wahr, J.M. 1996, Geophys. J. Int., 125, 173
Dziewonski, A.M., & Anderson, D.L. 1981, PEPI, 25, 297
Feissel-Vernier, M. 2003, A&A, 403, 105
Gegout, P., Hinderer, J., Legros, H., et al. 1998, PEPI, 106, 337
Gontier, A.-M., Lambert, S.B., & Barache, C. 2006, In: D. Barret et al. (Eds.), Proc. Journées SF2A 2006, 23
Koot, L., Rivoldini, A., de Viron, O., & Dehant, V. 2008, J. Geophys. Res., 113(B8), B08414
Lambert, S.B., & Gontier, A.-M. 2008, A&A, in press
Lambert, S.B., Dehant, V., & Gontier, A.-M. 2008, A&A, 481, 535
Lambert, S.B., & Dehant, V. 2007, A&A, 469, 777
Lambert, S.B. 2006, A&A, 457, 717
Ma, C., Arias, E.F., Eubanks, T.M., et al. 1998, AJ, 116, 516
Mathews, P.M., Buffett, B.A., Herring, T.A., & Shapiro, I.I. 1991, J. Geophys. Res., 96(B5), 8219
Mathews, P.M., Herring, T.A., & Buffett, B.A. 2002, J. Geophys. Res., 107(B4), 10.1029/2001JB000390
Rosat, S., Lambert, S.B., Florsch, N., et al. 2008, 2008 Earth Tide Symposium, Jena, Germany
Sasao, T., Okubo, S., & Saito, M. 1980, Proc. IAU Symp. 78, ed. E.P. Federov et al. (Hingham, Mass.: D. Reidel), 165
Vondrák, J., Weber, R., & Ron, C. 2005, A&A, 444, 297

SF2A 2008
C. Charbonnel, F. Combes and R. Samadi (eds)

AN ESTIMATE OF THE RELATIVISTIC PARAMETER γ USING VLBI

Lambert, S. B.[1] and Le Poncin-Lafitte, C.[2]

Abstract. This paper presents estimates of the post-Newtonian parameter γ from the analysis of 24 years of radio delays recorded by the various geodetic VLBI observing campaigns and the current permanent geodetic VLBI network.

1 Light deflection and VLBI measurements

In the weak field approximation, gravitational effects in Solar System are described using the parameterized post-Newtonian formalism, that has a dozen parameters among which the very well-known β and γ. Experiments of light deflection are particularly sensitive to γ and VLBI is an important technique to measure this effect when light rays coming from quasars graze the Sun. If ϕ is the angle between the Sun and the source as seen from the Earth, and b the impact parameter, the deflection angle is $\theta \approx (\gamma + 1)(GM/c^2b)(1 + \cos\phi)$, where $\gamma = 1$ in General Relativity (GR). A grazing ray at the Sun's limb is thus deflected by $1.7''$. The most recent attempt to measure γ by VLBI was done by Shapiro et al. (2004), using VLBI observations over 1979–1999. They found that γ is consistent with GR within 4×10^{-4}. Bertotti et al. (2005), found 2×10^{-5}, using Cassini spacecraft tracking time delays (this constitutes the current best determination).

A look at the observational history of extragalactic radio sources in the International VLBI Service for Geodesy and Astrometry (IVS) data base reveals that the VLBI observing schedule included a number of radio sources at less than 15° to the sun. This number was quite uniform during 1984–1996, and then substantially increased during 1996–2002. Later, sources at less than 15° have no longer been observed. Note also that 1992–1999, that contains a number of close approaches, is a period of low solar activity.

In this work, we aim at estimating γ using the additional 1999-2008 time period with respect to Shapiro et al., and dropping the 1979–1984 period which contains observations with poor geometries and early recording systems. We also want to test several time spans that may be more reliable for this kind of experiment.

2 Data analysis and results

All the VLBI analyses are run using the IVS OPAR analysis center facilities (Gontier et al. 2006) at the SYRTE department of the Paris Observatory. In a first step, we build up a radio source coordinate (RSC) catalogue that will be taken as a priori catalogue for further analyses. This is realized in a single inversion of 3,852 ionosphere-calibrated dual-frequency diurnal VLBI sessions reparted over 1984–2008. In such an inversion, the RSC must be constrained in order to avoid any global rotation of the frame. After several tests, we choose to apply a no-net rotation constraint on the coordinates of 262 sources that were selected by Lambert & Gontier (2008). This set of sources was shown to provide a materialization of the celestial reference system more stable than previous ones (Ma et al. 1998; Feissel-Vernier et al. 2006). Thus, the obtained RSC catalogue is aligned to the International Celestial Reference Frame (Ma et al. 1998; Fey et al. 2004) within 20 μas. To avoid perturbation of the RSC estimates by any variable geophysical processes (e.g., unmodeled Earth orientation or seasonal deformation of the network geometry), all observing site coordinates and velocities are estimated over the full time span, together with session-wise Earth orientation parameters, antenna axis offsets, and troposphere gradients and zenith delay.

[1] Observatoire de Paris, SYRTE, CNRS UMR8630, 61 av. de l'Observatoire, F-75014, Paris
[2] Observatoire de Paris, SYRTE, CNRS UMR8630, 61 av. de l'Observatoire, F-75014, Paris

In a second step, we launch inversions of the same VLBI sessions wherein (i) a mean value of γ is estimated over the full time span, and (ii) RSC are not globally constrained, but allowed to move within circles of 10^{-8} rad around the a priori position given by the a priori RSC catalogue previously set up. This second step is repeated for sessions within 1984–2002, and 1996–2002. Additionally, we also run similar a solution over the Shapiro et al.'s 1979–1999 time span for comparison purpose. (Nevertheless, the sessions used are not exactly the same, as well as the analysis strategy and the sofware package.) In all these solutions, station coordinates and Earth orientation parameters are estimated at each session, with appropriate loose constraints. Obtained values of γ are gathered in Table 1. The posfit rms delay that nears 27 ps means that the noise level is at the level of 250 μas in terms of angular positioning.

The solution over 1979–1999 confirms the results of Shapiro et al. with a slightly lower formal error that may originate from a different analysis strategy (e.g., constraints on radio source coordinates). The 1996–2002 solution obviously suffers from a small number of observations, bringing out less sources (with less observations) on which the adjustment of γ can be done. The solutions over 1984–2002 and 1984–2008 that include a large number number of sessions and delays both result in estimates of γ consistent with GR within 2×10^{-4}. The solution over 1984–2002, i.e., over the period that is both long and rich in close approaches, is the closest to the unity.

Table 1. Characteristics of the global solutions and estimates of γ.

	No. sessions	No. delays	No. sources	Postfit rms delay (ps)	γ
1984–2008	3,852	4,348,913	988	24.9	0.99986 ± 0.00015
1984–2002	3,040	2,857,624	781	27.0	0.99993 ± 0.00017
1996–2002	753	1,024,322	676	27.5	0.99940 ± 0.00022
1979–1999	2,598	2,115,509	723	27.4	0.99983 ± 0.00020

3 Conclusion

We show that the existing geodetic VLBI data can be used back to 1984 to get estimates of γ with a accuracy of 2×10^{-4}. The estimate of γ can even reach values close to 1 by 7×10^{-5} when using strictly the time span containing sessions with observations of sources at low elongations to the sun (less than 15°). The improvement with respect to the value of Shapiro et al. can be attributed to the extra three years of data (1999–2002) that are rich in close approaches, along with the improvement of the quality of the VLBI network and observations. Using the sessions after 2002, that no longer contains close approaches below 15°, makes the estimate of γ depart from the unity at the level of 1σ.

References

Bertotti, B., Iess, L., & Tortora, P. 2003, Nature, 425, 374

Feissel-Vernier, M., Ma, C., Gontier, A.-M., & Barache, C. 2006, A&A, 452, 1107

Fey, A. L., Ma, C., Arias, E. F., et al. 2004, AJ, 127, 3785

Gontier, A.-M., Lambert, S. B., & Barache, C. 2006, In: D. Barret et al. (Eds), Proc. Journées SF2A 2006, 27

Lambert, S. B., & Gontier, A.-M. 2008, A&A, in press

Ma, C., Arias, E. F., Eubanks, T. M., et al. 1998, AJ, 116, 516

Shapiro, S. S., Davis, J. L., Lebach, D. E., & Gregory, J. S. 2004, Phys. Rev. Lett., 92, 121101

SF2A 2008
C. Charbonnel, F. Combes and R. Samadi (eds)

RELATIVISTIC ASPECTS OF THE GAIA MISSION

Le Poncin-Lafitte, C.[1]

Abstract. Given the extreme accuracy reached in future global space astrometry, a mission such that GAIA will need a global relativistic modeling of observations. Outlining the importance of having a consistent relativistic approach all the way through the data analysis, we present also why GAIA observations will lead, in return, to an improvement of some General Relativity tests much beyond the current level.

1 Introduction

In 2000 the International Astronomical Union has adopted a general relativistic framework for modeling high-accuracy astronomical observations. Two fundamentals systems have been fixed: the Barycentric Celestial Reference System (BCRS) and the Geocentric Celestial Reference System (GCRS). The BCRS has been defined in such a way that it is covering the Solar System and observed sources. It is mainly very useful for the modeling of the dynamics of the solar system bodies and/or probe as well as the description of light propagation between light sources and an observer. The coordinate time of the BCRS is called the Barycentric Coordinate Time (TCB). It is however possible to use a scaled TCB for practical purpose, the so-called Dynamical Barycentric Time (TDB). The GCRS has been constructed in order that all gravitational fields generated by other bodies are seen as tidal potentials. The coordinate time of the GCRS is called Geocentric Coordinate Time (TCG). A scaled version of TCG exists and is called Terrestrial Time (TT) which is directly related to the International Atomic Time (TAI). The CGRS is suitable for the modeling of all physical processes in the immediate vicinity of the Earth. In addition, a local reference system, GCRS-like, can be constructed for any massless bodies, *i. e.* an observing satellite, and it is convenient to model any physical processes in the local vicinity of the satellite (Klioner 2004). By using this set of three relativistic reference systems, it is possible to draw a consistent relativistic scheme for the modeling of all kind of GAIA observations, as illustrated in Fig. 1.

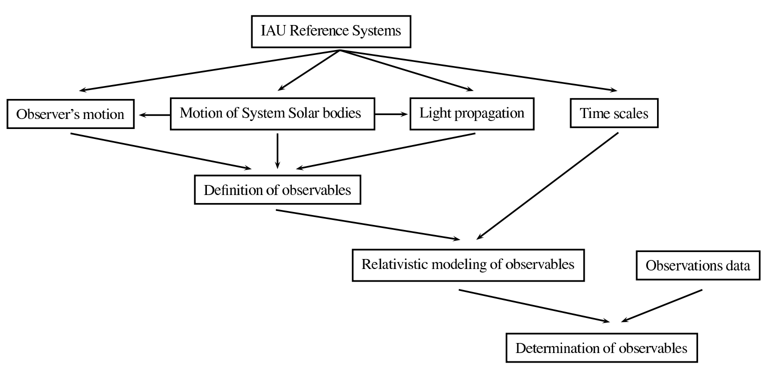

Fig. 1. Principles of relativistic modeling of astronomical observations.

[1] Observatoire de Paris, SYRTE CNRS/UMR 8630, 61 Avenue de l'Observatoire, F75014 Paris, France

2 modeling of the motion of the satellite/ Solar System bodies

It is well known that the equation of motion are ordinary differential equations of second order which can be solved numerically. The principal relativistic effects in the mass-monopole approximation for the gravitating bodies are the so-called Einstein-Infeld-Hoffmann equations of motion which can be written as follow

$$\begin{aligned} a^i_E &= -\sum_{B\neq E} G\,M_B\,\frac{r^i_{EB}}{r^3_{EB}} + \frac{G}{c^2}\sum_{B\neq E} M_B\,\frac{r^i_{EB}}{r^3_{EB}}\left\{\sum_{C\neq B}\frac{G\,M_C}{r_{BC}} + 4\sum_{C\neq E}\frac{G\,M_C}{r_{EC}}\right. \\ &\quad \left. +\frac{3}{2}\frac{\left(r^j_{EB}\dot{x}^j_B\right)^2}{r^2_{EB}} - \frac{1}{2}\sum_{C\neq E,B} G\,M_C\,\frac{r^j_{EB}\,r^j_{BC}}{r^3_{BC}} - 2\,\dot{x}^j_B\,\dot{x}^j_B - \dot{x}^j_E\,\dot{x}^j_E + 4\,\dot{x}^j_E\,\dot{x}^j_B\right\} \\ &\quad +\frac{1}{c^2}\sum_{B\neq E} G\,M_B\,\frac{r^j_{EB}}{r^3_{EB}}\left\{4\,\dot{x}^j_E - 3\,\dot{x}^j_B\right\}(\dot{x}^i_E - \dot{x}^i_B) - \frac{1}{c^2}\frac{7}{2}\sum_{B\neq E}\frac{G\,M_B}{r_{EB}}\sum_{C\neq E,B} G\,M_C\,\frac{r^i_{BC}}{r^3_{BC}} + \mathcal{O}(c^{-4}), \end{aligned} \tag{2.1}$$

where capital latin subscripts B, C and E enumerate massive bodies, M_B is the mass of body B, $\mathbf{r}_{EB} = \mathbf{x}_E - \mathbf{x}_B$, a dot signifying time derivative with respect to TCB.

Of course, on the first hand, modern planetary ephemerides use Eq. (2.1) as a basic one and they are usually distributed in TDB time scale. On the other hand, one of the most controversial question is relativistic time scales and their relations. Indeed, one consequence of relativity is that the relation between one moment of time from one reference system to another can be constructed if and only if the spatial positions of the event are specified. A particular case is the transformation from TCG to TCB at the geocenter, which reads

$$\frac{dTCG}{dTCB} = 1 + \frac{1}{c^2}\alpha(TCB) + \frac{1}{c^4}\beta(TCB) + \mathcal{O}\left(\frac{1}{c^5}\right), \tag{2.2}$$

with

$$\alpha(TCB) = -\frac{1}{2}v^2_E - \sum_A \frac{GM_A}{r_{GA}}, \tag{2.3}$$

$$\begin{aligned} \beta(TCB) &= -\frac{1}{8}v^4_E + \frac{1}{2}\left(\sum_A \frac{GM_A}{r_{EA}}\right)^2 + \sum_A\left(\frac{GM_A}{r_{EA}}\sum_{B\neq A}\frac{GM_B}{r_{AB}}\right) \\ &\quad + \sum_A \frac{GM_A}{r_{EA}}\left[4\mathbf{v}_A.\mathbf{v}_E - \frac{3}{2}v^2_E - 2v^2_A + \frac{1}{2}\mathbf{a}_A.\mathbf{r}_{EA} + \frac{1}{2}\left(\frac{\mathbf{v}_A.\mathbf{r}_{EA}}{r_{EA}}\right)^2\right], \end{aligned} \tag{2.4}$$

where capital latin subscripts A, B and C enumerate massive bodies, E corresponds to the Earth, $\mathbf{v}_E = \dot{\mathbf{x}}_E$ and $\mathbf{a}_E = \ddot{\mathbf{x}}_E$.

Let us also stress that TDB has been redefined by the last IAU general assembly as a fixed linear transformation of TCB. It means that each planetary ephemeride, usually distributed in TDB, "realizes" the transformation (2.2). Since the official time scale chosen to process the GAIA data is TCB, It will be then natural to have an access to the transformations $TT \to TDB$ and back from the ephemeride used in the processing itself. Taking into account that it is not very complicated to do a Chebyshev polynomials representation of the numerical integration of Eq. (2.2), one can expect that in the future, GAIA mission is a good opportunity to lead the ephemeride providers to construct consistent relativistic four-dimensional planetary ephemerides.

3 modeling of positional observations

First of all, the equation of light propagation relative to the BCRS should be derived and solved. It can be seen that five vectors are needed (see Fig. 2): $\mathbf{s}$ is the unit observed direction, $\mathbf{n}$ is the unit vector tangential to the light ray at the moment of observation, σ is the unit vector tangential to the light ray at $t = -\infty$, $\mathbf{k}$ is the unit coordinate vector from the source to the observer and $\mathbf{l}$ is the unit vector from the Solar System barycenter to the light source. The modeling (GREM, Klioner 2003) consists then in a sequence of transformations between these vectors:

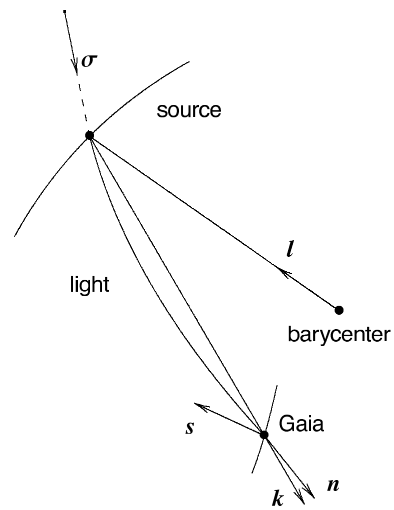

Fig. 2. Vectors used in the modeling of light propagation.

a) aberration: this step converts the observed direction to the source **s** into the coordinate velocity of the light ray **n** at the event of observation,

b) light deflection for source at past infinity: the vector **n** is converted into σ,

c) light deflection for finite sources: this step converts σ into the coordinate direction **k** going from the source to the observer,

d) parallax: **k** is converted into **l** going from the Solar System barycenter to the source,

e) proper motion: this step gives a description of the time dependence of **l** caused by the motion of the source with respect to the Solar System barycenter.

The most complicated part of the modeling lies on the description of light deflection. To reach the microarcsecond accuracy, it is needed to take into account the effects of monopole field of major celestial bodies as well as the quadrupole field of giant planets and gravitomagnetic fields due to the translational motion of deflecting bodies.

4 Synchronization of the onboard clock

Another important aspect is the conversion of BCRS time intervals $dTCB$ into the corresponding GAIA proper time intervals dTG. The general form of this transformation is similar to Eq. (2.2), but has to be calculated along the worldline of GAIA. It reads

$$\frac{dTG}{dTCB} = 1 + \frac{1}{c^2}\alpha'(TCB) + \frac{1}{c^4}\beta'(TCB) + \mathcal{O}\left(\frac{1}{c^5}\right) , \tag{4.1}$$

with

$$\alpha'(TCB) = -\frac{1}{2}v_G^2 - \sum_A \frac{GM_A}{r_{GA}} , \tag{4.2}$$

$$\begin{aligned}\beta'(TCB) = & -\frac{1}{8}v_G^4 + \frac{1}{2}\left(\sum_A \frac{GM_A}{r_{GA}}\right)^2 + \sum_A \left(\frac{GM_A}{r_{GA}} \sum_{B\neq A} \frac{GM_B}{r_{AB}}\right) \\ & + \sum_A \frac{GM_A}{r_{GA}} \left[4\mathbf{v}_A.\mathbf{v}_G - \frac{3}{2}v_G^2 - 2v_A^2 + \frac{1}{2}\mathbf{a}_A.\mathbf{r}_{GA} + \frac{1}{2}\left(\frac{\mathbf{v}_A.\mathbf{r}_{GA}}{r_{GA}}\right)^2\right] ,\end{aligned} \tag{4.3}$$

where all quantities, indexed with capital latin subscript G, refer to the satellite. GAIA will be observable from Earth ground stations several hours peer day. During all visibility periods, the clock of GAIA will be synchronize with the ground. Essentially, GAIA onboard clock will generate some time packet OBT_k, which differs from the "ideal" proper time TG because technical errors of the clock, and this information will be send to the ground station which will produce a time tag in Universal Coordinate Time UTC_k. The whole story is to be able to give a relation between all pairs $(OBT_K\,; UTC_K)$ and the corresponding relativistic pairs (TG_K, TCB_k) One possible approach is illustrated in Fig. 3 where numerous time scales and relativistic transformations are involved.

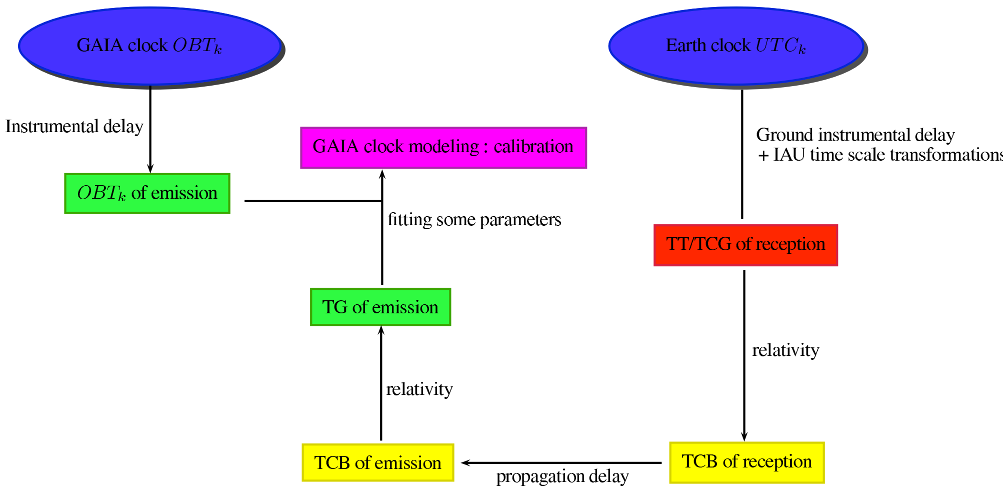

Fig. 3. Relativitistic scheme of onboard clock synchronization

5 Testing General Relativity?

Because the standard reduction modeling of GAIA is deeply based on General Relativity basic principles, GAIA data can be used to test many aspects of relativity itself. It is difficult to describe here all possible tests, so let us only give the main contributions of GAIA to fundamental physics:

- the PPN parameter γ will be measured with an accuracy between 10^{-6} and 5×10^{-7} in a wide range of angular distances from the Sun which constitutes a complete test of light deflection in Solar System,
- the PPN parameter β will be measured with an accuracy close to 10^{-4} from the observations of asteroïds (Hestroffer et al. 2007),
- local gravitational light deflection due to giant planet will be measured: the monopole deflection, the deflection due to translational motion of the planets and the deflection due to the quadrupole field of Jupiter (GAREX experiment of Crosta & Mignard 2006, Le Poncin-Lafitte & Teyssandier 2008).

References

Crosta, M.-T., Mignard, F. 2006, Classical and Quantum Gravity, 23, 4853

Hestroffer, D., Mouret, S., Berthier, J., Mignard, F., Tanga, P., 2008, IAU Symposium, 248, 266

Klioner, S. A., 2003, Technical report on the implementation of the GAIA relativistic model, available from the GAIA document archive

Klioner, S. A., 2004, Physical Review D, 69, 124001

Le Poncin-Lafitte, C., Teyssandier, P., 2008, Physical Review D, 77, 044029

Soffel, M., *et al.*, 2003, Astronomical Journal, 126, 2687

SF2A 2008
C. Charbonnel, F. Combes and R. Samadi (eds)

PIONEER 10 DATA ANALYSIS: INVESTIGATION ON PERIODIC ANOMALIES

Levy, A.[1], Christophe, B.[1], Reynaud, S.[2], Courty, J-M.[2], Bério, P.[3] and Métris, G.[3]

Abstract. The Pioneer Anomaly refers to the difference between the expected theoretical trajectory of the Pioneer 10 and 11 spacecrafts and the observed trajectory through Doppler measurements. It has been interpreted by the Jet Propulsion Laboratory (JPL) as a constant anomalous acceleration (Anderson et al. 2002). For this analysis, the Groupe Anomalie Pioneer (GAP) composed of several french laboratories has developped a specific trajectography software, ODYSSEY, which enables to test different anomaly models.

The paper will present, after a brief description of the software and the implemented models, the last results obtained: in addition to the constant anomaly, time dependent signatures of the anomaly have been noticed which can be described geometrically. The fit of the Pioneer 10 data with these new models yields a reduction of the standard deviation of the residual by a factor 2 with respect to the simple constant anomaly.

1 Introduction

The Pioneer Anomaly refers to the observed deviation from expectations of the trajectory of the Pioneer 10 and 11 spacecrafts, as observed through Doppler tracking. Precisely, the analysis performed at the Jet Propulsion Laboratory (JPL) have shown that the deviation can be described as a nearly constant and Sunward acceleration with a similar magnitude $(8.74\pm1.33)10^{-10}\mathrm{ms}^{-2}$ for the two spacecraft (Anderson et al. 2002).

The presence of this anomaly and its magnitude have been confirmed by different analysis software (Marwardt 2002, Olsen 2007). A number of mechanisms have been considered as attempts of explanations of the anomaly as a systematic effect generated by the spacecraft itself or its environment (see as an example (Nieto et al. 2005) but they have not led to a satisfactory understanding to date. If confirmed, the Pioneer signal might reveal an anomalous behaviour of gravity at scales of the order of the size of the solar system and thus have a strong impact on fundamental physics, astrophysics and cosmology.

An international collaboration has been built recently, within the frame of International Space Science Institute (ISSI), in order to re-analyse the Pioneer data. The Pioneer data which had been analysed by the Anderson team (Anderson 2002) have been made available by Slava Turyshev (JPL) in the framework of this collaboration. They consist in Orbit Data Files (ODF) which contain in particular Pioneer 10 Doppler data from November 30th, 1986 to July 20th, 1998.

The aim of the present paper is to report some results of the analysis of these data performed by a collaboration between three groups at Onera, OCA and LKB within the "Groupe Anomalie Pioneer". A dedicated software called ODYSSEY has been developed to this purpose. The first result is to confirm the existence and magnitude of the anomalous secular acceleration reported by Anderson et al. (2002), using different and as independent as possible tools. The main motivation of the present paper is to study the periodic variations of the anomaly, which are known to exist besides the constant anomaly. Especially, we will show here that this periodic anomaly can be at least partly represented in terms of a modulation of the Doppler signal as a function of a unique azimuthal angle having a physical meaning.

[1] ONERA/DMPH, 29 av. Division Leclerc, F-92322 Chatillon
[2] LKB, UPMC, case 74, CNRS, ENS, F-75252 Paris cedex 05, France
[3] Geoscience Azur, Université Nice Sophia-Antipolis, OCA, Avenue Copernic F-06130 Grasse, France

2 Development of the ODYSSEY software

The Pioneer 10/11 spacecrafts were tracked by the Deep Space Network (DSN) antennas. A S-Band signal at about 2.11 GHz is emitted at time t_1 by a DSN antenna and received onboard the spacecraft at time t_2. The frequency is multiplied by a constant ratio of 240/221 by a transponder and sent back to a ground antenna where it was received at time t_3. The Doppler shift is the difference between the up- and down- frequencies. In fact, the ODF observable is the average of the Doppler shift over a time span called compression interval (Moyer 2000). The ODF format, described in (Wackley 2000), also contains the compression time, the date of the middle of the compression interval, the emitted frequency and the receiving and transmitting DSN antenna identifiers.

To analyse the ODF data, a software called ODYSSEY has been developed at OCA within a collaboration with Onera. It is basically an interplanetary trajectory determination software. It performs numerical integration in rectangular coordinates of dynamical equations to propagate the position and velocity of the spacecraft and variational equations to propagate the sensitivity of the position and velocity with respect to the initial conditions of position and velocity and other parameters to be fitted. The values of the parameters to be estimated are obtained through a best fit procedure using the iterative least-squares method.

Maneuvers are taken into account as increments of velocity along the three directions. The dates of the maneuvers are provided by JPL and their amplitudes estimated as parameters in the best fit analysis.

The dynamical model to compute the motion of the spacecraft includes gravitational attraction by the main bodies of the solar system and direct radiation pressure. The motion of the spacecraft is computed using non relativistic gravitational equations. For the solar radiation pressure we use the same model as in (Anderson 2002).

The dynamical equations are integrated in the Barycentric Celestial Reference System (BCRS); The reference time scale is the Barycentric Coordinate Time (TCB). Positions of terrestrial stations are expressed in the International Terrestrial Reference System (ITRS); the reference time scale is the Coordinated Universal Time (UTC). The transition between ITRS and BCRS on the one hand, and TCB and UTC on the other hand, are performed according to 2003 International Earth Rotation Service (IERS) conventions. The positions of celestial bodies are obtained from DE 405 ephemeris from JPL in BCRS with a reference time scale is similar to the Barycentric Dynamical Time.

Special efforts have been devoted in the development of ODYSSEY for handling the calculation of the ODF observable. In a first step, the perturbations of the round-trip light time are not taken into account. The ODF observable, that is the average of the Doppler shift over the compression time, is computed through a numerical approximation using the 4-points Simpson method.

The instantaneous Doppler shift is calculated in terms of velocities of the endpoints, evaluated at the event times t_1, t_2 and t_3 (Markwardt 2002). As only t_3 is provided in ODF, t_2 and t_1 have to be determined, which is done iteratively using the relativistic light time equation.

In the second step of the computation of the observable, the perturbations which affect the propagation of the tracking signal are taken into account. The Shapiro time delay and the solar corona effect are modeled as in (Anderson 2002). For the determination of the electron density necessary to compute ionospheric effect, the International Reference Ionosphere (IRI) 2007 (Bilitza 2001) has been implemented. For the mapping functions of the tropospheric effect, the Global Mapping Functions (GMF) (Boehm 2006) have been implemented. All these perturbations are modeled as delays affecting the signal (except for the Shapiro delay, their effect in the light time equation is however negligible).

3 Confirmation of the existence of a constant anomaly

Our first aim was to study the secular Pioneer anomaly reported by Anderson et al. (2002). To this aim, we performed a best-fit with a constant anomalous acceleration a_P exerted on the probe and centered on the Sun.

The initial conditions as well as the three components of each maneuver are also fitted. Points with an elevation inferior to 20° are rejected so as to limit the effect of imperfections of atmospherical models. Outliers are also rejected when their difference with the expectation exceeds 100 Hz at the first iteration and 6σ at the following iterations with σ the standard deviation of the residuals at this iteration.

The analysis performed with the software ODYSSEY confirms that a better fit is obtained with a constant sunward acceleration. The value estimated by ODYSSEY for the anomalous acceleration is $a_P = 0.84 \pm$

$0.01\,\mathrm{nms}^{-2}$ with the formal error given at 1σ. This magnitude is compatible with that reported by Anderson et al.

The postfit residuals show a standard deviation of 9.8 mHz, which is largely improved with respect to a fit without a_P.

4 Study of the periodic variations of the Pioneer Anomaly

It can be emphasized that the level of the residuals is higher than the measurement noise. In order to highlight the potential existence of systematic structures in the residuals, we performed a spectral analysis of the residuals using the SparSpec software (Bourguignon et al. 2007). The result of this spectral analysis is shown on Fig. 1.

The presence of significant periodic terms is clear at the periods measured with respect to a day = 86400 s: $f_1 = 0.9974 \pm 0.0004\,\mathrm{day}$, $f_2 = \frac{1}{2}(09972 \pm 0.0004)$, and $f_3 = 189 \pm 32\,\mathrm{day}$. As 0.9972 day = 1.0 sidereal day, these periods are consistent with variations on one sidereal day, half a sidereal day, and half a year.

The presence of diurnal and seasonal variations in the residuals has also been reported by Anderson et al. (Anderson et al. 2002). Anderson et al. (2002) proposes modeling errors such as errors in the Earth's ephemeris, the orientation of the Earth's spin axis or the station's coordinates. However, these parameters are strongly constrained by other observational methods and it seems difficult to change them enough to explain the periodic anomaly.

The main motivation of the present paper is to test an alternative explanation where some perturbation would modify the propagation of the tracking signal along the path from the Earth antenna and the spacecraft. The idea is to represent such a perturbation, whatever its origin, as a function of the angle φ defined as the difference between the Earth Antenna (A) azimuthal angle and the Pioneer (P) azimuthal angle : $\varphi = \varphi_P - \varphi_A$. The main interest of this geometrical model is that it should simultaneously account for the orbital movement of the Earth around the Sun and the diurnal rotation of the Earth.

As this perturbation is supposed to be periodic, it will be represented by a few Fourier coefficients υ_n and υ'_n. The spectral analysis information led us to test the following model :

$$\begin{aligned}\Delta f &= \upsilon_1(\cos(\varphi_u) + \cos(\varphi_d)) + \upsilon'_1(\sin(\varphi_u) + \sin(\varphi_d)) \\ &+\upsilon_2(\cos(2\varphi_u) + \cos(2\varphi_d)) + \upsilon'_2(\sin(2\varphi_u) + \sin(2\varphi_d))\end{aligned} \tag{4.1}$$

Here φ_u and φ_d are the angles φ evaluated on the up- and down-links.

This model results in a spectacular improvement of the best fit residuals, with the standard deviation reduced to 5.5 mHz. The values of the fitted anomalous parameters are reported in table 1.

Table 1. Results of the best fit with periodic terms in the signal, with two different ionospheric models.

a_P (nms^{-2})	υ_1 (mHz)	υ'_1 (mHz)	υ_2 (mHz)	υ'_2
-0.836±0.001	124.3±9.3	-125.3±0.6	2.7±0.2	-4.8±0.1

The best fit with modulated terms shows that when these terms are looked for in a dedicated best fit procedure, they are unambiguously found to differ from zero. Especially, the yearly period corresponds to a large potential amplitude while it was not detected in the spectral analysis of the best fit residuals with only a secular anomaly. This can be explained by the fact that the fit of the initial conditions also induces terms at the at the daily and yearly periods. In particular, a change of the initial conditions may easily produce variations masking modulated terms (Reynaud & Jaekel 2005, Courty 2008).

An even more impressive demonstration of the improvement of the data analysis drawn by the inclusion of modulated terms comes from the spectral analysis of the residuals. This spectral analysis is represented on Fig. 2 for the best fit with modulated terms. It is drawn intentionnally at the same scale as Fig. 1 so that one can easily notice the global reduction of the main peaks in the spectrum as well as all the secondary peaks.

5 Conclusion

In the present paper, we have reported the first results of our re-analysis of the Pioneer 10 Doppler data for the 1986 to 1998 time span. The improvement of the data fit with a constant anomalous acceleration exerted on Pioneer 10 has been confirmed by this new data analysis.

The paper has then been focused on the study of periodic terms in the residuals. The main new result of the paper is that a large part of these diurnal and seasonal anomalies may be captured in a simple geometrical model where the light time on the tracking path is modified in a manner depending only on the azimuthal angle φ between the Sun-Earth and Sun-probe lines. This geometrical model could represent in a simple way the physical effects expected on light propagation in some metric extensions of general relativity which have been studied as potential candidates for the explanation of the secular Pioneer anomaly (Reynaud & Jaekel 2005). Nevertheless, the results of the paper cannot be considered as pointing to a particular possible explanation of the anomaly and similar effects could for example be obtained through a mismodeling of the solar corona model.

However, considering the modulated anomalies has allowed us to reduce by a factor of the order of two the standard deviation of the residuals. This suggests that the new analysis constitutes a richer characterization of the Pioneer data, now involving not only a secular acceleration but also modulated terms, which will have to be compared with any, existing as well as future, possible explanation of the anomaly.

6 Acknowledgement

This work has benefited of discussions with a number of people involved in the international collaborations devoted to the investigation of the Pioneer data. Special thanks are due to S.G. Turyshev (NASA JPL) for having led the ISSI team during which the ODF used in the seminal paper (Anderson 2002) were made available to the members of the collaboration. We are grateful for discussions with the members of this collaboration and especially with P. Touboul and B. Foulon (ONERA) and the members of the french collaboration GAP. Another special thanks is due to CNES for its support of the GAP.

References

Anderson, J. et al. 2002, Phys. Rev. D 65

Bilitza, D.,2001, Radio Science, 36 No. 2, 261-275

Boehm, J., Niell, A., Tregoning, P., & Schuh, H., 2006, Geo. Res. Lett., 33, L07304

Bourguignon, S., Carfantan, H., Bohm, T., 2007, A&A, 462, 379-387; SparSpec software is available at: http://www.ast.obs-mip.fr/Softwares

Courty, J.-M., Reynaud, S., Levy, A., Christophe, B., 2008, to be published in Space Science Reviews

Jaekel, M.-T., & Reynaud, S., 2006, Class. Quant. Gravity, 23, 7561-7579

Markwardt, C. 2002, arXiv:gr-qc/0208046v1

Moyer, T.D., 2000, Deep Space Communications and Navigation Series

Nieto, M.M. & Anderson, J.D., 2005, Class. Quant. Gravity, 22, 5343-5354

Olsen, O. 2007, A&A, 463, 393-397

Wackley, A. et al., 2000, Trk-2-18 Archival Tracking Data Interface, Document 820-13

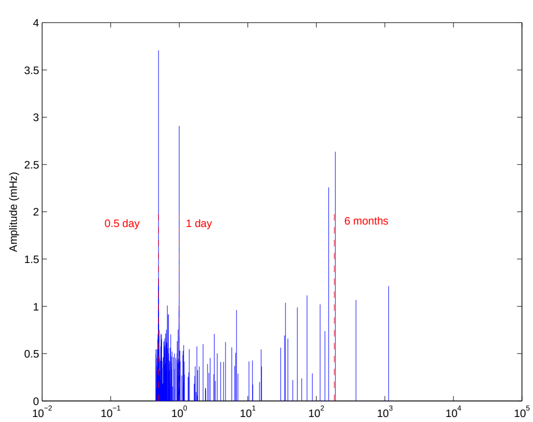

Fig. 1. SparSpec analysis of the residuals from the fit with a constant acceleration.

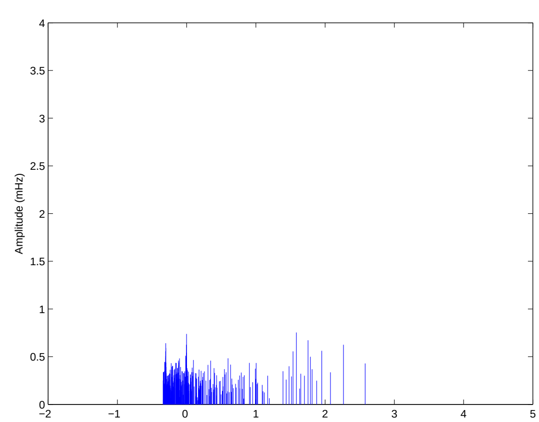

Fig. 2. SparSpec analysis of the residuals from the fit with a constant acceleration and periodic terms.

SF2A 2008
C. Charbonnel, F. Combes and R. Samadi (eds)

TITAN'S FORCED ROTATION - PART II: THE RESONANT WOBBLE

Noyelles, B.[1], Lemaître, A.[1] and Vienne, A.[2]

Abstract. Our knowledge of the gravity field of Titan has been recently improved thanks to the fly-bys of Cassini spacecraft, that provided us first values of Titan's J_2 and C_{22}, unfortunately without any indication of the polar inertial momentum C. Anyway, these data allowed us to give last year a first 3-dimensional description of the rotation of Titan, seen as a rigid body. In particular, we pointed out an interesting phenomenon forcing the wobble (i.e. the angular separation between Titan pole axis and angular momentum), that we suspected to be nearly resonant. This year we present a study of this resonance, involving a free libration around the Cassini equilibrium and a proper mode given by the orbital ephemerides. The resonant argument has been clearly identified, and its behaviour has been investigated using the Second Fundamental Model of Resonance. We show that in case of capture, the wobble might be pumped to several degrees. Moreover, we propose an original formula to estimate the contribution of the wobble in the tidal internal dissipation of a synchronous satellite. A significant wobble might cause a wrong estimation of the rotation of Titan.

1 Introduction

Last year Noyelles et al. 2007 we presented a 3-degree of freedom theory of Titan's rotation, seen as a rigid body. Such a study is possible since the fly-bys of Cassini spacecrafts that provided us information on Titan's gravity field, especially J_2 and C_{22}. Unfortunately, a third useful parameter, i.e. the polar inertial momentum C, remains unknown. That is the reason why we study Titan's rotation for several realistic values of C.

Our study showed an interesting behavior of Titan's wobble (i.e. the angular separation between Titan's polar axis and its angular momentum), when C is close to $0.35MR^2$ (see Fig.1).

2 The resonant Hamiltonian

We start from the following Hamiltonian:

$$\begin{aligned}\mathcal{H} &= \frac{nP^2}{2}+\frac{n}{8}\left[4P-\xi_q^2-\eta_q^2\right]\left[\frac{\gamma_1+\gamma_2}{1-\gamma_1-\gamma_2}\xi_q^2+\frac{\gamma_1-\gamma_2}{1-\gamma_1+\gamma_2}\eta_q^2\right] \\ &+n\left(\frac{d_0}{d}\right)^3\left(1+\delta_s\left(\frac{d_0}{d}\right)^2\right)\left[\delta_1(x^2+y^2)+\delta_2(x^2-y^2)\right] \end{aligned} \tag{2.1}$$

in which the used variables are the modified Andoyer's variables. In this Hamiltonian the notations are as follows:

- P is the norm of Titan's angular momentum
- η_q and ξ_q locate the angular momentum in the body frame
- n is Titan's mean motion

[1] University of Namur, Dept of Mathematics, 8 Rempart de la Vierge, B-5000 Namur, Belgium
[2] IMCCE - Paris Observatory / UPMC / USTL, CNRS UMR 8028, 77 avenue Denfert-Rochereau, 75014 Paris, France

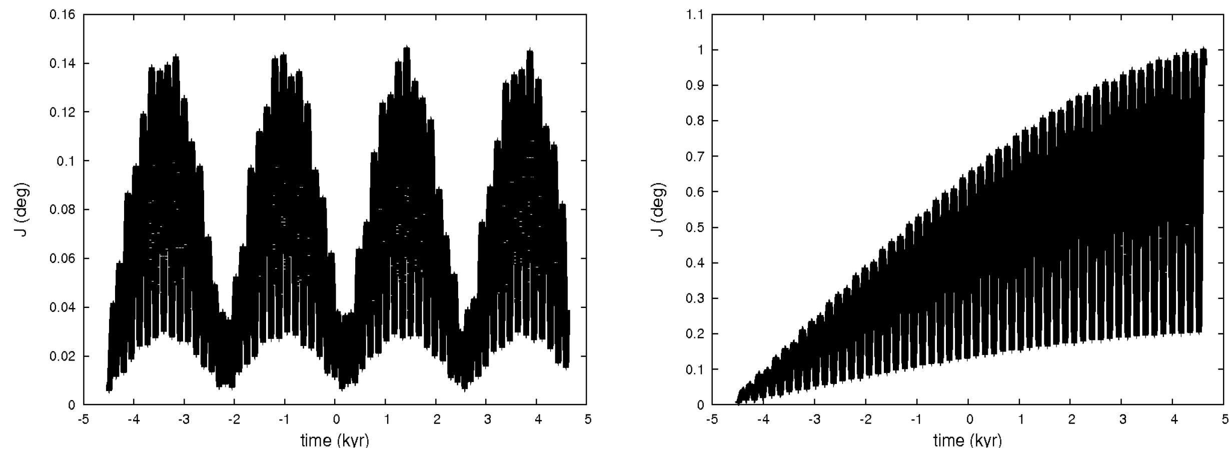

$C = 0.31MR^2$ $C = 0.35MR^2$

Fig. 1. Two different behaviors of the wobble J for 2 different values of the polar inertial momentum C. We note that for $C = 0.35MR^2$, J seems to have a quasi-resonant behavior, taking important values.

- (x, y, z) is the unit vector pointing to Saturn in Titan's reference frame
- γ_1, γ_2, δ_1 and δ_2 are associated to Titan's gravity field
- δ_s is associated to Saturn's oblateness coefficient J_2.

We now perform an analytical study requiring several canonical transformations, consisting in

1. Determining the equilibrium, and centering the Hamiltonian around it.
2. Untangling the proper modes Henrard & Lemaître 2005.
3. Doing a polar canonical transformation to express the small oscillations around the equilibrium in angle-action variables.

After these transformations, the Hamiltonian becomes

$$\begin{aligned} \mathcal{K} &= \mathcal{N} + \mathcal{P} \\ &= \omega_u U + \omega_v V + \omega_w W + \mathcal{P} \end{aligned} \tag{2.2}$$

in which $\mathcal{N}$ is the quadratic Hamiltonian depending only of the proper modes of the system (u, v, w, U, V, W), and $\mathcal{P}$ is the perturbation depending on the proper modes of the orbital motion.

Table 1. Synthetic representation of $\eta_q + \sqrt{-1}\xi_q = \sin J \exp(-\sqrt{-1}l)$, associated to the wobble, for $C = 0.31MR^2$. ϕ_6 and Φ_6 are proper modes of Titan's orbital dynamics. They are associated respectively to Titan's pericenter and ascending node.

N°	Amp. $\times 10^4$	Phase (°)	T (y)	Ident.	Cause
1	9.12391728	-51.69	306.33602	w	$\sqrt{W}$
2	6.01688587	51.69	-306.33605	$-w$	$\sqrt{W}$
3	5.73033451	158.48	351.70284	$\phi_6 - \Phi_6$	$e_6\gamma_6$
4	3.83212940	-158.48	-351.70284	$\Phi_6 - \phi_6$	$e_6\gamma_6$
5	0.63642954	-35.86	135.27368	$v - \Phi_6$	$\sqrt{V}\gamma_6$
6	0.38395548	35.86	-135.27368	$\Phi_6 - v$	$\sqrt{V}\gamma_6$

The Tab.1 gives the synthetic representation of the variable associated to the wobble, in the case of $C = 0.31MR^2$. We can see that the main forced contribution is $\phi_6 - \Phi_6$, with a period of 351.7 y. When C gets closer to $0.35MR^2$, the frequency of the proper mode w gets close to 350 y, so we can hint that the resonant argument is $w + \Phi_6 - \phi_6$. This has been checked in numerical simulations.

Starting from the Hamiltonian 2.2 we perform this last canonical transformation:

$$\begin{array}{ll} u & U \\ v & V \\ \theta = w + \Phi_6 - \phi_6 & \Theta = W \end{array}$$

giving this new Hamiltonian $\mathcal{T}$:

$$\mathcal{T} = \omega_u U + \omega_v V + \left(\omega_w + \dot{\Phi}_6 - \dot{\phi}_6\right)\Theta + \mathcal{T}_2. \tag{2.3}$$

We then average over every angle except the resonant one, considered as the only slow argument, and we obtain:

$$\mathcal{T} = \psi\Theta + \mu\Theta^2 + \epsilon\sqrt{2\Theta}\cos\theta. \tag{2.4}$$

This Hamiltonian is the classical *Second Fundamental Model of Resonance* Henrard & Lemaître 1983, describing the evolution of the system in deep resonance. Its equilibrium is the positive root of the cubic equation $x^3 - 3(\delta+1)x - 2 = 0$ with $\delta = -1 - sign(\psi\mu)\left|\frac{4}{27}\frac{\psi^3}{\mu\epsilon^2}\right|^{\frac{1}{3}}$. It corresponds to a forced value of the "free" amplitude of the wobble, forced by the resonance (see Tab.2).

Table 2. The wobble forced by the resonance.

$\frac{C}{MR^2}$	W_0 (forced)	$< J >$
0.34	(no real solution)	
0.35	0.342	80.368°
0.355	0.108	40.702°
0.3555	0.034	22.337°
0.355551	0.010	12.034°
0.35555146967191	0.009	11.413°
0.35555146967192	(no resonance)	

3 Internal dissipation

The differential gravitational attraction of Saturn on Titan raises a tidal bulge. The misalignement of the tidal bulge with the direction Titan-Saturn induces a loss of internal energy, that is usually expressed as:

$$\frac{dE}{dt} = \frac{21}{2}e^2\frac{k_2}{Q}f\frac{\mathcal{G}M_{♄}^2 nR^2}{a^6}. \tag{3.1}$$

In particular, we have $\frac{dE}{dt} \propto e^2$ because the misalignement of the tidal bulge is due to Titan's orbital eccentricity. If Titan's wobble J_0 is significant, it alters the orientation of the tidal bulge and thus it should be taken into account in the calculation of the internal dissipation. That is the reason why we propose this original formula :

$$\frac{dE}{dt} = \frac{3}{2}J_0^2\left(\frac{n+w}{w}\right)^2\frac{k_2}{Q}f\frac{\mathcal{G}M_{♄}^2 nR^2}{a^6} \tag{3.2}$$

and the total expression for the internal dissipation is now:

$$\frac{dE}{dt} = \left[\frac{21}{2}e^2 + \frac{3}{2}J_0^2\left(\frac{n+w}{w}\right)^2\right]\frac{k_2}{Q}f\frac{\mathcal{G}M_{♄}^2 nR^2}{a^6}. \tag{3.3}$$

A numerical application shows that the contribution of the wobble on the internal dissipation is predominant if $J_0 > 4.4°$, what is realistic. One can notice the term $n+w$ in the contribution of the wobble. It is the sum of two frequencies: the orbital frequency (that is also the spin rate) and the wobble frequency. It means that the frequency of the tidal excitation due to the wobble is not n (as it the case for the eccentricity) but $n + w \approx n$, because of a composition between the two motions (spin and wobble). If the wobble is significant, a measurement of the spin rate might be altered and a take a higher value than the actual spin rate.

4 Comparison with the observations

Recently, the Cassini RADAR Team measured a slightly super-synchronous rotation for Titan, the shift being about $+0.36°/y$ Stiles et al. 2008. An a priori neglected wobble could be an explanation, but at least another one exists: Tokano & Neubauer (2005) suggested that seasonal energy exchanges between Titan's atmosphere and its surface provoke a variation of the length of the day (i.e., the spin rate). Lorenz et al. (2008) interpret the measured super-synchronous rotation as the signature of an internal ocean, that decouples the rotation of Titan's crust from its mantle, and makes it highly sensitive to the seasonal energy exchanges. Unfortunately, one cannot discriminate a secular contribution to a seasonal one in Titan's measure of spin, because it has been computed from about 2-years irregularly spaced data. Their accuracy depends on the flybys of the spacecraft near Titan, and to the distance between Titan and the spacecraft. Moreover, the seasonal period is 29 years for Saturn and its satellites, far too large to be detected.

5 Conclusion

We have elaborated the first 3-degree of freedom theory of Titan's rotation, seen as a rigid body. This theory permitted us to enlight a likely resonance forcing the free wobble. This wobble might cause an alteration of the measure of the spin rate by Cassini spacecraft.

The next step is now to use a more realistic model for Titan, i.e. in modeling an internal ocean and also the atmosphere. Such a study has been initiated by Henrard (2008), in taking account of a liquid core in the rotation of Io. The goal is to obtain a convergence between the expected rotation and the observations.

This study has been published in Noyelles et al. (2008) and Noyelles (2008), in which the reader can find more explanations.

References

Henrard J., 2008, CM&DA, 101, 1

Henrard J. & Lemaître A., 1983, Celestial Mechanics, 30, 197

Henrard J. & Lemaître A., 2005, AJ, 130, 2415

Lorenz R., Kirk R.L., Stiles B.W. et al., 2008, Science, 319, 1649

Noyelles B., Lemaître A. & Vienne A., 2007, SF2A-2007: Proceedings of the Annual meeting of the French Society of Astronomy and Astrophysics held in Grenoble, France, July 2-6, 2007, Eds.: J. Bouvier, A. Chalabaev, and C. Charbonnel, p.113

Noyelles B., Lemaître A. & Vienne A., 2008, A&A, 478, 959

Noyelles B., 2008, CM&DA, 101, 13

Stiles B.W., Kirk R.L., Lorenz R.D. et al., 2008, AJ, 135, 1669

Tokano T. & Neubauer F.M., 2005, Geophysical Research Letters, 32, L24203

SF2A 2008
C. Charbonnel, F. Combes and R. Samadi (eds)

PROPER TIME VERSUS TCB USED FOR TIME DELAY INTERFEROMETRY IN THE LISA MISSION

Pireaux, S.[1]

Abstract. The three spacecraft $i, j, k = 1, 2, 3$ of the LISA (Laser Interferometer Space Antenna) joint ESA-NASA mission aim at the detection of gravitational waves (GW). They are to be launched in 2015, $L_{ij} \sim 5 \cdot 10^6$ kilometers apart, in a triangular configuration, each following a free-falling test mass. The test masses are inter-connected by double laser links forming an interferometer. Laser frequency (LF) and optical bench (OB) noises are several orders of magnitude larger than GW signals to be detected. Hence, Time Delay Interferometry (TDI) data pre-processing (summarized here) was developed to reach the gravitational wave detection level, allowing to get rid of (most of) LF and OB noises. TDI combination algebra, to be applied on the data, is given in terms of the coordinate time, t, corresponding to the Barycentric Coordinate Reference System (BCRS) and called TCB. However, local data at each spacecraft is recorded in terms of spacecraft proper time, $\overset{k}{\tau}$, requiring the use of relativistic time transformations $\overset{k}{\tau} - t$ provided here.

1 LISA, a challenge

LISA (LISA, 1998) will detect GW in the $[10^{-4}, 10^{-1}]$ Hz frequency band. A GW is a space-time perturbation. When passing by, it perturbs the free-falling test-mass motion. GWs are detected via the measurement of phase shift due to the interferometric arm-length variations ΔL_{ij}. This requires LISA arm-length to be known with a good precision: $\Delta L_{ij}/L_{ij} \sim 10^{-23}$. In LISA, LF and OB noises are orders of magnitude larger than GW signals ($\sim 10^{-13}$ versus $\sim 10^{-21}$ in fractional frequency units). However, through TDI data pre-processing, LF and OB noises can be reduced by more than 8 orders of magnitude. TDI pre-processing is based on the precise knowledge of photon flight time t_{ij} between two LISA spacecraft, while TDI ranging allows to measure $t_{ij} = L_{ij}/c + ...$ with c, the speed of light in vacuum.

2 TDI: a new metrology method

LISA has 6 independent laser links, leading to 12 interferometric measurements (inter or intra-satellites). TDI observables are time-delayed (with respect to t_{ij}) particular combinations of measurements from different laser links, in close loops, in which OB and LF noises are cancelled. Mathematically speaking, TDI observables are polynomials of delay operators that are applied on measurements. The TDI algebra (Nayak & Vinet 2005, Shaddock et al. 2003) is based on TDI generators, that is a set of TDI observables allowing to write any other as a linear combination of those; and is characterized by the numbers p, n, and m_{max}, defined in Figure 1 Left. Those numbers are function of the selected set of assumptions on t_{ij}, called 1st, 1.5th or 2nd generation (Figure 1 Left). The latter assumptions are verified only by certain orbit models (Figure 1 Middle).

On one side of the problem, the appropriate geometry model for LISA and TDI generation must be selected so that, through *TDI data pre-processing*, LF and OB noises are brought down to LISA specifications. Ideally, when only LF and OB noises are present and when the efficiency assumptions (Figure 1 Right) are verified, the efficiency of the TDI generations to remove LF and OB noise is optimal. It is however not a 100 % for the 2nd generation TDI, since the algebra for that generation is not exact. Furthermore, for the real LISA mission, there will be other noises than LF and OB, the true orbits will be more complex than the model verifying TDI 1st, 1.5th or 2nd generation assumptions, and the efficiency conditions will not be verified... thus lowering TDI

[1] Observatoire Royal de Belgique, Department 1, 1180 Brussels, Belgium

efficiency. In particular, the clocks (Ultra Stable Oscillators, USOs) aboard the 3 spacecraft do not beat the coordinate time t used in TDI. This is the topic of the present paper and it is addressed in Section 3. On the other side, *TDI ranging* measures t_{ij} via a minimization of residual LF/OB noise in TDI observables as, ideally, if only LF and OB noises are present and efficiency conditions are verified, the TDI-observables cancel for the appropriate t_{ij}.

TDI metrology requires a realistic geometry, that is laser link t_{ij} model (Chauvineau et al. 2005), orbital velocity v_k and position r_k models for spacecraft k (Pireaux & Chauvineau 2008); possibly including relativity.

3 Relativistic time scales in LISA

The clock abord spacecraft k beats its own proper time $\overset{k}{\tau}$ used to timestamp the data, not $t = TCB$ used in TDI (Pireaux 2007, in particular Figure 1). To find the time transformation $\overset{k}{\tau} - t$, we use the relativistic line element for a BCRS metric, leading to

$$ds^2 = c^2 d\overset{k}{\tau}{}^2 \simeq \left(1 - 2\frac{w_k}{c^2} - \frac{v_k^2}{c^2}\right) c^2 dt^2 \;\Rightarrow\; \overset{k}{\tau} - t \simeq \overset{k}{\tau}_0 - t_0 - \frac{\sqrt{GMa}}{2c^2}\left[3\left(\Psi_k - \Psi_{k0}\right) + e\;\left(\sin\Psi_k - \sin\Psi_{k0}\right)\right]$$

where we used a simple classical Keplerian orbit model (Nayak et al. 2006) with eccentric anomaly ψ_k, semi major axis a, Newtonian constant G, solar mass M and Newtonian solar potential at spacecraft k, w_k. This allows to compute numerical estimates for a one year mission as in Figure 2 (Pireaux 2007). We see that the difference in rate of spacecraft proper time versus TCB is of the order of $5 \cdot 10^{-8}$. The difference between spacecraft proper times and TCB exhibits an oscillatory trend with a maximum amplitude of $\sim 10^{-3}$ s.

Characteristics of the TDI algebra	TDI generations		
	1st	1.5th	2nd
delay assumptions	$t_{ij} = t_{ji}$ $t_{ij} = cst$	$t_{ij} \neq t_{ji}$ $t_{ij} = constant$	$t_{ij} \neq t_{ji}$ $t_{ij} \neq constant$
TDI algebra	1st module sysyguies over ring p=3	1st module sysyguies over ring p=6	?
m_{max} = nbr of different data-flow variables	6 or 9	9	9
p = nbr of delay operators	3	6	6 non-commutative
n = nbr of TDI generators in the minimal set	4	6	6 TDI to keep LF/OB within specifications but no algebra

Appropriate geometry model to fit delay assumptions	TDI generations		
	1st	1.5th	2nd
delay assumptions	$t_{ij} = t_{ji}$ $t_{ij} = cst$	$t_{ij} \neq t_{ji}$ $t_{ij} = constant$	$t_{ij} \neq t_{ji}$ $t_{ij} \neq constant$
orbit model	rigid, motionless LISA	rigid, rotates $\circlearrowright$ CM, 1st order in e Keplerian motion $\circlearrowright$ Sun	breathing of constellation
laser link model	Newtonian: $t_{ij} = L_{ij}/c$	Newtonian + Sagnac +aberration effects	Newtonian + Sagnac +aberration + relativity effects

TDI efficiency to remove LF/OB noises	TDI generations		
	1st	1.5th	2nd
delay assumptions	$t_{ij} = t_{ji}$ $t_{ij} = cst$	$t_{ij} \neq t_{ji}$ $t_{ij} = constant$	$t_{ij} \neq t_{ji}$ $t_{ij} \neq constant$
efficiency assumptions: - 3 ideal, identical, perfect spacecraft clocks (USO) - 3 clocks beating t - t_{ij} *exactly known*	100%		<100%
if efficiency assumptions not verified	<100%		

Fig. 1. Characteristics of TDI. See text and (Pireaux 2008) for details.

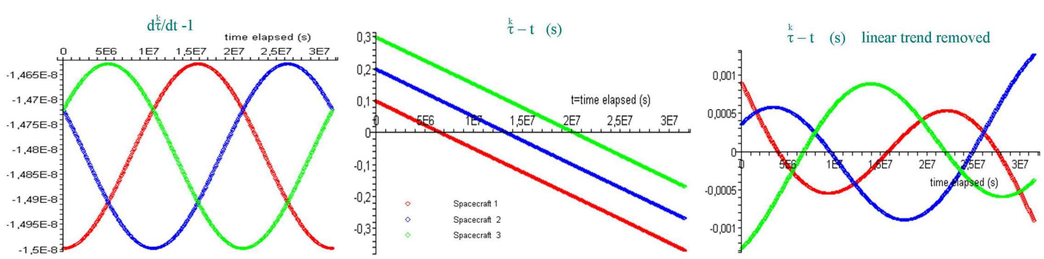

Fig. 2. Proper versus coordinate time in LISA, over one year. See text and (Pireaux 2007) for details.

References

Chauvineau, B., Pireaux, S., Regimbau, T., & Vinet, J-Y. 2005, Phys. Rev. D, 72, 122003
LISA Pre-Phase A Report, 2nd Ed. 1998: http://www.srl.caltech.edu/lisa/documents/PrePhaseA.pdf
Nayak, K.R., & Vinet, J-Y. 2005, CQG, 22, S437-S443
Nayak, K.R., Koshti, S., Dhurandar, S.V., & Vinet, J-Y. 2006, CQG, 23, 1763-1783
Petiteau et al. 2008, Phys. Rev. D, 77023002
Pireaux, S. 2007, CQG, 24, 2271-2281
Pireaux, S. 2008, proceedings of EFTF08, Toulouse, France, 23-25 March 2008
Pireaux, S., & Chauvineau, B. 2008, Cel. Mecha. , submitted (arXiv:0801.3637)
Shaddock, D.A., Tinto, M., Estabrook, F.B., & Armstrong, J.W. 2003, Phys. Rev. D, 68, 061303(R)

SF2A 2008
C. Charbonnel, F. Combes and R. Samadi (eds)

RELATIVISTIC ORBIT DETERMINATION WITH THE RMI (RELATIVISTIC MOTION INTEGRATOR) SOFTWARE FOR THE LISA MISSION

Pireaux, S.[1]

Abstract. The LISA constellation aims at the detection of gravitational waves. Precise ephemerides of its spacecraft are needed for orbit determination and for the so-called Time Delay Interferometry (TDI) data-pre-processing. We use the Relativistic Motion Integrator (RMI) to compute LISA ephemeris and confront this relativistic approach with a classical orbit model.

1 Introduction

The LISA mission (LISA, 1998), to be launched in 2015, is an interferometer that aims at the detection of gravitational waves in the $[10^{-4}, 10^{-1}]$ Hz frequency band. LISA is formed by three spacecraft, inter-connected by double laser links. Precise ephemerides of LISA spacecraft are needed not only for the sake of orbit determination but also to compute the photon flight time in laser links between spacecraft, required in data TDI pre-processing (Nayak & Vinet 2005; and references therein) which aims at lowering laser frequency and optical bench noises down to LISA specifications in order to reach the gravitational wave-detection level.

Before the present work, only *classical* ephemerides for LISA were available. Hence, relativistic effects in LISA orbit determination needed to be quantified.

2 Orbit models

The characteristics of the spacecraft orbits are the following: drag-free motion at an average interdistance of $L = 5$ million kilometers, rotation of the triangular constellation around its center of mass and around the Sun. We considered some simplifying assumptions, namely: no non-gravitational forces are applied on the spacecrafts, each one perfectly follows a free-falling test mass, itself perfectly shielded; planetary perturbations are neglected and the Sun is assumed non-rotating and spherical.

The generic method of the *Relativistic Motion Integrator (RMI)* (Pireaux et al. 2006) is to numerically integrate, instead of Newtonian equations plus relativistic corrections, the exact relativistic equation of motion (for a given metric, corresponding to a gravitational field at first Post-Newtonian -PN- order or higher). The Christoffel symbols, present in the relativistic equations, contain all gravitational effects, classical and relativistic, at corresponding order of the selected metric. According to the above cited LISA simplified assumptions, there is no non-gravitational force (geodesic motion), and we use the BCRS (Barycentric Coordinate Reference System) coordinates and Post-Newtonian (PN) metric IAU2000, as recommended by the IAU (International Astronomical Union).

Our generic *classical model* numerically integrates Newton‘s second law of motion, *without* any PN relativistic corrections, around the central body.

In particular for the LISA simplified assumptions, it implies Keplerian motion around the Sun without planets, with a LISA plane angle of $\pi/3 + 5/8 \cdot 1/60$ to minimise armlength variations, common orbit parameters for the three spacecraft (semi-major axis of 1 A.U., small orbital eccentricity, orbit inclination and orbital period of about 1 year), with a 2π phase off-set, as decribed in reference (Nayak et al. 2006).

Initial conditions for LISA spacecraft in RMI computation are the same as the selected classical Keplerian initial positions and velocities.

[1] Observatoire Royal de Belgique, Department 1, 1180 Brussels, Belgium

3 Comparison between numerical relativistic and classical orbit models for LISA

With the orbit models described in Section 2, we show that the numerical classical model for LISA orbits in the gravitational field of a non-rotating spherical Sun without planets can be wrong, with respect to the numerical relativistic version of the same model, by as much as about ten kilometers in radial distance during a year and up to about 60 kilometer in along track distance after a year (Fig. 1 Left and Center). Relativistic effects in spacecraft inter-distance are relevant since they lead to a significant correction in the photon time transfer t_{ij} between two spacecraft i and j, which is used in TDI (Fig. 1 Right). This correction adds up to (and is several orders of magnitude higher than) the relativistic effects in laser links for a classical LISA orbitography, studied in reference (Chauvineau et al. 2005). The above numerical results obtained with RMI were confirmed with an analytical 1PN development at first order in the small LISA eccentricity, $e_{LISA} \simeq 0.0096$, (Pireaux & Chauvineau 2008).

4 Conclusions and perspectives

LISA is a very complex mission and the TDI method must be validated. Hence the need for a LISA simulator. Such is LISACode (Petiteau et al. 2008); but the orbit model presently implemented in LISACode is classical, while the laser link model is relativistic. In the present paper, using RMI, we have quantified and demonstrated the relevance of the relativistic effects in LISA orbit determination.

LISA is a relevant example to use RMI. The strength of the RMI method is that it can be used to compute relativistic orbits for different missions (whether barycentric or planetocentric); only the central body parameters and initial conditions, mission parameters (number of satellites or planets) in the corresponding RMI modules would change. If the IAU 2000 metric is updated, only the metric module in RMI needs to be updated, no additional analytical developments must be recomputed. Indeed, RMI includes any gravitational contribution at the corresponding order of the metric (whether 1PN or higher). RMI is a coherent native relativistic approach, and it should be preferred to "Newton + relativistic correction" methods. In the future, the RMI software will use a symplectic integrator, instead of presently used Runge-Kutta of order 8. Non-gravitational forces will be implemented, as well as planetary perturbations, in particular for the LISA mission.

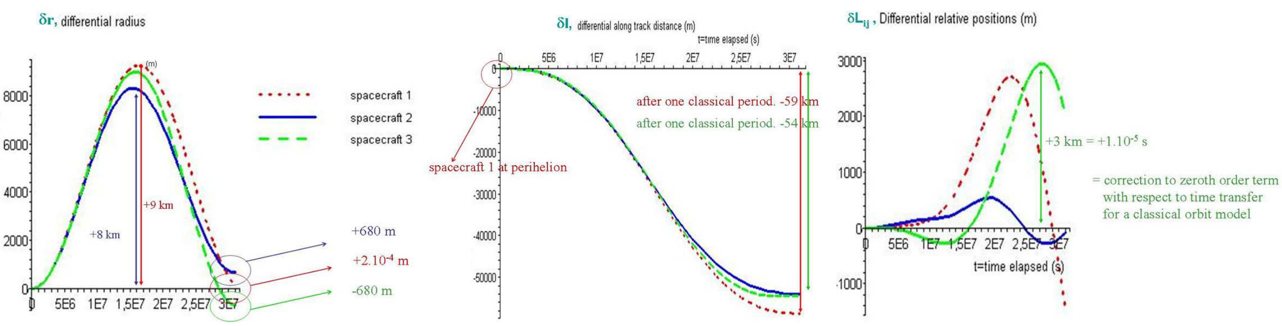

Fig. 1. Difference between numerical relativistic and classical position ephemerides for the LISA mission. **Left** : In radial barycentric distance (δr). **Center**: In along track distance (δl). **Right**: In the relative distance between spacecraft, $\delta L_{jk} = \delta(r_k - r_j)$ with $j, k = 1, 2, 3,\ j \neq k$.

References

Chauvineau, B., Pireaux, S., Regimbau, T., & Vinet, J-Y. 2005, Phys. Rev. D, 72, 122003

LISA Pre-Phase A Report, 2nd Ed. 1998: http://www.srl.caltech.edu/lisa/documents/PrePhaseA.pdf

Nayak, K.R., & Vinet, J-Y. 2005, CQG, 22, S437-S443

Nayak, K.R., Koshti, S., Dhurandar, S.V., & Vinet, J-Y. 2006, CQG, 23, 1763-1783

Petiteau et al. 2008, Phys. Rev. D, 77023002

Pireaux, S., & Chauvineau, B. 2008, Cel. Mecha., submitted (arXiv:0801.3637)

Pireaux, S., Barriot, J-P., & Rosenblatt, P. 2006, Acta. Astron., 59, 517-523

SF2A 2008
C. Charbonnel, F. Combes and R. Samadi (eds)

HYDROLOGICAL EFFECTS ON POLAR MOTION COMPARED TO GRACE OBSERVATIONS.

Seoane, L.[1], Nastula, J.[2], Bizouard, C.[1] and Gambis, D.[1]

Abstract. The influence of the continental hydrologic signals on the polar motion is not well known. Different models have been developed to evaluate and compare these effects to geodetic observations. Previous studies have shown large disagreements mainly due to the lack of global measurements of related hydrological parameters. The recent Gravity Recovery and Climatic Experiment (GRACE) mission allows us to compute excitation functions ($\chi_1 + i\chi_2$) of polar motion due to unmodelled variations like hydrological processes. We have compared this gravimetric-based excitation to the excitation estimated from a hydrological model and from geodetic observations for the period February 2003 to December 2006. The residuals of the geodetic excitation are not fully explained, neither by the hydrological model nor by the gravimetric data. However, considering annual variations, there is a good agreement between geodetic and gravimetric excitations especially in amplitude. The hydrological model-based excitation has significant discrepancies for the real component of the excitation χ_1. We found that all series show common interannual oscillations of nearly 1.3 year period coinciding with Amazon's water storage variations (Schmidt et al. 2007).

1 Introduction

The excitation of polar motion is to a large extent related to the mass redistribution of geophysical fluids. The importance of atmospheric and oceanic angular momentum signals at monthly and seasonal periods are well known. The role of the continental hydrologic signals, originated from land water, snow, and ice, is however less known. A number of previous studies have estimated hydrological excitation from climatologically measurements, numerical climate models and global hydrology models based upon the observed distribution of surface water, snow, ice and soil moisture (Kuehne & Wilson 1991; Chen et al. 2000). The hydrological part of polar motion excitation, can also be obtained, as a residual series, by removing atmospheric and oceanic signals from the mass term of the geodetically determined excitation of polar motion. The general conclusion of these studies is that the change in continental water storage plays a major role in the seasonal polar motion. However, the results do not agree among themselves and with the observed polar motion (Chen & Wilson 2005). This is mainly due to the lack of global measurements of related hydrological parameters.
Thanks to the Gravity Recovery and Climate Experiment (GRACE) mission, the mass redistribution is determined over the period February 2003 to December 2006. Data are tide free and non-tidal atmospheric and oceanic effects have been taken into account in the processing of the data. That means that gravity field solution is mostly of hydrological nature. This allows us to compare "gravimetric"-based excitation to the existing hydrological models, differences being possibly due to other Earth phenomena, for example, earthquakes.

2 Data and Methodology

2.1 *Gravimetric excitation of polar motion*

The determination of the GRACE satellites data is provided by four centres: Center for Space Research (CSR), GeoForschungsZentrum (GFZ), Jet Propulsion Laboratory (JPL) and Groupe de Recherche de Géodésie Spatiale (GRGS) in the form of normalized spherical harmonic coefficients.

[1] Observatoire de Paris, SYRTE, CNRS UMR 8630, 75014 Paris, France
[2] Space Research Center of the Polish Academy of Sciences, Bartycka 18a , 00-716 Warsaw, Poland

We use the latest version of the gravity field solution. All series are tide free. The non-tidal atmospheric and oceanic effects have been removed from the gravimetric data as a part of the de-aliasing. Then gravimetric-based excitation reflects variations from hydrological processes, post-glacial rebound, earthquakes and maybe unknowing Earth's geophysical phenomena. However, GRGS uses a barotropic oceanic model then baroclinic oceanic signal is as well in the data.
The "gravimetric" polar motion excitation is directly related to the (2,1) Stokes coefficients of the gravity field and off-diagonal inertia moments of the Earth in the terrestrial frame. The "gravimetric" citation is computed using the formula given by Chen et al. (2004).

2.2 Modeled hydrological excitation of polar motion

The Special Bureau for Hydrology of the International Earth Rotation and Reference System Service (IERS) provides the grids of the continental water storage estimated by the Climate Predicted Center (CPC). Hydrological excitations functions can be computed from these fields of using the formulation given by Chen & Wilson (2005).

2.3 Geodetic excitation of polar motion

The geodetic polar motion excitation in polar motion can be written as:

$$\chi = \chi_1 + i\chi_2 = p + i\frac{\dot{p}}{\sigma_c} \tag{2.1}$$

where $p = x - iy$ is the complex pole coordinate obtained from the Earth Orientation Parameters (EOP) series C04 (Gambis 2004) and σ_c is the frequency of the Chandler pulsation ($2\pi/433$ rad/days) with quality factor of 175. Polar motion derivative has been numerical approximated.
We have then to remove atmospheric and oceanic effects. For this purpose we use the Atmospheric Angular Momentum (AAM) series of the National Center for Environmental Prediction and National Center for Atmospheric Research reanalysis (Salstein et al. 1993) and the Oceanic Angular Momentum (OAM) series obtained from Estimating the Circulation and Climate of the Ocean model (Gross 2008).

2.4 Sampling and filtering of the excitation series

The different excitation functions used in our study have sampling comprised between 6 hours and one month. Applying Vondrak smoothing we make the series spectrally consistent. All those solutions are also interpolated

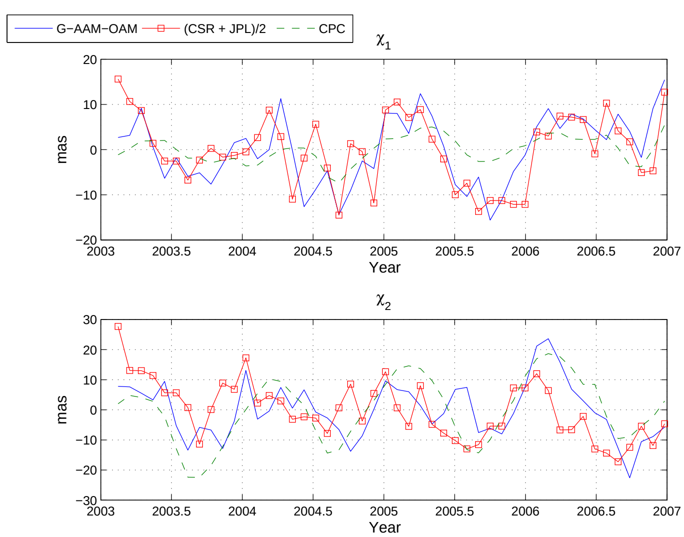

Fig. 1. Hydrological excitation from geodetic observations, CPC model and mean CSR and JPL gravimetric solutions

	χ_1		χ_2	
	Amplitude mas	Phase degree	Amplitude mas	Phase degree
G-AAM-OAM	6.9 ± 1.4	67.3 ± 12.0	9.2 ± 1.5	78.4 ± 9.3
CPC	3.6 ± 0.4	89.6 ± 6.8	13.6 ± 0.6	70.1 ± 28.5
CSR	4.7 ± 2.8	70.7 ± 34.9	8.6 ± 2.5	23.8 ± 16.7
GFZ	2.2 ± 2.4	20.8 ± 63.6	8.2 ± 2.3	10.8 ± 15.6
JPL	7.4 ± 1.4	78.3 ± 10.6	7.0 ± 1.2	31.8 ± 9.6
GRGS	5.3 ± 3.2	341.5 ± 34.7	13.0 ± 2.6	10.3 ± 11.2

Table 1. Annual variations of hydrological excitations.

at 30 day intervals.
We must be careful especially with the correlation significance because temporal span is not long enough (only 48 points). According to the Student-t test, critical value for 90% significance level of correlation is 0.18.

3 Analysis and Results

We compared gravimetric and modeled hydrological excitations to geodetic observations after removing atmospheric and oceanic contributions.
Considering correlations (not shown) with geodetic observations we find that CPC model-based, CSR and JPL gravimetric-based excitations have higher values than the critical value of the correlation coefficient. Fig. 1 shows hydrological excitation estimated from geodetic observations, CPC model and mean of CSR and JPL. We note that gravimetric excitation functions differ from geodetic observations up to 10 mas. Hence any difference between gravimetric and geodetic quantities can be associated to the inaccuracy of the gravity field solution or to the mis-modelling of the atmospheric and oceanic effects.
Table 1 shows annual variations of the different hydrological excitation series. We note that the annual oscillations of real component of the equatorial excitation (χ_1) computed from CSR and JPL gravity field observations agree in amplitude and phase with geodetic residuals whereas the hydrological excitation from CPC has not enough power. χ_2 amplitudes of all series are in agreement with geodetic one, but there are phase discrepancies. Only CPC series provide an correct phase.

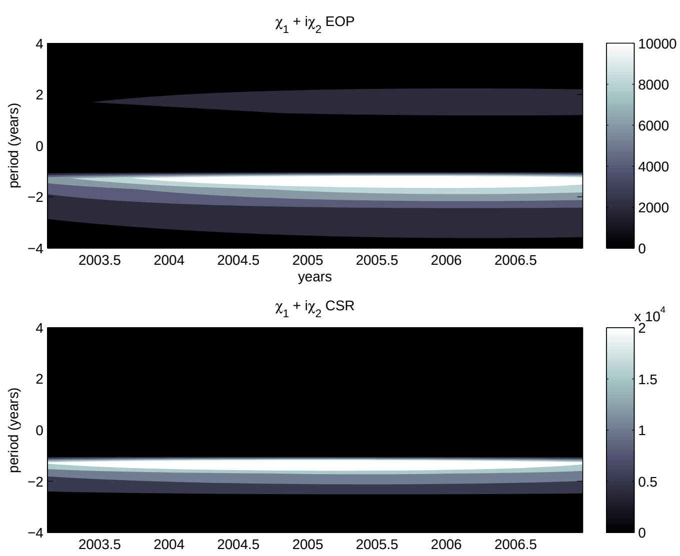

Fig. 2. Wavelet analysis for geodetic observations and CSR series of long period variations (longer than 1 year)

We also notice interannual period variations (greater than 1 year) in polar motion excitation functions: band-

pass filter of cut-off frequencies 1/4 and 1 cpy is applied to all series and wavelet analysis (Fig. 2) shows the existence of interannual oscillations with a maximum energy at the period of 1.3 year in the gravimetric observations as well as in the geodetic and in the modeled excitation (not shown). Over the same time span, February 2003 to December 2006, Schmidt et al. (2007) have as well detected the oscillations of 1.3 year period over the Amazon using GRACE's geoid computed by GFZ. We confirm that water storage variations in the Amazon or even in other world's basin have a significant influence in polar motion excitation.
Further improvements of GRACE or any other gravimetric mission data might help in the validation of hydrological signals due to center data processing computed from the hydrological models.
Interesting facts were found at long periods. We should confirm these results in the future using longer series of GRACE data.

We are grateful to Jean Michel Lemoine for providing different GRGS data sets.

References

Chen, J.L., Wilson, C. R., Chao, B.F., Shum, C.K. & Tapley, B.D. 2000, Hydrologic and oceanic excitations to polar motion and length-of-day variation, Geophys. J. Int., 141, pp. 149-156.

Chen, J.L., Wilson, C.R., Tapley, B.D. & Ries, J.C. 2004, Low Degree Gravitational Changes from GRACE: Validation and Interpretation, Geophys. Res. Lett., 31, L22607, doi:10.1029/2004GL021670.

Chen, J.L., & Wilson, C. R. 2005, Hydrological excitation of polar motion, 1993-2002, Geophys. J. Int., 160, pp. 833-839, doi:10.1029/2003GL018688.

Gambis, D. 2004, Monitoring Earth Orientation at the IERS using space-geodetic observations, J. Geod, 78, pp. 295-303.

Gross, R. 2008, An Improved Empirical Model for the Effect of Long-Period Ocean Tides on Polar Motion, J. Geodesy, submitted.

Kuehne, J. & Wilson, C.R. 1991, Terrestial water storage and polar motion, J. Geophys. Res., 96, pp. 4337-4345.

Salstein, D. A., Kann, D. M., Miller, A. J. & Rosen, R. D. 1993. The sub-bureau for atmospheric angular momentum of the International Earth Rotation Service: A meteorological data center with geodetic applications, Bull. Am. Meteorol. Soc., 74, pp. 67-80.

Schmidt, R., Petrovic, S, Guntner, A., Wunsch, J., Barthelmes, F. & Kusche, J. 2007, Estimating periodic components of water stock changes from GRACE and global hydrology models, 2007 GSTM Symposium.

SF2A 2008
C. Charbonnel, F. Combes and R. Samadi (eds)

QUASARS COMPILATION AND THE LARGE QUASAR ASTROMETRIC CATALOGUE (LQAC) : TOWARDS A DENSIFICATION OF THE ICRF

Souchay, J.[1], Andrei, A.H.[2], Barache, C.[1], Bouquillon, S.[1], Gontier, A.-M., Lambert, S. B.[1], Taris, F.[1], Le Poncin-Lafitte, C.[1], Arias, E.F.[3], Suchet, D.[1] and Baudin, M.[1]

Abstract.

In the recent years a huge and always increasing number of quasars have been detected and identified from various sky surveys. This leads to a large quantity of data with various and inhomogeneous informations in terms of astrometry, photometry, radioastronomy and spectroscopy. Therefore we have decided to make a general compilation of the largest number of recorded quasars obtained from all the available catalogues, with their best position estimates and by retaining the tabulated physical information available both at optical and radio wavelengths. This catalogue compilation named LQAC (Large Quasar Astrometric Catalogue) gives, for each quasar, the equatorial coordinates, multiband photometry, radio fluxes, redshift, luminosity distances and absolute magnitudes (Souchay et al. 2008b).

1 Introduction

The drastically increasing number of quasars discovered in the recent years through automatic surveys and very modern techniques as it is the case for the SDSS (Sloan Digital Sky Survey) recently motivated us to construct a complete compilation of all the quasars which have already been reckoned at the present time. This kind of systematic archiving has been successfully done in the last two decades by Véron-Cetty & Véron who up dated on a regular basis their compilation with a number of recorded sources ranging from roughly 2000 in 1984 to more than 85000 for the recent release (Véron-Cetty & Véron 2006). Among the various qualities of this compiled catalogue we can notice that it was regularly updated in order to follow the always increasing number of recorded quasars and it succeeded in being as complete as possible.

For the construction of the LQAC (Souchay et al. 2008b), our goals were similar to that of the aforementioned authors. We gathered the 12 largest quasar catalogues, 4 from radio interferometry programs, 8 from optical surveys and we carried out systematical cross-identifications of the objects. Informations concerning u,b,v,g,r,i,z,j,k photometry as well as redshift and radio fluxes at 1.4Ghz (20cm), 2.3Ghz (13cm), 5.0Ghz (6cm), 8.4Ghz (3.6cm) and 24Ghz (1.2cm) were also given when available. A small proportion of remaining objects not reckoned by the 12 catalogues and included in the Véron-Cetty & Véron (2006) compilation of quasars are added in our LQAC compilation, with a specific number indicating their catalogue of origin.

The aim of the LQAC was to give useful data concerning any quasar already detected at the present date without exception. Its construction contains some fundamental improvements (Souchay et al. 2008b) that we can summarize as follow : it concerns by far more quasars than in the previous catalogues; It gives the a priori most accurate determination of the celestial positions of the quasars, thanks to a compilation strategy in relation with the astrometric quality of the catalogues; It contains more informations concerning the photometric properties of the objects ; It priviligiates systematically large surveys with respect to small catalogues, for the sake of homogeneity; It gives clear and direct information about the cross-identification between the catalogues involved in the compilation. At last it proposes a determination of the absolute magnitudes of the quasars at two bandwidths (r and i) by using very up-to-date models of galactic extinction and new values of cosmological parameters.

[1] SYRTE, Observatoire de Paris, 61, av. de l'observatoire, 75014 Paris
[2] Observatorio Nacional/MCT, Rio de Janeiro // Observatorio do Valongo;UFRJ, Rio de Janeiro
[3] BIPM

Table 1. Characteristics of the main catalogs participating in our compilation of quasars named LQAC (Souchay et al. 2008b). The last column indicates the search radius chosen for cross-identifications. The symbol (*) indicates that for the cross-identification 3 different search radius have been considered.

Catalogue Name	Flag	Nature	Nbs of quasars	**Accuracy** (")	Search radius (")
ICRF-Ext2	A	radio	717	0.001	1
VLBA	B	radio	3 357	0.001	1
VLA-015	C	radio	1701	0.015	1
JVAS	D	radio	2 118	0.2	1
SDSS	E	optical	74 868	0.2	1
2QZ	F	optical	22 971	0.2	1
FIRST	G	radio	969	0.5	2
VLA+015	H	radio	157	0.2	2
HB	I	optical + radio	7 245	1.5	2-5-30 (*)
2MASS	J	infrared	-	0.2	1
GSC2.3	K	optical	-	0.2	1
B1.0	L	optical	-	0.2	1
V&V	M	optical+radio	85 189	1.0	2-5-10 (*)

2 Characteristics of the catalogues involved in the LQAC

In the LQAC a flag designates each catalogue participating to the compilation of quasars. The nomenclature of the flags is given by the Table 1. We give in the following some details about each main catalogue of the compilation.

• The ICRF-Ext.2 (Fey et al. 2004), second extension of the International Celestial Reference Frame , is the present realization of the ICRS (International Celestial Reference System) at radio frequencies . It contains 717 extragalactic sources which represent the basic frame with respect to which the position of any object in the celestial sphere should be measured. Although we are exclusively considering quasars in our compilation, we keep some particular objects (10 Active Galactic Nuclei and 10 BL LAC objects) thanks to their remarkable astrometric accuracy.

• The Very Long Baseline Array (VLBA) Calibrator Survey(VCS) consists in a catalogue containing milliarc-second accurate positions of more than 3000 extragalacic radio sources, mainly quasars (Fomalont et al. 2003). These positions have been derived from astrometric analysis of dual-frequency 2.3 and 8.4 GHz observations, using the Goddard Space Flight Center Calc/Solve package, with maps of the sources available for a majority of cases.

• The Very Large Array (VLA) consists in 27 radio antennas in a Y shaped configuration at St. Augustin (New Mexico). The 25-m antennas are linked electronically to give the same resolution as an antenna of 36 km across, with the sensitivity of a 130 meter dish (Claussen 2006). The VLA catalogue of quasars contains information concerning the accuracy of source positions. Therefore we decided to separate the original catlog in two parts, one with accuracy better (less) than 0.15" and another containing all the sources with accuracy worse than this value. The first sub catalogue, with flag"C", contains 1701 quasars with an astrometric precision around 10 mas whereas the second one, with flag "H" is much smaller with only 157 quasars with an accuracy around 0.2". For all objects, fluxes are given at 6 frequencies : 0.3GHz, 4GHz, 5GHz,8.4GHz,15Ghz, and 23GHz. Nevertheless, only a few of these flux determinations are given for the objects.

• The JVAS (Jodrell Bank-VLA Astrometric Survey) catalogue contains 2118 sources with 8.4 GHz flux information (Patnaik et al. 1992; Browne et al. 1998; Wilkinson et al. 1998).

• TheSloan Digital Sky Survey (SDSS) covers about one quarter of the sky, observed from a dedicated 2.5-m telescope located at Apache Point, New Mexico. Images are obtained in five broad optical bands (designated by u, g, r, i, z) covering the wavelength range of the CCD response from the atmospheric ultraviolet cutoff to the near infrared (see Fukugita et al. 1996 for details). The astrometric calibration (Pier et al. 2003) yields an accuracy per coordinate of 45 mas when reduced against the USNO CCD Astrograph catalogue (UCAC) and 75 mas when reduced against Tycho-2. The SDSS quasars input catalogue is by far the largest one, thanks to the DR5 release. It contains 74 868 objects (Schneider et al. 2005). Moreover it gives extensive photometric information for the quasars with magnitudes estimations in the u, b, v, g, r, i, z colors and a precise redshift evaluation.

• The 2-degree Field (2dF) QSO Redshift Survey, the second densiest one, quoted as 2QZ (Croom et al. 2004) is based on a pre-selection of quasars candidates from well defined criteria based on broadband u, b_j, r colors obtained from automated plate measurements (APM) of UKST photographic plates. The magnitude of the pre-selected objects is such that $16 < b_j < 20.85$. The survey area comprises 30 fields arranged in two $75° \times 5°$ declination strips, one passing across the South Galactic Cap, centered on $\delta = -30°$ and the other passing across the North Galactic Cap, centered on $\delta = 0°$.

• The FIRST radio survey (Gregg et al. 1996; Becker et al. 2001) has provided a new resource for constructing a large quasar sample, with positions accurate to better than 1", and with high radio sensitivity. One of the main tasks consisted in matching the radio catalogue from the NRAO VLA survey (Becker et al. 1995) with an optical catalogue provided by the Automated Plate Machine (APM) digitization of Palomar Sky Survey Plates. Optical selection was accompanied by several spectroscopic campaigns in order to refine the selection criteria.

• About fifteen years ago Hewitt & Burbridge(1993) have published a catalogue containing all known quasars with measured emission redshifts, complete to 1992, December 31. This catalogue contains 7245 objects, nearly all QSO's, with about 90 BLac objects. The information about the objects is exhaustive and very complete, containing positions, colors, magnitudes, emission-line redshifts, absorption, variability, polarization, as well as X-ray, radio and infrared data. An important problem of this catalogue is the poor accuracy of the equatorial coordinates for a significant proportion of the quasars in the list. In the next section we will describe how we deal with this disadvantage..

• The three catalogues 2MASS (Cutri et al. 2003), GSC2.3 (STScI, 2006) and B1.0 (Monet et al. 2003) do not bring new quasars to our sample, but thanks to cross identifications they enable one to cover gaps concerning photometric informations not provided by the pre-compiled catalogue.

3 Discussion and conclusion

Our final catalogue contains 113663 quasars. This is 25% bigger than the number of quasars recorded in the latest version of the Véron Cetty & Véron (2006) catalogue, which was the densiest compilation of quasars up to now. Souchay et al.(2008a) have discussed the external homogeneity of the data by comparing the equatorial coordinates, the redshifts and the magnitudes of objects belonging to two different catalogues. Moreover, they have used up-to-date cosmological parameters as well as recent models for galactic extinction and K-correction in order to evaluate at best the absolute magnitudes of the objects. In table 2, we gather the number of entries per item (magnitude, photometric band etc...). For comparison we present the corresponding number of entries of the Véron-Cetty & Véron catalogue. We plan to build up-dated versions of the LQAC in the future.

References

Becker, R.H., White, R.L., & Helfand, D.J. 1995, ApJ, 450, 559

Becker, R.H., White, R.L., Gregg, M.D., et al. 2001, ApJS, 135, 227

Browne, I.W.A., Patnaik, A.R., Wilkinson, P.N., & Wrobel, J.M. 1998, MNRAS, 293, 257

Claussen, M., 2006, VLA Calibrator Manual

Croom, S.M., Smith, R.J., Boyle, B.J., et al. 2004, MNRAS, 349, 1397

Table 2. Number of entries per item for each of the following catalogues : the VV2006 one (flag M) the A to L compilation, and the final LQAC catalogue. The difference between the numbers of the 4th. column and of the 3rd. one gives the contribution of the VV2006 to the LQAC.

	Véron-Cetty & Véron(2006) (M)	Compilation A to L	Compilation (LQAC) A to M	Percentage of completness
u	74 367	96 343	**99 665**	87.8
b	79 488	96 253	**106 801**	93.9
v	54 542	48 466	**75 396**	66.3
g	0	74 862	**74 862**	65.9
r	1 540	99 537	**100 811**	88.7
i	101	86 143	**86 238**	75.9
z	0	74 861	**74 861**	65.9
z	85182	101 535	**110 745**	97.4
J	9	13 647	**13 656**	12.0
K	3	13 647	**13 650**	12.0
1.4Ghz	8 405	1 811	**8 934**	7.8
2.3Ghz	0	3 234	**3 234**	2.8
5.0Ghz	3 585	862	**3951**	3.4
8.4Ghz	0	3 858	**3 858**	3.3
24Ghz	0	61	**61**	0.0

Cutri, R.M., Skrutskie, M.F., van Dyk, S., et al. 2003, NASA/IPAC Infrared Science Archive, http://irsa.ipac.caltech.edu/applications/Gator/

Fey, A.L., Ma, C., Arias, E.F., et al. 2004, AJ, 127, 3587

Fomalont, E.B., Petrov, L., MacMillan, D.S., et al. 2003, AJ, 126, 2562

Fukugita, M., Ichikawa, T., Gunn, J.E., et al. 1996, AJ, 111, 1748

Gregg, M.D., Becker, R.H., White, R.L., et al. 1996, AJ, 112, 407

Hewitt, A., & Burbidge, G. 1993, ApJS, 87, 451

Monet, D.G., Levine, S.E., Canzian, B., et al. 2003, AJ, 125, 984

Patnaik, A.R., Browne, I.W.A., Wilkinson, P.N., & Wrobel, J.M. 1992, MNRAS, 254, 655

Pier, J.R., Munn, J.A., Hindsley, R.B., et al. 2003, AJ, 125, 1559

Schneider, D.P., Hall, P.B., Richards, G.T., et al. 2005, AJ, 130, 367

Souchay,J., Lambert,S.B.,Andrei,A.H.,Bouquillon,S.,Barache,C.,Le Poncin-Lafitte,C.,2008, A& A Res. Note,485,299

Souchay, J.,Andrei,A.H.,Barache,C., Bouquillon,S., Gontier,A.M., Lambert, S.B, Le Poncin-Lafitte,C., Taris,F., Arias,F., Suchet,D., Baudin,M. 2008, accepted A&A

Véron-Cetty, M.-P., & Véron, P. 2006, A&A, 455, 773

Wilkinson, P.N., Browne, I.W.A., Patnaik, A.R., et al. 1998, MNRAS, 300, 790

SF2A 2008
C. Charbonnel, F. Combes and R. Samadi (eds)

DETERMINATION OF THE CORRECTIONS TO THE CELESTIAL POLE COORDINATES USING LLR OBSERVATIONS

Zerhouni, W.[1], Capitaine, N.[1] and Francou, G.[1]

Abstract. The Lunar Laser Ranging (LLR), which is one of the most accurate astrometric technique, has many applications in various domains including astronomy, gedoynamics and gravitational physics. It consists in determining the round-trip travel times of light pulses between stations on the Earth and reflectors on the surface of the Moon.

Analysis of LLR observations allows us to determine many parameters of the Earth-Moon system, such as station coordinates on the Earth, coordinates of the retro-reflectors on the lunar surface, lunar gravity field parameters,... Here, we focus on the determination of the Earth Orientation Parameters (EOP) especially, the direction towards the Celestial Intermediate Pole (CIP) in the Geocentric Celestial Reference System.

We have first calculated the LLR residuals over a period of more than 37 years, using IAU 2000A-2006 as a model of precession nutation (i.e MHB 2000 nutation of Mathews et al. 2002 and P03 precession of Capitaine et al. 2003) and the CIO based procedure. Second, we have determined the corrections to the the IAU 2000A-2006 X and Y coordinates every 70 days. The results obtained give an interesting estimation of the celestial pole coordinates, even if the accuracy is not at the same order as from VLBI because of the insufficient density of the observations.

1 Introduction

Analysis of LLR observations allows us to determine many parameters of the Earth-Moon system, such as station coordinates on the Earth, coordinates of the retro-reflectors on the lunar surface, lunar gravity field parameters,... Here, we focus on the determination of the Earth Orientation Parameters (EOP) especially, the direction towards the Celestial Intermediate Pole (CIP) in the Geocentric Celestial Reference System.

2 Calculation and results

In a first step, we have calculated the LLR residuals using the procedure described by Chapront et al. (1999,2002) for both stations of Cerga and McDonald over the periods 1984-2005 and 1969-2006 respectively. We have used the IAU 2006-2000A model of precession nutation (MHB 2000 as a model of nutation and P03 as a model of precession) and the CIO procedure (see IERS conventions 2003 and SOFA routines).

In a second step, we have estimated the correction to the X, Y celestial pole coordinates every 70 days with respect to the IAU 2006-2000A model of precession nutation. The results are represented on Fig.1.
In order to characterize the signal, we have made a new analysis with fitting :

- First, the long-term nutation parameters (18.6, 9.3 year, a secular term, and a constant term). The results are represented on Fig.2 (left).
- Second, the annual and semi annual terms. In this case we have removed the FCN (Free Core Nutation) using a model derived from VLBI analysis. The numerical results for the amplitudes show that the error is bigger than the estimation; this is because of the imperfect distribution of the observations. The results are represented on Fig.2 (right).

[1] SYRTE, Observatoire de Paris

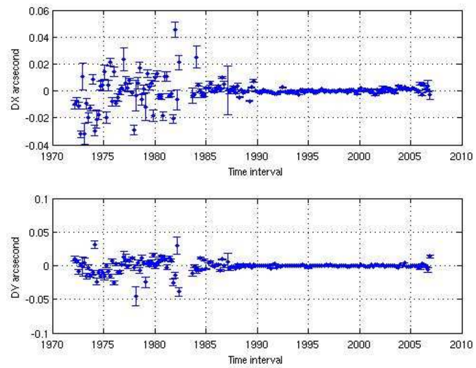

Fig. 1. DX, DY corrections to the celestial pole coordinates and their formal errors

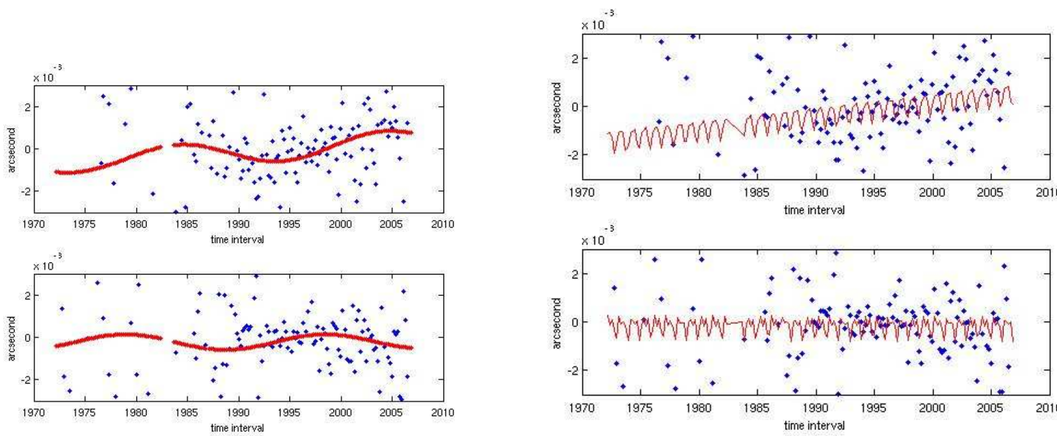

Fig. 2. Left in blue: correction DX, DY to the celestial pole coordinates - in red: the fitted terms (18.6, 9.3, secular and constant term) . **Right** in blue: correction DX, DY to the celestial pole coordinates - in red: the fitted terms (annnual, semi-annual, secular and constant term)

3 Conclusion

Fig.1 shows that from LLR observations, it is possible to have an estimation of the correction to the celestial pole coordinates (DX, DY). Due to the imperfect distribution of the observations, the accuracy is not at the same order as from VLBI.

References

Capitaine, N., Wallace, P.T., and Chapront, J. 2003, Expressions for IAU 2000 precession quantities, Astron. Astrophys., 412, 567-586

Chapront, J., Chapront-Touz, M. and Francou, G. 1999, Determination of the lunar orbital and rotational parameters and of the ecliptic reference system orientation from LLR measurements and IERS data, Astron. Astrophys., 343, 624-633

Chapront, J., Chapront-Touz, M. and Francou, G. 2002, A new determination of lunar orbital parameters precession constant and tidal acceleration from LLR measurements, Astron. Astrophys., 387, 700-709

Mathews, P.M., Herring, T.A., and Buffet, B.A. 2002, J.Geophys. Res, 107(B4), 10.1029/2001JB00390

McCarthy, D. D. 1996, IERS technical Note 21: IERS Conventions (1996)

IERS technical Note 32 : IERS Conventions (2003)

SOFA : www.iau-sofa.rl.ac.uk/

PCHE

High Energy Cosmic Phenomena

SF2A 2008
C. Charbonnel, F. Combes and R. Samadi (eds)

THE ANTARES NEUTRINO TELESCOPE A STATUS REPORT

Baret, B.[1] on behalf of the ANTARES Collaboration[1]

1 Introduction

ANTARES is a large volume neutrino telescope installed off La Seyne- sur-mer, France, at 2475m depth. Neutrino telescopes aim at detecting neutrinos as a new probe for a sky study at energies greater than 1 TeV. The detection principle relies on the observation, using photomultipliers, of the Cherenkov light emitted by charged leptons induced by neutrino interactions in the surrounding detector medium. The ANTARES detector is complete since June 2008 with 12 lines, comprising 75 optical detectors each, connected to the shore via a 40 km long undersea cable. The detector is now complete and working. It has already recorded several hundredth of atmospheric neutrino event candidates and is ready for physics analyses.

2 Scientific motivations

One of the major aims of neutrino astronomy is to contribute solving the fundamental question of the origin of high energy cosmic rays (HECR). Neutrinos can indeed escape from the core of the sources and travel with the speed of light through magnetic fields and matter without being deflected or absorbed. Therefore they can deliver direct information about the processes taking place in the core of the production sites and reveal the existence of undetected sources. At high energies, neutrinos are unmatched in their capabilities to probe the Universe. High energy neutrinos are produced in a beam dump scenario in dense matter via pion decay, when the accelerated protons interact with ambient matter or dense photon fields:

$$\begin{array}{ccccc} p + A/\gamma \rightarrow & \pi^0 + & \pi^{\pm} & & +N + ... \\ & \downarrow & \downarrow & & \\ & \gamma\gamma & \mu^{\pm} + \nu_\mu(\bar{\nu_\mu}) & & \\ & & \downarrow & & \\ & & e^{\pm} + \nu_e(\bar{\nu_e}) + \bar{\nu_\mu}(\nu_\mu) & & \end{array}$$

Good candidates for high energy neutrino production are active galactic nuclei (AGN) where the accretion of matter by a supermassive black holemay lead to relativistic ejecta (Halzen & Zas). Other potential sources of extra-galactic high energy neutrinos are transient sources like gamma ray bursters (GRB). As many models (Piras T.) for GRBs involves the collapse of a star, acceleration of hadrons follows naturally. The diffuse flux of high energy neutrinos from GRBs is lower than the one expected from AGNs, but the background can be dramatically reduced by requiring a spatial and temporal coincidence with the short electromagnetic bursts detected by a satellite. High Energy activity from our Galaxy has also been reported by ground based gamma-ray telescopes. Many astrophysical sources (Bednarek *et al.*) are candidates to accelerate hadrons and subsequently produce neutrinos. Such sources could only be observed by a northern neutrino telescope like Antares. Neutrino telescopes are also sensitive to signals due to the annihilation of neutralinos, gravitationally trapped inside the core of massive objects like the Sun, the Earth or the Galactic centre (Falchini E.). Finally, deep-sea neutrino telescopes enable researches in the fields of marine biology, oceanography and seismology.

[1] Laboratoire Astroparticules & Cosmologie, 10 rue A. Domon et L. Duquet, 75025 Paris Cedex 13 , France

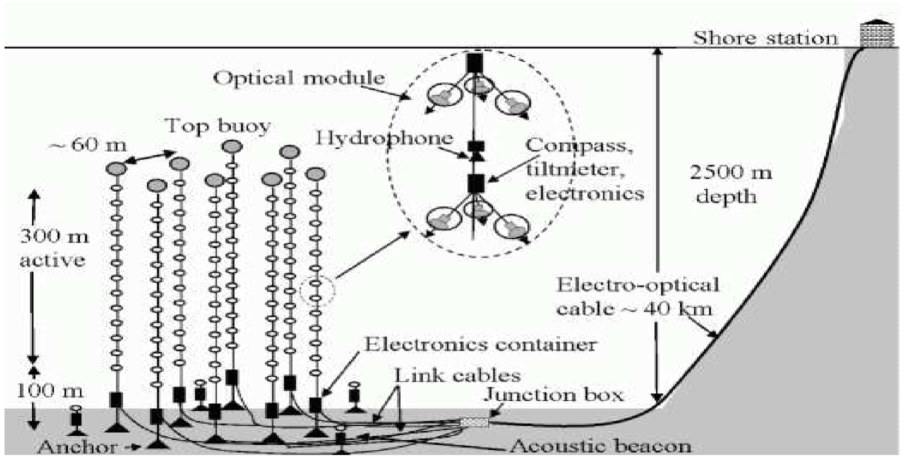

Fig. 1. Schematic layout of the Antares detector. The detector is connected to a junction box (deployed in December 2002) and operated from shore through an electro-optical cable. The actual detector has 12 lines.

3 Detection principle

The neutrino´ s advantage, the weak coupling to matter, is at the same time a big disadvantage. Huge volumes need to be monitored to compensate for the feeble signal expected from the cosmic neutrino sources. In this context, the water Cherenkov technique offers both a cheap and reliable option. The detection principle relies on the observation, using a 3 dimensional array of photodetectors, of the Cherenkov light emitted, in a transparent medium, by charged leptons induced by charged-current neutrino interactions in the surrounding de-tector medium. Thanks to the large muon pathlength, the effective detection volume in the muon channel is substantially higher than for other neutrino flavours. The higher the neutrino energy the smaller the deviation between the muon and the neutrino (typically $\Delta\theta \simeq (E_\nu(TeV))^{-0.6}$), thus enabling to point back to the source with a precision close to the one achieved by gamma-ray telescopes. Muon trajectories are reconstructed using the time and amplitude from the photodetector signals.
The energy of the event is estimated thanks to the energy deposited in the detector. Monte Carlo simulations for sea water predict a muon energy estimation by a factor of 2-3. Cosmic particles penetrating the atmosphere undergo a cascade of many secondary particles. Among them, high energy muons can reach the detector and constitute a very intense source of background. To suppress this background the detector concentrates on upward detection. As a result, the field of view is restricted to one half of the celestial sky (2π sr). Severe quality cuts criteria are then applied to the reconstruction to remove remaining mis-reconstructed muons. Atmospheric neutrinos produced in the atmospheric cascades can travel through the Earth and interact in the detector vicinity. To some extent this background is irreducible.
Fortunately, the atmospheric neutrino flux shows a dependency upon energy $dN/dE \propto E^{-3.7}$ while cosmic neutrinos are expected to exhibit a flux dependency $dN/dE \propto E^{-2}$. An excess of events above a certain energy can therefore be attributed to extraterrestrial neutrinos.

4 Detector description

Antares is a large European collaboration[1] which has deployed and now operates a 2475 m depth detector 40 km off La-Seyne-sur-Mer (Var, French Riviera) at a location 42o 50 N, 6o 10 E. The site benefits from the close infrastructures of the French sea science institute IFREMER. The sea water properties have been extensively studied revealing low light scattering, mainly forward (Antares Astrop. Phys. 2005) and an average optical background (induced by bacteria and 40 K decays) of 70 kHz per detection channel. The final detector consists of an array of 12 flexible individual mooring lines separated from each other on the sea bed by 60-80 m.

[1] for a complete list of antares member see http://antares.in2p3.fr

Figure 1 left shows a sketch of the detector. The lines are weighted to the sea bed and held nearly vertical by syntactic-foam buoys. Each line will be nequipped with 75 photomultipliers (Antares NIM A 2005) housed in glass spheres, referred to as optical modules (OM). The OMs are inclined by 45 o with respect to the vertical axis to ensure maximum sensitivity to upward moving Cherenkov light fronts. Expected performances, in particular in the frame of point source searches are described in (Aguilar J.A.).

The default readout mode (Antares 2006) of the detector is the transmission of the time and amplitude of any light signal above a threshold corresponding to 1/3 of a photo-electron for each OM. Time measurements are relative to a master reference clock signal distributed to each storey from shore via an electrooptical cable. The grouping of three optical modules in a storey allows local coincidences to be made to eventually reduce the readout rate. In addition the front end electronics (Fehr F.) allows a more detailed readout of the light signal than the standard time and amplitude mode. With this detailed readout it is possible to sample (up to 1 GHz) the full waveform of the signal with 128 channels, enabling special calibration studies of the electronics.

5 First results from deep-sea

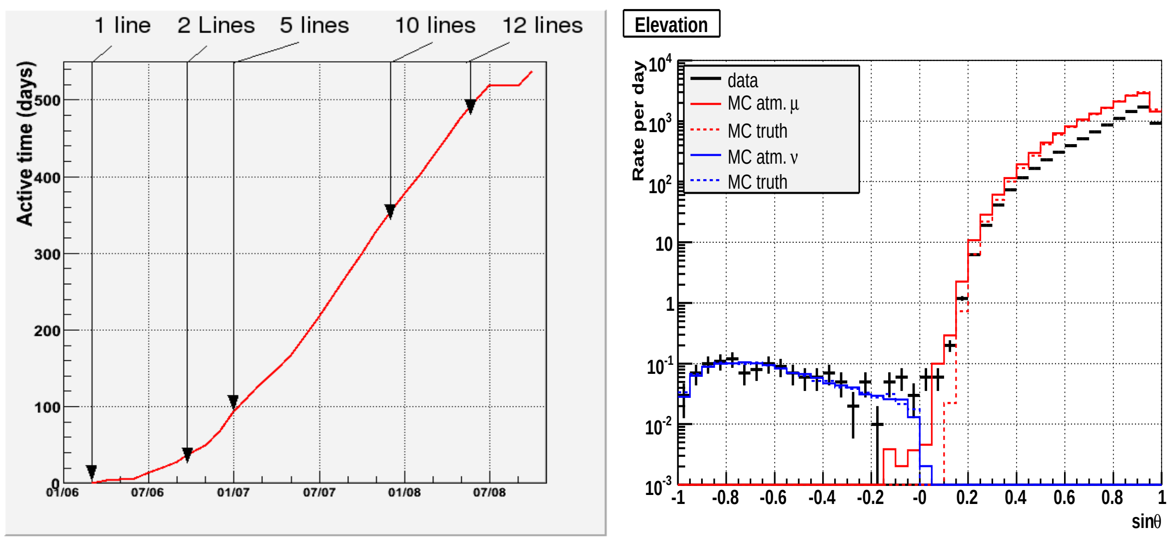

Fig. 2. Left : Integrated number of effective days of data taking since March 2006 taking into account all losses. **Right**: rate versus zenith angle ($\theta = 0$ for downgoing events) distribution after cuts. 5 lines detectector data are presented together with corersponding Monte Carlo simulation.

A mini-instrumented line equipped with 3 OMs (MILOM) and mainly dedicated to study environmental parameters (sea current, salinity, pressure, temperature...) has been in operation since spring 2005. The results of this line are presented in details in 10. Antares is today the largest neutrino telescope ever built in the northen hemisphere. Data with one line have been taken since March 2006, with 2 lines since October 2006, with 5 lines since january 2007 and 10 lines since december 2007. The telescope is now complete and operational with its 12 lines since june 2008. Figure 2 left gives an indication of the data taking efficiency since the connection of the first line, which has been continuously improving. The line motions are monitored by acoustic devices (high frequency long base line LBL) and by inclinometers regularly spread along the line, allowing redundancy. The system allows a location of each OM with a precision close to 10 cm. Timing calibration is ensured by a network of laser and LED beacons 11. According to the design specifications, a precision mesurement of 0.4 ns is achieved which guaranties an angular resolution within expectations ($< 0.5°$). The existing data are dominated by downward going muon bundles, the present trigger rate being roughly 5 Hz. The reconstruction program fits a single track to these events under the assumption that light is emitted under the Cherenkov angle w.r.t the muon path. The angular distribution obtained, after quality cuts, is shown on figure 2 right. As one can see, upward candidates are also present in the reconstructed sample (so far around 500 have been reconstructed), and both contributions are well understood. One of these neutrino candidates is displayed in figure 3. The detector is now ready for a large variety of physics studies.

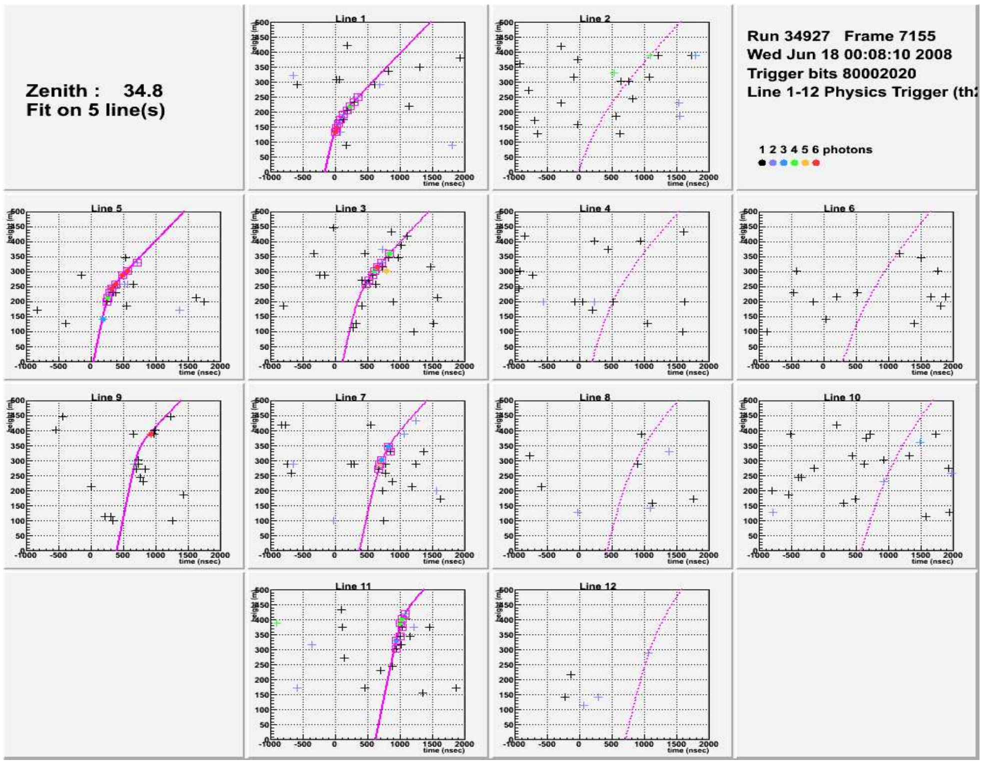

Fig. 3. An example of an atmospheric upward going neutrino induced muon candidate event. Each plot shows a single line hit time versus height distribution with the fitted hyperbola (intersection of the line and Cherenkov cone). The event has a reconstructed zenith angle of $34,8°$.

6 Conclusions

Great achievements have been made by the Antares collaboration in the last year. The detector is now complete working in nominal mode with 12 lines. Downward going muons and upward neutrino candidates are now continously reconstructed that validate the conceptual method and the chosen techniques. It now opens the path to excinting physics analyses. Very exciting times have started with a detector looking for neutrinos in a region of the celestial sky which has never been studied with such a level of sensitivity.

References

Halzen, F., & Zas, E. 1997, ApJ, 488, 669
Piran, T. 2004, Rev. Mod. Phys., 76
Bednarek, W., Burgio, G.F., & Montaruli, T. 2005, New Astron. Rev., 49, 1
Falchini, E., In ICRC, 2007
Antares. Astropart. Phys., 23:131-155, 2005
Antares. NIM A, 55:132-141, 2005
Aguilar, J.A., In ICRC, 2007
Antares. NIM A, 570:107-116, 2007
Circella, M., In ICRC, 2007
Antares. Astropart. Phys., 26:314-324, 2006
Fehr, F., In ICRC, 2007

SF2A 2008
C. Charbonnel, F. Combes and R. Samadi (eds)

THE CHINESE-FRENCH SVOM MISSION FOR GAMMA-RAY BURST STUDIES

Basa, S.[1], Wei, J.[2], Paul, J.[3], Zhang, S. N.[4] and the SVOM collaboration[5]

Abstract. We present the Space-based multi-band astronomical Variable Objects Monitor mission (SVOM) decided by the Chinese National Space Agency (CNSA) and the French Space Agency (CNES). The mission which is designed to detect about 80 Gamma-Ray Bursts (GRBs) of all known types per year, will carry a very innovative scientific payload combining a gamma-ray coded mask imagers sensitive in the range 4 keV to 250 keV, a soft X-ray telescope operating between 0.5 to 2 keV, a gamma-ray spectro-photometer sensitive in the range 50 keV to 5 MeV, and an optical telescope able to measure the GRB afterglow emission down to a magnitude limit $M_R = 23$ with a 300 s exposure. A particular attention will be also paid to the follow-up in making easy the observation of the SVOM detected GRB by the largest ground based telescopes.

Scheduled for a launch in 2013, it will provide fast and reliable GRB positions, will measure the broadband spectral energy distribution and temporal properties of the prompt emission, and will quickly identify the optical afterglows of detected GRBs, including those at very high redshift.

1 Introduction

The study of GRBs has the potential to expand and revolutionize our understanding of key astrophysical issues. In the coming years they will undoubtedly shed new light on the evolution of the young universe, particularly on the history of star formation, the metal enrichment of galaxies, and the re-ionization of the intergalactic medium. In parallel they will bring crucial insights on the mechanisms driving supernova explosions, the radiation processes at work in regions of space containing a huge energy density, and will provide reliable triggers for gravitational waves and high energy neutrinos detectors.

The recent interest in GRBs is illustrated by the growing number of instruments on ground and in space dedicated to their studies which are now under construction or under study. In order to fulfil these scientific promises, future studies must rely on the availability of a continuous flow of accurate positions, but also on the measure of many additional parameters (e.g. redshift, E-peak, jet break time, ...), which are crucial for the understanding of the phenomena itself and for their use as cosmological probes.

The Sino-French SVOM mission (Space-based multi-band astronomical Variable Objects Monitor) is conceived to:

- Permit the detection of all known types of GRBs.
- Provide fast and reliable GRB positions.
- Measure the broadband spectral shape of the prompt emission, from visible to MeV domains.
- Measure the temporal properties of the prompt emission, from visible to MeV domains.
- Quickly identify the afterglows of detected GRBs at X-ray and optical wavelengths, including those which are highly redshifted (z>6).

[1] Laboratoire d'Astrophysique de Marseille, Marseille, France.
Email: stephane.basa@oamp.fr

[2] National Astronomical Observatories of China, Beijing, China.

[3] AstroParticule et Cosmologie, Paris, France.

[4] Institute of High Energy Physics, Beijing, China.

[5] France: APC Paris, CEA-IRFU Saclay, CESR Toulouse, CNES, IAP Paris, INSU, LAM Marseille, LATT Toulouse, OHP Saint-Michel; China: CAS, CNSA, IHEP Beijing, NAOC Beijing, SECM Shanghai, XIOMP Xi'an; Italy: INAF-IASF Milano.

- Measure the broadband spectral shape of the early and late afterglow, from visible to X-rays domains.
- Measure the temporal evolution of the early and late afterglow, from visible to X-rays domains.

2 The SVOM mission

2.1 The concept

The constant advances in the field of GRB studies is made possible by the increasing synergy between space and ground instruments. The SVOM mission has been designed to optimize very precisely this synergy. The on-board instruments will permit the detection of the GRBs, their localization from arcminutes to arcsecondes accuracy, the study of the prompt emission, the early detection and follow-up of visible afterglows, and the primary selection of high-redshift candidates (z>6). The ground segment will permit the fast distribution of the alerts, the localization of GRBs with sub-arcsecondes precision and the multi-band photometry of the afterglow and the prompt for the longest events from the visible to the near-infrared domains.

These functions will be achieved by a set of wide and narrow field instruments. Such a combination requires a very specific observation scenario, which is based on the successful experience of the Swift mission (Gehrels et al., 2004):

1. the detection is done by a very wide field gamma-ray imaging instrument[1] able to derive on-board localization with few arcminutes accuracy;
2. the position is immediately transmitted to the scientific community through a VHF stations network;
3. in parallel the satellite slews rapidly and automatically (when safely possible, regarding to the pointing constraints) to position the GRB in the narrow field of view of the onboard instruments, an X-ray and an optical telescopes, which will study the afterglow and provide refined coordinates. The observations start less than 5 minutes after the detection.

The scientific objectives of the mission put a very special emphasis on two categories of GRBs: very distant events at redshift greater than 6, which constitute exceptional cosmological beacons, and faint/soft nearby events, which allow probing the nature of the progenitors and the physics at work in the explosion. These goals have a major impact on the design of the mission: the onboard hard X-ray imager must be sensitive down to 4 keV and able to compute image and rate triggers on-board, and the follow-up telescopes on the ground must be sensitive in the near infrared.

2.2 The scientific payload

To achieve all these functions, the SVOM mission will operate a set of four instruments in space that constitute the scientific payload of the satellite.

ECLAIRs is a 2D-coded mask imager sensitive from 4 to 250 keV, with a field of view (FoV) of $89° \times 89°$ and a localization accuracy better than 10', at 7 σ (Mandrou et al., 2008). It will deliver triggers by seeking continuously for the appearance of new transient sources in the hard X-ray energy domain, and by determining their localization on the sky (Schanne et al., 2007). When a new source candidate is detected, an alert will be automatically transmitted to the satellite and to the ground within 1 minute via a VHF network.

GRM (Gamma-Ray Monitor) is a set of two gamma-ray spectro-photometers sensitive in the range 50 keV to 5 MeV. It will cover the same FoV than ECLAIRs and provide a measurement of the peak energy, E-peak.

XIAO (X-ray Imager for Afterglow Observations) is a mirror focusing X-ray telescope operating from 0.5 to 2 keV, with a FOV of $23' \times 23'$ and a localization accuracy better than 10", at 5 σ (Mereghetti et al., 2008). It will reach a sensitivity of about 5-10 μCrab in 10 ks, at 5 σ. It will provide an intermediate step between the first localizations at several arcminutes given by Eclairs and the precise localizations that can be achieved with an optical telescope. The refined position will be also transmitted via the alert network.

VT (Visible Telescope) is a 45 cm visible telescope operating from 400 to 950 nm, with a FOV of $21' \times 21'$. It will reach a sensitivity of about 23 magnitudes, in the R band, in a 300 s exposure time, at 5 σ. Subimages,

[1]GRBs occurring anywhere, at any time, at an observed rate of one to two per day, a gamma-ray detector featuring a wide field-of-view and a long observing time is required.

centered on the position provided by XIAO, will be transmitted to the ground in order to detect quickly an optical emission from the GRB and refine its localization accuracy at less than 1”. This position will be also transmitted via the alert network.

2.3 The ground segment

Another key element of the SVOM mission is the two Ground Follow-up Telescopes (GFTs) (one managed by France, an other one by China). These robotic 1-meter class telescopes will point automatically their field-of view towards the space-given error box within tens of seconds after the alert reception and will provide panchromatic follow-up (visible to near-infrared). They will contribute to the improvement of the link between the scientific payload and the largest telescopes by measuring the celestial coordinates with an accuracy better than 0.5”, and by providing an estimate of its photometric redshift in less than 5 min after the beginning of the observations. These information will be available to the scientific community through an alert message. Evenly placed on the Earth (one in South America in a place to be defined, the other one in China), they will be in a position to start the research of the GRB optical emission immediately after the alert reception in more than 40 % of the cases.

All the alerts of any new transient candidate will be transmitted from the scientific payload to the ground in real-time via a VHF real-time network, which is based on the successful experience of the Hete-II mission[2] (Tamagawa et al., 2003). The prompt alert will be distributed to the GRB community in the first minutes after the on-board detection through the GCN network. Main characteristics of the burst, the useful ones for follow-up campaigns, will be determined from a subset of data downlinked in real-time through the VHF network, before the full data are available through the X-band. Between two burst alerts, this network will be also used continuously to downlink some housekeeping and technical data in order to monitor the instruments.

2.4 The follow-up program

Follow-up telescopes will play a decisive role in the scientific return of the SVOM mission by extending its capabilities to domains not covered by the scientific payload and the ground segment: deep near-infrared photometry, spectroscopy, polarimetry, large wavelength coverage (radio to Ultra High Energy), ...

A follow-up program will be systematically organized and will have to guarantee a uniform quality to the largest possible sample. Possible instruments which could be involved on the SVOM follow-up are:

Radio: ALMA, VLA, ...

Visible and infrared: Tarot, Raptor, 2.2m MPE, Falkes Telescopes, Liverpool Telescope, ... (robotic telescopes) and VLT (Hawk-I, XShooter), JWST, Subaru, ... (large telescopes).

Gamma-ray: Swift (if still in operation), Fermi, ...

UHE: Antares, Auger, CTA, Hess, Ice Cube, Magic, Milagro, ...

2.5 Observing strategy

The selected SVOM orbit is circular with an altitude of ∼600 km and an inclination angle of ∼30°, with a precession period of 60 days. To allow fast and systematic follow-up observations by ground-based telescopes, the satellite orientation is quasi anti-solar, granting that the bursts are discovered in the night part of the sky. Strong Galactic sources and the Galactic plane where heavy extinction prevents the detection of afterglows are avoided. Thanks to this strategy, about 75 % of the GRBs will be visible at the time of their detection from at least one of the three major ground-based observatories (Cerro Paranal, Mauna Kea and Roques de los Muchachos).

A majority of bursts will be immediately observable at the end of the satellite automatic slew maneuver: about 60% are observable immediately (starting observation 5 minutes after the detection, for at least 5 minutes), the rest being observable between 40 and 60 minutes later due to Earth obstruction, which may occur just few minutes after the trigger (Cordier et al., 2008).

---

[2]The main difference is due to the higher orbit inclination foreseen for SVOM satellite, which implies to spread VHF stations between ±30° of latitudes.

3 The scientific performances

The SVOM mission offers a very attractive combination of instruments. The burst observation rate for the Eclairs instrument is estimated to about 80 per year for a 7 σ level detection, with about 10 % of the events at a redshift larger than 6. Despite its smaller effective surface than the Burst Alert Telescope of Swift, Eclairs holds greater potential for the discovery of highly redshifted and faint gamma-ray bursts thanks to a low-energy threshold of 4 keV. Simultaneously, the GRM will be able to provide systematically a precise estimation of the peak energy parameter.

After the automatic satellite slew maneuver, XIAO, with a sensitivity close to the Swift X-Ray Telescope, and the VT, with a sensitivity significantly improved over the Swift UVOT, completed by the two GFTs on ground, will insure a systematic multi-wavelength follow-up for several hours. In particular the VT will allow the detection of nearly 75% of GRBs in the visible domain, during the first orbit (Akerlof & Swan) and, for the first time, to explore the realm of "dark GRBs". All these instruments are included in a chain allowing a refinement of the localization, from few arcminutes to sub-arcsecondes. All these alerts will be distributed to the scientific community in real time through the GCN alert network.

A significant fraction of the time will be also available for non-GRB science like the discovery or the follow-up of cataclysmic variables, active stars, active galactic nuclei, supernovae, ... It will be possible to propose a program consisting in an observation of a given target for typically few consecutive orbits (programs maximizing the simultaneous use of several instruments will be always favored). Such a program will have always a lower priority than the GRB core program: the capabilities to detect a GRB must not be affected and the observation is stopped whenever a GRB is detected and will only resume after completion of the follow-up campaign. Target of Opportunity (ToO) observations will be also accepted for unpredictable events discovered in the routine scrutiny of the SVOM data or proposed by external partners.

4 Conclusion

SVOM is a very ambitious multi-wavelength mission operating from the optical to the gamma-ray domains. It is designed to detect all known types of GRBs, to provide fast and reliable positions, to measure the broadband spectral shape and temporal properties of the prompt emission, and to quickly identify the optical and X-ray afterglows of detected events, including those ay very high redshift.

Scheduled for a launch in 2013 and for at least 3 years, it will open the door to systematic and accurate GRB studies, allowing a better understanding of the phenomenon and of the Universe!

Acknowledgement

The french contribution to the SVOM mission is completed under the responsibility and leadership of the Centre National d'Etudes Spatiales (CNES). The french authors are grateful to CNES support.

References

Akerlof & Swan 2007, ApJ, 671, 1868.

Cordier, B., 2008, Proc. Gamma-Ray Bursts 2007, Santa Fe, USA, AIP Conf. Proc., 1000, 585-588.

Gehrels, N. et al, 2004, ApJ 611, 1005-1020.

Mandrou, P. et al., 2008, Proc. Nanjing GRB Conference, Nanjing, China, 2008arXiv0809.1057M.

Mereghetti, S. et al., 2008, Proc.SPIE Astronomical Telescopes and Instrumentation 2008, Marseille, France, 2008arXiv0807.0893M.

Schanne, S. et al., 2007, Proc. 30^{th} International Cosmic Ray Conference, Merida, Mexico, 2007arXiv0711.3754S.

Tamagawa, T. et al., 2003, Proc. 28^{th} International Cosmic Ray Conference, Trukuba, Japan.

SF2A 2008
C. Charbonnel, F. Combes and R. Samadi (eds)

HESS-II PERFORMANCE IN THE LOW-ENERGY DOMAIN

Becherini, Y.[1], Djannati-Atai, A.[1] and Punch, M.[1]

Abstract. In mid-2009 a notable upgrade of the H.E.S.S. telescope system will take place: a new telescope with a 600 m^2 mirror area and very-high-resolution camera (0.07°) will be positioned at the centre of the present configuration, with the aim of lowering the threshold and enhance its sensitivity in the 100 GeV to several TeV energy range. HESS-II will permit the investigation of the lower energy γ-ray spectra in various cosmic accelerators, giving information on the origin of the γ-rays observed, and will detect AGNs with a redshift greater than 0.2 (being less affected by absorption by Extragalactic Background Light - EBL - in this energy range) and will search for new classes of very high energy γ-ray emitters (pulsars, microquasars, GRB, and dark matter candidates).

1 Introduction

By the end of 2009 the H.E.S.S. experiment will enter its Phase II and at that time the data taking configuration will consist of the four current telescopes (here called T1, T2, T3 and T4) plus the new very large HESS-II telescope (here called T5, see Deil et al.). We have developed a shower reconstruction strategy for the events hitting the very large telescope alone which consists of several consecutive steps: first of all we clean the images and evaluate the shower direction, then, knowing the basic parameters of the images and of the showers we can optimise and apply a cut for hadron rejection and a cut on the shape of the images, finally we estimate the event energy with the sample of selected events with a Neural Network (NN) approach.

2 Low-energy performance

We simulated gamma and proton showers between 20 and 150 GeV at a zenith angle of 18° assuming an optimal optical efficiency in the five telescopes. The γ-ray source is simulated on the optical axis, so the source is projected at the centre of the cameras, and the simulations are carried out over 500 m from the centre of the array. The local trigger configuration used in this analysis can be summarised as follows: for T1, ..., T4 we required a pixel threshold of 4 p.e. and a minimum number of pixels of 2.5, while for T5 we raised these values to 5 and 3.5 respectively. The event is then kept only if it has at least one telescope satisfying the local trigger condition.

Images are cleaned with the following filtering rule: a pixel is accepted if it has at least a charge of 7 p.e. and some neighbouring pixels having a charge greater than 5 p.e., then for the reconstruction of the shower parameters with the filtered pixels we use the Hillas algorithm, see Werner et al. . For pure Mono-telescope events, the shower direction has to be estimated from the measured parameters using relations derived from Monte Carlo simulations.

Analysis cuts. The optimisation of the background rejection cut (*cut 1*) for the pure T5 Mono events has been performed with the Fisher algorithm implemented in a multi-variate analysis. An additional cut (*cut 2*) is required in order to reject the events giving images at the border of the camera, and to reject the events hitting the telescope too close to the source direction, which give non-elliptical images.

Angular resolution. The angular resolution, defined as 68% containment radius for all the pure T5 Mono events after trigger and image filtering, is shown in Fig. 1 on the left with the upper continuous line, while the resulting curve after the background rejection cut and cut 2 is shown with the lower continuous line. The angular resolution for the pure T5 events after cuts $(1 + 2)$ is of the order of 0.25°.

[1] APC, AstroParticule et Cosmologie, CNRS - Univ. Paris VII, 10, rue A. Domon et L. Duquet, 75205 Paris Cedex 13, France

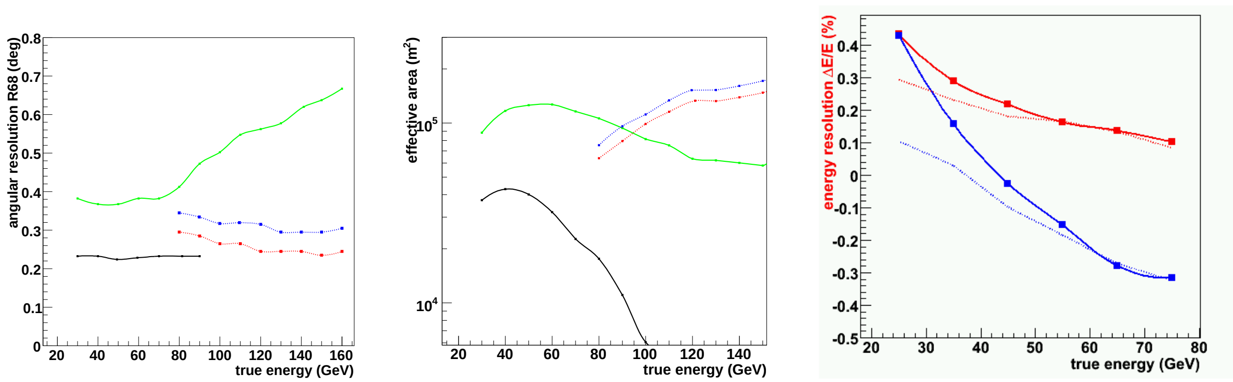

Fig. 1. Left: Angular resolution for the different HESS-II detection regimes: the upper continuous line shows the curve for the pure T5 Mono events after trigger and image filtering, while the lower continuous line shows the curve after the background rejection cut (cut 1) and cut 2. The remaining curves are obtained in the case of the semi-Stereo plus full-Stereo events at trigger and image filtering level (the upper dotted line is for the Hillas case while the lower dotted line is for the Model3D case, see Lemoine-Goumard et al.) and no analysis cuts were applied; the final stereo angular resolution is expected to be much better. Center: Effective area given in m^2 for the different HESS-II detection regimes: after trigger and image filtering (upper continuous line) and after cuts (lower continuous line) for the pure T5 events; after trigger and image filtering for the semi-Stereo and full-Stereo events for two different stereo reconstruction algorithms, the upper dotted line represents the results obtained with the *Hillas* algorithm, while the lower dotted line represents the *Model3D* resulting curve. Right: Energy resolution (upper continuous line) and bias curve (lower continuous line) obtained with a neural network approach in the case of the pure T5 Mono events. The dotted curves represent the resolution and the bias for the events having an impact parameter smaller than 130 m.

Effective area. For the calculation of the effective area, another quality cut on the squared angular deviation between the source position and the reconstructed direction θ^2 (*cut 3*) is applied: we select all the events having a $\theta^2 < 0.13$ deg^2. The effective area resulting after the three cuts is shown at the centre of Fig. 1: it has a maximum around 40 GeV then it drops dramatically at about 80 GeV where the semi-Stereo and full-Stereo detection regimes take over.

Energy resolution and bias. A dedicated study for the evaluation of the energy of the pure T5 events has been carried out using a NN approach trained with the events passing the three cuts mentioned. The resulting energy resolution defined as $\Delta E/E$ and bias defined as $< E > /E$ are shown in Fig. 1 on the right.

3 Conclusions

From our preliminary study of the performance of the HESS-II telescope we found the angular resolution for the pure T5 events to be of the order of 0.25° in the [30 GeV, 90 GeV] energy range after the hadron rejection and image shape cuts. The effective area after the additional cut on the angular resolution is found to be 4×10^4 m^2 at the maximum value of 40 GeV. Our current evaluation of the energy resolution varies from 40% to 20% as a function of the energy, while the bias spans from $+40\%$ to -40%: a more detailed study is needed in order to suppress this effect which is essentially due to the events having a large impact parameter.

References

Deil, C., et al. for the H.E.S.S. Collaboration, Gamma Ray Symposium 2008

Hofmann, W., Jung, I., Konopelko, A., et al. 1999, Astropart. Phys., 12, 135

Lemoine-Goumard, M., Degrange, B., & Tluczykont, M. 2006, Astropart. Phys., 25, 195-211

SF2A 2008
C. Charbonnel, F. Combes and R. Samadi (eds)

AUTONOMOUS RADIODETECTION OF HIGH ENERGY COSMIC RAYS AT THE PIERRE AUGER OBSERVATORY

Bellétoile, A.[1] and the Pierre Auger Collaboration

Abstract. The RAuger experiment is a prototype of an autonomous station for radiodetection of air showers that has been deployed on the southern site of the Pierre Auger Observatory. We report in this paper the first events for radio detection of high energy cosmic rays with a fully autonomous and self-triggered cluster of antennas in coincidence with the Auger surface detector. The experimental setup and results are discussed.

1 Introduction

As a complement to other techniques, like a particle detector array or a fluorescence telescope, radiodetection of ultra-high energy cosmic rays (UHECR) is a new method that could enable both an increase of the statistics and a reduction of systematic uncertainties on the determination of the air shower properties. Radiodetection aims to detect the electric field emitted by an air shower developping in the atmosphere. This electric field propagates through the atmosphere and can be detected over large distances by using a radio antenna. This offers a bolometric measurement of the air shower, in a way quite similar to the fluorescence technique. Thus it enables to probe the history of the shower development so that important information on both the nature and the energy of the primary particle can be accessed from the radio signal properties (Huege *et al* 2007, Meyer-Vernet *et al* 2007, Scholten *et al* 2008).

Experimental measurements were first attempted in the 60's, see (Allan 1971) for a complete review. Despite a validated observation in 1965 (Jelley *et al* 1965), experiments had to face difficulties of reproducibility and the technique was quickly abandoned to the profit of other methods that appeared more promising at that time. Recently, the growing interest in UHECR together with technical developments, in particular on fast ADC, gave a new impulse to this technique that is being re-investigated on modern experiments such as LOPES (Falcke *et al* 2005) in Germany and CODALEMA (Ardouin *et al* 2005) in France. Successful results obtained by those collaborations, both working in the 10^{17} eV energy range, motivates the exploitation of the radio detection technique at higher energy.

2 Radio@Auger

Increasing the observed energy by one order of magnitude requires a solution to new experimental constraints. The antenna array should be deployed over a large area, typically 10 km^2, which prohibits the use of cables between detectors and a central acquisition building as it is the case in both CODALEMA and LOPES experiments. Antennas should be mounted on fully autonomous stations that should provide power supply, accurate timing system as well as embedded electronics. In order to define an experimental strategy, a radiodetection R&D program on the southern site of the Pierre Auger Observatory was initiated in 2006 in a collective effort by the Auger, CODALEMA and LOPES groups.

One major item of the R&D program is the trigger system of such an autonomous detector. Indeed, on experiments like CODALEMA or LOPES, the antenna array is triggered by an associated particle detector array. This should not be feasible on a large array of antennas and a trigger based on the radio signal itself has to be achieved. The most advanced approach toward such a radio trigger was probably done by the

[1] LPSC, IN2P3-CNRS, Université Joseph Fourier, UMR 8109, 38000 Grenoble, France

CODALEMA collaboration that validated the autonomous detection and reconstruction of arrival direction of fast radio transients during a first operation phase (Ardouin *et al* 2005). Unfortunately, they could not firmly confirm at that time the CR origin of those transients.

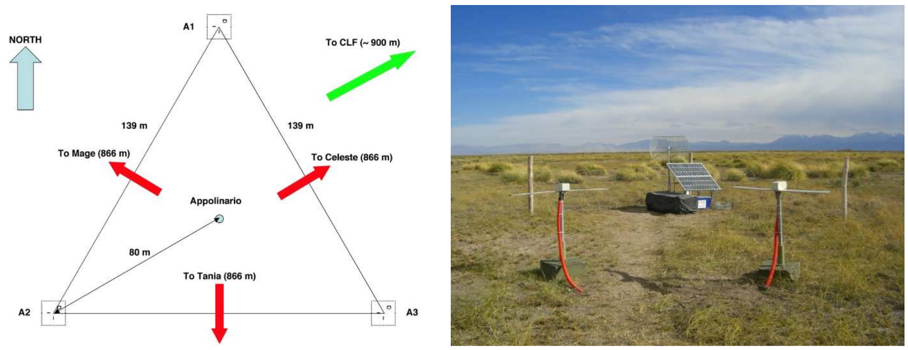

Fig. 1. Left : Global setup of the RAuger experiment. The 3 stations, namely A1, A2 and A3, are around the additionnal tank named Appolinario at the center of an elementary triangle of the Auger surface detector (not on the figure). The Central PC is at the CLF, 900 m away. **Right**: Detail of one of the 3 radio stations. The 2 short active dipoles (EW and NS) are at the foreground. The electronic box, solar panels and the WIFI antenna for data transmission are just behind.

The first phase of the R&D program started by the end of the year 2006 and is currently ending. During this phase, the CODALEMA collaboration in association with the Auger group developed an experimental prototype called RAuger for Radio at Auger to investigate the feasibility of a fully autonomous radio station and to perform in situ background measurements to qualify the southern site on a radio point of view.

3 Experimental Setup

The prototype has been deployed at the centre of one elementary triangle of the Auger surface detector array. One additional Cerenkov water tank was also installed in the centre of that triangle to locally lower the energy threshold of the Auger array. The RAuger experiment is made up of 3 fully autonomous radio detectors surrounding that additional tank as shown on fig 1 (left). The radio array pitch is 139 m and each station is at 80 m from the additional water tank.

The electric field is measured using two short active dipoles from the CODALEMA experiment on each radio station, see fig 1 (right). Those antennas are composed of two aluminium slabs of 0.6 m length and 0.1 m width. Antennas are horizontal, 1 m above the ground and oriented one in the North-South (NS) direction and the other in the East-West (EW) direction to measure independently the corresponding polarization of the electric field. The antenna has good performances in the 80 kHz-230 MHz band and is coupled to a low-noise high input impedance amplifier with a constant gain in this wide frequency domain. The performances of the system are presented in (Charrier 2007) and (Revenu 2007).

The technicality of the device lies in the nature of the trigger system. The antenna sensitivity to fast transients is hardly compatible with the fast electronic activity of the station. The electromagnetic compatibility of various components of the radio station becomes a crucial issue that requires to pay a special care to connectivity, shielding and ground loops. The EW polarization channel is divided in two parts, one is connected to the ADC, the other to a 50-70 MHz bandpass analogical filter to trigger the acquisition. This particular frequency band was chosen for its low radio activity that ensures a good signal to noise ratio. The filtered signal is compared to an adjustable threshold. When that threshold is passed, both signals, EW and NS polarization, are digitized in the full frequency band on an 8 bits ADC with a sampling rate of 500 MS/s for a 5 μs duration waveform.

The embedded electronics uses the Unified Board from Auger tanks with its GPS timing system that enables a timing of the events with a 10 ns accuracy. It masters the local data streams and sends it by a WiFi link to a Central PC installed at the Central Laser Facility (CLF), 900 m away. From that Central PC, the collected data are finally sent to the Auger building in Malargüe, Argentina and brought back to the laboratory via an ethernet link. The acquisition is frozen until data transmission has been acknowledged by the central PC. This leads to an acquisition dead time of approximately 2.7 s mainly due to the time transfer via serial ports of the Unified Board. RAuger is installed since November 2006 and is running in a quite stable mode since July 2007. The analysis presented here is performed on data taken between July 2007 and May 2008 corresponding to 318 days.

4 Detection in coincidence with Auger

The trigger rate of the system depends on many effects that are not fully understood yet. Among them, thunderstorms and stormy weather have been identified as playing an important role. Radio signals attributed to thunderstorm are broad and contain a massive amount of energy that can lead to the saturation of the ADC channel. Those particular features make them easily recognizable from the type of radio signal one can expect from an air shower.

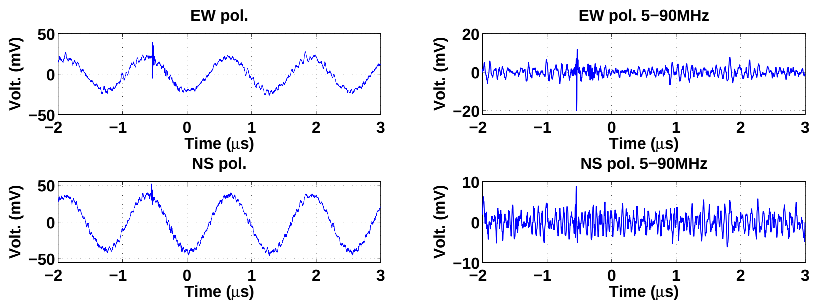

Fig. 2. Left : Illustration of one air shower detected with radio in coincidence with the Auger surface detector. The measured voltages are ploted versus time for both polarizations, EW top and NS bottom, in the full frequency bandwidth (from some 100 kHz to 100 MHz). The fast transients superimposed to radio background are clearly visible on both polarizations. The sinewave is due to LV19, a local radio station emitting at 790 kHz at Malargüe. **Right**: The same event is displayed but signals have been numerically filtered in the 5-90 MHz frequency band. Most of the radio background has been removed with that very large filter. Our system enables to use very low frequency bands.

During periods of stormy weather, many events have been detected in coincidence by the 3 radio stations. We have been able to triangulate the arrival directions of those events and in this way to confirm that the system enables good reconstruction. Unfortunately, none of those 3 fold events were identified as resulting from an air shower as they did not present time coincidence with the Auger surface detector. This lack of 3 fold events can be attributed to both, the high dead time of the system and hardware failures that occurred occasionaly on radio stations. As a test prototype, the station doesn't have the robustness one would expect from a dedicated instrument. Those aspects should be easily improved in a next generation of a radio detection station.

To identify cosmic ray events in coincidence, we are searching for time coincidences between Auger events and our radio events in a 10 μs window. The shower plane and the core are given by the Auger reconstruction. The fortuitous events rate is very small, of the order of $10^{-11}\ s^{-1}$, due to the small trigger rate of the antennas (the saturation corresponds to 0.37 events/s) and the small number of Auger events falling closer than 1 km (axis distance) from Appolinario (around 1.6 events/day). Integrated over a period of 318 days, the expected number of random coincidences is of the order of 10^{-4} so that the association of our coincidences with actual Auger events is unambiguous. The total number of coincidences with Auger is 25 in the considered period with energies ranging from 0.2 to 8 EeV.

Illustrative signals measured on one radio station for a 0.9 EeV event are given fig 2. The fast transients associated with the air shower is clearly visible in the full frequency band, superimposed to the radio-background, on both polarizations. Depending mainly on ionospheric conditions, it is possible to use frequencies down to 5 MHz with a good signal to noise ratio as shown fig 2 (right). It should be noticed that the lowest usable frequency is an important parameter as it has an influence upon the ability to detect distant air showers and to recover the original waveform of the radio signal. This lowest usable frequency should be considered for a

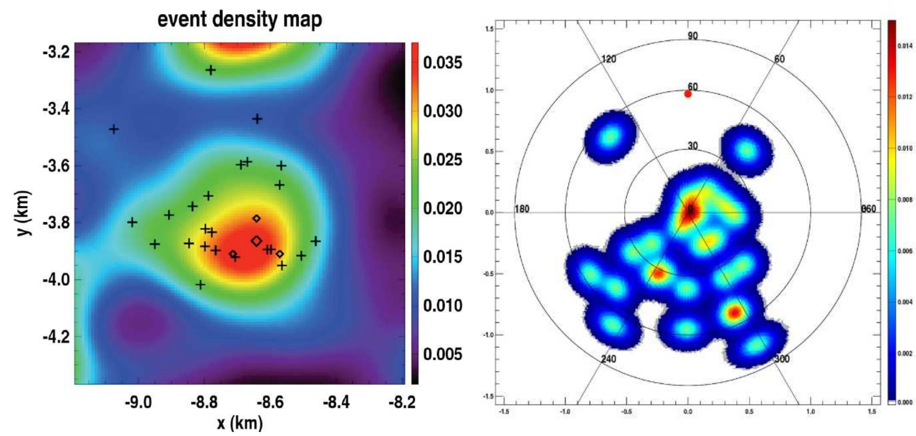

Fig. 3. Left :Event ground density map around Appolinario, computed from the Auger event list and smoothed by a 100 m width Gaussian. The Auger events with a radio counterpart are indicated by the black crosses. Appolinario is the largest diamond at the center and the 3 radio stations are the small ones around. **Right**: Sky map in local coordinates of the radio events seen in coincidence with Auger SD and smoothed by a 10^o Gaussian beam. The zenith is at the center, North at the top, East on the right. 80% of the events are coming from the South while the Auger SD events skymap is uniform in azimuth. The red dot towards the north at $\theta \sim 60^o$ is the location of the geomagnetic field.

future antenna array. The polarization measurement is also an interesting aspect as the ratio of the EW to the NS component should help a better understanding of the emission processes of the air shower.

Fig. 3 left show that the ground distribution of the 25 radiodetected events follows well the Auger SD event density map around Appolinario. This is not the case for the angular distributions. The azimuthal distribution of the radio events is not uniform as compared to that of the Auger SD events as it is visible on fig 3 right. It is found that 80 % (20/25) of the radio events are coming from the South as one should expect considering the direction of the geomagnetic vector in Argentina (see also Ardouin *et al* 2008).

5 Conclusion

Measurements show that the southern site of the Pierre Auger Observatory is very well suited for radiodetection. The low radio activity enables the use of a very low frequency band down to 5 MHz. The trigger based on the radio signal has been validated for the first time by the detection of air showers in coincidence with the Auger surface detector. The arrival direction of those events indicates a North-South asymmetry although the poor statistic and the weakness of this test prototype does not allow any quantitative conclusion. The prototype is not maintained anymore and should be replaced soon by a new generation of autonomous stations.

References

Allan H.R. , 1971, J.G. Wilson & S.A. Wouthuysen Eds, Progress in elementary particle and cosmic ray physics, 169

Ardouin D. *et al.* 2005, Nucl. Instrum. Meth. A 555, 148

Ardouin D. *et al*, submitted to Astroparticle Physics.

Charrier D. and the CODALEMA collaboration, 2007, Nucl. Instrum. Meth. A, 572, 481

Falcke H. *et al.* 2005, Nature, 435, 313

Huege T., Ulrich R., & Engel R. 2007, Astropart. Phys. 27, 392

Jelley J. V. *et al.* 1965, Nature, 205, 237

Meyer-Vernet N., Lecacheux A., & Ardouin D. 2008, A&A, 480, 1

Revenu B. and the CODALEMA collaboration, 2007, proc. of the 30th Int. Cosmic Ray Conf.

Scholten O., Werner K., & Rusydi F., 2008, Astropart. Phys., 29, 94

SF2A 2008
C. Charbonnel, F. Combes and R. Samadi (eds)

RADIATION PROCESSES AROUND ACCRETING BLACK HOLES

Belmont, R.[1], Malzac, J.[1] and Marcowith, A.[2]

Abstract. Accreting sources such as AGN, X-ray binaries or gamma-ray bursts are known to be strong, high energy emitters. The hard emission is though to originate from plasmas of thermal and/or non-thermal high energy particles. Not only does this emission allow to probe the unique properties of the matter in an extreme environment, but it also has a crucial backreaction on the energetics and the dynamics of the emitting medium itself. Understanding interactions between radiation and matter has become a key issue in the modelling of high energy sources. Although most cross sections are well known, they are quite complex and the way all processes couple non-linearly is still an open issue.

We present a new code that solves the local, kinetic evolution equations for distributions of electrons, positrons and photons, interacting by radiation processes such as self-absorbed synchrotron and bremsstrahlung radiation, Compton scattering, pair production/annihilation, and by Coulomb collisions. The code is very general and aimed to modelled various high energy sources. As an application, we study the spectral states of X-ray binaries, including thermalization by Coulomb collisions and synchrotron self-absorption. It is found that the low-hard and high-soft states can be modelled with different illumination but the same non-thermal acceleration mechanism.

1 Introduction

The hard emission of high energy sources such as X-ray binaries, AGN or gamma-ray bursts is expected to originate from high energy particles. In spite of large effort, understanding the properties of relativistic plasmas remains a challenge. At these high energies, Coulomb collisions become inefficient and the corresponding thermalisation timescale becomes longer than others, including radiation processes timescales. Then, kinetic and radiation processes contribute significantly to shaping the particle distribution; and understanding the highly non-linear, coupled evolution of particles and photons becomes a complicated issue that is best addressed numerically.

Although Monte Carlo simulations allow to deal with complex geometries (Pozdnyakov et al. 1980; Stern et al. 1995; Malzac & Jourdain 2000), they are often too time-consuming to be used for exploring the parameter space or real data fitting. For such purpose, codes solving the kinetic equations are more efficient for they can use simple prescriptions to account crudely for geometric effects (Lightman & Zdziarski 1987; Coppi 1992; Nayakshin & Melia 1998; Pe'er & Waxman 2005).

In the fist section, we present a new kinetic code developed to address the modelling of high energy plasmas. In the second section, we investigate the thermalization by synchrotron self-absorption in the corona of accreting black-hole and we apply the results to the X-ray binary Cyg-X1.

2 Simulating radiation and kinetic processes in high energy sources

2.1 Principle

The code developed is a one-zone code. Its abandons the detailed description of the sources geometry. Instead it focuses on the microphysics of radiation and kinetic processes and assumes a homogeneous sphere of fully

[1] Centre d'Etude Spatiale des Rayonnements (OMP; UPS; CNRS), 9 avenue du Colonel Roche, BP44346, 31028, Toulouse Cedex 4, France
[2] Laboratoire de Physique Théorique et d'Astroparticules, IN2P3/CNRS, Université MontpellierII, CC 70, place Eugène Bataillon, F-34095 Montpellier Cedex 5, France

magnetised plasma. The plasma properties are described by the distributions of particles and photons. Isotropy is assumed so that both particle and photon populations are described by only one-dimension energy distributions, which enables fast computation. Three distributions are considered, for photons, electrons and positrons. No assumption is made on the shape of the distributions (such as thermal or power-law for example) and the exact distributions are computed self-consistently from the microphysics. A thermal distribution of hot proton is also considered to account for Coulomb heating by hot protons. The code is time dependent and evolves simultaneously the three distributions.

2.2 Microphysics

At present stage, the code accounts for Compton scattering, cyclo-synchrotron pair production and annihilation, self-absorbed radiation, self-absorbed e-p bremsstrahlung, and Coulomb collisions (e-e and e-p). The exact cross sections are used for Compton scattering and pair production/annihilation. To achieve good accuracy in the computation of Compton scattering, a dedicated treatment is also used, which combines integration of the Klein-Nishina cross section over the distribution for large angle scattering and a Fokker-Planck treatment for small angle scattering. In addition to these elemental radiation processes, the code allows for photon injection to reproduce external illumination. It also includes prescriptions for additional heating/acceleration: the simulated plasma can be heated by thermal heating and/or non-thermal acceleration. The former process is modelled by an artificial Coulomb heating, the efficiency of which is imposed. The latter can be modelled either by injecting physically high energy particles into the system, or by second-order Fermi acceleration with a threshold. In contrast to previous studies our modelling of thermal and stochastic acceleration are fully consistent.

2.3 Numerical methods

The system evolution is described by a set of 3 coupled, integro-differential equations, one for each species. Solving numerically these equations is not trivial. First, the nature of integro-differential equations is very different to that of usual differential equations and the associated numerical schemes have been much less studied. Then, the energy ranges involved in high energy sources are wide: typically 20 orders of magnitude for Blazars spectra for example. The non-local nature of radiation processes implies to combine very small and very large terms, which is numerically challenging. Last, the various timescales involved can be drastically short. Photons for example can get a large amount of energy in one single Compton scattering event. To deal with these problems, the code uses a second order in energy, semi-implicit first order in time scheme and stores the cross sections as large tables.

The use of exact cross sections or suitable combinations of asymptotic expressions and the choice of specific numerical schemes enable the use of the code over very large energy ranges for photons (from radio or lower energy bands to TeV energies or higher) and for particles (from $p/mc = 10^{-7}$ to $p/mc = 10^{7}$). This numerical improvement and the implementation of numerous microphysical processes allow to use the code in many astrophysical applications as X-ray binaries, AGN, gamma-ray bursts... The code has now been tested extensively. Tests and methods are presented in more detail in Belmont et al. (2008).

3 The spectral states of accreting black holes

3.1 The Low-hard and High-soft states

As a first application of the code, we present a study on the spectral states of galactic accreting black holes. X-ray binaries exhibit a complex variability in the light curves and the spectra. Among other spectral states, two canonical states have now been identified in many sources: the so-called low-hard (LH) and high-soft (HS) states. The LH state has usually a rather low luminosity ($L < 0.1\% L_{\rm Edd}$) and a hard spectrum (with a photon index of $\Gamma \approx 1.5-2$). It is well reproduced with a thermal Comptonization model in a corona with a temperature $k_B T \approx 100$ keV. The HS state has a higher luminosity ($L \sim 1\% L_{\rm Edd}$). The spectrum is composed by a strong excess at a few keV and a soft high-energy tail ($\Gamma \approx 2.5 - 3.5$) extending at least to MeV energies. It cannot be reproduced by a thermal Comptonization model. Instead, it is modelled as the sum of a disk black-body emission and its Comptonization by accelerated, non-thermal particles.

The different nature of the Comptonization in both spectral states (thermal vs. non-thermal) is often assumed to originate from different heating processes (Coppi 1992; Poutanen & Coppi 1998). The corona in the

LH state is assumed to be heated by a thermal mechanism such as Coulomb heating by hot protons (Narayan & Yi 1994), whereas the particles in the HS states are thought to be accelerated by non-thermals processes such as reconnection in an active corona (Galeev et al. 1979). While the change in disk luminosity is naturally explained by a change of the innermost radius of the accretion disk (Esin et al. 1997), there is no explanation why one process should be switched on while the other is switched off during state transition.

3.2 *Thermalisation of non-thermal particles*

We have investigated the idea that particles may be accelerated only by non-thermal mechanisms and then thermalised with different efficiency depending on the spectral state. Particles can be thermalised by Coulomb collisions and synchrotron self-absorption. Although the latter effect is not as known as the former, it has been shown that exchange of synchrotron photons between particles can be very efficient in magnetised sources (Ghisellini & Svensson 1991; Ghisellini et al. 1998). To study the effect of thermalisation in the different

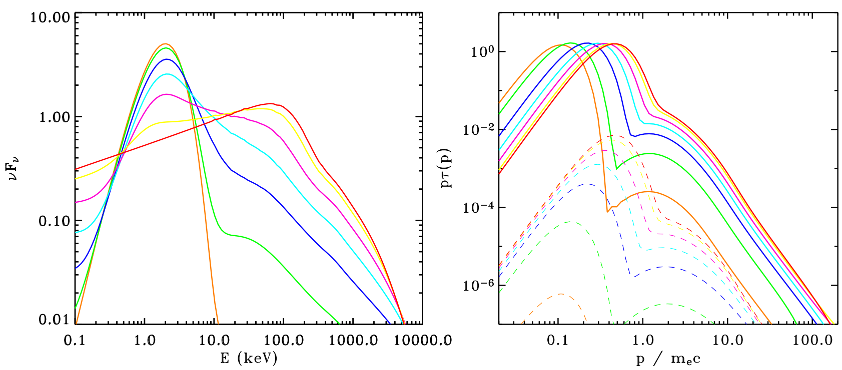

Fig. 1. Photon (left panel) and particle (right panel) distributions in steady state. The total energy is $L = 5.5 \times 10^{37}$ erg s^{-1} and the fraction of energy injected as soft photons is $0, 10, 30, 50, 70, 90$, and 99% for the red, yellow, pink, cyan, blue, green, and orange curves respectively. Dashed lines show the positron distribution. The system is characterized by its size: $R = 5 \times 10^7$cm, its optical depths $\tau = 2$, and the magnetic field strength $B = 2.5 \times 10^6$ Gauss. The temperature of the injected soft photons is $k_B T = 420$ eV and accelerated particles are injected with a power low distribution of slope $\Gamma_{\rm inj} = 3$ between $\gamma_{\rm min} = 1$ and $\gamma_{\rm max} = 10^3$.

states, we ran simulations with only non-thermal acceleration. The total injected power is the sum of the energy injected by accelerating particles and illuminating the corona. In steady state, it equals the source luminosity and was set to a constant. The faction of power injected as soft photons was varied. Figure 1 shows steady state photon and particle distributions. The particle distribution is composed by a high energy, non-thermal tail produced by non-thermal particle acceleration and a thermal, low energy part resulting from the thermalisation of high energy particles by synchrotron self-absorption and Coulomb collisions. For weak illumination, the thermalisation is efficient and produces a hot thermal component which produces the strong thermal comptonization spectra typical of LH states. As illumination increases, the cooling by inverse Compton increases, the temperature of the Maxwellian part decreases, and the thermal Comptonization becomes less efficient. For strong illumination, Comptonization by the non-thermal tail becomes dominant, and the spectra exhibits a power-law at high energy. As the flux of seed photons increases, the black-body component also becomes stronger, which gives eventually spectra very similar those observed in the HS state of X-ray binaries.

3.3 *Modelling the spectrum of Cyg-X1*

We also compared these results with real data. Figure 2 shows a comparison of two simulations with observations of Cyg-X1 in both states. Although these are not real fits to the data, both states are well reproduced.

4 Conclusion

We presented a new code for high energy plasmas. Compared to previous codes, it describes the microphysics more accurately, more processes have been included and general numerical schemes have been implemented.

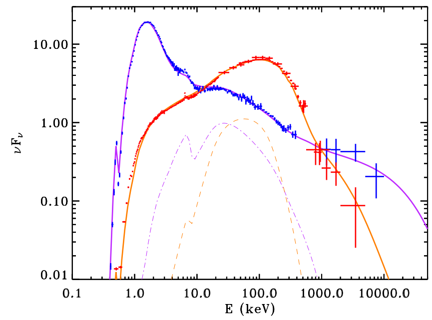

Fig. 2. Spectra of Cyg-X1. Crosses correspond to observations published in McConnell et al. (2002). Solid lines are the results of two simulations with $R = 10^8$cm, $B = (5.4; 41) \times 10^5$ Gauss, $\tau = (1.45; 0.12)$, $L_{\rm phot} = (0; 31) \times 10^{36}$ erg s^{-1}, $L_{\rm acc} = (8.8; 10) \times 10^{36}$ erg s^{-1}, and $\Gamma_{\rm inj} = (3.5; 2.1)$, for the (HS,LH) states respectively. A distance of $D = 2$ kpc was assumed. Absorption with $N_{\rm H} = 6 \times 21$ cm was modeld with the WABS model in XSPEC and reflection components were added to the simulations results.

This generality allows to use the code for many astrophysical situations.

The code was used to model the spectral states of accreting black holes. We found that high energy particles can be thermalised efficiently by synchrotron self-absorption and Coulomb collisions. As a result, non-thermal particle acceleration can naturally explain even the thermal, LH state of X-ray binaries and the state transition only results from a change in the illumination by the accretion disk. Such model was successfully applied to observations of cyg-X1 and more accurate data fitting will provide strong constrains on the source parameters.

References

Belmont, R., Malzac, J., & Marcowith A. 2008, in press for A&A

Coppi, P. S. 1992, MNRAS, 258, 657

Esin, A. A., McClintock, J. E., & Narayan, R. 1997, ApJ, 489, 865

Galeev, A. A., Rosner, R., & Vaiana, G. S. 1979, ApJ, 229, 318

Ghisellini, G., & Svensson, R. 1991, MNRAS, 252, 313

Ghisellini, G., Haardt, F., & Svensson, R. 1998, MNRAS, 297, 348

Lightman, A. P., & Zdziarski, A. A. 1987, ApJ, 319, 643

Malzac, J., & Jourdain, E. 2000, A&A, 359, 843

Malzac, J. & Belmont, R. 2008, MNRAS, submitted

McConnell, M. L., et al. 2002, ApJ, 572, 984

Narayan, R., & Yi, I. 1994, ApJL, 428, L13

Nayakshin, S., & Melia, F. 1998, ApJS, 114, 269

Pe'er, A., & Waxman, E. 2005, ApJ, 628, 857

Poutanen, J., & Coppi, P. S. 1998, Physica Scripta Volume T, 77, 57

Pozdnyakov, L. A., Sobol, I. M., & Syunyaev, R. A. 1980, Comptomization and radiation spectra of X-ray sources. Calculation of the Monte Carlo method, Rept. Pr-447 Acad. of Sci. USSR, Moscow, 1978 12 p

Stern, B. E., Begelman, M. C., Sikora, M., & Svensson, R. 1995, MNRAS, 272, 291

KHZ QUASI-PERIODIC OSCILLATIONS IN THE LOW-MASS X-RAY BINARY 4U 0614+09

Boutelier, M.[1], Barret D.[1] and Miller, M.C.[2]

Abstract. We report on a comprehensive analysis of the kilohertz ($\geq$ 400 Hz) quasi-periodic oscillations (kHz QPOs) detected from the neutron star low-mass X-ray binary 4U 0614+09 with the Rossi X-ray Timing Explorer (RXTE). With a much larger data set than previously analyzed (all archival data from February 1996 up to October 2007), we first investigate the reality of the 1330 Hz QPO reported by van Straaten et al. (2000). This QPO is of particular interest since it has the highest frequency reported so far. A thorough analysis of the same observation fails to confirm the detection. On the other hand, over our extended data set, the highest QPO frequency we measure for the upper kHz QPO is at $\sim$ 1224 Hz; a value which is fully consistent with the maximum values observed in similar systems. Second, we demonstrate that the frequency dependence of the quality factor ($Q = \nu/\Delta\nu$) and amplitude of the lower and upper kHz QPOs follow the systematic trends seen in similar systems. In particular, 4U 0614+09 shows a drop of the quality factor of the lower kHz QPO above $\sim$ 760 Hz. If this is due to an approach to the innermost stable circular orbit, it implies a neutron star mass of $\sim$ 1.9 $M_\odot$.

1 Introduction

Kilohertz quasi-periodic brightness oscillations (kHz QPOs) have been reported from 4U 0614+09 by Ford et al. (1997), van Straaten et al. (2000, 2002), Barret et al. (2006), and Mendez (2006). The peculiar properties of its kHz QPOs motivate the present work for two main reasons. First, among kHz QPO sources, 4U 0614+09 holds the record for the highest claimed QPO frequency, 1330 Hz (van Straaten et al. 2000), whereas in most sources the maximum frequency for the upper kHz QPO lies around 1200 Hz. This is of particular importance because it sets the most stringent constraints on the mass and radius of the NS, under the assumption that 1330 Hz is an orbital frequency (e.g., Miller et al. 1998). Unfortunately 4U 0614+09 tends to have a low count rate and broad QPOs compared to similar sources, hence its QPOs are challenging to characterize.

Second Barret et al. (2006) have performed a systematic study of the quality factor of the lower and upper kHz QPOs in six systems: 4U 1636-536, 4U 1608-522, 4U 1735-44, 4U 1728-34, 4U 1820-303 and 4U 0614+09. Using data available in the RXTE archive at the end of 2004, they found that all the sources except 4U 0614+09 showed evidence of a reproducible drop in the quality factor of their lower kHz QPOs at high frequency. This result is consistent with what is expected if the drop is produced by the approach of an active oscillating region to the innermost stable circular orbit (ISCO), a key feature of strong-gravity general relativity. For 4U 0614+09 only the rising part of the quality factor versus frequency curve was reported. The availability of more data in the RXTE archive, together with the developments of procedures adapted for broad and weak QPOs, led us to re-analyze all the archival data to search for the same effects seen in other sources.

2 Observations and data analysis

For the purpose of this paper, we have retrieved from the HEASARC archive science event mode data recorded by the RXTE Proportional Counter Array (PCA). The data set spans over eleven years from February 26th, 1996 to October 17th, 2007. We consider segments of continuous observation (ObsIDs): 763 ObsIDs were

[1] Centre d'Etude Spatial des Rayonnements, CNRS/UPS, 9 avenue du Colonel Roche, 31028 Toulouse Cedex 04, France
[2] University of Maryland Department of Astronomy and Maryland Astronomy Center for Theory and Computation, College Park, MD 20742-2421, USA

analyzed with a typical duration of 3000 seconds. For each ObsID, we have computed an average Power Density Spectrum (PDS) with a 1 Hz resolution, using events recorded between 2 and 40 keV. The PDS are normalized according to Leahy et al. (1983), so that the Poisson noise level is constant around 2. The PDS is then blindly searched for excesses between 300 Hz and 1400 Hz using a scanning technique, as presented in Boirin et al. (2000). Each excess (at most the 2 strongest) is then fitted with a Lorentzian with three free parameters; frequency, full width at half maximum and amplitude (the Poisson noise level is fitted separately above 1500 Hz: a frequency domain free of QPOs). The amplitude of the Lorentzian is then converted into a root mean square (RMS), expressed in fraction of the total source count rate.

As a result of this systematic analysis, in 235 ObsIDs we detected a single QPO above a 3σ threshold (single trial), and in 27 ObsIDs we found two simultaneous QPOs (in one ObsID, two QPOs were detected but not simultaneously). The remaining ObsIDs, which contained no QPOs, were removed from the subsequent analysis. The quality factor and RMS amplitude versus frequency of all detected QPOs are shown in Fig 1. The patterns identified in other similar systems by Barret et al. (2006) are also seen for 4U 0614+09. In particular, in the quality factor versus frequency plot, lower and upper QPOs occupy two distinct regions: the quality factor of lower QPOs is larger than the quality factor of upper QPOs and the quality factor of the upper QPOs rises steadily with frequency (note that the scatter in the quality factor of the lower QPOs is in part because it is not corrected for the frequency drift within the ObsID). Similarly, there is a clear trend for the RMS amplitude of the upper QPOs to decrease with increasing frequency, whereas the RMS amplitude of the lower QPOs increases first before reaching a plateau (but see below).

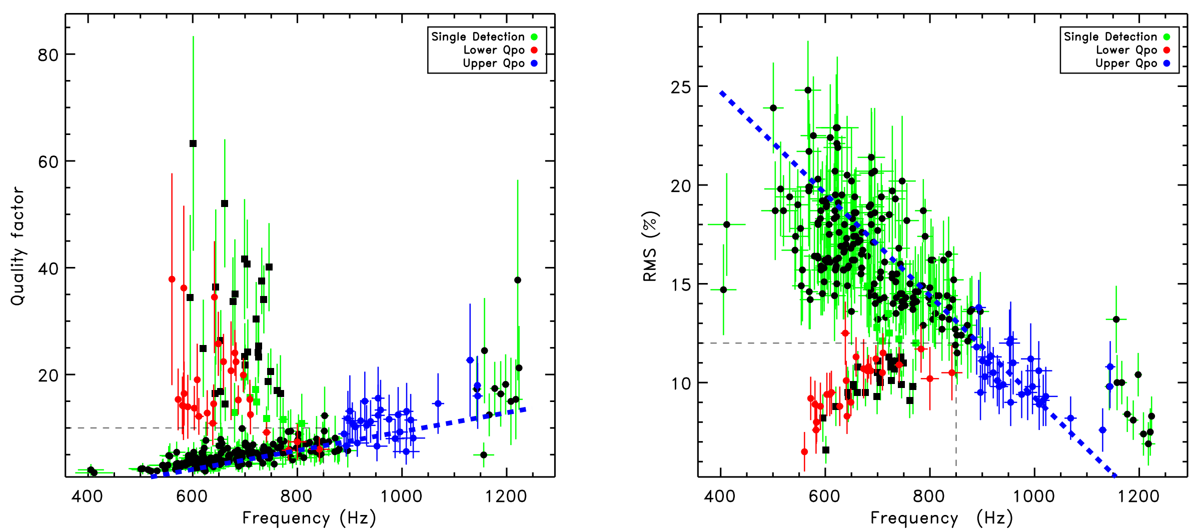

Fig. 1. Quality factor (left) and RMS amplitude (right) versus frequency of all detected QPOs. Each point represents the average over one ObsID. Red and blue filled circles are respectively for lower and upper twin QPOs. Black filled squares with green error bars are for single detected QPO identified as lower QPO. Black filled circles with green error bars are for single detected QPO identified as upper QPO.

2.1 On the 1330 Hz QPO

As can be seen from Fig 1, the highest QPO frequency detected in our systematic analysis is at about 1220 Hz; hence we do not detect any QPOs at frequencies similar to the one reported at 1330 Hz by van Straaten et al. (2000). This could be because our significance threshold of 3σ is close to the quoted single trial significance of the 1330 Hz QPO (3.5σ, van Straaten et al. 2000). We have repeated the analysis of van Straaten et al. (2000) for the ObsID 40030-01-04-00 in which the 1330 Hz QPO was reported (considering events from 5 keV to 97 keV). The strongest excess we could fit was at $\nu = 1328.4 \pm 26.5$ Hz, FWHM $= 46.2 \pm 70.2$ Hz, RMS $= 4.6 \pm 1.7$ %, hence with a low significance of 1.3 (the errors are computed with $\Delta\chi^2 = 1$). By looking at the count spectrum of the source, it dominates over the background up to 20 keV. We have thus computed a PDS using only events from 2 to 20 keV. The strongest excess of the PDS is no longer around 1330 Hz (a $\sim 1\sigma$ excess exists at 966 Hz). By initialising the parameters of the fit with the values of van Straaten et al. (2000), the Lorentzian parameters are badly constrained (as expected for a non significant excess) and discontinuity in the χ^2 curves prevents us from evaluating the errors. Restricting the energy range from 4 to 20 keV (to account for the fact that the RMS of the QPOs increases with energy) leads to a similar conclusion. From this, we conclude that the 1330 Hz QPO reported by van Straaten et al. (2000) was likely a statistical artifact.

2.2 *Average properties of kHz QPOs*

After having identified each QPO, either a lower QPO or an upper QPO, based on its position on Fig 1, one can align them using a shift-and-add technique (Mendez et al. 1998). This allows us to obtain a better description of their average properties; quality factor and RMS amplitudes. The results are presented in Fig. 2. This figure shows for the first time that the quality factor of the lower QPO starts by increasing with increasing frequency and then drops when it reaches a frequency around 700 Hz. Although this is not corrected for the frequency drift within each ObsID, it is worth mentioning that the maximum value of the quality factor of the lower QPO is only about 20, whereas in some other sources it goes up to 200 (see Barret et al. 2006 and Mendez 2006 for a discussion). At the same time, the quality factor of the upper QPOs increases steadily. The behaviour of the RMS amplitude of the lower QPO is consistent with other sources: it increases, saturates and then decreases with increasing frequency. On the other hand, for the upper QPO, there seems to be a discontinuity in the decrease of its amplitude around 1100 Hz. This effect, as well as the distribution of frequencies recovered from our analysis (revealing a possible gap around 1100 Hz) will be discussed in a forthcoming paper.

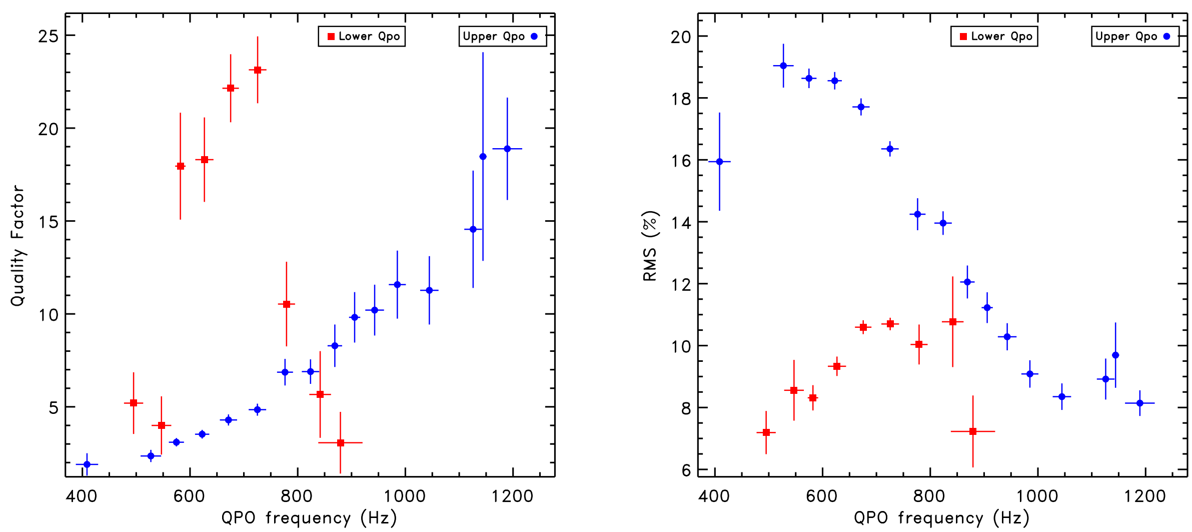

Fig. 2. Quality factor (left) and RMS amplitude (right) versus frequency after grouping the ObsIDs with QPOs of similar type and frequency (within a 50 Hz interval). Red filled squares are for lower QPO. Blue filled circles are for upper QPO. An abrupt drop of coherence of the lower QPO around 750 Hz is now revealed.

3 Conclusions

Based on a systematic analysis of all archival RXTE data for 4U 0614+09, the main results presented in this paper can be summarised as follows:

- We do not confirm the previous claim of a QPO at 1330 Hz. This is based on a thorough reanalysis of the observation from which the QPO was reported, and the fact that in our analysis, the highest frequency detected is at 1220 Hz; a value which is fully consistent with maximum frequencies observed in similar systems.

- We observe for the first time a drop of the quality factor of the lower QPO. Such a drop has been interpreted as being related to the oscillating region, crossing the innermost stable circular orbit, so our detection is consistent with that idea.

- The frequency difference is constant around 320 Hz, hence if the drop in quality factor for the lower kHz QPO is due to the ISCO, one can estimate the orbital frequency there. To do this we compute the maximum frequency of the lower QPO by extrapolating its quality factor to 0. This yields a limiting frequency of $\sim 920 - 930$ Hz, corresponding to an orbital frequency of 1250 Hz at the innermost stable orbit (ν_{ISCO}). As a safety check, we note that the maximum QPO frequency detected for the upper QPO is indeed lower than ν_{ISCO}. From this we can estimate the mass of the NS following the equation $\frac{M}{M_\odot} \approx \frac{\nu_{ISCO}}{2200\mathrm{Hz}} \times (1+0.75j)$ where $j = \frac{cJ}{GM^2} \sim 0.1-0.2$ is the dimensionless angular momentum of the star. This leads to a gravitational mass for the neutron star of 1.9 $M_\odot$, i.e. a relatively massive NS, but still consistent with realistic modern equations of state, which predict maximum masses for slowly rotating ($j << 1$) stars of $\sim 1.8 - 2.3$ $M_\odot$ (Akmal, Pandharipande & Ravenhall 1998; Lattimer & Prakash 2001; Klahn et al. 2006).

References

Akmal A., Pandharipande V. R., & Ravenhall D. G. 1998, PhRvC, 58, 1804

Barret, D., Olive, J.-F., & Miller, M. C. 2006, MNRAS, 370, 1140

Boirin, L., Barret, D., Olive, J. F., Bloser, P. F., & Grindlay, J. E. 2000, A&A, 361, 121

Ford, E., Kaaret, P., Tavani, M., Barret, D., Bloser, P., Grindlay, J. E., Harmon, B. A., Paciesas, W. S., & Zhang, S. N. 1997, ApJL, 475, L123+

Klähn T., Blaschke, D., Typel, S., van Dalen, E. N. E., Faessler, A.,Fuchs, C., Gaitanos, T., Grigorian, H., Ho, A., Kolomeitsev, E. E., Miller, M. C., Röpke, G., Trümper, J., Voskresensky, D. N., Weber, F., & Wolter, H. H. 2006, Phys. Rev. C, 74, 035802

van der Klis M. 2006, Advances in Space Research, 38, 2675

Lattimer J. M., & Prakash M. 2001, ApJ, 550, 426

Leahy, D. A., Darbro, W., Elsner, R. F., Weisskopf, M. C., Kahn, S., Sutherland, P. G., & Grindlay, J. E. 1983, ApJ, 266, 160

Mendez, M. 2006, MNRAS, 371, 1925

Mendez, M., van der Klis, M., van Paradijs, J., Lewin, W. H. G., Vaughan, B. A., Kuulkers, E., Zhang, W., Lamb, F. K., & Psaltis, D. 1998, ApJL, 494, L95

Mendez, M., & Belloni, T. 2007, MNRAS, 381, 790

Miller, M. C., Lamb, F. K., & Psaltis, D. 1998, ApJ, 508, 791

Strohmayer, T. E., Markwardt, C. B., & Kuulkers, E. 2008, ApJL, 672, L37

van Straaten, S., Ford, E. C., van der Klis, M., Mendez, M., & Kaaret, P. 2000, ApJ, 540, 1049

van Straaten, S., van der Klis, M., di Salvo, T., & Belloni, T. 2002, ApJ, 568, 912

SF2A 2008
C. Charbonnel, F. Combes and R. Samadi (eds)

TIME DEPENDENT MODELISATION OF TEV BLAZARS BY A STRATIFIED JET MODEL

Boutelier, T.[1], Henri, G. [1] and Petrucci, P-O.[1]

Abstract. We present a new time-dependent inhomogeneous jet model of non-thermal blazar emission. Ultra-relativistic leptons are injected at the base of a jet and propagate along it. We assume continuous reacceleration and cooling, producing a relativistic quasi-maxwellian (or "pile-up") particle energy distribution. The synchrotron and Synchrotron-Self Compton jet emissivity are computed at each altitude. Klein-Nishina effects as well as intrinsic gamma-gamma absorption are included in the computation. Due to the pair production optical depth, considerable particle density enhancement can occur, particularly during flaring states.Time-dependent jet emission can be computed by varying the particle injection, but due to the sensitivity of pair production process, only small variations of the injected density are required during the flares. The stratification of the jet emission, together with a pile-up distribution, allows significantly lower bulk Lorentz factors, compared to one-zone models. Applying this model to the case of PKS 2155–304 and its big TeV flare observed in 2006, we can reproduce *simultaneously* the average broad band spectrum of this source from radio to TeV, as well as TeV light curve of the flare with bulk Lorentz factor lower than 15.

1 Introduction

It is widely admitted that the blazar phenomenon is due to relativistic Doppler boosting of the non-thermal jet emission taking place in radio-loud Active Galactic Nuclei (AGN) whose jet axis is closely aligned with the observer's line of sight. Blazars exhibit very broad spectral energy distributions (SED) ranging from the radio to the gamma-ray band and dominated by two broad band components. In the Synchrotron Self Compton scenario (SSC), the lowest energy hump is attributed to the synchrotron emission of relativistic leptonic particles, and the highest one is attributed to the Inverse Compton process (IC) of the same leptons on the synchrotron photon field. Broad band observations of these objects are crucial to understand the jet physics and to put reliable constraints on jet parameters.

The most extreme class of blazars are the highly peaked BL lac sources (HBL), where the synchrotron/Inverse Compton components peak in the UV/X-ray/gamma-ray (GeV up to TeV) range. These objects are well known to be highly variable in all energy bands. Perhaps the most extreme example of this extraordinary variability behaviour has been caught by the HESS instrument with the big flare of PKS 2155–304 during summer 2006 (Aharonian et al. 2007).

In this case, the observed variability time scale (~ 200 sec) in the TeV range implies a minimum bulk Lorentz factor greater than 50 (Begelman, Fabian, & Rees 2008) assuming an homogeneous one zone model. However, such high values of the bulk Lorentz factor are in contradiction with constrains derived from other observational evidence (Urry & Padovani 1995; Henri & Saugé 2006 and references therein). Furthermore, one-zone models are unable to fit the entire spectrum, the low energy radio points being generally attributed to more distant emitting regions. We present here a new approach, unifying small and large scales emission regions: we consider that the radio jet is actually filled by the same particles originating from the high energy emitting region, at the bottom of the jet, that have propagated along it. We describe thus the emitting plasma by a continuous (although variable) particle injection, submitted to continuous reacceleration and radiative cooling. This model fits well into the two-flow framework originally proposed by Pelletier (1985) and Sol et al. (1989) where a non relativistic, but powerful MHD jet launched by the accretion disk, surrounds a highly relativistic plasma of electron-positron pairs propagating along its axis. The MHD jet plays the role of a collimater and an energy reservoir for the pair plasma, which is responsible for the observed broad band emission.

[1] Laboratoire d'Astrophysique de Grenoble–Université Joseph-Fourier/CNRS UMR 5571 –BP 53, F-38041 Grenoble, France

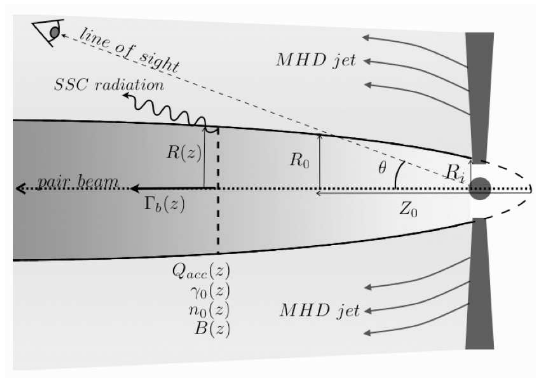

Fig. 1. Sketch of the jet geometry. See text for the signification of the different parameters.

2 Description of the model

2.1 Geometry of the model and particle energy distribution

We consider that the relativistic plasma propagates in a stationary funnel (associated to the last magnetic surface of the surrounding MHD jet) that we parametrize as a shifted paraboloid shape (power-law with an index ω). The magnetic field scales with the jet radius to the power $-\lambda$. We consider that the jet is continuously accelerating, starting from rest ($\Gamma_b = 1$ at $z = 0$) and reaching an asymptotic value $\Gamma_{b\infty}$ on a typical scale Z_0.

The MHD jet that surrounds the radiative pair plasma transfers its energy to the pairs via second order Fermi acceleration mechanism (particle-wave interaction). As a result of this acceleration mechanism, the energy distribution function (EDF) of the electron-positron plasma is assumed to be a relativistic maxwellian (or "pile-up") distribution (Saugé & Henri 2004 and references therein). As they propagate inside the structure, the particles lose energy via synchrotron and inverse Compton cooling. Particles are continuously re-heated by the surrounding MHD jet, via a Fermi II acceleration process. The acceleration rate $Q_{acc}(z)$ is parametrized as a power-law with an index $-\zeta$ and a normalisation factor Q_0. To avoid energy divergence, the heating is stopped after an altitude Z_c. The relativistic maxwellian's "temperature" γ_0 is determined by balancing radiative cooling and re-heating. Because of absorption of γ-ray photons via the pair creation process, new particles are created inside the jet, which yields to the increase of the particle flux $\Phi(z,t) = \int n(\gamma, z, t) S(z) \Gamma_b \beta_b c d\gamma$, where $S(z)$ is the surface of radial section of the jet. This quantity is computed via a continuity equation that takes into account the pair creation term. Fig. 1. displays the different parameters used in the model. More details about the parametrisation we use can be found in Boutelier et al. (2008).

2.2 The jet spectrum

We compute the emissivity at each altitude in the jet by assuming a SSC process for the radiative mechanism. The total intensity of the jet is then determined by integrating the emissivity all along the jet. Once injected at the base of the jet, the particles contribute first to the high energy part of the jet SED. As they propagate, their emissivity peaks progressively at lower energy, producing the low energy part of the spectrum. The spectral shape of the whole SED is not controlled by the local particle energy distribution (which is always locally a narrow pile-up), but rather by the z-dependencies of the jet radius, the magnetic field, and the acceleration rate. A constant injection rate would lead to a stationary emission pattern, which would be rather easy to fit. In reality, the observed instantaneous spectra are a complicated convolution of the whole history of the jet, keeping the memory of the whole past injection pattern. Boutelier et al. (2008) describes a procedure to extract the physical parameters of the jet from observed spectra, despite the fact that they do not correspond to a simple steady-state of the jet.

Table 1. Model parameters of the flaring and quiescent state. During the flaring state, the flux of injected particles varies between the indicated minimum and maximum values, following the injection pattern displayed in Fig. 2. The other parameters remain fixed. R_i, R_0, Z_0, Z_c are in unit of $10^{14}cm$ and are displayed on Fig. 1.

STATE		$\Phi(Z_i)$ $[10^{42}s^{-1}]$	$\Phi(Z_0)$ $[10^{42}s^{-1}]$	Q_0 $[s^{-1}]$	$\Gamma_{b\infty}$	R_i	R_0	Z_0	Z_c	B_0 $[G]$	ω	λ	ζ
	Max	2.09	70.1										
flaring	Aver.	1.84	24.4	6.5									
	Min	1.16	2.33		15	1.1	1.78	20	5×10^7	5	0.2	1.9	1.27
quiescent		1.16	1.55	2.5									

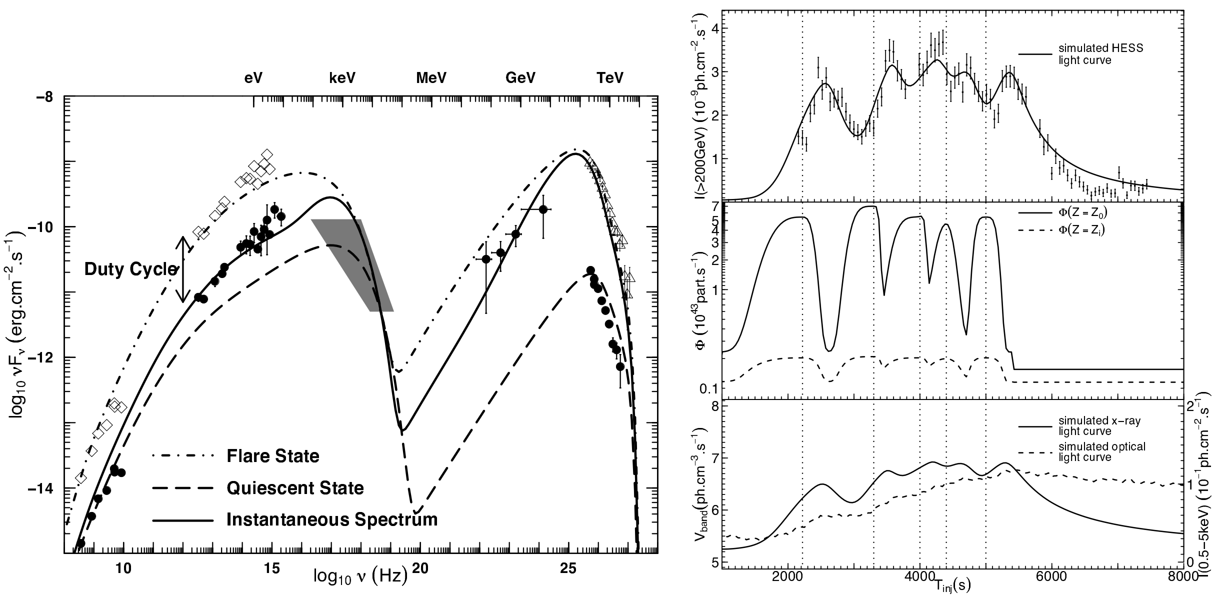

Fig. 2. Left : Fit of PKS 2155–304 data. **Filled dots:** average archival data (see text). **Empty triangles:** average HESS data from the big flaring night. **Empty diamonds:** "fake flaring" state low energy points **Shaded area:** enveloppe of archival X-ray data from BeppoSAX, SWIFT and XMM-Newton. **Dot-dashed line:** best fit of the " average fake flaring" spectrum. **Dashed line:** fit of the quiescent (∼average) spectrum. **Solid line:** example of an instantaneous **simulated spectrum**. **Right**: **Upper panel**: HESS light curve above 200 GeV superimposed with the model (solid line). **Middle panel**: time dependent particle injection function used in the simulation. **Lower panel**: predicted light curves in X-ray (dashed line, left y-scale) and optical (dot-dashed line, right y-scale). The dotted lines mark the maximum of the different bursts of the injection function.

3 Application to PKS 2155–304

We have tested our model to the big flare event observed by HESS in July 2006 in PKS 2155–304 . We apply the method described in Boutelier et al. (2008) to the SED of PKS 2155–304. The average spectrum of PKS 2155–304 in the low frequencies range ($\leq 10^{15}$ Hz), is constructed using archival data from the HEASARC archive website (http://heasarc.gsfc.nasa.gov/docs/archive.html). Based on the activity detected by HESS, we estimate that the duty-cycle is around 10%. Then to construct the "fake flaring" spectrum of this source, i.e. the spectrum expected if the jet was always in a flaring state, we combine the HESS data with the radio-to-optical ones corrected by a factor 10 (dot-dashed line in left plot of Fig. 2).

An average "fake flaring" spectrum is shown in the left side of Fig. 2 in dot-dashed line. The corresponding best fit model parameters are reported in Tab. 1. Interestingly we only need a Doppler factor $\Gamma_b = 15$ which is significantly below the values of ~ 50 inferred from one-zone model (Begelman, Fabian, & Rees 2008). The best fit parameters of the TeV quiescent state (derived from averaged H.E.S.S spectrum in Aharonian et al. 2005) are also reported in Tab. 1 and the solution has been overplotted in the left side of Fig. 2 (dashed line).

To reproduce the observed H.E.S.S. light curve during the big-flare event, we use an injection function $\Phi(z = 0, t)$ that is the sum of five "generalized Gaussian" shape, similar to the analysis made in Aharonian et al. (2007). Before the flare, the flux of particles $\Phi(z = 0, t)$ is assumed to be a crenel function that oscillates between quiescent and flaring states in agreement with the source duty cycle. At the right top of Fig. 2, we have reported the HESS light curve and the simulated one (solid line). The agreement between the simulated and the reported HESS light curve is very good. The instantaneous spectrum overplotted in solide lines on the left side of Fig. 2 agrees with the radio to TeV spectrum observed during the burst.

4 Discussion

Our time-dependent inhomogeneous jet model succeeds in reproducing *simultaneously* the broad band (from radio to TeV) spectrum of PKS 2155–304 as well as the TeV light curve during the big flare event of July 2006. The key idea of the method is to decompose the blazar spectrum in "quiescent", low luminosity states, and "flaring", high luminosity states. The high energy part of the spectrum, coming from small-scale inner regions, is assumed to be, at any time, in one of these pure states. On the other hand the low energy part is a convolution over a large scale of the past history of the jet : it is thus rather a time-averaged spectral state mixing quiescent and flaring states in proportions given by the source "duty-cycle". Moreover we do not require two different populations of emitting particles like in other models (e.g. Katarzyński et al. 2003) but simply a continuous (although variable) injection of particles at the base of the jet that propagate along the jet structure. Pair production plays an important role to amplify the initial variation, as can be seen with the variation of the particle flux along the jet during the flaring state (see Tab. 1 and the right side of Fig. 2 (middle)): the pair current is amplified by a factor 30 at the end of the jet, while the initial current varies only by a factor 2.

The model can also predict light curves at different wavelengths. As an example, the x-ray (2-10 keV) and optical (V band) light curves expected during the TeV flare have been plotted at the right bottom of Fig.2. The x-ray luminosity exhibits almost simultaneous variations but with a lower amplitude (about 5 times smaller). On the other hand, the optical light curve shows a very different behavior, increasing all along the flare. This is due to to the large size of the optical emitting region that plays the role of a low pass filter. Consequently, the optical luminosity integrates the recent past history of the jet. These results are compatible with simultaneous multiwavelength observations made during the “Chandra night” (Costamante, private communication).

In the present work, we do not specify the origin of the variability. Obviously, other plasma parameters can vary in addition to the injection density N_0. Most likely, variability can be triggered by a change in the acceleration rate described by Q_{acc}. In a plausible scenario, long term (year scale) variability implying the succession of quiescent and active states could be attributed to variations in the accretion rate, wheras the short (minute-scale) flares would be attributed to the instability to pair creation that develops only when the initial particle density is close to a critical threshold.

References

Aharonian, F., et al. 2007, ApJL, 664, L71

Aharonian, F., et al. 2005, A&A, 430, 865

Begelman, M. C., Fabian A. C., & Rees M. J. 2008, MNRAS, 384, L19

Boutelier, T., Henri, G., & Petrucci, P.-0. 2008, MNRAS, L102+

Henri, G., & Saugé, L. 2006, ApJ, 640, 185

Katarzyński, K., Sol, H., & Kus, A. 2003, A&A, 410, 101

Pelletier, G. 1985, in Plasma turbulence and Astrophysical Objects, Société Française de Physique (SFP)

Saugé, L., Henri, G. 2004, ApJ, 616, 136

Sol, H., Pelletier, G., & Asseo, E. 1989, MNRAS, 237, 411

Urry, C. M., & Padovani, P. 1995, PASP, 107, 803

SF2A 2008
C. Charbonnel, F. Combes and R. Samadi (eds)

ULTRA HIGH ENERGY COSMIC RAY HORIZONS

Busca, N.G.[1]

Abstract. We calculate the horizons of ultra high energy cosmic rays assuming different nuclei primaries ranging from proton to iron at ultra high energies ($6 \cdot 10^{19}$). We show that sources of ultra high energy protons and heavy nuclei can originate from distances up to $\sim$ 180 Mpc, while low and intermediate mass nuclei can only originate in the local universe ($<$ 50 Mpc.)

1 Introduction

Recent results from the Pierre Auger Observatory (Abraham et al. 2007) show a significant correlation between arrival directions of cosmic rays and nearby extragalactic objects, implying that the cosmic ray flux at ultra high energies is anisotropic. These results constitute evidence for the hypothesis that the propagation of ultra high energy cosmic rays is mainly constrained by photo-pion interactions with the cosmic radiation background, or, equivalently, that their flux is suppressed due to the GZK effect.

The observed anisotropy should be a reflection of the distribution of their sources in the nearby universe. In this work we use the Monte Carlo propagation code developed in (Allard et al. 2005) to calculate the distances that contain a given fraction of the sources of cosmic rays that arrive at Earth with an energy above a given energy threshold (E_{th}). We refer to these distances as the "horizon", and we calculate them as a function of E_{th}, for different source primaries.

2 Method

Consider the *integrated* cosmic ray flux at Earth, $d\mathcal{F}(E_{th}, z)$, produced by sources with a redshift between z and $z + dz$, and a given fraction f. We define the horizon $H(E_{th}, f)$ as the distance for which the following relation is satisfied:

$$f = \frac{\int_0^{z_{hor}} dz \frac{d\mathcal{F}(E_{th},z)}{dz}}{\int_0^{\infty} dz \frac{d\mathcal{F}(E_th,z)}{dz}} \tag{2.1}$$

The horizon is then readily obtained by $H(E_{th}, f) \simeq 4.22 \cdot 10^3 z_{hor}(E_{th}, f)$. We consider energies above 60 EeV, energy at which Auger observes the onset of anisotropy.

The evaluation of equation 2.1 is done by means of the Monte Carlo nuclei propagation code developed in (Allard et al. 2005). The code propagates nuclei from their sources, following all nuclear secondaries resulting from interactions with the radiation backgrounds. In the case of protons, the dominant interaction in the considered energy range is phtopion production off CMB photons. In the case of heavier nuclei, the dominant interaction is via the delta resonance which results in the "erosion" of the primary by loss of one or several nucleons.

We considered a power law energy distribution at injection with spectral indices ranging from -3 to -2. The assumed source distribution is homogeneous and redshift independent (at the energies considered only contribution from sources up to redshift 0.1 are relevant). We assumed nuclear primaries ranging from proton to iron.

[1] Laboratoire d'Astroparticules at Cosmologie,10, rue Alice Domon et Lonie Duquet, 75205 Paris Cedex 13

3 Results and Discussion

The interactions of protons and compound nuclei with the CMB are different and we discuss them separately. At the energies considered, the main energy loss mechanism is dominated by pion production for protons and by giant delta resonance interactions for nuclei. The interaction length, however, is dominated in both cases by pair production. Since this interactions are of very low inelasticity they will be ignored in the subsequent discussion.

The effects of photopion interactions on the propagation of protons are well known since (Greisen 1966 and Zatsepin and Kusmin 1966) and have been extensively studied in, e.g., (Berezinsky 2004). Above the threshold for pion production against CMB photons (at $\sim 6 \cdot 10^{19} eV$) the interaction length reduces to around 10 Mpc. These interactions are of large inelasticity ($\sim 20\%$).

The total interaction lengths for compound nuclei is dominated by delta resonance interactions with low density infra-red photons up to a threshold energy where interactions with the high density CMB photons become dominant. The cross section for the delta resonance process is approximately proportional to A. This fact, together with the fact that the energy of a photon in the rest frame of the nuclei is proportional to the gamma factor of the nuclei in the lab frame (Γ), implies that the interaction lengths for two nuclei with the same Γ factor differ by a factor given by the ratio of their mass numbers (the smaller interaction length corresponding to the heavier nucleus).

The first energy range dominated by interactions with infra-red photons corresponds to Γ smaller than $5 \cdot 10^9$. In this range the interaction length decreases from over 4Gpc$/A$ at $\Gamma \sim 5 \cdot 10^8$ to about $500/A$ Mpc at $\Gamma \sim 5 \cdot 10^9$.

At $\Gamma \sim 5 \cdot 10^9$ interactions with the denser CMB photons become dominant. Above this threshold, the interaction length decreases much more drastically, becoming smaller than 1Mpc$/A$ for $\Gamma \sim 10^{10}$. Note that while this Γ corresponds to an energy of $\sim 4 \cdot 10^{19}$ eV for He, it corresponds to an energy of $\sim 2 \cdot 10^{20}$ eV for Fe. Above this threshold energy, the universe becomes opaque for compound nuclei and photodisintegration down to pure nucleons is completed in a few megaparsecs.

These qualitative conclusions reflect in the horizons plotted in figures 1(left) and 1(right). Both figures show the horizon as a function of energy for two cases: figure 1(left) corresponds to requiring a given composition *at the sources* while figure 1(right), to requiring a given composition *at the Earth*. The displayed horizons correspond to a spectral index that fits the ultra high energy spectrum for each assumed composition. This implies spectral indices in the range between -2.3 and -2.0.

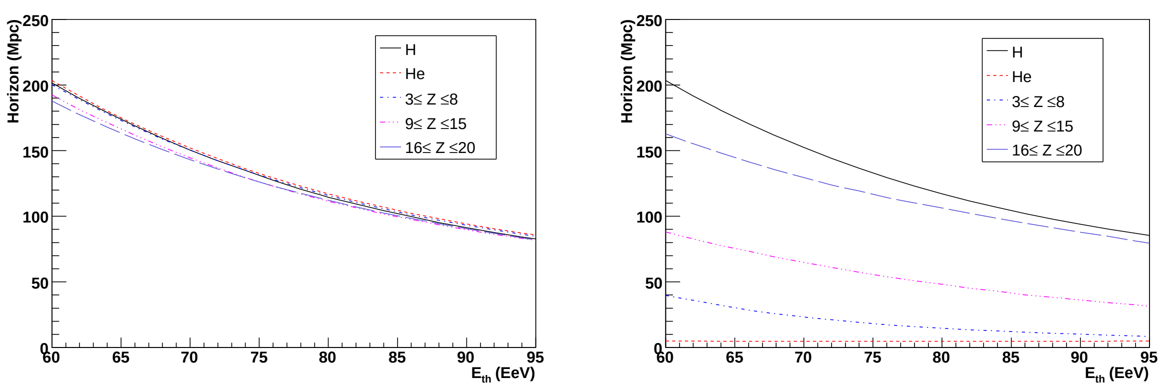

Fig. 1. Ultra high energy horizons. **Left**: assuming the indicated composition at the source (equal fraction of primaries in the indicated Z range). **Right**: requiring the indicated composition at Earth.

Figure 1(left) illustrates the fact that horizons are depend very little on source composition in the case of no particle identification at Earth. This observation is due to two facts: firts, light and intermediate nuclei photodisintegrate very quickly so the analysis reduces to the proton case and second, heavy nuclei have horizons that are very similar to those of protons. These two facts are evident in figure 1(right). Light and intermediate nuclei have horizons ranging between 4 Mpc for He and less than 90 Mpc for Si. The fact that heavy nuclei have a similar horizon to that of proton is a rather remarkable coincidence. The interaction processes in this energy range are different (photopion for proton and delta resonance for nuclei) as well as the responsible photon backgrounds (CMB for protons and infra-red for nuclei). The resulting interaction length is, however, of the same order of magnitude, resulting in similar propagation features.

4 Conclusions

In this work we calculate the horizons for ultra high energy cosmic rays in the energy range between 60 EeV and 100 EeV . They are defined as the distance to the Earth that contains a given fraction of their sources. We considered the case of different composition at the source and at the Earth.

We find that the horizons are very similar independent of the source composition. This is a consequence of the fact that light and intermediate nuclei photodisintegrate very quickly, resulting in an equivalent input flux which is almost composed of pure protons, and that heavy nuclei have a horizon which is very similar to that of proton. Their size evolve with energy, and is around 200 Mpc at 60 EeV and reduces to around 100 Mpc at 100 EeV.

However, if particle if particles can be identified at Earth, the results have a different interpretation. For example, for He particles arriving at Earth with an energy above 60 EeV, 90% of their sources are within 4 Mpc. For CNO or other heavier particles, up to Si, arriving at Earth with an energy above 60 EeV, 90% of the source are within 90 Mpc.

If particle identification ar Earth is ever possible, and the ultra high energy cosmic ray flux turned out to be dominated by light and intermediate nuclei, the perspectives for charged particle astronomy become extremely interesting: the flux is dominated by very nearby sources (at distances up to tens of Mpc), which should be few (unless source density is very high) and easy to identify even if deflections are not small.

References

Abraham, C. et al. 2007, Science, 318 (5852), 896

Allard D., Parizot E., Khan E., Goriely S., & Olinto A.V. 2005, A&A Letters 443, 29

Berezinsky, V.S., Grigorieva, S.I., & Hnatyk, B.I. 2004, Astropart. Phys., 21, 617

Greisen, K. 1966, Phys. Rev. Lett., 16, 748

Zatsepin, G.T., & Kuzmin, V.A., 1966, Sov. Phys. JETP, Lett 4, 78

SF2A 2008
C. Charbonnel, F. Combes and R. Samadi (eds)

PROBING PULSAR WINDS WITH GAMMA-RAY BINARIES

Cerutti, B.[1], Dubus, G.[1] and Henri, G.[1]

Abstract.
We report on our current studies of high energy radiation from gamma-ray binaries, systems which emit most of their energy above an MeV. Gamma-gamma absorption and anisotropic inverse Compton scattering processes were previously investigated in the context of the young pulsar wind scenario. Here, we report on the gamma-ray emission that would originate from the unshocked pulsar wind itself, instead of originating at the shock between pulsar and stellar wind. The comparison of the theoretical spectral energy distributions with EGRET, HESS and MAGIC observations constrains the particle energy and the shock geometry. The classical pulsar wind model appears incompatible with the data. Alternative models such as the striped pulsar wind may be favored.

1 Introduction

Three gamma-ray binaries have been firmly detected in the TeV energy domain: PSR B1259-63 (Aharonian et al. 2005b), LS 5039 (Aharonian et al. 2005a) and LSI +61°303 (Albert et al. 2006). These systems are composed of a massive O/Be type star and a compact object and emit most of their energy above an MeV. A young 48 ms pulsar was detected in PSR B1259-63 (Johnston et al. 1992) but the nature of the compact object in the other two binaries is still undecided. Lack of accretion signs and similarities with PSR B1259-63 favor the presence of a young pulsar (Maraschi & Treves 1981; Martocchia et al. 2005; Dubus 2006b). This hypothesis provides a common scenario to explain the emission from these systems. The gamma-ray emission would be due to particle acceleration at the collision site between the relativistic pulsar wind and the wind of the massive star. Pulsar wind nebula (PWN) of young plerions are known to emit high and very high energy (see the contribution by F. Dubois in this volume). In gamma-ray binaries, the external photon density is high ($\sim 10^{14}$ ph/cm^3 for LS 5039). An intense gamma-ray flux is expected due to inverse Compton scattering of the stellar photons onto the electrons from the PWN. Because of their tight orbits, gamma-ray radiation can be used to probe the pulsar wind at very small scales (0.01-0.1 AU to be compared with isolated PWN size $\sim$ 0.1 pc). In the classical model of the Crab nebula (Rees & Gunn 1974; Kennel & Coroniti 1984), the pulsar wind nebula is described as being composed of an *unshocked* relativistic cold wind expanding freely until the ram pressure is balanced by the surrounding medium. In the *shocked* region, particles are ramdomized and accelerated. High energy emission from the shocked pulsar wind was previously investigated for LS 5039 and constraints on the magnetic field, the particle distribution and the total energy injected were formulated at the termination shock (Dubus, Cerutti & Henri 2008). According to the pulsar wind model, high energy emission is expected to originate from the region upstream the shocked region as well. We investigate the theoretical spectral signature from the unshocked pulsar wind in gamma-ray binaries and compare it with observations.

2 The unshocked pulsar wind

The rotation of a highly magnetized compact star induces huge electric fields at the surface, sufficiently strong to inject and accelerate electrons and ions into the magnetosphere. Interactions between the magnetic field and the electrons and pair cascading produce a relativistic wind of electrons-positrons, released beyond the light cylinder. The model of plerions PWN describes the unshocked pulsar wind as being isotropic, radial and

[1] Laboratoire d'Astrophysique de Grenoble, UMR 5571 CNRS, Université Joseph Fourier, BP 53, 38041 Grenoble, France

monoenergetic with a bulk Lorentz factor $\gamma_0 \sim 10^6$ far from the light cylinder. The magnetic energy density is assumed to be entirely converted into the kinetic energy of the particles in the wind. The magnetic field is thought to be frozen into the plasma of pairs. Consequently, no synchrotron radiation is expected from this region. However, inverse Compton scattering of stellar photons onto the relativistic electrons is still possible. Previous investigations of the inverse Compton signature from the unshocked pulsar wind were carried out by Bogovalov & Aharonian (2000) for the Crab pulsar and by Ball & Kirk (2000) for the system PSR B1259-63 and found a typical line-like spectrum. Here, we look at the emission from a truncated pulsar wind at a distance R_{shock} averaged along the orbit for different injected bulk Lorentz factor γ_0 in gamma-ray binaries.

3 The Compton emission line

3.1 A line-like signature

Because of the relative position of the massive star, the pulsar and the observer, the inverse Compton emission is highly anisotropic. Spectral calculations are based on the anisotropic inverse Compton scattering equations derived in Dubus, Cerutti & Henri (2008). Ultra-relativistic electrons emit most of their radiation in a narrow cone of semi-aperture angle $1/\gamma_e \ll 1$ due to boosting effects. Assuming the wind expands radially, the observer sees only the emission from the electrons moving toward him. The pulsar wind is observed as a point-like gamma-ray source.

Figure 1 presents computed spectra from a monoenergetic pulsar wind with $\gamma_0 = 10^5$ applied to LS 5039, taking into account the inverse Compton cooling of the pairs and ignoring gamma-gamma absorption. Spectra present a typical sharp peak at an energy which depends on the bulk Lorentz factor γ_0 and whose amplitude on the size of the emitting region R_{shock}. At the superior conjunction (left panel), Compton cooling is efficient because electron/photon interaction is almost head-on. For small emitting region (orbital separation $d \gg R_{shock}$) the pairs do not have enough time to radiate before reaching the shock, producing less gamma-rays. When the region is extended enough, pairs can cool down efficiently and the amplitude of the spectrum attains a maximum value set by the total injected power into the wind L_p. Cooled electrons then start to contribute to the low energy tail in the scattered spectrum. Details can be found in Cerutti, Dubus & Henri (2008).

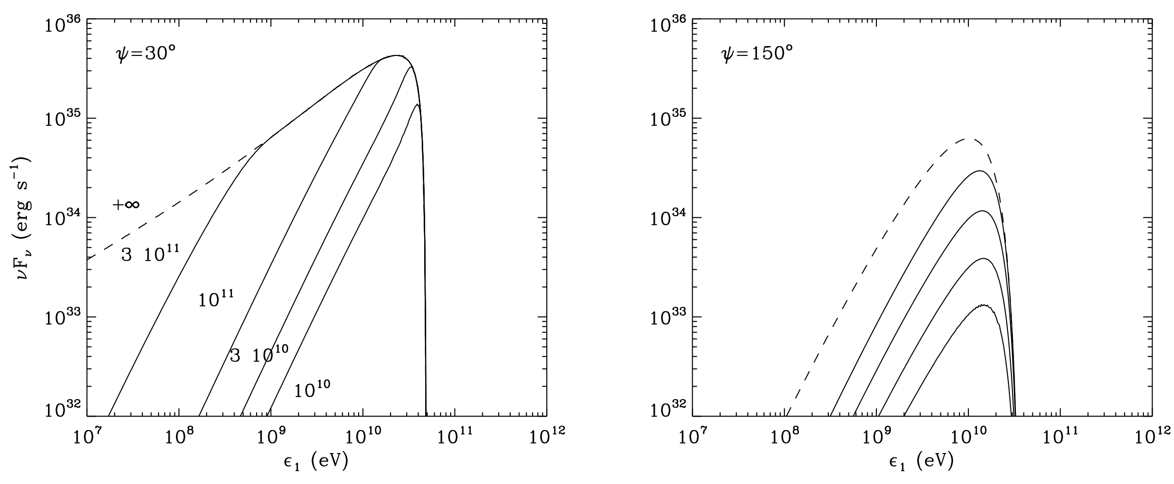

Fig. 1. Spectrum from the unshocked pulsar wind applied to LS 5039 with $\gamma_0 = 10^5$ and $L_p = 10^{36}$ erg/s. Spectra are calculated at the superior (left panel) and inferior (right panel) conjunctions for different PWN size $R_{shock} = 10^{10}$ (bottom), 3 10^{10}, 10^{11}, 3 10^{11} cm and $+\infty$ (dashed line), where ψ is the viewing angle massive star-pulsar-observer.

3.2 Observational constraints

The intense photon density available in gamma-ray binaries produces a strong line-like signature at every orbital phases in the complete spectral energy distribution. Figure 2 presents computed spectra for LS 5039 averaged along the orbit, taking into account gamma-gamma absorption calculated in Dubus (2006a). The size of the compact PWN depends on the ratio of the flux wind momentum of the two stars. The orbital parameters and the mass loss rate inferred from optical observations of the massive star suggest a likely size for the nebula of 10% of the orbital separation, assuming a pulsar luminosity of $L_p = 10^{36}$ erg/s.

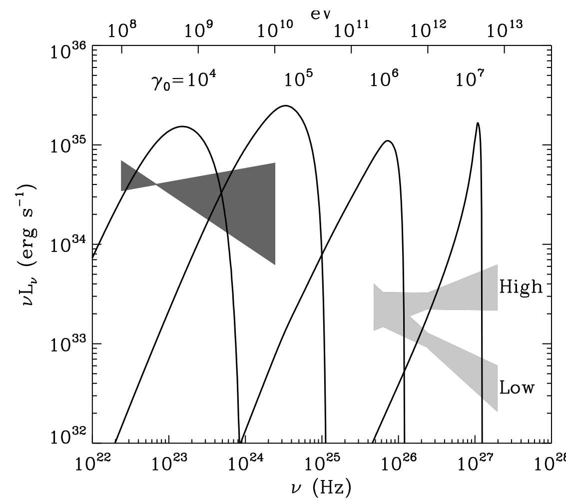

Fig. 2. Orbital averaged spectra for LS 5039 and comparison with EGRET (dark bowtie) and HESS (light bowtie) observations. The pulsar luminosity is set at $L_p = 10^{36}$ erg/s, the nebula size at $R_{shock}/d = 0.1$ and the bulk Lorentz factor at $10^4 - 10^7$.

If we stick to the cold pulsar wind model, the contribution from the unshocked pulsar wind should be a significant contributor to the observed flux. Comparison with EGRET and HESS observations (Hartman et al. 1999; Aharonian et al. 2006) constrains the Lorentz factor to a few 10^5 or $\gamma_0 > 10^7$. Stronger limits are expected with future GLAST, HESS-2 or CTA measurements.

Several possibilities may reduce this emission to a level consistent with observations. A reduction of the total injected power would diminish the amplitude of the peak. This hypothesis is not viable since it would entail a diminution of the shocked pulsar wind emission as well. A smaller nebula size would also decrease the contribution of the peak but measurements of the stellar wind parameters (McSwain et al. 2004) do not seem to support this possibility. Moreover, a stronger magnetic field would be expected at the collision site, inhibiting the formation of TeV gamma-rays. Another possibility to consider is that the pulsar wind is anisotropic as deduced from X-rays observations of several plerions. A smaller emission is expected if the pulsar has a more pole-on orientation with respect to the observer. The probability to observe the effect of such an anisotropy remains small ($\sim 5\%$ for each system). Alternatively, the monoenergetic assumption of the unshocked pulsar wind may be incorrect. An injected power-law distribution for the electrons gives spectra difficult to distinguish from the shocked component (e.g. Sierpowska-Bartosik & Torres 2008).

4 The striped wind: a promising alternative?

The *striped wind* is a more realistic model to describe the pulsar wind of an oblique rotator (see the contribution of J. Pétri in this volume). A striped current sheet separates the opposite magnetic field lines originating from the opposite magnetic poles of the neutron star. The alternating magnetic field could be dissipated and accelerate particles close to the equatorial plane. Independently of the dissipation process considered, an upper limit of the Lorentz factor can be formulated based on a causality condition (Arons 2008). Dissipation will occur if the associated timescale t_{diss} is smaller than the time for a stripe to reach the termination shock region t_{flow}. The condition $t_{diss} < t_{flow}$ is fulfilled if $\Gamma < \sqrt{\beta_{eff} R_{shock}/R_{lc}}$, where β_{eff} quantifies the efficiency of the dissipation process and R_{lc} is the radius of the light cylinder. In gamma-ray binaries $R_{shock}/R_{lc} \sim 10^4$ so that if the bulk Lorentz factor of the pulsar wind $\Gamma > 100$, the wind does not have enough time to dissipate. Hence it remains highly magnetized up to the shock, reducing the observational signature of the unshocked wind. Particle-in-cells simulations tend to show that the magnetic energy density is converted into ultra-relativistic particles at the termination shock (Pétri & Lyubarsky 2007). The conditions in the shocked region seem unchanged compared with the classical picture. Further theoretical and numerical works are necessary to predict accurate observational features from the striped pulsar wind. This model remains a promising alternative to understand the high energy emission from the unshocked pulsar wind in gamma-ray binaries.

5 Conclusion

Gamma-ray binaries are particularly interesting objects for the study of pulsar winds at very small scales. The stellar photons act as a probe of the inner structure of pulsar winds. Scattered photons at high energy to the observer betray the physical conditions at the collision site and upstream the termination shock. The study of the emission from the unshocked pulsar wind appears incompatible with the classical model of pulsar wind to the benefit of alternative models such as the striped wind.

References

Aharonian, F.A., et al. (HESS collaboration) 2005a, Science, 309, 746
Aharonian, F.A., et al. (HESS collaboration) 2005b, A&A, 442, 1
Aharonian, F.A., et al. (HESS collaboration) 2006, A&A, 460, 743
Albert, J., et al. (MAGIC collaboration) 2006, Science, 312, 1771
Arons, J. 2008, in 40 Years of Pulsars, ASP Conf. Proc., 983, 200
Ball, L., & Kirk, J.G. 2000, Astroparticle Physics, 12, 335
Bogovalov, S.V., & Aharonian, F.A. 2000, MNRAS, 313, 504
Cerutti, B., Dubus, G., & Henri, G. 2008, A&A, 488, 37
Dubus, G. 2006a, A&A, 451, 9
Dubus, G. 2006b, A&A, 456, 801
Dubus, G., Cerutti, B., & Henri, G. 2008, A&A, 477, 691
Hartman, R.C., et al. 1999, ApJS, 123, 79
Johnston, S., et al. 1992, ApJ, 387, L37
Kennel, C.F., & Coroniti, F.V. 1984, ApJ, 283, 694
Maraschi, L., & Treves, A. 1981, MNRAS, 194, 1L
Martocchia, A., Motch, C., & Negueruela, I. 2005, A&A, 430, 245
McSwain, M.V., et al. 2004, ApJ, 600, 927
Pétri, J., & Lyubarsky Y.E., 2007, A&A, 473, 683
Rees, M.J., & Gunn, J.E. 1974, MNRAS, 167, 1
Sierpowska-Bartosik, A., & Torres, D.F. 2008, MNRAS submitted [arXiv:0801.3427]

SF2A 2008
C. Charbonnel, F. Combes and R. Samadi (eds)

SEARCH FOR CLUMPY DARK MATTER IN THE GALAXY WITH H.E.S.S.

Charbonnier, A.[1], Maurin, D.[1], Brun, P.[2], Farnier, C.[3], Glicenstein, J.-F.[2], Jacholkowska, A.[1], Martineau-Huynh, O.[1], Moulin, E.[2], de Naurois, M.[1], Tavernet, J.-P.[1], Vincent, P.[1] and Vivier, M.[2]

Abstract. According to N-body simulations, dark matter should be distributed in the Galaxy into structures of various masses. We have modelled the distribution of these sub-structures, so as to produce a map of the expected γ-ray flux. The identification of this signal by H.E.S.S. is a challenge, because it is shadowed by the hadronic and electronic backgrounds. The most massive sub-structures of the galactic halo are the dwarf spheroidal galaxies. We present a preliminary analysis of H.E.S.S. observations on Carina dwarf to put constraints on WIMP models.

1 The H.E.S.S. experiment

The H.E.S.S. experiment, dedicated to the observation of very high energy γ-rays, consists of an array of four telescopes located in Namibia. The system is fully operational since 2004. When a high energy particle enters the atmosphere, it gives birth to an atmospheric shower of particles with velocities higher than the speed of light. Cerenkov light is thus emitted and detected by the H.E.S.S. telescopes.

The main challenge lies in the discrimination between photons and hadrons, and the reconstruction of the energy and the direction of the incoming photons. The energy threshold is around 100 GeV. The success of H.E.S.S. relies on the stereoscopy and the characteristics of the cameras, which combine a good time resolution, high sensitivity, high granularity and a large field of view (5°).

2 Dark matter distribution

Many astrophysical observations as well as cosmological studies converge to the Λ-CDM paradigm (cosmological constant and cold dark matter). Dark matter particles are expected to be stable, massive, neutral and weakly interacting (the so-called WIMPs). They cannot be explained by the standard model of particle physics. Two candidates are often considered: the neutralino which is the lightest stable particle coming from the minimal supersymmetric models (MSSM) and the lightest Kaluza Klein (KK) particle from extra-dimension models.

N-body simulations and analytical frameworks have provided a description of the distribution of cold dark matter. Our Galaxy may be settled in a dark matter halo which contains a large amount of sub-structures. We modelled the distribution of these clumps in the Galaxy with a Monte Carlo approach, with the following main features (see Lavalle et al. 2008): i) the mass of the clumps ranges between 10^{-6} and 10^{12} $M_\odot$; ii) the mass and the spatial distributions are assumed to be not correlated; iii) the normalisation is constrained by astrophysical observations (number of satellite galaxies in the Milky Way and estimation of the total Galactic mass according to the velocity dispersion of stars); iv) the density profile in each clump is identical on all scales.

3 Search for dark matter

WIMPs are expected to self-annihilate and produce a γ-ray flux Φ_γ along the line of sight ψ:

$$\frac{\mathrm{d}\Phi_\gamma}{\mathrm{d}E_\gamma}(E_\gamma, \psi, \Delta\Omega) = \frac{\mathrm{d}\Phi^{\mathrm{PP}}}{\mathrm{d}E_\gamma}(E_\gamma) \times \Phi^{\mathrm{astro}}(\psi, \Delta\Omega) \ . \tag{3.1}$$

[1] LPNHE, Université Pierre et Marie Curie Paris 6, Université Paris Diderot Paris 7, IN2P3/CNRS, F-75252 Paris, France
[2] IRFU/DSM/CEA, CE Saclay, F-91191 Gif-sur-Yvette, Cedex, France
[3] LPTA, Université Montpellier II, CNRS/IN2P3, CC70, Place Eugène Bataillon, F-34095 Montpellier Cedex 5, France

E_γ is the photon energy and $\Delta\Omega$ the angular resolution of the instrument. The first term $\Phi^{\rm PP}$ is related to the particle physics model describing WIMP annihilation, and the second term $\Phi^{\rm astro}$ takes into account the dark matter distribution (clumps of the Galaxy and dwarf spheroidal galaxies).

3.1 Sub-structures of dark matter

Fig. 1 (left panel) presents one realisation of the sky map obtained for $\Phi^{\rm astro}$, considering only sub-structures of the Galaxy. It reveals the presence of spots on top of a diffuse background. With an optimistic model for particle physics (Fornengo et al. 2004), the expected flux from these foreground sub-halos is about $\sim 6.1 \cdot 10^{-13}\ \gamma\ {\rm cm}^{-2}\ {\rm s}^{-1}$, below the H.E.S.S. sensitivity. Moreover, the clump position is unknown, the hadronic and electronic diffuse backgrounds are important, and the smooth dark matter contribution should also be added to the sky map.

3.2 Dwarf spheroidal galaxies

Dwarf spheroidal galaxies are dark matter-dominated objects, according to velocity dispersion measurements. They are located off-galactic plane and are expected to be free of astrophysical backgrounds. At present three of them have been observed with H.E.S.S.: Sagittarius and Canis Major (Aharonian et al. 2008, 2009), and we present here a preliminary analysis of Carina. No γ-ray excess has been found, which allows to exclude some WIMP models. Fig. 1 (right panel) presents the exclusion plot in the $\langle\sigma v\rangle - m_\chi$ plane, for a total observation time of 2.7 h and a standard analysis. No natural MSSM and KK models can be excluded.

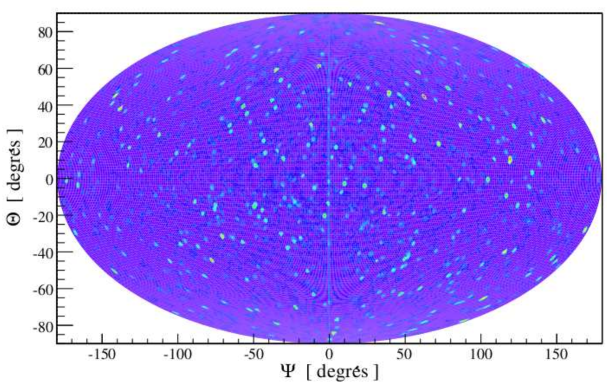

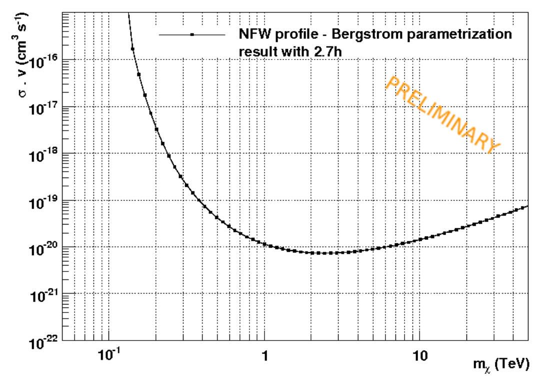

Fig. 1. Left panel: $\Phi^{\rm astro}$ from galactic clumps. **Right panel:** preliminary exclusion plot from Carina observations.

4 Conclusion

The sub-structures studied are not within reach of H.E.S.S. and probably not of H.E.S.S. II, but rather for the next generation of Cerenkov array as CTA (Cerenkov Telescope Array). Stronger constraints from dwarf galaxies could be set with larger observational time. The combination of existing observations on several dwarfs should also be investigated.

References

Lavalle, J., Yuan, Q., Maurin, D. & Bi, X.-J. 2008, A&A, 479, 427

Fornengo, N., Pieri, & Scopel, S. 2004, Phys. Rev. D., 70, 103529

Aharonian, F. A & al. (H.E.S.S. Coll.), 2008, Astropart. Phys., 29, 55

Aharonian, F. A & al. (H.E.S.S. Coll.), 2009, ApJ to appear (arXiv:0809.3894)

SF2A 2008
C. Charbonnel, F. Combes and R. Samadi (eds)

IMPLICATIONS OF THE COSMIC RAY SPECTRUM FOR THE MASS COMPOSITION AT THE HIGHEST ENERGIES

Decerprit, G.[1], Allard, D.[1], Busca, N.G.[1], Parizot, E.[1] and Olinto, A.V.[1,2]

Abstract. The significant attenuation of the cosmic-ray flux above $\sim 5\,10^{19}$ eV suggests that the observed high-energy spectrum is shaped by the so-called GZK effect. This interaction of ultra-high-energy cosmic rays (UHECRs) with the ambient radiation fields also affects their composition. We review the effect of photo-dissociation interactions on different nuclear species and analyze the phenomenology of secondary proton production as a function of energy. We show that, by itself, the UHECR spectrum does not constrain the cosmic-ray composition at their extragalactic sources. While the propagated composition (i.e., as observed at Earth) cannot contain significant amounts of intermediate mass nuclei (say between He and Si), whatever the source composition, and while it is vastly proton-dominated when protons are able to reach energies above 10^{20} eV at the source, we show that the propagated composition can be dominated by Fe and sub-Fe nuclei at the highest energies, either if the sources are very strongly enriched in Fe nuclei (a rather improbable situation), or if the accelerated protons have a maximum energy of a few 10^{19} eV at the sources. We also show that in the latter cases, the expected flux above $3\,10^{20}$ eV is very much reduced compared to the case when protons dominate in this energy range, both at the sources and at Earth.

1 Introduction

The measurement of the composition of ultra-high-energy cosmic-ray (UHECRs) and the inference of their source composition are among the main questions involved in the understanding of their enigmatic origin. The common hypothesis is a transition from a heavy composition to a light composition between 10^{17} eV and a few times 10^{18} eV. The shape of the GZK feature which results in a flux suppression and the energy at which it occurs could restrain the composition. In this paper we investigate the constraints placed by these observables on the source composition as well as on that expected at Earth.

2 The method : Nuclei propagation in the Universe

We model the propagation of all nuclei from a uniform and continuous distribution of sources. Departing from a given redshift, z = 5, we consider them propagating, facing photonic background of CMB and IR/Optical/UV. Computing all relevant photodisintegration mean free paths for each interaction process, we finally derive all the interactions experienced by nuclei. Pair production [Rachen 1996] and adiabatic losses result in a decrease of the Lorentz factor of the nucleus, whereas photodisintegration processes trigger the ejection of several nucleons from the parent nucleus, which make a critical difference with the well known proton case. The lowest energy (10-20 MeV) disintegration process is the Giant Dipole Resonance (GDR). Around 30 MeV the quasi-deuteron (QD) process becomes comparable to the GDR and dominates the total cross section at higher energies. Finally, the photopion production of nuclei becomes relevant above 150 MeV.

3 Results : spectrum predictions for various source composition hypotheses

We turn to the calculations of propagated spectra assuming various source compositions. The propagated spectra that best fit Auger spectra for pure He, CNO and Si source compositions are shown in the present

[1] Laboratoire Astroparticule & Cosmologie (APC), Université Paris 7/CNRS, 10 rue Alice Domon 75205 Paris Cedex 13
[2] The University of Chicago, 5640 S. Ellis, Chicago, IL60637, USA

paper. These extreme examples show that for light or intermediate source composition, the spectrum after propagation is expected to be rich in proton and that a large proton abundance observed above a few 10^{19} eV would not strongly constrain the source composition.

The case of a heavy source composition

The case of a heavy source composition (pure Fe) is displayed in Fig. 1. It can provide good fits as well to the data ($\beta = 2.3$ for Auger) though the shapes are different from the proton cases. One can see that the expected composition is still heavy on Earth with a low abundance of secondary protons. The implication of a heavy source composition on the composition at the Earth is then very different from the other cases we studied, but current data do not allow us to distinguish between the proton dominated and the heavy dominated shapes.

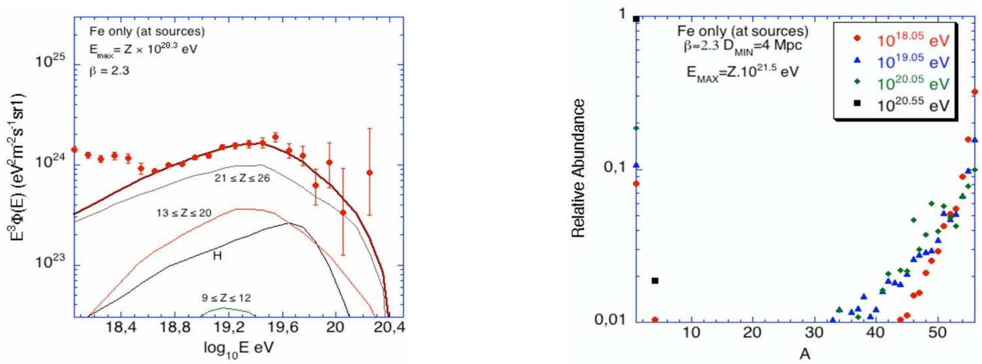

Fig. 1. Propagated spectra obtained assuming a pure iron source composition compared to Auger spectra (left) and relative abundances of the different isobar between A=1 and 56, expected on Earth in four different energy bins (right).

Another surprising yet acceptable fit

Acceptable fits of the data can be obtained with a mild increase of the overall abundance of heavy elements at the source. With $E_{max} = Z \times 4\,10^{19}$ eV and $\sim 30\%$ of Fe nuclei at the sources, one can see [Decerprit & al, 2008] that the agreement with data is reasonable and that the composition, proton dominated at low energy, becomes gradually heavier and very dominated by Fe above 50 EeV.

4 Discussion & conclusion

In this paper, we extract conclusive results about the UHCER composition from the data. In the case of a source composition dominated by protons or light nuclei, we always derive a good fit of the data and a propagated composition enriched in protons, as well as a GZK-like cut-off. If heavy nuclei are present at the source, the proton enrichment is expected to stop between $\sim 5\,10^{19}$-$\sim 2\,10^{20}$ eV, so that it leaves a distinctive signature on the elongation rate [cf. Allard 2007]. In the case of heavy source compositions, conclusions are radically different but fits remain compatible with current data and show propagated spectra dominated by heavy nuclei. Finally, we have shown that current experimental spectra are compatible either with proton-dominated UHECRs or with the "nuclear GZK cut-off" coming from the photodisintegration of heavy dominated UHECRs. Though current data do not allow to distinguish between them, it is likely that future data, as expected from the Pierre Auger observatory, will provide better constraints.

References

Allard, D., Busca, N., Decerprit, G., Olinto, A. V., & Parizot, E. 2008, to be published in JCAP, astro-ph/0805.4779

Allard, D., Parizot, E., & Olinto, A. V. 2007, A&A, 473, 59

Rachen, J. P. 1996, PhD thesis of the Bohn University

SF2A 2008
C. Charbonnel, F. Combes and R. Samadi (eds)

THE CTA PROJECT

de Naurois, M. for the CTA consortium[1]

Abstract. During the last few years, very high energy (VHE) gamma-ray astronomy has emerged as a truly observational discipline, largely driven by the European-led HESS and MAGIC experiments. More than 70 VHE gamma-ray sources have been detected, representing different galactic and extragalactic source populations such as young shell type supernova remnants, pulsars wind nebulae, giant molecular clouds, Wolf-Rayet stars, binary pulsars, microquasars, the Galactic Center, Active Galactic Nuclei and a large number of yet unidentified Galactic objects. The CTA project is aiming at building a very powerful multi-functional tool for spectral, temporal and morphological studies of galactic and extragalactic sources of VHE gamma-rays, with an unprecedented sensitivity (improved by one order of magnitude compared to the previous generation experiments) and a superior angular resolution. The current plan for CTA consists of two observatories, one in each Hemisphere, with 10 GeV-∼1 TeV and 10 GeV-100 TeV energy coverage in the Northern and Southern Hemisphere respectively. We will report on the scientific motivation, design status and expected performances of the CTA project, as well as on its current status.

1 Introduction

Since the pioneering work of the Whipple experiment in the 1980's, gamma-ray astronomy as emerged as a new window on the non-thermal Universe. Unprecedented sensitivity achieved by the third generation experiments such as HESS, MAGIC, VERITAS and CANGAROO led to the discovery of more than 70 Very High Energy sources, both galactic and extragalactic, and belonging to various categories such as young shell type supernova remnants, pulsars wind nebulae, giant molecular clouds, Wolf-Rayet stars, binary pulsars and microquasars. A large fraction of these object line up on the Galactic Plane, thus demonstrating the close correlation between these gamma-ray emitters and the distribution of matter in our Galaxy (see Fig. 1).

These spectacular astrophysics results, comprising high resolution spectra, precise imagery and timing measurement, have generated a considerable interest from the astrophysics and particle physics community and were recognized by the award of the Descartes Prize to the HESS collaboration for 2006. The very broad variety of achievable science has spawned the urgent wish for a next generation, more sensitive and more flexible facility, able to serve a very fast growing community of users. The proposed CTA facility - an array of Cerenkov telescopes built on proved technologies but at an industrial scale - is aiming at pushing the Atmospheric Cerenkov technique further on, with a factor of ten in sensitivity (Fig. 2, **left**) and a factor of five in angular resolution. This improvement, leading to the probable discovery of ∼1000 sources, is comparable with the gap between the EGRET and Fermi space telescopes and will allow in-depth studies of known classes of gamma emitters, together with a strong discovery potential for new classes of sources that are below the sensitivity of current instruments.

In order to cover the full sky, it is planned to build two stations, one in the northern hemisphere and the other one in the southern hemisphere. The full energy range will be three or four orders of magnitude, from about 10 GeV up to about 100 TeV (depending on the final design) with a milliCrab sensitivity in the core energy range.

CTA was considered as "Emerging Proposal" in the 2006 road-map report of the European Strategy Forum on Research Infrastructures (ESFRI) and is now included in the updated road-map. The construction of CTA as a next-generation facility for ground-based very-high-energy gamma-ray astronomy has been recently promoted to the status of "fully supported project" by the ApPEC/ASPERA committee.

[1] LPNHE, IN2P3 - CNRS - Universits Paris VI et Paris VII, 4 place Jussieu, 75252 Paris Cedex 05, FRANCE

An important aspect of the CTA project is the time overlap with the Fermi space telescope, successfully launched in 2008 and which is now renewing our view of the GeV Universe. Multi-wavelength observations are indeed a key to the Non Thermal Universe, and this imposes a short schedule for the CTA design study and construction phase.

2 Science motivation

The large list of astrophysics cases for CTA, can be roughly split into *guaranteed science* and *new discovery potential*. Both parts cover both the galactic and extragalactic domains.

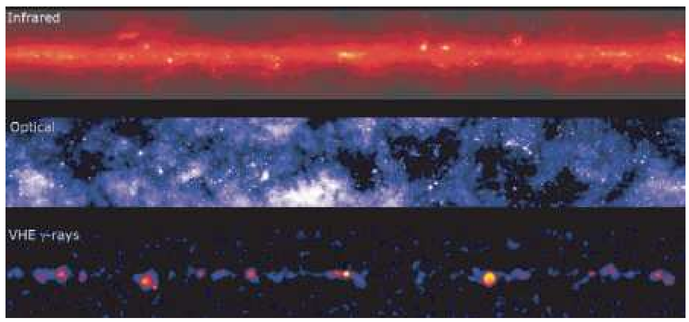

Fig. 1. The inner regions of the galactic plane seen in multi-wavelength observations. The H.E.S.S. observations at TeV energies reveal many sources, lining up on the plane, and mostly associated with supernova remnants and pulsar wind nebulæ.

In the galaxy, many TeV gamma sources have been discovered, in particular during the H.E.S.S. survey of the inner galactic regions (see Fig. 1). These sources mainly belong to the categories of supernova remnants (SNRs), pulsar wind nebula (PWNs), binary systems and diffuse emission attributed to the interaction of cosmic rays with the interstellar medium, with some still unidentified sources and a few additional peculiar sources, such as the Galactic Center. The variety of sources allows to address various physics subjects such as acceleration of charged particles in astrophysical sources which is linked to the origin of cosmic rays (CR) mystery. Indeed, almost one century after their discovery by Victor HESS in 1912, the sources of the bulk of CR observed at earth are still not firmly identified, although many arguments point towards supernova remnants as prime candidates. The solid detection of TeV radiation from a population of SNRs and the precise measurement of their spectra from below the GeV domain (with the Fermi Space Telescope) up to 100 TeV will help disentangling between the leptonic and hadronic acceleration scenarios and thus make a decisive contribution to the solution of this mystery. The upper energy range, close to the *knee*, is of particular interest in this regard.

Pulsar Wind Nebula form the most numerous class of known Very High Energy emitters, some of them being amongst the most efficient known accelerators. Third generation instruments have in some cases observed an energy-dependent morphology in these systems, and thus started to investigate the details of particle acceleration and cooling. The major task for CTA regarding PWNs will be to probe the physics of pulsar wind by the mean of better sensitivity and angular resolution.

Pulsar magnetospheres are also known to act as efficient cosmic accelerators, yet there is no accepted model for this particle acceleration, a process which involves electrodynamics with very high magnetic fields as well as the effect of general relativity. Two broads categories of models (*polar-cap* and *outer-gap* models), differ by the location on the magnetosphere where the particle acceleration takes place, and predict different behavior in the 10-50 GeV domain. The recent discovery of pulsation from the Crab nebula by the MAGIC collaboration (Teshima, M., 2008) above 25 GeV, with a dedicated trigger setup, stresses the discovery potential of a more sensitive instruments such as CTA in this domain.

Amongst Very High γ-ray emitters, four are binary systems, consisting of a compact object (neutron star or black hole) orbiting around a massive star. In these objects, the periodic change of environment along the orbit can induce a modulation of the acceleration efficiency and of the cooling mechanisms, thus resulting in a modulation of the spectral signature, as was observed in LS 5039 by the H.E.S.S. experiment (Aharonian, A. *et al*, 2006). This offers a unique view on the system, allowing to probe how the acceleration mechanism react to changing environment. Moreover, microquasars can be understood as scaled down version of the giants Active Galactic Nuclei, however with much smaller dynamical time scales. Microquasars therefore offer a chance to understand the physics of accretion and ejection in accreting black holes.

The increased sensitivity and energy coverage of CTA will increase the number of VHE γ-ray blazars and allow the detection of more distant ones. By disentangling between intrinsic spectral curvature and propagation effects, this will provide a handle on the extragalactic diffuse gamma-ray background, which is closely related to the formation of large structures in the Universe. Modeling of accretion and ejection mechanisms will also benefit from the improved sensitivity as it will allow to sample faster variability.

In addition to detailed study of the aforementioned sources of TeV γ-rays, CTA offers a significant discovery potential in fundamental physics: weakly interacting dark matter particles are expected to concentrate at the center of massive structures, where their annihilation could lead to a detectable gamma-ray signal. Prime targets for CTA in these regards are Globular Clusters or Dwarf Galaxies where less conventional sources are expected to hide a possible annihilation signal. Improved angular resolution will limit the confusion problem, whereas increased energy coverage will increase the reachable mass range and allow the detection of spectacular spectral features that are needed to reject conventional signal explanations. Other potential discovery from CTA would be the detection of non-Newtonian gravity through its effect on the time of propagation of very high energy photons. This would require a large sample of highly variable blazars at different distances, in order to investigate relation between propagation time lags and distance.

3 The CTA design study

The CTA consortium is performing a Design Study (DS) for the optimization of the performance of the planned observatory and to study its possible implementation. The primary targets of the DS are:

- to narrow down the multidimensional space of design options and technology options, optimizing the relation between performance and cost of the facility,
- to lay out a clear path for how such a facility can be constructed and operated using proved industrial technologies, and ensuring high performances and availability of the system,
- to build and test prototype telescope(s) that are suitable for mass production for a large array of telescopes

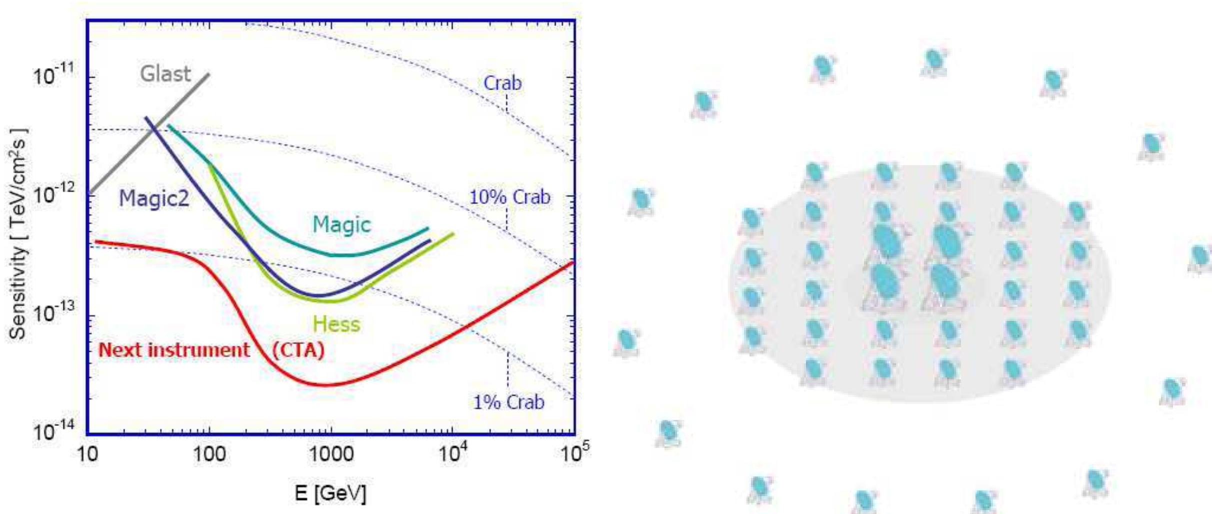

Fig. 2. Left: Sensitivity aimed with CTA, compared with the existing experiments and with the flux of the Crab Nebula (standard candle for Very High Energy Gamma-Ray Astronomy). The exact value will depend on the real layout of the system. **Right**: Possible layout for the CTA southern array.

A duration of about four years is foreseen for the Design Study and prototyping. Examples of the system optimization include telescope layout (Fig. 2, **right**), field of view and pixel size, as well as full integration of electronic components into a single ASIC. In a possible design scenario, the southern hemisphere array of CTA will consist of two types of telescopes with different mirror size in order to cover the full energy range. The low energy instrumentation might consist of 23-28 m telescopes with a moderate field of view (FoV) of the order of 3-4 deg, while the high energy instrumentation above about 100 GeV will be equipped with large cameras with up to 6-8 deg FoV, installed in 12-15 m telescopes. This will not only allow effective surveys of the galactic plane and the investigation of extended sources and diffuse radiation, but will also result in an improved high energy performance with an expected additional improvement in count rate with respect to small FoV instrumentation. The northern hemisphere array will consist of the low energy instrumentation only, and focuses on the observation of extragalactic objects. For future upgrades the implementation of high QE photon detectors might be envisaged, which possibly results in an even higher sensitivity.

While in 2008 the focus is on the optimization of possible layouts of the telescope system and on the evaluation of possible technical implementations, the year 2009 will be used to construct and test components of prototypes. During 2010-2011 prototype telescope(s) shall be constructed and finally tested in the field, before the actual construction of the array from 2010 for fully operational system in 2018.

4 Conclusions

The new Cerenkov Telescope Array (CTA) project intends to build in a short time scale a large facility that is well beyond possible upgrades of existing instruments. Its much improved sensitivity, it's unprecedented angular resolution and its larger energy coverage will guarantee a high level of science return, together with a large discovery potential in fundamental physics. Of the order of $\sim$1000 sources are expected, including new types of sources that are below the capabilities of current instruments. Being run as an observatory open to external astronomers, CTA will bring one more piece to the multi-wavelenth coverage of the Universe, and intends to become one of the major player in astronomy for the next decade.

5 Acknowledgments

We wish to thank all the scientists in 34 institutes in 15 countries who are contributing and participating in the Cerenkov Telescope Array (CTA) project.

References

"The Cherenkov Telescope Array project". http://www.cta-observatory.org/

"The H.E.S.S. project". http://www.mpi-hd.mpg.de/hfm/HESS

"The MAGIC Telescope". http://wwwmagic.mppmu.mpg.de/

"The VERITAS project". http://veritas.sao.arizona.edu/

"The CANGAROO telescope system". http://icrhp9.icrr.u-tokyo.ac.jp/

Teshima, M. 2008, ATel #1491

Aharonian, A. *et al* 2006, A&A, 460, 743-749

NEUTRINO DETECTION OF TRANSIENT SOURCES WITH OPTICAL FOLLOW-UP OBSERVATIONS

Dornic, D.[1], Basa, S.[2], Brunner, J.[1], Busto, J.[1], Boër, M.[3], Klotz, A.[3,4], Escoffier, S.[1], Gendre, B.[2], Le Van Suu, A.[3], Mazure, A.[2], Atteia, J.L.[5] and Vallage, B.[6]

Abstract. The ANTARES telescope has the opportunity to detect transient neutrino sources, such as gamma-ray bursts (GRBs), core-collapse supernovae (SNe), flares of active galactic nuclei (AGNs)... To enhance the sensitivity to these sources, we are developing a new detection method based on the observation of neutrino bursts followed by an optical detection. The ANTARES Collaboration is implementing a fast on-line event reconstruction with a good angular resolution. These characteristics allow to trigger an optical telescope network in order to identify the nature of the neutrinos (and high energy cosmic-rays) sources. This follow-up can be done with a network of small automatic telescopes and required a small observation time. An optical follow-up of special events, such as neutrino doublets in coincidence in time and space or single neutrino having a very high energy, would not only give access to the nature of the sources but also improve the sensitivity for neutrino detection from SNe or GRBs.

1 Introduction

The ANTARES neutrino telescope [1] is located 40 km off shore Toulon, in the South French coast, at about 2500 m below sea level. The complete detector is composed of 12 lines, each including 75 photomultipliers on 25 storeys, which are the sensitive elements. Data taking started in 2006 with the operation of the first line of the detector. The construction of the 12 line detector was completed in May 2008. The main goal of the experiment is to detect high energy muon induced by neutrino interaction in the vicinity of the detector.

Among all the possible astrophysical sources, transients offer one of the most promising perspectives for the detection of cosmic neutrinos thank to the almost background free search. The detection of these neutrinos would be the only direct probe of hadronic accelerations and so, the discovery of the ultra high energy cosmic ray sources without ambiguity.

In this paper, we discuss the different strategies implemented in ANTARES for the transient sources detection.

2 Transient sources detection strategies

To detect transient sources, two different methods can be used [2]. The first one is based on the search for neutrino candidates in conjunction with an accurate timing and positional information provided by an external source: the triggered search. The second one is based on the search for ”special neutrino events” coming from the same position within a given time window: the rolling search.

[1] CPPM, Faculte des Sciences de Luminy, 163 avenue de Luminy, 13288 Marseille Cedex09, France
[2] LAM, BP8, Traverse du Siphon, 133376 Marseille Cedex 12, France
[3] OHP, 04870 Saint Michel L'Observatoire, France
[4] CESR, Observatoire Midi-Pyrénées, CNRS, Université de Toulouse, BP 4346, 31028 Toulouse Cedex 04, France
[5] LATT, Observatoire Midi-Pyrénées, CNRS, Université de Toulouse, 14 avenue E. Berlin, 31400 Toulouse, France
[6] CEA-IRFU, centre de Saclay, 91191 Gif-Sur-Yvette, France

2.1 The triggered search

Classically, GRBs or flare of AGNs are detected by gamma-ray satellites which deliver an alert to the Gamma-ray bursts Coordinates Network (GCN [3]). The characteristics of this alert are then distributed to the other observatories. The small difference in arrival time and position expected between photons and neutrinos allows a very efficient detection even with a low energy threshold due to the very low expected background. This method has been implemented in ANTARES mainly for the GRBs detection since the end of 2006. Today, the alerts are primarily provided by the Swift [4] and the Integral [5] satellites. Data triggered by more than 250 alerts have been stored up to now.

Due to the very low background rate, even the detection of a small number of neutrinos correlated with GRBs could set a discovery. But, due to the relatively small field of view of the gamma-ray satellites (for example, Swift has a 1.4 sr field of view), only a small fraction of the existing bursts are triggered. Moreover, the choked GRBs without photons counterpart can not be detected by this method.

2.2 The rolling search

This second method, originally proposed by Kowalski and Mohr [6], consists on the detection of a burst of neutrinos in temporal and directional coincidence. Applied to ANTARES, the detection of a doublet of neutrinos is almost statistically significant. Indeed, the number of doublet due to atmospheric neutrinos is of the order of 0.05 per year when a temporal window of 900 s and a directional one of 3° x 3° are defined.

It is also possible to search for single cosmic neutrino events by requiring that the reconstructed muon energy is higher than a given energy threshold (typically above a few tens of TeV if a Waxman−Bahcall flux is considered). This high threshold reduces significantly the atmospheric neutrino background [7].

In contrary to the current gamma-ray observatories, a neutrino telescope covers at least a half hemisphere if only up-going events are analyzed and even 4π sr if down-going events are considered. When the neutrino telescope is running, this method is around 100% efficient. Moreover, this method requires no hypothesis on the period during which the neutrinos are emitted with respect to the gamma flash, a parameter not really constrained by the different models. More importantly no assumption is made on the nature of the source and the mechanisms occurring inside.

The main drawback of the rolling search is that a detection is not automatically associated to an astronomical source. To overcome this problem, it is fundamental to organize a complementary follow-up program. This program can be done with a small optical telescope network. The observation of any transient sources will require a quasi real-time analysis and a very good angular precision. It will be described in detail in section 4.

3 The ANTARES neutrino triggers

ANTARES is implementing a new on-line event reconstruction (named BBfit). This analysis strategy contains a very efficient trigger based on local clusters of photomultiplier hits and a simple event reconstruction. The two main advantages are a very fast analysis (between 5 and 10 ms per event) and a good angular resolution. The minimal condition for an event to be reconstructed is to contain a minimum of six storeys triggered on at least two lines. To select a high purity sample of up-going neutrino candidates, one quality cut is applied to the result of the χ^2 minimisation of the muon track reconstruction based on the measured time and amplitude of the hits. In order to obtain a fast answer, the on-line reconstruction does not use the dynamic reconstructed geometry of the detector lines. This has the consequence that the angular resolution is degraded with respect to the one obtained with the standard off-line ANTARES reconstruction (of about 0.2 - 0.3°) which includes the detector positioning.

In order to set the cuts used for the special event selection, we have analysed the data taken from December 2007 to May 2008 (around 109 active days) with a 10 line detector. During this period, around 350 up-going neutrino candidates were recorded. The figure 1 shows the elevation distribution of the well reconstructed muon events which pass the quality cuts during this period. This plot shows as the same time the down-going atmospheric muons and the up-going neutrino candidates. It also illustrates the very low contamination of the bad reconstructed atmospheric muons in the up-going sample.

In order to obtain an angular resolution lower than the field of view of the telescope (around 1.9°), we select reconstructed events which trigger several hits on at least 3 lines. The dependence of this resolution with the

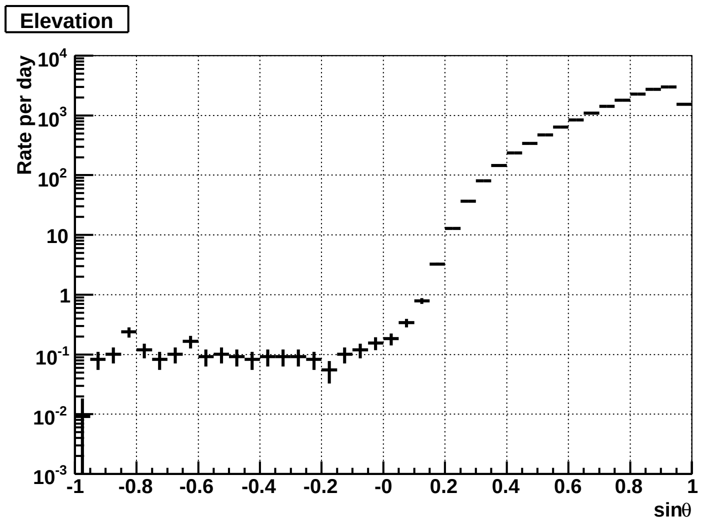

Fig. 1. Elevation distribution of the well reconstructed muon tracks recorded with the 10 line detector (Dec 2007 to May 2008). The region where the elevation is negative represents the up-going part of the distribution.

number of lines used in the fit is shown in the figure 2. For the high energy events, this resolution can be as good as 0.5 degree.

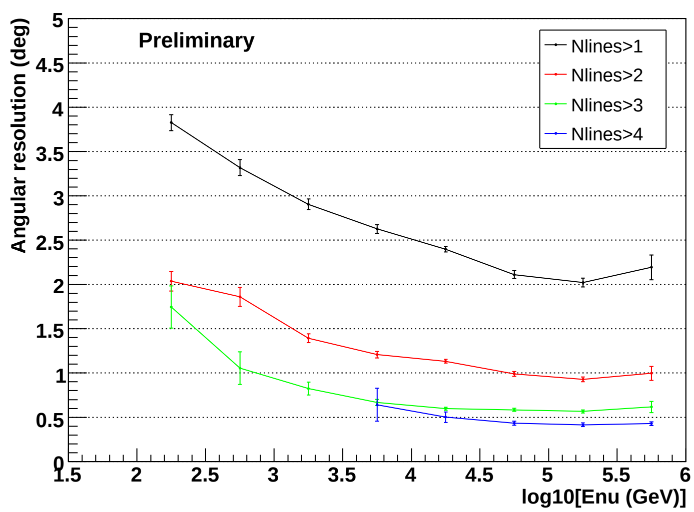

Fig. 2. Angular resolution evolution with energy for the event with at least 2, 3, 4 and 5 lines used in the fit.

An estimation of the energy in the on-line reconstruction is indirectly determined using the number of hits of the event and the total amplitude of these hits. In order to select events with an energy above a few tens of TeV, a minimum of about 20 hits and about 200 photoelectrons per track are required. These two different trigger logics applied on the 10 line data period select six events in about 109 active days.

4 Optical follow-up network

ANTARES is organizing a follow-up program in collaboration with TAROT (*Télescope à Action Rapide pour les Objets Transitoires*, Rapid Action Telescope for Transient Objects; [8]). This network is composed of two 25 cm optical telescopes located at Calern (South of France) and La Silla (Chile). The main advantages of the TAROT instruments are the large field of view of 1.86° x 1.86° and their very fast positioning time (less than 10 s). These telescopes are perfectly tailored for such a program. Since 2004, they observe automatically the alerts provided by different GRB satellites [9].

As it was said in the section 2, the rolling search method is sensitive to all transient sources which produced high energy neutrinos. Different observation strategies will be defined according to the different source types. For example a GRB afterglow requires a very fast observation strategy in contrary to a core collapse supernovae for which the signal will appear several days after the neutrino signal.

Such a program would not require a large observation time. Depending on the neutrino trigger settings, an alert sent to TAROT by this rolling search program would be issued at a rate of about one or two times per month.

5 Summary

The detection of neutrinos from transient sources is favorized by the fact that external triggers are provided by spacecraft currently in operation. The follow-up of interesting events would improve significantly the perspective for neutrino detection from transient sources. These special events are selected with two complementary triggers: search of a neutrino doublet (the most sensitive) or a single high energy event. The most important point of the rolling search method is that it is sensitive to any transient source. The confirmation by the optical telescope of a neutrino alert will give not only the nature of the source but also allow to increase the precision of the source direction determination in order to target other observatories (for example very large telescopes for the redshift measurement).

The key of the success of the search method is to analyze all the events on a very fast way while keeping a good angular precision. This good angular resolution will be an advantage not only to reduce the background and also to increase the probability to find an optical counterpart. The ANTARES Collaboration has an agreement with TAROT to develop this Target-of-Opportunity program. The implementation of this new technique has already started and we expect to send the first alert by the end of 2008.

References

Antares Collaboration, Proposal, arXiv:astro-ph/9907342v1

Basa, S., Dornic, D. et al. 2008, arXiv:astro-ph/0810.1394

GCN network, http://gcn.gsfc.nasa.gov

Barthelemy, S.D., Barbier, L.M., Cummings, J.R., et al. 2005, Space Science Reviews, 120, 143

Meregheti, S., et al. 2003, Astron. Astrophys., 411, 291

Kowalski, M., & Mohr, A. 2007, Astroparticle Physics, 27, 533

D. Dornic et al, arXiv:astro-ph/0810.1452

Bringer M., Boer M., et al. 1999, A&AS, 138, 581

Klotz, A., Boer, M., Atteia, J.L., & Gendre, B. 2008, AJ, submited

SF2A 2008
C. Charbonnel, F. Combes and R. Samadi (eds)

THE HIGH-ENERGY PICTURE OF GRS 1915+105 WITH *SPI/INTEGRAL*

Droulans, R.[1] and Jourdain, E.[1]

Abstract. We report the results of two years of INTEGRAL/SPI monitoring of the Galactic microquasar GRS 1915+105. From July 2004 to May 2006, the source has been observed twenty times with long (~100 ks) exposures. We present an analysis of the SPI data and focus on the description of the high-energy (> 20 keV) output of the source. We find the 20 – 500 keV spectral emission of GRS 1915+105 to be bounded between two limit states. In particular, it seems that these high-energy states are not correlated to the temporal behavior of the source, suggesting that there is no immediate link between the macroscopic characteristics of the coronal plasma and the the variability of the accretion flows. All spectra are well fitted by a thermal comptonization component plus an extra high-energy powerlaw. This confirms the presence of thermal and non-thermal electrons around the black hole.

1 Introduction

GRS 1915+105 is among the most notorious accreting black holes in our Galaxy. Not only it is one of the brightest and most variable X-ray sources in the sky (see Castro-Tirado et al. 1992 for a first detection report and Belloni et al. 2000 for detailed variability analysis), but it is also the first galactic object in which superluminal plasma ejections have been observed (Mirabel & Rodriguez 1994).

Yet, most of the recent studies (see Fender & Belloni 2004 for a review) focus on the astonishing X-ray properties, the soft γ-ray emission (> 100 keV) being generally observed at poor signal to noise ratio. Understanding the high-energy behavior of the source is nevertheless very important as it is assumed to trace the physical processes occurring at the innermost regions surrounding the black-hole (e.g. Galeev et al. 1979 or Malzac 2007 for a review). Featuring good spectral resolution and sensitivity up to several MeV, the γ-ray spectrometer SPI (Vedrenne et al. 2003) aboard the INTEGRAL observatory is a good instrument to tackle this issue.

Here we present all SPI observations on GRS 1915+105 from July 2004 to May 2006. We focus on gaining the most accurate high-energy picture of the source, mainly through extensive spectral analysis. Emphasis is given to four observations which we found to be of particular interest.

2 Results

From July 2004 to May 2006, the source has been observed twenty times with long (~100 ks) exposures. The total $20 - 50\,keV$ light-curve from our observational period shows relevant long-term variability, the averaged source flux per observation ($\approx$ one-day) spanning between 90 and $380\,mCrab$. On the shorter science-window timescale ($\approx 2\,ks$), the obtained individual light-curves show generally lower variability. Within a single observation, the source flux varies at most by a factor of 2. As GRS 1915+105 is well known for being very variable in X-rays, we also considered SPI-simultaneous 1.2 – 12 keV ASM light-curves to compare the X- and soft γ-ray behavior of the source. We used XSPEC 11.3.2 (Arnaud 1996) for spectral analysis. Each observation-averaged spectrum is fitted with a basic powerlaw model which gives a good description of most of the data. The photon index is found to range from 2.8 to 3.5.

2.1 Observations 295 and 423

From the ASM light-curves (figure 1 left) , we see that for both observations GRS 1915+105 shows very similar X-ray activity, summarily characterized by low flux and almost no variability. The temporal properties in the $20 - 50\,keV$ band

[1] CESR / CNRS – Universite de Toulouse, 9 Av. du Colonel Roche, 31028 Toulouse Cedex 04, France

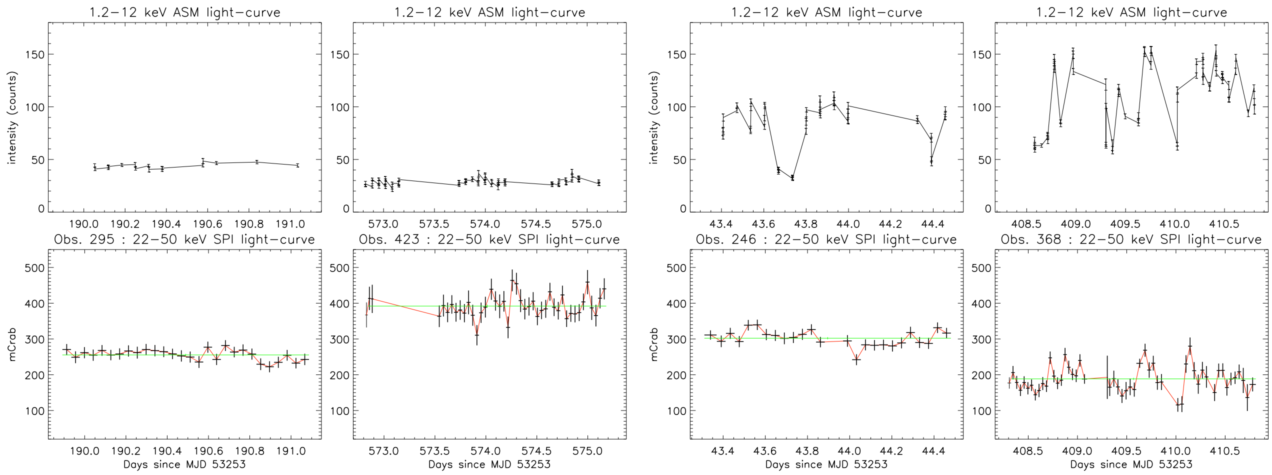

Fig. 1. ASM and SPI light-curves. **Left** : Observations 295 and 423. **Right**: Observations 246 and 368.

are also quite alike, with little variability during both observations. However, spectral characteristics are found to be significantly different, with respective photon indices of 3.5 and 2.8. We will now further investigate these differences through more detailed spectral modelling.

A simple powerlaw model gives a rather poor fit for observation 295. Pure thermal comptonization models like COMPTT (Titarchuk 1994) can also be ruled out ($\chi^2/\nu = 72/26$). Assuming that the low-energy part is nonetheless produced through thermal comptonization, one needs to add a further spectral component. We thus chose to add a powerlaw as a phenomenological description of the observed high-energy tail. Given the error amplitude above 100 *keV*, we arbitrarily fixed the photon index to the standard value 2.0. The resulting fit ($kT_e = 16.3\,keV$ and $\tau = 0.57$) is in very good agreement with our data ($\chi^2/\nu = 17/25$) and the *F-TEST* indicates a probability of $\sim 10^{-9}$ that this improvement has been a chance event. As a last step we applied Poutanen and Svensson's COMPPS model (1996). Note that COMPPS is more constraining than COMPTT+PL as it requires both components (thermal and non-thermal) to be linked, whereas the former does not. Equally good fitting results ($\chi^2/\nu = 17/25$) for both models confirmed the observed $20-500\,keV$ emission to most likely originate from thermal and non-thermal comptonization processes.

For observation 423, the basic powerlaw fit is clearly unacceptable ($\chi^2/\nu = 83/27$) due to the marked curvature around 50 *keV*, leaving clear evidence for thermal processes. However, a thermal component alone is not able to account for the observed emission above 200 *keV*. We thus keep the hybrid comptonization models ($\chi^2/\nu = 37/25$ for COMPTT+PL and $\chi^2/\nu = 37/24$ for COMPPS) as our preferred description for the spectrum from observation 423.

2.2 Observations 246 and 368

Considering the (2 *ks* timescale) lightcurves from observation 368, we find the same variability pattern in X-rays as in the $20-50\,keV$ SPI band (figure 1 right), indicating that both bands are probably sampling the temporal behavior of the same component. For observation 246 there seems to be a similar correspondence, although less clear due to lower variability amplitude in the SPI band. Both spectra are fitted with thermal + non-thermal comptonization models (COMPTT+PL and COMPPS) which provide the best agreement to the data.

2.3 Composite spectra

In order to go further in the description of the high-energy tail of GRS 1915+105, we decided to compile consistent information from different observations. Improved statistics on the resulting composite spectra would indeed allow us to put better constraints on the parameters of the fitted models. The first group of observational data is characterized by a rather low $20-50\,keV$ flux ($\sim 200\,mCrab$) and a very soft spectral shape ($\Gamma \approx 3.45$); hereafter we will call it the *soft sample*. The second group on the other hand has hard colors ($\Gamma \approx 2.90$) and a high flux ($\sim 330\,mCrab$) in the $20-50\,keV$ band; it will accordingly be called the *hard sample*. As a result, our two samples are likely to describe the boundary comptonization states between which the source seems to be continuously switching.

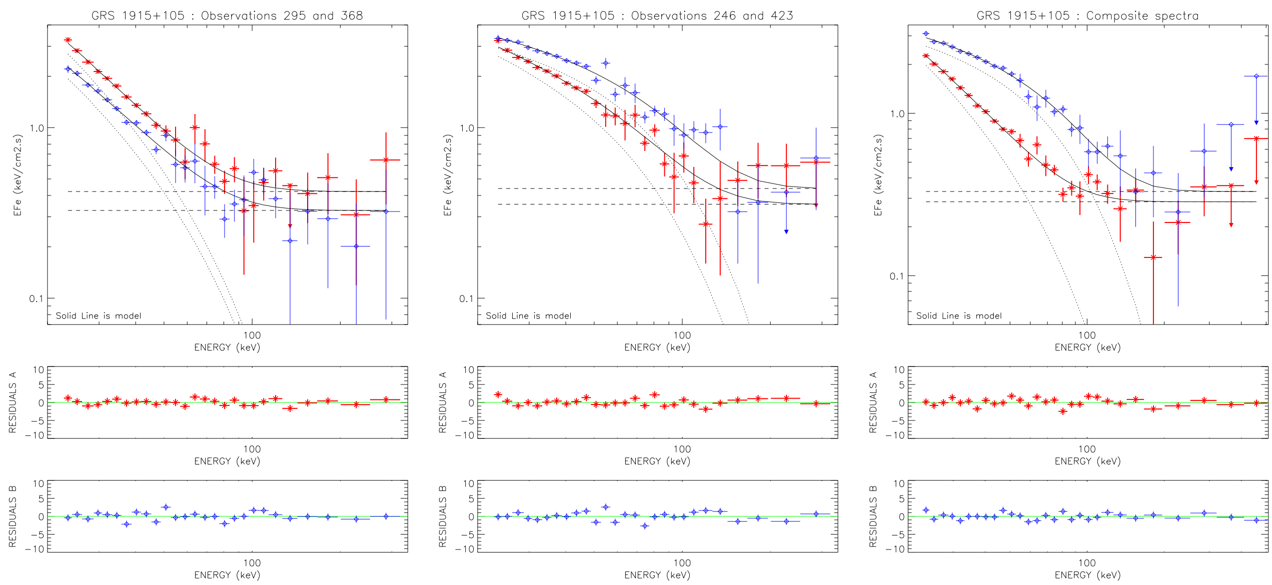

Fig. 2. COMPTT+PL best fits. **Left** : Observations 295 (red stars) and 368 (blue diamonds). **Middle** : Observations 246 (red stars) and 423. **Right** : Soft sample (red stars) and hard sample.

	COMPTT						PL			
Obs ID	kT_{bb} (keV)	kT_e (keV)	τ	$\gamma_{\min}$	Γ_e	F_{comptt}	α	K_{pl}	χ^2/ν	FTEST
246	1.0f	$18.2^{+1.1}_{-1.0}$	0.97	-	-	3.64	2.0f	$3.48^{+1.05}_{-0.96}$	27/25	4×10^{-2}
295	1.5f	$16.3^{+1.2}_{-0.9}$	0.57	-	-	2.73	2.0f	$3.95^{+0.66}_{-0.56}$	17/25	2×10^{-9}
368	1.5f	$13.4^{+1.0}_{-0.9}$	0.86	-	-	1.94	2.0f	$3.28^{+0.54}_{-0.56}$	29/25	1×10^{-6}
423	1.0f	$19.2^{+1.0}_{-1.0}$	1.20	-	-	4.91	2.0f	$4.27^{+1.29}_{-1.38}$	37/25	8×10^{-2}
SS	1.5f	$16.5^{+0.6}_{-0.6}$	0.62	-	-	2.07	2.0f	$2.75^{+0.28}_{-0.29}$	31/25	3×10^{-10}
HS	1.0f	$17.7^{+0.7}_{-0.7}$	1.28	-	-	4.13	2.0f	$3.31^{+0.91}_{-0.95}$	19/25	8×10^{-4}

Table 1. Spectral fitting of the four highlighted observations and the composite samples. For each spectrum the COMPTT + PL parameters are given. Seed photon temperature is fixed to standard values. COMPTT errors are calculated on kT_e while fixing τ to its best fit value. F_{comptt} denotes the integrated 20-500 keV energy flux from the thermal component and is given in units of $\times10^{-9} ergs/cm^2/s$. K_{pl} is the flux normalization at 100 keV of the non-thermal powerlaw and is given in units of $\times10^{-5} photons/cm^2/s/keV$

3 Discussion

We interpret the $20-500$ keV emission of GRS 1915+105 as a conjunction of thermal and non-thermal comptonization. Given the similarities of the observed temporal properties, the ASM band is likely to sample the same emission component as the $20-50$ keV SPI band. This is in agreement with the results of Done et al. (2004) who show that except for ultrashort disc-dominated X-ray spikes the accretion disc has no significant effect above 3 keV (see also Rodriguez et al. 2008). The spectra obtained during observations 295 and 368 on one hand and 246 and 423 on the other show that for different X-ray classes (i.e. different temporal behavior of the hot accretion flow) the high energy spectra can be very similar. Conversely, observations 295 and 423 show that within stable emission episodes, there can be significant differences in the spectral behavior of the source. Assuming that the $3-50$ keV emission originates from the comptonizing corona (see Malzac 2007 or Done et al. 2007 for details), this clearly indicates that there is no correlation between the temporal variability and the macroscopic properties of the comptonizing accretion flow.

3.1 The limit states

Modelling the soft sample spectrum reveals the intersection point of the two components to be around 60 keV. At higher energies, the non-thermal processes dominate. Both the thermal and non-thermal components have approximately the same luminosity above 20 keV. If these two components originate from the same population, the electrons are found to thermalize around Lorentz factor $\gamma_{min} = 1.3$. The mildly hot Compton cloud ($kT_e \approx 15\,keV$) is found to be marginally optically thick ($\tau \approx 2.7$) which is an expected configuration for black-hole binaries in a very high state (Done & Kubota 2006). We suggest that our soft composite spectrum gives a template high-energy representation of GRS 1915+105 in low coronal luminosity states.

Concerning the hard sample spectrum, the luminosity of the non-thermal component is found to be roughly the same as for the previously discussed soft sample. However, the intersection point of the two components is now around 110 keV (which corresponds to Lorentz factor $\gamma_{min} \approx 1.39$), showing that the main difference lies in the properties of the comptonizing thermal electrons of the corona. The plasma is found to be either hotter for similar optical depth or optically thicker for similar electron temperature (or a mixture of both), thus enhancing the higher observed $20-50\,keV$ flux. Even though this situation cannot be completely resolved due to the observational $kT-\tau$ degeneracy, spectral fits with COMPPS indicate that most probably there has been a significant increase in opacity, whereas electron temperature remains between 14 and 18 keV. In any case, this does not affect the estimation of the total $20-500\,keV$ luminosity issued from thermal Compton scatterings, which is found to be enhanced at least by a factor of 2 in comparison with the soft sample. We interpret our spectrum as a template for the high-energy emission of GRS 1915+105 in high coronal luminosity states.

4 Summary and Conclusion

We have conducted detailed high-energy spectral analysis of the GRS 1915+105 microquasar through all available SPI data from July 2004 to May 2006. We can summarize our findings as follows:

We found the $\sim$ one day averaged $20-500\,keV$ spectral emission to be always between two boundary states, *hard* and *soft*, which we illustrated through spectral modelling. We confirm that INTEGRAL-SPI observes no high-energy cutoff for GRS 1915+105 (Rodriguez et al. 2008). More precisely, we suggest that the high-energy cutoff from thermal comptonization is drowned by an additional non-thermal component. We found the non-thermal component to be statistically required in both composite samples. The spectral differences we observed in hard X-rays ($20-50\,keV$) are most likely coupled to the evolution of the thermal electron plasma. The bolometric luminosity issued out of thermal comptonization varies by a factor of 2 between soft and hard samples. In contrast, the obtained fits indicate that the non-thermal component is rather stable. This implies that both components are not necessarily linked, i.e. they could originate from dissociated electron populations. Given the length of the high-energy observations (SPI ≈ 3 *days* or OSSE ≈ 15 *days*), it is difficult to investigate the connections between the various X-ray classes and the high-energy spectra. Yet we pointed out that there is no direct correlation between the observed variability patterns and our $20-500\,keV$ SPI spectra. This shows that the macroscopic properties of the comptonizing thermal electrons evolve independently from the temporal behavior of the source, i.e. independently from the fluctuations of the accretion flow.

References

Arnaud, K.A., 1996, in Jacoby, G.H., Barnes, J., eds, ASP Conf. Ser. Vol.101, San Francisco, p.17

Belloni, T., Klein-Wolt, M., Méndez M., et al. 2000, A&A, 355, 271

Castro-Tirado, A.J., Brandt S., & Lund, N. 1992, IAUC, 5590, 2

Done, C., Wardziński, G., & Gierliński, M. 2004, MNRAS, 349, 393

Done, C.& Kubota, A. 2006, MNRAS, 371, 1216

Done, C., Gierliński, M., & Kubota, A., 2007, A&AR Volume 15, Issue 1, 1

Fender, R.P., & Belloni, T. 2004, ARA&A, 42, 317

Galeev, A.A., Rosner, R., & Vaiana, G.S. 1979, ApJ, 229, 318G

Malzac, J. 2007, ApJS, 170, 175

Mirabel, I.F., & Rodríguez, L.F. 1994, Nature, 371, 46

Poutanen, J., & Svensson, R. 1996, ApJ, 470, 249

Rodriguez, J., Shaw, S.E., Hannikainen, D.C. et al. 2008, ApJ, 675, 1449R

Titarchuk, L. 1994, ApJ, 434, 313

Vedrenne, G., Roques, J.P, Schönfelder, et al. 2003, A&A, 411, L63

SF2A 2008
C. Charbonnel, F. Combes and R. Samadi (eds)

HIGH ENERGY EMISSION IN PULSAR WIND NEBULAE

Dubois, F.[1] and for H.E.S.S. Collaboration

Abstract. Pulsar wind nebulae (PWNe) are extended structures of shocked relativistic particles powered by a pulsar at very high energy. Interaction between these particles and the surrounding medium produces very high energy photon emission. Observation by imaging Cherenkov telescopes system in an energy scale from about 100 GeV to 100 TeV, shows various morphologies, depending on many parameters : age, ambiant medium distribution, magnetic fields. The H.E.S.S. experiment allowed to find out many sources, like Vela X or HESS J1825-137, usefull for morphology analysis. Last results obtained with H.E.S.S. and implications on the evolution model of PWNe will be presented here.

Introduction

Pulsar wind nebulae emit in a wide energy range, from radio to TeV γ-rays. Radio and X-ray observations allowed us to discover characteristics about magnetic fields, evolution in pulsar vicinity, as it will be described in the first part. Observing PWNe at higher energy gives new information to explain the complex evolution of these sources et better define their properties.

1 An evolving definition

Thanks to observations in new energy ranges, PWNe definition is evolving, by finding out new properties for each energy range. From the first observations, the following properties were found:

- a filled center or blob like form,
- a flat radio spectrum with a spectral index between 0 to -0.3,
- a well-organized internal magnetic field with high integrated linear polarisation at high radio frequencies.

With the growing accuracy of instruments for X-ray astronomy, the definition of PWNe has been broadened:

- a torus and a jet near the pulsar, and a jet aligned with the pulsar spin axis (see Pavlov et al. 2003),
- evidence for particles re-acceleration between light cylinder and shock radius, providing a hard X-ray spectral index between -1.5 to -2. near the shock,
- evidence for synchroton cooling beyond the shock with spectral index between -2. to -2.5.

Here are only the main properties. A more exhaustive list can be found in de Jager & Djannati-Ataï (2008).

[1] LAPP, Laboratoire de Annecy-le-vieux de Physique des particles, UMR/IN2P3-CNRS, Université de Savoie, 9 Chemin de Bellevue - 74941 Annecy-le-Vieux, France

2 Pulsar Wind Nebulae discovery

The H.E.S.S. experiment has observed the South hemisphere sky since 2003 and found many γ-ray sources like supernovae remnants, active galactic nuclei, pulsar wind nebulae and many other unidentified sources. Some sources of the last type could be associated with a pulsar, with a position offset.
The γ-ray emission from HESS J1912+101 was discovered thanks to the H.E.S.S. galactic survey (Aharonian et al. 2008). This source (Fig. 1) does not show any apparent counterpart in other wavelengths. The best candidates to explain this emission are the supernova remnant 44.6+1.1 (white ellipse on Fig. 1, top-right) in one hand, and the pulsar PSR J1913+1011 on the other hand. In the first case, emission would be due to interaction of accelerated particles with dense molecular clouds. However, X-ray observations do not show any counterpart, which would be expected in this case.

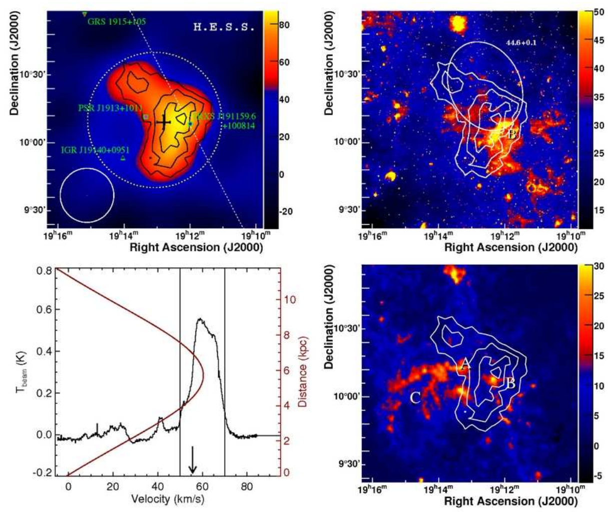

Fig. 1. Top, left: γ-ray excess distribution. Top, right: radio emission using the Spitzer telescope. The region marked as "B" is a complex of molecular clouds and HII-regions. The white ellipse illustrates the position and the extension of the SNR 44.6+0.1. Bottom, left: Velocity profile of ^{13}CO intensity at 110.2GHz. The arrow marks the velocity corresponding to the nominal distance of PSR J1913+1011. Bottom, right: ^{13}CO intensity, integrated in the velocity range 50-70km.s^{-1}

The second candidate can be also the engine of this emission. The shifted position is explained by the proper motion of the pulsar, as it is shown in Fig. 1 (bottom-left). The asymmetric emission, in this case, would be due to molecular clouds, observed with CO line at 110.2 GHz.

3 Morphology analysis

The γ-ray source HESS J1825-137 is a well-known example of energy dependent and asymmetrical morphology emission. It is associated to X-ray PWN G18.0-0.7 and the pulsar PSR J1826-1334. The shifted pulsar position compared to the TeV emission is also explained by an evolution in an inhomogeneous medium : nebula is evolving where the density is lower. This phenomena is confirmed by simulation of pulsar nebula in a nonuniform mdium (Blondin et al. 2001): after a free expansion, the reverse shock collides with the pulsar wind during the Sedov period. An inhomogeneous medium causes an asymmetrical collision and hence an asymmetrical evolution of the PWN.

An other property discovered with HESS J1825-137 is the energy dependent morphology. As shown in Fig. 2 , γ-ray emission is much more extended than X-ray emission. Furthermore, this dependance is also apparent at TeV energy: the source extension increases with decreasing energy (Fig. 4). As a result, the spectrum is softer far away the pulsar position and harder near the pulsar (see Fig. 4). This can be well explained by particles cooling: the older ones, far away, had more time to loose their energy by synchrotron cooling.

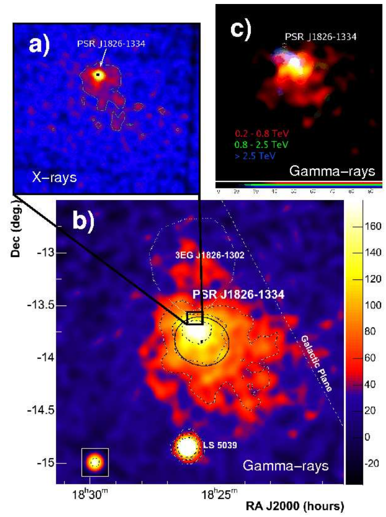

Fig. 2. a)X-ray emission observed with XMM-Newton space-base telescope. b)γ-ray excess map. c) TeV γ-ray excess integrated in 3 energy ranges : 0.2-0.8 TeV (red), 0.8-2.5 Tev (green) and above 2.5 TeV (blue).

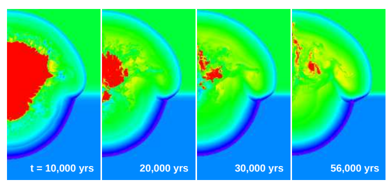

Fig. 3. Simulation of pulsar wind nebula evolution in an inhomogeneous medium (Blondin et al. 2001).

4 Mechanism of emission

High energy emission is mainly due to two mechanisms. The hadronic model describes photon emission as the result of interaction between accelerated protons and cold protons. The leptonic model includes interactions with leptons like synchrotron emission where magnetic density dominates, and Inverse Compton emission, due to interactions between particles and photons from Cosmic Ray Background (CMB), infrared interstellar medium, or synchrotron photon, where radiation density is dominating. In the PWNe case, a purely leptonic model better fits the Crab data (see Fig. 5).
An other example favoring leptonic model is given by VelaX. With the hypothesis of acceleration during the early age of the pulsar, and using the 40ms period of the pulsar, the energy needed for a dominating hadronic emission would be higher than the energy given by the pulsar itself (van der Swaluw & Wu 2001).

Conclusion

Discovery of new sources by the H.E.S.S. experiment leads to a better characterization of pulsar wind nebulae and exhibits new properties: an expanded, often asymmetric emission, an energy dependent morphology due to particles cooling. In many cases, leptonic model is prefered to hadronic model to explain observed spectra. PWNe multiwavelength analysis provide us information about evolution and physical properties of the surrounding media.

Acknowlegdement

The support of the Namibian authorities and of the University of Namibia in facilitating the construction and operation of H.E.S.S. is gratefully acknowledged, as is the support by the German Ministry for Education and Research (BMBF), the Max Planck Society, the French Ministry for Research, the CNRS-IN2P3 and the

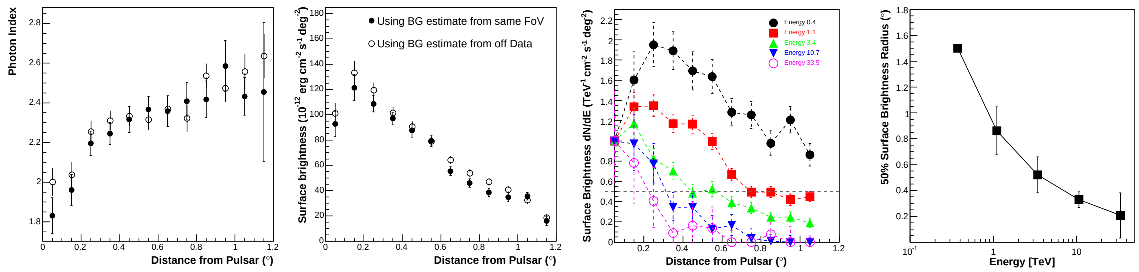

Fig. 4. Left: Spectral index and brightness dependence. The closed points are obtained by using a reflected background substraction. The opened points are derived using off-data (from Aharonian et al. 2006). Right: Relative surface brightness for energies between 0.2 TeV to 9 TeV (see also Funk 2007)

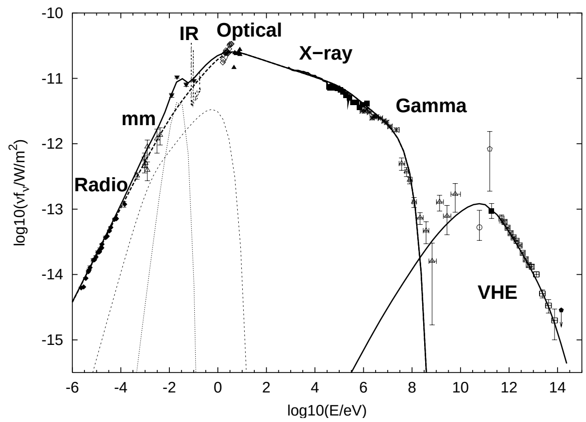

Fig. 5. Spectral energy density of Crab Nebula: spectrum fitted by a pure leptonic model (Horns & Aharonian 2004)

Astroparticle Interdisciplinary Programme of the CNRS, the U.K. Science and Technology Facilities Council (STFC), the IPNP of the Charles University, the Polish Ministry of Science and Higher Education, the South African Department of Science and Technology and National Research Foundation, and by the University of Namibia. We appreciate the excellent work of the technical support staff in Berlin, Durham, Hamburg, Heidelberg, Palaiseau, Paris, Saclay, and in Namibia in the construction and operation of the equipment.

References

Aharonian, F. et al. 2008, A& A, 484, 435

Aharonian, F. et al. 2006, A& A, 460, 365

Blondin, J.M.,Chevalier,R.A., & Frierson, D.M. 2001, ApJ, 563, 806

de Jager, O. J. & Djannatï, A. 2008, arXiv:0803.0116 to appear in Springer Lecture Notes: "Neutron stars and pulsars: 40 years after their discovery", eds. W. Becker

Horns, D. & Aharonian, F. 2004, The Integral Universe, SP-552, 439

Funk, S. 2007, 30th International Cosmic Ray Conference, 00, 30

Pavlov, G.G. et al. 2003, ApJ, 591,1157

van der Swaluw, E., & Wu, Y. 2001, ApJ, 555, L49

SF2A 2008
C. Charbonnel, F. Combes and R. Samadi (eds)

A GLOBAL ENERGETIC MODEL FOR MICROQUASARS: PRELIMINARY RESULTS AND SPECTRAL ENERGY DISTRIBUTIONS

Foellmi, C.[1], Petrucci, P.-O.[1], Ferreira, J.[1], Henri, G.[1] and Boutelier, T.[1]

Abstract. We present preliminary results and observables from a model of microquasar based on a theoretical framework where stationary, powerful, compact jets are launched and then accelerated from an inner magnetized disk. This model aim at providing a consistent picture of microquasars in all their spectral states. It is composed of an outer standard accretion disk down to a variable transition radius where it changes to a magnetized disk, called the Jet Emitting Disk (JED). The theoretical framework providing the heating, we solve the radiative equilibrium and obtain the JED structure. Our JED solutions are rich, and reproduce the already known scheme where a cold optically-thick and a hot optically-thin solutions bracket a thermally unstable one. We present the model and preliminary results, whith a first attempt at reproducing the observed SED of XTE J1118+480.

1 Introduction

Microquasars are stellar binaries with a short period in which one of the two components is a stellar-mass black-hole. The secondary component is a normal star filling its Roche lobe, and loosing mass through the first Lagrangian point. The ejected matter organizes itself in an accretion disk, from which jets are launched. Microquasar are one piece of a chain of objects with Active Galactic Nuclei and Gamma Ray Bursts, sharing the same ingredients and physics (Mirabel 2004).

Various theoretical works have been made to model the accretion disk, with the goal of reproducing the observations. The first kind of observations that is attempted to be reproduced is the spectral energy distribution (SED), which results from the combination of model *components* and the consistency with which they are combined, and the physical radiative processes occuring therein. Other observables, such as for example time-lag observed in X-rays or Quasi-Periodic Oscillations, are usually being modeled with more or less dedicated work, and reflects more the behavior of a given component (the disk for QPOs, e.g. Tagger & Varnière 2006, and the jet for time-lags, see for instance Kylafis et al. 2008).

Our own approach is the following: based on a *consistent* dynamical framework describing how jets are launched from a disk (see Ferreira 1997 and references therein), we build a microquasar model comprising an outer standard accretion disk down to a transition radius, and an inner disk from which jets are lauched, called the Jet Emitting Disk (JED). This model is a global attempt at explaining the general behavior of microquasars in all their spectral states (see Ferreira et al. 2006, Petrucci et al. 2008). Our goal here is to explore the richness of the solutions given by the radiative equilibrium of the JED, and produce theoretical SEDs that can be tested against observations.

2 The model

Our model for microquasars is based on the theoretical framework described in Ferreira et al. (2006, see in particular their Fig. 1). We model the outer standard accretion disk, from the transition radius r_j onwards, with a multi-temperature blackbody spectrum, following Makishima et al. (1996). In the inner JED, comprised between the last stable orbit $r_{\rm ISCO} = 6R_g$ and r_j, we consider a one-temperature plasma with thermal particules only, and follow Mahadevan (1997) for the Bremsstrahlung, Esin et al. (1996) for the Synchrotron.

[1] Laboratoire d'Astrophysique de Grenoble, OSUG, U. Joseph Fourier, CNRS UMR 5571, 38400 Saint-Martin d'Hères, France

We approximate the Compton cooling by using the parameter η of Dermer et al. (1991), which gives the mean gain of energy in a Compton diffusion. We then solve the conservation of energy and the conservation of photons, assuming that in all cases, the compton intensity spectrum follows a power-law with a Wien bump at high energy. In order to obtain the three parameters of the comptonized spectrum, we link the Wien's bump normalisation γ and the power-law index α (see Wardzinski & Zdziarski, 2000, Equ. 23).

In our computations we consider two sources of photons that are being comptonized: the Synchrotron self-Compton on the inner JED photons (internal Compton), and the external Compton on photons coming from the standard accretion disk, and reaching the JED. This later contribution appeared to be of central importance in some cases where the transition radius r_j. The correct inclusion of these photons for the comptonization deserves a full and detailed geometrical treatment. As for now, we have simply considered that half of the photons coming from the inner radius of the standard accretion disk (i.e. at r_j) only are seen in the JED for comptonization by hot electrons.

3 Radiative equilibrium of the disk and the JED solution

In order to compute theoretical SEDs, we need to compute the radiative equilibrium of the disk. We make the hypothesis, a posteriori verified, that the total pressure is dominated by the gaz pressure. Moreover, the vertical equilibrium of the disk links the temperature T_e to the disk scale height $\epsilon \equiv h/r$. Consequently, the cooling is only a function of ϵ. We compute the cooling by using the individual SEDs of each independant radius of the disk, and adding an advection term (which becomes significant only at $\epsilon \sim 0.1$). The heating of the disk is also a function of ϵ only, as provided by the theoretical framework (see Combet & Ferreira 2008). We then solve the equation $Q^-(\epsilon) = Q^+(\epsilon)$ (see Fig 1), where $Q^-(\epsilon) = Q_{\mathrm{Bremsstrahlung}} + Q_{\mathrm{Synchrotron\ Compton}} + Q_{\mathrm{External\ Compton}} + Q_{\mathrm{Advection}}$.

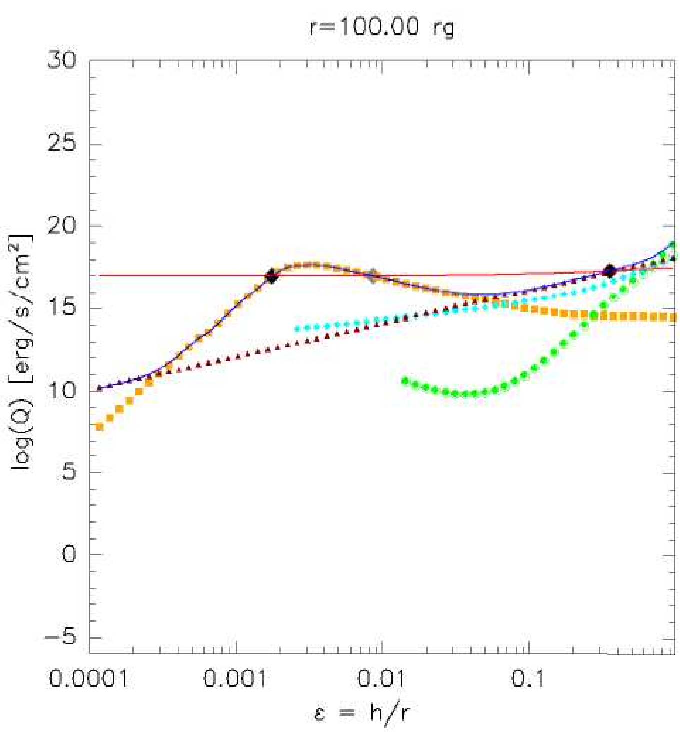

Fig. 1. The radiative equilibrium is computed here for the JED radius $r = 100R_g$. The various cooling contributions are indicated by dots of various shapes. In orange, the Bremsstrahlung, cyan the external Compton, green the SSC, brown the advection. The red and blue lines indicate the heating and the total cooling respectively.

Interestingly, our novel accretion disk solution often leads to three solutions of the thermal equilibrium: a cold optically-thick and a hot optically-thin thermally stable ones, and one middle thermally unstable solution

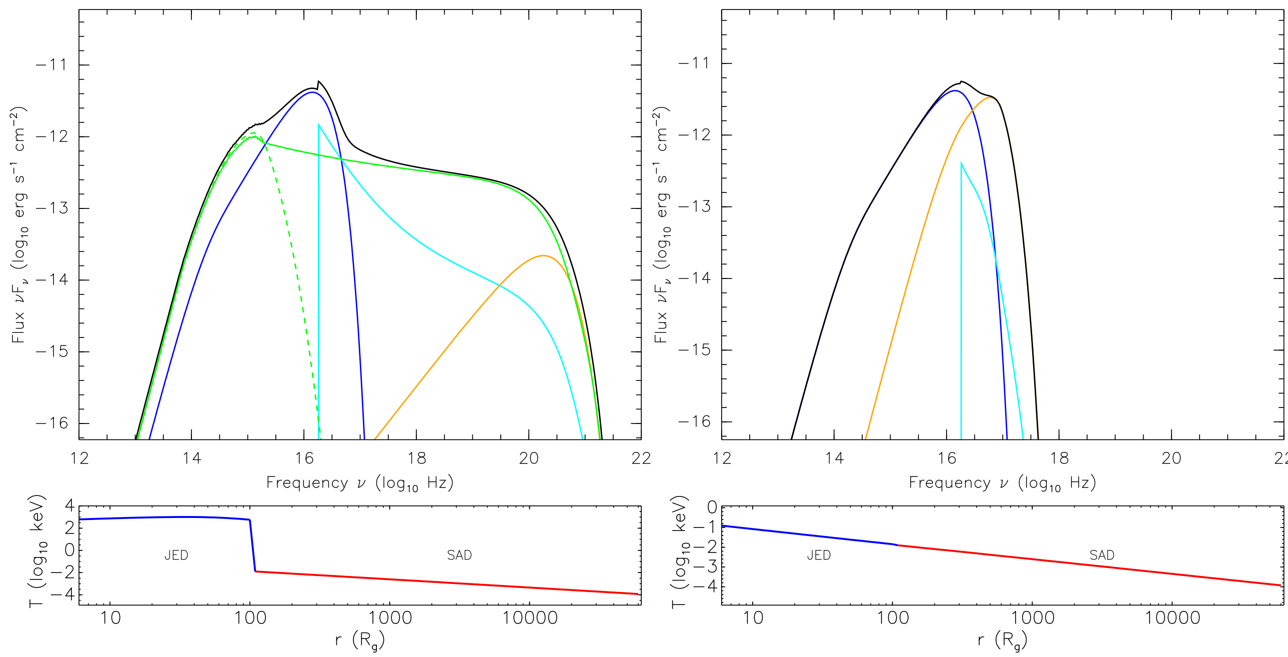

Fig. 2. Example of theoretical SEDs. Left: using the "hot" stable solution. Right: using the "cold" stable solution. The input parameters are identical to both figures: an accretion rate $\dot{M} = 10^{-2} M_{\rm Edd} = 10^{-2} L_{\rm Edd}/c^2$, an internal disk radius $r_i = 6R_g$, a transition radius between the standard accretion disk and the JED $r_j = 100R_g$, a magnetization $\mu = 1.0$, and the sonic Mach number $m_s = 1.0$, for an object with $M_{bh} = 10M_\odot$, an inclination angle $i = 70°$ and a distance of 10 kpc. The black line indicate our final SED, the jet is in red, the Bremsstrahlung in orange, the standard accretion disk in blue, the external Compton in cyan. The synchrotron is indicated in dashed green (it is not counted in the final SED), while the SSC is shown in plain green.

(see black losanges in Fig. 1). One interesting output of our model is that we are able to produce a hard X-ray spectrum even with thermal particles, and with the clear advantage of having consistently taken into account the power extracted for the jet. This is illustrated in Fig. 2. However, the jet is weakly radiative, and radiate through an unknown distribution of non-thermal particles. We thus model the jet emission by a pure synchrotron emission model, following Heinz & Sunyaev (2003). We have then attempted to manually reproduce the observed SED of the galactic microquasar XTE J1118+480 (see Markoff et al. 2001), as shown in Fig. 3.

4 Perspectives

At that stage, our model can be tested against observational SEDs when data is available over a large frequency domain (as shown above), but mostly when the object is in the so-called low/hard state. Preliminary tests have shown that we cannot reproduce the high/soft state because of the absence in our model of a component that can produce the hard-tail power-law observed during these stages. In the future, we will tackle this issue along with the developement of a more realistic jet emission model. Our final goal is to be able to explore the hardness-intensity diagram and reproduce an hysteresis pattern.

References

Belloni, T., Homan, J., Casella, P., van der Klis, M., Nespoli, E., Lewin, W.H.G., Miller, J.M., & Méndez, M. 2005, A&A, 440, 207

Combet, C., Ferreira, J. 2008, A&A, 479, 481

Dermer, C.D., Liang, E.P., & Canfield, E. 1991, ApJ, 369, 410

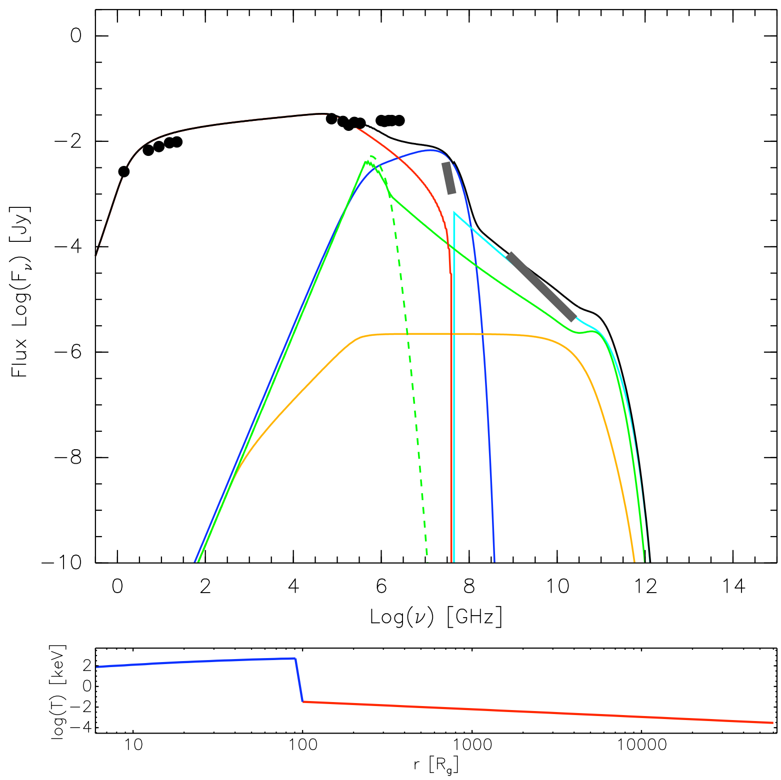

Fig. 3. Manual fit of the observed SED of XTE J1118+480 taken from Markoff et al. (2001). The bottom panel shows the corresponding disk where the red line is the standard accretion disk, and in blue the hot JED disk. Parameters are: $M_{bh} = 6.M_\odot$, $\dot{M} = 0.2M_{\rm Edd}$ and $D = 1.8$ kpc taken from Markoff et al. (2001) and a hot JED disk with $r_j = 100R_g$. The jet synchrotron model follows Heinz & Sunyaev (2003).

Ferreira, J., Petrucci, P.-O., Henri, G., Saugé, L., & Pelletier, G. 2006, A&A, 447, 813

Ferreira, J. 1997, A&A, 319, 340

Esin, A., Narayan, R., Ostriker, E., & Yi, I. 1996, ApJ, 465, 312

Heinz, S., &, Sunyaev, R.A. 2003, MNRAS, 343, 59

Kylafis, N.D., Papadakis, I.E., Reig, P., Giannios, D., & Pooley, G.G. 2008, eprint arXiv, astro-ph/0807.2910

Mahadevan, R. 1997, ApJ, 477, 585

Makishima, K., Maejima, Y., Mitsuda, K., Bradt, H.V., Remillard, R.A., Tuohy, I.R., Hoshi, R., & Nakagawa, R. 1986, ApJ, 308, 635

Markoff, S., Falckem H., & Fender, R. 2001, 372, 25

Mirabel, I.F. 2004, Proceedings of the 5th INTEGRAL Workshop on the INTEGRAL Universe (ESA SP-552), 552, 175

Petrucci, P.-O., Ferreira, J., Henri, G., & Pelletier G. 2008, MNRAS, 385, L88

Tagger, M., & Varnière, P. 2006, ApJ, 652, 1457

Wardzinski, G., & Zdziarski, A.A. 2000, Mon. Not. R. Astron. Soc., 314, 183

STOCHASTIC MODEL OF ACCELERATION TO ULTRA HIGH ENERGY

Fraschetti, F.[1]

Abstract. In the past year, the HiRes and Auger collaborations have reported the discovery of a high-energy cutoff in the ultra-high-energy cosmic-ray (UHECR) spectrum, and an apparent clustering of the highest energy events towards nearby active galactic nuclei (AGNs). Consensus is building that such 10^{19}-10^{20} eV particles are accelerated within the radio-bright lobes of these sources, but it is not yet clear how this actually happens. We report (to our knowledge) the first treatment of particle acceleration in such environments from first principles, showing that energies of order 10^{20} eV are reached in 10^7 years for protons. This prediction appears to be consistent with the Auger observations. However, our findings reopen the question regarding whether the high-energy cutoff is due solely to propagation effects, or whether it represents the maximum energy permitted by the acceleration process itself.

1 Introduction

The understanding of the origin of Ultra-High-Energy Cosmic Rays (UHECRs) still represents one the major challenges of theoretical astrophysics. Recently the observations by Pierre Auger Observatory (PAO), demonstrating a low fraction of high-energy photons in the Cosmic Ray distribution, rule out the top-down models, in which the UHECRs represent the decay products of high-mass particles created in the early Universe (Semikoz et al. 2007). The measured photon flux is also in conflict with scenarios in which UHECRs are produced by collisions between cosmic strings or topological defects (Bluemer et al 2008; Auger 2008b). On the other hand, such extremely energetic particles may still be produced via astrophysical acceleration mechanisms (Fraschetti 2008; Torres & Anchordoqui 2004 and other references cited therein).

Moreover the long sought GZK cutoff (Greisen 1966; Zatsepin & Kuz'min 1966) in Cosmic Ray spectrum due to interactions of primary protons with the CMB has been claimed to have been observed by the High Resolution Fly's Eye (Abbasi et al. 2008). A spectral steepening at the expected energy $E_{GZK} \sim 4 \times 10^{19}$ eV has also been observed by PAO (Auger 2008c).

The PAO has confirmed that active galactic nuclei (AGN) located within ~ 75 Mpc are correlated with the arrival directions of UHECRs (Auger 2008a). However, the question remains open regarding the mechanism of acceleration to such high energies and the origin of the observed cutoff in the spectrum, i.e., whether it is due solely to the GZK effect, or it also points to an intrinsic limit to the acceleration efficiency.

UHECRs generation scenarios include the so-called first-order Fermi acceleration in GRBs, Pulsar Wind Bubbles, and also relativistic second order Fermi acceleration (Fermi 1949). We report here a treatment of propagation and acceleration of individual particle in the lobes of radio-bright AGNs from first principles (Fraschetti & Melia 2008), considering the acceleration of charged particles via random scatterings (a second-order process) with fluctuations in a turbulent magnetic field.

2 Model of magnetic turbulence

In our treatment, we follow the three-dimensional motion of *individual* particles within a time-varying field. By avoiding the use of equations describing statistical averages through the phase space distribution function of a given population of particles, we mitigate our dependence on unknown factors, such as the diffusion coefficient. We also avoid the need to use the Parker approximation (Padmanabhan 2001) in the transport equation. For

[1] LUTh, Observatoire de Paris, CNRS-UMR8102 and Université Paris VII, 5 Place Jules Janssen, F-92195 Meudon Cédex, France

simplicity, we assume that the magnetic energy is divided equally between the two components: background and turbulence; the actual value of this fraction does not produce any significant qualitative differences in our results. For many real astrophysical plasmas, the magnetic turbulence seems to be in accordance with the Kolmogorov spectrum; a more recent numerical analysis of MHD turbulence confirms the general validity of the Kolmogorov power spectrum (Cho et al. 2003). In addition, renormalization group techniques applied to the analysis of MHD turbulence also favour a Kolmogorov power spectrum (for more details, see Verma 2004).

We calculate the trajectory of a test particle with charge e and mass m in a magnetic field $\mathbf{B}(t,\mathbf{r}) = mc\mathbf{\Omega}(t,\mathbf{r})/e$, where c is the speed of light in vacuum. The particle motion is obtained as a solution of the Lorentz equation

$$\frac{d\mathbf{u}(t)}{dt} = \delta\mathcal{E}(t,\mathbf{r}) + \frac{\mathbf{u}(t)\times\mathbf{\Omega}(t,\mathbf{r})}{\gamma(t)} \,, \tag{2.1}$$

where $\mathbf{u}$ is the three-space vector of the four-velocity $u^\mu = (\gamma, \gamma\mathbf{v}/c)$, t is the time in the rest frame of the source, and γ is the Lorentz factor $\gamma = 1/\sqrt{1-(v/c)^2}$. The quantity $\mathbf{\Omega}$ in equation (2.1) is given by $\mathbf{\Omega}(t,\mathbf{r}) = \mathbf{\Omega}_0 + \delta\mathbf{\Omega}(t,\mathbf{r})$, where $\mathbf{\Omega}_0 = e\mathbf{B}_0/mc$ and $\mathbf{B}_0$ is the background magnetic field. The time variation of the magnetic field, however, induces an electric field $\delta\mathcal{E}(t,\mathbf{r}) = (e/mc)\mathbf{E}(t,\mathbf{r})$ according to Faraday's law. We ignore any large-scale background electric fields; this is a reasonable assumption given that currents would quench any such fields within the radio lobes of AGNs.

We follow the prescription of (Giacalone & Jokipii 1994) for generating the turbulent magnetic field, including a time-dependent phase factor to allow for temporal variations. The procedure of building the turbulence calls for the random generation of a given number N of transverse waves $\mathbf{k}_i$, $i = 1,..,N$ at every point of physical space where the particle is found, each with a random amplitude, phase and orientation defined by angles $\theta(k_i)$ and $\phi(k_i)$. This form of the fluctuation satisfies $\nabla\cdot\delta\mathbf{\Omega}(t,\mathbf{r}) = 0$. We write

$$\delta\mathbf{\Omega}(t,\mathbf{r}) = \sum_{i=1}^{N} \Omega(k_i)\hat{\xi}_\pm(k_i) e^{\left[i(k_i x' - \omega_i t + \beta(k_i))\right]} \,, \tag{2.2}$$

where the polarization vector is given by

$$\hat{\xi}_\pm(k_i) = \cos\alpha(k_i)\hat{\mathbf{y}}' \pm i\sin\alpha(k_i)\hat{\mathbf{z}}' \,. \tag{2.3}$$

The primed reference system (x', y', z') is related to the lab-frame coordinates (x, y, z) via a rotation in terms of $\theta(k_i)$ and $\phi(k_i)$ (Fraschetti & Melia 2008). For each k_i, there are 5 random numbers: $0 < \theta(k_i) < \pi$, $0 < \phi(k_i) < 2\pi$, $0 < \alpha(k_i) < 2\pi$, $0 < \beta(k_i) < 2\pi$ and the sign $\pm$ indicating the sense of polarization. We use the dispersion relation for transverse non-relativistic Alfven waves in the background plasma: $\omega(k_i) = v_A k_i cos\theta(k_i)$, where $v_A = B_0/\sqrt{4\pi m_p n}$ is the non-relativistic Alfven velocity in a medium with background magnetic field B_0 and number density n, being m_p the proton mass, and $\theta(k_i)$ is the angle between the wavevector k_i and B_0. The background plasma is assumed to have a background number density $n \sim 10^{-4}$ cm^{-3}, a reasonable value for the radio lobes of AGNs.

The amplitudes of the magnetic fluctuations are assumed to be generated by Kolmogorov turbulence, so

$$\Omega(k_i) = \Omega(k_{min})\left(\frac{k_i}{k_{min}}\right)^{-\Gamma/2} \,, \tag{2.4}$$

where k_{min} corresponds to the longest wavelength of the fluctuations and $\Gamma = 5/3$. Finally, the quantity $\Omega(k_{min})$ is computed by requiring that the energy density of the magnetic fluctuations equals that of the background magnetic field: ${B_0}^2/8\pi$.

We choose N=2400 values of k evenly spaced on a logarithmic scale; considering that the turbulence wavenumber k is related to the turbulent length scale l by $k = 2\pi/l$, we adopt a range of lengthscales from $l_{min} = 10^{-1}\, v_0/\Omega_0$ to $l_{max} = 10^9\, v_0/\Omega_0$, where v_0 is the initial velocity of the particle and Ω_0 is its gyrofrequency in the background magnetic field. Thus the dynamic range covered by k is $k_{max}/k_{min} = l_{max}/l_{min} = 10^{10}$ and the interaction of particle with the turbulent waves is gyroresonant at all times. The particles propagating through this region are released at a random position inside the acceleration zone, which for simplicity is chosen to be a sphere of radius $\mathcal{R}$, with a fixed initial velocity u_0 pointed in a random direction. The initial value of the Lorentz factor $\gamma_0 = \sqrt{1+{u_0}^2} \sim 1.015$ is chosen to avoid having to deal with ionization losses for the protons.

Assuming that both the radio and CMB intensity fields are isotropic, we take these energy losses into account using the following angle-integrated power-loss rate:

$$-\frac{dE}{dt} = \frac{4}{3}\sigma_T(m)c\gamma^2\left(\frac{B^2}{8\pi} + U_R + U_{CMB}\right) , \quad (2.5)$$

where $\sigma_T(m) = 6.6524 \times (m_e/m)^2\, 10^{-25}$ cm^2 is the Thomson cross section for a particle of mass m, $B^2/(8\pi) = (2{B_0}^2)/(8\pi)$ is the total energy density of the magnetic field, and U_R is the photon energy density inside a typical Radio Lobe, for which we assume a standard luminosity density corresponding to the Fanaroff-Riley class II of galaxies (with a luminosity $L = 5 \times 10^{25}$ W Hz^{-1} sr^{-1} at 178 MHz), and $\mathcal{R}$ is the radius of the acceleration zone. For the CMB, we use $U_{CMB} = aT^4 = 4.2 \times 10^{-13}$ erg cm^{-3}. In Fig. 1, we plot the time evolution of the particle Lorentz factor γ for three representative values of the background field B_0: 10^{-7}, 10^{-8}, and 10^{-9} gauss. We see the particle undergoing various phases of acceleration and deceleration as it encounters fluctuations in **B**.

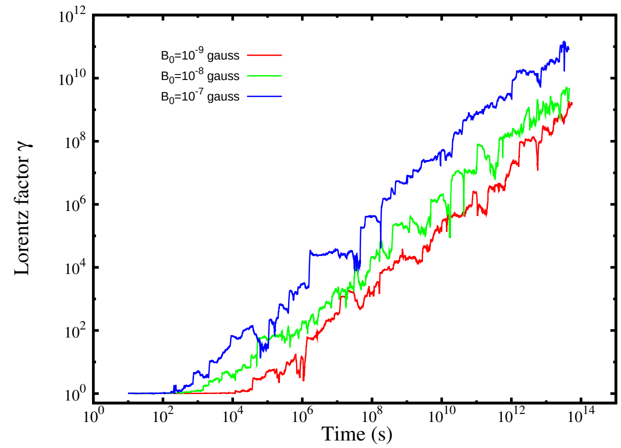

Fig. 1. Simulated time evolution of the Lorentz factor γ for a proton propagating through a time-varying turbulent magnetic field. The particle is followed until it leaves the acceleration zone and enters the intergalactic medium. The acceleration timescale Δt is inversely proportional to the background field B_0. Therefore, as expected, a larger B_0 produces a more efficient acceleration.

In a region where magnetic turbulence is absent or static, a given test particle propagates by "bouncing" randomly off the inhomogeneities in **B**, but its energy remains constant. The field we are modeling here, however, is comprised of transverse plane waves (see equation 2.2), and collisions between the test particle and these waves produces (on balance) a net acceleration as viewed in the lab frame. A sampling of parameter space is shown in Fig. 2.

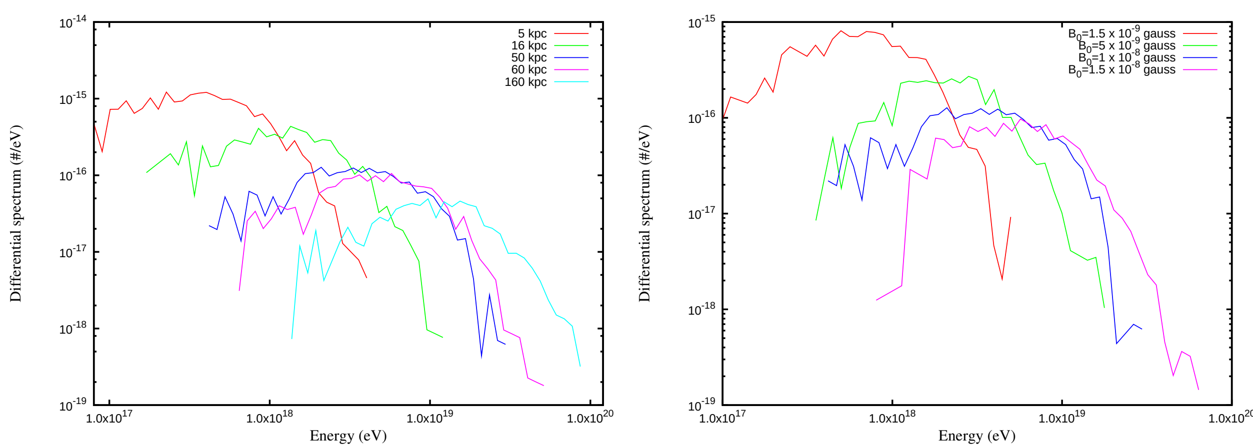

Fig. 2. Left: Calculated differential spectra for 500 protons with $B_0 = 10^{-8}$ gauss and for different values of the size of the acceleration region, assumed to be a sphere of radius spanning the interval $\mathcal{R} = [5 - 160]$ kpc. The dependence of the energy cutoff on $\mathcal{R}$ is evidenced. This result shows that the cutoff in the observed spectral distribution can be due to the competition between two distint effects: propagation through the CMB and intrinsic properties of the accelerator. Moreover, the slope in the region $E > 4 \times 10^{18}$ eV strongly depends on R. This diagram supports the view that the steeper CR spectrum below $\log(E/eV) \approx 18.6$ likely represents a population of galactic cosmic rays. **Right:** Calculated differential spectra for 500 protons with $R = 50$ kpc and for different values of the turbulent magnetic energy. In this case B_0 spans the interval $B_0 = 1.5 \times [10^{-9} - 10^{-8}]$ gauss.

In Fig. 3, we compare a theoretical differential injection spectrum for a population of 1,000 protons with energy $E > 4 \times 10^{18}$ eV with a power law in arbitrary units of index -2.6. We infer that for a radius $\mathcal{R} = 50$ kpc, B_0 should lie in the range $[0.5 - 5] \times 10^{-8}$ gauss. The observed spectrum may be affected by the cosmological evolution in source density. However, a likelihood analysis (Gelmini et al 2007) of the dependence of the observed distribution on input parameters has already shown that, in the case of pure proton-fluxes of primaries, for $\alpha \sim 0$, where α is the evolution index in the source density, the HiRes observations are compatible with a power-law injection spectrum with index -2.6 (Fraschetti & Melia 2008). Thus, in a more conservative interpretation, the result presented here provides the injection spectrum from a single source.

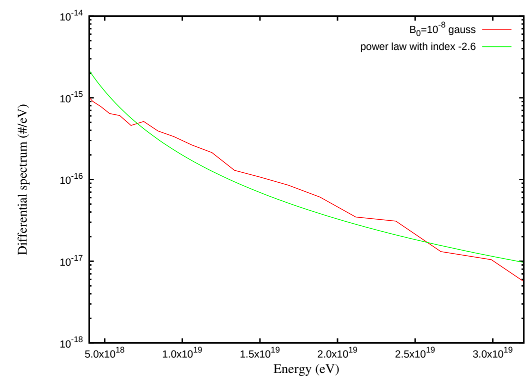

Fig. 3. Calculated differential spectrum for 1,000 protons in the energy range $\log(E/eV) = [18.6 - 19.5]$ for the selected parameters $B_0 = 10^{-8}$ gauss and $\mathcal{R} = 50$ kpc.

3 Conclusion

It is worth emphasizing that this calculation was carried out without the use of several unknown factors often required in approaches involving a hybrid Boltzmann equation to obtain the phase-space particle distribution. In addition, we point out that the acceleration mechanism we have invoked here is sustained over 10 orders of magnitude in particle energy, and the UHECRs therefore emerge naturally—without the introduction of any additional exotic physics—from the physical conditions thought to be prevalent within AGN giant radio lobes.

The importance of elucidating the mechanism of acceleration of UHECRs is confirmed by the growing number of dedicated experiments which will join Auger South: Auger North, the JEM-EUSO mission (Allard 2008), etc. The UHECR source identification will continue to improve. Eventually, we should be able to clarify whether the cutoff in the CR distribution is indeed due to propagation effects, or whether it is primarily the result of limitations in the acceleration itself. As energies as high as $\sim 10^{20}$ eV may be reached within typical radio lobes, it is possible that both of these factors must be considered in future refinements of this work.

References

Abbasi, R. U. *et al.* [HiRes Collaboration], 2008, Phys. Rev. Lett., 100, 101101
Allard, D., in these proceedings
The Auger Collaboration, 2007, Science, 318, 939
The Auger Collaboration, 2008a, Astropart. Phys. 29, 188
The Auger Collaboration, 2008b, Astropart. Phys., 29, 243
The Auger Collaboration, 2008c, Phys. Rev. Lett., 101, 061101
Bhattacharjee, P. & Sigl G. 2000, Phys. Rep., 327, 109
Bluemer, J., for the Auger Collaboration (http://arXiv.org/abs/astro-ph/0807.4871)
Cho, J., Lazarian, A., Vishniac, E.T. 2003, ApJ, 595, 812
Fermi, E. 1949, Phys. Rev., 75, 1169
Fraschetti, F. 2008, Phil. Trans. A of Royal Society, 366
Fraschetti, F., & Melia, F. 2008, Mon. Not. Roy. Astron. Soc., in press (http://arxiv.org/abs/astro-ph/0809.3686)
Gelmini, G., Kalashev, O., & Semikoz, D.V. (http://arxiv.org/abs/astro-ph/0702464)
Giacalone, J., & Jokipii, J.R. 1994, ApJ, 430, L137
Greisen, K. 1966, Phys. Rev. Lett., 16, 748
Padmanabhan, T. 2001, Theoretical Astrophysics Vol II, Cambridge University Press.
Semikoz, D. V., for the Auger Collaboration (http://arXiv.org/abs/astro-ph/0706.2960).
Torres, D.F., & Anchordoqui, L.A. 2004, Rep. Prog. Phys., 67, 1663
Verma, M.K. 2004, Phys. Rep., 401, 229
Zatsepin, G.T., & Kuz'min, V. A., 1966, Sov. J. of Exp. and Theor. Phys. Letters, 4, 78

SF2A 2008
C. Charbonnel, F. Combes and R. Samadi (eds)

THE LUMINOSITY OF GRB AFTERGLOWS AS DISTANCE ESTIMATOR

Gendre, B.[1], Galli, A.[2] and Boër, M.[3]

Abstract. We investigate the clustering of afterglow light curves observed at X-ray and optical wavelengths. We have constructed a sample of 61 bursts with known distance and X-ray afterglow. GRB sources can be divided in three classes, namely optical and X-ray bright afterglows, optical and X-ray dim ones, and optically bright -X-ray dim ones. We argue that this clustering is related to the fireball total energy, the external medium density, the fraction of fireball energy going in relativistic electrons and magnetic fields. We propose a method for the estimation of the GRB source redshift based on the observed X-ray flux one day after the burst and optical properties. We tested this method on three recently detected SWIFT GRBs with known redshift, and found it in good agreement with the reported distance from optical spectroscopy.

1 Introduction

Long Gamma-Ray Bursts (GRBs) (for a review, see Meszaros 2006) are linked to the final stages of the stellar evolution. As these objects are extremely luminous and can be detected up to large distance, they are interesting for studies of cosmology in the redshift range 1-15. However, the use of GRB for cosmological studies needs to build a robust indicator of their distance, whenever possible based on their intrinsic properties.

Hints of standardization of the X-ray afterglow luminosities were first discovered by Boër & Gendre (2000), who found evidences for clustering in the X-ray luminosity of BeppoSAX afterglows, and confirmed later by Gendre & Boër (2005). In the following we will refer to these articles respectively as paper I and II. This study was completed by Nardini et al. (2006) and Liang & Zhang (2006) who found independently that optical afterglows were also clustered in luminosity, and by Gendre et al. (2008b) who extended this study towards infrared wavelengths. We have tried to derive a method for estimating the burst distance based on that property. In Section 2 we present the luminosity clusterings. In section 3 we present our method of GRB distance estimation from the X-ray afterglow light curve. We test this method on several GRBs detected recently by SWIFT, and we propose an estimation of the redshift for two previously detected GRBs of unknown distance.

2 Luminosity clustering

2.1 X-ray clustering

Our sample of GRBs with known redshift and X-ray afterglow observations includes all afterglows observed by BeppoSAX, XMM-Newton, Chandra, and SWIFT prior to the 1st of August 2006 with a t_{90} larger than 2.0 seconds (in order to exclude short bursts). Data analysis is explained in detail in Gendre et al. (2008a). The results are displayed in Fig. 1. The groups reported in papers I and II are apparent. We note however some dispersion during the first part of the light curves. We interpret this as a consequence on the error on the T_a measurement. We refer to the bright group as *xI* and the dimmer one as *xII*, as in paper II. Height bursts do not follow this relation. We consider that these low luminosity events form a specific group, referred as *xIII* in the following.

[1] Laboratoire d'Astrophysique de Marseille/CNRS/Universit de Provence
[2] IASF-Roma
[3] Observatoire de Haute-Provence/CNRS

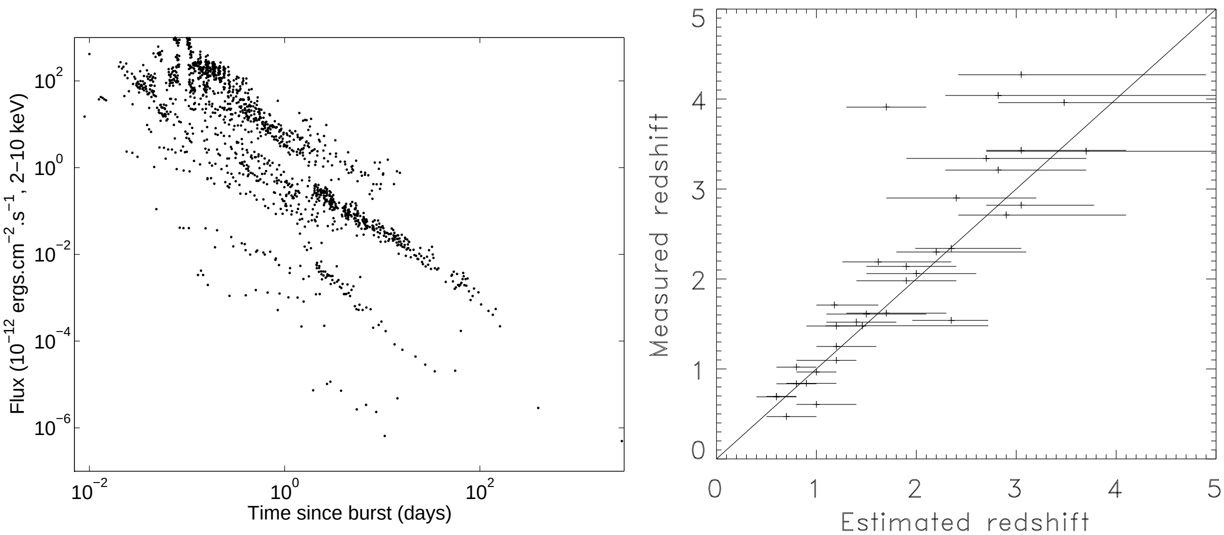

Fig. 1. Left: the light curves of our sample, corrected for distance effects (see text). The groups reported in papers I and II are clearly seen. Right: Comparison of the estimated redshift versus the measured one for the bursts defining our sample. The solid line corresponds to equality.

2.2 The optical afterglows

Nardini et al. (2006) and Liang & Zhang (2006) have shown that optical afterglow light curves also display a clustering effect. They found two groups, and we will refer to them as *oI* and *oII* for the bright and dim group respectively. While an *oI* burst can belong to *xI* or *xII*, *oII* bursts are dim both at optical and X-ray wavelengths.

2.2.1 The nature of the clustering

The optical and X-ray data define 3 groups : *xI-oI* events, *xII-oI* events, *xII-oII* events, plus the outliers *xIII* events. We propose that the presence of different groups is ascribed to different families of ϵ_e and ϵ_B values:

- a family of 'magnetized fireball' that produces the group *xII-oI*. In such a case the fireball transfers only a low fraction of its energy into relativistic electrons.

- a family of 'less magnetized fireball' that produces the groups *xI-oI* and *xII-oII*. The fraction of total energy going into magnetic fields is roughly one order of magnitude lower than group *xII-oI*. These two groups can be related to an high and low fraction of energy going in relativistic electrons, respectively.

3 Estimation of GRB source distance

To date, most of the redshift measurements made on GRB afterglows were done by optical spectroscopic or photometric observations. However, not all GRBs can be followed in optical. On the other hand, after the launch of the SWIFT satellite, nearly all GRBs have an homogeneous X-ray follow-up. Hence, a distance measurement method based solely on X-ray observations could be very interesting if one wants to use a large sample of GRB sources for cosmological studies. We used the observed luminosity clustering in X-ray to derive a distance estimator. Table 1, which provides the redshift needed to comply with the relation for both groups for a given observed flux, is directly usable to estimate that estimator. Note that the belonging group can be fixed only through broad-band modeling. In practical, this leads to two redshift estimates. If the bursts has an optical afterglow there is a possible way to decide which of the estimate is valid: if a GRB afterglow is observed by UVOT (or in the B band for ground based telescopes) then it cannot belong to group I, and the ambiguity on the redshift determination is cleared.

Table 1. Flux to redshift conversion. This table should be used as an estimate of the redshift for bursts observed by any X-ray observatory. The flux is given in the 2-10 keV band at 1 day after the burst (observer frame). The redshift has been calculated for an energy index of 1.2, the uncertainty is 30%.

Flux (erg s^{-1} cm^{-2})	Group I redshift	group II redshift
1×10^{-14}	—	4.43
2×10^{-14}	—	3.28
3×10^{-14}	—	2.72
4×10^{-14}	—	2.35
5×10^{-14}	—	2.12
6×10^{-14}	7.80	1.96
7×10^{-14}	7.09	1.83
8×10^{-14}	6.38	1.75
9×10^{-14}	6.05	1.68
1×10^{-13}	5.78	1.62
2×10^{-13}	4.10	1.26
3×10^{-13}	3.48	1.09
4×10^{-13}	3.05	0.96
5×10^{-13}	2.82	0.89
6×10^{-13}	2.59	0.82
7×10^{-13}	2.42	0.77
8×10^{-13}	2.29	0.73
9×10^{-13}	2.10	0.69
1×10^{-12}	1.99	0.66
2×10^{-12}	1.50	0.50
3×10^{-12}	1.29	—
4×10^{-12}	1.16	—
5×10^{-12}	1.06	—
6×10^{-12}	0.99	—
7×10^{-12}	0.94	—
8×10^{-12}	0.89	—
9×10^{-12}	0.83	—
1×10^{-11}	0.79	—
2×10^{-11}	0.56	—
3×10^{-11}	0.50	—

We calibrated this method by deriving the estimated redshift for the bursts of our sample (for which the group is known), and comparing this value with the measured redshift. The results are displayed in Fig. 1. The estimated redshift agrees with the measured one for most of the bursts. The only discrepancies arises at low redshift: as a conservative approach we prefer to restrict the validity of our method to source located at redshifts larger than 0.5.

The distance estimation of several events with no known redshift, good temporal sampling and spectral informations is presented in table 2. GRB 980519 was observed in U band Jaunsen et al. (2001). As the Lymann α cut-off cross the U band at $z \sim 2.8$, this burst should not have been observed in the high distance hypothesis. U observations can indeed solve the problem of group classification, and we propose a redshift measurement for GRB 980519 of 1.4 ± 0.2. For the same reason, GRB 040827 has $z = 1.9 \pm 0.3$, since an optical afterglow has been observed (Malesani et al 2004).

Several GRB were recently detected by SWIFT and their distance derived using optical spectroscopy. We thus have a sample of bursts which allows to test this correlation independently. To simulate actual conditions for an unknown event we used the SWIFT count rate light curve available from their web site, and we apply a mean spectral index of 1.2 for the count-to-flux conversion. The results are indicated in Table 3, indicating an agreement in accordance with the error estimated previously.

Table 2. Redshift estimates derived from the relation using either the group I and II hypotheses for pre-SWIFT bursts without known distance.

GRB name	Redshift group I	estimate group II
GRB 980329	4.2 ± 1.2	1.2 ± 0.2
GRB 980519	3.8 ± 0.7	1.4 ± 0.2
GRB 990704	3.5 ± 0.9	1.3 ± 0.3
GRB 990806	$4.7^{+1.6}_{-0.7}$	1.6 ± 0.3
GRB 001109	2.3 ± 0.7	0.8 ± 0.2
GRB 001025A	5.8 ± 1.8	2.2 ± 0.4
GRB 020322	5.0 ± 1.5	1.5 ± 0.3
GRB 040106	3.4 ± 0.5	1.0 ± 0.2
GRB 040223	$5.5^{+2.0}_{1.2}$	1.7 ± 0.2
GRB 040827	8.0 ± 2.0	1.9 ± 0.3

Table 3. Redshift estimates derived from the relation using either the group I and II hypotheses for SWIFT bursts with known distance.

GRB name	Group I estimate	Group II estimate	Measured redshift
GRB 070529	7.8	1.96	2.44
GRB 070611	6.05	1.68	2.04
GRB 070721B	—	3.28	3.62

4 Conclusions

We have investigated the clustering of afterglow light curves observed previously in X-ray and in optical. Adding SWIFT bursts to the previous sample reported in paper II, we still confirm our previous findings. On a sample of 61 events the X-ray light curves cluster in two groups, with a significance larger than 6 σ. We compared the classification within each group in X-ray and in optical, and found three classes: *bright* optical and X-ray afterglows, *dim* ones, and optically *bright*-X-ray *dim* ones.

Using the observed X-ray afterglow properties of GRBs, we propose a new, simple, method for the determination of the source distance based on X-ray data; optical photometry in U and V bands may help to clear the degeneracy between the two estimates found. We apply this method to a sample of GRB source of unknown redshift. We propose an estimation of the redshift for GRB 980519 (1.4 ± 0.2) and for GRB 040827 (1.9 ± 0.3).

BG acknowledge support from COFIN grant 2005025417, and from the Centre Nationnal d'Etudes Spatiales. We are pleased to thank Alessandra Corsi, Giulia Stratta. This work made use of data supplied by the UK Swift Science Data Centre at the University of Leicester.

References

Boër, M. & Gendre, B. 2000, A&A, 361, L21

Gendre, B., Boër, M., 2005, A&A , 430, 465

Gendre, B., Galli, A., & Boër, M., 2008a, ApJ, 683, 620

Gendre, B., Pelisson, S., Boër, M. Basa, S., Mazure, A., 2008b, A&A, submitted

Jaunsen, A.O., Hjorth, J., Björnsson, G., et al., 2001, ApJ, 546, 127

Liang, E. & Zhang, B., 2006, ApJ, 638, L67

Malesani, D., D'Avanzo, P., Melandri, A., et al., 2004, GCN # 2685

Meszaros, P, 2006, Rep. Prog. Phys., 69, 2259

Nardini, M., Ghisellini, G., Ghirlanda, G., et al., 2006, A&A, 451, 821

SF2A 2008
C. Charbonnel, F. Combes and R. Samadi (eds)

RISING OPTICAL AFTERGLOWS SEEN BY TAROT

Gendre, B.[1], Klotz, A.[2], Stratta, G.[3], Preger, B.[3], Piro, L.[4], Pelangeon, A.[5], Galli, A.[4], Cutini, S.[3], Corsi, A.[4], Boër, M.[6] and Atteia, J.L.[5]

Abstract. We present the multi-wavelength study of those gamma-ray bursts observed by TAROT. These events are characterized by the presence at early time of a rising in their optical light curves lasting a few hundred of seconds. In one case (GRB 060904B), a flare occurs at similar time in the X-ray band, while in the other cases the X-ray light curves appear smooth during the optical rise. We investigate the possible nature of this behavior and conclude that a multi-component emission is mandatory to explain the optical-to-X-ray afterglow.

1 Introduction

Since the discovery of Gamma-Ray Burst (GRB) afterglows, in 1997 (Costa et al. 1997), tens of GRB optical afterglows have been detected by ground-based rapid response telescopes. Early optical afterglow data play a relevant role to obtain information on the physics of the central engine, and possibly to constraint the initial Lorentz factor of the fireball (*e.g* Zhang et al. 2003). This paper is devoted to the analysis of the GRB observations made by TAROT during the period 2001-2007 when the first telescope started to be fully operational.

2 GRB observations with TAROT

TAROT observed 59 GRBs between 2001 and 2007. During that period, 13 optical transients were detected. Six of them are time resolved allowing the measure of the decay index. 12 GRBs were observed when the gamma emission was still active amongst them 3 were positively detected by TAROT. Figure 1 displays all the detected optical emissions and the first upper limit in the case of negative detections. Half of the afterglows with detectable OT exhibit an increase in brightness until few hundreds of seconds (GRB 050904, GRB 060904B, GRB 070420, GRB 071010A).

3 A rising in detail : GRB 060904B

The optical light-curve of GRB 060904B is shown in Fig. 1. Before the end of the prompt phase, the optical emission features a rise, reaching R=16.8 at maximum. During that rising part, the X-ray and gamma-ray emissions features a giant flare, well fit by a Band model and an hard-to-soft behavior, characteristic of prompt related emission (Klotz et al. 2008). Several phenomena can contribute to a late rising of the optical afterglow (see Klotz et al. 2008), all of them imply a double component to explain the observed emission.

[1] Laboratoire d'Astrophysique de Marseille/CNRS/Universit de Provence
[2] Centre d'Etude Spatiale des Rayonnements/CNRS/Universit Paul Sabatier
[3] ASI Science Data Center
[4] IASF-Roma
[5] Laboratoire d'Astrophysisque de Toulouse/CNRS
[6] Observatoire de Haute Provence/CNRS

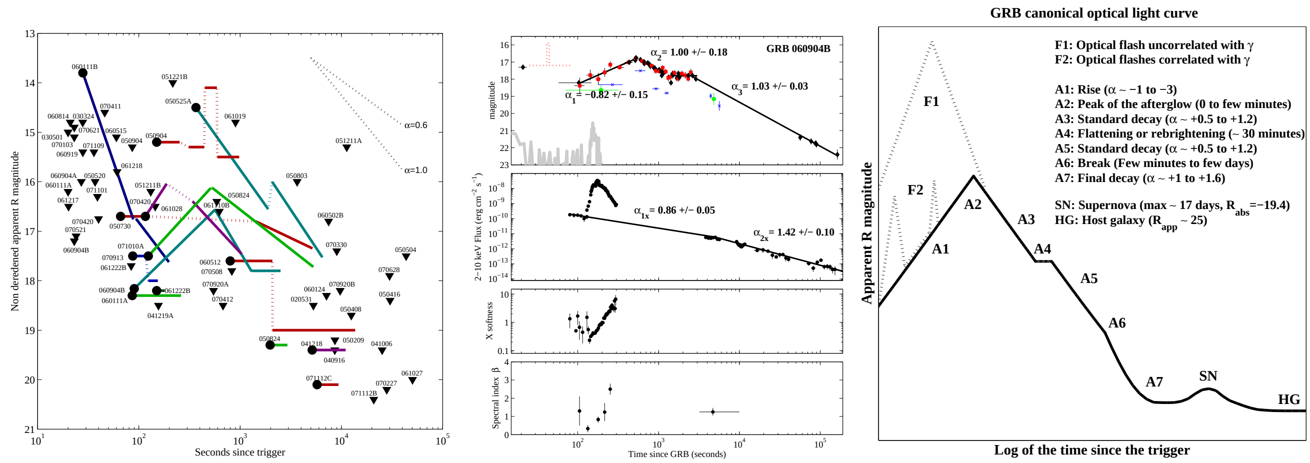

Fig. 1. Left : the TAROT data: upper limits for the first time bin (triangles) and light curves of the detected sources (thick lines). The upper right slopes illustrate some typical afterglow decays. Middle : Time resolved parameters of GRB 060904B. Top panel: Optical light-curve. Red squares are TAROT data (plus the limiting magnitude during 23s to 83s indicated by the dotted line). Black diamonds are R measurements of other observatories. Green disk and blue x are from literature for V and B band respectively. The BAT light curve is displayed as the light gray curve offseted arbitrarily. Fits are based on a power law. Second panel: X-Ray light-curve from XRT data. The count rate has been converted to flux units using the best fit spectral model of late afterglow. Third panel: softness ratio defined by (0.3-1.5 keV)/(1.5-10 keV). Bottom panel: X-ray band spectral index. Right : Canonical optical light curve of a typical GRB.

4 Toward a canonical light curve

Ten years of GRB optical observations allow to derive a global view of their light curves (presented in figure 1). Components F1 and F2, two type of flash emissions, have been observed only when the GRB is still in its active phase: F1 variations are not correlated with the gamma–ray activity, while F2 emission follows the gamma–ray activity. Often, neither F1 nor F2 are detected. A1 is only observed when the peak of the afterglow A2 occurs tens to hundreds seconds seconds after the GRB. A3 is the usual afterglow power law decay. The A4 flattening is more rare and occurs usually between 15 and 30 min in the source rest frame (see discussion in Klotz et al. 2005). The nature of the A6 break, previously supposed to be the jet break, is now under debate (e.g. Covino et al. 2006). The SN component is the supernova light curve signature that has been detected only for the nearest sources. The final HG segment is the host galaxy background flux. TAROT observations are usually sensitivity limited to the A5 phase.

B. Gendre. acknowledges support from the CNES. The TAROT telescope has been funded by the *Centre National de la Recherche Scientifique* (CNRS), *Institut National des Sciences de l'Univers* (INSU) and the Carlsberg Fundation. It has been built with the support of the *Division Technique* of INSU. We thank the technical staff contributing to the TAROT project: G. Buchholtz, J. Eysseric, M. Merzougui, C. Pollas, and P. & Y. Richaud. S. Cutini, B. Preger & G. Stratta acknowledge support of ASI contract 1/024/05/0.

References

Costa, E., Frontera, F., Heise, J., et al, 1997, Nature, 387, 783

Covino, S., Malesani, D., Tagliaferri, G., et al. 2006 Il Nuovo Cimento C, 121, 1171

Klotz, A., Boër, M., Atteia, J.L., et al., 2005, A&A 439, L35

Klotz, A., Gendre, B., Stratta, G., et al., 2008, A&A, 483, 847

Zhang, B., Kobayashi, S., Meszaros, P., 2003, ApJ, 595, 950

SF2A 2008
C. Charbonnel, F. Combes and R. Samadi (eds)

THE ACTIVE GALACTIC NUCLEI SEEN AT VERY HIGH ENERGY

Gérard, L.[1]

Abstract. AGNs are a class of objects emitting over a very broad energy range. Most AGNs observed at VHE are Blazars, so named because they have jets which are orientated towards us. In this case, the observed γ-rays, produced by the particle acceleration and emission processes in the jets, benefit from boosting by the Lorentz factor, so that their energies can reach the TeV. The first TeV Blazar, Mkn421, was discovered in 1992 with the Whipple observatory. Today, the known γ-ray sky contains over 20 of these objects, with the detections being carried out mainly by MAGIC and VERITAS for the Northern hemisphere and by H.E.S.S. for the Southern hemisphere. The present generation of Čerenkov telescopes has improved the quality of the spectral characterization and is now sensitive enough to detect variability on time-scales of minutes for the brightest sources. The detected TeV AGN study is essential for the comprehension of the processes taking place in the jets which are at the origin of the γ emission. The spectra of the farthest sources also highly constrain the density of the extragalactic background light.

1 Introduction

Imaging Čerenkov telescopes are observing the sky at very high energies (VHE; > 100 GeV). Thanks to the improvement of the detection technology, the number of active galactic nuclei (AGN) seen at VHE and the quality of the data has both increased in the past few years. Detected AGNs at VHE will be reviewed before giving the panorama of the types of studies that can now be carried out on this type of objects.

2 Description of Active Galactic Nuclei

It is now believed that most galaxies host in their centre a super massive black hole. For 10% of the observed galaxies the massive black hole accretes matter via an accretion disk: the galactic nucleus is active. Jets can then be formed, in which the matter is ejected at velocity close to the speed of light. Those jets host very strong magnetic fields where charged particles are accelerated. The accelerated particles radiate over the whole electromagnetic spectrum, from the Radio to VHE. The spectrum from radio to X-ray can be mainly explained by the synchrotron radiation of the electrons within the magnetic fields. On the other hand the emission at VHE can be explained through two different scenarios: leptonic and hadronic ones. In the leptonic scenario, the VHE photons are produced via inverse Compton whereas in the hadronic scenario they are produced via the disintegration of pions, created by the collision of an accelerated proton with the ambient medium.

There are different types of AGNs now united within the same classification which explain the different aspects from one AGN to another by the various orientations taken by the jets in relation with the line of sight. At VHE the AGNs seen are mostly Blazars, AGNs whose jets are pointing towards us. Indeed this is a very favorable geometry since under this angle the signal is amplified in intensity and in energy by the Lorentz boost.

The radiation processes producing the VHE photons are known, but the nature and the proportion of the particles (leptons and/or hadrons) involved is yet to be clarified. The observation of AGNs at VHE is essential to understand the mechanisms taking place within those objets and the particles responsible for the emission.

[1] Laboratoire APC ,CNRS, Université Paris Diderot, 10 rue Alice Domon et Léonie Duquet, Paris, France

3 A growing catalogue of AGN at VHE

The first detected AGN at VHE was Mkn 421, observed by Whipple in 1992. Whipple, together with HEGRA, CAT, 7 Tel Array and Durham Mark VI constitute the first generation of Čerenkov telescopes to see AGNs at VHE. The new generation benefit from various improvements such as fine imaging, broader collecting area, faster electronics and stereo technology for H.E.S.S, Veritas and Cangaroo. MAGIC was working with one telescope benefiting from a very large mirror area, but a second one has been constructed and MAGIC II will also benefit from stereo technique. In the Northern hemisphere, MAGIC and more recently VERITAS are observing the sources, Whipple is still operating, monitoring the brightest sources. H.E.S.S. is carrying out the observations from the Southern hemisphere.

Up to today, the VHE γ-ray sky contains 22 AGNs (see table 1), from a redshift of 0.004 to $\sim$0.2. H.E.S.S. discovered PG 1553+113 whose redshift is not well determined but considered > 0.250. MAGIC claimed the detection of 3C 279 the farthest seen AGN at VHE at a redshift of 0.536. Fifteen of thoses sources were added to the catalogue thanks to the technical improvements of the new generation of telescopes, and there are more discoveries to come, with the present instruments and with the next generation. All the AGNs seen at VHE are Blazars except for M87, the first non-blazar seen at VHE. The photons from this source don't benefit from the Lorentz boost but M87 is quite close and therefore can be detected. The majority of Blazars observed at VHE are BL Lacertae divided in different families considering the energy position of their double spectral structure composed of the synchrotron peak and the inverse Compton peak.

AGNs	**Redshift**	**Type**	**First Detection**	
			Year	**Instrument**
M87	0.004	FRI	2003	HEGRA
Mkn 421	0.030	HBL	1992	Whipple
Mkn 501	0.034	HBL	1996	Whipple
1ES 2344+514	0.044	HBL	1998	Whipple
Mkn 180	0.046	HBL	2006	MAGIC*
1ES 1959+650	0.047	HBL	1999	7-Tel. Array
BL Lac	0.069	LBL	2008	MAGIC*
PKS 0548-322	0.069	HBL	2007	H.E.S.S.*
PKS2005-489	0.071	HBL	2005	H.E.S.S.*
RGB J0152+017	0.080	HBL	2007	H.E.S.S.*
W Comae	0.102	IBL	2008	VERITAS*
PKS2155-304	0.116	HBL	1999	Mark VI
H 1426+428	0.129	HBL	2002	Whipple
1ES 0806+524	0.138	HBL	2008	VERITAS*
1ES 0229+200	0.139	HBL	2006	H.E.S.S.*
H 2356-309	0.165	HBL	2006	H.E.S.S.*
1ES 1218+304	0.182	HBL	2006	MAGIC*
1ES 1101-232	0.186	HBL	2006	H.E.S.S.*
1ES 0347-121	0.188	HBL	2007	H.E.S.S.*
1ES 1011+496	0.212	HBL	2007	MAGIC*
PG 1553+113	>0.250	HBL	2006	H.E.S.S.*
3C 279	0.536	FSRQ	2008	MAGIC*

Table 1. *AGNs detected at VHE, classified by increasing redshift. The HBL (High-energy-peaked BL Lacs), LBL (Low-energy-peaked BL Lacs) and IBL (Intermediate BL Lacs) are BL Lacertae (BL Lacs), a subcategory of Blazars. The SED of BL Lacs is dominated by synchrotron emission at low energy and inverse Compton (IC) emission at high energy, a double peak structure. The FRI (Fanaroff and Riley type 1) are radio galaxies. The FSRQ (Flat Spectrum Radio Quazar) are Blazars without radio emission. The instruments with a * are from the new generation.*

4 Tools to understand those objects

4.1 The multi-wavelength campaigns

Since the AGNs emit over a very broad energy range, getting a global view of the objects is the motivation to organize multi-wavelengths campaigns. A good illustration of such a campaign is given by that led on PKS 2155-304 during the the months of October and November 2003 (see paper 2), involving H.E.S.S., Rossi X-Ray Timing Explorer (RXTE), Robotic Optical Transient Search Experiment (ROTSE) and Nançay Radio Telescope (NRT). The spectral energy distribution (SED) of the source with the data obtained during the campaign is shown in Fig. 1. The experimental data set gives constraints to the emission models. Considering the leptonic and the hadronic radiative models presented on the SED (Fig. 1) the discrimination is yet to be done and could be achieved with H.E.S.S II [1] thanks to its lower energy threshold.

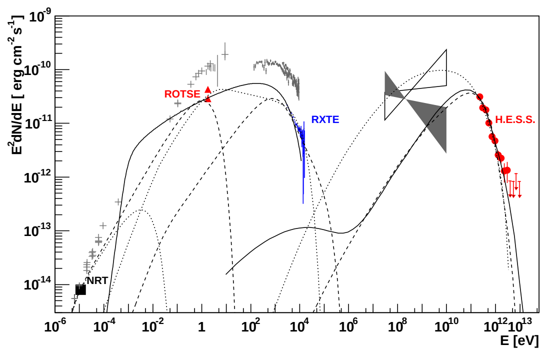

Fig. 1. *Spectral energy distribution of the AGN PKS2155-304. The coloured and labeled points represent data taken during the multi-wavelengths campaign in October and November 2003. The SED is from paper 2.*

When multi-wavelength campaigns are carried out on a source in a very bright state the data set obtained is well enough sampled to study the correlation between X-ray and γ-ray fluxes. This scenario happened during Mkn 421 multi-wavelength campaign in 2001 (see paper 3), and that of PKS 2155-304 in 2006 (see proceeding 4). In each case both sources have been observed during a flaring state allowing the evolution of their flux with time to be measured. For Mkn 421, a linear correlation has been found considering the whole period of observation. A more complex behavior is revealed when looking at intra-night flux correlations. On certain nights a quadratic correlation has been found which is understood within the frame-work of 1 zone synchrotron self-Compton (SSC) emission model (for more detail see paper 3). On the other hand the correlation between the X-ray and γ-ray fluxes of PKS 2155-304 show a cubic correlation, this can be explained only by a 2 zone SSC emission model. For more details on the interpretation of correlation between X-ray and γ-ray fluxes see paper 4. The complexity of those behavior is challenging the emission models.

4.2 AGNs' variability

On the brightest sources, the study of VHE AGNs' variability is now possible on short time-scales thanks to the high sensitivity of the instruments. Spectral variability measured during Mkn 421 (2001 and 2004) and Mkn 501 (2005, see paper 5) flaring states show, in each case, a hardening spectrum when the flux increases. PKS 2155-304 flared twice in 2006 (see paper 6 for the first flare). In the case of PKS 2155-304 2006 flares the behavior might be more complex (see proceeding 9).

Temporal variability of the VHE flux is observed on some AGNs ,on month scale even day scale for the brightest sources. For M87, time variability on day scale has been observed, so the size of the emission region was then constrained by causality to be of the order of the Schwartchild radius (see paper 1). PKS 2155-304 first

[1] A fifth telescope is to be added to the present H.E.S.S telescope array, the new telescope will be operational in autumn 2009, H.E.S.S.II . This telescope will be 30m in diameter, bigger than the other H.E.S.S. telescopes; this size should lower the energy threshold down to around 30GeV.

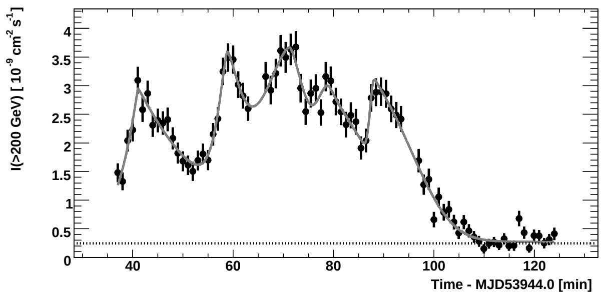

Fig. 2. *PKS 2155-304 light curve on minutes intervales, 2006 flare, fitted by 5 flares and a constant component. (from paper 6)*

flare in 2006 was an historical event. Time variability of the order of the minutes was measured (see Fig. 2), this was a first for AGNs at VHE but also considering other wavelengths. Such variability also puts constraints on the size of the emission region; hadronic radiative models are not good candidates to explain such a rapid variability. This highly sampled data set allows other type of variability studies: descriptioon as random process (see proceeding 10), constraints quantum gravity (see 8), etc.

5 Constraining the extragalactic background light

The study of AGNs at VHE also contributes constraining the extragalactic background light (EBL). The EBL is the accumulated light from all galaxies and the first stars. A VHE photon colliding with an infrared EBL photon will produce an electron positron pair. Therefore, the farther the VHE photon is coming from the higher is the probability for this photon to be absorbed by the EBL . The VHE spectrum of a fairly distant AGN can give contraints on the density of the EBL, with simple assumptions on the emission spectrum. By observing the unexpectedly hard spectra of H 2356-309 (z=0.165) and 1ES 1101-232 (z=0.186) H.E.S.S. gave a very constraining value for the upper limit of EBL density, close to the lower limit given by the galaxy counting (see paper 7). This is an important achievement since a direct measure of the EBL is made very difficult by the zodiacal light.

6 Conclusion

The catalogue of VHE AGNs contains 22 sources, and we're still counting. The quality of the data taken in observations of AGNs at VHE and other energies now allows fine correlation studies between X-ray and γ-ray emission; it also opens the short time-scales variability studies. The emission models are then better constrained and the understanding of the objects improve. Besides, the EBL density has been highly constrained thanks to the observation of hard spectra from fairly distant sources.

References

Aharonian, F. et al., Science, 2005, 314, 1424

Aharonian, F. et al., A&A, 2005, 442, 895

Fossati, G. et al., ApJ, 2008, 677, 906-925

Costamante, L. et al., High Energy Phenomena in Relativistic Outflows (Dublin), 2007, proceeding

Katarzyński, K. et al., A&A, 2005, 433, 479-496

Aharonian, F. et al., ApJ, 2007, 664, L71-L74

Aharonian, F. et al., Nature, 2006, 440, 1018-1021

Aharonian, F. et al., Phys. Rev. Letter, 2008, accepted for publication

Lenain, J. et al., International Symposium on High Energy Gamma-Ray Astronomy (Heidelberg), 2008, proceeding

Superina, G. et al., Workshop on Blazar Variability across the Electromagnetic Spectrum (Palaiseau), 2008, proceeding

SF2A 2008
C. Charbonnel, F. Combes and R. Samadi (eds)

DARK MATTER SEARCHES WITH H.E.S.S: NEARBY DWARF GALAXIES AND IMBH MINI-SPIKES

Moulin, E.[1], Vivier, M. [1], Brun, P.[1], Glicenstein, J-F.[1] and the H.E.S.S. Collaboration[2]

Abstract. WIMP pair annihilations produce high energy gamma-rays, which can be detected by IACTs such as the H.E.S.S. array of Imaging Atmospheric Cherenkov telescopes. Nearby dwarf galaxies and mini-spikes around intermediate-mass black holes (IMBHs) in the Galactic halo are possible targets for the observation of these annihilations. H.E.S.S. observations on the nearby dwarf galaxy candidate Canis Major is reported. Using a modelling of the unknown dark matter density profile, constraints on the velocity-weighted annihilation cross section of DM particles are derived in the framework of Supersymmetric (pMSSM) and Kaluza-Klein (KK) models. Next, a search for DM mini-spikes around IMBHs is described and constraints on the particle physics parameters in various scenarios are given.

1 Introduction

WIMPS (Weakly Interacting Massive Particles) are among the best motivated particle dark matter candidates. The WIMP annihilation rate is proportional to the square of the DM density integrated along the line of sight. Celestial objects with enhanced DM density are thus primary targets for indirect DM searches. Among these are the Galactic Center, nearby external galaxies and substructures in galactic haloes. In this paper, we report on H.E.S.S. results towards a dwarf galaxy candidate, Canis Major, and on a search for DM mini-spikes around IMBHs.

2 Canis Major overdensity

The nature of the Canis Major (CMa) overdensity (whether it is a Galactic warp or a dwarf galaxy) has been debated since its discovery in 2004. The scenario in which it is presented as a dwarf galaxy makes it a potentially interesting target for DM searches. CMa is located at ∼8 kpc from the Sun towards the Galactic anti-center direction. Observations of CMa by H.E.S.S. have been carried out in 2006. After standard quality criteria, the CMa dataset amounts to 9.6 hours (Aharonian et al. (2009)).

The DM mass profile of dwarf galaxies is usually estimated using velocity dispersion measurements of their stellar population as well as their luminosity profile. This modelling was for instance carried out by Aharonian et al. (2008a) for the Sgr dwarf galaxy. In the case of CMa, no such observational data are available. The CMa dark mass distribution was assumed to have a cusped NFW (Navarro-Frank-White) halo profile. The parameters of the NFW profile are determined by solving a three-equation system in a Λ-CDM cosmology with the virial mass, the scale radius and the density profile normalisation taken as unknown quantities (see Aharonian et al. (2009) for details on the procedure). The tidal disruption of CMa by the Galactic gravitational field was taken into account. For a typical CMa mass of 10^8 $M_\odot$, the line-of-sight-integrated squared density is $\sim 10^{25}$ $GeV^2 cm^{-5}$.

Halo independent constraints on the annihilation signal have been derived for various neutralino masses. In the center of the field of view, H.E.S.S. reaches a sensitivity of 10^2 $GeV^2 cm^{-2} s^{-1}$ for 1 TeV higgsino-like neutralino annihilating in W and Z pairs. The right hand side of Fig. 1 shows the constraints on σv. 95% C.L. exclusion limits reach $\sim 5\times 10^{-24}$ $cm^3 s^{-1}$ in the 500 GeV - 10 TeV DM particle mass range assuming a total halo mass of 3×10^8 $M_\odot$ (Aharonian et al. (2009)).

[1] CEA/DSM/IRFU, CE Saclay, 91191 Gif-sur-Yvette, France
[2] http://www.mpi-hd.mpg.de/hfm/HESS/

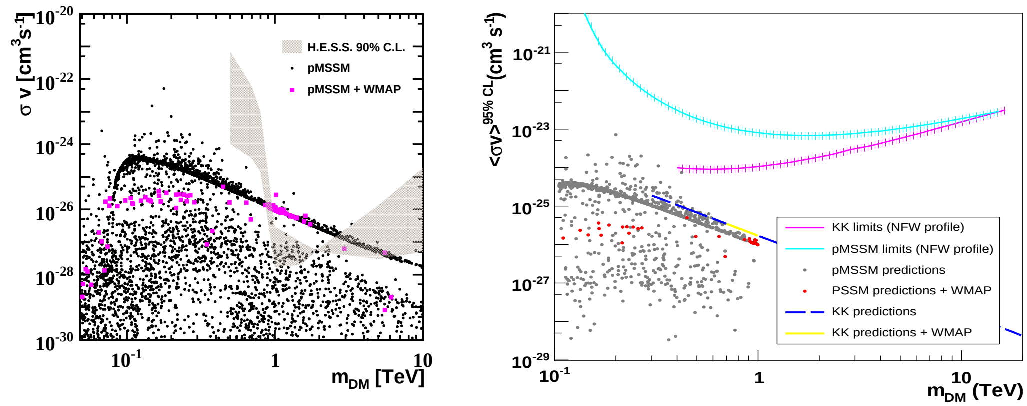

Fig. 1. Left: Constraints on the IMBH γ-ray production scenario for different neutralino parameters, shown as upper limits at 90% C.L. on σv as a function of the mass of the DM particle, in scenario B (grey shaded area). The DM particle is assumed to be a neutralino pair annihilating into $b\bar{b}$ or $\tau^+\tau^-$ pair. SUSY models from the pMSSM (black points) are plotted together with those satisfying the WMAP constraints on the cold DM density (magenta points). Right : Upper limits at 95% C.L. on σv as a function of the DM particle mass in the case of a NFW profile and an assumed CMa total mass of 3×10^8 $M_\odot$. The shaded area correspond to the 1σ error bars on σv for pMSSM and KK DM particles. pMSSM and KK models are also plotted with those satisfying the WMAP+SDSS constraints on the cold DM density.

3 Dark matter mini-spikes in IMBH scenarios

Mini-spikes around IMBHs have been recently proposed as promising targets for indirect DM detection (Bertone et al. (2005)). The growth of massive black holes affects the surrounding distribution of DM. The profile of the final DM overdensity, called mini-spike, depends on the initial distribution of matter, but also on astrophysical processes such as gravitational scattering of stars and mergers. Ignoring astrophysical effects, and assuming adiabatic growth of the black hole, starting from a NFW profile, a spike with a power-law index 7/3 is obtained. In the so-called scenario B of Bertone et al. (2005), the IMBH has a mass of $\sim10^5$ $M_\odot$. The gamma-ray flux from these objects can be calculated, assuming a particle physics model for the WIMP. The scenario B of Bertone et al. (2005) leads to gamma-ray fluxes accessible to H.E.S.S. For a 5 TeV neutralino mass, the mean integrated gamma-ray flux is $4.5\times10^{-11}\text{cm}^{-2}\text{s}^{-1}$ (Aharonian et al. (2008b)).

H.E.S.S. observations (2004-2006) of the Galactic plane lead to the discovery of more than 20 very high energy gamma-ray sources. Some of them have been identified as counterparts of sources already discovered at other wavelength. However, almost half of the sources have no obvious counterpart and are still considered unidentified. The detailed study of these sources shows that they have intrinsic spatial extensions greater than ∼5', while mini-spikes are expected to be point-like sources for H.E.S.S. Their spectra is also inconsistent with a DM spectrum with a WIMP mass $\leq$ 10 TeV. H.E.S.S. has detected so far no IMBH candidate in its Galactic plane survey data.

Constraints are derived on the scenario B for neutralino or LKP annihilations. The left panel of Fig. 1 shows the exclusion limit at the 90% C.L. on σv as a function of the neutralino mass. The neutralino is assumed to annihilate into $b\bar{b}$ and $\tau^+\tau^-$ with 100% BR, respectively. The limits on σv are at the level of 10^{-28} $\text{cm}^{-3}\text{s}^{-1}$ for the $b\bar{b}$ channel for neutralino masses in the TeV energy range.

References

F. Aharonian, et al. 2008a, Astropart. Phys.,29, 55

F. Aharonian, et al. 2008b, to be published in Phys. Rev. D, arXiv:0806.2981

F. Aharonian, et al. 2009, to be published in Astrophys. J., arXiv:0809.3894

G. Bertone, A. R. Zentner, and J. Silk 2005, Phys. Rev. D72, 103517

SF2A 2008
C. Charbonnel, F. Combes and R. Samadi (eds)

HOW POLARIZATION AND SCATTERING CAN REVEAL GEOMETRIES, DYNAMICS, AND FEEDING OF ACTIVE GALACTIC NUCLEI

Goosmann, R. W.[1], Gaskell, C. M.[2] and Shoji, M.[2]

Abstract. Gaskell et al. (2007) introduced polarization reverberation mapping as a new technique to explore the structure of active galactic nuclei. We present modeling results for the time-dependent polarization signal expected from scattering inside a centrally illuminated spheroid. Such a model setup describes a larger corona surrounding the compact source of an active nucleus. Time-delays between the polarized and the total flux are computed and related to the geometry of the cloud and the viewing angle. When including the in-flow dynamics of the cloud, it is possible to constrain its optical depth and velocity, which enables estimations of the mass inflow rate.

1 Introduction

Multiple reprocessing and scattering in the central engine of active galactic nuclei (AGN) are a major challenge to the spectral analysis. To disentangle the various media present in the inner parts of an AGN, the radiative transfer has to be modeled coherently. Scattering induces polarization that can be exploited to constrain the emission and reprocessing geometry. The Monte-Carlo radiative transfer code STOKES (Goosmann & Gaskell 2007) is designed to model polarization in a wide range of astronomical applications. In its most recent version, time-dependent effects are included, which allows to interpret results from polarization reverberation mapping (Gaskell et al. 2007). In this proceedings note we present STOKES reverberation modeling for the polarized echo of a centrally illuminated scattering cloud.

2 Constraining the shape of a spheroidal scattering cloud

We model the time-resolved, polarized flux of a centrally illuminated, constant density, and Thomson scattering spheroid. The vertical half-axis of the spheroid is denoted by a, the horizontal half-axis by b. We define $b = 10$ light-days and evaluate the aspect ratios $a/b = 1/10$, $3/10$, $5/10$, and $7/10$ at viewing angles of $i = 10°$, $30°$, and $60°$ (measured from the spheroid's symmetry axis). The Thomson optical depth τ along b is set to unity.

At first, we assume a short flash of unpolarized light to be emitted at the center of the spheroid. We trace for each viewing angle the time evolution of the escaping radiation. The resulting lightcurves of the polarized flux, i.e. the percentage of polarization p multiplied by the total flux F, are shown in the top row of Fig. 1. With increasing a/b the maxima of the curves shift toward higher values and their shape becomes more symmetric and shallow. For a given a/b, the normalization of the lightcurves increases with i while the position of the maximum moves toward shorter delays. Except for the flattest spheroid, the light-crossing distances indicated by the maxima of the lightcurves exceed the horizontal extension (20 light-days) of the spheroid. This clearly indicates multiple scattering effects.

Next, we randomly vary the intensity of the central source and conduct a cross-correlation analysis between $p \times F$ and F. The results are shown in the bottom row of Fig. 1. The correlation between the total and the polarized flux is always strong. The resulting delays depend on a/b and i and the dependencies correspond to those of the single light flashes studied before. Note that a degeneracy appears for the dependence on i when the shape of the scattering cloud approaches a sphere (see the case of $a/b = 7/10$). This, of course, is expected from symmetry considerations.

[1] Observatoire Astronomique de Strasbourg, 11 rue de l'Université, F-67000 Strasbourg, France
[2] Department of Astronomy, University of Texas, Austin, TX 78712-0259, USA

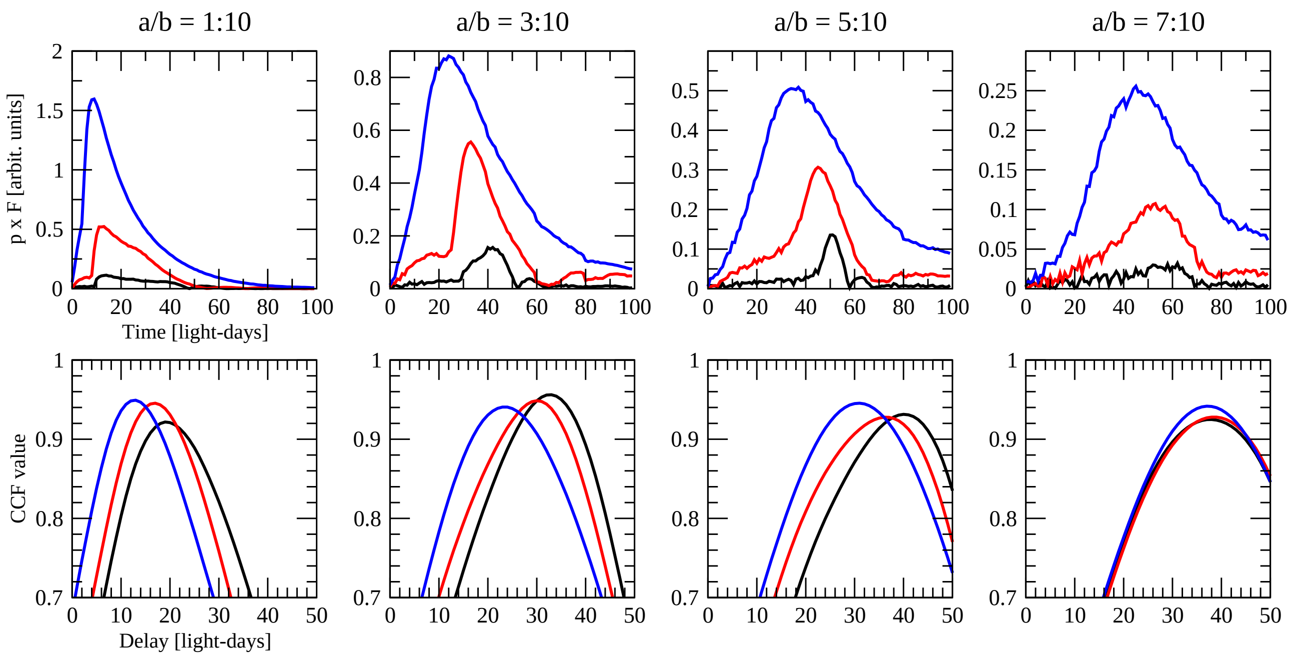

Fig. 1. Top: lightcurves for the polarized flux of a light flash emitted at the center of a spheroidal scattering region with aspect ratio a/b. The viewing angles $i = 10°$ (black), $30°$ (red), and $60°$ (blue) are evaluated. Bottom: cross-correlation functions between the total flux and the polarized flux echo when the intensity of the central source varies.

3 Determining the optical depth and velocity of in-falling matter

The correlations shown in Fig. 1 could be used to constrain the geometry of the scattering cloud if the inclination of the system is known. But the time-delays of the polarization echo also depend on τ. To put constraints on τ the dynamics of the scattering medium can be exploited, as was recently shown in Gaskell & Goosmann (2008) for scattering inflows in AGN. In Fig. 2 we show the effects of multiple scattering inside an in-falling medium. The resulting blue-shifting of emission lines is observed in AGN, and our modeling with STOKES has shown that the shifting and the resulting line profile do not strongly depend on the geometry of the inflow but mainly on its velocity and optical depth. These quantities are closely related to the inflow rate of the material and thus to the possible growth rate of the supermassive black hole.

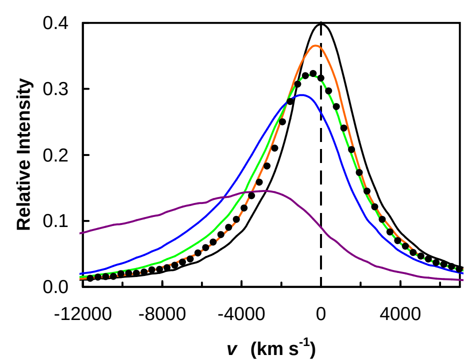

Fig. 2. Calculated shifts of an emission line by electron or Rayleigh scattering (see Gaskell & Goosmann 2008, for details of the computation). The top black solid curve shows a Lorentzian line profile before scattering. The other solid curves show the blue-shifting caused by an external spherical shell of scatterers with an inflow velocity of -1000 km/s. In order of increasing blue-shifting and decreasing peak flux, the curves show the effects of $\tau = 0.5$ (red), 1.0 (green), 2.0 (blue), and 10 (purple). The dots show the blue-shifting caused by a cylindrical distribution of scatters with $\tau = 20$ inflowing at -1000 km/s.

References

Gaskell, C. M., & Goosmann, R. W. 2008, arXiv:0805.4258

Gaskell, C. M., Goosmann, R. W., Merkulova, N. I., Shakhovskoy, N. M., & Shoji, M. 2007, arXiv:0711.1019

Goosmann, R. W., & Gaskell, C. M. 2007, A&A, 465, 129

SF2A 2008
C. Charbonnel, F. Combes and R. Samadi (eds)

XMM-NEWTON VIEW OF THE ECLIPSING BURSTER LOW-MASS X-RAY BINARY AX J1745.6-2901

Grosso, N.[1], Porquet, D.[1] and Boirin, L.[1]

Abstract. From March 31 to April 4, 2007, three XMM-Newton observations were performed to monitor the X-ray activity of Sgr A* and its neighboring X-ray transient sources. Two X-ray transient sources in outburst were detected during this multi-wavelength observation campaign. We focus here on the transient source in outburst located at about 1.5′ South-West from Sgr A*, which exhibited deep eclipses and type-I X-ray bursts. We identify this source with the eclipsing burster low-mass X-ray binary discovered by ASCA, AX J1745.6-2901. These XMM-Newton observations allow us to refine the period of the eclipse and the position of AX J1745.6-2901. Finally, we observed with XMM-Newton several dips from AX J1745.6-2901, which is the first dipper of the Galactic center region.

1 Introduction

From March 31 to April 4, 2007, three XMM-Newton observations were performed to monitor the X-ray activity of Sgr A* and its neighboring X-ray transient sources (Porquet et al. 2008). Two X-ray transient sources in outburst were detected during this multi-wavelength observation campaign (Porquet et al. 2007).

2 Astrometry

The X-ray transient source in outburst located at about 1.5′ South-West from Sgr A* is inside the 6″-radius error box of Swift J174535.5-290135.6, which was detected by the Swift X-Ray Telescope in late February 2006 (Kennea et al. 2006), and simultaneously detected with JEM-X aboard INTEGRAL (Chenevez et al. 2006). In the three observations, the error box of the XMM-Newton source encloses the 0.2″-radius error box of the Chandra source CXOGC J174535.6-290133 (Muno et al. 2003). A renewed activity of Swift J174535.5-290135.6 has been reported by Swift and INTEGRAL on mid-February 2007 (Kuulkers et al. 2007; Wijnands et al. 2007). Therefore, these XMM-Newton observations indicate an outburst duration of at least 7 weeks for this X-ray transient.

The ASCA source AX J1745.6-2901 (hereafter AX), with an estimated positional uncertainty of 24″ in radius, is located at 36″ of the XMM-Newton source. AX is an eclipsing X ray burster with an eclipse period of 8.356±0.008 h (Maeda et al. 1996).

3 X-ray light curves

Figure 1 shows the X-ray light curves obtained in the 2–10 keV energy range with the EPIC pn spectro-imager. We observed seven deep eclipses –with a period consistent with the period of AX– as well as four type-I X-ray bursts. Type-I X-ray burst are thermonuclear flashes of the matter accreted on the surface of a weakly magnetized neutron star (Joss 1977, 1978). Therefore, we identify this XMM-Newton source with the eclipsing X-ray burster AX. Several dips are also observed before the eclipses. Dipping phenomena and eclipses are present together when the X-ray binary is viewed under an elevated inclination ($\sim 75° - \sim 80°$), i.e., close to an edge-on view (Frank et al. 1987). In this viewing configuration, at each orbital rotation, the bulge of the accretion disk passes in front of the compact object, followed by the low-mass donor star, causing first dips and then an eclipse in the X-ray light curve.

[1] Observatoire astronomique de Strasbourg, Université de Strasbourg, CNRS, INSU, 11 rue de l'Université, 67000 Strasbourg, France

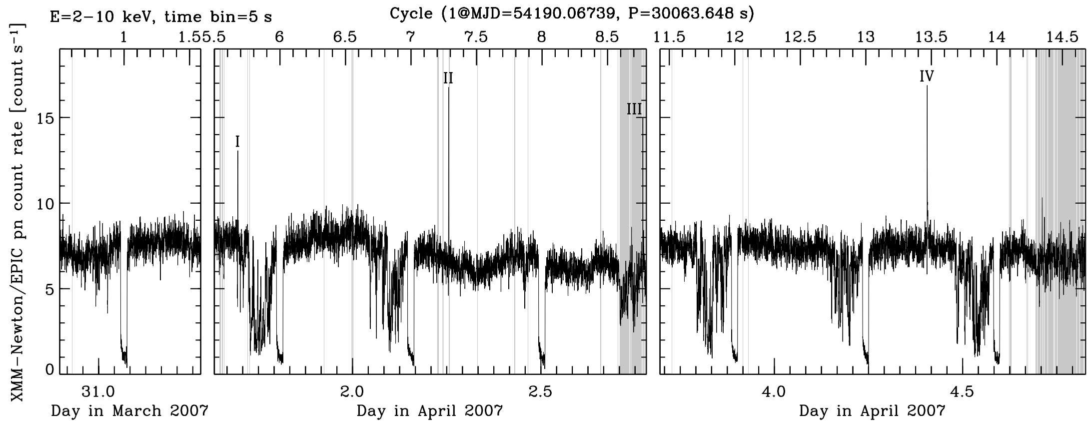

Fig. 1. EPIC pn X-ray light curve of AX J1745.6-290. The grey vertical stripes indicate the time intervals of high flaring-background where the scientific mode was switched off. Type-I X-ray bursts are labelled with Roman numbers.

4 Orbital period

We evaluate using a light curve folding method an orbital period of 30063.8 s with a 90% confidence error of 0.5 s. This level of accuracy allows us to track back the eclipse phase down to the epoch of the first observation of the X-ray eclipse with ASCA in 1994 (Maeda et al. 1996). We find that it corresponds to cycle -13161, which helps us to refine the orbital period to: 30063.648 s (i.e., 8.351013 h) with an uncertainty of 0.004 s. Our improved linear ephemeris of the eclipse allows us to identify an unnoticed egress in a short Chandra observation of CXOGC J174535.6-290133 in June 2006. Therefore, we unambiguously identify the Chandra source with the ASCA source.

5 Summary

We have unambiguously identified AX with CXOGC J174535.6-290133 (Porquet et al. 2007), which provides a better determination of the position of this low-mass X-ray binary for multi-wavelength follow-up observations. We have also improved the accuracy of the orbital period, and the linear ephemeris of the eclipse center.

The XMM-Newton project is an ESA Science Mission with instruments and contributions directly funded by ESA Member States and the USA (NASA).

References

Chenevez, J., Sanchez-Fernandez, C., Kuulkers, E., et al. 2006, The Astronomer's Telegram, 756

Frank, J., King, A. R., & Lasota, J.-P. 1987, A&A, 178, 137

Joss, P. C. 1977, Nature, 270, 310

Joss, P. C. 1978, ApJ, L123

Kennea, J. A., Burrows, D. N., Campana, S., et al. 2006, The Astronomer's Telegram, 753

Kuulkers, E., Shaw, S., Chenevez, J., et al. 2007, The Astronomer's Telegram, 1005

Maeda, Y., Koyama, K., Sakano, M., Takeshima, T., & Yamauchi, S. 1996, PASJ, 48, 417

Muno, M. P., Baganoff, F. K., Bautz, M. W., et al. 2003, ApJ, 589, 225

Porquet, D., Grosso, N., Goldwurm, A., et al. 2007, The Astronomer's Telegram, 1058

Porquet, D., Grosso, N., Predehl, P., et al. 2008, A&A, 488, 549

Wijnands, R., Klien Wolt, M., Kuulkers, E., et al. 2007, The Astronomer's Telegram, 1006

SF2A 2008
C. Charbonnel, F. Combes and R. Samadi (eds)

LIMITS ON AN ENERGY DEPENDENCE OF THE SPEED OF LIGHT FROM A FLARE OF THE ACTIVE GALAXY PKS 2155-304

Jacholkowska, A.[1]

Abstract. The study of time-lags in light curves with Wavelet methods or Cross-correlation functions for distant astrophysical sources like active galaxies, as a function of energy, may lead to a detection of Lorentz symmetry breaking or effects due to Quantum Gravity in extra-dimension models. In this paper a search for such timelags during the H.E.S.S. observations of the exceptional Very High Energy flare of the active galaxy PKS 2155-304 on 28 July in 2006 is presented. Since no significant time-lag value was found on the minute level, the 95% Confidence Limit on the Quantum Gravity scale is set to $0.5 - 0.7\ 10^{18} GeV$, considering only a linear term in the standard photon dispersion relation.

Introduction

A Quantum Gravity theory provides a unified picture based on the Quantum Mechanics and the General Relativity, thus leading to a common description of the four fundamental forces. The Quantum Gravity effects in the framework of the String Theory (Ellis et al. 2000) where the gravitation is considered as a gauge interaction, are resulting from a graviton-like exchange in a background classical space-time. In most of the String Theory models implying large extra-dimensions these effects would take place at the Planck scale, thus leading to no 'spontaneous' Lorentz Symmetry breaking, as it may happen in models with 'foamy' structure of the quantum space-time (Amelino-Camelia et al. 1998, Ellis et al. 2000) or in models based on the General Relativity with Loop Quantum Gravity (Gambini & Pullin 1999, Alfaro et al. 2002) which postulates discrete (cellular) space-time in the Planckian regime. As a result, one may expect a spontaneous violation of the Lorentz Symmetry at high energies to be the generic signature of Quantum Gravity.

1 Extra-dimension models and Quantum Gravity

In models developed by (Ellis et al. 2002), photons propagate in vacuum which may exhibit a non-trivial refractive index due to its foamy structure on a characteristic scale approaching the Planck length or equivalently Plank energy ($E_{\rm P} = 1.22 \times 10^{19}$ GeV). This implies a light group velocity increasing as a function of energy of the subluminal photon, in contrary to the dispersion effects in any field theoretical vacuum or plasma. In general, the Quantum Gravity scale is supposed to be close to Planck energy and the standard photon dispersion relation in second order in energy can be written as:

$$c' = c\ \left(1 \pm \xi \frac{E}{E_{\rm P}} \pm \zeta^2 \frac{E^2}{E_{\rm P}^2}\right). \tag{1.1}$$

As suggested by (Amelino-Camelia et al. 1998) the tiny effects can add up to measurable time delays for photons from cosmological sources. Simultaneously-emitted photons of energies E_1 and E_2 which travel over a distance L will arrive at the observer with a time delay $\Delta t = t_1 - t_2$ per energy difference $\Delta E = E_1 - E_2$:

$$\frac{\Delta t}{\Delta E} = \frac{L}{\Delta E}\ \left(\frac{1}{c_1'} - \frac{1}{c_2'}\right) \approx \mp\xi \frac{L}{E_{\rm P} c} \quad \text{for} \quad \Delta E \ll E_{\rm P}, \tag{1.2}$$

[1] LPNHE, Université Pierre et Marie Curie Paris 6, Université Denis Diderot Paris 7,
CNRS/IN2P3, 4 Place Jussieu, F-75252, Paris Cedex 5, France

when conserving only the linear term in the development. Here, the cosmological expansion of the universe is neglected.

The energy dispersion is best observed in sources that show a fast flux variability, are at cosmological distances and are observed over a wide energy range. Therefore in the past, Gamma Ray Bursts and Very High Energy (VHE) flares of active galaxies have been the primary targets of these "time-of-flight" studies, which provide the least model dependent test of Lorentz symmetry. A caveat of time-of-flight measurements is that dispersion might be introduced due intrinsic source effects, which could cancel out or enhance the dispersion due to modifications to the speed of light. The most solid results on the Quantum Gravity scale of the order of $10^{16} GeV$ are provided by GRB observations with different redshifts as they take into account the possible time lags originating from source effects, resulting in limits of $\xi < 1300$ (Ellis et al. 2006, Bolmont et al. 2008). Before this study, the dispersion measurements for active galaxies exist only for two sources, Mkn 421 and Mkn 501. Both are located at a similar redshift of ~0.03. For Mkn 421 no energy-dependent time delay was found during a VHE flare in 1996 by the Whipple collaboration (Biller et al. 1999). For Mkn 501 an indication of higher energy photons lagging the lower energy ones was reported during a VHE flare in 2005 by the MAGIC collaboration (Albert et al. 2007).

2 Analysis of the PKS2155-304 flare and results on Quantum Gravity

In the present study, photon time delays were searched for during the VHE flare of the active galaxy PKS 2155-304 observed by the High Energy Stereoscopic System (H.E.S.S.) on July 28 in 2006. PKS 2155-304 is located at a redshift of z = 0.116 , equivalent to a distance of 490 Mpc (for a Hubble constant of 71 km s^{-1} Mpc^{-1}). The light curve shows fast variability (~ 200 s) and covers an energy range of a few TeV with no significant spectral variability (Aharonian et al. 2007). Together with the unprecedented photon statistics (~ 10000 photons) at these energies, this flare provides a perfect testbed. The data presented here were analyzed using the standard H.E.S.S. analysis, described in detail in (Aharonian et al. 2006). Time delays between light curves of different energies were studied in order to quantify a possible energy dispersion.

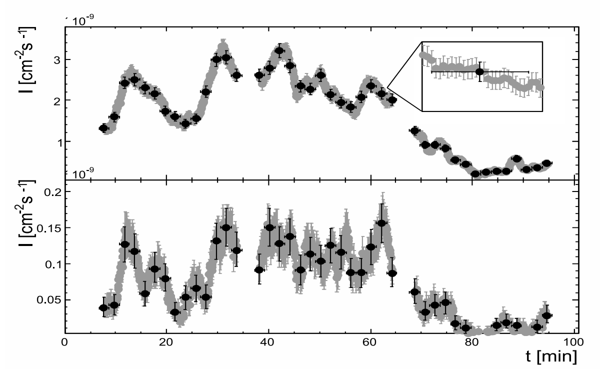

Fig. 1. Black points show the integral flux VHE light curves measured on July 28 from PKS 2155-304 by H.E.S.S. between 200-800 GeV (upper panel) and >800 GeV (lower panel), binned in two-minute time intervals. The zero time point is set to MJD 53944.02. Gray points show the oversampled light curve, meaning that the original time bins were subsequently shifted by five seconds. The inlay in the upper panel illustrates this in a zoom, where the horizontal error bar shows the two minute time duration from the original light curve.

The spectral time properties of the PKS2155-304 flare were investigated with 2 methods: Continuous Wavelet Transform (CWT) (Mallat 1998) and Modified Cross-Correlation Function (MCCF) (Li et al. 2004, Edelson & Krolik 1998). Both analyses of the light curves were done in similar two energy domains as shown in Fig. 1. To evaluate precisely the position of the sharp transitions, referred below as extrema, the CWT method was used as it is widely applied in the time lag studies of the GRB light curves 6, 7. This method relies on very different aspects of the light curves from those studied later by MCCF and provides independent crosschecks of the systematic errors. As in analyses described in (Ellis et al. 2003), the search for extrema (maxima and minima) in the light curves was done with a Mexican Hat wavelet function. The LastWave package (Bacri 2004) used in this analysis provides, for each light curve considered, a list of extrema candidates with their positions and first and second derivative. The extrema were later associated in pairs between the light curves in the two energy ranges following an algorithm based on the Lipschitz coefficient as in (Mallat 1998, Ellis et al. 2003) which characterizes the regularity of each extremum. Since tiny quantum gravity effects are to be probed, the value of the time bin-width of 60 seconds was found to be optimal as the statistics is concerned, for this study. Light curves have been constructed in the two energy bands (between 0.21 to 0.25 TeV and above 0.6 TeV) from the photon-tagged sample used in the MCCF analysis, resulting in a mean energy difference of 0.92 TeV. To evaluate the time-lag error, photon lists were generated from the real data using a parametric bootstrap model, obtained from a polynomial spline fit to the light curves in time bins of one minute and a fit of the energy distribution of the events in the real data. Samples composed of hundreds of Monte Carlo experiments were analyzed and the values of the error were found to range between 30 and 36 seconds with mean values of the reconstructed smearing different by at most 15 s. The results from error calibration have also shown that there is no major systematic bias on the mean time lag estimation induced by the method in use.

The mean time lag for two pairs of extrema identified with CWT method was found to be 27 seconds. After correction for the systematic shift deduced with the error calibration procedure, we set a 95% confidence limit to 100 s TeV^{-1} on a possible time lag.

The MCCF analysis (Li et al. 2004, Edelson & Krolik 1998), applied to oversampled light curves was used to cross-check the results obtained with CWT. To optimize the energy gap between two energy bands, while keeping good event statistics in both, the correlation analysis was performed on the light curve between 200 and 800 GeV and above 800 GeV (see Fig. 1). The mean difference of the photon energies between the two bands is 1.0 TeV. In order to measure the time delay, the central peak of the MCCF distribution was fitted by a Gaussian function plus a first-degree polynomial, resulting in a maximum at $\tau_{\mathrm{peak}} = 20$ s. The error of the measured time lag is determined by propagating the flux errors via simulations. Simulated light curves were generated for each energy band, by varying the flux points of the original oversampled light curve within its measurement errors, taking into account the correlations between bins. It was found that the Cross Correlation Peak Distribution (CCPD) has an RMS of 28 s and for 21% of the simulations the time delay is negative. Therefore the measured time delay of 20 s is considered to be not significant. The response of the MCCF to dispersion in energy was determined by injecting artificial dispersion into the H.E.S.S. data and measuring its effect on the CCPD.

A 95% confidence upper limit on a linear dispersion of 73 s TeV^{-1} was found. The accuracy of the MCCF method was also verified with the bootstrap simulation Monte Carlo and the CCPD of these simulations confirmed the previously measured error on the time delay. Artificially introduced dispersion was always recovered within the expected accuracy.

The impact of other possible systematic effects has also been investigated: selection of gamma-like events, choice of the energy domain or varying binning in the light curves changing the results at most by 0.5σ. For the wavelet method, various cuts on the CWT parameters have been applied and lead to negligible changes in the extrema identification and pair association. The probability of accidental associations in pairs has been evaluated to be $< 1\%$ with dedicated Monte Carlo simulations of random spikes in the light curve.

The measured limits are the most constraining limits from time-of-flight measurements to date: $\xi < 24.2$ (or ξ^{-1} $E_p > 5.0 \times 10^{17}$ GeV) from CWT and $\xi < 17.6$ (or ξ^{-1} $E_p > 6.9 \times 10^{17}$ GeV) from MCCF for the linear dispersion term, a slightly better result due to a larger lever arm in energy.

Conclusions

The results from PKS2155-304 flare on July 2006 are complementary to those from Mrk501 2005 flare observation by MAGIC, where a significant positive time-lag was detected with statistics lower by an order of magnitude. It should be underlined that in case of PKS2155-304 flare the analyses of variability of the light curves were performed with two orthogonal approaches and with a very robust estimation of the time-lag error. The measured time-lag of the order of few minutes with Mrk 501 would imply values above 10 minutes for PKS2155-304 redshift, if the Quantum Gravity interpretation was maintained.

In future, the large lever arm in energy of the GLAST mission will open a new era in this domain. As for the proposed Cherenkov Telescope Array (CTA), the population studies of the active galaxy data with redshift, will provide competitive results on Lorentz Symmetry breaking independently of the source induced effects.

Acknowledgments

The support of the Namibian authorities and of the University of Namibia in facilitating the construction and operation of H.E.S.S. is gratefully acknowledged, as is the support by the German Ministry for Education and Research (BMBF), the Max Planck Society, the French Ministry for Research, the CNRS-IN2P3 and the Astroparticle Interdisciplinary Programme of the CNRS, the U.K. Science and Technology Facilities Council (STFC), the IPNP of the Charles University, the Polish Ministry of Science and Higher Education, the South African Department of Science and Technology and National Research Foundation, and by the University of Namibia.

References

Ellis, J., Mavromatos, N. E., Nanopoulos, D. V., & Volkov, G., 2000, Genaral Relativity and Gravitation, 32, 1777

Ellis, J., Mavromatos, N. E., Nanopoulos, & D. V., 2002, Phys Rev D, 61, 027503

Amelino-Camelia, G., Ellis, J., Mavromatos, N. E., Nanopoulos, D. V., & Sarkar S., 1998, Nature, 395, 762

Alfaro, J., Morales-Tecotl, H. A., & Urrutia, L. F., 2002, Phys Rev D, 65,103509

Gambini, R., & Pullin J., 1999, Phys Rev D, 59, 124021

Ellis, J., Mavromatos, N. E., Nanopoulos, D. V., Sakharov A. S., & Sarkisyan E. K. G., 2006, ApJ, 25, 402

Bolmont, J., Jacholkowska, A., Atteia, J.-L., Piron, F., & Pizzichini G., 2008, ApJ, 676, 532

Biller, S. D., et al., WHIPPLE Collaboration, 1999, Phys. Rev. Lett.,83,2108

Albert J., et al., MAGIC Collaboration, 2007, ApJ, 669, 862

Aharonian, F., et al., H.E.S.S. Collaboration, 2007, Ap. Lett., 664, L71

Aharonian, F., et al., H.E.S.S. Collaboration, 2006, Astrophysics and Astronomy, 457, 899

Li, T.-P., Qu, J.-L., Feng, H., Song, L.-M., & Chen L., 2004, Chinese Journal for A&A, 4, 583

Edelson, R. A., & Krolik J. H., 1998, ApJ, 333, 646

Mallat, S., 1998, Academic Press, San Diego

Ellis, J., Mavromatos, N. E., Nanopoulos, D. V., & Sakharov, A. S., 2003, A&A, 402, 409

Bacry, H., 2004, LastWave version 2.0.3

SF2A 2008
C. Charbonnel, F. Combes and R. Samadi (eds)

OBSERVATIONS OF SHELL-TYPE SUPERNOVA REMNANTS WITH H.E.S.S.

Komin, N.[1]

Abstract. It is widely believed that the shells of supernova remnants (SNRs) are the sources of the Galactic Cosmic Rays up to energies of about 10^{15} eV. These high-energy hadrons interact with ambient material, and the subsequent neutral pion decay produces gamma rays in the GeV and TeV energy range.

H.E.S.S., a system of ground-based imaging Cherenkov telescopes dedicated to the observation of gamma rays with energies of several hundred GeV up to tens of TeV, is an ideal instrument for the observations of high-energy gamma-ray emission from SNRs. In the recent years H.E.S.S. observed a number of SNRs. Firm detections have been reported from the well-known SNRs RX J1731-3946 and RX J0852-4622 as well as the interaction of W28 with molecular clouds. Further on, the Galactic scan conducted with H.E.S.S. revealed several other SNRs.

In this talk I will discuss some of the SNRs observed so far and discuss the implications with respect to Cosmic Ray acceleration.

1 Introduction

Shell-type supernova remnants (SNRs) are believed to be the sources of Galactic Cosmic Rays with energies up to 10^{15} eV. Supernova explosions can deliver the entire energy density observed in Cosmic Rays (); and particle acceleration is predicted to occur in the shock front of the supernova remnant (see e.g.). Non-thermal X-ray emission from supernova remnants, which is interpreted as being synchrotron radiation, proves the acceleration of electrons. The acceleration of hadrons, however, is still debated. Relativistic protons produce in interactions with ambient material π^0 mesons; the disintegration of these mesons subsequently produces gamma rays in the GeV and TeV energy regime. Gamma-ray astronomy is therefore an ideal tool to study hadron acceleration in supernova remnants.

The High Energy Stereoscopic System (H.E.S.S.) is an imaging Cherenkov telescope array dedicated to the observations of very high energy (VHE) gamma rays with energies of more than 100 GeV, up to several tens of TeV. Located in Namibia on the southern hemisphere it, is in an ideal place to observe the central part of the Galactic plane. In the first years of observations a number of shell-type supernova remnants have been detected, a not complete list is discussed in this paper.

2 H.E.S.S. observations of SNRs

2.1 *RX J1713−3964*

The supernova remnant RX J1713−3964 (also called G 347.3-0.5) was one of the first sources observed with H.E.S.S. and the first confirmed extended VHE gamma-ray source (; ;). An image of the gamma-ray excess is shown in the left panel of Fig. 1. The gamma-ray morphology follows that seen in X-rays, indicating that X-rays and gamma rays originate in the same region. The detection of gamma-rays with energies up to 100 TeV proves particle acceleration up to 10^{15} eV. Whether these particles are electrons or protons cannot be concluded from gamma-ray observations alone. Further assumptions have to be made as gamma-ray emission can be both, inverse Compton radiation of electrons and π^0-decay emission from protons.

The recent detection of an energy cut-off in the X-ray spectrum and the modelling of the entire electromagnetic emission of the supernova remnant () showed that the observed emission can be explained as being of

[1] CEA/Irfu/SPP, Centre de Saclay, 91191 Gif-sur-Yvette CEDEX, France

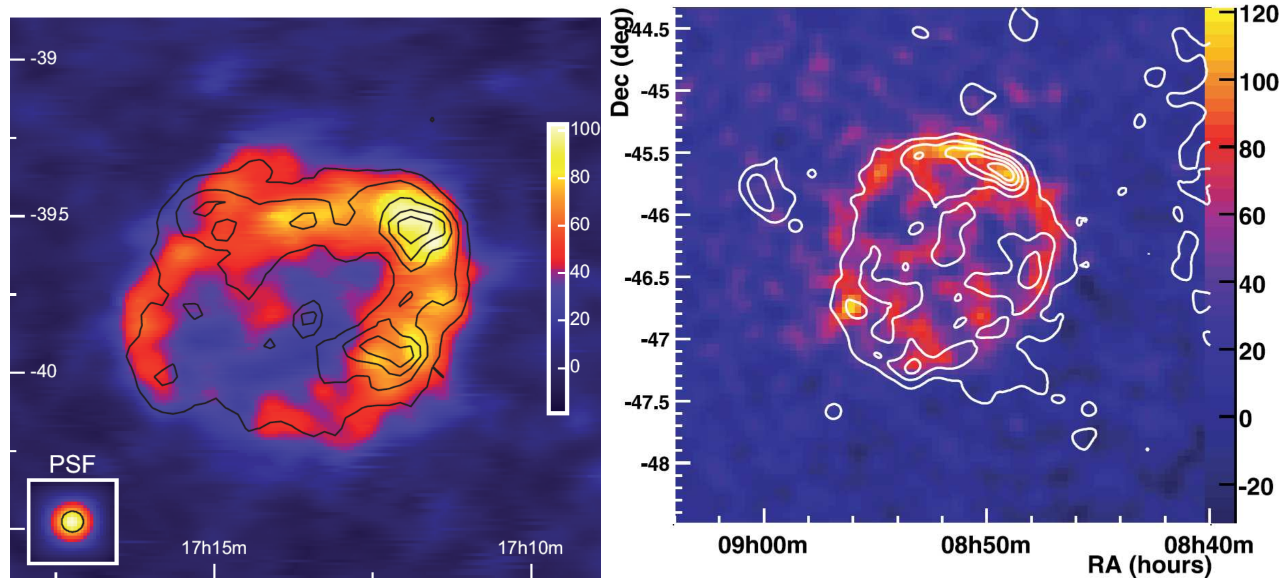

Fig. 1. H.E.S.S. gamma-ray images (colour scale) for shell-type supernova remnants with overlaid X-ray emission contours. *Left panel:* RX J1713−3964 with ASCA X-ray data (). *Right panel:* RX J0852−4622 with ROSAT X-ray contours ().

hadronic origin under assumption of a high magnetic field around 200 μG. However, a solely electronic model would be possible as well, assuming a magnetic field of 14 μG and the requirement of two distinct electron components.

2.2 RX J0852−4622

The second extended TeV source discovered by H.E.S.S. is the supernova remnant RX J0852−4622 (also called G 266.2−1.2 or Vela Junior). As shown in the right panel of Fig. 1 the gamma-ray morphology is a clear shell with a diameter of 2° which follows the X-ray morphology (). Detailed modelling of the emission over all wavelength () showed that the emission is consistent with a hadronic scenario in the case of a high magnetic field of about 120 μG. Such a high field is further supported by the observation of very thin X-ray filaments (). A pure electronic scenario would require quite a low magnetic field of about 6 μG, contradicting the expected magnetic field amplification in supernova remnant shells ().

2.3 RCW 86

A third object in the class of shell-type SNRs with gamma-ray emission, non-thermal X-ray emission and only faint radio emission is RCW 86 (also known as G315.4−2.3 or MSH 14−63) (). The gamma-ray emission shows an almost complete shell (left panel of Fig. 2). The X-ray morphology (right panel of Fig. 2), however, is a rather bipolar structure with the brightest part of the emission in the south-west; and therefore the case of RCW 86 is somewhat different to the objects discussed before. Comparison of X-ray and gamma-ray emission in a leptonic scenario leads to a magnetic field of about 20 μG. Given the large uncertainties in age and distance to the remnant, a hadronic scenario would be possible as well.

2.4 W 28

The case of W 28 (also called G 6.4−0.1) is completely different to the sources discussed above. The shell of W 28 was seen only in radio. X-ray observations show only thermal emission from the interior of the SNR. This remnant is rather old, 35 – 150 kyr, and it is expected that the highest energy electrons (those that produce non-thermal X-ray emission) have already lost their energy, so that no synchrotron emission is seen anymore in X-rays. The left panel of Fig. 3 shows the gamma-ray excess map obtained with H.E.S.S. (). Gamma-ray

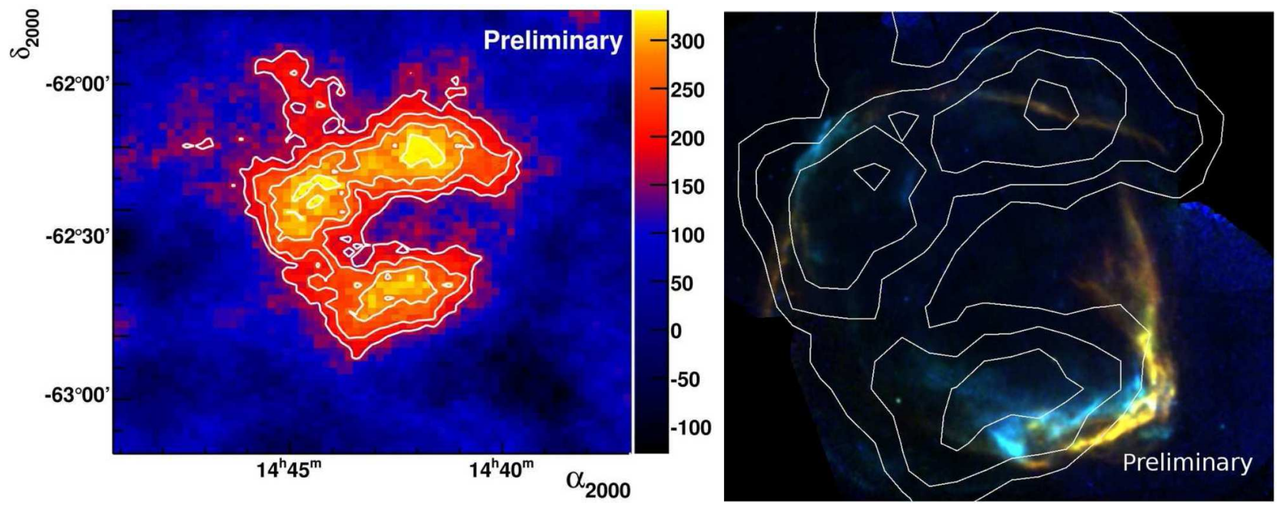

Fig. 2. Shell-type supernova remnant RCW 86 (). *Left panel:* H.E.S.S. gamma-ray excess image (colour scale) with overlaid 3, 4, 5, 6 σ significance contours. *Right panel:* XMM X-ray image (colour scale) with H.E.S.S. significance contours.

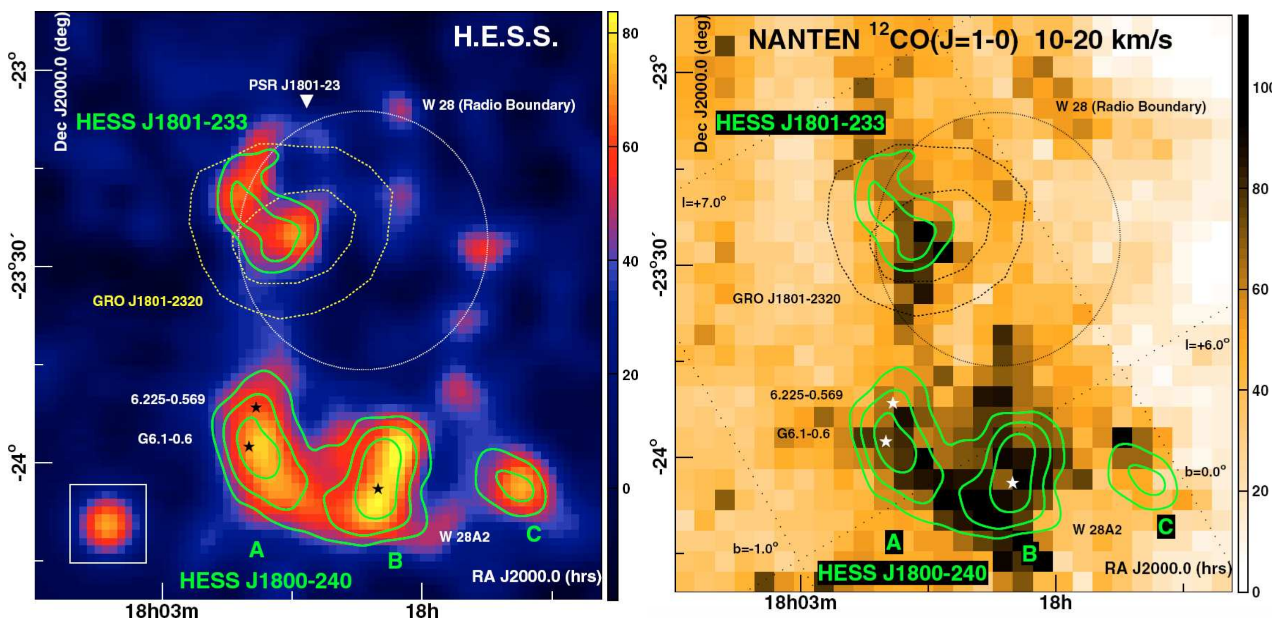

Fig. 3. Supernova remnant W 28 (). *Left panel:* H.E.S.S. gamma-ray excess map with overlaid 4, 5 and 6 σ significance contours. The extension of the radio shell is indicated by a white dashed circle. *Right panel:* CO emission (colour scale) indicating molecular clouds with overlaid H.E.S.S. significance contours.

emission is detected from the direction of W 28, but it is not directly connected to the SNR. It is, however, correlated with molecular clouds seen in radio, as shown in the right panel of Fig. 3. Molecular clouds are regions of high matter density, therefore providing additional target material for the proton-proton interactions. Even though other possible counterparts for the gamma-ray emission exist, the correlation with regions of high density in the vicinity of the SNR makes it likely that protons were accelerated in the supernova shell.

3 Discussion

Shell-type supernova remnants are established as gamma-ray emitters. The morphology of young remnants generally show a good agreement between gamma-ray and X-ray morphologies. The emission of non-thermal X-rays interpreted as synchrotron emission of relativistic electrons is a proof for particle acceleration in the remnant's shells. Under certain assumptions on the parent electron distribution and for low to moderate magnetic fields the observed gamma-ray emission can be interpreted as being inverse Compton scattering of electrons off ambient photon fields. On the other hand, the gamma-ray emission can be easily powered by proton interactions assuming the transfer of about 10% of the supernova's explosion energy to protons. This scenario requires a higher magnetic field in order to suppress inverse Compton emission. Magnetic fields are expected to be amplified in the SNR's shock (); therefore the acceleration of protons in SNR shells seems to be likely. The disentanglement of leptonic and hadronic emission remains an open question.

In old SNRs no inverse Compton emission is expected and any gamma-ray radiation can be attributed to proton interactions assuming sufficient target material is provided. The detection of gamma-ray emission from the direction of W 28 coincident with molecular clouds is a striking example for possible hadronic emission. Other possible counterparts for this emission, and the problem of connecting the SNR with the clouds and gamma-ray emission in general, are and will remain the major problems in this kind of observations.

4 Conclusion

Gamma-ray observations show that shell-type SNRs are indeed possible accelerators of protons and thus possible sources of the Cosmic Rays. The remaining problem of discriminating inverse Compton and hadronic emission can be overcome by the observation of further features in the gamma-ray spectrum. *Fermi*/LAT (recently launched) and H.E.S.S. II (under construction) will extend the observable gamma-ray spectrum to lower energies. Future observatories like CTA will allow the study of the high-energy end of the spectrum.

The final proof of hadron acceleration in SNRs would be the detection of neutrinos from the supernova remnant shells. With the work discussed above, gamma-ray observations can identify the most promising targets for the search of neutrino emission.

References

Ginzburg, V. L., Syrovatskii, S. I., "The Origin of Cosmic Rays", New York: Macmillan, 1964

Malkov, M. A., O'C Drury, L., 2001, Reports on Progress in Physics, 64, 4

H.E.S.S. collaboration, F. Aharonian et al., 2004, Nature, 432, 75

H.E.S.S. collaboration, F. Aharonian et al., 2006, Astron. Astrophys. 449, 223

H.E.S.S. collaboration, F. Aharonian et al., 2007a, Astron. Astrophys., 464, 235

Tanaka et al. 2008, arXiv:0806.1490

H.E.S.S. collaboration, F. Aharonian et al., 2005, Astron. Astrophys., 437, L7

H.E.S.S. collaboration, F. Aharonian et al., 2007b, Astrophys. Journal, 661, 236

Bamba, A. et al., 2005, Astrophys. Journal, 632, 294

Völk, H. J., Berezhko, E. G., Ksenofontov, L. T., 2005, Astron. Astrophys., 433, 229

Hoppe, S., Lemoine-Goumard, M., for the H.E.S.S. collaboration, ICRC 2007

H.E.S.S. collaboration, F. Aharonian et al., 2005, Astron. Astrophys., 481, 401

SF2A 2008
C. Charbonnel, F. Combes and R. Samadi (eds)

THE OPTICAL DEPTH OF THE UNIVERSE SEEN THROUGH ULTRAHIGH ENERGY COSMIC RAY SPECTACLES

Kotera, K.[1] and Lemoine, M.[1]

Abstract. We provide an analytical description of the transport of ultrahigh energy cosmic rays in a universe made up of magnetized scattering centers, with negligible magnetic fields between them. Magnetic deflection is no longer a continuous process: it is rather dominated by scattering events. We calculate the optical depth of the Universe to cosmic ray scattering and discuss its phenomenological consequences for various source scenarios. It is found that part of the correlation reported recently by the Pierre Auger Observatory between active galactic nuclei and the arrival directions of ultrahigh energy cosmic rays may be affected by a scattering delusion. This experiment may be observing in part the last scattering surface of particles, rather than their source population.

1 Introduction

The problem of the origin of ultrahigh energy cosmic rays is higly related to their propagation in the extragalactic medium. Our lack of knowledge on the distribution of the magnetic fields on very large scales hinders significantly our study on that domain. At extremely high energies ($E > 6 \times 10^{19}$) though, one can reasonably assume that the ambient extragalactic magnetic field plays a negligible role in the propagation of particles, the only notable deflecting regions being localized magnetized spots. Radio halos, magnetized galactic winds, clusters of galaxies and filaments of large scale structures are altogether numerous, magnetized and spatially extended enough in order to influence the trajectory of ultrahigh energy cosmic rays.

We study here different modes of propagation of ultrahigh energy particles in such a model of magnetized universe. According to the parameters of scattering centers, the energy of the observed particles, and the direction in the sky, the Universe can appear more or less opaque to cosmic ray scattering.

2 Optical depth and last scattering surface for cosmic ray scattering

Out of simplicity, we will assume here that the scattering centers are distributed homogeneously in the Universe, with a typical mean free path to interaction. It is shown in Kotera & Lemoine (2008) that an inhomogeneous distribution is quite similar to the case where the dominant scattering centers are filaments. The details of the interaction between a particle and each type of magnetized structure is described in this paper.

The optical depth τ characterizes the number of scatterings along a path length l. In order to study the angular spread of the cosmic ray images on the detector, we also define the effective optical depth $\tau_{\rm eff}$, which becomes unity when the path length l is such that the particle has suffered a deflection of order unity. We write: $\tau = l/\overline{d}$ and $\tau_{\rm eff} = l/l_{\rm scatt}$, where $\overline{d}$ is the mean free path to interaction with any scattering center, and $l_{\rm scatt}$ the scattering length of cosmic rays in the medium, corresponding to the distance over which the deflection becomes of order unity. To make concrete estimates, we assume that one type of scattering center dominates, with typical interaction length d_i: $\tau \simeq 3.1\,(l/100\,{\rm Mpc})(d_i/32\,{\rm Mpc})^{-1}$. The fiducial value $d_i = 32\,{\rm Mpc}$ corresponds to spherical scattering centers of density $n_i = 10^{-2}\,{\rm Mpc}^{-3}$ and radius $r_i = 1\,{\rm Mpc}$; it is also a typical value for the interaction distance to filaments of the large scale structure.

A simple calculation shows that the flux received from sources located within a distance l increases as l. Hence most of the flux comes from sources located at distance $l_{\rm max}(E)$, the energy loss distance (by pions and pair production) of a particle of a given energy. Replacing l by $l_{\rm max}$ in the definitions of τ and $\tau_{\rm eff}$, one obtains the dependence in energy of these quantities, as shown in Figure 1 for one particular type of scattering center.

[1] Institut d'Astrophysique de Paris, UMR7095 - CNRS, Université Pierre & Marie Curie, 98 bis boulevard Arago F-75014 Paris, France

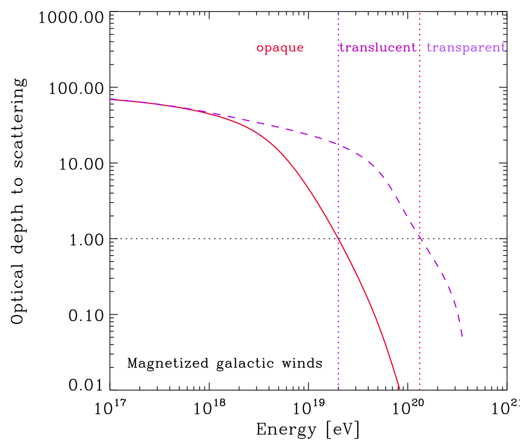

Fig. 1. Optical depth to cosmic ray scattering by magnetized galactic winds, with number density $n_{\rm gw} = 10^{-2}\,{\rm Mpc}^{-3}$, magnetic field intensity $B_{\rm gw} = 3 \cdot 10^{-8}\,{\rm G}$, coherence length $\lambda_{\rm gw} = 50\,{\rm kpc}$, and radius $r_{\rm gw} = 0.8\,{\rm Mpc}$. Solid line: optical depth $\tau_{\rm eff}$ to scattering by an angle of order unity; dashed line: optical depth τ.

In this figure, the horizontal dotted line indicates an optical depth of order unity, while the vertical dotted lines indicate at which energy $\tau_{\rm eff} = 1$ and $\tau = 1$ respectively, from left to right. As indicated on the figure, these lines delimit the energy ranges in which the Universe appears opaque ($\tau > \tau_{\rm eff} > 1$), translucent ($\tau > 1 > \tau_{\rm eff}$) or transparent ($1 > \tau > \tau_{\rm eff}$) to cosmic ray scattering. Interestingly, for this example, the Universe is translucent at energies close to the threshold for pion production $E_{\rm GZK} \simeq 6 \cdot 10^{19}\,{\rm eV}$.

Since the sources of protons with energies beyond the pion production threshold are bound to reside within $100 - 200\,{\rm Mpc}$, one may expect the optical depth of scattering centers to vary with the direction of observation, just as the matter density. In order to discuss the influence of such variations on existing and upcoming data, we have constructed sky maps of the matter concentration using the PSCz catalog of galaxies (Saunders et al., 2000).

The integrated column density of baryonic matter $N_{\rm g}/\langle N_{\rm g}\rangle$ up to a distance l is shown in Fig. 2 for maximal distances: $l = 80,\, 160\,{\rm Mpc}$ (we adopt $H_0 = 70\,{\rm km/s/Mpc}$). In order to correct for the incompleteness of the catalog, we have followed the prescriptions of Saunders et al. (2000) and smoothed the galaxy distribution with a variable gaussian filter, making use of the `HEALPix` library (Górski et al., 2005). The overall resolution of the maps is of order $7°$.

These maps provide an estimate of the optical depth to cosmic ray scattering in the case where the scattering centers are distributed as the galaxies, with a possible bias. A relation of proportionality between the quantity $N_{\rm g}/\langle N_{\rm g}\rangle$ shown in Figure 2 and the optical depth τ, that enables a more precise reading of those skymaps can be found in Kotera & Lemoine (2008).

3 Consequences for cosmic ray transport

In this section, we discuss the phenomenological consequences of the above model of cosmic ray transport with respect to the signatures of different source models, discussing in particular the absence or existence of counterparts.

The optically thin regime, in which $l_{\rm max} < \overline{d} < l_{\rm scatt}$, is trivial in terms of particle propagation: most particles travel in straight line, without interacting in the intergalactic medium, hence one should expect to see the source directly in the arrival direction of the highest energy events. However, in the case of gamma-ray burst sources, the spreading of arrival times through the interaction with cosmic magnetic fields is essential to reconcile the gamma-ray burst rate with the rate of ultrahigh energy cosmic ray detection (Waxman, 1995). In the absence of scattering (hence time delay), such a bursting source would be essentially unobservable as the occurrence rate is much too low when compared to the lifetime of the experiment.

In the intermediate 'translucent' regime ($\overline{d} < l_{\rm max} < l_{\rm scatt}$), the total deflection remains smaller than unity.

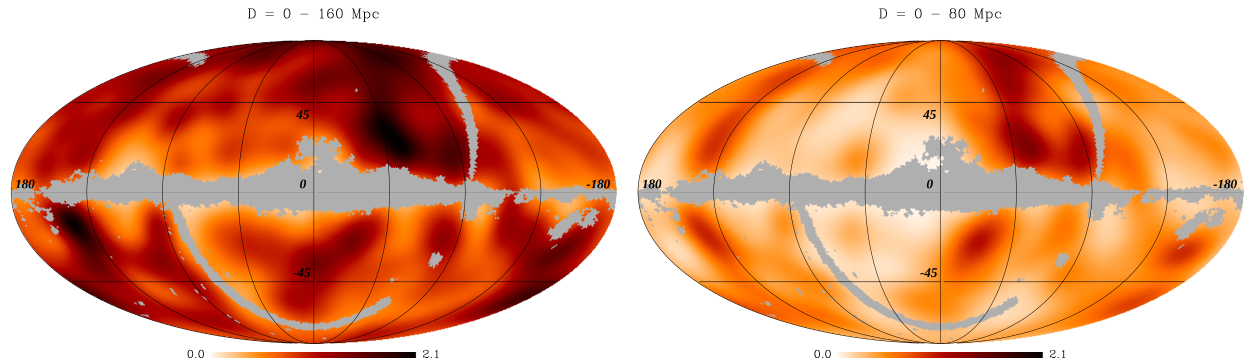

Fig. 2. Integrated galaxy column density as derived from the PSCz catalog of galaxies up to the maximal distances $l = 80\,\mathrm{Mpc}$ and $l = 160\,\mathrm{Mpc}$ (Mollweide projection). The contours give the column density N_{g} in units of the mean column density $\langle N_{\mathrm{g}} \rangle = \langle n_{\mathrm{g}} \rangle \times 160$ Mpc, with $\langle n_{\mathrm{g}} \rangle$ the mean galaxy density. The grey mask indicates the regions of the sky that are not covered by the PSCz catalog (Saunders et al., 2000).

One may thus describe the transport as nearly ballistic with a non-zero time delay as measured relatively to straight line propagation. The total time delay aquired over a path length δt and the typical deflection angle $\delta\alpha$ between the source direction and the particle arrival direction can be calculated as a function of τ, using random walk arguments.

As $\delta\alpha$ depends on τ, which is itself direction dependent (as shown in Fig. 2), the angular deflection will depend on the observed region of the sky. This property is also valid for the time delay, as $\delta t \propto \tau$. This is particularly interesting if the sources of cosmic rays were bursting sources (like gamma-ray bursts): the time delay and its dispersion induced by the interactions with scattering centers can artificially enhance the flux of particles. Hence the probability of observing particles produced by bursting sources will be lower by a factor τ in regions where $\tau < 1$, as compared to regions where the optical depth is greater than unity. Conversely, if the source is not of the bursting type, one might see it directly in the arrival direction if the source lies in a hole of the foreground scattering center distribution.

The opaque regime corresponds to $\tau > \tau_{\mathrm{eff}} > 1$. In this case, cosmic rays diffuse from the source to the detector as in a random billiard. The arrival direction of high energy events will point back to the source (either of bursting or continously emitting) only if this latter is located at a distance closer than l_{scatt}. Note that the same delusive effect of finding a scattering center in the arrival direction of cosmic rays occurs in this regime just as in the translucent regime.

4 Discussion on the recent data from the Pierre Auger Observatory

The Pierre Auger Observatory (PAO) has recently released the largest catalog of events above $5.7 \times 10^{19}\,\mathrm{eV}$ (Abraham et al., 2008), in which 20 out of 27 events originate from within 3 degrees of an active galactic nucleus located within 75 Mpc.

This correlation is puzzling for two reasons: the AGN used in this analysis are mainly Seyfert galaxies that are not favoured candidates for particle acceleration to ultrahigh energy. Second, the distance at which the maximum correlation is observed seems to be much lower than l_{max}, the source distance scale from which the maximum flux should be observed. Two main possibilities are advocated in the community to solve this latter incoherence: the energy scale measured by PAO may be underestimated by 30%, or it might be due to a selection bias of the observed particles. In light of the analysis developed above, we suggest that this correlation may actually pinpoint scattering centers correlating with AGN, rather than the sources of ultrahigh energy cosmic rays.

We estimate the fraction of events that are likely to be contaminated by such pollution by calculating the fraction of galaxies in the PSCz catalogue that lie within 3° of an AGN which is itself located closer than 75 Mpc. We obtain that 31% of events above $6 \times 10^{19}\,\mathrm{eV}$ could correlate with the AGN, assuming that the PSCz galaxies provide an unbiased tracer of the cosmic ray source population and that the magnetic deflection is much smaller than the search radius of 3°. Now, if we repeat the same procedure, taking into account magnetic deflections, the fraction of contaminated events increases as the assumed magnetic deflection angle $\delta\alpha$ becomes of order of a few degrees: it equals 39% for $\delta\alpha = 1°$, 48% for $\delta\alpha = 3°$, then decreases, being 45% for $\delta\alpha = 5°$ and 43% for $\delta\alpha = 7°$.

The above estimates indicate that, within the assumptions of the above discussion, the delusion should not affect all events of PAO, but a significant fraction nonetheless, possibly as high as $\simeq 50\,\%$. Moreover, they also indicate that intergalactic magnetic deflection could be larger than 3° and yet produce a relatively significant false correlation with AGN. This fraction of contaminated events is likely to be enhanced if ultrahigh energy cosmic rays originate from gamma-ray bursts. Indeed, as discussed in Section 3, one expects in this case the number of events in regions of low foreground density to be smaller by a factor of order τ (τ being the optical depth measured in such directions) when compared to that coming from regions of optical depth greater than unity.

In conclusion, it appears that the counterparts seen by PAO seem unlikely to be the sources of ultrahigh energy cosmic rays. One possible interpretation of the observed correlation is that PAO is mistaking the last scattering centers with the sources, which can be either continuously emitting or bursting sources. If the energy scale of PAO was underestimated by 30%, it may have detected the invisible sources within a few megaparsecs, in which case, no other counterpart (gamma rays, neutrinos...) will ever be seen in their direction, as they will have passed through Argentina more than 10^3 years ago. It appears that the most efficient way find the sources of ultrahigh energy cosmic rays will be to look for a signature of one type of sources at the highest energies ($> 10^{20}$ eV).

References

Kotera, K. and Lemoine, M., 2008, Phys. Rev. D, 77, 123003

Saunders, W. et al., 2000, MNRAS, 317, 55

Górski, K. M. et al., 2005, ApJ, 622, 759G

Waxman, E., 1995, Phys. Rev. L, 75, 386

Abraham, J. et al. (The Pierre Auger Collaboration), 2008, Astroparticle Physics, 29, 188

SF2A 2008
C. Charbonnel, F. Combes and R. Samadi (eds)

ON THE RESULTS OF THE PIERRE AUGER OBSERVATORY

Lemoine, M.[1]

Abstract. This paper discusses the correlation recently reported by the Pierre Auger Observatory (PAO) of the arrival directions of the highest energy cosmic rays with active galactic nuclei (AGN) located within 75 Mpc. It is argued that these correlating AGN do not have the power required to be the sources of those particles. It is further argued that the current PAO data disfavors giant radio-galaxies (both Fanaroff-Riley type I and II) as sources of ultra-high energy cosmic rays. The reported correlation with AGN should thus be understood as follows: the AGN trace the distribution of the local large scale structure, in which the actual sources of ultrahigh energy cosmic rays camouflage. The most promising theoretical candidates for these sources are then gamma-ray bursts and magnetars. One important consequence of the above is that one will not detect counterparts in gamma-rays, neutrinos or gravitational waves to the sources of these observed ultrahigh energy cosmic rays, since the cosmic rays are delayed by extragalactic magnetic fields on timescales $\sim 10^4 - 10^5$ yrs much larger than the emission timescale of these sources.

1 Introduction

The Pierre Auger Observatory has become the largest cosmic ray detector ever built. Among the first results published so far, the announcement of a correlation of 20/27 arrival directions of the highest energy events ($E > 5.7\times10^{19}\,$eV) with nearby ($d < 75\,$Mpc) active galactic nuclei (Abraham *et al.* 2007, 2008) has triggered a surge of interest in AGN models of ultrahigh energy cosmic ray origin as well as forecast studies of neutrino and gamma-ray expected signals from these objects. However, the fact that the correlating AGN are intrinsically weak seems to have been ignored or gone unnoticed (for exceptions, Moskalenko et al. 2008, George et al. 2008, Ghisellini et al. 2008). The term "AGN" stands for a broad class of galaxies and covers a huge range of luminosities $\sim 10^{40} - 10^{48}\,$erg/s. Whereas the typical model of ultrahigh energy cosmic ray origin in AGN refers to strongly beamed Fanaroff-Riley II (FR II) sources with giant radio lobes (e.g. Rachen & Biermann 1993), 19 out of 20 correlating AGN in the PAO dataset belong to the Seyfert or LINER class, only one being a Fanaroff-Riley I (FR I) radio-galaxy.

As emphasized in the PAO papers, one cannot exclude that actual sources of ultrahigh energy cosmic rays are distributed as the correlating AGN. As argued in Section 2, this interpretation is most likely the correct one. This has strong implications for the sources of ultrahigh energy cosmic rays, as discussed in Section 3. The present discussion, which draws heavily from the arguments presented in Lemoine & Waxman (2008), concludes that, quite ironically, the current data actually disfavors the acceleration of the highest energy cosmic rays in AGN, be they powerful or not, but instead point to bursting sources such as gamma-ray bursts (Vietri 1995, Waxman 1995) or spinning down magnetars (Arons 2003).

2 On AGN as sources of ultrahigh energy cosmic rays

The Hillas criterion gives a phenomenological bound to the maximal energy $E_{\rm max}$ that can be produced by a source of size R and magnetic field B (Hillas 1984). It relies on the statement that the particle must spend at least a Larmor time in the source, leading to: $E_{\rm max,20} = 11\,ZB_0R_0$, with $E_{\rm max,20} \equiv E_{\rm max}/10^{20}\,$eV, $B_0 \equiv B/1\,$G and $R_0 \equiv R/1\,$pc (Z denotes the charge of the accelerated particle). The above inequality can actually be recast as a lower limit on the magnetic luminosity of the source (Norman *et al.* 1995), which for spherical symmetry and non-relativistic motion with speed βc reads: $L_{\rm B} \simeq B^2R^2\beta c/2 \geq 1.2\times10^{45}\,\beta Z^{-2}E_{20}^2\,$erg/s.

[1] Institut d'Astrophysique de Paris, CNRS - UMPC, 98 bis boulevard Arago, 75014 Paris

One can actually obtain a more stringent bound on L_B by considering the acceleration process in more detail (Lyutikov & Ouyed 2005, Waxman 2005, Lemoine & Waxman 2008). To this effect, one writes the acceleration timescale as: $t_{\rm acc} = \mathcal{A} t_{\rm L}$, and assumes an outflow with bulk Lorentz factor γ and half-opening angle Θ. In the comoving frame, the maximal energy is limited by the condition $t_{\rm acc} < t_{\rm dyn} = R/(\gamma\beta c)$, with R the distance to the origin the outflow, the quantity $t_{\rm dyn}$ defining the dynamical timescale. This can be rewritten as a lower bound on $L_B = R^2\Theta^2\gamma^2\beta c B^2/4$ (L_B is calculated in the laboratory or source frame):

$$L_B \geq 0.65 \times 10^{45}\,\Theta^2\gamma^2\mathcal{A}^2\beta^3c^2Z^{-2}E_{20}^2\,\mathrm{erg/s}\ , \tag{2.1}$$

with E_{20} the observed energy in units of $10^{20}\,$eV. This bound is more severe than that derived from the Hillas criterion for several reasons. First of all, one must expect $\mathcal{A} > 1$ (and possibly $\mathcal{A} \gg 1$). For instance, non-relativistic Fermi acceleration leads to $\mathcal{A} \sim \alpha/\beta_{\rm sh}^2$ for Fermi-I at a shock of velocity $\beta_{\rm sh}c$ or $\alpha/\beta_{\rm A}^2$ for Fermi-II (with $\beta_{\rm A}c$ the Alfvén velocity), and $\alpha > 1$ is the ratio of the scattering timescale in the magnetic turbulence to the Larmor time (see Casse et al. 2002). Ultra-relativistic shock acceleration has been shown to be inefficient at ultrahigh energies in the sense that $\mathcal{A} \propto r_{\rm L}$ (see Pelletier et al. 2008 for a recent discussion). Moderately relativistic shock acceleration seems to be the most efficient acceleration process, but still one expects $\mathcal{A} \sim \alpha$, so that $\mathcal{A} \sim 1$ can be seen as a limiting regime of maximally efficient acceleration, for moderately relativistic shocks and assuming a Bohm diffusion regime $\alpha = 1$.

In these respects, Eq. (2.1) is very restrictive because very few sources are capable of emitting such magnetic power. One can check that the bound remains robust in the limit $\beta \to 0$, since $\mathcal{A}^2 \propto \beta_{\rm sh}^{-4}$ then more than compensates for this term. Similarly, as $\Theta \to 0$, lateral escape losses become prominent and one obtain a very similar bound albeit with a slightly different dependence on parameters (see Lemoine & Waxman 2008). It is furthermore natural to expect $Z \sim 1$ in regards of the tiny cosmic abundance of iron and other heavy nuclei.

Even then, this does not suffice. One should also require that the acceleration timescale be smaller than the energy losses timescales. The comparison does not directly depend on L_B but also on the magnetic field and radiation energy densities, so that additional parameters are to be considered. Such constraints allow to rule out acceleration of particles in the central regions of the powerful AGN (Norman et al. 1995, Henri et al. 1999).

This discussion shows that Seyfert galaxies (and more generally, radio quiet AGN) do not have the power to accelerate particles up to $10^{20}\,$eV since their bolometric luminosities lie below $10^{45}\,$ergs/sec. In the dataset of the Pierre Auger Observatory released so far, only one of the correlating AGN is a radio-galaxy possessing a large scale radio jet (Centaurus A), all others are Seyfert galaxies (with a few possible LINERs). Extending the search for counterparts to deeper distances (130 Mpc) or larger radii, Moskalenko et al. (2008) and Nagar & Matulich (2008) have noted a correlation of eight out of the twenty seven events with the lobes of extended radio-galaxies.

Centaurus A had been previously considered as a possible source of ultrahigh energy cosmic rays, even though it is classified as a low power BL Lac: its bolometric luminosity $L_{\rm bol} \sim 10^{43}\,$erg/s and its jet kinetic power $L_{\rm jet} \simeq 2\times10^{43}\,$erg/s. Through the modelling of the spectral energy distribution of the nucleus, Chiaberge et al. (2001) find $L_B \sim 10^{42}\,$ergs/sec, which misses the above bound by three orders of magnitude. Note that the paper of Romero et al. (1995), which argues that acceleration can take place in the X-ray knots of the inner jet contains flawed estimates for the maximal energy. These authors match the acceleration timescale with the energy loss timescale, but do not compare it to the escape timescale; and yet, this comparison would yield a maximal energy $\sim 10^{18}\,$eV, in agreement with the inferred magnetic luminosity and Eq. (2.1).

More generally, FR I radio-galaxies, TeV blazars and BL Lac objects do not seem to possess significant power to accelerate particles up to $10^{20}\,$eV, since their inferred magnetic luminosities are of order $L_B \sim 10^{42} - 10^{44}\,$ergs/s (Celotti & Ghisellini 2008). According to this study (done in the framework of leptonic models), only flat spectrum radio quasars (i.e. the most powerful FR II sources) seem capable of producing jets with $L_B > 10^{45}\,$ergs/s.

In proton blazar models, the magnetic field in the blazar zone is typically one order of magnitude larger than in leptonic models. In this case, acceleration might occur to ultrahigh energy in the blazar zone. However, in order to escape further expansion losses in the magnetized jets, the accelerated protons would have to be converted into neutrons, which would decay back to protons on a distance scale $\sim 0.9E_{20}\,$Mpc, i.e. outside the jet. One should therefore observe a correlation of the arrival directions with blazars, not with radio-galaxies seen offside (Rachen 2008). Since the Pierre Auger Observatory reports no correlation with blazars, and since blazars are too rare objects to be able to explain the number of events observed, this scenario fails.

Hence, in the class of radio-galaxies, only the most powerful FR II could potentially accelerate particles to ultra-high energies. However, in the sample of radio-galaxies that correlate with some events of the Pierre Auger dataset, constructed by Nagar & Matulich (2008), there is no FR II source, only three radio-galaxies of an intermediate FR I/FR II type. Furthermore, the highest energy PAO event, with $E = 1.48 \pm 0.27 \times 10^{20}$ eV, lies 28° away from the closest FR II (NGC 4261) within 130 Mpc in the catalog of Massaglia (2007). The closest blazar located closer than 150 Mpc lies 115° away from this event. At energies above 10^{20} eV, magnetic deflection should not exceed a few degrees (see Kotera & Lemoine 2008, Kashti & Waxman 2008 for a recent analytical discussion, and Dolag et al. 2004, Sigl et al. 2004 for numerical simulations). Large deflection angles at such energy are also disfavored from a purely empirical point of view since they would imply isotropic arrival directions of particles above 6×10^{19} eV, in direct contradiction with the PAO results.

All in all, the PAO data argue against the origin of ultrahigh energy cosmic rays in AGN, be they powerful or not. Intriguingly, a fraction of events seem to cluster in the direction to Cen A, with a small probability of chance coincidence (Gorbunov et al. 2008). However, one must keep in mind that Cen A lies in front of the Centaurus supercluster (at 50 Mpc) and the Shapley supercluster (200 Mpc), which represent some of the most important concentrations of matter in the local Universe. As discussed in Lemoine & Waxman (2008), the small occurence probabilities are not conclusive because they are calculated a posteriori, and because the significance fluctuates strongly with the assumptions made on the distribution and distance scale of the sources.

3 Discussion

The correlation of the Pierre Auger Observatory is thus mostly accidental, in the sense the correlating AGN trace the matter distribution, hence the source distribution. It is useful to note at this stage that the HiRes experiment does not confirm the correlation seen by the Pierre Auger Observatory (Abbasi et al. 2008). Kotera & Lemoine (2008) have observed that the distance scale of these correlating AGN (75 Mpc) is too small when compared to the expected source distance scale ($\sim$ 150 Mpc) and have suggested that the apparent correlation may be imaging the last scattering surface of ultrahigh energy cosmic rays rather than the source distribution. If the PAO energy scale had been underestimated by $\sim 30\%$, the two distance scales would agree (Abraham et al. 2007). Independently of this issue of the energy scale, Kashti & Waxman (2008) have shown that the PAO arrival directions are consistent with a source population tracing the large scale structure, with a preference for a source population biased towards dense regions of the intergalactic medium.

This discussion leads us to the conclusion that the sources of ultrahigh energy rays are invisible. The lack of clear counterpart, together with the hint of correlation of the arrival directions with the large scale structure suggest that these sources camouflage in more common galaxies and that they are of the bursting type. Given an expected deflection angle $\delta\theta \sim 3°$, the time delay suffered by ultrahigh energy protons is $\delta t \simeq \delta\theta^2 d/4c \simeq 10^5$ yrs (Waxman & Miralda-Escudé 1996), which sets an upper bound on the source activity timescale. Theoretical models which fall in this class are gamma-ray bursts (Vietri 1995; Waxman 1995), and magnetar spin-down (Arons 2003).

One fundamental consequence of bursting sources is that no counterpart, be it gamma-rays, X-rays, neutrinos or gravitational waves, should be found in the arrival directions of the highest energy events since these particles have passed by us δt ago and these sources are non-repeating. In order to confirm the origin of the highest energy cosmic rays in such sources, one must now collect more ultrahigh energy events at the highest energies possible, in order to search for specific signatures of bursting models, notably the departure from a continuous power law spectrum associated with a smaller number of contributing sources, or the energy clustering of events from a same source (Miralda-Escudé & Waxman 1996, Waxman & Miralda-Escudé 1996).

Quite certainly, much work also remains to be done on a theoretical level in order to improve our understanding of acceleration processes in these objects, and on the observational level, using multi-messenger astronomy.

References

Abbasi, R. U., et al. (The HiRes Collaboration), 2008, arXiv:0804.0382

Abraham, J. et al. (The Pierre Auger Collaboration), 2007, Science, 318, 938

Abraham, J. et al. (The Pierre Auger Collaboration), 2008, Astropart. Physics, 29, 188

Arons, J. 2003, ApJ, 589, 871

Casse, F., Lemoine, M., & Pelletier, G. 2002, PRD, 65, 023002

Chiaberge, M., Capetti, A., & Celotti, A. 2001, MNRAS, 324, L33

Dolag, K., Grasso, D., Springel, V., & Tkachev, I. 2005, JCAP, 1, 9

George, M. R., Fabian, A. C., Baumgartner, W. H., Mushotzky, R. F., & Tueller, J. 2008, MNRAS 388, L59

Ghisellini, G., Ghirlanda, G., Tavecchio, F., Fraternali, F., & Pareschi, G. 2008, arXiv:0806.2393

Gorbunov, D. S., Tinyakov, P. G., Tkachev, I. I., & Troitsky, S. V. 2008, arXiv:0804.1088

Henri, G., Pelletier, G., Petrucci, P. O., & Renaud, N. 1999, Astropart. Physics, 11, 347

Hillas, A. M. 1984, ARAA, 22, 425

Kashti, T., & Waxman, E. 2008, JCAP, 5, 6

Kotera, K., & Lemoine, M. 2008, PRD, 77, 123003

Lyutikov, M., & Ouyed, R. 2005, arXiv:astro-ph/0507620

Massaglia, S., 2007, Nuc. Phys. B Proc. Supp. 168, 302

Miralda-Escude, J., & Waxman, E. 1996, ApJ, 462, L59

Moskalenko, I. V., Stawarz, L., Porter, T. A., & Cheung, C. C. 2008, arXiv:0805.1260

Nagar, N. M., & Matulich, J. 2008, arXiv:0806.3220

Norman, C. A., Melrose, D. B., & Achterberg, A. 1995, ApJ, 454, 60

Pelletier, G., Lemoine, M., & Marcowith, A., 2008, arXiv:0707.3459

Rachen, J. P., & Biermann, P. L. 1993, AA, 272, 161

Rachen, J., 2008, in Proceedings of "Rencontres de Blois 2008 - Challenges in particle astrophysics", Blois (France), May 18-23 2008, ed. J. Dumarchez

Romero, G. E., Combi, J. A., Perez Bergliaffa, S. E., & Anchordoqui, L. A. 1996, Astropart. Physics, 5, 279

Sigl, G., Miniati, F., & Enßlin, T. A. 2004, PRD, 70, 043007

Vietri, M. 1995, ApJ, 453, 883

Waxman, E. 1995, Phys. Rev. Lett., 75, 386.

Waxman, E., & Miralda-Escude, J. 1996, ApJ, 472, L89

SF2A 2008
C. Charbonnel, F. Combes and R. Samadi (eds)

QUARK MATTER AT THE INTERIOR OF NEUTRON STARS

Oertel, M.[1]

Abstract. The density at the center of a neutron star reaches several times nuclear matter saturation density. At this density, the properties of strongly interacting matter are not well known. Exotic phases, such as hyperon matter, can appear. It is even possible that there is a phase transition to deconfined quark matter. Recent studies suggest that the phase structure of QCD in this domain is very rich. I will present the main characteristics of quark matter at high density as well as some observable consequences.

1 Introduction

The structure of the QCD phase diagram is one of the most exciting topics in the field of strong interactions (for reviews see, e.g., Alford et al. 2007). For a long time the discussion was restricted to two phases: the hadronic phase and the quark-gluon plasma (QGP). The former contains "our" world, where quarks and gluons are confined to color-neutral hadrons, whereas in the QGP quarks and gluons are deconfined.

At large enough density, nuclear matter is expected to undergo a phase transition to the deconfined phase, where quarks and gluons are free to move in the medium. Unfortunately, this transition is not well understood, since QCD lattice calculations cannot yet be performed at large density, i.e., at large chemical potential. Experimentally, in ultra-relativistic heavy ion collisions the transition to the deconfined phase is expected to occur at high temperature but essentially at zero baryon density. On the other hand, neutron stars are believed to contain very high baryon density in their interior, where the transition to the deconfined phase could occur. It has been argued by several authors that the properties of neutron stars can be strongly affected by the presence of a core where a quark phase or a mixed hadron-quark phase is present. The fact that the quark phase - if present - is likely to be a color superconductor has recently attracted much attention.

The intention of this talk will not be to discuss all the different possible color superconducting phases, but I will focus on some examples in order to discuss the main concepts of high density quark matter and the possible impact on neutron star phenomenology.

2 Color superconducting quark matter

Since QCD on the perturbative level provides an attractive interaction between quarks in certain channels, it is rather obvious to think of color superconducting phases in analogy with the Cooper mechanism for electrons responsible for the well-known electromagnetic superconductivity. Based on this idea, color superconducting phases were discussed already in the 70's (cf. for example Barrois 1977) and 80's (Bailin & Love 1984). But until quite recently not much attention was payed to this possibility. This changed dramatically after it was discovered that due to non-perturbative effects, the gaps which are related to these phases could be of the order of $\Delta \sim 100$ MeV (Alford et al. 1998; Rapp et al. 1998), much larger than expected from the early perturbative estimates. Since in standard weak-coupling BCS theory the critical temperature is given by $T_c \simeq 0.57\,\Delta(T=0)$, this also implies that T_c is much larger than the typical temperature of a neutron star older than some minutes. It was concluded that color superconducting phases could be relevant for compact stars (Weber 1999).

Rather soon after the beginning of this new era, it was noticed that there is probably more than one color superconducting phase in the QCD phase diagram. Due to the large number of quark degrees of freedom –color, flavor, and spin– there are many channels where diquark condensation is neither forbidden by Pauli principle

[1] LUTH, Observatoire de Paris, CNRS, Université Paris Diderot, 5 place Jules Janssen, 92195 Meudon Cedex, France

nor by symmetries. Thus the interactions have to decide about the actual condensation pattern realized at a given density or a given chemical potential and temperature.

In order to describe quark matter at the interior of a compact star, it is important to consider electrically and color neutral matter in β-equilibrium. In addition to the quarks we also allow for the presence of leptons, especially electrons and muons. As we consider stars older than a few minutes, when neutrinos can freely leave the system, lepton number is not conserved.

At large density, for chemical potentials much larger than the strange quark mass, three-flavor pairing, i.e. including up-, down-, and strange quarks (CFL phase), is energetically favored. The neutrality conditions are in favor of the CFL phase at moderate densities, too, since in particular the condition for electrical neutrality induces a considerable mismatch between the Fermi-momenta of up- and down quarks and renders therefore a standard BCS-type two-flavor pairing (2SC phase) difficult. Unfortunately there is actually no means to treat the problem of quark matter at densities relevant for neutron stars from first principles. This means, that although the general ideas are clear, the details of the phase diagram depend on the exact interaction model chosen. In general, models where the quark masses are generated dynamically, like in NJL-type models (cf. Buballa 2005 for a review) allow for a two-flavor pairing window, whereas in Bag models only three-flavor phases exist even at moderate densities if neutrality is imposed (cf. for example Alford & Reddy 2003). Several other possibilities, such as crystalline phases, where the mismatch of Fermi-momenta is compensated by a nonzero momentum of the diquark condensate, or gapless phases, have been considered in the literature, too. In the two-flavor case, the remaining quarks can form "exotic" phases, like spin-1 condensates. For recent versions of the phase diagram of neutral color superconducting quark matter, see for example Ruester et al. (2005).

Concerning the value of the strange quark mass, let us mention the work by Nickel et al. (2006). They show that within a self-consistent Dyson-Schwinger approach, the screening of gluons at the relevant densities for neutron stars lowers the strange quark mass such that within this self-consistent treatment the CFL phase stays favored over two-flavor pairing all the way down to hadronic matter. The calculations are, however, very involved, such that this model has for the moment not been applied to neutron stars.

3 Compact stars with a color superconducting quark matter core

This section will be devoted to the study of the composition of a neutron star including the possibility of a quark matter core or even a pure quark star. In general, as already mentioned above, it is very difficult to establish on first principles the properties of quark matter at the relevant densities. In the literature mainly two types of models are used: Bag models and NJL-type models. For the phenomenology of neutron stars, the main difference is that within the latter the quark masses are generated dynamically and the strange quark mass is still rather high for densities at the interior of a neutron star. This leads to a gravitational instability within these models if strange quark states become populated (cf. Baldo et al. 2003). That means, that in contrast to Bag model studies, only two-flavor quark matter can exist in hybrid stars and in particular, no pure quark stars exist within NJL type models because they require the existence of absolutely stable strange quark matter. And even the parameter window allowing for hybrid stars with two-flavor quark matter is in general rather small (cf. Buballa 2005).

One often studied observable is the mass-radius relation of a non-rotating star. This is interesting in the context of pure quarks stars, because they are self-bound objects and the mass-radius relation has therefore a very different behavior than for normal neutron stars. In particular, for very small masses and radii, it follows a $M \sim R^3$ curve and the resulting radii are smaller for a given mass than for neutron stars. This means that the discovery of an object with a small radius and a typical neutron stars mass would be a strong indication for a quark star. Another possibility is that recent QPO observations could exclude parts of the mass-radius diagram and be in favor of a quark star interpretation, too (cf. Boutelier, M. 2008).

For hybrid stars, the situation is less obvious. Due to the additional degrees of freedom, the EOS in general becomes softer if one includes a possible quark phase. This means that the maximal masses become smaller. The same phenomenon can be observed for purely hadronic stars but allowing for the presence of hyperons, i.e. baryons containing in contrast to nucleons at least one strange quark, in the denser part of the star. Since color superconducting quark matter has a lower energy than normal quark matter, the maximum mass is even further reduced if quark matter is color superconducting. This can be seen from Fig. 1, where the mass-radius relation for different compact star configurations obtained by integrating the TOV equation for static non-rotating objects is displayed (cf. Buballa et al. 2004). The dash-dotted line represents purely hadronic

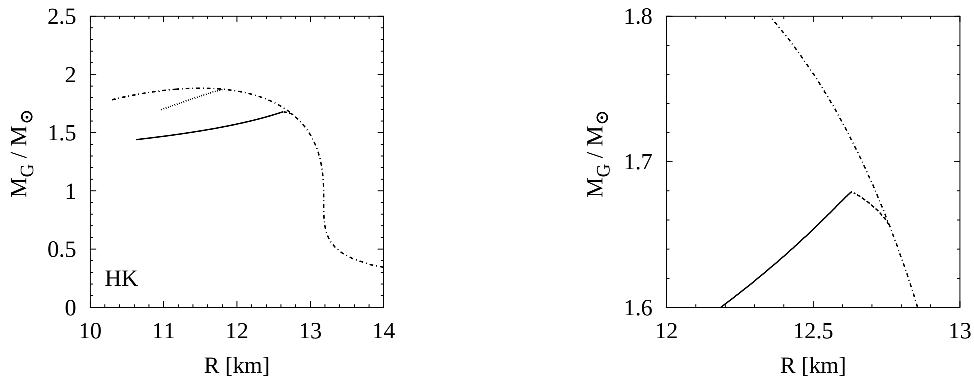

Fig. 1. Mass-radius relation of compact star configurations with a chiral $SU(3)$ model for the hadronic phase (Hanauske et al. 2000) and an NJL-type model for the quark phase including color superconductivity. The right panel shows the details of the phase transition region.

configurations, the dotted line configurations with a normal quark-matter core and the solid one configurations with color superconducting quark-matter cores in the 2SC and CFL phase. The phase transition part of the figure is again shown in more detail on the right hand side of Fig. 1. It can be seen that there is only a very small region, where stable hybrid stars exist. Note, however, that the star becomes unstable at the 2SC-CFL phase transition, such that we only find a hybrid star with a two-flavor quark core. The reason is, as explained above, the high strange quark mass in NJL-type models as applied here.

The existence of a hybrid star with a quark matter core can, however, not be ruled out if a high mass neutron star (typically with a mass above two solar masses) is observed, because the EOS of quark matter is not known well enough. A small repulsive vector interaction, for instance, could stiffen the quark matter EOS of state such that maximum masses above two solar masses can be accommodated (cf. Alford et al. 2005).

Many other possible signatures revealing the existence of a (color superconducting) quark matter core or even a pure quark star have been discussed. One interesting idea is based on the gravitational wave signal of neutron stars spiraling into black holes in binary systems (for a recent numerical simulation see Etienne et al. 2008). A step in the density profile at the interior of the neutron star resulting from a first order phase transition changes the form of the gravitational wave signal. Although the sensitivity of present detectors very probably is not sufficient, this could perhaps be detected in future gravitational wave detectors.

The above mentioned ideas are mainly based on the existence or not of a phase transition inside the neutron star. The superfluid or superconducting character of the matter only plays a minor role. There are, however, observables which are strongly influenced by superfluidity or superconductivity. First of all, let us mention the cooling behavior. The cooling of a neutron star is governed by neutrino emissivity and specific heat. The contribution to both quantities of particles paired in a scalar condensate (the dominant channel for almost all superfluid or superconducting phases inside a neutron star from the crust to a possible quark matter core) is suppressed exponentially at low temperatures as $\exp(-\Delta/T)$, where Δ is the energy gap in the spectrum and T the temperature. That means, quark matter in the CFL phase, where all quarks are paired, has a very low specific heat and neutrino emissivity. Unfortunately, this does not lead to any observable signal, since the cooling of the star is then dominated by the outer (hadronic) layers with higher specific heat and neutrino emissivity. The situation is different for two-flavor color superconducting phases, because there are quarks which remain unpaired or which pair in exotic condensates, such as spin-1, with much lower critical temperatures. This could give rise to rapid cooling due to direct Urca processes on unpaired quarks in early times before the temperature falls below the critical temperature for the "exotic" condensates. A more detailed discussion of the influence of two-flavor color superconducting phases on the cooling curves of neutron stars can be found in Popov et al. (2006).

The time of arrival of supernova neutrinos is another possible signal of a phase transition to CFL quark matter inside a neutron star. The most spectacular idea in this context is the following one: the neutrino mean free path is much longer in CFL matter than in all other phases inside a neutron star. A phase transition to CFL matter during the cooling down of the star could thus liberate all the previously trapped neutrinos and result in an increasing neutrino luminosity at the end of the supernova neutrino signal (Carter & Reddy 2000). It is, however, not clear whether this scenario survives a detailed simulation of supernova neutrino transport.

Another interesting field are the elastic properties such as r-mode instabilities. r-modes are oscillatory modes which transfer angular momentum from the star into gravitational radiation. At some critical spin frequency an instability exists which leads to an exponentially growing r-mode. In fact, the r-mode instability is very likely to impose the upper bound on observed spinning rates of pulsars since the mass-shedding limit is in general much higher than the observed frequencies. The damping of this instability is governed by viscosity. Here again, the contributions of gapped modes to the viscosity are damped exponentially. This means, the observation of millisecond pulsars with spin rates of several hundreds of Hz is inconsistent with a star formed uniquely of CFL quark matter because in that case the damping would be so low that the resulting maximum frequency is of the order of Hz or even below (cf. Madsen 2000).

In conclusion one should say that it is difficult to obtain information on the composition of neutron star matter from the different observations, but there are many interesting ideas for possible improvements in the (near) future.

References

Alford, M., Blaschke,D., Drago, A., Klähn, T., Pagliara, G. and Schaffner-Bielich, J.,2007, Nature 445, E7.

Alford, M., Rajagopal, K., and Wilczek, F., 1998, Phys. Lett. B 422, 247.

Alford,M., Rajagopal, K., Reddy,S. and Wilczek, F., 2001, Phys. Rev. D 64, 074017.

Alford, M. and Reddy, S., 2003, Phys. Rev. D 67, 074024.

Alford, M.G., Schmitt,A., Rajagopal. K. and Schäfer, T., 2007, arXiv:0709.4635 [hep-ph].

Bailin, D. and Love, A., 1984, Phys. Rep. 107 , 325.

Baldo,M., Buballa,M., Burgio,F., Neumann, F., Oertel, M. and Schulze, H.J., 2003, Phys. Lett. B 562, 153.

Barrois, B., 1977, Nucl. Phys. B 129, 390.

Boutelier, M., these proceedings.

Buballa, M., 2005, Phys. Rept. 407, 205.

Buballa, M., Neumann,F., Oertel, M. and Shovkovy, I., 2004, Phys. Lett. B 595, 36.

Carter, G.W. and Reddy, S. , 2000, Phys. Rev. D 62, 103002.

Etienne, Z.B., Faber, J.A., Liu, Y.T., Shapiro, S.L., Taniguchi, K., and Baumgarte, T.W., 2008, Phys. Rev. D 77, 084002.

M. Hanauske, D. Zschiesche, S. Pal, S. Schramm, H. Stöcker, and W. Greiner, 2000, Astrophys. J. 537, 50329.

Madsen, J., 2000, Phys. Rev. Lett. 85, 10.

Nickel,D., Alkofer, R. and Wambach, J., 2006, Phys. Rev. D 74, 114015.

Pisarski, R.D., and Rischke, D.H., 1999, Phys. Rev. D 60, 094013.

Popov,S., Grigorian, H. and Blaschke, D., 2006, Phys. Rev. C 74, 025803.

Rapp, R., Schäfer, T., Shuryak, E.V., and Velkovsky, M., 1998, Phys. Rev. Lett. 81, 53.

Weber, F., 1999, Acta Phys. Polon. B30, 3149.

SF2A 2008
C. Charbonnel, F. Combes and R. Samadi (eds)

UPPER LIMIT ON THE DIFFUSE FLUX OF UHE TAU NEUTRINOS FROM THE PIERRE AUGER OBSERVATORY

Payet, K., on behalf of the Pierre Auger Collaboration.[1]

Abstract. The Pierre Auger Observatory is able to discriminate showers induced by Ultra High Energy neutrinos from every other primaries. More particularly, it is sensitive to Earth-skimming ν_τ that interact in the Earth's crust to produce a τ lepton that may emerge and trigger an extensive air shower used to sign the presence of the initial neutrino. The data from 1 January 2004 to 31 August 2007 contains no such neutrino candidate, but is used to place a limit on the flux of ν_τ at EeV energies. The result from the Pierre Auger Observatory gives a limit in the energy range $2 \times 10^{17} eV < E_\nu < 2 \times 10^{19}$eV for an E_ν^{-2} differential energy spectrum. The limit set at 90% C.L. is $E_\nu^{-2} dN_{\nu_\tau}/dE_\nu < 1.3 \times 10^{-7}$ GeV cm^{-2} s^{-1} sr^{-1}.

1 Introduction

Through the last years, the observation of ultra-high energy (UHE) neutrinos has become one of the challenges of astroparticle physics. Many models, either astrophysical or exotic models, predict a substantial flux of neutrinos. One of the most certain contribution to this neutrino flux are the so-called GZK-neutrinos (Engel et al. 2001) produced in the decay of pions and kaons, from the interaction of ultra-high energy protons with the CMB. Such a mechanism provides a substantial flux of muon and electron neutrinos at the point of interaction. But given the large distances traveled by the particles, an observer can expect equal fluxes of electron, muon and ν_τ at the observation point, due to flavour mixing and neutrino oscillations. During the last years, an increasing effort has been put forward to develop a new generation of dedicated neutrino telescopes, that are relevant for an energy range of 10^{-6} to 10^{-1} EeV. An Ultra-high energy cosmic-ray detector such as the Pierre Auger Observatory (Abraham et al. 2004), although it was not developed for the detection of neutrinos, may have equal or even better potential in the UHE range of 10^{-1} to 10^{2} EeV, where the GZK-neutrinos are expected. In fact, it has been pointed out recently that the detection potential could be enhanced by the presence of τ neutrinos, due to oscillations, in the cosmic neutrinos flux. Upward-going UHE ν_τ that graze the Earth just below the horizon (also called "Earth-skimming neutrinos") have a quite high probability to interact in the crust and produce a τ lepton which, if produced close enough from the surface, may emerge and trigger an extensive air shower which may be detected by the surface detector (SD) array of the Pierre Auger Observatory, provided it does not decay too far from the ground. After giving a brief description of the Pierre Auger observatory in section 2, and discussing the issues of the detection and identification of UHE neutrinos in section 3, we will present the result of the search for UHE ν_τ with the SD in section 4.

2 The Pierre Auger Observatory

The Pierre Auger Observatory is located near the town of Malargüe, in the province of Mendoza, Argentina and has just reached completion. The originality of the Pierre Auger Observatory is that it combines two different techniques for the detection of Extensive Air Showers (EAS), that were originally used separately in previous experiments.

The Fluorescence Detector (FD) is composed of 4 buildings, each one housing 6 fluorescence telescopes designed to cover the entire SD. These instruments detect the ultraviolet light emitted by the nitrogen molecules of the air that are excited by the secondary charged particles of the EAS. The amount of light detected by the

[1] LPSC, Université Joseph Fourier Grenoble 1, CNRS/IN2P3, INPG, Grenoble, France

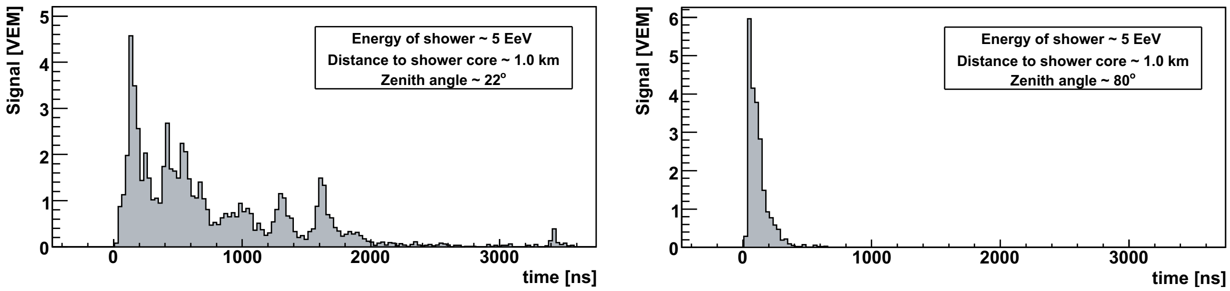

Fig. 1. FADC traces of stations at 1 km from the shower core for two real showers of 5 EeV. Left panel: Shower with electromagnetic component ($\theta \simeq 22^\circ$); Right: muonic signal ($\theta \simeq 80^\circ$)

telescopes is directly related to the energy of the EAS and thus offers a relatively precise measurement of the energy of the primary particle, allowing to limit the systematic uncertainties due to Monte Carlo (MC) simulations. The FD however suffers from its 10% duty cycle, especially when searching for rare events such as neutrinos.

The SD consists in an array of 1600 water Cherenkov tanks arranged in a hexagonal grid of 1.5 km covering a total area of 3000 km^2 and is used to sample the secondary particles of the EAS at the ground level. Each of these tanks contains 12 tons of purified water instrumented with $3 \times 9''$ photomultiplier tubes sampled by 40 MHz Flash Analog Digital Converters (FADCs). The signal in each tank is calibrated in units of Vertical Equivalent Muon (VEM) that is defined as the signal produced by a vertical muon crossing the tank. Contrarily to the FD, the SD has a 100 % duty cycle that provides a non negligible sensitivity to UHE neutrinos events.

3 Detection of UHE neutrinos

UHE particles that interact in the atmosphere produce EAS that contain muons and an electromagnetic (EM) component of electrons, positrons and photons. The muonic component can penetrate deeply in the atmosphere due to the long decay time of the muons. The EM component however is attenuated much faster and becomes negligible for showers traveling more than 2000 g cm^{-2} through the atmosphere. Protons and iron nuclei interact quickly in the upper layers of the atmosphere which means that at large zenith angles ($> 75^\circ$), where the atmosphere gets thicker, showers produced by such primaries have to travel through an important quantity of matter (typically more than 3800 g cm^{-2}) before reaching the ground. Such showers are thus dominated by muons arriving at the detector in a thin and flat shower front. This is not necessarily the case for Earth-skimming ν_τ as they produce a τ lepton that is likely to emerge and decay close to the detector, triggering a shower that can reach the detector with a still important EM component. Looking for such "young" showers at large zenith angles is the best way to discriminate between UHE neutrinos and other primaries.

For this purpose we can use two important informations from the SD: the arrival times of the shower front in the different tanks give an estimate of the zenith angle of the shower, while the time duration of the signal in the tanks signs the presence of EM component. A shower front composed only of high energy muons produces a narrow FADC trace whereas EM component induces broad signals (see Figure 1).

Devising a selection criterion for UHE ν_τ implies the use of different simulations. First the τ decay is simulated using the TAUOLA package (Jadach et al 1993) and the secondary particles created are then injected in the AIRES code (Sciutto 2002) to simulate the developement of the shower in the atmosphere. Such EAS generated by the product of the decaying τ lepton were simulated with energies between 10^{17} and 3×10^{20} eV, zenith angles from 90.1° to 95.9° and for different altitudes of the decay point above the Pierre Auger Observatory in the range $0 - 2500$ m. Then, the shower secondary particles at the ground level are injected in a detailed simulation of the SD (Ghia 2007). Based on these simulations, a set of conditions has been designed to select showers induced by Earth-skimming ν_τ and reject those induced by other primaries. As stated above, this criterion can be separated into two parts. First, the FADC traces of the different tanks present in the event are examined to find broad signals as shown in the figure 1. For this purpose each tank for which the main segment of the FADC trace has 13 or more neighbouring bins over a threshold of 0.2 VEM and for which the ratio of the integrated signal over the peak height exceeds 1.4 is tagged as an "EM tank". And the "young shower" condition is fulfilled if at least 60% of the tanks in the event are successfully tagged.

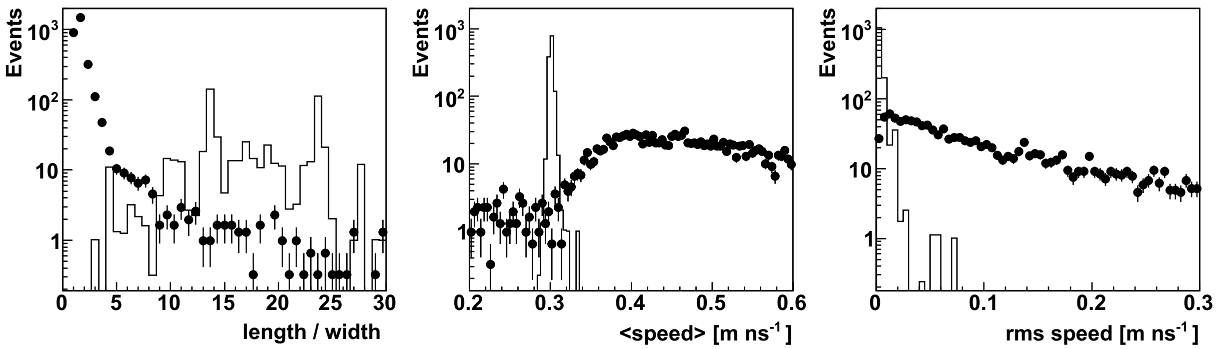

Fig. 2. Distributions of discriminating variables for showers initiated by τs decaying in the atmosphere, generated by ν_τs with energies sampled from an E_ν^{-2} flux (histogram), and for real events passing the "young shower" selection (points). Left: length/width ratio of the footprint of the shower on the ground; middle: average speed between pairs of stations; right: r.m.s scatter of the speeds.

Along with this EM condition, the event must also be compatible with a very inclined shower. The triggered tanks are thus required to have an elongated pattern on the ground by assigning a length and a width to the pattern and restricting its ratio (length/width > 5) and the apparent speed of the signal moving across the ground along the azimuthal direction is required to be very close to the speed of light (as expected for very inclined showers), in the range $(0.29, 0.31)$ m ns^{-1} with an r.m.s scatter below 0.08 m ns^{-1}. In figure 2, we show the distributions of the different discriminating variables for real events and simulated τ showers.

These conditions allow to reject the background from UHECR-induced showers and retain more than 80% of the simulated ν_τ showers.

4 Results

The conditions defined above were applied to the data set and over the whole period no neutrino candidate was found. The data of the Pierre Auger Observatory can thus be used to place a limit on the diffuse flux of UHE ν_τ. For this purpose we must calculte the exposure of the observatory. The total exposure must take into account the fact that the detector has grown while it was being constructed and is thus the time integral of the aperture for a given configuration. This aperture is then folded with the $\nu_\tau \to \tau$ conversion probability and the identification efficiency $\epsilon_{\rm ff}$. The latter is evaluated thanks to the selection criteria presented above and to the knowledge of the instantaneous configuration of the detector at a given time. It is a function of the τ energy E_τ, the altitude above ground of the central part of the shower h_c, the position (x, y) of the shower in the surface S covered by the array, and the time t.

The conversion probability is obtained using a MC simulation of the propagation of ν_τ and τ leptons inside the Earth. Such a simulation takes into account the different relevant processes: charged current and neutral current weak interactions for both particles; decay and electromagnetic energy losses through bremsstrahlung, pair production and photonuclear interaction for the τ lepton. Folding the conversion probability with the τ decay probability as a function of the flight distance gives the differential probability $d^2P_\tau/(dE_\tau dh_c)$ of obtaining an emerging τ lepton of energy E_τ that will produce a shower with central part at an altitude hc.

The expression for the exposure as a function of neutrino energy $\mathrm{Exp}(E_\nu)$, with θ and Ω the zenith and solid angles, is then:

$$\mathrm{Exp}(E_\nu) = \int_\Omega d\Omega \int_0^{E_\nu} dE_\tau \int_0^\infty dh_c \left[\frac{d^2p_\tau}{dE_\tau dh_c} \times \int_T dt \int_S dxdy \cos\theta \epsilon_{\rm ff} \left[E_\tau, h_c, x, y, t\right] \right] \tag{4.1}$$

This exposure is calculated using MC techniques and the estimated statistical uncertainty is below 3%. Simulating interactions in the relevant energy range requires the use of parton distribution and structure functions that have to be extrapolated to energies where no data is available. This is the main source of systematic uncertainties of this work. The uncertainty in the exposure due to the ν cross-section is estimated to be 15%. The 40% difference among existing calculations for the τ energy losses is used as the systematic uncertainty. Also, we consider a 30% uncertainty due to the polarization of the decaying τ lepton. We considered only

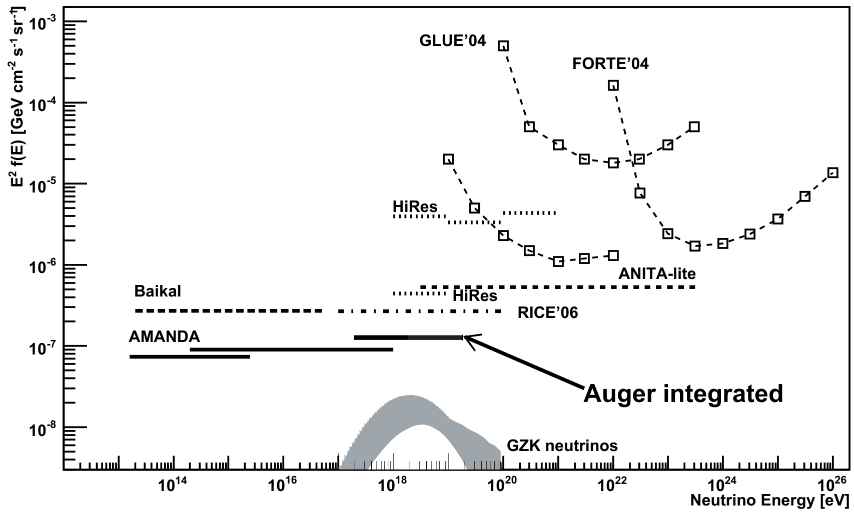

Fig. 3. Limits at 90% C.L. for a diffuse flux of ν_τ from the Pierre Auger Observatory. Limits from other experiments are converted to a single flavour assuming a 1:1:1 ratio of the 3 neutrino flavours and scaled to 90% C.L. where needed. The shaded curve shows the range of expected fluxes of GZK neutrinos from (Engel et al. 2001; Allard et al 2006).

extrapolations that follow the behaviour observed in the regions with experimental data. We also consider a 18% uncertainty from neglecting the contribution of the mountains around the Pierre Auger Observatory to the emerging τ flux and adopt a 25 % systematic uncertainty for the simulations of the EAS and the detector.

The limit set at 90% C.L. is then calculated using the following formula (integrated format):

$$K_{90} = \frac{2.44}{\int \Phi(E_\nu).Exp(E_\nu)dE_\nu} \tag{4.2}$$

This value defines a limit flux K_{90}/E_ν^2 that would lead to 2.44 detected neutrinos for the considered exposure. Assuming a $\Phi(E_\nu) = E_\nu^{-2}$ differential flux of ν_τ, and adopting the most pessimistic scenario for the systematic uncertainties, we obtain:

$$K_{90} = 1.3 \times 10^{-7}\text{GeV cm}^{-2}\text{ s}^{-1}\text{ sr}^{-1} \tag{4.3}$$

The limit is shown in figure 3. In the most optimistic scenario for the systematics, the K_{90} value is divided by a factor ~ 3.

The data collected with the SD of the Pierre Auger Observatory provides at present the most sensitive bound on neutrinos at EeV energies, the most relevant energies to explore the GZK neutrinos. The Pierre Auger Observatory will continue to take data for about 20 years over which time the limit should improve by over an order of magnitude if no neutrino candidate is found.

The full list of references may be found in the original paper (Abraham et al. 2008).

References

Engel, R., Seckel, D. and Stanev, T. 2001, Phys. Rev. D 64 093010

Abraham, A. *et al.* [Pierre Auger Collaboration] 2004, Nucl. Instrum. Method A523 50

Jadach, S. *et al.* 1993, Comput. Phys. Comm 76 361

Sciutto, S. 2002, http://www.fisica.unlo.edu.ar/auger/aires/, version 2.6.0

Ghia, P. L.[Pierre Auger Collaboration] 2007, 30th ICRC, arXiv:0706.1212 [astro-ph]

Allard, D. *et al.* 2006, JCAP 0609, 005

Abraham, A. *et al.* [Pierre Auger Collaboration] 2008, Phys. Rev. Lett. 100, 211101

SF2A 2008
C. Charbonnel, F. Combes and R. Samadi (eds)

MODELLING THE HIGH ENERGY EMISSION OF PULSARS

Pétri, J.[1,2]

Abstract. To date, seven gamma-ray pulsars are known, showing pulsed emission up to tens of GeV and associated light-curves with a double-pulse structure. We study this pulsed high-energy emission in the framework of the striped wind model. By numerical integration of the time-dependent emissivity in the current sheets, we compute the phase-dependent spectral variability of the inverse Compton radiation. Several light curves and spectra are presented. Pulses are a direct consequence of relativistic beaming. Our model is able to explain some of the high-energy (10 MeV-10 GeV) spectral features and behavior of several gamma-ray pulsars, like Geminga and Vela.

1 Introduction

The high-energy, pulsed emission from rotating magnetized neutron stars is usually explained in the framework of either the polar cap or the outer gap models. In both of these models, the radiation is produced within the light cylinder.

An alternative site for the production of pulsed radiation has been investigated (Kirk et al. 2002) based on the idea of a striped pulsar wind, originally introduced by Coroniti (1990) and Michel (1994). Emission from the striped wind originates outside the light cylinder and relativistic beaming effects are responsible for the phase coherence of the radiation. It has already been shown that this model can satisfactorily fit the optical polarization data from the Crab pulsar (Pétri & Kirk 2005).

We use an explicit asymptotic solution for the large-scale field structure related to the oblique split monopole (Bogovalov 1999). We calculate the properties of the phase-resolved and spectral variability of the pulsed emission and compare our results with high-energy observations of several gamma-ray pulsars.

2 THE STRIPED WIND MODEL

The model used to compute the high-energy pulse shape and the phase-resolved spectrum arising from the striped wind is briefly presented in this section. The geometrical configuration is as follows. The magnetized neutron star is rotating at an angular speed Ω_* directed along the (Oz)-axis i.e. the rotation axis is $\vec{\Omega}_* = \Omega_* \vec{e}_z$. We use a Cartesian coordinate system with coordinates (x, y, z) and orthonormal basis $(\vec{e}_x, \vec{e}_y, \vec{e}_z)$. The stellar magnetic moment $\vec{m} = m\,\vec{e}_m$, assumed to be dipolar, makes an angle χ with respect to the rotation axis. This angle is therefore defined by $\cos\chi = \vec{e}_m \cdot \vec{e}_z$. The inclination of the line of sight with respect to the rotational axis, and defined by the unit vector $\vec{n}$, is denoted by ζ, we have $\cos\zeta = \vec{n} \cdot \vec{e}_z$. It lies in the (Oyz) plane. Moreover, the wind is expanding radially outwards at a constant velocity V close to the speed of light denoted by c.

Our model involves some geometrical properties related to the magnetic field structure and some dynamical properties related to the emitting particles. Furthermore, in order to compute the light curves and the corresponding spectra, we need to know the emissivity of the wind due to inverse Compton scattering. This is explained in the next paragraphs.

2.1 Magnetic field structure

We adopt a geometrical structure of the wind based on the asymptotic magnetic field solution given by Bogovalov (1999). Outside the light cylinder, the magnetic structure is replaced by two magnetic monopoles with equal and opposite intensity. The current sheet sustaining the magnetic polarity reversal arising in this solution, expressed in spherical coordinates (r, θ, φ) is defined by $r_s(\theta, \varphi, t) = \beta\, r_L\, [\pm \arccos(-\cot\theta\, \cot\chi) + c\,t/r_L - \varphi + 2\,l\,\pi]$ where $\beta = V/c$, $r_L = c/\Omega_*$ is the

[1] Centre d'étude des Environnements Terrestre et Planétaires, 10-12 avenue de l'Europe 78140 Vélizy
[2] Laboratoire de Radio-Astronomie, École Normale Supérieure, 24 rue Lhomond 75005 Paris

radius of the light cylinder, t is the time as measured by a distant observer at rest, and l an integer. Because of the ideal MHD assumption, this surface is frozen into the plasma and therefore moves also radially outwards at a constant speed V. Strictly speaking, the current sheets are infinitely thin. However, as was already done in the study of the synchrotron polarization of the pulsed emission (Pétri & Kirk 2005) we release this prescription. Indeed, the current sheet are assumed to have a given thickness, parameterized by the quantity Δ_φ. Moreover, inside the sheets, the particle number density is very high while the magnetic field is weak. In whole space, the magnetic field is purely toroidal and given by

$$B_\varphi = B_{\rm L} \, \frac{R_{\rm L}}{r} \, \eta_\varphi \tag{2.1}$$

The strength of the magnetic field at the light-cylinder is denoted by $B_{\rm L}$. In the original work of Bogovalov (1999) , the function η_φ is related to the Heaviside unit step function and can only have two values ± 1, leading to the discontinuity in magnetic field. In order to make the transition more smooth, we redefine the function η_φ by

$$\begin{aligned} \eta_\varphi &= \tanh(\Delta_\varphi \, \psi) \\ \psi &= \cos\theta \, \cos\chi + \sin\theta \, \sin\chi \, \cos\left[\varphi - \Omega_* \, (t - \frac{r}{V})\right] \end{aligned} \tag{2.2}$$

With this expression, the transition layer has a thickness of approximately Δ_φ.

2.2 Particle distribution function

The innermost regions of the pulsar magnetosphere is believed to be a site of high-energy pair production feeding the wind with ultra-relativistic electrons and positrons. For these emitting particles, we adopt an isotropic distribution function in momentum space in the comoving frame of the wind. It is given by a power law in energy, with a sharp low and high-energy cut-off, $\gamma_{\rm min}$ and $\gamma_{\rm max}$ respectively, such that the particle number density at time t and position $\vec{r}$ with energy between γ and $\gamma + d\gamma$ is

$$n_e(\gamma, \vec{r}, t) \, d\gamma = K_e(\vec{r}, t) \, \gamma^{-p} \, d\gamma \tag{2.3}$$

with $\gamma_{\rm min} \le \gamma \le \gamma_{\rm max}$ and $K_e(\vec{r}, t)$ is related to the number density of emitting particles in the current sheet. The particular form of the magnetic field in the current sheets, decreasing like a tangent hyperbolic function tanh as given in Eq. (2.1), suggests to use a plasma density profile dictated by the exact solution of the relativistic Harris current sheet, namely a secant cosines hyperbolic function sech, see for instance Pétri & Kirk (2007). We thus adopt the following expression for the density

$$K_e(\vec{r}, t) = \frac{(N - N_0) \, {\rm sech}^2(\Delta_\varphi \, \psi) + N_0}{r^2} \tag{2.4}$$

N_0 sets the minimum density in the stripes, between the current sheets, whereas N defines the highest density inside the sheets. However, in order to allow different peak intensities in the light curves, we choose different maximum densities in two consecutive sheets, namely N_1 and N_2. The radial motion of the wind at a fixed speed imposes an overall $1/r^2$ dependence on this quantity, due to conservation of particle number. However, adiabatic losses in the current sheets due to pressure work will cool down this distribution function in such a way that K_e decreases with an additional factor $1/r^{2/3(p+2)}$, see Kirk (1994). As already done in a previous work, we assume the emission commences when the wind crosses the surface defined by $r = r_0 \gg r_{\rm L}$. Let us now discuss the exact form of the emissivity functions in the striped wind for the inverse Compton radiation.

2.3 Inverse Compton emissivity

We assume an isotropic distribution of mono-energetic target photons ε with density $n_\gamma(\varepsilon)$ in the observer frame. The total emissivity is denoted by $j_{\rm ic}^{\rm obs}$. Knowing the inverse Compton emissivity, the light curves are obtained by integration over the whole wind region. This wind is assumed to extend from a radius r_0 to an outer radius $r_{\rm s}$ which can be interpreted as the location of the termination shock. Therefore, the inverse Compton radiation at a fixed observer time t is given by

$$I_{\rm ic}^{\rm obs}(t) = \int_{r_0}^{r_{\rm s}} \int_0^\pi \int_0^{2\pi} j_{\rm ic}^{\rm obs}(\vec{r}, t_{\rm ret}) \, r^2 \sin\theta dr d\theta d\varphi \tag{2.5}$$

The retarded time is expressed as $t_{\rm ret} = t - \|\vec{R}_0 - \vec{r}\|/c \approx t - R_0/c + \vec{n} \cdot \vec{r}/c$. The approximation is valid if the observer, located at $\vec{R}_0$, is very far away from the radiating system, $R_0 \gg r_{\rm s}$. Eq.(2.5) is integrated numerically. We compute the inverse Compton intensity for several frequencies from far below the low cut-off frequency to far over the high frequency cut-off. We are therefore able to predict the phase resolved spectral variability and the pulse shape simultaneously. The results and applications to some γ-ray pulsars are discussed in the next section.

3 APPLICATION TO γ-RAY PULSARS

We apply the aforementioned model to inverse Compton scattering of low-energy photons from the cosmic microwave background with typical energy of $\varepsilon_{\rm cmb} = k_B\, T_{\rm cmb} = 2.36 \times 10^{-4}$ eV and energy density of 2.65×10^5 eV/m^3. We focus on 2 pulsars, namely, Vela and Geminga.

3.1 Geminga pulsar

In our best fit, we choose an inclination of the magnetic moment with respect to the rotation axis of $\chi = 60^o$. In order to obtain a phase separation of 0.5 between the two pulses, we have to adopt an inclination of the line of sight $\zeta = 90^o$. The Lorentz factor of the wind is $\Gamma = 10$.

Results for the light-curve above 100 MeV and the definition of the different phase intervals is shown in Fig. 1. The rising and falling shape of both pulses are well fitted by our model. The corresponding spectra are shown in Fig. 2. The spectral variability is reproduced with satisfactory accuracy except for the OP phase for which the intensity is overestimated.

3.2 Vela pulsar

In our best fit, we choose an inclination of the magnetic moment with respect to the rotation axis of $\chi = 60^o$ and an inclination of the line of sight $\zeta = 76^o$. The Lorentz factor of the wind is $\Gamma = 16$.

Results for the light-curve above 100 MeV and the definition of the different phase intervals is shown in Fig. 1. The corresponding spectra are shown in Fig. 2. The spectra within the two pulses, P1/2, IP1, LW2 and TW1 are well reproduced as well as the cut off energy around a few GeV. The other phases still need some intensity level readjustment.

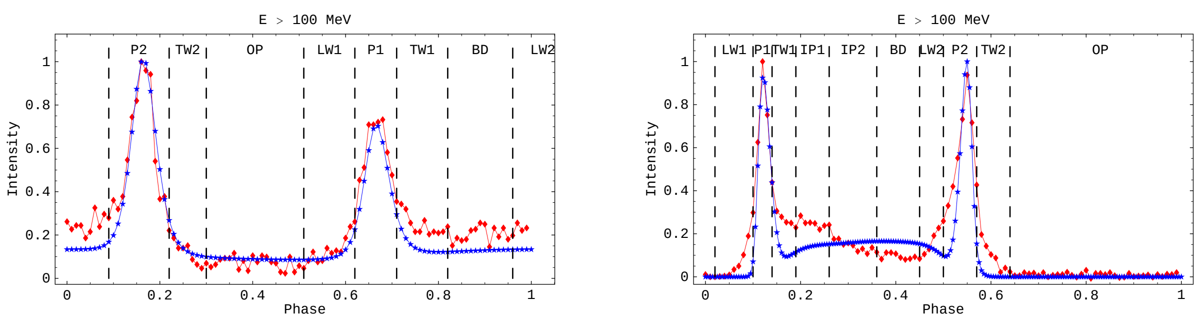

Fig. 1. Gamma-ray light curve above 100 MeV of Geminga, on the left and Vela, on the right, fitted with the inverse Compton emission from the striped wind.

4 CONCLUSION

In the striped wind model, the pulsed high-energy emission from pulsars arises from regions well outside the light-cylinder. By computing the inverse Compton emission on the CMB photons, we were able to fit the EGRET data of the light-curves and spectra for several gamma-ray pulsars such as Vela and Geminga.

References

Bogovalov, S. V. 1999, A&A, 349, 1017

Coroniti, F. V. 1990, ApJ, 349, 538

Fierro, J. M., Michelson, P. F., Nolan, P. L., & Thompson, D. J. 1998, ApJ, 494, 734

Kirk, J. G. 1994, in Saas-Fee Advanced Course 24: Plasma Astrophysics, ed. A. O. Benz & T. J.-L. Courvoisier, 225

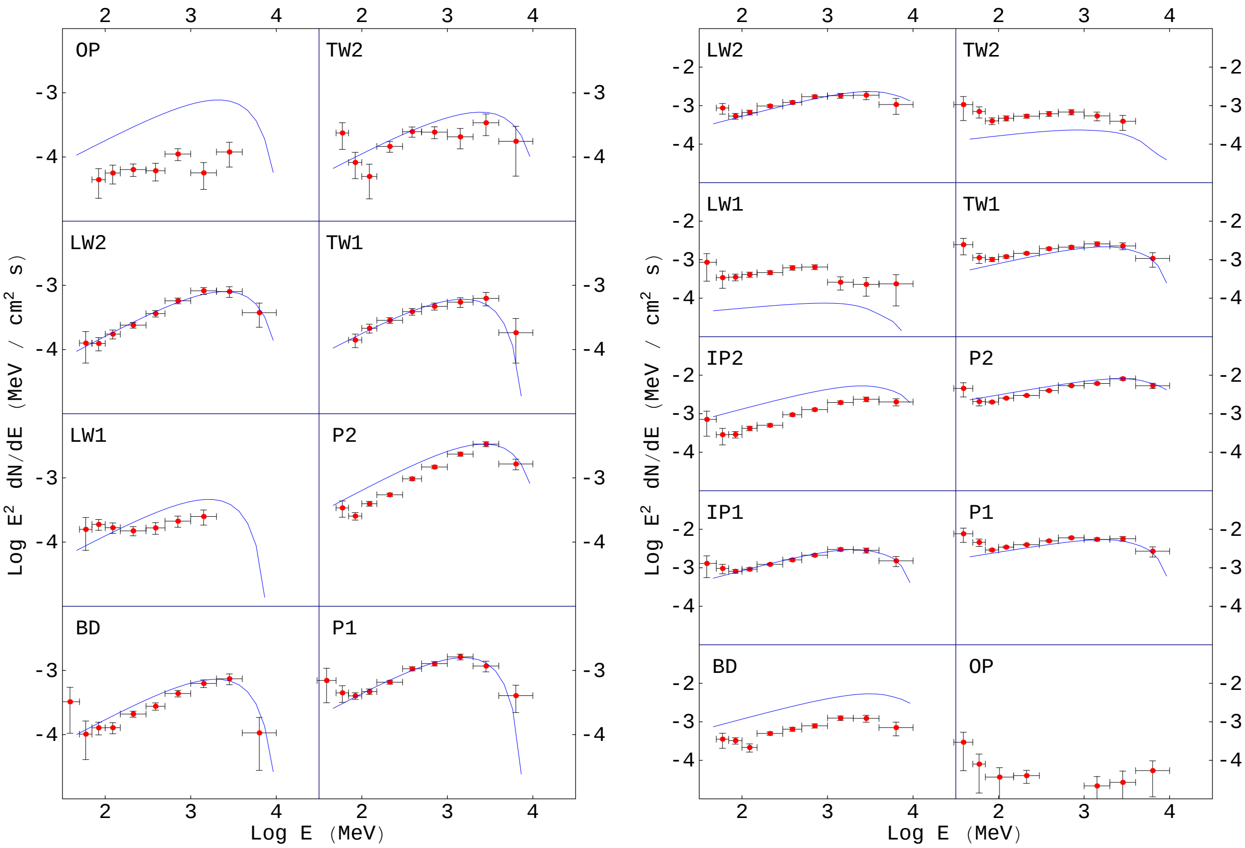

Fig. 2. Phase-resolved inverse Compton emission from the Geminga pulsar, on the left and the Vela pulsar, on the right, for different phase intervals: bridge (BD), off-pulse (OP), interpulse 1/2 (IP1/IP2), leading wing 1/2 (LW1/LW2), peak 1/2 (P1/P2), trailing wing 1/2 (TW1/TW2), for the definition of the intervals see Fierro et al. (1998).

Kirk, J. G., Skjæraasen, O., & Gallant, Y. A. 2002, A&A, 388, L29
Michel, F. C. 1994, ApJ, 431, 397
Pétri, J. & Kirk, J. G. 2005, ApJL, 627, L37
Pétri, J. & Kirk, J. G. 2007, Plasma Physics and Controlled Fusion, 49, 1885

SF2A 2008
C. Charbonnel, F. Combes and R. Samadi (eds)

SUZAKU OBSERVATIONS OF MRK 841 AND THE PROBLEM OF THE SOFT EXCESS IN SEYFERT GALAXIES

Ponti, G.[1], Petrucci, P.-O.[2], Matt, G.[3], Mouchet, M.[1,4], Boisson, C.[4], Longinotti, A.L.[5], Costantini, E.[6], Cappi, M.[7] and Goncalves, A.C.[4]

Abstract. We show preliminary results from the study of the first of 2 long (∼50 ks) Suzaku observations of the bright Seyfert 1 galaxy Mrk 841. This source is characterized by a strong soft excess, which has been modelled assuming two different physical interpretations: reflection onto a relativistic ionised disc and absorption by a relativistic wind. Both models give similar results from a statistical point of view, but the high energy data seems to favour an ionized disc reflection interpretation.

1 Introduction

The origin of the soft excess in Seyfert galaxies is still not understood. It has been recently realized that its characteristic temperature (when fitted by a simple black body) is remarkably constant over many range of AGN luminosity and black hole masses (Czerny et al. 2003; Gierlinski & Done 2004; Crummy et al. 2006; Ponti et al. 2006), favouring an origin through atomic processes instead of disc black body emission. Recent studies suggest two appealing explanations. The soft excess: either it is due to ionized reflection from the accretion disc or it may be the result of a strong relativistic ionized wind produced in the inner parts of the accretion disc.

Mkn 841 is a bright Seyfert 1 galaxy (z=0.0364), one of the rare Seyfert 1 detected by OSSE at more than 3 σ (Johnson et al. 1997). It is known for its large spectral variability (e.g. Nandra et al. 1995), its strong soft excess, the first ever detected in a type 1 AGN (Arnaud et al. 1985). Several XMM-Newton observations of this source confirm the presence of the soft excess and iron line complex and reveal their extreme and puzzling spectral and temporal behaviors (Petrucci et al. 2007). Different explanations have been proposed, but they could not be disentangled due to the lack of high energy observations.

2 Observations and Results

Suzaku caught Mrk 841 in similar flux states during the two observations. We show here the results of the XIS and XHD-Pin detectors for the first pointing only, the second observation yielding similar results. In all models used to fit the Suzaku data, we included a primary power law continum, a neutral iron line and reflection component from cold, distant, material.

The soft excess has been modelled assuming different physical precesses. In particular, we explored the possibility that it is due to either a relativistic ionized disc reflection (Ross & Fabian 2005; KDBLUR in Xspec) or to a relativistically smeared ionized absorption (Gierlinski & Done 2004; SWIND1 in Xspec).

Results are shown and described in Figures 1 and 2. From a statistical point of view the two models are equivalent: both scenarios provide a good fit in the 0.5-10 keV band which is where the data has a higher

[1] Laboratoire Astropaticule et Cosmologie, Univeriste Paris 7, 10 rue Alice Domon et Leonide Duquet, 75205 Paris Cedex 13, France
[2] Laboratoire d'astrophysique de Grenoble, BP 43, 38041 Grenoble Cedex 9, France
[3] Dipartimento di Fisica, Universita degli Studi Roma Tre, via della Vasca Navale 84, 00146 Roma, Italy
[4] Observatoire de Paris, Section de Meudon, LUTH, 5 place Jules Janssen, 92195 Meudon Cedex, France
[5] XMM-Newton Science Operation Center, European Space Astronomy Center, ESA, Apartado 50727, E-28080 Madrid, Spain
[6] SRON National Institute for Space Research, Sorbonnelaan 2, 3584 CA Utrecht, The Netherlands
[7] INAF/IASF Bologna, via Gobetti 101, 40129 Bologna, Italy

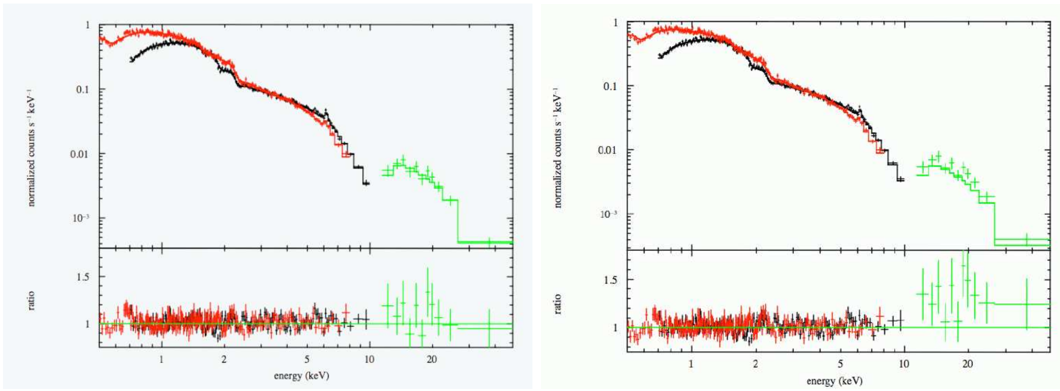

Fig. 1. Left: Suzaku mean spectrum fitted with a disc ionized reflection (Ross & Fabian 2005) convolved with a LAOR kernel (KDBLUR in Xspec) and **Right:** fitted with a relativistic ionized absorption model (Gierlinski & Done 2004) using the SWIND1 model in Xspec. The two models gives similar results from a statistical point of view. Nevertheless, the reflection model better reproduce the pin data.

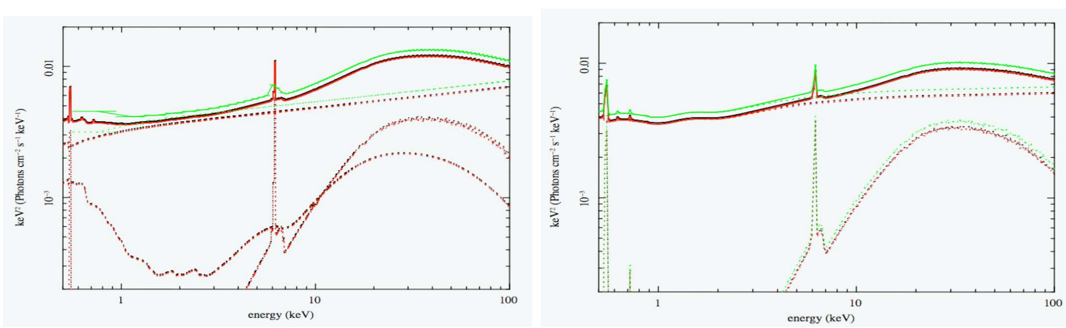

Fig. 2. Both best fit models are composed by a primary power law, a neutral iron line and its associated reflection continuum (assuming cosmic abundances). The soft excess has been modelled assuming a relativistic ionized disc reflection (left panel) or a relativistic smeared ionized absorption (right panel).

statistical weight. However, the high energy residuals in the Suzaku/PIN data seem to favour the reflection model, although no firm conclusion can be achived due to the large statistical and sistematic errors in this spectral range. The best fit parameters indicate that in both physical scenarios extreme relativistic effects must be involved. In particular in the absorption interpretation a smearing of the narrow absorption features of $\sim$0.3 c is required, while in the reflection interpretation a disc reflectivity index of $\sim$3.8 is required.

References

Arnaud, K. A., Branduardi-Raymont, G., Culhane, J. L., et al. 1985, MNRAS 217, 10

Crummy, J., Fabian, A. C., Gallo, L., & Ross, R. R. 2006, MNRAS 365, 1067

Czerny, B., Nikołajuk, M., Różańska, A., et al. 2003, A&A, 412, 317

Gierlinski, M. & Done, C. 2004, MNRAS, 349, L7

Johnson, W. N., Zdziarski, A. A., Madejski, G. M., et al. 1997, AIPC, 410, 283

Nandra, K., Turner, T. J., George, I. M., et al. 1995, MNRAS, 273, 85

Petrucci, P. O., Ponti, G., Matt, G., et al. 2007, A&A, 470, 889

Ponti, G., Miniutti, G., Cappi, M., et al. 2006 MNRAS 368, 903

Ross, R.R. & Fabian, A.C. 2005, MNRAS, 358, 211

SF2A 2008
C. Charbonnel, F. Combes and R. Samadi (eds)

X-RAY HICCUPS FROM SGR A* OBSERVED ON APRIL 4, 2007

Porquet, D.[1]

Abstract. Our Galaxy hosts at its dynamical center Sgr A*, the closest supermassive black hole. Remarkably, its luminosity is several orders of magnitude lower than the Eddington luminosity. Thanks to *Chandra* and *XMM-Newton*, we are able to detect X-ray flares from Sgr A*, providing new exciting perspectives for the understanding of the processes at work in the Galactic nucleus. On April 4, 2007, we observed for the first time within a time interval of roughly half a day, an enhanced incidence rate of X-ray flaring, with a bright flare (peak amplitude of ∼100 above the quiescent luminosity) followed by three flares of more moderate amplitude (amplitudes ∼25–40). This is the first time that a such level of X-ray flaring activity from Sgr A*, both in amplitude and frequency, is reported. This bright flare represents the second brightest X-ray flare from Sgr A* on record. This new bright flare exhibits similar light-curve shape (nearly symmetrical), duration (∼3 ks) and spectral characteristics to the very bright flare observed in October 3, 2002 by *XMM-Newton*. Based on a fully self-consistent analysis approach, we established that the two brightest X-ray flares observed so far from Sgr A* exhibited similar (well constrained) soft spectra.

1 Introduction

Located at the center of our Galaxy, Sgr A* is the closest supermassive black hole to the solar system at a distance of about 8 kpc. Its mass of about $3–4\times10^6\,M_\odot$ has been determined thanks to the measurements of star motions (e.g., Schödel et al. 2002, Ghez et al. 2003). Amazingly, this source is much fainter than expected from accretion onto a supermassive black hole. Its bolometric luminosity is only about 3×10^{-9} $\mathrm{L_{Edd}}$. In particular, its 2–10 keV "quiescent" X-ray luminosity is only about $2.4\times10^{33}\,\mathrm{erg\,s^{-1}}$ within a radius of 1.5″ (Baganoff et al. 2003). Hence, Sgr A* radiates in X-rays at about 11 orders of magnitude less than its corresponding Eddington luminosity. This has motivated the development of various radiatively inefficient accretion models to explain the dimness of the Galactic Center black hole, e.g., Advection-Dominated Accretion Flows, jet-disk models, Bondi-Hoyle with inner Keplerian flows (see Baganoff et al. 2003, and references therein). The recent discovery of X-ray flares from Sgr A* has provided new exciting perspectives for the understanding of the processes at work in the Galactic nucleus. The first detection of such events was found with *Chandra* in October 2000 (Baganoff et al. 2001). The bulk of X-ray flares detected (up to April 2007, see below) have weak to moderate peak flux amplitudes with factor of about 2–45 compared to the quiescent state (e.g., Bélanger et al. 2005, Eckart et al. 2006, Hornstein et al. 2007, Marrone et al. 2008). Only one very bright flare with a flux amplitude of about 160 was observed in October 2002 (Porquet et al. 2003). It is noteworthy that its peak luminosity of $\sim3.6\times10^{35}\,\mathrm{erg\,s^{-1}}$ was comparable to the bolometric luminosity of Sgr A* during its quiescent state. The light curves of the X-ray flares can exhibit short (e.g., 600 s, Baganoff et al. 2001; 200 s, Porquet et al. 2003) but deep drops close to the flare maximum. This short-time scale could indicate that the X-ray emission is emitted from a region as small as $7R_\mathrm{S}$ ($\sim 13\,R_\odot$).

2 X-ray hiccups observed on April 4th 2007

We report here the main results of our Sgr A* observation campaign (PI: D. Porquet, ∼230 ks, splitted up into three observations) performed with *XMM-Newton* from March 30 to April 4, 2007. The detailed analysis and interpretation are reported in Porquet et al. (2008). On April 4th, 2007, for the first time, a high level of flaring activity were reported with four X-ray flares, one bright and three moderate, detected in half a day. The bright flare is the second brightest X-ray flare detected so far from Sgr A*.

[1] Observatoire astronomique de Strasbourg, Université de Strasbourg, CNRS, INSU, 11 rue de l'Université, 67000 Strasbourg, France

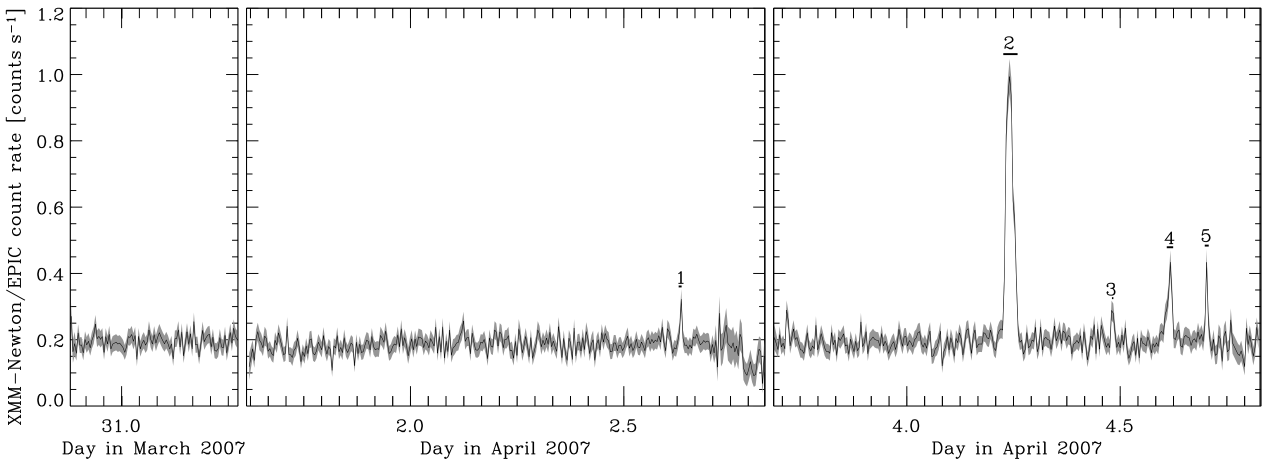

Fig. 1. *XMM-Newton*/EPIC (pn+MOS1+MOS2) light curves of Sgr A* in the 2–10 keV energy range obtained in Spring 2007. The light curves are corrected from soft-proton flaring background. The time interval used to bin the light curve is 350 s. The X-ray flares are labeled from 1 to 5. The horizontal lines below these labels indicate the flare durations. The quiescent level of Sgr A* corresponds to only 10% of the non-flaring level of these light curves.

2.1 X-ray light curves of Sgr A*

In Fig. 1 are reported the EPIC (pn+MOS1+MOS2) background subtracted light curves of Sgr A* in the 2–10 keV energy range, with a time bin interval of 350 s. During the first and second observations, the light curves are almost flat, with a non-flaring level of X-ray emission consistent with the level commonly observed (e.g., Porquet et al. 2003). Only 10% of this 2-10 keV non-flaring level comes from Sgr A* in its quiescent state. Indeed, inside the 10″-radius *XMM-Newton* extraction region centered on Sgr A* (excluding Sgr A* and any transient sources in outburst), 90% of the 2–10 keV non-flaring level comes mainly from one point source associated with the complex of stars IRS 13, the candidate pulsar wind nebula G359.95-0.04, and a diffuse component (Baganoff et al. 2003). We identify any significant deviation from the non-flaring level as possible flare. A flare (#1) was observed on April 2, 2007. On April 4, one bright flare (#2), with a peak amplitude of ∼100 (with a detection of $\sim 21\sigma$) above the quiescent luminosity was observed followed shortly by three moderate flares (#3: $\sim 6\sigma$; #4: $\sim 6\sigma$; and #5: $\sim 8\sigma$). The bright flare has a duration of ∼2.8 ks, similar to the duration that was observed for the (brightest) flare of October 2002 (∼2.9 ks; Porquet et al. 2003). Its light curve is almost symmetrical, but no significant deep drop (i.e., about 50% of flux decrease) is observed in contrast to the moderate flare of September 2000 (Baganoff et al. 2001) and the very bright flare of October 2002 (Porquet et al. 2003). The time gaps between two consecutive flares starting from flare #2 are 5.3, 3.0 and 1.8 hours. Therefore, four flares were observed in a time interval of only half a day. This is the first time that a such level of X-ray flaring activity from Sgr A*, both in amplitude and frequency, is reported. When the time coverage of the NIR observations allowed simultaneous observations with *XMM-Newton*, the NIR counterparts of these X-ray flares have been observed: flare #2 was observed with VLT/NACO (Dodds-Eden et al. 2008, in prep.), and flares #1, #4, and #5 were observed with HST/NICMOS (Yusef-Zadeh et al. 2008, in prep.). This strengthens the relationship observed up to now between X-ray and NIR flares when there is a simultaneous X-ray/NIR observation coverage: all X-ray flares have an NIR flare counterpart, while all NIR flares are not each time associated with an X-ray flare counterpart (e.g., Eckart et al. 06, Hornstein et al. 2007).

2.2 Spectral analysis of the X-ray flares

We report here the spectral analysis of the four flares observed on April 4th, 2007. We used as extraction region for each instrument, a 10″-radius region centered on the position of Sgr A* determined during the bright flare time interval. We would like to emphasize that the determination of the time interval of the X-ray flare is crucial to prevent from any bias in the spectral analysis, especially in cases of weak and moderate flares. To extract the background spectrum we used the same region, but limited to the non-flaring level time interval. We performed the spectral analysis of the bright flare #2, and of the sum of the three following moderate flares (i.e., #3+#4+#5) to increase the statistics. Instead of using the χ^2 statistic, which is not appropriate

Table 1. Best fit parameters (using W statistic) of the EPIC flare spectra for absorbed power-law continuum, taking into account dust scattering. $N_{\rm H}$ values are given in units of $10^{22}\,{\rm cm}^{-2}$. The mean unabsorbed fluxes for the flare period in the 2–10 keV energy range are in units of $10^{-12}\,{\rm erg\,cm^{-2}\,s^{-1}}$. The errors are given at the 90% confidence level.

Flare	$N_{\rm H}^{(a)}$	Γ	$F_{2-10\,\rm keV}^{\rm mean\ (b)}$	C/d.o.f.
April 2007				
#2	$12.3^{+2.1}_{-1.8}$	$2.3^{+0.3}_{-0.3}$	$16.1^{+3.1}_{-2.2}$	2560/2998
#3+#4+#5	$8.8^{+4.4}_{-3.2}$	$1.7^{+0.7}_{-0.6}$	$5.0^{+1.8}_{-1.0}$	2117/2998
October 3, 2002				
	$12.3^{+1.6}_{-1.5}$	$2.2^{+0.3}_{-0.3}$	$25.3^{+3.6}_{-2.7}$	2728/2998

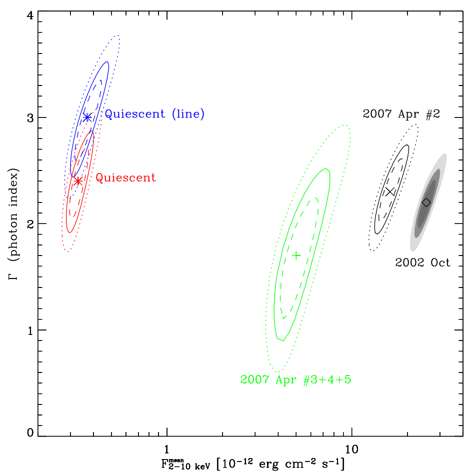

Fig. 2. Confidence regions of the photon index versus unabsorbed flux in the 2–10 keV energy range of the X-ray flares from Sgr A* for an absorbed power-law model taking into account the dust scattering. The dashed, continuous, and dotted contour levels correspond to confidence levels for two interesting parameters of 68%, 90%, 99%, respectively (i.e., to $\Delta C = 2.3$, 4.61, 9.21, respectively). The confidence regions corresponding to the quiescent state of Sgr A* are inferred from the spectral analysis of four archived Chandra observations, using the same spectral models (red contour levels) or including a Gaussian emission line (blue contour levels).

for the fitting of spectra with low counts (e.g., #3 + #4 + #5), we use a modified version of `cstat` statistic called the W statistic (Wachter et al. 1979) that must be used for *unbinned* background-subtracted spectra to prevent from information loose and hence bias of the fitting results. We fit the spectra in the 1–10 keV energy range. On Table 1, the parameter fits for both the bright flare and the sum of the moderates flares are reported, assuming an absorbed power law continuum including the effect of the dust scattering. The parameter fits for the bright flare are well constrained and show a well constrained soft photon index of 2.3±0.3. Though, the best fit parameters for the sum of the weak flares are much less constrained, they are consistent with those of the bright flare within the error bars.

We have made the first detailed comparison of X-ray flare properties observed with *XMM-Newton* (this April 2007 campaign and previous observations) based on a fully self-consistent analysis approach (for more details, see Porquet et al. 2008). We showed that only the *XMM-Newton* data of the brightest flare that occurred on October 2002 flares can be used for a safe comparison with the April 2007 data. In Fig. 2 are reported the confidence regions of the photon index versus the unabsorbed flux, at the confidence levels of 68%, 90%, and 99% (corresponding to ΔC=2.3, 4.61, and 9.21, respectively, for two interesting parameters). The fluxes of the flares span a large range, i.e., about a factor 5. The flare #2 has a flux lower than the October 2002 flare at the 90% confidence level, but has similar well constrained best fit values.

3 Summary and discussions

On April 4, 2007, with *XMM-Newton* we observed an unprecedented level of X-ray flaring activity from Sgr A*, both in amplitude and frequency, with four X-ray flares occurring within only half a day: one bright flare (peak amplitude of ~100 above the quiescent luminosity) followed shortly by three moderate ones (peak amplitude ~25–40). The flare #2 is the second brightest X-ray flare detected so far from Sgr A*. This new bright flare exhibits similar light-curve shape (nearly symmetrical), duration ($\sim$3 ks) and spectral characteristics to the very bright flare (peak amplitude of $\sim$160) observed in October 3, 2002 by *XMM-Newton* (Porquet et al. 2003). We have made the first detailed comparison of X-ray flare properties observed with *XMM-Newton* (this April 2007 campaign and previous observations) based on a fully self-consistent analysis approach (see Porquet et al. 2008 for more details), and showed that the two brightest X-ray flares observed so far from Sgr A* exhibited similar well constrained soft spectra (Γ=2.2–2.3$\pm$0.3). We show that such statement cannot be done for moderate flares. This result brings strong constraints on any model proposed to explain the flaring behavior of Sgr A*. Besides, such quick succession of several events separated by only a few hours, might argue against a disruption mechanism that relies on the temporary storage of mass and energy, if all the corresponding accretion energy is released during the flare. The accretion rate (e.g., Melia 2007) in this system might not produce a transient accumulation of mass between flares of sufficient magnitude. If instead the flares are due to a magneto-rotational instability, then the energy liberated during the flare must also be accumulated over the short inter-burst period. The low mass accretion rate, from which the energy is derived, might argue against this type of mechanism as well. On the other hand, if the flare arises from the infall of a clump of gas (e.g., Liu et al. 2006) then there would be less restriction on how often these could come in. Genzel et al. (2003) have shown that the total energy release $\geq 10^{39.5}$ erg during a flare requires a gas accreted mass of a few times 10^{19} g (assuming a radiation efficiency of $\sim$10%), i.e., comparable to that of a comet or a small asteroid. Recently, Cadez et al. (2006) have argued that the flares could be produced by tidal captures and disruptions of such small bodies. The comet/asteroid/planetesimal idea for depositing the additional mass and energy to initiate a flare is attractive. The distance from Sgr A* at which such a small body would get tidally disrupted is the Roche radius, which is for a rigid body:

$$\frac{R_{\mathcal{R}}}{R_{\rm S}} = 13.2 \times \left(\frac{M_{\rm BH}}{4\times 10^6 M_\odot}\right)^{-2/3} \times \left(\frac{\rho_p}{1\,{\rm g\,cm^{-3}}}\right)^{-1/3},$$

where $M_{\rm BH}$ is the black hole mass and ρ_p is the density of the rigid body. Thus, for a black-hole mass of $4\times 10^6\ M_\odot$ and a density of $1\,{\rm g\,cm^{-3}}$, this corresponds to $13.2\,R_{\rm S}$, in good agreement with the size of the region where the flares are thought to occur. The flaring rates would then depend on processes occurring much farther out, so the fact that so many flares are seen so close together on some days, and much less frequently at other times, would simply be due to stochastic events. However, it would still be difficult to distinguish between a compact emission region and emission within a jet, since these disruption events could still end up producing an ejection of plasma associated with the flare itself.

References

Baganoff, F. K., Bautz, M. W., Brandt, W. N., et al. 2001, Nature, 413, 45

Baganoff, F. K., Maeda, Y., Morris, M., et al. 2003, ApJ, 591, 891

Bélanger, G., Goldwurm, A., Melia, F. et al. 2005, ApJ, 635, 1095

Čadež, A., Calvani, M., Gomboc, A., Kostić, U. 2006, AIP Conf, 861, 566

Eckart, A., Baganoff, F. K., Schödel, R. et al. 2006, A&A, 450, 535

Genzel, R., Schödel, R., Ott, T. et al. 2003, Nature, 425, 934

Hornstein, S. D., Matthews, K., Ghez, A. M. et al. 2007, ApJ, 667, 900

Liu, S., Melia, F., Petrosian, V. 2006, ApJ, 636, 798

Marrone, D. P., Baganoff, F. K., Morris, M., et al. 2008, ApJ, 682, 373

Melia, F. 2007, The Galactic supermassive black hole ed. F. Melia (Princeton, NJ: Princeton University Press)

Porquet, D., Predehl, P., Aschenbach, B., et al. 2003, A&A, 407, L17

Porquet, D., Grosso, N., Predehl, P., et al. 2008, A&A, 488, 549

Schödel, R., Ott, T., Genzel, R., et al. 2002, Nature, 419, 694

Wachter, K., Leach, R., & Kellogg, E. 1979, ApJ, 230, 274

SF2A 2008
C. Charbonnel, F. Combes and R. Samadi (eds)

POSITRON ANNIHILATION IN THE MILKY WAY

Prantzos, N.[1]

Abstract. I review our current understanding of positron sources in the Galaxy, on the basis of the reported properties of the observed 511 keV annihilation line. It is argued here that most of the disk positrons propagate away fom the disk (due to the low density environment) and the resulting low surface brightness annihilation emission is currently undetectable by SPI/INTEGRAL. It is also argued that a large fraction of the disk positrons may be transported via the regular magnetic field of the Galaxy into the bulge and annihilate there. These ideas may alleviate current difficulties in interepreting INTEGRAL results.

1 Introduction

The origin of the Galactic electron-positron annihilation radiation remains problematic ever since the original detection of its characteristic 511 keV line (e. g. Diehl et al. 2006 and references therein). Recent observations of the line intensity and spatial morphology with the SPI instrument aboard INTEGRAL put severe constraints on its origin, since it appears that 1.5±0.1 10^{43} e^+/s are annihilated in the bulge alone and 0.3±0.2 10^{43} e^+/s in the disk, i.e. that the bulge/disk ratio of annihilating positrons is $B/D \sim$ 3-9 (Knödlseder et al. 2005).

Weidenspointer et al. (2008) find a significant asymmetry in the disk emission (factor 1.7 between positive and negative latitudes). They also find that the observed distribution of low-mass X-ray binaries in the hard state has a remarkable similarity to the 511 keV longitude profile; they suggest then that those objects may be the main sources of positrons in the disk, with a sizeable (but insufficient) contribution to the bulge emission.

In this short review, I discuss the Galactic positron sources in the light of recent developments. I argue that, *if* it is assumed that *positrons annihilate near their sources*, then none of the proposed positron production sites, either conventional or “exotic”ones, completely satisfies the observational constraints. Furthermore, I argue that a large fraction of the disk positrons, produced by thermonuclear supernovae (SNIa) or other sources, may be transported via the regular magnetic field of the Galaxy into the bulge, where they annihilate. This increases both the bulge positron annihilation rate and the bulge/disk ratio, alleviating considerably the constraints imposed by the SPI/INTEGRAL data analysis. In fact, I argue that the SPI data are compatible with values of B/D as low as 0.5, because positrons can propagate away from their sources and fill a rather large volume (of low surface brightness), much larger than the relatively thin disks adopted in the analysis of SPI data. This property is crucial to the success of the scenario proposed here, which depends also on the poorly known properties of the Galactic magnetic field. In any case, the issue of positron propagation in the ISM and the magnetic field of the Galaxy appears to be crucial for our understanding of the 511 keV emission.

2 Positron sources in the Galaxy

Thermonuclear supernovae (SNIa) are prolific e^+ producers, releasing on average 3 10^{54} positrons (from the decay of $\sim$ 0.7 $M_\odot$of ^{56}Co), but most of them annihilate inside the SN. Assuming that N_{e^+} positrons escape each SNIa and that the rate of SNIa in the Galactic bulge and disk *per unit stellar mass* is R_{Ia} (given by observations of SNIa in external galaxies), one finds that the e^+ production rate from ^{56}Co radioactivity of SNIa is $L = M \; R_{Ia} \; N_{e^+}$, where M is the stellar mass of the system. N_{e^+} is currently the major uncertainty of the problem. Original estimates, based on late optical lightcurves of SNIa, gave $N_{e^+} \sim$ 8 10^{52} or an escaping

[1] Institut d’Astrophysique de Paris, 98bis Bd Arago, 75014 Paris

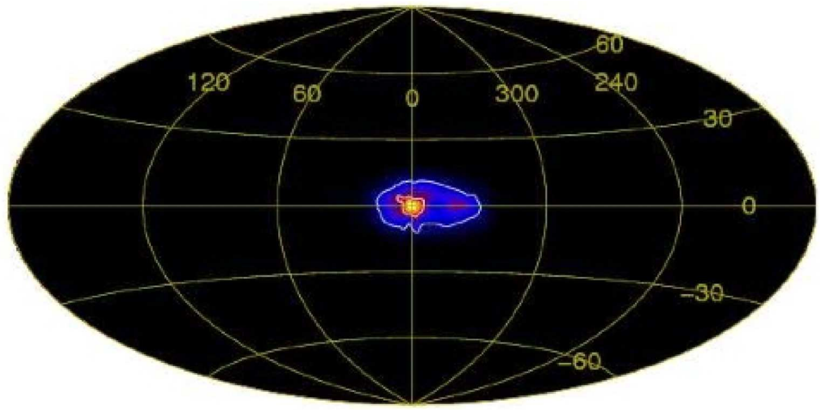

Fig. 1. Image of the Galactic 511 keV emission, after 5 years of SPI/INTEGRAL data (Weidenspointner et al. 2008). A strong bulge emission and a weak asymmetric disk are seen.

fraction $f \sim 0.03$ (Milne et al. 1999).[1] Taking into account the masses of the MW disk and bulge, as well as the corresponding SNIa rates, this number leads to a positron emissivity L_D=$1.95^{+0.98}_{-0.93}$ 10^{43} e^+/s for the disk and L_B=$0.17^{+0.083}_{-0.081}$ 10^{43} e^+/s for the bulge (see e.g. Prantzos 2006). Those estimates suggest that the disk e^+ emissivity is slightly larger than the total galactic e^+ annihilation rate required by SPI observations, but it is much larger than the one of the bulge, contrary to observations.

In the case of the disk positrons, a major source is undisputably the radioactivity of ^{26}Al. The observed decay of the $\sim$ 2 $M_\odot$ of ^{26}Al per Myr (see Diehl, this volume) provides about 0.4 10^{43} e^+/s, i.e. close to the value given by the latest SPI data for the disk positron annihilation rate. However, the 1.8 MeV map of ^{26}Al does not show the degree of asymmetry claimed in Weidenspointner et al. (2008) for the disk 511 keV emission.

Among the other astrophysical sources of positrons, X-ray binaries (XRBs) or some related class of objects, appear as plausible candidates. Low-mass XRBs (LMXRBs) were suggested in Prantzos (2004), who noticed that their observed longitude distribution in the Galaxy is strongly peaked towards the central regions, not unlike the one of the 511 keV emision. He also noticed, however, that most of the strongest sources (counting for 80% of the total Galactic X-ray flux) are evenly distributed in the Galactic plane, with no preference for the bulge; if their positron emissivity scales with (some power of) their X-ray flux, then LMXRBs cannot be at the origin of the bulge Galactic positrons.

According to Weidenspointner et al. (2008), the observed asymmetry in the disk 511 keV emission[2] matches closely the Galactic distribution of LMXRBs in their hard state (factor 1.7 in both cases between positive and negative Galactic longitudes) and this similarity suggests that disk positrons mostly originate from this particular class of compacts objects. It should be noted, however, that in all probability, at least half of the disk 511 keV emissivity is due to ^{26}Al, which displays only a small degree of asymmetry. The remaining 511 keV emission (i.e. once the ^{26}Al contribution is removed) is certainly even more asymmetric (factor $>$2.5) and no known source matches such an asymmetric profile; thus, it seems premature to conclude that hard-state LMXRBs are at the origin of Galactic positrons.

Guessoum et al. (2006) find that another sub-class of XRBs, micro-quasars, are interesting positron producers. Altough it is not known whether their jets contain mostly positrons or protons, theoretical estimates evaluate their individual positron emissivity up to $\sim$ $10^{41}e^+$/s. Coupled with their estimated number in the Milky Way (of the order of 100), that value suggests that micro-quasars may be interesting candidates.

If the Galactic SNIa positron emissivity evaluated in the first paragraph of this section is close to the real one, but the source of the observed bulge emission turns out to be different, it should then be a rather strange

[1] Observations of the late *bolometric* lightcurves of two SNIa (Sollerman et al. 2004; Strinziger and Sollerman 2007) are compatible with zero escaping fraction (or N_{e+}=0) *in the framework of 1-D models for SNIa*. In "canonical" 1-D models, ^{56}Co is produced and remains in the inner part of the SNIa. However, hydrodynamical 3-D models and recent observations (Tanaka et al. 2008) suggest that a sizeable fraction of ^{56}Co may be found in the outermost, highest velocity layers, from which positrons may, perhaps, escape. In any case, the (presently unknown) configuration of the SNIa magnetic field is crucial for the issue of e^+ escape.

[2] Note that this finding is not confirmed in a recent analysis by Bouchet et al. 2008.

coincidence. We argue here that transport of disk positrons to the bulge through the Galactic magnetic field may inverse the Disk/Bulge ratio of e^+ annihilation rates. The arguments are valid for any other source producing positrons of $\sim$ 1 MeV, such as those resulting from radioactivity or X-ray binaries, or microquasar jets.

3 Positron propagation in the Galaxy

Positrons released in the ISM (especially in its less dense regions, like e.g. outside spiral arms or outside the thin gaseous layer) propagate affected by the Galactic magnetic field. The large scale regular magnetic field (MF) of the Milky Way is composed of a toroidal (disk) component (probably bisymmetric) and a poloidal (halo) component, probably in the form of a A0 dipole (see Han 2004 and references therein also Fig. 1). At Galactocentric distance r=8 kpc the toroidal component has a strength of a few μG (Beck et al. 1996) and dominates the poloidal one (a few tenths of μG). However, the former varies as 1/r, while the latter as $1/r^3$ and should therefore dominate in the inner Galaxy.

Positron propagation is strongly affected by the irregular (turbulent) component of the galactic MF, which is comparable in intensity with the regular one near the local disk. Unfortunately, the properties of the irregular component away from the disk plane are even less well understood than those of the regular components (e.g. Han 2004). Prouza & Smida (2003) assume that the turbulent component occupies 80% of the volume inside spiral arms, 20% of the volume outside spiral arms and within vertical distance $|z|$ <1.5 kpc and only 1% of the volume at larger distances. On the other hand, cosmic ray propagation models indicate that the size of the cosmic ray "halo" (CRH, i.e. the region inside which cosmic rays diffuse on inhomogeneities of the magnetic field) is $z_{CRH} > 3$ kpc, based on measurements of unstable/stable ratios of secondary nuclei (Strong & Moskalenko 2001). If e^+ escape from the CRH then positron propagation at large distances from the disk will be dominated by the regular MF, i.e. the poloidal field. In those conditions, a fraction of the positrons produced from disk SNIa will ultimately find their way into the bulge.

Taking into account the SPI data (see Sec. 1) and the SNIa emissivity of positrons in the disk and the bulge (Sec. 2) it turns out that in order to explain the observed bulge annihilation rate by SNIa, the fraction of disk positrons channeled to the bulge must be $f_{ESC} \sim$ 0.5, (i.e. $\sim$ 10^{43} e^+/s from the disk have to join the 0.17 10^{43} e^+/s produced in the bulge and annihilate in that region.

This fraction may not be unreasonable. For instance, reacceleration of e^+ by shock waves of SNIa may considerably increase the thermalization (travel) time of positrons τ_{SD}. On the other hand, the positron confinement time in the disk may be shorter than the standard value of $\tau_{CONF} \sim$ 10^7 yr. The reason is that, because of their low energy (and correspondingly low gyroradius in the Galactic MF) 1 MeV positrons may diffuse very little on the density fluctuations of the MF, and thus they may escape more easily than the higher energy particles of standard Galactic cosmic rays. These arguments are discussed further in Prantzos (2006), while Jean et al. (2006) find that low energy positrons may travel distances of several kpc in the hot, tenuous interstellar medium (which dominates away from the disk of the Milky Way).

In Prantzos (2006) it is also argued that the SNIa disk positrons may not only leave the disk, but also enter the bulge by avoiding the "magnetic mirror" effect. The reason is that their velocity has a dominant component which is always parallel to the lines of the regular magnetic field of the Galaxy. When positrons are still in the cosmic ray halo, they diffuse on the turbulent component of the MF at small scales, but at large scales their diffusive motion follows the regular (toroidal) component. The configuration of the Galactic MF can vary only smoothly between the regions where the various components of the regular field (toroidal in the disk and poloidal away from it) dominate. The toroidal field changes smoothly into a poloidal one and positrons leaving the former enter the latter with a velocity essentially parallel to its field lines; this minimizes the losses due to the mirror effect.

It is then concluded that 1) MeV positrons produced in the disk may propagate away from it, and 2) they may also be chanelled to the bulge and annihilate there. In Fig. 2 we calculate the Galactic gamma-ray profile from positron annihilation, as seen with three different levels of sensitivity (appearing in the bottom of each panel). We assume that the Milky Way e^+ annihilation rate results from i) a bulge with annihilation rate L=1.2 10^{43} e^+/s (resulting from transfer of $\sim$ 50% of the disk SNIa positrons plus those produced by the bulge SNIa population), ii) a "thick disk" (scaleheight 3 kpc) from the remaining SNIa positrons, and iii) a thin disk (from positrons released by ^{26}Al decay and annihilating in the thin gaseous layer). Of course, such a symmetric model does not reproduce the small disk asymmetry reported in Weidenspointer et al. (2008).

We show quantitatively (and with more details in Prantzos 2006) that the SPI/INTEGRAL data are fully

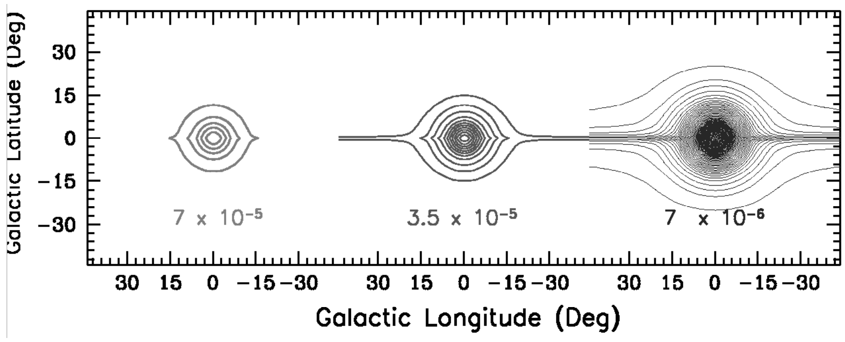

Fig. 2. Simulated profile of the 511 keV emission of the Milky Way in galactic coordinates, as seen at three different levels of detector sensisitivity (indicated in the bottom of each panel, in ph/cm^2/s). The adopted composite model for the positron annihilation (bulge + thin disk + thick disk) is described in Sec. 3.

compatible even with bulge/disk ratio of e^+ annihilation rates lower than 1, provided that sufficiently (but not unreasonably) extended positron distributions are considered. The model proposed here exploits a range of possibilities, given our poor understanding of the Galactic magnetic field and of the propagation of low energy positrons in it. Its assumptions may be tested, through future observational and theoretical developments. Multi-wavelength studies of SNIa, including the infrared, will determine ultimately the typical positron yield of those objects. A small 511 keV emission outside the bulge is currently seen by SPI/INTEGRAL and, given enough exposure, the spatial extent of that emission will be determined (by INTEGRAL or a future instrument); an extended disk emission will prove that positrons travel indeed far away from their sources. The morphology of the Galactic magnetic field, and especially the presence of a poloidal component, will be put on more sound basis through further measurements (e.g. Han 2004).

References

Beck, R., Brandenburg, A., Moss D., et al. 1996, ARAA 34, 155

Bouchet, L., Jourdain, E., & Roques, J. P. 2008, ApJ 679, 1315

Diehl, R., Prantzos, N., & von Ballmoos, P. 2006, NuPhA 777, 70

Guessoum, N., Jean, P. , & Prantzos, N. 2006, A&A 457, 753

Han, J. L. 2004, in "The Magnetized Interstellar Medium", B. Uyaniker et al. (eds.), Copernicus GmbH (Katlenburg-Lindau), p.3

Jean, P., Knödlseder, J., Gillard W., et al. 2006, A&A, 445, 579

Knödlseder, J., Jean, P., Lonjou, V., et al. 2005, A&A, 441, 513

Milne, P., The, L.-S., & Leising, M., 1999, ApJS 124, 503

Prantzos, N. 2004, in "The INTEGRAL Universe", ESA SP-552, p. 15

Prantzos, N. 2006, A&A, 449, 869

Prouza, M., & Smida, R. 2003, A&A 410, 1

Sollerman, J, Lindahl, J., Kozma, C., et al. 2004, A&A 428, 555

Stritzinger, M., & Sollerman, J. 2007, A&A 407, L1

Strong, A., & Moskalenko, I. 2001, Adv. Sp. Res. 27, 717

Tanaka, M., Mazzali, P., Benetti, S. et al. 2008, ApJ 677, 448

Weidenspointner, G., Skinner, G., Jean, P., et al. 2008, Nature 451, 159

SF2A 2008
C. Charbonnel, F. Combes and R. Samadi (eds)

PEERING THROUGH THE STELLAR WIND OF IGR J19140+0951 USING RXTE AND INTEGRAL OBSERVATIONS

Prat, L.[1], Rodriguez, J.[1] and Hannikainen, D.C.[2]

Abstract. IGR J19140+0951 was discovered by the satellite *INTEGRAL* in 2003. This is a High Mass X-ray binary, in which the compact object is deeply embedded in the wind coming from the supergiant companion star. Due to the high level of photoelectric absorption, this type of source couldn't be detected without hard X-rays observations. The spectra obtained in the 3–80 keV range using *RXTE* and *INTEGRAL* have allowed us to perform a precise spectral analysis of the system along its binary orbit. We were able to confirm the supergiant nature of the companion star and the neutron star nature of the compact object. Using a simple stellar wind model to describe the evolution of the photoelectric absorption, we were able to restrict the orbital inclination angle to the range 37–75°. Finally, we have detected a so-called "soft excess" in at least four observations, for the first time for this source. Such soft excesses have been reported in several HMXBs in the past. We discuss the possible origin of this excess, and suggest, based on its spectral properties and occurrences close to the superior conjunction, that it may be explained as the reprocessing of the X-ray emission originating from the neutron star by the surrounding ionized gas.

1 Introduction

High Mass X-ray Binaries (HMXBs) are binary systems consisting of a compact object orbiting a massive companion star. Prior to the launch of the INTErnational Gamma-ray Astrophysics Laboratory (*INTEGRAL*) in 2002, most of the known HMXBs contained a Be companion. In Be-type HMXBs, the compact object emits strong X-ray flashes when it crosses the equatorial plane of the companion star, where a thick disk of matter originating from the stellar wind is present. O and B-type stars have more isotropic stellar winds which absorb the X-ray emission of the compact object, rendering them almost undetectable below a few keV. Thanks to its sensitivity in the soft gamma-ray range, however, *INTEGRAL* has found many such systems in the past few years (see e.g. Liu et al. 2006; Bodaghee et al. 2007). In this perspective, the use of X-ray spectroscopy at different orbital phases makes it possible to probe the stellar wind, providing two-dimensional information on the density and ionization structure of the wind. For instance, the soft excess that is present in the soft X-ray spectra of many HMXBs, whose origin is still quite mysterious, is linked to the physics of the wind close to the compact object, especially the region where the fast moving stellar wind collides with the slow moving and highly ionized gas surrounding the compact object (Hickox et al. 2004).

IGR J19140+0951 was discovered by *INTEGRAL* in March 2003 (Hannikainen et al. 2003). Prior to our study, it was identified as a HMXB with an orbital period of 13.552 days (Wen et al. 2006), likely composed of a neutron star (Rodriguez et al. 2005) orbiting a B0.5 I type supergiant companion star (Hannikainen et al. 2007). Thus, it is a good candidate to study the properties of the obscured X-ray binaries.

2 Spectral analysis

Our data cover the period March 2004–September 2007 with 32 observations taken simultanously by the two satellites. They were reduced using the latest software packages available (for more details on the analysing process and on the results presented here, we refer to Prat et al. 2008). Since IGR J19140+0951 is a fairly faint

[1] DSM/IRFU/Service d'Astrophysique, CEA/Saclay, F-91191 Gif-sur-Yvette, France
[2] Metsähovi Radio Observatory, Helsinki University of Technology TKK, Metsähovintie 114, FI-02540 Kylmälä, Finland

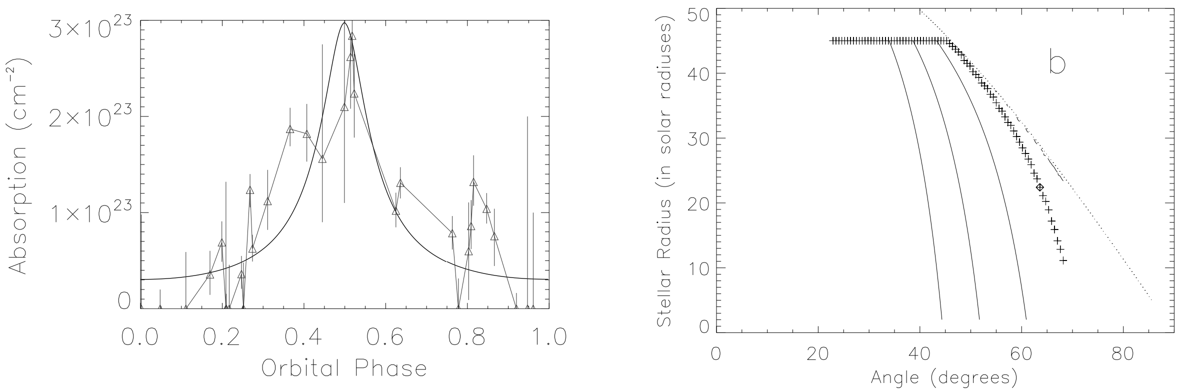

Fig. 1. Left : Model absorption (continuous line) and experimental absorption (△ symbols), for the stellar model with parameters $M_\star = 20M_\odot$, $R_\star = 21R_\odot$ and $\beta = 0.5$. Phase 0 corresponds to when the compact object is located between the Earth and the companion star (inferior conjunction). **Right :** Most probable orbital inclination, as a function of the companion radius, for a typical set of parameters. The + symbols correspond to the most probable orbital inclination, confidence contours are drawn at the 25, 68 and 90% confidence levels. The dotted line is the "eclipse limit": points above this line are excluded as it would imply an eclipse of the neutron star by its companion, which is not observed.

source, we also corrected the spectra for the Galactic X-ray background (GXB), using the parameters measured by Valinia & Marshall (1998). This correction aimed mostly at minimizing the errors on the measure of the photoelectric absorption, by removing the Galactic contribution and keeping only the absorption intrinsic to the source.

We tested several models in analysing the spectra, starting with phenomenological models. The data were well fitted using an absorbed power law combined with a high energy cut-off. An iron fluorescent line at 6.4 keV is present in the observations where the source is detected at a high enough significance. Note that the high energy cut-off is only detected in the observations where the source flux is sufficiently high, thus giving enough precision at the high energy end of the spectra. The presence of this cut-off allowed us to identify the emission process as thermal Comptonization, which is quite common for this type of source. This is also confirmed by the good fitting results obtained with the more physical Comptonization model `COMPTT`, in XSPEC notations.

The photoelectric absorption $N_{\rm H}$ undergoes strong variations, well correlated with the orbital phase (Fig. 1, left). Since the orbit of the X-ray source is probably almost circular, one possible explanation for the observed change in $N_{\rm H}$ relies on an inclined orbit for the system. Qualitatively, when the neutron star is behind its companion its light has to travel a longer distance through a denser part of the stellar wind, so the absorption in the soft X-rays increases. Therefore, at the superior conjunction we should observe a maximum in the absorption, which is indeed the case.

The unabsorbed flux undergoes strong variations that are not correlated with the orbital phase; this may be a consequence of the details of the accretion process. The stellar wind is not perfectly homogeneous and the accretion onto the neutron star, following the magnetic field line to the magnetic poles, is a highly unstable and complicated process (see e.g. Takata et al. 2006, and references therein, for a review of the emission processes). Since our observations are spread over several years, it is not surprising that the source flux is highly variable. This may also be a direct consequence of the clumpiness of the stellar wind: depending on the times of the observation, the compact object may be in the course of accreting a denser portion of the wind (Blay et al. 2008). Unfortunately, the rather short exposure times and the too long periods between successive observations restrained precise characterisations of this clumpiness.

3 Soft Excess detection

But a more interesting characteristic is the detection of a so called "soft excess". During our study, some spectra exhibited an excess in the soft X-ray part of the spectra, which we modeled by adding a black body component to the model. This feature has already been observed in many X-ray binaries (see Hickox et al. 2004, for a review). Its origin is mysterious, but can be linked to the immediate environment of the neutron star, and explained qualitatively by the following scenario. The stellar wind of massive stars is mostly accelerated by bound-bound transitions of atoms. The neutron star, due to its high energy emission, ionizes the surrounding material, so the already ionized gas around the neutron star is no longer accelerated by the stellar radiation field. When the compact object moves along its orbit, the hot gas will gradually be overtaken by the stellar wind. This will lead to the formation of a "tail" trailing the neutron star.

As the gas in this tail is ionized, its absorption will be lower, but its precise effect on the emission is not clear. Since the soft excess is only visible around the superior conjunction (between phases 0.40 and 0.75), one possibility is that the hard X-ray emission may be scattered around the tail. The precise study of this effect, however, would require better spectral resolution in the soft X-ray range than what is available on *RXTE*.

4 Wind model

In order to constrain several parameters for the system, we used a simple "β-law" wind model: it adequately describes the strong stellar winds of B-type stars, which is usually taken to be stationary and spherically symmetric. See e.g. Levine et al. (2004) for a precise description of the method. Using the evolution of the photoelectric absorption, we were able to constrain the inclination of the system and the mass-loss rate of the companion star. For the most probable stellar radius of 21 $R_\odot$, the lower inclination limit is constrained between 37 and 42° (Fig. 1, right), with χ^2 being at a minimum in the range 55–63°. Fig. 1, left, shows the best-fit model against the experimental normalized data, with a good agreement. The mass-loss rate, $\dot{M}_\star$, is constrained to the range 0.6–1.0$\times10^{-7}$ $M_\odot$/year, which is consistent with what is expected for a B0.5 type supergiant.

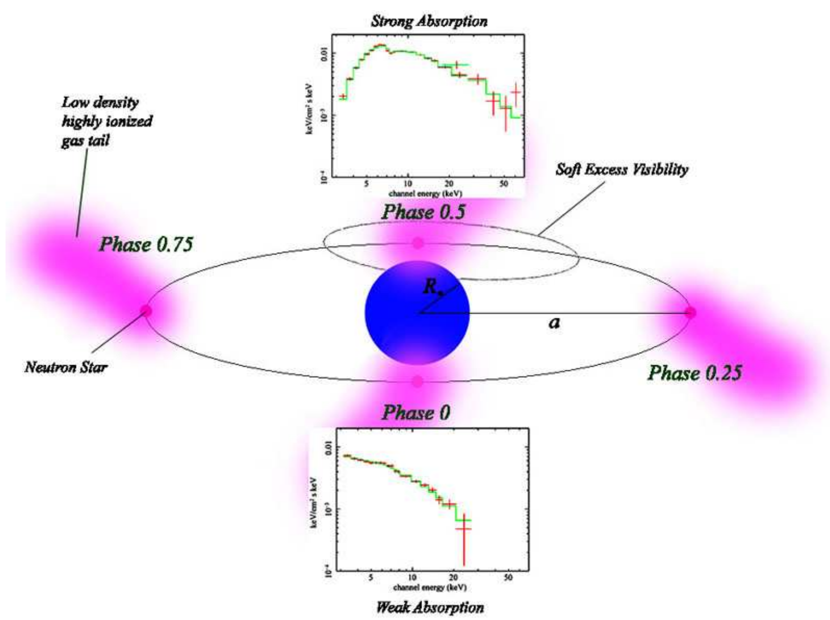

Fig. 2. Diagram of IGR J19140+0951 as it could be seen from the Earth. The orbital inclination of the system is taken to be $\sim 65°$.

Fig. 2 summarizes schematically our main results. We found that photoelectric absorption highly correlates with the orbital phase of the system. Using a simple stellar wind model we found a rather high orbital inclination, $\sim 65°$. We have detected a soft excess in some observations, just before the superior conjunction, in the area indicated on the figure. This may be explained by a cloud of highly ionised gas surrounding the neutron star. Because of its ionisation, this gas is less accelerated by the stellar wind and, while being gradually overtaken by the wind, tends to form a “tail”. This tail could scatter the hard X-ray emission from the compact object and thus explain the soft excess feature. However, these results remain qualitative, as a precise determination of the geometry of the stellar wind would require a better sensitivity in the soft X-ray range, which could be achieved for instance with the use of the *XMM* or *Chandra* satellites.

5 Conclusions

The study of X-ray binaries is challenging since it is often difficult, if not impossible, to identify their visible and infrared counterparts. Even if an infrared counterpart were observed, the distance to some systems prohibits the measurement of the orbital characteristics. Our study shows that X-ray observations can overcome these limitations and produce very precise inferences. The *RXTE* and *INTEGRAL* observations of IGR J19140+0951 have led to good measurements of the orbital period of the system, constraints on its inclination angle, and the diagnostic of the type of the companion star (supergiant O or B)

Moreover, we can use the compact object to probe the stellar wind of the companion. In the case of IGR J19140+0951, we diagnosed the wind density, the probable presence of clumps, and the wind structure around the neutron star. More precise observations could lead to constraints on the mass and radius of the companion, and better constraints on the stellar wind. This allows the study of new *INTEGRAL* sources, either distant or highly absorbed, and ultimately the determination of new useful data for X-ray binary evolution scenarios.

References

Blay, P., Martnez-Nez, S., Negueruela, I., Pottschmidt, K., Smith, D. M., et al. 2008, astro-ph/08064097

Bodaghee, A., Courvoisier, T. J.-L., Rodriguez, J., et al. 2007, A&A, 457, 585

Hannikainen, D., Rawlings, M. G., Muhli, P., et al. 2007, MNRAS, 380, 665

Hannikainen, D., Rodriguez, J., & Pottschmidt, K. 2003, IAUC, 8088

Hickox, R. C., Narayan, R., & Kallman, T. R. 2004, ApJ, 614, 881

Liu, Q. Z., van Paradijs, J., van den Heuvel, E. P. J. 2006, A&A, 455, 1165

Levine, A. M., Rappaport, S., Remillard, R., & Savcheva, A. 2004, ApJ, 617, 134

Prat, L., Rodriguez, J., & Hannikainen, D. 2008, MNRAS, 389, 301

Rodriguez, J., Cabanac, C., Hannikainen, D., et al. 2005, A&A, 432, L17

Takata J., Shibata, S., Hirotani, K., & Chang, H.-K. 2006, MNRAS, 366, 1310

Valinia, A., & Marshall, F. E. 1998, ApJ, 505, 134

Wen L., Levine, A., Corbet, R., & Bradt, H. 2006, ApJS, 163, 372

SF2A 2008
C. Charbonnel, F. Combes and R. Samadi (eds)

ATMOSPHERIC EFFECTS ON EXTENSIVE AIR SHOWERS OBSERVED WITH THE SURFACE DETECTOR OF THE PIERRE AUGER OBSERVATORY

Rouillé d'Orfeuil, B.[1]

Abstract. Atmospheric parameters, such as pressure (P), temperature (T) and density ($\rho \propto P/T$), affect the development of extensive air showers (EAS) initiated by energetic cosmic rays (CRs). We have studied the impact of atmospheric variations on EAS by means of the surface detector of the Pierre Auger Observatory, analyzing the dependence on P and ρ of the counting rate of events. We show that the observed behaviour is explained by a model including P and ρ and validated with full EAS simulations.

1 Introduction

The properties of the primary CRs have to be inferred from EAS, which are typically sampled by an array of detectors at ground level. As the atmosphere is the medium in which the shower evolves, its state affects the shower development. Changes in the atmosphere are expected to have an effect also on the measured signal. We have studied the atmospheric effects on EAS by means of the surface detector (SD) of the Pierre Auger Observatory (Abraham et al. 2004) designed to study CRs from $\approx 10^{18}$ eV up to the highest energies. The signals in the detectors are fitted in each event to find the signal at a 1000 m core distance, S(1000), which is used to estimate the primary energy. The atmosphere is continuously monitored by meteorological stations at the detector site and balloon-borne sensors provide measurements of T and P as a function of the height h.

2 Atmospheric effects on EAS

An increase (decrease) of P, which measures the vertical air column density above ground, corresponds to an increased (decreased) matter overburden and implies that the shower is in a more (less) advanced stage when it reaches the ground level. On the other side, a decrease (increase) of ρ increases (decreases) the Molière radius r_M and thus broadens (narrows) the lateral extent of the EAS. The impact on S(1000) can then be modelized using a Gaisser-Hillas and a Nishimura-Kamata-Greisen profile, which describe the longitudinal and the lateral distribution of the electromagnetic component of the EAS, respectively. In fact, the relevant value of r_M is the one corresponding to the air density ρ^* two radiation lengths (X_0) above ground (Greisen 1963) in the direction of the incoming shower. On time scales of one day or more, the temperature gradient ($\mathrm{d}T/\mathrm{d}h$) in the lowest layers of the atmosphere is constant. Therefore the variation of ρ^* on temporal scales of one day essentially follows that of ρ. An additional effect is related to the diurnal variations of $\mathrm{d}T/\mathrm{d}h$. During the day the surface of the Earth is heated, producing a steeper $\mathrm{d}T/\mathrm{d}h$ whereas during the night $\mathrm{d}T/\mathrm{d}h$ becomes smaller. As a result, the amplitude of the diurnal variation in T is smaller at 2 X_0 above ground than at ground level. It is then useful to separate the daily modulation from the longer term one introducing the average daily density ρ_d and the instantaneous departure from it, $\rho - \rho_d$. The energy reconstructed with no correction is $E_r \propto [\mathrm{S}(1000)]^B$ where $B \approx 1$ (Abraham et al. 2008). The primary energy $E_0(\theta, P, \rho)$ that would have been obtained for the same shower at the reference pressure P_0 and density ρ_0 is related to E_r as: $E_0 = E_r\,[1 - \alpha_P(P - P_0) - \alpha_\rho(\rho_d - \rho_0) - \beta_\rho(\rho - \rho_d)]^B$ where the coefficients $\alpha_{P,\rho}$ and β_ρ depend on the zenith angle θ. Assuming that the cosmic ray spectrum is a pure power law $\mathrm{d}J/\mathrm{d}E \propto E^{-\gamma}$, the rate $R(\theta, P, \rho)$ of events at a given zenith angle is:

$$R = R_0\,[1 + a_P(P - P_0) + a_\rho(\rho_d - \rho_0) + b_\rho(\rho - \rho_d)] \tag{2.1}$$

with $R_0 = R(\theta, P_0, \rho_0)$ and coefficients $a_{P,\rho} = (B\gamma - 1)\alpha_{P,\rho}$ and $b_\rho = (B\gamma - 1)\beta_\rho$.

[1] Laboratoire AstroParticule et Cosmologie, 10 rue A. Domon et L. Duquet, 75205 Paris Cedex 13, France

3 Modulation of the measured rate of events

To study the modulation of the events rate with the ground weather parameters we use the data taken from 1 January 2005 to 31 December 2007 that have $\theta < 60°$. The value of the air density ρ at ground is deduced from P and T measured at the meteorogical stations. Rather than using the raw number of triggering events, we measured the rate as a function of time, to account for temporal variation of the active detection area. Assuming that the rate of events computed each hour follows a Poisson distribution, a maximum likelihood fit gives the estimated values of the coefficients in eq.(2.1). The result is shown in Fig. 1.

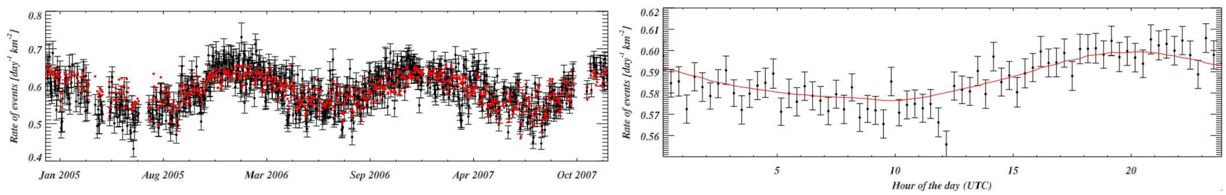

Fig. 1. Left: daily modulation of the measured (black points) and fitted (red points) rate of events. Right: diurnal modulation (black) and fitted (red) events rate.

4 Comparison of the experimental results with model and simulations

We now compare the atmospheric coefficients derived from data and simulations with those expected from the model (Fig. 2). The Corsika code with the QGSjetII model for high energy hadronic interaction, was used to simulate a set of proton showers at $10^{18.5}$, 10^{19} and $10^{19.5}$ eV in 5 different atmospheres and at various θ. The atmospheric profiles used are a parametrisation of the seasonal averages of several radio soundings carried out at the detector site, but, being averages on large time scales, do not account for the diurnal variations of T.

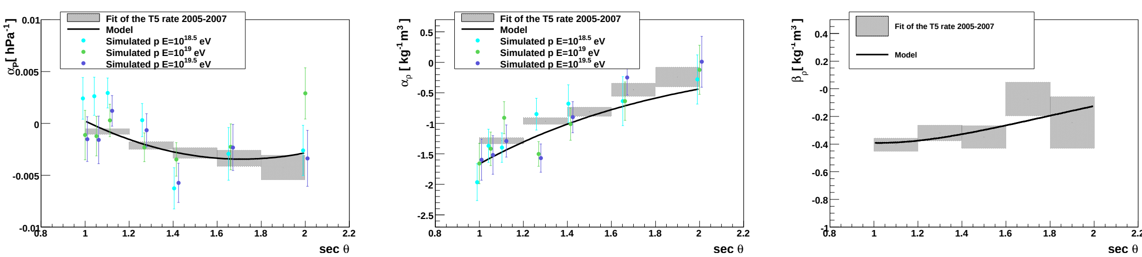

Fig. 2. Comparison of the α_P (left), α_ρ (center) and β_ρ (right) coefficients, as a function of $\sec\theta$ obtained from data (grey shaded rectangle), simulations (bullets) and model (continuous line).

5 Conclusion

We have studied the effect of atmospheric variations on EAS using 3 years of data collected by the SD of the Pierre Auger Obsrvatory. We observe a significant modulation of the event rate, both on seasonal scale ($\sim 10\%$) and on shorter time scale ($\sim 2\%$ on average during a day). This modulation is due to the impact of the density and pressure changes on the EAS development, and in turn on S(1000). Comparing the coefficients deduced from data, shower simulations in different atmospheric profiles and expectations from the model, a remarkable agreement is obtained, not only for the overall size of the effect but also for the θ dependence.

References

Abraham, J., et al., 2004, NIM A, **523**, 50
Greisen, K., 1956 Progress in Cosmic Ray Physics, **3**
Abraham, J., et al., 2008, PRL, **101**, 061101

SF2A 2008
C. Charbonnel, F. Combes and R. Samadi (eds)

MEASUREMENT OF THE UHECR ENERGY SPECTRUM USING DATA FROM THE SURFACE DTETCTOR OF THE PIERRE AUGER OBSERVATORY

Rouillé d'Orfeuil, B.[1]

Abstract. We report a measurement of the cosmic ray energy spectrum based on the high statistics collected by the surface detector of the Pierre Auger Observatory. High-energy cosmic rays are measured by recording the extensive air shower of secondary particles they produce in the atmosphere. The properties of the CR, such as its energy, have to be inferred from the air showers. The methods developed to determine the spectrum from reconstructed observables are described in detail. The hybrid nature of the Pierre Auger Observatory, which combines a fluorescence detector and a surface detector, allows the energy calibaration of the observables. The methods are simple and robust and do not rely on detailed numerical simulation or any assumption about the chemical composition of the CRs.

1 Introduction

The Pierre Auger Observatory (Abraham et al. 2004), located near Malargüe, Argentina (35.2° S, 69.5°W) at 1400 m a.s.l., is designed to study cosmic rays (CRs) from $\approx 10^{18}$ eV up to the highest energies. Two different techniques are used to detect the extensive air showers (EAS) initiated by the highest energy CRs. Firstly, a collection of telescopes is used to collect the fluorescence light emitted from nitrogen excited by charged particles. The fluorescence detector (FD) provides a nearly calorimetric, model-independant energy measurement, because the ultra-violet light is proportional to the energy deposited by the EAS along its path. This method can be used only when the sky is moonless and dark, and thus has roughly a 10% duty cycle (Dawson 2007). The second method uses 1600 water-Cherenkov detectors to sample the photons and charged particles of the EAS at ground level. It is laid out over 3000 km^2 on a triangular grid of 1.5 km spacing. The surface detector (SD) trigger condition, based on a 3-stations coincidence, makes the array fully efficient above about 3×10^{18} eV. The signal at a 1000 m core distance, S(1000), is used to estimate the primary energy. The SD, with its near 100% duty cycle, gives the large sample used here (Suomijarvi et al. 2007). A subsample of EAS detected by both instruments, the hybrid events, are very precisely measured (Perrone et al. 2007) and provide an invaluable energy calibration tool. Indeed, the comparison of the shower energy, measured using the FD, with the S(1000) for the hybrid events is used to calibrate the energy scale for the SD.

2 Analysis procedure

A cosmic ray of 10^{19} eV arriving vertically typically produces signals in 8 stations. Signals are quantified in terms of the response of a water tank to a single relativistic muon passing vertically and centrally through it (a vertical equivalent muon or VEM). Calibration of each sations is carried out continuously with 2% accuracy (Bertou 2006). The signals are fitted in each event to find the VEM size at 1000 m (Newton 2006). The uncertainty in every S(1000) is found, accounting for statistical fluctuations of the signals, systematic uncertainties in the assumption of the fall-off of the signal with distance and the shower-to-shower fluctuations (Ave et al. 2007). Above 10^{19} eV the uncertainty in S(1000) is about 10%.

The longitudinal development of EAS in the atmosphere is measured using the fluorescence detectors. The light produced is detected as a line of illuminated pixels in one or more fluorescence telescope cameras. The

[1] Laboratoire AstroParticule et Cosmologie, 10 rue A. Domon et L. Duquet, 75205 Paris Cedex 13, France

signal, after correcting for attenuation due to Rayleigh and aerosol scattering, is proportional to the number of fluorescence photons emitted in the field of view of the pixel. Cherenkov light produced at angles close to the shower axis can be scattered towards the pixels: this contamination is accounted for (Unger et al. 2007). A Gaisser-Hillas function (Gaisser & Hillas 1977) is used to reconstruct the shower profile which provides a measurement of the energy of the EAS deposited in the atmosphere. To derive the primary energy, an estimate of the missing energy carried into the ground by muons and neutrinos must be made based on assumptions about the mass of cosmic rays and of the appropriate hadronic model. For a primary beam mixture of protons and iron, simulations of showers with the QGSJET01 model indicate a correction of 10% (Barbosa et al. 2004). The systematic uncertainty is 4%. Systematic uncertainties in the FD energy measurement have been estimated. Measurements, made in combination with the fluorescence detectors, are used to measure the quality and transmission properties of the atmosphere. In particular, the vertical aerosol optical depth (VAOD) profile (Ben-Zvi et al. 2007) is found every 15 min by observing the light scattered from a centrally-located laser yielding an hourly average. The average correction to E_{FD} from the VAOD measurement is +5% at 3×10^{18} eV rising to +18% at 5×10^{19} eV, reflecting the increase of the average distance of such events from an FD. The largest uncertainties are in the absolute fluorescence yield (14%), the absolute calibration of the FD (10%) and the reconstruction method (10%). Systematic uncertainties from atmospheric aerosols, the dependence of the fluorescence spectrum on temperature and on humidity are each at the 5% level. These uncertainties are independent and added in quadrature give 22% for E_{FD}.

The present data set is taken from 1 January 2004 to 31 August 2007 while the array has been growing from 154 to 1388 stations. Only events with zenith angle $\theta < 60°$ and reconstructed energy $E > 3 \times 10^{18}$ eV are considered. Candidate showers are selected on the basis of the topology and time compatibility of the triggered detectors (Allard et al. 2005). The SD with the highest signal must be enclosed within an active hexagon, in which all six surrounding detectors were operational at the time of the event. Thus it is guaranteed that the intersection of the axis of the shower with the ground is within the array, and that the shower is sampled sufficiently to make reliable measurements of $S(1000)$ and of the shower axis. For this analysis, the array is fully efficient, so the acceptance at any time is determined by the geometric aperture of the array (Allard et al. 2005). The integrated exposure reaches 6992 km^2 sr yr, which is a factor of 2 and 3 larger than the exposure obtained by HiRes (Abbasi et al. 2008) and AGASA (Takeda et al. 2003), respectively.

The decrease of $S(1000)$ with zenith angle arising from the attenuation of the shower and from geometrical effects is quantified by applying the constant integral intensity cut method (Hersil et al. 1961), justified by the approximately isotropic flux of primaries. An energy estimator for each event, independent of θ, is $S_{38°}$, the $S(1000)$ that EAS would have produced had it arrived at the median zenith angle, 38°. Using information from the fluorescence detectors the energy corresponding to each $S_{38°}$ can be estimated almost entirely from data except for assumptions about the missing energy. The energy calibration is obtained from a subset of high-quality hybrid events (Perrone et al. 2007). Statistical uncertainties in $S_{38°}$ and E_{FD} were assigned to each event: averaged over the sample these were 16% and 8%, respectively. The correlation of $S_{38°}$ with E_{FD} is shown in Fig. 1 (left), together with the least-squares fit of the data to a power-law, $E_{FD} = a \cdot S_{38°}^b$. The best fit yields $a = (1.49 \pm 0.06(\mathrm{stat}) \pm 0.12(\mathrm{syst})) \times 10^{17}$ eV and $b = 1.08 \pm 0.01(\mathrm{stat}) \pm 0.04(\mathrm{syst})$ with a reduced χ^2 of 1.1. $S_{38°}$ grows approximately linearly with energy. The energy resolution, estimated from the fractional difference between E_{FD} and the derived SD energy, $E = a \cdot S_{38°}^b$, is shown too in Fig. 1 (right). The root-mean-square deviation of the distribution is 19%, in good agreement with the quadratic sum of the $S_{38°}$ and E_{FD} statistical uncertainties of 18%. The calibration accuracy at the highest energies is limited by the number of events: the most energetic is $\sim 6 \times 10^{19}$ eV. The calibration at low energies extends below the range of interest.

The energy spectrum based on $\sim 20,000$ events is shown in Fig. 2. Statistical uncertainties and 84% confidence-level limits are calculated according to (Feldman & Cousins 1998). Systematic uncertainties on the energy scale due to the calibration procedure are 7% at 10^{19} eV and 15% at 10^{20} eV, while a 22% systematic uncertainty in the absolute energy scale comes from the FD energy measurement. The spectrum is fitted by a smooth transition function with the suppression energy of 4×10^{19} eV defined as that at which the flux falls below an extrapolated power law by 50%. To examine the spectral shape at the highest energies, we fit a power-law function between 4×10^{18} eV and 4×10^{19} eV, $J \propto E^{-\gamma}$, using a binned likelihood method (Hague et al. 2007). A power-law is a good parameterization: the spectral index obtained is $2.69 \pm 0.02(\mathrm{stat}) \pm 0.06(\mathrm{syst})$

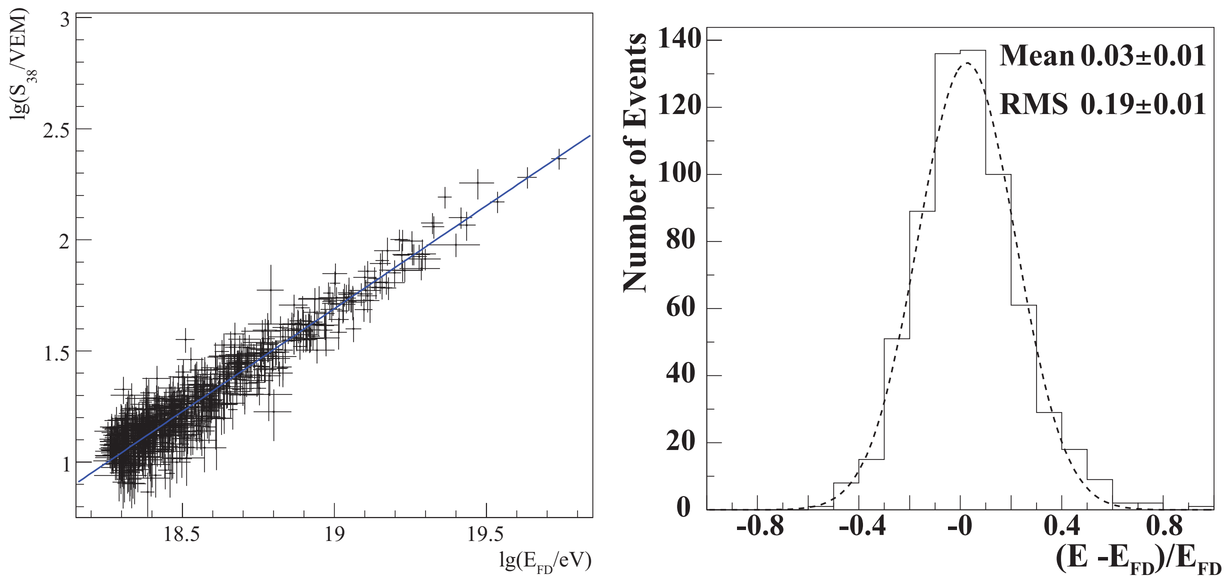

Fig. 1. Left: Correlation between $\lg S_{38^\circ}$ and $\lg E_{FD}$ for the 661 hybrid events used in the fit. The full line is the best fit to the data. Right: the fractional differences between the two energy estimators.

(reduced $\chi^2 = 1.2$), the systematic uncertainty coming from the calibration curve. The numbers expected if this power-law were to hold above 4×10^{19} eV or 10^{20} eV, would be 167 ± 3 and 35 ± 1 while 69 events and 1 event are observed. The spectral index above 4×10^{19} eV is $4.2 \pm 0.4(\text{stat}) \pm 0.06(\text{syst})$. A method which is independent of the slope of the energy spectrum is used to reject a single power-law hypothesis above 4×10^{18} eV with a significance of more than 6 standard deviations, a conclusion independent of the systematic uncertainties currently associated with the energy scale. In Fig. 2 the fractional differences with respect to an assumed flux $\propto E^{-2.69}$ are shown. HiRes I data (Abbasi et al. 2008) show a softer spectrum where our index is 2.69 while the position of suppression agrees within the quoted systematic uncertainties.

3 Conclusion

We reject the hypothesis that the cosmic-ray spectrum continues with a constant slope above 4×10^{19} eV, with a significance of 6 standard deviations. This result is independent of the systematic uncertainties in the energy scale. A precise measurement of the energy spectrum, together with anosotropy and mass composition studies in this energy range, will shed light on the origin of the highest energy particles observed in nature.

References

Abraham, J., et al., 2004, NIM A, **523**, 50

Dawson, B., et al., 2007, in Proceedings of the 30th ICRC, Merida, Mexico, #0976

Suomijarvi, T., et al., 2007, in Proceedings of the 30th ICRC, Merida, Mexico, #0299

Perrone, L., et al., 2007, in Proceedings of the 30th ICRC, Merida, Mexico, #0316

Bertou, X., et al., 2006, NIM A, **568**, 839

Newton, D., et al., 2007, Astropart. Phys., **26**, 414

Ave, M., et al., 2007, in Proceedings of the 30th ICRC, Merida, Mexico, #0297

Unger, M., et al., 2008, NIM A, **588**, 433

Gaisser, T.K., & Hillas, A.M., 1977, in Proceedings of the 15th ICRC, **8**, 353

Barbosa, H., et al., 2004, Astropart. Phys., **22**, 159

Ben-Zvi, S., et al., 2007, in Proceedings of the 29th ICRC, Merida, Mexico, #0399

Allard, D., et al., 2005, in Proceedings of the 29th ICRC, Pune, India, **0**, 101-106

Abbasi, R.U, et al., 2008, PRL, **100**, 101

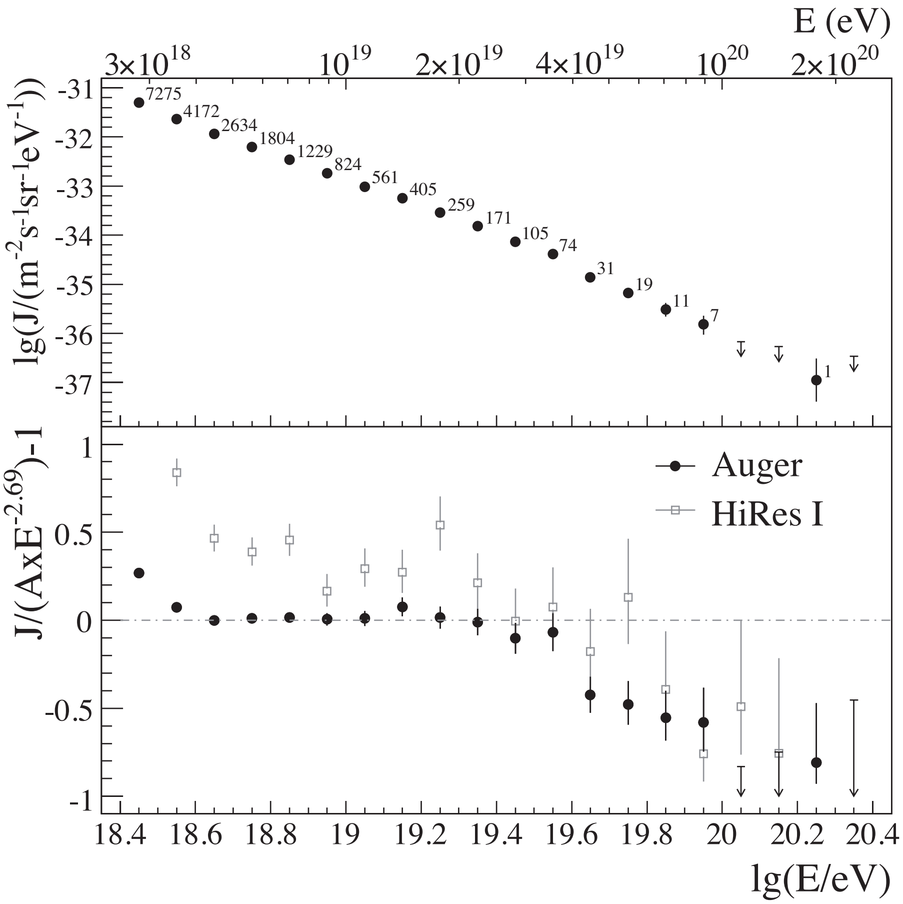

Fig. 2. Upper panel: The differential flux J as a function of energy, with statistical uncertainties. Lower Panel: The fractional differences between Auger and HiRes I data (Abbasi et al. 2008) compared with a spectrum with an index of 2.69.

Takeda, M., et al., 2003, Astropart. Phys., **19**, 447

Feldman, G.J., & Cousins, R.D., 1998, Phys. Rev. D, **57**, 3873

Hague, J.D., et al., 2007, Astropart. Phys., **27**, 455

MULTIWAVELENGTH STUDY OF X-RAY SOURCES IN THE GLOBULAR CLUSTER NGC 2808: CHANDRA, XMM-NEWTON, HST AND ATCA OBSERVATIONS

Servillat, M.[1], Dieball, A.[2], Webb, N. A.[1], Knigge, C.[2], Maccarone, C.[2], Barret, D.[1], Cornelisse, R.[3], Long, K. S.[4], Shara, M. M.[5] and Zurek, D. R.[5]

Abstract. We aim to detect and identify the faint X-ray sources belonging to Galactic globular clusters in order to understand their role in the evolution of globular clusters. We present a new Chandra X-ray observation of the Galactic globular cluster NGC 2808. Previous observations with XMM-Newton and ultraviolet observations with the Hubble Space Telescope are re-investigated to help identify the Chandra sources associated with the cluster. From statistical analysis, 16 sources are very likely to be linked to NGC 2808. We found one likely neutron star low-mass X-ray binary in quiescence and 8 cataclysmic variable candidates in the core of NGC 2808. The other core sources are also cataclysmic variable candidates, but some of the faintest could possibly be chromospherically active binaries or millisecond pulsars. This significant population of close binaries is likely to play an important role in slowing down the core collapse of this cluster. We found a possible deficit of X-ray sources compared to 47 Tuc which could be related to the metallicity content and the complexity of the evolution of NGC 2808. From X-rays and radio (ATCA) observations, we found no evidence of an intermediate mass black hole in NGC 2808 and derived mass constraints of several hundreds solar masses.

1 Introduction

Globular clusters (GCs) are old, gravitationally bound stellar systems which can have extremely high stellar densities, especially in their core regions. In such an environment, dynamical interactions between the cluster members are inevitable, leading to a variety of close binary (CB) systems and other exotic stellar objects. The observed overabundance of neutron star (NS) low-mass X-ray binaries (LMXBs) in GCs relative to the Galactic field was explained by the dynamical processes occurring in the dense cores of GCs (Fabian et al. 1975). Observations also support the fact that quiescent LMXBs (qLMXBs) in GCs scale with the cluster encounter rate (Gendre et al. 2003; Pooley et al. 2003), implying that qLMXBs are formed through dynamical processes in the dense cores. As white dwarfs (WDs) are far more common than NSs, we would then also expect many more CBs containing an accreting WD primary, i.e. cataclysmic variables (CVs). The dynamically-formed CBs are expected to be found in the cores of GCs, where the stellar densities are at a maximum (Hurley et al. 2007).

CBs are important for our understanding of GC evolution, since the binding energy of a few, very close binaries can rival that of a modest-sized GC (e.g. Hut et al. 2003 and references therein). In the core, binaries are subject to encounters and hard binaries become harder while transferring their energy to passing stars. The presence of many CBs could lead to violent interactions, which heat the cluster, delay the core collapse, and promote its expansion. This depends critically on the number of CBs, which is still poorly known. Faint X-ray sources belonging to the clusters have been identified as qLMXBs, CVs, active binaries (ABs, generally RS CVn systems), or millisecond pulsars (MSPs). These sources are thus directly connected with the CB population, and their study is of interest for the understanding of the dynamical evolution of globular clusters.

[1] CESR, Observatoire Midi-Pyrénées, CNRS, Université Paul Sabatier, 9 avenue du Colonel Roche, BP 44346, 31028 Toulouse Cedex 4, France – e-mail: `mathieu.servillat@cesr.fr`

[2] Department of Physics and Astronomy, University of Southampton, SO17 1BJ, UK

[3] Instituto de Astrofisica de Canarias, Via Lactea, La Laguna E-38200, Santa Cruz de Tenerife, Spain

[4] Space Telescope Science Institute, Baltimore, MD 21218, USA

[5] Department of Astrophysics, American Museum of Natural History, New York, NY 10024, USA

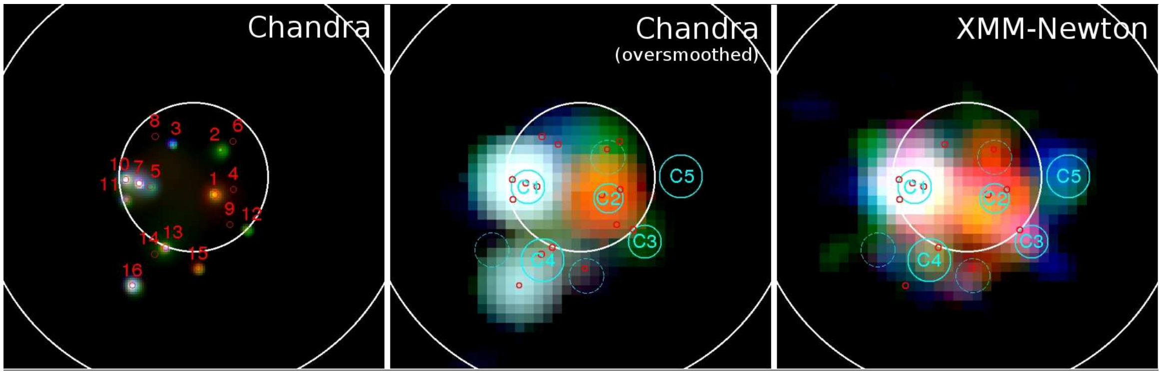

Fig. 1. Images of the core of NGC 2808. Colours correspond to different energy bands, red: 0.5–1.5 keV, green: 1.5–3 keV, blue: 3–8 keV. The absolute 1σ positional error for each source is represented as a circle, red (small) for Chandra and blue (large) for XMM-Newton. Core and half-mass radii are shown. **Left:** Chandra image, smoothed using the adaptative smooth tool *csmooth*. **Center:**: Chandra image, over smoothed with a Gaussian filter to be compared with the XMM-Newton image. **Right:** XMM-Newton combined image (pn, MOS1 and MOS2), smoothed with a Gaussian filter. Only Chandra detected sources which could have been detected by XMM-Newton are represented (small red circles).

As these faint X-ray sources can have similar emissions in X-ray observations, multiwavelength studies are needed in order to constrain their nature. We performed such a multiwavelength study of the globular cluster NGC 2808, which is massive, dense, with an intermediate metallicity (Harris 1996). This GC is known to harbour an elongated horizontal branch, and a triple main sequence in its colour–magnitude Diagram, related to the evolution of the helium and metallicity content of the cluster (Piotto et al. 2007).

2 Data

NGC 2808 has been observed with the Chandra ACIS-I instrument on 2007 June 19–21. The data reduction has been presented in Servillat et al. (2008b), and led to 56.9 ks of clean observation, down to a limiting flux of $F_{0.5-8\mathrm{keV}} \sim 0.9 \times 10^{-15}$ erg cm^{-2} s^{-1}, corresponding to a limiting luminosity of $L_{0.5-8\mathrm{keV}} \sim 1.0 \times 10^{31}$ erg s^{-1} (at the distance of the cluster). We found 16 sources in the half-mass radius that are statistically associated with the cluster. Two sources are variable during this observation. One additional variable source is just outside this radius, and also likely to be linked to the cluster.

NGC 2808 has been previously observed with the XMM-Newton EPIC instruments on 2005 February 1st (28 months before the Chandra observation). The data reduction led to 38 and 30 ks of clean observation for MOS and pn detectors, respectively (Servillat et al. 2008a). It reached a limiting flux of $F_{0.5-8\ \mathrm{keV}} \sim 4.0 \times 10^{-15}$ erg cm^{-2} s^{-1}, corresponding to a limiting luminosity of $L_{0.5-8\ \mathrm{keV}} \sim 4.2 \times 10^{31}$ erg s^{-1} for sources in the core of NGC 2808. Five sources were found within the half-mass radius and are statistically associated with the cluster. However, several sources remained unresolved.

The Chandra and XMM-Newton images are in general very similar (Figure 1). XMM-Newton source C5 is clearly missing in the Chandra observation, and Chandra source 16 was not detected with XMM-Newton. We found that Chandra source 16 has varied by a factor of at least ~ 5. XMM-Newton source C5 has also varied by a factor of at least ~ 5 (Servillat et al. 2008b).

The core of NGC 2808 has been observed with the STIS instrument on board the HST in January/February 2000. The dataset in far ultra-violet (FUV, 1590 Å) and near ultra-violet (NUV, 2700 Å) is presented by (Dieball et al. 2005). After alignment of the Chandra and HST images, we found 10 possible FUV counterparts to 8 X-ray sources (Servillat et al. 2008b). Statistically, one would expect 5–6 matches by chance, thus 2 or 3 real matches. Three sources have probabilities that indicate that they may be associated with a FUV source: Chandra sources 7 and 14 which are located in the CV region in the colour–magnitude diagram, and Chandra source 10 which is in the blue horizontal branch.

We used the optical catalogue obtained by Piotto et al. (2002) with the HST PC detector to look for optical counterparts. Nearly all of the optical counterparts found are either located on the main sequence, red giant branch or red horizontal branch. However, two of the optical sources are on the blue horizontal branch (Chandra 8 and 11) and four sources are in the optical blue straggler region (Chandra 3, 4, 9 and 12). There are four sources that are faint and blue with $B - V < 0.4$ and $V > 20.4$ mag, as expected for CVs (corresponding to Chandra 8 and 11).

3 Discussion

3.1 Identification of sources

From their colour and luminosities, it is possible to propose a possible nature for several sources (see Servillat et al. 2008b for a detailed discussion): Chandra source 1 is a qLMXB candidate hosting a neutron star. Its XMM-Newton spectrum is well fitted by a neutron star hydrogen atmosphere model (Servillat et al. 2008a; Webb & Barret 2007); Chandra sources 7, 10 and 16 are among the brightest sources ($> 10^{32}$ erg s^{-1}) and are thus CV candidates; Chandra sources 2, 5, 11, 12, 13 and 15 have a lower luminosity and could be either CVs or ABs; The other sources which are detected with 4–6 counts are not constrained by their X-ray emission and could be either CVs, ABs or MSPs.

X-ray and UV emission from Chandra sources 7 et 14 are consitant and compatible with the expected emission of CVs. Chandra sources 3 and 16, and XMM-Newton C5 showed variability more likely to come from CVs rather than ABs. Chandra sources 8 and 11 have optical counterparts which could indicate that they are CVs. This lead to 8 CV candidates in the core of NGC 2808. Chandra source 17 is close to the half-mass radius of NGC 2808, and showed an eruption compatible with a CV or an AB linked to the cluster.

3.2 Deficit of X-ray sources: does metallicity play a role?

Assuming a completeness in the detection of sources at a luminosity of $L_{0.5-8\mathrm{keV}} \sim 2 \times 10^{31}$ erg s^{-1}, we can estimate the number of expected X-ray sources in NGC 2808. Taking into account the specific encounter frequency of NGC 2808, as defined in Pooley & Hut (2006), and our completeness limit, we expect 30 ± 6 X-ray sources by dynamical formation (Pooley & Hut 2006). In 47 Tuc, which is similar in mass, density and concentration to NGC 2808, about 31 ± 3 X-ray sources are detected above our completeness limit (Heinke et al. 2005). However, we detected only 11 sources in the half-mass radius of NGC 2808 and above the completeness limit, which is significantly lower than the expected number of dynamically formed X-ray sources.

Metallicity seems to be a key parameter that could highly affect the number of X-ray sources in GCs at a given age. Indeed, due to the lower opacity, metal poor stars are generally hotter and more compact. Concerning interacting binaries, which are generally X-ray sources, this could determine if, when and how mass transfer occurs (de Mink et al. 2007). NGC 2808 and 47 Tuc have very different metallicities, which could explain the differences in the number of detectable X-ray sources. In the same way, Kundu et al. (2007) found that metal-rich extragalactic GCs host three times as many LMXBs than metal-poor ones.

3.3 X-ray to UV ratios of selected CVs: a look at intermediate polars?

From the UV observations, ~ 30 CV candidates were detected (located in the CV region of the colour–magnitude diagram). With Chandra, we obtained 8 CV candidates (at most 15). If we take into account only significant matches, we found 2 UV counterparts that have UV properties clearly compatible with the CV hypothesis (Chandra sources 7 and 14). It seems that X-ray and UV emission from CVs are decorrelated, as the brightest X-ray sources in NGC 2808 are generally not the brightest UV sources.

We estimated a F_X/F_{NUV} ratio for several CVs belonging to different classes, where F_{NUV} is the flux density between 2500–3000 Å (corresponding to the NUV observations), and F_X the flux in the band 0.5–8 keV. Polars have ratios greater than 5000 and intermediate polars appear to have ratios greater than 2000 (see discussion in Servillat et al. 2008b). The detection limit of the NUV observation is 6×10^{-19} erg cm^{-2} s^{-1} Å^{-1}, and the limit in X-rays is 9×10^{-16} erg cm^{-2} s^{-1}. Therefore, the X-ray/NUV ratio for the CV candidates detected in UV is lower than ~ 1500. The ~ 30 CV candidates detected in UV and not in X-rays are thus likely to be mostly non-magnetic systems (such as the dwarf nova YZ Cnc with a ratio of ~ 500, Hakala et al. 2004).

Most intermediate polars (IPs) in the field are more luminous than 10^{31} erg cm^{-2} s^{-1} in X-rays (Verbunt et al. 1997, see also the Intermediate Polar Home Page maintained by K. Mukai, where 12 out of 14 have luminosities above this limit). We should have detected most of these in our Chandra observation if their emission is similar to IPs in the field. This would lead to a maximum of ~ 14 IPs (we exclude Chandra source 14 whose X-ray/NUV ratio is lower than 2000, and Chandra source 1 which is a qLMXB candidate). The proportion derived is $\sim 30\%$ of the detected CV candidates (in UV and X-rays), and $\sim 7\%$ of the expected GC CV population (estimated to be ~ 200 CVs, Ivanova et al. 2006). This is somewhat higher, but still coherent with the proportion of IP candidates in the field, which can be estimated to $\sim 5\%$ from the catalogue of Ritter & Kolb (2003, updated Feb. 2008).

The estimation of the fraction of IPs in GCs is particularly interesting as an excess of IPs was proposed to explained the lack of CV outburst observed in GCs (Dobrotka et al. 2005). Due to the incompleteness of our observations, this result does not allow us to confirm or rule out a possible excess of IPs in NGC 2808. However, with a deeper sample, this method could allow us to better quantify the proportion of IPs.

3.4 Observational constraints on an intermediate mass black hole and millisecond pulsars

According several authors (e.g. Miocchi 2007), NGC 2808 is a good candidate for hosting an intermediate mass black hole (IMBH, 10^3–10^4 $M_\odot$). If such an IMBH exists in NGC 2808, it should be located at the center of mass of the cluster due to mass segregation. We reduced radio data from the ATCA observatory (Maccarone & Servillat 2008), and found no radio source in the core of NGC 2808. The limiting flux was used to derive a mass constrain. We estimated the material density in the cluster, and considered the most probable parameters for the fraction of the Bondi rate accretion, the efficiency of this accretion and the correlation between X-ray and radio power (see Maccarone & Servillat 2008, for a detailed estimation). This yield limits on the black hole mass of 370 $M_\odot$ (most probable limit), and 2100 $M_\odot$ (most conservative limit). A similar approach can be used with the X-ray data. No sources are found at the center of mass of the cluster, which lead to mass limits of several hundreds of solar masses (Servillat et al. 2008a,b). Along with other mass limits for several globular clusters, these results cast doubt on suggestions that globular clusters may follow the same $M_{BH} - \sigma$ relation as galaxies (Maccarone & Servillat 2008).

The non detection of radio sources in the core also implies that the number of MSPs associated with NGC 2808 could be lower than the number of MSPs in 47 Tuc. Again, metallicity could be a key parameter that would highly affect the number of MSPs in GCs.

References

de Mink, S. E., Pols, O. R., & Yoon, S. 2008, AIPC, 990, 230

Dieball, A., Knigge, C., Zurek, D. R., Shara, M. M. & Long, K. S. 2005, ApJ, 625, 156

Dobrotka, A. and Lasota, J.-P. and Menou, K. 2006, ApJ, 640, 288

Fabian, A. C., Pringle, J. E. & Rees, M. J. 1975, MNRAS, 172, 15P

Gendre, B., Barret, D., & Webb, N. A. 2003, A&A, 403, L11

Hakala, P., Ramsay, G., Wheatley, P., Harlaftis, E. T., & Papadimitriou, C. 2004, A&A, 420, 273

Harris, W. E. 1996, AJ, 112, 1487

Heinke, C. O., Grindlay, J. E., Edmonds, P. D., et al. 2005, ApJ, 625, 796

Hurley, J. R., Aarseth, S. J. & Shara, M. M. 2007, ApJ, 665, 707

Hut, P., Shara, M. M., Aarseth, S. J., et al. 2003, New Astronomy, 8, 337

Ivanova, N., Heinke, C. O., Rasio, F. A., et al. 2006, MNRAS, 372, 1043

Kundu, A., Maccarone, T. J. & Zepf, S. E. 2007, ApJ, 662, 525

Maccarone, T. J. & Servillat, M. 2008, MNRAS, 389, 379

Miocchi, P. 2007, MNRAS, 381, 103

Piotto, G., King, I. R., Djorgovski, S. G., et al. 2002, A&A, 391, 945

Piotto, G. and Bedin, L. R. and Anderson, J., et al. 2007, ApJ, 661, L53

Pooley, D. & Hut, P. 2006, ApJ, 646, L143

Pooley, D., Lewin, W. H. G., Anderson, S. F., et al. 2003, ApJ, 591, L131

Ritter, H. & Kolb, U. 2003, A&A, 404, 301

Servillat, M., Dieball, A., Webb, N. A., et al. 2008a, A&A, in press, arXiv 0808.2661

Servillat, M., Webb, N. A. & Barret, D. 2008b, A&A, 480, 397

Verbunt, F., Bunk, W. H., Ritter, H. & Pfeffermann, E. 1997, A&A, 327, 602

Webb, N. A. & Barret, D. 2007, ApJ, 671, 727

SF2A 2008
C. Charbonnel, F. Combes and R. Samadi (eds)

X-RAY BURSTS FROM THE GALACTIC CENTER: THE CASE OF SLX 1737–282 AND GRS 1741.9–2853

Trap, G.[1,2], Falanga, M.[2], Goldwurm, A.[1,2] and Terrier, R.[1]

Abstract. The center of our galaxy harbors a whole population of neutron stars in low mass X-ray binaries. Most of these systems are characterized by regular fast rises followed by exponential decays of their X-ray luminosities, on timescales ranging from seconds to hours. These "X-ray bursts" are now firmly believed to result from unstable thermonuclear burning of accreted material onto the surface of the neutron stars. In early 2007, while surveying the Galactic Center, the *INTEGRAL* satellite recorded a new long burst from the faint ultra-compact binary candidate SLX 1737–282 as well as several short ones from the faint transient source GRS 1741.9–2853. We take these recent detections as an opportunity to briefly discuss our current observational and phenomenological understanding of these phenomena, with a particular emphasis on low accretion rate bursters.

1 X-ray bursts

An X-ray ray burster is a binary system consisting of a neutron star ($\sim 1.4\,M_\odot$) accreting matter from a low mass companion star ($< M_\odot$). The latter fills its Roche lobe and pours matter onto the neutron stars via an accretion disk, which accounts for most of the persistent X-ray flux of the source. On the surface of the neutron star, the accreted matter, mostly hydrogen and helium, reaches suitable temperature and pressure conditions for nuclear fusion. However these nuclear reactions are generally highly dependent on temperature and develop in a medium where the pressure is usually frozen either by quantum degeneracy or hydrostatic equilibrium. As a result, a slight increase of the temperature is not regulated by an expansion of the burning material, but instead enhances the fusion rate, which in turn increases the temperature and so forth, leading to a thermonuclear runaway (Mestel 1952, Schwarzschild & Härm 1965). This translates observationally in recurrent quick elevations of the count rate of the source, followed by exponential decays, called X-ray bursts. The duration of the decay is variable from bursts to bursts and has given rise to a classification in three categories: (i) *short bursts* lasting 10–100 s, separated by a few hours, (ii) *intermediate long bursts* lasting 10–20 min, separated by several weeks and *superbursts* lasting 1–3 h, separated by several months (fig.1 left).

1.1 Short bursts phenomenology

Short X-ray bursts were dicovered by Grindlay et al. (1976) and have been intensively studied over the last 30 years (see Lewin et al. 1993, Strohmayer & Bildsten 2006 and Galloway et al. 2008 for reviews). Early on, Fujimoto et al. (1981) showed that the nature of the nuclear fusion at stake in short X-ray bursts should be highly dependent on the accretion rate, $\dot{m}$, of the neutron star. Defining $x = \dot{m}/\dot{m}_{\rm Edd}$, where $\dot{m}_{\rm Edd}$ is the accretion at the Eddington luminosity, one classically distinguishes 5 different regimes:

1. $x \lesssim 10^{-6}$: Hydrogen (H) burns stably via pycnonuclear and thermonuclear (*pp*-process) reactions that do not depend strongly on temperature. So no X-ray bursts can be observed.

[1] AstroParticule & Cosmologie (APC) / Université Paris VII / CNRS / CEA / Observatoire de Paris – Bât. Condorcet, 10, rue Alice Domon et Léonie Duquet, 75205 Paris Cedex 13, France.
[2] Service d'Astrophysique (SAp) / IRFU / DSM / CEA Saclay – Bât. 709, 91191 Gif-sur-Yvette Cedex, France.

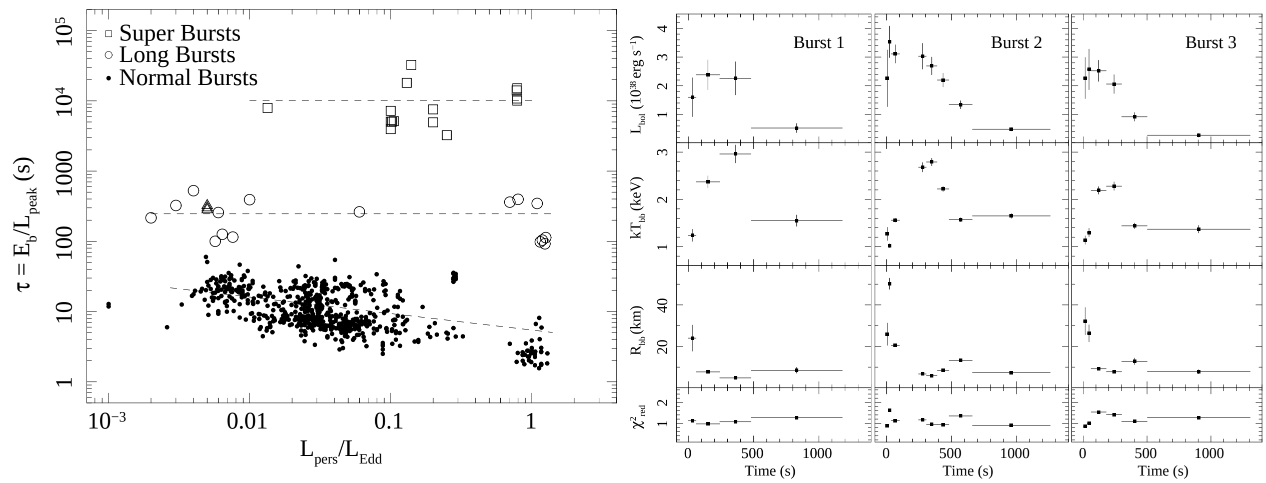

Fig. 1. Left : Duration of observed X-ray bursts as a function of persistent luminosity. **Right**: Spectral evolution of 3 intermediate long bursts from SLX 1737–282 recorded by *INTEGRAL*. The third panels clearly show the photospheric radius expansion of the neutron star. (Figures from Falanga et al. 2008).

2. $10^{-6} \lesssim x \lesssim 0.01$: H burns through the cold CNO cycle. The reaction rate is thus limited by proton captures, which depends a lot on temperature. H burning is then unstable and has two possible outcomes. If the column depth is high enough ($> 5 \times 10^7\,\mathrm{g\,cm^{-2}}$), the triple-$\alpha$ reaction can burn helium (He) unstably thus producing an He flash in a H-rich environment. Otherwise, a pure and weak H flash develops (only ~ 5 times the persistent luminosity) and sedimentation builds a thick pure He layer beneath the H burning shell (Peng et al. 2007, Cooper & Narayan 2007).

3. $0.01 \lesssim x \lesssim 0.1$: H burns into He via the hot CNO cycle, which is limited by β-decays independent of temperature. H burning is thus stable and heats the He layer building up underneath, until He ignites unstably beacause of the high temperature dependence of the triple-α reaction. One sees a powerful pure He flash, lasting only ~ 10 s. In general the energy release is so quick, due to the rapidity of strong interactions, that the burst reaches the Eddington luminosity. Consequently the atmosphere of the neutron star experiences a photo radius expansion (PRE).

4. $0.1 \lesssim x \lesssim 1$: H is piling up faster than it is depleted by steady burning, so that He ignites unstably in a H-rich environment. The flashes involve the *rp*-process to produce heavy elements and last longer (~ 100 s), due to a series of slow β-decays governed by the weak interaction. Note that close to $x \sim 1$, He should start to burn stably between bursts, leading to "delayed mixed bursts" (Narayan & Heyl 2003).

5. $1 \lesssim x$: Temperature due to accretion is so high that both H and He burn steadily through hot CNO and stable triple-α reactions respectively. The bursting behavior thus completely stops.

1.2 Superburst and intermediate long bursts phenomenology

Superbursts are rare events, seen in sources which displays mainly short bursts. The basic scenario is that these short events produce heavy elements that settle down under the surface, in particular carbon, which detonates once in a while, producing a superburst. On the condition that the inner crust of the neutron star is hot enough, this model predicts recurrence times, energetics and durations in good agreement with the observations so far (Cumming & Bildsten 2001).

As for intermediate long bursts, recent theoretical developments have suggested that they should involve the burning of a thick layer of He. The first option is that the source has a low $\dot{m}$, so that we are in case 2 of paragraph 1.1. Weak H flashes produce a thick He layer that ignites when the proper column density is reached. The second possibility is that the companion star is a pure He donor, in an ultra-compact binary system for instance (see section 2.). Indeed, if $\dot{m}$ and the crustal heating are low enough, and in the absence of heating from hydrogen burning, then ignition of He can be delayed until a sufficiently thick layer of fuel has been accumulated. Though the burning of He is rapid, the cooling time is long (10–20 min) because of the thickness of the layer in which the heat is deposited (Cumming et al. 2006).

2 SLX 1737–282

SLX 1737–282 is a Galactic Center burster (fig.2 left) from which exclusively intermediate long bursts have been recorded so far. It is the only such source in the galaxy known to date. We recently reported the observations of 3 new long bursts (fig.1 right) from the source with the *INTEGRAL* satellite (Falanga et al. 2008). From the presence of PRE (fig.1 right, third panels) we are able to derive the source distance (7.3 kpc) and have evidence that the bursts resulted from He burning.

On the other hand, the estimated persistent bolometric luminosity of the source is rather low: $L_{\rm pers} \sim 0.005\,L_{\rm Edd}$. By working out the accretion column of the bursts and the expected recurrence time, we find that our observations of an apparent recurrence time of $\sim$ 86 days and burst energetics of $\sim 10^{41}$ erg, are in good agreement with pure He bursts. Yet, at this low $\dot{m}$ ($\sim 0.005\,\dot{m}_{\rm Edd}$) we should observe the presence of H in the flashes (see paragraph 1.1), unless the companion is a pure He star and no H can be accreted. As a matter of fact, we favor this latter explanation, as it is in line with the fact that SLX 1737–282 has recently been classified as an ultra-compact binary candidate (in't Zand et al. 2007). Indeed disk instability models of low mass X-ray binaries show that steady and low $\dot{m}$ systems must have short orbital periods ($P_{\rm orb} \lesssim 2\,$h), otherwise they would turn out to be transient (Dubus et al. 1999). Thus, as binaries evolution models demonstrate, SLX 1737–282 should be a system with a H-poor Roche lobe-filling companion (to persistently sustain the accretion), driven by gravitational radiation (for conservative mass transfer). This respectively sets contraints on the companion equation of state (fig.8 in Falanga et al. 2008) and the companion mass-orbital period plane (fig.9 in Falanga et al. 2008). As a result, we suggest that the companion star in SLX 1737–282 is likely to be a He white dwarf.

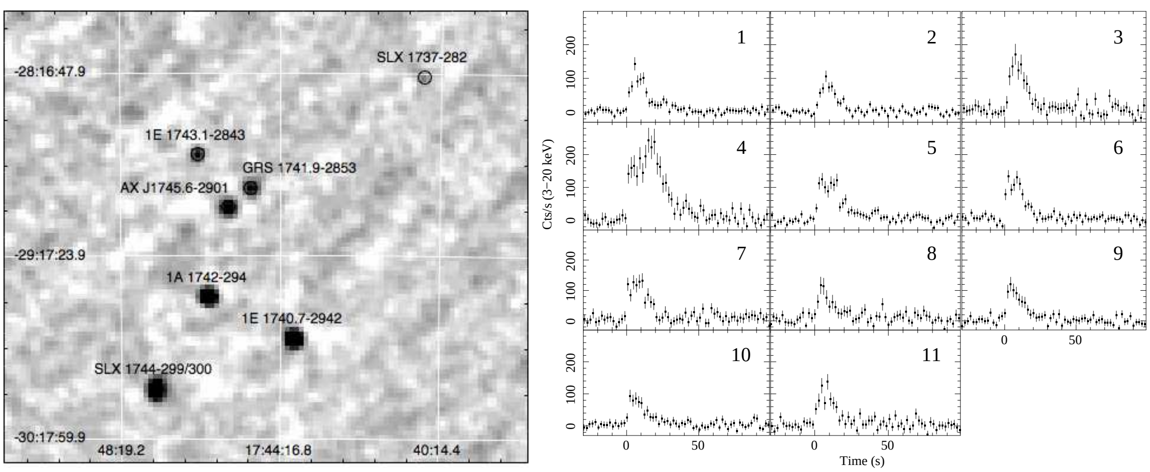

Fig. 2. Left : Mosaic of the Galactic Center in the 3–20 keV band, by the *INTEGRAL*/JEM-X1 module, from February to April 2007. The galactic plane runs from upper left to bottom right and the very center of the galaxy almost coincides with the low mass X-ray binary AX J1745.6–2901. **Right** : Short burts detected by *INTEGRAL*/JEM-X during the 2005 and 2007 outbursts of GRS 1741.9–2853.

3 GRS 1741.9–2853

GRS 1741.9–2853 is a faint transient burster from the Galactic Center (fig.2 left). In early 2007, a new outburst from the source has been followed by the *INTEGRAL* and *XMM-Newton* satellites. During this event, we have detected a total of 9 short X-ray bursts, 7 with *INTEGRAL*/JEM-X and 2 with *XMM-Newton*. By analysing archival data, we have also found 4 bursts with JEM-X during another outburst of GRS 1741.9–2853 in 2005 (see fig.2 right). From the brightest burst, we put an upper limit on the source distance at $\sim$ 8 kpc (Trap et al. 2008).

Interestingly, at the beginning and end of the outbursts, the source displayed bursts when its persistent luminosity was no bigger than $\sim 10^{36}\,{\rm erg\,s^{-1}} \sim 1\%\,L_{\rm Edd}$. This potentially makes GRS 1741.9–2853 an interesting probe of the low $\dot{m}$ burning regime (case 2, paragraph 1.1).

4 Conclusions and perspectives

SLX 1737–282 is the best example for which the observations convincingly match the theory of intermediate long bursts as being thermonuclear explosions of a thick He shell accreted from a pure He donor. A conclusive confirmation of this scenario would still be the detection of an optical modulation revealing a short period and so an ultra-compact nature.

More generally, with the systematic study of low $\dot{m}$ bursters, an interesting new field has started to emerge within the burst community (Cornelisse et al. 2004). There is now growing interest for the poorly studied nuclear regime in which H fusion is unstable. Theoretical work (Peng et al. 2007) has recently provided clues to bridge the gap between short and intermediate long burst, through unstable H burning. From an observational viewpoint, Boirin et al. (2007) put forward that unstable H burning may be responsible for bursts multiplets. These bursts at low accretion rates could even have some relevance in the mechanism of soft X-ray transients outbursts (Kuulkers et al. 2008). As we will argue in a forthcoming paper, a *transient* and *low accretion rate* burster like GRS 1741.9–2853 is an interesting target for further investigation of this burning regime.

References

Boirin, L., Keek, L., Mendez, M., et al. 2007, A&A, 465, 559

Cooper, R., & Narayan, R. 2007, ApJ, 661, 468

Cornelisse, R., in't Zand, J. J. M., Kuulkers, E., et al. 2004, Nucl. Phys. B, 132, 518

Cumming, A., & Bildsten, L. 2001, ApJ, 559, L127

Cumming, A., Macbeth, J., in't Zand, J. J. M., & Page, D. 2006, ApJ, 646, 429

Dubus, G., Lasota, J.-P., Hameury, J.-M., & Charles, P. 1999, MNRAS, 303, 139

Falanga, M., Chenevez, J., Cumming, A., et al. 2008, A&A, 484, 43

Fujimoto, M. Y., Hanawa, T., & Miyaji, S. 1981, ApJ, 247, 267

Galloway, D., Muno, M., Hartman, J. M., Psaltis, D., & Chakrabarty, D. 2008, arXiv:astro-ph/0608259v2

Grindlay, J., Gursky, H., Schnopper, H. et al. 1976, ApJ, 205, L127

in't Zand, J. J. M., Jonker, P. G. & Markwardt, C. B. 2007, ApJ, 465, 953

Kuulkers, E., in't Zand, J. J. M., & Lasota, J.-P. 2008 arXiv:astro-ph/0809.3323

Lewin, W. H. G., van Paradijs, J., & Taam, R. E. 1993, Space Sci. Rev., 193, 15

Mestel, L. 1952, MNRAS, 112, 598

Narayan, R., & Heyl, J. 2003, ApJ, 599, 419

Peng, F., Brown, E. F., & Truran, J. W. 2007, ApJ, 654, 1022

Schwarzschild, M., & Härm, R. 1965, ApJ, 142, 855

Strohmayer, T., & Bildsten, L. 2006, Compact Stellar X-ray Sources, ed. W. Lewin & M. van der Klis (Cambridge University Press)

Trap, G., Falanga, M., Goldwurm, A. et al. 2008, In prep.

SF2A 2008
C. Charbonnel, F. Combes and R. Samadi (eds)

NUMERICAL STUDY OF STATIONARY BLACK HOLES: LOCAL HORIZON PROPERTIES AND THE KERR SOLUTION

Vasset, N.[1] and Novak, J.[1]

Abstract. This work focuses on a numerical implementation of the local physics of black hole astrophysical spacetimes. This is done by imposing boundary conditions on a certain formulation of Einstein Equations, namely the fully constrained formalism(FCF) of Bonazzola et al.(2004). We here make use of the Isolated Horizon formalism of Ashtekar et al. (1999), aiming at a local characterization of a black hole region. This horizon can be seen as an intuitive physical object (contrary to, e.g., the event horizon). We thus solve the Einstein Equations, using 3+1 formalism, on 3-slices of spacetime excised by marginally trapped surfaces. We are then able to recover the Kerr spacetime outside the black hole region only by prescribing that our grid boundary behaves indeed like an Isolated Horizon. Contrary to some earlier works, we take into account the non-conformal part of our 3-metric, making use of a no-boundary method on the horizon. Our spacetime is then perfectly stationary.We compare our results with previous ones, and show accuracy results, involving among others a verification of the virial theorem, and a refined Penrose inequality studied in Jaramillo et al. (2007).

1 Introduction

Trying to accurately describe black holes solutions as evolving physical objects in numerical simulations is of direct interest in astrophysics. We focus here on a particular approach, trying to describe black holes as physical objects represented by their horizons, and using numerical excision techniques. Defining the physical laws for event horizons of black holes has been tried some time ago (see Thorne et al.(1986)). However, being global objects, applying evolution laws to event horizons is almost impossible due to their non causal behaviour. Alternative local characterizations, based on the concept of trapped surfaces, have been recently formulated. We will use here the isolated horizon formalism, prescribing the physics of non-evolving black hole regions.

Following the prescription of Gourgoulhon & Jaramillo (2006) and pursuing the numerical explorations of Cook and Pfeiffer (2004) and Jaramillo et al. (2007) among others, we try to numerically implement those objects as boundary conditions imposed on (3+1) Einstein Equations, in a 3-slice excised by a 2-surface. This is done here using the Fully Constrained Formalism (FCF) of Bonazzola et al. (2004), with spectral method high accuracy resolutions using the LORENE library (http://www.lorene.obspm.fr). We drop out the usual conformal flatness hypothesis for our simulation, so that we can exactly recover a stationary rotating vacuum slice of spacetime. Issues raised by this approach require a particular handling of boundary conditions for the non conformally flat equation. In our case, no additional boundary condition is required.

2 Trapped surfaces and Isolated Horizons as a local description of black hole regions

We refer the reader to Ashtekar and Krishnan(2004) for a review. The global concept of a trapped surface relies on the concept of expansion: this is defined as the area rate of change along geodesics orthogonal to a 2-surface in a spacetime (negative if the area is decreasing along the geodesics from the surface, positive otherwise). A spacelike closed 2-surface is said to be a trapped surface if expansions along the two future null geodesics normal to the surface are less than zero. This clearly characterizes strong local curvature. A marginally outer trapped surface in an asymptotically flat spacetime has the expansion along the outer null geodesics normal

[1] Laboratoire Univers et Théories, CNRS UMR 7182, Observatoire de Meudon, Place Jules Janssen, 92195 Meudon, France

to the surface to be exactly zero. If the cosmic censorship holds, there is an equivalence between a marginally outer trapped surface and the presence of a black hole region enclosing it. These surfaces are always situated inside the event horizon.

Isolated horizons are aimed at describing stationary vacuum black hole regions. They are defined as 3-dimensional tubes foliated by marginally outer trapped surfaces, and with a null vector field as generator. We prescribe in addition that the metric is not evolving along the generators. A consequence is that any slice of an isolated horizon has in addition a vanishing shear tensor. The shear 2-tensor is a geometrical quantity on the 2-surface that measures the geometrical strain undergone by this surface.

This formalism has been extensively studied as a *diagnosis* for simulations involving black holes, where marginally trapped surfaces are found *a posteriori* with numerical tools called apparent horizon finders (Lin et al. 2004). We here want to impose properties on a surface that will turn out to be an Isolated Horizon,and simulate what happens outside of it. This approach has been made by Cook and Pfeiffer (2004) and Jaramillo et al. (2007) for the single black hole case. The main improvement in this work is the dropping out of the conformal flatness hypothesis, leading to more accurately stationary data in the rotating case.

3 A fully constrained formalism of Einstein Equations

For technical details, the reader is referred to Bonazzola et al. (2004) or Gourgoulhon (2007).

The 3+1 formalism of General Relativity, foliates a 4-dimensional globally hyperbolic variety with spatial 3-slices endowed with an induced 3-metric γ_{ij} and an extrinsic curvature K_{ij}. The 4-metric of an asymptotically flat, globally hyperbolic variety $(\mathcal{M})$ writes:$g_{\mu\nu}dx^{\mu}dx^{\nu} = -N^2dt^2 + \psi^{-4}\tilde{\gamma}_{ij}(dx^i + \beta^i dt)(dx^j + \beta^j dt)$, where N, ψ, β^i and γ_{ij} are respectively the lapse scalar, the conformal factor, the shift vector and the conformal metric. We also make the decomposition $\tilde{\gamma}^{ij} = f^{ij} + h^{ij}$, where f^{ij} is the flat metric associated with our 3-slice, and h^{ij} The deviation of the metric from conformal flatness. Setting arbitrarily $h^{ij} = 0$ before caluclations is called the conformal flatness approximation (or Isenberg-Wilson-Matthews theory of gravity).

This decomposition allows us to write the 3+1 Einstein system (see Gourgoulhon 2007). We will place ourselves in the FCF of Bonazzola et al. (2004). We fix the gauge to be the Dirac gauge: the divergence of the metric with respect to a flat derivative associated with the 3-slice must vanish. Moreover, we seek to find data on a 3-slice that are stationary in our coordinate system (all the time derivatives vanish). Under these approximations, the 3+1 system writes:

$$\Delta\psi = \mathcal{S}_{\psi}(h^{ij}, K^{ij}, N, \psi, \beta^i) \tag{3.1}$$

$$\Delta(N\psi) = \mathcal{S}_{N\psi}(h^{ij}, K^{ij}, N, \psi, \beta^i) \tag{3.2}$$

$$\Delta\beta^i + \frac{1}{3}\mathcal{D}^i\mathcal{D}_j\beta^j = (\mathcal{S}_{\beta^k}(h^{kj}, K^{kj}, N, \psi, \beta^k))^i \tag{3.3}$$

$$\Delta h^{ij} - \frac{\psi^4}{N^2}\mathcal{L}_{\beta}\mathcal{L}_{\beta}h^{ij} = \mathcal{S}^{ij}_{h^{kl}}(h^{kl}, N, \psi, \beta, K^{kl}) \tag{3.4}$$

The $\mathcal{S}_X$ are nonlinear sources. The three first equations, in ψ, $N\psi$ and β^i, stem from the Einstein Hamiltonian and Momentum constraints. In a fully constrained evolution scheme, they are solved at each timestep. The last tensor elliptic equation comes from the Einstein dynamical equation in the case of stationarity. Several works deal with initial data by simply applying the conformal flatness hypothesis, and do not solve it. Here we will solve it numerically for a single black hole numerical spacetime in stationarity. We will use the excision technique for this calculation, and a set of boundary conditions coming from the isolated horizon formalism.

4 Boundary conditions for Einstein Equations, Numerical resolution

We try to simulate the space 3-slice outside of an excised sphere fixed at a radius $r_H = 1$ in our spherical coordinates. Following the prescriptions of Cook and Pfeiffer (2004) and Gourgoulhon & Jaramillo (2006), we find boundary conditions for our elliptic equations (3.2), (3.3),(3.4) by prescribing the sphere to be an isolated horizon slice: If we write $\beta^i = \tilde{b}\tilde{s}^i - V^i$, where $\tilde{s}^i$ is the spacelike outer unit normal to the excised surface, we adapt our coordinates to the geometry of our horizon by setting our time evolution vector to be null on that surface: $\tilde{b} = \frac{N}{\psi^2}$. This ensures the horizon stays at a fixed radius during time evolution. The vanishing of the shear translates into a Dirichlet condition for the other part of the shift, being proportional to the rotational symmetry vector: $V^i = \Omega_r(\frac{\partial}{\partial\phi})^i$, where Ω_r is the rotation rate parameter of the horizon in our coordinates. The vanishing expansion gives an approximate Neumann condition for variable $N\psi$: $4\partial_r(N\psi) = -\frac{N}{\psi}K_{ij}\tilde{s}^i\tilde{s}^j - N\frac{D_i\tilde{s}^i}{\psi^3}$. Finally, we set arbitrarily the boundary condition on the lapse to be a fixed value of 0.3.

There remains the boundary condition on the equation for h^{ij}. We will use for the resolution the scalar variables A and $\tilde{B}$ described in Cordero et al. (2008), and adapted to the Dirac Gauge choice. With the Dirac gauge constraints and an additional determinant condition, the tensor equation reduces to 2 elliptic scalar equations($\mathcal{L}_\beta$ is the Lie derivative along β^i):

$$\Delta A - \frac{\psi^4}{N^2}\mathcal{L}_\beta\mathcal{L}_\beta A = A_{\mathcal{S}}(h^{ij}, N, \psi, \beta, K^{ij}) \tag{4.1}$$

$$\tilde{\Delta}\tilde{B} - \frac{\psi^4}{N^2}\mathcal{L}_\beta\mathcal{L}_\beta\tilde{B} = \tilde{B}_{\mathcal{S}}(h^{ij}, N, \psi, \beta, K^{ij}) \tag{4.2}$$

$\tilde{\Delta}$ is a modified elliptic laplace operator, and $A_{\mathcal{S}}$ and $\tilde{B}_{\mathcal{S}}$ are the A and $\tilde{B}$ potentials associated to the tensor source. Once these two quantities are known, one can entirely reconstruct the tensor h^{ij} using the Dirac gauge and the determinant condition. The gauge is then satisfied by construction at each step.

From these two scalar equations, we have been able to exhibit approximate equations by linear operators acting on A and $\tilde{B}$, and with particular properties. We decompose all our operators and unknowns into spherical harmonics. Using the condition $\tilde{b} = \frac{N}{\psi^2}$, we are able to simplify the double Lie derivative operator and separate radial terms from the others, so that we can approximately write (for example for $A(r,\theta,\phi) = \Sigma A_{lm}(r)Y_l^m(\theta,\phi)$):

$$[-\alpha(r-r_H) - \delta(r-r_H)^2]\frac{d^2}{dr^2}A_{\ell m} + \frac{2}{r}\frac{d}{dr}A_{\ell m} - \frac{\ell(\ell+1)}{r^2}A_{\ell m} = A_{\mathcal{S}} + \frac{\psi^4}{N^2}(\mathcal{L}_\beta\mathcal{L}_\beta A)^{**}_{\ell m}. \tag{4.3}$$

α and δ are real numbers determined by the data.

The ordinary differential operator on the left is singular; a search for analytical homogeneous solutions gives a Kernel of dimension one for usual values of α and δ. By fixing the behaviour of the fields at infinity, there is no further need for a boundary condition on the excised frontier for solving the equation. The same analysis holds for the operator acting on $\tilde{B}$.

This is not an actual proof that our two scalar equations do not need any boundary condition prescription, because the right hand side depends (non-linearly) on the variable. However, we implement our resolution iteratively by inverting at each step these weakly singular operators; our system being convergent, this indicates that indeed, no boundary condition has to be imposed globally for the determination of h^{ij}. The question remains open why it is actually the case, and whether this result applies to more general cases involving isolated horizons.

Our simulation is made on a LORENE 3D spherical grid, using spherical harmonics decomposition for the angular part and spectral multidomain Chebychev decomposition for the radial part. The mapping consists in 4 shells and an outer compactified domain, so that infinity is inside our grid and we have no boundary condition to put at a finite radius. We impose the values of all the fields to be equivalent at infinity to those of a flat 3-space. Except for stationarity, all simulations are done with no assumption of coordinate symmetry.

Having set the shape and the location of the surface in our coordinates, and the lapse being set to a fixed value of 0.3, we are only left with one parameter which is the horizon rotation parameter Ω_r. We generate two sets of initial data, spanning the rotation parameter from zero (Schwarzschild solution) to 0.3. One set will give the solution for the whole differential system, while the other will give the Conformally Flat Data, where instead of solving the equation for the h^{ij} variable, we set it to zero (this is the most commonly used approximation for black hole initial data: however, we know that the Kerr spacetime does not admit any conformally flat slices).

Figure 1 presents the relative accuracy obtained for the Einstein constraints in the non conformally flat case, as well as the accuracy for the Einstein Dynamical equation in the non conformally flat and conformally flat case (this is the only equation not solved in this case). We actually see a major improvement, showing the discrepancy between the usual conformal flatness approximation that one uses generically to simulate rotating spacetimes in numerical relativity, and the actual stationary Kerr solution. Another test of stationarity can be the comparison between the ADM mass and the Komar mass at infinity, the latter being tentatively defined with the supposed Killing vector $(\frac{\partial}{\partial\phi})^i$ (We don't impose any Killing symmetry, except on the horizon: Although we know, by the Black Hole rigidity theorem, that an accurate resolution of Einstein Equations would impose this vector to be so). This is done in figure 2. The comparison between the ADM mass and the Komar mass is

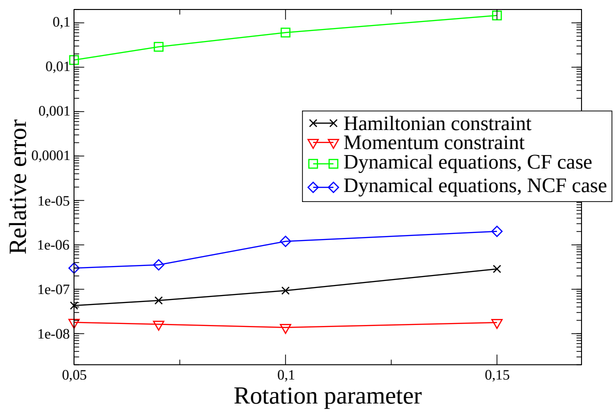

Fig. 1. Accuracy for Einstein Equations resolution

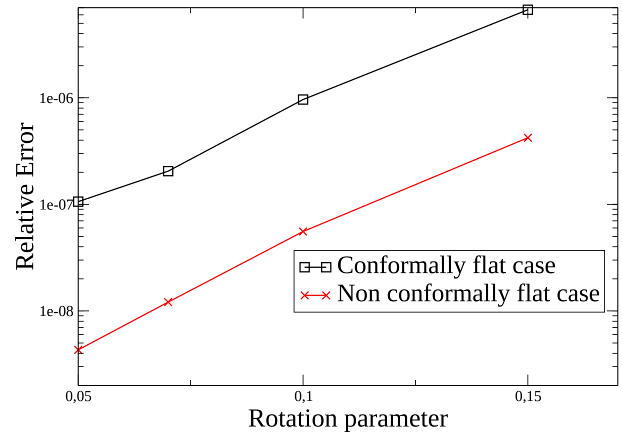

Fig. 2. Relative difference between the ADM and Komar mass in conformally flat and non-conformally flat cases

directly linked to the virial theorem of General Relativity put forth by Gourgoulhon & Bonazzola (1994). The concordance between those masses is equivalent to the vanishing of the virial integral.

We also have computed the accuracy of verification of a Penrose-Like inequality studied in Jaramillo et al. (2007), being the following:

$$\epsilon_A = \frac{\mathcal{A}}{8\pi(M_{ADM}^2 + \sqrt{M_{ADM}^4 - J^2})} \leq 1 \tag{4.4}$$

$\mathcal{A}$ is the area of the horizon, and M_{ADM} and J are respectively the ADM mass and the Komar angular momentum associated with the 3-slice. Being a little more stringent that the actual Penrose inequality, it is supposed to be verified for all spacetimes containing an apparent horizon, and it is an equality only for actual Kerr apparent horizons. We find an accuracy of 3.10^{-8} at most for this equality in our case. This is another strong hint of the accuracy of our spacetime solution.

To our knowledge, it is the first time the non conformally flat part is numerically computed in a black hole spacetime using only a prescription on the stationarity of the horizon. Further accuracy tests, including geometrical properties of the horizon and the spacetime will be presented in an upcoming paper. The authors warmly thank Eric Gourgoulhon and Jose Luis Jaramillo for numerous fruitful discussions.

References

Ashtekar, A., & Krishnan, B. 2004, Liv.Rev.Rel.2004-10

Bonazzola, S., Gourgoulhon, E., Grandclément, P., & Novak, J. 2004, Phys. Rev. D, 70, 104007

Cordero, I., Ibanez, J.M., Gourgoulhon, E., Jaramillo, J.L., & Novak, J. 2008, Phy.Rev.D, 77, 084007

Cook, G.B, & Pfeiffer, H. 2004, Phys.Rev.D, 70, 104016

Gourgoulhon, E. 2007, 3+1 Formalism and Bases of Numerical Relativity, gr-qc/0703035

Gourgoulhon, E., & Bonazzola, S., 1994, Clas.Quant.Grav., 11, 443-452

Gourgoulhon, E., & Jaramillo, J.L., 2006, Phys.Rep., 423, 159

Jaramillo, J.L., Ansorg, M., & Limousin, F. 2007, Phys.Rev.D, 74, 087502

Jaramillo, J.L., Ansorg, M., & Vasset, N. 2007, ERE07 proceedings, gr-qc/0712.1741

Lin, L.M., & Novak, J. 2007, Class.Quant.Grav., 24, 2665

Thorne, K., Price, R., & MacDonald, D. 1986, Black Holes: The membrane paradigm, Yale University Press

SF2A 2008
C. Charbonnel, F. Combes and R. Samadi (eds)

ON THE GINI-STATISTIC AND THE SEARCH FOR VARIABILITY IN A HESS PKS 2155-304 TIME SERIES

Venter, L.A.[1]

Abstract. The Gini statistic (V_n) considers individual photons and is standard normally distributed for exponentially distributed arrival times. The statistic can identify segments in a light curve within which the count rate changes and may therefore indicate the presence of variability. V_n is calculated for data from constant count rate and simple assumed intrinsic source simulations, windowing the photon lists on time-intervals between 10 s and 500 s. Plots of V_n vs. time show that peak values of the statistic identify sufficiently sharp changes in the slope of a light curve. Qualitatively, V_n(t) identifies small flares that *are* 'visible' in the light curve and thus does not add information. Ultimately, both the binning and Gini (V_n) approaches are limited by the uncertainties of low counts and Poissonian statistics.

1 Introduction

Cherenkov telescope γ-ray observations produce photon lists which list the arrival times of the photons. The HESS PKS2155-304 flare of July 28, 2006 (Aharonian 2007), sparked great interest because of the very short time scales that are evident in the light curve, which could be identified due to the high count rate.

Possonian statistical variations in the emission from a quiescent source can produce spurious short time-scale flare-like events. Very simply, the time scales that characterize a single flare are defined by points where the slope of the light curve changes, i.e. *change points.* Since the Gini-statistic discriminates between a constant count rate and any change in the count rate, it might be able to find variability (O. de Jager 2007 private comm.).

The Gini test is a powerful test for exponentiality against a range of alternatives (Gail & Gastwirth 1978). The statistic has a null-hypotheses, H_0: The photon list is a realization of a constant count rate source. Let t_i be the photon arrival times, $x_i = t_{i+1} - t_i$ the time differences and $x_{(i)}$ the ordered statistics. Then V_n, the normalized Gini statistic, calculated as $G_n = \left[\sum_{i=1}^{n-1} i(n-i)(x_{(i+1)} - x_{(i)})\right] / \left[(n-1)\sum_{i=1}^{n} x_i\right]$ and $V_n = (G_n - 1/2)[12(n-1)]^{1/2}$, is standard normally distributed for constant count rate data. However, the statistic does not distinguish between a constant count rate and a count rate that changes linearly with time. A large value may indicate *a change in the slope* of the light curve and may thus point out change points. If we calculate V_n within a time window T, $V_n \rightarrow$ for n$\rightarrow \infty$, if $x_{(i+1)} > x_{(i)}$ within the window, at least for some subset of $x_{(i)}$.

2 Calculation and analysis

A window of width T (T = 20 s... 500 s) is allowed to slide in steps of 10 s from the beginning to the end of a photon list, as described in de Villiers (2007). V_n can be plotted versus time for each window. Figure 1 shows an assumed source and the associated V_n values for different window sizes. Two or three peaks in V_n may be associated with a single flare. Narrow (small T) windows insufficiently sample around a possible change point to produce larger V_n values. On the other hand, wide windows (large T) may sample multiple change points and so resolution is diminished.

Figure 2(left) shows the light curve of the HESS July 28 flare (run 3), 30 s bins. The count rate changes substantially at a number of points, which may indicate time scales of varying source components, but the

[1] Observatoire de Paris, LUTH, Place Jules Janssen, 92195 Meudon, France

SF2A 2008
C. Charbonnel, F. Combes and R. Samadi (eds)

VERY HIGH ENERGY γ-RAY ASTRONOMY: REVIEW OF THE LATEST RESULTS

de Oña Wilhelmi, E.[1]

Abstract. The field of Very High Energy (VHE, E>100 GeV) gamma-ray astronomy has undergone a major revolution over the last four years, thanks to the results obtained by the new imaging Air Cherenkov Telescopes (IACTs). The latest generation of Cherenkov telescopes, such as H.E.S.S., VERITAS, and MAGIC, has increased the observation energy range from 100 GeV to multi-TeV, which allowed the field to enjoy a period of rapid growth, today boasting a source catalogue containing about 50 emitters of VHE gamma-rays from a variety of classes, including supernova remnants, blazars, pulsars, and microquasars. Other kinds of objects, such as pulsars, galaxy clusters or GRBs, are expected to produce also VHE gamma-rays. Furthermore, a large number of new unidentified sources without obvious counterparts at lower wavelength have been discovered. We will review the latest results published and discuss the most interesting cases.

1 Introduction

The window of ground-based gamma astronomy was opened in 1989 by the observation of a strong signal from the first TeV gamma source, the Crab Nebula, by the Whipple collaboration. Since then, increasing progress has been made in this new field of astronomy and discoveries of new sources have been made by newer ground-based VHE γ-ray instruments. Those instruments can be classify in two groups: Instruments with high sensitivity, the so-called imaging Cherenkov telescopes (IACTs) such as VERITAS (Holder et al. 2008), MAGIC (Bastieri et al. 2008), H.E.S.S. (Djannati-Ataï et al. 2008) and CANGAROO (Enomoto et al 2008), which operates in the energy range from 0.05 to 50 TeV, have large collection areas ($>10^4$m^2), good angular resolution (typically $\sim$0.05^o) and high capacity of background rejection using the *imaging* technique, but are limited by a small aperture (0.003 sr) and the request of observations under dark night conditions (10% duty cycle). IACTs allow to study in detailed the energy spectra and sources morphology, and are able to perform surveys of limited regions of the sky. The second group (Milagro (Abdo et al. 2007), Tibet (Amenomori et al. 2007) and ARGO) is characterized on the contrary by large aperture (> 2 sr) and high duty cycle (>90%) instruments, operating in a slightly higher energy range (1 - 100 TeV) but with limited angular resolution (0.3-0.7^o) and lower sensitivity than the one of the telescopes. These later instruments are optimum to carry on unbiased sky survey and study very extended sources not accessible by the imaging telescopes.

Over the last years, the number of known VHE gamma-ray sources increased rapidly: the last count gives more than 70 sources, among them 7 or more supernova remnants, about 20 pulsar wind nebulae and 20 unidentified sources, four binary systems, diffuse emission from clouds and 23 extragalactic sources. Fig. 1 shows the updated VHE γ-ray sky map (Wagner 2008).

A brief overview of the field is presented here. Since there will be another contribution dedicated to extra-galactic sources, and due to the limited space, I will only cover the most relevant results on Galactic sources.

2 Galactic sources

The H.E.S.S. telescope has conducted recently an extension of the scan of the inner Galactic Plane Survey (GPS) (Aharonian et al. 2005), which has supposed a major breakthrough in the Galactic field. The survey, covering the yet unexplored range in longitude between [-85^o,60^o] and [-2.5^o,2.5^o] in latitude, has revealed more than two dozens of new VHE sources, consisting of shell-type SNRs, pulsar wind nebulae, X-ray binary

[1] Laboratoire d'Astroparticule et Cosmologie-APC CNRS, Universit P7, Observatoire de Paris, CEA

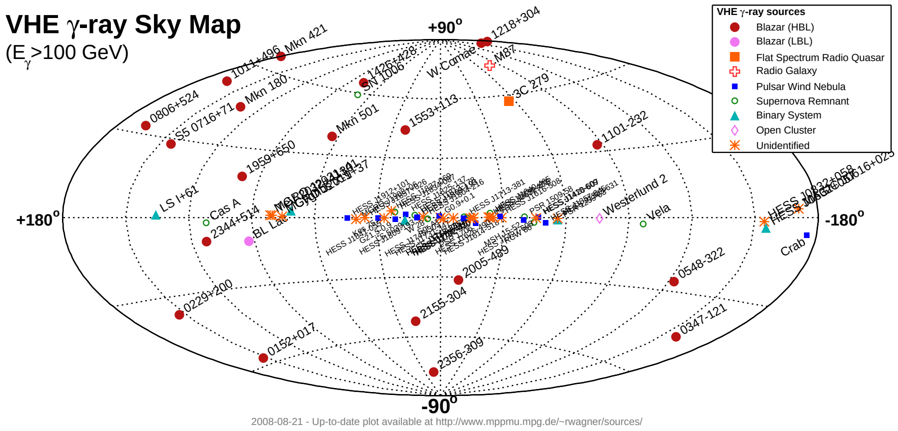

Fig. 1. The VHE γ-ray sky map

systems, a putative young star cluster, yet unidentified objects, the so-called dark sources, in which not obvious counterparts at other energy wavelengths are found (see e.g. Aharonian et al. (2006), Aharonian et al. (2008)), and the diffuse emission in the central 100 pc of the Milky Way, being able to locate the Galactic Center γ-ray source with a precision of 6", consistent with the black hole Srg A* but excluding the nearby remnant Sgr A East. MAGIC and VERITAS had contribute to the galactic field with the discovery of the γ-ray binary LSI +61 303 (Albert et al 2006), the stellar mass black hole binary Cygnus X-1 (Albert et al 2007), the supernova remnant IC443 (Albert et al. 2007) and they have confirmed several sources such as the first unidentified source, HEGRA TeV J2032+4130 (Aharonian et al. 2002).

The water Cherenkov detector Milagro has also survey the sky during 7 years of operation (2358 days of data to the North of 30^o longitude), announcing the discovery of three low-latitude sources and 4 lower significance hot-spots, as well as evidence for diffuse emission along the Galactic Plane. Fig. 2 shows the results of these observations. Note that the scan overlaps with the H.E.S.S. one between 35^o and 60^o, allowing a comparison between the sources detected in this region.

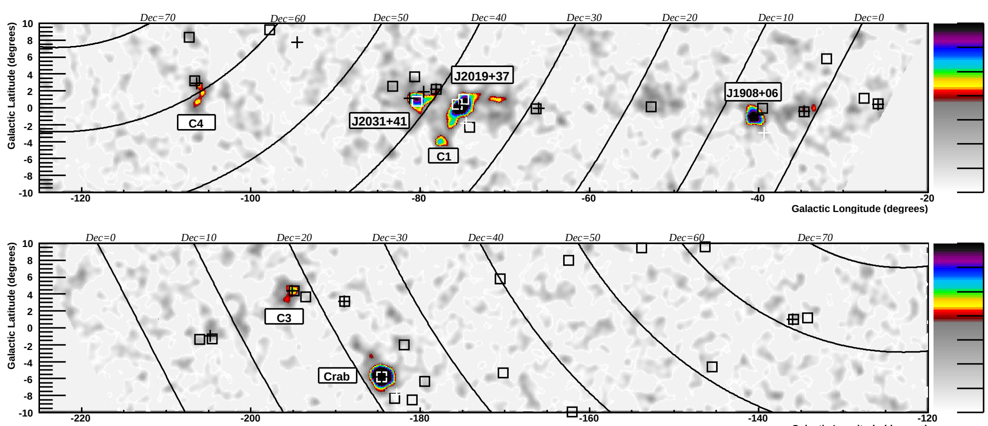

Fig. 2. Milagro observation of the Galactic Plane.

2.1 Supernova remnants

Shell-type supernova remnants (SNRs) are considered as prime acceleration sites for the galactic cosmic-rays, at most up 10^{15} eV. Up to 7 firm detections are seen in TeV γ-rays: IC 443, RX J0852-4622 (Katagiri et al 2005), RCW 86 (Hoppe & Lemoine-Goumard 2007), RX J1713.7-3946 (Aharonian et al. 2006), W28 (Aharonian et al. 2008), Cas A and SN 1006 (Melitta-Godo et al. 2008). Three of them have been resolved (RX J0852-4622, RCW 86 and RX J1713.7-3946) with unpreceding angular resolution, proving thus the acceleration of particle responsable of the VHE emission in the shell (see Fig. 3). Two mechanisms have been proposed to explain the VHE emission, through synchrotron radiation and Inverse Compton scattering produced by a population of electrons, or through collisions of accelerated protons with gas. The close correlation between γ-ray emission and X-ray emission, like in the case of RX J1713.7-3946, may favor a leptonic scenario, although it requires 10 μG magnetic field, while the filaments seen in X-ray images of SNR are often interpreted as evidence for rapid cooling of electrons as they move away from the shock fronts, which requires much higher fields in the 100 μG range. On the contrary, older SNRs such as IC 443 and W28, show a good agreement with dense molecular cloud, being so a strong argument for the presence of protons accelerated by the remnant.

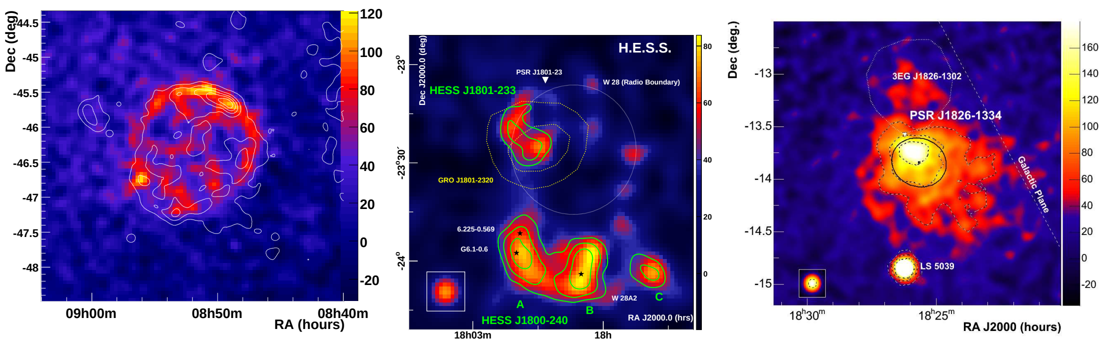

Fig. 3. Left: RX J0852-4622, together with X-ray contours from the ROSAT All Sky Survey >1.3 keV. **Middle:** the VHE emission from W28, coincident with an enhancement of ^{12}CO (J=1-2) data. **Right:** the PWN J1825-137

2.2 Pulsar wind nebulae

Pulsar wind nebulae represents the major Galactic source population revealed by the H.E.S.S. scan, being the Crab Nebula the first VHE γ-ray source. But they differ from the Crab Nebula in that they are typically very extended sources (few tens of pc), associated with very young, energetic pulsars, and the TeV emission is mostly displaced with respect to the pulsar position. HESS J1825-137 (in Fig. 3) can be considered as the prototype of such objects. The VHE emission and morphology can be explained by cooling of particles suffering radiative energy losses as they flowing away from the pulsar, resulting in the shrinking of the source towards the pulsar with increasing energy.

2.3 Unidentified sources

A large number of TeV γ-ray sources remain unidentified, that is, do not have a plausible counterpart at lower energies, where both, leptonic and hadronic models, predict in general synchrotron emission from charge particles, although highly suppressed in the latter case. They show rather hard spectral index and are mostly extended (see i.e. Fig. 4). In some cases, this could be due to lack of deep observations at other wavelength, but on some other cases, the VHE emission could be identify with pure protons accelerators, or explained with a leptonic population with a cutoff in the TeV range, in which case, in the KN regime high energy γ-rays can still be produced, but the synchrotron radiation peaks below the X-ray range and escapes detection. The scan performed by Milagro shows 3 new sources which remained unidentified, MGRO J2019+37 and MGRO J2031+41, on the Cygnus region, and MGRO J1908+06, located around 40^o on the Galactic plane. Fig. 4 shows the differential flux at 20 TeV of the H.E.S.S. and Milagro sources in the overlapping region of their scan. The two horizontal blue lines show the Milagro sensitivity at 20 TeV for a declination of 0 and 10^o, corresponding to the range of longitude of the H.E.S.S. sources above 35^o longitude.

HESS J1908+063 has been identified with MGRO J1908+06 but the two other Milagro sources are still being investigated by MAGIC and VERITAS.

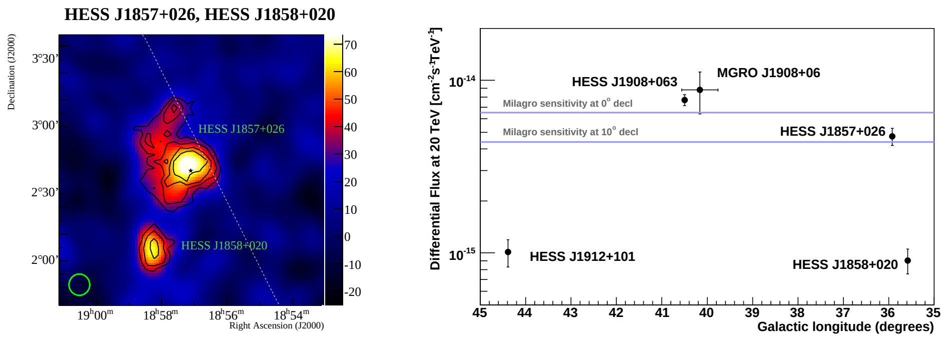

Fig. 4. On the left, one of the unidentified source discovered during the GPS, on the right, sources detected by Milagro and H.E.S.S. in their Galactic Plane Scan

3 Summary

The field of VHE astronomy has been consolidated in the last years, and has opened and answered many scientific topics. The future generation of telescopes Cherenkov, MAGIC II and H.E.S.S. II, and CTA in the following years, are expected to increase the sensitivity 10 orders of magnitude and extend the energy coverage from 1 GeV to 100 TeV, providing thus, together with HAWC (based on Milagro technology) full-sky coverage at sensitivity better than 0.1 Crab.

References

Abdo, A.A. et al. (MILAGRO Collaboration), 2007, ApJ, 658, 33.

Aharonian, F. A., et al. (H.E.S.S. Collaboration) 2005, Science, 307, 1938.

Aharonian, F. A., et al. (H.E.S.S. Collaboration) 2006, ApJ, 636, 777.

Aharonian F. et al. (H.E.S.S. Collaboration), 2008, A&A, 477, 353.

Aharonian et al. (HEGRA Collaboration) 1001 A&A, 393, L37.

Aharonian F. et al. (H.E.S.S. Collaboration), 2008, A&A, 481, 401.

Melitta-Godo et al. (H.E.S.S. Collaboration), 2008 Proc. of the Heidelberg Intern. Symposium on High-Energy Gamma-Ray Astronomy.

Albert, J. et al. (MAGIC Collaboration), 2006, Science, 312, 1771.

Albert, J. et al. (MAGIC Collaboration), 2007, ApJL, 665, L51.

Albert, J. et al. (MAGIC Collaboration), 2007, ApJ 664, L87.

Amenomori, M. et al. (Tibet Collaboration), 2007, Proc. 30th ICRC.

Bastieri, D. et al. (MAGIC Collaboration), 2008, NIM A, 588, 1.

Djannati-Ataï, A. et al. (HESS Collaboration), 2008, submitted to Elsevier, arXiv:0808.2841.

Enomoto, R. et al. (CANGAROO Collaboration), 2008, Proc. of the Heidelberg Intern. Symposium on High Energy Gamma-Ray Astronomy.

Holder, J., et al. (Veritas Collaboration), 2008, Proc. of the Heidelberg Intern. Symposium on High Energy Gamma-Ray Astronomy.

Hoppe, S. & Lemoine-Goumard, M. for the H.E.S.S. Collaboration, 2007, in Proc. of the 30th ICRC, Merida, arXiv:0710.4057v1.

Katagiri et al. 2005, ApJ 619, L163.

Wagner, R. 2008, "http://www.mppmu.mpg.de/ rwagner/sources/"

PCMI

Interstellar Medium

SF2A 2008
C. Charbonnel, F. Combes and R. Samadi (eds)

INVESTIGATING DISK DISSIPATION: THE CASE OF CQ TAU AND MWC 758

Chapillon, E.[1,2,3], Guilloteau, S.[1,2], Dutrey, A.[1,2] and Piétu, V.[3]

Abstract. The Herbig Ae stars are the massive analogs of the TTauri stars. Very few disks surrounding these kind of stars have been studied in detail. To better constraint the disks parameters (temperature and density) we observed the disks around CQ Tau and MWC 758 with the IRAM array in continuum and CO line emissions. The disks properties are derived using a standard parametric model. The two sources show a surprising low CO abundance (assuming a standard gas-to-dust ratio). We use the Meudon PDR code to study the chemistry. For CQ Tau we find that photodissociation of CO is a viable mechanism to explain the CO depletion without modifying the gas-to-dust ratio. However, we find in both sources that the temperature of large grains can be low enough to prevent CO from being released from the grain surfaces. In addition the low inclination of the CQ Tau disk challenges the UX Ori classification of this star. We conclude that CO does not appear as a direct tracer of the gas-to-dust ratio.

1 Introduction

Planetary formation takes place in the protoplanetary disks of gas and dust surrounding young stars. However, the overall properties of these disks are not yet well constrained by current observations. It is now generally admitted that the disks surrounding intermediate mass Herbig Ae (HAe) stars are warmer (and generally more massive) analogs of those surrounding lower mass TTauri stars. Accurate disk orientation, sizes, temperatures, and CO abundances are available for a few objects only: AB Aur (Piétu et al. 2005), MWC 480 (Simon et al. 2000; Piétu et al. 2007), and HD 163296 (Isella et al. 2007) have been studied in CO isotopologues, all having relatively massive and extended disks. However, the transition between Class II object (where the protoplanetary disk is made of gas and dust) and Class III (where the disk contains mainly dust) is poorly knwown. To study this transition phase between Class II and Class III, we observed the low mass disks around two intermediate mass pre-main-sequence (PMS) HAe stars CQ Tau and MWC 758.

2 Observations and data analysis

We have studied CQ Tau and MWC 758, two HAe ($\sim 2\,\mathrm{M}_\odot$) located at about 140pc in the Taurus complex. The disk around CQ Tau has been imaged at different wavelengths. So far, this is one of the oldest HAe star ($\sim$ 10 Myrs) surrounded by a resolved dust and gas disk (Mannings & Sargent 1997; Testi et al. 2001). Moreover, CQ Tau appears as a peculiar HAe star exhibiting an UX Ori like variability (Natta et al. 1997). The disk around MWC 758 has also been barely resolved in CO by Mannings & Sargent (1997, 2000). Both disks appeared significantly weaker and smaller in CO lines than the previously studied disks around HAe stars.

We have observed CQ Tau and MWC 758 in ^{12}CO J=21 line and 1.3mm continuum with the IRAM array (1.5" angular resolution) see figure 1. MWC 758 was also imaged in ^{12}CO J=10 (2.5" resolution). The data were fitted in the uv plane using a standard flaring disk model, with power-law distributions for all primary quantities (surface density $\Sigma(r) = \Sigma_0(r/r_0)^{-p}$, temperature $T(r) = T_0(r/r_0)^{-q}$, velocity $V(r) = V_0(r/r_0)^{-v}$, and scale height $H(r) = H_0(r/r_0)^{-h}$), following the method described in detail by Piétu et al. (2007). Results are presented in table.1. The disks are very similar, notably in size (200AU in CO) and mass (1–3 $10^{-3}\mathrm{M}_\odot$).

[1] Université Bordeaux 1, LAB, UMR 5804, 2 rue de l'Observatoire, BP 89,33270 Floirac, France
[2] CNRS/INSU - UMR 5804, BP 89, 33270 Floirac, France
[3] IRAM 300, rue de la piscine 38406 Saint Martin d'Hères France

(1)	(2)	(3)	(4)	(5)	(6)	(7)
Source	CQ Tau		MWC 758			
Data	^{12}CO J=2→1	Dust	^{12}CO J=2→1	^{12}CO J=1→0	^{12}CO	Dust
V_{LSR} (km.s^{-1})	6.17 ± 0.04		5.79 ± 0.01	5.90 ± 0.02	5.80 ± 0.02	
Orientation, PA (°)	-36.7 ±1.3	-36 ± 18	-31 ±1	-23 ±3	-31 ±1	-38 ± 7
Inclination, i (°)	29.3 ±1.7	29 ± 9	18 ±6	16 ±1	16 ±4	40 ± 20
Velocity(*), (km.s^{-1})	4.0 ± 0.2		3.6 ± 1.1	[4.00]	4.0 ± 0.6	
Velocity exponent, v	0.51 ± 0.02		0.51 ± 0.03	0.47 ± 0.07	0.50 ± 0.02	
Stellar mass, M_* ($M_\odot$)	1.8 ± 0.2		1.5 ± 0.7 [1.80]	[1.80]	1.80 ± 0.5	
Σ (*), (cm^{-2})	$1.7 \pm 0.1\,10^{16}$	$1.7 \pm 0.3\,10^{22}$	$3.5 \pm 0.7\,10^{16}$	$1.6 \pm 2.4\,10^{16}$	$4.7 \pm 0.9\,10^{16}$	$6.0 \pm 2.0\,10^{22}$
Σ_{mass} (*) (g.cm^{-2})		0.075 ± 0.015				0.3 ± 0.1
Exponent p	2.3 ± 0.2	1.3 ± 0.1	2.7 ± 0.5	[3]	2.9 ± 0.4	1.5 ± 0.4
Outer radius R_{out}, (AU)	200 ± 20	200 ± 30	300 ± 20	230 ± 30	270 ± 15	180 ± 40
Temperature(*),(K)	150 ± 50 [150]		37 ± 6	24 ± 4	30 ± 1	
Exponent q	0.7 ± 0.5 [0.5]		0.05 ± 0.20	0.6 ± 0.3	0.37 ± 0.15	
δV (*), (km.s^{-1})	0.32 ± 0.09		0.50 ± 0.03	0.28 ± 0.10	0.44 ± 0.02	
Scale height(*), (AU)	22		15		11	
β		0.70 ± 0.04				1.0 ± 0.15

Table 1. Best parameters. Column (1) contains the parameter name. Columns (2) and (4) indicate the parameters derived from ^{12}CO J=2→1, column (5) parameters derived from ^{12}CO J=1→0, and columns (3) and (7) parameters derived from the dust emission, using the disk temperature from ^{12}CO and the dust emissivity from $\kappa_\nu(\nu) = 0.1(\nu/10^{12}\mathrm{Hz})^\beta \mathrm{cm}^2\mathrm{g}^{-1}$ (Beckwith et al. 1990). Column (6) indicates the results of a simultaneous fit to both CO lines. Note that the P.A. is that of the disk axis. δV is the local line width (sum of thermal + turbulent component see Pietu et al. 2007 for a description of the convention). Σ is the surface density ($(\mathrm{H}+2\mathrm{H}_2)/2$) and Σ_{mass} the mass surface density assuming a g/d ratio of 100. (*) values at 100 AU. Square brackets indicate fixed parameters. The error bars correspond to 1 σ level of uncertainties.

Note that the masses are quite low comparing to the standard TTauri disks ($\sim 10^{-2} M_\odot$). Both disks are in Keplerian rotation. The dust emissivity spectral index ($\beta = 0.7$–1) indicates that grain growth has occurred in those sources. One surprising result is the low CO abundance ($\sim 10^{-6}$ instead of the standard value of 10^{-4}) assuming the standard value of 100 for the gas-to-dust ratio (g/d) i.e., CO is depleted by a factor of about 100. Although the two sources are quite similar, CQ Tau is hotter and less dense by a factor 5 than MWC 758.

The hight CO depletion suggests that the g/d ratio may be much lower than our assumed value of 100 because we are observing disks in the process of dissipating their gaseous content. Since the temperature of these two disks is large, depletion of CO due to sticking on grains cannot be invoked in a simple way.

3 Chemistry modeling

We use the PDR code from the Meudon group (Le Petit et al. 2006 and reference therein) to study the chemistry of the disks. The model is a 1D stationary plane-parallel slab of gas and dust illuminated by an ultraviolet (UV) radiation field. We use a chemical network similar to that of Goicoechea et al. 2006. No freeze-out onto grains is considered. We take into account a power-law grain size distribution $n(a) \propto a^{-\gamma}$ following HilyBlant et al. 2009 with a_+ and a_- being the maximum and minimum cutoff radii, respectively. The resulting extinction curve is calculated using the Mie theory for homogeneous isotropic spherical particles. To have a two-dimensional molecular distribution we compute the model at different radii in the disk. The output of this 1+1D model is the vertical distribution of molecular abundance calculated at different radii. As an input, we impose temperature and vertical density laws as derived from Table 1 at each radius. We investigate several g/d ratio (10–100 to mimic gas dispersal) under various UV field conditions (Draine field with a scaling factor $\chi = 10^3$–10^4), and different maximum grain size (a_+=1μm–1mm to mimic grain growth). The dust mass is constant in all our simulations. The thermal balance is calculated. The results for the CQ Tau structure are presented on figure 3.

4 Discussion

Figure 3 (bottom) suggests that a case with $a_+ \geq 1$ mm and $g/d \simeq 100$ can explain CO column densities of the order of $10^{16}\mathrm{cm}^{-2}$ around 200AU for CQ Tau. Figure 3 (top) allows us to conclude that the case with $a_+ = 1\mu$m cannot explain the observed CO column densities, even with a low g/d ratio. For CQ Tau this is in agreement with the spectral index we measure ($\beta = 0.7$), which indicates that significant grain growth has occurred as also found by Testi et al.2003. This result suggests that grain growth, or more precisely the enhancement of the UV

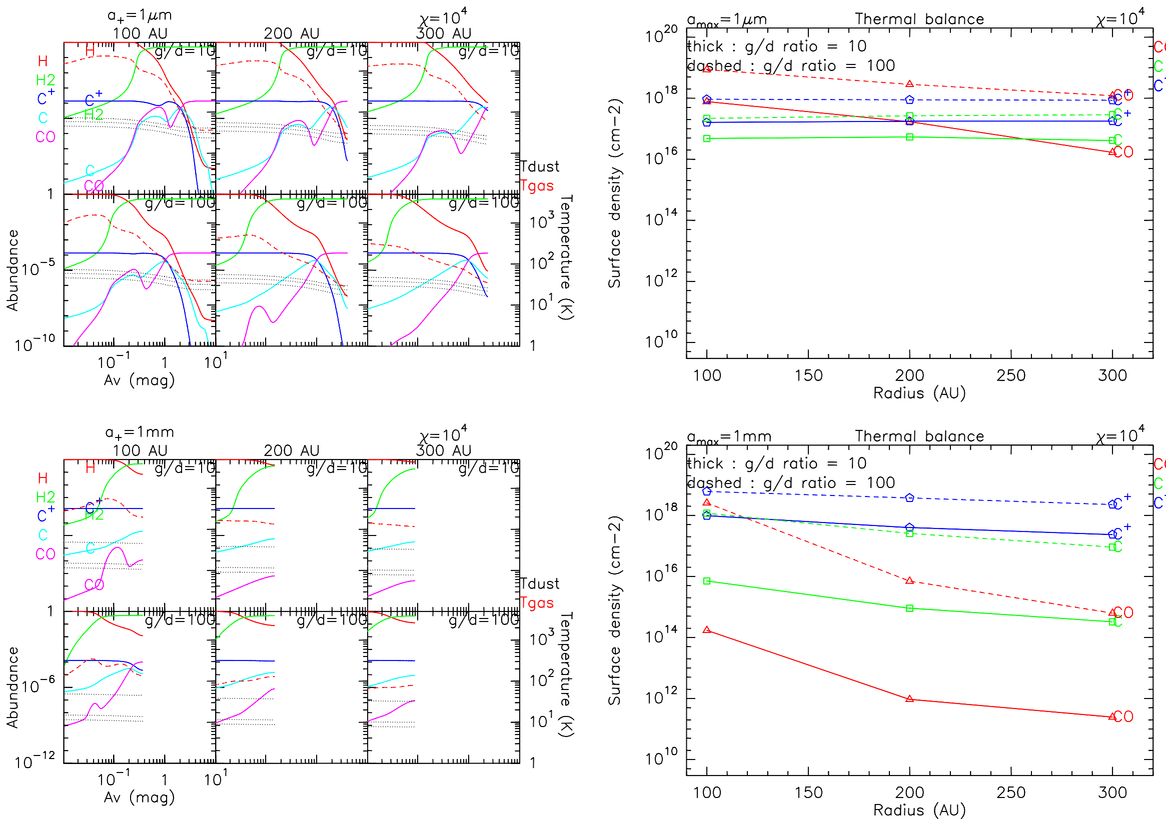

Fig. 1. Left: Vertical distribution through the disk of the abundance of H,H_2, C^+, C and CO and gas (dashed line) and dust (dotted line) temperature at the radii 100, 200 and 300 AU for the models with standard UV field ($\chi = 10^4$ at 100 AU), a_+=1μm (top) and app=1mm (bottom). Dust temperature is plotted for tree grain sizes: a_+, $a_-$and $(a_+ + a_-)/2$. **Right:** Radial distribution of the surface density of C^+, C and CO for the model with standard UV field ($\chi = 10^4$ at 100 AU), a_+=1μm (top) and a_+=1mm (bottom).

penetration resulting from grain growth, is the dominant process explaining the measured CO column density. The observed CO temperature and the temperature calculated from the (approximate) thermal balance are in reasonable agreement for CQ Tau, around 60 − 100 K.

MWC 758 poses a different challenge, as the observed gas temperature is much lower, about 30 K, while the estimated CO column density is similar. Taken at face value, the results of the thermal balance study would favor the low g/d ratio solution (i.e., $g/d = 10$), which results in a somewhat more efficient cooling. However, there are several significant uncertainties in our modeling procedure. For example, the amount of small grains which controls the photo-electric heating is poorly constrained, and therefore the efficiency of this process may be overestimated in our model. Similarly, the gas-grain coupling is dominated by the small grains, because of their larger cross section and higher temperature, and remains also rather uncertain. Furthermore, we use a simple approximation for the diffusion of UV photons toward the disk plane, and even the unattenuated UV flux is uncertain. Note that the photodissociation is totally dominated by the UV excess (900–1200Å see Figure 2), while the stellar UV flux will play a role in the heating processes. .

A totally different alternative to explain the low CO-to-dust ratio resides in the thermal history. Although the observed CO gas (and presumably small dust) is too warm to allow efficient sticking to grains, we find that the temperature of large grains can be low enough to prevent CO from being released from the grain surfaces.

In any case, our study clearly indicates that a low apparent CO abundance does not necessarily imply a low gas-to-dust ratio, and thus that CO is not an unambiguous tracer of this ratio.

Besides, the accurate determination of the inclination of CQ Tau ($29^\circ \pm 2$) challenges the UX ori hypothesis for this source since this phenomenon require that the disk inclination to be larger than $\sim 45^o$ (Natta & Whitney2000). Moreover, Eisner et al. 2004 have measured the inclinaison of the inner disk axis in near infra-

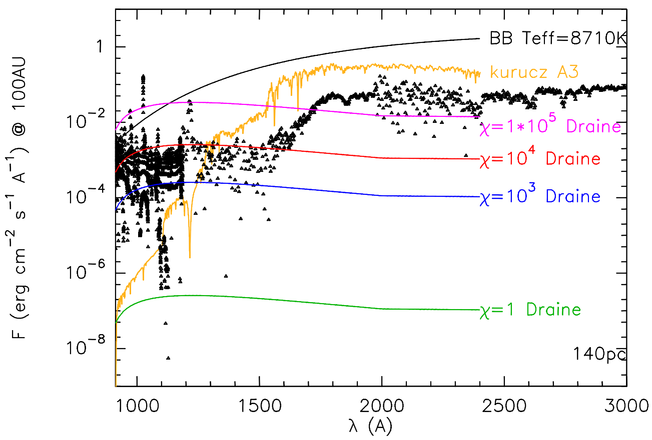

Fig. 2. Flux at 100 AU of FUSE and IUE observations MWC 758 (points), an A3V star according to the Kurucz atlas, a black body with the same temperature as an A3 star and several scaled Draine fields. The curved labeled 10^5 is calculated to have the same integrated intensity between 912 and 2400 Å as the observations. The star is assumed to be at 140 pc.

red. They found $48 \pm 5°$. This result suggests that the disk may be warped by dynamical interactions with (yet undetected) inner bodies, but such large warps have never been observed so far.

More details about this study can be found in Chapillon et al. 2008

We acknowledge all the PdBI IRAM staff, Pierre Hily-Blant, Franck Le Petit, Thierry Forveille, Gail Schaeffer and Claire Martin-Zaïdi. This research was supported by the INSU program PCMI.

References

Beckwith, S.V.W., Sargent, A.I., Chini, R.S., & Guesten, R. 1990, AJ, 99, 924
Chapillon, E., Guilloteau, S., Dutrey, A., & Piétu, V. 2008, A&A 488, 565, 578
Eisner, J.A., Lane, B.F., Hillenbrand, L.A., Akeson, R.L., & Sargent, A.I. 2004, ApJ, 613, 1049
Goicoechea, J.R., Pety, J., Gerin, M., et al. 2006, A&A, 456, 565
Grady, C.A., Woodgate, B.E., Bowers, C.W. et al. 2005, ApJ, 630, 958
Hily-Blant, P., Dartois, E., Dutrey, A., et al. 2009 (A&A submitted)
Isella, A., Testi, L., Natta, A., et al. 2007, A&A, 469, 213
Le Petit, F., Nehmé, C., Le Bourlot, J., & Roueff, E. 2006, ApJS, 164, 506
Mannings, V., & Sargent, A.I. 1997, ApJ, 490, 792
Mannings, V., & Sargent, A.I. 2000, ApJ, 529, 391
Natta, A., Grinin, V.P., Mannings, V., & Ungerechts, H. 1997, ApJ, 491, 885
Natta, A., & Whitney, B.A. 2000, A&A, 364, 633
Piétu, V., Guilloteau, S., & Dutrey, A. 2005, A&A, 443, 945
Piétu, V., Dutrey, A., & Guilloteau, S. 2007, A&A, 467, 163
Simon, M., Dutrey, A., & Guilloteau, S. 2000, ApJ, 545, 1034
Testi, L., Natta, A., Shepherd, D.S., & Wilner, D.J. 2001, ApJ, 554, 1087

SF2A 2008
C. Charbonnel, F. Combes and R. Samadi (eds)

DUST PROCESSING IN PHOTODISSOCIATION REGIONS MID-IR EMISSION MODELLING OF NGC2023N

Compiègne, M.[1,2], Abergel, A.[1], Verstraete, L.[1] and Habart, E.[1]

Abstract. This study is done in the context of dust evolution and its interaction with the gaseous phase throughout the interstellar medium evolution cycle. We focus on the mid-IR spectral variations of the dust emission across photodissociation regions, observed with both ISO and Spitzer satellites. We use a dust emission model coupled with a radiative transfer model in order to study the excitation effects on these spectral variations. We show that in NGC2023N, radiative transfer effects cannot account for the observed spectral variations. Thus, we interpret these variations in term of changes of the relative abundance between polycyclic aromatic hydrocarbons (PAHs, mid-IR bands carriers) and very small grains (VSGs, mid-IR continuum carriers). We conclude that the PAH/VSG abundance ratio is about 5 times lower in the dense deep part than in the diffuse illuminated part of the PDR where dust properties seem to be the same as in the diffuse high galactic latitude medium. Consequently, we conclude that dust must evolve from "dense properties" to "diffuse properties" at the small spatial scale of the dense illuminated ridge.

1 Introduction

Dust plays a key role for the physics and the chemistry of photodissociation regions (PDRs) which are important IR emitters in galaxies. ISO observations revealed a systematic diminution of the ratio between aromatic infrared bands (AIBs, attributed to polycyclic aromatic hydrocarbons, PAHs) and mid-IR continuum (attributed to very small grains, VSGs) in PDRs (e.g. Abergel et al., 2002). Rapacioli et al. (2005) and Berné et al. (2007) have interpreted these variations in term of chemical properties evolution of carbonaceous emitters (PAHs $\Leftrightarrow$ VSGs evolution) using the single value decomposition method and the blind signal separation method. A limitation of these methods is that it does not take into account possible variation due to radiative transfer effects. We present a study of dust mid-IR emission in NGC2023 North (hereafter NGC2023N) using a dust model coupled to a radiative transfer model. We interpret the AIB / continuum variations observed with Spitzer/IRS and ISOCAM in term of PAH/VSG relative abundance evolution. More details are given in Compiègne et al. (2008).

2 Observed and modelled spectral variations

NGC2023N is excited by a B1.5V star (HD37903) embedded in the L1630 molecular cloud. This PDR exhibits a strong mid-IR spectral variation as shown by Abergel et al. (2002). Fig.1 shows this variation that occurs at the dense illuminated ridge traced by $H_2\, \nu = 1-0\, S(1)\, 2.12\mu$m emission. The AIB (7-9$\mu$m)/continuum (22-24$\mu$m) ratio goes from a value of 1.9 in the diffuse illuminated part to a value of 0.4 in the deep dense part of the PDR. The left panel of Fig.2 shows both the modelled and observed spectrum of the diffuse illuminated part. The modelled spectrum is obtained using the dust model described in Compiègne et al. (2008). The used exciting radiation field corresponds to a B1.5V star located at 0.3 pc and extinguished with $A_V \sim 1.25$ (for details, see Compiègne et al., 2008). Cirrus dust properties allow us to reproduce the spectrum of the diffuse illuminated part of NGC2023N. The right panel of Fig.2 shows the modelled evolution of the AIB (7-9μm)/continuum (22-24μm) ratio as a function of optical depth in the PDR (for details, see Compiègne et al., 2008) for $n_H = 10^4$ and $10^5\, cm^{-3}$ (Field et al., 1998). The required extinction of $A_V \sim 12$ to account for the value of 0.4 of the ratio at the deep dense location with only excitation effects is not in accordance with the raise of the 22-24μm observed intensity from ~70 MJy sr^{-1} to ~100 MJy sr^{-1} between the diffuse illuminated part and this location.

[1] Institut d'Astrophysique Spatiale, UMR8617, CNRS, Université Paris-sud XI, bâtiment 121, F-91405 Orsay Cedex, France
[2] Canadian Institute for Theoretical Astrophysics, University of Toronto, 60 St. George Street, Toronto, ON M5S 3H8, Canada

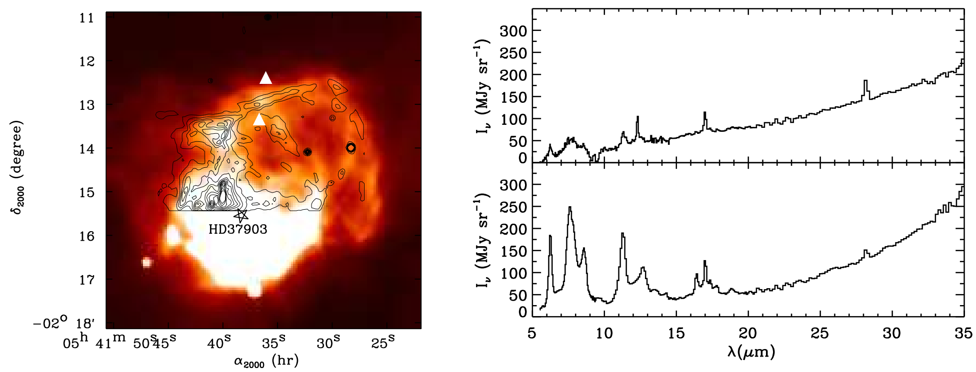

Fig. 1. NGC2023 as seen by ISOCAM/LW2 (5-8.5μm). Contours show the $H_2\,\nu = 1-0\,S(1)\,2.12\mu$m emission observed with SOFI. **Spectra:** ISOCAM/CVF and IRS spectra of the diffuse illuminated part (southern triangle on the map) and of the deep dense part (northern triangle on the map) of the PDR.

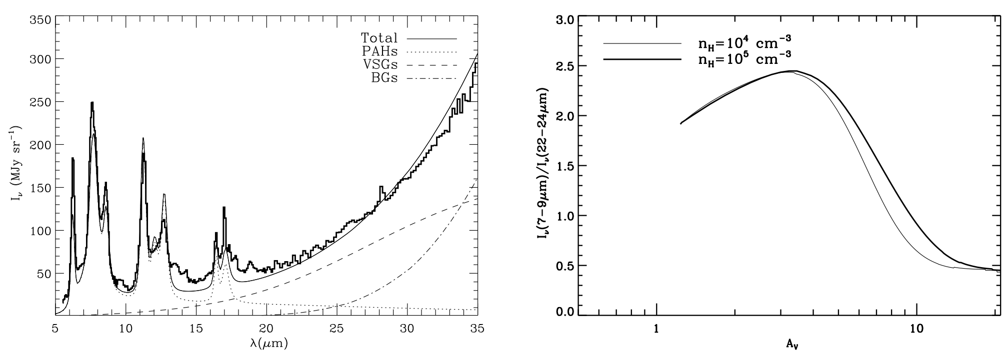

Fig. 2. Left: Spectrum of the diffuse illuminated part observed (thick line) and modelled (thin line). Used dust properties are those of Cirrus. **Right:** Modelling of the AIBs/continuum ratio evolution across the PDR for two different densities.

3 Conclusion

The modelling of the mid-IR emission in NGC2023N shows that radiation transfer effects can not explain the observed spectral variations. We conclude that PAH/VSG relative abundance is ~5 times lower in the deep dense part of the PDR than in the diffuse illuminated part where dust properties seem to be the same as in Cirrus. Thus, dust must evolve from “dense” to “diffuse” properties at the small spatial scale of the PDR. The strong evolution of the PAH relative abundance between the dense and diffuse medium in PDRs has importance for the physics and the chemistry of these regions, for the interpretation of extragalactic sources spectra or also concerning the use of AIBs as a tracer of the star formation activity.

References

Abergel, A., Bernard, J.P., & Boulanger, F., et al. 2002, A&A, 389, 239

Berné, O., Joblin, C., Deville, Y., et al. 2007, A&A, 496, 575

Compiègne, M., Abergel, A., Verstraete, L., & Habart, E. 2008, A&A, in press (arXiv 0809.5026)

Field, D, Lemaire, J-L, Pineau des Forts, G, et al. 1998, A&A, 333, 280

Rapacioli, M., Joblin, C., & Boissel, P. 2005, A&A, 429, 139

SF2A 2008
C. Charbonnel, F. Combes and R. Samadi (eds)

FORMATION AND PROPERTIES OF MOLECULAR CLOUD CORES

Dib, S.[1,2], Galván-Madrid, R.[3,4], Kim, J.[5] and Vázquez-Semadeni, E.[4]

Abstract. In this paper, we review some of the properties of dense molecular cloud cores. The results presented here rely on three-dimensional numerical simulations of isothermal, magnetized, turbulent, and self-gravitating molecular clouds (MCs) in which dense core form as a consequence of the gravo-turbulent fragmentation of the clouds. In particular we discuss issues related to the mass spectrum of the cores, their lifetimes and their virial balance.

1 The simulations

We performed 3D numerical simulations of magnetized, self-gravitating, and turbulent isothermal MCs using the TVD code (Kim et al. 1999) on grids with 256^3 and 512^3 cells (Vázquez-Semadeni et al. 2005; Dib et al. 2007a; Dib et al. 2008a). The basic features of these simulations are: Turbulence is driven until it is fully developed (at least for 2 crossing timescales) before gravity is turned on. The Poisson equation is solved to account for the self-gravity of the gas using a standard Fourier algorithm. Turbulence is constantly driven in the simulation box following the algorithm of Stone et al. (1998). The kinetic energy input rate is adjusted such as to maintain a constant rms sonic Mach number $M_s = 10$. Kinetic energy is injected at large scales, in the wave number range $k = 1 - 2$. Periodic boundary conditions are used in the three directions. In physical units, the simulations have a linear size of 4 pc, an average number density of $\bar{n} = 500$ cm^{-3}, a temperature of 11.4 K, a sound speed of 0.2 km s^{-1}, and an initial *rms* velocity of 2 km s^{-1}. The Jeans number of the box is $J_{box} = 4$ (number of Jeans masses in the box is $M_{box}/M_{J,box} = J^3_{box} = 64$, where $M_{box} = 1887$ M$_\odot$). The simulations vary by the strength of the magnetic field in the box with $B_0 = 0, 4.6, 14.5$, and 45.8 μG for the non-magnetized, the strongly supercritical, the mildly supercritical, and the subcritical cloud models, respectively. Correspondingly, the plasma beta and mass-to-magnetic flux (normalized for the critical value for collapse $M/\phi = (4\pi^2 G)^{-1/2}$; Nakano & Nakamura 1978) values of the box are $\beta_{p,box} = \infty, 1, 0.1$, and 0.01, and $\mu_{box} = \infty, 8.8, 2.8$, and 0.9, respectively. Cores are identified using a clump-finding algorithm that is based on a density threshold criterion and a friend-of-friend approach as described in Dib et al. (2007a). We restrict our selection of cores to epochs where the Truelove criterion (Truelove et al. 1997) is not violated in any of them. Thus, the derived properties of our numerical cores can be best compared to those of starless prestellar cores.

[1] Service d'Astrophysique, DSM/Irfu, CEA/Saclay, F-91191 Gif-sur-Yvette Cedex, France; email: sami.dib@cea.fr
[2] Lebanese University, Faculty of Sciences, Department of Physics, El Hadath, Beirut, Lebanon
[3] Harvard-Smithsonian Center for Astrophysics, 60 Garden Street, Cambridge, MA 02138, USA; rgalvan@cfa.harvard.edu
[4] Centro de Radioastronomía y Astrofísica, Universidad Nacional Autónoma de México, 58089, Morelia, Michoacán, Mexico; e.vazquez@astrosmo.unam.mx
[5] Korea Astronomy and Space Science Institute, 61-1, Hwaam-dong, Yuseong-gu, Daejeon 305-348, Korea; jskim@kasi.re.kr

2 Core mass function

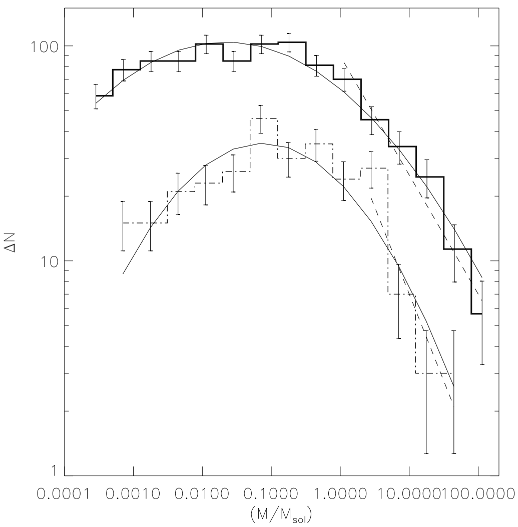

Fig. 1. Core mass function for cores identified at density thresholds of 20 and 50 times the average density (full thick and dot-dashed line respectively). Over-plotted to the CMF is a lognormal fit (full line) and power law fits in the intermediate to high mass regimes (dashed lines).

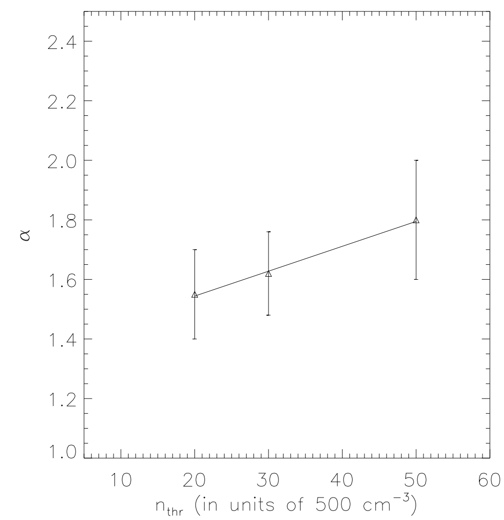

Fig. 2. Slope of the CMF in the intermediate and high mass regimes as a function of the density threshold. The slope of the CMF is steeper when cores are identified with higher density tracers/thresholds.

One important area of modern astrophysics revolves around characterizing the initial mass function of stars (i.e. mass function of stars at their birth), and assessing whether it is universal (i.e. independent of environment) or not. Early determinations of the IMF have been obtained by Salpeter (1955) who showed that the field star population can be described by a power law of the form $dN/dM = M^{\alpha}$ with $\alpha \sim -2.35$ in the intermediate to high mass regimes. Subsequent determinations of the IMF, particularly that of stellar clusters, have derived values of α that are in the range $\sim [-1.8, -2.7]$ (e.g., Massey et al. 1995; Sharma et al. 2007). A related important issue is that of the relationship between the IMF and the core mass function (CMF). Observations of dense cores in nearby star forming regions tend to indicate that their mass distribution is not very different from that of the IMF (e.g., Motte et al. 1998; Johnstone & Bally 2006) which would indicate that the shape of the IMF might be already set in the early gaseous phase. Using our above described simulations, we have constructed the CMF at several density thresholds. Fig. 1 displays the CMF for cores identified at the density thresholds of $n_{thr} = 20\bar{n} = 10^4$ cm^{-3} and $50\bar{n} = 2.5 \times 10^4$ cm^{-3}. The derived values of the slopes in the intermediate to high mass regimes show a steepening of the slope of the CMF with increasing threshold. Equivalently, the width of the CMF decreases with increasing threshold when the CMFs are fitted with a lognormal distribution. Our statistics of cores does not allow us to probe the values of the slopes for cores identified at higher density thresholds, e.g., in the range of $200\bar{n} = 10^5$ cm^{-3} at which all cores are gravitationally bound. However, an extrapolation of the slope-threshold relation in Fig. 2 seems to indicate that values of the slopes in the range [-2.5,-3] can be expected for these threshold values. Nonetheless, it shoud be noted that the power law shape (or lognormal) of the CMF can be substantially modified as time evolves under the influence of various physical processes such as gas accretion and core coalescence (Dib et al. 2007b; Dib 2007; Dib et al. 2008a,b,c)

3 Virial balance

In Dib et al. (2007a) and Dib & Kim (2007), we investigated the detailed virial balance of the cores formed in the simulations. By calculating all the terms of the virial theorem, we could show that the cores are dynamical, out of equilibrium structures. In each model, there is a mixed populations of gravitationally bound cores, cores that are bound by external compressions, and unbound dispersing objects. We compare the diagnostic of the gravitational boundedness of cores using the detailed virial balance to that made using other simplified

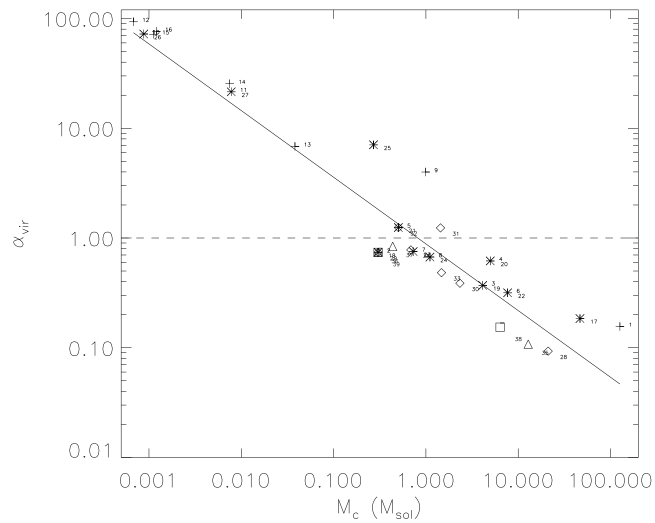

Fig. 3. The virial parameter as a function of the mass for the clumps and cores in the mildly magnetically supercritical simulation after $t = 1.6$ Myr of turning on self-gravity.

indicators, such as the virial parameter α_{vir} which compares the sum of the kinetic and thermal energy to gravity, the mass to magnetic flux ratio which compares the importance of magnetic support against gravity, and the Jeans number which compares the importance of thermal support against gravity. In all simulations, we find a trend in which, for gravitationally bound cores, the virial balance of such objects indicates that their inner parts (i.e., when cores are defined at high density thresholds) are more gravitationally bound than when the same objects are identified with lower density tracers (inner+outer parts). The simplified indicators seemed to indicate a different result in which the extended objects are more gravitationally bound than their inner parts. The discrepancy is nonetheless not very surprising considering the fact that the simplified indicators describe only a part of the energetic balance of the cores and that all of them neglect the surface energy terms that appear in the virial theorem. A comparison of the mass-virial parameter relation $\alpha_{vir} = M_c^{\beta}$ for the different simulated clouds (and at different epochs) with the observations (e.g. Bertoldi & McKee 1992; Williams et al. 2000) shows that the closest agreement with the observations is obtained for the case of the mildly magnetically supercritical cloud model. The value of β in this model is found to be ~ -0.6 (Fig. 3) in contrast to values of $\beta > -0.5$ for the strongly supercritical and non-magnetic cases. This seems to indicate that real molecular clouds in nearby star forming regions and in which cores are observed to form might be in a state of near magnetic criticality or slight super-criticality.

4 Cores lifetimes

In Vázquez-Semadeni et al. (2005) the time evolution of the cores was studied for simulations of different initial mass-to-magnetic flux ratio. Galván-Madrid et al. (2007) performed mesurements of the core lifetimes as a function of the density threshold n_{thr} used to define the cores for the likely case of MCs that are slightly magnetically supercritical (see above). The prestellar lifetimes of the cores ranged between a few to several free-fall times, with a mean value of $\tau_{pre} \sim 6\ t_{ff}$, where $t_{ff} \equiv (3\pi/32G\rho)^{1/2}$. Fig. 4 displays the lifetimes of the cores in the simulations against their threshold density (which is similar to the initial mean volume density). The observational data compiled by Ward-Thompson et al. (2007) is overplotted (filled squares). There is good agreement between the prestellar lifetimes of the simulations and the observations. Galván-Madrid et al. (2007) also performed indirect estimations of the starless-to-protostellar core ratio. They found that it decreases from ~ 5 at $n_{thr} \sim 10^4$ cm^{-3} to ~ 1 at $n_{thr} \sim 10^5$ cm^{-3}, in rough agreement with observational estimates (e.g., Lee & Myers 1999; Hatchell et al. 2007).

S. D. would like to thank the organizers of the SF2A-PCMI Dynamique workshop for the invitation to speak.

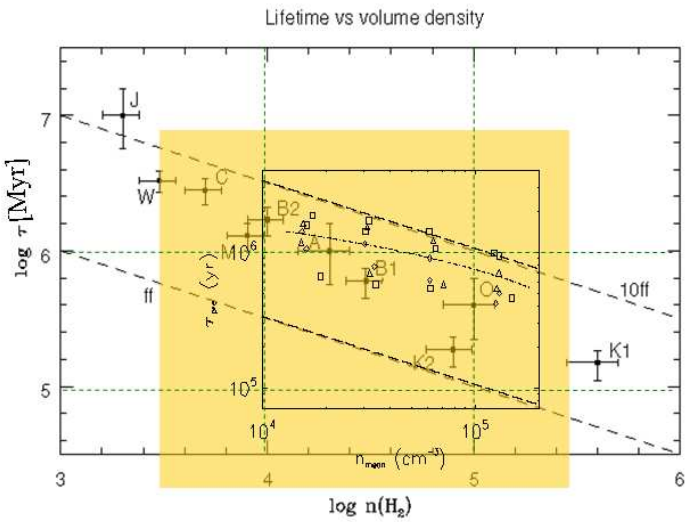

Fig. 4. Duration of the prestellar stage for the collapsing cores in the simulations as a function of their mean density. Diamonds, triangles, and open squares correspond to different runs. The loci of $\tau_{pre} = 1\ t_{ff}$ and $\tau_{pre} = 10\ t_{ff}$ are marked by the lower and upper long-dashed lines respectively. The linear fit to the simulation measurements ($\tau_{pre} \simeq 6\ t_{ff}$) is marked by the dash-dotted line. Over-plotted to the simulations are observational data points (filled squares, taken from Ward-Thompson et al. 2007).

References

Bertoldi, F., & McKee, C. F. 1992, ApJ, 395, 140

Dib, S., Kim, J., Vázquez-Semadeni, E., Burkert, A., & Shadmehri, M. 2007a, ApJ, 661, 262

Dib, S., Kim, J., & Shadmehri, M. 2007b, MNRAS, 381, L40

Dib, S. 2007, JKAS, 40, 157

Dib, S., & Kim, J. 2007, in Small Ionized and Neutral Structures in the Diffuse Interstellar Medium, ed. M. Haverkorn, & M. Goss (ASP Conference Series), p. 166

Dib, S., Brandenburg, A., Kim, J., Gopinathan, & M., André, P. 2008a, ApJ, 678, L105

Dib, S., Shadmehri, M., Gopinathan, M., Kim, J., & Henning, T. 2008b, in Massive Star Formation: Observations Confront Theory, ed. H. Beuther, H. Linz, & T. Henning (ASP Conference Series), p. 282

Dib, S., Shadmehri, M., & Audit, E., 2008c, in preparation

Galván-Madrid, R., Vázquez-Semadeni, E., Kim, J., & Ballesteros-Paredes, J. 2007, ApJ, 670, 480

Hatchell, J., Fuller, G. A., Richer, J. S., Harries, T. J., & Ladd, E. F. 2007, A&A, 468, 1009

Johnstone, D., & Bally, J. 2006, ApJ, 653, 383

Kim, J., Ryu, D., Jones, T. W., & Hong, S. S. 1999, ApJ, 514, 506

Lee, C. W., & Myers, P. C. 1999, ApJS, 123, 233

Massey, P., Johnson, K. E., & Degioia-Eastwood, K. 1995, ApJ, 454, 151

Motte, F., André, P., & Neri, R. 1998, A&A, 336, 150

Nakano, T. & Nakamura, T. 1978, PASJ, 30, 671

Salpeter, E. E. 1955, ApJ, 121, 161

Sharma, S., Pandey, A. K., Ojha, D. K., Ghosh, S. K., Mahesh., G., Bhatt, B. C., & Sagar, R. 2008, ApJ, 135, 1934

Stone, J. M., Ostriker, E. C., & Gammie, C. F. 1998, ApJ, 508, L99

Truelove, J. K., Klein, R. I., McKee, C. F., Holliman, J. H., II; Howell, L. H., & Greenough, J. A. 1997, ApJ, 489, L179

Vázquez-Semadeni, E., Kim, J., Shadmehri, M., & Ballesteros-Paredes, J. 2005, ApJ, 618, 344

Ward-Thompson, D., André, P., Crutcher, R., Johnstone, D., Onishi, T., & Wilson, C. 2007, in Protostars and Planets V, ed. B. Reipurth, D. Jewitt, & K. Keil (Tuscon:Univ. of Arizona Press), 33

Williams, J. P., Blitz, L. & McKee, C. F. 2000, in Protostars and Planets IV, ed V. Manning, A. Boss, & S. Russel, (Tuscon:Univ. Arizona Press), p. 97

SF2A 2008
C. Charbonnel, F. Combes and R. Samadi (eds)

MAGNETOHYDRODYNAMIC TURBULENCE

Galtier, S.[1]

Abstract. A short review is given on MHD turbulence for strong and wave turbulence, and for incompressible as well as compressible fluids. The role of anisotropy *versus* isotropy is discussed and important issues are raised.

1 Turbulence in Navier-Stokes fluids

Turbulence is one of the main problems in theoretical physics. For that reason, any exact results appear almost as a miracle. In his third 1941 turbulence paper, Kolmogorov found that an exact and nontrivial relation may be derived from Navier-Stokes equations – which can be seen as the archetype equations for describing turbulence – for the third-order longitudinal structure function (Kolmogorov, 1941). Because of the rarity of such results, the Kolmogorov's four-fifth's law is considered as one of the most important results in turbulence (Frisch, 1995). Basically, the four-fifth's theorem makes the following link between a two-point measurement, separated by a distance $\mathbf{r}$, and the distance itself (in 3D):

$$-\frac{4}{5}\varepsilon^v r = \langle (v'_\parallel - v_\parallel)^3 \rangle \,, \tag{1.1}$$

where $\langle\rangle$ denotes an ensemble average, the parallel direction $\parallel$ is the one along the vector separation $\mathbf{r}$, v is the velocity and ε^v is the mean (kinetic) energy dissipation rate per unit mass. To obtain this exact result the assumptions of homogeneity and isotropy are made (Batchelor, 1953). The former assumption is satisfied as long as we are at the heart of the fluid (far from the boundaries) and the latter is also satisfied if no external agent (like, for example, rotation or stratification) are present. Additionally, we need to consider the long time limit for which a stationary state is reached with a finite ε^v and we take the infinite Reynolds number limit ($\nu \to 0$) for which the mean energy dissipation rate per unit mass tends to a finite positive limit. Therefore, the exact prediction is valid, at first order, in a wide inertial range. This prediction is well supported by the experimental data (Frisch, 1995). Note that this type of law has been extended by Yaglom (Yaglom, 1949) to scalar passively advected (by still an incompressible fluid), such as the temperature or a pollutant in the atmosphere.

The four-fifth's law is a fundamental result used to develop scaling law models like the famous – but not exact – 5/3-Kolmogorov spectrum. For higher-order correlation functions, significant deviation from a linear law deduced directly from the four-fifth's law is found in experiments and direct numerical simulations: this deviation which has led to the development of several models is called intermittency.

2 Incompressible MHD Turbulence

2.1 Homogeneity and isotropy assumptions

For astrophysical fluids, the Navier-Stokes description is a rather poor model and we generally prefer to use the magnetohydrodynamics approximation which describes quite well the large-scale plasma dynamics. The question of the existence of an exact relation between a two-point measurement, separated by a distance $\mathbf{r}$, and the distance itself is naturally addressed. A positive answer was given by Politano & Pouquet only in 1998 (see

[1] Institut d'Astrophysique Spatiale, Bât. 121, Université Paris-Sud XI, 91405 Orsay, France; Institut Universitaire de France

also Chandrasekhar (1951)) for incompressible MHD turbulence. The addition in the analysis of the magnetic field and its coupling with the velocity field renders the problem more difficult and, in practice, we are dealing with a couple of equations. In this case, the possible formulation in 3D is:

$$-\frac{4}{3}\varepsilon^{\pm} r = \langle (z'^{-}_{\parallel} - z^{-}_{\parallel}) \sum_i (z'^{+}_i - z^{+}_i)^2 \rangle \,, \tag{2.1}$$

where the parallel direction $\parallel$ is still the one along the vector separation $\mathbf{r}$, $\mathbf{z}^{\pm} = \mathbf{v} \pm \mathbf{b}$ is the Elsässer fields (with $\mathbf{b}$ normalized to a velocity field) and $\varepsilon^{\pm}$ is the mean energy dissipation rate per unit mass associated to the Elsässer energies. To obtain these exact results the assumptions of homogeneity and isotropy are still made, and we also consider the long time limit for which a stationary state is reached with a finite $\varepsilon^{\pm}$ and we take the infinite (magnetic) Reynolds number limit ($\nu \to 0$ and $\eta \to 0$) for which the mean energy dissipation rates per unit mass tend to a finite positive limit. Therefore, the exact prediction is again valid, at first order, in a wide inertial range. Some comments have to be made on these 4/3's law. First, we do not really make a distinction between the viscosity ν and the magnetic resistivity η in the treatment which means that we basically assume a unit magnetic Prandtl number. Second, the isotropy assumption, which mainly appears in the development of the kinematics (Batchelor, 1953), is stronger for magnetized fluids since most of the situations found in astrophysics is far from isotropy. A good example is the solar wind where *in situ* measurements demonstrate the anisotropic nature of turbulence. Nevertheless, the use the 4/3's law gives interesting results (Sorriso-Valvo, 2007; MacBride et al., 2008). Another example is given by the Sun where many thin coronal loops are well observed which are considered as a signature of anisotropy (see *e.g.* Bigot et al., 2008). Note finally that an extension of this 4/3's theorem to 3D Hall-MHD has been obtained recently (Galtier, 2008) which provides a relevant tool to investigate the non-linear nature of the high frequency magnetic field fluctuations in the solar wind (see, *e.g.* , Goldstein et al., 1994; Markovskii et al., 2006; Galtier & Buchlin, 2007).

The four-third's law is a fundamental result which may be used to develop scaling law models for different-order correlation functions. However, the situation is not as clear as for neutral fluids since there are two time-scales in MHD: the eddy-turnover time and the Alfvén time. The former time is associated to the transfer time for Navier-Stokes turbulence; the latter time has to be seen as the time of interaction between two counter-propagating Alfvén wave packets (see Fig.1) During a collision, there is a deformation of the wave packets in such

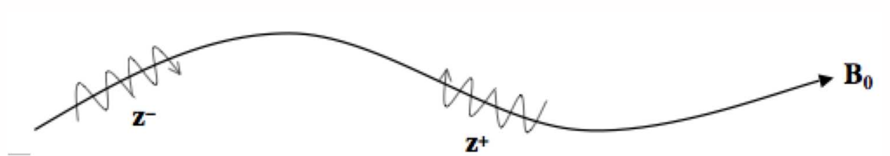

Fig. 1. Alfvén wave packets propagating along a magnetic field line.

a way that energy is transferred mainly at smaller scales. The multiplicity of collisions leads to the formation of a well extended power law energy spectrum whose index lies between $-5/3$ (Kolmogorov's prediction) or $-3/2$ (Iroshnikov-Kraichnan's (1964-1965) prediction). The precise value is still the subject of many discussions.

2.2 Beyond isotropy

The weakness of the Iroshnikov-Kraichnan (IK) phenomenology is the apparent contradiction between the presence of Alfvén waves and the absence of an external uniform magnetic field. The external field is supposed to be played by the large-scale magnetic field but its main effect, *i.e.* anisotropy, is not included in the description. One of the most important difference between neutral and magnetized fluids is the possibility in the latter case to have a large-scale field which cannot be removed by a galilean transform. This large-scale component corresponds to a large-scale magnetic field $\mathbf{B_0}$ (see Fig. 1). The role of a uniform magnetic field has been widely discussed in the literature and, in particular, during the last two decades (see, *e.g.* , Montgomery & Turner, 1981; Shebalin et al., 1983; Ng & Bhattacharjee, 1996; Verma, 2004). At strong $\mathbf{B_0}$ intensity, one of the most clearly established results is the bi-dimensionalization of MHD turbulent flows with a strong reduction of nonlinear transfers along $\mathbf{B_0}$. In the early eighties, it was shown that a strong B_0 leads to anisotropic turbulence with an energy concentration near the plane $\mathbf{k} \cdot \mathbf{B_0} = 0$, a result confirmed later on by direct numerical simulations in two and three space dimensions. From an observational point of view, we have also several evidences that astrophysical (and laboratory) plasmas are mostly in anisotropic states like in the solar wind (Bruno & Carbone, 2005) or in the interstellar medium (Elmegreen & Scalo, 2004; Scalo & Elmergreen, 2004).

The effects of a strong uniform magnetic field may be handled through an analysis of resonant triadic interactions (Shebalin et al., 1983) between the wavevectors $(\mathbf{k}, \mathbf{p}, \mathbf{q})$ which satisfy the relation $\mathbf{k} = \mathbf{p} + \mathbf{q}$, whereas the associated wave frequencies satisfy, for example, $\omega(\mathbf{k}) = \omega(\mathbf{p}) - \omega(\mathbf{q})$. The Alfvén frequency is $\omega(\mathbf{k}) = \mathbf{k} \cdot \mathbf{B_0} = k_\parallel B_0$, where $\parallel$ defines the direction along $\mathbf{B_0}$ ($\perp$ will be the perpendicular direction to $\mathbf{B_0}$). The solution of these three-wave resonant conditions directly gives, $q_\parallel = 0$, which implies a spectral transfer only in the perpendicular direction. For a strength of B_0 well above the *r.m.s.* level of the kinetic and magnetic fluctuations, the nonlinear interactions of Alfvén waves may dominate the dynamics of the MHD flow leading to the regime of (weak) wave turbulence where the energy transfer, stemming from three-wave resonant interactions, can only increase the perpendicular component of the wavevectors, while the nonlinear transfers is completely inhibited along $\mathbf{B_0}$ (Galtier et al., 2000).

Another important issue discussed in the literature is the relationship between perpendicular and parallel scales in anisotropic MHD turbulence (see Higdon, 1984; Goldreich & Sridhar, 1995; Boldyrev, 2006). In order to take into account the anisotropy, Goldreich & Shridar (1995) proposed a heuristic model based on a critical balance between linear wave periods and nonlinear turnover time scales, respectively $\tau_A \sim \ell_\parallel / B_0$ and $\tau_{NL} \sim \ell_\perp / u_\ell$ (where $\ell_\parallel$ and $\ell_\perp$ are the typical length scales parallel and perpendicular to $\mathbf{B_0}$), with $\tau_A = \tau_{NL}$ at all inertial scales. Following the Kolmogorov arguments, one ends up with a $E(k_\perp, k_\parallel) \sim k_\perp^{-5/3}$ energy spectrum (where $\mathbf{k} \equiv (\mathbf{k}_\perp, k_\parallel)$ and $k_\perp \equiv |\mathbf{k}_\perp|$) with the anisotropic scaling law

$$k_\parallel \sim k_\perp^{2/3} . \tag{2.2}$$

A generalization of this result has been proposed recently (Galtier et al., 2005) in an attempt to model MHD flows in both the weak and strong turbulent regimes, as well as in the transition between them. In this heuristic model, the time-scale ratio $\chi = \tau_A / \tau_{NL}$ is supposed to be constant at all scales but not necessarily equal to unity. The relaxation of this constraint enables to still recover the anisotropic scaling law (2.2) and to find a universal prediction for the total energy spectrum $E(k_\perp, k_\parallel) \sim k_\perp^{-\alpha} k_\parallel^{-\beta}$, with $3\alpha + 2\beta = 7$. According to direct numerical simulations (see, *e.g.* Cho et al., 2000; Maron & Goldreich, 2001; Shaikh & Zank, 2007), the anisotropic scaling law between parallel and perpendicular scales (2.2) seems to be a robust result and an approximately constant ratio χ, generally smaller than one, is found between the Alfvén and the nonlinear times. This sub-critical value of χ implies therefore a dynamics mainly driven by Alfvén waves interactions.

In the weak turbulence limit, the time-scale separation, $\chi \ll 1$, leads to the destruction of some nonlinear terms, including the fourth-order cumulants, and only the resonance terms survive (Zakharov et al., 1992; Galtier et al., 2000) which allows to obtain a natural asymptotic closure for the wave kinetic equations. In absence of helicities and for $k_\perp \gg k_\parallel$, the dynamics is then entirely governed by shear-Alfvén waves, the pseudo-Alfvén waves being passively advected by the previous one. In the case of an axisymmetric turbulence, and in the absence of cross-correlation between velocity and magnetic field fluctuations, the exact power law solution is $E(k_\perp, k_\parallel) \sim k_\perp^{-2} f(k_\parallel)$, where f is an arbitrary function taking into account the transfer inhibition along $\mathbf{B_0}$. First evidences of this regimes by direct numerical simulations are now obtained (Perez & Boldyrev, 2008; Bigot et al., 2008).

3 Compressible MHD Turbulence

Compressible turbulence has many applications in astrophysics and, in particular, in the interstellar medium where the plasma is thought to be highly compressible. For example, radio wave scintillation observations reveal a nearly Kolmogorov spectrum of density fluctuations in the ionized interstellar medium. Unfortunately, the previous exact results – the 4/5's law – has no equivalent even for compressible neutral fluids. It is therefore more difficult to predict the scaling-laws for intermittency although astrophysical data are available (see *e.g.* Burlaga, 1991). Under some restricted conditions ($\beta \ll 1$), wave turbulence may apply to compressible MHD and give some exact results (Kuznetsov, 2001, Chandran, 2005). It is shown that three-wave interactions transfer energy to high-frequency fast waves and, to a lesser extend, high-frequency Alfvén waves with a strong anisotropy. In strong turbulence, one has also to make the distinction between Alfvén waves, fast and slow magneto-acoustic waves. In this regime, direct numerical simulations are the best way to extract any scaling laws (see *e.g.* Kowal et al., 2007). Basically, a different behavior is found for sub and supersonic flows with in the latter case a strong dependence in the sonic Mach number.

4 Conclusion

Many questions are still opened in astrophysical turbulence but super-computers can now reveal some new features which, conjointly with theoretical efforts, will certainly help to deeper understand the complex dynamics of MHD fluids and , in particular, in the compressible case.

Aknowledgments

This work was supported by the ANR project no. 06-BLAN-0363-01 “HiSpeedPIV”.

References

Batchelor, G.K. 1953, The theory of homogeneous turbulence, Cambridge Univ. Press
Bigot, B., Galtier, S., & Politano, H., 2008, Astron. Astrophys., in press
Boldyrev, S., 2006, Phys. Rev. Lett., 96, 115002
Burlaga, L.F., 1991, J. Geophys. Res., 96, 5847
Bruno, R., & Carbone, V., 2005, Living Rev. Solar Phys., 2, 1
Chandran, B.D.G., 2005, Phys. Rev. Lett., 95, 265004
Chandrasekhar, S., 1951, Proc. Roy. Soc. A, 204, 435
Cho, J., & Vishniac, E.T., 2000, ApJ, 539, 273
Elmegreen, B.G., & Scalo, J., 2004, Annu. Rev. Astron. Astrophys., 42, 211
Frisch, U. 1995, Turbulence: the legacy of A.N. Kolmogorov, Cambridge Univ. Press
Galtier, S., Nazarenko, S.V., Newell, A.C., & Pouquet, A., 2000, J. Plasma Phys., 63, 447
Galtier, S., Pouquet, A., & Mangeney, A., 2005, Phys. Plasmas, 12, 092310
Galtier, S., & Buchlin, E., 2007, ApJ, 656, 560
Galtier, S., 2008, Phys. Rev. E, 77, 015302(R)
Goldreich, P., & Sridhar, S., 1995, ApJ, 438, 763
Goldstein, M.L., Roberts, D.A., and Fitch, C.A., 1994, J. Geophys. Res., 99, 11519
Higdon, J.C., 1984, ApJ, 285, 109
Iroshnikov, P.S., 1964, Soviet Astron., 7, 566
Kolmogorov, A.N., 1941, Dokl. Akad. Nauk SSSR, 32, 16
Kowal, G., Lazarian, A., & Beresnyak, A., 2007, ApJ, 658, 423
Kraichnan, R.H., 1965, Phys. Fluids, 8, 1385
Kuznetsov, E.A., 2001, JETP, 93, 1052
MacBride, B.T., Smith, C.W., & Forman, M.A., 2008, ApJ, 679, 1644
Markovskii, S.A., Vasquez, B.J., Smith, C.W., & Hollweg, J.V., 2006, ApJ, 639, 1177
Maron, J., & Goldreich, P., 2001, ApJ, 554, 1175
Montgomery, D., &Turner, L., 1981, Phys. Fluids, 24, 825
Ng, C.S., & Bhattacharjee, A., 1996, ApJ, 465, 845
Perez, J.C. & Boldyrev, S., 2008, ApJ, 672, L61
Politano, H., & Pouquet, A., 1998, Phys. Rev. E, 57, R21
Scalo, J., & Elmegreen, B.J., 2004, Annu. Rev. Astron. Astrophys., 42, 275
Shaikh, D., & Zank, G., 2007, ApJ, 656, L17
Shebalin, J.V., Matthaeus, W.H., & Montgomery, D., 1983, J. Plasma Phys., 29, 525
Sorriso-Valvo, L., Marino, R., Carbone, V., Noullez, A., Lepreti, L., Veltri, P., Bruno, R., Bavassano, B., & Pietropaolo, E., 2007, Phys. Rev. Lett., 99, 115001
Verma, M.K., 2004, Phys. Rep., 401, 229
Yaglom, A.M., 1949, Dokl. Akad. Nauk SSSR, 69, 743
Zakharov, V.E., L’vov, V., & Falkovich, G.E. 1992, Kolmogorov Spectra of Turbulence I: Wave Turbulence, Springer-Verlag, Berlin

SF2A 2008
C. Charbonnel, F. Combes and R. Samadi (eds)

HI AND CO STUDY OF CIRCUMSTELLAR ENVIRONMENTS

Libert, Y.[1], Le Bertre, T.[1], Gérard, E.[2] and Winters, J.M.[3]

Abstract. Circumstellar shells around red giants are built over long periods of time that may reach several 10^6 years. They may therefore extend over large sizes ($\sim$ 1 pc, possibly more) and different complementary tracers are needed to describe their global properties. We have undertaken a programme designed to gauge the properties of matter in the external parts of circumstellar shells around AGB stars and to relate them to those of the central sources. We present 21-cm H I and CO rotational line data obtained on an oxygen-rich semi-regular variable, RX Lep. These emissions indicate a stellar outflow at a velocity of $\sim$ 4 km s^{-1} and a rate of $\sim 2\ 10^{-7}$ M$_\odot$ yr^{-1}, for a duration of $\sim 5\ 10^4$ years. The modeling of the H I line-profiles obtained at several different positions shows that the outflow is slowed down by the ambient ISM, and that the external parts of the circumstellar shell are dominated by gas at $\sim$ 200 K, as in the well-known "detached shell" around the carbon star Y CVn. The H I source is elongated in a direction opposite to the proper motion of the central star, as it is presently being discovered in more and more cases.

1 Introduction

Low and intermediate mass stars ($\sim$ 0.8 to 6 M$_\odot$, on the zero-age main sequence) lose a large part of their mass ($\sim$ 0.2–5 M$_\odot$) during their evolution from the main sequence until their final fate, as white dwarfs of $\sim$ 0.6–1 M$_\odot$. This process is believed to take place mainly during the asymptotic giant branch (AGB) phase, although for the low mass stars ($\sim$ 0.8 to 2 M$_\odot$) a significant fraction ($\sim$ 0.2 M$_\odot$) might be lost during the first red giant branch phase. Therefore AGB stars are surrounded by expanding circumstellar shells that are built during several 10^4 years or more, and that may extend over large distances. Molecular line emissions show that some sources may reach a size of the order of 0.1 pc in radius (e.g. IRC +10216, Fong et al. 2003). This is certainly a lower limit, since molecular species are expected to be photo-dissociated by the ambient interstellar radiation field. Indeed, IRAS has revealed that many AGB stars are associated with extended emissions at 60 and 100 μm (Young et al. 1993a) indicative of sizes that could reach 1 pc. However the continuum infrared emission cannot provide clues on the kinematics in these external parts of circumstellar shells.

With this line of thought, and taking advantage of the refurbishment of the Nançay Radiotelescope, we started in 2001 a systematic observing programme aimed at using the atomic hydrogen line at 21-cm as a diagnostic tool for the circumstellar environment around late type giants. The idea of observing H I in late-type giants was not new, but the attempts to detect it were until recently largely unsuccessful (e.g. Zuckerman et al. 1980), so that only one AGB star, Mira, had been detected (Bowers & Knapp 1988). This was surprising because hydrogen should be the most common element in late-type star ouflows. For a stellar effective temperature, $T_{\rm eff}$, larger than 2500 K hydrogen should be in atomic form from the atmosphere outwards (Glassgold & Huggins 1983). On the other hand, for $T_{\rm eff} < 2500$ K, it should be in molecular form from the atmosphere out to a radius, typically 0.1 pc, at which H_2 is expected to be photo-dissociated by the interstellar radiation field, unless self-shielding preserves it in clumps.

In this contribution we present the results that we have obtained on one of the best observed sources in our programme, RX Lep. A complete report on this source can be found in Libert et al. (2008).

[1] LERMA, UMR 8112, Observatoire de Paris, 61 av. de l'Observatoire, F-75014 Paris, France
[2] GEPI, UMR 8111, Observatoire de Paris, 5 place J. Janssen, F-92195 Meudon Cedex, France
[3] IRAM, 300 rue de la Piscine, F-38406 St Martin d'Hères, France

2 RX Lep

RX Lep is an oxygen-rich semi-regular variable of type M6III (HR 1693), probably in the early-phase of the AGB. The central star effective temperature has been estimated to be 3300 K by Dumm & Schild (1998). Therefore following Glassgold & Huggins (1983) we expect that circumstellar hydrogen is mostly in atomic form.

The parallax measured by Hipparcos (Perryman et al. 1997) places RX Lep at 137 pc from the Sun. The proper motion, corrected for the Sun motion towards the apex (Dehnen & Binney 1998), is 35 mas yr^{-1} in right ascension (RA) and 58 mas yr^{-1} in declination (Dec). This translates to a motion in the plane of the sky of $44\,km\,s^{-1}$ in the North-East direction (PA $\sim 31°$).

With the SEST we have detected RX Lep in the CO (2-1) line. We derive a stellar radial velocity $V_{lsr} = 28.9\,km\,s^{-1}$, in agreement with previous data obtained in the optical range. From the line profile and using the method of Winters et al. (2003), we obtain an expansion velocity, $V_{exp}= 4.2\ km\,s^{-1}$, and a mass-loss rate, $\dot{M} \sim 1.7\ 10^{-7}\ M_{\odot}\ yr^{-1}$. Combining with the Hipparcos proper motion, we get a 3-D space velocity of 53 $km\,s^{-1}$.

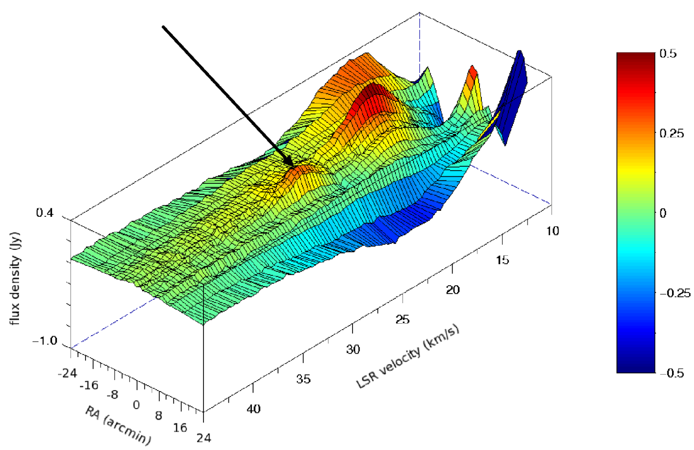

Fig. 1. 3-D position-velocity representation of the H I flux density; West is to the left. The arrow points to the expected location of the source.

RX Lep was observed in the H I line at 21 cm with the Nançay Radiotelescope between February 2005 and February 2008. At 21 cm, the telescope beam has an FWHM of 4′ in RA and 22′ in Dec. We have mapped the emission in the position-switch mode with steps of 2′ in RA and 11′ in Dec, i.e. half the beam FWHM in both directions. The main difficulty in observing the H I emission from circumstellar shells arises from the overlapping interstellar emission (see Gérard & Le Bertre 2004) and this is probably one of the main reasons for the lack of success in previous investigations (the other one being the selection of cold targets in which hydrogen is mostly molecular). We have developped a new approach in order to analyze this confusion, and to extract genuine circumstellar emission (Libert et al. 2008). In Fig. 1, we show a position-velocity diagramme in which the RX Lep emission can be discriminated against the interstellar emission. However, this has been possible only because in the direction of RX Lep and in the spectral range around its radial velocity the confusion by interstellar emission stays moderate, and also because the source is relatively bright.

The resulting spectral map is presented in Fig. 2. RX Lep is clearly detected on the central position and at several offset positions. The line profile is quasi-gaussian with an FWHM = 3.8 $km\,s^{-1}$, and a central velocity, $V_{lsr}= 28.8\ km\,s^{-1}$, in excellent agreement with the velocity derived from the CO line. The profile does not seem to vary significantly with position. In our survey of H I emission, quasi-gaussian line profile is the rule rather than the exception (Gérard & Le Bertre 2006). This type of line-profile is an indication of a slowing down of the stellar outflows in the external part of circumstellar shells. For instance the emission from the carbon star Y CVn is well reproduced by a model in which the stellar outflow is expanding up to a distance at which it is slowed down by the surrounding circumstellar matter that has been accumulating over time (Libert et al. 2007a, b). This circumstellar matter forms a slowly expanding shell (Young et al. 1993b), sometimes referred to as a “detached shell”. The same modeling provides a satisfactory fit to the line profiles obtained towards RX Lep, when assuming that the central star has undergone a constant outflow of matter ($V_{exp}= 4.2\ km\,s^{-1}$,

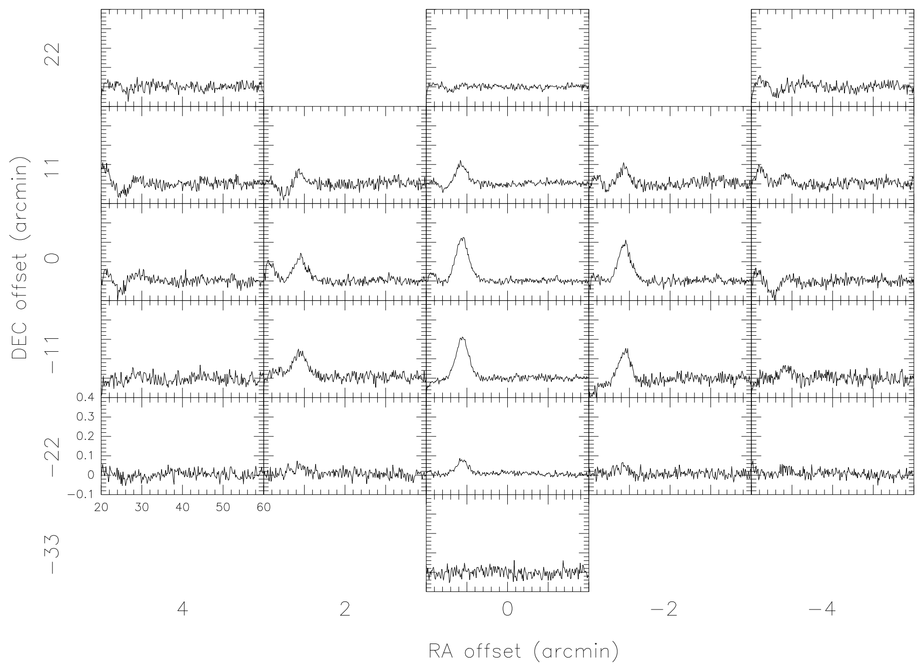

Fig. 2. H I map of RX Lep. The steps are 2′ in RA and 11′ in Dec.

$\dot{M} = 1.7\ 10^{-7}\ M_\odot\ yr^{-1}$) for 4.3 10^4 years.

In contrast to Y CVn, for which the spatial distribution of the emission is roughly circular and centered on the central star, we find that for RX Lep it is clearly offset to the South-West and elongated along the North-South direction. This can be seen on the map by comparing the flux on the central position to that 2′ West, or that 11′ South. Assuming a gaussian distribution of the brightness, we estimate the size (FWHM) of the source at 2.3′ in the East-West direction and 15′ in the North-South direction, and the offset with respect to the central star at –0.4′ in RA and –4.4′ in Dec. Therefore the source seems elongated and offset in a direction which is approximately opposite to that given by the proper motion.

3 Discussion

There is growing evidence that the external parts of circumstellar shells are shaped by their motion relative to the ambient ISM. Using the VLA Matthews & Reid (2007) have found that the H I emission discovered recently around RS Cnc (Gérard & Le Bertre 2003) is elongated in a direction opposite to its proper motion. The same morphology is apparent in Mira (Matthews et al. 2008). The latter case is particularly interesting because GALEX has discovered in the FUV (∼ 1500 Å) a 2-degree long tail associated to Mira (Martin et al. 2007). The H I emission correlates with the FUV on large scales, but not on smaller scales ($\lesssim 1'$). Finally, Ueta et al. (2006) have imaged with Spitzer the nebula discovered by IRAS around R Hya (Young et al. 1993a). At 70 μm it has a parabolic structure with a summit located ahead of the star in the direction of the space motion, suggesting an association with a bow-shock interface. This interpretation is corroborated by the presence of Hα emission co-spatial to the nebula. Wareing et al. (2006) have modeled this source and predicted the existence of a tail of ram-pressure-stripped AGB material stretching downstream.

All these elements suggest that the elongated shape of RX Lep is connected to its motion through the ISM. Villaver et al. (2003) have performed numerical simulations of the evolution of a low mass star moving through the ISM. They find that circumstellar shells are progressively distorted and become elongated in the direction of motion (e.g. left panel in their figure 1). There is perhaps a 25° difference between the RX Lep proper motion and the elongation of the shell. It might be due to the intrinsic motion of the local ISM. Such intrinsic motions have already been identified in the solar neighborhood (Lallement et al. 1995).

Based on this discussion, we propose for RX Lep the schematic description shown in Fig. 3. The central star is losing matter at a rate of $\sim 2\ 10^{-7}\ M_\odot\ yr^{-1}$. The outflow is slowed down at a termination shock, ~ 0.02 pc

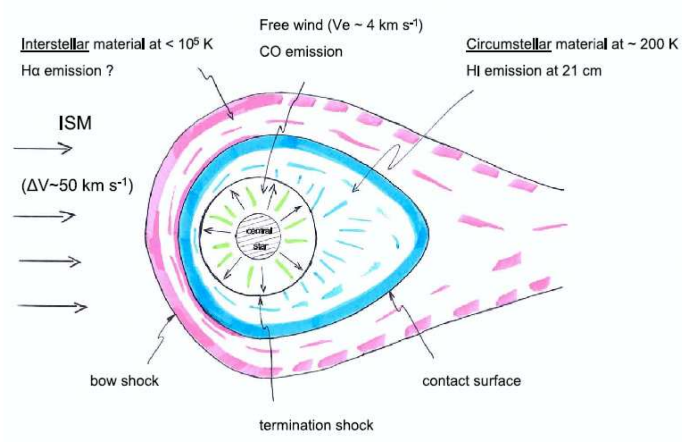

Fig. 3. Cartoon description of the RX Lep circumstellar environment (adapted from Villaver et al. 2003, cf left panel in their figure 1). The drawing is not to scale; the H I emission comes from an elongated region of $\sim 0.1\,\mathrm{pc} \times 0.7\,\mathrm{pc}$.

from the central star, leading to the formation of a "detached shell" of circumstellar matter at ~ 200 K, which, except for the shape, looks quite similar to that of Y CVn. The H I emission that we have detected comes predominantly from this region that is elongated due to the space motion of the central star. Outside the contact surface we have a region dominated by the interstellar material that has been flowing through the bow shock and that we probably cannot detect at 21 cm because it has been excited to a temperature of $\sim 50\,000$ K.

4 Conclusion

Our previous study of the H I emission around Y CVn has illustrated how the ambient ISM can slow down stellar outflows (Libert et al. 2007a, b). The present study illustrates a second effect, i.e. the shaping of circumstellar shells by their motion through the ISM. This second effect was predicted by Villaver et al. (2003). The discovery by GALEX of an extended tail associated to Mira shows that this shaping can lead to a disruption of the external regions of circumstellar shells, and ultimately to the injection of circumstellar material in the ISM.

The circumstellar environment of RX Lep provides an excellent illustration of this shaping phenomenon. The combination of CO and H I data was essential to get a global description of this circumstellar shell.

In our H I survey (Gérard & Le Bertre 2006) we have found several other cases of asymmetrical distribution of the intensity. The effect seems to be general and therefore the 21-cm line provides a useful tracer of the dynamic interaction between the external regions of circumstellar shells and the ISM.

Acknowledgements
We are grateful to Dr. Lynn Matthews for helpful discussions, and acknowledge financial support by the PCMI and the ASA.

References

Bowers P.F., Knapp G.R., 1988, ApJ, 332, 299
Dehnen W., Binney J.J., 1998, MNRAS, 298, 387
Dumm T., Schild H., 1998, New Astronomy, 3, 137
Fong D., Meixner M., Shah R.Y., 2003, ApJ, 582, L39
Gérard E., Le Bertre T., 2003, A&A, 397, L17
Gérard E., Le Bertre T., 2004, Proc. "*SF2A-2004*", F. Combes, D. Barret, T. Contini, F. Meynadier & L. Pagani (eds.), p. 295
Gérard E., Le Bertre T., 2006, AJ, 132, 2566
Glassgold A.E., Huggins P.J., 1983, MNRAS, 203, 517
Lallement R., Ferlet R., Lagrange A.M., Lemoine M., Vidal-Madjar A., 1995, A&A, 304, 461

Libert Y., Gérard E., Le Bertre T., 2007a, MNRAS, 380, 1161
Libert Y., Le Bertre T., Gérard E., 2007b, Proc. "*SF2A-2007*", J. Bouvier, A. Chalabaev & C. Charbonnel (eds.), p. 253
Libert Y., Le Bertre T., Gérard E., Winters J.M., 2008, A&A, in press (arXiv:0809.3265)
Martin D.C., Seibert M., Neill J.D., et al., 2007, Nature, 448, 780
Matthews L.D., Libert Y., Gérard E., Le Bertre T., Reid M.J., 2008, ApJ, 684, 603
Matthews L.D., Reid M.J., 2007, AJ, 133, 2291
Perryman M.A.C., Lindegren L., Kovalevsky J., et al., 1997, A&A, 323, L49
Ueta T., Speck A.K., Stencel R.E., et al., 2006, ApJ, 648, L39
Villaver E., García-Segura G., Manchado A., 2003, ApJ, 585, L49
Wareing C.J., Zijlstra A.A., Speck A.K., et al., 2006, MNRAS, 372, L63
Winters J.M., Le Bertre T., Jeong K.S., Nyman L.-Å., Epchtein N., 2003, A&A, 409, 715
Young K., Phillips T.G., Knapp G.R., 1993a, ApJS, 86, 517
Young K., Phillips T.G., Knapp G.R., 1993b, ApJ, 409, 725
Zuckerman B., Terzian Y., Silverglate P., 1980, ApJ, 241, 1014

SF2A 2008
C. Charbonnel, F. Combes and R. Samadi (eds)

DYNAMICAL EFFECTS OF COSMIC RAYS IN THE INTERSTELLAR MEDIUM

Marcowith, A.[1]

Abstract. We give a short review of the connection between cosmic-rays (CRs) and the macroscopic structures in the interstellar medium (ISM). Two complementary energy regimes provide information on the interaction of CRs with the interstellar matter. The low energy CR (LECRs) with $E \leq GeV$ usually dominate the energy density of the CR spectrum. The LECRs are of prime importance in the chemistry of diffuse and dark clouds. They can be investigated in the X and gamma-ray wavebands through the spallation reactions and iron fluorescence radiation. The highest energies (HECRs) with $E \gg GeV$ probe the ISM medium over larger scales. The recent detection of gamma radiation from the galactic ridge by the telescope Tcherenkov H.E.S.S. shows a non uniform CR distribution with respect to the local measurements. Some sites where the CRs should have a dynamical effect are finally briefly discussed.

1 Introduction

The Cosmic Ray spectrum has three main dimensions: a mass spectrum, an energy spectrum and an angular spectrum. The CR spectrum is composed of 99% of nuclei and 1% of electrons and positrons. About 89% of nuclei are protons, 9% are helium nuclei and about 1% of metals. CRs have a composition close to solar except for some particular elements produced by spallation reaction; the Lithium-Beryllium and Boron group and the sub-iron elements (Longair 1994). The energy spectrum at energies beyond the GeV can be described by a scale invariant spectrum up to the so-called CR knee at 3×10^{15}eV with an index $s \simeq 2.7$. Beyond, the spectrum softens with an index $s \simeq 3$. The highest energies show several substructures around 3×10^{17} eV and is likely associated with an extragalactic component (Nagano & Watson 2000). The spectrum seems to cut off at energies of a few 10^{20} eV (Abbasi et al 2008). Finally, the CR angular spectrum is isotropic to a level of 0.1% up to the CR knee (Iyono et al 2005). Beyond the Auger experiment has recently found some anisotropy (Abraham et al 2007). The galactic and extragalactic sources of the GeV-EeV component is still a matter of debate (Drury et al 2001, Berezinsky et al 2006). Several arguments (energy budget, diffusive shock acceleration, composition) favor the supernova remnants as a probable sources of the galactic CR component (GCR). At energies $E \leq$ GeV, the CR spectrum is modulated by the solar wind and the effective spectrum is unknown. We will see that several evidences exist for the presence of MeV CR particles in the ISM (see section 2). Higher energies (TeV-PeV) can be searched through the interplay of high energy instruments (see section 3).

The local energy density of CRs at energies close to 1 GeV is $e_{\rm CR} \simeq 1{\rm eV/cm}^3$. This energy density is of the same order of the energy density of the magnetic field and of the gas (Ferrière 2001). This fact has some important physical consequences on different domains of modern astrophysics. First as mentionned above, the assumption of an homogenous CR distribution applied all over the Galaxy implies that the supernova are the probable sources of CRs up to the knee or even a few hundred of PeV (even if no definite theoretical proof does exist). The high energy density of CRs is also important in the mechanism of the Parker instability (see Parker 1992). The CR pressure produces magnetic field loops necessary for the realisation of an $\alpha\omega$ dynamo, the principal mechanism of magnetic field generation in the Galaxy (see a review by Kulsrud 1999). The variations of CR pressure in the molecular clouds can also have an effect in the process of the cloud collapse in the star formation regions (see section 2). Finally, in some star forming regions, recent X-ray observations have concluded to an energy crisis; Cooper et al (2004) for instance reported that the mechanical energy injected by the stellar winds

[1] Laboratoire de Physique Théorique et d'Astroparticule
CNRS, Université Montpellier-II, place Eugène Bataillon, 34095 Montpellier Cédex, France

and the supernovae are not recovered in the kinetic energy of the observed expanding structures. Butt & Bykov (2008) argued that the missing energy can be injected into CRs and in turbulent motions.
The two next sections discuss observationnal evidences of the interaction of CRs with the ISM matter. The section 4 presents some aspects of the dynamical effects of CRs and discusses some interesting perspectives.

2 Low energy (MeV-GeV) CRs

2.1 Induced chemistry in the ISM

Several ion species produced in CR-ISM matter interaction are of prime interest in the chemistry of the ISM; H_3^+,HCO^+, CO, H_3O^+ .... For instance, H_3^+ is at the init of an important chain in interstellar chemical reactions:

$$H_2 \ + \ CR \rightarrow H_2^+ \ + \ e^- \ ,$$

$$H_2 \ + \ H_2^+ \rightarrow H_3^+ \ + \ H \ .$$

The H_3^+ abundances included in a network of chemical reactions allow the calculation of the local CR ionisation rate ξ (expressed in s^{-1}). Solar values are $\xi_\odot = 3 \times 10^{-17}\ \mathrm{s}^{-1}$. High ionisation rates typically $10 \times \xi_\odot$ are found in diffuse clouds (Mc Call et al 2003, van der Tak 2006), whereas low rates typically $\sim \xi_\odot/10$ have been found in some dark (opaque and dense) clouds (Caselli et al 2002). High irradiation rates have also been found in star forming or active regions ξPer and SgrB2 (Oka et al 2005). The factor 40 of enhancement of low energy CR irradiation in the central part of the galaxy corroborates the conclusions deduced from the diffuse TeV emission of the GC (Aharonian et al 2006) where a CR flux enhancement above 1 TeV by a factor 3-9 is found with respect to the local values (see section 3). There are however some possible biases to explain these high rates, noticably if the clouds are dynamically evolving (Lintott & Rawlings 2006). A possible explanation of the diffuse/dark clouds effect has been advanced recently by Padoan & Scalo (2005). The authors invoked the effect of the CR self-confinement associated with the generation of resonantly interactiong waves produced by the streaming instability. The LECR with a streaming velocity larger than the Alfvèn speed do generate Alfvèn waves, the scattering off the waves by the particles exclude the latter from the densest parts; the inner parts of a molecular cloud (Cesarsky & Völk 1978). Padoan & Scalo did found a CR density scaling $n_{\mathrm{i}}^{1/2}$ (n_{i} is the local ion density).

2.2 Spallation reactions

A possible signature of the acceleration of low energy particles in the ISM can be obtained from the interaction of CRs with the ambient medium. Several processes are associated with these interactions (see Tatischeff 2003). Energetic particles can produce continuum X-rays through Inverse Bremsstrahlung radiation (the interaction between an energetic ion and an electron) or by direct Bremsstrahlung radiation from electron/positron secondary pairs. The interaction produces also several X and gamma-ray lines: fluoresence of the Iron line (see the case of SgrB2 clouds treated in Park et al 2004), the nuclear lines excited by the CRs like ^{12}C producing a line at 4.4MeV or a line at 6.13 MeV for the oxygen 16, at 1.63 MeV for the Neon 20, at 0.845 MeV for the Iron 56 (Ramaty & Lingenfelter 1979). The gamma-ray continuum is produced by a combinaison of Inverse Compton, Bremsstrahlung radiation and neutral pion decay. Up to now any of these signatures have been found in the Galaxy (to the exception of X- and gamma-ray radiation from the Sun). However, some hints of CRs interaction have been observed again in molecular complexes in the Perseus OB2 region. In particular, Knauth et al (2000) did observed a ratio $[^7Li/^6Li] \sim 2$ in clouds close to the star ø Persei itself close a cluster of massive stars IC348 in the superbubble Perseus OB2. This ratio has to be compared to local meteoritical values close to 12. Such a ratio can be explained by the interplay of spallation reactions producing the ^7Li and ^6Li in important quantities. These radiation are now tracked by the INTEGRAL satellite and will be among the major scientific goals of the next generation of Compton telescopes.

3 High energy (TeV-PeV) CRs

There have been a recent revival interest of the expected signature of gamma-ray radiation produced by neutral pion decay from molecular clouds. This interest results from the last observations of the Tcherenkov telescopes and with the launch of the GLAST-Fermi satellite. The H.E.S.S. telescope has detected several supernova

remants (SNR) as well as diffuse radiation from the galactic ridge (see the review by Hinton et al 2006 and the references therein). Even if the origin of the gamma-ray radiation is still matter of debate (Inverse Compton radiation or neutral pion decay), several hints in favor of the interaction of the SNR with molecular clouds have been advanced (Aharonian et al 2008 and 2009 in the W28 and CTB37A cases respectively). The MAGIC telescope has recently detected some gamma-ray radiation from the SNR IC443 (Albert et al 2007). One way to ascertain the neutral pion decay origin is to produce comparitive maps in gamma-rays and in CO or to search for maser radiation. In particular several OH masers at 1720 MHz have been observed to be associated with TeV gamma-rays.
The penetration properties of CRs into molecular clouds have been investigated in a long series of work; Skilling & Strong (1976), Cesarsky & Völk (1978), Dogel' & Sharov (1990), Aharonian (2001). The effect is controlled by several processes: radiative/adiabatic losses, advection by the turbulent flow, diffusion into the magnetised medium, reacceleration by stochastic Fermi acceleration, the distance to the accelerator. Gabici et al (2007) have developped a phenomenological model of gamma-ray emission in a passive cloud embedded in a flux of CRs. The energy limit of the self-exclusion of CRs appears to depend on the cloud and turbulence parameters: the cloud density profile, the spectral index and level of the turbulence. If the gamma-ray as well as the secondary emission are not strongly sensitive to these parameters, the core emission appears extremely variable once a parameter study is undertaken. A typical core size of a pc can be resolved by Tcherenkov telescopes like H.E.S.S. and this investigation shows that TeV observations can serve as a tool to constrain the above parameters.

4 Dynamical effect of Cosmic-Rays: perspectives

The cosmic rays have an important dynamical action in the Galaxy since their energy density is approximately equal to the energy density of the galactic magnetic field and to the energy density of the interstellar gas. The CR pressure $P_{\rm cr}$ is essential in maintaining the equilibrium distribution of the gas and the magnetic field in the gravitational field above the galactic plane. The dynamical effects of CRs have also to be searched in the CR pressure gradient; i.e. in the force exerted on the magnetised fluid and not only in the local energy density of the particles. The dynamical role of CRs on the ISM structures is a subject still widely underdevelopped. It seems important to look after different situations depending on the distance of the source to the interacting site. One particular aspect connected with the work of Padoan & Scalo (2005) is the induced effect of a strong CR gradient on the dynamics of the MC core. In effect, the transition from the diffuse to the dark part of the cloud marks the position of the maximum reflexion of the CR by the self-generated waves. The position coincides also with the strongest CR gradient. The pressure gradient on the core collapse process is still to be clarified. But this effect is likely strongly dependent on the CR diffusivity in the clouds still badly known. The distance of the cloud to the CR source also dictates the main instability at the origin of the interaction; the cloud is then active or passive.

Snodin et al (2007) did investigated in a general way the effect of the CR diffusivity on macroscopic structures of the ISM. This diffusivity depends strongly on the CR spatial diffusion coefficient parallel and perpendicular to the mean magnetic field. The coefficients rely on the local properties of the turbulence. Because of this diffusive properties, the CR gas is generally found to be more uniformly distributed than the thermal gas and the magnetic field. A connexe aspect is the loosely known properties of the CR diffusion in the Galaxy. The secondary to primary ratios indicate the CR diffusion coefficient at energies of $\sim GeV$ is around $D_0 \simeq 10^{28}$ cm^2/s. However recent developments in theory of magnetohydrodynamical (MHD) turbulence find anisotropic solutions where most of the energy cascade proceeds perpendicularly to the mean magnetic field (Goldreich & Sridhar 1995 and S.Galtier in these proceedings). This type of turbulence has been shown to be highly inefficient to confine the CRs (Yan & Lazarian 2004) precisely because of this anisotropy; both linear and non-linear calculations of wave-particle interaction give estimations of the diffusion coefficients $D \gg D_0$. A correct calculation of the dynamical role of the CRs strongly depends on a better understanding of their interaction process with the electromagnetic instabilities pervading the interstellar space.

5 Conclusion

The CRs spectrum is now investigated from the MeV to Eev range. Only (till the exploration of the local ISM by the Voyager I and II missions) indirect measurements through the ionisation of the molecular clouds or the spallation reactions do probe the CR spectrum at low energies. At higher energies, the recent experimental improvements the Tcherenkov telescope technics as well as the launch of the GLAST-Fermi satellite allow (or will allow) a detailed probe of the interaction of CRs with large scale structures in the ISM. The H.E.S.S.experiment has already shown a non uniform distribution at high energies with an enhanced flux from the galactic ridge. The dynamical effects of CRs have been investigated mostly in the context of the so-called Parker instability. It however appears that the CR gradients close or far from the sources may induce important effects in the dynamical evolution of the structures in the ISM especially in connection with the star formation cycle.

The author thanks P. Hennebelle, K. Ferrière and C. Joblin for the organisation of the interdisciplinary meeting on the dynamical processes in the universe held during the SF2A 2008 workshop.

References

Abbasi, R.U. et al, 2008, PRL, 100, 1101

Abraham, J. et al, 2007, Science, 318, 938

Aharonian, F.A. et al 2009, accepted.

Aharonian, F.A. et al 2008, A&A, 481, 401

Aharonian, F.A., 2001, SSR, 99, 187

Albert, J. et al, 2007, 664, L87

Berezinsky, V. et al, 2006, PRD, 74, 043005

Butt, Y. & Bykov, A., 2008, ApJ, 677, L21

Caselli, P. et al, 2002, ApJ, 565, 344

McCall, B.J. et al, 2003, Nature, 422, 500

Cesarsky C.J. & Völk, H.J., 1978, A&A, 70, 367

Cooper, R.L. et al, 2004, ApJ, 605, 751

Dogel' V. & Sharov, G.S., 1990, A&A, 229, 259

Drury, L.O.'C. et al, 2001, SpSR, 99, 329

Ferrière, K., 2001, RMP, 73, 1031

Gabici, S. et al, 2007, ApSS, 309, 465

Goldreich, P. & Sridhar, S., 1995, ApJ, 438, 763

Hinton, J.A. et al, 2006, JPhCS, 54, 140

Iyono A. et al, 2005, proceedings of the 29^{th} ICRC conference, 101

Knauth, D.C. et al, 2000, Nature, 405, 656

Kulsrud, R., 1999, ARA&A, 37, 37

Lintott, C.J. & Rawlings, J.M.C., 2006, A&A, 448, 425

Longair, M.S., 1994, High energy Astrophysics, Cambridge university press.

Oka, T. et al, 2005, ApJ, 632, 882

Nagano M. & Watson, A.A., RMP, 72, 689

Padoan, P. & Scalo, J., 2005, ApJ, 624, L97

Park, S. et al, 2004, ApJ, 603, 548

Parker, E.N., 1992, ApJ, 401, 137

Ramaty, R. & Lingenfelter, R.E., 1979, Nature, 278, 127

Skilling, J. & Strong, A.W., 1976, A&A, 53, 253

Snodin, A.P. et al, 2006, MNRAS, 373, 643

van der Tak, F.F.S. et al, 2006, A&A, 454, L99

Tatischeff, V., 2003, EAS Publications Series, Volume 7, 2003, Final Stages of Stellar Evolution. Edited by C. Motch and J.-M. Hameury,

Yan H. & Lazarian, A. 2004, ApJ, 614, 757

SF2A 2008
C. Charbonnel, F. Combes and R. Samadi (eds)

MOBILITY OF D ATOMS ON POROUS AMORPHOUS WATER ICE SURFACES UNDER INTERSTELLAR CONDITIONS

Matar, E.[1], Congiu, E.[1], Dulieu, F.[1], Momeni, A.[2] and Lemaire, J.-L.[1]

Abstract. We report here the results of a set of experiments on the mobility of deuterium at 10 K on porous amorphous solid water (p-ASW) ice under interstellar conditions, using a temperature programmed desorption technique. Beams of O_2 and D_2 were irradiated on the surface of a p-ASW ice film and the mobility of D atoms at 10 K was investigated via their property of reacting with the O_2 molecules.

1 Introduction

Mobility of hydrogen atoms on the icy mantles of interstellar dust grains has been at the centre of numerous debates over the years, since it is crucial for the formation of the H2 molecule and hydrogenated species in the interstellar medium. Some theoretical works have predicted that atoms are mobile on amorphous surfaces (Buch & Zhang 1991), which have been corroborated by modelling of experimental data (Hornekaer & al. 2003). However, there is not a general consensus on these results, neither theoretically (Smoluchowski 1981) nor experimentally (Perets 2005). Here we will try to shed some light on this important question.

2 Methods, Results and Conclusions

To do this, we have conducted a laboratory study concerning the mobility of hydrogen atoms with the FORMOLISM (FORmation of MOLecules in the InterStellar Medium) set-up (which has been described elsewhere, e.g. Amiaud & al. 2007). In a UHV chamber, O2 molecules are deposited on porous amorphous water ice substrates of two different thickness at two different surface temperatures, 10 K and 25 K. Then the surface is exposed to varying amounts of cold D atoms (50 K). Temperature-programmed desorption (TPD) experiments are subsequently used to monitor simultaneously desorptions of both O2 molecules left on the surface and D2 molecules. The latter come from both the D2 undissociated fraction in the D beam and that of D atoms that have recombined on the surface.

In a first experiment we deposit 0.5 ML of O2 on a 20 ML porous ASW film held at 10 K. This experiment shows that the desorbing quantity of O2 decreases with respect to the increase of the amounts of D atoms. This decrease is explained by the destruction of O2 molecules by the D atoms beam. Our results show a competition between two mechanisms: D2 formation and O2 destruction. When O2 molecules are within the reach of D atoms their destruction is then favored over the formation of D2. From the TPD traces shown in Fig. 1, we notice that the decrease of the O2 signal is initially proportional to the increase of the exposure time of D atoms. The second experiment is done in order to validate the result of the first experiment on a very thick and porous ASW surface (250 ML) and by depositing O2 molecules at 10 K and at 25 K to induce their mobility. The results show very clearly that the desorbing signal of O2 still decreases (though slower than in the first experiment) with the increase of the deposited D amounts. This indicates that, even on a very thick and porous ASW surface, D atoms are able to diffuse and find the deeply hidden O2.

The experimental data we present are best explained if D atoms are mobile on the ice surface during the time of the experiment (before the TPD heating ramp), thus supporting the chemical models that include the mobility of H atoms at 10 K.

[1] Université de Cergy-Pontoise & Observatoire de Paris, LERMA, UMR 8112 du CNRS, 95000 Cergy-Pontoise, France
[2] LCAM, Universite Paris-Sud, Orsay, France

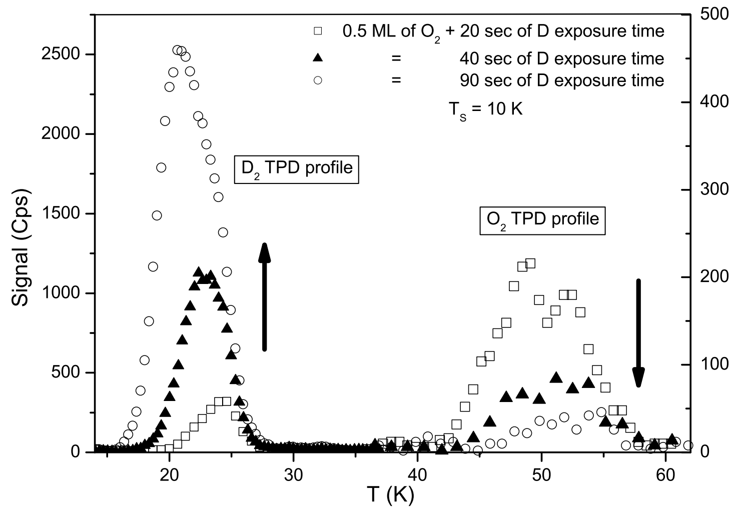

Fig. 1. TPD profiles of D2 and O2 for different exposure times of D atoms at constant O2 dose on 20 ML p-ASW. The decrease of the O2 signal is linked to the increase of the exposure time of D atoms (as indicated by the arrows)

References

V. Buch, and Q. Zhang, ApJ., 379 (1991) 647

L. Hornekaer, A. Baurichter, V. V. Petrunin, D. Field, and C. A. Luntz, Science, 302 (2003) 1943

R. Smoluchowski, Astr. Space Sci. 75 (1981) 353-363

H. B. Perets, O. Biham, G. Manico, V. Pirronello, J. Roser, S. Swords, and G. Vidali, ApJ, 627 (2005) 850

Amiaud, L., Dulieu, F., Fillion, J.-H., Momeni, A., Lemaire, J. L, J. Chem. Phys., 127 (2007) 144709

SF2A 2008
C. Charbonnel, F. Combes and R. Samadi (eds)

INTERSTELLAR DUST ON THE EVE OF HERSCHEL AND PLANCK

Miville-Deschênes, M.-A.[1]

Abstract. In this contribution I review some of the key scientific questions that animate the interstellar dust community a few months before the launch of Herschel and Planck. Great progress have been made in the past 25 years on the subject of interstellar dust using infrared observations from space. With the advent of sub-millimeter and millimeter observations with Herschel and Planck, new scientific challenges are coming and exciting discoveries are to be expected. In particular Herschel and Planck will bring key information 1) on the growth process of dust grains, the first step toward the formation of planetesimals, 2) on the structure of the interstellar medium and its link with interstellar turbulence, 3) on the physical conditions of the Galactic halo clouds which are thought to have some cold dust, 4) on the properties of the interstellar magnetic field and 5) on the interstellar PAHs using their spinning dust emission in the millimeter.

1 Introduction

Even though interstellar dust weights less than one percent of the whole interstellar matter it plays an important role in the physics of the interstellar medium (ISM). Dust grains act as catalysis for chemical reactions (especially H_2), they participate in the heating of the diffuse gas through the photo-electric effect and they absorb starlight allowing molecules to survive. With its size distribution spanning the range from big molecules to micron size particles, dust grains can be used as a tracer of the dynamical conditions of the ISM. As it absorbs and gets heated by starlight interstellar dust is a reliable tracer of the star formation activity. Also, being well mixed with the gas, dust emission and extinction is often used to trace the structure of the ISM. Interstellar dust is a complex subject as it involves solid state physics, laboratory experiments, interplanetary samples analysis, numerical simulations (radiative transfer, aggregate growth...), modeling and observations from the ultra-violet to the radio, in emission, extinction and polarization.

Great progress have been made on the subject of interstellar dust since the 1980s, thanks to infrared observations from space with IRAS, COBE, ISO and Spitzer. Moving to the sub-millimeter and millimeter range with Herschel and Planck, we expect to live a similar evolution in our understanding of the interstellar medium in general and of big dust grain in particular. Herschel and Planck will bring key informations on the structure of the ISM, from a few arc-seconds to the whole sky, and from cirrus clouds to dense cores. They will help characterized in detail the evolution of big grains and especially their growth process. Planck will also make a significant contribution as it will make the first all-sky survey of the polarized dust emission, giving access for the first time to the properties of the interstellar magnetic field through all phases of the ISM. Its wavelength range will also allow to describe in more detail the spinning dust emission in the millimeter. In this contribution I present the context in which the interstellar dust community is preparing for Planck and Herschel by giving examples of recent studies and comments on the expected progress.

2 From PAHs to big grains

The emission from interstellar dust is observed from the near-infrared to the radio. It corresponds to the emission from dust grains of size ranging from big molecules to tenths of micron. The size distribution of dust grains is the result of an evolution through a variety of processes tightly related to the dynamics of the ISM. Low energies collisions with the gas leads to accretion of atoms or molecules, and grain-grain collisions produce

[1] Institut d'Astrophysique Spatiale (CNRS), Université Paris-Sud, bâtiment 121, 91405, Orsay, France

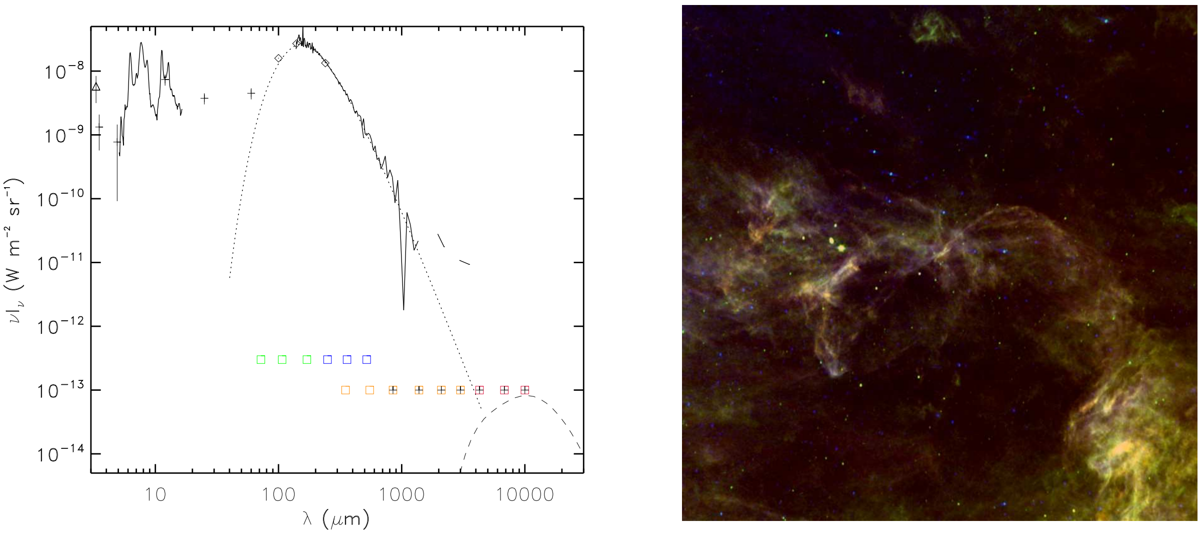

Fig. 1. Left: Emission spectrum from interstellar dust, for a gas column density of $N_H = 10^{20}$ cm^{-2}. Data used in this figure are from ISO, Arome, DIRBE and FIRAS (see Boulanger (1999) for details). The dotted line is a modified black-body spectrum at 17.5 K with $\beta = 2$. The dashed line represents a typical spinning dust emission spectrum, normalized to the 23 GHz map of Miville-Deschênes et al. (2008). The color squares show the central wavelength of the PACS (green), SPIRE (blue), Planck-HFI (orange) and Planck-LFI (red) channels. The Planck polarized channels are indicated with additional crosses. **Right:** $25° \times 25°$ RGB image of the North Celestial Loop as observed by IRAS. Red is 100 μm, green is 60 μm and blue is the average of 12 and 25 μm. Data are from the IRIS dataset (Miville-Deschênes & Lagache 2005). The color variations seen in this image of a diffuse high Galactic latitude cloud, uniformly heated by the interstellar radiation field, reveal variations of the relative abundance of smaller to bigger grains. These variations are seen at all scales in this image which implies that dust grains evolve rather rapidly, even in these diffuse environments.

grain growth (coagulation). At higher energies, typical of interstellar shocks, grains are eroded by the gas or fragmented in grain-grain collisions (Guillet et al. 2007).

Interactions with the radiation field also modify grains. Photons can activate chemical reactions, modify grain structure and even destroy the smaller particles. These smallest dust grains (the PAHs for Polycyclic Aromatic Hydrocarbons) have been the subject of many studies in the past 20 years especially with ISO and Spitzer. Their emission spectrum is now well characterized. The strong emission features of PAHs in the mid-infrared allows to study in details the interstellar physical conditions in photo-dominated regions and the physical properties of these particles, especially their charge state (Flagey et al. 2006). Based on this knowledge, Compiègne et al. (2007) observed the signature of neutral PAHs in a HII region away from the PDR which put constraints on the evolution of these particles in moderate radiation fields. Recently Berné et al. (2007) presented a study based on mid-infrared spectroscopic observations of PDRs obtained with Spitzer. Their detailed analysis of the PAH emission is in favor of a scenario where some PAHs would be the result of fragments detached from bigger grains (the so-called Very Small Grains - VSGs) by photo-evaporation.

PAH emission is now routinely observed in PDRs, at the surface of molecular clouds and in translucent and diffuse clouds. Recently it has also been observed at the surface of disks around Herbig Ae stars at 11.3 μm with VISIR on the VLT (Doucet et al. 2007). These observations offer a new opportunity to study the flaring structure of disks and the evolution of dust grains in the first phases of star and planet formation. Understanding the growth process of interstellar grains is essential in the context of planet formation but it seems that it is an efficient mechanisms even in molecular clouds. There are some observational evidences that grain growth through grain-grain collision can lead to grains with a more open structure, mid-way between compact spheres and fluffy aggregates (Dominik & Tielens 1997). These grains would have a higher surface/mass ratio than compact spheres which modifies their absorption and emission efficiency, leading to a lower equilibrium temperature (Stepnik et al. 2003) and to a modification of their emission spectrum in the far-infrared to millimeter range (Boudet et al. 2005; Meny et al. 2007). Observational evidences of this effect came recently from the detection

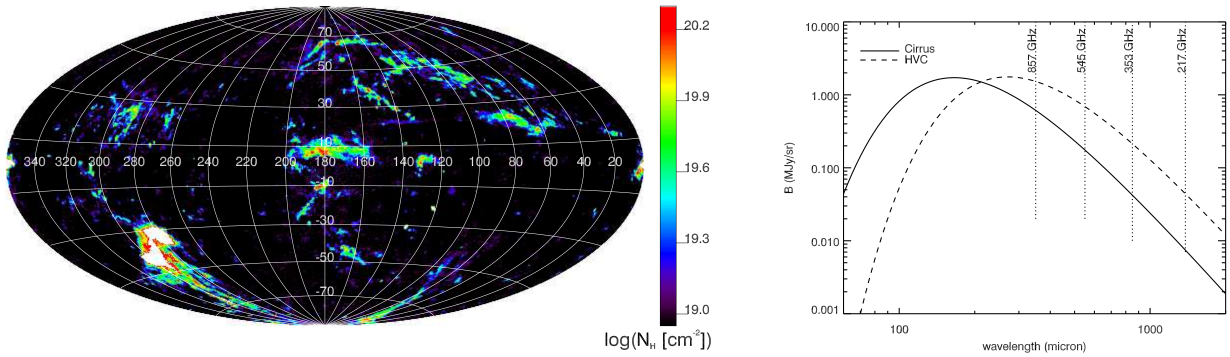

Fig. 2. Left: All-sky map of the High-Velocity Clouds (HVC) at 21 cm as given by the Leiden-Argentine-Bonn survey. The map is centered on the Galactic anti-center region. The bright region at (l∼290, b∼-40) are the Magellanic Clouds. **Right:** Comparison of thermal dust emission for a typical cirrus (T_{dust} = 17.5 K) and a HVC (T_{dust} = 10.7 K). The vertical dotted lines show the expected brightness sensitivity for the four highest frequencies of Planck-HFI after 14 months of observations.

of 304 cold dense cores by the Archeops experiment (Désert et al. 2008).

For now most of the information on the big grain emission in the submm-mm range comes from dedicated observations of selected targets (using SCUBA, PRONAOS, ARCHEOPS for example) or from the all-sky survey of FIRAS on-board COBE. This last experiment provided the only all-sky map of the submm interstellar emission to date but with very limited sensitivity (see the noise level on the spectrum in Fig. 1 - left) and low angular resolution (7°). Planck will improve significantly the situation by providing all-sky maps of the big grain emission at the same resolution than IRAS (5'). In addition, with its better angular resolution (∼ 10" for PACS and ∼ 30" for SPIRE) Herschel will allow to study in greater details the properties of dust emission at small scales in selected regions. This situation is comparable to the leap forward that has been done on the understanding of the PAH emission with the all-sky surveys of IRAS at 12 and 25 μm and the higher resolution observations done with the ISO and Spitzer satellites. With their wavelength range covering the big grain emission (see Fig. 1) and their better angular resolution, Herschel and Planck will certainly modify greatly our understanding of the bigger dust grains and especially of their growth process.

3 Dust, the structure and the mass of the interstellar medium

Being relatively well mixed with the gas, dust grains offer a way to trace the structure of the interstellar medium. This is only true when dust grains are uniformly heated by the radiation field. If not, radiative transfer has to be taken into account to separate contributions from the density and radiation field variations to the emission structure observed (Heitsch et al. 2007). Coupled with the knowledge of how three-dimensional fluctuations are projected on a two-dimensional observed sky, statistical methods can be used to estimate the power spectrum of the density field of interstellar matter in three dimensions in diffuse clouds (see an example of such a diffuse region in Fig. 1 - right). Miville-Deschênes et al. (2007) used this technique to highlight the fact that the density field of interstellar matter follows a power law with a spectral of -3 on average. Furthermore these authors studied the behavior of the non-Gaussianity of the emission fluctuations and could come up with a prescription to simulated realistic non-Gaussian interstellar emission maps. A similar analysis was done by Ingalls et al. (2004) who used 24 μm Spitzer / 25 μm IRAS data of the Gum nebular region to estimate the structure of the medium and the depth of the emitting medium, which corresponds in this case to the depth to which the UV radiation penetrates in the cloud to heat the Very Small Grains.

Observations in the submm-mm range with Herschel and Planck will allow to trace the structure and mass of big grains, including the colder component which is too cold to have a detectable emission in the IRAS bands. Therefore these new experiments will provide a more complete view of interstellar structure, from diffuse to molecular clouds, which is an important aspect of our understanding of the dynamical processes involved in the evolution of matter.

These submm-mm observations will also allow to study the properties of clouds in the Galactic halo and especially High-Velocity Clouds (HVCs - see Fig. 2 - left for an all-sky view of the 21 cm from HVCs). The location and mass of these clouds is still very uncertain but they could well represent the infall of fresh and metal poor gas that is needed to explain the star formation activity of the Galaxy. If, as was shown by Miville-Deschênes et al. (2005), the high-velocity clouds have dust, it has to be cold because of the great distance from radiation source, which would allow Planck to detect them (see Fig. 2 - right). The observation of dust emission from HVCs with Herschel and Planck would provide a new way of estimating the structure, the distance (using the dust temperature) and the mass of these enigmatic clouds.

4 Anomalous microwave emission

One of the greatest challenges of observing the Cosmic Microwave Background (CMB) in the 20-200 GHz range resides in the separation of the CMB and foreground emission. This task is facilitated by the fact that the intensity of the emission from the Galactic interstellar medium reaches a minimum in this range. On the other hand, even if the Galactic emission is weak, it is still stronger than the CMB over a significant fraction of the sky. In addition the identification of the cosmological signal is complicated by the fact that several interstellar emissions are superimposed in this frequency range: free-free, synchrotron, thermal dust and the so-called "anomalous emission" that is either attributed to energetic synchrotron (Bennett et al. 2003) or to small spinning dust grains (Draine & Lazarian 1998). The spectral shape and intensity of the emission is sketched in Fig. 1 (dashed line).

The attribution of the anomalous emission to synchrotron has two important drawback. First the correlation between the anomalous emission and the dust 100 μm emission extends down to low column density cirrus clouds, where there is no star forming activities and no local production of cosmic rays (see Davies et al. (2006)). Second the anomalous emission has been shown to be essentially unpolarized (Battistelli et al. 2006; Miville-Deschênes et al. 2008) which is in favor of the spinning dust hypothesis as it is not expected to be polarized, from theory (Draine & Lazarian 1998) and from extinction measurements of small dust grains (e.g. Martin 2007).

Recently Miville-Deschênes et al. (2008) revisited the analysis of the Galactic emission in the WMAP data. Using a joint analysis of intensity and polarization at 23 GHz they could estimate the anomalous emission over the whole sky (see Fig. 3 - left). This emission is strongly correlated to dust extinction (E(B-V)) which is also in favor of an emission mechanism involving dust grains. Here again, with its better angular resolution and sensitivity, Planck will allow to significantly improve our knowledge of this emission (see Fig. 1).

5 Polarization and magnetic field

Polarization from dust is observed in extinction in the UV to the near-infrared. It is also observed in emission in the far-infrared and submm but observations are still very sparse and mostly confined to bright molecular clouds (Vaillancourt 2007) or to the Galactic plane (Benoit et al. 2004; Ponthieu et al. 2005). Our lack of knowledge of the properties of dust polarized emission, and especially of its power spectrum, is one of the main concern for the analysis of the polarized CMB.

These observations imply that dust grains are aligned on the Galactic magnetic field even if the exact mechanism responsible for this alignment is still a matter of debate. Therefore the Planck/HFI polarization maps of dust thermal emission will provide an unprecedented perspective on the Galactic magnetic field structure in interstellar clouds. For the first time, a detailed study of the structure and intensity of the magnetic fields within nearby interstellar clouds, in relation with their density and velocity structure, will be conducted. Theoretical and numerical simulations studies showed the obvious importance of the magnetic field on the structure and dynamics of the ISM and on the regulation of the star formation efficiency. This is an area of the physics of the interstellar medium where observations has brought very little constraints up to now. In that respect the all-sky maps of dust polarization (and also synchrotron polarization) that Planck will provide will make a significant break-through in our understanding of the ISM.

The analysis of the WMAP 23 GHz polarization data (see Fig. 3) by Miville-Deschênes et al. (2008) gives a first idea on how submm-mm polarization observations can be used to estimate the parameters of the large-scale spiral structure of the magnetic field but also of its turbulent part. With the frequency range sensitive to polarization extending up to 353 GHz, the Planck data will allow to use such method jointly on the dust and synchrotron polarized emissions, and therefore better constrain the properties of the large scale Galactic magnetic field. In addition, the higher sensitivity of the Planck data will allow to perform local statistical

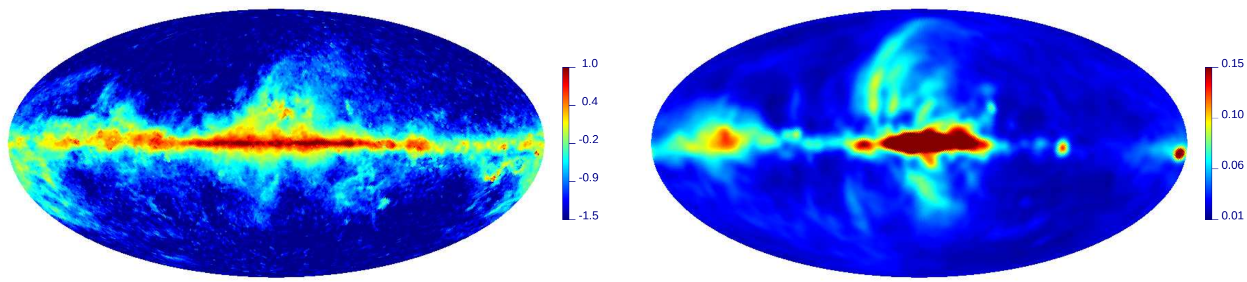

Fig. 3. Left: Anomalous emission at 23 GHz as observed by WMAP (Miville-Deschênes et al. 2008). Units are in $\log_{10}$(mK CMB). **Right:** WMAP polarized intensity at 23 GHz (in mK CMB), smoothed at 5 degrees. At this frequency the interstellar emission is strongly dominated by synchrotron. Planck will provide the first all-sky map of polarized dust emission.

analysis of the polarization angle compared with the amplitude of turbulent motion (the Chandrasekhar-Fermi method) which allow to infer the amplitude of the magnetic field in molecular and cirrus clouds.

Polarization might also help to resolve a long-standing debate about dust emission. The modeling of the dust emission spectrum and of the extinction curve leads to the presence of two populations of big grains, one silicate based and one made of carbonaceous matter. Up to now observations can not indicate whether these grain populations are physically separated or if they compose a mixture. These two dust populations should have different signature in polarization which should help to make progress in this area.

6 Conclusion

Our understanding of interstellar dust has improved spectacularly in the last 25 years, thanks to space observatories like IRAS, COBE, ISO and Spitzer. The combination of all-sky surveys and of higher-resolution observations of specific regions have brought the field of interstellar dust to a high level of complexity. In particular significant progress have ben made in the understanding of the properties and evolution of the smallest dust particles that can be observed in the mid-infrared. The observations of the diffuse PAH emission that were a challenge in the 1980s are now routinely done.

The field of interstellar dust is about to live a similar leap forward with the upcoming Herschel and Planck missions that will provide all-sky surveys and dedicated high-resolution observations of the submm and mm emission from big interstellar grains. In addition Planck will provide detailed mapping of the spinning dust emission, making a direct link with the knowledge obtained recently on interstellar PAHs. Planck will also provide polarization maps in 7 bands, giving access to the structure and intensity of the magnetic field, one of the key information still to be characterized in the ISM. Planck and Herschel will also make important contributions to long-standing questions regarding, for example, the silicate vs carbonaceous grains modeling, the mechanism of grain alignment on the magnetic field, high-velocity clouds, and the grain growth process. It is thus with excitement that we stand on the eve of Herschel and Planck.

References

Battistelli, E. S., Rebolo, R., Rubino-Martin, J. A., Hildebrandt, S. R., Watson, R. A., Gutierrez, C. & Hoyland, R. J. 2006, ApJ, 645, L141–L144.

Bennett, C. L., Halpern, M., Hinshaw, G. et al. 2003, ApJS, 148, 1–27.

Benoit, A., Ade, P., Amblard, A. et al. 2004, A&A, 424, 571–582.

Berné, O., Joblin, C., Deville, Y. et al. 2007, A&A, 469, 575–586.

Boudet, N., Mutschke, H., Nayral, C., Jäger, C., Bernard, J. P., Henning, T. & Meny, C. 2005, ApJ, 633, 272–281.

Boulanger, F. Dust emission and ism components. In A. R. Taylor, T. Landecker, G. J, editor, *New perspective on the interstellar medium*, page 173. Astronomical Society of the Pacific, 1999.

Compiègne, M., Abergel, A., Verstraete, L., Reach, W. T., Habart, E., Smith, J. D., Boulanger, F. & Joblin, C. 2007, A&A, 471, 205–212.

Davies, R. D., Dickinson, C., Banday, A. J., Jaffe, T. R., Gorski, K. M. & Davis, R. J. 2006, MNRAS, 758, 758.

Désert, F. X., Macías-Pérez, J. F., Mayet, F. et al. 2008, A&A, 481, 411–421.

Dominik, C. & Tielens, A. G. G. M. 1997, ApJ, 480, 647.

Doucet, C., Habart, E., Pantin, E., Dullemond, C., Lagage, P. O., Pinte, C., Duchêne, G. & Ménard, F. 2007, A&A, 470, 625–631.

Draine, B. T. & Lazarian, A. 1998, ApJ, 508, 157–179.

Flagey, N., Boulanger, F., Verstraete, L., Miville-Deschênes, M. A., Noriega Crespo, A. & Reach, W. T. 2006, A&A, 453, 969.

Guillet, V., Pineau Des Forêts, G. & Jones, A. P. 2007, A&A, 476, 263–277.

Heitsch, F., Whitney, B. A., Indebetouw, R., Meade, M. R., Babler, B. L. & Churchwell, E. 2007, ApJ, 656, 227–241.

Ingalls, J. G., Miville-Deschênes, M. A., Reach, W. T. et al. 2004, ApJS, 154, 281–285.

Martin, P. G. In Miville-Deschênes, M.-A. & Boulanger, F, editors, *Polarization 2005*, pages 165–188. EAS Publications Series, Volume 23, 2007.

Meny, C., Gromov, V., Boudet, N., Bernard, J. P., Paradis, D. & Nayral, C. 2007, A&A, 468, 171–188

Miville-Deschênes, M. A. & Lagache, G. 2005, ApJS, 157, 302–323.

Miville-Deschênes, M. A., Boulanger, F., Reach, W. T. & Noriega-Crespo, A. 2005, ApJ, 631, L57–L60.

Miville-Deschênes, M. A., Lagache, G., Boulanger, F. & Puget, J. L. 2007, A&A, 469, 595–605.

Miville-Deschênes, M. M. A., Ysard, N., Lavabre, A., Ponthieu, N., Macías-Pérez, J. F., Aumont, J. & Bernard, J. P. 2008, A&A, in press. arXiv:0802.3345

Ponthieu, N., Macías-Pérez, J. F., Tristram, M. et al. 2005, A&A, 444, 327–336.

Stepnik, B., Abergel, A., Bernard, J. P. et al. 2003, A&A, 398, 551.

Vaillancourt, J. E. In Miville-Deschênes, M.-A. & Boulanger, F, editors, *Polarization 2005*, pages 147–164. EAS Publications Series, Volume 23, 2007.

SF2A 2008
C. Charbonnel, F. Combes and R. Samadi (eds)

THE MEXICAN MILLION MODELS DATABASE: A VIRTUAL OBSERVATORY FOR GASEOUS NEBULAE

Morisset, C.[1]

Abstract. The 3MdB (Mexican Million Models database) is a large database of photoionization models for H II regions. The number of free parameters for the models is close to 15, incluing the description of the ionizing SED and the description of the ionized gas. The outputs of the models are more than 70 emission line intensities, the ionic fractions and temperatures. All the parameters and outputs are included in the MySQL database, giving the possibility to the user to search into the database for example for all the models that reproduce a given set of observations.

1 Introduction

The study of the ionized interstellar medium is mainly based on the analysis of the observed emission line intensities. From line ratios one may determine physical and chemical parameters of the nebulae such as the electron temperature, the electron density and the abundances of the most common elements. The characteristics of the ionizing spectrum can also be determined from the line intensities. The interaction between the ionizing source and the gas is computed a photoionization code (e.g. Cloudy, see Ferland et al. 1998) allowingto constructu numerical models of H II regions, including the intensities of the emission lines. Such models can then be compared to the observations and a fit can be defined. I present here a new database of photoionization models, which can be used to look for models that are reproducing a given observation or a given catalog of observations. This tool can be understand as a kind of H II regions virtual observatory where line intensities from millions of models can be mined.

2 P-space and O-space

One can describe a (photoionization) model as a link from the parameter-space (P-space) to the observable-space (O-space). The parameter-space is describing an object in terms of effective temperature, luminosity, size of the nebula, radial density variation, abundances, presence of dust, etc. This can be seen as the set of inputs required to compute the model. The object in the observable-space is described by the set of the emission line intensities. This is also the set of outputs of the photoionization model. The dimension of the P-space is the number of free parameters needed to describe a model, it can easily reach a value of 15 for 1D models (as when running Cloudy), many more for 3D models where the description of the density distribution is more complexe (using e.g. Cloudy_3D, see Morisset 2006). The dimension of the O-space is the number of emission line intensities that one can obtain from the photoionization code. It can be seven hundreds of lines! In the O-space we find the results of the modeling process (what we classically call the models, projections from the P-space into the O-space using a code) and also the observations of "real" objects. Actually, taking into account the error bars around each observed value of emission line intensity transform the observed objects to an hyper-boxes around the observed values (in the O-space). The relation between the shape in the P-space and the corresponding shape in the O-space is far from being linear. For example, a rectangule in the P-space does not transform into a rectangular plane in the O-space, but rather into a complex hyper-shape. This is illustrated by Fig. 2 in Stasińska et al. (2006) where a regular grid in the P-space (of 2 dimensions U and Z) transforms into a curved

[1] Instituto de Astronomía, Universidad Nacional Autónoma de México; Apdo. postal 70–264; Ciudad Universitaria; México D.F.; 04510 México. e-mail: Chris.Morisset@gmail.com

shape into the O-space. The reverse is also true: a rectangular shape into the O-space is not obtained by a rectangular shape in the P-space: this is why it is not possible to easily obtain the parameters of the models that adjust a given observation. The action of fitting an observation by some models is finding the models which are close to a given observation in the O-space. Considering the errors on the observations, this means finding the models that fall in the hyper-box around the point that represent the object in the O-space. Due to the high non-linearity of the transformation between the P- and the O-space, there is no simple way to go from an observation to the set of physical parameters that describe the object. There are various ways to find the set of values in the P-space that reproduce an observed object (a point in the O-space, or an hypercube if we take the error bars into account): By running models and figuring out what are the effect in O-space of changing something in the P-space or by automatic Khi2 method: for example Cloudy can optimize a set of parameter to fit a set of observations. Generally these methods lead to a definition of the "best" model fitting the observations of an object. One can also use regular grids of models: this method can be very useful to see the effects of changing one parameter on the observables. It gives the possibility of finding various models that fit the same observation (within the errors) The last method is to use irregular grids of models. This is the case of a grid that can be adapted to increase the density of models in P-space where this is useful. Such an approach needs observations to know which locus in the P-space is "good" (it falls in a "good" locus in the O-space : where there is observed objects). For this one can use a kind of genetic algorithm, see next section.

3 A genetic algorithm for the definition of new models

To define a genetic algorithm, we must considere two phases: a phase of selection of parents and a phase of reproduction with random evolution, leading to children The selection of the parent models is performed in the O-space, in the hyper-boxes around the observations, the sizes of the hypercube being the acceptable error on each observable (e.g. emission line intensity). Any model that falls within an hyper-box around an observation is a model selected for the reproduction (it is a parent model). A new generation of models is generated from the set of parent models. The values of the parameters for the children are determined randomly around the values of the parent models, within a given range. Each parent will generate a given number of children.

4 The 3MdB

The Mexican Million Models database (supported by CONACyT grant 49737) is a project of a huge photoionization model database, where the user can search easily and quickly for models that reproduce a given set of observations. There are more than 15 parameters that can be varied to describe a model. First the ionizing SED can be described as a Planck function, as a stellar atmosphere model, in this case the stellar metallicity and the surface gravity may also be provided. There is also a possibility to describe the SED in terms of stellar cluster. Secondly the ionized gas: the inner radius of the nebula, the hydrogen density, the abundances of the main elements, the presence of dust (composition, density), a filling factor for the gas. Once the model is computed the corresponding entry in the database is completed by adding to the parameters the intensities of more than 70 emission lines. A entry in the 3MdB is: a point in the P-space (defined by the values of all the parameters), the corresponding point in the O-space (the values of the observables, i.e. line intensities), plus a set of other characteristics of the models. The genetic algorithm described in Sec.3 is used to compute the values of the parameters for the new generation models. The observations that are used for the selection of the parent models are from various catalogs, such as part of the SDSS like the one used by Izotov et al. (2006). The database contains 1,350,000 models (October 2008). The increasing rate of the database is 350 models/hour. It actually run on a 2-double-core AMD 64 bits processors computer. The data are in MySQL tables, driven by IDL routines calling Cloudy, reading the outputs and filling the database.

References

Ferland, G. J. Korista, K.T. Verner, D.A. Ferguson, J.W. Kingdon, J.B. and Verner, E.M. 1998, PASP, 110, 761

Izotov, Y. I., Stasińska, G., Meynet, G., Guseva, N. G., & Thuan, T. X. 2006, A&A, 448, 955

Morisset, C. 2006, in IAU Symposium, Vol. 234, Planetary Nebulae in our Galaxy and Beyond, ed. M. J. Barlow & R. H. Mendez, 467–468

Stasińska, G., Cid Fernandes, R., Mateus, A., Sodré, L., & Asari, N. V. 2006, MNRAS, 371, 972

SF2A 2008
C. Charbonnel, F. Combes and R. Samadi (eds)

A FIRST STEP FOR THE UNDERSTANDING OF DISEQUILIBRATED ORTHO TO PARA RATIOS FOUND IN SPACE : STUDIES OF NUCLEAR SPIN CONVERSION OF H_2O IN RARE GAS MATRICES

Pardanaud, C.[1], Michaut, X.[1], Fillion, J.H.[1], Vasserot, A.-M.[1] and Abouaf-Marguin, L.[1]

Abstract.
As a first step before studying ices of astrophysical interest, we have investigated the parameters involved in the nuclear spin conversion of water isolated in rare gas matrices at low temperatures (4.2 K). In these environments, the water molecule rotates almost freely and is able to perform translational oscillations within the cage made of rare gas atoms. We present here a study, in the mid-infrared, of H_2O in neon, argon, krypton and xenon matrices. In all the matrices, we observed an acceleration of the nuclear spin conversion as the concentration of water in the sample increased. Calculations performed by our group show clearly that intermolecular magnetic interactions are responsible for this concentration dependence. The intermolecular process is found to slow down from neon to xenon because the lattice parameter continuously increases from neon to xenon. For diluted samples we measured times between 100 and 700 minutes depending upon the rare gas atom. It is then surprising that these times observed in cryogenic matrices are much shorter than months estimated in ice by Tikhonov & Volkov (2002) at 77 K.

1 Introduction

Water molecules represent the major species liberated as the comets approach close to the Sun. Recent observations using infrared or sub-millimetric sensitive telescopes (Crovisier 2006) allow to access to the quantum states of the molecules and specially to their nuclear spin states. In case of water, molecules are named *ortho* or *para* according as the spins of the protons are parallel (total nuclear spin I=*1*) or anti-parallel (total nuclear spin I=*0*). In gaseous phase, each rotational state is associated with only one of the nuclear magnetic species and in the high temperature limit ($\geq$ 50 K), due to spin degeneracy 1/4 of the molecules are *para*, while 3/4 are *ortho*. Below 50 K, the OPR ($ortho - to - para$) ratio at the Boltzmann equilibrium becomes strongly temperature dependent. From the OPR measured in different comets, so-called spin temperatures have been extracted and compared to the temperatures associated with other degrees of freedom of the molecules (kinetic, rotational, vibrational). The results (Crovisier 1998, 2006; Kawakita et al. 2006; Bonev et al. 2007) showed that for most of the molecules observed in different comets (C/1995 O1-Hale Bopp, C/2001 A2-LINEAR,C/2001 Q4-NEAT,..), the measured spin temperatures are spread around a mean value of 30 K while rotational temperatures are between 25 and 100 K (Bonev et al. 2007). The origin of these non equilibrated nuclear spin states is not understood yet but, if this disequilibrium have been kept constant for billions of years, the OPR would be a clue of the temperature formation of the protosolar nebulous. In this context, it is important to know the possibility for different cold media like gas (Tudorie et al. 2006), solid (Tikhonov & Volkov 2002), or surface (Tudorie et al. 2007) to conserve or not nuclear spin states disequilibria at low temperatures. We studied first nuclear spin conversion (NSC) in rare gas solids for which measurements were performed but not completely explained yet (Michaut et al. 2004 and references therein).

[1] Laboratoire de Physique Moléculaire pour l'Atmosphère et l'Astrophysique-UMR CNRS 1043, Université Paris 6, 4 place Jussieu, 75252 Paris cedex 5

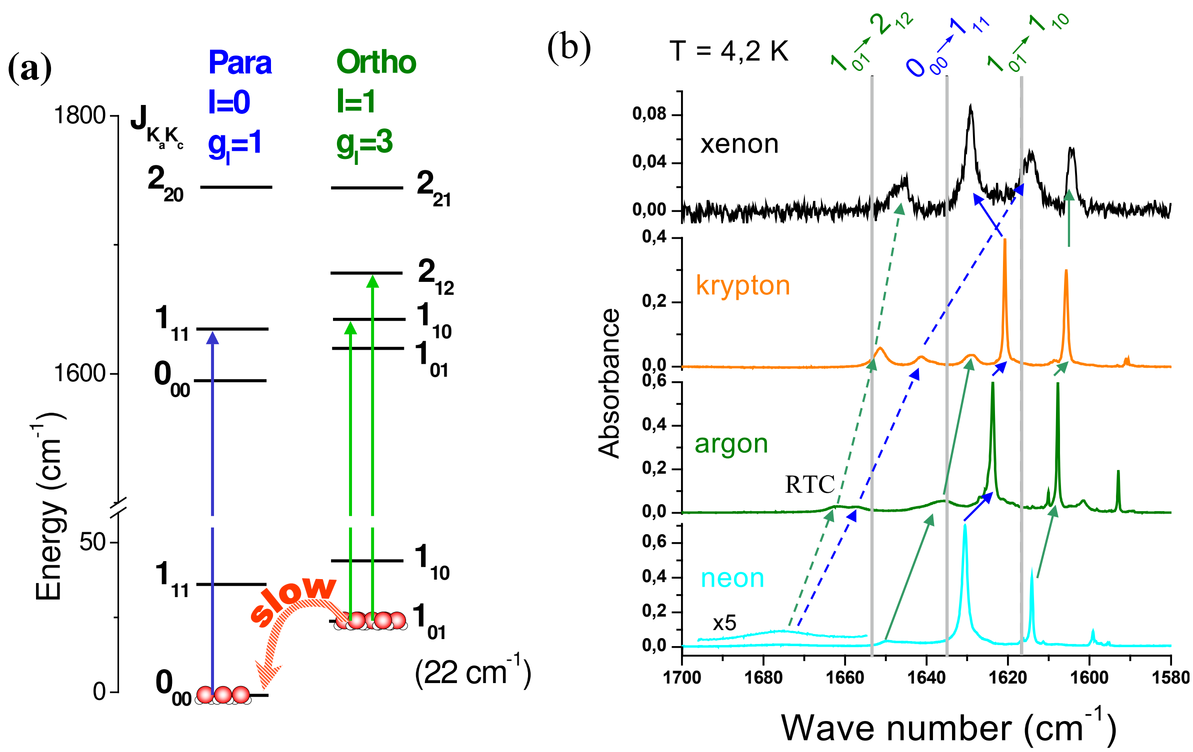

Fig. 1. Vibrational bending mode ν_2 of water. (a) Populated rotational energy levels of water molecules at low temperature and main infrared transitions observed in rare gas matrices at 4.2 K (b) Experimental spectra recorded at 4.2 K just after a fast cooling from 20 K in the different matrices. The vertical lines indicate the position of the rovibrational lines for the free molecule. RTC =Rotation-Translation-Coupling.

2 Experimental procedure

The experimental details have been described elsewhere (Pardanaud et al. 2007). The solid sample is prepared using the "spray on" technique. The gaseous mixture of H_2O (doubly distilled and outgassed), and RG=Rare Gas (Air Liquide Company, > 99.999% purity), is prepared by standard manometric procedures in a stainless steel and pyrex device. This gaseous sample is deposited onto a gold-coated copper plane mirror cooled to temperatures ranging from 4.2 K (for neon) to 35 K (for xenon) by a closed-cycle helium cryogenerator. After deposition (at 20 K for argon), the sample is first cooled down slowly to preserve optical quality of the polycrystalline layer. The light from a FTIR Bruker IFS 113v spectrometer is reflected on the mirror and thus goes twice through the solid sample before being analysed. The spectra are recorded with 0.15 cm^{-1} resolution. Due to the weakness of the electric interactions between the molecule and the atoms of the cage, it is known that the molecule can vibrate, and quasi-freely rotate (Michaut et al. 2004). The mid-infrared spectrum of the molecule is then similar to the one expected in gas at low temperature. The Figure 1.a shows the rovibrational energy diagram of water molecules in the bending region ν_2. As H_2O is an asymmetric rotor, rotational energy levels are labeled using 3 quantum numbers : the total angular momentum J and its projections K_A and K_C on the principal inertial axis of the molecule. The figure 1.b shows typical spectra of H_2O isolated in the various rare gas matrices at 4.2 K, recorded just after a fast cooling from 20 K, for a concentration H_2O/RG=1/2000. As NSC is slow the OPR value is frozen from 20 K to 4.2 K : thus the water molecules are not in Boltzmann equilibrium at that time.

The time evolution (Michaut et al. 2004) shows that the *ortho* lines decrease to the benefit of the *para* lines. As the integrated intensity of a line is proportional to the fractional population of the molecules on the initial energy level of the transition, following the time evolution of the intensity allows to measure the needed time

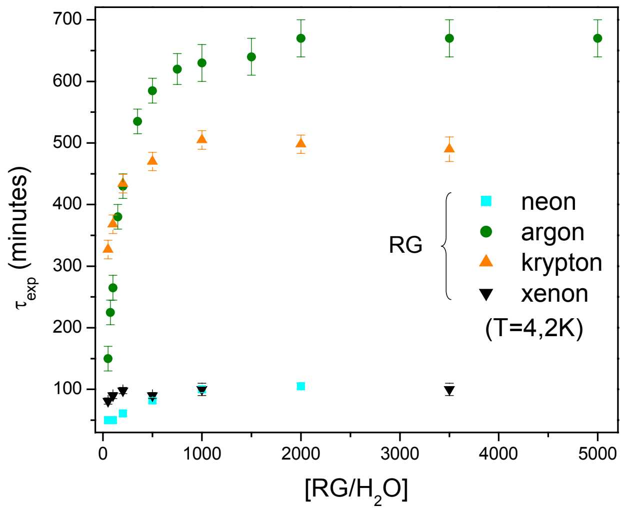

Fig. 2. Evolution of the experimental time of conversion with water dilution at 4.2 K for Ne, Ar, Kr and Xe.

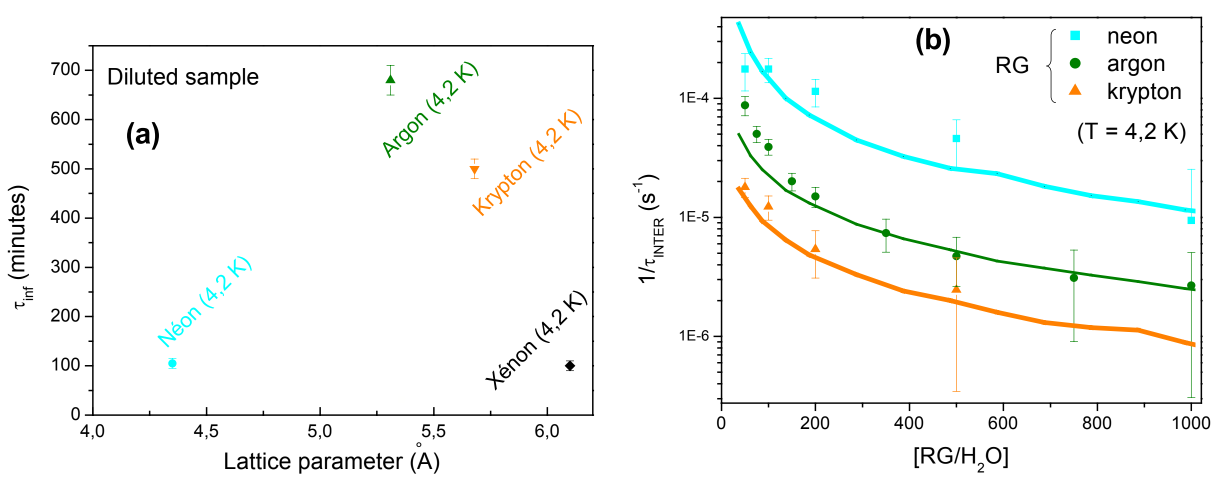

Fig. 3. Comparison of the NSC in the four matrices. (a) Diluted sample. (b) Concentrated samples. The intermolecular part of the experimental data (see text) are compared to the contributions of magnetic intermolecular interactions (lines) calculated using spin-spin interactions between water molecules randomly spread in the solid.

for the system to recover the Boltzmann equilibrium. The experimental data are fitted using single exponential decay and the characteristic conversion time τ_{exp} can be measured in various experimental conditions (Michaut et al. 2004; Pardanaud et al. 2007; Abouaf-Marguin et al. 2007).

3 Results and discussion

We have shown previously that nuclear spin conversion of water in argon is strongly dependent on the dilution from 2000 down to 50 at 4.2 K. We calculated the possible contribution of magnetic interactions between water molecules embedded in the sample. We used a numerical procedure to randomly distribute water molecules in a perfect argon lattice. The magnetic dipoles of the two protons of one molecule produce an inhomogeneous magnetic field between the two protons of a neighbouring interacting molecule. This magnetic gradient allows then the molecules to experience Rabi oscillations between the two nuclear spin states. Collisions with the rare gas atoms of the cage are then necessary to make the molecules to transfer their rotational energy to the matrix through phonons emission. This last mechanism allows the molecules to be finally trapped in the lowest energy level and thus to be converted. Calculations show that the conversion through this process is concentration dependent at low dilution ($Ar/H_2O \leq 2000$), as this process is distance dependent. Calculations also shows that for high dilutions ($Ar/H_2O \geq 2000$), these interactions can not contribute efficiently to the NSC and can not explain the conversion time of $\tau_{inf} = 680 \pm 30$ minutes measured experimentally. It seems then that for each concentration, two mechanisms coexist. The second mechanism must be concentration independent and responsible for the nuclear spin conversion for molecules infinitely diluted in the sample. To eliminate *external* effects, we checked the influence of different parameters like IR radiation from the spectrometer, presence of a metallic sample holder, or atmospheric impurities. We showed (Abouaf-Marguin et al. 2007) that no one of these parameters can explain the observed behavior. Thus the nuclear spin conversion is due to an "intrinsec" interaction with the matrix. Solid argon does not have magnetic isotopes but it hinders the rotation of the H_2O molecule. Then the only explanation of this conversion is the enhancement of intramolecular spin rotation coupling by the matrix so that the lowest *ortho* and *para* energy levels are connected, which is strictly forbidden for the isolated molecule.

We have also checked, by changing the rare gas, the influence of a small change of the environment. Figure 2 shows the evolution of τ_{exp} in function of the dilution of water in the sample for the four rare gas matrices. For higher concentrations ($Ne/H_2O \leq 500$, $Ar/H_2O \leq 2000$, $Kr/H_2O \leq 1000$) the NSC constant vary strongly leading to the conclusion that the intermolecular process is also active in Ne and Kr. Figure 3.b shows the evolution with RG/H_2O of the conversion constant due to magnetic intermolecular interaction, denoted as $1/\tau_{inter}$ and obtained by assuming that intra and intermolecular mecanisms can be decoupled following the simple law : $1/\tau_{exp} = 1/\tau_{inf} + 1/\tau_{inter}$. For a given dilution, results from the model and experiments show a good agreement. NSC from intermolecular origin is more active in Ne, than in Ar, than in Kr, because the mean distance between water molecules increases from Ne to Kr, as does the lattice parameter. However, only a tendancy has been pointed out in Xe where no clear variation has been found even when Xe/H_2O=50.

Figure 3.a shows the matrix effect on NSC in the diluted domain : a factor of ∼7 on the conversion times is encountered without any kind of continuity. The difference of mass from Ne to Xe and the presence of magnetic isotopes in Kr and Xe may play an important role.

4 Conclusions

To conclude, we showed that nuclear spin conversion is very sensitive to magnetic interactions as well as to the environment of molecules. As the decrease of mean distances between molecules in the solid enhances the NSC, this process might be very fast in pure ice. However as rotation is blocked in ice, the mechanism to liberate the excess energy might be more complicated. So it is difficult to extrapolate to pure ice which is the suitable medium for direct applications to astrophysics. Efforts are made by our group to investigate NSC in ice and to understand why conversion times observed in cryogenic matrices are so short compared to the durations of months estimated in ice at 80 K (Tikhonov & Volkov 2002).

References

Abouaf-Marguin, L., Vasserot, A.-M., Pardanaud, C., & Michaut, X. 2007, accepted in CPL

Bonev, B. P., Mumma, M. J., Villanueva, et al. 2007, ApJ 661, L97

Crovisier, J. 2006, Molecular Physics 104, 2737

Crovisier, J. 1998, Faraday Discuss. 109, 437

Kawakita, H., Dello Russo, N., Furusho, R., et al. 2006, ApJ 643, 1337

Michaut, X., Vasserot, A.-M., & Abouaf-Marguin, L. 2004, Vib. Spectrosc. 34, 83

Pardanaud, C., Vasserot, A.-M., Michaut, X., & Abouaf-Marguin, L. 2007, J. Mol. Struc. DOI:10.1016/J.molstruc.2007.03.023

Tikhonov,V. I., & Volkov, A. A. 2002, Science 296, 2363

Tudorie, M., et al. 2006, A&A DOI20064952

Tudorie, M., Khelkhal, M., Cosléou, J., Cacciani, P. 2007, Surf. Sci. 601, 1630

SF2A 2008
C. Charbonnel, F. Combes and R. Samadi (eds)

DYNAMICAL ASPECTS OF STELLAR PHYSICS

Zahn, J.-P.[1], Brun, A.-S.[2,1] and Mathis, S.[2,1]

Abstract. Several manifestations of the dynamics of stellar interiors are briefly presented, with emphasis on the most recent developments in their numerical simulation.

1 Introduction

For someone who contemplates the night sky, stars seem to behave as inert objects: their brightness does not change, except for a few of them, which are purposely called variable stars. But this is a false impression: in fact stars are extremely dynamic, as illustrated by the closest of all, our Sun. Observed through a telescope, its surface displays granules that have a lifetime of about 10 minutes. Moreover, a few dark spots are visible in general, which can be followed as they cross the disk. From their migration one can deduce the rotation of the Sun, and detect that the equator rotates faster than the regions of higher latitude. The number of spots varies with time, on a cycle of about 11 years, during which the location where they appear decreases in latitude. And when we observe the Sun in selected wavelengths, many more phenomena are revealed, such as eruptions, flares, coronal mass ejections, and these are also related with the activity cycle.

The physical processes causing this dynamical behavior have now been identified, in the Sun as well as in other stars: they are seated in the interior and the main players are thermal convection, the rotation and the magnetic field. Modeling their effects benefits greatly from the ever increasing computer resources, although it still encounters severe limitations when dealing with turbulent and highly stratified flows. We shall illustrate this here with some recent examples.

2 Thermal convection

The thermal energy which is released by the nuclear reactions in the core of stars is transported by radiation as long as the medium is transparent enough. Near the surface of solar-type stars, this is no longer the case, because the ions recombine in atoms and molecules, which increases the opacity; the temperature gradient then steepens until it becomes superadiabatic, leading to thermal convection. There, heat is transported by hot eddies moving upward and cold eddies mowing downward, and these are the motions observed as granulation at the surface of the Sun.

Surface convection is now being modeled in exquisite detail by high resolution 3-dimensional numerical simulations, where the transfer of radiation has been treated with care. The pioneers in this field were Stein and Nordlund (1998); Fig. 1 shows one of their early simulations, where the computational domain was chosen such as to accommodate 20 - 30 granules, with a resolution of $253 \times 253 \times 163$. The result is compared with pictures of the solar granulation - the agreement is excellent. Moreover, the spectral line profiles deduced from such simulations match perfectly those observed on the Sun, and they can be used to determine the surface abundance of various chemical elements (Asplund et al. 2004).

A complementary approach to model convection in solar-type stars is to treat globally the whole convection zone, except for the upper layers where the density contrast would be too high. But both sphericity and rotation are then taken in account. Figure 2 displays a simulation performed by Brun and Toomre (2002) with the ASH

[1] LUTH, Observatoire de Paris-CNRS-Université Paris-Diderot, Place Jules Janssen, F-92195 Meudon, France
[2] DSM/IRFU/Service d'Astrophysique, CEA Saclay, F-91191 Gif-sur-Yvette, France; and AIM-UMR 7158-CEA-CNRS-Université Paris 7, France

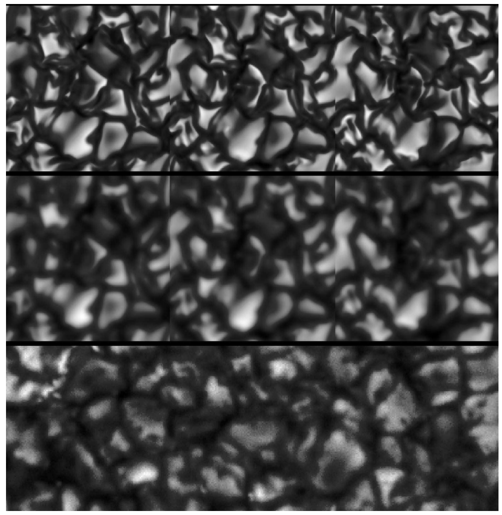

Fig. 1. Comparison of solar granulation as predicted by the numerical simulations performed by Stein & Nordlund (1998) (top row) and observed by the Swedish Solar Telescope in La Palma (bottom row). Each row presents 3 images at 1 minute intervals. In the middle row the computed image has been smoothed to account for the effect of atmospheric turbulence (courtesy ApJ).

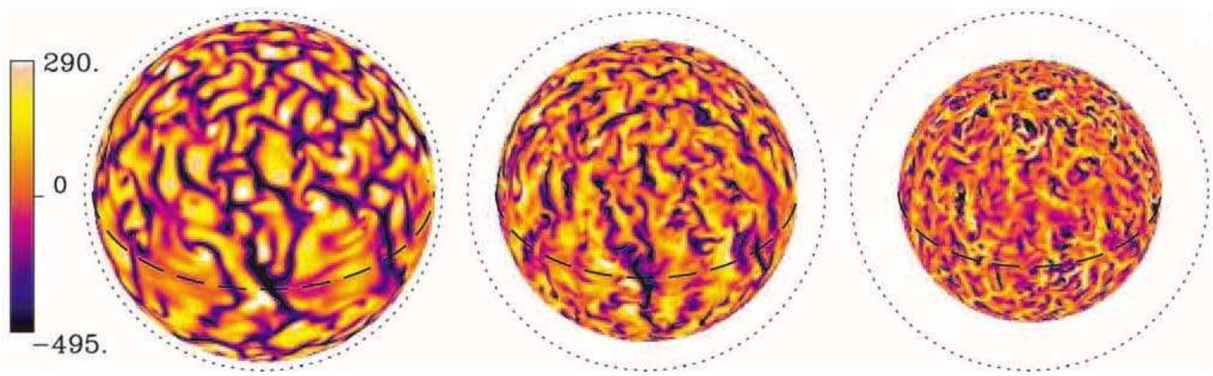

Fig. 2. Numerical simulation of solar convection, performed by Brun & Toomre (2002); the figure displays the pattern of the vertical velocity at different depths (0.95, 0.84 and 0.73 $R_\odot$). The upflows are in bright orange and the downflows in dark purple tones; the dashed circle indicates the position of the surface (courtesy ApJ).

code (for anelastic spherical harmonics) which has been specially designed to run on massive parallel computers; the resolution is $192 \times 512 \times 1024$. The main results of such simulations are that the strongest downflow lanes extend over the whole convection zone and that the equator is rotating faster than the higher latitudes, as observed on the Sun. Also, the large banana cells, that were present in earlier low resolution simulations, no longer show up here, because the level of turbulence could be substantially increased. For a recent account on global solar convection, see Miesch et al. (2008).

3 Towards a consistent model for the solar dynamo

According to the widely accepted paradigm (Parker 1955), the solar dynamo consists of two steps. In the Ω-step, the poloidal (meridian) field is sheared through the differential rotation into a toroidal (azimuthal) component. In the α-step, that toroidal field is twisted back into a poloidal field by the convective motions, that are rendered 'helical' by the Coriolis force. In Parker's original view, both mechanisms were supposed to operate in the convection zone, but since the discovery of the tachocline through acoustic sounding, it became plausible that the Ω-step takes place in that thin shear layer, which connects the differential rotation of the

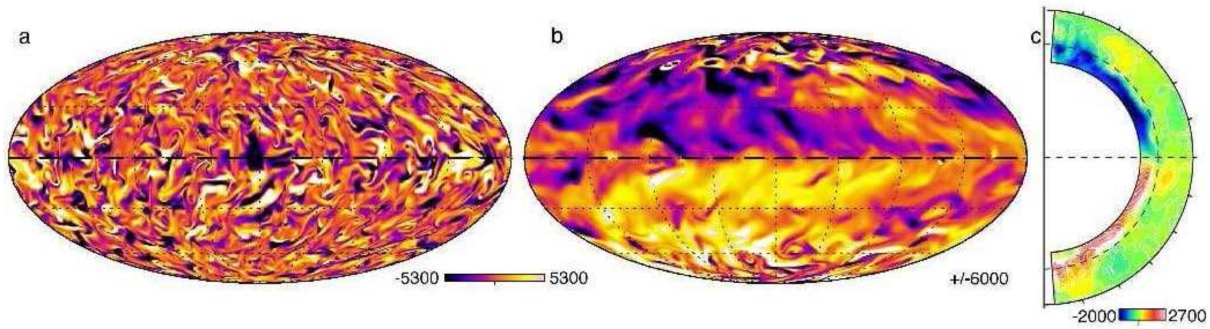

Fig. 3. Dynamo action in the solar convection zone: the Ω mechanism. Mollweide projections at one instant of the azimuthal field in the middle of the convection zone (**a**: 0.84 $R_\odot$) and in the underlying radiative region (**b**: 0.67 $R_\odot$). Panel **c**: meridional view of the azimuthal field averaged in time and longitude (Browning et al. 2007; courtesy ApJ).

convection zone, above, with the uniform rotation of the radiative interior.

Recent simulations by Browning et al. (2006) seem to confirm that expectation. A seed field grows to finite amplitude, where it is maintained for high enough magnetic Reynolds number (Rm$=v\ell/\eta$ where v is the rms velocity, ℓ the size of the convective eddies and η the magnetic diffusivity). As shown in Fig. 3, in the convection zone the longitudinal field is turbulent and not structured on large scale; once it is pumped down, by penetrating plumes, into the stable layer below (i.e. the tachocline), it is sheared into a well organized toroidal field. The calculations were run with a resolution of $98 \times 512 \times 1024$. In this simulation the α-effect, which closes the dynamo loop, is operating in the bulk of the convection zone.

4 Rotation induced mixing in stellar radiation zones

Until recently, stellar radiation zones were deemed as being motionless, except for their rotation. But now a new picture emerges, where these zones are the seat of slow flows, that are turbulent in spite of their low velocity because their characteristic scale is so large (of the order of the radius of the star). For instance a large scale circulation arises in the immediate vicinity of a differentially rotating convection zone, in the tachocline we have encountered above (Spiegel & Zahn 1992). A similar circulation occurs also in the bulk of the radiation zone, whenever angular momentum requires to be transported from one depth to the other. For instance, when a star looses angular momentum through a wind, that angular momentum is extracted from the deep interior by a large scale flow (Zahn 1992; Maeder & Zahn 1998; Mathis & Zahn 2004). That transport shapes the angular velocity profile, rendering it non uniform, and the shear of the differential rotation becomes unstable and generates turbulence. This turbulence produces mixing, and modifies the evolution of the star by carrying hydrogen rich material into the nuclear core.

These transport processes can be easily implemented in a stellar evolution code if one assumes that the turbulence generated by the shear is able to reduce the differential rotation in latitude to a point where the star can be considered in 'shellular' rotation, with the angular velocity depending only on depth. Then the problem reduces to one dimension, but with the transport of angular momentum keeping its advective character.

This rotation driven circulation explains well why on the surface of massive stars some chemical elements are observed (such as nitrogen) that have been synthesized in the core (Talon et al. 1997; Maeder & Meynet 2000). It also predicts that solar-type stars should have a fast rotating central region, but it is the contrary that is observed, through helioseismology. This means that another, more powerful process is responsible for the transport of angular momentum in these stars, and is able to render their rotation uniform.

5 Angular momentum transport in stellar radiation zones: magnetic stresses or internal gravity waves?

One candidate for this transport is the magnetic field, which can easily render the rotation uniform along the field lines of the poloidal field. However such a field, which can only be of fossil origin, will eventually connect with the convection zone above, and it should imprint the differential rotation of that zone on the radiative interior, which is not observed. Our simulations (Brun & Zahn 2006) seem to confirm that, although the results may depend somewhat on the boundary conditions applied on the top of the radiation zone (see Garaud & Garaud 2008).

Internal gravity waves are another candidate: these are waves whose restoring force is buoyancy, in a stably stratified medium. Some are excited at the edge of a convection zone and travel into the adjacent radiative region. They transport angular momentum, which they deposit at the location where they are dissipated through radiative damping, as was first pointed out by Press (1981).

Preliminary calculations by Talon et al. (2002) showed that low frequency gravity waves could indeed extract the angular momentum from the core of late-type stars, and render their rotation quasi uniform. This transport was then implemented in stellar evolution codes, together with the rotational mixing described above, and it led to results that agree very well with the observations, such as the lithium depletion in solar-type stars, both of populations I and II (Charbonnel & Talon 2005). The main weaknesses of this modeling is that it depends on the energy spectrum one assumes for these waves and that the picture given above can be modified by the Coriolis acceleration for low-frequency waves, but we should be able soon to study them with numerical simulations of penetrative convection.

6 Perspectives

Great progress has been recently achieved in understanding the dynamical behavior of stellar interiors, thanks to numerical simulations, as we have seen in those few examples. But such simulations must be validated by observational constraints, and these are provided presently by a score of instruments, ground based or in space. To mention only a few, of the most recent ones: while the mini-satellites MOST and CoRoT are probing the interior of stars through asteroseismology, the spectropolarimeters ESPaDOnS (CFHT Hawaii) and NARVAL (Pic du Midi) are mapping the magnetic field at their surface. Both to be launched in 2009, the next asteroseismic mission will be Kepler, and SDO (Solar Dynamics Observatory) promises to be as successful as SoHO, which started operating in 1995 and is still providing first rate data. No doubt, understanding the dynamical aspects of stellar physics has a bright future!

References

Asplund, M., Grevesse, N., Sauval, A. J., Allende Prieto, C., & Kiselman, D. 2004, A&A, 417, 751

Browning, M. K., Miesch, M. S., Brun, A. S., & Toomre, J. 2006, ApJ, 648, L157

Brun, A. S., & Toomre, J. 2002, ApJ, 570, 865

Brun, A. S., & Zahn, J.-P. 2006, ApJ, 457, 665

Charbonnel, C., & Talon, S. 2005, Science, 309, 2189

Garaud, P., & Garaud, J.-D. 2008, to appear in MNRAS (arXiv:0806.2551)

Maeder, A., & Meynet, G. 2000, ARA&A, 38, 143

Maeder, A., & Zahn, J.-P. 1998, A&A, 334, 1000

Mathis, S. & Zahn, J.-P. 2004, A&A, 425, 229

Miesch, M. S., Brun, A. S., DeRosa, M. L. & Toomre, J. 2008, ApJ, 673, 557

Parker, E. N. 1955, ApJ, 122, 293

Press, W. H. 1981, ApJ, 245, 286

Spiegel, E. A., & Zahn, J.-P. 1992, A&A, 265, 106

Stein, R. F., & Nordlund, Å. 1998, ApJ, 499, 914

Talon, S., Kumar, P. & Zahn, J.-P. 2002, ApJ, 574, L175

Talon, S., Zahn, J.-P., Maeder, A., & Meynet, G. 1997, A&A, 322, 209

Zahn, J.-P. 1992, A&A, 265, 115

PNC

Cosmology

SF2A 2008
C. Charbonnel, F. Combes and R. Samadi (eds)

A SYMMETRIC MILNE UNIVERSE : A SECOND CONCORDANT UNIVERSE?

Benoit-Lévy, A.[1] and Chardin, G.[2]

Abstract. The Standard Model of Cosmology predicts a rather strange composition for the energy content of our Universe: ≈70% of unknown Dark Energy and ≈25% of undetected Dark Matter, whereas ordinary matter accounts for just ≈5%. Although this representation fits rather well cosmological observations, it lacks physical meaning and is therefore unsatisfactory. We study here an alternative universe with equal quantities of matter and antimatter, in which antimatter is supposed to present a negative active gravitational mass, resulting in a coasting Milne cosmology. We present here some characteristics of this symmetric Milne universe and show that it is very surprisingly consistent with Big-Bang Nucleosynthesis, Cosmic Microwave Background and Type Ia Supernovae.

1 Introduction

In this contribution, we present the unconventionnal cosmology of a universe containing equal quantities of matter and antimatter which is supposed to present a negative gravitationnal mass. The principal motivation for this comes from General Relativity through the work of B. Carter (Carter 1968) on Kerr-Newmann metric. A Kerr-Newmann geometry with the charge, mass and spin of the electron will connect two spaces; if in the first one the ring is seen as an electron, in the second one, symmetries in the metric reverse the sign of the charge and the mass. This symmetry strongly evokes antimatter and the Kerr-Newmann solution appears as a positron in this second space.

The main consequence of this assumption is that on scales larger than the typical separation between matter and antimatter the Universe appears as gravitationally empty and is therefore characterized by a linear scale factor $a(t) \propto t$.

This symmetric Milne universe, due to the time dependence of the scale factor, does not have an horizon and therefore no inflation scenario is required. The age of the Universe is simply given by $t_H = H_0^{-1} \approx 14 \times 10^9$ years, which solves the age problem for the Universe just as ΛCDM does, but without Dark Energy. Requiring neither Dark Energy, nor Dark Matter or inflation, the symmetric Milne Universe is devoid of any free parameters.

2 Time-temperature relation and Big-Bang Nucleosynthesis (BBN)

General considerations about linearly evolving universe has been developped in (Gehlaut et al. 2003; Kaplinghat et al. 2000). As the temperature evolves as $T \propto t^{-1}$ (instead of $T \propto t^{-1/2}$ in standard cosmology), timescale is drasticaly modified during BBN. As an example, the age of the Universe at a temperature of 1 MeV is three years instead of the standard 1 s. Despite this tremendous quantity of time, a thermal nucleosynthesis of helium-4 and lithium-7 is possible as weak interactions decouple at a temperature around $T \approx 80$ keV. In order to obtain the observed abundance of helium-4, a very high baryonic density, characterized by the baryon to photon ratio η is required: $\eta = 8 \times 10^{-9}$, more that ten times the standard value. It should be noted that this high baryonic density, predicted by BBN removes the need for non-baryonic Dark Matter. Deuterium and helium-3 are strongly depleted and need to be somehow produced shortly after BBN. Presence of separated domains of matter and antimatter naturally provides a means to produce deuterium and helium-3 in adequate quantities.

[1] CEA/IRFU & IN2P3/CSNSM
[2] Université Paris Sud 11 & IN2P3/CSNSM

3 Type Ia Supernovae

Distance measurements of SNIa since 1998 are usually interpreted as demonstrating an accelerated expansion and that our Universe is composed of ≈70% of an unknown Dark Energy component. Fig 1(left) shows the Hubble Diagram for the Type Ia SNe of the first year of the SNLS (Astier et al. 2006). Whereas, the Einstein-de Sitter model seems rather clearly excluded, the difference between Milne and ΛCDM is much subtler. We fitted the data against the symmetric Milne Universe and obtained a value for the absolute magnitude which differs from that of ΛCDM by ≈0.1 magnitude. On fig. 1(right), we present the residuals for these two models which turn to be very similar and hard to distinguish.

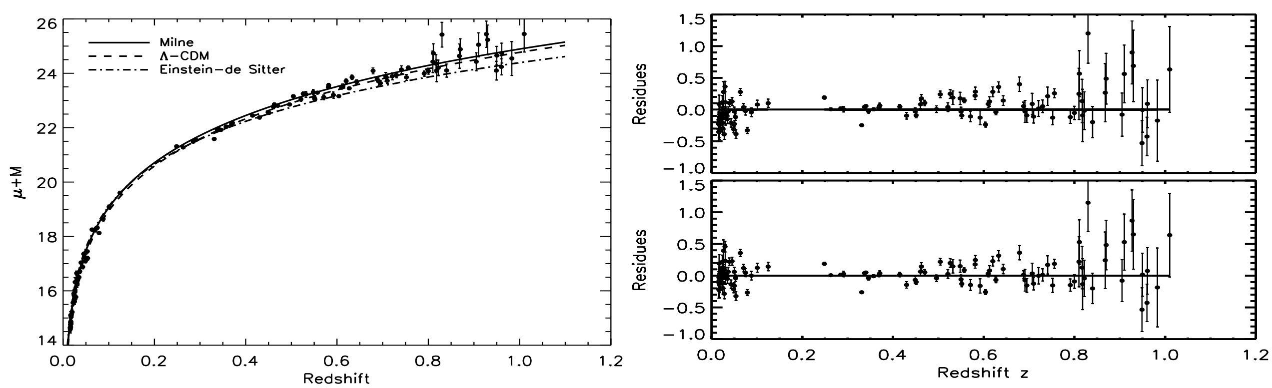

Fig. 1. *Left.* Hubble diagram for Milne, Λ-CDM and Einstein-de Sitter models. *Right.* Residuals of the Milne (top) and the Λ-CDM (bottom) adjustment for the first year SNLS data. It is clear from this figure that the difference between the two models is marginal within the present systematic errors.

4 Cosmic Microwave Background

Precise measurements of the first acoustic CMB peak usually lead to the conclusion that our Universe has a nearly zero spatial curvature. A priori, an open space such as the Milne universe is expected to give a very small value for the angular scale of first acoutic peak. Formally, this scale corresponds to the angle under which is seen the sound horizon at decoupling. For the symmetric Milne universe, this angle reads $\theta = \left(\int c_s d\eta\right)\left(\frac{\sinh(\ln(1+z_{dec}))}{1+z_{dec}}\right)^{-1}$, where c_s is the speed of sound in the baryon-photon fluid (grossly equal to $c/\sqrt{3}$) and z_{dec} is the redshift of decoupling. The integration should be made between the epoch of generation of sound waves around the QGP transition and decoupling.

Very surprisingly, the integration yields $\theta \approx 1^\circ$, which is the observed scale.

5 Conclusion

The symmetric Milne universe, containing equal quantities of matter and antimatter with negative mass reveals itself to be surprisingly in good agreement with main cosmological tests. Despite unresolved questions, it should be seen as a serious and much simpler alternative to standard ΛCDM cosmology, without unobserved Dark Energy and Dark Matter components.

References

Carter, B. 1968, Phys. Rev., 174, 1559

Gehlaut, S. *et al.*2003, astro-ph/0306448

Kaplinghat, M. *et al.*2000, Phys. Rev. D, 61, 103507

Astier, P. *et al.*2006 A&A, 447, 31

SF2A 2008
C. Charbonnel, F. Combes and R. Samadi (eds)

COSMOLOGY AND ASTROPHYSICS WITH EXACT INHOMOGENEOUS MODELS

Célérier, M.-N.[1]

Abstract. It is commonly stated that we have entered the era of precision cosmology. The successes of the Concordance model are built on using a homogeneous background metric combined with first order perturbation theory. However, as we map out the universe around us — its mass distribution and flow patterns — in ever greater detail, the non-linear behaviour of cosmic structures becomes increasingly apparent. The homogeneity assumption — so essential in developing the basics of cosmology — must now be considered just a zeroth order approximation, and similarly linear perturbation theory a first order approximation. Since inhomogeneous solutions of Einstein's field equations provide models of both small and large structures that are fully non-linear, they seem to be best appropriate to properly interpret observations. We give here some instructive examples pertaining to inhomogeneous astrophysics and cosmology, from structure formation to the reproduction of cosmological data.

Structure formation is generally studied either in N-body simulations or in the linear perturbation formalism. However, the linear approach is no more valid once the density contrast becomes too large and it does not take into account the influence of the structure shape. The limitations of the N-body simulations are: the use of Newtonian mechanics, the assumption of a uniform Hubble expansion and the finite number of particles. Thus investigations based on exact solutions are mandatory.

Exact spherically symmetric inhomogeneous models, such as Lemaître–Tolman–Bondi (LTB) and Lemaître (otherwise known as Misner-Sharp) were used to describe: the formation of a galaxy with a central blackhole (Krasiński & Hellaby, 2004a), the formation and evolution of galaxy clusters and voids (Krasiński & Hellaby, 2002; Krasiński & Hellaby, 2004b) and the influence of radiation on void formation (Bolejko, 2006a). These investigations demonstrate that velocity perturbations are more efficient in generating structures than density perturbations are and that until several million years after last scattering radiation cannot be neglected in models of structure formation.

To estimate how two neighboring structures influence each other evolution, the evolution of a double structure in quasi-spherical Szekeres (QSS) models (inhomogeneous without symmetries) was compared with that of single structures in other models. In the studied QSS models, the growth of the density contrast as shown in Fig. 1 appears to be 5 times faster than in LTB models and *8 times faster* than in the linear approach (Bolejko, 2006b).

A QSS model for a triple structure was also studied by Bolejko (2007). An overdense region at the origin is followed by a small void which spreads to a given r coordinate. At a larger distance from the origin, the void is huge and its larger side is adjacent to an overdense region. Where the void is large, it evolves much faster than the underdense region closer to the "centered" cluster. The exterior overdense region close to the void along a large area evolves much faster than the more compact supercluster at the centre. This suggests that, in the Universe, small voids surrounded by large high densities evolve much more slowly than large isolated voids.

In cosmology, the last decade has witnessed a phenomenal increase of the available data. Analyzed in the framework of FLRW homogeneous solutions, they have yielded the Concordance model where more than 95% of the Universe content is of unknown nature. Hence the need of studying if these observations could not be given a more natural explanation in the framework of exact inhomogeneous models, even if other promizing

[1] LUTH, Observatoire de Paris, CNRS, Université Paris VII, 92195 Meudon, France

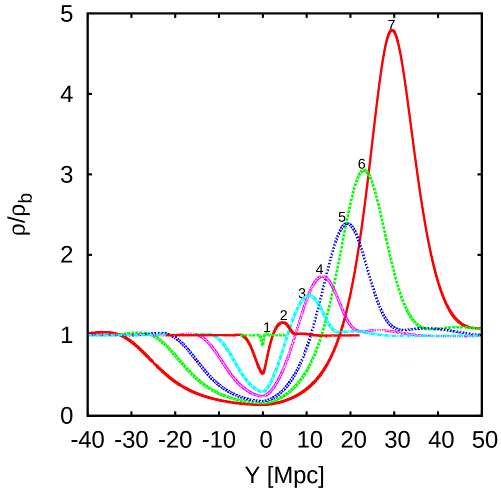

Fig. 1. Evolution of the density profile from 100 Myr after BB (1) to the present time (7).

averaging methods are currently put forward.

The horizon problem develops sooner or later in any cosmological model exhibiting a space-like singularity. Inflation adds a slice of de Sitter space-time to an otherwise space-like singularity FLRW model. It thus only postpones the occurence of the horizon problem to a future region of the observer's worldline. A delayed Big-Bang provides a permanent solution to the problem within of a particular class of LTB models exhibiting a non space-like singularity (Célérier & Schneider, 1998; Célérier, 2000; Célérier & Szekeres, 2002).

The luminosity distance-redshift relation obtained from the SN Ia data analyzed in the framework of an a priori homogeneous Universe yields an apparent accelerated expansion. However, recent studies show that these data can be reproduced by fitting the parameter functions of inhomogeneous solutions – LTB or LTB Swiss-cheese – without any "dark energy" component (see, e.g., Célérier, 2007, for a review).

This very short summary shows that there is still much to be learned about the effects of exact non-linear inhomogeneities in Geneneral Relativity. The Universe, as we observe it, is very inhomogeneous. There are groups and clusters of galaxies, huge cosmic voids and large elongated filaments and walls. In cosmology, however, the homogeneous and isotropic models of the FLRW class are used almost exclusively and structure formation is described by an approximate perturbation theory. This works well as long as the perturbations remain small, but cannot be applied once they become large and evolution becomes non-linear. The phenomena of fully relativistic inhomogeneous evolution do occur and cannot be ignored. This is where the methods of inhomogeneous cosmology must come into play.

References

Krasiński, A., & Hellaby, C. 2004a, Phys. Rev., D69, 043502
Krasiński, A., & Hellaby, C. 2002, Phys. Rev., D65, 023501
Krasiński, A., & Hellaby, C. 2004b, Phys. Rev., D69, 023502
Bolejko, K. 2006a, MNRAS, 370, 924
Bolejko, K. 2006b, Phys. Rev., D73, 123508
Bolejko, K. 2007, Phys. Rev., D75, 043508
Célérier, M.-N., & Schneider, J. 1998, Phys. Lett., A249, 37
Célérier, M.-N. 2000, A& A, 362, 840
Célérier, M.-N., & Szekeres, P. 2002, Phys. Rev., D65, 123516
Célérier, M.-N. 2007, New Adv. Phys., 1, 29

SF2A 2008
C. Charbonnel, F. Combes and R. Samadi (eds)

THE SZ EFFECT : BIASES INTRODUCED ON COSMOLOGICAL PARAMETER ESTIMATION USING PLANCK

Taburet, N.[1], Aghanim, N.[1], Douspis, M.[1] and Langer, M.[1]

Abstract. We examine the biases induced on cosmological parameters when the presence of secondary anisotropies is not taken into account in Cosmic Microwave Background analyses. We develop an exact analytical expression applicable when any additive signal (systematics, foregrounds) is neglected in the analysis. We then apply it, in the context of the upcoming *Planck* experiment, to the case of the thermal Sunyaev-Zel'dovich residual signal that remains after cluster extraction. We show that analyses neglecting the presence of this signal introduce important biases on the values of the cosmological parameters n_s and τ, at least 6.5 and 2.9 times larger than the expected precision on these parameters. The $\Omega_{\rm b}$ parameter is also biased to a lesser extent.

1 Introduction

The future Cosmic Microwave Background (CMB) experiments, such as *Planck*, will measure with unequalled sensitivities the amplitude of the CMB temperature and polarisation anisotropies up to angular scales of a few arcminutes in multiple frequency bands. These measurements will allow us to constrain cosmological parameters with a relative precision of the order of one percent. In this context, additional contributions to the signal (galaxies, point sources, secondaries arising from the interaction of CMB photons with matter after decoupling, etc.) can no more be neglected and a precise quantification of the biases on the parameters is needed.

The secondary anisotropy we focus on is that which dominates at small scales (e.g. Aghanim et al. 2008): the thermal Sunyaev-Zel'dovich (SZ) effect (Sunyaev & Zel'dovich 1972). The SZ effect is made of two contributions: the inverse Compton scattering of the CMB photons off the hot electrons of the intra-clusters gas, called the thermal SZ, and a Doppler shift caused by the motion of the clusters with respect to the CMB reference frame, called the kinetic SZ. The thermal SZ effect thus decreases the CMB intensity in the Rayleigh Jeans part of the black body spectrum and increases it in the Wien part. Using this characteristic spectral signature and the upcoming multifrequency surveys, one will be able to detect and extract galaxy clusters. Nevertheless we will be left, in the temperature anisotropy maps, with some level of residual SZ contribution from undetected clusters that generate some power excess at small scales.

We present a method we developed to calculate the biases on parameters induced by any signal that adds to or subtracts from the primary signal. We then apply this method to the case of the thermal SZ residuals in the context of the future *Planck* mission and discuss our results.

2 Biases induced by an additive contribution

Several studies have estimated the expected precision on the cosmological parameters that one can reach given the characteristics of an instrument (sky coverage, beam, sensitivity...) This information must be completed by an estimation of the sensitivity of the measurements to any secondary signal added to the primary. We present a general method to calculate the bias induced, on parameter estimation, by any additive signal (instrumental systematics, astrophysical contaminants).

As a reference used to estimate cosmological parameters, we consider a signal $C_\ell^{\rm D}$ that is the sum of a primary signal ($C_\ell^{\rm CMB}(\hat{\theta})$) that depends on the cosmological parameters $\hat{\theta}$ and of an additional signal ($C_\ell^{\rm add}$)

[1] Institut d'Astrophysique Spatiale, Université Paris Sud 11 & CNRS (UMR 8617), Bât 121, 91405 ORSAY Cedex

that may, or may not, contain cosmological information. When this additional signal is taken into account in the parameter estimation one obtain the "true" cosmological parameters ${}_1\hat{\theta}$. On the contrary, when one fits the total signal with the primary only, one obtains a biased parameter set ${}_2\hat{\theta}$. We derived (Taburet et al. 2008) an analytical expression of the biases on the parameters : $\hat{b} ={}_2\hat{\theta} -{}_1\hat{\theta}$. Considering that the associated errors to each $C_\ell^{\rm D}$ data point have a Gaussian distribution, we showed that the biases on the parameters are $\hat{b} = \mathbf{G}^{-1}\hat{V}$, where

$$\begin{aligned} G_{ij} \quad = \quad & \sum_{\ell,X,Y} \mathrm{cov}_\ell^{-1}(C_\ell^X C_\ell^Y) \left[\left.\frac{\partial C_\ell^{X\mathrm{mod}}}{\partial\theta_i}\right|_{\hat{\theta}={}_1\hat{\theta}} \left.\frac{\partial C_\ell^{Y\mathrm{mod}}}{\partial\theta_j}\right|_{\hat{\theta}={}_1\hat{\theta}} + \left.\frac{\partial C_\ell^{X\mathrm{mod}}}{\partial\theta_j}\right|_{\hat{\theta}={}_1\hat{\theta}} \left.\frac{\partial C_\ell^{Y\mathrm{mod}}}{\partial\theta_i}\right|_{\hat{\theta}={}_1\hat{\theta}} \right. \\ & \left. - C_\ell^{X\mathrm{add}} \left.\frac{\partial^2 C_\ell^{Y\mathrm{mod}}}{\partial\theta_i\partial\theta_j}\right|_{\hat{\theta}={}_1\hat{\theta}} - C_\ell^{Y\mathrm{add}} \left.\frac{\partial^2 C_\ell^{X\mathrm{mod}}}{\partial\theta_i\partial\theta_j}\right|_{\hat{\theta}={}_1\hat{\theta}} \right] \end{aligned} \tag{2.1}$$

and

$$V_i = \sum_{\ell,X,Y} \mathrm{cov}_\ell^{-1}(C_\ell^X C_\ell^Y) \left[C_\ell^{Y\mathrm{add}} \left.\frac{\partial C_\ell^{X\mathrm{mod}}}{\partial\theta_i}\right|_{\hat{\theta}={}_1\hat{\theta}} + C_\ell^{X\mathrm{add}} \left.\frac{\partial C_\ell^{Y\mathrm{mod}}}{\partial\theta_i}\right|_{\hat{\theta}={}_1\hat{\theta}} \right]. \tag{2.2}$$

with $C_\ell^{X\mathrm{mod}} = C_\ell^{X\mathrm{CMB}}$ and X, Y = TT, EE, TE. The expression of the coefficients of the covariance matrix, $\mathrm{cov}_\ell(C_\ell^X C_\ell^Y)$, can be found in Zaldarriaga & Seljak (1997), and the numerical values that we used can be found in the *The Scientific Programme of Planck* (also known as the *Planck Blue Book*, The Planck Colaboration 2006).

Our method presents multiple advantages : it is applicable to calculate the biases induced by any kind of additive signal. In contrast to previous studies (e.g. Zahn et al. 2005; Amara & Réfrégier 2008) the formula we derived is applicable even when the additive signal is dominant over the primary.

The biases on the investigated parameters become relevant only if they are larger than the expected confidence intervals. The latter can be computed through a Fisher matrix analysis. The 68.3% confidence interval on one parameter (the others being known) is given by

$$\delta\theta_i = \sqrt{F_{ij}^{-1}}, \tag{2.3}$$

where the Fisher matrix coefficients are

$$F_{ij} = \sum_\ell \sum_{X,Y} \mathrm{cov}_\ell^{-1}(C_\ell^X C_\ell^Y) \frac{\partial C_\ell^X}{\partial\theta_i} \frac{\partial C_\ell^Y}{\partial\theta_j}. \tag{2.4}$$

3 The thermal SZ residuals

In the context of the large upcoming multifrequency surveys (*Planck*, SPT...) and using the typical signature of the thermal SZ effect, one will be able to detect galaxy clusters through their SZ effect. It will allow us to build up SZ cluster catalogues and also to remove some of the thermal SZ signal from the CMB maps so as to retrieve the best primary CMB signal. We will however be left with some SZ residual signal in the temperature maps. It is thus important to quantify the biases on the cosmological parameters if the thermal SZ residuals are neglected in the *Planck* data analysis. Our approach is first to estimate which galaxy clusters will remain undetected, then to calculate the associated SZ residual signal and use it in equations (2.1) and (2.2) to get an estimate of the biases.

First we build up the theoretical selection function that determine the minimal mass $M_{\rm lim}(z)$ for a cluster at redshift z to be detected by the *Planck* instrument through its SZ contribution. We consider that a galaxy cluster is detected if its beam-convolved Compton parameter emerges from the confusion noise and if its integrated signal is above the instrumental limit, σ_Y, simultaneously in the 3 channels where the SZ signal is the strongest (100, 143 and 353 GHz).

Then we calculate the SZ residual angular power spectrum due to the undetected clusters. For each multipole ℓ, the contribution comes from each galaxy cluster (poisson contribution) and from the correlation between clusters. Following Komatsu & Kitayama (1999) who have shown that the latter is negligible compared to the former for $\ell > 300$, we consider only the poissonian contribution (Komatsu & Seljak 2002):

$$C_\ell = f_\nu^2 \int_0^{z_{\rm rec}} dz \frac{dV}{dz} \int_{M_{\rm Min}}^{M_{\rm Max}} dM \frac{dn(M,z)}{dM} \left|\tilde{y}(M,z)\right|^2 \tag{3.1}$$

where f_ν represents the frequency dependency of the SZ effect. The comoving volume V and the mass function $n(M,z)$ depend on the cosmology, and $\tilde{y}(M,z)$ depends on both the cosmology and the intra-cluster gas distribution (that we describe by an isothermal β-model). $M_{\rm Max} = M_{\rm lim}(z)$ is the highest mass of undetected clusters at redshift z.

Figure 1 shows that the detected clusters (difference between the dashed and the dot-dashed curves) contribute mainly at large scales, while the residual contributes at small scales where the primary CMB signal vanishes. For multipoles higher than 2000, the SZ contribution after extracting clusters detected at $3\sigma_Y$ dominates over the primary CMB signal.

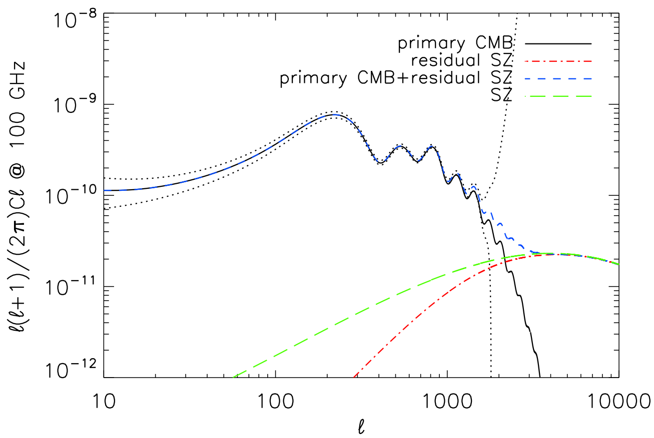

Fig. 1. At 100 GHz, primary CMB (solid line), SZ angular power spectrum of the whole cluster population (long-dashed green line), residual SZ spectrum after the extraction of clusters above 3 times the instrumental noise simultaneously at 100, 143 and 353 GHz (dot-dashed red line), primordial CMB + residual SZ spectrum (dashed blue line). The black dotted lines represent the $1\sigma_Y$ noise of the 100 GHz *Planck* channel.

4 Results and discussion

We apply the method outlined in section 2 to the *Planck* mission in order to estimate the biases introduced on the Ω_Λ, $\Omega_{\rm b}$, H_0, $n_{\rm s}$, σ_8 and τ parameters when the additive signal constituted by the thermal SZ residuals is neglected in the data analysis. The black solid lines on figure 2 represent the 68.3% confidence ellipses on these 6 parameters using the TT, TE and EE power spectra when a coherent analysis that takes into account the primary CMB and the SZ residuals dependency on the cosmological parameters is carried out (reference model). The distance between the centre of these and the centre of the shifted ellipses (dotted red and dashed green) represents the biases on the parameters when the thermal SZ residuals (respectively after a 1 and a 5 σ_Y cluster detection) are not taken into account in the analysis of the CMB signal.

First, and unsurprisingly, the biases induced on Ω_Λ and H_0 are negligible. At most, for a large residual contribution, they reach roughly 0.08 and 0.6 in units of the 1σ errors on the parameters. On the contrary, as expected, the parameters σ_8, and to a higher extent $n_{\rm s}$, $\Omega_{\rm b}$ and τ, which are the most sensitive to a power excess at large scales, and are also degenerate with each other, are significantly affected. An excess of power at high ℓ and a slight shift of the fourth and fifth CMB peaks towards smaller scales, due to SZ residuals, can be respectively accounted for by over-estimating the values of σ_8 and $\Omega_{\rm b}$. Since the amplitude of the CMB power spectrum strongly depends on σ_8, a relatively small variation of σ_8 is enough to fit the power excess. As a result, the bias on this parameter is rather small. For $\Omega_{\rm b}$ the biases are 1.4 and 2.4 in units of the error on Ω_b, for the 1 and $5\sigma_Y$ cases respectively. Higher $\Omega_{\rm b}$ and σ_8 values add more power at all multipoles, while the SZ residuals contribute significantly only at $\ell > 1000$. The resulting excess at large scales is thus accounted for by increasing the spectral index n_s, redistributing power from large to small scales ($\ell > 1200$). It is also compensated by a decrease of the optical depth τ, that reduces the CMB power. As a consequence, fitting data containing primary CMB and SZ secondary residual with a pure primary CMB spectrum induces quite an

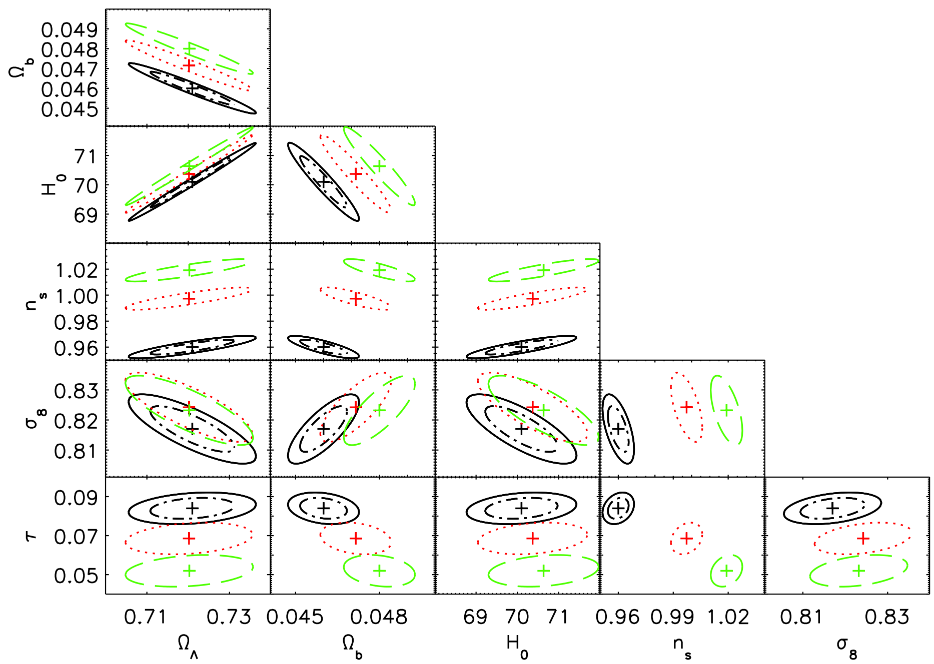

Fig. 2. 68.3% joint confidence regions for Ω_Λ, Ω_b, H_0, n, σ_8 and τ (solid line) obtained with the expected *Planck* TT, TE and EE spectra computed for the reference cosmological model. The dotted (red) and long dashed (green) shifted ellipses represent the 68.3% joint confidence regions around the biased parameters when respectively the $1\sigma_Y$ and $5\sigma_Y$ residual SZ contributions are not taken into account.

important bias on n_s and τ.

We show that a neglected thermal SZ residual signal in future high sensitivity high resolution CMB experiments introduces strong biases on the values of n_s, σ_8 and Ω_b. The high values of the biases emphasise the need of a coherent analysis (as was already pointed out in Douspis et al. 2006) of the CMB signal that includes full cosmological dependency of the SZ signal. One should also consider the importance of taking into account other additional signals contributing to the power excess at small scales, such as extragalactic point sources that also contribute to biasing the parameters when neglected.

References

Aghanim, N., Majumdar, S., & Silk, J. 2008, Reports of Progress in Physics, 71, 066902

Amara, A. & Réfrégier, A. 2007, arXiv:0710.5171

Douspis, M., Aghanim, N., & Langer, M. 2006, A&A, 456, 819

Komatsu, E. & Kitayama, T. 1999 ApJ, 526, L1

Komatsu, E. & Seljak, U. 2002, MNRAS, 336, 1256

Sunyaev, R.A. & Zel'dovich, Y.B. 1972, Comments Astrophys. Space Phys., 4, 173

Taburet, N., Aghanim, N., Douspis, M., & Langer, M. 2008, arXiv:0809.1364, submitted to MNRAS

The Planck Colaboration 2006, arXiv:astro-ph/0604069

Zahn, O., Zaldarriaga, M., Hernquist, L., & McQuinn, M. 2005, ApJ, 630, 657

Zaldarriaga, M. & Seljak, U. 1997, Phys.Rev.D, 55, 1830

SF2A 2008
C. Charbonnel, F. Combes and R. Samadi (eds)

PRIMORDIAL MOLECULES AND GRAVITATIONAL COLLAPSES

Vonlanthen, P.[1] and Puy, D.[1]

Abstract. We analyze the formation of molecules based on carbon, nitrogen, oxygen and fluorine during the Dark Ages in two different contexts: the standard Big Bang nucleosynthesis model on the one hand and a particular, non-standard nucleosynthesis scenario on the other hand. The latter is particularly efficient in creating heavy nuclei. We also study, in these two different frames, the influence of the molecular H_2 and HD cooling functions on the gas temperature of a collapsing cloud.

1 Dark Ages chemistry of heavy elements

The cosmological gas hosted various chemical reactions and different molecules were created during the Dark Ages, the main ones being molecular hydrogen and HD. Heavy nuclei such as C, N, O or F were formed in very negligible amounts in the standard Big Bang nucleosynthesis model, because of the inexistence of stable elements with mass numbers 5 or 8 and because of the growing importance of the coulombian repulsion. For this reason, we expect molecules based on these elements to be produced in very small quantities. However, heavy nuclei can be efficiently synthesized in some non-standard nucleosynthesis models, in which small parts of the Universe have a high baryonic density, while most of the volume of the Universe is characterized by the usual, small baryon-to-photon ratio. We will here consider the particular non-standard nucleosynthesis scenario of Rauscher et al. (1994). This model is particularly efficient in creating heavy nuclei. In this scenario, the formation of such nuclei is a consequence of baryon density inhomogeneities, which induce local variations of the neutron-proton ratio. Heavy nuclei are then synthesized by neutron captures in neutron rich regions. In this particular nucleosynthesis case, the most abundant element is not hydrogen, but helium.

We compute the chemistry of H, D, He, Li, C, N, O and F from $z = 10^4$ to $z = 10$, using a large set of reactions that come mainly from the UMIST database (www.udfa.net) for the heavy elements C, N and O. We take the rates discussed in Puy et al. (2007) for the fluorine chemistry. We solve the complex set of differential equations governing the Dark Ages chemistry in the two distinct frames discussed above (we will call them standard and non-standard). Our results can be seen in Fig. 1. The main heavy molecules like CH, OH or NH and their respective molecular ions are created in amounts up to eleven orders of magnitude higher in the non-standard chemistry case. Globally, we obtain much lower abundances than in similar studies (e. g. Lipovka et al. 2007). We think that this is due, at least partly, to our much more extended reaction set.

2 Molecular cooling and gravitational collapses

Once primordial molecules are synthesized, they play a determining role in the formation of the first (Population III) stars. In particular, they are believed to be the only agent likely to cool down the primordial clouds undergoing gravitational collapses. We define the molecular thermal function $\Psi_{\rm mol}$ of a given molecule as the difference between its heating function $\Gamma_{\rm mol}$ (energy gain via radiative excitation of a rotational level followed by collisional deexcitation) and its cooling function $\Lambda_{\rm mol}$ (energy loss via collisional excitation followed by radiative deexcitation). For $\Psi_{\rm H_2}$, we compute rotational level populations for levels up to $J = 20$ at each timestep and consider collisions of H_2 with H and He. We use the very recent collision rates of Wrathmall, Gusdorf & Flower (2007) for collisions with H, and Le Bourlot et al. (1999) for collisions with He. For the computation of $\Psi_{\rm HD}$, the first eight levels are considered. We use the collision rates from Flower & Roueff (1999) for collisions with

[1] Université Montpellier II - GRAAL, CNRS - UMR 5024, place Eugène Bataillon, 34095 Montpellier, France

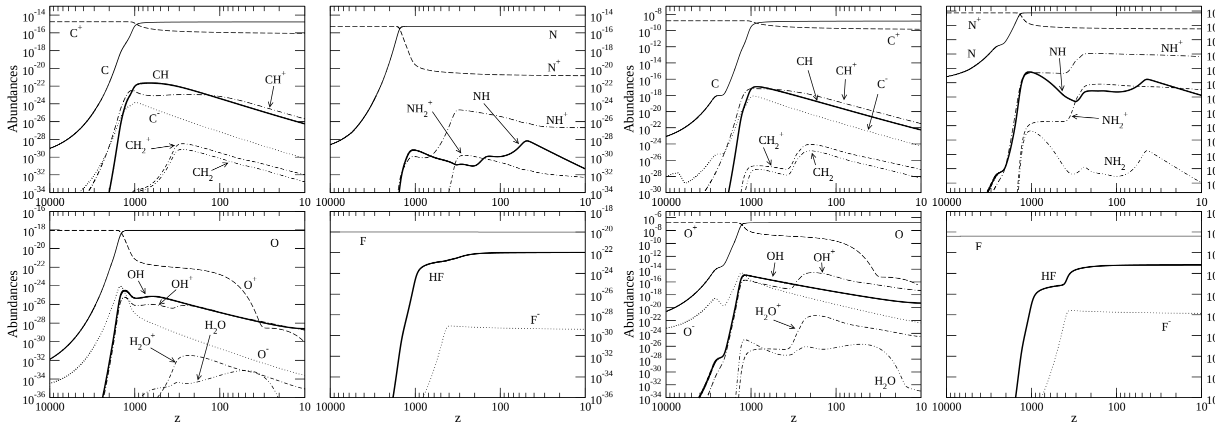

Fig. 1. Dark Ages chemistry of carbon, nitrogen, oxygen and fluorine. **Left:** Standard Big Bang chemistry. **Right:** Chemistry in the particular, non-standard model of Rauscher et al. (1994).

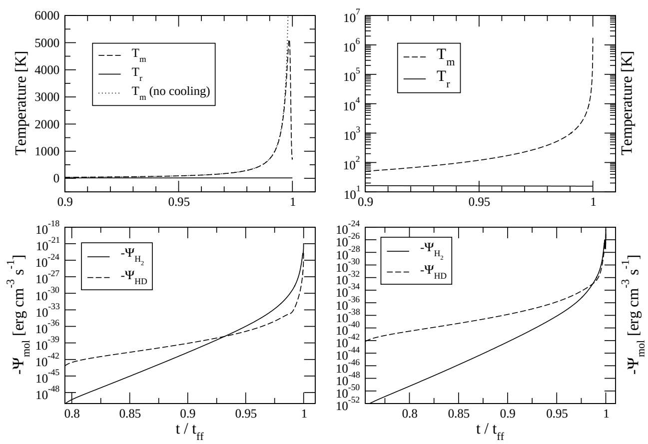

Fig. 2. Top: Evolution of the gas ($T_{\rm m}$) and radiation ($T_{\rm r}$) temperatures. **Bottom:** Evolution of $\Psi_{\rm H_2}$ and $\Psi_{\rm HD}$.

H, He and H_2. Fig. 2 shows the evolution of $\Psi_{\rm H_2}$, $\Psi_{\rm HD}$ and the gas temperature $T_{\rm m}$ inside a collapsing 10^{10} $M_\odot$ cloud. We use a 1D model of a perfectly homogeneous, spherical cloud. The left column shows the collapse in the case of the standard chemistry. We see that the cooling is dominated first by $\Psi_{\rm HD}$. Then, when $T_{\rm m} \sim 60$ K, $\Psi_{\rm H_2}$ becomes dominant. The most interesting point is that after almost one free fall time, $T_{\rm m}$ starts to decrease, illustrating the efficiency of primordial molecules as cooling agent. The right column of Fig. 2 considers the same collapse, but this time in the non-standard chemistry scenario of Rauscher et al. (1994). Indeed, HD is more abundant in this case than H_2, and $\Psi_{\rm HD}$ could dominate the thermal properties of the collapsing gas. Unfortunately, Fig. 2 leads to the conclusion that the molecular cooling is less efficient in that case by a factor of the order of 2000. As a consequence, $T_{\rm m}$ never decreases.

References

Flower, D. R., & Roueff, E. 1999, MNRAS, 309, 833

Le Bourlot, J., Pineau des Forêts, G., & Flower, D. R. 1999, MNRAS, 305, 802

Lipovka, A., Saucedo, J., & Lipovka, N. M. 2007, astro-ph/0703547

Puy, D., Dubrovich, V., Lipovka, A., Talbi, D., & Vonlanthen, P. 2007, A&A, 476, 685

Rauscher, T., Applegate, J. H., Cowan, J. J., Thielemann, F.-K., & Wiescher, M. 1994, ApJ, 429, 499

Wrathmall, S. A., Gusdorf, A., & Flower, D. R. 2007, MNRAS, 382, 133

PNG

Galaxies

SF2A 2008
C. Charbonnel, F. Combes and R. Samadi (eds)

THE COMA CLUSTER FAINT GALAXY POPULATION

Adami, C.[1], Biviano, A.[2], Cuillandre J.C.[3], Durret, F.[4], Gavazzi, R.[4], Ilbert, O.[1], Le Brun, V.[1], Mazure, A.[1], Pello, R.[5], Picat, J.P.[5], Scheidegger, R.[6] and Ulmer, M.P.[6]

Abstract.
We present preliminary results of new Vimos spectroscopy of faint Coma cluster dwarf galaxies (R≥21). About 1000 spectra where measured along the line of sight. We also present our most recent results regarding spectral characteristics of low surface brightness galaxies, deep galaxy luminosity function, and galaxy orientations in the cluster.

1 Preliminary results of new Vimos spectroscopy of faint Coma cluster dwarf galaxies

We got ∼1000 spectra of faint Coma line of sight galaxies (R∼[21,23]) using the VLT/VIMOS instrument in 2008. Despite the very defavourable Coma declination / VLT latitude, we were able to observe 3 masks at airmasses close to 1.7 and seing of the order of 1.2. The targets were partly selected on the photometric redshift basis and partly randomly in order to increase the number of targets. All data are reduced and we started the analysis of the spectra, measuring first the redshift of the targets. Using 60% of the data, we have a redshift measurement success rate of ∼80%, leading to more than 400 successful measurements (S/N in [3,6] for most of the targets). Among them slightly less than 100 galaxies are part of the Coma cluster. The expected minimum number of galaxies inside the Coma cluster given the target selection was 70, so we are in good agreement with the predictions. This already represents a major breakthrough because spectroscopically, basically nothing was known fainter than R=21. We also confirm the very diffuse shape of the faint Coma cluster galaxies. At least part of them are faint low surface brightness galaxies detected in Adami et al. (2006). Very few of these galaxies have emission lines and the majority of the sample is consistent with post starburst objects. More detailled results will be given in a forthcoming paper.

2 Spectral characteristics of the Coma cluster faint low surface brightness galaxies

As a continuation of our study of faint Low Surface Brightness Galaxies (Adami et al. 2006) in one of the densest nearby ($z = 0.023$) galaxy regions known, the Coma cluster, we used here u* (Megacam), B, V, R, and I (CFH12K) band data in order to put constraints on the Coma cluster faint low surface brightness galaxy spectral characteristics. By comparing the broad band spectral energy distribution with population synthesis models, we infered photometric redshifts (to confirm the Coma cluster membership), ages, dust extinction and photometric types. A large part of our sample is consistent with being in Coma. Assuming that all fLSBs are part of the Coma cluster, the spectral fits agree with our previous interpretation, i.e. galaxies on the extended color magnitude relation are relatively old, the reddest ones exhibiting similar ages, and the bluest ones being

[1] LAM, OAMP, Université Aix-Marseille & CNRS, Pôle de l'Etoile, Site de Château Gombert, 38 rue Frédéric Joliot-Curie, 13388 Marseille 13 Cedex, France
[2] INAF / Osservatorio Astronomico di Trieste via G.B. Tiepolo 11 - 34143 Trieste, Italy
[3] Canada-France-Hawaii Telescope Corporation, Kamuela, HI 96743
[4] Institut d'Astrophysique de Paris, CNRS, UMR 7095, Université Pierre et Marie Curie, 98bis Bd Arago, 75014 Paris, France
[5] Laboratoire d'Astrophysique de Toulouse-Tarbes, Université de Toulouse, CNRS, 14 Av. Edouard Belin, 31400 Toulouse, France
[6] Department Physics & Astronomy, Northwestern University, Evanston, IL 60208-2900, USA

the youngest. Besides the fact that we confirm the detection of 683 fLSBs in u* compared to our previous BR detections, we show that a majority are part of the Coma cluster. These objects can tentatively be divided into 3 classes: (a) those that have evolved passively after an initial burst of star formation (the fLSB primordial population of the cluster); (b) those that have been removed from massive old galaxies, and (c) those that have been torn away from the outer regions of blue galaxies.

3 Photometric redshifts as a tool to study the Coma cluster galaxy luminosity function

We apply photometric redshift techniques to an investigation of the Coma cluster galaxy luminosity function (GLF) at faint magnitudes, in particular in the u* band where basically no studies are presently available at these magnitudes. Cluster members were selected based on probability distribution function from photometric redshift calculations applied to deep u*, B, V, R, I images covering a region of almost 1 deg^2 (completeness limit R$\sim$24). In the area covered only by the u* image, the GLF was also derived after a statistical background subtraction. Global and local GLFs in the B, V, R, and I bands obtained with photometric redshift selection are consistent with our previous results based on a statistical background subtraction (Adami et al. 2007a and b). The GLF in the u* band shows an increase in the faint end slope towards the outer regions of the cluster: the $u*$ GLF slope varies from $\alpha \sim -1$ in the cluster center to $\alpha \sim -2$ in the cluster periphery. The analysis of the multicolor type spatial distribution reveals that late type galaxies are distributed in clumps in the cluster outskirts, where X-ray substructures are also detected and where the GLF in the u* band is steeper. The concentrations of faint late type galaxies in the cluster outskirts could explain these very steep slopes, assuming a short burst of star formation in these galaxies when entering the cluster.

4 Galaxy orientations in the Coma cluster

Models of large scale structure formation predict the existence of preferential orientations for galaxies in clusters. In this context, we have searched for preferential orientations of very faint galaxies in the Coma cluster (down $I_{Vega}$$\sim$-11.5). By applying a deconvolution method to deep u* and I band images of the Coma cluster, we were able to recover orientations down to very faint magnitudes, close to the faintest dwarf galaxies No preferential orientations are found in more than 95% of the cluster area, and the brighter the galaxies, the fewer preferential orientations we detect. The minor axes of late type galaxies are radially oriented along a northeast - southwest direction and are oriented in a north - south direction in the western X-ray substructures. For early type galaxies, in the western regions showing significant preferential orientations, galaxy major axes tend to be oriented perpendicularly to the north - south direction. In the eastern significant region and close to NGC 4889, galaxy major axes also tend to point toward the two cluster dominant galaxies. In the southern significant regions, galaxy planes tend to be tangential with respect to the clustercentric direction, except close to (α=194.8, δ=27.65) where the orientation is close to -15 deg. Early and late type galaxies do not have the same behaviour regarding orientation. Part of the orientations of the minor axes of late type galaxies and of the major axes of early type galaxies can be explained by the tidal torque model (e.g. Peebles 1969) applied both to cosmological filaments and local merging directions. Another part (close to NGC 4889) can be accounted for by collimated infalls (e.g. Torlina et al. 2007). For early type galaxies, an additional region ($\alpha = 194.8, \delta = 27.65$) shows orientations that probably result from local processes involving induced star formation.

References

Adami, C.; Durret, F.; Mazure, A.; et al., 2007, A&A 462, 411 (a)

Adami, C.; Picat, J. P.; Durret, F.; et al., 2007, A&A 472, 749 (b)

Adami, C.; Scheidegger, R.; Ulmer, M.; et al., 2006, A&A 459, 679

Peebles P.J.E., 1969, ApJ 155, 39

Torlina L., De Propris R., West M.J., 2007, ApJ 660, L97

SF2A 2008
C. Charbonnel, F. Combes and R. Samadi (eds)

THE HERSCHEL REFERENCE SURVEY

Boselli, A.[1] and the SPIRE extragalactic group

Abstract. In order to study the dust properties of different galaxies in the nearby Universe, the SPIRE extragalactic group selected a volume limited (15< D <25 Mpc), complete sample of 323 galaxies spanning the whole range in morphological type (from ellipticals to late-type spirals) and luminosity (8.5 < log L_H < 12 $L_{H}\odot$, -22 < M_B < -16) extracted from 2MASS, to be observed in guaranteed time (114 h) with Herschel. The 250-360-520 μm SPIRE data, combined with those collected at other frequencies, will be used to trace the dust properties of normal galaxies and provide a reference sample for studies at high redshift.

1 Introduction

During their evolution, the different stellar populations of galaxies produce and inject into the interstellar medium metals that congregate to form dust particles of different size and composition. This dust, heated by the general stellar radiation field, re-emit the absorbed energy in the far-IR. In normal galaxies, those objects dominating in number the nearby universe, the emitting dust has a modified black body spectrum with a peak at $\sim$ 200 μm rapidly decreasing at longer wavelengths (Boselli et al. 2003). Because of the quiescent star formation activity of these objects, however, most of the dust has a relatively cold temperature ($\sim$ 20 K) and is emitting in the submillimetric domain. The total dust amount of normal galaxies can thus be measured only by means of observations in the 200-1000 μm spectral range.

All physical (star formation activity, gas content, metallicity; Boselli et al. 2001; 2002; Zaritsky et al. 1994; Gavazzi et al. 2004), structural (concentration index, light profile; Boselli et al. 1997; Gavazzi et al. 2000; Scodeggio et al. 2002), kinematical (shape of the rotation curve; Catinella et al. 2006) and stellar population (stellar spectral energy distribution; Gavazzi et al. 2002; Boselli et al. 2003) properties of galaxies are strongly related to their total stellar mass (downsizing effect) and marginally to their morphological type. Tracing the statistical dust properties of normal galaxies can thus be done by observing a large and complete sample of objects spanning the largest possible range in luminosity and Hubble type.

Although accessible to ground based facilities such as SCUBA, the observation of such large samples of normal, quiescent galaxies would be too time consuming (more than 20 hours per galaxy) (Dunne et al. 2000). Given its large field of view (4'x4') and its sensitivity ($\sim$ 7 mJy for a 5 σ detection for a point source in 1 hour integration), SPIRE on Herschel is the ideal instrument for such a survey. For such a purpose, the SPIRE extragalactic group selected a volume limited, complete sample of 323 galaxies to be observed in 114.5 hours of guaranteed time in the three SPIRE bands at 250, 360 and 520 μm.

2 The sample and the observations

To span the largest possible range in mass, the sample has been selected in the K band (from 2MASS) since near-IR luminosities are linearly related to the total dynamical mass of galaxies (Gavazzi et al. 1996). A distance constraint of 15 < D < 25 Mpc has been introduced to construct a volume limited sample. This distance range limits distance uncertainties due to local peculiar motions and secure the presence of low-luminosity, dwarf galaxies, non accessible at higher redshift. To minimize galactic cirrus contamination, galaxies have been selected at high galactic latitude ($b > +55^o$) and in low galactic extinction regions (A_B < 0.2; Schlegel et al. 1998). Our sample contains all early-type galaxies (E-S0-S0a) with $K_{Stot} \leq 8.7$ (65 objects) and late-type with

[1] Laboratoire d'Astrophysique de Marseille

$K_{Stot} \leq 12$. A different limit for early-type galaxies has been adopted to avoid the dust poor ellipticals whose emission would be hardly detected within reasonable integration times.

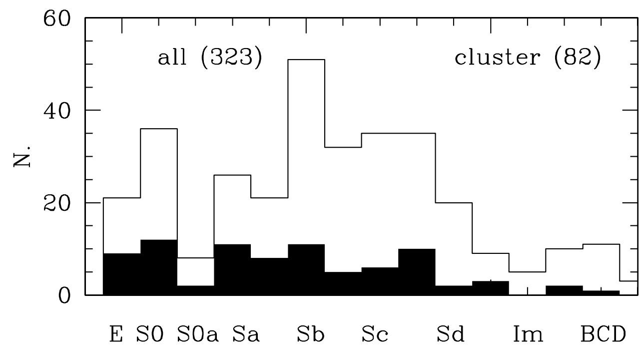

Fig. 1. The morphology distribution of the Herschel Reference Sample (HRS).

Figure 1 shows the histogram of the morphology distribution of the selected sample. As selected, the sample includes both relatively isolated and cluster object (Virgo) and is thus ideal for a statistical study on the effects of the environment on the dust properties of galaxies. Dwarf irregulars and blue compact galaxies, here undersampled in spite of the selected large range in luminosity, will be the targets of another SPIRE key program. As selected, the sample is representative of the K band luminosity function (Figure 2).

Pointed observations will be done with integration times of 30 minutes for ellipticals and lenticulars, and 12 minutes for late-types. Given a slewing overhead of 3 minutes per observation, this will ensure an efficient use of the telescope. For early-type galaxies the integration time has been determined by assuming a lower limit to their total dust mass of $\sim 10^4$ M$\odot$ as determined from IRAS observations (Bregman et al. 1998). With 30 minutes of integration a detection limit of 11 mJy at $\sim 4\ \sigma$ will be achived. For spirals the integration time is dictated by the need of detecting the cold dust emission outside the optical radius. By combining ISOPHOT (Alton et al. 1998) and SCUBA (Valahakis et al. 2005) observations of extended sources with spectral energy distribution of normal galaxies of different type (Boselli et al. 2003), and assuming a standard dust to gas ratio we estimate that 12 minutes of integration are sufficient to detect the cold dust associated to the extended HI disc. With 12 minutes of integration time we will get to a detection limit of 22 mJy at $\sim 5\ \sigma$.

3 Science projects

The selected sample will allow us to trace for the first time the variation of the cold dust properties (dust mass and temperature, dust to gas ratio,...) of normal galaxies along the Hubble sequence and as a function of luminosity. Combined with multifrequency datasets, the SPIRE data will be used to study the role of dust in the physics of the interstellar medium. Through the shielding of the interstellar radiation field, in particular of the UV light, dust participate in the cooling of the gas and thus plays a major role in the process of star formation. Dust is also an important catalyst in the formation of the molecular hydrogen, and thus is critical entity for the study of the feedback. Modeling the energetic balance between emitted and absorbed light, UV to sub-millimetric spectral energy distributions of these 323 galaxies will be used to quantify the dust obscuration in different objects. This analysis will allow us to define standard recipes for correcting UV and optical data, a useful tool for the interpretation of all modern surveys.
The presence of dust shells and discs in ellipticals will be used to study their hierarchical formation history. By studying the relationship between dust mass and other global properties of ellipticals we will determine how much dust is produced by the old stellar population and how much is the result of mergers.
The comparison of cluster and isolated galaxies will allow us to make a detailed study on the effects of the environment on the dust properties of galaxies, and thus understand whether the hot and dense cluster in-

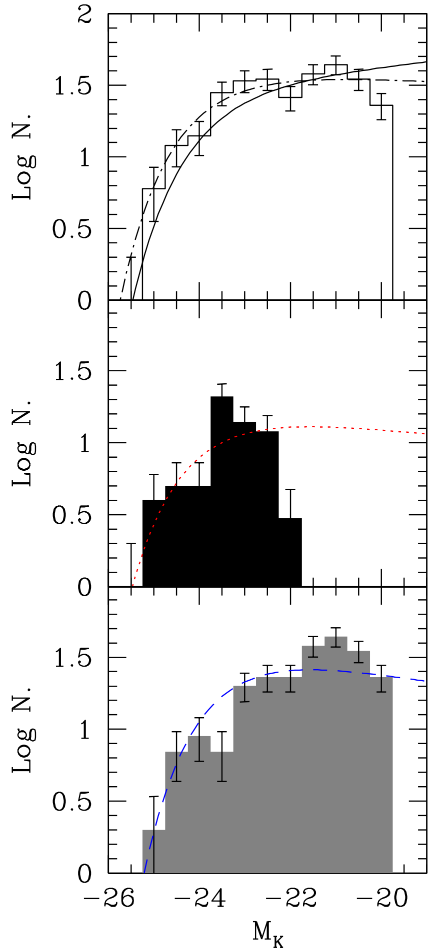

Fig. 2. The K band luminosity distribution of the HRS for all galaxies is compared to the 2MASS K band luminosity function of Kochanek et al. (2001) (black solid line) and Cole et al. (2001) (black dotted-dashed line)(upper panel). The K band luminosity distributions of the E-S0-S0a (central panel) and Sa-Sd-Im-BCD (lower panel) galaxies in the HRS are compared to the Kochanek et al. (2001) K band luminosity function of early-type (red dotted line) and late-type (blue dashed line) galaxies. Poisson errors are also indicated.

tergalactic medium can be polluted through the gas stripping process of late-type galaxies (Boselli & Gavazzi 2006). This dataset will be used to measure the local luminosity and dust-mass functions and distributions, important benchmarks for the deep Herschel surveys planned by the SPIRE team, providing at the same time a unique reference sample for any statistical study.

4 Corollary data

The proposed analysis can be done only once corollary data covering the whole electromagnetic spectrum will be available. Given its definition, the Herschel reference sample is easily accessible for ground based and space facilities: the selected galaxies are in fact relatively bright ($m_B < 15$ mag) and extended (∼ 2-3 arcmin). UV data at 1500 and 2300 Å will be taken from the GALEX all sky survey or the UV atlas of nearby galaxies (Gil de Paz et al. 2006), optical and near-IR images will be secured by the SDSS (Abazajian et al. 2005) and 2MASS (Jarrett et al. 2003) surveys. These data will be used to trace the underlying stellar population and

reconstruct the star formation history of the target galaxies.
Far-IR data in the 10-200 μm spectral range, needed for characterizing the whole dust emission and thus constraining dust masses and temperatures, will be taken from the AKARI/ASTRO-F survey at a similar spatial resolution ($\sim$ 20-30 arcsec, depending on the wavelength). Radio continuum data are already available from the NVSS survey (Condon et al. 1998), while HI data will be obtained thanks to the ALFALFA survey (Giovanelli et al. 2005).
Dedicated spectroscopic observations in drift scan mode, needed to measure the metal content of the target galaxies as well as their underlying stellar population at higher spectral resolution than with imaging, has been almost completed with CARELEC at the OHP 1.93m telescope. We are also undergoing Hα imaging observations (needed to measure the present day star formation activity) at the San Pedro Martir Observatory. 12CO(1-0) and 12CO(3-2) observations of the sample galaxies are under way at the Kitt Peak 12m and JCMT telescopes, while HI mapping at the Westerbork radiotelescope.

References

Abazajian, K., et al. 2005, 129, 1755

Alton, P., Trewhella, M., Davies, J., et al. 1998, A&A, 335, 807

Boselli, A., Tuffs, R., Gavazzi, G., Hippelein, H. & Pierini, D. 1997, A&AS, 121, 507

Boselli, A., Gavazzi, G., Donas, J., & Scodeggio, M. 2001, AJ, 121, 753

Boselli, A., Lequeux, J., & Gavazzi, G. 2002, A&A, 384, 33

Boselli, A., Gavazzi, G., & Sanvito, G. 2003, A&A, 402, 37

Boselli, A., & Gavazzi, G. 2006, PASP, 118, 517

Bregman, J., Snider, B., Grego, L., & Cox, C. 1998, ApJ, 499, 670

Catinella, B., Giovanelli, R., & Haynes, M. 2006, ApJ, 640, 751

Condon, J., et al. 1998, AJ, 115, 1693

Dunne, L., Eales, S., Edmunds, M., Ivison, R., Alexander, P., & Clements, D. 2000, MNRAS, 315, 115

Gavazzi, G., Pierini, D., Boselli, A. 1996, A&A, 312, 397

Gavazzi, G., Franzetti, P., Scodeggio, M., Boselli, A., & Pierini, D. 2000, A&A, 361, 863

Gavazzi, G., Bonfanti, C., Sanvito, G., Boselli, A., & Scodeggio, M. 2002, ApJ, 576, 135

Gavazzi, G., Zaccardo, A., Sanvito, G., Boselli, A., & Bonfanti, C. 2004, A&A, 417, 499

Gil de Paz, A., Boissier, S., Madore, B., et al. 2007, ApJS, 173, 185

Giovanelli, R., Haynes, M., Brian, K., et al. 2005, AJ, 130, 2598

Jarrett, T., Chester, T., Cutri, R., Schneider, S. & Huchra, J. 2003, AJ, 125, 525

Schlegel, F., Finkbeiner, D., & Davis M. 1998, ApJ, 500, 525

Scodeggio, M., Gavazzi, G., Franzetti, P., Boselli, A., Zibetti, S., & Pierini, D. 2002, A&A, 384, 812

Valahakis, C., Dunne, L., & Eales, S. 2005, MNRAS, 364, 1253

Zaritsky, D., Kennicutt, R., & Huchra, J. 1994, ApJ, 420, 87

SF2A 2008
C. Charbonnel, F. Combes and R. Samadi (eds)

AN OPTICAL VIEW OF THE 4 MPC X-RAY FILAMENT OF ABELL 85

Boué, G.[1], Durret, F.[2], Adami, C.[3], Mamon, G.[2], Ilbert, O.[4] and Cayatte, V.[5]

Abstract. The merging cluster Abell 85 (z=0.055) has a filament discovered in X-rays at least 4 Mpc in length, interpreted as due to groups falling on to the main cluster. We present here an optical study of this filament, based on deep broad band optical imaging and on Hα imaging, with the aims of: 1) analyzing the faint end slopes of galaxy luminosity functions in various wavelength bands and in various regions, which are expected to be influenced by physical processes (mergers, tides, infall); 2) searching for star formation in the filament galaxies, as expected if this region is undergoing merging processes.

1 Introduction

Large scale structure formation scenarios predict that matter is concentrated in filaments, with clusters at their intersection. However, due to their faintness, such filaments are difficult to detect directly. We discovered in X-rays a filament at least 4 Mpc in length in the merging cluster Abell 85 (z=0.055) and interpreted it as due to groups falling on to the main cluster (Durret et al. 1998, 2003, 2005). We test here the idea that merging processes trigger star formation in galaxies by obtaining narrow band Hα imaging of this cluster. We also present the results obtained with deep broad band imaging. A full description of this work can be found in Boué et al. (2008).

2 Galaxies with Hα emission

Based on broad and narrow band imaging obtained at the ESO 2.2m telescope with the WFI camera, 101 galaxies are detected in the Hα filter, out of which 23 have redshifts in the cluster, 2 have spectroscopic redshifts outside the cluster and 56 have photometric redshifts indicating they are probably outside the cluster. Most galaxies detected in Hα and belonging to the cluster are concentrated in the filament, suggesting that star formation is indeed triggered in the filament (Fig. 1). A Serna & Gerbal (1996) analysis of the overall spectroscopic sample for the whole Megacam region suggests that the filament is indeed a gravitationally bound region.

3 Galaxy luminosity functions

Galaxy luminosity functions (GLFs) were computed in the u*, g', r' and i' bands from deep Megaprime/Megacam images processed at the TERAPIX data center. The background contribution was subtracted statistically using the four CFHTLS Deep fields, and the cosmic variance was found to be the main source of error. The global GLFs are displayed in Fig. 2 in the four bands. The best fit slopes are -1.5 ± 0.15. The local GLFs computed in 16 subregions have shapes differing from one zone to another: they are more richly populated in the south part of the cluster and in the south east (where the X-ray filament is) than in the southwest.

[1] IMCCE, UMR 8028, Observatoire de Paris, 77 Av. Denfert-Rochereau, 75014 Paris
[2] IAP, CNRS UMR 7095 et Université Pierre et Marie Curie, 98bis Bd Arago, 75014 Paris
[3] LAM, Pôle de l'Etoile, site de Château-Gombert, 38 rue F. Joliot-Curie, , 13388 Marseille Cedex 13
[4] Institute for Astronomy, 2680 Woodlawn Dr., University of Hawaii, Honolulu, Hawaii 96822, USA
[5] Observatoire de Paris, LUTH, UMR 8102 et Université Denis Diderot , 5 place Janssen, 92195 Meudon

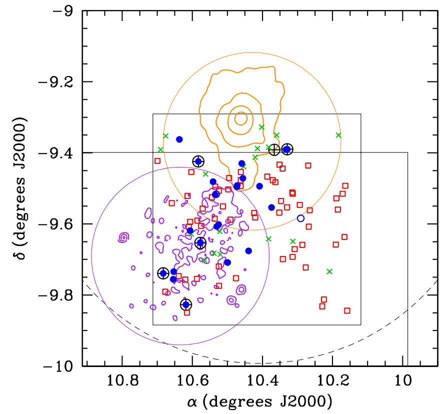

Fig. 1. Positions of the galaxies detected in Hα, with blue circles for galaxies with spectroscopic redshifts in the cluster and red squares for galaxies with no spectroscopic redshift. Black circled galaxies show Hα in their SDSS spectrum. The two large circles show the two XMM fields with isocontours superimposed. The dashed circle indicates the virial radius.

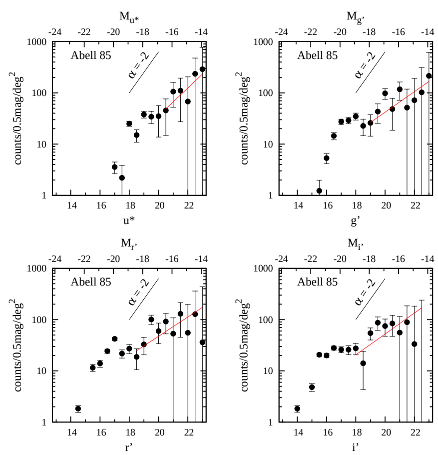

Fig. 2. Global luminosity functions for the south part of the cluster and filament region of Abell 85.

4 Conclusions

The filament of Abell 85, discovered in X-rays, is confirmed in the optical, and our results agree with the previous interpretation that the filament is made of groups falling on to the cluster. Our Hα detections may be preferentially concentrated in the filament but the statistics are too low to draw a firm conclusion.

References

Boué, G., Durret, F., Adami, C., Mamon, G., Ilbert, O., & Cayatte, V. 2008, A&A in press, arXiv:0807.4262

Durret, F., Forman, W., Gerbal, G., Jones, C., & Vikhlinin, A. 1998, A&A, 335, 41

Durret, F., Lima Neto, G.B., Forman, W., & Churazov, E. 2003, A&A 403, L29

Durret, F., Lima Neto, G.B., & Forman, W. 2005, A&A 432, 809

Serna, A., & Gerbal, D. 1996, A&A 309, 65

SF2A 2008
C. Charbonnel, F. Combes and R. Samadi (eds)

HI KINEMATICS AND DYNAMICS OF M31

Chemin, L.[1], Carignan, C.[2] and Foster, T.[3]

Abstract. We report on final results from recent deep HI observations of M31 obtained with the DRAO aperture synthesis telescope. Many emission lines can be detected along the line-of-sights. The total HI mass is composed by about 70% of a main spectral component attributed to the thin HI disc and 30% of an additional component, Part of this latter additional emission ($\sim$ 70%) is due to a newly discovered gas component, which we refer to as an "anomalous" component similar to the one observed in a few other galaxies. The gas distribution, warp parameters and rotation curve are presented, as well as results from mass distribution models of the rotation curve of M31.

1 Introduction

Mapping the neutral hydrogen in Local Group galaxies is never easy due to the extreme proximity of the galaxies. The main problems are caused by the contamination by the Milky-Way HI and by the difficulty to obtain many field-of-views on telescopes to fully map the galaxies. Nevertheless, the large field-of view, high sensitivity and spectral resolution of the DRAO synthesis telescope are used to obtain the most extended and deepest HI gas distribution of M31.

2 Results

The main results from this HI study of M31 which total integrated emission is shown in Figure 1 can be summarized as follows.

- A large fraction of the field-of-view is filled by several emission lines. Up to five lines can be detected in some spectra, which is more than the two usually known in M31. Two lines are detected in $\sim$65% of the spectra, three lines in $\sim$32% of them, four lines in $\sim$11% of them and five lines in $\sim$2% of them.

- The total HI mass of M31 is 5.1×10^9 $\mathcal{M}_\odot$. The thin HI disc traced by the brightest main spectral component contains 70% of this mass.

- The rotation curve is peculiar, admitting a central velocity dip at 5 kpc in the inner HI ring, two distinct flat parts, the first one at 265 km s^{-1} in the outer HI ring and extending over $\sim$ 9 kpc and the second one at $\sim$ 222 km s^{-1} in the outer disc and extending over $\sim$ 7 kpc (Fig. 1). Except in the perturbed region around $R = 5$ kpc, the axisymmetry of the gas rotation is very good between the two disc halves so that the velocity uncertainties are mostly below 10 km s^{-1}.

- The warp parameters are derived up to 33 kpc. The kinematical major axis is observed to continuously twist as a function of radius from $R = 19$ kpc while the inclination roughly remains constant throughout the HI disc at an average value of $75^o \pm 3^o$.

[1] Observatoire de Paris, GEPI & Université Paris 7, 5 pl. Janssen, 92195 Meudon, France, e-mail: laurent.chemin@obspm.fr
[2] Université de Montréal, Dept. de Physique, C.P. 6128, succ. centre ville, Montréal, QC, Canada H3C3J7
[3] Brandon University, Dept. of Physics & Astronomy, Brandon, MB, Canada R7A 6A9

- Though its effects in the datacube are spectacular by causing duplicated emission lines, the warp of M31 is thus not strong, contrary to what has been thought for a long time. The wiggles in the inclination profile arising at $R \sim 26$ kpc are fully responsible of the creation of part of the multiple emission lines. The mass attributed to the duplicated emission by the disc warping is small, probably at most $\sim 10\%$ of the total HI mass.

- The remaining 30% of the total HI mass enclosed in all other spectral lines than the rotating disc is thus made of $\sim 30\%$ from the warp contamination and $\sim 70\%$ from additional mechanisms. The latter "anomalous" gas component may have internal (expanding gas clouds in star forming regions) and/or external (extraplanar HI halo, intermediate or high velocity clouds) origins. No forbidden velocities are detected in the datacube, implying that if gas accretion occurs in M31 from extraplanar sources, it is not done from apparent counter-rotating orbits.

- A tight relationship is shown between HI structures and diffuse stellar structures (evidenced in Ibata et al. 2007), the G1 clump and the HI "loop" at the extremity of the SW approaching half. The HI kinematics indicates that the loop is bound to the disc, probably suggesting that the G1 clump is also bound to the disc. To the North-East, a relation between HI spurs and the NE stellar clump is also evidenced.

- Mass-model fittings of the rotation curve are made complicated due to the peculiar shape of the rotation curve. The central dip cannot be modelled in any fittings. The HI data seem to rule out the "universal" Navarro-Frenk-White cusp, which barely coexists with the bulge potential. The best fitted halo shape is for core-dominated or ΛCDM Einasto halos, thus for a constant or slowly decreasing inner mass density profile (Fig. 1).

- A dynamical mass of $\mathcal{M}_{\rm Dyn} = (3.2 \pm 0.3) \times 10^{11}\ \mathcal{M}_\odot$ enclosed within a radius of 33 kpc is derived. An extrapolation to the virial radius of 190 kpc leads to a total mass of $\mathcal{M}_{\rm Vir} \sim 5.0 \times 10^{11}\ \mathcal{M}_\odot$ for M31.

The results and analysis will be presented in Chemin, Carignan & Foster (2008).

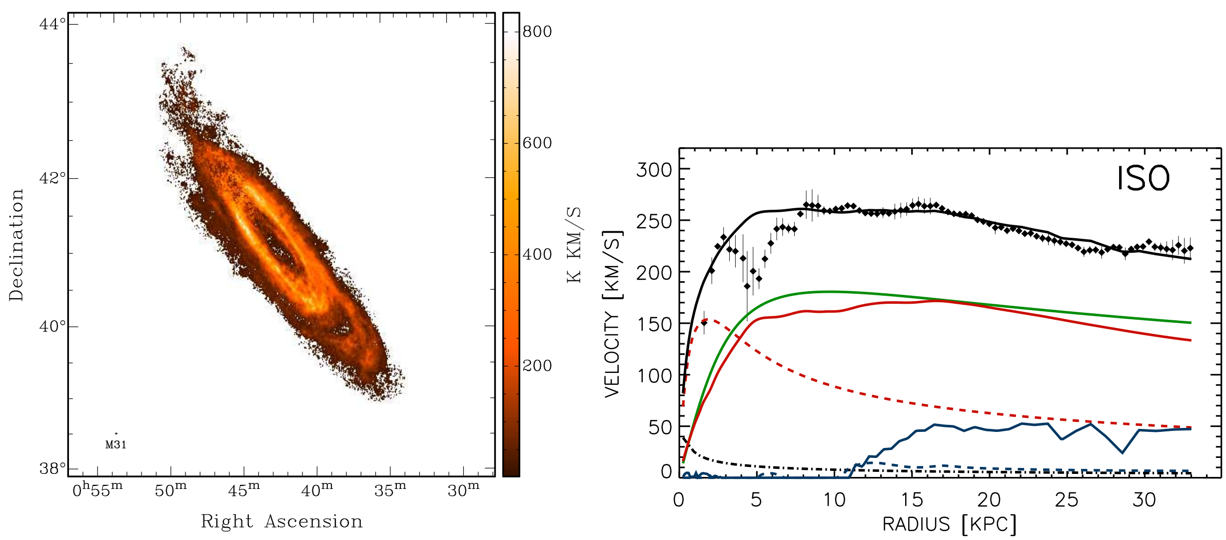

Fig. 1. Total integrated HI emission of M31 (left) and mass distribution models of the M31 HI rotation curve (right). A black dashed-dotted line is for the black hole contribution, blue lines for the neutral and molecular gaseous discs, red lines for the stellar disc and bulge, a green line for the dark matter halo and a black solid line for the overall model.

References

Chemin, L., Carignan, C., & Foster, T. 2008, submitted to ApJ

Ibata, R., Martin, N. F., Irwin, M., Chapman, S., Ferguson, A. M. N., Lewis, G., & McConnachie, A. W. 2007, ApJ, 671, 1591

THE GALMER DATABASE: MODELING COLORS AND SPECTRA

Di Matteo, P.[1], Chilingarian, I.[2], Melchior, A.-L.[2], Combes, F.[2] and Semelin, B.[2]

Abstract. The GalMer database is a library of thousands of simulations of galaxy interactions and mergers. We followed the evolution of the baryonic (gas and stars) and dark matter components through a Tree-SPH code (Semelin & Combes, 2002), including star formation recipes and metal enrichment. Different galaxy morphologies, mass ratios and orbital parameters are simulated, in order to study statistically the main physical processes related to galaxy encounters (see Di Matteo *et al*, 2007; Di Matteo *et al*, 2008a, 2008b). All the simulations are available at the web address *http://galmer.obspm.fr*, together with the tools for the on-the-fly analysis. Here we present some applications of this database.

1 Broadband photometric colors and spectra

We developed a technique to model spectrophotometric properties of interacting galaxies using results of GalMer simulations to trace kinematics, star formation and chemical enrichment history. Spectra, broadband photometric colors, and luminosity-weighted line-of-sight velocities are modeled by using PEGASE.HR (Le Borgne *et al*, 2004) and PEGASE.2 (Fioc & Rocca-Volmerange, 1999).

We pre-compute only once a grid of simple stellar populations (SSPs) corresponding to a given IMF (Miller & Scalo, 1979 in our case) and the grid of ages and metallicities, and we then apply it to all the particles. For each spatial bin, the dust extinction associated to each gas particle is computed using column density (to get AV) and the prescription of Fitzpatrick (1999) (to get the wavelength dependence). It is then applied to the total spectral energy distribution computed along the line of sight (excluding the current particle). This is done by co-adding the pre-computed SSPs from the grid mentioned above with the weights corresponding to a contribution of each age and metallicity contained in the SFH (star formation history) and CEH (chemical enrichment history). The dust extinction is then derived from the column density of gas, assuming a Galactic ratio and using the prescription of Fitzpatrick (1999), and applied to the total spectrum or SED as it was computed at the previous step. Then the total spectrum of the current particle is blue- or redshifted according to its radial velocity.

Figs. 1 and 2 show the resulting photometric colors and optical spectra for a simulated Sa galaxy, evolving isolated.

References

Di Matteo, P., Combes, F., Melchior, A.-L., & Semelin, B. 2007, A&A, 468, 61

Di Matteo, P., Combes, F., Melchior, A.-L., & Semelin, B. 2008a, A&A, 477, 437

Di Matteo, P., Bournaud, F., Martig, M., Combes, F., Melchior, A.-L., & Semelin, B. 2008b, A&A accepted, astro-ph/0809.2592

Fioc, M. & Rocca-Volmerange, B. 1999, A&A, 344, 393

Fitzpatrick, E.L. 1999, PASP, 111, 63

Le Borgne, D., Rocca-Volmerange, B., Prugniel, P., Lançon, A.,Fioc, M., & Soubiran, C. 2004, A&A, 425, 881

Miller, G. E. & Scalo, J. M. 1979, ApJS, 41, 513

Semelin, B. & Combes, F. 2002, A&A, 388, 826

[1] Observatoire de Paris - Section de Meudon, GEPI; 5 Place Jules Janssen, 92195 Meudon, France
[2] Observatoire de Paris, LERMA; 61, Avenue de l'Observatoire, 75014, Paris, France

Fig. 1. Photometric colors of an Sa galaxy, evolved isolated, 500 Myr after the beginning of the simulation. Three different line-of-sights are shown, corresponding to an edge-on view (left image), an inclination of 30 deg (central image) and a face-on view (right image). Color composition is as follows: B=g', G=r', R=z'.

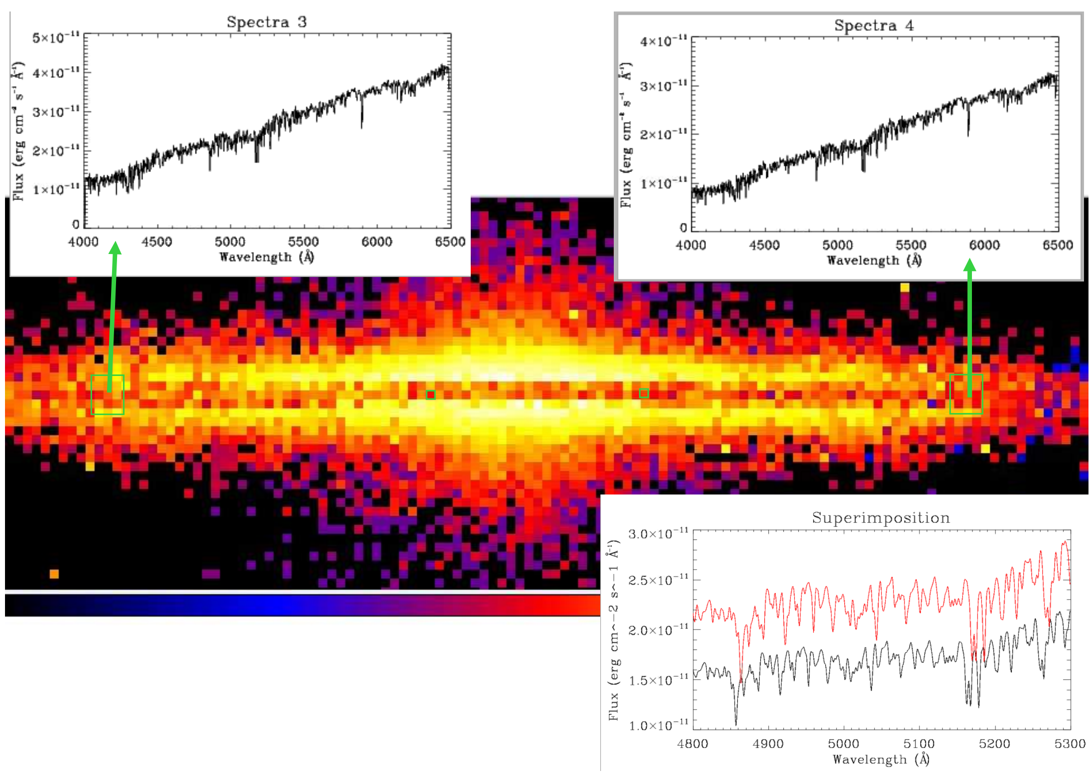

Fig. 2. Spectra of an Sa galaxy, evolved isolated 550 Myr after the beginning of the simulation. The spectra correspond to regions located about 12 kpc away from the galaxy center and to a 1 kpc $\times$ 1 kpc area. The underlying galaxy image is in B-band. The panel on the bottom right shows a comparison of the two spectra, revealing the rotation of the galaxy disk (blue and redshift).

SF2A 2008
C. Charbonnel, F. Combes and R. Samadi (eds)

H_2 ENERGETICS IN GALAXY-WIDE SHOCKS
INSIGHTS IN STARBURST TRIGGERING AND GALAXY FORMATION

Guillard, P.[1] and Boulanger, F.[1]

Abstract.
Spitzer space telescope observations led to the surprising detection of a diverse set of extragalactic sources whose infrared spectra are dominated by line emission of molecular hydrogen. The absence or relative weakness of typical signs of star formation (like dust features, lines of ionized gas) suggest the presence of large quantities of H_2 gas with no (or very little) associated star formation. We use the Stephan's Quintet (SQ) galaxy collision to define a physical framework to describe the H_2 formation and emission in galaxy-wide shocks. SQ observations show that exceptionally turbulent H_2 gas is coexisting with a hot, X-ray emitting plasma. The extreme mid-IR H_2 emission from the shock exceeds that of the X-rays. These observations set a new light on the contribution of H_2 to the cooling of the interstellar medium, on the relation between molecular gas and star formation, and on the energetics of galaxy formation.

These observations can be interpreted by considering that the shock is moving through an inhomogeneous medium. They suggest that most of the shock energy is transferred to bulk kinetic energy of the H_2 gas. The turbulent energy of the post-shock gas drives a mass cycle across the different gas phases where H_2 is forming out of the hot/warm gas. This interpretation puts the H_2 emission into a broader context including optical and X-ray observations. We propose that the turbulence in the clouds is powered by a slow energy and momentum transfer from the bulk motion of the gas and that the dissipation of this turbulent energy in turn is powering the H_2 emission.

1 Introduction

Recently, Spitzer IRS (Infra-Red Spectrometer) observations led to the unexpected detection of extremely bright mid-IR ($L > 10^{41}$erg s^{-1}) H_2 rotational line emission from warm gas towards the group-wide shock in Stephan's Quintet (hereafter SQ) (Appleton et al. 2006). This first result was quickly followed by the detection of bright H_2 line emission from more distant galaxies (Egami et al. 2006, Ogle et al. 2007) and from the NGC 1275 and NGC 4696 cooling flows (Johnstone et al. 2007). These H_2-bright galaxies may represent an important signature of galaxy evolution, but this unusual emission accompanied by little (or no) star formation has not yet been explained. Because of the absence or relative weakness of star forming signatures (dust features, ionized gas lines) in the mid-infrared Spitzer spectra, their exceptional H_2 luminosity may trace a *burst* of kinetic energy dissipation associated with galaxy interaction, gas infall or AGN feedback. In § 2 we briefly present the H_2-luminous compilation of objects observed by *Spitzer*. In § 3 we summarize the results obtained from our model (P. Guillard et al. 2008) of the SQ post-shock gas. Then § 4 discuss the implications of these results on our understanding of the kinetic energy dissipation in these systems.

2 An Emerging Population of H_2-Bright Sources

Fig. 1 shows a sample of this new class of extremely luminous H_2 emission galaxies, up to 10^{10} $L_\odot$ in pure rotational molecular hydrogen emission lines and relatively weak total IR emission(Ogle et al. 2009, in prep.). The most contrasted examples show bright H_2 emission lines with no spectroscopic signature (dust or ionized gas lines) of star formation (Appleton et al. 2006, Ogle et al. 2007). In many of these galaxies, molecular gas has been detected through the mid-IR H_2 rotational lines prior to any CO observation. The same properties

[1] Institut d'Astrophysique Spatiale, UMR 8617, CNRS, Université Paris-Sud 11, 91400 Orsay

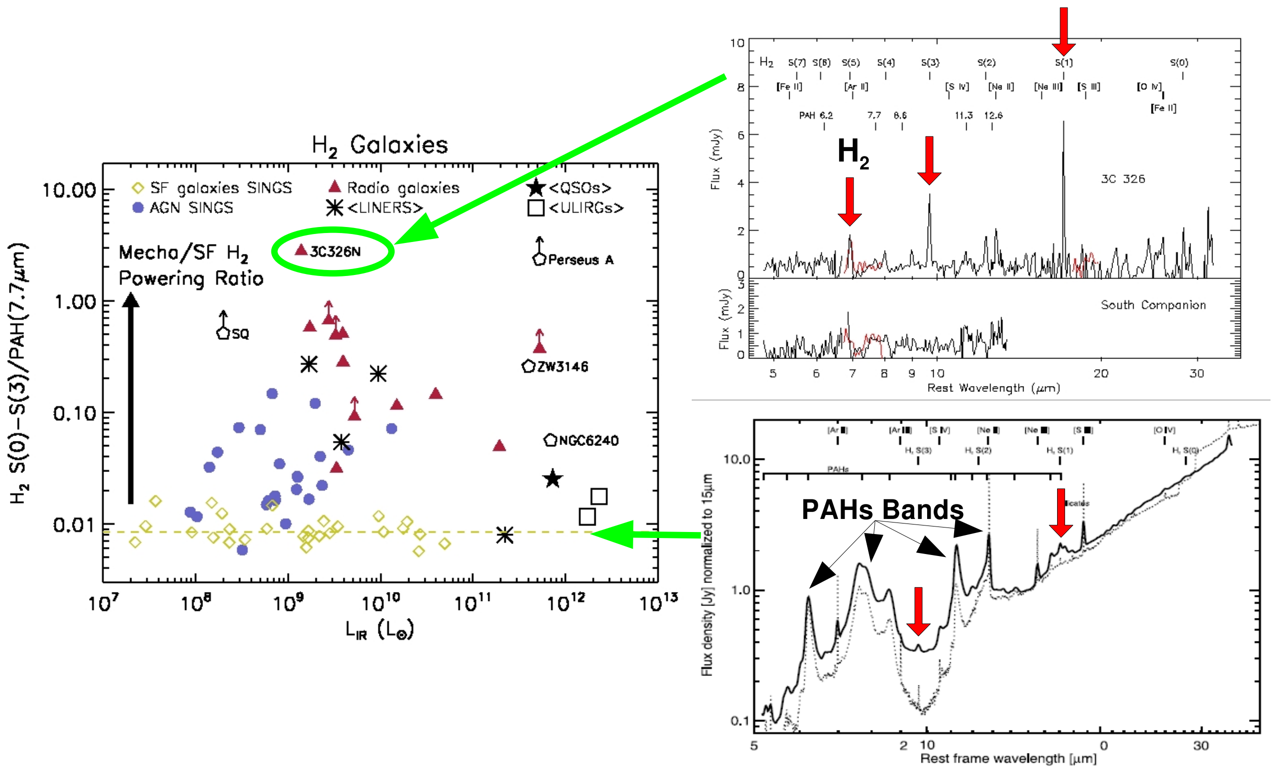

Fig. 1. The H_2 rotational lines emission is compared with the PAH emission in the 7.7 micron band (left side). The large black symbols represent averages for samples of galaxies. The smaller symbols represent individual galaxies. At all IR luminosities, the observations reveal galaxies with excess H_2 emission on top of the Star Formation (SF) contribution defined by SF dominated galaxies (dashed line). These H_2-Galaxies (MOHEGs) include active galactic nuclei galaxies (Seyferts, LINERs and radio galaxies), cooling flows (Perseus A, ZW3146) and colliding galaxies/mergers (SQ and NGC 6240). The excess H_2 emission reveals large (up to 10^{10} $M_\odot$) quantities of warm ($T > 150$ K) molecular gas. On the right side we show for comparison an example of spectra of the 3C326 H_2-luminous radio-galaxy (from Ogle et al. 2007) with respect to normal star forming galaxies (adapted from Brandl et al. 2006)

of the H_2 emission are observed in different types of objects that characterize key-processes at work in galaxy formation and evolution: gas accretion, galaxy interactions, gas ejection due to star formation or to the action of the central black hole on its environment. In each case, H_2 lines appear to have an unexpected contribution to the gas cooling.

3 The Stephan's Quintet: a ideal laboratory to study H_2 Energetics in Galaxy-Wide Shocks

SQ is a nearby (94 Mpc) H_2-luminous source where observations provide a clear astrophysical context to study the origin of the H_2 emission. A wide (5×25 kpc) shock is creating by a galaxy (NGC 7318b) colliding into a tidal tail at a relative velocity of $\sim 1\,000$ km s^{-1}. Evidence for a galaxy-wide shock comes from observations of X-rays from the hot post-shock gas (Trinchieri et al. 1003, 2005), strong radio synchrotron emission from the radio emitting plasma (Sulentic et al. 2001) and shocked-gas excitation diagnostics from optical emission lines (Xu et al. 2003). The surprise comes out from *Spitzer* observations that show that this gas also contain molecular hydrogen with an H_2 linewidth of 870 km s^{-1} (Appleton et al. 2006). The main energy reservoir is the bulk kinetic energy of the gas. A minor fraction of the collision energy is used to heat the hot plasma. The H_2 surface brightness is larger than the X-ray emission from the same region, thus the H_2 line emission dominates over X-ray cooling in the center of the shock. As such, it plays a major role in the energy dissipation and evolution of the post-shock gas.

We propose a scenario where a large-scale shock wave overtakes an inhomogeneous pre-shock medium (Guil-

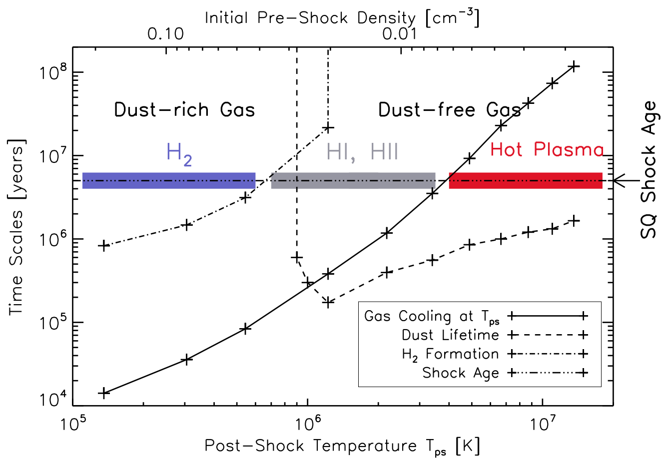

Fig. 2. The multiphasic post-shock medium. The dust lifetime, H_2 formation and gas cooling (full line) time scales in the SQ post-shock gas are plotted as a function of the post-shock temperature. Each shock velocity corresponds to a post-shock temperature or density. The ordering of the timescales separates the 3 main phases of the post-shock gas. The comparison of the H_2 formation time scale with the SQ shock age ($\sim 5 \times 10^6$ yr, indicated by the position of the bars) show where H_2 molecules can form (blue bar).

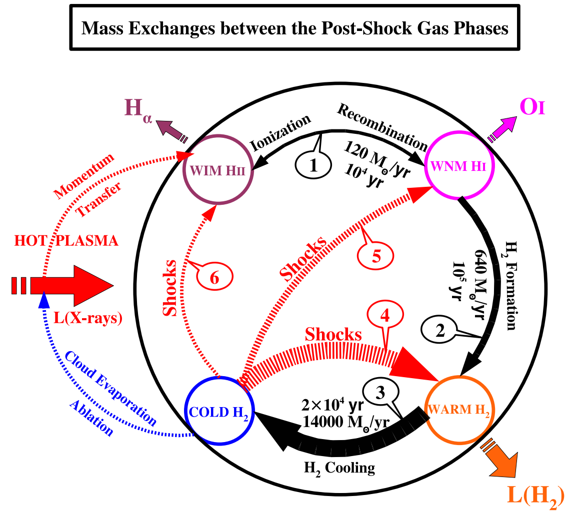

Fig. 3. Schematic view at the gas evolutionary cycle proposed in our interpretation of Stephan's Quintet optical and H_2 observations. Arrows represent the mass flows between the H II, warm H I, warm and cold H_2 gas components. They are numbered for clarity. The dynamical interaction between gas phases drives the cycle. The mass flow values and associated timescales are derived from the H_α, OI, and H_2 luminosities and model calculations. Heating of the cold H_2 gas (red arrows) is necessary to account for the increasing mass flow from the ionized gas to cold H_2 phases.

lard et al. 2008, submitted). The collision speed is the shock speed in the low density volume filling gas. The post-shock pressure of the hot gas drives slower shocks into denser gas. The post-shock gas is thus heated to a range of temperatures that depend on the pre-shock gas density. Our model quantifies the gas cooling, dust destruction, H_2 formation and excitation in the post-shock medium (Fig. 2).

Schematically, the low density volume filling pre-shock gas, shocked at high velocities ($\sim$ 600 km s^{-1}) becomes a dust-free X-ray emitting plasma. The cooling timescale of the hot gas is more than one order of magnitude greater than the shock age (5×10^6 yr). Therefore the post-shock plasma does not have the time to cool down and form molecular gas since the shock was initiated. Denser gas is heated at lower temperatures and dust survives. In the context of the SQ shock, we show that these clouds have time to cool down and form H_2 before being disrupted. We show that the cooling of the HII or HI gas cannot explain the observed H_2 emission, but that low-velocity ($5 - 20$ km s^{-1}) shocks driven into molecular fragments can account for it. We propose that these shocks are generated by cloud fragments collisions. The supersonic turbulence in the molecular fragments is powered by a slow energy and momentum transfer from the bulk motion of the gas. The turbulent energy of the post-shock gas drives a mass cycle across the different gas phases where H_2 is forming out of the hot gas.

4 The Cycling of Gas across ISM Phases

In this section, we place the Spitzer H_2 detection in the broader context set by optical observations. We propose a picture of the post-shock gas evolution that sketches the dynamical interaction between gas phases. This interpretation introduces a physical framework that may apply to H_2 luminous galaxies in general.

A schematic cartoon of the evolutionary picture of the post-shock gas which arises from our data interpretation is presented in Fig. 3. It sketches a global view that we detail here. Black and red arrows represent the mass flows between the H II, warm H I, warm and cold H_2 gas components of the post-shock gas. The large arrow to the left symbolizes the relative motion between the warm and cold gas and the surrounding plasma. Each of the black arrows is labeled with its main associated process: gas recombination and ionization (arrow number 1), H_2 formation (2) and H_2 cooling (3). The values of the mass flows and the associated timescales are derived from observations and our model calculations (see Guillard et al. 2008 for details).

A continuous cycle through gas components is excluded by the increasing mass flow needed to account for the H_α, OI, and H_2 luminosities. Heating of the cold H_2 gas towards warmer gas states (red arrows) needs to occur. It is the dissipation of the gas mechanical energy that powers these red arrows. The post-shock molecular cloud fragments are likely to experience a distribution of shock velocities, depending on their size and density. Arrow number 4 represents the low velocity magnetic shocks excitation of H_2 gas that can account for the H_2 emission (described in Guillard et al.). More energetic shocks may dissociate the molecular gas (arrows number 5). They are necessary to account for the low H_α to O I luminosity ratio. Even more energetic shocks may ionize the molecular gas (arrow number 6). This would bring cold H_2 directly into the H II reservoir.

Turbulent mixing of hot, warm and cold gas are an alternative mass input of H II gas. Turbulent mixing layers result from cloud gas shredding into fragments that become too small to survive evaporation due to heat conduction (see e.g. Begelman & Fabian, 1990). Turbulent mixing is represented by the thin blue arrow towards the surrouding plasma, to the left of our cartoon. Turbulent mixing produces intermediate temperature gas that is thermally instable. This gas cools back to produce H II gas that enters the cycle (thin red arrow). It is relevant to our scenario to note that cold gas in mixing layers probably preserves its dust content. It is only heated to a few 10^5 K, well below temperatures for which thermal sputtering becomes effective. Further, metals from the dust-free hot plasma that is brought to cool are expected to accrete on dust when gas cools and condenses.

5 Concluding remarks

Our understanding of the dynamical interaction between gas phase is inspired by numerical simulations (e.g. Audit & Hennebelle 2005) which have changed our perspective on the interstellar medium phases from a static to a dynamical picture. The interaction with the hot plasma supplies mechanical energy and momentum to the warm gas as discussed in the context of cold gas observations in clusters by Pope et al. 2008. In our interpretation it is this energy input which drives turbulence and the gas cycle.

Many galaxy collisions and mergers are observed to trigger IR-luminous bursts of star formation. However, the absence of spectroscopic signatures of photoionization (dust or ionized gas lines) in the center of the SQ shock (Xu et al. 2003) show no or little star formation in this region. Our interpretation is that the bulk kinetic energy of the gas colliding flows is not completely dissipated. Within this dynamical understanding of the post-shock gas, cold molecular is not a mass sink. The fact that there is no star formation at the centre of the shock shows that it is not long-lived enough to allow formation of gravitationally instable molecular fragments. Within a more general framework, interacting H_2 luminous galaxies may represent an intermediate phase in the evolution of mergers, prior to the starburst.

References

Appleton, P. N., Xu, K. C., Reach, W., et al. 2006, ApJ, 639, L51
Audit, E. & Hennebelle, P. 2005, A&A, 433, 1-13
Begelman, M.C. & Fabian, A.C. 1990, MNRAS, 244, 26
Egami, E., Rieke, G. H., Fadda, D., & Hines, D. C. 2006, ApJ, 652, L21
Guillard, P., Boulanger, F., Pineau des Forêts, G., Appleton, P.N., 2008, A&A, submitted
Johnstone, R. M., Hatch, N. A., Ferland, G. J., et al. 2007, MNRAS, 382, 1246
Ogle, P., Antonucci, R., Appleton, P. N., & Whysong, D. 2007, ApJ, 668, 699
Pope, E.; Pittard, J.; Hartquist, T. & Falle, S. 2008, MNRAS, 389, 1259
Sulentic, J. W., Rosado, M., Dultzin-Hacyan, D., et al. 2001, AJ, 122, 2993
Trinchieri, G., Sulentic, J., Breitschwerdt, D., & Pietsch, W. 2003, A&A, 401, 173
Xu, C. K., Lu, N., Condon, J. J., Dopita, M., & Tuffs, R. J. 2003, ApJ, 595, 665

SF2A 2008
C. Charbonnel, F. Combes and R. Samadi (eds)

ROTATION ON SUB-KPC SCALES IN THE STRONGLY LENSED Z~ 3 'ARC&CORE' AND IMPLICATIONS FOR HIGH-REDSHIFT GALAXY DYNAMICS

Nesvadba, N., P., H.[1, 2], Lehnert, M. D.[2] and Frye, B.[3]

1 IFU observations of gravitationally lensed and field galaxies at z$\sim 2-3$

Redshifts z$\sim$2$-$3 represent the cosmologically most important epoch of star formation and galaxy evolution. Detailed studies of individual galaxies during this epoch are now possible with integral-field spectrographs (IFUs). The emerging picture is however far from simple. Even adaptive optics (AO) assisted observations reach resolutions of only $\sim$ 1 kpc, making it difficult to infer even the basic physical mechanism driving the kinematics. Forster Schreiber et al. (2006) (hereafter FS06) argue that at least a subsample of blue, star-forming galaxies at somewhat lower redshifts, z$\sim$ 2.5, may show the signs of large, spatially-extended, rotating disks. Law et al. (2007) emphasize however that UV selected z$\sim$2$-$3 galaxies have irregular kinematics, which are likely not dominated by large-scale gravitational motion, but may be more related to merging or gas cooling. Moreover, none of these scenarios may be easily generalized to the overall population of high-z galaxies. To ensure observational success, only bright and large sources are being targeted with IFUs. This bears the risk that the targets will not be good representatives of the overall high-z galaxy population, but may be biased towards the most actively star forming and disturbed galaxies such as (minor and major) mergers.

To investigate whether this worry is substantiated we compare IFU samples of z$\sim$2$-$3 galaxies with galaxies at similar redshifts, where the observational constraints are alleviated by the additional boost of a gravitational lense. We do this in two steps: (1) Detailed comparison of a lensed and unlensed z$\sim$ 3 LBG with rest-frame optical IFU data. (2) A comparison of rest-frame optical line widths in unlensed z$\sim$2$-$3 galaxies with IFU data and lensed galaxies. Both comparisons suggest that existing IFU samples may be seriously biased.

2 The "arc&core": The first z$\sim$3 galaxy with a rotation curve on sub-kpc scales

Due to a fortuitous lensing configuration of the z=3.2 strongly lensed LBG (SLLBG) 'arc&core', we see a zoom into the inner $\sim$ 1 kpc and several more peripheral patches magnified by factors $\sim$ 20. Most strikingly, [OIII]λ5007 line emission reveals a smooth velocity gradient of 190 km s^{-1} at a spatial resolution of $\sim$ 200 pc in the source plane (Nesvadba et al. 2006), that resembles rotation curves of spiral galaxies at low redshift (Fig. 1). Line widths are uniform and relatively narrow, decreasing from σ=97$\pm$9 km s^{-1} in the inner 'core' to σ=62 $\pm$ 15 km s^{-1} in the outer 'arc'. The overall properties of the 'arc&core' appear rather average compared to samples of LBGs in the field, raising confidence that rotation on sub-kpc scales is not uncommon for high-z galaxies, and consistent with inside-out disk formation scenarios. Such scales are significantly smaller than what is found from IFU observations of unlensed galaxies at slightly lower redshifts.

An important measure to quantify the amount of random to ordered motion in galaxies is the ratio between velocity gradient v and Gaussian line width σ, v/σ. For the arc&core, v/σ $\sim$3, while the galaxies of FS06 have $v/\sigma \sim 1$, suggesting that field galaxies studied with IFUs are kinematically more strongly disturbed. This may be a result of somewhat different selection criteria (the z$\sim$ 2.5 sample has a UV color selection, but not strictly the Lyman-break technique). However, even the z=3.2 LBG Q0347-383 C5 (a classical LBG) shows the same trend. C5 consists of two separate, unresolved line emitting clumps with a relative velocity shift of 33

[1] Marie-Curie Fellow
[2] GEPI, Observatoire de Paris, CNRS, Universite Denis Diderot; 5, Place Jules Janssen, 92190 Meudon, France
[3] Dublin City University, School of Physics, Glasnevin, Dublin 9, Ireland

km s^{-1}, but much greater line widths $\sigma \sim 85$ km s^{-1} (Fig. 1), perhaps indicative of a merger of two subunits. The co-moving space density of bright LBGs like C5 is consistent with theoretically predicted merger rates (Nesvadba et al. 2008).

A comparison based on only two galaxies cannot be conclusive, but the number of strongly lensed LBGs at z$\sim$2$-$3 with deep IFU data sets is small, and the arc&core is the only SLLBG in the literature with a spatially resolved rotation curve. We thus compare with the integrated line widths of 5 z$\sim$ 3 SLLBGs with near-IR spectroscopy in the literature. We find significantly more narrow lines in the integrated spectra of SLLBGs compared to the spatially resolved maps of FS06. The spatial resolution of the field galaxies approximately corresponds to the size of the lensed galaxies in the source plane, so we compare spectra extracted from similarly large regions. Similarly to the above detailed comparison of two LBGs with IFU data, this may suggest that great care is warranted when generalizing IFU observations to the overall population of high-z galaxies.

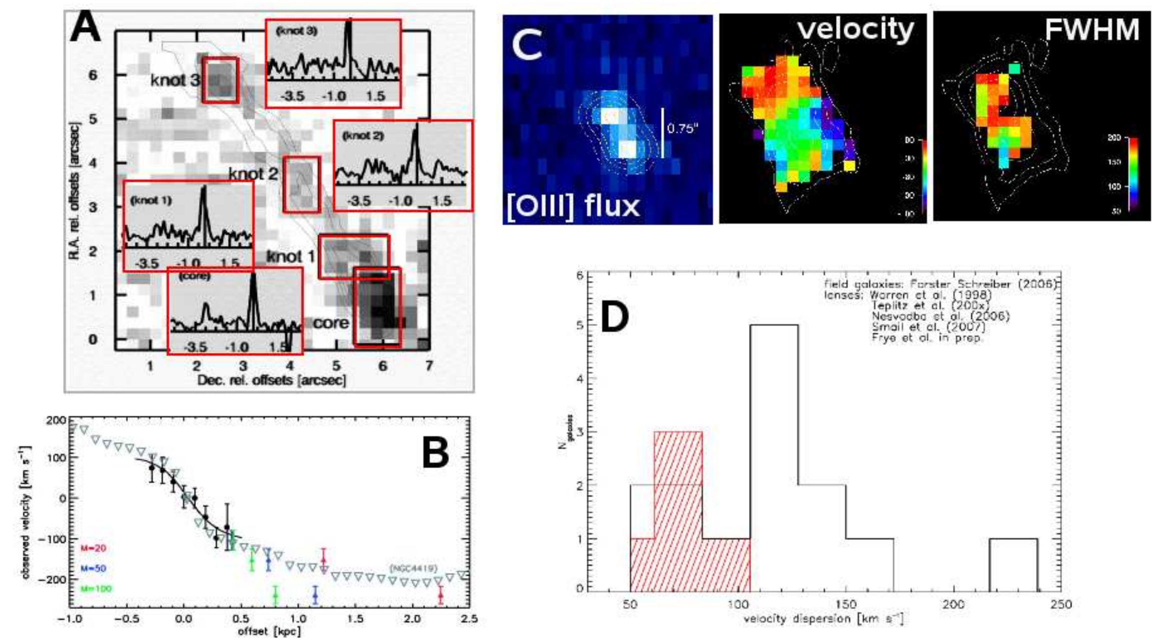

Fig. 1. *(A) [OIII]λ5007 line image of the 'arc&core'. Insets show spectra extracted from the apertures highlighted in red. (B) Relative velocities within the "core" (black dots) and the "arc" (red,blue and green triangles) closely resemble the rotation curve of a $\leq 10^{10}$ $M_\odot$ disk galaxy (black line: model, gray upside-down triangles: Rotation curve of the $\mathcal{L}^*$ sprial galaxy NGC4419 in the Virgo cluster). (C) (left to right) [OIII] morphology, velocities and FWHMs of the bright, unlensed LBG Q0347-383 C5. Morphology and kinematics are consistent with two interacting subunits. (D) Comparison of the line widths in lensed galaxies (red hatched histogram) with the sample of z$\sim$ 2.5 galaxies with IFU data (FS06). The lensed galaxies have widths in the lower tail of the unlensed sample.*

References

Forster Schreiber, N. et al. 2006, ApJ 645, 1062
Law D. et al. 2007, ApJ, 669, 929
Nesvadba N. P. H. et al. 2006, ApJ, 650, 693
Nesvadba N. P. H. et al. 2008, A&A, 479, 67
Smail et al. 2004, ApJL 654, 33
Teplitz et al. 2000, ApJL 533, 65
Warren et al. 1998, MNRAS 299, 1215

SF2A 2008
C. Charbonnel, F. Combes and R. Samadi (eds)

OUTFLOWS, BUBBLES, AND THE ROLE OF THE RADIO JET: DIRECT EVIDENCE FOR AGN FEEDBACK AT Z$\sim$2

Nesvadba, N., P., H.[1,2] and Lehnert, M. D.[1]

Abstract. To accommodate the seemingly "anti-hierarchical" properties of galaxies near the upper end of the mass function within our hierarchical paradigm, current models of galaxy evolution postulate a phase of vigorous AGN feedback at high redshift, which effectively terminates star formation by quenching the supply of cold gas. Using the SINFONI IFU on the VLT, we identified kpc-sized outflows of ionized gas in z$\sim$2$-$3 radio galaxies, which have the expected signatures of being powerful AGN-driven winds with the potential of terminating star formation in the massive host galaxies. The bipolar outflows contain up to few$\times 10^{10}$ M$_\odot$ in ionized gas with velocities near the escape velocity of a massive galaxy. Kinetic energies are equivalent to $\sim 0.2\%$ of the rest mass of the supermassive black hole. We discuss the results of this on-going study and the global impact of the observed outflows.

1 The role of AGN feedback for galaxy evolution in the early universe

AGN feedback is now a critical element of state-of-the-art models of galaxy evolution tailored to solve some of the outstanding issues at the upper end of the galaxy mass function. Observationally, a picture emerges where AGN feedback is most likely related to the mechanical energy output of the synchrotron emitting, relativistic plasma ejected during the radio-loud phases of AGN activity: Giant cavities in the hot, X-ray emitting halos of massive galaxy clusters filled with radio plasma are robust evidence for AGN feedback heating the gas on scales of massive galaxy clusters (e.g., McNamara & Nulsen, 2007). Best et al. (2006) analyzed a large sample of early-type galaxies from the SDSS catalog with FIRST and NVSS radio data and found that heating by the radio source may well balance gas cooling over 2 orders of magnitude in radio power and in stellar mass.

However, since most of the growth of massive galaxies was completed during the first few Gyrs after the Big Bang, observations at low redshift can only provide evidence that AGN feedback is able to *maintain* the hot, hydrostatic halos of massive early-type galaxies (*"maintenance mode"*). If we want to observe directly whether AGN feedback indeed quenched star formation and terminated galaxy growth in the early universe (*"quenching mode"*), we have to search at high redshift. With this goal, we started a detailed analysis of the rest-frame optical line emission in powerful, z$\sim$2$-$3 radio galaxies with integral field spectroscopy, where we may plausibly expect the strongest signatures of AGN-driven winds.

2 Powerful radio galaxies at z$\sim$ 2$-$3: Dying starbursts in the most massive galaxies?

The observed properties of HzRGs suggest they may be ideal candidates to search for strong, AGN-driven winds: They have large stellar (Seymour et al. 2007) and dynamical (Nesvadba et al. 2007a) masses of $\sim 10^{11-12}$ M$_\odot$ and reside in significant overdensities of galaxies suggesting particularly massive underlying dark-matter halos (e.g., Venemans et al. 2007). Large molecular gas masses in some sources (e.g., Papadopoulos et al. 2000) and submillimeter observations suggest that some HzRGs at redshifts z$\geq 3-4$ are dust-enshrouded, strongly star-forming galaxies with FIR luminosities in the ULIRG regime. Interestingly, the fraction of submillimeter-bright HzRGs shows a rapid decline from >50% at z>2.5 to $\leq$15% at z<2.5 (Reuland et al. 2004). This suggests that HzRGs may be particularly massive galaxies near the end of their phase of active star formation. They also host particularly powerful AGN. Thus, they are good candidates to search for the kinematic signatures of AGN-driven winds.

[1] GEPI, Observatoire de Paris, CNRS, Universite Denis Diderot; 5, Place Jules Janssen, 92190 Meudon, France
[2] Marie-Curie Fellow

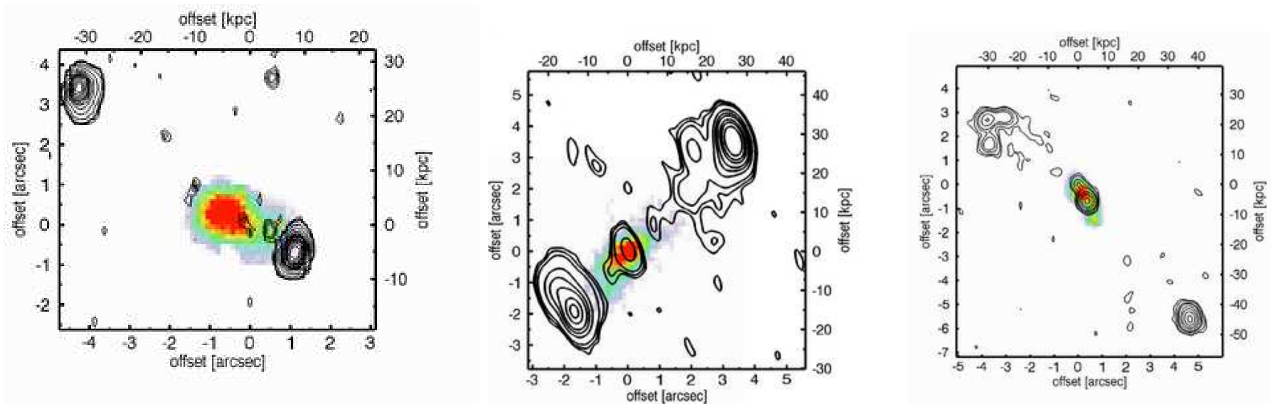

Fig. 1. *(left to right:)* [OIII]λ5007 emission line morphologies of MRC0316-257 at z=3.1, MRC0406-244 at z=2.4 and TXS0828+193 at z=2.6. Contours indicate the line-free continuum morphology for MRC0406-244 and TXS0828+193, and the 4.8 GHz radio core for MRC0316-257, where we did not detect the continuum.

3 Observational evidence for AGN-driven winds in z$\sim$2$-$3 radio galaxies

To directly investigate whether HzRGs may be the sites of powerful, AGN driven winds, we collected a sample of HzRGs at redshifts z$\sim$2$-$3 with rest-frame optical near-infrared spectral imaging obtained with SINFONI on the VLT. Including scheduled observations, our total sample will consist of 29 galaxies spanning wide ranges in radio power and radio size. We also include galaxies with compact, and probably young, radio sources. We will in the following concentrate on the analysis of a first subsample of 6 galaxies, 4 with extended jets with radii between 10 and 50 kpc, 2 with more compact radio sources <10 kpc in radius. For details see Nesvadba et al. (2006, 2007a, 2008).

3.1 Continuum and emission line morphologies

Using an integral-field spectrograph, we were able to extract continuum-free line images as well as line-free continuum images from our three-dimensional data cubes (Fig. 1). We find that in all cases, the continuum emission is relatively compact, but spatially resolved in some cases, with half-light radii $\leq$ 5 kpc. Radio-loud AGN activity is often related to an on-going merger. However, we only identify one continuum knot per galaxy. For the merger scenario, this may suggest an advanced stage where the galaxies are seperated by less than the $\sim$ 4 kpc spatial resolution of our data. Alternatively, since SINFONI is relatively inefficient in detecting low surface-brightness continuum emission, nuclear activity may have been triggered by other processes like minor mergers or perhaps cooling flows in cluster environments.

The extended, distorted morphologies of HzRGs with extended jets seen in broad-band imaging are mostly due line contamination, originating from emission line regions that extend over several 10s of kpc, and are significantly larger than the continuum (Nesvadba et al. 2008), but extend to smaller radial distances than the radio lobes. The same is found from Lyα longslit spectroscopy (e.g., Villar-Martin 2003). Overall, different emission lines in the same galaxy show similar morphologies. In the galaxies with *compact* radio sources, the line emission appears also compact. This may suggest a causal relationship between the advance of the jet and the extent of the high surface brightness emission line gas.

3.2 Kinematics, outflow energies, and physical properties of the ionized gas

We fitted spectra extracted from individual spatial resolution elements to construct two-dimensional maps of the relative velocities and line widths (Fig. 2). Typically, the velocity maps show two bubbles with relatively homogeneous internal velocity, and projected velocities relative to each other of 700$-$1000 km s^{-1}, reminiscent of back-to-back outflows extending from near the radio core. MRC1138-262 has a more complex structure with at least 3 bubbles. Line widths are generally large, indicating strong turbulence, with typical FWHMs $\sim$500$-$1200 km s^{-1}. Areas with wider lines may be due to partial overlap between bubbles.

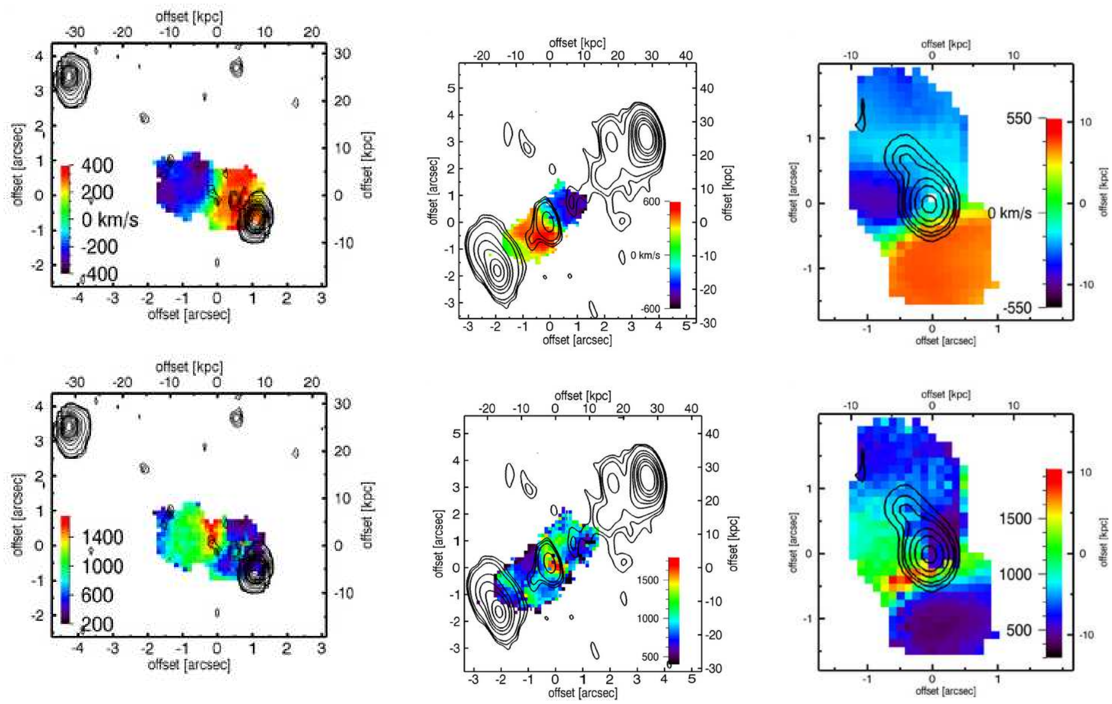

Fig. 2. *top, left to right:* Maps of relative velocities (in km s^{-1}) for MRC0316-257 at z=3.1, MRC0406-244 at z=2.4, and TXS0828+193 at z=2.6. *bottom, left to right*: Maps of FWHMs (in km s^{-1}) for the same galaxies. Contours show the jet morphologies. For TXS0828+193, the lobes are outside of the area shown.

Filamentary morphologies and low gas filling factors suggest that the UV-optical line emission may originate from clouds of cold gas that are being swept up by an expanding hot medium, most likely related to the overpressurized 'cocoon' of gas heated by the radio jet. In such a scenario the velocity of the clouds may yield an estimate of the kinetic energy injection rate necessary to accelerate the gas to the observed velocities of up to $\sim 10^{45}$ erg s^{-1} (Nesvadba et al. 2006). The size and velocities of the outflow suggest dynamical timescales of few $\times 10^7$ yrs. Maintaining the observed outflows over such timescales requires total energy injections of $\sim 10^{60}$ erg. This is in the range of what is observed for AGN driven bubbles in massive clusters at low redshift (e.g., McNamara & Nulsen, 2006, and references therein). The observed velocities and kinetic energies are also in the range of escape velocities and binding energies expected for galaxies with masses of few $\times 10^{11}$ M$_\odot$ (Nesvadba et al. 2006). This may suggest that much of the gas participating in the outflows may ultimately be unbound from the underlying gravitational potential.

3.3 Molecular and ionized gas budgets

Having measured Hα line fluxes, we are able to roughly estimate ionized gas masses assuming case B recombination (see Nesvadba et al. 2008 for details). For galaxies where we also measured Hβ, we correct for extinction of $A_V \sim 1-4$ mag and find ionized gas masses of up to few $\times$ 10^{10} M$_\odot$. (Without the correction, estimates are few $\times 10^9$ M$_\odot$, Nesvadba et al. 2008.) This exceeds the amount of ionized gas found in any other high-redshift galaxy population by several orders of magnitudes, including galaxies with starburst-driven winds. Nesvadba et al. (2007b) investigated a spatially-resolved, starburst driven wind in a strongly star-forming submillimeter-selected galaxy at z$\sim$2.6 with of order few$\times 10^6$ M$_\odot$ in ionized gas in the wind. Compact radio galaxies have lower entrained gas masses, but in the range of what would be expected for less evolved outflows with similar entrainment rates as the galaxies with large radio lobes (Nesvadba et al. 2007a).

Molecular gas masses in strongly star-forming galaxies at high redshift are also typically in the range of few $\times 10^{10}$ M$_\odot$ (e.g., Neri et al. 2003), and are a necessary prerequisite to fuel the observed starbursts with star formation rates of few 100 M$_\odot$ yr^{-1}. However, not all HzRGs have been detected in CO. TXS0828+193 specifically, which is part of our sample, appears to have less than $\sim 10^{10}$ M$_\odot$ in molecular gas (Nesvadba et al., in prep.). This illustrates that the AGN winds may affect a significant fraction of the overall interstellar medium of strongly star-forming, massive galaxies in the early universe. Since the velocities are near the expected escape velocity of a massive galaxy and underlying dark-matter halo (§3.2), much of this gas may actually escape.

4 Global impact of AGN driven winds

Four out of four HzRGs with extended radio jets show evidence for outflows with with kinetic energies of up to 10^{60} erg over dynamical timescales of 10^7 yrs, and the preliminary analysis of our full sample suggests that this is far from being unusual. Nesvadba et al. (2006, 2008) estimate that the outflow energies correspond to $\sim 10\%$ of the jet kinetic luminosity. If this coupling efficiency between jet and interstellar medium is typical for HzRGs with similarly powerful radio sources, then the redshift-dependent luminosity function of Willott et al. (2001) suggests that at redshifts z$\sim 1-3$, AGN-winds release an overall energy density of about 10^{57} erg s^{-1} Mpc^{-3}. Some of this energy release may contribute to heating and increasing the entropy in extra-galactic gas surrounding the HzRG, and to enhance gas stripping in satellite galaxies, so that subsequent merging with satellites will be relatively dissipationless. This may later contribute to preserving the low content in cold gas and old, luminosity weighted ages of the highly metal-enriched stellar population in massive galaxies to the present day, in spite of possible continuous accretion of satellite galaxies over cosmologically significant periods (Nesvadba et al. 2008).

If the outflows are related to the nuclear activity, then the ultimate energy source powering the outflow is accretion onto the supermassive black hole in the center of the galaxy. Thus, models of galaxy evolution often parameterize the efficency of AGN feedback by the energy equivalent of the rest mass of the black hole. Since we have reason to believe that HzRGs approximately fall onto the low-redshift M-σ relationship between the mass of the supermassive black hole and velocity dispersion of the host, we can use the stellar mass estimates of Seymour et al. (2007) to roughly estimate the black hole mass of our targets. We find that of order 0.1% of the energy equivalent of the black hole mass in HzRGs is being released in kinetic energy of the outflows. A similar estimate based on the global energy density released by powerful radio galaxies estimated above, and the local black hole mass density yields a very similar result, $\sim 0.2\%$. This is very close to what is assumed in galaxy evolution models (e.g., Di Matteo et al. 2005), and highlights the likely importance of the observed outflows on galaxy evolution.

References

Baum S. & McCarthy, P.J., 2000, AJ 119 2634
Benson et al. 2003, ApJ, 599,38
Best P., Kaiser C., Heckman T., & Kauffmann, G., 2006, MNRAS, 368, 76
Di Matteo T. et al. 2005, Nature 433 604
McNamara B. & Nulsen P., 2007, ARA&A, 45, 117
Nesvadba N. P. H., et al. 2006, ApJ, 650, 693
Nesvadba N. P. H., et al. 2007a, A&A, 475, 145
Nesvadba N. P. H., et al. 2007b, A&A, 475, 145
Nesvadba N. P. H., et al. 2008, A&A accepted, astro-ph/0809.5171
Papadopoulos, P., Rottgering, H., van der Werf, P., 2000, ApJ, 528,626
Pipino, A. & Matteucci, F. 2004, MNRAS 357, 968
Reuland et al. 2004, MNRAS, 353 377
Seymour, N. et al. 2007, ApJS, 171, 353
Venemans, B. et al., 2007, A&A 461,823
Villar-Martin et al. 2003, MNRAS 357,273
Willott et al. 2001, MNRAS 322,536

SF2A 2008
C. Charbonnel, F. Combes and R. Samadi (eds)

BAYESIAN ANALYSIS OF GALAXY SEDS FROM FUV TO FIR

Noll, S.[1], Burgarella, D.[1], Marcillac, D.[2], Giovannoli, E.[1] and Buat, V.[1]

Abstract. Photometric data of galaxies ranging from rest-frame far-UV to far-IR allow to derive galaxy properties in a robust way by fitting the attenuated stellar emission and the related dust emission at the same time. For this purpose we have written a code which uses model spectra composed of the Maraston stellar population models, synthetic attenuation functions based on a modified Calzetti law, spectral line templates, and the Dale & Helou dust emission models. Depending on the input redshifts filter fluxes are computed for the model set and compared to the galaxy photometry by carrying out a Bayesian analysis. The code is tested by analysing a subset of the SINGS sample of nearby galaxies. We illustrate the quality of the results by comparing them to literature data and discuss the importance of IR data for the reliability of the fitting.

1 Project

Rest-frame UV-to-IR spectral energy distributions (SEDs) of star-forming galaxies at given redshifts enable us to derive physical galaxy properties with a high reliability, since dust extinction and dust emission can be studied at the same time. For this reason, we have developed the observer-friendly programme package *CIGALE* (*C*ode *I*nvestigating *GAL*axy *E*mission) following a Bayesian approach (cf. Burgarella et al. 2005).

2 Procedure

CIGALE uses a grid of model templates based on one or two stellar population models of Maraston (2005) or PEGASE (Fioc & Rocca-Volmerange 1997) with different ages and exponentially decreasing star-formation rates (SFRs) characterised by the e-folding time τ. The use of Maraston (2005) models is preferred, since thermally pulsating asymptotic giant branch stars are considered. The stellar spectra are extinguished by Calzetti et al. (2000) dust attenuation curves modified by multiplying a power law (allowing for different slopes) and adding an optional Gaussian 2175 Å bump. The latter is suggested by the frequent detection of UV bumps in distant, UV-luminous galaxies (Noll et al. 2007). The re-emission of the dust-absorbed energy in the IR is considered by consistently adding dust emission templates of Dale & Helou (2002), which are parameterised by the slope of the power-law distribution of dust mass over heating intensity. Finally, the UV-to-IR spectra are corrected by empirical interstellar emission and absorption templates based on spectra of Kinney et al. (1996) and Noll et al. (2004).

For the redshifts of the objects under investigation filter fluxes are derived for each model and compared to the observed data by computing χ^2. Then, *CIGALE* performs a Bayesian analysis by using the distribution of χ^2-selected 'good' models in the parameter space in order to derive expectation values and standard deviations for the galaxy properties describing the models used.

3 Results from a SINGS test sample

We test the quality of the code by using a sample of 52 local SINGS galaxies (Kennicutt et al. 2003) for which photometry of Dale et al. (2007) in 16 filters between GALEX FUV and MIPS 160 μm is available. Combining

[1] Observatoire Astronomique de Marseille-Provence, 38 rue Frédéric Joliot-Curie, 13388 Marseille Cedex 13, France
[2] Institut d'Astrophysique Spatiale, Bât. 121, Université Paris XI, 91405 Orsay, France

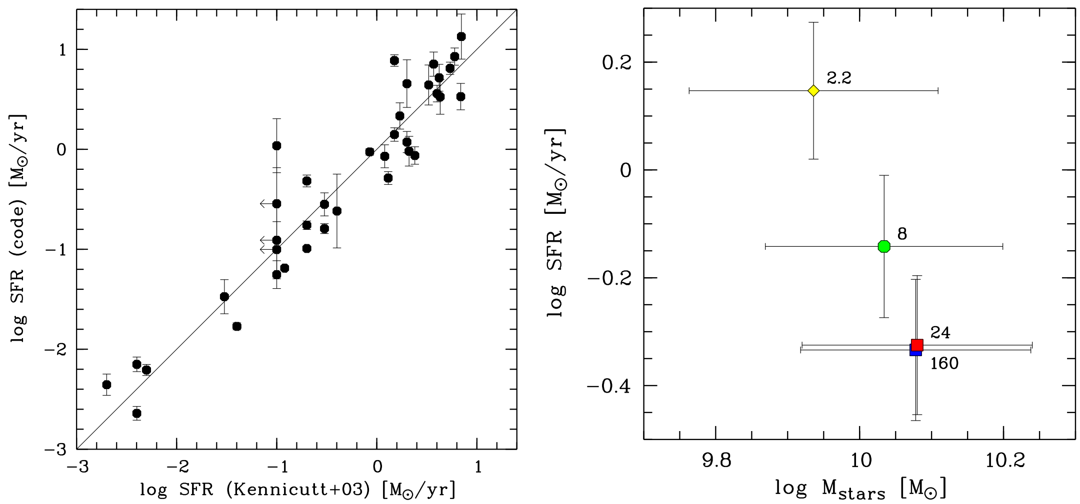

Fig. 1. *Left:* Comparison of the SFRs of our SINGS subsample derived from the code and those of Kennicutt et al. (2003) based on Hα emission. *Right:* Sample means and mean errors for the total stellar mass and SFR of our SINGS subsample for different filter combinations. The wavelength in μm of the last filter in the filter set is indicated near the symbols.

a 10 Gyr and a $\leq$ 0.2 Gyr-old model with different τ and mass ratios for solar metallicity, and a large set of attenuation curves (allowing for different $E(B-V)$ in both model components) and dust emission templates, we find good agreement between the measured and best-model filter fluxes. Typical systematic deviations are about 0.1 mag only.

The *CIGALE* results show good agreement with literature data derived in a different way. For example, our SFRs and the Hα-based ones in Kennicutt et al. (2003) differ by marginal 0.02 ± 0.04 dex on average only. Reducing the number of filters in the IR causes a significant deterioration of the fitting results, in particular, for the SFR, if no filter is available which traces the dust emission.

4 Conclusions

The new SED-fitting code *CIGALE* works and is ready for use at higher redshifts. Photometric data from rest-frame UV to IR are essential to obtain reliable galaxy properties.

References

Burgarella, D., Buat, V., & Iglesias-Páramo, J. 2005, MNRAS, 360, 1413

Calzetti, D., Armus, L., Bohlin, R.C., et al. 2000, ApJ, 533, 682

Dale, D.A., & Helou, G. 2002, ApJ, 576, 159

Dale, D.A, Gil de Paz, A., Gordon, K.D., et al. 2007, ApJ, 655, 863

Fioc, M., & Rocca-Volmerange, B. 1997, A&A, 326, 950

Kennicutt, R.C. Jr., Armus, L., Bendo, G., et al. 2003, PASP, 115, 928

Kinney, A.L., Calzetti, D., Bohlin, R.C., et al. 1996, ApJ, 467, 38

Maraston, C. 2005, MNRAS, 362, 799

Noll, S., Mehlert, D., Appenzeller, I., et al. 2004, A&A, 418, 885

Noll, S., Pierini, D., Pannella, M., & Savaglio, S. 2007, A&A, 472, 455

SF2A 2008
C. Charbonnel, F. Combes and R. Samadi (eds)

MASS ASSEMBLY AND CHEMICAL EVOLUTION OF GALAXIES ALONG COSMIC TIME WITH THE MASSIV SURVEY

Queyrel, J.[1], Contini, T.[1], Epinat, B.[2], Garilli, B.[3], Lamareille, F.[1], Le Fèvre, O.[2], Vergani, D.[4], Kissler-Patig, M.[5], Lemoine-Busserole, M.[6], Perez-Montero, E.[1] and the MASSIV collaboration[7]

1 Introduction

Nowadays, powerful telescopes allow to have deep insight into formation and evolution of galaxies since very early epochs. Thanks to these new instruments it is possible to acquire a very good knowledge of the dynamical, physical and chemical properties of high redshift galaxies, putting strong constraints on galaxy evolution models. Here we present first results of the MASSIV (Mass Assembly Survey with SINFONI in VVDS) project, an ESO-VLT Large Program with the 3D NIR spectrograph SINFONI, aimed at observing a representative sample of about 100 star-forming galaxies in the redshift range $z \sim 1 - 2$, picked-up from the VVDS (VIMOS VLT Deep Survey). The measurement of nebular emission-lines (Hα, [OIII], [NII], etc) in the datacubes gives access to dynamical and chemical properties of galaxies through velocity and emission-line ratios maps. This allows to follow the evolution with cosmic time of the fraction of rotating disks, spheroids and mergers as well as of fundamental scaling relations such as the Tully-Fisher and Mass-Metallicity relations.

2 Sample selection and observations

For this ESO Large Programe (PI: T. Contini), a sample of 140 galaxies has been selected from the VVDS. They are chosen to be star forming galaxies at $1 < z < 2$ – a crucial period in the evolution of the universe – so that they present emission-lines giving acces to their physical properties. Selecting galaxies in the VVDS allows to build a statistical and representative sample of galaxies at high redshift.

The VIMOS VLT Deep Survey (Le Fèvre et al. 2005) aims at following the evolution of galaxies, AGNs and large-scale structures with spectroscopic redshifts and multiwavelength dataset. It is a purely I-band apparent magnitude limited survey which makes it the least biased survey of the distant universe available today. About 150 galaxies meet the constraints – star-forming, right redshift to avoid bright OH sky lines, bright star close enough for AO/LGS observations – defined for the MASSIV project.

In the J and H bands ($R \sim 2000$) the IFU technology gives acces to a spectrum with nebular emission-lines for each pixel in the FoV. Data reduction is performed with the SINFONI pipeline which substracts the sky background, flat-fields the images, calibrates in wavelength and recontructs the final datacube. Each observation block is spatialy centered considering an offset of the telescope from a bright star. With the assistance of the AO-LGS we are able to study very accurately the properties of the galaxies over their spatial extent.

[1] Laboratoire d'Astrophysique de Toulouse - Tarbes, France
[2] Laboratoire d'Astrophysique de Marseille, France
[3] INAF, Milano, Italy
[4] INAF, Bologna, Italy
[5] ESO, Germany
[6] Oxford University, UK
[7] `http://www.ast-obs-mip.fr/massiv`

3 Kinematics, physical and chemical properties

Deep insights in galaxies properties are made possible by 3D-spectroscopy. The spectra in each spaxels allow to produce velocity maps and flux (ratio) maps, in order to derive the rotational and dispersion velocities, dynamical mass, SFR, chemical abundances, etc. In association with the morphology deduced from HST and CFHTLS images, it will be possible to disentangle rotating disks, spheroids, clear mergers, etc. Figure 1 shows an example of such an analysis performed on a galaxy at $z \sim 1$ observed in April 2008 in the J band. Comparisons with simulated datacubes (produced by cosmological simulations, e.g. Horizon) are also foreseen.

4 Tully-Fisher and Mass-Metallicity relations

The relation between galaxy luminosity and maximal rotation velocity is well known in the local universe as the TF-relation. Investigating how it evolves with redshift is the goal of many studies (e.g. Flores et al. 2006). The use of rotation curves deduced from velocity maps, contrary to those produced with long-slit spectroscopy, is a far better way to estimate $V_{\rm rot}$ and derive the TF-relation at $1 < z < 2$.

Many physical processes have been evoked to explain the origin of the mass-metallicity relation (outflows, downsizing, etc), so that evolutionary models need to reproduce it. If this relation is well constrained at $z \sim 0$ (Tremonti et al. 2004; Lamareille et al. 2004), we need to precise its evolution with redshift. Recent studies show an evolution toward lower metallicities (Erb et al. 2006; Maiolino et al. 2008; Lamareille et al. 2008; Contini et al. 2008), but strong efforts are still to be made to ripen our knowledge (see fig 1).

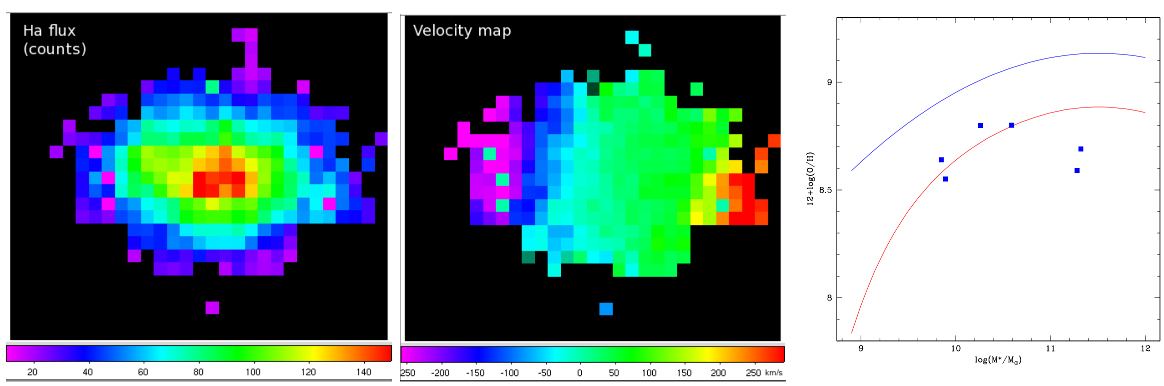

Fig. 1. Left and Middle. Hα flux and velocity maps of VVDS140217425 ($z = 0.9792$) obtained with SINFONI. **Right.** Mass-Metallicity relation of 6 VVDS galaxies (blue squares) at $z \sim 1.4$ (Queyrel et al. 2008). The relations at $z \sim 0$ in blue (Tremonti et al. 2004) and at $z \sim 2$ in red (Erb et al. 2006) are also shown for comparison.

References

Contini, T., Lamreille, F., Perez-Montero, E., et al. 2008, *in prep*

Erb, D. K., Shapley, A. E.,Pettini, M., et al. 2006, ApJ, 644, 813

Flores, H., Hammer, F., Puech, M., Amram, P., Balkowski, C. 2006, A&A, 455, 107

Lamareille, F.,Mouhcine, M.,Contini, T.,Lewis, I., Maddox, S. 2004, MNRAS, 350, 396

Lamareille, F., Brinchmann, J., Contini, T., et al. 2008 *submited to A&A*

Le Fèvre, O.,Vettolani, G.,Garilli, B., et al. 2005, A&A, 139, 845

Maiolino, R.,Nagao, T.,Grazian, A., et al. 2008, A&A, 488, 463

Queyrel, J., Contini, T., Lemoine-Busserolle, M., et al. 2008, *submited to A&A*

Tremonti, C. A., Heckman, T. M., Kauffmann, G., et al. , 2004, A&A, 613, 898

SF2A 2008
C. Charbonnel, F. Combes and R. Samadi (eds)

OBSERVATIONS OF A Z = 0.9 CLUSTER OF GALAXIES

Ulmer, M.P.[1], Adami, C.[2], Durret, F.[3], Lima-Neto, G.[4], Covonne, G.[5], Ilbert, O.[2], Cypriano, E.[6], Allam, S.[7], Kron, R.[8], Mahoney, W.[7] and Gavazzi, R.[3]

Abstract.
The cluster Cl 1257+4738 was found by comparing a ROSAT image with red ground based images, taken to determine if the red galaxies were young dusty ones or old early type galaxies. This adds another cluster to the handful of clusters with z larger than about 0.9. Each one provides new insights as to the relationship between the evolution of galaxies and the ICM. We acquired Chandra, XMM-Newton, Spitzer IRAC plus MIPS 24 data to study this relationship between galaxies and the ICM.

1 Introduction

It is becoming increasingly clear that the redshift range between ∼0.8 and 1.0 is particularly interesting for comparing star formation histories of galaxies in clusters and in the field, as well as studying relationship of galaxy infall and heating of the intracluster medium (e.g. Gilbank 2008).

Cluster formation is thought to start by $z = 2$ (e.g. Fassbender 2008). We might expect selection effects to favor finding the more X-ray luminous clusters when observing apparently faint clusters at high redshift. This is not the case, however. For example, the compilation by Ota et al. (2006) shows that 50% of the cluster sample between $z = 0.3$ and 0.56 have a bolometric X-ray luminosity ($L_{X,bol}$) greater than 10^{45} ergs s^{-1} compared to only 20% of the sample above $z = 1$ (e.g. Fassbender 2008). These X-ray luminosity observations suggest that in the redshift range between about 1 and 2, clusters are growing, but have not reached their peak X-ray luminosity even by $z \sim 1$.

In comparison, we estimate the free fall times for clusters (with a typical radius of 1 Mpc and masses between $0.5 - 5 \times 10^{14}$ M$_\odot$) of the order of 2.2 Gy − 0.7 Gyr (Sarazin 1986). The free fall time goes as the square root of the inverse of the cluster mass. In contrast, the elapsed time between $z = 2$ (the assumed initial infall epoch) and 1 is on the order of about 2.6 Gyrs (Ω_m=0.27, Ω_Λ=0.73, H_0=71 km/s/Mpc). Thus, the redshift range near 1 can be seen on theoretical grounds to favor finding clusters of $0.5 - 5 \times 10^{14}$ M$_\odot$ that have just completed their infall, while higher mass systems should be more mature.

In the process of our search for moderately distant (i.e. $z \sim 1$) clusters of galaxies that are detectable via their X-ray emission, we report here the discovery of a cluster with $z = 0.866$, RX J1257.2+4738 (hereafter for brevity referred to as RX J1257).

We report here a preliminar study based on extensive space-based and ground-based observations including Chandra, XMM, *Spitzer*, Gemini, Subaru, and ARC. That work will be reported in a forthcoming paper.

[1] Department Physics & Astronomy, Northwestern University, Evanston, IL 60208-2900, USA
[2] LAM, OAMP, Université Aix-Marseille & CNRS, Pôle de l'Etoile, Site de Château Gombert, 38 rue Frédéric Joliot-Curie, 13388 Marseille 13 Cedex, France
[3] Institut d'Astrophysique de Paris, CNRS, UMR 7095, Université Pierre et Marie Curie, 98bis Bd Arago, 75014 Paris, France
[4] Instituto de Astronomia, Geofísica e C. Atmosf./USP, R. do Matão 1226, 05508-090 São Paulo/SP, Brazil
[5] INAF – Osservatorio Astronomico di Capodimonte, Naples, Italy
[6] Department of Physics and Astronomy, University College London, London WC1E 6BT, UK
[7] California Institute of Technology, USA
[8] University of Chicago, Department of Astronomy and Astrophysics, 5640 South Ellis Avenue, Chicago, IL 60637, USA

2 Observations

We got Chandra (37 ksec) and XMM (15.94 ksec) X-ray data. These data allowed us to remove point sources and to fit a temperature of the intracluster gas ($3.6^{+2.9}_{-1.2}$ keV).

We got visible (i', z'), near infrared (J, Ks) and infrared (Spitzer: 4 IRAC bands and 24μ MIPS) data. This allowed us to compute photometric redshifts in order to discriminate between cluster members and field galaxies. We extracted a catalog of objects using Sextractor in double-image mode.

Finally, we measured 45 Gemini/Gmos spectroscopic redshifts along the cluster line of sight.

3 Cluster mass and substructures

We found a cluster mass of about $1 - 5 \times 10^{14}$ $M_\odot$. We also applied the SernaGerbal (SG: Serna & Gerbal 1996) method to our redshift catalog. The method reveals the existence of 2 groups, constituting independent structures inside the redshift catalog. The first group is a 3 galaxy low mass structure (4.5×10^{12} $M_\odot$) located beyond the cluster outskirts. The other group is located in the cluster center, roughly coincident with the X-ray emission, with a mass of $6.1 \times 10^{14} M_\odot$ (velocity dispersion of 598 km s^{-1} computed with 18 galaxies). Within this group, 2 other subgroups are detected, with masses of $\sim 10^{14}$ (velocity dispersion of 289 km s^{-1}) and 2.2 10^{13} $M_\odot$ (velocity dispersion of 255 km s^{-1}). These masses from X-ray and from galaxy velocity dispersion measurements are consistent and are in the correct range to call RX J1257 a rich cluster. However, since the velocity dispersion of the substructures are based on only 5 and 3 galaxies, respectively, these masses should only be taken to demonstrate the concistency between the X-ray estimated mass and the velocity dispersion mass.

4 Cluster collapse

We judge that this cluster is just in the process of formation and has not become relaxed because of: (a) the large fraction of galaxies that lie outside the core detectable X-ray emission or that lie inside and that are late type objects; (b) the bimodal nature of both the X-ray emission and the galaxy distribution; (c) the majority of the spectroscopically confirmed cluster members (more than 90%) were detectable in the MIPS 24 μm channel which suggest the presence of dust and star formation with some even being within the X-ray contours that indicates the system is young; (d) the detected level of substructures using the Serna-Gerbal method; (e) the kT on the high side relative to the predicted $L_{X,bol}$-kT relation line.

5 A comprehensive picture

The results briefly presented here combined with previous work on IR-X-ray observations of cluster of galaxies leads to a scenario in which the majority of the red galaxies in high z clusters are red due to dust rather than being red and dead. The less massive the cluster, the younger it will be in terms of having not yet completed infall, compared to more massive clusters. Then a system such as RX J1257 should, as we found here, have a high fraction of red dusty galaxies. Some of these will even be inside the core region as the cluster is still so young. The more massive the cluster, the fewer of these galaxies will be found in the core, and the more quickly the galaxies will progress from being red to blue to being red again.

References

Fassbender, R. 2008, astroph: 0806.0861

Gilbank, D. G., Yee, H. K. C., Ellingson, E., et al. 2008, ApJl, 677, L89

Ota, N., Kitayama, T., Masai, K., & Mitsuda, K. 2006, ApJ, 640, 673

Sarazin C. 1986, Rev.Mod.Phys. 58, 1

Serna, A., & Gerbal, D. 1996, A&A 309, 65

SF2A 2008
C. Charbonnel, F. Combes and R. Samadi (eds)

ANTARCTIC PROSPECTS FOR HYPERLEDA

Vauglin, I.[1] and Prugniel, P.[1]

Abstract. The outstanding atmospheric conditions of the Dôme C give a unique opportunity to survey deeply large areas of the sky in thermal infrared reaching unusual sensitivity limits for ground-based observations. The project of a 3m-class telescope, WHITE, is developed to take benefit of these characteristics.

We present the specific contribution of the HyperLeda to such project and some science cases related to the physics of the Local Universe which requires the approach of HyperLeda.

1 Interest of Dôme C for infrared extragalactic astronomy

Ground-based observations in the thermal infrared (typically from 3 μm and beyond) has to face difficult observing conditions because of only partially clear atmospheric windows and a hugh, rapidly variable background emission. At Dôme C, the extreme temperatures (down to $-80°$C) and dryness (< 0.2 mm PWV) offer unique conditions of transparency and stability of the sky (Fossat 2008). It allows to benefit from remarkable atmospheric transmission in the infrared bands, totally unsual in other terrestrial sites. The very low temperature of the atmosphere implies a very low temperature of the whole telescope infrastructure and instrument leading to a considerable gain, especially in K, L, M bands: up to 4 magnitudes, that extragalactic astronomy will benefit.

1.1 The WHITE project

To make the best use of the exceptional atmospheric characteristics of Dôme C, French members of the ARENA group propose to build a Wide field (0.5 deg in diameter) High resolution (0.3 arcsec using GLAO from the ice) Infrared (1 to 5μm) 3m-class TElescope called WHITE (Wide-field High-resolution Infrared TElescope). Observations could be perform during night and day time. WHITE will be dedicated to carry out surveys: a deep extragalactic field over a few square degrees, a complete survey of the Magellanic Clouds, a high angular resolution survey to detect dusty supernovae up to $z \sim 0.5 - 0.7$. The project is detailed in Burgarella et al. (2008).

The White team closely collaborates with the Australian group led by J. Storey who has a similar project called Pilot (Storey J. et al. 2007) to join the two projects. Pilot is funded for a detailed design study by Australian financial sources.

1.2 HyperLeda involvement

Processing, archiving and distributing the data play a major role in the project to guarantee an optimal scientific return and widest visibility. The goal is to provide homogeneous and high quality data in the shortest delay to the users' community.

Our team proposes to use its expertise in this field (HyperLeda database, DENIS survey, Virtual Observatory) to contribute to the design and deployment of the data processing and archiving of WHITE.

[1] CRAL-Observatoire de Lyon, CNRS UMR 5574, Université de Lyon, 69561 Saint-Genis-Laval cedex, France

1.2.1 Data handling and processing

Because of poor data transfert capabilities from Concordia to elsewhere, the data processing has to be performed on the site and in quasi-real time. The raw and reduced data are then transferred off-line to the remote operation center. Before proceeding to the detection and extraction of the sources we must performed: (i) Determination of the precise astrometric solution and (ii) Determination of the PSF. The standard processing pipeline will use a classical source extraction method (sextractor) applied on the integrated image, and for each source a time variability will be characterized.

1.2.2 Data products

The catalogues of extracted sources and the meta-data of the observations will be distributed through HyperLeda. They will be cross-identified with the database HyperLeda in order to construct multi-wavelength spectral energy distributions. For some observations, and in particular for the legacy surveys, some added-value data-products will also be produced. Besides, all the observations of the deep fields or multi-epoch programs will be co-added to achieve the deepest detection.

1.2.3 Virtual observatory

In order to validate and test the complete observational chain, including the data-processing and analysis, we will simulate astrophysical fields, observe them with a virtual telescope -that is simulating the effects of the atmosphere, of the telescope and of the detectors- and process them as real observations. Realistic fields, including source confusion (crowded fields), will be provided using various physical hypotheses. The simulations and the virtual telescope will be made available at an early phase of the instrument in order to assess the performances.

2 The added-value of using HyperLeda

One of our main goal using HyperLeda is to study the physics of galaxies (scaling relations) and their distribution in the Local Universe. Therefore, surveys and catalogues must be combined to derive accurate description of the galaxies. For this purpose, HyperLeda produces homogeneous data, in particular homogeneous estimates of distances, masses and classification (morphological, spectral and activity). Hence, HyperLeda is a database with added scientific value. For WHITE, the multi-wavelength cross-identification will be a critical issue because a field in the M-band is considerably different than in the optical or even in the K-bands. The HyperLeda team developed a long expertise in this field. HyperLeda will provide to the user's community the access to the science-ready data, plus a multi-wavelength cross-identification and physical data on the objects.

K-, L- and M-band observations are of prime importance, specifically for two subjects we are working on:

- the Cepheids PLC-relation, which could give a direct unbiased determination of the distance of any galaxies in which Cepheids have been observed, provided that we dispose of mid-IR observations to minimize the effect of the unknown extinction in the host galaxy,

- the determination of the powerful physical engine in the Ultra-Luminous InfraRed Galaxies (ULIRGs) with the differentation between ULIRGs whith unobscured AGN − having no absorption features and a flat continuum − and ULIRGs with an obscured AGN activity − showing absorption lines at 3.4 μm (due to aliphatic hydrocarbon dust grains) and at 4.6 μm (due to CO gas) together with a steep reddened continuum.

The White telescope at Dome C will give unique opportunity to obtain high quality data on ULIRGs and to obtain intrinsic colors for the Cepheids.

References

Burgarella, D., Le Roux, B., Langlois, M., et al. 2008, Proceedings of the SPIE, 2008SPIE.7012E..82B

Fossat, E. 2008, in The Astrophysical Science Cases at Dome C, ed. H. Zinnecker, H. Rauer & N. Epchtein

Storey, J., Ashley, M., Burton, M., & Lawrence, J. 2007, EAS Publications Series, Volume 25, 255

Vauglin, I., Gravilović, N., & Prugniel, P. 2008 in The Astrophysical Science Cases at Dome C, ed. H. Zinnecker, H. Rauer & N. Epchtein (EDP Science)

PNP

Planets

SF2A 2008
C. Charbonnel, F. Combes and R. Samadi (eds)

THE TIMESCALE FOR GIANT PLANET FORMATION : CONSTRAINTS FROM THE ROTATIONAL EVOLUTION OF EXOPLANET HOST STARS

Bouvier, J.[1]

Abstract. The timescale over which planets may form in the circumstellar disks of young stars is one of the main issues of current planetary formation models. We present here new constraints on planet formation timescales derived from the rotational evolution of exoplanet host stars.

1 Introduction

The time it takes to form giant gaseous planets in the circumstellar disks of young stars is still a poorly constrained parameter. On the theoretical side, models predict planet formation timescales in the range from $\sim$1 Myr to 10 Myr, depending on the processes at work (e.g. Ida & Lin 2004; Alibert et al. 2005; Guillot & Hueso 2006; Lissauer & Stevenson 2007). On the observational side, protoplanetary disk lifetimes, as measured by the decay of either infrared excess (dust) or line emission (gas) in pre-main sequence stars, appear to vary from star to star, in the range from $\leq$1 Myr up to about 10 Myr (e.g. Lawson et al. 2004; Hillenbrand et al. 2005; Jayawardhana et al. 2006; Meyer et al. 2007). Why do some stars dissipate their disk on very short timescales while other retain their disk up to $\sim$10 Myr ? Is rapid disk dissipation the result of prompt planet formation in the disk ? Or, on the contrary, are long-lived disks required to allow for planet formation ?

Indirect clues may be gained by investigating the imprint the planet formation process may have left on the properties of exoplanet host stars. Israelian et al. (2004) reported that solar-type stars with massive planets are more lithium depleted than their siblings without detected massive planets, a result recently confirmed by Gonzalez (2008). We investigate here whether enhanced lithium depletion in exoplanet host stars may result from their specific rotational history, which in turn is tightly coupled to the evolution of their circumstellar disk during the pre-main sequence. In this way, we attempt to relate giant planet formation to lithium abundances, angular momentum evolution, and disk lifetimes.

2 The rotational evolution of solar-mass stars

Figure 1 shows models we developped to investigate the rotational evolution of solar-type stars, from their birth up to the age of the Sun. The models dicussed here were originally developped by Bouvier et al. (1997) and Allain (1998). The rotational evolution of solar-mass stars is driven by a number of physical processes acting over the star's lifetime. During the early pre-main sequence (PMS), the star is magnetically coupled to its accretion disk (cf. Bouvier et al. 2007). As long as this interaction lasts, the star is prevented from spinning up (in spite of contraction) and evolves at constant angular velocity (Matt & Pudritz 2005). The disk lifetime, a free parameter of the model, thus dictates the early rotational evolution of the star. When the disk eventually dissipates, the star begins to spin up as it contracts towards the zero-age main sequence (ZAMS). Depending on the initial velocity and disk lifetime, a wide range of rotation rates can be obtained on the ZAMS (Bouvier et al. 1997). The lowest initial velocities and longest disk lifetimes result in the slowest rotation rates on the ZAMS. On the opposite, high initial velocities and/or short disk lifetimes lead to fast rotation on the ZAMS. Finally, as the stellar structure stabilizes on the ZAMS, at an age of about 40 Myr for a solar-mass star, the braking by a magnetized wind becomes the dominant process and effectively spins the star down on the early

[1] Laboratoire d'Astrophysique, Observatoire de Grenoble, Université J. Fourier, CNRS, BP 53, 38041 Grenoble, Cedex 9, France

main sequence (MS). As the braking rate scales with surface velocity (Kawaler 1988), fast rotators are spun down more efficiently than slow ones, and this leads to a rapid convergence towards uniformly slow rotation by the age of the Sun. Indeed, after a few Gyr, the surface rotational velocity of solar-type stars has lost memory of the past rotational history.

Internal differential rotation is an important additional parameter of the model. We consider here a radiative core and a convective envelope that are each in rigid rotation, but whose rotation rate may differ (Allain 1998). We therefore introduce a coupling timescale between the inner radiative zone and the outer convective envelope, τ_c, which measures the rate of angular momentum transfer between the core and the envelope (MacGregor & Brenner 1991). A short coupling timescale corresponds to an efficient core-envelope angular momentum transport and, as a consequence, little internal differential rotation. On the opposite, a long coupling timescale leads to the developement of a large rotational velocity gradient between the core and the envelope. This model parameter, τ_c, governs internal differential rotation, and is therefore expected to be of prime importance for rotationally-induced mixing and associated lithium depletion during the evolution of solar-type stars.

The models are confronted to the observed rotation rates of solar-type stars at various ages (e.g. Irwin et al. 2008). We aim here at reproducing the lower and upper envelopes of the observed rotational distributions, in order to contrast the evolution of slow and fast rotators and relate it to lithium depletion. A model for fast rotators is compared to observations in Fig. 1. Starting from an initial period of 1.2 d, the star remains coupled to its disk for 5 Myr, then spins up to a velocity of order of 160 km s^{-1} on the ZAMS, and is eventually spun down by a magnetized wind on the MS to the Sun's velocity. The model reproduces reasonably well the PMS spin up and the rapid MS spin down observed for fast rotators between 5 and 500 Myr. In order to reach such an agreement, the core-envelope coupling timescale has to be short, $\tau_c \sim 10$ Myr, which implies little internal differential rotation in fast rotators.

Fig. 1 also shows a model for slow rotators. The initial period is 10 d and the star-disk interaction lasts for 5 Myr in the early PMS. As the star approaches the ZAMS, both the outer convective envelope and the inner radiative core spin up. Once on the ZAMS, the outer envelope is quickly braked, while the core remains in rapid rotation. This behaviour results from an assumed weak coupling between the core and the envelope, with $\tau_c \sim 100$ Myr. On the early MS, the rapidly-rotating core transfers angular momentum back to the envelope, which explains the nearly constant surface velocity over several 100 Myr in spite of magnetic braking. We thus find that a long core-envelope coupling timescale is required to account for the observed rotational evolution of slow rotators, which implies the developement of a large velocity gradient at the core-envelope boundary.

3 Lithium depletion, rotation, and the lifetime of protoplanetary disks

The modeling of the rotational evolution of solar-type stars seems to imply that internal differential rotation is much larger in slow rotators than in fast ones. This should have a strong impact on lithium abundances, as the efficiency of rotationally-induced lithium burning is expected to scale with differential rotation (Zahn 2007). This model prediction is supported indeed by measurements of lithium abundances in the Pleiades open cluster, at an age of 100 Myr. Soderblom et al. (1993) found that rapidly rotating solar-type stars in the Pleiades exhibit higher lithium abundances than slow rotators, which indicates that lithium depletion already takes place during the PMS/ZAMS, and is more pronounced in slow than in fast rotators.

Different rotational histories may thus be reflected in the lithium abundance pattern of mature solar-type stars, leading to a *dispersion* of lithium abundances at a given age and mass, long after the circumstellar disks have disappeared. The models above suggest that enhanced lithium depletion is associated to low surface rotation on the ZAMS. Then, the fact that mature solar-type stars with massive exoplanets are lithium-depleted compared to similar stars with no planet detection seems to indicate that massive exoplanet hosts had slow rotation rates on the ZAMS.

Why were massive exoplanet host stars slow rotators on the ZAMS ? Two main parameters dictate the rotation rate at the ZAMS : the initial velocity and, most importantly, the disk lifetime. For a given disk lifetime, the lower the initial velocity, the lower the velocity on the ZAMS. Conversely, for a given initial velocity, the longer the disk lifetime, the lower the velocity on the ZAMS. This is because the magnetic star-disk interaction during the PMS is far more efficient than solar-type winds in extracting angular momentum from the star (Bouvier 2007; Matt& Pudritz 2007). Disk lifetimes varying from star to star in the range 1-10 Myr are required to account for the distribution of rotational velocities on the ZAMS (Bouvier et al. 1997). Statistically, however, the slowest rotators on the ZAMS are expected to be the stars who had initially low rotation rates *and*

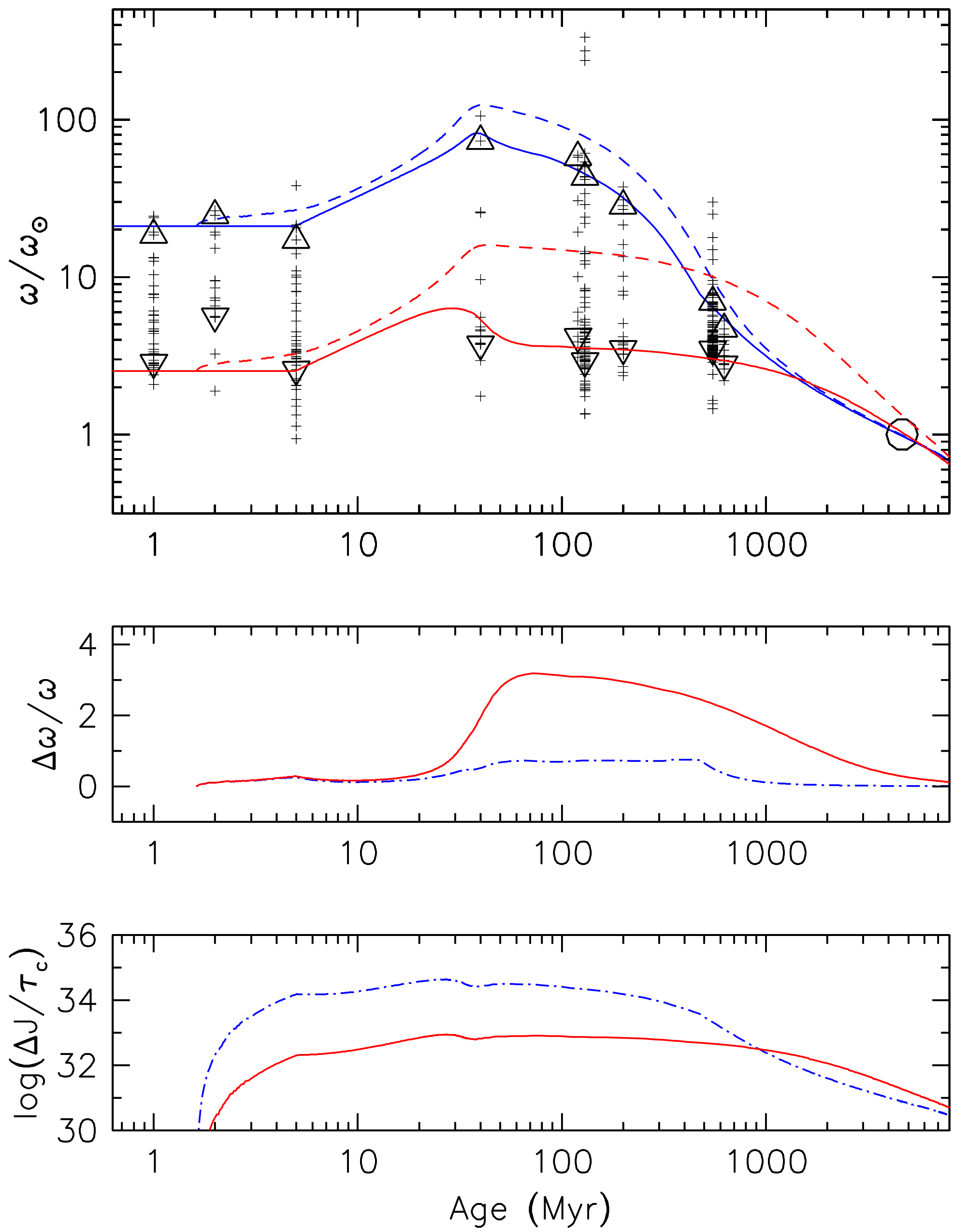

Fig. 1. Rotational models for slow and fast solar-mass rotators. *Data :* The 10th and 75th percentiles of the observed rotational period distributions of solar-type stars (0.8-1.1 $M_\odot$) were converted to angular velocity and are plotted as direct and inverted triangles as a function of time. Individual measurements of rotational periods converted to angular velocities are also shown in order to illustrate the statistical significance of the various samples. *Models :* Rotational evolution models are shown for slow and fast 1 $M_\odot$ rotators. For each model in the upper panel, surface rotation is shown as a solid line, and the rotation of the radiative core by a dashed line. With a core-envelope coupling timescale τ_c of only 10 Myr, little differential rotation develops in fast rotators. In contrast, the 100 Myr core-envelope coupling timescale in slow rotators results in a large velocity gradient at the base of the convective zone. A disk lifetime of 5 Myr is assumed for both models. *Lower panels :* The velocity shear at the base of the convective zone $(\omega_{\rm rad} - \omega_{\rm conv})/\omega_{\rm conv}$, and the angular momentum transport rate $\Delta J/\tau_c$ (g cm^2 s^{-2}) from the core to the envelope are shown for slow (solid line) and fast (dotted-dashed line) rotators.

the longest-lived disks. An initially slowly-rotating star with a short-lived disk would strongly spin up during the PMS and reach the ZAMS as an intermediate or fast rotator.

Long-lived disks thus appear as a necessary condition for massive planet formation and/or migration on a timescale $\geq$5 Myr. Long lasting disks may indeed be the common origin for slow rotation on the ZAMS, lithium depletion and massive planet formation. Interestingly enough, the Sun hosts massive planets. Even though the solar system gaseous planets are located further away from the Sun than massive exoplanets are from their host stars, the Sun is strongly lithium deficient. According to the scenario outlined above, the Sun would thus have been a slow rotator on the ZAMS.

4 Conclusions

Based on what we currently know of the rotational properties of young stars, of the lithium depletion process in stellar interiors and of the angular momentum evolution of solar-type stars, it seems likely that the lithium-depleted content of massive exoplanet host stars is a sequel to their specific rotational history. This history is predominantly dictated by star-disk interaction during the pre-main sequence. Rotationally-driven lithium depletion in exoplanet host stars can be at least qualitatively accounted for by assuming protoplanetary disk lifetimes of order of 5-10 Myr. Such long-lived disks may be a necessary condition for planet formation and/or migration around young solar-type stars, at least for the class of giant exoplanets detected so far. A full account of this work is given in Bouvier (2008).

References

Alibert, Y., Mordasini, C., Benz, W., & Winisdoerffer, C. 2005, A&A, 434, 343

Allain, S. 1998, A&A, 333, 629

Bouvier, J. 2007, IAU Symposium, 243, 231

Bouvier, J. 2008, A&A, 489, L53

Bouvier, J., Forestini, M., & Allain, S. 1997, A&A, 326, 1023

Bouvier, J., Alencar, S. H. P., Harries, T. J., Johns-Krull, C. M., & Romanova, M. M. 2007, Protostars and Planets V, 479

Gonzalez, G. 2008, MNRAS, 386, 928

Guillot, T., & Hueso, R. 2006, MNRAS, 367, L47

Hillenbrand, L. A. 2005, arXiv:astro-ph/0511083

Ida, S., & Lin, D. N. C. 2004, ApJ, 616, 567

Irwin, J., Hodgkin, S., Aigrain, S., et al. 2008, MNRAS, 384, 675

Israelian, G., Santos, N. C., Mayor, M., & Rebolo, R. 2004, A&A, 414, 601

Jayawardhana, R., Coffey, J., Scholz, A., Brandeker, A., & van Kerkwijk, M. H. 2006, ApJ, 648, 1206

Kawaler, S. D. 1988, ApJ, 333, 236

Lawson, W. A., Lyo, A.-R., & Muzerolle, J. 2004, MNRAS, 351, L39

Lissauer, J. J., & Stevenson, D. J. 2007, Protostars and Planets V, 591

MacGregor, K. B., & Brenner, M. 1991, ApJ, 376, 204

Matt, S., & Pudritz, R. E. 2005, ApJl, 632, L135

Matt, S., & Pudritz, R. E. 2007, IAU Symposium, 243, 299

Meyer, M. R., Backman, D. E., Weinberger, A. J., & Wyatt, M. C. 2007, Protostars and Planets V, 573

Soderblom, D. R., Jones, B. F., Balachandran, S., et al. 1993, AJ, 106, 1059

Zahn, J.-P. 2007, EAS Publications Series, 26, 49

SF2A 2008
C. Charbonnel, F. Combes and R. Samadi (eds)

CO IN THE ATMOSPHERES OF SATURN AND URANUS. OBSERVATIONS AT MILLIMETER AND SUBMILLIMETER WAVELENGTHS.

Cavalié, T.[1], Billebaud, F.[1], Dobrijevic, M.[1], Fouchet, T.[2], Lellouch, E.[2], Brillet, J.[1], Encrenaz, T.[2], Moriarty-Schieven, G. H.[3] and Wouterloot, J.[3]

Abstract. An external supply of oxygenated compounds exists in outer planets. Carbon monoxide has been detected in each giant planet. The source of CO has been proved to be dual (internal and external) in Jupiter and Neptune, but this is still unclear in the case of Saturn and Uranus. Therefore, constraining the amount of CO in the troposphere and stratosphere of these planets would help solve this problem. We performed observations of Saturn and Uranus at millimeter and submillimeter wavelengths in the CO (1-0), (2-1) and (3-2) lines. Observations were carried out with the IRAM 30-m telescope (Pico Veletta, Spain) in September 2006 and with the JCMT 15-m telescope (Hawaii, USA) in January 2008. We have recorded broad multi-band spectra of each planet. The results of these observations are presented and discussed.

1 Introduction

Water and carbon dioxide have been detected in the stratosphere of the outer planets (Feuchtgruber et al. 1997, 1999; Lellouch et al. 1997; Burgdorf et al. 2006). The large abundances detected above the tropopause cold trap implied an external supply for these compounds (Moses et al. 2000; Lellouch et al. 2002). The possible external sources are interplanetary dust particles (IDP), large comet impacts and local sources (rings and satellites).

Carbon monoxide has been detected in the atmospheres of the outer planets (Beer 1975; Noll et al. 1986; Encrenaz et al. 2004; Marten et al. 1993). The question of the origin of CO is more complicated to address because this compound does not condense at the tropopause of the giant planets. So, convective transport can bring CO from the deep interiors of the planets to the shallow atmosphere. Therefore, CO can be of internal and/or external origin. It is thus important to reliably measure the relative contributions of the internal and external sources of CO. A way of achieving these measurements is to observe independently the CO abundance in the troposphere and in the stratosphere.

Bézard et al. (2002) and Lellouch et al. (2005) have shown that there is an internal and an external source of CO on Jupiter and Neptune (respectively). In the atmospheres of Saturn and Uranus, the situtation is still unclear. The CO has been detected in the infrared range on both planets. From the latest published data, Noll & Larson (1991) could not distinguish between a internal source (1-ppb, uniform with altitude) and an external source (25-ppb above the tropopause). In the atmosphere of Uranus, Encrenaz et al. (2004) favored an external origin (30-ppb above the tropopause) but could not rule out an internal source (upper limit of 20-ppb, uniform with atitude). To better constrain the origin of CO, we have observed the $J=1 \rightarrow 0$, $J=2 \rightarrow 1$ and $J=3 \rightarrow 2$ transitions of CO in the atmospheres of Saturn and Uranus, using the IRAM (Institut de RadioAstronomie Millimétrique) 30-m telescope and the JCMT (James Clerk Maxwell Telescope) 15-m telescope. The observations are presented in Sect. 2. Our radiative transfer model is described in Sect. 3. Preliminary results are given in Sect. 4.

[1] Laboratoire d'Astrophysique de Bordeaux, 2 rue de l'Observatoire BP 89, 33271 Floirac cedex, France
[2] Observatoire de Paris-Meudon, 5 place Jules Janssen, 92195 Meudon, France
[3] Joint Astronomy Center, 660 N. A'ohoku Place, University Park, Hilo, Hawaii 96720, USA

CO line	Single band width [GHz]	Tunings [GHz]
(1-0)	0.5	114.503, 114.887, 115.271
(2-1)	1.0	229.002, 229.770, 230.538, 231.306, 232.074
(3-2)	1.0	343.545, 344.045, 344.545, 345.045, 345.545
		346.045, 346.545, 347.045, 347.545, 348.045

Table 1. Tunings used during the observations of Saturn and Uranus as a function of the observed line. The width of each sub-band is also given.

2 Observations

Saturn and Uranus were observed at the frequency of the CO (1-0) and (2-1) lines with the IRAM 30-m telescope in September 2006. Besides, we observed the CO (3-2) line in the atmosphere of Saturn with the JCMT 15-m telescope in January 2008. Because synthetic computations predict that the lines are broad, we used Lellouch et al. (2005) observing technique. It consists in observing a large frequency range (3 to 5-GHz) by using multiple short integrations of 0.5 to 1-GHz sub-bands with significant overlaps between contiguous sub-bands. The different tunings which have been set are given in Table 1. The initial spectral resolution was 1-MHz. The observations have been carried out with heterodyne receivers in wobbler or position switching mode. The (1-0) line could not be explored beyond 115.5-GHz because of the presence of the terrestrial O_2 line. Contrary to the IRAM observations, observations of Mars have also been carried out at the same time as the observations of Saturn with the JCMT antenna in order to obtain an absolute calibration of the spectrum in terms of brightness temperature. So the IRAM observations are interpreted in terms of line-to-continuum ratios whereas the JCMT spectrum is interpreted in terms of absolute brightness temperature.

Before connecting the sub-bands together, each one was reduced individually. The ripples which appear on every sub-bands of one spectrum have been removed by a Fourier analysis and a polynomial baseline subtraction. Then, the sub-bands have been reconnected by averaging them on their overlaping parts and rescaled one to another. Finally, the spectral resolution has been smoothed to 16-MHz on each spectrum to decrease the noise level.

The CO is not detected on the IRAM spectra whereas an absorption feature is detected on the JCMT spectrum of Saturn. Thus, 3-σ upper limits have been determined from the IRAM spectra and simple CO vertical distributions have been tested in the case of the JCMT spectrum.

3 Modeling

Synthetic spectra have been computed with a standard 1D line-by-line non-scattering radiative transfer model, which accounts for the approximate spherical geometry of the planets. The planetary disk and limb contributions were taken into account. More details (opacity sources, thermal profiles) are given in Cavalié et al. (2008).

Two kinds of vertical distributions of CO have been tested. The first one (Type I hereafter) is modeled with two parameters: q_{CO} and the level below which q_{CO} is set to 0, noted p_0. This distribution reflects an external source. When fixing upper limits, the p_0 level is fixed to the tropopause level ($p_0 \sim$100-mbar). The second one (Type II) consists in a uniform distibution with altitude. This distribution reflects an internal source. The only parameter which has to be fixed is the CO mixing ratio q_{CO}.

4 Preliminary results

4.1 Upper limits

Because no absolute calibration has been performed on the IRAM spectra and because the rings do not contribute significantly to the total flux, the ring contribution has been neglected when modeling the (1-0) and (2-1) CO lines. The spectra which lead to the best upper limits are the spectra centered on the CO (2-1) line.

The upper limits derived from the IRAM observations of Saturn and Uranus are given in Table 2. The upper limits derived from the observation of Saturn improve the previously published ones (Rosenqvist et al. 1992) but are far from the detection level of Noll & Larson (1991). The values obtained in the case of Uranus are

	Saturn			Uranus		
Telescope	CO distribution	CO origin	q_{CO}	CO distribution	CO origin	q_{CO}
IRAM 30-m	Type I (p_0=100-mbar)	External	$<6.3\times10^{-8}$	Type I	External	$<2.7\times10^{-8}$
	Type II	Internal	$<3.9\times10^{-8}$	Type II	Internal	$<1.8\times10^{-8}$
JCMT 15-m	Type I (p_0=16-mbar)	External	2.5×10^{-8}			

Table 2. Upper limits derived from the 230-GHz spectra of Saturn and Uranus observed with the IRAM 30-m telescope (Cavalié et al. 2008) and detection level in the atmosphere of Saturn from the 345-GHz JCMT observations.

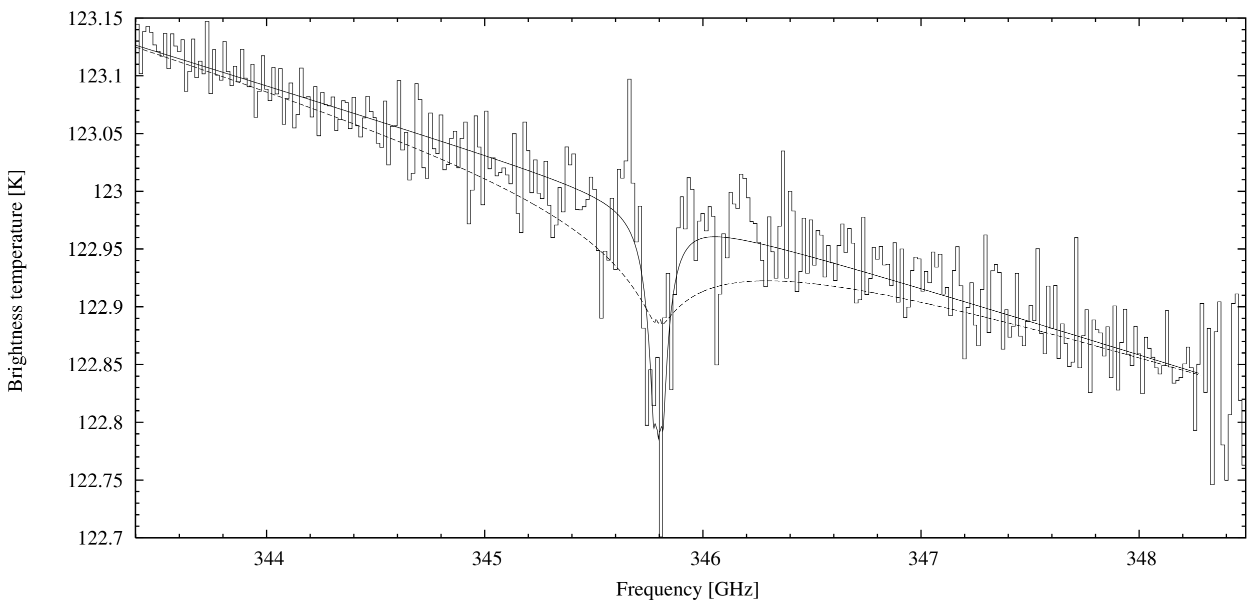

Fig. 1. Observed spectrum of Saturn at 345-GHz. The CO (3-2) line is detected. Solid line: best fit model with a Type I distribution (q_{CO}=2.5$\times10^{-8}$ and p_0 = 16-mbar); long-dashed lines: best fit model with a Type II distribution (q_{CO}=1$\times10^{-9}$).

consistent with previously published upper limits (Marten et al. 1993) but are slightly lower than the detection level of Encrenaz et al. (2004).We suggest that their detection level might have been slightly overestimated from their modeling.

4.2 Absolute brightness temperature of Saturn at 345-GHz

The observations of Saturn with the JCMT telescope at 345-GHz have been calibrated by observing Mars at the same time. Following Griffin et al. (1986) and using Ulich (1981) and Wright (1976), the brightness temperature of Mars at the time of the observations is 205.5±5.7-K at 345-GHz. From this value, we can determine the brightness temperature of Saturn at 345-GHz. We obtain:

$$T_b = (123 \pm 13)\ \mathrm{K}$$

This measurement gives a new absolute determination of Saturn brightness temperature in the submillimeter range. The ring inclination angle was 7°.

4.3 Detection of the CO (3-2) line at 345-GHz in the spectrum of Saturn

The CO (3-2) line has been detected from our observations of Saturn (see Fig. 1). The line contrast has an uncertainty of a factor of 2 because of the data reduction scheme. If we use the Noll & Larson (1991) CO

Type I distribution ($q_{\rm CO}$=2.5$\times$10^{-8} and $p_0 \simeq$ 100-mbar), we obtain an absorption which is too large. The best fit model is computed by adjusting the p_0 level to 16-mbar. By testing the Type II distribution, we only obtain a rough fitting of the observed line. The absorption feature obtained is too broad.

The main result of these observations are the derival of new upper limits on the CO mixing ratio in the atmospheres of Saturn and Uranus from millimeter observations (Cavalié et al. 2008) and the detection of the CO (3-2) line in the atmosphere of Saturn. This observation confirms the detection of CO in the infrared. The values of the CO mixing ratio we derive from this observation are consistent with Noll & Larson (1991). They also permit to better constrain the p_0 level of the simplified Type II vertical distribution. From our observations, we favor an external origin for CO in the atmosphere of Saturn, but new observations should be performed to directly measure the CO abundance in the stratosphere of the planet. Moreover, photochemical modeling of the supply of oxygenated compounds to the atmosphere of Saturn should provide more realistic vertical profiles to test and compare with this observation.

References

Beer, R. 1975, ApJ, 200, L167

Bézard, B. 2002, Icarus, 159, 95

Burgdorf, M., et al 2006, Icarus, 184, 634

Cavalié, T., et al 2008, A&A, 484, 555

Encrenaz, T., et al 2004, A&A, 413, L5

Feuchtgruber, H., et al 1997, Nature, 389, 159

Feuchtgruber, H., et al 1999, The Universe as seen by ISO. Eds. P. Cox & M. F. Kessler. ESA-SP, 427, 133

Griffin, M., et al. 1986, Icarus, 65, 244

Lellouch, E., et al 1997, BAAS, 29, 992

Lellouch, E., et al 2002, Icarus, 159, 112

Marten, A., et al 1993, ApJ, 406, 285

Moses, J., et al. 2000, Icarus, 145, 166

Noll, K., et al 1986, ApJ 309, L91

Noll, K., & Larson, H., 1991, Icarus, 89, 168

Rosenqvist, J., et al. 1992, ApJ, 92, L99

Ulich, B., 1981, Astron. J., 86, 1619

Wright, E., 1976, ApJ, 210, 250

RECENT OBSERVATIONS OF THE OH 18-CM LINES IN COMETS WITH THE NANÇAY RADIO TELESCOPE

Colom, P.[1], Crovisier, J.[1], Biver, N.[1] and Bockelée-Morvan, D.[1]

The OH 18-cm lines have been systematically observed in comets with the Nançay radio telescope since 1973 (Crovisier et al. 2002). These observations allow us to evaluate the cometary water production rate and its evolution with time, and to study several physical processes such as the excitation mechanisms of the OH radio lines, the expansion of cometary atmospheres, their anisotropy in relation with non-gravitational forces, the Zeeman effect in relation to the cometary magnetic field. Between 1973 and 1999, 52 comets have been successfully observed at Nançay. The radio telescope has been upgraded in 2000, and observations are now made with a sensitivity increased by about a factor of two. As of mid 2008, the returns of 40 comets were observed at Nançay with the refurbished instrument (Table 1). The observations are organized in a data base; the part from 1982 to 2002 is publicly available (Crovisier et al. 2002; `http://www.lesia.obspm.fr/planeto/cometes/basecom/`). New analyses have been performed of the OH line shapes in terms of coma expansion velocity (Tseng et al. 2007) and of the correlation between visual magnitudes and OH production rates (Crovisier 2005; Jorda et al. 2008). Among the last comets observed at Nançay are 9P/Tempel 1 prior to its visit by Deep Impact (Biver et al. 2007), the two main fragments of 73P/Schwassmann-Wachmann 3 during their passage close to the Earth in 2006 (Colom et al. 2006; Biver et al. 2008a), the day-time comet C/2006 P1 (McNaught) close to the Sun (Biver et al. 2008c), 17P/Holmes just after its outburst in October 2007 (Biver et al. 2008b), and 8P/Tuttle in winter 2007-2008, also during its close approach to the Earth.

References

Biver, N., Bockelée-Morvan, D., Boissier, J., et al. 2007, Icarus, 187, 253

Biver, N., Bockelée-Morvan, D., Crovisier, J., et al. 2008a, in Asteroids, Comets, Meteors 2008, Abstract 8149, Lunar and Planetary Institute Contribution No 1405, Houston (CD-ROM)

Biver, N., Bockelée-Morvan, D., Wiesemeyer, H., et al. 2008b, in Asteroids, Comets, Meteors 2008, Abstract 8146, Lunar and Planetary Institute Contribution No 1405, Houston (CD-ROM)

Biver, N., Wiesemeyer, H., Paubert, G., et al. 2008c, in Asteroids, Comets, Meteors 2008, Abstract 8247, Lunar and Planetary Institute Contribution No 1405, Houston (CD-ROM)

Colom, P., Crovisier, J., Biver, N., et al. 2006, in SF2A-2006: Semaine de l'Astrophysique Française, ed. D. Barret, F. Casoli, G. Lagache, A. Lecavelier, & L. Pagani, 389

Crovisier, J. 2005, Int. Comet Quarterly, 27, 3

Crovisier, J., Colom, P., Gérard, E., Bockelée-Morvan, D., & Bourgois, G. 2002, A&A, 393, 1053

Jorda, L., Crovisier, J., & Green, D. W. E. 2008, in Asteroids, Comets, Meteors 2008, Abstract 8046, Lunar and Planetary Institute Contribution No 1405, Houston (CD-ROM)

Tseng, W.-L., Bockelée-Morvan, D., Crovisier, J., Colom, P., & Ip, W.-H. 2007, A&A, 467, 729

[1] LESIA, Observatoire de Paris, 5 place Jues Jansse, F-92195 Meudon

Table 1. The comets observed at Nançay since 2000.

comet	perihelion [yymmdd]	q [AU]	range of observations [yymmdd]	r_h range a) [AU]	N b)	c)	
C/1999 S4 (LINEAR)	000726.17	0.765	000706–000803	0.76–0.86	20	L	
C/1999 T1 (McNaught-Hartley)	001213.47	1.172	001115–010130	1.17–1.40	40	L	
C/2000 W1 (Utsunomiya-Jones)	001226.56	0.321	001212–010107	0.33–0.49	11	L	
73P/Schwassmann-Wachmann 3	010127.71	0.937	001201–010310	0.96–1.23	31	J	
45P/Honda-Mrkos-Pajdušáková	010329.89	0.528	010103–010315	0.60–1.14	27	J	d)
24P/Schaumasse	010502.66	1.205	010310–010630	1.22–1.43	47	J	
C/2001 A2 (LINEAR)	010524.52	0.779	010402–010712	0.96–1.22	56	L	
16P/Brooks 2	010719.82	1.835	010417–010510	1.93–2.01	18	J	d)
19P/Borrelly	010914.73	1.358	010719–011129	1.36–1.50	54	J	
C/2000 WM_1 (LINEAR)	020122.67	0.555	011004–020420	0.75–2.10	104	L	
153P/2002 C1 (Ikeya-Zhang)	020318.98	0.507	020227–020620	0.51–1.90	78	H	
C/2002 F1 (Utsunomiya)	020422.90	0.438	020409–020620	0.46–1.37	34	L	
46P/Wirtanen	020826.76	1.059	020720–020816	1.07–1.17	19	J	d)
C/2002 O6 (SWAN)	020909.46	0.495	020821–020902	0.52–0.65	9	L	
C/2002 X5 (Kudo-Fujikawa)	030129.00	0.190	030101–030409	0.19–1.71	64	L	
C/2002 V1 (NEAT)	030218.30	0.099	021231–030426	0.10–1.37	62	L	
C/2002 Y1 (Juels-Holvorcem)	030413.24	0.714	030301–030427	0.72–1.10	18	L	
2P/Encke	031229.88	0.338	031018–040122	0.35–1.44	40	J	
C/2004 F4 (Bradfield)	040417.09	0.168	040506–040520	0.66–1.00	13	L	
C/2002 T7 (LINEAR	040423.10	0.615	031102–040620	0.61–2.93	67	L	
C/2003 T3 (Tabur)	040429.02	1.481	040204–040413	1.50–1.89	29	L	
C/2001 Q4 (NEAT)	040515.97	0.962	040502–040613	0.96–1.08	42	L	
C/2003 K4 LINEAR)	041013.72	1.024	040601–041113	1.03–2.28	92	L	
C/2004 Q2 (Machholz)	050124.84	1.203	041001–050122	1.21–2.09	78	L	
C/2003 T4 (LINEAR)	050403.65	0.850	041009–050401	0.85–2.85	120	L	
9P/Tempel 1	050705.32	1.506	050304–050710	1.51–1.92	95	J	
C/2006 A1 (Pojmanski)	060222.18	0.555	060216–060331	0.57–0.98	20	L	
73P/Schwassmann-Wachmann 3 (B)	060607.92	0.939	060407–060721	0.94–1.28	62	J	
73P/Schwassmann-Wachmann 3 (C)	060606.95	0.939	060302–060720	0.94–1.61	76	J	
4P/Faye	061115.46	1.667	060915–061019	1.69–1.78	25	J	
C/2006 M4 (SWAN)	060928.73	0.783	061027–061115	0.96–1.18	13	L	
C/2006 P1 (McNaught)	070112.80	0.171	070110–070120	0.17–0.34	7	L	
96P/Machholz 1	070404.62	0.125	070319–070604	0.19–1.48	39	H	
2P/Encke	070419.30	0.339	070501–070601	0.46–1.01	25	J	
17P/Holmes	070504.50	2.053	071025–071108	2.44–2.49	10	J	
C/2007 F1 (LONEOS)	071028.76	0.402	071018–071111	0.40–0.54	21	L	
8P/Tuttle	080127.02	1.027	071203–080128	1.03–1.31	49	H	
46P/Wirtanen	080202.50	1.057	080103–080121	1.07–1.13	16	J	
C/2007 W1 (Boattini)	080624.89	0.850	080401–010831	1.67–0.85	119	L	
6P/d'Arrest	080814.96	1.353	080614–080806	1.36–1.53	36	J	

a) lowest and highest heliocentric distance of the observations;
b) number of observations in the data base;
c) L: long-period comet; H: Halley-family comet; J: Jupiter-family comet;
d) no detection.

THE CHEMICAL DIVERSITY OF COMETS: RECENT RESULTS FROM RADIO OBSERVATIONS

Crovisier, J.[1], Biver, N.[1], Bockelée-Morvan, D.[1], Boissier, J.[2] and Colom, P.[1]

A fundamental question in cometary science is whether or not the different dynamical classes of comets are correlated with different chemical compositions (Bockelée-Morvan et al. 2005). The dynamical classes point to various reservoirs of comets. If these latter are associated with different sites of formation, one would expect a diversity in the chemical composition of comets, due to different initial conditions. From the ground or Earth orbit, radio and infrared spectroscopic observations of a now significant sample of comets indeed revealed deep differences in the relative abundances of cometary ices. However, no obvious correlation with dynamical classes is found (Biver et al. 2002; Crovisier 2007; Crovisier et al. 2008). Further results came, or are expected, from space exploration. This means of investigation, by nature limited to a small number of objects, is unfortunately focussed on short-period comets (mainly from the Jupiter family). But it provides ground truth for remote sensing. Our database of spectroscopic radio observations has been recently enriched by the Jupiter-family comets 9P/Tempel 1, 73P/Schwassmann-Wachmann and 17P/Holmes, and the Halley-type comet 8P/Tuttle (Biver et al. 2007, 2008a, 2008b, 2008c).

References

Biver, N., Bockelée-Morvan, D., Boissier, J., et al. 2007, Icarus, 187, 253

Biver, N., Bockelée-Morvan, D., Crovisier, J., et al. 2002, Earth Moon and Planets 90, 323

Biver, N., Bockelée-Morvan, D., Crovisier, J., et al. 2008a, in Asteroids, Comets, Meteors 2008, Abstract 8149, Lunar and Planetary Institute Contribution No 1405, Houston (CD-ROM)

Biver, N., Bockelée-Morvan, D., Wiesemeyer, H., et al. 2008b, in Asteroids, Comets, Meteors 2008, Abstract 8146, Lunar and Planetary Institute Contribution No 1405, Houston (CD-ROM)

Biver, N., Wiesemeyer, H., Paubert, G., et al. 2008c, in Asteroids, Comets, Meteors 2008, Abstract 8247, Lunar and Planetary Institute Contribution No 1405, Houston (CD-ROM)

Bockelée-Morvan, D., Crovisier, J., Mumma, M. J. & Weaver, H. A., 2005, in: Comets II, Festou, M.C., Keller, H.U. & Weaver, H A. (Eds.), Univ. Arizona Press, Tucson, 391

Crovisier, J. 2007, in Proceedings of the XVIIIèmes Rencontres de Blois: Planetary Science: Challenges and Discoveries, (in press), arXiv:astro-ph/0703785

Crovisier, J., Biver, N., Bockelée-Morvan, D. & Colom, P. 2008, Planet. Space Scie (in press), arXiv:0808.3843

[1] LESIA, Observatoire de Paris, 5 place Jues Jansse, F-92195 Meudon
[2] IRAM, 300 rue de la Piscin, F-38406 Saint Martin d'Hères

SF2A 2008
C. Charbonnel, F. Combes and R. Samadi (eds)

NUV RADII OF THE EXTRASOLAR PLANET HD 209458B

Désert, J. M.[1], Vidal-Madjar, A. [1], Lecavelier des Etangs, A. [1], Hébrard, G. [1] and Ferlet, R. [1]

Abstract.
Extrasolar planetary transits are powerful tools to probe their atmosphere and thus extract key physical properties of planets, like their mean densities, chemical compositions, or atmospheric structures. Every 3.5 days, the transits of the gaseous planet orbiting HD 209458 offer the opportunity to investigate the spectral features of its atmosphere. We present here NUV transmission spectroscopy of the transiting extrasolar planet HD209458b using HST/ACS. We present the data analysis of the seven HST orbits which were used to observe two transits of HD209458b. We found a radius of $R_P = 1.4\ R_{jup} +/- 0.05$ consistent with previous measurements. Due to various systematics, the radius of the planet in the NUV cannot be extracted with a high precison.

1 Introduction

In the case of HD 209458b, absorptions of several percents for H I Lyman-α, O I and C II have been measured in the hydrodynamically escaping upper atmosphere (Vidal-Madjar 2003, 2004, 2008, Désert et al. 2004, Lecavelier Des Etangs 2007, Ehrenreich et al. 2008) and a hot layer of hydrogen have been detected (Ballester et al. 2007). More recently, Rayleigh scattering by H_2 molecules has been identified (Lecavelier et al. 2008b) from sets of HST/STIS observations (Charbonneau et al. 2002, Knutson et al. 2007, Sing et al. 2008a,b). From the same datasets, the possible presence of TiO/VO as been studied (Désert et al. 2008).

2 Observations

The observing program was originally designed to observe HD 209458b with HST/STIS. After STIS failure, it has been possible to execute the program with HST/ACS during Cycle 13. The program (GO10145) consists in $3 + 2$ visits, performed with the ACS/HRC and the ACS/SBC. The results obtained using ACS/SBS with PR110L prism spectroscopy around the Lyman-α line are presented in a separated paper (Ehrenreich et la. 2008). The two other visits are composed of 7 orbits $(4 + 3)$. Each orbit was plan to be a sequence of direct image filters and prism PR200L spectra at various exposure times. The normal observing technique for all ACS-HRC PR200L spectroscopy is to obtain a direct image of the field followed by the dispersed prism image. This combination allows the wavelength calibration of individual target spectra by reference to the corresponding direct images. We obtain few exposures of 0.1s, 3.6 s, 40 s, and 540 s during the two transit observed. All the images were saturated.

3 Analysis

3.1 Slitless spectroscopy

HRC PR200L Slitless spectroscopy yields spectral 2D calibrated images. The spectral image is composed of the stellar halo surrounding the stellar center position, the red pile-up resulting from the built up of photons on a few detector pixels which appear when using a prism the saturation zone and the stellar continuum between 150 and 400 nm. The spectral resolution significantly diminishes toward the red. For bright objects, such as

[1] Institut d'astrophysique de Paris, CNRS (UMR 7095), Université Pierre et Marie Curie, 98 bis boulevard Arago, 75014 Paris, France

HD 209458, this effect can lead to blooming of the HRC CCD from filled wells; the overfilled pixels bleed in the detector Y direction. The tilt of the prism causes a deviation of about 300 pixels between the position of the direct object and the region of the dispersed spectrum on the CCD.

3.2 Spectra extraction

All the effect described previously make this extraction very difficult. We used the flat-fielded spectral images to extract the spectra. Since there is no slit in the ACS, the Point Spread Function of the target modulates the spectral resolution. The so called background is the sum of the effects of the real background, the halo, and the diffraction spikes. Due to the quasi central symmetry of the image, we considered that a good evaluation of the background was to consider the opposite pixels from the star. The current calibration of the wavelength solution used in the aXe data reduction software assumes the use of these apertures. At 3500 Å, the dispersion drops to 105 Å per pixel Lyman-$\alpha$and is 563 Å per pixel at 5000 Å.

3.3 Fitting the transit light curve

We parameterized the transit light curve with 4 variables: the planet-star radius ratio $R_p/R_\star$, the stellar radius to orbital radius ratio $a/R_\star$, the impact parameter b, and the time of mid-transit T_c0. We used the transit routine `OCCULTNL` developed by Mandel & Agol (2002) where limb-darkening corrections are taken into account. We then performed a least-squares fit to our data over the whole parameter space.

4 Results and conclusion

We extracted the NUV radius of HD 209458b at 2 bandpasses. We are able to detect the stellar MgII doublet at 2 800 Å. We found a radius of $R_P = 1.4\ R_{jup} +/-0.05$ in agreement with the radius of 1.3263 $R_{jup} +/-0.0018$ found in the visible (Knutson et al. 2007) obtain from STIS/HST observations.

Although ACS is very sensitive, the error bars derived here are large since they include various systematics that affect the determination of the radius of the planet. The telescope jitter, dithering and intra-pixel sensitivity variations are responsible for severe fluctuations observed in individual spectra. We conclude that dithering should not be used for precision photometry when levels of 0.01% are needed. Finally, the exposures were all saturated which introduce not linearity effects and thus make the comparison between consecutive wavelength difficult. The error bars we derived are to large to draw any firm conclusion on the detection of absorbers potentially present in the atmosphere and which could be observed in this wavelength domain.

COS will reach the domain of 1200-3000 Å. This domain include the ACS one but with a much better resolution and sensitivity, allowing the detection of supplementary absorber in this region.

References

Ballester, G. E., Sing, D. K., & Herbert, F. 2007, Nature, 445, 511

Charbonneau, D., Brown, T. M., Noyes, R. W., & Gilliland, R. L. 2002, ApJ, 568, 377

Désert, J. -M., Vidal-Madjar, A., Lecavelier des Etangs, A., et al. 2008, arXiv:0809.1865

Désert, J.-M., Vidal-Madjar, A., Lecavelier Des Étangs, A., et al. 2004, Extrasolar Planets: Today and Tomorrow, 321, 205

Ehrenreich, D., Lecavelier Des Etangs, A., Hébrard, G., et al. 2008, A&A, 483, 933

Ehrenreich, D., Hébrard, G., Lecavelier des Etangs, A., et al. 2007, ApJL, 668, L179

Knutson, H. A., Charbonneau, D., Noyes, et al. 2007a, ApJ, 655, 564

Lecavelier Des Etangs, A., Vidal-Madjar, A., Désert, J.-M., et al. 2008, A&A, 485, 865

Lecavelier Des Etangs, A. 2007, A&A, 461, 1185

Vidal-Madjar, A., Désert, J.-M., & Sing, D. 2008b, A&A, 485, 865

Mandel, K., & Agol, E. 2002, ApJ, 580, L171

Sing, D. K., Vidal-Madjar, A., Desert,J. -M. et al. 2008b, arXiv:0802.3864

Sing, D. K., Vidal-Madjar, A., Lecavelier des Etangs, A., et al. 2008b, ArXiv e-prints, 803, arXiv:0803.1054

Vidal-Madjar, A., Lecavelier des Etangs, A., Désert, J.-M., et al. 2008, ApJL, 676, L57

Vidal-Madjar, A., et al. 2004, ApJ, 604, L69

Vidal-Madjar, A., Lecavelier des Etangs, A., Désert, J.-M. et al. 2003, Nature, 422, 143

SF2A 2008
C. Charbonnel, F. Combes and R. Samadi (eds)

ETHANE, ACETYLENE AND PROPANE DISTRIBUTION IN SATURN'S STRATOSPHERE FROM CASSINI/CIRS LIMB OBSERVATIONS

Guerlet, S.[1], Fouchet, T.[1] and Bézard, B.[1]

Abstract. We present an analysis of limb observations performed by the Composite InfraRed Spectrometer (CIRS) instrument onboard the Cassini spacecraft, in order to investigate the temperature and composition of Saturn's stratosphere. Spectra were acquired at twenty different latitudes between 80°S and 45°N from March 2005 to January 2008, which corresponds to mid-summer in the southern hemisphere. We used a line-by-line radiative transfer model, coupled to an iterative retrieval algorithm, to determine the vertical temperature profile of the stratosphere at each latitude. Then, we derived the volume mixing ratio vertical profiles of various hydrocarbons: ethane, acetylene and propane.

Our results show an equatorial maximum of the abundance of acetylene at 1 mbar, almost twice as high as expected from photochemical models, which can be explained by a descent of air at the equator. As already observed in 2002 and 2004 by Greathouse et al. (2005) and Howett et al. (2007) at 2 mbar, we note that the volume mixing ratio of ethane slightly increases towards the South pole, which is evidence for a meridional circulation. As for propane, its meridional distribution suggests that its chemical lifetime in Saturn's stratosphere may be shorter than predicted.

1 Introduction

In Saturn's upper atmosphere, methane photolysis by solar UV initiates a complexe hydrocarbon chemistry, which by-products are transported downwards by eddy diffusion. Saturn's 29.5-years seasonal cycle modulates this photochemistry, as well as the stratospheric temperatures, through temporal and latitudinal changes in solar insolation. In addition, the meridional hydrocarbon distribution is also affected by atmospheric dynamics such as horizontal diffusion and advection, which are still poorly known.

In this study, we analyzed a set of limb data acquired by the Composite InfraRed Spectrometer (CIRS) onboard the Cassini spacecraft. We retrieved the acetylene (C_2H_2), ethane (C_2H_6) and propane (C_3H_8) vertical and meridional stratospheric distributions. In particular, we retrieved the propane distribution with a spatial coverage never achieved before. By taking advantage of the limb viewing geometry, where infrared radiation is emitted through a large optical path and a narrow altitude range, we also improved the vertical extent and resolution with respect to previous nadir observations. These three species, having various chemical lifetimes, are affected in different ways by atmospheric dynamics. Comparing their volume mixing ratios (*vmr*) inferred from observations to photochemical models thus provides a way of tracing dynamical phenomena.

2 Instrument and data

2.1 CIRS instrument

The Fourier-spectrometer CIRS comprises three focal planes covering the mid-infrared region, two being used in this study:

- Focal Plane 3 (FP3), covering the 600 - 1100 cm^{-1} (9 μm to 16 μm) spectral range ;
- Focal Plane 4 (FP4), covering the 1100 - 1400 cm^{-1} region (7 μm to 9 μm).

[1] LESIA - Observatoire de Paris

Both FP3 and FP4 consist in a linear array of 10 squared detectors, with an individual field of view (IFOV) of 0.273x0.273 mrad. Depending on the spacecraft distance to Saturn, the projected IFOV on the planet varied from 50x50km to 100x100km (one to two scale heights). During a limb observation, the two 10-detectors arrays of FP3 and FP4 were set perpendicular to the limb, so that each detector probed a different altitude.

2.2 Data selection

Spectra analyzed hereafter were acquired at 15 cm^{-1} spectral resolution during four dedicated fly-bys between March, 2005 and August, 2006, which corresponded to summer in the Southern hemisphere (since 2002, until equinox in 2009). The latitudinal coverage extended from 45°S to 45°N, every 5°, where most latitudes have been sampled two or three times. We also investigated a few data sets acquired at 1 and 3 cm^{-1}, including more southern latitudes at 70°S and 80°S.

3 Method

We used a line-by-line radiative transfer model to calculate synthetic spectra. It included opacity from CH_4, CH_3D, C_2H_6, C_2H_2, C_3H_8, C_3H_4, C_4H_2 and collision-induced opacity from H_2-He and H_2-H_2. The atmospheric grid consisted in 360 layers from 10 bar to 10^{-8} bar. It was coupled with an iterative inversion algorithm adapted from Conrath et al. (1998), in order to retrieve the atmospheric state (temperature, hydrocarbon vertical profiles) from the measured spectra.

As a molecular emission intensity depends on both its abundance and temperature, we proceeded in two steps. First, we retrieved the temperature vertical profile from the methane ν_4 emission band at 1305 cm^{-1} (assuming it is uniformly mixed with a *vmr* of 4.5 x10^{-3} (Flasar et al. 2005)), providing information in the 1 mbar - 2 μbar region. In order to retrieve the temperature between 20 mbar and 1 mbar, we simultaneously inverted the 600-660 cm^{-1} continuum emission induced by H_2-He and H_2-H_2 collisions. Then, this temperature profile was incorporated in the model, so that we could retrieve the C_2H_6 *vmr* profile from its ν_9 emission band (centered at 822 cm^{-1}), the C_2H_2 profile from its ν_5 emission band (730 cm^{-1}) and the C_3H_8 profile from its ν_{21} band (748 cm^{-1}).

The two latter molecules had to be inverted simultaneously, as the propane ν_{21} Q-branch is located in the same region as the C_2H_2 ν_5 R-branch. The calculated kernels (which represent how the intensity at a wavenumber i is a function of a state parameter at a level z) showed that CIRS observations were sensitive in the range 5 mbar-10 μbar for C_2H_2 and C_2H_6, and in the range 5 mbar to 0.5 mbar for C_3H_8.

Figure 1 shows an example of a comparison between synthetic and observed emission bands of ethane, acetylene and propane at two given pressure levels (all the different pressure levels probed by CIRS have not been plotted for the sake of clarity) and Fig. 3 the corresponding retrieved profiles.

4 Results and discussion

4.1 Stratospheric temperature

The temperature structure is discussed in details in Fouchet et al. 2008. The main feature is an equatorial oscillation, analogous to the Earth's quasi-biennal oscillation (QBO), resulting from interactions between vertically propagating waves and the mean zonal flow. Regarding the seasonal response, we find a larger north to south temperature gradient at $\sim$ 1 mbar than at $\sim$ 0.01 mbar. The thermal inertia being larger at low altitudes, this is not expected from the thermal response of the atmosphere.

4.2 Hydrocarbon distribution

Results about the meridional distribution of the C_2H_6, C_2H_2 and C_3H_8 volume mixing ratio at 1 and 0.1 mbar are displayed in Fig. 3.

We first note that all three hydrocarbon meridional distributions exhibit a maximum at the equator at 1 mbar. This is in good agreement with photochemical models which predict that mean insolation being greater at the equator, it should coincide with a larger hydrocarbon production and thus a larger abundance. However, especially for C_2H_2, our derived maximum at the equator is larger than predicted: at 1 mbar, we note a 80°S-to-equator enhancement of about 4, in contrast to the expected factor of 2 (Moses et al., 2005). This enhancement

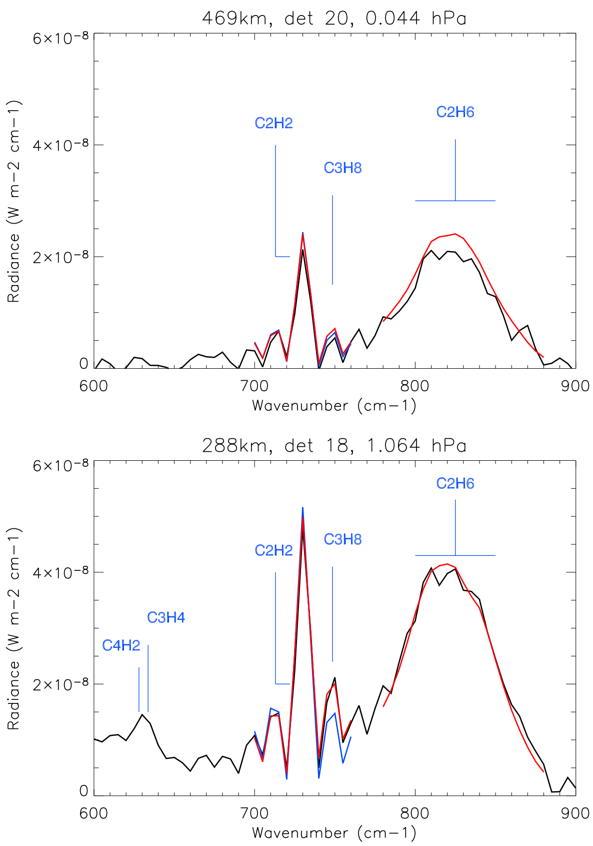

Fig. 1. Synthetic spectra (in red and blue) plotted over observed spectra (in black) at 20°S from two different detectors, thus two different altitudes. The model that do not account for propane opacity (in blue) fails to reproduce the acetylene R-branch intensity around the 1-mbar pressure level

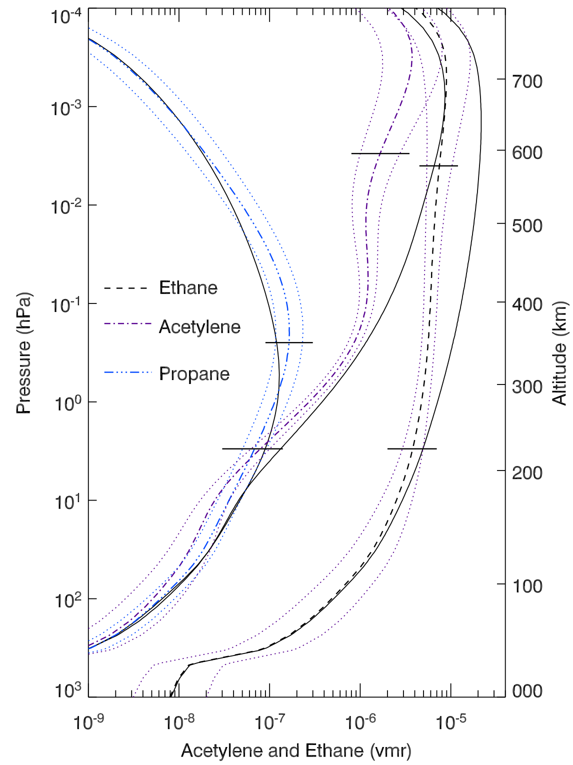

Fig. 2. The corresponding retrieved profiles of C_2H_6, C_2H_2 and C_3H_8 in dashed and dotted-dashed lines. The a priori profiles are in solid lines, the error bars in dotted lines and the horizontal bars represent the vertical limits in sensitivity.

can be explained by a descent of rich-hydrocarbon air at the equator, initiated by the equatorial oscillation, and would affect preferentially C_2H_2 because its vertical profile has a steeper gradient than compared to C_2H_6.

Another unexpected feature is the region of strong hydrocarbon abundance around 25°N, observed at the 0.1-mbar pressure level and above for both C_2H_2 and C_2H_6. It seems to be correlated with the area undergoing ring shadowing at this season. It may be associated with a downwelling branch of the meridional circulation.

The global meridional distribution of the three hydrocarbons can be analyzed in terms of their net photochemical lifetimes. Below the 0.1-mbar level, these lifetimes are supposed to be longer than Saturn's year, so that their distributions should reproduce the yearly averaged solar insolation (decreasing towards both poles). At 1 mbar, apart from the equatorial region, C_2H_2 distribution agrees very well, qualitatively, with this prediction (cf Fig 3) whereas C_2H_6 is found to slightly increase towards the South Pole. This trend for C_2H_6 has already been observed by Greathouse et al. (2005) and Howett et al. (2007) at 1 and 2 mbar and interprated as caused by meridional circulation from equator to South Pole. It can be explained by the fact that C_2H_6 have a much longer lifetime (about 600 years at 1 mbar) than C_2H_2 ($\sim$ 100 years at 1 mbar): as the two molecules are transported towards the South Pole, C_2H_2 is more rapidly chemically destructed than C_2H_6, which explains why we only observe an enhancement for C_2H_6 and constrains the dynamical timescale to lie between 100 and 600 years at 1 mbar.

On the other hand, the propane abundance is found to gradually increase from 45°N to 80°S at 1 mbar (cf Fig. 3) by a factor of 2.5. Although its chemical lifetime is not well constrained because of the lack of laboratory data, it is supposed to be intermediate between C_2H_6 and C_2H_2 lifetimes at 1 mbar. We thus expect

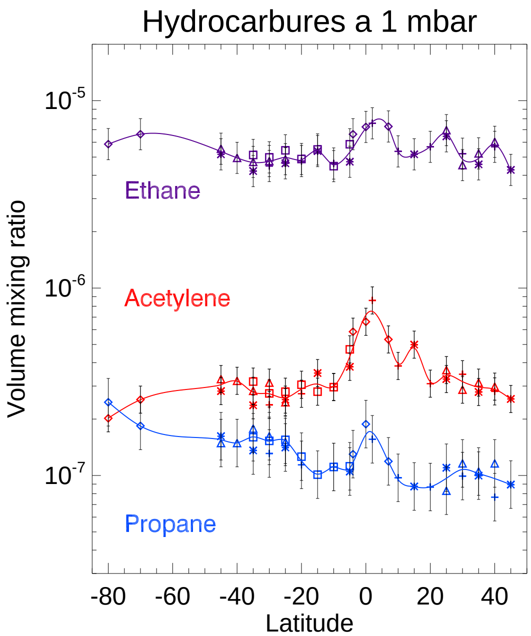

(a)

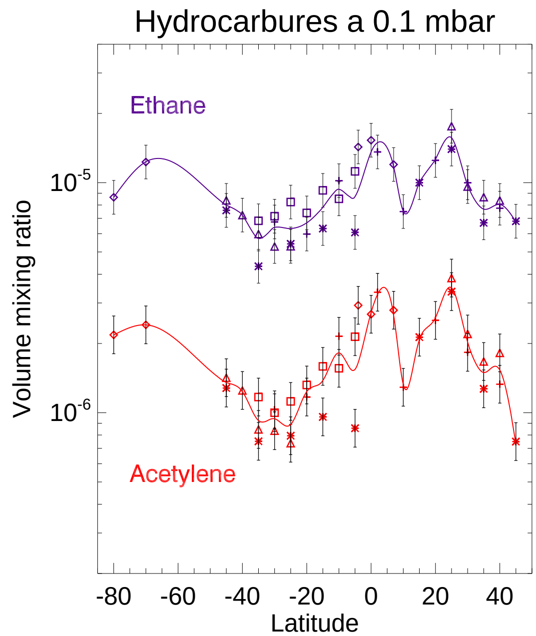

(b)

Fig. 3. Meridionnal hydrocarbon variations at the 1-mbar (left) and the 0.1-mbar (right) pressure levels.

the propane distribution to be less affected by meridional transport than C_2H_6. However, the North-to-South gradient is found greater for propane than for ethane. This anomaly can be explained if the C_3H_8 lifetime at 1 mbar is shorter than or similar to Saturn's season, leading to an increase of C_3H_8 towards southern latitudes due to the increasing solar insolation, at odds with predictions from photochemical models.

Eventually, at 0.1 mbar, we find that the two molecules display very similar distributions, meaning that the two molecules are transported, chemically produced and destructed on same timescales. This is consistent with photochemical models that predict they have similar chemical lifetimes at this pressure level (Moses & Greathouse, 2005).

References

Conrath, B.J. et al., 1998, Icarus, 135, 501-517

Flasar, F. M. et al., 2004, Space Sci. Rev., 115, 169-297

Flasar, F. M. et al., 2005, Science, 307, 1247-1251

Fouchet, T. et al., 2008, Nature, 7192, 200-202

Greathouse, T. et al., 2005, Icarus, 177, 18-31

Greathouse, T. et al., 2006, Icarus, 181, 266-271

Howett, C. et al, 2007, Icarus, 190, 556-572

Moses, J. and Greathouse, T., 2005, J. Geophys. Res, 110

Moses, J. et al., 2000, Icarus, 143, 244-298

SF2A 2008
C. Charbonnel, F. Combes and R. Samadi (eds)

MISALIGNED SPIN-ORBIT IN THE XO-3 PLANETARY SYSTEM?

Hébrard, G.[1], Bouchy, F.[1], Pont, F.[2], Loeillet, B.[1,3], Rabus, M.[4], Bonfil, X.[6,5], Moutou, C.[3], Boisse, I.[1], Delfosse, X.[6], Desort, M.[6], Eggenberger, A.[6], Ehrenreich, D.[6], Forveille, T.[6], Lagrange,A.-M.[6], Lovis, C.[7], Mayor, M.[7], Pepe, F.[7], Perrier, C.[6], Santos, N. C.[5,7], Queloz, D.[7], Ségransan, D.[7], Udry, S.[7] and Vidal-Madjar, A.[1]

Abstract. The SOPHIE Consortium started a large program of exoplanets search and characterization in the Northern hemisphere with the new spectrograph SOPHIE at the 1.93-m telescope of Haute-Provence Observatory, France. The objectives of this program are to characterize the zoo of exoplanets and to bring strong constraints on their processes of formation and evolution using the radial velocity technique. We present here new SOPHIE measurements of the transiting planet host star XO-3. This allowed us to observe the Rossiter-McLaughlin effect and to refine the parameters of the planet. The unusual shape of the radial velocity anomaly during the transit provides a hint for a nearly transverse Rossiter-McLaughlin effect. The sky-projected angle between the planetary orbital axis and the stellar rotation axis should be $\lambda = 70^\circ \pm 15^\circ$ to be compatible with our observations. This suggests that some close-in planets might result from gravitational interaction between planets and/or stars rather than migration. This result requires confirmation by additional observations.

1 Presentation

Accurate radial velocity measurements are an efficient and powerful technique for research and characterization of exoplanetary systems. They allow the statistic of known systems to be extended by completing the mass-period diagram of exoplanets, in particular toward lower masses and longer periods, as the measurements accuracy is improving. In addition, parameters of the transiting planets could be measured thanks to spectroscopic transit observations (the Rossiter-McLaughlin effect), and Doppler follow-up are mandatory to establish the planetary nature and characterize the parameters of the transiting candidates obtained from photometric surveys.

The SOPHIE instrument replaces the ELODIE spectrograph at the 1.93-m telescope of Haute-Provence Observatory. SOPHIE is a fiber-fed, cross-dispersed, environmentally stabilized echelle spectrograph dedicated to high-precision radial velocity measurements (Bouchy et al. 2006). Since its first light on the sky in summer 2006, SOPHIE was used in particular for Doppler follow-up of photometric surveys for planetary transits search. SOPHIE allowed the discovery of transiting planets found by SuperWASP (Collier Cameron et al. 2007, Pollacco et al. 2008), CoRoT (Barge et al. 2008, Alonso et al. 2008, Bouchy et al. 2008) and HAT (Bakos et al. 2007) surveys, as well as the parameters of these new planets to be characterized.

[1] Institut d'Astrophysique de Paris, UMR7095 CNRS, Université Pierre & Marie Curie, 98bis boulevard Arago, 75014 Paris, France
[2] Physikalisches Institut, University of Bern, Sidlerstrasse 5, 3012 Bern, Switzerland
[3] Laboratoire d'Astrophysique de Marseille, Univ. de Provence, CNRS (UMR 6110), BP 8,13376 Marseille Cedex 12, France
[4] Instituto de Astrofísica de Canarias, La Laguna, Tenerife, Spain
[5] Centro de Astrofísica, Universidade do Porto, Rua das Estrelas, 4150-762 Porto, Portugal
[6] Laboratoire d'Astrophysique de Grenoble, CNRS (UMR 5571), Université J. Fourier, BP53, 38041 Grenoble, France
[7] Observatoire de Genève, Université de Genève, 51 Chemin des Maillettes, 1290 Sauverny, Switzerland

2 The SOPHIE Consortium

Together with the advent of this new instrument, the SOPHIE Consortium has been established to carry out a program of detection and characterization of extrasolar planets (Bouchy 2008). Using 120 to 160 nights per year, this large program aims at covering several aspects of exoplanetary science. In particular, we perform a moderate-precision survey ($7 - 10\,\mathrm{m/s}$) of FGK stars, with the aim of monitoring and characterizing known transiting hot Jupiters, as well as detecting new transiting planets. For this latter goal, the main interest of radial velocity surveys, by comparison with photometric surveys, is to detect planets transiting in front of stars brighter than $m_V \simeq 9$. The few known planets transiting in front of bright stars are the ones that allow the most accurate parameters determination and the studies of the planetary atmospheres.

As part of the SOPHIE Consortium program, the detection of three exoplanets have been published up to now: HD 43691b and HD 132406b (Da Silva et al. 2008), and HD 45652b (Santos et al. 2008). These planets are respectively 2.5, 5.6 and 0.5 $\mathrm{M_{Jup}}$ for $M_\mathrm{p} \sin i$, and 37, 975 and 44 days for the orbital periods. There were first found from the ELODIE survey and then monitored by SOPHIE (and by CORALIE at the Euler 1.2-m Swiss Telescope in the case of HD 45652b). SOPHIE data show 9.0, 4.1, and 7.3 m/s dispersion around the fitted orbits for these three targets respectively. Spectroscopic transits of the massive planet HD 147506b were also observed by the SOPHIE Consortium, allowing a refinement of the parameters of this system (Loeillet et al. 2008). Moreover, a study of the stellar activity of the transiting planet host star HD 189733 from SOPHIE Consortium data is presented by Boisse et al. (2008).

3 XO-3b with SOPHIE

3.1 Observations and data reduction

Johns-Krull et al. (2008) announced the detection of XO-3b, which is an extra-solar planet transiting its F5V parent star with a 3.2-day orbital period. There was a quite large uncertainty on the parameters of this system. Johns-Krull et al. (2008) presented a spectroscopic analysis favoring large masses and radii, whereas their light curve analysis suggests lower values. Winn et al. (2008) solved the issue from accurate photometric transit observations, and favored lower values ($R_\mathrm{p} = 1.22 \pm 0.07\ \mathrm{R_{Jup}}$).

We acquired 36 spectra of XO-3 ($m_V = 9.91$) with SOPHIE during the night of January 28th, 2008, where a full coverage of the planetary transit was observed. The airmass ranged from 1.2 to 3.1 during this ∼6-hour observation sequence. Another 19 spectra were acquired at other orbital phases during the following two months.

Through the SOPHIE pipeline, the spectra are extracted and cross-correlated with numerical masks, then the resulting cross-correlation functions are fitted by Gaussians to get the radial velocities. We eliminated the first eight spectral orders of the 39 available ones from the cross-correlation; these blue orders are particularly noisy, especially for the spectra obtained at the end of the transit, when the airmass was high. We corrected the Moon contamination thanks to the second aperture, targeted on the sky.

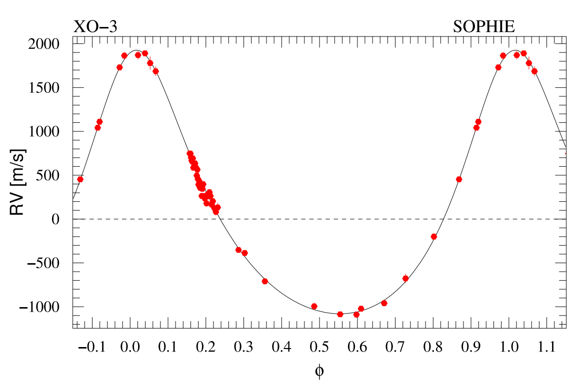

Fig. 1. Phase-folded radial velocity SOPHIE measurements of XO-3 (corrected from the velocity $V_r = -12.045\,\mathrm{km\,s^{-1}}$) as a function of the orbital phase and Keplerian fit to the data. Fig. 2 (top panel) displays a magnification on the transit night measurements (around $\Phi = 0.2$).

3.2 *Refined orbit*

We made a Keplerian fit of the SOPHIE measurements performed outside the transit (Fig. 1). The dispersion of the data around the fit is 29 $\mathrm{m\,s^{-1}}$, in agreement with the estimated errors on the individual radial velocities. The derived orbital parameters are reported by Hébrard et al. (2008); they agree with the Johns-Krull et al. (2008) parameters but the error bars are reduced by factors of three to six. They agree also with updated parameters from Winn et al. (2008). The residuals show no trend that might suggest the presence of another companion in the system over two months.

3.3 *Transverse Rossiter-McLaughlin effect?*

The radial velocities of XO-3 measured with SOPHIE during the transit are plotted on the top panel of Fig. 2. Surprisingly, they do not show the ordinary anomaly seen in case of prograde transits, but the typical shape for a transverse Rossiter-McLaughlin effect. The sky-projected angle between the planetary orbital axis and the stellar rotation axis should be $\lambda = 70° \pm 15°$ to be compatible with our observations.

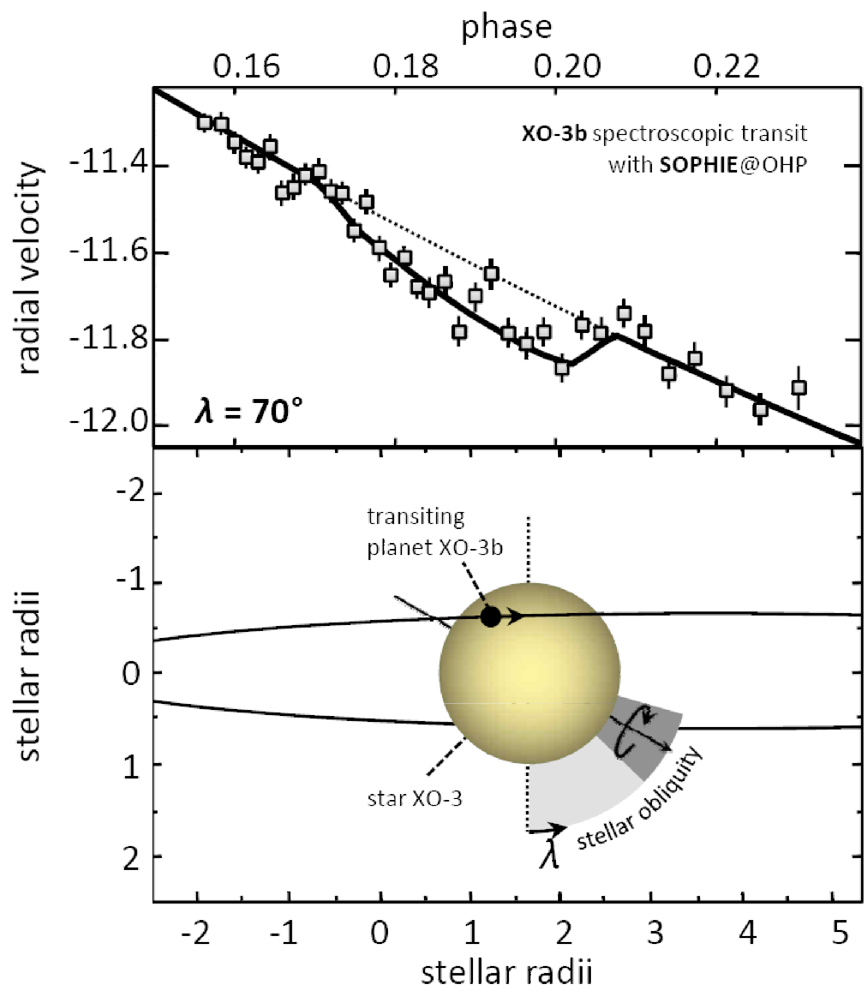

Fig. 2. *Top:* Rossiter-McLaughlin effect models with $\lambda = 70°$. The squares are the SOPHIE radial-velocity measurements of XO-3 with 1-σ error bars as a function of the orbital phase. The solid and dotted lines are the Keplerian fits with and without Rossiter-McLaughlin effect. *Bottom:* Schematic view of the XO-3 system with nearly transverse transit, as seen from the Earth. The stellar spin axis is shown, as well as the planet orbit and the λ misalignment angle (or stellar obliquity). The range $\lambda = 70° \pm 15°$ which is favored by our observations is shown.

The model of the Rossiter-McLaughlin anomaly is over-plotted on the top panel of Fig. 2; it produces a good fit of the data, centered on the expected mid-transit and with the adequate duration and depth (see also Hébrard et al. 2008). The SOPHIE measurements performed just before and after the transit are well described by the Keplerian orbit model. The 43 $\mathrm{m\,s^{-1}}$ dispersion of the data from these transverse models remains slightly above the computed uncertainties on radial velocity measurements.

4 Discussion

A schematic view of the XO-3 system in this nearly transverse configuration is shown in Fig. 2, bottom panel. The SOPHIE observation remains noisy, and we consider this result as a tentative detection of a spin-orbit misalignment rather than a firm detection. Indeed, the end of the transit was observed at large airmasses, which could possibly bias the radial velocity measurements in a way that is difficult to quantify. Other spectroscopic transits of XO-3b should thus be observed.

Narita et al. (2008) also found a possible spin-orbit misalignment, in the case of the eccentric planet HD 17156b; however Barbieri et al. (2008) and Cochran et al. (2008) found $\lambda \simeq 0°$ for this system from extra observations. The timescale for spin-orbit alignment through tidal dissipation is much longer than the timescale for orbital circularization. There are thus no obvious reasons to exclude an eccentric, transverse system. A strong spin-orbit misalignment would favor formation that invokes planet-planet or planet-star scattering rather than inward migration due to interaction with the accretion disk. This suggests in turn that some close-in planets might result from gravitational interactions in multi-body systems (Takeda 2008; see also Papaloizou & Terquem 2001).

Tidal frictions might be high enough to tune the stellar rotation velocity close to the velocity of its companion on its orbit at the periastron. The expected pseudo-synchronized stellar rotation is $V_{\mathrm{rot}} \simeq 30\frac{R_\star}{\mathrm{R}_\odot}\,\mathrm{km\,s^{-1}}$. The XO-3 rotation velocity, $V \sin I = 18.5\,\mathrm{km\,s^{-1}}$, is clearly smaller than the pseudo-synchronized velocity. However, we note that a spin-orbit misalignment would tend to reduce the pseudo-synchronized rotation velocity of the star. Pseudo-synchronization might thus be possible if actually there is a spin-orbit misalignment in the XO-3 system.

We thank the technical team at Haute-Provence Observatory for their support with the SOPHIE instrument and the 1.93-m OHP telescope. Financial supports for the SOPHIE Consortium from the "Programme national de planétologie" (PNP) of CNRS/INSU, France, and from the Swiss National Science Foundation (FNSRS) are gratefully acknowledged.

References

Alonso, R., Auvergne, M., Baglin, A., et al. 2008, A&A, 482, L21

Bakos, G. A., Shporer, A., Pal, A., et al. 2007, ApJ, 671, L173

Barbieri, M., et al. 2008, in *Transiting Planets*, IAU 253, Boston, May 2008

Barge, P., Baglin, A., Auvergne, M., et al. 2008, A&A, 482, L17

Boisse, I., et al. 2008, A&A in press

Bouchy, F., 2008, this volume

Bouchy, F., and the Sophie team, 2006, in 10th Anniversary of 51 Peg-b eds. L. Arnold, F. Bouchy & C. Moutou, 319

Bouchy, F., Queloz, D., Deleuil, M., et al. 2008, A&A, 482, L25

Cochran, W. D., Redfield, S., Endl, M., Cochran, A. L., ApJ, 638, L59

Collier Cameron, A., Bouchy, F., Hébrard, G., et al. 2007, MNRAS, 375, 951

Da Silva, R., Udry, S., Bouchy, F., et al. 2008, A&A, 473, 323

Hébrard, G., Bouchy, F., Pont, F., et al. 2008, A&A, 488, 763

Johns-Krull, C. M., McCullough, P. R., Burke, C. J., et al. 2008, ApJ, 677, 657

Loeillet, B., Shporer, A., Bouchy, F., et al. 2008, A&A, 481, 529

Narita, N., Enya, K., Sato, B., et al. 2007, PASJ, 59, 763

Papaloizou, J. C. B., Terquem, C., 2001, MNRAS, 325, 221

Pollacco, D., Skillen, I., Collier Cameron, A., et al. 2008, MNRAS, 385, 1576

Santos, N. C., Udry, S., Bouchy, F., et al. 2008, A&A in press (arXiv:0805.1019)

Takeda, G. 2008, in *Transiting Planets*, IAU 253, Boston, May 2008

Winn, J. N., Holman, M. J., Torres, G., et al. 2008, ApJ, in press [arXiv:0804.4475]

SF2A 2008
C. Charbonnel, F. Combes and R. Samadi (eds)

SPECTROSCOPY AND NUCLEAR SPIN CONVERSION OF A MOLECULE OF ASTROPHYSICAL INTEREST IN RARE GAS MATRICES : METHANE

Lekic, A.[1], Stienlet, J.[1], Pardanaud, C.[1], Michaut, X.[1], Fillion, J.-H.[1], Vasserot, A.-M.[1] and Abouaf-Marguin, L.[1]

Abstract. Many hydrogenated species observed in space in cold media, exist in different nuclear spin configurations. In cometary's atmospheres and in interstellar molecular clouds, the relative populations of these 'nuclear spin isomers' deviate significantly from the thermal equilibrium. Experimental studies are therefore required to understand the parameters governing the nuclear spin enrichment and conversion in astrophysical conditions, especially in presence of ice. We present new experimental results of the nuclear spin conversion dynamics for CH_4 trapped in rare gas matrices between 4K and 20K. Results revealed for methane are compared to those obtained with water.

1 Introduction

Methane and other hydrogenated molecules of astrophysical interest like H_2, H_2O, H_2CO, NH_3, CH_3OH, or C_2H_4 play an important role for the chemistry in the interstellar medium (ISM) and in the protosolar nebula. Because of the spin 1/2 of the protons, these molecules exist in different nuclear spin configurations. In case of four protons as it is for methane, they are called *ortho*, *para* and *meta* isotopomers depending whether the total nuclear spins are *I=1*, *I=0* or *I=2*, respectively. Due to the Pauli's exclusion principle and the properties of symmetry of rovibrational and spin wave functions of the molecule, each species can be identified by its own rotation-vibration spectrum. In the high temperature limit ($> 50\ K$), it is known that 9/16 of the molecules are *ortho*, 5/16 are *meta* while 2/16 are *para*. Below 50 K, the E/A and F/A ratios become strongly temperature dependent. From these ratios of molecules measured in cometary *comae* (Crovisier 2006; Kawakita *et al* 2006) or in dark clouds (Dickens & Irvine 1999), it is expected to determine the formation conditions of molecules in space, and especially the formation temperature. However, very few experimental data are available concerning nuclear spin conversion in relevant astrophysical conditions.

2 Results and discussion

As a first step before studying ices of astrophysical interest, we have investigated the parameters involved in the nuclear spin conversion of methane isolated in rare gas matrices at low temperatures (between 4.5 K and 20 K). In these environments, the hydrogenated molecule vibrates and rotates almost freely within the cage made of rare gas atoms (Michaut 2004). The rovibrational spectra were recorded in the wavenumber range of 400-4000 cm^{-1} with a resolution of 0.15 cm^{-1} using a Bruker 113V FTIR spectrometer. After a fast cooling from 20 K to 4.2 K, populations of the nuclear spin species do not follow the Boltzmann distribution due to slow nuclear spin conversion. By following the time evolution of the transitions associated with each nuclear spin species, we have measured conversion times in various conditions. At 4.2 K, due to the presence of CH_4 as impurity, argon matrices can be stabilized in *Face Centered Cubic (FCC)* or *Hexagonal Close-Packed (HCP)* crystalline structures. We observed that the nuclear spin conversion is four times faster in the *HCP* structure than in the *CFC* one while the dimensions of the cage are similar in both cases. The strong acceleration of the nuclear spin conversion observed in case of water as the concentration of molecules increases in the sample is

[1] Laboratoire de Physique Moléculaire pour l'Atmosphère et l'Astrophysique-UMR CNRS 7092, Université Paris 6, 4 place Jussieu, 75252 Paris cedex 5

less important for methane (cf figure 1). The calculations performed by our group in the case of H_2O showed that intermolecular magnetic interactions are responsible for this concentration dependence. It seems then that $CH_4 - CH_4$ magnetic interactions are less efficient than for $H_2O - H_2O$ pairs. To confirm this fact, calculations are in progress in our group. For more diluted samples, we measured a characteristic times (100-700 minutes) depending of the molecule, the nature of the rare gas atom and the symmetry of the cage. It is then surprising that characteristic times in cryogenic matrices are much shorter than months estimated in ice (Tikhonov & Volkov 2002) at 77 K. These data strongly suggest that the environment of the molecule plays a crucial role on the nuclear spin conversion of hydrogenated molecules.

3 Conclusions

To conclude, we showed that nuclear spin conversion is very sensitive to intermolecular magnetic interactions as well as to the environment of molecules. As the decrease of mean distances between molecules in the solid enhances the NSC, this process might be very fast in pure ice. However, as rotation is blocked in ice, the mechanism to liberate the excess energy might be different, preventing any direct extrapolation of theses results to the astrophysical context. Efforts are made by our group to experimentally investigate NSC in ice.

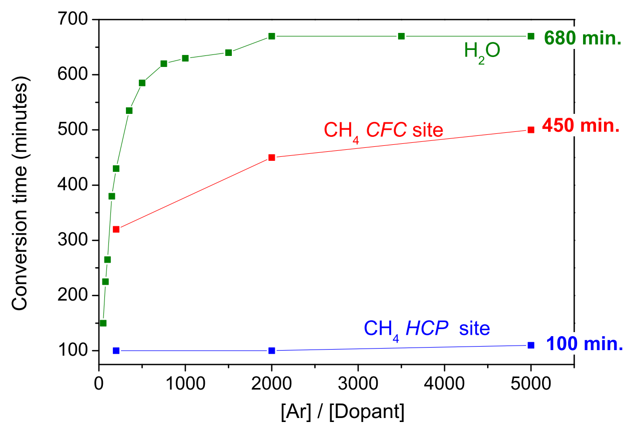

Fig. 1. Evolution of the nuclear spin conversion time of H_2O and CH_4 isolated in solid Ar in function of the dilution of dopant ([Rare Gas]/[Molecule]) at 4.2 K. On the right side of the figure are indicated the conversion times measured in the most diluted samples

References

Crovisier, J. 2006, Molecular Physics 104, 2737

Kawakita, H., Dello Russo, N., Furusho, R., *et al* 2006, ApJ 643, 1337

Dickens,J. E. & Irvine,W. M. 1999, ApJ, 518, 733

Michaut, X., Vasserot, A.-M., & Abouaf-Marguin, L. 2004, Vib. Spectrosc., 34, 83

Tikhonov,V. I., & Volkov, A. A. 2002, Science 296, 2363

SF2A 2008
C. Charbonnel, F. Combes and R. Samadi (eds)

COLLISION-INDUCED THERMODYNAMIC EVOLUTION OF PLANETESIMALS IN THE PRIMORDIAL EDGEWORTH-KUIPER BELT

Marboeuf, U.[1], Petit, J.-M.[1] and Mousis, O.[1]

Abstract. Kuiper Belt Objects and cometary nuclei are considered to be among the most primitive bodies of the outer Solar system. However, their composition may not reflect that of the primordial planetesimals from which they formed since these latter might have experienced some physico-chemical differentiation, due to the heating of impacts. Here, we examine the implications of collisional effects on the physical and chemical differentiation of the planetesimals located in the primitive Edgeworth-Kuiper Belt by using a cometary nucleus model that ensures conservation of mass and energy during and after the impact. We then discuss the influence of the composition (dust fraction and CO/H_2O ratio) and of the adopted values for heat capacity and conductivity within the matrix. We observe that deep modifications of the physical composition in the planetesimals are only possible in the case of a poorly dusty planetesimal without CO inside the body. In all other cases, variations of the parameters show that collisions induce modifications on the initial physical and chemical composition only in the subsurface layers.

1 Introduction

Kuiper Belt Objects (hereafter KBOs) and cometary nuclei are considered to be among the most primordial objects of the outer solar system. However, 90% of the mass of the Kuiper belt was lost through collisions and ejections by dynamical interactions with Neptune (Stern and Colwell 1997; Leinhardt et al. 2008). Due to the heating generated by collisions during this period, and since they might have experienced some physico-chemical differentiation, the composition of these bodies might not reflect that of the primordial planetesimals. Here, we investigate the post-impact thermochemical evolution of a cometary nucleus located in the outer solar system.

2 Insertion of the collision energy in planetesimals

The nucleus model employed in this work is the 1D model described by Marboeuf et al. (2008). This model takes a sphere (initially homogenous) composed of a porous predefined mixture of water ice and dust with different ices in specified proportions. The collision between the projectile and target is characterized in terms of the fraction f^c of kinetic energy delivered in the form of heat to the target by the impactor itself. We neglect the destruction or erosion which can be caused to the target by the impactor. Original accretion and radioactive heating are also neglected in our calculations. Immediately after collision, impact heat is transfered to the nucleus and its propagation within the cometary nucleus is described following the approach of Orosei et al. (2001) and Mousis et al. (2005). We also assume that the impact strength for a porous icy target impacted by a porous icy projectile is $Q^*_D \leq 5.10^4$ $(J.m^{-3})$ (Ryan et al. 1999). This value implies that the largest impactor size cannot exceed $\sim$ 3–5% of the target's one.

3 Choice of the parameters

At the beginning of the computation, the objects share a similar composition. The main physical parameters and initial composition defining our model of planetesimal are standard for comet nuclei. According to Kouchi et al. (1994) and Chick and Cassen (1996), planetesimals of the Kuiper Belt are expected to be formed from

[1] Laboratoire UTINAM, UMR-CNRS 6213, Observatoire de Besancon, 41 bis avenue de l'observatoire, 25010 Besancon France

amorphous ice and the initial temperature is assumed equal to 30 K. The orbital elements (semi-axis $a = 35$ AU, excenticity $e = 0$) are those of a generic member of the primitive Kuiper Belt. The size of the target is assumed to be 10 km and the size of the impactor is set to 300 m (see Sect. 2). Since the composition (dust/ice mass ratio and CO/H_2O mol ratio) and values of the heat capacity and conductivity remain poorly known within planetesimals, we considered a range of plausible values for each of these parameters in order to investigate their influence on the result of collisions. To this end, we adopt $3.T$ and 1200 $J.Kg^{-1}.K^{-1}$ for the heat capacity of the dust's grains (T being the local temperature of the matrix), 10^{-4} and 10 $W.m^{-1}.K^{-1}$ for the heat conductivity of the dust's grains, 0.1, 1 and 10 for the dust/ice mass ratio, and 0 and 10% for the CO/H_2O mol ratio.

4 Results

We have first investigated the influence of different values of the dust's heat capacity on the post-impact evolution of the target. A low dust's heat capacity ($C_d = 3.TJ.Kg^{-1}.K^{-1}$) induces the crystallisation of the target's ice on a depth of order 1–2 times the size of the impactor, after one collision, whereas a higher value ($C_d = 1200J.Kg^{-1}.K^{-1}$) inhibits the crystallisation. In this case, several consecutive impacts are needed in order to start the crystallisation process. In the same time, the value of the heat conductivity of dust's grains, it poorly influences the amplitude of crystallisation in the target. Poor (great) conductivities for dust's grains ($K_d = 10^{-4}W.m^{-1}.K^{-1}/K_d = 10W.m^{-1}.K^{-1}$) increases (decreases) the depth of crystallisation in the planetesimal. In addition, the choice of the heat capacity, and then of the dust/ice mass ratio, strongly influences the evolution of crystallisation in the target. A small dust/ice mass ratio ($\frac{M_d}{M_i} = 0.1$) in the planetesimals results in the crystallisation of the nucleus for any values of the dust's heat capacity and conductivity, and immediately after the first collision. Inversely, at greater dust/ice mass ratio ($\frac{M_d}{M_i} = 10$), several successive collisions are needed to start the crystallisation within the target's matrix. Moreover the presence of CO in the pores of the planetesimals weakens the alteration of their structure and composition after collisions because it partially absorbs the energy coming from the impacts and crystallisation when it escapes from the nucleus, due to sublimation.

5 Conclusions

We have studied the post-impact thermochemical evolution of a cometary nuclei located in the outer solar system. The composition and the structure of a cometary nucleus can be affected by the choice of its thermodynamic parameter. We observe that deep modifications of the ice's structure in the planetesimals are only possible in the case of a poorly dusty planetesimal ($\frac{M_d}{M_i} = 0.1$) without CO inside the body. In all other cases, variances of the parameters show that the collisions induce modifications on the initial physical and chemical composition only in the subsurface layers.

References

Chick, K. M. and Cassen, P. 1997. Astrophysical Journal 477, 398

Kouchi, A., Yamamoto, T., et al. 1994. Astronomy and Astrophysics 290, 1009-1018

Leinhardt, Z. M., Stewart, S. T., et al. 2008. The Solar System Beyond Neptune 195-211

Marboeuf, U., Petit, J.-M. et al. 2008. Astronomy and Astrophysics, submitted

Mousis, O., Marboeuf, U., et al. 2005. Monthly Notices of the Royal Astronomical Society 362, L40-L44

Orosei, R., Coradini, A., et al. 2001. Advances in Space Research 28, 1563-1569

Ryan, E. V., Davis, D. R., et a. 1999. Icarus 142, 56-62

Stern, S. A. and Colwell, J. E. 1997. Astrophysical Journal 490, 879

SF2A 2008
C. Charbonnel, F. Combes and R. Samadi (eds)

THE ROSSBY WAVE INSTABILITY AND PLANET FORMATION: 3D NUMERICAL SIMULATIONS

Méheut, H.[1], Casse, F. [1], Varnière, P. [1 2] and Tagger, M.[1 3]

Abstract. Models of planet formation do not explain yet the growth of planetesimals as in certain ranges of grain size collisions are too slow compared to estimated planet formation time. The Rossby wave instability (RWI) may solve this problem by the formation of Rossby vortices in the accretion disc, speeding up the accumulation of grains in their centre (Varniere & Tagger, 2006). Up to now, only two dimensions numerical studies of the RWI have been done. In this proceeding we present the results of three dimensions numerical simulations of the non-linear evolution of the RWI in a non magnetized disc and its vertical structure.

1 Introduction

The planet formation model based on gravitational collapse is a too slow mechanism as far as the collisions between grains with a size higher than one centimeter or meter, will destroy them. The other difficulty of this model is that the grains should fall on to the central star in a few thousand years. In order to speed up the planet formation, it has been proposed (Barge & Sommeira, 1995) that vortices in the protoplanetary disc would speed up the process by trapping the dust in their center. However vortices in discs are sheared away by differential rotation (Tagger, 2001) and should not be able to survive on the planet formation timescale. This difficulty could be overcome by the Rossby-Wave Instability (Lovelace et al., 1999) which under certain conditions can create long-lived, high-amplitude vortices (Varniere & Tagger, 2006).

The analytical study of this instability (Lovelace et al., 1999) was done in the case of a two dimensional disc and predicted the RWI linear evolution. This work has been confirmed by 2D numerical simulations of the linear evolution (Li et al., 2000) and have been extended to the non linear stage (Li et al., 2001). Other simulations of the RWI have been performed in the context of planet formation with a dead zone lying in the protoplanetary disc (Varniere & Tagger, 2006, Lyra, et al., 2008). Rossby wave instability may have already been seen in three dimensional numerical simulations (Machida & Matsumoto, 2003) but was not identified and therefore not studied in details. The point of the present simulations is to study the development and the vertical structure of this instability when it appears in a 3D accretion disc.

After a brief discussion about the Rossby wave instability, its characteristics and trigger mechanism,we show the numerical setup and initial conditions of the simulations. The results are presented in paragraph 4 and 5, and in the last part conclusions are given.

2 The Rossby wave instability

The Rossby wave instability was introduced by Lovelace et al. (1999) as a solution for the angular momentum transport in a un-magnetized disc. It is a hydrodynamical instability that occurs when the radial profile of the specific vorticity shows a local extremum:

$$\partial_r \mathcal{L} = 0 \tag{2.1}$$

$$\mathcal{L} = \frac{(\vec{\nabla} \times \vec{v})_z}{\Sigma} \tag{2.2}$$

[1] APC, Université Paris Diderot
[2] LAOG, Grenoble
[3] LPCE, Orleans

where r and z are the coordinates of the cylindrical basis (r, θ, z), $\vec{v}$ is the velocity of the fluid, and Σ is the surface density of the disc.

This condition may be fulfilled within a protoplanetary disc at the edge of the dead zone (defined as the radial interval where the ionization is too low to couple the gas with the magnetic field). Varniere & Tagger (2006) found that the dead zone naturaly creates the conditons to trigger the RWI: MHD instabilities such as the magneto-rotational instability (Balbus & Hawley, 1991) cause accretion outside the dead zone that creates a minimum of the density at its inner edge and a density maximum at its outer edge. These density extrema lead to extrema of the specific vorticity $\mathcal{L}$.

The RWI is a non axisymetric instability characterised by the formation of a Rossby vortex at the position of the extremum of $\mathcal{L}$ and density waves outside the vortex zone. Rossby vortices are usually discussed in meteorology and planetary atmosphere in general (Jupiter great red spot). In an accretion disc, a vortex would be sheared due to differential rotation, unless being sustained by some process; the RWI is one of the processes able to do so. Differential rotation is also responsible of the coiling of the compressional waves into spirals, as in spiral galaxies.

3 Setup

The 3D simulations of the RWI were done by the mean of the hydrodynamical module of the Versatile Advection Code (VAC,Toth, 1996) solving the adiabatic equations. The resolution in cylindrical coordinates $(r/r_0, \theta, z/r_0)$ is $300 \times 256 \times 32$ or 64 cells on the computational domain $[0.8, 10.] \times [0., 2\pi] \times [0., 0.8]$ with r_0 the radius of the inner edge of the disc.

The initial density profile is a usual profile with a surface density varying as $(r/r_0)^{-1/2}$ where we add an overdensity (a bump) at a radius of $3r_0$, to satisfy the instability condition.

$$\rho(r, 0) = 10^{-2} + r^{-1/2}\Big(1 + th\big(\frac{r/r_0 - 1.5}{0.1}\big)\Big)\Big(1. + e^{-\frac{(r/r_0 - 3.)^2}{10^{-2}}}\Big) \tag{3.1}$$

The radial velocity and vertical density profile were chosen in order for the disc to be in equilibrium. The axisymmetry of the disc is broken due to small perturbations of the radial velocity that are of the order of 10^{-4} the keplerian velocity.

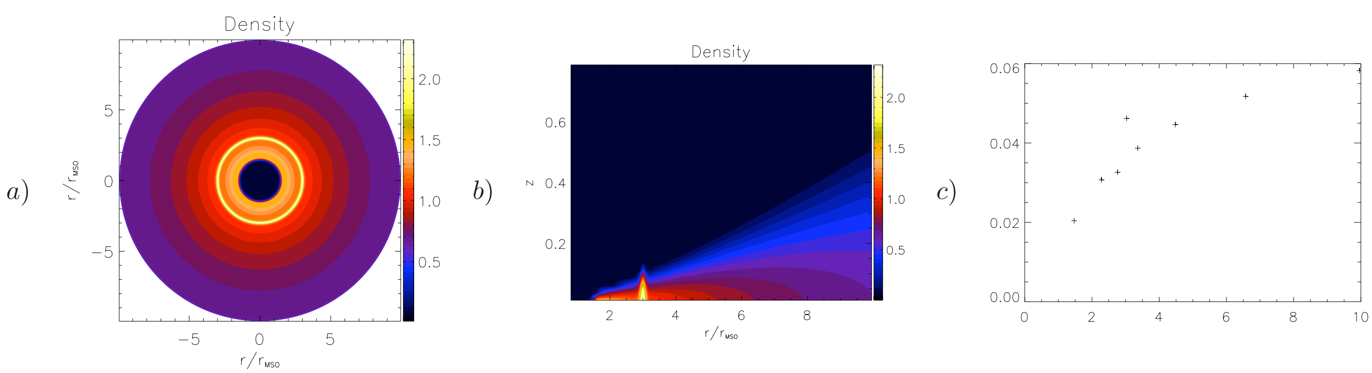

Fig. 1. Initial density profile of the disc, cut in the midplane (a) and vertical cut (b). c) Evolution of the aspect ratio h/r of the disc with the radius r.

These initial conditions have been chosen such that the Rayleigh stability criterion is ensured everywhere, despite the strong radial pressure gradient near the overdensity. The equilibrium of the disc have been checked with analogous simulations without the velocity perturbations.

4 RWI identification

The first aim of these 3D simulations was to show that the RWI can develop near the overdensity, at the edge of the dead zone of a proto-planetary disc. The instability can be identified thanks to its two components, vortices and density waves that appear clearly in the simulations. Those two components can be seen on the density profile on fig 2. In the following plots, we display the physical quantities once have been subtracted the axisymmetric component of each quantity.

4.1 Acoustic waves

The density waves are clearly identified when plotting the compressible part of the velocity ($\vec{\nabla}.\vec{v}$). An interesting point is that the bump zone is known to be a forbidden zone for the density waves and it is clear on fig 2 b) that those waves are only seen outside this zone.

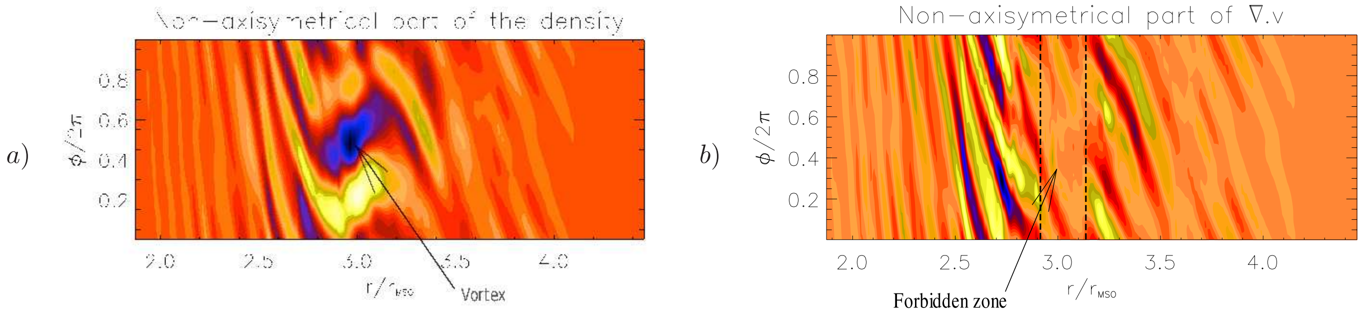

Fig. 2. The two plots are representations of the disc in a cartesian grid, where the radius of the disc is in asbscissa and the θ angle is in ordinate ($\phi = \theta/2\pi$). The plots are cut of the disc between $r/r_0 = 1.8$ and 4.2 . a) Non-axisymetrical part of the density of the disc, the two parts of the instability can be seen: the vortex and the acoustic waves. b) The plot of the non-axisymetrical part of $\vec{\nabla}.\vec{v}$ shows the compressible waves that are localised outside the bump zone.

4.2 Vortices

The second aim of the simulations was to know if this instability can help for the planet formation, that is the structure of the vortices in the vertical direction. In the planet formation model, it is usually supposed that the dust grains are concentrated in the mid-plane of the disc due to a lower thermal velocity for a given gas temperature; that is why it is important to know if the vortex occurs in the vertical structure of the disc and where it is located.

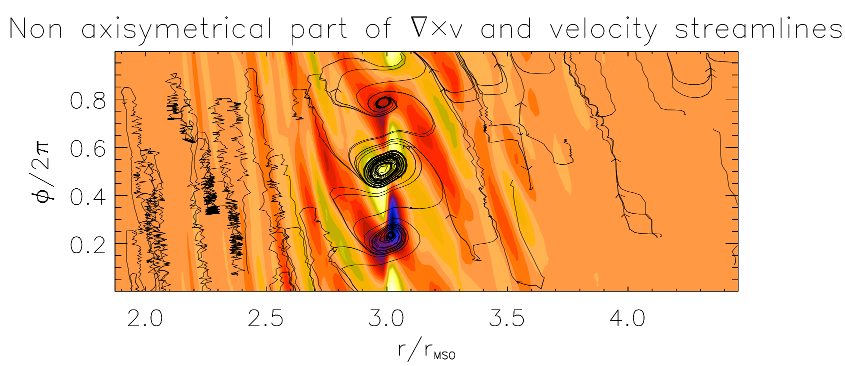

Fig. 3. The same projection as before is used. The color plot is the nonaxisymetric part of the vorticity $(\vec{\nabla} \times \vec{v})_z$ in the disc, it is concentrated around the position of the bump. The black lines are the streamlines of the non-axisymetric part of the velocity showing the vortices.

The vortices can be observed by plotting the vorticity of the stream that is the vertical projection of $\vec{\nabla} \times \vec{v}$ as can be seen on fig 3. The exact location of the vortices is confirmed by the velocity stream lines. The radius where we placed the extremum of $\mathcal{L}$ is clearly the radius of the center of the vortices and is a key parameter for the instability observed here.

5 Vertical structure of the vortices

Figure 4 shows the maximum value of the vorticity in function of z. This comparison with the density profile shows that when the disc has a vertical extension of ten cells, the vortex has a vertical extension over several cells before its amplitude diminishes with the density. The vortex is then more vertically extended than the density. This vertical extension of the vortex is coherent with the instability linear theory and with the planet formation mechanism because it will favour the agglomeration of dust.

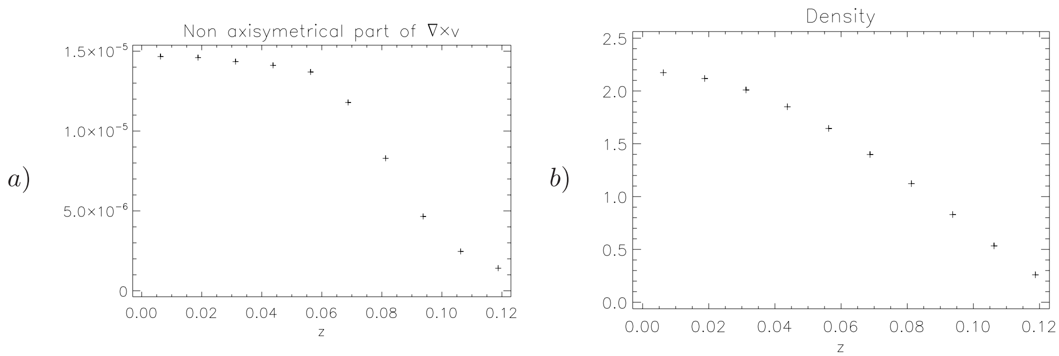

Fig. 4. Vorticity (a) and density (b) in function of the height z. This figure shows a vertical extension of the vortices as far as the vorticity decreases slower than the density

6 Conclusion

We have presented the first fully 3D simulations of the RWI. The radial and vertical structures of the instability are in agreement with the linear theory. The vortices exhibit finite vertical extension and survive during several disc rotations. These simulations confirm the physics of the instability, and its ability to help planet formation by creating strong long-lived vortices in a differentially rotating disc.

However only a few keplerian orbits of the vortices have been simulated here, future studies will include longer simulations to see the long time evolution of the vortices. A better vertical resolution is also needed to have a better idea of the vortices structure, and for such a simulation an adaptive mesh refinement (AMR) grid will be used. A two fluid simulations including the solid grains with a more realistic disc including the magnetised and dead zone would also be an interesting development of this work. In an other context we aim to study the RWI instability in order to understand the microquasar high frequency quasi-periodic oscillations.

References

Balbus, S.A., Hawley, J.F.,1991, ApJ,376,214

Barge, P. & Sommeira, J.. 1995, A&A, 295, L1

Li, H., Finn, J.M.., Lovelace, R.V.E., Colgate, S.A., 2000, ApJ, 553, 1023

Li, H., Colgate, S.A., Wendroff, B., Liska, R., 2001, ApJ, 551, 874

Lovelace, R.V.E, Li, H., Colgate, S.A., Nelson, A.F., 1999, ApJ, 513, 805

Lyra, W., Johansen, A., Klahr, H., Piskunov, N., arXiv:0807.2622v1

Machida, M., Matsumoto, R., 2003, ApJ, 585, 429

Tagger, M., 2001, A&A, 380, 750

Tagger, M. & Varniere, P., 2006, ApJ, 652, 1457

Varniere, P. & Tagger, M., 2006, A&A, 446, L13

SF2A 2008
C. Charbonnel, F. Combes and R. Samadi (eds)

A MODEL FOR THE KHZ QPO IN NEUTRON STAR BINARIES

Méheut, H.[1] and Tagger, M.[2]

Abstract. Twin quasi-periodic oscillations have been observed in the emission spectrum of neutron star binaries. The models that have been proposed do not succeed to explain the frequency difference between the two kHz QPO, which is close but distinct from the rotation frequency of the neutron star. I will present a new model based on the dynamics of the gas trapped in the neutron star magnetosphere.

1 Introduction

Neutron star binaries are at the center of numerous investigations since they are the laboratory of extreme physics such as high magnetic field and strong gravity. These extreme conditions can be explored thanks to the X-ray emission of the accretion disk of the neutron star. The millisecond variability is one of the key-points of this emission since it originates in the inner part of the disk exposed to the stronger gravitational field.

The kHz quasi-periodic oscillations have been widely studied since their discovery in 1996 by the RXTE satellite. Various theoretical models have been proposed, but none of them was really convincing. Here we present a new model for the kHz QPO in neutron star binaries, based on the dynamics of the gas in the inner part of the accretion disk.

2 Observations and first models

2.1 Observations

Twin kHz QPO have been discovered in low-mass X-ray binaries containing a low magnetic field neutron star at diverse X-ray luminosities. Here is an example of such observations:

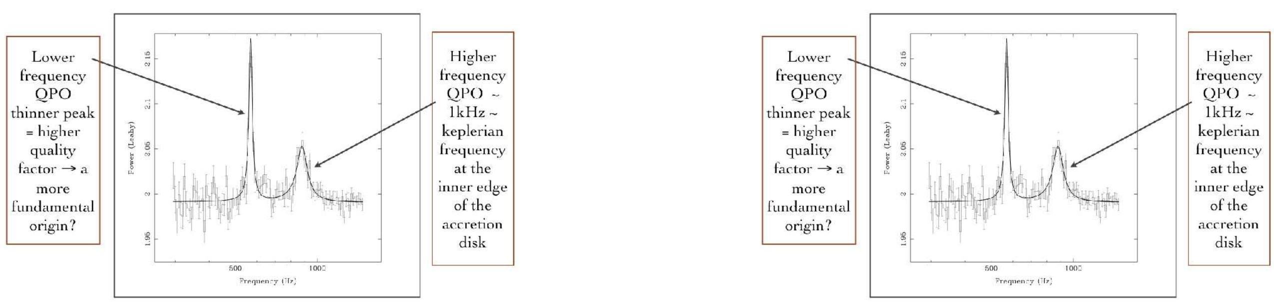

Fig. 1. *Left:* Power spectrum of a neutron star binary showing twin kHz QPO (Mendez et al., 1998) *Right:* Variation of the peaks separation as a function of the lower QPO frequency in 4U 1728-34 (Mendez & van der Klis, 1999)

One interesting point of twin QPO is that for the same neutron star binaries, their frequencies may evolve but the difference between the two peaks $\Delta\nu$ is constant and close to the rotation frequency of the neutron star for a wide range of variations of ν.

---

[1] APC, Universite Paris Diderot
[2] LPCE, Orleans

2.2 Firsts models

After the discovery of the twin kHz QPOs, their intrinsic fundamental nature has been suggested and different models have been proposed. Two main classes of models can be distinguished: those based on a beat frequency (van der Klis, 2000) and the relativistic precession models (Stella & Vietry, 1999). None of them were fully convincing and twin QPO are still not clearly understood.

3 A model based on the dynamics of a magnetospheric disc

In the model presented here, we assume that the lower frequency is the keplerian frequency at the inner edge of the keplerian disk: this is a fundamental frequency much better adapted to explain the higher quality factor of the lower QPO. We then seek to explain the higher frequency QPO by the presence of a warped disk in the neutron star magnetosphere.

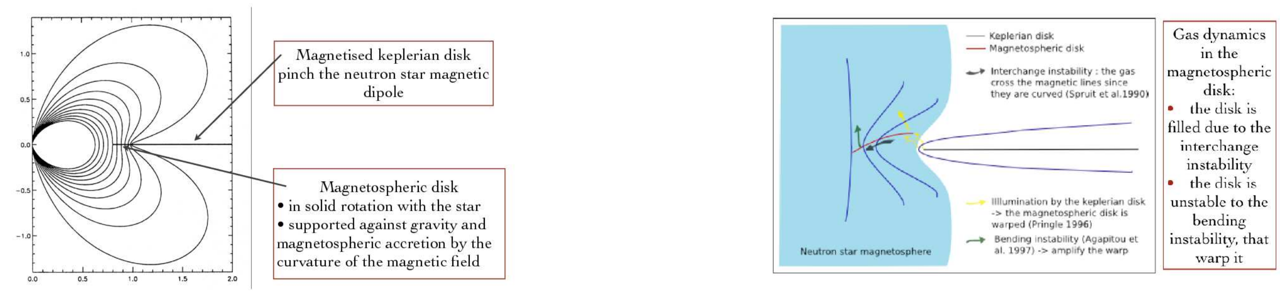

Fig. 2. *Left:* Geometry configuration of the model (Lepeletier & Aly, 1998) *Right:*

The dispersion relation of the bending instability can be written in this magnetic configuration:

$$(\omega - m\Omega_*)^2 = \Omega_K^{d2} + \frac{r(\Omega_K^2 - \Omega^2)}{B_z}\frac{\partial B_z}{\partial r} + \frac{2B_r^2}{\Sigma}|k| + \frac{L}{\Sigma d} + i\frac{L}{\Sigma}|k|, \tag{3.1}$$

with ω the frequency of the instability and $\frac{r(\Omega_K^2-\Omega^2)}{B_z}\frac{\partial B_z}{\partial r}$ depending on the position of the inner edge of Keplerian disk thus on Ω_K^d.

4 Conclusion

In this model the lower QPO is the fundamental one, it is the keplerian frequency at the inner edge of the accretion disk, and the higher frequency QPO is due to a bending instability in the magnetospheric disk. This model can explain the behaviour of the QPO frequency difference. However this model is still under development.

References

Agapitou, V., Papaloizou, J. & Terquem,C. 1997, MNRAS, 631, 645

Lepeltier, T., & Aly, J.J., 1996, A&A, 645,665

Mendez, M., van der Klis, M.,Wijnands,R., Ford, E.C., van Paradjis J., & Vaughan, B.A., 1998, ApJ, 505:L23-26

Spruit, H.C., & Taam, R.E., 1990, A&A, 475,493

Stella, L., Vietri, M., 1999, Phys,Rev.Let, 82,17:20

van der Klis, M., 2000, Ann.Rev.A&A, 717, 760

Mendez, M., & van der Klis, M., 1999. ApJ, 517:L51■54

SF2A 2008
C. Charbonnel, F. Combes and R. Samadi (eds)

DETECTION OF ANTHRACENE IN THE UV SPECTRUM OF COMET 1P/HALLEY

Moreels, G.[1], Clairemidi, J.[1], Mousis, O.[1] and Bréchignac, P.[2]

Abstract. Following the detection of three small PAHs, naphthalene, phenanthrene and pyrene in dust grains collected by the Stardust probe in the environment of Comet 81P/Wild 2, we reprocessed the UV spectra of Comet 1P/Halley recorded by the Vega-TKS spectrometer. The near-UV cometary spectra were compared with laboratory spectra of anthracene obtained under laser-induced fluorescence conditions. Four main peaks coincide at 362, 367.5, 373 and 382.5 nm. This shows that anthracene is present in the innermost coma of Comet 1P/Halley and comes in addition to the previous detection of phenanthrene and pyrene.

1 Introduction

Naphthalene, phenanthrene and pyrene were recently identified in comet 81P/Wild2 samples collected during the Stardust mission (Sandford et al. 2006; Clemett et al. 2007). In addition, by using a model for the infrared emission of dust based on a statistical mix of PAHs with an average size $\sim$1 $\AA$ for pyrene (Li & Draine 2001), Lisse et al. (2006) also detected infrared signatures of PAHs at 6.2 and 7.6 μm in Spitzer spectra of comet 9P/Tempel 1 ejecta. These new findings led us to re-investigate the UV part of TKS spectra in order to search for new fluorescence bands of PAHs, as these compounds are quite efficient in emitting near UV and blue luminescence when exposed to UV radiation. In this paper, we present a set of four spectra of the inner coma of comet 1P/Halley, each one being an average of four individual spectra taken at different projected distances between 421 and 932 km from the nuclei. The data are compared with a fluorescence spectrum of anthracene obtained in the laboratory under simulated cometary conditions. Both types of spectra, cometary and laboratory, present comparable features that allow a confident identification of anthracene in 1P/Halley.

2 Spectra of Halley's inner coma

Spectra of Halley's inner coma in the near UV were obtained on March 9, 1986 with the TKS spectrometer onboard the Vega2 spacecraft. In the inner coma at $p \leq 3000$ km, during the approach and encounter period, intense fluorescence broad band emissions (10–50 kRayleighs / nm) gradually emerged as the spacecraft approached the comet. The spectra recorded during this session exhibit a noticeable variability which reflects the inhomogeneities of the cometary medium close to the nucleus. A selection of them is displayed in Fig. 1, where a number of fluorescence bands are seen in the 340–390 nm spectral range.

Polyatomic molecules which emit fluorescence radiation in the near UV are numerous. Our search was oriented towards methanol and formaldehyde, since these molecules have been detected in several comets, and towards PAHs which present fluorescence bands in the UV and visible. In the UV, methanol in the gaseous phase shows a weak absorption band at $\lambda \sim 180$–200 nm. The molecule is dissociated and produces mainly formaldehyde or, with a lower rate, methoxy radicals. At shorter wavelengths, $\lambda < 150$ nm, the dissociation products are methyl and OH ($^2\Sigma$) radicals. As a result, methanol does not seem to be a possible fluorescence carrier of the observed emission. In the case of formaldehyde, its fluorescence spectrum presents ten regularly spaced bands but none of them coincide with the reported emission features between 358 and 385 nm.

Among the large family of PAHs, we identified phenanthrene (Moreels et al. 1994) and pyrene (Clairemidi et al. 2004) from TKS spectra of Halley's inner coma. These two PAHs were also identified in the samples of

[1] Observatoire de Besançon, Institut UTINAM, CNRS-UMR 6213, BP 1615, 25010 Besançon Cedex, France; guy.moreels@obs-besancon.fr
[2] Laboratoire de Photophysique Moléculaire, CNRS, Univ. Paris-Sud, Bât. 210, 91405 Orsay Cedex, France

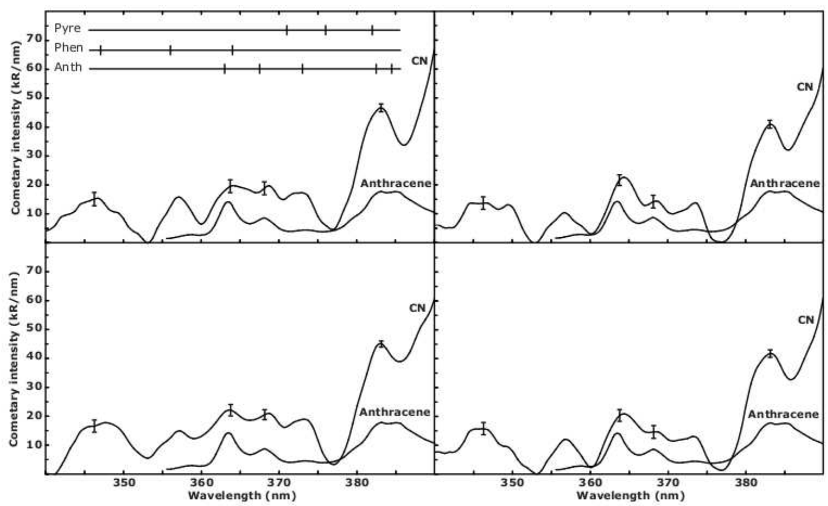

Fig. 1. Comparison of cometary spectra with the laboratory spectrum of anthracene. The CN emission band is not subtracted from the cometary spectrum. The laboratory spectrum of anthracene, shown with arbitrary intensity units, is presented below the cometary spectrum. The cometary spectrum shown in each panel is an average of four different individual spectra taken at different projected distances p between 421 and 932 km. Four main peaks coincide at 363, 367.5, 373 and 382.5 nm. Error bars are plotted at the wavelengths of several PAHs emission bands. Marks in the upper left panel denote the location of the anthracene, phenanthrene and pyrene features.

the comet 81P/Wild 2 collected by Stardust (Sandford et al. 2006; Clemett et al. 2007), and presented as a good match to the material excavated by the Deep Impact experiment from comet 9P/Tempel 1, as observed by the Spitzer Space Telescope at 5–35 μm (Lisse et al. 2006). PAHs are considered to be the best candidates as possible carriers of the cometary emission, because their fluorescence bands are expected to be located in the 330–385 nm spectral range.

3 Identification of Anthracene

The identification of some of these bands in comet 1P/Halley as being anthracene has been done on the basis of comparisons between the cometary spectra and emission spectra obtained in the laboratory, under conditions which provide valuable simulation of the astrophysical situation, i.e. super-cooled gas phase molecules in a collision-free regime. The experimental conditions are described in Hermine (1994), Moreels et al. (1994) and Clairemidi et al. (2004). The characteristics of the experiment (very low temperature and absence of collisions) provide an appropriate simulation of the cometary conditions. The fluorescence spectra correspond to the recording of the dispersed emission resulting from excitation at a fixed laser wavelength.

The photophysical properties of the anthracene molecule must be invoked in order to derive from experimental data the expected emission spectrum of the molecule if present in the cometary environment. This is done with the help of the diagrams presented in Fig. 2. The central part of the figure is an energy levels scheme following partly the traditional Jablonski's representation. The fluorescence excitation spectrum of jet-cooled anthracene is reported on the left hand side of the figure, while the standard solar spectrum is recalled on the right hand side. The central scheme consists of three piles of vibrational energy levels built above the vibrationless electronic singlet states: the ground state S_0 (right), the first excited singlet S_1 (middle), and the fourth excited singlet S_4 (left). Note that the second and third excited singlet states are not represented since, as apparent from the fluorescence excitation spectrum (left), the $S_2 \leftarrow S_0$ and $S_3 \leftarrow S_0$ transitions have negligible oscillator strengths. The metastable triplet states are not shown either, although they contribute to the reduction of the fluorescence quantum yield by inter-system crossing non radiative transitions. It thus appears that only the vibronic bands belonging to the $S_1 \leftarrow S_0$ and $S_4 \leftarrow S_0$ electronic transitions are efficient to excite the fluorescence of anthracene. Excitation of the S_4 state is immediately followed by fast non radiative transitions of internal conversion to the S_1 state (waving horizontal arrow in the figure), as evidenced by the fact that the fluorescence is emitted in the wavelength range of the $S_1 \leftarrow S_0$ transition.

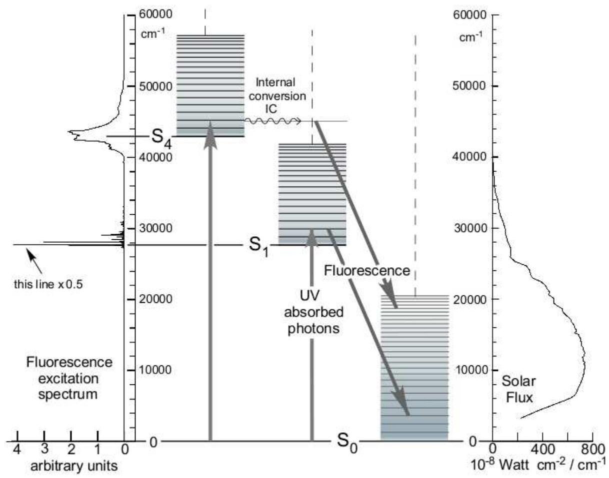

Fig. 2. Energy levels diagram showing the allowed electronic transitions within the singlet states of anthracene. On the left hand side, the fluorescence excitation spectrum of the jet-cooled molecules is reproduced (Hermine 1994). On the right hand side, the solar spectrum is shown for comparison. Note that the S_2 and S_3 states are not represented since they do not contribute to the excitation because of their very low oscillator strengths. Triplets which contribute to the reduction of the fluorescence quantum yield by non-radiative transitions are not shown for overall clarity.

The experimental study shows that excitation through the various vibronic bands of the $S_1 \leftarrow S_0$ transition gives rise to a dispersed emission spectrum which is red-shifted relative to the origin transition at 361 nm, always similar when the excitation wavelength is varied and which evolves towards an essentially stable spectrum when intramolecular vibrational redistribution (IVR) is established (Bréchignac & Hermine 1994). It is clear from the solar spectrum in Fig. 2 that the flux available for excitation to S_4 is significantly smaller than it is for excitation to S_1. Interestingly enough the quantum yield is also reduced from 0.67 (at the origin of S_1) to 0.02 (at the high energy side of the S_4 band). Consequently, the contribution of the fluorescence from S_1 is expected to be about 20 times larger than that from S_4. The laboratory photophysical studies thus led us to adopt as expected cometary spectrum the spectrum with λ_{exc}= 344 nm reported by Lambert et al (1984), which is reproduced in the four panels of Fig. 1.

We selected for this figure cometary spectra where the fluorescence bands of anthracene at 363, 367.5, 373, 382.5 and 384.5 nm are present. As the medium probably contains a mixture of PAHs, the simultaneous presence in the four spectra of the fluorescence bands of anthracene at 363, 367.5, 382.5–384.5 nm constitutes a strong criterion for identifying this molecule. The main fluorescence bands of phenanthrene located at 347, 356, 364 nm are also seen. In the case of pyrene, the bands located at 371, 376 and 382 nm are hardly seen in the spectra that were chosen in the present work. As a result, the spectra shown in Fig. 1 suggest the identification of anthracene in Halley's comet but also confirm the presence of phenanthrene.

Following the same approach as in our previous cometary PAHs works (Moreels et al. 1994; Bréchignac & Hermine 1994, Clairemidi et al. 2004), i.e. relying on the absolute oscillator strength for $S_1 \leftarrow S_0$ absorption and fluorescence quantum yields from S_1 (near λ_{exc} = 344 nm, Q $\simeq$ 0.2) (Hermine 1994), integrating the cometary intensity in anthracene bands (from Fig.1) and assuming the expansion velocity is 1 km/s, it is possible to derive the production rate of anthracene: $Q_{anthracene} \sim 10^{26}$ molecules s^{-1}.

This value may be compared with the production rate of C_2, estimated to be 6×10^{27} molecules s^{-1} for March 9, the encounter day (Krasnopolsky et al. 1986). Comparing the production rate of anthracene to the estimated production rate of water mentioned by Krasnopolsky et al. (1986), $Q_{H_2O} = 2 \times 10^{30}$ molecules s^{-1}, and by Encrenaz et al. (1988) for P/Halley, $Q_{H_2O} = 10^{30}$ molecules s^{-1}, we derive a maximum abundance of anthracene relative to water of 5×10^{-5} to 1×10^{-4}. Note that Bockelée-Morvan et al. (1995) found a lower PAH abundance relative to water ($\sim 1.5 \times 10^{-6}$ to 10^{-5}) in a set of seven comets, but their derived abundances depend on modeling assumptions which are still uncertain and there is a significant diversity among comets, namely in the dust/gas ratio and in the composition of the coma.

In the same conditions the cometary intensity in phenanthrene bands from Fig. 1 would lead to $Q_{phenanthrene}$ ranging from 6×10^{26} to 10^{27} molecules/s. The order of magnitude is similar to our previous determination

(Moreels et al. 1994) although weaker by a factor of $\simeq 2$. Such a difference can be explained by the fact that the spectra in Fig. 1 have been selected to clearly show up the anthracene bands, in contrast to our previous work. The higher abundance of phenanthrene compared to anthracene could be explained by the fact that it is more stable than anthracene (see e.g. Fig. 2 p.4, Bjørseth 1983).

This reveals a clear variability in the spectra which must have its origin in the heterogeneity of the material composition along the time-varying line-of-sight. Such a behavior is fully consistent with the evidence of highly anisotropic jets in Halley's coma, and is expected to be emphasized if the PAHs molecules are indeed outgassed from the dust particles themselves, possibly released by the fragmentation of clumps. Such a process is also proposed by Green et al. (2007) to explain the impact counts data recorded in the Wild 2 coma during the Stardust closest approach.

4 Summary and discussion

The recent identification of PAHs in the cometary dust grains collected during the Stardust mission (Clemett et al. 2007) led us to re-investigate the spectra of Halley's inner coma recorded by the TKS spectrometer. We compared the cometary data with laser induced fluorescence spectra obtained under cooled molecular jet conditions. Using anthracene vapour, four main peaks located at 363, 367.5, 373 and 382.5 nm were identified in the laboratory spectrum of the 3-ring PAH, as well as in the cometary spectra. In addition, the spatial distribution of the emission exhibits a p^{-1} variation which shows that its carrier, anthracene, is emitted by the nucleus or by dust packs in the coma. The identification of anthracene confirms the previously reported detection of phenanthrene (Moreels et al. 1994), and pyrene (Clairemidi et al. 2004). It should be noted that the structure of individual spectra is not uniform for the whole set of TKS data. This reveals some heterogeneity in the composition of clumps or of dust grains as pointed by the Stardust results (Clemett et al. 2007). The chemistry capable of producing such PAHs is likely to create, under similar conditions, a whole family of polycyclic aromatic molecules. In particular, the presence of naphthalene is not excluded from our spectra but difficult to determine definitely because the expected spectrum presents only one broad (~ 25 nm) band without characteristic features (Bréchignac & Hermine 1994). These detections imply that other PAHs might also be present in comet Halley and give rise to characteristic emission spectra.

References

Bjørseth A., 1983, Handbook of polycyclic aromatic hydrocarbons, Marcel Dekker, INC. (New York 10016)

Bockelée-Morvan D., Brooke T. Y., Crovisier J., 1995, Icarus, 116, 18

Bréchignac P., Hermine P., 1994, in A.I.P. Conf. Proc. 312, Molecules and Grains in Space, ed. I. Nenner (New York: AIP), 613

Clairemidi J., Bréchignac P., Moreels G., Pautet D., 2004, P&SS, 52, 761

Clemett S. J., Nakamura-Messenger K., McKay D. S., Sandford S. A., 2007, LPI, 38, 2091

Encrenaz T., D'Hendecourt L., Puget J. L., 1988, A&A, 207, 162

Green S. F., et al., 2007, ESASP, 643, 35

Hermine P., 1994, PhDT, Université Paris XI, Orsay

Krasnopolsky V. A., et al., 1986, Nature, 321, 269

Lambert W.R, Felker P.M., Zewail A.H., 1984b, J. Chem. Phys. 81, 2217

Li A., Draine B. T., 2001, ApJ, 554, 778

Lisse C. M., et al., 2006, Science, 313, 635

Moreels G., Clairemidi J., Hermine P., Bréchignac P., Rousselot P., 1994, A&A, 282, 643

Sandford S. A., et al., 2006, Science, 314, 1720

SF2A 2008
C. Charbonnel, F. Combes and R. Samadi (eds)

PHOTOCHEMICAL ENRICHMENT OF DEUTERIUM IN TITAN'S ATMOSPHERE: NEW LIGHTS FROM CASSINI-HUYGENS

Moudens, A.[1], Cordier, D.[1,2], Mousis, O.[3], Lunine, J.I.[4] and Vuitton, V.[4,5]

Abstract. We reinvestigate a scenario initially proposed by Pinto et al. (1986) and Lunine et al. (1999), dealing with the photochemical enrichment of deuterium in the atmosphere of Titan, which is based on the possibility that the initial methane reservoir accessible to the atmosphere was larger than what is seen today, in light of the recent Cassini-Huygens measurements (Bézard et al. 2007). We show that this photochemical mechanism is not efficient enough in the atmosphere of Titan to explain its current D/H value, even if the current atmospheric reservoir of CH_4 is postulated to exist since 4.5 Gyr.

1 Photochemical model

We define R as the ratio of the total mass of CH_4 expelled from the interior of Titan and constituting the initial reservoir to the current atmospheric mass of CH_4. If photochemistry is the only source of methane destruction one can write

$$R = f^{\frac{1}{1-q}}, \tag{1.1}$$

with f the ratio of D/H observed in Titan's current atmospheric CH_4 to protosolar D/H. $q = k_2/k_1$, k_2 and k_1 being the respective rates for CH_3D and CH_4 destructions. Alternatively, R can be expressed as it follows:

$$R = \frac{m_{\mathrm{CH_4}}\, F\, \tau}{M_{\mathrm{CH_4}}}, \tag{1.2}$$

where $m_{\mathrm{CH_4}}$ is the mass of a CH_4 molecule, F the net photolytic destruction rate of CH_4, τ the time elapsed since the formation of the initial CH_4 reservoir up until now and $M_{\mathrm{CH_4}}$ is the cumulated mass of atmospheric CH_4 per unit of area, determined by using the Huygens probe data, namely the atmospheric density (HASI data) and CH_4 mole fraction profiles (GCMS data). The fractionation of deuterium in methane photochemistry is plotted in Fig. 1.

2 Results and conclusion

Figure 1 shows our calculations of the deuterium enrichment f. Assuming a protosolar D/H in the CH_4 initially released from the interior of Titan, it can be seen that the photolytic fractionation between CH_4 and CH_3D is never efficient enough to allow a sufficient increase of the atmospheric D/H to match the observed one, even on a 4.5 Gyr timescale. Thus, a higher D/H ratio than the protosolar value must be advocated in the CH_4 of Titan prior its outgassing from the crust. The needed initial enrichment f_0 ranges between 3.2 and 4.0 after 0.6 Gyr, and between 2.2 and 3.2 after 4.5 Gyr of the reservoir existence. Our results substantially differ from those obtained by Lunine et al. (1999) who showed that the deuterium enrichment via photolysis was almost

[1] Institut de Physique de Rennes, CNRS, UMR 6251, Université de Rennes 1, Campus de Beaulieu, 35042 Rennes, France
[2] Ecole Nationale Supérieure de Chimie de Rennes, Campus de Beaulieu, 35700 Rennes
[3] Université de Franche-Comté, Institut UTINAM, CNRS/INSU, UMR 6213, Observatoire des Sciences de l'Univers de Besanon, France
[4] Lunar and Planetary Laboratory, University of Arizona, Tucson, AZ, USA
[5] Université Joseph Fourier, Laboratoire de Planétologie de Grenoble, CNRS/INSU, France

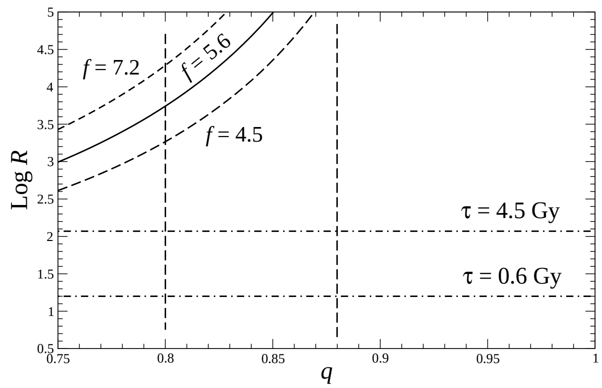

Fig. 1. The fractionation of deuterium in CH_4 photochemistry: plotted is R, namely the initial mass of the methane reservoir, normalized to the mass of the current reservoir (Eq.1). Three curves are shown, corresponding to different present-day deuterium enrichments measured in methane by Cassini/CIRS, with respect to the protosolar D/H abundance. The solid curve corresponds to the central value reported by Bézard et al. 2007 (D/H=$1.32^{+0.15}_{-0.11} \times 10^{-4}$) and the dashed curves are related to extreme values obtained with uncertainties. The D/H ratio in the methane initially acquired by Titan is assumed to be protosolar. The two horizontal lines represent values that would be acquired by R if τ of the actual methane reservoir reaches 0.6 or 4.5 Gyr (see Eq.2). The two vertical lines represent limits on plausible values of q. It can be seen that, whatever the considered value of τ, the reservoir of Titan's atmospheric methane is not initially massive enough to allow a substantial D/H photolytic enrichment that would match the observed values.

efficient enough to explain the current D/H value. Indeed, Lunine et al. (1999) assumed that the satellite was formed in a dense and warm Saturn's subnebula, and that the CH_4 incorporated in Titan was the result of the gas phase conversion of CO in the subnebula. In this scenario, a slight deuterium enhancement in CH_4 would have occurred in the subnebula gas phase, due to a fractionation effect at high temperature and prior the formation of ices and their trapping into proto-Titan. This slight oversolar D/H value in the CH_4 outgassing from the interior of Titan, combined with photolytic enrichment over 4.5 Gyr, would have sufficiently enriched the D/H in CH_4 to allow it to be consistent with the current atmospheric value. However, in the present work, by considering recent data on Titan's atmosphere acquired by Cassini-Huygens, we show that the minimum value required for f_0 is still higher than the one expected from the production of CH_4 in a warm and dense subnebula. We conclude that the isotopic fractionation in the atmosphere of Titan and the isotopic exchange in the Solar nebula are two complementary processes to explain the observed D/H value in methane. The relative importance of these two mechanisms dep ends on the epoch from which started the actual outgassing event.

References

Bézard, B., Nixon, C.A., Kleiner, I., & Jennings, D. E. 2007, Icarus, 191, 397

Fulchignoni, M., et al. 2005, Nature, 438, 785

Hörst, S. M., et al. 2008, Journal of Geophysical Research (Planets), in press

Lunine, J. I., Yung, Y. L., & Lorenz, R. D. 1999, Planet. Spa. Sci., 47, 1291

Mousis, O., Gautier, D., & Coustenis, A. 2002, Icarus, 159, 156

Niemann, H. B., et al. 2005, Nature, 438, 779

Pinto, J. P., Lunine, J.I., Sang-Joon Kim, & Yuk L. Yung 1986, Nature, 319, 388

Vuitton, V., Yelle, R. V., & Cui, J. 2008, Journal of Geophysical Research (Planets), 113, 5007

SF2A 2008
C. Charbonnel, F. Combes and R. Samadi (eds)

SEQUESTRATION OF ETHANE IN THE CRYOVOLCANIC SUBSURFACE OF TITAN

Mousis, O.[1] and Schmitt, B.[2]

Abstract. Saturn's largest satellite, Titan, has a thick atmosphere dominated by nitrogen and methane. The dense orange-brown smog hiding the satellite's surface is produced by photochemical reactions of methane, nitrogen and their dissociation products with solar ultraviolet, which lead primarily to the formation of ethane and heavier hydrocarbons. In the years prior to the exploration of Titan's surface by the *Cassini-Huygens* spacecraft, the production and condensation of ethane was expected to have formed a satellite-wide ocean one kilometer in depth, assuming that it was generated over the Solar system's lifetime. However, *Cassini-Huygens* observations failed to find any evidence of such an ocean. Here we describe the main cause of the ethane deficiency on Titan: cryovolcanic lavas regularly cover its surface, leading to the percolation of the liquid hydrocarbons through this porous material and its accumulation in subsurface layers built up during successive methane outgassing events. The liquid stored in the pores may, combined with the ice layers, form a stable ethane-rich clathrate reservoir, potentially isolated from the surface.

1 Introduction

Any discussion on the reservoirs of ethane condensate at the surface of Titan should take into account the recently revised condensation rate of 5.9×10^{-14} g cm^{-2} s^{-1} for this molecule, consistent with Cassini CIRS observations (Atreya et al. 2006). This lower ethane condensation rate implies a reduction of the depth of the initially expected satellite-wide ocean to a value of $\sim$155 m, if methane was continuously released over Titan's life. This value is even smaller if we consider Titan's recent thermal evolution models supporting the idea that the methane outgassing has occurred episodically (Tobie et al. 2006). If the actual atmospheric methane is outgassing at the current rate since only $\sim$0.6 gigayears (Gyr) (Tobie et al. 2006), the depth of the hypothetical global ethane ocean reaches no more than $\sim$20 m. Indirect evidence has been obtained for the presence of lakes at high latitudes in the northern hemisphere during several Cassini Radar flybys of Titan (Stofan et al. 2007; Lorenz et al. 2008). But with a likely current inventory of 3×10^4–3×10^5 km^3 of liquid (Lorenz et al. 2008), these lakes are not expected to store more than about 20% of the produced ethane. This value can even be lower if we consider alternative photochemical models which lead to the condensation of twice as much ethane and predict the presence of substantial amounts of liquid propane (Vuitton & Yelle 2005).

The apparent deficiency in liquid ethane on Titan has been interpreted as supporting the theory that ethane mostly condenses onto smog particles forming different types of thick deposits, including dunes and dark areas (Hunten 2006). However, the haze production rate is only 8 to 50% of the ethane value (Atreya et al. 2006). With all the liquid and solid condensates taken into account, the liquid-to-solid volume ratio ranges between 2.5 and 23. No granular material, even extremely microporous, can adsorb more than 30% of its volume in its pores at saturation. Any liquid above this value will wet the saturated haze, up to the point where the plastic and then the liquid limits of the material are reached. With liquid-to-solid volume ratios larger than 2.5, these limits are largely exceeded and the rheological properties of such wet material are incompatible with the stability of the observed dunes. In the most favorable case, the dunes and the wetter dark flat area could probably retain up to 20% of the total liquid inventory, but the remaining 80% should escape the haze deposits and migrate to other reservoirs.

An alternative interpretation is that a liquid ocean would fill the empty space of the upper crust consisting in a 10,000 m regolith layer generated by impacts during Titan's early history (Kossacki & Lorenz 1996). After

[1] Université de Franche-Comté, Institut UTINAM, CNRS/INSU, France; olivier.mousis@obs-besancon.fr
[2] Université Joseph Fourier, Laboratoire de Planétologie de Grenoble, CNRS/INSU, France; Bernard.Schmitt@obs.ujf-grenoble.fr

4.5 Gyr of Titan's evolution, the porosity of this layer would decrease to 1–4%, allowing the incorporation of a liquid ocean with an equivalent depth of ∼100–400 m (Kossacki & Lorenz 1996). However, these calculations do not consider the porosity closing off and the depth below which it becomes isolated from the surface. On Earth, the porosity close-off in pure water ice is ∼10% for Greenland's ice cap, but for the finer grain size of the regolith this value is probably even higher. The resulting amount of trapped liquid is then lower than predicted. Moreover, the *Cassini* Radar and optical images show that the satellite surface is geologically young (Elachi et al. 2005). Therefore, it is unlikely that large extents of the early regolith remain currently in contact with the atmosphere since the deposition of photochemical debris, pluvial erosion or deposition, tectonic processes or cryovolcanism may have contributed to their burial.

None of the aforementioned ethane trapping scenarios is fully supported by the *Cassini-Huygens* observations of Titan (Atreya et al. 2006; Elachi et al. 2005; Stofan et al. 2007). However, the detection of cryovolcanic features (Elachi et al. 2005; Lopes et al. 2007), together with the theoretical estimates of strong resurfacing rates (about 50 m of "cryolava" deposited per 10^6 yr; Elachi et al. 2005), lead us to propose a geological process that solves the ethane deficiency issue in a manner which is in agreement with our current knowledge of Titan: the incorporation of liquid hydrocarbons in the porous cryovolcanic subsurface. However, note that, at present, no extensive cryovolcanic deposits have yet been clearly identified on the surface of Titan but the presence of some distinct cryovolcanic features makes our scenario worth developing.

2 Cryovolcanism on Titan

We investigate the conditions of such incorporation by considering two different mechanisms of cryovolcanism and methane delivery:

Ascent of liquid from the subsurface ocean. The methane coming from the saturated deep ocean (Tobie et al. 2006; Fortes et al. 2007), is transported close to the surface of Titan in ammonia-water pockets which erupt through the ice shell and lead to cryovolcanism (Mitri et al. 2006). The release of dissolved methane creates gas-rich eruptions and very porous cryovolcanic materials since, even with only 1% of dissolved methane, the gas volume expelled largely exceeds that of the cryovolcanic ice.

Destabilization of clathrates in the ice shell of Titan. In this case, clathrates of methane stored in the close subsurface are destabilized by ascents of hot thermal plumes and melt (Tobie et al. 2006). The cryolava expelled to the surface of Titan releases the large amount of methane initially trapped in clathrates. A very porous ice is produced from this clathrate decomposition (Schmitt 1986).

In both cases, a highly porous icy material is generated, probably similar to basaltic lava flows. Since the cooling of the cryolava is expected to take less than one year to decrease down to Titan's surface temperature (Lorenz 1996), it should be fast enough to allow the preservation of most of the porosity created by the methane release.

3 Trapping of liquid hydrocarbons in the subsurface layers

The liquid composition formed on Titan's surface can be inferred if it is considered in thermodynamic equilibrium with the atmosphere and that the organic materials mixed with the fluid have only minor effects on this equilibrium. With a methane mole fraction of $\sim 4.9 \times 10^{-2}$ measured near the surface by *Huygens* (Niemann et al. 2005), the predicted mole fractions of methane, ethane and nitrogen are ∼0.35, ∼0.60 and ∼0.05 in the liquid, respectively (Dubouloz et al. 1989). We adopt these fractions as the nominal composition of the liquid currently present at and below the surface of Titan.

We now consider two different Titan evolution scenarios and estimate the equivalent depth of a global liquid layer condensed on its surface: over a 0.6 Gyr period of cryovolcanism (Tobie et al. 2006), and over the lifetime of the Solar system (4.55 Gyr). In the first case, the thickness of the liquid layer is ∼30 m, including 21, 8 and 1 m of ethane, methane and nitrogen, respectively. In the second case, the thickness increases to 225 m, with 155, 62 and 8 m of ethane, methane and nitrogen, respectively. If the upper layers of Titan's subsurface are mostly constituted by an homogeneous deposit of cryolavas with a mean porosity of 25%, icy crust thicknesses of only ∼120 and 900 m are required to bury these oceans for the two scenarios. Even if the porosity is 10%, ice crust thicknesses of only 300 and 2250 m deep, respectively, are required.

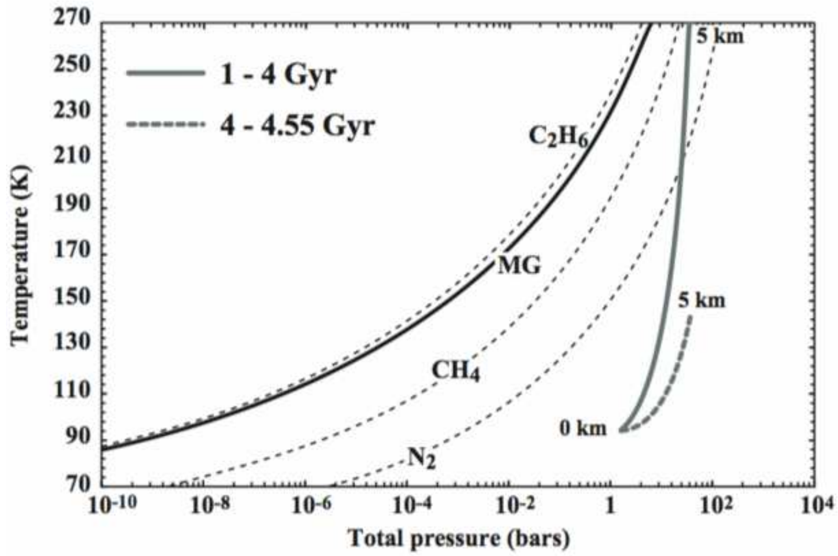

Fig. 1. From left to right: equilibrium pressures of C_2H_6, multiple guest (MG in the figure), CH_4 and N_2 clathrates as a function of temperature (black curves). The hydrostatic pressure within a column of CH_4-C_2H_6-N_2 liquid is also represented as a function of local temperature in the porous subsurface of Titan at two different periods of its thermal history. The first temperature profile (grey curve) corresponds to the 1–4 Gyr period of Titan's evolution. During this period, the upper water ice crust is conductive and its thickness does not exceed ~5 km. A linear temperature profile can then be constructed between an assumed temperature of ~94 K at the surface and ~270 K at the inner ice-ocean interface. The second temperature profile (dotted grey curve), which is valid at epochs later than 4 Gyr, postulates the existence of a ~50 km thick icy crust. In the outer conductive layer of the icy crust, about 15 km deep, the temperature varies linearly between ~94 K and ~250 K. In our calculation, we only consider the first 5 km of the icy crust since it can largely contain all the liquid hydrocarbons generated over Titan's life (see text).

Presuming that the liquid at a given depth is in thermal equilibrium with the ice surrounding the pores, we consider two different temperature profiles derived from Titan's interior models and covering its overall thermal history (Tobie et al. 2006). Assuming that the ice porosity remains open within the first 5 km of the icy shell, the two hydrostatic pressure-vs-temperature curves in a column of liquid are calculated and compared to the stability curves of clathrates in Fig. 1. The equilibrium pressure curve of the multiple guest clathrate (hereafter MG clathrate) is determined for the nominal liquid composition. The equilibrium pressure curves of methane, ethane and nitrogen single guest clathrates are determined by fitting the available laboratory data and their equations are of the form $\log P_{eq} = A/T + B$, where P_{eq} and T are the partial equilibrium pressure (bars) and the temperature (K) of the considered species, respectively. Table 1 shows the values of constants A and B from our fits to laboratory measurements. Equilibrium pressure curves for MG clathrate formed from the liquid mixture, can be expressed as (Hand et al. 2006):

$$P_{eq,MG} = \left[\sum_i \frac{y_i}{P_{eq,i}} \right]^{-1} \tag{3.1}$$

where y_i is the mole fraction of the component i in the fluid phase. Figure 1 displays the dissociation pressures of methane, ethane, nitrogen and MG clathrates as a function of temperature. At a given temperature, these clathrates are stable at pressures equal or higher than their equilibrium pressures. They are also more stable than the liquid with corresponding composition provided sufficient water ice is available. In both cases, the column of liquid is located within the thermodynamic stability domains of ethane, methane and MG clathrates. The methane-ethane-nitrogen liquid filling the pores of Titan's icy crust thus likely forms, at all depths, a MG clathrate with the available water ice.

4 Discussion

Although the hydrostatic stability of the liquid column is achieved at any depth for both types of temperature profiles when the column is filled up to the surface (hydrostatic pressure always larger than the equilibrium vapour pressure of the liquid), this is not the case for a shallow column of liquid accumulated at great depths, and thus at higher temperatures. For example, if the porosity close-off currently occurs at 3 km depth the vapour pressure at the bottom of the liquid column (123 K) is larger than 2 bars and requires at least 300 m of liquid to stabilize. For porosities of 10–25%, a minimum equivalent ocean depth of 30–75 m is necessary, larger than the total amount of liquid produced in the scenario of recent methane outgassing. In such cases the liquid may ascend the column under the vapor pressure and erupt. However the much colder upper crust layers will probably recondense the boosting gas before it reaches the surface. Clathrate formation provides a more efficient way to stabilize the stored methane-ethane-nitrogen mixture at great depth. Its formation also greatly reduces the equilibrium gas pressure and thus stabilizes the remaining liquid phase. With our current knowledge of clathrate formation, the amount of liquid trapped in the form of MG clathrate remains difficult to estimate. Indeed, the extent of clathrate formation from the liquid phase can be limited by the very slow (and poorly known) kinetics at these low temperatures and the availability of water ice to clathration around the pores. Finally, the formation process of clathrates strongly reduces the porosity of the crust. With a volume expansion of the clathrate structure of $\sim$20% compared to that of water ice, its formation in an ice layer with an initial porosity of 25% reduces this quantity to 10%, namely the close-off value observed in terrestrial ice caps. So clathrate formation may well induce its self isolation by closing the pore network that allowed the liquid hydrocarbons to percolate the ice down to these dept hs.

References

Atreya, S. K., Adams, E. Y., Niemann, H. B., Demick-Montelara, J. E., Owen, T. C., Fulchignoni, M., Ferri, F., & Wilson, E. H. 2006, PSS, 54, 1177

Dubouloz, N., Raulin, F., Lellouch, E., & Gautier, D. 1989, Icarus, 82, 81

Elachi, C., et al. 2005, Science, 308, 970

Fortes, A. D., Grindrod, P. M., Trickett, S. K., & Vočadlo, L. 2007, Icarus, 188, 139

Hand, D. P., Chyba, C. F., Carlson, R. W., & Cooper, J. F. 2006, Astrobiology, 6, 463

Hunten, D. M. 2006, nature, 443, 669

Kossacki, K. J., & Lorenz, R. D. 1996, PSS, 44, 1029

Lopes, R. M. C., et al. 2007, Icarus, 186, 395

Lorenz, R. D. 1996, PSS, 44, 1021

Lorenz, R. D., et al. 2008, GRL, in press.

Mitri, G., Showman, A. P., Lunine, J. I., & Lopes, R. 2006, 37th Annual Lunar and Planetary Science Conference, 37, 1994

Niemann, H. B., et al. 2005, nature, 438, 779

Schmitt, B. 1986, Ph.D. Thesis

Stofan, E. R., et al. 2007, nature, 445, 61

Tobie, G., Lunine, J. I., & Sotin, C. 2006, nature, 440, 61

Vuitton, V., & Yelle, R. V. 2005, Bulletin of the American Astronomical Society, 37, 734

SF2A 2008
C. Charbonnel, F. Combes and R. Samadi (eds)

MAPPING THE CLOUDS OF TITAN OVER 3.5 YEARS WITH VIMS/CASSINI: IMPLICATIONS FOR TITAN CLIMATOLOGY

Rodriguez, S.[1,2], Le Mouélic, S.[1,3], Rannou, P.[4,5], Sotin, C.[1,6], Tobie, G.[1,3], Barnes, J.W.[7], Griffith, C.A.[8], Hirtzig, M.[9], Pitman, K.M.[6], Brown, R.H.[8], Baines, K.H.[6], Buratti, B.J.[6], Clark, R.N.[10] and Nicholson, P.D.[11]

Abstract. The N_2-rich atmosphere of Saturns largest moon Titan contains a few percent of methane (CH_4) (Kuiper 1944) which dissociates to produce a plethora of organic compounds, the most abundant of which is ethane (C_2H_6) (Yung et al. 1984; Toublanc et al. 1995). Methane and ethane are involved in a cycle similar to the terrestrial hydrological cycle, including clouds, rain, surface or sub-surface liquids and evaporation (Flasar 1998; Tokano 2001; Rannou et al. 2006). Clouds are visible consequences of meteorological activity on Titan. The Cassini spacecraft, in orbit in the Saturnian system since July 2004, has provided an unprecedented view of Titans clouds. We present here the first comprehensive map of cloud events, detected from the Visual and Infrared Mapping Spectrometer onboard the Cassini spacecraft. We detect more than one hundred and fifty cloud events between July 2004 and December 2007. Three categories of clouds have been identified: 1) bursts of clouds at the south pole, 2) a long lived widespread cloud system at the north pole, and 3) transient temperate clouds centered around 40°S which may display longitudinal variations. These observations are consistent with control of the cloud spatial distribution dominated by the global atmospheric circulation, possibly combined with some geographic forcing (gravity waves imposed by Saturns tides and local surface sources of methane), mostly observable at temperate latitudes. Global circulation models (GCM) predict dramatic changes in the cloud activity as Titans equinox approaches (2009). Such long-term variations should be observed during the extension of the Cassini mission.

1 Introduction

Methane on Titan plays a role similar to that of water on Earth. Gaseous methane can condense in the form of liquids or solids at specific latitudes and altitudes and can occasionally precipitate onto the surface, feeding surface and sub-surface reservoirs of liquid methane. Because methane humidity remains low near the surface, liquid methane evaporates, thus maintaining this exotic, active meteorological cycle (Flasar 1998; Tokano 2001; Rannou et al. 2006). Ethane and other condensable byproducts are also thought to condense and form clouds, mostly in high latitudes regions during the winter season (Rannou et al. 2006; Griffith et al. 2006). Clouds on Titan were detected as early as 1995 through ground-based telescopic observations (Griffith et al. 1998) and have been regularly observed since. The regular flybys of Titan by the Cassini spacecraft provide a unique opportunity to track the cloud activity. The search for Titans clouds location and the monitoring of their

[1] Université de Nantes, Laboratoire de Planétologie et Géodynamique, Nantes, France
[2] Laboratoire AIM, Université Paris 7/CNRS/CEA-Saclay, DSM/IRFU/SAp, France
[3] CNRS, UMR-6112, Nantes, France
[4] Groupe de Spectrométrie Moléculaire et Atmosphérique, Université de Reims Champagne-Ardenne, France
[5] Service dAéronomie, Université Versailles-St-Quentin, France
[6] Jet Propulsion Laboratory, California Institute of Technology, Pasadena, CA, USA
[7] NASA Ames Research Center M/S 244-30, Moffett Field, CA
[8] Lunar and Planetary Lab and Steward Observatory, University of Arizona, Tucson, AZ, USA
[9] AOSS, PSL, University of Michigan, Ann Arbor, MI, USA
[10] USGS, Denver Federal Center, Denver, CO, USA
[11] Cornell University, Astronomy Department, Ithaca, NY, USA

long-term activity contribute to the global understanding of Titans climate and meteorological cycle, which are key questions to be addressed by the Cassini-Huygens mission.

Investigations from ground-based telescopes using adaptive optics facilities (allowing direct imaging) gathered the first statistical constraints on the location and lifetime of Titans clouds, revealing in particular the variability and periodicity of outbursts of the large South Polar clouds (Brown et al. 2002; Bouchez & Brown 2005; Schaller et al. 2006a, 2006b; Hirtzig et al. 2006). Ground-based observations also reported in 2004 the first detection of a temperate-latitude cloud system occurring at 40^oS (Roe et al. 2005a, 2005b). Since its insertion into Saturns orbit in July 2004, the Cassini mission has viewed Titans clouds in unprecedented detail with, on average, a monthly close flyby of Titan. The Cassini view widely complements the ground-based observations and provides new constraints on the seasonal evolution of Titans meteorology. Several southern and other discrete clouds were observed during the first flybys by using the Cassinis Imaging Science Subsystem (ISS) camera (Porco et al. 2005) and the Visual and Infrared Mapping Spectrometer (VIMS) (Griffith et al. 2005, 2006; Baines 2005). This latter instrument acquires hyperspectral images in 352 contiguous spectral channels between 0.3 and 5.2 μm (Brown et al. 2003), allowing the detection of clouds not only from their morphologies in simple imagery but also from their spectral behavior. Here, we present the first comprehensive mapping of Titans clouds detected in the full VIMS dataset between the Cassini insertion in July 2004 and December 2007 (i.e. during 39 Titans flybys).

2 Titan's clouds detection with VIMS: Methods and results

The atmosphere of Titan is opaque at infrared wavelengths, except for seven narrow spectral windows where methane absorption is the weakest (at λ = 0.93, 1.08, 1.27, 1.59, 2.03, 2.75 and 5 μm). Because clouds are efficient reflectors in the near-infrared and substantially reduce the path-length of solar photons in Titans atmosphere, their spectra present a broadening of all spectral windows with particularly broad and bright windows at 2.75 and 5 μm. We found that the most robust automated detection criterion to separate pixels that contain cloudy spectral component from any other components is to use the simultaneous widening of the 2.75 and 5 μm windows. Taking a single window or a combination of two other windows leads systematically to false positive detections. We produce, for each VIMS datacube, histogram distributions for the 2.75 and 5 μm windows areas. Two-sigma conservative thresholds on the two areas distributions are automatically calculated in order to only select these cloudy pixels. The reliability of the thresholds is controlled and finely tuned up with the help of reference images. Note that, if the deliberate choice of a conservative threshold allow us to avoid false positive and assure us that each detection is real, it can lead to the non-detection of optically thin or very low clouds, of clouds that are much smaller than a VIMS pixel, or clouds that are too close to the limb. This can also lead to the warping of the shape of some clouds, as the clouds edges are the most delicate part to detect.

Between July 2004 (flyby T0) and December 2007 (T38), VIMS acquired more than 10,000 images of Titan. By eliminating redundant, night side, limb viewing, very low time exposure and also very small images, we reduced the dataset down to 1,600 images useful for the purpose of cloud detection. This still represents several millions of spectra, which prohibits the effective use of a manual detection technique. We therefore developed a semi-automated algorithm to detect clouds in VIMS images, using mainly the simultaneous broadening of the 2.75-μm and 5-μm windows. Clouds show up at three distinct latitudes: the south polar region (poleward of 60^oS), the north polar region (poleward of 50^oN), and a narrow belt centered at 40^oS.

Our observations show that the southern pole wide cloud system faded at the beginning of 2005. Ten months later (October 2005), a cloud event appeared. This second outburst, (also reported by Schaller et al. (2006a)), lasts less than two months, significantly shorter than previous south pole events. A large cloud reappears again at the south pole nine months later in September 2006, and some clouds sporadically burst equatorward of 60^oS in continually smaller and more transient patches in October 2006, January 2007, and April 2007. June 2007 marks the reappearance of another huge, but very brief (less than one month), south pole cloud burst, almost exactly nine months after the last occurrence in September 2006. Thus, over three and a half years of VIMS observations, the south polar cloud appears quasi-periodically with a period of 8 to 9 months. However, these periodic bursts appear more erratic and less intense as Titan equinox approaches and the maximum solar illumination progressively shifts towards northern latitudes.

This study clearly shows the predicted stability of the north polar cloud (Griffith et al. 2006; Le Mouélic et al. 2008) as we have systematically detected it over the 2004-2007 period. We generally observe this extensive meteorological event poleward of 50-60^{o}N. All of these clouds are spectrally different from the southern clouds (presumably made of liquid/solid methane), because they show up in our detection algorithm with significantly less signal at 5 μm than any other cloudy features. This indicates lower backscattering at 5 μm and is consistent with clouds composed of micron sized particles made of solid ethane intimately mixed with aerosols, within the north polar haze cap (Rannou et al. 2006; Griffith et al. 2006).

We also detect numerous isolated and transient tropical clouds between 55^{o}S and 30^{o}S (more than one hundred). A few small clouds, whose areas never exceed 4000 km2 and therefore are undetectable in ground-based observations, are also observed closer to the equator (up to 15^{o}S). The density distribution in latitudes of all temperate clouds peaks at 40^{o}S latitude, within a narrow 25^o wide latitude band. Most of these clouds are elongated in the east-west direction, as it was previously observed (Roe et al. 2005a, 2005b; Griffith et al. 2005; Baines et al. 2005), due to strong zonal winds of tens of meter per second (Porco et al. 2005). They do not appear uniformly distributed around Titan, confirming with a better statistic previous ground-based observations (Roe et al. 2005b). Our longitudinal distribution peaks every 90^o at 30^{o}E, 120^{o}E, -150^{o}E and -60^{o}E, shifted 30^o towards the east from the sub-Saturn, trailing, anti-Saturn and leading points respectively. The peak in the direction of Saturn is two times larger than the others. The 90^o periodicity strongly suggests that the longitudinal distribution of tropical clouds may be connected to tidal forcing caused by the strong tides Titan experiences during its elliptic orbit around Saturn. The non-uniformity of the distribution may also partly be due to localized geological processes as suggested by Roe et al. (2005b). The temperate clouds appeared during two time periods, in 2004 and between August 2006 and August 2007. Except in October 2005 (Schaller et al. 2006b) and January 2006 (this work), we did not observe any temperate clouds for a long period between December 2004 and August 2006, perhaps due to the combination of less frequent Titans flybys by Cassini (one flyby every two months on average during this period against two per month on average after) and a momentary decline in cloud activity. The 40^{o}S clouds reappeared after this quiet phase until mid-2007 but their activity tended to progressively decrease during late 2007.

3 Comparison with the Global Circulation Model (GCM) from Rannou et al. (2006)

The cloud layer as monitored by VIMS shows that significant atmospheric changes occurred during the observing time period. Since clouds trace the atmospheric circulation, these changes give new insight into Titan's global wind pattern and its seasonal evolution, just before equinox. Most of the clouds reported here can be understood in the framework of the global atmospheric circulation triggered by seasonal solar insolation variations. Titan's global circulation in the troposphere and lower stratosphere is characterized by a Hadley-type cell with an ascending branch at mid-latitude (30-40^o) in the summer hemisphere, and two descending branches near $\pm 60^o$ (Tokano 2001; Rannou et al. 2006). Models also predict small slant cells near the poles, and especially the summer pole, triggered by the temperature contrast in the polar region (Rannou et al. 2006). In the upper stratosphere and the mesosphere, the circulation is dominated by a large thermally direct cell similar to the Brewer-Dobson circulation on Earth. Before the forthcoming northern spring equinox in 2009, this circulation has an ascending branch in the southern hemisphere and a descending branch in the north polar region. According to Titan's Global Circulation Model (GCM)(Rannou et al. 2006; Mitchell et al. 2006), ascending motions of methane-rich air in the troposphere result in the formation of methane clouds, owing to adiabatic cooling. Clouds are then predicted in the convergence zone of the troposphere circulation, at 40^o in the summer hemisphere, and near 12 km altitude, which represents an analog of the cloud belt in the inter-tropical convergence zone on Earth and on Mars. Clouds are also predicted very near the summer pole, in the troposphere, where methane, driven from warmer region, condenses and can generate convective structures (Rannou et al. 2006; Hueso & Sanchez-Lavega, 2006; Barth & Rafkin, 2007). The downwelling stratospheric circulation, in the northern (winter) region, drives an ethane and aerosol enriched stratospheric air into the cold tropopause of the polar night (above 40 km) which lead to the formation of clouds identified as ethane clouds (Griffith et al. 2006). The three classes of clouds reported in this work are observed at the latitudes predicted by the GCM. The observed stability of the north polar clouds is interpreted, with GCM, as the result of a constant incoming flux of ethane and aerosols from the stratosphere, producing a mist of ethane (and probably other products) droplets of few micrometers which slowly settles down. On the other hand, the summer hemisphere clouds timing predicted by GCM weakly reproduces our observations. The GCM (Rannou et al. 2006) and mesoscale models (Hueso & Sanchez-Lavega, 2006; Barth & Rafkin, 2007) show that summer hemisphere clouds produced by wet methane convection should be sporadic by nature (with lifetimes of several hours to few days due to sedimentation, rainfall and dissipation). This variability is readily observed in our data. Yet, predictions show that the southern cloud activity should progressively decrease as the equinox approaches, which is a consequence of a change in the south polar circulation pattern. Although the GCM prediction only gives a statistically averaged view of the cloud activity, this southern declining meteorological activity is not observable in our data. According to the GCM, the south polar clouds should have disappeared in mid-2005 and the mid-latitudes clouds should have progressively fade out since 2005. The global trend of the evolution of the southern clouds activity that we observe with VIMS is qualitatively different: the southern clouds are still observable even late in 2007 and are particularly active at 40^oS since mid-2007. This may indicate that methane is resupplied and clouds can form in Titans low atmosphere in a more efficient way than GCM can predict, especially at temperate latitudes, probably because GCM do not take into account of gravity waves and/or cryovolcanism. In late 2007, polar clouds occurrences seem to be less frequent in our data and the mid-latitude clouds are scarcer and tend to disappear. These slight declining trends in southern cloud activity may indicate that we are probably witnessing the forthcoming seasonal circulation turnover as we approach the equinox, but with a different timing pattern than forecasted by the GCM. The timing of cloudy events monitored by VIMS just before the circulation turnover strongly depends on the underlying atmospheric processes. This makes a new constraint for climate models to understand the details of cloud formation on Titan.

4 Perspectives

In the coming decade, we expect that the complete reversal in the general circulation of Titans atmosphere will be probed through the long-term joint monitoring by Cassini and ground-based facilities with observations of positions, altitudes and morphologies of Titans clouds. Furthermore, the cloud locations may give useful hints about the distribution of possible surface methane reservoirs. For instance, an asymmetry in the climatology of the cloud layer may explain the observed north/south asymmetry in the distribution of clouds, lakes and seas. In the near future, it will be of prime importance to carry on comparing close flyby observations, as those presented in this report, with ground-based data to avoid a misinterpretation about Titans cloud distribution. Relating space-based and Earth-based views, using the longest time interval possible, is compulsory to prepare for the development and interpretation of Titan post-Cassini nominal mission observations.

References

Baines, K.H., et al. 2005, EM&P 96, 119.
Barth, E.L., & Rafkin, S.C.R. 2007, GRL 34, L03203.
Bouchez, A.H., & Brown, M.E. 2005, ApJ 618, L53.
Brown, M.E., Bouchez, A.H., & Griffith, C.A. 2002, Nature 420, 795.
Brown, R.H., et al. 2003, Icarus 164, 461.
Flasar, F.M. 1998, P&SS 46, 1109.
Griffith, C.A., Owen, T., Miller, G.A., & Geballe, T. 1998, Nature 395, 575.
Griffith, C.A., et al. 2005, Science 310, 474.
Griffith, C.A., et al. 2006, Science 313, 1620.
Hirtzig, M., et al. 2006, A&A 456, 761.
Hueso, R., & Sanchez-Lavega, A. 2006, Nature 442, 428.
Kuiper, G.P. 1944, ApJ 100, 329.
Le Mouélic, S., et al. 2008, 39th Lunar and Planetary Science Conference, LPI Contribution No. 1391, 1649.
Mitchell, J.L., Pierrehumbert, R.T., Frierson, D.M..W., & Caballero, R. 2006, PNAS 103, 18421.
Porco, C.C., et al. 2005, Nature 434, 159.
Rannou, P., Montmessin, F., Hourdin, F., & Lebonnois, S. 2006, Science 311, 201.
Roe, H.G., Bouchez, A.H., Trujillo, C.A., Schaller, E.L., & Brown, M.E. 2005a, ApJ 618, L49.
Roe, H.G., Brown, M.E., Schaller, E.L., Bouchez, A.H., & Trujillo, C.A. 2005b, Science 310, 477.
Schaller, E.L., Brown, M.E., Roe, H.G., & Bouchez, A.H. 2006a, Icarus 182, 224.
Schaller, E.L., Brown, M.E., Roe, H.G., Bouchez, A.H., & Trujillo, C.A. 2006b, Icarus 184, 517.
Tokano, T. 2001, Icarus 153, 130.
Toublanc, D., et al. 1995, Icarus 113, 2.
Yung, Y.L., Allen, M., & Pinto, J.P. 1984, Astrophys. J. Suppl. 55, 465.

SF2A 2008
C. Charbonnel, F. Combes and R. Samadi (eds)

DO CLATHRATE HYDRATES HAVE ANY INFLUENCE ON THE ATMOSPHERE OF MARS?

Thomas, C.[1], Picaud, S.[1], Mousis, O.[1] and Ballenegger, V.[1]

Abstract. Recent observations have evidenced traces of methane heterogeneously distributed in the Martian atmosphere (Krasnopolsky et al. 2004). However, because the lifetime of CH_4 in the atmosphere of Mars is estimated to be around 250-430 years on the basis of gas-phase chemistry (Krasnopolsky et al. 2004), its actual sources on Mars remain controversial. Among other assumptions, it has been proposed (Chastain & Chevrier 2007) that clathrate hydrates located in the subsurface of Mars could be at the origin of the small quantities of CH_4 detected. In the present work, we have calculated the relative abundance of CH_4 in clathrate hydrates on Mars, using a statistical model based on the theory of van der Waals and Platteeuw (1959). The results show that methane enriched clathrate hydrates could be stable in the subsurface of Mars only if a primitive methane-rich atmosphere has existed or if a subsurface source of CH_4 has been (or is still) present.

1 Introduction

Recently, a small quantity of methane ($\sim$ 10 ppbv) has been detected in the atmosphere of Mars by the Planetary Fourier Spectrometer (PFS) onboard the *Mars Express* spacecraft (Formisano et al. 2004). The photochemical mean lifetime of the martian atmospheric methane is $\sim$ 300-600 years (Krasnopolsky et al. 2004; Formisano et al. 2004), and so it should not still exist today. To explain its presence, several scenarios have been invoked, like the release of methane from a subsurface reservoir, or the existence of an active biological (organisms living in the near subsurface of the planet; Formisano et al. 2004; Krasnopolsky et al. 2004; Krasnopolsky 2006) or geological (e.g. olivine hydratation in the martian regolith or crust; Oze & Sharma 2005) primary source of methane. The martian atmospheric methane could also come from the decomposition of possible methane clathrate hydrates in the near-subsurface (Prieto-Ballesteros et al. 2006; Chastain & Chevrier 2007). Indeed, because they can trap methane over large timescales, clathrate hydrates could be a secondary reservoir, filled either by ancient or by current methane sources (Prieto-Ballesteros et al. 2006; Chastain & Chevrier 2007).

Such a mechanism has recently been studied by Chastain & Chevrier (2007) with the program CSMHYD developed by Sloan (1998), and for a model of an atmosphere containing only CO_2 and CH_4. We reinvestigate here this work, by using a statistical thermodynamic model based on experimental data and on the original work of van der Waals & Platteeuw (1959). This model enables calculations at lower temperatures than the CSMHYD, and for an initial gas phase containing more species. It is thus possible to study the composition of clathrate hydrates formed from the martian atmosphere, at temperatures even as lower as the extreme ones measured in the polar caps ($\sim$ 130 K; Kieffer et al. 2001)

2 Model

To carry out this study, we have used the same approach as in our previous studies devoted to the trapping of noble gases by clathrate hydrates on Titan (Thomas et al. 2007, 2008), based on the statistical model proposed by van der Waals & Platteeuw (1959). In such an approach the relative abundance f_K of a guest species K in a clathrate hydrate (of structure I or II) is defined as the ratio of the average number of guest molecules of species K in the clathrate hydrate over the average total number of incorporated molecules, as :

[1] Institut UTINAM, CNRS/INSU, UMR 6213, 25030 Besançon Cedex, France

$$f_K = \frac{b_L y_{K,L} + b_S y_{K,S}}{b_L \sum_J y_{J,L} + b_S \sum_J y_{J,S}}, \tag{2.1}$$

where the sums in the denominator run over all species present in the system, and b_S and b_L are the number of small and large cages per unit cell, respectively. This statistical approach relies on the representation of the interactions between the guest species K and the water molecules forming the surrounding cage by a spherically averaged Kihara potential. As a consequence, the calculations of the relative abundances of a guest species trapped in clathrate hydrate strongly depend on the accurate determination of the interaction parameters.

In this study, we have used the set of parameters for the Kihara potential determined by Parrish & Prausnitz (1972) from experimentally measured clathrate hydrate properties. Unfortunately this set does not provide the complete list of Kihara parameters required by the molecules studied in our system. As a consequence, for the CO molecule, we have used the parameters given by Diaz Peña et al. (1982). The parameters used in this study are given in Table 1.

Table 1. Kihara parameters used in the present study. σ is the Lennard-Jones diameter, ϵ is the depth of the potential well, and a is the radius of the impenetrable core. These parameters derive from $^{(a)}$ Parrish & Prausnitz (1972), $^{(b)}$ Jager (2001), $^{(c)}$ Diaz Peña et al. (1982).

Molecule	σ(Å)	ϵ/k_B(K)	a(Å)
$CH_4^{(a)}$	3.2398	153.17	0.300
$O_2^{(a)}$	2.7673	166.37	0.360
$CO^{(c)}$	3.101	134.95	0.284
$N_2^{(a)}$	3.2199	127.95	0.350
$CO_2^{(a)}$	2.9681	169.09	$0.6805^{(b)}$
$Xe^{(a)}$	3.1906	201.34	0.280
$Ar^{(a)}$	2.9434	170.50	0.184
$Kr^{(a)}$	2.9739	198.34	0.230

3 Results

This model has been used to calculate the composition of clathrate hydrates formed in the near subsurface of Mars as a function of the temperature and of the gas phase composition, from a martian atmosphere containing CO_2, N_2, O_2, CO, Kr, Xe and Ar[1], together with CH_4. Three different initial gas phase abundances of CH_4 have been studied. In each case, the ratios between CO_2, N_2, O_2, CO, Kr, Xe and Ar are taken equal to those measured in the present martian atmosphere, and the sum of all initial gas phase abundances is equal to 1. The largest value of CH_4 initial gas phase abundance (50%) is typical of methane-rich conditions in which CH_4 is supplied from below by microbial or geological processes or from above from ancient atmospheres. In contrast, the lowest values (0.01% and 1%) are more typical of recent atmospheric compositions.

The figure 1 shows the evolution with temperature of the relative abundances f_K in clathrate hydrates of all the species initially present, and for the three different abundances of CH_4 considered. For each case, the relative abundances of Ar, N_2, O_2, CO, Kr and CH_4 slightly increase with the formation temperature, whereas that of CO_2 and Xe slightly decrease, irrespective of the initial gas phase abundances. However, the trapping of Ar, N_2, O_2, CO, Kr and Xe is always weak, whereas the incorporation of CH_4 and CO_2 in clathrate hydrates strongly depends on their initial gas phase abundances. Indeed, Figs. 1.a and 1.b show that CH_4 is poorly trapped when its initial gas phase abundance is lower than a few percent, whereas in such a situation, CO_2 fills almost entirely the clathrate hydrates. On the contrary, considering a methane-rich initial gas phase leads to a strong competition between the trapping of CO_2 and that of CH_4 (Fig. 1.c).

To show the trapping efficiency, we have calculated the ratio between the relative abundance f_K of a given gas in the multiple guest clathrate hydrate and its initial gas phase abundance x_K (Thomas et al. 2007, 2008).

[1] The present martian atmosphere contains 95% of CO_2, 2.7% of N_2, 0.13% of O_2, 0.07% of CO, 2.10^{-5}% of Kr, 8.10^{-6}% of Xe and 1.6% of Ar (Moroz 1998).

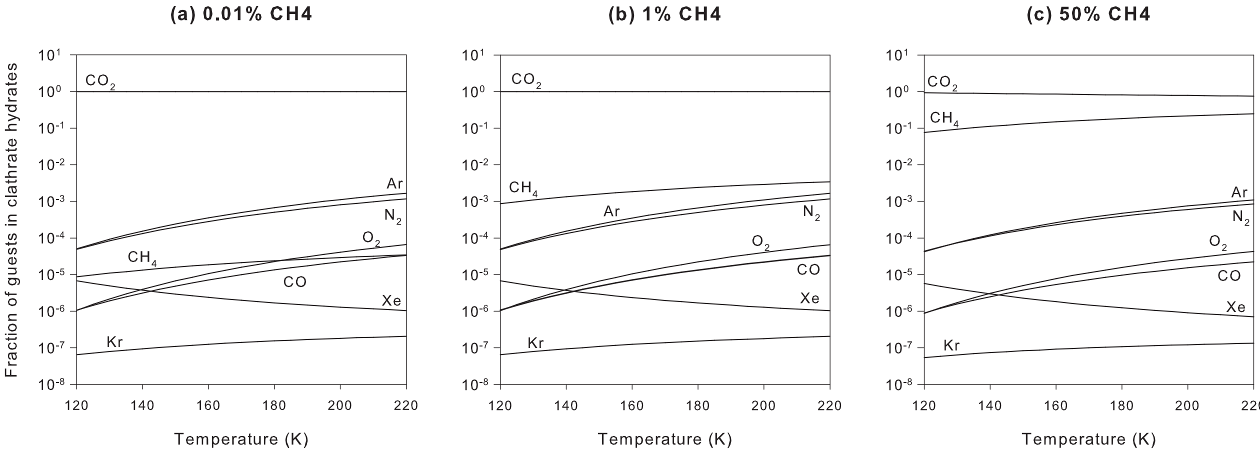

Fig. 1. Relative abundances of CH_4, CO_2, CO, O_2, N_2, Ar, Kr and Xe in clathrate hydrates as a function of temperature for the different methane abundances considered in the present work.

These abundance ratios have been calculated at the particular point on the dissociation curves corresponding to the present average atmospheric pressure on Mars, i.e. $P = 7$ mbar, and they are given in Table 2 together with the x_K and f_K values.

Table 2. Relative abundances of CH_4, CO_2, CO, O_2, N_2, Ar, Kr and Xe in the initial gas phase (x_G) and in clathrates (f_G), and abundance ratios. These ratios are calculated at $P = 7$ mbar, and at the corresponding temperature on the dissociation curves.

gaz	x_G	f_G	abundance ratio	gaz	x_G	f_G	abundance ratio
CH_4	1×10^{-4}	1.66×10^{-5}	0.166	Ar	1.61×10^{-2}	2.71×10^{-4}	1.68×10^{-2}
	0.1	1.77×10^{-2}	0.177		1.50×10^{-2}	2.62×10^{-4}	1.75×10^{-2}
	0.5	0.127	0.254		0.81×10^{-2}	1.69×10^{-4}	2.11×10^{-2}
CO_2	0.957	0.999	1.046	N_2	2.72×10^{-2}	2.20×10^{-4}	0.81×10^{-2}
	0.861	0.982	1.143		2.40×10^{-2}	2.05×10^{-4}	0.85×10^{-2}
	0.478	0.873	1.829		1.36×10^{-2}	1.54×10^{-4}	1.13×10^{-2}
Xe	8.04×10^{-8}	2.75×10^{-6}	34.27	CO	7.03×10^{-4}	5.45×10^{-6}	0.77×10^{-2}
	7.24×10^{-8}	2.71×10^{-6}	37.51		6.33×10^{-4}	5.11×10^{-6}	0.81×10^{-2}
	4.02×10^{-8}	2.42×10^{-6}	60.20		3.52×10^{-4}	3.48×10^{-6}	0.99×10^{-2}
Kr	2.01×10^{-7}	1.14×10^{-7}	0.568	O_2	1.31×10^{-3}	7.71×10^{-6}	0.59×10^{-2}
	1.81×10^{-7}	1.09×10^{-7}	0.603		1.18×10^{-3}	7.17×10^{-6}	0.61×10^{-2}
	1.01×10^{-7}	8.14×10^{-8}	0.810		0.65×10^{-3}	4.60×10^{-6}	0.70×10^{-2}

Table 2 shows that in such conditions, the abundance ratio of CH_4 increases with its initial gas phase abundance, but it remains lower than 1 in all situations, indicating that the trapping efficiency of CH_4 in the multiple guest clathrate hydrates considered here is quite low. On the contrary, with an abundance ratio always larger than 1, CO_2 is trapped in clathrate hydrates with a high efficiency. Thus, although the trapping of CH_4 becomes more and more efficient when its initial gas phase abundance increases, it remains much less efficient than the trapping of CO_2. Note that Table 2 also shows that the trapping of Xe (and in a lesser extent that of Kr) by clathrate hydrates is very efficient. However, Xe, Kr, Ar, CO, N_2 and O_2 have abundances almost negligible in the multiple guest clathrate hydrates considered in the present study.

4 Conclusion

Our calculations show that CO_2 and, in a lesser extent CH_4, are strongly trapped in the multiple guest clathrate hydrates considered here, even when additional gases such as Ar, Kr, Xe, CO, O_2 and N_2 are present in the initial gas phase. Indeed, these latter gases do not influence the composition of the corresponding clathrate hydrate, although some of them are strongly trapped (Xe and Kr).

Although we have considered an initial gas phase containing more species than the one studied by Chastain & Chevrier (2007), our results are mostly similar to those they obtained, that is in presence of CO_2, a methane-rich clathrate hydrate can be thermodynamically stable only if the gas phase is itself strongly enriched in CH_4.

As a consequence, if methane-rich clathrate hydrates exist on Mars, they cannot have been formed from the present martian atmosphere (poor in methane; Mumma et al. 2003; Formisano et al. 2004; Krasnopolsky et al. 2004; Geminale et al. 2008), but only from an early martian atmosphere, richer in CH_4 than the present one.

References

Chastain, B. K., & Chevrier, V. 2007, Planet. Space Sci., 55, 1246

Diaz Peña, M., Pando, C., & Renuncio, J. A. R. 1982, J.Chem.Phys., 76, 325

Formisano, V., Atreya, S., Encrenaz, T., Ignatiev, N., & Giuranna, M. 2004, Science, 306, 1758

Geminale, A., Formisano, V., & Giuranna, M. 2008, Planet. Space Sci., 56, 1194

Jager, M. 2001, Ph.D. Thesis.

Kang, S. P., Lee, H., Lee, C. S., & Sung, W. M. 2001, Fluid Phase Equilibria, 185 (1-2), 101

Kieffer, H. H., & Titus, T. N. 2001, Icarus, 154, 162

Krasnopolsky, V. A., Maillard, J. P., & Owen, T. C. 2004, Icarus, 172, 537

Krasnopolsky, V. A. 2006, Icarus, 180, 359

Mumma, M. J., Novak, R. E., DiSanti, M. A., & Bonev, B. P. 2003, Bulletin of the American Astronomical Society, 35, 937

Oze, C., & Sharma, M. 2005, Geophysical Research Letters, 32, 10203

Parrish, W. R., & Prausnitz, J. M. 1972, Industrial and Engineering Chemistry: Process Design and Development, 11 (1), 26. Erratum : Parrish, W. R., & Prausnitz, J. M. 1972, Industrial and Engineering Chemistry: Process Design and Development, 11 (3), 462

Prieto-Ballesteros, O., Kargel, J. S., Farén, A. G., Fernández-Remolar, D. C., Dohm J. N., & Amils, R. 2006, Geology, 34, 149

Sloan, E. D., Jr. 1998, Clathrate hydrates of natural gases, ed . M. Dekker (New York)

Thomas, C., Mousis, O., Ballenegger, V., & Picaud, S. 2007, A&A, 474, L17

Thomas, C., Picaud, S., Mousis, O., & Ballenegger, V. 2008, Planet. Space Sci., in press.

van der Waals, J. H., & Platteeuw, J. C. 1959, Adv. Chem. Phys., 2, 1

PNPS

Stellar Physics

SF2A 2008
C. Charbonnel, F. Combes and R. Samadi (eds)

DIGIT, GASPS, DEBRIS AND DUNES: FOUR HERSCHEL OPEN TIME KEY PROGRAMS TO SURVEY THE DUST CYCLE IN CIRCUMSTELLAR DISKS

Augereau, J.-C.[1], Absil, O.[1], Bouvier, J.[1], Duchêne, G.[1,2], Lestrade, J.-F.[3], Maret, S.[1], Martin-Zaïdi, C.[1], Ménard, F.[1], Morbidelli, A.[4], Olofsson, J.[1], Pantin, E.[5], Pinte, C.[6] and Thébault, P.[7]

Abstract. Four accepted Herschel open time key programs, DIGIT, GASPS, DEBRIS and DUNES, will study the evolution of the dust grains in circumstellar disks around young and Main Sequence stars. There is a strong implication of the french community in these four projects which represent a total of 930 hours (>38 days) of Herschel observing time. The DIGIT and GASPS projects will focus on the first stages of planet formation, while the DEBRIS and DUNES projects will search for extra-solar Kuiper Belt analogs around nearby Main Sequence stars. In this paper, we give an overview of the scientific goals of the four projects and of the numerical tools that we will be providing to the teams to model and interpret the Herschel observations from these programs.

1 Introduction

Early 2009, the ESA far-infrared and sub-millimeter space observatory, Herschel, will be launched from the Guiana Space Centre, Kourou (French Guiana), using an Ariane 5 ECA shared with the Planck satellite. With a 3.5 m effective telescope diameter, Herschel will be the largest mirror ever built for a space telescope until the JWST flies. It will be placed on a Lissajous orbit about the second Lagrange point of the Earth-Sun system (L2). Out of the three instruments onboard Herschel, PACS and SPIRE will be of particular interest for the study of the cold circumstellar material about young and Main Sequence stars.

PACS offers imaging photometry at 70, 100 and 160 μm, and 5×5 pixels ($47''\times47''$) integral field spectroscopy with a resolution of a few thousands between 55 and 210 μm. It offers major advances over previous instruments, in particular its higher sensitivity will provide well-characterized SEDs of faint objects, allowing for instance detection of lines a factor of $\sim$100 fainter than possible with ISO/LWS and enabling searches for weak solid-state emission features and a higher spectral resolution (R = 1500 –3000 vs. 200 for ISO/LWS). The much higher spatial resolution (9.4$''$ PACS pixel vs. about 80$''$ LWS beam) will furthermore significantly reduce background confusion compared to previous space missions. The SPIRE instrument will offer photometry in 3 channels (240, 350, and 500 μm, simultaneously), and a spectroscopy mode for wavelengths between 194 and 672 μm and with resolutions ranging (at 250 μm) between a few tens to a thousand.

Out of the 62 Open Time Key Program (hereafter OTKP) proposals that were submitted late Octobre 2007, 21 have been (partly) approved, with 10 belonging to the ISM/Star Formation category. These 10 programs include the GASPS, DIGIT, DUNES and DEBRIS projects discussed in this paper. The GASPS and DIGIT OTKPs will essentially focus on the evolution and dissipation processes of gaseous disks during the planet forming period, while DEBRIS and DUNES will perform systematic surveys of nearby Main Sequence stars to search for extra-solar analogs to our Kuiper belt.

[1] Laboratoire d'Astrophysique de Grenoble, LAOG, BP 53 Grenoble Cedex 9, France
[2] Department of Astronomy, 601 Campbell Hall, University of California Berkeley, Berkeley, CA 94720-3411, USA
[3] LERMA/CNRS, Observatoire de Paris, 77 Av. Denfert Rochereau, 75014 Paris, France
[4] Observatoire de la Côte d'Azur, Boulevard de l'Observatoire, B.P. 4229, 06304 Nice Cedex 4, France
[5] CEA, Irfu, Service dAstrophysique, Centre de Saclay, 91191 Gif-sur-Yvette, France.
[6] School of Physics, University of Exeter, Stocker Road, Exeter EX4 4QL, United Kingdom
[7] Stockholm Observatory, Albanova Universitetcentrum, SE-10691 Stockholm, Sweden

2 Planet-forming disks: GASPS and DIGIT

With a total of 400 h, the GASPS (Gas in Protoplanetary Systems) project is the largest of the OTKP accepted in the ISM/Star formation category. The GASPS team is lead by B. Dent in Edinburgh (UK) and consists of 38 CoIs (`http://www.laeff.inta.es/projects/herschel/index.php`). GASPS will perform an unbiased PACS survey of atomic and molecular gas and dust in more than 250 disks covering a wide range of ages (1–30 Myr), disks masses ($10^{-2}M_\odot$–$10^{-5}M_\odot$), and stellar types (A to M). The majority of the targets lie in 6 of the closest ($<$ 160 pc) young stellar clusters with well defined ages: Taurus, Upper Sco, TW Hya, Tuc Hor, Beta Pic and Eta Cha. The primary goal of GASPS, as the project name states, is a gas census using the far-infrared fine structure lines of carbon and oxygen as probes of atomic gas, together with water lines to probe the molecular gas. But GASPS will also spend a small fraction (5%, 20h) of the observing time on 70 and 170 μm photometry, to define the SED in the same wavelength range as the line data. Together these data will provide a broad picture of disks as they transition from molecular, through atomic, to mainly dusty composition.

The french astronomers involved in GASPS will primarily contribute to analysis and modeling of the observations of the dusty component of the disks, using the radiative transfer code developed at LAOG by Pinte et al. (2006). We will search for the signatures of the dust structure (such as dust settling) which are most obvious (break in the SED slope, change in absolute flux) and can be probed with appropriate color-magnitude and color-color diagrams. Combined with literature data and ancillary observations (accepted IRAM, CARMA, AKARI, SMA, APEX programs for instance), the modeling of the spectral energy distribution will provide a parametrization of the global disk structure and a self-consistently calculated temperature profile through out the disk that will serve as inputs to the chemistry models available to the team. SED fitting of individual objects is gonna be performed by generating large grids of models using the new cluster funded by the ANR project "Dusty Disks" (PI. F. Ménard).

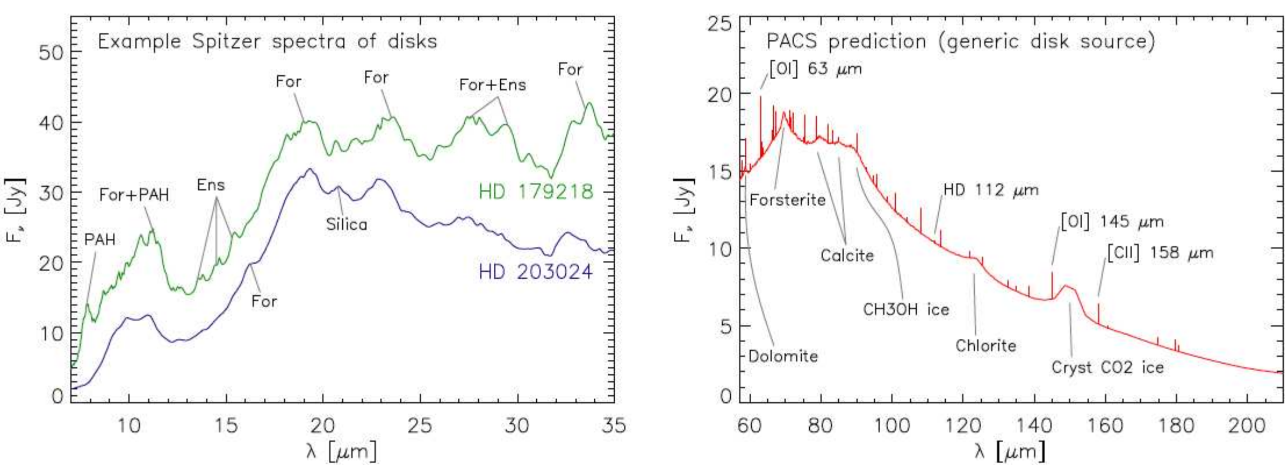

Fig. 1. *Left*: Spitzer spectra (arbitrary units) of two Herbig Ae star sources showing the richness in solid-state features. "For" stands for crystalline forsterite and "Ens" for crystalline enstatite. *Right*: Model spectrum (courtesy of K. Dullemond) of a disk around a Herbig Ae star of $L_* = 30L_\odot$ at a distance of 120 parsec. The dust of the model disk consists of 15% ice (mixture of H_2O , CO_2 and CH_3OH), 10% crystalline forsterite, 0.5% dolomite, 0.5% calcite, 20% chlorite, and the rest amorphous olivine. This composition is illustrative, and does not represent the complete inventory of dust/ice species that Herschel can discover. Most of the gas lines are H_2O, but their overall normalization is arbitrary, so as to show their position and typical relative strengths. The other gas lines (annotated) are mockup lines shown at a strength consistent with the range of predictions.

The DIGIT OTKP (250 h, P.I. Neal Evans, Texas, `http://peggysue.as.utexas.edu/DIGIT/`, 27 CoIs) aims at following the evolution of dust, ice and gas in time from objects embedded in cloud cores through the dissipation of disks. The main tool will be PACS spectral observations of a sample selected to probe the full evolutionary sequence and span a wide range of masses, luminosities, and other variables like environment. PACS offers imaging photometry (dust), broad spectral scans from 57 to 210 μm (dust, ice, strong gas lines), and targeted spectral scans (weak gas lines) well-suited to the goals of DIGIT.

The DIGIT sample is drawn from previous studies, particularly those for which high-quality Spitzer-IRS

Table 1. Targets for the DUNES (140 h) and DEBRIS (140 h) OTKPs

Spectral Class	Observed by DUNES	Observed by DEBRIS	DEBRIS targets shared with DUNES	DUNES targets shared with DEBRIS
M	0	89	8	0
K	54	57	9	35
G	52	48	25	41
F	27	71	50	22
A	0	83	14	0
Total	133	348	106	98

5–40μm spectra exist and show solid-state features than can be ascribed to amorphous and crystalline silicates. A key component of the DIGIT observing program will be full high-S/N spectral scans from 57 to 210 μm of about 23 disk sources with strong continuum. For 12 weaker disk sources, we focus on specific spectroscopic features (e.g. forsterite 69 μm feature), and for 30 of the most evolved disks, we will obtain sensitive searches for residual dust and gas. For the brighest sources, the far-infrared features to be observed will provide critical information on the thermal and mixing history, aqueous content and processing, and elemental composition of the cooler dust at larger disk radii. DIGIT will search for hydrosilicates (e.g. Montmorillonite, Serpentine) and carbonates (e.g. Calcite, Dolomite) that may have formed by aqueous alteration and expected to appear in the most evolved disks. This study represents an extension of the analysis of Spitzer spectra for a hundred of disks around young stars performed by Olofsson et al. (these proceedings) in Grenoble.

3 Exo-Kuiper belts: DUNES and DEBRIS

The DUNES (DUst around NEarby Stars, PI Carlos Eiroa, Spain, 40 CoIs, `www.mpia-hd.mpg.de/DUNES/`) and DEBRIS (Disc Emission via Bias-free Reconnaissance in the Infrared/Sub-millimeter, PI Brenda Matthews, Canada, 27 CoIs) OTKPs are aimed at performing sensitivity-limited (DUNES) or flux-limited (DEBRIS) surveys of faint exo-solar analogues to the Edgeworth-Kuiper Belt (EKB) in statistical samples of nearby stars. These so-called debris disks, which contain much less dust mass than young disks (typically 10^{-3}–$10^{-1} M_\oplus$), survive over billions of years, pointing towards the presence of large reservoirs of colliding asteroid- and evaporating comet-like bodies. Therefore, dust in debris disks is intimately connected to its parent bodies, invisible left-over planetesimals. Observing the dust emission is a powerful way to shed light onto their spatial and size distributions, properties and composition, and ultimately, their accretion history. Furthermore, dust sensitively responds to the gravity of planetary perturbers and thus can be used as a tracer of planets.

DUNES and DEBRIS have very similar objectives and were therefore awarded the same number of hours (140 h for each program) by the time allocation committee. The two teams were requested to coordinate their observing effort since a significant fraction of the targets in the original lists overlapped. The division of common targets has been based on the PACS/100 sensitivity. DEBRIS adopts a flux-limited approach, while DUNES requires the stellar photosphere to be at least detected with a Signal-to-Noise ratio larger than 3 at 100 μm. This fundamental difference in observing strategy directly translates into differences in numbers of targets for each program as the DUNES approach is more observing time-consuming (see Table 1). DUNES will finally observe 133 FGK-type nearby Main Sequence stars and this sample includes known planet-hosting stars (20 as of July 2008) while DEBRIS will observe 348 stars including A and M-type stars, with some shared between the two teams as indicated in the last two columns of Tab. 1. Both the DUNES and DEBRIS surveys are driven by PACS 100/160 observations as the main tool to detect cold dust, with SPIRE photometry used for follow-up (42 targets for DUNES, 100 for DEBRIS). DUNES will in addition observe 49 targets with PACS 70/160 to get some redundancy with existing Spitzer MIPS 70 μm observations and to improve the 160 μm sensitivity.

The PACS and SPIRE observations, combined with ancillary data, will be interpreted using state-of-the-art models developed within the teams to infer the individual properties of the dust disks (mass, temperature, distance, grain size distribution), and to statistically discuss the incidence and evolution of planetesimal belts too faint to be detected from the ground, and too cold to be detected with previous space missions, including with Spitzer. The detected systems will be compared to our own EKB to evaluate whether the solar system is peculiar or rather common. For some of the targets, the observing time has been tailored to able the detection of exo-EKBs as faint as a few times our own EKB which as fractional bolometric luminosity of about 10^{-7} (see Figure 2). Furthermore, since truncated cold disks may be a strong indication of interior planets, resembling the roles played by Neptune and Jupiter in the solar system, they would constitute the best candidates for probing the presence of long-orbital period exo-planets in the solar neighbourhood.

The french CoIs are deeply involved in the modeling aspects of the two programs, providing radiative transfer tools (e.g. Augereau et al. 1999, Pinte et al. 2006) as well as expertise on dynamical modeling of planetary systems (e.g. Morbidelli et al. 2008, Reche et al. 2008). The DUNES modeling effort will in fact be lead by the LAOG CoIs. We will also provide complementary ground-based (sub-)millimeter observations (e.g. survey of disks about M-type stars by Lestrade et al. 2007) as well as near-IR interferometric observations to search for hot exo-zodiacal dust in regions not probed by HERSCHEL (e.g. Absil et al. 2008).

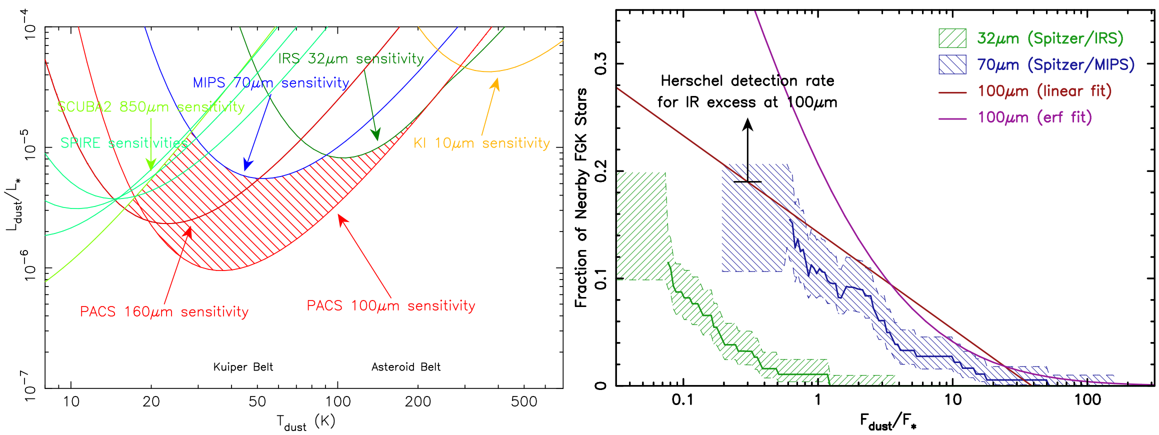

Fig. 2. *Left panel*: Detection limits for a G5V star at 20 pc, following the Bryden et al. (2006) approach. The assumed $1\,\sigma$ fractional flux accuracies are 20% for Spitzer/MIPS at $70\,\mu$m, 2.5% for Spitzer/IRS at $32\,\mu$m, 10% for PACS $100\,\mu$m (i.e. SNR=10), and 100% for PACS $160\,\mu$m (SNR=1). *Right panel*: Spitzer detection rates of IR excess as a function of the fractional monochromatic dust flux, $F_{\rm dust}/F_{*}$. For Spitzer/MIPS at $70\,\mu$m, 182 F5-K5 stars were observed by Bryden et al. (2006) and Beichman et al. (2006b). For Spitzer/IRS spectra at $32\,\mu$m, 187 F0-M0 stars were observed by Beichman et al. (2006a, 2008). Uncertainties in the underlying distribution due to small number statistics (shaded regions) are large below the detection limits of each instrument/wavelength.

4 Conclusion

The GASPS, DIGIT, DUNES and DEBRIS observations build on the heritage of previous space missions and the four teams will provide to the community a rich database to address the physical and chemical evolution of protostellar and protoplanetary sources, and to study planet formation. The archive will also be invaluable for planning future ground and space missions, aiming in particular at detecting photons from exo-planets. The significant french contribution to the 4 OTKPs is intimately related to the excellent, worldwide visibility of our work in the field of star and planet formation, and in particular through the development of versatile numerical models that will be used to interpret the soon coming HERSCHEL data.

References

Absil, O., et al. 2008, A&A, 487, 1041

Augereau, J. C., Lagrange, A. M., Mouillet, D., Papaloizou, J. C. B., & Grorod, P. A. 1999, A&A, 348, 557

Lestrade, J.-F., Wyatt, M. C., Bertoldi, F., Dent, W. R. F., & Menten, K. M. 2006, A&A, 460, 733

Morbidelli, A., & Levison, H. F. 2008, Physica Scripta Volume T, 130, 014028

Pinte, C., Ménard, F., Duchêne, G., & Bastien, P. 2006, A&A, 459, 797

Reche, R., Beust, H., Augereau, J.-C., & Absil, O. 2008, A&A, 480, 551

SF2A 2008
C. Charbonnel, F. Combes and R. Samadi (eds)

THE CIRCUMBINARY DUSTY DISK OF UPSILON SGR REVEALED BY MID-IR INTERFEROMETRIC OBSERVATIONS WITH THE VLTI/MIDI

Bonneau, D.[1], Netolický, M.[4,2], Chesneau, O. [1], Harmanec, P.[3], Koubský, P.[4], Mourard , D.[1] and Stee, P.[1]

Abstract. The first mid-IR interferometric observations of a hydrogen-deficient binary star, υ Sgr, were carried out using the MIDI/VLTI instrument between April 2007 and May 2008. The dusty circumbinary envelope is resolved in the N band ($8 - 13.5\mu m$), and has a typical size of 20 x 14 mas. The calibrated fringe visibilities, the mid-IR spectrum and the SED were fitted using models computed with the radiative transfer code MC3D using several mixtures of carbon and silicate dust, in order to determine the geometry and chemical composition of the envelope. The best model we obtain is a geometrically thin and dense disk with an inner radius of $R_{in} \simeq 6.0$AU and a scale height $h_{100} \simeq 3.5$AU. The inclination of the disk is $i \simeq 50°$ and its position angle is $PA \simeq 80°$. The chemical composition of the dust is approximatelya ratio of 60% of carbon dust and 40% of silicate dust. We constrained for the first time the geometry and the chemistry of the circumbinary dusty envelope of υ Sgr. It is now clear that the components of υ Sgr are massive stars ($> 10\ M_\odot$) and the results are compatible with evolutionary scenario proposed by Delgado & Thomas (1981) of a binary with massive components experiencing several phases of important mass transfer leading to the hydrogen-deficient primary star. However, complementary spectro-interferometric observations in the near infrared and the visible are mandatory to investigate the complex structure of the inner circumstellar environment and directly resolve the stellar components of the υ Sgr system.

1 Introduction

The massive, hot and very luminous stars are the principal source of UV flux in the Galaxy and their evolution is affected by a powerful stellar wind which has effects on the circumstellar medium and the stellar formation. The determination of the fundamental parameters of massive stars suffers from a great uncertainty. Close massive binary stars are complex objects as well from the observational point of view as from the modeling point of view. The study of binary systems with (initially) massive objects is particularly attractive. Accretion discs, gaseous streams, jets, and scattering envelopes were found by combining spectroscopic, photometric and interferometric observations and studied in the well known interacting binary β Lyrae (Harmanec et al. 1996; Harmanec 2002; Ak et al. 2007). The system υ Sgr (HD 181615) with a A type low mass supergiant, is the brightest member of the type of extremely hydrogen-deficient binaries stars (HdB stars; Schönberner & Drilling 1983). The HdB stars are in a second phase of mass transfer where the primary has ended the core helium burning phase (Delgado & Thomas 1981). The distance of υ Sgr determined by Hipparcos was recently revised to $d = 595^{+94}_{-72}$ pc (van Leeuwen 2007). The system υ Sgr is known as a single-lined spectroscopic binary ($P =$ 137.9 d, $e = 0.0$, $dP/dt =$ -24 s/y; Koubský et al. 2006). The secondary orbit was determined from the study of the IUE spectra ($M_p/M_s \approx 0.64$; Dudley & Jeffery 1990), however, the detection of the secondary lines is uncertain due to the poor quality of the data. The presence of circumstellar matter in the υ Sgr system is evidenced by the complex Hα absorption/emission profiles but also by the strong infrared excess, and in particular by the prominent silicate dust signature at 9.7μm (Treffers et al. 1976). Nariai (1967) proposed that the displaced Hα absorption is formed in a supersonic flow generated as the gas is transferred from the primary via the L1 point, adopts a

[1] UMR 6525 H. Fizeau, Univ. Nice Sophia Antipolis, CNRS, OCA, Av. Copernic, F-06130 Grasse, France
[2] Masaryk University, Department of Theoretical Physics and Astrophysics, 611 37 Brno, Czech Republic
[3] Astronomical Institute of the Charles University, V Holešovičkách 2, 180 00 Praha 8, Czech Republic
[4] Astronomical Institute of the Academy of Sciences, 251 65 Ondřejov, Czech Republic

form of a cone directed toward the secondary and partly escapes from the system in the form of an outflowing spiral arm encircling the whole binary. Koubský et al. (2006) have tentatively suggested an alternative model in which υ Sgr might be a non-eclipsing analog of the β Lyr system (the peculiar spectrum of the primary would come from the rim of a disk, while the blue-shifted absorption would originate from the slowly precessing bipolar jets). This paper presents the first detection of the dusty circumbinary envelope of υ Sgr and the best model obtained from interferometric and photometric data using the MC3D code.

2 Mid-Infrared observations

2.1 Interferometric Observations

The observations were carried out with the instrument MIDI of the Very Large Telescope Interferometer (VLTI) in operation at the ESO Paranal Observatory (Leinert et al. 2003), using the 1.8m Auxiliary Telescopes (ATs) and 8m Unit Telescopes (UTs). υ Sgr was observed from April till August 2007 and in May 2008 with 6 baselines ranging from 20 meters up to 125 meters. The observations were performed using the PRISM dispersive element giving a spectral resolution of $R \sim 30$ in the N-band. In order to calibrate the visibilities of the science target, we used observations of calibrating stars selected from the MIDI calibrator list using the SearchCal tool available at JMMC[1]. The data obtained with MIDI instrument have been reduced using IDL-based MIA+EWS software. A description of the data reduction steps can be found in Leinert et al. (2004). We have followed the standard reduction process. As seen in Fig. 1-Left, the dataset offers a reasonable coverage of the u-v space, but there is only 1 measurement in position angle range from $90° - 180°$ which is the main source of uncertainty for the determination of the orientation and inclination angles derived from the observed visibilities.

2.2 First results

The images recorded using the MIDI star acquisition modes at 8.7 μm clearly show a perfect Airy pattern, which FWHM is $\approx 225\ mas$ meaning that υ Sgr is unresolved at the UTs focus ($D = 8.2m, 1.22\lambda/D = 0.267''$). On the other hand, the decrease of the visibility with increasing base length shows clearly that the dusty envelope of υ Sgr observed at $\lambda \sim 10\mu m$ is resolved by the VLTI. As a first-order model approximation of the source our calibrated visibility curves are fitted with 2D elliptical Gaussian with $FWHM \approx 20 \times 14mas$, inclination $i \approx 45°$ and position angle $P.A. \approx 76°$.

3 Radiative Transfer Modeling

The interferometric mid-IR calibrated visibilities have been combined with the spectral energy distribution (SED) to constrain the physical parameters of the dusty envelope of υ Sgr using a model computed with the radiative transfer code MC3D.

3.1 Photometric data of υ Sgr

For υ Sgr, we have adopted the value $E(\mathrm{B-V}) = 0.20$ is adopted by Dudley & Jeffery (1990). Assuming $R_V = 3.1$, this color excess gives a total visual absorption $A_V \approx 0.6$. From this small value for the interstellar absorption and the large infrared excess of the source, it comes out that the circumstellar dust around υ Sgr should exhibit a small self-absorption. Given the asymmetry of the source, the dust cannot be distributed in a spherical shell but rather in a disk that does not intercept the line-of-sight and that must be seen at low or intermediate inclination.

The dereddened SED of υ Sgr was derived from UV, visual, near-IR and mid-IR measured flux compiled by Trams et al. (1991) can be fitted by two blackbodies (one for the stellar radiation at $T = 12000\,\mathrm{K}$, the other for the radiation from the dusty envelope at $T = 950\,\mathrm{K}$). We derived the luminosity of the central source $L \simeq 39000 L_\odot$ using the revised Hipparcos distance.

As suggested by the 10 μm feature present in the MIDI and IRAS spectra, we can expect some silicates in the dusty envelope of the binary. It might be inconsistent however, to restrict the chemical composition just to the silicate dust, as the primary source is now a HdB star.

[1] http://www.mariotti.fr/

parameter	value
$R_{\rm in}$ [AU]	$\simeq 6.0$
i	$\simeq 50°$
α	$\simeq 2.0$
β	$\simeq 0.7$
h_{100} [AU]	$\simeq 3.5$
$\log(M_{\rm d}/M_\odot)$	≈ -3.5
$M_{\rm am.C}/M_{\rm d}$	$\simeq 0.6$

Table 1. Parameters of the best model visibility fit.

3.2 *Visibility and photometry modeling*

For the interpretation of the interferometric data and the observed SED, we used the MC3D radiative transfer code (Wolf et al. 1999) based on Monte-Carlo method for emitting, scattering, absorbing and reemitting the photons. The code assumes a spherical source located in the center of the coordinate system and spherical dust grains. The density of the dust shell is computed according to the model of the stratified dusty disk (Shakura & Sunyaev 1973), the density of witch is defined with the 2D law:

$$\varrho(r,z) = \varrho_{100}\Big(\frac{100}{r}\Big)^{\alpha} \exp\Big[-\frac{1}{2}\Big(\frac{z}{h(r)}\Big)^{2}\Big]$$

with $h(r) = h_{100}\big(\frac{r}{100}\big)^{\beta}$. r is the radial distance in the midplane of the disk, h_{100} is the scale height at the distance of $r = 100\,\mathrm{AU}$, α the density parameter in the midplane and β is the vertical density parameter. The central source is described the effective temperature $T_{\rm eff}$ and the luminosity L (see Fig.1-Center). The MC3D code then makes it possible to calculate the SED and the intensity map of the source which is converted into visibility map. Computed SED and visibilities are fitted on the data to estimate the parameters of the best model. The dust is supposed to be a mixture of astronomical silicate and amorphous carbon. We assumed the grain size distribution of (Mathis et al. **?**) $\frac{{\rm d}n(a)}{{\rm d}a} \sim a^{-3.5}$, where a is the dust grain radius assumed to range from 0.01 to 1.00 μm. Because our poor current knowledge about the geometry of the binary orbit and its surrounding, the parameter space of the models we had to explore was large. The only fixed parameters were the parameters of the central source ($T_{\rm eff}$, $L/L_\odot$) and the sublimation temperature of 1500 K adopted for all the models. The outer radius of the model grid was kept to be $R_{\rm out} = 100\,\mathrm{AU}$, which corresponds to a maximum angular size of $\sim 400mas$ consistent with the unresolved image taken with VLT UT telescope. The geometry of the disk is defined by α, β, h_{100}, $R_{\rm in}$, the inclination i and the $P.A.$, together with the composition and the total mass M_d of the dust. In the first step of the fitting procedure we focused on finding the brightness distribution on the sky giving the best fit of the visibilities, which are very sensitive to the geometry of the dusty envelope. In the second step, based on this best models we tried to find the best fit of the SED, taking a particular care of reproducing the 10μm silicate feature. The evaluation of the quality of the visibility fit was made using the reduced χ^2. The parameters of the best model are shown in Table 1. If we assume that the dusty disk lies in the same plane as the binary, the inclination of the model could put more constrains on the binary system. Our value for i is consistent with the constrains mentioned in Koubský et al. (2006). Also it would be noted that the $P.A.$ of the model is almost perpendicular to the observed orientation of the polarization $P_{\rm obs} = 172°$ (Yudin 2001). The image of the disk given by the best model is shown in Fig.1-Right.

4 Conclusion

The VLTI-MIDI observations provided evidence for a thin, flat circumbinary disk around the hydrogen-deficient binary υ Sgr whose inner rim lies close to the radius of sublimation temperature. The chemical composition of the dust (60 % of carbon and 40% of silicate) could be a consequence of several episodes of mass transfers in agreement with the evolutionary scenario proposed by Delgado & Thomas 1981, leading to the hydrogen-deficient primary. These observations allowed us to constraint the the inclination and the position angle of the system, and given these constraints and the spectroscopic observations reported in Koubský et al. (2006), it is now clear that the components of υ Sgr are massive stars ($> 10\ M_\odot$). The results obtained here pushed the

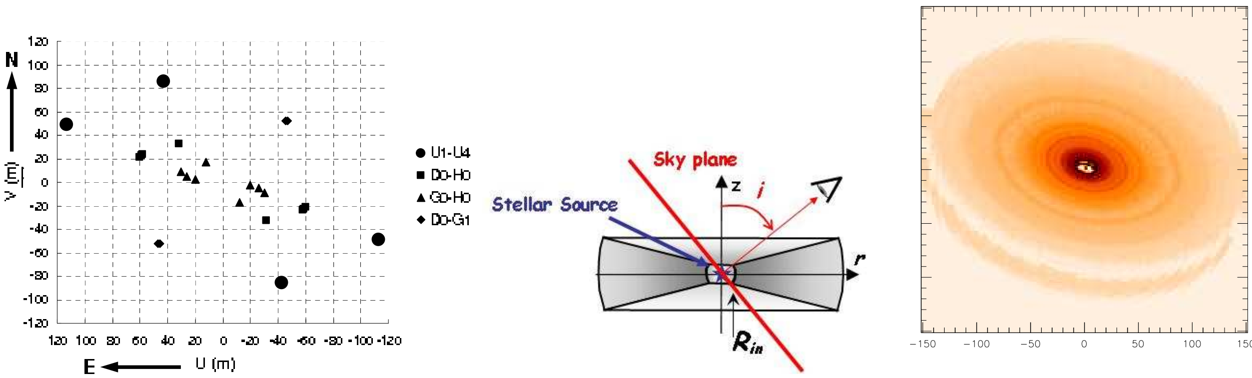

Fig. 1. Left: The uv coverage over the time of observations of the VLT baselines using UTs (U1-U4) and ATs (D0-H0, G0-H0, D0-G1). Center: Cut of the 3D model of disk used by the MC3D code. Right: The intensity map at 13 μm for the best visibility model. The intensity levels of the image corresponds to the square root of the real image.

knowledge of this peculiar HdB a step forward. However, there are still many open issues: e.g. the explanation of the peculiar spectrum of the 'invisible' component and the verification of the radial velocity curve of the secondary, that can be tested only at visible or UV wavelengths. The disk inner rim can be best studied in the near-IR using short baselines ($\leq$40m). The binary system, with a semi-major axis of $\sim 2mas - 4mas$, can be resolved with an interferometer, in the near-infrared (with baselines longer than ($\leq$80m), or better in the visible (continuum and some chosen lines) using the VEGA recombiner of the CHARA interferometer (Mourard et al. 2009).

Acknowledgements. The research of P. Harmanec was supported by the grants 205/06/0304, and 205/08/H005 of the Czech Science Foundation and also from the Research Program MSM0021620860 *Physical study of objects and processes in the solar system and in astrophysics* of the Ministry of Education of the Czech Republic. The visit of M. Netolický to OCA, where he was trained in modern VLTI software techniques and their application, was funded from the OPTICON grant R113-CT-2004-001566 JRA 4.

References

Ak, H., et al. 2007, A&A, 463, 233

Delgado, A. J., & Thomas, H.-C. 1981, A&A, 96, 142

Dudley, R.E., & Jeffery, C.S. 1990, MNRAS, 247, 400

Harmanec, P., Morand, F., Bonneau, D., et al. 1996, A&A, 312, 879

Hamanec, P. 2002, AN, 323, 87

Koubský, P., Harmanec, P., Yang, S., Netolicky, M., et al. 2006, A&A, 459, 849

Leinert, Ch., Graser, U., Przygodda, F., et al. 2003, Ap&SS, 286, 73

Leinert, Ch., van Boekel, R., Waters, L.B.F.M., et al. 2004, A&A, 423, 537

van Leeuwen, F., 2007, A&A, 474, 653

Mourard, D., Perraut, K., Bonneau D. et al. 2008, astroph

Nariai, K. 1967, PASJ, 19, 564

Schönberner & D., Drillind, J.S. 1983, ApJ, 268,225

Shakura, N. I., & Syunyaev, R. A. 1973, A&A, 24, 337

Trams, N.R., Waters, L.B.F.M., Lamers, H.J.G.L.M., et al. 1991, A&ASS 87, 361

Treffers, R., Woolf, N.J., Fink, U. and Larson, H.P. 1976, ApJ, 207, 680

Wolf, S., Henning, T., & Stecklum, B. 1999, A&A, 349, 839

Yudin, R. V. 2001, VizieR Online Data Catalog, 336, 80912

SF2A 2008
C. Charbonnel, F. Combes and R. Samadi (eds)

BROWN DWARFS IN THE HYADES CLUSTER

Bouvier, J. et al.[1]

Abstract. We present the results of a search for brown dwarfs (BDs) and very low-mass (VLM) stars in the 625 Myr-old, metal-rich ([Fe/H]=0.14) Hyades cluster. We performed a deep (I$\sim$23, z$\sim$22.5) photometric survey over 16 deg^2 around the cluster center. We report the discovery of the first 2 BDs in the Hyades cluster, with a spectral type T1 and T2, respectively. Their optical and near-IR photometry, as well as their proper motion, are consistent with them being cluster members. According to models, their mass is about 50 Jupiter masses at an age of 625 Myr. We also report the discovery of 3 new very low-mass stellar members and confirm the membership of 15 others.

1 The CFHT survey of the Hyades cluster

The Hyades is one of the richest open clusters and the closest to the Sun. Perryman et al. (2008) derived its main structural and kinematical properties based on Hipparcos measurements : a distance of 46.3±0.27 pc, an age of 625±50 Myr, and a metallicity [Fe/H] of 0.14±0.05. The large proper motion of the cluster ($\mu \simeq$100 mas yr^{-1}) can be easily measured from imaging surveys over a timeframe of only a few years, which helps in assessing cluster's membership.

Wide-field optical images were obtained in the I and z bands with the CFHT 12K camera, a mosaic of 12 CCD arrays with a pixel size of 0.21" which provides a FOV of $42' \times 28'$. The survey consists of 53 mosaic fields covering a total of 16 square degrees. The survey is at least 90% complete down to I$\sim$23.0 and z$\sim$22.5, a limit which varies only slightly with seeing conditions (0.6-0.8 arcsec).

2 Hyades brown dwarfs

PSF photometry was performed on the I and z-band images with a modified version of SExtractor (Bertin & Arnouts 1996). The (I, I-z) color magnitude diagram (CMD) is shown in Figure 1. A total of 125 Hyades candidate members were selected in this CMD from their location relative to model isochrones. Follow up K-band imaging was obtained for 108 candidate members using the 1k×1k CFHT WIRCAM camera. The (I, I-K) CMD for these candidate members is shown in Figure 1. In addition, proper motion was computed from pairs of optical and infrared images obtained 2 or 3 years apart. The proper motion vector diagram of 107 optically selected Hyades candidate members is shown in Figure 1.

Based on photometry and astrometry, we eventually identified 20 candidates which consistently qualify as probable Hyades members. Of these, 15 were already listed as possible or probable Hyades members in the Prosser & Stauffer's Open Cluster Database. The remaining 5 probable members we report here are new. They include 3 very low-mass stars ($\sim$0.14 $M_\odot$) and 2 objects well within the substellar regime.

Our survey thus identifies the first 2 Hyades BD candidates (CFHT-Hy-20, 21), with an estimated mass of about 50 Jupiter masses, and a very low-mass star (CFHT-Hy-19) close to the stellar/substellar limit (75 jupiter masses). We obtained low resolution infrared spectra for these 3 objects using TNG/NICS (Fig. 1). Fitting the observed spectra with those of template field dwarfs observed with the same instrument, we derive a spectral type of M8, T2 and T1 for CFHT-Hy-19, 20 and 21, respectively.

[1] Laboratoire d'Astrophysique, Observatoire de Grenoble, Université J. Fourier, CNRS, BP 53, 38041 Grenoble, Cedex 9, France

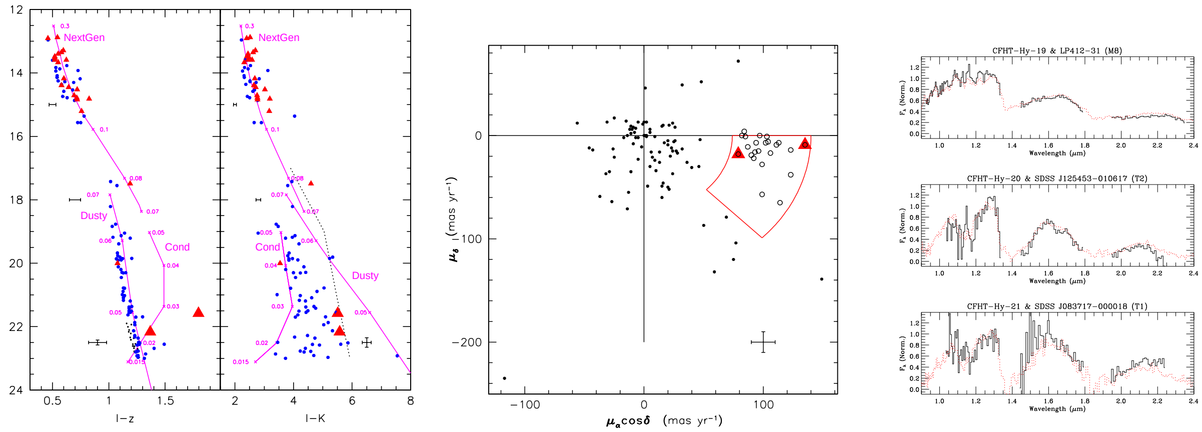

Fig. 1. Left: (I, I-z) and (I, I-K) CMDs of optically selected candidated followed up with CFHT IR in the K-band. Small dots : 17 optically selected candidates without follow up IR photometry. Large dots : optically selected candidates whose proper motion is inconsistent with Hyades membership (cf. central panel). Triangles : candidates whose proper motion is consistent with Hyades membership. The stellar/substellar boundary occurs at I$\simeq$17.8 mag. The 2 most promising substellar cluster candidates are shown by large triangles. NextGen (0.07-0.3 $M_\odot$), Dusty (0.04-0.07 $M_\odot$) and Cond (0.015-0.05 $M_\odot$) 600 Myr isochrones are shown and labelled with mass (Baraffe et al. 1998; Chabrier et al. 2000). In the (I, I-K) CMD, the dotted line indicates the locus of M8-T5 field dwarfs. The rms photometric error is shown as bars. **Center**: Proper motion vector diagram for 107 optically selected candidates followed up in the K-band (see text). The expected proper motion for Hyades members is shown by the (red) box. Within these boundaries, 23 optically selected candidates (empty circles) are found to share the proper motion of the cluster, including 2 BDs (large triangles). Typical rms errors on the ppm measurements are shown by a cross. **Right**: Near-infrared Amici low resolution spectra of CFHT-Hy-19, 20 and 21 (solid lines from top to bottom). In each panel we also show the closest matching field dwarf spectrum (dotted line) from the low resolution Amici spectral library (Testi et al. 2001).

3 Conclusion

Our survey is complete in the mass range from less than 50 Jupiter masses up to 0.20 $M_\odot$. In this mass range, we identified 18 very low-mass stars, down to the stellar-substellar limit, as well as 2 brown dwarfs with a spectral type T1 and T2. These are the first T-dwarfs identified in the Hyades cluster at an age of 625 Myr[1], and also the only known instances of metal-rich ([Fe/H]=0.14) methane dwarfs. Additional spectroscopy of these lowest mass Hyades members is scheduled on Gemini in the fall of 2008. A full account of these results is given in Bouvier et al. (2008).

References

Baraffe, I., Chabrier, G., Allard, F., & Hauschildt, P. H. 1998, A&A, 337, 403

Bertin, E., & Arnouts, S. 1996, A&AS, 117, 393

Bouvier, J., Meeus, G., Kendall, T., et al. 2008, A&A, 481, 661

Chabrier, G., Baraffe, I., Allard, F., & Hauschildt, P. 2000, ApJ, 542, 464

Hogan, E., Jameson, R. F., Casewell, S. L., et al. 2008, MNRAS, 388, 495

Perryman, M. A. C., et al. 1998, A&A, 331, 81

Testi, L., D'Antona, F., Ghinassi, F., Licandro, J., Magazzù, A., et al. 2001, ApJ 552, L147

[1]Since then, Hogan et al. (2008) reported the discovery of 12 L-dwarfs in the cluster.

SF2A 2008
C. Charbonnel, F. Combes and R. Samadi (eds)

NUMERICAL STUDIES OF THE VISHNIAC INSTABILITY IN SUPERNOVA REMNANTS

Cavet, C.[1], Nguyen, H. C.[1,3], Michaut, C.[1], Falize, E.[1,2], Bouquet, S.[1,2] and Di Menza, L.[3]

Abstract. Vishniac instability has been theoretically studied in supernova remnants where it is supposed to explain the fragmentation of the interstellar medium. However its role is not fully demonstrated in these objects. Numerical simulations with the HYDRO-MUSCL hydrodynamic code has been realised to simulate this instability in order to compare the numerical growth rate with the Vishniac analytical solution.

1 Introduction

Among the instabilities arising in astrophysical systems, and in particular in supernova remnants (SNRs), the Vishniac instability is not very well known. In their original analysis of global perturbations, Vishniac (1983) and Ryu & Vishniac (1987) identified the criteria that allows to compute the growth of a perturbation in a thin shell of shocked matter. The instability depends on the direction of two opposite forces: the thermal pressure p_{th} due to hot SNR gas (pushe outwards) and the ram pressure p_{ram} due to the accretion of the surrounding interstellar matter (ISM) on the shock front (compresse inwards). If the ISM is uniform, the two pressures keep the same directions and the shock front is stable; but in the case of non-uniform ISM, the shock front is distorted, the two forces do not counterbalance and oscillations can develop and grow. In a linear stability analysis, Vishniac (1983) used the infinitely thin shell approximation to study the perturbation equations and numerically solved the corresponding system. In a recent study (Cavet *et al*, 2007) an analytical solution for the growth rate has been determined in this case, but this approximation does not allow to access the general instability criteria. Aiming to investigate the more realistic physical cases of a thin shell with finite thickness, the growth rate is calculated through numerical simulations of perturbed radiative blast waves, and compared with the analytical one.

2 Numerical simulations

Numerical simulations are performed with the HYDRO-MUSCL code developed by our team. This Eulerian code solving hydrodynamic equations, uses a regular cartesian grid and an adaptative time step. The underlying numerical method is a MUSCL-Hancock finite volume scheme and a HLLC Riemann solver (Toro, 1999). In order to perform 2D cylindrical hydrodynamic simulations for the propagation of a shock wave in the ISM, we induce an initial explosion by depositing a strong amount of energy in the form of p_{th} at the center of a box. In a first simulation, we study the initial phase of the shock evolution where the gas is adiabatic (the polytropic index is $\gamma = 5/3$) and then the shock radius can be approximated with the Sedov law (see Keilty *et al*, 2000). The simulation is stopped at (t_0, r_0) *i.e* when the radius evolves according to the self-similar solution and when the density on the shock front reaches the strong shock limit. We use this result as input data in the following simulation. In the second calculation, axial velocities are directly modified in data in order to obtain the snowplow radius evolution and radiative losses are taken into account by $\gamma = 1.1$. We introduce high-density spots ($\rho_{spot} \propto \rho_{shock}$) ahead of the shock wave to perturb the shock front and let the system evolve. The analytical form of this perturbative spots are (Ryu & Vishniac, 1987): $\widetilde{\rho} = \rho/\rho_{ISM} = \delta\tilde{\rho}_i(\xi)\ Y_{lm}(\theta, \Phi)\ t^s$.

[1] LUTH, Observatoire de Paris, CNRS, Université Paris-Diderot, Meudon, France
[2] Département de Physique Théorique et Appliquée (DPTA), CEA Bruyères le Châtel, 91297 Arpajon Cedex, France
[3] Laboratoire de Mathématiques, Université Paris-Sud, Orsay, France

To determine the initial profile of these spots, we have to evaluate the function $\delta\tilde{\rho}_i(\xi)$ of the dimensionless spatial parameter ξ. In the analytical part, this function is not explicitly estimated and only determined by numerical means. We have obtained an approximated value $\delta\widetilde{\rho}_i(\xi) \approx -(2a-2)\xi^{2a-3}$ with the method developed in Kushnir *et al* (2005). Then in the numerical simulations we introduce a finite number of spots to take into account the perturbative mode number l and we add a bi-dimensional spot shape in order to reproduce the deformation profile according to r, θ, ϕ.
Numerically we observe that the two spots create radial oscillations both on density and pressure, and density perturbation on the shock front. We remarke also that in the two local pressure deformations of the shell shape, p_{th} and p_{ram} are not aligned as in the analytical pattern. Thus in this numerical configuration, the Vishniac instability criteria γ and $\delta\widetilde{\rho}_i(\xi)\, Y_{lm}$ are fulfilled. In order to observe the evolution of the growth rate s of this small perturbations and to compare s with the theoretical results, we let run the simulation during $t = 10 \times t_0$. In Fig. 1 we superpose ten snapshots of the density profile projected on the y-axis and normalized for the shock

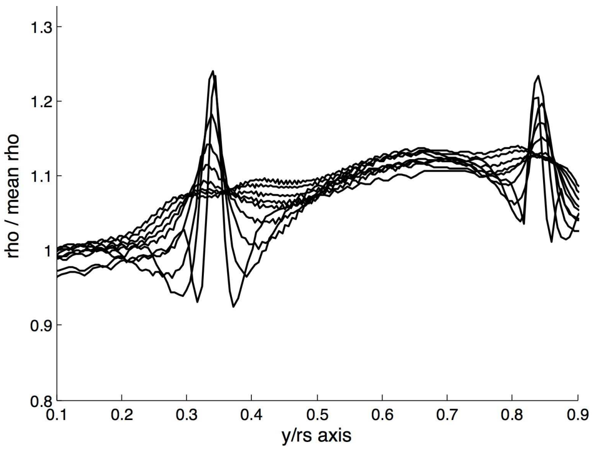

Fig. 1. Ten dimensionless density profiles $\widetilde{\rho}$ versus y-axis

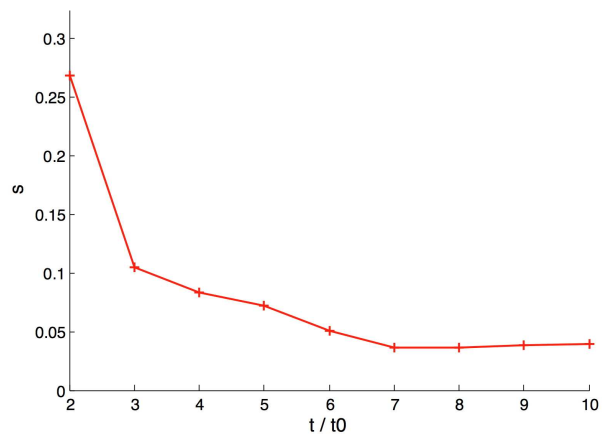

Fig. 2. Evolution of perturbation growth rate s versus t

front value which enables to measure the normalized peak oscillations $\delta\widetilde{\rho}$ during this period. We estimate the growth rate by the relation: $s = [\ln(\delta\widetilde{\rho}) - \ln(\delta\widetilde{\rho}(1)\; Y_{lm})] / \ln t$ where $\delta\widetilde{\rho}(1) = 1.8$. Figure 2 shows the evolution of the growth rate $s(t)$ and its stabilization to a limit value $s = 3.7 \times 10^{-2}$ clearly observed. Compared to Vishniac prediction, this value seems too low. However, we have chosen a small mode number $l \sim 8$ due to the presence of only two high density spots. If we increase the number of initial spots, l is also increasing and can reach the optimal mode number $l = 40$ of the theoretical pattern. However due to numerical constraints it is not easy to multiply initial high-density spots on the way of the thin shell. In future simulations, we will improve the stability study using a multi-processor version of HYDRO-MUSCL code. We will combine this new simulations with profiles of perturbed shell designed by analytical tools that will enable a better control of spatial shape and thus of the value of the mode number l. Furthermore an experiment of the Vishniac instability realized by our team is planned on the LIL high-power facility (Bordeaux, France) in 2009.

References

Vishniac, E.T. 1983, ApJ, 274, 152

Ryu, D., & Vishniac, E.T. 1987, ApJ, 313, 820

Cavet, C., Michaut, C., & Falize, E. 2008, SF2A-2007: Proceedings of the Annual meeting of the French Society of Astronomy and Astrophysics held in Grenoble, France, July 2-6, 2007, Eds.: J. Bouvier, A. Chalabaev, and C. Charbonnel, p.443, EDP-Sciences, Conference Series

Kushnir, D., Waxman, E., & Shvarts, D. 2005, ApJ, 634, 407

Keilty, K.A., Liang, E.P., Ditmire, T., Remington, B.A., Shigemori, K., & Rubenchik, A. 2000, ApJ, 533, 890

Toro, E.F. 1999, Riemann solvers and numerical methods for fluid dynamics, Springer

SF2A 2008
C. Charbonnel, F. Combes and R. Samadi (eds)

HIGH-RESOLUTION THERMAL IR IMAGING OF MWC300 WITH VLT/VISIR

Domiciano de Souza, A.[1], Kervella, P.[2], Bendjoya, Ph.[1] and Niccolini, G.[1]

Abstract. B[e] stars are expected to possess dusty circumstellar environments, which are responsible for a strong infrared (IR) excess. Using single-dish diffraction-limited imaging in the thermal infrared domain, we aim at measuring the angular extension of the dusty environment of the galactic B[e] MWC 300. We obtained diffraction-limited images of MWC 300 at 11.25 μm using the BURST mode of the VLT/VISIR instrument. MWC 300 is partially, but statistically significantly, resolved by VISIR so that we could measure the size of its dusty envelope for the first time. By assuming a 2D circular Gaussian intensity distribution and using different image analysis methods we measured a FWHM angular size of 69 ± 10 mas. For a distance of 1.8 kpc, we obtain a linear size of 125 ± 18 AU $= (1.87 \pm 0.26) \times 10^{13}$ m for the circumstellar dust emitting in the mid-IR. This measured size is shown to agree with a model that was calculated with a Monte Carlo radiative transfer code for dust envelopes. The flux of MWC 300 at 11.25 μm is estimated as 84.5 ± 1.4 Jy $= (20.0 \pm 0.3) \times 10^{-13}$ W/m^2/μm. The VLT/VISIR now offers the possibility of obtaining mid-IR diffraction-limited images with a high signal-to-noise ratio. The MWC 300's size as directly measured in this work is compatible with the theoretical size of a nearly edge-on dusty disc estimated in previous works. Interferometric data at milliarcsec angular resolution are required to reveal details on this dusty envelope.

1 Introduction

MWC 300 (V431 Sct) is a galactic B[e] star, being most probably a supergiant B[e] with a luminosity $\log L/L_\odot = 5.1 \pm 0.1$ and located at a distance $d = 1.8 \pm 0.2$ kpc (Miroshnichenko et al. 2004; hereafter M04). Interferometric and/or imaging instruments can nowadays attain the required angular resolutions for directly measuring the mid-IR size of MWC 300 and of other supergiant B[e] stars (e.g., Domiciano de Souza et al. 2007).

We present here results from diffraction-limited images of MWC 300 at 11.25 μm using the BURST mode of the VLT/VISIR instrument. This work is based on observations performed at the European Southern Observatory, Chile under ESO Program 078.D-0295(A). A detailed description of the results is given by Domiciano de Souza et al. (2008).

2 Observations and data reduction

We used the VISIR instrument (Lagage et al. 2004), installed at the Cassegrain focus of the Melipal telescope (UT3) of the VLT (Paranal, Chile). Under standard conditions at Paranal (median seeing of 0.8" at 0.5 μm), the 8 m telescope is not diffraction-limited in the mid-IR (seeing ≈ 0.4" vs. 0.3" diffraction).

To overcome this limitation, a specific mode of the instrument called the BURST mode was introduced by Doucet et al. (2007). Its principle is to acquire very short exposures ($\Delta t \leq 50$ ms), to keep the complete integration within a fraction of the coherence time (≈ 300 ms at Paranal in the mid-IR). The detector is therefore read very quickly, and the resulting images freeze the turbulence. It is subsequently possible to select the best images presenting a single speckle ("lucky imaging"), so they are diffraction-limited.

We observed MWC 300 during the first half of the night of October 3-4, 2006. A series of BURST mode observations of this star and its main PSF calibrator η Ser (HD 168723, spectral type K0III-IV) was obtained in the PAH2 filter, whose central wavelength is $\lambda = 11.25$ μm. The main PSF calibrator, η Ser, was chosen in the Cohen et al. (1999) catalogue of spectrophotometric standards for infrared wavelengths so that its flux is

[1] Lab. H. Fizeau, CNRS UMR 6525, Univ. de Nice-Sophia Antipolis, Observatoire de la Côte d'Azur, F-06108 Nice cedex 2
[2] LESIA, Observatoire de Paris, CNRS UMR 8109, UPMC, Université Paris Diderot, 5 Place Jules Janssen, F-92195 Meudon

Table 1. Log of the VISIR observations of MWC 300 and its main (PSF1: η Ser) and secondary (PSF2: α Eri) PSF calibrators.

#	MJD[1]	Star	DIT[2]	N exp.[3]	θ (")[4]	AM[5]
img A	0.0044	MWC 300	10	1200 × 8	0.8	1.15
img B	0.0120	MWC 300	10	1200 × 14	1.1	1.21
img C	0.0238	MWC 300	10	1200 × 14	1.0	1.24
PSF1	0.0451	η Ser	10	1200 × 14	1.0	1.46
PSF2	0.1877	α Eri	20	1200 × 14	0.8	1.21

[1] modified Julian date of the middle of the exposures on the target, minus 54 012.

[2] Detector Integration Time given in milliseconds for one frame.

[3] number of image exposures in the form *nb. of frames per file* × *nb. of files.*

[4] seeing in the visible ($\lambda = 0.5\,\mu$m) as measured by the observatory DIMM sensor, in arcseconds.

[5] average airmass of the observation.

absolutely calibrated, providing a convenient photometric reference for accurately estimating the absolute flux of MWC 300. We estimated the flux of MWC 300 at 11.25 μm to be 84.5 ± 1.4 Jy = $(20.0 \pm 0.3) \times 10^{-13}$ W/m^2/μm. This value is in good agreement with other measured fluxes in the mid-IR: for example M04 found 76.5 Jy at 10.79 μm, and the MSX observations give 70.0 Jy at 8.28 μm and 93.6 Jy at 12.13 μm (Egan et al. 2003). A secondary PSF (PSF2: α Eri) has also been used in the data analysis.

The journal of the VISIR observations is given in Table 1. During the observations, the seeing quality in the visible varied from 0.8 to 1.1".

2.1 Raw data processing

The fluctuations of the thermal background were removed through the classical subtraction of the chopped and nodded images, to produce data cubes of about 10 000 images covering 6.8" × 6.8". After a precentering at the integer pixel level, the images were sorted by their maximum intensity, used as a proxy of the Strehl ratio (e.g., Born & Wolf 1999). The 40% best images of each cube were then resampled up by a factor 10 using a cubic spline interpolation, and the star image was subsequently centered using Gaussian fitting, at a precision level of a few milli arc seconds (much smaller than the original pixel scale). The field of view was trimmed to 2.25" × 2.25" to reduce the computing time. The resulting cubes were eventually averaged to obtain the master images of MWC 300 and the PSFs used in our image analysis.

The final averaged images of MWC 300 and η Ser are shown in Fig. 1. We can see up to 3 or 4 Airy rings in all MWC 300 images. We note that the data signal-to-noise ratio (SNR) is quite high, reaching $\simeq 2500 - 3500$ per pixel in the core of the MWC 300 images; for the PSF1 the SNR reaches $\simeq 1900$ per pixel. Thanks to these high SNRs one can determine that the core of the MWC 300 images are statistically significantly wider than the core of the PSF, suggesting that the target was partially resolved by VISIR.

3 Image analysis

We applied different methods to estimate MWC 300's size at 11.25 μm from the partially resolved VISIR images:

1. Size estimation assuming that the central peaks of all images (MWC 300 and PSFs) can be represented by a 2D circular Gaussian (hereafter 2DCG).

2. Size estimation by fitting the MWC 300 images with a 2DCG convolved with the observed PSF image. Here we assume that the real intensity distribution of MWC 300 is given by a 2DCG profile.

3. Size estimation by direct image deconvolution of the MWC 300 images by the PSFs. The only assumption about MWC 300 adopted for the deconvolution is that it has a positive intensity distribution, i.e., the positivity criterion commonly used in image processing.

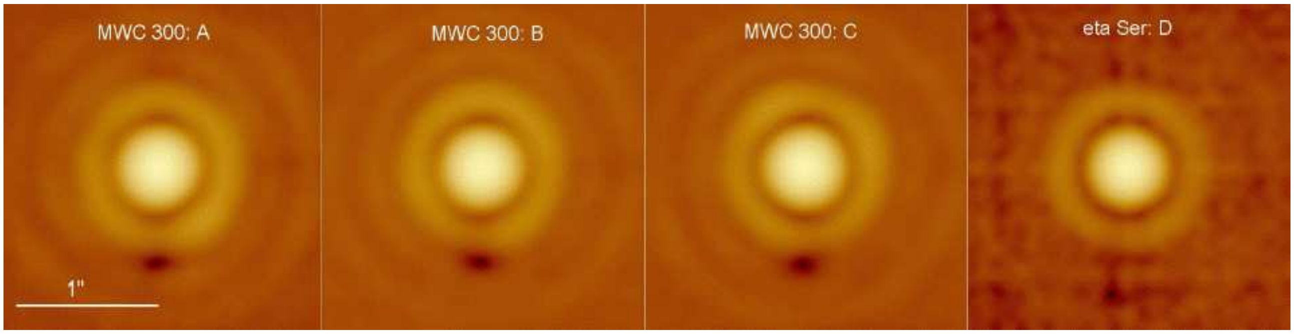

Fig. 1. Final averaged images of MWC 300 and η Ser (PSF) in logarithmic scale (see text and Table 1 details about the observations). At least 3 Airy rings are visible in MWC 300.

Table 2. Typical size of MWC 300 (2D circular Gaussian FWHM in units of mas) from different methods for the VISIR images A, B, and C.

Method applied:	A	B	C	$\overline{\text{FWHM}} \pm \sigma$
Analytical estimation	70	62	57	63 ± 7
Fit of 2DCG convolved with PSF	81	72	67	73 ± 7
Richardson-Lucy deconvolution	80	68	60	69 ± 10

The main results are summarized in Table 2 and the details of each method used are given by Domiciano de Souza et al. (2008). In the following we describe the results from the decovonlution method, which is the one imposing less *a priori* constraints on the data.

3.1 Imaging by Richardson-Lucy deconvolution

We thus performed a Richardson-Lucy deconvolution using the software package Airy[1] (Correia et al. 2002) version 4.0, developed within the CAOS problem-solving environment. The size of the deconvolved images diminishes regularly at each iteration, reaching a plateau after a few hundred iterations. To estimate the size of the deconvolved images and more easily compare it with the sizes from the other methods, we fitted a 2DCG to measure the corresponding FWHM after each iteration. Figure 2(left) shows the FWHM of the MWC 300 deconvolved images as function of the deconvolution iteration.

The deconvolution process was repeated until 1000 iterations to make sure that the FWHM of the deconvolved images converged to a minimum or a plateau in our case. We present in Table 2 the average FWHM calculated on the central peak of the deconvolved images at the plateau regime. This plateau regime is considered to have been reached when the FWHM varies by less than 0.2% between two iterations. The final results do not strongly depend on this value.

The sizes obtained from deconvolution are compatible with the first two methods, especially with those from the fit of a 2DCG convolved with the PSF. As an example of a deconvolved image, we also show in Fig. 2(left) the average of images A, B, and C of MWC 300 deconvolved by the PSF1 at iteration 1000. The more intense secondary structures in the deconvolved image are residuals from the first Airy ring, probably caused by the fact that the SNR of the MWC 300 images is larger than for the PSF.

Since the deconvolution does not impose any a priori assumption on MWC 300, we chose the average size and uncertainty from this method as the more realistic size estimation from the VISIR data: FWHM $= 69 \pm 10$ mas. From our angular size estimation (FWHM $= 69 \pm 10$ mas from the deconvolution), the linear FWHM of MWC 300 at 11.25 μm is $\text{FWHM}_{\text{linear}} = 125 \pm 18$ AU $= (1.87 \pm 0.26) \times 10^{13}$ m (assuming a distance $d = 1.8$ kpc given by M04). For a central star radius $R_* = 29\ R_\odot$, from M04, we have $\text{FWHM}_{\text{linear}} = 924 \pm 131 R_*$.

[1] available at http://fizeau.unice.fr/caos/

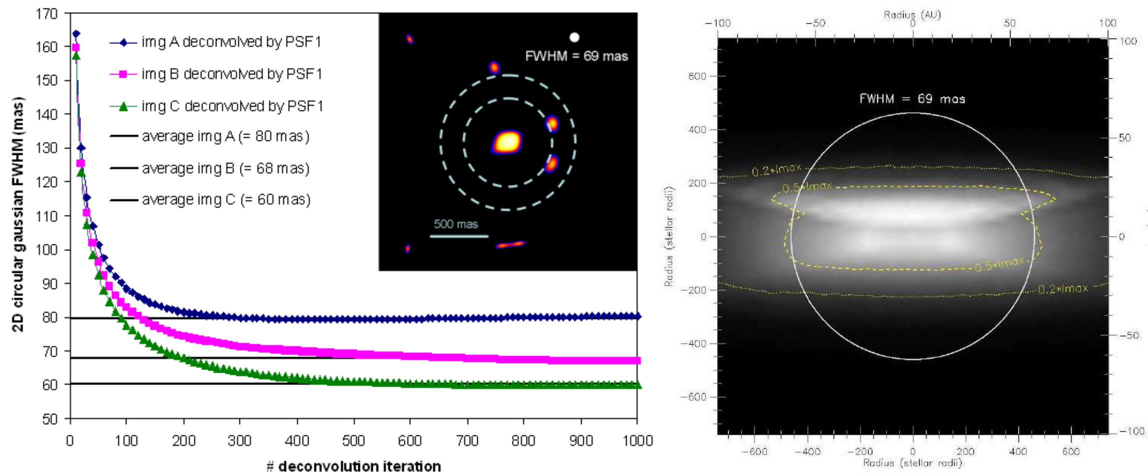

Fig. 2. *Left:* FWHM from a fit of a 2DCG to the center of each deconvolved image of MWC 300 as a function of the iteration number. After a few hundred iterations, the MWC 300 deconvolved images converge to an almost constant FWHM. The average FWHM of each MWC 300 deconvolved image calculated on the plateau regime is compatible with the estimations from other methods (Table 2). The upper right image shows the average of images A, B, and C deconvolved by the PSF1 at iteration 1000 (log. scale). The dashed rings indicate the first Airy ring region. The 2DCG FWHM from the deconvolution method is indicated. *Right:* Image of MWC 300 calculated with a Monte Carlo radiative transfer code (Niccolini & Alcolea 2006). This 11.25 μm image corresponds to a nearly equator-on disc (inclination of the polar axis to the line of sight is 80°). Note that the size of the image at half intensity (dashed contour) agrees with the FWHM size measured with VISIR (circle).

4 Modelling by Monte Carlo radiatif transfer

For a more quantitative analysis of our size estimation, we computed a model dusty disc with the help of a Monte Carlo continuum radiative transfer code (Niccolini & Alcolea 2006). The model input parameters are those of M04, except for the mass of the disc ($M = 0.01 M_{\odot}$) and for the density profile, which in our case is given by a Gaussian law from $R_1 = 147 R_*$ to $3450 R_*$, followed by a $\rho \propto r^{-4}$ power-law. The synthetic image at 11.25 μm, shown in Fig. 2(right), well agrees with the measured VISIR FWHM. The adopted model gives dust temperatures above ~ 600 K within the measured FWHM.

References

Born, M. & Wolf, E. 1999 Principles of Optics, 7th ed. Cambridge, England: Cambridge University Press

Cohen, M., Walker, R. G., Carter, B., et al. 1999, AJ, 117, 1864

Correia, S., Carbillet, M., Boccacci, P., et al. 2002, A&A, 387, 733

Domiciano de Souza, A., Kervella, P., Bendjoya, P., & Niccolini, G. 2008, A&A, 480, L29

Domiciano de Souza, A., Driebe, T., Chesneau, O., et al. 2007, A&A, 464, 81

Doucet, C., Habart, E., Pantin, E. et al. 2007, A&A, 470, 625

Egan, M.P., Price, S.D., Kraemer K.E., et al. 2003, The Midcourse Space Experiment Point Source Catalog Version 2.3, AFRL-VS-TR-2003-1589

Lagage, P.O. et al. 2004, The ESO Messenger 117, 12

Miroshnichenko, A. S., Levato, H., Bjorkman, K. S. et al. 2004, A&A, 417, 731

Niccolini, G., & Alcolea, J. 2006, A&A, 456, 1

SF2A 2008
C. Charbonnel, F. Combes and R. Samadi (eds)

IMPACT OF LARGE-SCALE MAGNETIC FIELDS ON STELLAR STRUCTURE AND PROSPECTIVES ON STELLAR EVOLUTION

Duez, V.[1], Mathis, S.[1], Brun, A.-S.[1] and Turck-Chièze, S.[1]

Abstract. The influence of large-scale magnetic fields on stellar structure and stellar evolution is semi-analytically considered. The magnetic field is derived for a given axisymmetric azimuthal current, and is non force-free, acting thus directly on the stellar structure by modifying the hydrostatic balance. We discuss the relative importance of the various terms associated with the magnetic field in the mechanical and thermal balances before implementing its effects in a 1D stellar evolution code in a way that preserves its geometrical properties. Our purpose is illustrated by the case of an internal magnetic field matching at the surface of an Ap star with an external potential and multipolar magnetic field.

1 Introduction

Though the traditional picture describing the stellar structure and the stellar evolution has succeeded in answering to many questions of the stellar physicists during the last century, some facts indicate today that there is a need for a model that goes far beyond the standard stellar evolution model. The discrepancy between the helioseismology-deduced sound speed and the one found using new solar abundances (Turck-Chièze *et al.*, 2004), or the flat rotation profile observed through helioseismic inversions in the radiation zone (Mathur *et al.* 2008) are two major examples highlighting the necessity to introduce the influence of the rotation, the magnetic field and the internal waves in the equations describing the stellar structure, to reach a complete physical picture of stellar interiors.

We here focus on the impact of a large-scale magnetic field on the stellar structure and we present how the geometry of the magnetic field can be modeled by considering non force-free magneto-hydrostatic (MHS) equilibria using a Grad-Shafranov approach (see also our PNST contribution). This allows us to discuss the relative importance of the various terms associated with the magnetic field. A pertubative treatment is performed on an Ap-type star with an axisymmetric dipolar magnetic field matching at the stellar surface with a potential field. The perturbations of the structural quantities are obtained and the limits of this approach underlined.

2 Non force-free magneto-hydrostatic equilibria

The more natural way to take into account the dynamical processes that might influence the stellar evolution secularly, namely the influence of the rotation and the magnetic field, in a unidimensional stellar evolution code, is to project their respective terms acting upon the structure on the vectorial spherical harmonics basis (Mathis & Zahn 2004, 2005). In the case of the magnetic field however, the poloidal and toroidal components remain arbitrary in the model when initial conditions are considered. Assuming magneto-hydrostatic equilibria provides constraints on these magnetic initial configuration.

Moreover, since observations reveal that about 5 percents of the A-type stars present an external magnetic field organized over large scales, so a magnetic field of dynamo or fossil origin lies certainly in a non-negligible proportion of main sequence star's radiation zones and can probably influence significantly their evolutionary tracks, since they are likely to be non force-free. We provide here a way to model any MHS equilibrium that fulfill all the exposed requirements, by supposing any prescription for the toroidal current.

[1] CEA/DSM/IRFU/SAp, CE Saclay, F-91191 Gif-sur-Yvette Cedex, France; AIM, UMR 7158, CEA - CNRS - Université Paris 7, France

2.1 Axisymmetric magnetic field and Grad-Shafranov-Poisson equation

In the present work, we assume that the magnetic field ($\boldsymbol{B}$) is axisymmetric. In this case we can express its components in function of a poloidal magnetic flux fonction $\Psi(r,\theta)$ and of a toroidal potential function $F(r,\theta)$ ($\hat{\mathbf{e}}_\varphi$ being the azimuthal unit vector) such that $\boldsymbol{B}(r,\theta)$ remains divergenceless :

$$\boldsymbol{B} = \frac{1}{r\sin\theta}\nabla\Psi\times\hat{\mathbf{e}}_\varphi + \frac{1}{r\sin\theta}\,F\,\hat{\mathbf{e}}_\varphi. \tag{2.1}$$

On the other hand, Ampere's law in the MHD classical approximation is given by $\nabla\times\boldsymbol{B} = \mu_0\,\boldsymbol{j}$, where $\boldsymbol{j}$ is the current density and μ_0 the vacuum permeability. Projected along the azimuthal direction, one gets

$$\mu_0\;j_\varphi = \frac{1}{r}\frac{\partial}{\partial r}\left(rB_\theta\right) - \frac{1}{r}\frac{\partial B_r}{\partial\theta}. \tag{2.2}$$

It leads to the Grad-Shafranov-Poisson equation (hereafter called the GSP equation):

$$\Delta^*\Psi = -\mu_0 r\sin\theta\;j_\varphi \quad \text{where} \quad \Delta^*\Psi \equiv \frac{\partial^2\Psi}{\partial r^2} + \frac{\sin\theta}{r^2}\frac{\partial}{\partial\theta}\left(\frac{1}{\sin\theta}\frac{\partial\Psi}{\partial\theta}\right). \tag{2.3}$$

2.2 The current density function

The formalism is derived in order to take as an input of the model any given toroidal current density $j_\varphi(r,\theta)$. Here, to illustrate our purpose a simple function is chosen, taken on the form: $j_\varphi(r,\theta) = j_{\varphi_0}\,j_{\varphi_r}(r)\,j_{\varphi_\theta}(\theta)$. The radial function is taken as $j_{\varphi_r} = \sin\left(\pi r/R_*\right)/\left(\pi r/R_*\right)$ if $0 \le r \le R_*$ (R_* is the star's radius) and $j_{\varphi_r} = 0$ otherwise and the angular function as dipolar: $j_{\varphi_\theta} = \sin\theta$. The magnetic strength B_0 giving the amplitude j_{φ_0} is determined according to the fact that at its maximum, the magnetic pressure is equal to $B_0^2/2\mu_0$.

2.3 Non Force-Free Condition

It is supposed that magnetic fields force-free everywhere, though they are stable, are unlikely to exist in stellar interiors, since such fields require an unrealistic Lorentz force at the stellar surface in order to avoid the field itself to vanish. Let us start then from the non force-free MHS equilibrium :

$$\rho\,\boldsymbol{g} - \nabla P_{\text{gas}} + \boldsymbol{F_{\mathcal{L}}} = \boldsymbol{0}, \tag{2.4}$$

where ρ is the density, $\boldsymbol{g}$ the local gravity field, P_{gas} the gas pressure and $\boldsymbol{F_{\mathcal{L}}} = \boldsymbol{j}\times\boldsymbol{B}$ the Lorentz force.
Requiring the toroidal component of the Lorentz force $F_{\mathcal{L}_\varphi}$ to vanish everywhere writes as $\frac{\partial\Psi}{\partial r}\frac{\partial F}{\partial\theta} - \frac{\partial\Psi}{\partial\theta}\frac{\partial F}{\partial r} = 0$. The non-trivial values for F are thus obtained by setting $F(r,\theta) = F(\Psi)$. For a regular function, we can make a serial expansion $F(\Psi) = \sum_{n=0}^{\infty}\alpha_n\Psi^n$. We only keep the first-order term since the zeroth-order one leads to a singular toroidal magnetic field at the center. Let then consider $F(\Psi) = \alpha\Psi$ where α is taken as $\alpha = 1/R_*$ based on a dimensional analysis. The magnetic field topology is now completely determined by the function Ψ.

2.4 The GSP solutions

We solve the equation (2.3) using the Green's functions method (cf. Morse & Feshbach, 1953; Payne & Melatos, 2008, Duez *et al.*, 2008b). The general expression for the flux function Ψ inside the star is given by

$$\Psi(r,\theta) \;=\sum_{l=0}^{\infty} -\mu_0\,\mathcal{N}_l^{-1}\sin^2\theta\,C_l^{3/2}(\cos\theta)\int_0^{R_*} g_l^*(r',r)\left[\int_0^{\pi} j_\varphi(r',\theta')\,C_l^{3/2}(\cos\theta')\sin^3\theta' d\theta'\right]r'^3 dr', \tag{2.5}$$

where $C_l^{3/2}(\cos\theta)$ is the Gegenbauer polynomial of latitudinal order l and the normalization coefficient is defined by $\mathcal{N}_l = \frac{2(l+1)(l+2)}{(2l+3)}$. For multipolar boundary conditions the Green's function is given by $g_l^*(r,r') = -\frac{1}{(2l+3)}\frac{r^l}{r'^{l+1}}$ if $r < r'$, $g_l^*(r,r') = -\frac{1}{(2l+3)}\frac{r'^{l+2}}{r^{l+3}}$ if $r > r'$.
Outside the star, the expression obtained for the flux function is:

$$\Psi_{\text{ext}}(r,\theta) = \sum_{l=1}^{\infty}\frac{\alpha_l}{l}\sqrt{\frac{2l+1}{4\pi}}\frac{R_*^{l+1}}{r^l}\sin\theta\;P_l^1(\cos\theta), \tag{2.6}$$

$P_l^1(\cos\theta)$ being the associated Legendre polynomial of azimuthal degree $m = 1$. The coefficients α_l are determined so that the internal solution $\Psi_{\text{int}}(r,\theta)$ matches the potential external one $\Psi_{\text{ext}}(r,\theta)$ at $r = R_*$.

3 Hierarchy of the physical quantities aimed to be implemented in a stellar evolution code

3.1 The necessity to take into account the geometrical nature of the field

3.1.1 Goldreich's β parameter

This parameter, defined by Goldreich (1991) as

$$\beta_{\mathrm{Gold.}} = \left(< B_{\mathrm{h}}^2 > - < B_{\mathrm{r}}^2 >\right) / \left(< B_{\mathrm{h}}^2 > + < B_{\mathrm{r}}^2 >\right) \tag{3.1}$$

where the r and h subscripts stand for the vertical and horizontal directions, has been understood by several authors as a parameter aimed to mimic the geometrical effects of the field once implemented in 1D models. Computing this quantity for a given axisymmetric MHS equilibrium (see Fig. 1, left), we show that this quantity has at least to be taken as a function of the radius to reproduce correctly the field's geometry properties.

3.1.2 Magnetic pressure gradient *versus* magnetic tension force

We would like to pinpoint here also the necessity to take into account the whole Lorentz force action on the hydrostatic balance: the one induced by the magnetic pressure gradient $\nabla P_{\mathrm{mag}} \equiv (1/2\,\mu_0)\,\nabla \boldsymbol{B}^2$ as well as the one induced by the magnetic tension force $\boldsymbol{F}_{\mathcal{L}}^{T} \equiv (1/\mu_0)\,(\boldsymbol{B}\cdot\nabla)\,\boldsymbol{B}$. As shown in Fig. 1 (right), the latter is actually required to counterbalance the effects of the former as the field tends toward a force-free state. It is thus a quantity of importance in the vicinity of the axis of symmetry and at the stellar surface where the field has to be force-free for stability reasons.

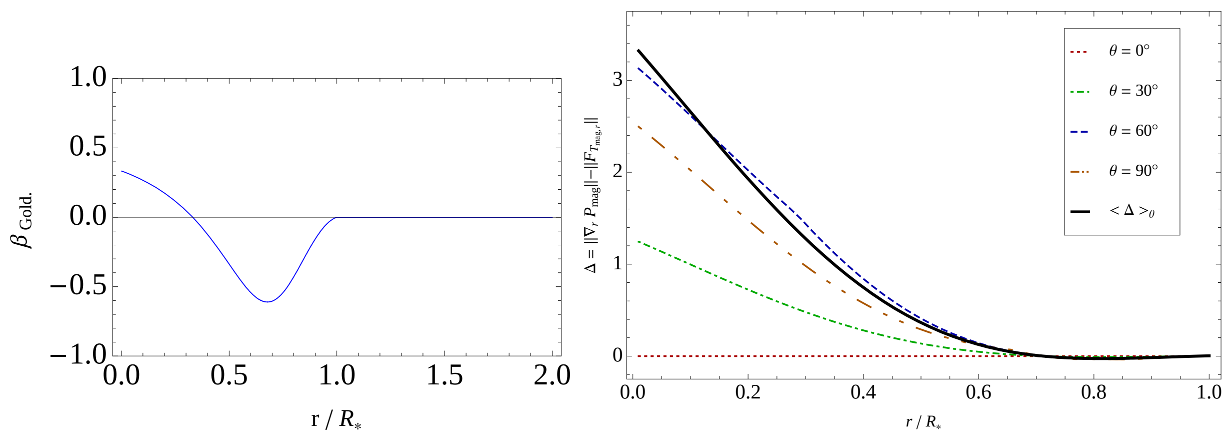

Fig. 1. Left : Amplitude of the parameter $\beta_{\mathrm{Gold.}}$ as a function of the radius. **Right**: Absolute difference Δ between the radial components of the magnetic pressure force and the magnetic tension one (normalized with respect to $B_0^2/\mu_0 R_*$) at several latitudes ($\theta = 0°$, $\theta = 30°$, $\theta = 60°$ and $\theta = 90°$, in dashed lines) and latitudinally-averaged (solid line). Notice that on the axis of symmetry or in the vicinity of the surface, both forces counterbalance each other, leading to a force-free state.

3.2 Perturbations induced on the energetic quantities by a magnetic field on an Ap-star model

The direct contribution of the magnetic field to the change in the energetic balance through ohmic heating or through Poynting's flux is computed by integrating their respective expressions detailed by Duez *et al.* (2008a) over the sphere. It is found that at $r = R_*$ we have $L_* = 3.04\times10^{35}\,\mathrm{erg\,s^{-1}}$, whereas the luminosity generated by ohmic heating is $L_\Omega = 5.39\times10^{24}\mathrm{erg\,s^{-1}}$ and the one generated by the Poynting flux is $L_{\mathrm{Poynt}} = 3.15\times10^{25}\mathrm{erg\,s^{-1}}$. The ratio of the classical luminosity over its magnetic contribution is then at the surface $L_*/\left(L_\Omega + L_{\mathrm{Poynt}}\right) = 8.24\times10^9$, *i.e.* the energetic perturbations are much weaker than the perturbations generated by the Lorentz force. We can then conjecture that a first approach, consisting in limiting the impact of a large-scale magnetic field only to its impact upon the hydrostatic balance will be justified and that the impact of the magnetic terms on the energetic balance is a higher order perturbation.

3.3 Perturbations induced on the structural quantities by a magnetic field on an Ap-star model

A first-order perturbative treatment is performed in the high-β regime ($\beta = \frac{P_{\rm gas}}{P_{\rm mag}}$) to highlight the structural deformations associated with the modification of the hydrostatic equilibrium due to the magnetic field. From our previous remark, the only perturbation taken into account is the one arising from the introduction of the Lorentz force, which is assumed to be weak compared to the gravitational field and to the gaseous pressure gradient. Following Sweet (1950) and Mathis & Zahn (2004, 2005), the equation for the amplitude of the gravitational potential fluctuation $\widehat{\phi}_l$ over the non-magnetic state is derived :

$$\frac{1}{r}\frac{\mathrm{d}^2}{\mathrm{d}r^2}\left(r\widehat{\phi}_l\right) - \frac{l(l+1)}{r^2}\widehat{\phi}_l - \frac{4\pi G}{g_0}\frac{\mathrm{d}\rho_0}{\mathrm{d}r}\widehat{\phi}_l = \frac{4\pi G}{g_0}\left[\mathcal{X}_{\boldsymbol{F}_{\mathcal{L}};l} + \frac{\mathrm{d}}{\mathrm{d}r}\left(r\mathcal{Y}_{\boldsymbol{F}_{\mathcal{L}};l}\right)\right], \tag{3.2}$$

where $\mathcal{X}_{\boldsymbol{F}_{\mathcal{L}};l}$ and $\mathcal{Y}_{\boldsymbol{F}_{\mathcal{L}};l}$ are respectively the projections of the radial and the latitudinal $\boldsymbol{F}_{\mathcal{L}}$ components on the Legendre polynomials (cf. these proceedings, "Impact of Large-Scale Magnetic Fields on Solar Structure").
The expressions for the normalized perturbations in gravitational potential $\tilde{\Phi}_l$, density $\tilde{\rho}_l$, pressure $\tilde{P}_l$ ($\tilde{X}_l = \widehat{X}_l/X_0$), and radius c_l have been derived by Mathis, Le Poncin-Lafitte & Duez (2008) and are shown in Fig. 2 (for the modes $l = 0$ and $l = 2$) in the case of an Ap-type star. For kG fields, despite the weakness of the gravitational multipole moment of order 2, it appears that the first-order approach is insufficient to draw any conclusion about the fluctuations in pressure and density at the stellar surface, since these are higher than their unperturbed values owing to the sudden drop of the latter near the surface. However for weaker field, of about 10^2 lower than the value considered here, the treatment is suitable since the fluctuations are proportional to the squared field amplitude. This sudden increase of the perturbation near the surface is in agreement with the value of the plasma parameter β which is lower than unity in this region, indicating that magnetic effects have a crucial impact on the structure of the subsurface layers of such a star. It is then necessary to implement directly the full set of modified equations including the magnetic field in a stellar evolution code.

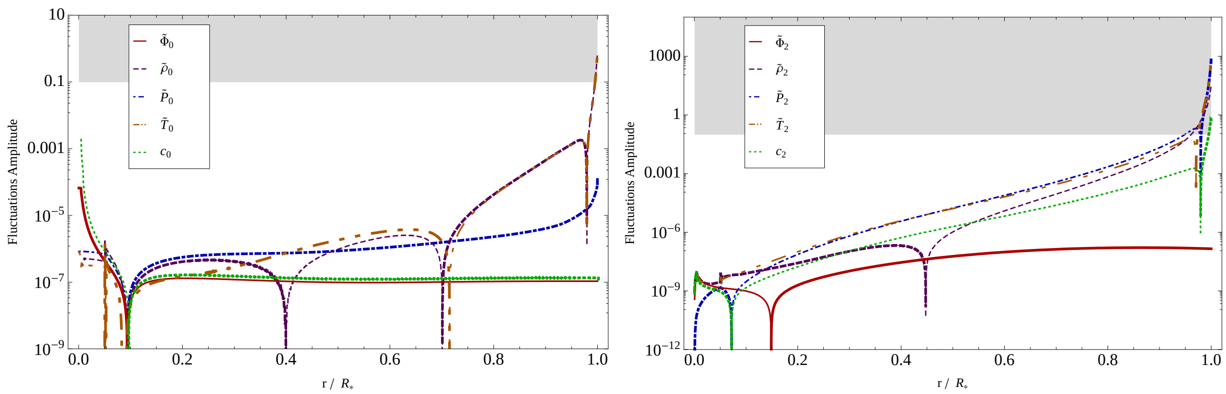

Fig. 2. Normalized modal fluctuations with $l = 0$ (**Left**) and $l = 2$ (**Right**) in gravitational potential, density, pressure, temperature and radius, for a dipolar field in an Ap-type star whose strength at the stellar surface is $B_{\rm surf} = 10\,$kG. Bold lines represent negative values. The gray filled area corresponds to the regime where the perturbative approach is invalid an corresponds to the low-β regime.

References

Duez, V., Brun, A.-S., Mathis, S., Nghiem, P.A.P. & Turck-Chièze, S. 2008, in Mem. S.A.It., 79, 716

Duez, V., Mathis, S., Brun, A.-S. & Turck-Chièze, S. 2008, ApJ (submitted)

Goldreich, P., Murray, N., Willette, G. & Kumar, P. 1991, ApJ, 370, 752

Mathis, S. & Zahn, J.-P. 2004, A&A, 425, 229

Mathis, S. & Zahn, J.-P. 2005, A&A, 440, 653

Mathis, S., Le Poncin-Lafitte, C. & Duez, V. 2008, A&A, in preparation

Mathur, S., Eff-Darwich, A., Garcia, R.A. & Turck-Chièze, S. 2008, A&A, 484, 517

Morse, P. M., Feshbach, H. 1953, Method of Theoretical Physics, McGraw Hill Book Company

Payne, D. J. B. & Melatos, A. 2004, MNRAS, 351, 569

Turck-Chièze, S., Couvidat, S., Piau, L. et al. 2004, Phys. Rev. Let. 93, 21, 1102

SF2A 2008
C. Charbonnel, F. Combes and R. Samadi (eds)

IMPACT OF LARGE-SCALE MAGNETIC FIELDS ON SOLAR STRUCTURE

Duez, V.[1], Mathis, S.[1], Brun, A.-S.[1], Turck-Chièze, S.[1] and Le Poncin-Lafitte, C.[2]

Abstract. We here focus on the impact of large-scale magnetic fields on the solar structure from its core up to its surface by treating semi-analytically the Magneto-HydroStatic (MHS) equilibria of a self-gravitating spherical shell. Then, the modifications of the internal structure of the Sun introduced by such a field are deduced, and the resulting multipolar gravitational moments are obtained.

1 Introduction

With the ongoing development of the Sun-Earth interaction studies and the coming launch of PICARD, it is of primordial importance to get a better understanding of the processes which are at the origin of the solar variability. In particular, since the tachocline can play an important role on the generation of the large-scale magnetic field in the innermost layers of the Sun, conversely the proper modeling of the internal magnetic field can improve our understanding of the fundamental phenomena acting in this region. We here depict how a large-scale magnetic field can have an impact on the solar structure. For this purpose, we consider an internal magnetic field confined below the convection zone by solving a non force-free magneto-hydrostatic (MHS) equilibrium, using a Grad-Shafranov approach. A pertubative treatment is then performed on a solar model, allowing us to derive the amplitude of the fluctuations over the gravitational potential and the thermodynamic quantities at the surface of the Sun for an internal field with a 7MG strength, which is the upper limit proposed by Friedland & Gruzinov (1991) to adjust it to present observables.

2 Formalism

The magnetic field configuration is derived for a field which is assumed to be axisymmetric, in magneto-hydrostatic equilibrium and non force-free following the formalism presented in these proceedings by Duez *et al.* (to which we will refer hereafter as Paper I). The main difference lies in the change of boundary conditions: here the field is assumed to be confined below the convection zone ($r \leq R_b$, where R_b is the radiation-convection border), and the equilibrium modeled is thus similar to the one reached in a spheromak experiment as the toroidal field vanishes at the boundary. However, the main differences with spheromaks experiments where magnetohydrodynamic instabilities tend to reorganize the plasma towards a force-free state are that the Lorentz force does not vanish here and that $\beta \gg 1$ ($\beta = P_{\rm gas}/P_{\rm mag}$). This non force-freeness induces perturbations on the structural quantities by modifying the hydrostatic balance that will be quantified.

2.1 *Magnetic field topology*

The magnetic field is derived as in Paper I, to the exception of the Green's function which are modified owing to the new boundary conditions according to $g_l(r,r') = \frac{1}{(2l+3)}\left[\frac{r'^{l+2}}{R_b^{2l+3}} - \frac{1}{r'^{l+1}}\right] r^l$ if $r < r'$ or $g_l(r,r') = \frac{1}{(2l+3)}\left[\frac{r^l}{R_b^{2l+3}} - \frac{1}{r^{l+3}}\right] r'^{l+2}$ if $r > r'$; thus the flux function Ψ vanishes at $r = R_b$ and so does the magnetic field.

[1] CEA/DSM/IRFU/SAp, F-91191 Gif-sur-Yvette Cedex, France; AIM, UMR 7158, CEA - CNRS - Université Paris 7, France
[2] Observatoire de Paris, SYRTE CNRS/UMR 8630, 61 Avenue de l'Observatoire, F-75014 Paris, France

2.2 Perturbation of the structural quantities

A first-order perturbative treatment is performed in the high-β regime to highlight the structural modifications associated with the adjustment of the hydrostatic equilibrium due to the magnetic field. Our complete study (Duez *et al.*, 2008) has shown that as a first approximation, the only perturbation to take into account is the one arising from the introduction of the Lorentz force which is assumed to be weak compared with the gravitational field and with the gaseous pressure gradient. The equation for the perturbation of the gravific potential is derived following Mathis *et al.* (2008). First, we expand all the quantities X (the gravific potential, the density, the pressure, the temperature) around the non-magnetic state X_0 as $X(r,\theta) = X_0(r) + \sum_{l\geq 0} \widehat{X}_l(r) P_l(\cos\theta)$. Next, the components of the Lorentz force (resp. radial and latitudinal) are projected on the Legendre polynomials:

$$F_{\mathcal{L},r}(r,\theta) = \sum_l \mathcal{X}_{\boldsymbol{F}_{\mathcal{L}};l}(r)\, P_l(\cos\theta) \qquad F_{\mathcal{L},\theta}(r,\theta) = -\sum_l \mathcal{Y}_{\boldsymbol{F}_{\mathcal{L}};l}(r)\, \partial_\theta P_l(\cos\theta)\,. \tag{2.1}$$

The equation ruling the amplitude of the gravific potential perturbation induced by the magnetic field ($\widehat{\phi}_l$) is then given by

$$\frac{1}{r}\frac{\mathrm{d}^2}{\mathrm{d}r^2}\left(r\widehat{\phi}_l\right) - \frac{l(l+1)}{r^2}\widehat{\phi}_l - \frac{4\pi G}{g_0}\frac{\mathrm{d}\rho_0}{\mathrm{d}r}\widehat{\phi}_l = \frac{4\pi G}{g_0}\left[\mathcal{X}_{\boldsymbol{F}_{\mathcal{L}};l} + \frac{\mathrm{d}}{\mathrm{d}r}\left(r\mathcal{Y}_{\boldsymbol{F}_{\mathcal{L}};l}\right)\right] \tag{2.2}$$

while the perturbations of density ($\widehat{\rho}_l$) and of pressure ($\widehat{P}_l$) are obtained: $\widehat{\rho}_l = \frac{1}{g_0}\left[\frac{\mathrm{d}\rho_0}{\mathrm{d}r}\widehat{\phi}_l + \mathcal{X}_{\boldsymbol{F}_{\mathcal{L}};l} + \frac{\mathrm{d}}{\mathrm{d}r}\left(r\mathcal{Y}_{\boldsymbol{F}_{\mathcal{L}};l}\right)\right]$ and $\widehat{P}_l = -\rho_0\widehat{\phi}_l - r\mathcal{Y}_{\boldsymbol{F}_{\mathcal{L}};l}$. Finally, it is interesting to get diagnosis from the stellar radius variation induced by the magnetic field. The definition of the radius of an isobar is then given by: $r_P(r,\theta) = r\left[1 + \sum_{l\geq 0} c_l(r) P_l(\cos\theta)\right]$ where $c_l = -\frac{1}{r}\frac{\widehat{P}_l}{\mathrm{d}P_0/\mathrm{d}r} = \frac{\rho_0}{\mathrm{d}P_0/\mathrm{d}r}\left(\frac{1}{r}\widehat{\phi}_l + \frac{\mathcal{Y}_{\boldsymbol{F}_{\mathcal{L}};l}}{\rho_0}\right)$.

3 Results

Results for the normalized perturbations in gravitational potential $\tilde{\Phi}_l$, density $\tilde{\rho}_l$, pressure $\tilde{P}_l$ (where $\widetilde{X}_l = \widehat{X}_l / X_0$), and radius c_l are shown in Fig. 1 (for the modes $l = 0$ and $l = 2$) for a field's strength of $B_0 = 7\,\mathrm{MG}$. Using the continuity of ϕ at the surface (at $r = R_\odot$), we derive the expression to evaluate the gravitational multipolar moments : $J_l = \left(\frac{R_\odot}{GM_\odot}\right)\widehat{\phi}_l\,(r = R_\odot)$. The surface values are $\tilde{\rho}_0 = -1.67\times 10^{-1}$, $\tilde{P}_0 = -5.91\times 10^{-1}$, $c_0 = -1.17\times 10^{-4}$, $J_0 = 1.17\times 10^{-4}$; $\tilde{\rho}_2 = 2.92\times 10^{-3}$, $\tilde{P}_2 = 1.03\times 10^{-2}$, $c_2 = 2.04\times 10^{-6}$ and $J_2 = -2.05\times 10^{-6}$ which means that the configuration associated with such a dipolar magnetic field is prolate.

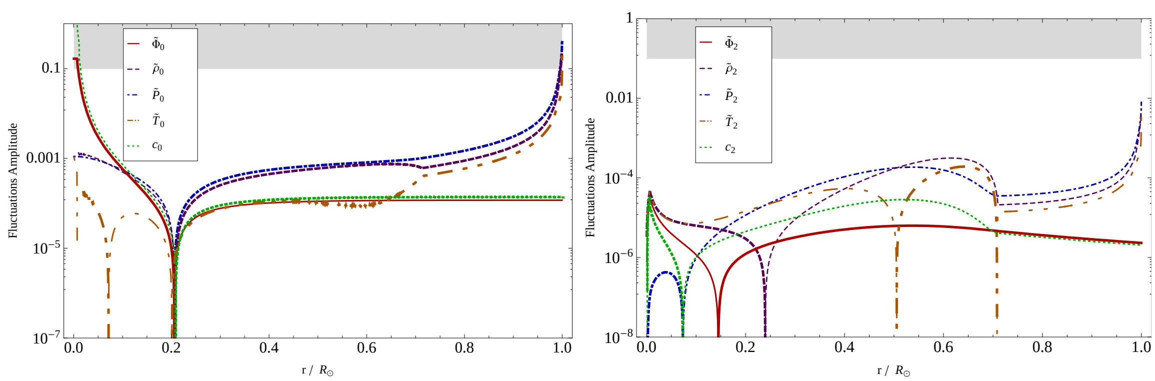

Fig. 1. Normalized modal fluctuations with $l = 0$ (**Left**) and $l = 2$ (**Right**) in gravitational potential, density, pressure, temperature and radius, for a dipolar field buried in the solar radiation zone with a strength of $B_0 = 7\,\mathrm{MG}$.

References

Duez, V., Mathis, S., Brun, A.-S., & Turck-Chièze, S. 2008, ApJ, submitted
Mathis, S., Le Poncin-Lafitte, C., & Duez, V. 2008, A&A, in preparation
Friedland, A., & Gruzinov, A. 2004, ApJ, 601, 570

SF2A 2008
C. Charbonnel, F. Combes and R. Samadi (eds)

THE MAGNETIC FIELD OF THE SUPERGIANT STAR ζ ORI A

Escolano, C.[1], Bouret, J.-C.[2], Donati, J.-F.[3], Martins, F.[4], Lanz, T.[5], Marcolino ,W.[6] and Howarth, I.[7]

Abstract. We present the results obtained on the O9.7 supergiant ζ Ori with the spectropolarimeter NARVAL at the 2M Telescope Bernard Lyot atop Pic du Midi (France). We detected the presence of a weak magnetic field of about 50-100G, making ζ Ori the third O star known to host a magnetic field and the first magnetic O star with a 'normal' rotationnal velocity. The magnetic field of Zeta Ori is the weakest magnetic field ever detected on a massive star and is lower than the thermal equipartition limit (about 100 G). By fitting synthetic spectra (obtained from NLTE stellar atmosphere models), we derived the physical properties of ζ Ori. This lattest is a 40 $M_\odot$ star, with a radius of 25 $R_\odot$ and appears quite evolved with an age of 5-6Myr. Despite its evolutionnary status, ζ Ori does not show signs of nitrogen surface enrichment. Concerning the wind of ζ Ori, we estimated a mass loss rate of about 2×10^{-6} $M_\odot.yr^{-1}$. The magnetic topology of ζ Ori is apparently more complex than a simple dipole and involves two main magnetic polarities located on both sides of the northern hemisphere. Our data also suggest that ζ Ori rotates in about 7.0 days and is about 40 degrees away from pole-on to an Earth-based observer. Despite its weakness, the detected field appears sufficient to affect significantly the wind structure: the corresponding Alfvén radius is however very close to the surface of the star, thus generating a rotational modulation in wind lines different than that reported on the two other known magnetic O stars.

Finally, the rapid rotation of ζ Ori with respect to θ^1 Ori C is surprising since both stars have similar unsigned magnetic fluxes (once rescaled to the same radius). This may indicate that the field of ζ Ori is not a fossil remnant (as opposed to that of θ^1 Ori C and HD191612) but rather the result of exotic dynamo processes produced through MHD instabilities.

1 Introduction

Magnetic fields are detected in a large fraction of cool stars (typically solar-type and later stars), with a complex topology due to dynamo mechanisms occuring in the outer convective layers. In comparison, only a handle of massive stars are known to host a magnetic field, principally chemically peculiar A and B stars. Among O stars, only HD191612 and θ^1 Ori C have a magnetic field.

In massive and luminous stars, it is commonly admitted that the field is not of dynamo origin (the outer layers of these stars being not convective but radiative) but rather a fossil field trapped when the star formed. Theoretical models predict that these fields have a strong impact on the evolution of the star, modifying the internal rotation and enhancing the transport and mixing of species, resulting in a surface chemical enrichment (Maeder & Meynet 2003, 2004, 2005). They can also influence the stellar winds, by confining it along the field lines (ud Doula & Owocki 2002).

Nevertheless, these theoretical findings suffer of a lack of observationnal and statistical support, due to the relative difficulty to detect magnetic fields in the most massive stars. The limited knowledge we have about the

[1] LAM-UMR 6110, CNRS & Univ. de Provence, 38 rue Frédéric Joliot-Curie, F-13388 Marseille cedex 13, France
[2] LAM-UMR 6110, CNRS & Univ. de Provence, 38 rue Frédéric Joliot-Curie, F-13388 Marseille cedex 13, France
[3] LATT-UMR 5572, CNRS & Univ. de Toulouse, 14 Av. E. Belin, F-31400 Toulouse, France
[4] GRAAL-ULR 5024, CNRS & Univ. de Montpellier II, Place Bataillon, F-34095 Montpellier, France
[5] Department of Astronomy, University of Maryland, College Park, MD 20742, USA
[6] LAM-UMR 6110, CNRS & Univ. de Provence, 38 rue Frédéric Joliot-Curie, F-13388 Marseille cedex 13, France
[7] Dept. of Physics and Astronomy, University College London, Gower Street, London WC1E6BT, UK

existence and the statistical properties of magnetic fields in massive O stars is mostly due to the fact that these fields are difficult to detect. Absorption lines of O stars are both relatively few in number in the optical domain, and generally rather broad, decreasing dramatically the size of the Zeeman signatures that their putative fields can induce. With the advent of the new generation spectropolarimeters, such as ESPADONS at CFHT and NARVAL at TBL, detection of the expectedly weak magnetic fields in massive stars becomes within range.

In this context we embarked in october 2007 a campaign of detection of magnetic fields in massive O stars, using the spectropolarimeter NARVAL. Among the observed stars, we found a magnetic field in the O9.7 supergiant ζ Ori. We present here the results obtained from the spectropolarimetric analysis of this star.

2 Observations

ζ Ori A was observed during seven nights in 2007, from October 18 to October 25; the spectropolarimetric observations were collected with NARVAL at TBL and the spectropolarimetric data were reduced with the fully automatic reduction package Libre ESpRIT (Donati et al. 1997; Donati et al., in prep). The spectra cover wavelengths between 370 and 1050 nm and the resolving power is R=65000. In total, 292 circular-polarization sequences were obtained, each consisting of four individual subexposures taken in different polarimeter congurations. We applied Least-Squares Deconvolution (LSD; Donati et al. 1997) to all observations, with a line list especially constructed for ζ Ori, keeping only the lines unaffected by wind contributions (emission, shift in wavelength). From those lines we produced a mean circular polarization profile (LSD Stokes V profile), a mean check (N for null) profile and a mean unpolarized profile (LSD Stokes I profile) for each spectrum. On Oct. 24, the detection probability exceeds 99%, with a reduced-χ^2 value (compared to a null-field, $V = 0$ profile) of 1.33. Similar (though less clear) Zeeman signatures are also observed during the other nights.

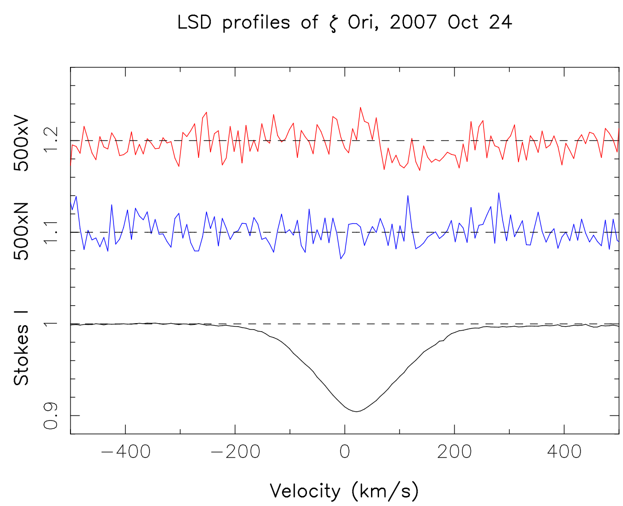

Fig. 1. LSD Stokes V (top), null N (middle) and Stokes I profiles of ζ Ori acquired on october 24. The V and N profiles are expanded by a factor 500 and shifted upwards by 1.2 and 1.1 respectively for more clarity. We can observe a Zeeman signature in the Stokes V profile while the null profile does not show spurious signal.

3 Spectral analysis: physical parameters

We performed the (unpolarized) spectral analysis with NLTE, line-blanketed models calculated with the radiative transfer code CMFGEN (Hillier & Miller 1998; Hillier et al. 2003). Effective temperature was derived from HeI and HeII photospheric lines while surface gravity was derived from the wings of hydrogen Balmer lines (H_δ, H_β and H_ϵ). We gave particular interest to CNO abundances, which were derived from the photospheric lines of each element. An interesting point is that ζ Ori does not show any enrichment in nitrogen or depletion in carbon. The wind parameters ($\dot{M}$ in particular) were derived from the H_α profile. Since this profile showed variations throughout the run, we derived a maximum and a minimum value of the mass loss rate $\dot{M}$ when H_α presented a maximum (respectively minimum) emission (Fig. 2).

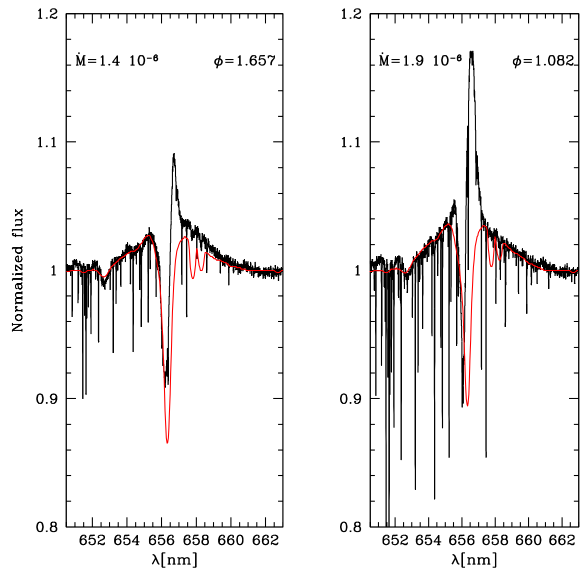

Fig. 2. Example of determination of the stellar parameters, here the minimum and the maximum mass loss rates based on the wings of the H_α profile. In black bold line is represented the spectrum observed with Narval and the red line is our best fit model.

Spectral type	O9.7 Ib
Distance (pc)	414.
Rotation Period (d)	7.0
v sin i (km.s^{-1})	110.
T_{eff} (K)	29500
log g (cgs)	3.25
log L ($L_\odot$)	5.7
M_* ($M_\odot$)	48.
ξ_t (km.s^{-1})	10.
$\dot{M}$ ($M_\odot$.yr^{-1})	1.4 - 1.9
v_∞ (km.s^{-1})	2100.
f_∞	0.1
v_{cl} (km.s^{-1})	200.
v_{rad} (km.s^{-1})	45.
y	0.1
C/$C_\odot$	1.
N/$N_\odot$	1.
O/$O_\odot$	0.5

Fig. 3. Summary of the physical parameters derived from the spectral analysis.

Fourier transforms of photospheric lines indicate a rotationnal velocity of 110 km.s^{-1}. In addition we estimated a rotation period of 7 days based on the cycle of variations of different lines. This implies that ζ Ori is seen at 40 degrees away from pole-on to an Earth-based observer.

4 Spectropolarimetric analysis: magnetic field

The Zeeman signatures were modelled with the imaging code designed by Donati et al. (2006). The code reconstructs the magnetic topology at the surface of the star using spherical harmonics expansion. The reconstruced field is mapped in Fig. 4, assuming either a simple dipole field or a more complex magnetic geometry (limited to $\ell = 3$). The second, more complex, topology was preferred since it provides a unit χ^2_ν fit to the data while a simple dipole gave a χ^2_ν significantly larger than 1. The reconstructed magnetic field has a strength of ± 61 G and an inclination angle of 83 degrees with respect to the rotation axis.

Calculation of the wind confinment parameter showed that the magnetic field measured on ζ Ori is just sufficient not to confine, but to distort the wind, which is compatible with the observed variability in H_α profile and some other lines.

When compared to the other two massive magnetic stars, one would expect ζ Ori to rotate, if not as slowly as HD 191612 (whose intrinsic magnetic flux is much higher), at least more slowly than θ^1 Ori C (whose intrinsic magnetic flux is similar) given its later evolution stage; this is however not what we observe. No more than speculations can be proposed at this stage. One possibility is that the magnetic field of ζ Ori is not of fossil origin (as opposed to that of θ^1 Ori C and HD 191612) but rather dynamo generated, making the rotational evolution of ζ Ori and θ^1 Ori C hardly comparable. The detected magnetic field is indeed much weaker than the critical limit above which MHD instabilities are inhibited (about six times the equipartition field or 600 G in the case of ζ Ori (Aurière et al. 2007) and may thus result from exotic dynamo action; the non-dipolar nature of the detected field could be additional evidence in favour of this interpretation, fossil fields being expected to have very simple topologies in evolved stars.

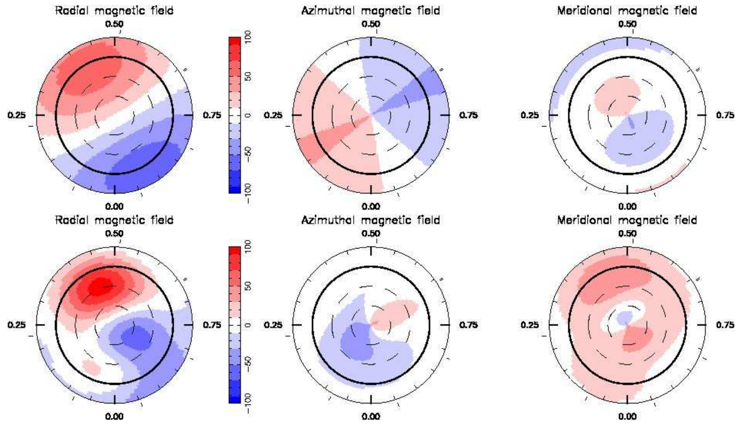

Fig. 4. Reconstructed magnetic topology of ζ Ori. The top figure assumes a dipolar field while the bottom figures assumes a more complex topology. For each topology, the three field components are displayed from left to right and the fluxes are labelled in G. The star is represented in flattened polar projection. The equator is represented by the bold circle and the parallels in dashed lines. The radial ticks depicted around each plot represent the phases of observations.

5 Conclusion

We made a complete spectropolarimetric analysis of the supergiant O9.7 star ζ Ori. We derived its stellar and wind parameters and highlighted the presence of a magnetic field. It is clear that this magnetic field has an impact on the wind of ζ Ori, through the spectral modulations we observed. The different characteristics of the field also ask the question of its origin; while a fossil field is generally admitted for massive stars, the field of ζ Ori would be likely dynamo generated.

New observations through several periods are necessary to confirm and expand our results, allowing a more precise determination of the rotation period and giving more constraints on the magnetic topology of ζ Ori. Moreover, this will bring informations on an hypothetic variation of the magnetic strength on a timescale of one year.

References

Aurière M., Wade G.A., Silvester J., Lignières F., Bagnulo S., Bale K., Dintrans B., Donati J.F., Folsom C. P., & Gruberbauer M. 2007, A&A, 475, 1053

Bouret, J.-C., Donati, J.-F., Martins, F., Escolano, C., Marcolino, W., Lanz, T., & Howarth, I. D., 2008, MNRAS, 389, 75

Donati, J.-F., & Brown S. 1997, A&A, 326, 1135

Donati, J.-F., Semel M., Carter B. D., Rees D. E., & Collier Cameron A. 1997, MNRAS, 291, 658

Donati J.-F., Howarth I., Jardine M., Petit P., Catala C., Landstreet J., Bouret J.-C., Alecian E., Barnes J., Forveille T., Paletou F., & Manset N. 2006, MNRAS, 370, 629

Hillier D.J., Lanz T., Heap S.R., Hubeny I., Smith L.J., Evans C.J., Lennon D.J., & Bouret J.C. 2003, ApJ, 588, 1039

Hillier D.J., & Miller D.L. 1998, ApJ, 496, 407

Maeder A., & Meynet G. 2003, A&A, 411, 543

Maeder A., & Meynet G. 2004, A&A, 422, 225

Maeder A., & Meynet G. 2005, A&A, 440, 1041

ud-Doula A., & Owocki S. P., 2002, ApJ, 576, 413

SF2A 2008
C. Charbonnel, F. Combes and R. Samadi (eds)

CONVECTIVE MIXING AND DUST CLOUDS IN BROWN DWARF ATMOSPHERES

Freytag, B.[1], Allard, F.[1], Ludwig, H.-G.[2], Homeier, D.[3], Steffen, M.[4] and Sharp[1], C.

Abstract. To investigate the mechanism that controls the formation and gravitational settling of dust grains as well as the mixing of fresh condensable material into the atmosphere of brown dwarfs, we performed 2D radiation-hydrodynamics simulations with CO5BOLD. We find that direct convective overshoot does not play a major role. Instead, the mixing in the clouds is controlled by gravity waves.

1 Introduction

Temperatures in the atmospheres of brown dwarfs are so low that dust particles can form. These grains should sink under the influence of gravity into deeper layers and vanish from the atmosphere clearing it from condensable material. However, observed spectra can only be reproduced by models accounting for dust formation and its resulting greenhouse effect in the visible layers. The approaches to model dust within classical 1D hydrostatic stellar atmosphere models presented in Helling et al. (2008) all rely on not well justified assumptions about the extent of the cloud layers or the amount of mixing. Time-dependent RHD models can describe self-consistently the mixing of material beyond the classical boundaries of a convection zone, as demonstrated for instance for main-sequence A-type stars (Freytag et al. 1996) or for M dwarfs (Ludwig et al. 2002, 2006).

2 Radiation-hydrodynamics simulations including dust

We performed 2D radiation-hydrodynamics simulations of brown dwarf atmospheres with CO5BOLD, see Freytag et al. (2002), Wedemeyer et al. (2004). The adopted dust scheme is based on a simplified version of the dust model used in Höfner et al. (2003). It includes a simple treatment of the formation and destruction of Forsterite as well as its gravitational settling, its advection, and its interaction with the radiation field.

There is a clear separation between the convection zone in the lower part and the atmosphere with inhomogeneities induced by gravity waves in the upper half of Fig. 1. As shown in Fig. 2 (left panel) the convective velocities fall significantly from the peak value inside the convection zone (on the right) to the top of the unstable layers, and even further (overshooting region). The scale height of *exponentially decreasing overshoot velocities* is so small that they do not induce significant mixing in the cloud layers. Above a local minimum in the vertical velocities, *gravity waves* dominate, instead. Their mixing efficiency increases rapidly with height – not only due to the increase in amplitude but also due to the increasing non-linearity. Figure 2 (center) shows the vertical extent of the dust clouds. At temperatures just low enough to allow the onset of dust formation, local temperature fluctuations modulate the dust density on short time scales given by the typical wave period. This leads to a *variation in the vertical thickness of the clouds*. In layers within the clouds, temperatures fluctuate causing evaporation/condensation cycles. Grain settling is balanced by *mixing induced by gravity waves*. However, at some height, the gravitational settling of dust grains becomes more efficient than the mixing and dust density and opacity drop rapidly. At the top of the clouds, braking waves occur and a local *dust convection zone* is forming. The influence of dust onto the temperature structure is demonstrated in Fig. 2 (right panel).

[1] Centre de Recherche Astrophysique de Lyon, UMR 5574: CNRS, Université de Lyon, École Normale Supérieure de Lyon, 46 allée d'Italie, F-69364 Lyon Cedex 07, France
[2] Observatoire de Paris-Meudon, GEPI-CIFIST, 92195 Meudon, France
[3] Institut für Astrophysik Göttingen, Georg-August-Universität, Friedrich-Hund-Platz 1, D-37077 Göttingen, Germany
[4] Astrophysikalisches Institut Potsdam, An der Sternwarte 16, D-14482 Potsdam, Germany

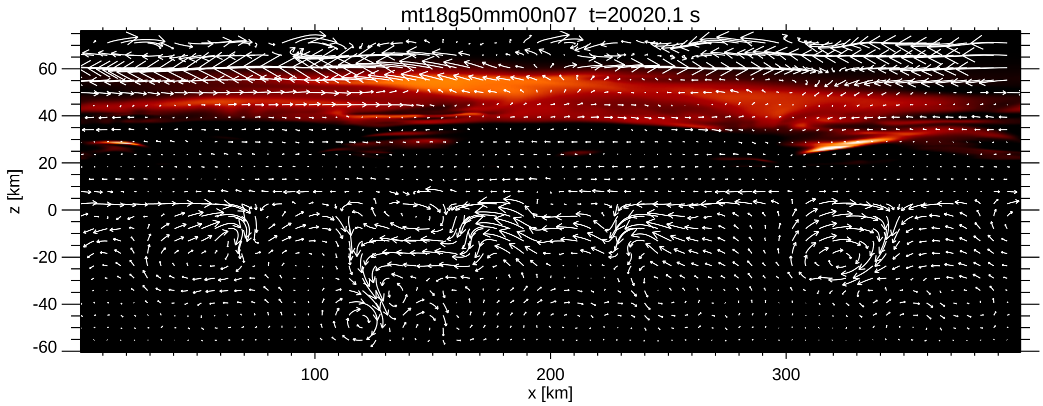

Fig. 1. This snapshot from a brown dwarf simulation with $T_{\rm eff}$=1858 K, log g=5 shows the velocity field as pseudo-streamlines and color-coded the dust concentration.

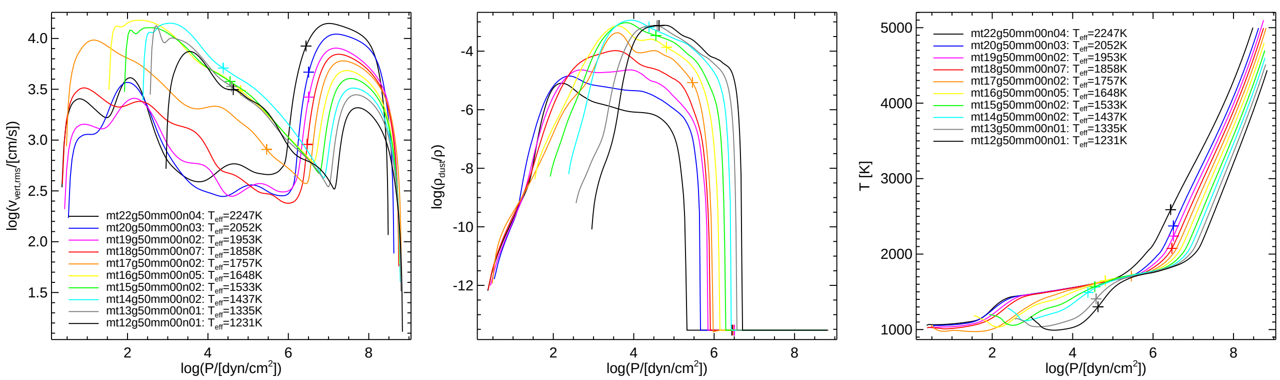

Fig. 2. Various quantities over logarithm of pressure for various effective temperatures (see legend) and log g=5. The plus signs mark the layers with Rosseland optical depth unity. From left to right: logarithm of rms vertical velocity, logarithm of dust concentration, mean temperature.

3 Conclusions

Our 2D radiation hydrodynamical models of brown dwarf atmospheres show that – instead of exponentially declining overshoot – gravity waves dominate the mixing of the upper atmospheric layers with amplitudes growing with height. The induced mixing is sufficient to balance the settling of dust grains. Dust concentration and cloud thickness are modulated by the waves.

Models with higher effective temperature show a high-altitude haze of optically thin clouds. At lower effective temperatures thick and dense clouds exist – but mostly below the visible layers, that are essentially depleted of the material that went into the dust. In between, dust is an important opacity source in the atmosphere.

References

Freytag, B., Ludwig, H.-G., & Steffen, M. 1996, A&A, 313, 497

Freytag, B., Steffen, M., & Dorch, B. 2002, Astronomische Nachrichten, 323, 213

Helling, C., Ackerman, A., Allard, F., et al. 2008, MNRAS, accepted, ArXiv e-prints, 809

Höfner, S., Gautschy-Loidl, R., Aringer, B., & Jørgensen, U. G. 2003, A&A, 399, 589

Ludwig, H.-G., Allard, F., & Hauschildt, P. H. 2002, A&A, 395, 99

Ludwig, H.-G., Allard, F., & Hauschildt, P. H. 2006, A&A, 459, 599

Wedemeyer, S., Freytag, B., Steffen, M., Ludwig, H.-G., & Holweger, H. 2004, A&A, 414, 1121

SF2A 2008
C. Charbonnel, F. Combes and R. Samadi (eds)

DIRECT NUMERICAL SIMULATIONS OF THE κ-MECHANISM

Gastine, T.[1] and Dintrans, B.[1]

Abstract. We present a purely-radiative hydrodynamic model of the κ-mechanism that sustains radial oscillations in Cepheid variables. We determine the physical conditions favourable for the κ-mechanism to occur by the means of a configurable hollow in the radiative conductivity profile. By starting from these most favourable conditions, we complete nonlinear direct numerical simulations (DNS) and compare them with the results given by a linear-stability analysis of radial modes. We find that well-defined instability strips are generated by changing the location and shape of the conductivity hollow. For a given position in the layer, the hollow amplitude and width stand out as the key parameters governing the appearance of unstable modes driven by the κ-mechanism. The DNS confirm both the growth rates and structures of the linearly-unstable modes. The nonlinear saturation that arises is produced by intricate couplings between the excited fundamental mode and higher damped overtones. These couplings are measured by projecting the DNS fields onto an acoustic subspace built from regular and adjoint eigenvectors and a 2:1 resonance is found to be responsible for the saturation of the κ-mechanism instability.

1 Introduction

Eddington (1917) discovered an excitation mechanism of stellar oscillations that is related to the opacity in ionisation regions: the κ-mechanism. This mechanism can only occur in regions of a star where the opacity varies so as to block the radiative flux during compression phases (Zhevakin 1953; Cox 1958). Ionisation regions correspond to a strong increase in opacity, leading to the "opacity bumps" that are responsible for the local driving of modes. These ionisation regions have nevertheless to be located in a very precise region of a star, neither too close to the surface nor to deep into the stellar core, in order to balance the damping that occurs in other regions. It defines the so-called *transition region* which is the limit between the quasi-adiabatic interior and the strongly non-adiabatic surface. For classical Cepheids that pulsate on the fundamental acoustic mode, this transition region is located at a temperature $T \simeq 40\,000$ K corresponding to the second helium ionisation (Baker & Kippenhahn 1965). However, the bump location is not solely responsible for the acoustic instability. A careful treatment of the κ-mechanism would involve dynamical couplings with convection, metallicity effects and realistic equations of state and opacity tables (Bono et al. 1999). The purpose of our model is to simplify the hydrodynamic approach while retaining the *leading order* phenomenon -the opacity bump location- such that feasible DNS of the κ-mechanism can be achieved.

2 Hydrodynamic model

We focus our study on radial modes propagating in Cepheids and thus only consider the 1-D case. Our model represents a *local zoom* about an ionisation region and is composed by a monatomic and perfect gas ($\gamma = c_p/c_v = 5/3$), with both a constant gravity $\vec{g}$ and a constant kinematic viscosity ν. The ionisation region is represented by a parametric conductivity hollow that mimics a bump in opacity as (Gastine & Dintrans 2008a):

$$K_0(T) = K_{\max}\left[1 + \mathcal{A}\frac{-\pi/2 + \arctan(\sigma T^+ T^-)}{\pi/2 + \arctan(\sigma e^2)}\right] \text{ with } \mathcal{A} = \frac{K_{\max} - K_{\min}}{K_{\max}} \text{ and } T^\pm = T - T_{\text{bump}} \pm e, \quad (2.1)$$

where T_{bump} is the hollow position in temperature, while σ, e and $\mathcal{A}$ denote its slope, width and relative amplitude, respectively. Examples of common values of these parameters are provided in Fig. 1.

[1] Laboratoire d'Astrophysique de Toulouse-Tarbes, CNRS et Université de Toulouse, 14 avenue Edouard Belin, F-31400 Toulouse, France

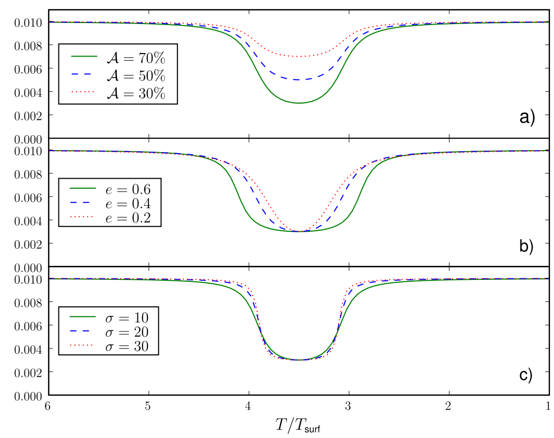

Fig. 1. Influence of the hollow parameters on the conductivity profile for $K_{\max} = 10^{-2}$ and $T_{\rm bump} = 3.5$: amplitude $\mathcal{A}$ (**a**), width e (**b**) and slope σ (**c**).

3 Linear stability analysis

We are interested in small perturbations about the hydrostatic and radiative equilibria. The layer is fully radiative and the radiative flux perturbation reads under the diffusion approximation:

$$\vec{F}' = -K_0\vec{\nabla}T' - K'\vec{\nabla}T_0, \tag{3.1}$$

where the "0" subscripts mean equilibrium quantities and primes denote Eulerian ones. The linearised perturbations obey to the following dimensionless equations:

$$\left\{\begin{array}{lcl} \lambda T' &=& \dfrac{\gamma}{\rho_0}\left(K_0\dfrac{d^2T'}{dz^2} + 2\dfrac{dK_0}{dz}\dfrac{dT'}{dz} + \dfrac{d^2K_0}{dz^2}T'\right) - (\gamma-1)T_0\dfrac{du}{dz} + \dfrac{F_{\rm bot}}{K_0}u, \\ \lambda u &=& -\dfrac{\gamma-1}{\gamma}\left(\dfrac{dT'}{dz} + \dfrac{d\ln\rho_0}{dz}T' + T_0\dfrac{dR}{dz}\right) + \dfrac{4}{3}\nu\left(\dfrac{d^2u}{dz^2} + \dfrac{d\ln\rho_0}{dz}\dfrac{du}{dz}\right), \\ \lambda R &=& -\dfrac{du}{dz} - \dfrac{d\ln\rho_0}{dz}u, \end{array}\right. \tag{3.2}$$

where $R \equiv \rho'/\rho_0$ denotes the density perturbation, u the velocity, $F_{\rm bot}$ the imposed bottom flux. We seek normal modes of the form $\exp(\lambda t)$ with $\lambda = \tau + i\omega$ (unstable modes correspond to $\tau > 0$).

In order to investigate the influence of the hollow shape on stability, we fix the value of σ and vary the other parameters ($T_{\rm bump}$, $\mathcal{A}$ and e). For each case, we first compute the equilibrium fields and second, the eigenvalues with their corresponding eigenvectors are completed using the LSB spectral solver (Valdettaro et al. 2007). Figure 2 displays the obtained instability strips for the fundamental mode and two main results appear: (i) a particular region in the layer ($T_{\rm bump} \in [1.8, 2.3]$) favours the appearance of unstable modes; (ii) both a minimum width and amplitude ($e_{\min} \simeq 0.15$ and $\mathcal{A}_{\min} \simeq 45\%$) are needed to destabilise the system.

4 Direct numerical simulations

To confirm the instability strips discovered previously in the linear-stability analysis, we perform direct numerical simulations of the *nonlinear* problem. We start from the favourable initial conditions determined by the previous parametric surveys and advance in time the hydrodynamic equations thanks to the high-order finite-difference Pencil Code[2].

[2]See `http://www.nordita.org/software/pencil-code` and Brandenburg & Dobler (2002).

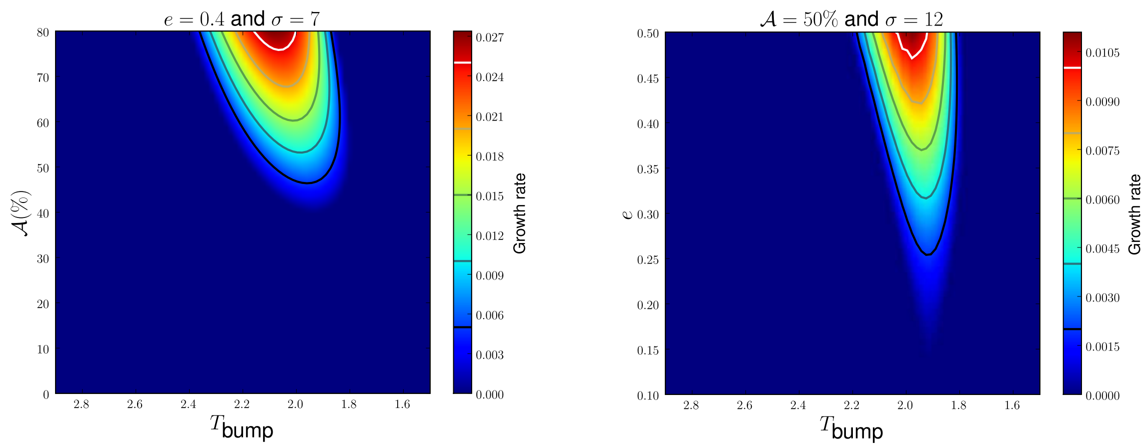

Fig. 2. *Left panel*: Instability strip for the fundamental mode in the plane ($T_{\rm bump}$, $\mathcal{A}$) for $e = 0.4$, $\sigma = 7$. *Right panel*: Instability strip for the fundamental mode in the plane ($T_{\rm bump}$, e) for $\mathcal{A} = 50\%$, $\sigma = 12$.

To determine which modes are present in the DNS in the nonlinear-saturation regime, we first perform a temporal Fourier transform of the momentum field $\rho u(z,t)$ and plot the resulting power spectrum in the (z,ω)-plane (Fig. 3a, left). With this method, acoustic modes are extracted because they emerge as "shark fin profiles" about definite eigenfrequencies (Dintrans & Brandenburg 2004). We next integrate $\widehat{\rho u}(z,\omega)$ over depth to obtain the mean spectrum (Fig. 3b, left). Several discrete peaks corresponding to normal modes appear but the fundamental mode close to $\omega_0 = 5.439$ clearly dominates. Finally, the linear eigenfunctions are compared to the mean profiles computed from a zoom taken in the DNS power spectrum about eigenfrequencies $\omega_0 = 5.439$ and $\omega_2 = 11.06$ (Fig. 3c, left).The agreement between the linear-stability analysis (eigenfunctions in dotted blue lines) and the DNS (profiles in solid black lines) is remarkable. In summary, Fig. 3 (left) shows that several overtones are present in this DNS, even for long times. However, because these overtones are linearly stable, some underlying energy transfers must occur between modes through nonlinear couplings.

To study this nonlinear interaction, we adopt a powerful method already used to study the sound generation by airplanes in aeroacoustics or by compressible convection in astrophysics (Bogdan et al. 1993). It is based on the projection of the DNS fields onto a basis shaped from the regular and adjoint eigenvectors that are solutions to the linear-oscillation equations. By using projections onto these two respective sets of eigenvectors, the time evolution of each acoustic mode propagating in the DNS is obtained. The kinetic energy content of each mode is also available in this formalism, highlighting the energy transfer between modes. As our problem only consists in an initially static radiative zone, the velocity field that develops is only due to acoustic modes, that is,

$$E_{\rm kin}^{\rm tot} = E_{\rm waves} = \sum_{n=0}^{\infty} E_n, \tag{4.1}$$

where E_n, is the energy contained in the n-acoustic mode.

The right panel of Fig. 3 displays the time evolution of the kinetic energy content $E_n/E_{\rm kin}^{\rm tot}$ for $n \in [\![0,\ 6]\!]$. After the linear transient growth of the fundamental mode, a given fraction of energy is progressively transferred to upper overtones and the nonlinear saturation is achieved above $t \simeq 150$. These nonlinear couplings mainly involve the $n = 0$ and $n = 2$ modes because their energy ratios are dominant (more than 98% of the total energy). The reason for this favored coupling lies in the period ratio existing between these two modes: the fundamental period is $P_0 = 2\pi/\omega_0 \simeq 1.155$, while the $n = 2$ one is $P_2 \simeq 0.568$ such that the corresponding period ratio is close to one half ($P_2/P_0 \simeq 0.491$). This $n = 2$ mode, which represents about 10% of the total kinetic energy, is involved in the nonlinear saturation of the κ-mechanism instability through a 2:1 resonance with the fundamental mode. Such a resonance is usual in celestial mechanics with, e.g., Jupiter's moons Io ($P = 1.769$d), Europa ($P = 3.551$d) and Ganymede ($P = 7.154$d) and it is well known that it helps to stabilise orbits. In our case, this stabilisation takes the form of a nonlinear saturation: the linear growth of the fundamental mode is balanced by the pumping of energy from the linearly-stable second overtone behaving in that case as an energy sink, leading to the full limit-cycle stability.

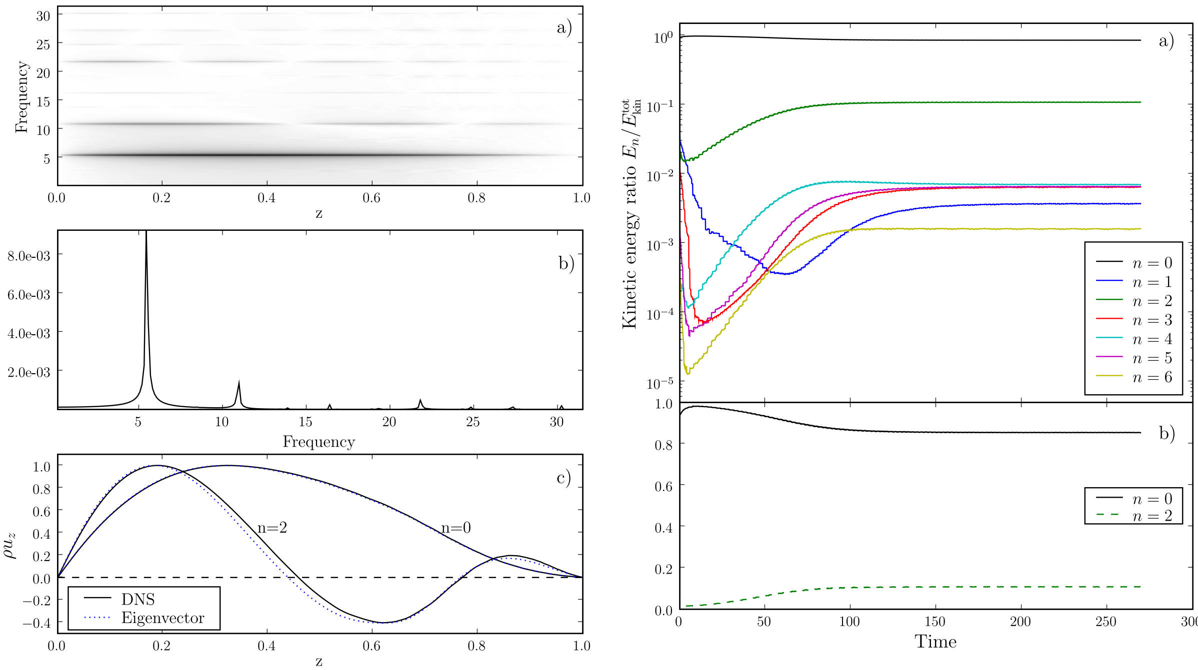

Fig. 3. *Left panel*: a) Temporal power spectrum for the momentum in the $(z,\ \omega)$ plane. **b)** The resulting mean spectrum after integrating in depth. **c)** Comparison between normalised momentum profiles for $n = (0,\ 2)$ modes according to the DNS power spectrum (solid black lines) and the linear-stability analysis (dotted blue lines). *Right panel*: a) Kinetic energy ratio for $n \in [\![0,\ 6]\!]$ in a logarithmic y-scale. **b)** Zoom for the $n = 0$ and $n = 2$ modes only.

5 Conclusion

Direct numerical simulations (DNS) of the κ-mechanism that excite stellar oscillations are performed. We first compute the most favourable setups using a linear-stability analysis of radial modes propagating in a 1-D layer of gas. In our model, a configurable hollow in the radiative conductivity profile mimics the opacity bump responsible for the layer destabilisation. The instability strips found in the linear study are outstandingly confirmed by the DNS and we show that the nonlinear saturation that arises involves a 2:1 resonance between the linearly-unstable fundamental mode and the linearly-stable second overtone.

References

Baker, N. & Kippenhahn, R. 1962, Zeitschrift für Astrophysik, 54, 114

Bogdan, T. J., Cattaneo, F., & Malagoli, A. 1993, ApJ, 407, 316

Bono, G., Marconi, M., & Stellingwerf, R. F. 1999, ApJS, 122, 167

Brandenburg, A. & Dobler, W. 2002, CoPhC, 147, 471 [`arXiv:astro-ph/0111569`]

Cox, J. P. 1958, ApJ, 127, 194

Dintrans, B. & Brandenburg, A. 2004, A&A, 421, 775 [`arXiv:astro-ph/0311094`]

Eddington, A. S. 1917, The Observatory, 40, 290

Gastine, T. & Dintrans, B. 2008, A&A, 484, 29 [`arXiv:astro-ph/0711.1276`]

Gastine, T. & Dintrans, B. 2008, A&A, in press [`arXiv:astro-ph/0804.0345`]

Valdettaro, L., Rieutord, M., Braconnier, T. & Fraysse, V. 2007, JCoAM, 205, 382 [`arXiv:physics/0604219`]

Zhevakin, S. A. 1953, Russ. A. J., 30, 161

SF2A 2008
C. Charbonnel, F. Combes and R. Samadi (eds)

FIRST RESULTS ON BE STARS WITH COROT

Gutiérrez-Soto, J.[1,2], Neiner, C.[2], Hubert, A.-M.[2], Floquet, M.[2], Huat, A.-L.[2], Diago, P. D.[3], Fabregat, J.[2,3], Leroy, B.[1], de Batz, B.[2], Andrade, L.[4], Emilio, M.[5], Facanha, W.[4], Frémat, Y.[6], Janot-Pacheco, E.[4], Martayan, M.[2,6], Suso, J.[3] and Garrido, R.[7]

Abstract. In this paper we present an overview of the analysis of some of the Be stars observed with the CoRoT satellite up to this date. Be stars are very fast-rotating B-type stars which may pulsate as β Cephei or SPB stars. CoRoT has already observed 5 bright Be stars in the seismology fields and several tens of fainter ones in the exoplanet fields with an unprecedented quality and with a time duration from 20 to 150 days. Multiple frequencies are detected in the majority of the stars. Pulsations, outbursts, beating phenomenon, rotation, amplitude variability, etc. have been found in their light curves. In order to complement this study, ground-based spectroscopic data have also been analysed for the stars located in the seismology fields.

1 Introduction

Be stars are non-supergiant B stars that show or have shown at one or another moment emission in Balmer lines. It is generally agreed that the origin of this emission is the presence of an equatorial circumstellar disk, fed by discrete mass-loss events. For a complete review of the Be phenomenon and its properties, see Porter & Rivinius (2003).

Short-term variations are present in these stars due to non-radial pulsations or/and rotational modulation. The spectroscopic analysis led by Rivinius et al. (2001) of μ Cen suggested that non-radial pulsations combined to the near break-up rotational velocity are probably the mechanism responsible for the mass ejection. However, μ Cen is, up to now, the only known Be star for which this behaviour could be shown.

Recently, the Canadian mission MOST observed during several weeks 5 Be stars with spectral types ranging from 09.5V to B8V. Modes typical of β Cep and/or SPB stars have been identified, suggesting that pulsations are present in all rapidly rotating Be stars (see eg. Saio et al. 2007).

The observation of Be stars with the CoRoT satellite (Baglin et al. 2002) is providing photometric time series with an unprecedented quality that will allow us to perform a deep study of the role of non-radial pulsations and their relation with the Be star outbursts. The CoRoT mission is providing 5 months of continuous observations of 1 or 2 bright Be stars (seismo fields) per long run. In addition, CoRoT is observing simultaneously many faint Be stars (exo fields) per long run. Moreover, some bright and faint stars are being observed during shorter periods of observations (short runs).

Here we present the first results obtained from the analysis of the light curves of the Be stars observed with CoRoT in the exo fields during the initial run (IR1) in the Galactic anticenter direction as well as in the seismo fields in the first short run (SRC1) and long run (LRC1) in the Galactic center direction.

[1] LESIA, Observatoire de Paris
[2] GEPI, Observatoire de Paris
[3] Observatori Astronòmic de la Universitat de València
[4] University of Sao Paulo, Brazil
[5] Universidade Estadual de Ponta Grossa, Brazil
[6] Royal Observatory of Belgium
[7] Instituto de Astrofísica de Andalucía

2 Results

2.1 SEISMO fields

The analysis of two Be stars observed in the seismology fields of CoRoT, namely HD 181231 and HD 175869, are presented in this section.

HD 181231 is a B5IVe star that showed low-amplitude variability with a frequency at 0.67 c d^{-1} from ground-based observations (Gutiérrez-Soto et al. 2007). The CoRoT light curve of 156.6 days shows a beating due to the presence of multiple frequencies. About 30 significant frequencies have been detected. The three largest-amplitude frequencies are 1.24, 0.62 and 0.69 c d^{-1}, with semi-amplitudes of 1.6, 1.2 and 1.1 mmag respectively. The phase diagram with the frequency 0.62 c d^{-1} (upper panel of Fig. 1) shows a double wave with different maximum and minimum, while the frequency 0.69 c d^{-1} shows a single-wave diagram (lower panel of Fig. 1).

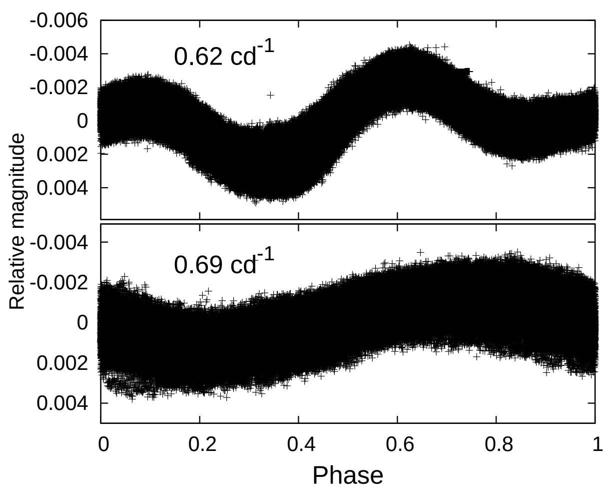

Fig. 1. Phase diagram of the star HD 181231 with the frequency 0.62 c d^{-1} (upper panel) and 0.69 c d^{-1} (lower panel).

Ground-based spectroscopic data of this star were also obtained with FEROS at the 2.2m telescope in La Silla as part of a large program (PI Ennio Poretti) and at the Pic du Midi with the NARVAL spectropolarimeter (PI Coralie Neiner). The line-profile of the Mg II 4481 shows variations with the frequency 0.69 c d^{-1}. Following Telting & Schrijvers (1997) we estimate a ℓ-value of $3-4$ from the phase distribution of these variations.

HD 175869 is a B8IIIVe star found to be non-variable from Hipparcos data. The CoRoT light curve of 27.2 days shows low-amplitude variations of the order of 0.2 mmag. A frequency compatible with the rotational frequency and its 5 harmonics are detected. Other significant low-amplitude frequencies with amplitudes of few ppm are also found.

2.2 EXO fields

To date, 7 confirmed Be stars were observed in the exo fields of CoRoT during the initial run. They show emission in the Hα line in the spectra taken with the CAFOS spectrograph at the 2.2m telescope in Calar Alto (PI Juan Fagregat). They have spectral types earlier than B5. All these stars are highly variable in the CoRoT light curves. Most of them present a beating of several close frequencies. As it is often observed in Be stars, the detected frequencies range from 0.4 to 4 c d^{-1}. The semi-amplitudes range from 40 to a few 0.01 mmag. Here we present a brief discussion of each individual star:

The CoRoT light curve of the star 102904910 shows beating of several frequencies. Many peaks around the frequencies 3.97, 3.84 and 1.92 c d^{-1} are clearly detected in the periodogram. We also find changes in the amplitude of the frequencies during the observations.

The light curve of the star 102791482 shows variability with large amplitude. The semi-amplitude of the largest-amplitude frequency is 40 mmag. The frequency analysis results on multiple frequencies (some tens) and many combinations.

The star 102766835 presents a long-term trend larger than the 58-day duration of the run and a beating of several frequencies. After removing this long-term trend, we find many frequencies around 0.93 and 0.88 c d^{-1} and their combinations. We noticed that even after prewhitening for a large number of frequencies (~ 50), some signal that appears to be non-sinusoidal is still present suggesting that the signal is not sinusoidal.

The analysis of the light curves of the stars 102761769, 102725623 and 102964342 yields several frequencies with low amplitudes. The largest semi-amplitudes in these stars range from 0.2 to 0.6 mmag.

The star 102719279 shows several fadings in its CoRoT light curve (see Fig. 2). A fading is due to an ejection of matter or outburst, but due to the inclination angle ($i \sim 90$), the material in the envelope is shadowing the star (see *Hubert & Floquet 1998* for some examples with Hipparcos data). From the light curve we see that a strong outburst occurs approximately at Julian day 2454151-2454152 (2606-2607 in the plot). Note that the outbursts produce a fading of ~0.1 mag in the light curve. The amplitude of the oscillations increases until the strongest outbursts occurs, and then suddenly the amplitude decreases while the average magnitude increases slowly to approximately reach the same level as before the outbursts. It is important to highlight that the outburst occurs when the amplitude of the variations is the largest.

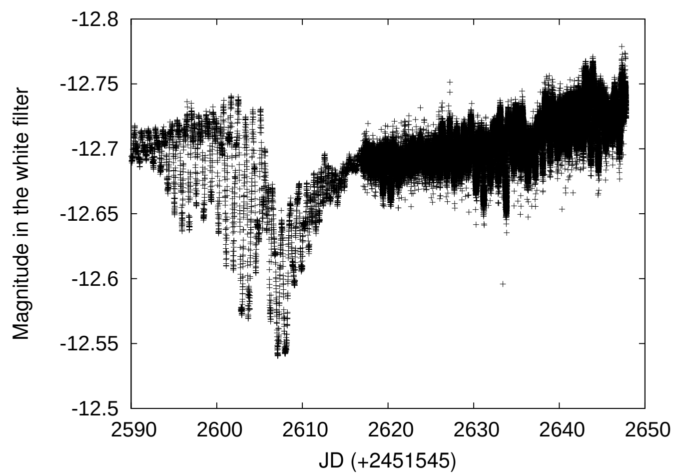

Fig. 2. Light curve of the star 102719279, observed in the exo fields.

From the Fourier analysis of the whole light curve, we detected several close frequencies around 1.16 c/d, the double 2.32 c d^{-1}, and around 0.98 c d^{-1}. As we noticed that the amplitudes of the variations change very much before and after the outbursts, we performed a Fourier analysis for both datasets. We clearly see in Fig. 3 that the amplitude of the peaks changes dramatically for the frequencies close to 1 (the peak disappears) and 1.16 c d^{-1} (the amplitude decreases from 20 to 5 mmag). Therefore, there is a link between the outbursts and the change in amplitude in this star.

3 Discussion and conclusions

The high precision, the high duty-cycle and the long-duration of the CoRoT observations have allowed us to detect many low-amplitude frequencies which would have never been detected from ground-based observations.

As a summary we can conclude that Be stars are highly variable, as all the Be stars studied here present short-term variations and most of them show a beating produced by multiple frequencies. For some stars, a change of amplitude of the oscillations the light curve has been observed. Finally, a link between amplitude variations and outbursts is found in one Be star.

These variations are probably due to the presence of non-radial pulsations, since multiple frequencies have been clearly detected. In addition, we have shown that an outburst occurred when the amplitude of the oscillations was the largest in a Be star. This results suggests that the oscillations may be linked to the ejection of matter in this star, as it was observed in the Be star μ Cen by Rivinius et al. (2001).

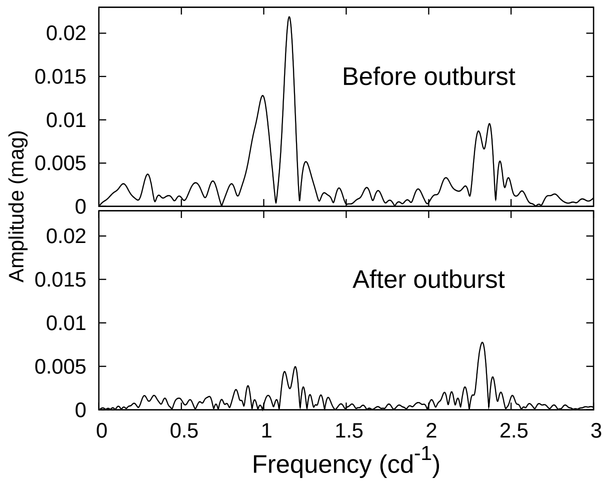

Fig. 3. Periodogram of the light curve of the star 102719279 before and after the outburst.

However, some questions are still opened after analyzing the CoRoT data. Some stars show double wave phase diagrams with 2 unequal minima for some frequencies, which would be in favor of the rotational modulation hypothesis (Balona 1990). For example inhomogeneities ejected from the central star attached with a magnetic field could produce these variations. Non-radial pulsations and rotational signatures were observed at the same time in few Be stars (eg. ω Ori, Neiner et al. 2003). However, no sign of magnetic field has been detected so far in the Corot Be stars studied here. Finally note that in addition to these frequencies, other frequencies clearly associated with pulsations are detected. Pulsating models taking into account the effects of fast rotation are then required in order to discriminate between rotation and pulsations and determine the internal structure of Be stars.

We wish to thank the CoRoT team for the acquisition and reduction of the CoRoT data. The FEROS data are being obtained as part of the ESO Large Programme LP178.D-0361 (PI: E. Poretti). This research is also based on data obtained at the Télescope Bernard Lyot (Pic du Midi).

References

Baglin, A., Auvergne, M., Catala, C., et al. 2002, in Radial and Nonradial Pulsations as Probes of Stellar Physics, ed. C. Aerts, T. R. Bedding, & J. Christensen-Dalsgaard, IAU Colloq., 185, ASP Conf. Ser., 259, 626

Balona 1990, MNRAS, 245, 92

Gutiérrez-Soto, J., Fabregat, J., Suso, J. et al. 2007, A&A, 476, 927

Hubert, A.-M. & Floquet, M., 1998, A&A, 335, 565

Porter, J.M. & Rivinius, Th. 2003, PASP, 115, 1153

Rivinius, Th., Baade, D., Štefl, S. et al. 2001, A&A, 369, 1058

Saio, H., Cameron, C., Kuschnig, R. et al. 2007, ApJ, 654, 544

Telting, J. & Schrijvers, C. 1997, A&A, 317, 723

SF2A 2008
C. Charbonnel, F. Combes and R. Samadi (eds)

THE COMPLEX ENVIRONMENT OF THE FAST ROTATING STAR ACHERNAR

Kervella, P.[1], Domiciano de Souza, A.[2], Kanaan, S.[2], Meilland, A.[3], Spang, A.[2] and Stee, P.[2]

Abstract. We report recent observations of Achernar (α Eri) and its circumstellar environment obtained with interferometric and single-telescope techniques. We also briefly summarize the SIMECA modeling of the near-infrared polar envelope detected by interferometry around this star. From these results, the close environment of Achernar appears to be shaped at least by the fast stellar wind pushed by the von Zeipel effect and possibly by interactions between the two stars Achernar A and B.

1 Introduction

Achernar is the brightest and nearest Be star. Domiciano de Souza et al. (2003) and Kervella & Domiciano de Souza (2006, hereafter K06) established that its photosphere is extremely flattened, and that an elongated circumstellar envelope (CSE) is present along the direction of its polar axis. Kanaan et al. (2008), reproduced these observations using the SIMECA modeling code. Recently, Kervella & Domiciano de Souza (2007) discovered a close-in companion, that proved to be an early A-type dwarf (Kervella et al 2008) on a close-in orbit. After a summary of our recent observations in Sect. (2), we summarize the SIMECA modeling results in Sect. (3).

2 Observations

Achernar was extensively observed by long-baseline interferometry with the VLTI instruments VINCI (near-IR, Kervella et al. 2004) and more recently MIDI (thermal IR, Ratzka et al. 2007). The VINCI data revealed the spectacular flattening of its photosphere ($\rho_{\rm eq}/\rho_{\rm pol} \approx 1.41$, K06) and the presence of an elongated CSE aligned with the polar axis of the star. This CSE contributes approximately 5% of the photospheric flux in the K band ($2.2\,\mu$m), and 13% in the N band ($10\,\mu$m; Kervella et al. *in prep.*), with a typical FWHM extension of approximately $10\,R_\star$ (Fig. 1). Unfortunately, our baseline coverage along the equator of the star is limited both in azimuth and spatial resolution, hence we constrain only marginally the equatorial CSE properties.

The stellar companion of Achernar discovered by Kervella & Domiciano de Souza (2007) orbits A on an apparently excentric orbit (Fig. 2). Although the parameters of this orbit are still to be determined, the approach of B at periastron could be sufficiently close to trigger the ejection of material from either Achernar A and/or B (based on its early spectral type, Achernar B could also be a fast rotator).

3 SIMECA modeling

Kanaan et al. (2008, hereafter Ka08) presented a SIMECA model based of the K06 interferometric observations as well as the historical spectroscopic observations of this star. The SIMECA code (Stee & Bittar 2001) allows to model the environment of active hot stars, producing line profiles, spectral energy distributions, and intensity maps. Ka08's best model for the epoch of VINCI observations (2002-2003) is a polar wind with an opening angle of $\approx 20°$ (the model parameters are listed in their Table 1), but little or no equatorial disk component. In this model, the overheated polar caps of Achernar (due to the von Zeipel effect, see von Zeipel 1924) eject a fast stellar wind that radiates free-free emission in the K band. Based on the observed historical variations of

[1] LESIA, Observatoire de Paris, CNRS UMR 8109, UPMC, Univ. Paris Diderot, 5 place Jules Janssen, 92195 Meudon, France
[2] Lab. H. Fizeau, CNRS UMR 6525, Univ. de Nice-Sophia Antipolis, Observatoire de la Côte dAzur, 06108 Nice, France
[3] Max-Planck-Intitut für Radioastronomie, Auf dem Hugel 69, 53121 Bonn, Germany

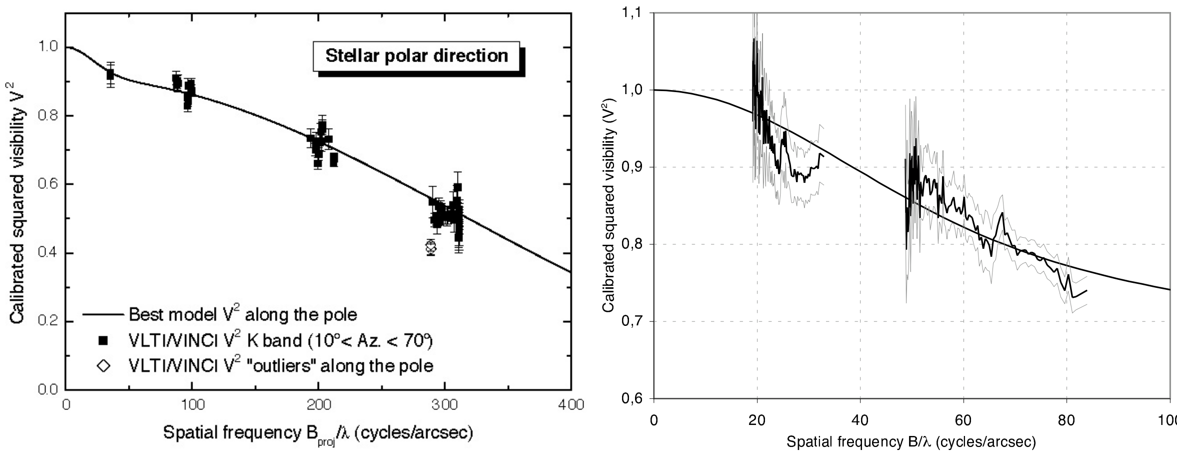

Fig. 1. Left: Interferometric observations of Achernar along its polar axis in the near-IR with VINCI (K06). **Right:** MIDI visibilities in the thermal IR (Kervella et al., *in prep.*). The adjustment of a model of the polar photosphere + Gaussian CSE is shown as a solid curve in both cases.

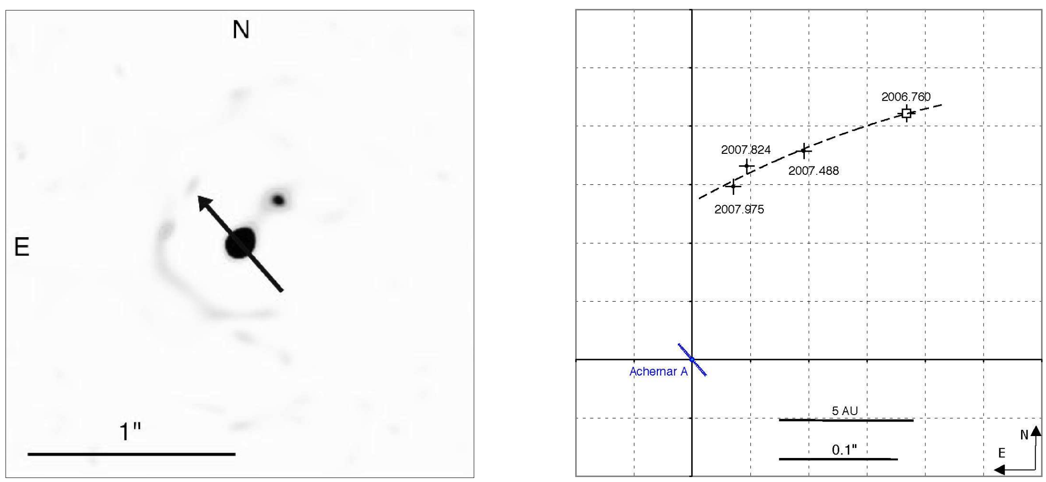

Fig. 2. Left: Deconvolved VISIR image of Achernar and its companion ($\lambda = 8.7\,\mu$m) obtained by Kervella & Domiciano de Souza (2007). **Right:** Portion of the orbit of Achernar B over approximately one year (Kervella et al. 2008).

the Hα profile, Ka08 also modeled the pseudo-periodic formation and dissipation of the equatorial disk (period of 10-15 years) by an outburst scenario in which the matter is briskly ejected from the stellar surface and then expands in the CSE with $v_{exp} \sim 0.2\,\mathrm{km.s^{-1}}$.

4 Conclusion

The SIMECA modeling of Achernar proposed by Ka08 reproduces well the VINCI observations in the near-IR K band. The passage at periastron of the close-in companion Achernar B is possibly the trigger of the Be episodes, that seem to have a 10-15 years periodicity. We did not detect an equatorial CSE, but the VLTI interferometric observations obtained up to now have a limited sensitivity along the equatorial direction of Achernar A.

Based on observations made with ESO Telescopes at Paranal Observatory under an unreferenced commissioning program with VINCI in P70, programs 078.D-0295(A) and (B) with VISIR, 279.D-5064(A) with NACO, and 078.D-0295(C), (D) and (E) with MIDI. This research used the SIMBAD and VizieR databases at the CDS, Strasbourg (France), and NASA's ADS bibliographic services. The Programme National de Physique Stellaire (PNPS) with the Bonus Qualité Recherche (BQR) from the Observatoire de la Côte dAzur are acknowledged for their financial supports. We also received the support of PHASE, the high angular resolution partnership between ONERA, Observatoire de Paris, CNRS, and University Denis Diderot Paris 7.

References

Domiciano de Souza, A., Kervella, P., Jankov, S., et al. 2003, A&A, 407, L47

Kanaan, S., Meilland, A., Stee, Ph., et al. 2008, A&A, 486, 785 (Ka08)

Kervella, P., Ségransan, D., & Coudé du Foresto, V. 2004a, A&A, 425, 1171

Kervella, P., & Domiciano de Souza, A. 2006, A&A, 453, 1059 (K06)

Kervella, P., & Domiciano de Souza, A. 2007, A&A, 474, L49

Kervella, P., Domiciano de Souza, A., Bendjoya, Ph. 2008, A&A, 484, L13

Ratzka, T., Leinert, C., & Henning, T. 2007, A&A, 471, 173

Stee, P., & Bittar, J. 2001, A&A, 367, 532

von Zeipel, H. 1924, MNRAS 84, 665

SF2A 2008
C. Charbonnel, F. Combes and R. Samadi (eds)

RESOLVING WITH SINFONI THE H_2 EMISSION FROM T TAU'S DISK

Labadie, L.[1], Gustafsson, M.[1], Herbst, T. M.[1] and Kasper, M.[2]

Abstract. We present spatially resolved near IR observations of the H_2 emission in the vicinity of T Tau N using SINFONI, the integral field spectrograph of the VLT. The gas is detected as a ring-like structure within ~80-100 AU from the star. The velocities of the H_2 are close to the systemic velocity of T Tau N, and an analysis of the excitation mechanisms plays in favor of a scenario where the H_2 is linked to the atmosphere of the circumstellar disk. The possible excitation scenarii are evoked here. Eventually, when detected in the disk, H_2 is also a strong tracer of the status of potential planet formation.

1 Introduction

Studying circumstellar disks is essential in understanding the evolutionary path from young gaseous disks to mature planetary systems. Many investigations have focused on broad band studies of the SED, or on scattered light from the disk itself. The detection of molecular line emission from species like CO or HCO^+ is also used as a tracer of the disk. However, these molecules can freeze out on the grains and become undetectable even when the disk still exists. Molecular H_2 in the disk has the advantage of being the main constituent and the last part of the gas to be bound up during the process of planet formation. Therefore, it remains in the disk even after CO or dust have become undetectable. In that sense, H_2 remains a good tracer for exploring the disk evolution since it may be observable for a longer period of time. Several groups have undertaken the study of H_2 IR rovibrational lines, mainly through long slit spectroscopy (Carmona et al. 2007; Bary et al. 2003 & 2008). However this technique is less immediate in terms of spatial distribution since it focuses on one specific position angle. Other authors have focused on the observation of pure rotational lines in the MIR (Martin-Zaidi et al. 2007) or on fluorescent H_2 in the UV (Walter et al. 2003). Here we focus on the circumstellar environment of T Tau, the prototype of the corresponding class of objects. T Tau is a triple star system, with a southern binary ~0.7" away from the northern component and showing a separation of ~0.1". All components are actively accreting and believed to host disks (Duchêne et al. 2005). The north component likely harbors a nearly face-on disk with $i \sim 19°$ (Herbst et al. 1997; Akeson et al. 1998). We used the integral field spectrograph SINFONI at the VLT to obtain diffraction limited K band images with a spectral resolution of 4000 (Gustafsson et al. 2008).

2 IFU principles and observations

SINFONI is based on the use of an optical slicer that samples the image into 32 sections and rearranges them into a pseudo-slit, which input is then spectrally dispersed through a grism. A spectral cube of 2048 images is reconstructed afterwards. The spatial information is maintained within each slice. T Tau N was observed on 30^{th} October 2004 in the K band (1.94 – 2.45 μm), with the 100 mas pixel scale for a FOV of 3.2". The standard star Hip025657 was observed at same airmass and with the same optical setup to correct for the telluric features. We used the SINFONI reduction pipeline to reconstruct the data cube. This final cube contains spatial information in X and Y directions, and spectral information in the Z direction. Among the various spectral lines, the observable H_2 rovibrational lines are : v=1-0 S(1) at 2.1218 μm; v=1-0 S(0) at 2.223 μm; v=2-1 S(1) at 2.2477 μm; v=1-0 Q(1) at 2.4066 μm.

[1] Max-Planck Institut für Astronomie; Königstuhl, 17 – 69117 Heidelberg – Germany
[2] European Southern Observatory; Karl-Schwarzschild-Str. 2 – 85748 Garching – Germany

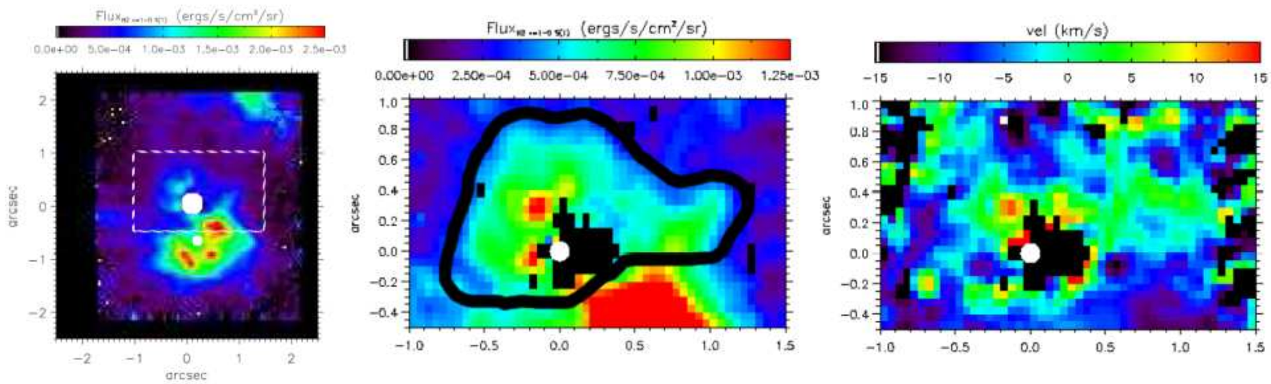

Fig. 1. Molecular H_2 maps around T Tau N. See the text for explaination

2.1 Velocities maps

Fig. 1.a shows the H_2 v=1-0 S(1) emission in the T Tau system in the 3"x3" FOV. T Tau N is represented as a large white dot and T Tau S as a smaller one. The strong emission close to T Tau S was already detected by Herbst et al. (2007) and corresponds to an outflow, as well as the emission seen in the right upper corner. A weaker emission is detected in a ring-like structure around T Tau N, which escaped previous detection. This emission is contained within the white box in Fig. 1.a. Fig. 1.b is a zoom in the vicinity of T Tau N. The region used for further analysis is confined inside the black contour. The emission south-west of T Tau N corresponds to outflows from T Tau S. Fig. 1.c presents the velocities map of the H_2 emission relative to the system velocity. Although the resolution of SINFONI is 70 km/s, much higher accuracy can be obtained through a Lorentzian fit of the line position. The velocity map shows small variations between -10 km/s and 10 km/s in the ring-like structure.

2.2 Gas kinematics

In our data, we have full access to the spectral distribution of the emitting gas. We have derived the radial velocity corresponding to every H_2 emitting position by fitting a Gaussian profile to the unresolved line profiles on a pixel by pixel basis. The velocities have been corrected for the Earths motion toward T Tau at the time of observation and are quoted with respect to the heliocentric velocity of T Tau N of 19.1 $\pm$ 1.2 km/s (Hartmann et al. 1986). The H_2 emission shows small variations between -10km/s and +10km/s with respect to the intrinsic velocity of T Tau N. There is no evidence of Keplerian rotation of the disk. However, if the inclination of the disk is $\sim 20°$, the radial velocity component of Keplerian rotation around a $2M_\odot$ star is only $\sim$5km/s at 10 AU and $\sim$2km/s at 100 AU. Such small velocity differences within the disk would be difficult to detect with the present data. In order to improve the signal-to-noise ratio, we constructed a global H_2 profile of the ring-like structure by adding all spectral profiles of H_2 v=1-0 S(1) emitting positions within the mask in Fig. 1.b (black continuous line). This also allows a direct comparison with previous spatially unresolved measurements of H_2 in the circumstellar environment of T Tauri stars. The Lorentzian fitting function provides the best match to the instrumental profile of SINFONI which dominates the unresolved H_2 profile. The profile is found to peak close to the rest velocity of T Tau N. From the Lorentzian fit we find the peak velocity to be 2.5 $\pm$ 2.1km/s (1-σ uncertainty). Considering the uncertainty in the rest velocity of T Tau N of 1.2km/s (Hartmann et al. 1986), the velocity of the H_2 emission is consistent with the rest velocity of the star within the errors. The same was found to be true of the H_2 emission from disks around other stars (Bary et al. 2003; Carmona et al. 2007).

3 Origin of the H_2 emission and excitation mechanisms

From gas kinematics, it appears that the extended H_2 emission is linked to the system of T Tau N. Could this emission correspond to a scenario in which the gas is part of a face-on disk atmosphere? Which mechanisms would then drive the excitation? Considering the scenario of a pure outflow exciting the gas, this appears not much plausible because of the typically high velocities of an outflows (60–200 km/s) and their property of being collimated, which are both unobserved with these data. The option of an envelope cleared out by a bipolar outflow and which inside walls sustain shocks from a wide-angle wind could be plausible, but this would require poorly collimated outflow compared to what is typically found in other T Tauri stars. Finally, we consider the case of the wide-angle low velocity wind that impinges on the atmosphere of a flared disk. SED modeling and observed H_2 extent suggests that the disk is $\sim$85 AU, with a total mass of $\sim 0.15\,M_\odot$. Concerning the excitation mechanism, two scenarii are suggested: shocks from a stellar wide-angle wind interacting with a flared disk, or irradiation by UV photons and X-rays. Both cases require a substantial disk around T Tau N. In the latter case however, models and observations indicate that the irradiation from the central star does not excite the H_2 much further than 20 AU, which is in contradiction with our observations (Herczeg et al. 2006). Consequently, the most likely scenario is the one of a wind-angle wind which shocks are able to excite out to 85 AU the H_2 located of an almost face-on disk around T Tau N.

References

Akeson, R. L., Koerner, D. W. & Jensen, E. L. N. 1998, ApJ, 505, 358
Bary, J. S., Weintraub & D. A., Kastner, J. H. 2003, ApJ, 586, 1136
Carmona, A., Van den Ancker, M. E., Henning, Th., et al. 2007, A&A, 476, 853
Duchêne, G., Ghez, A. M., McCabe, C., et al. 2005, ApJ, 628, 832
Gustafsson, M., Labadie, L., Herbst, T. M., et al. 2008, A&A, 488, 235
Hartmann, L., Hewett, R., Stahler, S., et al. 1986, ApJ, 309, 275
Herbst, T. M., Hartung, M., Kasper, M., et al. 2007, AJ, 114, 744
Herczeg, G. J., Linsky, J. L., Walter, F. M., et al. 2006, ApJ, 165, 256
Martin-Za¨di, C., Lagage, P. O., Pantin, E., et al. 2007, ApJ, 666, 117
Walter, F. M., Herczeg, G., Brown, A., et al. 2003, AJ, 126, 3076

SF2A 2008
C. Charbonnel, F. Combes and R. Samadi (eds)

POLARIZED HYDROGEN EMISSION LINES IN MIRA STAR

Lèbre, A.[1], Gillet, D.[2] and Fabas, N.[1]

Abstract. We present the very first results of a full spectropolarimetric study (in the four Stokes parameters I, Q, U and V) performed with NARVAL at TBL, on the Mira star o Cet. We focus on the high level of time variable linear polarization detected in Hydrogen emission lines.

1 Introduction

Mira stars are cool, evolved and variable stars. They are radially pulsating stars with long period of luminosity. The prototype of the class, o Cet (or Mira), has a pulsation period of about 332 days and, from maximum to minimum light, its spectral type varies from M5 to M9. A cool and very extended stellar atmosphere is present, surrounded with a circumstellar envelope.
Among the peculiar features of Miras 'spectra, emission lines are detected. The series of Hydrogen Balmer lines are observed in emission during about 80% of the luminosity period. They are supposed to be formed in the radiative wake of a hypersonic shock wave propagating periodically throughout the stellar atmosphere.
From september 2007 to february 2008, we have performed spectropolarimetric observations of o Cet with NARVAL@TBL. We have observed the star around its mimimum light (on september 4, 2007) and around its consecutive maximum light (january 20 and february 10, 2008) with the aim to explore the magneto-electric nature of the shock wave propagating throughout the stellar atmosphere.

2 Spectropolarimetric study

Spectropolarimetric signatures are well detected in the 4 Stokes parameters (IQUV) associated to Balmer Hydrogen lines (from Hα to Hδ). In figure 1, we present our NARVAL observations focussing on Hβ and Hδ lines. Those signatures appear to be time variable, being much more visible and structured at the maximum light, when the shock is emerging from the photosphere and is propagating with a high intensity.
From the Q and U Stokes parameters, linear polarization in the Balmer lines has been estimated. We confirm, in the Hβ line, the high level of linear polarization already reported by McLean & Coyne (1978) for o Cet at its 1977 maximum of luminosity. Moreover in figure 2, we present - in Hβ - the time variable nature of this linear polarization. Indeed, our NARVAL observations show that the linear polarization rate, in all the Balmer lines, appears to be time variable, and non-existent at the minimum light.
We suggest that the origin of this polarization phenomenon associated to Balmer emission lines lies in the shock wave structure itself. More precisely it would be due to a magneto-electric field located just behind the shock front, i.e, in the region where emissions are formed.

References

McLean I.S, Coyne G.V., 1978, ApJ, 226, L145

[1] GRAAL, Université Montpellier II, CNRS, Place E. Bataillon, 34095 Montpellier
[2] Observatoire de Haute Provence, CNRS, OAMP, 04870 Saint Michel l'Observatoire

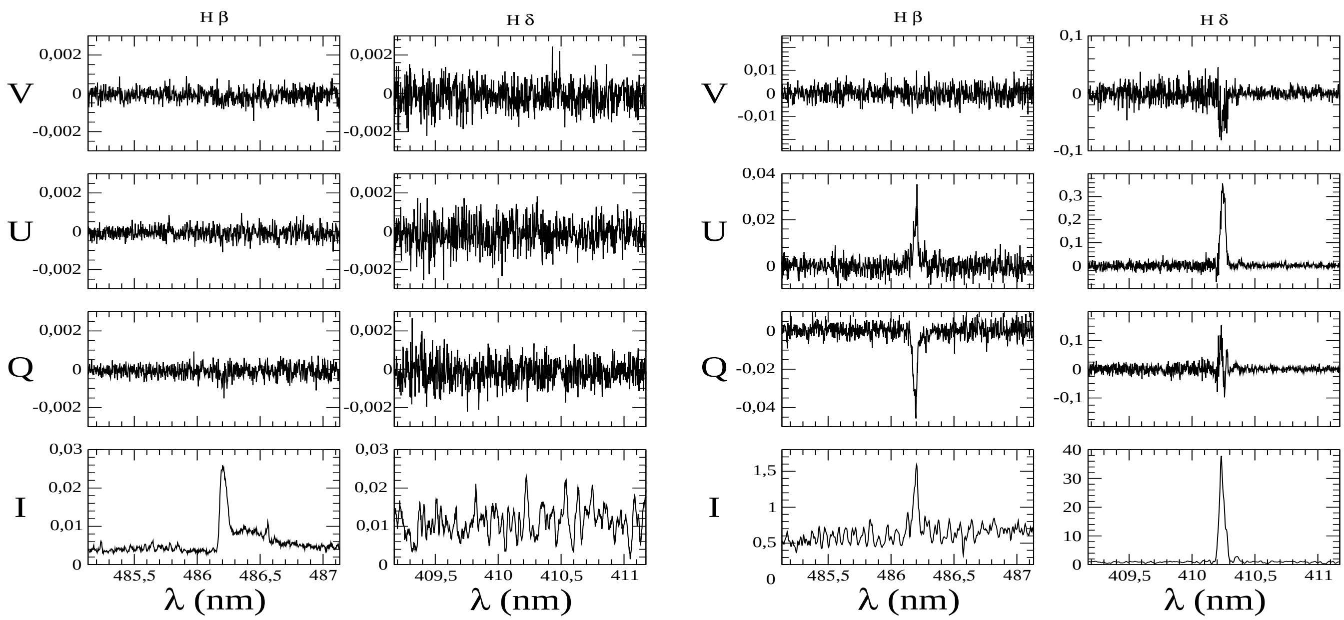

Fig. 1. Stokes parameters (IQUV) around Hβ and Hδ lines, for o Cet observed at its minimum light (left-side plots) and at its maximum light (right-side plots). At maximum light (february 2008), spectropolarimetric signatures are clearly detected in the 4 Stokes parameters and on both Balmer lines, while they are faint or absent in the observations around minimum light (september 2007).

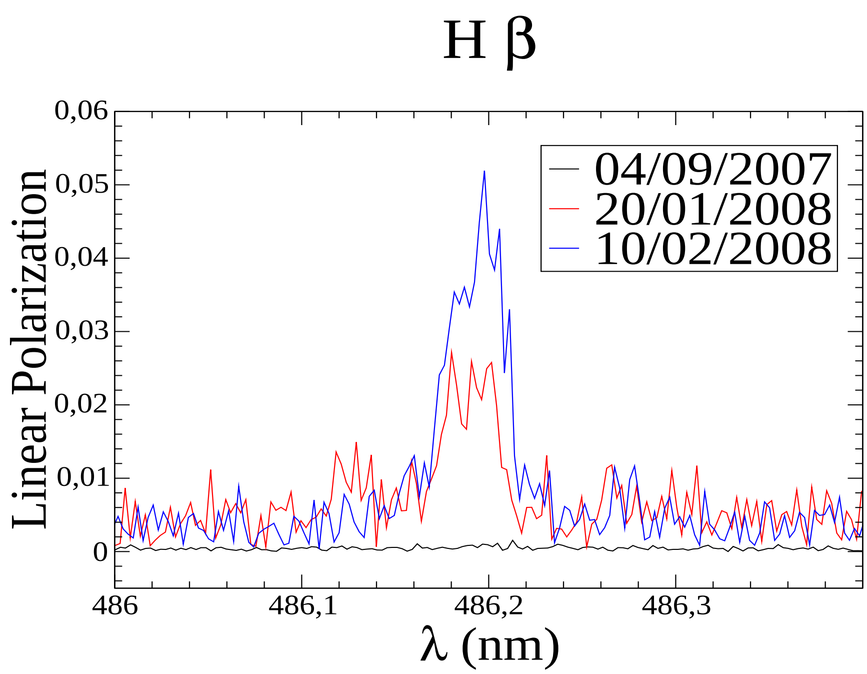

Fig. 2. Linear polarization rate in the Hβ line. From minimum to maximum light, it appears strongly variable suggesting a sharp link with the mechanism responsible of the emission line itself : the structure of the shock wave propagating throughout the stellar atmosphere.

SF2A 2008
C. Charbonnel, F. Combes and R. Samadi (eds)

BLUE EDGE OF THE δ SCUTI STARS VERSUS RED EDGE OF THE SPB STARS. HOW WILL COROT DATA HELP ?

Lefèvre, L.[1], Michel, E.[1], Aerts, C.[2], Kaiser, A.[3], Neiner, C.[1], Poretti, E.[4], Garrido, R.[5], Baglin, A.[1], Auvergne, M.[1], Catala, C.[1], Weiss, W.[3], Balaguer-Nùñez, L.[6], Maceroni. C.[7] and Ribas, I.[8]

Abstract. This work is intended to illustrate the possibilities offered by the CoRoT satellite observations to study the different instability strips (IS), and through them, physical processes and specific features of stellar interiors. The CoRoT space mission, launched on December 27^{th} 2006, has been developped and is operated by CNES, with the contribution of Austria, Belgium, Brasil , ESA, Germany and Spain. It enabled us to observe oscillations from stars down to a noise level of less than a ppm, much lower than the limit usually obtained from the ground. The number of available targets will have more than tripled by the end of the mission and these data might help testing the "purity" of the IS (i.e. the presence/absence of photometrically constant stars within) and lead to the discovery of new classes of pulsating stars (Degroote et al. 2008). We address this problem in the frame of the B and A main sequence stars.

Observations and discussion

The CoRoT mission has 2 main scientific programs : *stellar seismology* and *search for extrasolar planets*. Figure 1 represents HR diagrams realized thanks to the CoRoT *seismofield* and *exofield* observations. They both have their own importance as the former offers data with a very low noise level while the latter offers more statistics.

B stars : SPB stars and Be stars

Slowly pulsating B stars are variable mid-B-type wich pulsate in the range of 3-20 μHz and later types of Be stars have pulsational characteristics similar to that of SPB stars. The red edge of the SPB instability strip is essentially sensitive to the accumulation of elements of the iron group at a certain depth in the star (Miglio et al. 2007). All the studied stars in these classes clearly show variability in the expected frequency range. Among them are low amplitude (less than 100 ppm) pulsators that could be detected thanks to the low noise-level of the seismology field.

A stars : δ Scuti stars

δ Scuti stars usually pulsate within the 50 to 600 μHz frequency range. The red edge (RE) of the δ Scuti IS can be attributed to the coupling between oscillations and convection. The position of the blue edge (BE), however, is dependant on the abundance of Helium inside the star. This small sample (8 stars) revealed a few stars with no identified variability down to the *ppm level* within the δ Scuti theoretical IS. Firm values of $T_{\rm eff}$ and M_V, along with determination of their *vsini* and chemical abundancies will help answering the questions about the occurrence of variability in the IS and physical parameters ruling it.

[1] Observatoire de Paris, CNRS, Université Paris Diderot; 5 place Jules Janssen, 92190 Meudon, France
[2] Katholieke Universiteit Leuven, Inst. voor Sterrenkunde, B-3001 Leuven, Belgium
[3] Institut für Astronomie, Türkenschanzstrasse 17, 1180 Vienna, Austria
[4] INAF-Osservatorio Astron. di Brera, Via E. Bianchi 46,I-23807 Merate (LC), Italy
[5] Instituto de Astrofsica de Andaluca-CSIC, Apdo 3004, 18080 Granada, Spain
[6] Dept d'Astronomia i Meteorologia, Univ. de Barcelona, Av. Diagonal, 647, 08028 Barcelona, Spain
[7] INAF-Osservatorio Astr. di Roma, via Frascati 33, I-00040 Monteporzio C. Italy.
[8] IEEC, CSIC, Campus UAB, Fac. de Cincies, Torre C5, E-08193 Bellaterra, Spain.

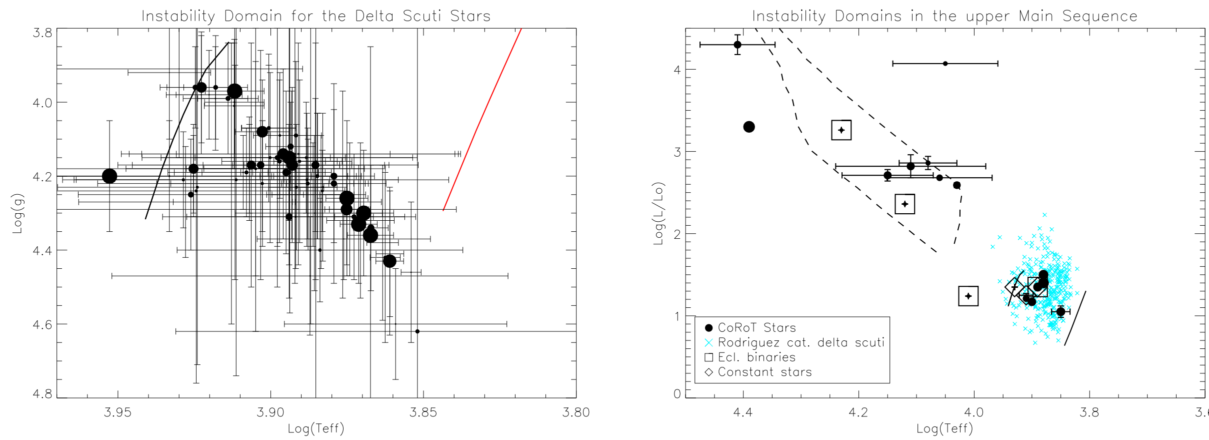

Fig. 1. Left : δ Scuti-like pulsators from the IRa01 for the exofield. The diagram shows the empirical RE and BE (Dupret et al. 2004). The size of the symbols is scaled to the amplitude of the most prominent frequency (300 to 30000 ppm: Kaiser, A., Priv. Com.). **Right** : HR Diagram with A and B stars observed from IR01 to LRa01 for the seismofield. The parameters were retrieved from various sources, i.e. Frémat et al. (2006), Poretti et al. (2007), Morel & Aerts (2007) and Miglio et al. (in prep.). The dashed lines represent the BE and RE of the IS for SPB stars (Miglio et al. 2007) and the solid lines represent the BE and RE of the δ Scuti IS. Symbol size also scales with amplitude (350 to 37000 ppm). Squares represent eclipsing binary stars and diamonds are overplotted on "non-variable" stars.

Conclusions

This preliminary work is intended to stress the potential of the CoRoT satellite to probe the existing limits between the different types of excitations and variations. To this purpose, the *exofield* is of utter importance as it contains the greater numbers of stars. The *seismofield*, however, with very low detection limits and precise individual stellar parameters will bring valuable complementary information. On one hand, our results show that all the B-stars considered here are found variable. If confirmed, these results would suggest that the pulsation mechanisms in these stars can be apprehended with a limited amount of parameters. On the other hand, we found A-stars that are constant down to the *ppm* level. This will help assessing which parameters are needed to understand the pulsational instability in this domain of the HR diagram.

AK and WW were supported by the Austrian Research Promotion Agency (FFG-ARL). EP acknowledges financial support from the ASI Project ASI/INAF/ I/015/07/0, WP 03170.

References

CoRoT Book, 2006, ESA-SP-1306, 538P

Degroote, P. et al. 2008, Communications in Asteroseismology, in preparation

Dupret, M.-A., Grigahcène, A., Garrido, R., Gabriel, M., & Scuflaire, R. 2004, A&A, 414, L17

Frémat, Y. , Neiner, C., Hubert, A.-M., et al. 2006, A&A, 451,1053-1063

Miglio, A., Montalbán, J., & Dupret, M.-A. 2007, Communications in Asteroseismology, 151, 48

Miglio, A., Degroote, P.-O., et al., 2008, in preparation

Morel, T., & Aerts, C. 2007, Communications in Asteroseismology, 150, 201

Poretti, E., Rainer, M., Uytterhoeven, et al. 2007, Memorie della Societa Astronomica Italiana, 78, 624

SF2A 2008
C. Charbonnel, F. Combes and R. Samadi (eds)

TURBULENT RESISTIVITY CHARACTERIZATION IN ACCRETION DISC MRI TURBULENCE.

Lesur, G.[1] and Longaretti, P-Y.[2]

Abstract. The magneto-rotational instability (MRI) is widely recognized as the most promising process to provide a turbulent transport satisfying the observational constraints. Although nearly all disk models make reference to this instability as the source of turbulence, important aspects of the MRI-driven turbulent transport properties are not well-known, in particular concerning the "resistive" transport. We have performed local simulations of the MRI to quantify this problem. We find that the resistive transport is systematically smaller than the angular momentum transport for a given configuration, and that the resistivity tensor is anisotropic.

1 Introduction

The origin of angular transport in accretion disks has always been a central problem in the disk community. The first α model (Shakura & Sunyaev 1973) already assumed a strong level of turbulence, leading to an effective viscosity orders of magnitude higher than molecular viscosity. However, the physical origin of this turbulence in disks is still largely discussed.

In a seminal paper, Balbus & Hawley (1991) have identified an MHD instability, the magnetorotational instability (MRI) that drives turbulence in the nonlinear regime. This instability has been extensively studied, mainly with local unstratified (Hawley et al. 1995) and stratified (Stone et al. 1996) 3D simulations, and global (Hawley 2000) disk simulations. These simulations have shown that MRI turbulence was an efficient way to transport angular momentum, although the role of microphysical processes was largely underestimated (Lesur & Longaretti 2007; Fromang et al. 2007).

MRI turbulence may also produce resistive transport (transport of magnetic fields) in discs. This transport is a key ingredient of accretion-ejection models (see, e.g. Ferreira 1997; Casse & Ferreira 2000 and references therein). This turbulent resistivity η_T is parameterized with the Shakura-Sunyaev ansatz as $\eta_T = \alpha_\eta v_A H$ (v_A is the Alfvén speed); stationary accretion ejection models require an anisotropy of the turbulent resistivity transport limited to a factor of order unity, and a very efficient turbulent tranport with $\alpha_\eta \lesssim 1$.

In any case, turbulent resistivity is an issue in its own right, and in this paper, we present new numerical results aimed at quantifying more precisely the resistive transport due to MRI turbulence. We first describe the physics and the numerical methods we used to study turbulence in disks. Then, we introduce the basics of the turbulent resistivity model, and we present the methodology used along with some preliminary results. Last, our findings are discussed along with some future line of work.

2 Shearing-box equations and numerical method

MRI-related turbulence has been extensively studied in the literature, and we will recall here only briefly the basic equations for the shearing-box model. The reader is referred to Hawley et al. (1995), Balbus (2003) and Regev & Umurhan (2008) for an extensive discussion of the properties and limitations of this model. Since MHD turbulence in discs is subsonic, we will work in the incompressible approximation, which allows us to eliminate

[1] Department of Applied Mathematics and Theoretical Physics, Centre for Mathematical Sciences, University of Cambridge, Wilberforce Road, Cambridge CB3 0WA, UK
[2] Laboratoire d'Astrophysique de Grenoble, UJF CNRS, BP, 53 38041 Grenoble CEDEX 9 FRANCE

sound waves and density waves. We also neglect vertical stratification, consistently with the local shearing-box model (Regev & Umurhan 2008). We include in our description a molecular viscosity and resistivity to minimize the artifacts of numerical dissipation.

The shearing-box equations are found by considering a Cartesian box centred at $r = R_0$, rotating with the disc at angular velocity $\Omega = \Omega(R_0)$ and having dimensions (L_x, L_y, L_z) with $L_i \ll R_0$. Assuming $R_0\phi \to x$ and $r - R_0 \to -y$, one eventually obtains the following set of equations for the deviations $\boldsymbol{v}$ from the local Keplerian profile:

$$
\begin{aligned}
\partial_t \boldsymbol{v} + \boldsymbol{\nabla}\cdot(\boldsymbol{v}\otimes\boldsymbol{v}) &= -\boldsymbol{\nabla}\Pi + \boldsymbol{\nabla}\cdot(\boldsymbol{B}\otimes\boldsymbol{B}) - Sy\partial_x\boldsymbol{v} \\
&\quad +(2\Omega - S)v_y\boldsymbol{e_x} - 2\Omega v_x\boldsymbol{e_y} + \nu\boldsymbol{\Delta}\boldsymbol{v}, \qquad (2.1)\\
\partial_t\boldsymbol{B} &= -Sy\partial_x\boldsymbol{B} + SB_y\boldsymbol{e_x} \\
&\quad +\boldsymbol{\nabla}\times(\boldsymbol{v}\times\boldsymbol{B}) + \eta\boldsymbol{\Delta}\boldsymbol{B}, \qquad (2.2)\\
\boldsymbol{\nabla}\cdot\boldsymbol{v} &= 0, \qquad (2.3)\\
\boldsymbol{\nabla}\cdot\boldsymbol{B} &= 0. \qquad (2.4)
\end{aligned}
$$

The boundary conditions associated with this system are periodic in the x and z direction and shearing-periodic in the y direction (Hawley et al. 1995). These equations involve the mean shear $S = -r\partial_r\Omega = (3/2)\Omega$ (a Keplerian rotation profile is assumed) . The generalized pressure term $\Pi = P/\rho_0 + \boldsymbol{B}^2/2$. Finally, the magnetic field is expressed in Alfvén-speed units, and all the velocities are given in units of SL_z. These equations are solved numerically using a Fourier Galerkin representation of (2.1)–(2.4) in a sheared frame (see Lesur & Longaretti 2005).

2.1 Turbulent resistivity definition

If MRI turbulence can be modelled as a turbulent resistivity on large scales (an assumption supported by our numerical results), one can define a large scale mean field $\bar{\boldsymbol{B}}$ and velocity $\bar{\boldsymbol{V}}$ plus fluctuating (turbulent) fields $\boldsymbol{b}$ and $\boldsymbol{v}$. We assume $\langle\boldsymbol{b}\rangle = 0$ and $\langle\boldsymbol{v}\rangle = 0$ where $\langle\rangle$ denotes an ensemble (or time, under ergodic hypothesis) average. The averaged induction equation reads:

$$\partial_t\bar{\boldsymbol{B}} = \boldsymbol{\nabla}\times(\bar{\boldsymbol{V}}\times\bar{\boldsymbol{B}}) + \nabla\times\bar{\boldsymbol{\mathcal{E}}} + \eta\Delta\bar{\boldsymbol{B}} \qquad (2.5)$$

where we have defined the mean electromotive force (EMF) $\bar{\boldsymbol{\mathcal{E}}} = \langle\boldsymbol{v}\times\boldsymbol{b}\rangle$ and we have used the definition $\langle\boldsymbol{B}\rangle \equiv \bar{\boldsymbol{B}}$ (same for $\bar{\boldsymbol{V}}$). The turbulent resistivity hypothesis assumes (in tensorial notations):

$$\bar{\mathcal{E}}_i = -\eta^T_{ik}\bar{J}_k \qquad (2.6)$$

where η^T is the (constant) turbulent resistivity tensor[1]. To confirm this model and compute turbulent resistivity coefficients, we have to find a linear correlation between the components $\bar{\mathcal{E}}_j$ and $\bar{J}_i$.

2.2 Numerical protocol

To compute the turbulent resistivity, one needs a mean current, which is not naturally present in local (shearing box) simulations. To produce this current, we have chosen to impose a large scale and *non homogeneous* field in the box. This method differs from the test field technique of Brandenburg and coworkers (see, e.g. Brandenburg et al. 2008 and references therein); the relative strengths and weaknesses of the two methods will be discussed elsewhere.

In practice, the current is produced in our Galerkin representation by forcing the largest Fourier mode in one direction to a given value B_0. To trigger the MRI, we impose a mean vertical field $B^0_z = 0.1$ for which the largest mode $k_z = 2\pi/L_z$ becomes unstable with a growth rate $\gamma \simeq S/2$. The aspect ratio is $L_x\times L_y\times L_z$=$4\times2\times1$. The factor 2 in L_y allow us to trigger more easily secondary instabilities in the strong mean vertical field cases (see Goodman & Xu 1994 and Bodo et al. 2008). The resolution used is $128\times128\times64$, similar in cell size to the one

[1]A more general relation $E_i = -\eta^T_{ijk}\partial_j B_k$ where η^T_{ijk} is an antisymmetric tensor is sometimes considered. We won't use it here for simplicity, as only one component of $\partial_j B_k$ is used at any given time.

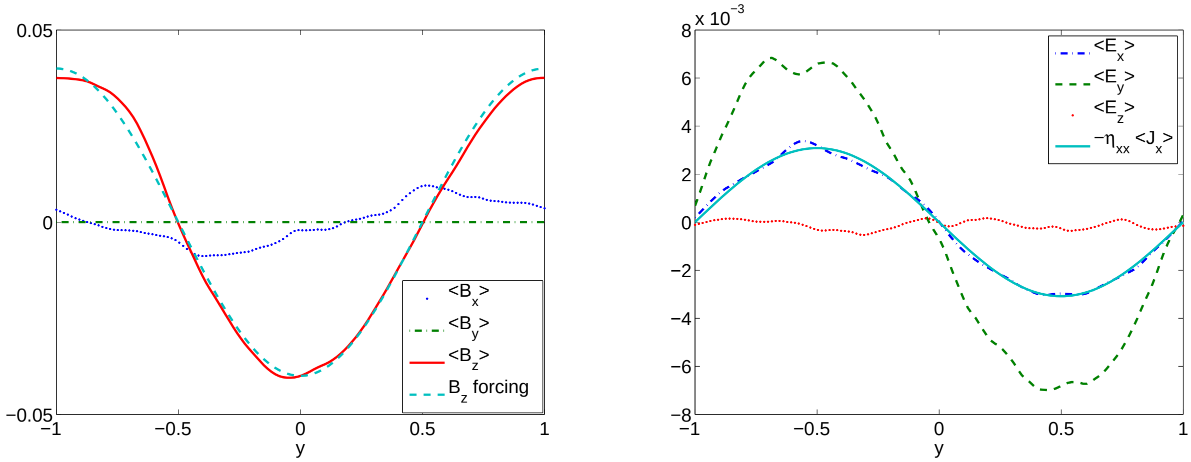

Fig. 1. Mean field (left) and emfs (right) from run ZY4 with $B_z^0 = 0.1$ and $\delta B^0 = 0.04$. We also plot the best fits corresponding to the turbulent resistivity model. We measure in this case $\eta^T_{xx} = 5.6 \times 10^{-2} SL_z^2$.

model	δB^0	$\eta^T_{xx}/(SL_z^2)$	$\eta^T_{yx}/(SL_z^2)$	$\alpha \equiv \nu^T/(SL_z^2)$
ZY1	0.01	3.6×10^{-2}	2.9×10^{-2}	1.5×10^{-1}
ZY2	0.02	3.7×10^{-2}	8.5×10^{-2}	1.5×10^{-1}
ZY3	0.03	3.6×10^{-2}	6.8×10^{-2}	1.5×10^{-1}
ZY4	0.04	2.4×10^{-2}	5.6×10^{-2}	1.3×10^{-1}
ZY5	0.08	1.1×10^{-2}	1.1×10^{-2}	7.8×10^{-2}

Table 1. Main results from the $B_z(y)$ configuration. α is the Shakura-Sunyaev like coefficient (see Lesur & Longaretti 2007 for a proper de?nition) computed from each run, and ν^T is the associated turbulent viscosity. Apart from runs ZY4 and ZY5, turbulence efficiency is constant and the turbulent Prandtl number appears to be systematically smaller than 1.

used in Lesur & Longaretti (2007). The Reynolds number is always $Re = SL_z^2/\nu = 1600$ and $Pm = \nu/\eta = 1$. Each simulation is integrated over 500 shear times, and the averages are computed from the 400 last shear times, to avoid initial conditions artefacts.

To postprocess the results, we first compute the time average $\bar{\boldsymbol{B}}$ and $\bar{\mathcal{E}}$. We then use a script which extract the mean current and compute the correlation with the emfs, giving in the end one component of the η^T tensor for one run. Note that using this procedure, we can in theory compute the resistivity associated with $B_z(y)$, $B_x(y)$ and $B_x(z)$ configurations. In this paper, we will only explore the $B_z(y)$ configuration. Similar results follow in the other configurations, and will be reported elsewhere.

3 Results

To illustrate our method we consider the following structure for the mean magnetic field (radially varying vertical field):

$$\bar{B}_z = B_z^0 + \delta B^0 \cos\Big(\frac{2\pi y}{L_y}\Big), \tag{3.1}$$

We show on Fig. 1 an example of a simulation result with $\delta B^0 = 0.04$. The profiles are computed from an average in time and in the (x, y) plane. From this figure, one get a classical diagonal resitivity term of $\eta^T_{xx} \sim 5.6 \times 10^{-2}$. We also find an non diagonal term $\eta^T_{yx} = 8 \times 10^{-2}$. We have repeated this kind of experience for various set of parameters, which are summarized on Tab. 1.

One may note a saturation process (models ZY4-ZY5), which may be due to the fact that increasing δB_0 to high values leads to strong modification of the background field. Since B_z^0 corresponds to the maximum of the growth rate for the $k_z = 2\pi/L_z$ mode, this means that increasing δB^0 always weakens the instability. This explanation is confirmed by the decrease of the turbulent transport α.

According to Tab. 1, we can state that, on average

$$\eta^T_{xx} \sim 0.2\nu^T = 0.2\alpha S L_z^2. \tag{3.2}$$

In a $B_x(y)$ configuration (radially varying azimuthal field) one obtains instead $\eta^T_{zz} \sim 0.6\nu^T = 0.6\alpha S L_z^2$.

4 Conclusions

We have presented a systematic method to determine the turbulent resistivity associated with MRI turbulence in accretion discs. We have exemplified this method in the configuration of a radially varying vertical magnetic field, using nonlinear spectral simulations of turbulence. Although these results are rather preliminary, two clear trends are noticeable. First, we find that the turbulent resistivity η^T is always smaller than the turbulent viscosity ν^T. However, it is far from being negligible, and we may define a turbulent Prandtl number $Pm^T = \eta^T/\nu^T$, which is found to be of the order of 0.2—0.6. Second, we find that the turbulent resistivity is an anisotropic tensor, as expected. In particular, the toroidal field (B_x) diffuses about 3 times more rapidly than the poloidal field (B_z), in the radial direction. We also find that a non diagonal term of the turbulent resistivity tensor is non zero. As shown by Lesur & Ogilvie (2008), such terms might play an important role for disc dynamos and large scale magnetic field generation.

These results seem to suggest that the turbulent resistivity generated by the magneto-rotational instability is about and order of magnitude too weak to allow for the existence of stationary accretion-ejection structure although the anisotropy is in the right range, but further work is required to get a complete characterization of the turbulent resistivity. In particular, one needs to quantify resistivity in the presence of a vertical structure for the magnetic field. However, this configuration is not easy to compute as it excites very strong channel solutions (Goodman & Xu 1994) which leads to unphysical results. To get a more precise scaling as a function of α, one may try to vary the mean vertical field amplitude B_z^0. Although our preliminary results seem to show a good agreement with (3.2) for weaker fields, more work is required to get a complete picture. Finally, the impact of the (molecular) Prandtl number, which is known to be strong on the transport efficiency (Lesur & Longaretti 2007), is yet to be studied for the turbulent resistivity.

References

Balbus, S. A. 2003, ARA&A, 41, 555

Balbus, S. A. & Hawley, J. F. 1991, ApJ, 376, 214

Bodo, G., Mignone, A., Cattaneo, F., Rossi, P., & Ferrari, A. 2008, Accepted in A&A, 805

Brandenburg, A., Rädler, K.-H., Rheinhardt, M., & Käpylä, P. J. 2008, ApJ, 676, 740

Casse, F. & Ferreira, J. 2000, A&A, 353, 1115

Ferreira, J. 1997, A&A, 319, 340

Fromang, S., Papaloizou, J., Lesur, G., & Heinemann, T. 2007, A&A, 476, 1123

Goodman, J. & Xu, G. 1994, ApJ, 432, 213

Hawley, J. F. 2000, ApJ, 528, 462

Hawley, J. F., Gammie, C. F., & Balbus, S. A. 1995, ApJ, 440, 742

Lesur, G. & Longaretti, P-Y. 2005, A&A, 444, 25

Lesur, G. & Longaretti, P.-Y. 2007, MNRAS, 378, 1471

Lesur, G. & Ogilvie, G. I. 2008, A&A, 488, 451

Regev, O. & Umurhan, O. M. 2008, A&A, 481, 21

Shakura, N. I. & Sunyaev, R. A. 1973, A&A, 24, 337

Stone, J. M., Hawley, J. F., Gammie, C. F., & Balbus, S. A. 1996, ApJ, 463, 656

SF2A 2008
C. Charbonnel, F. Combes and R. Samadi (eds)

SEARCH FOR VARABILITY IN ULTRA-COOL DWARFS SPECTROSCOPIC INVESTIGATION FOR CORRELATED VARIABILITY

Listowski, C.[1], Goldman, B.[1], Bailer-Jones, C. A. L.[1] and the CLOUDS collaboration

Abstract.
Some Ultra-cool dwarfs have cloudy atmospheres and are rapid rotators. Thus patterns can appear in the cloud coverage, leading to surface heterogeneities. Photometric and spectroscopic variations have already been reported in M-type, L-type and T-type ultra-cool dwarfs. However some detections are tentative because of the very low variation amplitudes. We present results for three ultra-cool dwarfs monitored in infrared, in low resolution, with the NTT-SOFI spectrograph, using the blue and red arms, corresponding to wavelength ranges of 0.95–1.64μm and 1.53–2.52μm respectively: DENIS-P J104814.9-395604 (M9), Kelu1 (L2) and 2MASS J15074769-1627386 (L5). We find these objects variable in both SOFI arms (Kelu1 being rather stable in the blue arm, compared to the other two objects).

1 Introduction

The very late M dwarfs (M9), the L and T dwarfs have like some planets and exoplanets a cloudy atmosphere. These objects are therefore of a high interest for variability investigations. The presence of a cloud coverage and the fact that brown dwarfs are rapid rotators provide the observator with an interesting work: studying a variable weather on these objects. Photometric and spectroscopic variations have already been reported (Clarke et al. 2003; Bailer-Jones 2008; Goldman et al. 2008). These variations can be due to either the rotational modulation of the dwarf or to dynamical atmospheric processes. Binarity and magnetic fields might also be the cause of variations.
DENIS1048 is an old cool dwarf at the hydrogen burning mass limit. Kelu1 and 2M1507 are both L-type brown dwarf. We analyse the infrared data of the SOFI spectrograph by looking for correlated variability in the spectra of these ultra-cool dwarfs. Many elements are involved at the same time in these processes. Correlations in different features (for instance species depleting at the same time) suggest that the observed variability is real (Bailer-Jones 2008; Goldman et al. 2008)

2 Method

We use the following method developped by Bailer-Jones (2008). We use the free software environment for statistical computing and graphics (www.r-project.org):
1.Each set of normalized relative spectra is converted into a matrix in that each row is a spectrum and each column a flux time series at a given wavelength.
2. Each row is binned with a binning factor, F, by taking the mean of the fluxes and the mean of the wavelengths values.
3. Correlations are computed between columns. The matrixes ,displayed with a color-scale , are symmetric. They are computed by taking the absolute value of the coeffcients. The distribution of correlation coefficients is also provided. From dark red to yellow the correlation coefficients rise.
4. A random correlation matrix is computed as well as the corresponding distribution, in order to compare it with the observed correlations.

[1] Max-Planck-Institute for Astronomie, Knigstuhl, D-69117 Heidelberg, Germany

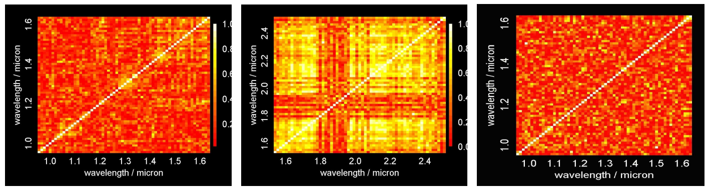

Fig. 1. Left : Kelu1. Example of correlation matrix in the blue arm. **Middle**: Kelu1. Example of correlation matrix in the red arm. **Right**: A random correlation matrix.

3 Which method to use for computing the relative spectra?

Since we had the choice for computing the relative spectra (for the cancellation of the Earths atmsosphere) between a standard star and a reference star simultaneously monitored in the slit, we compared correlation matrixes computed with both of them.

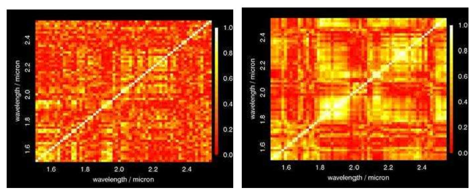

Fig. 2. Left: Correlation matrix for DENIS1048's relative spectra computed with the reference star simultaneously monitored in the slit with the science object. **Right** : Correlation matrix for DENIS1048's relative spectra (red arm) computed with the standard star.

The very yellow patterns in the 'standard' case suggest we may conclude that for a variability investigation a standard star does not provide a good enough cancellation of the Earths atmosphere, so that one should always manage to have a reference star in the slit, while monitoring the science object.

4 Detected variability and perspective

Given the random matrixes we can conclude the observed variations are real. DENIS-P J104814.9-395604 (M9) shows strong variations in the wavelength range 0.95–1.64μm with a very high scattering in the distribution of correlation coefficients. One might think that this very peculiar patterns would be due to the different groups of FeH lines, abundant at these wavelengths. A small range of the red part, the 1.6–1.8μ one, exhibits a very correlated pattern that might be due to FeH which is dominant in these wavelengths in M9 dwarfs, and present many absorption lines whose variations may be correlated. Kelu1 seems to be much more stable in the blue part than the other two objects. However the mean of the absolute values of the correlation coefficients in the red part is for Kelu1 more than twice higher than for the other two objects whereas it is the smallest in the blue part. Except for the water bands, all the species like FeH and CO would be correlated to each other.Finally our three science targets seem to be good candidates for further investigations of spectral and/or photometric variability. Kelu1 was already investigated with both technics (Clarke et al. 2002, 2003) but DENIS-P J104814.9-395604 and 2MASS J15074769-1627386 are still waiting for further investigations in variability.

References

Bailer-Jones, C. A. L., 2008, MNRAS, 384, 1145

Clarke, F. J., Tinney, C. G., & Covey, K. R. 2002, MNRAS, 332, 361

Clarke, F. J., Tinney, C. G., & Hodgkin, S. T., 2003, MNRAS, 341, 239

Goldman, B., et al. 2008,cA&A, 487, 277

THE WFI Hα SPECTROSCOPIC SURVEY

Martayan, C.[1,2], Baade, D.[3] and Fabregat, J.[4]

Abstract. This document presents the results from our spectroscopic survey of Hα emitters in galactic and SMC open clusters with the ESO Wide Field Imager in its slitless spectroscopic mode. First of all, for the galactic open cluster NGC6611, in which, the number and the nature of emission line stars is still the object of debates, we show that the number of true circumstellar emission line stars is small. Second, at low metallicity, typically in the Small Magellanic Cloud, B-type stars rotate faster than in the Milky Way and thus it is expected a larger number of Be stars. However, till now, search for Be stars was only performed in a very small number of open clusters in the Magellanic Clouds. Using the ESO/WFI in its slitless spectroscopic mode, we performed a Hα survey of the Small Magellanic Cloud. 3 million low-resolution spectra centered on Hα were obtained in the whole SMC. Here, we present the method to exploit the data and first results for 84 open clusters in the SMC about the ratios of Be stars to B stars.

1 Observations, data-reduction, and spectroscopic analysis

Observations were performed in 2002, at the 2.2m of the ESO at la Silla equiped with the Wide Field Imager in its slitless spectroscopic mode (Baade et al. 1999). This kind of instrumentation is not sensitive to the ambient diffuse nebula and displays only emission lines, which come from circumstellar matter like in the case of Be stars. Be stars are very fast rotating stars, which are surrounded by a circumstellar decretion disk. This instrumentation allowed Martayan et al. (2008a) to find true cirumstellar emission line stars in the Eagle Nebula and NGC6611 open cluster located in the Milky Way, while slit-spectroscopic observations show strong nebular lines. Only a small number of true emission line stars (less than 10) was found.

In the Milky Way, we used broad bandpass filter centered in Hα, but in the Magellanic Clouds due to the crowding of the fields, we used a narrow bandpass filter also centered in Hα. The exposure times range from 120 to 600s, and the resolving power is low ($\sim$100). In the SMC, 14 images were obtained, $\sim$8000 spectra were treated in 84 SMC open clusters among the 3 million obtained for the whole SMC, and in NGC6611 $\sim$10000 spectra were treated. In the LMC, 5 million spectra were obtained.

The data-reduction was performed using IRAF tasks and the spectra extraction with SExtractor (Bertin & Arnouts 1996). The analysis of spectra and emission line stars detection were done using lecspec and ALBUM codes by Martayan et al. (2008a,b). To classify the stars in SMC open clusters, we cross-correlated our WFI catalogues with OGLE ones (Udalski et al. 1998) to obtain the photometry (B, V, I) for each star and various information for each open cluster (E[B-V], age, reddening). More than 4000 stars of SMC open clusters were classified. An example of colour-magnitude digrams is shown for different open clusters in the SMC in Fig. 1.

2 Metallicity effect

At low metallicity, the stellar winds are less efficient than at high metallicity, as a consequence the stars retain more angular momentum and rotate faster in the SMC than in the MW (Martayan et al. 2007, Hunter et al. 2008). It is then expected that there are more Be stars in the SMC than in the MW. To enlighten this

[1] Royal Observatory of Belgium, 3 avenue circulaire 1180 Brussels, Belgium
[2] GEPI, Observatoire de Paris, CNRS, Université Paris Diderot; 5 place Jules Janssen 92195 Meudon Cedex, France
[3] European Organisation for Astronomical Research in the Southern Hemisphere, Karl-Schwarzschild-Str. 2, D-85748 Garching b. Muenchen, Germany
[4] Observatorio Astronómico de Valencia, edifici Instituts d'investigació, Poligon la Coma, 46980 Paterna Valencia, Spain

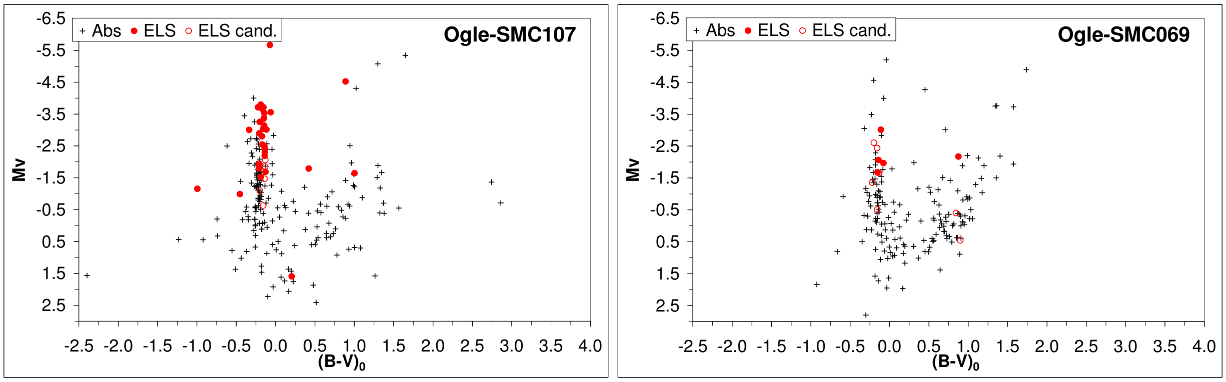

Fig. 1. Left: SMC open cluster OGLE-SMC107 (NGC330). **Right**: SMC open cluster OGLE-SMC069. Black dots correspond to the absorption stars, red full circles to definite emission line stars, and red empty circles to candidate emission line stars.

potential effect, the stars from 83 of the 84 open clusters treated in the SMC were grouped in order to avoid the variability of the rates of Be stars to B stars from a cluster to another. The rates of Be stars to B stars by spectral-type categories are then compared with those obtained in the Milky Way with data from McSwain & Gies (2005, 55 open clusters). In each spectral-type category, the proportion of Be stars to B stars is twice to 4 times higher in the SMC than in the MW. This result quantifies the trend seen in the preliminary studies of Maeder et al. (1999) or Wisniewski & Bjorkman (2006). About Oe stars, the rate is ∼1.5 times higher in the SMC than in the MW.

Furthermore, the distribution of the Be stars by spectral types peaks at the spectral-type B2 in the SMC open clusters. The same behaviour is seen for early-type Be stars in the MW (Zorec & Frémat 2005 in the field or in open clusters with data from McSwain & Gies 2005).

3 Conclusion

We conducted a large slitless spectroscopic survey in the Magellanic Clouds and in 2 open clusters in the Milky Way with the ESO/WFI in its slitless spectroscopic mode. In the open cluster NGC6611 and the Eagle Nebula (M16), we show that there is only a small number of true emission line stars. With the stars from 83 open clusters in the SMC, we show that there are twice to four times more Be stars in the SMC than in the MW open clusters. The exploitation of the spectra in the SMC field and in the whole LMC (field and open clusters) is currently ongoing.

C.M. acknowledges funding from the ESA/Belgian Federal Science Policy in the framework of the PRODEX program (C90290). C.M. thanks support from ESO's DGDF 2006,

References

Baade, D., Meisenheimer, K., Iwert, O., et al., 1999, Msngr, 95, 15

Bertin, E. & Arnouts, S., 1996, A&AS, 117, 393

Hunter, I., Lennon, D. J., Dufton, P. L., et al., 2008, A&A, 479, 541

Maeder, A., Grebel, E. K., Mermilliod, J.-C., 1999, A&A, 346, 459

Martayan, C., Frémat, Y., Hubert, A.-M., et al., 2007, A&A, 462, 683

Martayan, C., Floquet, M., Hubert, A.-M., et al., 2008a, A&A, in press, astroph08061430

Martayan, C., Baade, D., Hubert, A.-M., et al., 2008b, The 2007 ESO instrument calibration workshop, 595

McSwain, M. V. & Gies, D. R., 2005, ApJS, 161, 118

Udalski, A., Szymanski, M., Kubiak, M., et al., 1998, AcA, 48, 147

Wisniewski, J. P. & Bjorkman, K. S., 2006, ApJ, 652, 458

Zorec, J. & Frémat, Y., 2005, SF2A-2005: Semaine de l'Astrophysique Francaise, 361

SF2A 2008
C. Charbonnel, F. Combes and R. Samadi (eds)

THE GAIA SATELLITE: A TOOL FOR EMISSION LINE STARS AND HOT STARS

Martayan, C.[1,2], Frémat, Y.[1], Blomme, R.[1], Jonckheere, A.[1], Borges, M.[3], de Batz, B.[2], Leroy, B.[4], Sordo, R.[5], Bouret, J.-C.[6], Martins, F.[7], Zorec, J.[8], Neiner, C.[2], Nazé, Y.[9], Alecian, E.[10], Floquet, M.[2], Hubert, A.-M.[2], Briot, D.[2], Miroshnichenko, A.[11], Kolka, I.[12], Stee, P.[13], Lanz, T.[14] and Meynet, G.[15]

Abstract. The Gaia satellite will be launched at the end of 2011. It will observe at least 1 billion stars, and among them several million emission line stars and hot stars. Gaia will provide parallaxes for each star and spectra for stars till V magnitude equal to 17. After a general description of Gaia, we present the codes and methods, which are currently developed by our team. They will provide automatically the astrophysical parameters and spectral classification for the hot and emission line stars in the Milky Way and other close local group galaxies such as the Magellanic Clouds.

1 Introduction: The Gaia space mission

The Gaia space mission will be launched in 2011/2012. It will orbit at the anti-solar L2 point. Its lifetime is expected to be 5 years. Onboard, there are 3 different instruments: ASTRO, which will provide astrometric measurements (parallaxes, proper-motions) for all stars down to V magnitude 20 with an accuracy 200 times better than Hipparcos. There are 2 spectrophotometers BP/RP (R$\sim$100, 320–660nm and 650–1000nm) and a low/medium resolution spectrograph called the Radial Velocity Spectrometer (R=5000 to 11500, 847-874nm, designed for GK stars). This last one will provide spectra for stars till V magnitude equal to 17, and will be used to determine the radial velocity of the stars (see Viala et al. 2008). It is expected that 1 billion of stars will be observed by Gaia, on average 70 times in 5 years (but only 40 times for the RVS). Among them, using the IMF from Kroupa (2001), it is estimated that there are, at maximum, 68 million of hot stars (HS), and 6 million of emission line stars (ELS). Due to the huge quantity of data (200 teraBytes by year), all the data-reduction and the scientific analysis must be performed automatically via new software based on java programming language.

[1] Royal Observatory of Belgium, 3 avenue circulaire 1180 Brussels, Belgium
[2] GEPI, Observatoire de Paris, CNRS, Université Paris Diderot; 5 place Jules Janssen 92195 Meudon Cedex, France
[3] Fizeau, Observatoire de la Côte d'Azur, France
[4] LESIA, Observatoire de Paris, 5 place Jules Janssen 92195 Meudon Cedex, France
[5] Padova Astronomical Observatory, Italy
[6] Laboratoire d'Astrophysique de Marseille, France
[7] GRAAL-Université Montpellier 2, France
[8] Institut d'Astrophysique de Paris, France
[9] Institut d'Astrophysique de Liège, Belgium
[10] RMC Kingston, Canada
[11] University of North Carolina at Greensboro, USA
[12] Tartu Observatory, Estonia
[13] Fizeau, Observatoire de la Côte d'Azur, France
[14] Dpt of Astronomy, University of Maryland, USA
[15] Observatoire de Genève, Switzerland

2 Introduction: Hot stars and Emission Line Stars

The hot stars are defined as stars with effective temperature higher than 7500K. They concern main sequence OBA stars but also Supergiant O stars, etc. The emission line stars are the stars with emission lines in their spectra (in the RVS domain but also in others parts of the spectrum). From time to time, some ELS exhibit emission lines in the UV-Visible part of the spectrum but not in the RVS domain, in which CaII triplet and/or Paschen lines are present. This is the case for example of the late-type Be stars. More generally, ELS can be found everywhere in the HR diagram, they range from hot to cool stars and from young to evolved stars. As examples, one can cite the WR, LBV, Oe, Of, Be, supergiant Oe to Ke, PNe, HBe/Ae, B[e], Mira Ceti e, TTauri, UV Ceti, Flare stars, etc.

With Gaia, we shall obtain for these stars:

- with ASTRO: the proper motions and distances,
- with the BP/RP spectrophotometry: the ELS detection (for example in Hα), the stellar photometric classification, and photometric fundamental parameters.
- With the RVS spectrograph: the ELS detection, the radial velocity, the spectroscopic fundamental parameters, the stellar spectral classification.
- An indice of the spectroscopic and photometric variability of the stars because they will be observed several times during the 5 years of the mission.
- Indications about potential behaviour differences between HS and ELS from our Galaxy and close local group galaxies, because the bright stars of these galaxies, which correspond mainly to hot stars, will be observed by Gaia.

Combining these informations, we shall determine:

- 3D static and dynamic maps. These 2 maps allow to study the open cluster membership, the site of origin of the stars, the site of formation, and then to characterize the stars.
- The fundamental parameters and spectral classification of stars and where possible the parameters of the disks.
- Statistical links between the lines (amount of emission between Hα and Pa for example).
- With the distance, one can provide statistical relation between Mv and spectral types and find potential outliers among OB stars. This deviation could be interpreted in term of fast rotation effects (see Lamers et al. 1997).
- The interstellar reddening of the stars to correct their photometry. The remaining reddening will be interpreted as due to circumstellar matter/disk (Be, HBe/Ae stars).
- Previously unknown ELS (Be, WR), in case of Be stars, the Be phenomenon is transient and a Be star could be seen like a B star at one epoch and several years after seen like a Be star (due to the disk variability).
- The evolutionary status of Be stars. It will be possible to compare the status determined spectroscopically and photometrically via derredened abolute magnitudes.
- An index on the deviation from the expected behaviour of WR stars.
- The correct classification of B[e] stars. 50% of them are currently badly or not classified: SgB[e], PN[e], HB[e] because their distance is not yet known.
- The percentage of binarity. This is an important issue to understand the behaviour of some stars: what is the rate of binaries among Be stars? 75% according to McSwain & Gies (2005) or 30% according to Porter & Rivinius (2003)? What is the rate of binaries among hot stars? 60% for O stars according to Sana (2008), 30% according to Porter & Rivinius (2003) for B stars.

3 Algorithms and methods

In this section, we briefly present the methods of algorithms currently developed in order to obtain the astrophysical parameters of the stars and reach the goals enumerated above. They are elaborated in Coordination Unit 6, in the Coarse Characterization of Sources scientific module (managed by C. Martayan), in Coordination Unit 8, in the Extended Stellar Parametrizer scientific module (managed by Y. Frémat), in the Hot Stars scientific module (managed by R. Blomme), and in the Emission Line Stars scientific module (managed by C. Martayan).

3.1 Photometric detection of ELS and pre-classification of HS/ELS

The first possibility to detect the ELS and to pre-classify the HS is to use photometric colour-colour or colour-magnitude diagrams. To do that, with the BP/RP spectrophotometry, it is possible to obtain magnitudes in different filters similar to the classical Johnson or Geneva filters and draw the corresponding diagrams. Among them, to detect the ELS, the CMD (R-Hα vs. V-I) could be very useful as shown by Keller et al. (1999). Note that due to the low resolution, only stars with strong emission in Hα could be detected.

It is also possible to do the same kind of study with the RVS. We computed magnitude-filters in the RVS, defined in areas with CaII lines or Pa lines or both, and in the continuum. The magnitudes are then normalized to the size of the filters. Theoretical magnitudes are computed in filters where there are Pa+Ca lines (filter PaCa) and only one single Pa line (filter PaS that corresponds to the Pa14 line, which is the alone Pa line not blended with CaII lines in the RVS domain). Then the difference between the theoretical magnitude and the observed magnitude in the 2 filters are obtained (PaCa$_{th}$-PaCa$_{obs}$ and PaS$_{th}$-PaS$_{obs}$). The difference between 2 filters in the continuum is also determined in order to have an index on the slope of the spectrum and split the stars by categories (hot/cool stars). The first tests on simulated spectra (from CU2 team) for Be, WR stars and normal stars (from O to M stars) show that with the PaCa diagram, the ELS with strong or medium emission in the RVS are detected (above a threshold defined by the upper limit of the normal stars). We also used observed spectra both for ELS and HS from various ground-based spectrographs, which are correctly pre-classified with these diagrams (ELS or absorption). With the PaS diagram, we pre-classify the stars in spectral-types because the filter PaS allows to know whether the star contains or not Pa lines and then whether the star is a hot star or not).

3.2 Fundamental parameters determination

The fundamental parameters determination for hot stars is performed using grids of NLTE models with winds. The observed spectrum is fitted with theoretical ones using the Simplex downhill method (Nelder & Mead 1965). First tests based on 1089 synthetic spectra with noise added, Teff, logg, Vsini randomly chosen were performed. They indicate that in case of B stars, 61% of Teff are determined with an error bar of 10%, 65% of logg are determined with an error-bar of $\pm$0.25dex ($\pm$6%), 66% of Vsini are determined with an error-bar of $\pm$50%. In case of O stars, the error-bars are greater than for B stars, because the lines in the RVS spectra are weak. Due to its design, for HS the RVS displays only hydrogen lines (Pa lines) and from time to time weak HeII lines, which implies a poor precision on the Vsini. Full results are detailed in Frémat et al. (2007, 2008 in preparation), and Martayan et al. (2008). Moreover, the parameters derived for the HS will be useful for improving the galaxy models, in which there is a lack of HS population.

The same method of minimization/determination could be used to fit the emission lines with theoretical models to obtain parameters for the stellar winds and/or circumstellar matter/disks. Another technique for classical Be stars can use the relation between the strength of emission in Hα and Pa lines. However, it is necessary to remove the amount of emission due to CaII lines in the Ca–Pa blends. Using data from Briot (1981), we obtained an interpolated distribution of cleaned Pa emission in the RVS domain using the Pa14 line as beginning point.

3.3 Spectral classification

There are different possibilities to spectroscopically classify the stars. The first one is to use the Teff-logg plane and calibrations, which link fundamental parameters to spectral types (Zorec 1986, Bouret et al. 2003). The second one is to use the equivalent widths of the lines and calibrations from Andrillat et al. (1995), and

Carquillat et al. (1997). However, to do that, we have to detect the presence of a line, to determine the parameters of the lines (the wavelength, the intensity in emission or absorption, the equivalent width). For detecting the lines, we developed different algorithms based on local signal to noise ratio variations, the local slope variation, and by gaussian fitting (see Viala et al. 2008, Frémat et al. 2007). In case of high signal to noise ratio (better than 20), the different methods provide good lines detection. In case of bad signal to noise ratio (lower than 20), from time to time wrong lines are detected. The automatic identification is currently tested. It is based on a cross-correlation of the theoretical and observed wavelength -differences between consecutive lines. The EWs, FWHM, I, are then determined and added to the tables of observed lines and identified lines. Details will be given by Martayan et al. (in preparation).

3.4 Classification with neural networks approach

We explore also other kind of classication methods based on the neural network approach or on the decision tree via the WEKA library. These algorithms need training samples of spectra for each kind of stars in order to teach the neural networks. Then, they are tested with tests samples in order to determine the reliability of their automatic classification. Finally, after having defined the rates of good/bad classification, they are used in the true data. Currently, the first tests based on magnitude in filters (defined above) provide an excellent classification of stars, but the 1000 spectra used here are synthetic noise-free ones and we need more true observed spectra for each kind of object (ELS, HS) to correctly supervise the learning of the neural networks.

An important issue for these methods as well as for the other algorithms currently developed is to obtain in the near future enough observed spectra to test and improve them before the launch of Gaia. In addition, it will be useful for a more complete scientific analysis of the stars to have a dedicated telescope/instrument (probably a multi-objects spectrograph) for the follow-up of the Gaia targets.

4 Conclusion

The Gaia satellite is one of the most ambicious space mission of the next decades. It will provide some astrophysical parameters for 1 billion of stars and among them for several million of hot stars and emission line stars both in the Milky Way and close local group galaxies. They will allow to elaborate 3D static and dynamic maps, statistical studies, giving new clues about the behaviour of the stars (origin, evolution, variability, binarity). Different methods and algorithms are currently developed by our team in order to detect and identify the lines, to determine the fundamental parameters of the stars, and also to provide their spectral classification.

C.M. acknowledges funding from the ESA/Belgian Federal Science Policy in the framework of the PRODEX program (C90290). C.M. thanks the SOC of the Gaia session for the invitation to present a talk and the AS-Gaia France for the financial support.

References

Andrillat, Y., Jaschek, C. & Jaschek, M., 1995, A&A, 299, 493

Bouret, J.-C., Lanz, T., Hillier, D. J., Heap, S.R ., et al., 2003, ApJ, 595, 1182

Briot, D., 1981, A&A, 103, 5

Carquillat, M. J., Jaschek, C., Jaschek, M., Ginestet, N., 1997, A&AS, 123, 5

Frémat, Y., Barrado, D., Barro, L., Jonckheere, A., et al., 2007, GAIA-C8-SP-OPM-BL-001-02

Keller, S. C., Wood, P. R. & Bessell, M. S., 1999, A&AS, 134, 489

Kroupa, P., 2001, MNRAS, 322, 231

Lamers, H. J., Harzevoort, J. M., Schrijver, H., Hoogerwerf, R., et al., 1997, A&A, 325, 25

Martayan, C., Barrado, D., Barro, L., Blomme, R., et al., 2008, GAIA-C8-SP-OPM-BL-001-04

McSwain, M. V. & Gies, D. R., 2005, ApJS, 161, 118

Nelder, J. A. & Mead, R., 1965, the Computer Journal, 7.4, 308

Porter, J. M. & Rivinius, T., 2003, PASP, 115, 1153

Sana, H., 2008, IAUS, 250, 554

Viala,Y., Blomme, R., Dammerdji, Y., Delle-Luche, C., et al., 2008, GAIA-C6-SP-OPM-YV-004

Zorec, J., 1986, PhD thesis, Université Paris VII

SF2A 2008
C. Charbonnel, F. Combes and R. Samadi (eds)

MOLECULAR HYDROGEN IN THE DISK OF THE HERBIG STAR HD 97048

Martin-Zaïdi, C.[1], Lagage, P.-O.[2], Pantin, E.[2], Habart, E.[3], Ménard, F.[1], Augereau, J.-C.[1] and Pinte, C.[4]

Abstract. We present high-resolution spectroscopic mid-infrared observations of the circumstellar disk around the Herbig Ae star HD 97048 with the *VLT Imager and Spectrometer for the mid-InfraRed* (*VISIR*). We detect the S(1) pure rotational line of molecular hydrogen (H_2) at 17.035 μm arising from the disk around the star. This detection reinforces the claim that HD 97048 is a young object surrounded by a flared disk at an early stage of evolution. The emitting warm gas is located within the inner 35 AU of the disk. This detection implies that particular physical conditions, such as a $T_{gas} > T_{dust}$, are present in the inner disk surface layer. We do not detect the S(2) and S(4) H_2 lines, but we derive upper limits on the integrated line fluxes which allow us to estimate an upper limit on the gas excitation temperature. This limit on the temperature sets new contraints on the mass of warm gas in the inner regions of the disk.

1 Introduction

Circumstellar (CS) disks surrounding pre-main sequence stars are thought to be the location of planet building. The characterization of the gaseous component, which initially represents 99% of the total disk mass, is a key research question towards an understanding of protoplanetary disks and planet formation. However, from previous observations, little is known about the gas compared to the dust. Molecular hydrogen (H_2) is the main constituent of the molecular cloud from which the young star is formed and is also expected to be the main component of the CS disk. H_2 is the only molecule that can directly constrain the mass reservoir of warm and hot molecular gas in disks. Indeed, the detection of H_2 excited by collisions allows us to measure the temperature and density of the warm gas. Unfortunately, direct observation of H_2 is difficult. Electronic transitions occur in the ultraviolet to which the Earth's atmosphere is opaque, and rotational and ro-vibrational transitions at infrared (IR) wavelengths are faint because of their quadrupolar origin. Recently, Carmona et al. (2008) discussed the detectability of H_2 mid-IR lines by modeling the surface layers of a gas-rich disk, seen face-on, surrounding a Herbig Ae star (HAe) at 140 pc from the Sun. By assuming that the gas and dust were well-mixed in the disk, a gas-to-dust ratio of about 100, and that $T_{gas} = T_{dust}$, those authors demonstrated that mid-IR H_2 lines could not be detected with the existing instruments. Surprisingly, H_2 rotational lines have been detected in the disk around one HAe, namely AB Aur, with the high spectral and spatial resolution TEXES spectrometer (Bitner et al. 2007). These detections demonstrate that H_2 can be observed in the mid-IR domain when particular physical conditions exist in disks.

VISIR has a sufficiently high spectral and spatial resolution (Lagage et al. 2004) to pick up such narrow gas lines from the disks. In addition, high spectral resolution is a key element to disentangle the H_2 line from the absorption lines due to the Earth's atmosphere. The spectral ranges covered by *VISIR* offer access to the most intense pure rotational lines of H_2: the S(1) line at 17.0348 μm, S(2) at 12.2786 μm, and S(4) at 8.0250 μm. The S(0) transition close to 28 μm is not observable from the ground due to the Earth's atmospheric absorption, and the S(3) line at 9.6649 μm, is located amidst a forest of telluric ozone features, and is thus only observable for extremely favorable Doppler shifts.

[1] Laboratoire d'Astrophysique de Grenoble, CNRS, Université Joseph-Fourier, UMR5571, Grenoble, France
[2] Laboratoire AIM, CEA/DSM - CNRS - Université Paris Diderot, DAPNIA/Service d'Astrophysique, Bat. 709, CEA/Saclay, 91191 Gif-sur-Yvette Cedex, France
[3] Institut d'Astrophysique Spatiale, 91405 Orsay, France
[4] School of Physics, University of Exeter, StockerRoad, Exeter EX4 4QL, United Kingdom

Table 1. Summary of the observations. Airmass and seeing intervals: from the beginning to the end of the observations.

λ μm	t_{exp} (s)	Airmass	Optical seeing (")	Slit (")	R	Stand. Star	Asteroid
17.0348	1800	1.72-1.79	0.52-0.66	0.75	14 000	HD89388	CERES
12.2786	960	1.81-1.87	1.97-2.16	0.4	13 600	HD91056	VESTA
8.0250	1872	1.66-1.69	0.51-0.65	0.4	13 300	HD92305	VESTA

HD 97048 is a nearby, relatively isolated Herbig A0/B9 star located in the Chameleon cloud at a distance of 180 pc (van den Ancker et al. 1998). Its age has been estimated from evolutionary tracks to be of the order of 3 Mys (kindly computed by L. Testi and A. Palacios). This star is known to be surrounded by an extended CS disk. The *VISIR* imaging observations of this star have revealed an extended emission of PAHs (Polycyclic Aromatic Hydrocarbons) at the surface of a flared disk (Lagage et al. 2006; Doucet et al. 2007). This is the only Herbig star for which the flaring of the disk has been observed by direct imaging. This geometry implies that a large amount of gas should be present to support the flaring structure and that the disk is at an early stage of evolution. This star is thus one of the best candidates to study the gas component in the disks of HAes.

2 Observations and data reduction

HD 97048 was observed at 3 different periods. The observations at 17.035 μm presented in Martin-Zaïdi et al. (2007), were performed in 2006 June 22, the 8.025 μm observations in 2007 April 07, and the 12.278 μm observations in 2007 July 03 (Martin-Zaïdi et al. 2008, in prep). The three sets of observations were obtained with the high resolution spectroscopic mode of *VISIR*. The exposure time, slit width, and atmospheric conditions during the observations are presented in Table 1. For all the three observations, the standard "chopping and nodding" technique was used to suppress the large sky and telescope background dominating at mid-IR wavelengths (for details on the observation technique see Martin-Zaïdi et al. 2007). Asteroids and standard stars were observed just before and after observing HD 97048, at nearly the same airmass and seeing conditions as the object. In order to correct the spectra from the Earth's atmospheric absorption, we divided each spectrum of HD 97048 by that of the corresponding asteroid (which has a much better signal-to-noise ratio than that of the standard star), and used the standard stars' observed and modeled spectra (Cohen et al. 1999) to obtain the absolute flux calibration. The wavelength calibration is done by fitting the observed sky background features with a model of Paranal's atmospheric emission. We note that $A_v = 0.24$ mag for HD 97048 (Valenti et al. 2000), thus we have not corrected the spectra for dust extinction, since it is negligible in our wavelength range for any $A_v < 40$ mag (Fluks et al. 1994).

3 Data analysis

As shown in Fig. 1, we have detected the H_2 pure rotational S(1) line near 17.03 μm. In the flux-calibrated spectrum, the standard deviation (σ) of the continuum flux was calculated in regions less influenced by telluric absorption, and close to the feature of interest. We deduced a 6σ detection in amplitude for the line, corresponding to a signal-to-noise ratio of about 11σ for the line, when integrating the signal over a resolution element (6 pixels). The line is not resolved as we can fit it with a Gaussian with a full width at half maximum (FWHM) equal to a spectral resolution element of 30 $\mathrm{km\,s^{-1}}$ (see Fig. 1). From our fit, assuming the emission arises from an isothermal mass of optically thin H_2, we derived the integrated flux in the line (see Table 2).

Once the spectrum is corrected from the Earth's rotation, and knowing the heliocentric radial velocity of HD 97048 (+21 $\mathrm{km\,s^{-1}}$; Acke et al. 2005), we estimated, from the wavelength position of the Gaussian peak, the radial velocity of H_2 to be about 4 ± 2 $\mathrm{km\,s^{-1}}$ in the star's rest frame. We thus considered that the radial velocity of the H_2 is similar to that of the star, implying that the emitting gas is bound to the star. The H_2 line is not resolved spatially. Given the *VISIR* spatial resolution of about 0.427" at 17.03 μm, and the star distance (180 pc from the sun), we can assess that the emitting H_2 is located within the inner 35 AU of the disk. We calculated the corresponding column density for the $J = 3$ rotational level (see Table 2; for details about the method see Martin-Zaïdi et al. (2007).

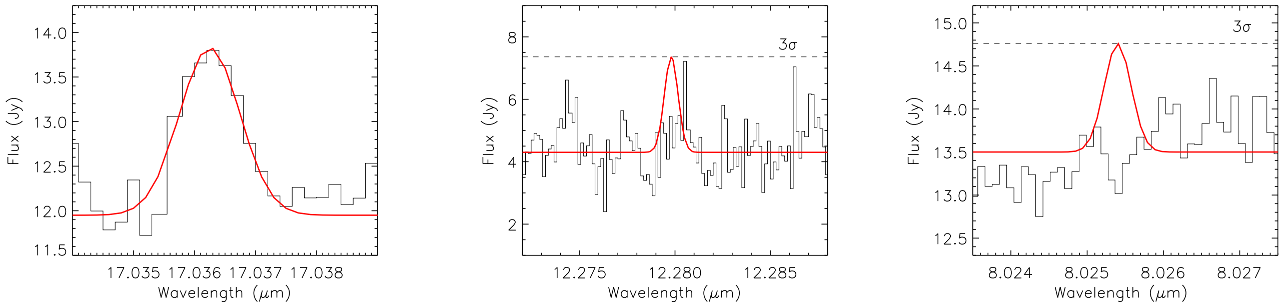

Fig. 1. *(Left):* H_2 S(1) emission line from the disk of HD 97048. *(Middle and Right):* regions of the HD 97048 spectrum where the S(2) and the S(4) lines, respectively, could have been observed. Gaussians with amplitudes of 3σ line-flux upper limits are overplotted. For each plot: black line: observed spectrum; red line: gaussian fit with FWHM equal to a spectral resolution element.

HD 97048 spectra showed no evidence for H_2 emission neither at 12.278 μm nor at 8.025 μm (Fig. 1). From the flux-calibrated spectra, we calculated the standard deviation (σ) for wavelength ranges relatively unaffected by telluric absorption, and close to the wavelengths of interest. The 3σ upper limits on the integrated line fluxes were calculated by integrating over a Gaussian of FWHM equal to a spectral resolution element and an amplitude of about 3σ flux, centered on the expected wavelength for the S(2) and S(4) lines respectively (Fig. 1). From the limits on integrated intensities and by assuming that the emitting H_2 is optically thin at LTE, we estimated the upper limits on the column densities of the corresponding upper rotational levels of each H_2 transition (see Table 2).

Table 2. Integrated fluxes, Intensities and column densities of each observed mid-IR transitions of H_2. v_{up} and J_{up} are respectively the vibrational and rotational upper levels of the transition of interest.

Wavelength (μm)	Transition	v_{up}	J_{up}	Integrated flux (ergs s^{-1} cm^{-2})	Intensity (ergs cm^{-2} s^{-1} sr^{-1})	$N_{J_{up}}(H_2)$ (cm^{-2})
17.035	S(1)	0	3	2.4×10^{-14}	5.7×10^{-3}	1.29×10^{21}
12.278	S(2)	0	4	$<5.5\times10^{-14}$	$<2.6\times10^{-2}$	$<7.46\times10^{20}$
8.025	S(4)	0	6	$<2.6\times10^{-14}$	$<2.9\times10^{-2}$	$<5.54\times10^{19}$

4 Discussion

Our high resolution spectroscopic observation of the S(1) pure rotational line of H_2 at 17.03 μm of HD 97048 has revealed the presence of significant amounts of warm gas in the inner 35 AU of the disk. This detection confirms that HD 97048 is a young object surrounded by a circumstellar disk at an early stage of evolution. Indeed photoevaporation of the gas and planet formation are expected to clear up the inner part of the disk within about 3 million years (Takeuchi et al. 2005).

The estimates of the column densities of the $J = 3$, $J = 4$, and $J = 6$ rotational levels of H_2 allowed us to plot the excitation diagram of the molecule (see Fig. 2). Assuming that all three levels are populated by thermal collisions (LTE), we estimated that the temperature of the observed gas should be less than 920 K. However, as shown by Martin-Zaïdi et al. (2007) from the observation of the S(1) line, such a detection can only be explained if the physical conditions of the gas differ from LTE ones. Indeed, the S(1) line detection implies that particular conditions have to be assumed for the gas and dust, such as $T_{gas} > T_{dust}$, and that the H_2 gas is likely excited by other mechanisms than thermal collisions. In any case, even if these three levels are not thermally populated, their populations give strong constraints on the gas kinetic temperature. Indeed, the kinetic temperature is given by the population of the first rotational levels (namely $J = 0$ and $J = 1$), and is always lower than the excitation temperature given by the higher energy levels. Our upper limit on

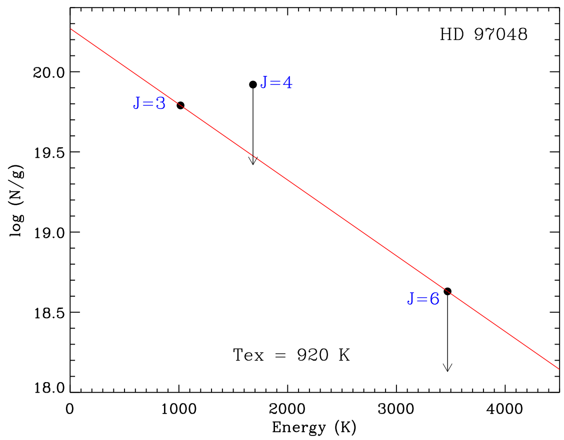

Fig. 2. Excitation diagram for H_2 towards HD 97048. If the three rotational levels are populated by thermal collisions, their populations follow the Boltzmann law, and the gas temperature should be less than 920 K (red line).

the temperature of about 920 K is thus reliable whatever the mechanisms responsible for the excitation of the observed gas.

This constraint on the temperature of the gas confirms the estimates by Martin-Zaïdi et al. (2007) concerning the mass of warm H_2 in the inner 35 AU of the disk. Indeed, those authors have derived masses of the warm gas in the range from 10^{-2} to nearly 1 M_{Jup} (1 $M_{Jup} \sim 10^{-3}$ $M_{\odot}$), depending on the adopted temperature and assuming LTE. Theses masses are lower than those of Lagage et al. (2006), who have estimated a minimum mass of gas in the inner disk to be of the order of 3 M_{Jup}. But it should be pointed out that mid-IR H_2 lines are only probing warm gas located in the surface layer of the disk, when a higher mass of colder gas is expected to be present in the interior layers of the disk. In any case, the finding of warm H_2 reinforces the claim that a large amount of cold gas is present in the disk to support its flaring geometry (Lagage et al. 2006).

References

Acke, B., van den Ancker, M.E., & Dullemond, C.P. 2005, A&A, 436, 209

Bitner, M.A., Richter, M.J., Lacy, J.H., et al. 2007, ApJL, 661, L69

Carmona, A., van den Ancker, M.E., Henning, T., et al. 2008, A&A, 477, 839

Cohen, M., Walker, R.G., & Witteborn, F.C. 1999, LPI Contributions, 969, 5

Doucet, C., Habart, E., Pantin, E., et al. 2007, A&A, 470, 625

Fluks, M.A., Plez, B., The, P.S., et al. 1994, A&AS, 105, 311

Lagage, P.-O., Doucet, C., Pantin, E. et al. 2006, Science, 314, 621

Lagage, P.-O., Pel, J.W., Authier, M., et al. 2004, The Messenger, 117, 12

Martin-Zaïdi C., et al. 2008, in prep

Martin-Zaïdi, C., Lagage, P.-O., Pantin, E., & Habart, E. 2007, ApJL, 666, L117

Takeuchi, T., Clarke, C.J., & Lin, D.N.C. 2005, ApJ, 627, 286

Valenti, J.A., Johns-Krull, C.M., & Linsky, J.L. 2000, ApJS, 129, 399

van den Ancker, M.E., de Winter, D., & Tjin A Djie, H.R.E. 1998, A&A, 330, 145

SF2A 2008
C. Charbonnel, F. Combes and R. Samadi (eds)

IS IT NECESSARY TO GO BEYOND THE PONCTUAL MASS APPROXIMATION FOR TIDAL PERTURBER IN CLOSE SYSTEMS?

Mathis, S.[1] and Le Poncin-Lafitte, C.[2]

Abstract. With the discoveries of very close star-planet systems with planet orbiting sometimes at several star radius but also with well-known situations in our solar system where natural satellites are very close to their parent planet the validity of the ponctual mass approximation for the tidal perturber (respectively the parent star or planet when we study the close planet or natural satellite dynamics) has to be examined. In this short paper, we consider this problematic using results coming from a complete formalism that allows to treat the tidal interaction between extended bodies. We focus on its application to a simplified configuration.

1 Context

In celestial mechanics, one of the main approximation done in the modelling of tidal effects (star-star, star-innermost planet or planet-natural satellites interactions) is to consider the tidal perturber as a point mass body. However a large number of extrasolar Jupiter-like planets orbiting their parent stars at a distance lower than 0.1 AU have been discovered during the past decade (Mayor *et al.*, 2005). Moreover, in Solar System, Phobos around Mars and the inner natural satellites of Jupiter, Saturn, Uranus and Neptune are very close to their parent planets. In such cases, the ratio of the perturber mean radius to the distance between the center of mass of the bodies can be not any more negligeable compared to 1. Furthermore, it can be also the case for very close but separated binary stars. In that situation, neglecting the extended character of the perturber have to be relaxed, so the tidal interaction between two extended bodies must be solved in a self-consistent way with taking into account the full gravitational potential of the extended perturber, generally expressed with some mass multipole moments, and then to consider their interaction with the tidally perturbed body. In the litterature, not so many studies have been done (Borderies, 1978-1980; Ilk, 1983; Borderies & Yoder, 1990; Hartmann, Soffel & Kioustelidis, 1994; Maciejewski, 1995).

2 General formalism

Several years ago, Hartmann, Soffel & Kioustelidis (1994) introduced in Celestial Mechanics an interesting tool, based on Cartesian Symmetric Trace Free (STF) tensors, to treat straighforwardly the couplings between the gravitational fields of extended bodies. These tensors are fully equivalent to usual spherical harmonics but in addition a set of STF tensors represents an irreductible basis of the rotation group SO3 (Courant & Hilbert 1953). It means that using algebraic properties of STF tensors, these objects become a powerful tool to determine the coupling between spherical harmonics in an elegant and compact way. However, as these tensors are not widely used in celestial mechanics, Mathis & Le Poncin-Lafitte (2008) (hereafter MLP08) first recall their definition and fundamental properties and stress their relation with usual spherical harmonics. Then, the multipole expansion of gravitational-type fields is treated. First, the well-known external field of such body is derived using STF tensors; classical identities are provided. Next, the mutual gravitational interaction between two extended bodies and the associated tidal interaction are derived. We show how the use of STF tensors leads

[1] CEA/DSM/IRFU/SAp, CE Saclay, F-91191 Gif-sur-Yvette Cedex, France; AIM, UMR 7158, CEA - CNRS - Université Paris 7, France
[2] Observatoire de Paris, SYRTE CNRS/UMR 8630, 61 Avenue de l'Observatoire, F-75014 Paris, France

to an analytical and compact treatment of the coupling of their gravitational fields. We deduce the general expressions of tidal and mutual interaction potentials expanded in spherical harmonics. Using the classical Kaula's transform (Kaula, 1962), we express them as a function of the Keplerian orbital elements of the body considered as the tidal perturber. These results are then used to derive the external gravitational potential of such tidally perturbed extended body. Introducing a third body, its mutual interaction potential with the previous tidally perturbed extended body is defined that allows us to derive the disturbing function using the results obtained with STF tensors and the Kaula's transform. The dynamical equations ruling the evolution of this system are obtained.

3 Case of an extended axisymmetric deformed perturber

Here, our goal is to quantify the term(s) of the disturbing function due to the non-ponctual behaviour of the perturber B and to compare it to the one in the ponctual mass case. To achieve this aim, some assumptions

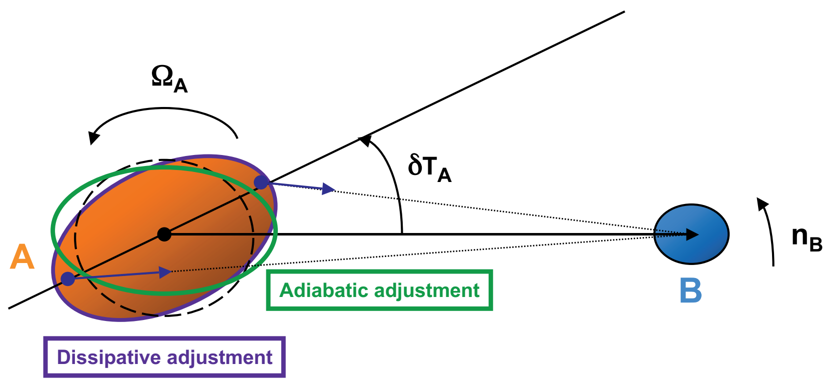

Fig. 1. Classical tidal dynamical system. The extended body B is tidally disturbing the extended body A which adjusts itself with a phase lag δ_{T_A} due to its internal friction processes. The dynamics of B is then studied. Ω_A and n_B are respectively the spin frequency of A and the mean motion of B.

are done. First, we adopt the quadrupolar approximation for the response of A to the tidal excitation by B; thus, using the calculations of MLP08, the disturbing function is then given by

$$\begin{aligned}\mathcal{R} \;=\; & -\frac{G}{M_B}\frac{4\pi}{5}k_2^{\mathrm{A}}R_{\mathrm{A}}^5 \sum_{m_{\mathrm{A}},l_{\mathrm{B}},m_{\mathrm{B}},j,p,q} \left\{ \left|Z_{\mathrm{T_A};2,m_{\mathrm{A}},L_{\mathrm{I}}}\left(\nu,K;\Psi_{2+l_{\mathrm{B}},m_{\mathrm{A}}+m_{\mathrm{B}},j,p,q}\right)\right| \left[\gamma_{l_{\mathrm{B}},m_{\mathrm{B}}}^{2,m_{\mathrm{A}}}\right]^2 \left|M_{l_{\mathrm{B}},m_{\mathrm{B}}}^{\mathrm{B}}\right|^2 \right.\\ & \times \frac{1}{a_{\mathrm{B}}^{2(2+l_{\mathrm{B}}+1)}} \left[\kappa_{2+l_{\mathrm{B}},j}\right]^2 \left[d_{j,m_{\mathrm{A}}+m_{\mathrm{B}}}^{2+l_{\mathrm{B}}}\left(\varepsilon_{\mathrm{A}}\right)\right]^2 \left[F_{2+l_{\mathrm{B}},j,p}\left(I_{\mathrm{B}}\right)\right]^2 \left[G_{2+l_{\mathrm{B}},p,q}\left(e_{\mathrm{B}}\right)\right]^2 \\ & \left.\times \exp\left[i\,\delta_{\mathrm{T_A};2,m_{\mathrm{A}},L_{\mathrm{I}}}\left(\nu,K;\Psi_{2+l_{\mathrm{B}},m_{\mathrm{A}}+m_{\mathrm{B}},j,p,q}\right)\right]\right\} = \sum_{L_{\mathrm{I}}}\mathcal{R}_{L_{\mathrm{I}}}, \end{aligned} \tag{3.1}$$

where $L_{\mathrm{I}} = \{m_{\mathrm{A}}, l_{\mathrm{B}}, m_{\mathrm{B}}, j, p, q\}$; indexes definition is given in MLP08. G is the universal constant of gravity. M_{B} is the mass of B and R_{A} is the radius of A. k_2^{A} is the Love's number of A that gives the linear adiabatic response of A to the tidal perturbation exerted by B. $Z_{\mathrm{T_A}}$ describes the dissipation of the tidal kinetic energy by viscous friction and thermal diffusion (ν and K are respectively the (turbulent) viscosity and the thermal diffusivity).

On the other hand, the gravific potential of B is expanded as $V^{\rm B}(\mathbf{r}) = G\sum_{l_{\rm B}\geq 0} M^{\rm B}_{l_{\rm B},m_{\rm B}} Y_{l_{\rm B},m_{\rm B}}(\theta,\varphi)/r^{l_{\rm B}+1}$ where the $M^{\rm B}_{l_{\rm B},m_{\rm B}}$ are the gravitational multipole moments of B and (r,θ,φ) are the spherical coordinates which have the center of mass of B for origin. $a_{\rm B}$, $e_{\rm B}$ and $I_{\rm B}$ are respectively the semi-major axis, the eccentricity and the inclination of the relative orbit of B. $\Psi_{L,M,j,p,q}$ is a function of the three other keplerian elements of this orbit, of the A angular velocity $\Omega_{\rm A}$ and of its precession angle. $\varepsilon_{\rm A}$ is the obliquity of A. $\gamma^{L_2,M_2}_{L_1,M_1}$ and $\kappa_{L,j}$ are coupling coefficients, which are detailed in MLP08. $d^{L}_{j,M}$, $F_{L,j,p}$ and $G_{L,p,q}$ are respectively obliquity, inclination and eccentricity special functions.

Since we are interested in the amplitude of $\mathcal{R}_{L_{\rm I}}$, we focus on its norm ($|\mathcal{R}_{L_{\rm I}}|$). On the other hand, as we know that the dissipative part of the tide is very small compared to the adiabatic one (cf. Zahn 1966), we can assume that $|Z_{T_{\rm A}}|\approx 1$ in this first step.

Let us first derive the terms $|\mathcal{R}_{L_{\rm I}}|$ due to the non-ponctual terms of the gravific potential of B which have a non-zero average in time over an orbital period of B, $\left\langle V^{\rm B}_{\rm N-P}\right\rangle_{T_{\rm B}}(\mathbf{r}) = 1/T_{\rm B}\int_0^{T_{\rm B}} V^{\rm B}_{\rm N-P}(t,\mathbf{r})\,{\rm d}t$ that corresponds to the axisymmetric rotational and permanent tidal deformations (see Zahn 1977) (the same procedure can of course be applied to the non-stationnary and non-axisymmetric deformations, but we choose here to focus only on $\left\langle V^{\rm B}_{\rm N-P}\right\rangle_{T_{\rm B}}$ to illustrate our purpose). Then, as the considered deformations of B are axisymmetric, we can expand them using the usual gravitational moments of B (J_{l_B}) as

$$V^{\rm B}(\mathbf{r}) = \frac{GM_{\rm B}}{r} + \left\langle V^{\rm B}_{\rm N-P}\right\rangle_{T_{\rm B}} \quad \text{where} \quad \left\langle V^{\rm B}_{\rm N-P}\right\rangle_{T_{\rm B}} = G\sum_{l_{\rm B}>0}\left(M^{\rm S_B}_{l_{\rm B},0}+M^{\rm T_B}_{l_{\rm B},0}\right)\frac{Y_{l_{\rm B},0}(\theta,\varphi)}{r^{l_{\rm B}+1}}, \tag{3.2}$$

with $M^{\rm S_B}_{l_{\rm B},0}+M^{\rm T_B}_{l_{\rm B},0} = -\frac{J_{l_{\rm B}}M_{\rm B}R_{\rm B}^{l_{\rm B}}}{\mathcal{N}^0_{l_{\rm B}}}$ where $M^{\rm S_B}_{l_{\rm B},0}$ and $M^{\rm T_B}_{l_{\rm B},0}$ are respectively the gravitational multipole moments induced by the permanent rotational and tidal deformations of B; $M_{\rm B}$ is the mass of B. $\mathcal{N}_{L,M}$ is the spherical harmonics ($Y_{L,M}$) normalization constant. Then, we obtain

$$\begin{aligned}\left|\mathcal{R}^{J_{l_{\rm B}}}_{L_{\rm I}}(a_{\rm B},e_{\rm B},I_{\rm B},\varepsilon_{\rm A})\right| &= \frac{G}{M_B}\frac{4\pi}{5}k_2^{\rm A}R_{\rm A}^5\left[\gamma^{2,m_{\rm A}}_{l_{\rm B},0}\right]^2\left|M^{\rm S_B}_{l_{\rm B},0}+M^{\rm T_B}_{l_{\rm B},0}\right|^2\\ &\quad\times\frac{1}{a_{\rm B}^{2(2+l_{\rm B}+1)}}\left[\kappa_{2+l_{\rm B},j}\right]^2\left[d^{2+l_{\rm B}}_{j,m_{\rm A}}(\varepsilon_{\rm A})\right]^2\left[F_{2+l_{\rm B},j,p}(I_{\rm B})\right]^2\left[G_{2+l_{\rm B},p,q}(e_{\rm B})\right]^2.\end{aligned} \tag{3.3}$$

On the other hand, the term $|\mathcal{R}_{L_{\rm I}}|$ associated to $M_{\rm B}$, namely the disturbing function in the case where B is assumed to be a ponctual mass, is given by:

$$\begin{aligned}\left|\mathcal{R}^{M_{\rm B}}_{L_{\rm I}}(a_{\rm B},e_{\rm B},I_{\rm B},\varepsilon_{\rm A})\right| &= \frac{G}{M_B}\frac{4\pi}{5}k_2^{\rm A}R_{\rm A}^5\left[\gamma^{2,m_{\rm A}}_{0,0}\right]^2\left|M^{\rm S_B}_{0,0}\right|^2\frac{1}{a_{\rm B}^6}\left[\kappa_{2,j}\right]^2\left[d^{2}_{j,m_{\rm A}}(\varepsilon_{\rm A})\right]^2\left[F_{2,j,p}(I_{\rm B})\right]^2\left[G_{2,p,q}(e_{\rm B})\right]^2\\ &= \frac{G}{M_B}\frac{4\pi}{5}k_2^{\rm A}R_{\rm A}^5 M_{\rm B}\frac{1}{a_{\rm B}^6}\left[\kappa_{2,j}\right]^2\left[d^{2}_{j,m_{\rm A}}(\varepsilon_{\rm A})\right]^2\left[F_{2,j,p}(I_{\rm B})\right]^2\left[G_{2,p,q}(e_{\rm B})\right]^2\end{aligned} \tag{3.4}$$

since $M^{\rm B}_{0,0} = \sqrt{4\pi}M_{\rm B}$. We now consider the ratio $\left|\mathcal{R}^{J_{l_{\rm B}}}_{L_{\rm I}}\right|/\left|\mathcal{R}^{M_{\rm B}}_{L_{\rm I}}\right|$, focusing on the configuration of minimum energy. In this state, the spins of A and B are aligned with the orbital one so that $\varepsilon_{\rm A}=I_{\rm B}=0$ (that leads to $j=m_{\rm A}$ and $p=(2-m_{\rm A}+l_{\rm B})/2$) and the orbit is circular ($e_{\rm B}=0$). Then, we consider:

$$\mathcal{E}_{m_{\rm A},l_{\rm B}} = \frac{\left|\mathcal{R}^{J_{l_{\rm B}}}_{L_{\rm I}}(a_{\rm B},0,0,0)\right|}{\left|\mathcal{R}^{M_{\rm B}}_{L_{\rm I}}(a_{\rm B},0,0,0)\right|}. \tag{3.5}$$

Using eqs. (3.3-3.4), we get its expression in function of $J_{l_{\rm B}}$ and of $(R_{\rm B}/a_{\rm B})$:

$$\mathcal{E}_{m_{\rm A},l_{\rm B}} = \frac{1}{4\pi}\left[\frac{1}{\mathcal{N}^0_{l_{\rm B}}}\frac{\gamma^{2,m_{\rm A}}_{l_{\rm B},0}}{\gamma^{2,m_{\rm A}}_{0,0}}\frac{\kappa_{2+l_{\rm B},m_{\rm A}}}{\kappa_{2,m_{\rm A}}}\frac{F_{2+l_{\rm B},2,\frac{l_{\rm B}}{2}}(0)}{F_{2,2,0}(0)}\right]^2 J^2_{l_{\rm B}}\left(\frac{R_{\rm B}}{a_{\rm B}}\right)^{2l_{\rm B}}. \tag{3.6}$$

As it has been emphasized by Zahn (1966-1977), the main mode of the dissipative tide ruling the secular evolution of the system is $m_{\rm A}=2$. We thus define $\mathcal{E}_{l_{\rm B}}$ such that

$$\mathcal{E}_{l_{\rm B}} = \mathcal{E}_{2,l_{\rm B}} = \left[\frac{1}{3}F_{2+l_B,2,\frac{l_B}{2}}(0)\right]^2 J^2_{l_{\rm B}}\left(\frac{R_{\rm B}}{a_{\rm B}}\right)^{2l_{\rm B}}, \tag{3.7}$$

which can be recast into

$$\log\left(\mathcal{E}_{l_B}\right) = 2\left[\log\left[\frac{1}{3}F_{2+l_B,2,\frac{l_B}{2}}(0)\right] + \log J_{l_B} - l_B \log\left(\frac{a_B}{R_B}\right)\right]. \tag{3.8}$$

Finally, keeping only into account the quadrupolar deformation of B (J_2), we get:

$$\log\left(\mathcal{E}_2\right) = 2\left[\log\left(\frac{5}{2}\right) + \log J_2 - 2\log\left(\frac{a_B}{R_B}\right)\right]. \tag{3.9}$$

This gives us the order of magnitude of the terms due to the non-ponctual behaviour of B compared to the one obtained in the ponctual mass approximation. It is directly proportional to the squarred J_2, thus increasing with ε_Ω^2 (where $\varepsilon_\Omega = \Omega_{\mathrm{B}}^2/\Omega_{\mathrm{c}}^2$, Ω_{B} being the angular velocity of B and $\Omega_{\mathrm{c}} = \sqrt{\frac{GM_{\mathrm{B}}}{R_{\mathrm{B}}^3}}$) in the case of the rotation-induced deformation and with $\varepsilon_{\mathrm{T}}^2$ (where $\varepsilon_{\mathrm{T}} = q\left(R_{\mathrm{B}}/a_{\mathrm{B}}\right)^3$ where $q = M_{\mathrm{A}}/M_{\mathrm{B}}$) in the tidal one, while it increases as $\left(R_{\mathrm{B}}/a_{\mathrm{B}}\right)^4$. Therefore, as it is shown in Fig. (2), the non-ponctual terms have to be taken into account for strongly deformed perturbers ($J_2 \geq 10^{-2}$) in very close systems ($a_{\mathrm{B}}/R_{\mathrm{B}} \leq 5$) while they decrease rapidly otherwise.

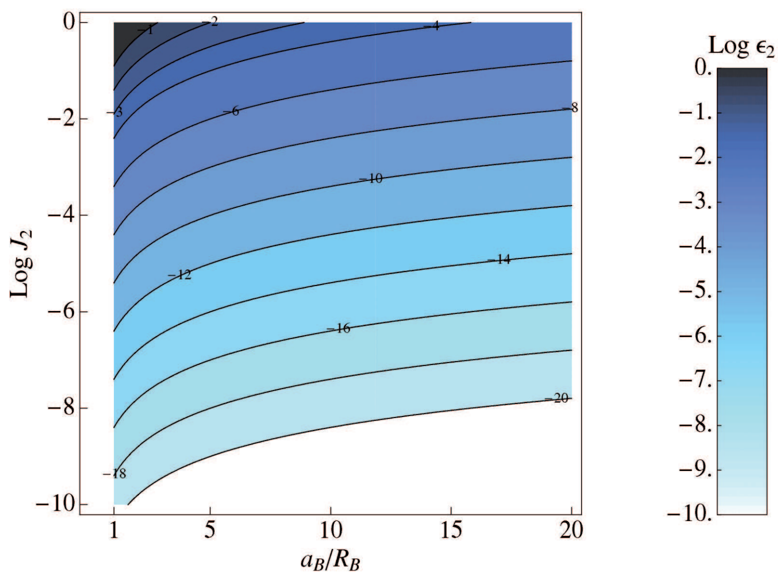

Fig. 2. Log $\mathcal{E}_2$ in function of $a_{\mathrm{B}}/R_{\mathrm{B}}$ and of J_2.

References

Borderies, N. 1978, Celestial Mechanics, 18, 295

Borderies, N. 1980, A&A, 82, 129

Borderies, N., Yoder, C. F. 1990, A&A, 233, 235

Courant, R. & Hilbert, D. 1953, Methods of Mathematical Physics, Interscience, New York

Hartmann, T., Soffel, M. H., Kioustelidis, T. 1994, Celestial Mechanics and Dynamical Astronomy, 60, 139

Ilk, K. H. 1983, Ph. D. Thesis, Technischen Universitaet, Munich Bayerische Akademie der Wissenschaften

Kaula, W. M. 1962, The Astronomical Journal, 67, 300

Maciejewski, A. J. 1995, Celestial Mechanics and Dynamical Astronomy, 63, 1

Mathis, S., Le Poncin-Lafitte, C. 2008, A&A, submitted (astro-ph 0711.1801)

Mayor, M., Pont, F., Vidal-Madjar, A. 2005, Progress of Theoretical Physics Supplement, 158, 43

Zahn, J.-P. 1966, Annales d'Astrophysique, 29, 313 & 489

Zahn, J.-P. 1977, A&A, 57, 383

SF2A 2008
C. Charbonnel, F. Combes and R. Samadi (eds)

AGB MASS LOSS AND CARBON STARS IN THE GALACTIC HALO

Mauron, N.[1]

Abstract. The mass loss of stars on the asymptotic giant branch (AGB) is a critical phenomenon for stellar evolution, but the AGB superwinds are not fully understood and physically modelled. One of the important characteristics that we would like to know is how mass loss depends on metallicity. At low metallicity, evolved AGB stars are carbon stars. From a systematic survey for cool carbon stars in the Galactic halo, we have identified 16 very dusty objects located far (> 2 kpc) from the Galactic plane and at distances of 2 to 20 kpc (Mauron 2008). One of these objects had been detected in CO by Groenewegen et al. (1997), its circumstellar expansion velocity is very small (3 km/s), and it is deficient in oxygen. We suggest that detection of CO from these 16 halo very dusty C stars might yield key information on mass loss at low metallicity.

1 Introduction

The AGB stars play an important role in stellar and galactic evolution. Stars with initial masses of ~ 1 to ~ 7 solar masses evolve to white dwarfs and lose a large fraction of their initial mass. The strength of this high mass loss (superwinds) determines the lifetimes of stars on the AGB and their populations. Another crucial aspect of the AGB is the return of matter into the interstellar medium. The AGB superwinds contribute to the ISM enrichment with fresh nuclear products and with grains. However, despite the key role of the AGB superwind, its mechanism remains difficult to explain.

A large number of observations of AGB winds close to the Sun have been done in the last years. The winds have been observed thanks to their CO millimeter emission and their infrared excess due to dust, and we have a rich sample for which mass-loss rates, the dust abundance and the expansion velocity have been measured. These observations have been used to explain mass loss (see, e.g. Habing & Olofsson 2004). The generally accepted mass-loss scenario is levitation of matter by pulsation and shocks, followed by dust condensation. Then, radiation pressure on grains leads to the outflow. However, the detailed physics and chemistry of these phenomena are not well established. For example, it appeared recently that silicate grains cannot drive outflows (Woitke 2006, Hofner & Andersen 2007). We also ignore why mass loss is modulated with a characteristic time of ~ 500 years. The best example of this modulation is the incomplete concentric shells of IRC+10216 (Mauron & Huggins 1999) and similar shells can also be seen in the AGB remnant halos of many post-AGB stars. This time interval is neither the pulsation period nor the interval between thermal pulses. Therefore, some important characteristics of the mass-loss mechanism are not explained.

Another important question about these AGB superwinds is whether they depend on the metallicity of the stars. At low metallicity, AGB stars are mainly carbon (C) stars because only a small amount of dredge-up carbon is needed to make the photosphere C-rich. Consequently, AGB stars in metal-poor galaxies like the Magellanic Clouds or Fornax are in large majority C stars. It is not clear whether mass-loss could depend on metallicity (Mattsson et al. 2008, Matsuura et al. 2007). The AGB stars in these external galaxies and particularly their infrared emission have been observed for many years and especially recently with *Spitzer*, and this permits to quantify the amount of dust in their circumstellar envelopes. However, these stars are too distant (~ 50 kpc or more) for their CO millimeter emission to be detected. Consequently, one ignores two important quantities which are the dust-to-gas ratio and the wind expansion velocity. It is therefore of great interest to search and find metal-poor C star closer to us than the Magellanic Clouds. For this reason, it is interesting to examine the population of AGB C stars in the Galactic halo.

[1] GRAAL, CNRS-UM2, place Bataillon, Montpellier France

2 The C stars in the Galactic halo

The AGB C stars located in the halo have been found with very different methods. Among a sample of C stars discovered with objective-prism plates, Bothun et al. (1991) noted that several of them were very red and were probably AGB stars. Because AGB C stars have a large $B-R$ color index, Totten & Irwin (1998) selected very red point sources on the digitized APM Schmidt plates taken at high galactic latitude. Follow-up spectroscopy allowed them to discover 36 cool halo C stars. Forty-one were known previously, so that Totten and Irwin (1998) could list a sample of 77 halo C stars, with some of them being CH-type stars. Because cool C stars are bright at near-infrared wavelengths, the publication of the 2MASS catalog offered the opportunity to select candidate stars with 2MASS JHK colors typical of AGB C stars and verify these candidates by follow-up spectroscopy. With this method, 100 new AGB C stars at $|b| > 20\,$deg. could be discovered (Mauron et al. 2004, Mauron 2008 and references therein).

Among the ~ 150 cool halo C stars, several have an important infrared excess. While the J-K color is between 1.4 and 2 for most AGB C stars, there are 16 C stars with J-K$\,>3$. These 16 dusty C stars are unusual because they are at large distances from the galactic plane, between ~ 2 and 10 kpc. Therefore, they do not belong to the usual population of AGB C stars close to the Sun which have a scale height of 200 pc. In addition, one of these stars was detected in CO emission and the expansion velocity is only 3 km/s (Groenewegen et al. 1997). Comparing the CO and the dust loss-rate, these authors found that the star is deficient in oxygen, so that the low expansion velocity may be a sign of low metallicity. We have obtained an estimate of mass loss rates for the 16 halo C stars by using the K-[12] color, and we have found that the $\dot{\mathrm{M}}$ values are between 1.0 and 12×10^{-6} $\mathrm{M}_\odot\,\mathrm{yr}^{-1}$ (Mauron 2008). Taking into account their distances, between 2 and 20 kpc, their winds should be detectable in the CO millimeter lines. This will inform us on the frequency of wind velocities as low as 3 km/s and on the possible link between a low metallicity and a low wind velocity.

3 Conclusions

The AGB phase is important for stellar and galactic evolution, but one of the important phenomena, mass loss, is not completely understood. How mass loss depends on metallicity is not clear, and we propose that a detailed study of 16 dusty halo C stars might give some crucial information. These stars are well above the galactic plane, in contrast with usual AGB stars of the solar neighbourhood, and their mass loss rates are strong, of the order of 4 10^{-6} $\mathrm{M}_\odot\,\mathrm{yr}^{-1}$. It should be possible to detect most of these objects in CO, and to see if any low expansion velocity is correlated with low metallicity.

References

Bothun, G.L., Elias, J.H., Mac Alpine, G., et al. 1991, AJ, 120, 2220

Groenewegen, M.A.T., Oudmaijer, R.D., & Ludwig, H.-G. 1997, MNRAS, 292, 686

Habing, H.J., & Olofsson, H. 2004, Asymptotic Giant Branch stars (New-York, Springer)

Höfner, S., & Andersen, A.C. 2007, AA, 465, L39

Matsuura, M., Zijlstra, A.A., Bernard-Salas, J., et al. 2007, MNRAS, 382, 1889

Mattsson, L., Wahlin, R., Höfner, S., & Eriksson, K. 2008, AA, 484, L5

Mauron, N., Huggins, P.J. 1999, AA, 3049,203

Mauron, N., Azzopardi, M., Gigoyan, K., & Kendall, T. 2004, AA, 418, 77

Mauron, N. 2008, AA, 482, 151

Totten, E.J., & Irwin, M.J. 1998, MNRAS, 294, 1

Woitke, P. 2006, AA, 460, L9

SF2A 2008
C. Charbonnel, F. Combes and R. Samadi (eds)

PROBING THE ROLE OF PROTOSTELLAR FEEDBACK IN CLUSTERED STAR FORMATION : OUTFLOWS IN THE COLLAPSING PROTOCLUSTER NGC 2264-C.

Maury, A. J.[1] and André, P.[1]

Abstract. We study the amount of turbulent support injected by protostellar outflows in the NGC 2264-C collapsing protocluster. Using HERA at the IRAM 30 m telescope, we took extensive maps of NGC2264-C in ^{12}CO(2–1), ^{13}CO(2–1), and C^{18}O(2–1). We found widespread high-velocity ^{12}CO emission, testifying to the presence of numerous outflows in the region. We carried out a detailed analysis of the properties of these outflows, including a quantitative evaluation of the total momentum flux injected by outflows in the protocluster. We show that protostellar feedback due to outflows doesn't provide enough energy to efficiently support the whole NGC 2264-C protocluster against global collapse.

1 Introduction

1.1 Clustered star formation and protostellar feedback processes.

It is now well established that a large fraction of young stars in giant molecular clouds form in groups and clusters rather than in isolation (e.g. Lada & Lada 2003).

Three main classes of models have been developed to link the IMF to the cluster formation process. The first one is a scenario based on turbulent fragmentation of the parent molecular cloud (e.g. Elmegreen 1997; Padoan & Nordlund 2002). This scenario produces an IMF-like core mass distribution as observed, and the IMF results primarily from the properties (e.g. power spectrum) of the turbulence. The second class of models emphasizes the role of protostellar feedback in regulating the star formation process (e.g. Norman & Silk 1980, Adams & Fatuzzo 1996). Here, the IMF is determined by the stars themselves through the collective effects of their feedback on both individual cores and the parent cloud. A third scenario exists, however, according to which interstellar turbulence plays no direct role in shaping the IMF, and the distribution of stellar masses is entirely determined by competitive accretion between already formed protostars and dynamical interactions between individual cluster members (e.g. Bonnell et al. 1998, Bate et al. 2003).

On the observational side, millimeter studies both in the continuum (Motte, André & Neri 1998) and molecular lines emission (André et al. 2007) are the best tool to study the very early phases of clustered star formation. Also, millimeter observations of molecular clouds have revealed supersonic linewidths, which are presumably due to turbulent motions. Theory suggests that turbulent motions can be treated as an additional pressure, so that supersonic turbulence increases the effective Jeans mass supported against collapse, $M_J^{eff} = (\frac{\pi}{G})^{3/2} \times \rho^{-1/2} \times c_{s,eff}^3$, where $c_{s,eff}$ is the effective sound speed (such that $c_{s,eff}^2 = c_s^2 + \frac{\langle v^2 \rangle}{3}$).

Recently, Li & Nakamura (2006) discussed the possible effects of protostellar outflows on clustered star formation. In particular, they argued that, due to its short decay time (e.g. Mac Low et al. 1998), the "interstellar turbulence" initially present in a cluster-forming cloud is quickly replaced by turbulent motions generated by protostellar outflows. The protostellar outflow-driven turbulence dominates for most of a protocluster's lifetime and acts to maintain the cluster-forming region close to overall virial equilibrium for several dynamical times, avoiding global free-fall collapse.

As the role of protostellar feedback in cluster-forming clouds is still a matter of debate, detailed studies of the dynamical effects of protostellar outflows in young protoclusters, where outflows are particularly strong and numerous, are required to fully understand the process of clustered star formation.

[1] CEA/DSM/DAPNIA, Service d'Astrophysique, CEA Saclay, Orme des Merisiers, 91191 Gif-sur-Yvette, France

1.2 Our target region : the protocluster NGC2264-C.

The NGC 2264-C protocluster is located in the Mon OB1 molecular cloud complex at a distance $d \sim 800$ pc, and has an LSR velocity of $\sim +7$ km.s^{-1}.
In 1972, Allen discovered in this region a bright embedded IR source, hereafter called IRS1, associated with IRAS 06384+0932, and also known as Allen's source. NGC 2264 has been the target of many molecular line studies, including an unbiased CO (J=1 $\rightarrow$ 0) survey for molecular outflows by Margulis et al. (1988) which revealed that IRS1 is associated with a molecular outflow, named NGC 2264-C. Also, a search for dense gas via a multitransitional CS study has been conducted, revealing molecular clumps.
Performing 30m observations with, e.g., MAMBO and HERA, Peretto et al. (2006) first completed a comprehensive mm continuum/line study of the cluster-forming clump NGC 2264-C (Peretto et al. 2006). Their 1.2 mm continuum mosaic of NGC 2264-C resolved the internal structure of the region, uncovering a total of 12 compact prestellar/protostellar cores. Their HCO^+(3–2) and CS line observations, combined with radiative transfer modelling, established the presence of *large-scale collapse motions*, converging onto the most massive core (C-MM3 with $M \sim 40\,M_\odot$, near the center of NGC 2264-C. Moreover, high-resolution PdBI observations in low-optical depth tracers of the inner part of NGC 2264-C allowed them to resolve a strong dynamical interaction in the central part of NGC 2264-C.
Detailed comparison of these 30m/PdBI observations with numerical SPH simulations of the evolution of a 1000 $M_\odot$ Jeans-unstable, isothermal clump (Peretto et al. 2007) confirms the view that NGC2264-C is an elongated clump collapsing/fragmenting along its long axis. The SPH simulations of Peretto et al. (2007) indicate that NGC 2264-C is observed at a very early stage of global clump collapse, typically $\lesssim 10^5$ yr after the start of dynamical contraction. A significant shortcoming of their present SPH simulations, however, is that they only produce the observed level of clump fragmentation when the total mass of dense ($> 10^4\,\mathrm{cm}^{-3}$) gas in the model is a factor of ~ 10 lower than in the actual NGC 2264-C clump. This pointed to the **need for extra support against gravity**, not included in the present simulations, such as support provided by magnetic fields or from feedback from protostellar outflows.
Because it is well documented and known to exhibit outflow activity, the NGC 2264-C protocluster is an ideal laboratory for probing the initial conditions of clustered star formation and evaluating the impact of outflow feedback on early protocluster evolution.

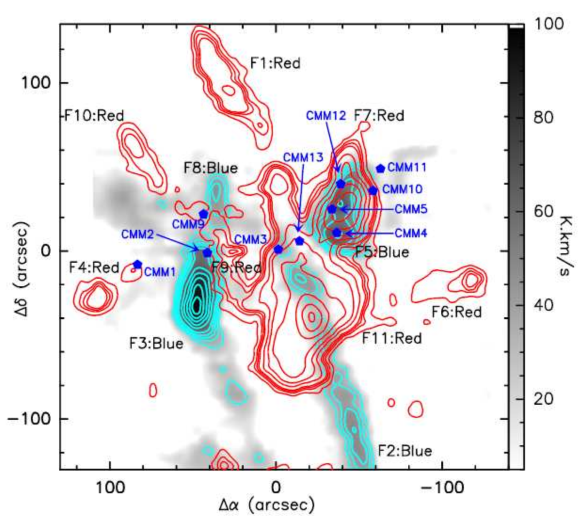

Fig. 1. ^{12}CO(2–1) map of the NGC 2264-C protocluster. The background image and blue contours show the levels of intensity integrated between -27 km/s and 2 km/s in the blue-shifted part of CO(2–1) line, from 5 to 98 K.km.s^{-1}. Red contours are levels of intensity integrated between 13 km/s and 34 km/s in the red-shifted part of the line, from 5 to 110 K.km.s^{-1}. The eleven outflows discovered are labelled by F1 to F11. Blue markers refer to the positions of millimetric peaks found (Peretto et al. 2006, 2007)

1.3 ^{12}CO(2–1) mapping of the NGC 2264-C protocluster

We thus initiated a mapping study of the outflow already detected by Margulis et al. (1988) in NGC 2264-C, with higher angular resolution and better sensitivity. Our goal was to assess the momentum injection rate due to outflows in this protocluster and examine whether outflows could affect the global dynamical evolution of the protocluster.

Observations of the ^{12}CO(2–1), C^{18}O(2–1) and ^{13}CO(2–1) emission lines from the NGC 2264-C protocluster were taken with the IRAM-30 m telescope between October and November 2006 using the HEterodyne Receiver

Array HERA together with the VESPA autocorrelator backend. The resulting map has a size of $3.3' \times 3.3'$ (equivalent to ~ 0.6 pc^2 at the distance of the protocluster). We detected a total of eleven sub-regions or "lobes" exhibiting high-velocity emission in the ^{12}CO(2–1) map (see Fig.1.). These eleven lobes are spatially distributed around the millimeter continuum cores identified by Peretto et al. (2006, 2007), and four of these lobes can be directly associated with Class 0 - like objects. Moreover, some of the outflows lobes that were found exhibit very colllimated shapes (see bipolar outflow made of F1 and F2 in Fig.1. for an example) and very high LSR velocity features (up to +33 km/s in the case of the blue-shifted lobe F10).

1.4 Momentum flux

To quantify the effective feedback of these eleven outflows on the protocluster, we led a quantitative study consisting in computing the momentum flux injected by the protostellar outflows in the region. Details about the method used can be found in Maury et al. 2008 (in prep).

Following Scoville et al. (1986) we first evaluated the gas mass carried out by each outflow independently, by integrating the excess ^{12}CO(2–1) emission both over the adequate velocity range, and spatially over the outflow extent (see Fig. 2.). The masses of entrained gas vary from outflow to outflow, and the total mass carried out by outflows over the whole NGC 2264-C protocluster is estimated to 37×10^{-2}M$_\odot$ ($\pm5\times10^{-2}$M$_\odot$).

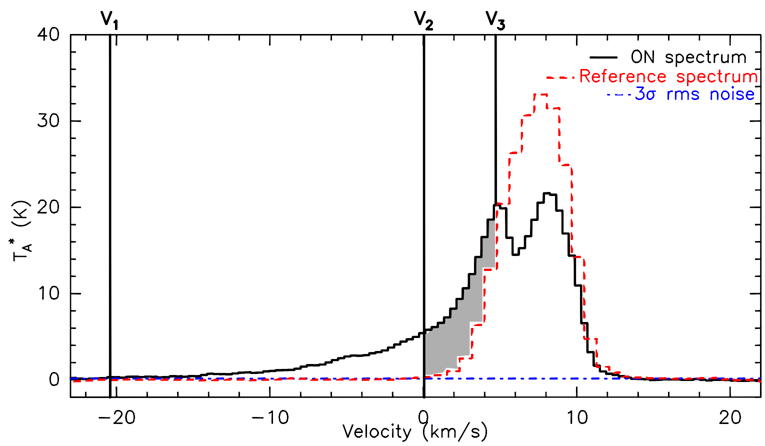

Fig. 2. Excess ^{12}CO(2–1) emission at blue-shifted velocities in outflow F3. The dashed spectrum represents the ^{12}CO(2–1) reference spectrum. The solid spectrum is extracted from the candidate outflow F3 spectra. Vertical solid lines illustrate the velocity ranges used in the computation of the outflow masses. [V$_1$; V$_2$] is the interval used for the calculation of the minimum mass : no emission being seen in the reference spectrum, all the emission seen in the spectrum extracted from F3 region is due to outflow. [V$_2$; V$_3$] is the velocity interval used to compute the additionnal outflow low-velocity mass, by integrating the ^{12}CO(2–1) emission corresponding to the area highlighted in grey.

We then used our mass estimates to compute the momentum flux of each outflow :
$F_{out} = M_{out} \times V_{char}/t_{dyn}$, with V_{char} the characteristic velocity of the flow (mean outflow velocity observed in the map over the entire extent of the outflow), and t_{dyn} the dynamical time of the outflow.
A correction factor for inclination of the outflow axis with the line of sight(l.o.s.) has to be taken into account when evaluating V_{char} and t_{dyn}, leading to a final inclination factor $f(i) = \frac{\sin(i)}{\cos^2(i)}$ (cf. Bontemps & al. 1996) on the momentum flux.
For each outflow, the minimum momentum flux was computed using the minimum computed value of entrained gas, and without correction for any inclination effect ($f(i) = 1$).
The maximum momentum flux of each outflow was computed by using the maximum computed value of entrained gas. Also, we assumed random outflow orientations in our dataset in this case, and therefore applied a correction factor $\langle f(i) \rangle = 2.9$ (corresponding to a mean statistic inclination angle i$\sim 57.3°$).

The momentum fluxes vary from outflow to outflow, and the total momentum flux injected by outflows over the whole NGC 2264-C protocluster is estimated to 10×10^{-4} M$_\odot$.km.s^{-1}.yr^{-1} ($\pm7\times10^{-4}$ M$_\odot$.km.s^{-1}.yr^{-1}).

1.5 Conclusions

We discovered eleven outflows emerging from compact Class 0-like protostellar sources in the NGC2264-C complex (see Fig. 1.). Most of them are powerful ones (if compared to Class 0 outflows studied by Bontemps & al. 1996), strengthening the idea that NGC2264-C is forming luminous intermediate-mass objects.

The maximum total force due to the eleven ^{12}CO(2–1) protostellar outflows is found to be:

$$\mathbf{F}_{out} \approx \mathbf{1.7{\times}10^{-3}\ M_{\odot}.km.s^{-1}.yr^{-1}}.$$

In order to discuss wether or not such a force applied to the NGC 2264-C protocluster has to be taken into account in the energy budget, we estimated the support needed to keep the whole protocluster (mass of ≈1600 $M_{\odot}$ in a 0.4pc radius) in hydrostatic equilibrium.
The pressure gradient needed to keep a spherical clump with a mass distibution such as $\rho(\mathrm{r}) = \frac{a^2}{2\pi G r^2}$ and M(R=0.4pc) = 1600 $M_{\odot}$ (where a is the isothermal sound speed, and G is the gravitational constant) in hydrostatic equilibrium is:

$$\frac{dP}{dr} = \text{- G}\ \frac{\rho(r).m(r)}{r^2} \implies P{=}\frac{GM^2}{8\pi R^4} \quad \text{for a spherical shell of radius R.}$$

Therefore, the total force needed to balance gravity at radius $R = 0.4$ pc in the NGC 2264-C protocluster is:

$$\mathbf{F} = \frac{GM^2}{2R^2} = \mathbf{40{\times}10^{-3}\ M_{\odot}.km.s^{-1}.yr^{-1}}$$

If we compare this value to the largest force exerted by the eleven outflows on the surrounding protocluster, we conclude that the total momentum flux injected by the eleven outflows is too small by an order of magnitude to provide significant support against collapse in NGC 2264-C. One should consider either cumulative effects of outflows on a longer timescale, or numerous weaker outflows not detected in this study to bring additionnal support against gravity through protostellar outflows (Maury et al. 2008, in prep.).

We show that the energy injected by outflows into cloud turbulent motions is much too low to efficiently support the whole collapsing protocluster. We conclude that the extra support needed to explain the global dynamics of the NGC2264-C protocluster could have another origin, such as magnetic support.

References

André P., Belloche, A., Motte, F., & Peretto, N. 2007, A&A, 472, 519
Bate, M., Bonnell, I., Bromm, V. 2003, MNRAS, 339, 577
Bonnell, I.A., Bate, M. R., & Zinnecker, H. 1998, MNRAS, 298, 93
Bontemps, S., André, P., Terebey, S., & Cabrit, S 1996, A&A, 314, 477
Elemegreen, B.G., 1997, ApJ, 486, 944
Lada, C.J. & Lada, E.A., 2003, ARA&A, 41, 57
Li, Z.-Y., & Nakamura, F., 2006, ApJ, 640, 187
Mac Low, M.-M., Klessen, R.S., Burkert, A., & Smith, M.D., 1998,
Margulis, M., Lada, C.J., & Snell, R.L., 1988, ApJ, 333, 316
Motte, F., André, P.,& Neri, R. 1998, A&A, 336, 150
Norman, C., & Silk, J., 1980, ApJ, 238, 158
Padoan, P. & Nordlund, A., 2002, ApJ, 576, 870
Peretto, N., André, P., Belloche, A., 2006, A&A, 445, 979
Peretto, N., Hennebelle, P., André, P., 2007, A&A, 464, 983
Scoville et al., 1986, ApJ, 303, 416

SF2A 2008
C. Charbonnel, F. Combes and R. Samadi (eds)

COROT FIRST RESULTS - LOOKING INSIDE THE STARS

Michel, E.[1], Baglin, A.[2] and the CoRoT Team

Abstract. CoRoT has now proven its ability to measure stellar luminosity variations down to the part-per-million level, over long and quasi uninterrupted periods (up to 150 days). These data carry a wealth of information on the interior of very different stars in various evolution stages. The three first runs are being analysed by the CoRoT community, unveiling stellar oscillations with unprecedented sensitivity and precision. With a few examples, we illustrate how CoRoT is opening a new era in stellar seismology and in stellar physics more generally.

The backbone of this new era is constituted of an ambitious program of seismology projects including CoRoT(2007-...), Kepler (2009-...), Siamois (2012?-...), Song (2012?-...), Plato (2017?-...),... It is also relying on the impressive progresses made simultaneously in theoretical developments of transport processes in stars (modeling rotation and elements mixing or segregation), in High angular resolution observations (bringing radii and oblateness measurements), spectropolarimetry (with Espadon, Narval,...), and will make intensive use of the distances determined with GAIA (2011-...).

We are now looking inside the stars.

The results presented at this conference can be found in Michel et al. (2008), see also http://www.univie.ac.at/tops/CoAst/ vol. 156.

Acknowledgements

The CoRoT (Convection Rotation and planetary Transits) space mission, launched on December 2006, was developed and is operated by CNES, with participation of the Science Program of ESA, ESA's RSSD, Austria, Belgium, Brazil, Germany and Spain.

References

Michel, E., et al. 2008, Communications in Asteroseismology, 156, in press
http://www.univie.ac.at/tops/CoAst/

[1] Observatoire de Paris, LESIA-CNRS(UMR 8109)- Univ. Paris 6-Univ. Paris 7
[2] Observatoire de Paris, LESIA-CNRS(UMR 8109)- Univ. Paris 6-Univ. Paris 7

SF2A 2008
C. Charbonnel, F. Combes and R. Samadi (eds)

COAGULATION AND CRYSTALLIZATION OF SILICATES IN PROTOPLANETARY DISKS: A C2D SPITZER/IRS SURVEY

Olofsson, J.[1], Augereau, J.-C.[1], Monin, J.-L.[1] and the c2d IRS team

Abstract. Silicates are observed in almost every place where dust can survive: in the interstellar medium (ISM), in the Earth mantle, in comets and it is now common knowledge that there are also present in circumstellar disks around young stars. The ISM sub-micron sized silicates are highly amorphous (>99%), while the silicate Mg-rich crystallinity fraction can reach 60% in comets like Hale-Bopp in the Solar System. The silicates have to be exposed to high temperatures to crystallize, and their presence in long-period comets suggests that dust has been heavily processed and transported in the disk. Statistical studies of planet forming disks are keys on understanding if these processes are generic and can occur in other protoplanetary systems.

As part of the Cores to Disks (c2d) Legacy Program, we obtained more than a hundred of Spitzer/IRS spectra of T Tauri stars, in the spectral range 5-35 μm, where many crystalline features are present. We find that most of these objects ($\sim$ 70%) show silicate emission features, either attributed to amorphous or crystalline grains. Studying the 10 μm feature, we find that grain growth has occured and their quasi-systematic presence in the disks upper layers indicate ongoing turbulent vertical mixing. We will also show that crystalline dust grains are present in the outer/deeper cold regions of the disk, with typical temperatures of about 100 K, which suggests efficient radial transport mechanisms. Overall, our study shows that vertical and radial transport seem to be generic dynamical processes in disks, challenging theoretical disk evolution and planet formation models.

1 Introduction

Silicates dust grains in the interstellar medium (ISM) are known to be largely amorphous ($\sim$ 99%) and with a typical sub-micronic grain size (e.g. Gail et al. 1998). On the other side, studies of comets in the Solar System present high crystallinity fraction. For example, Wooden et al. (1999) showed that 60% of the silicate grains in comet Hale-Bopp are crystalline grains, while Jupiter Family comets have a slightly lower crystallinity fraction (of about 35%), but still high compared to the ISM. This difference can be explaned considering a radial dependance of the mineralogy inside the disk. Therefore, it is meaningful to consider silicate crystalline grains as being tracers of the history of the circumstellar disk. During this stage of evolution, silicate grains are expected to be heavily processed, by coagulation, fragmentation and crystallization, caused by stellar radiation, thermal agitation, collisions, for instance.

The first observations of silicates in circumstellar disks have been obtained from the ground. Because of the atmosphere, only the 10 μm feature, produced mainly by amorphous grains, could be observed. Thanks to ISO satellite, mid to far-IR spectroscopy of disks around Herbig Ae/Be stars (hereafter, HAeBe) that are more massive than the Sun, could be achieved. Acke & van der Acker (2004), showed that 52% of HAeBe stars present the 10 μm feature, and 23% of them show the 11.3 μm feature, which is associated to forsterite, an Mg-rich crystalline silicate. Spitzer satellite then became available and several surveys were led (e.g. Furlan et al. 2006, Kessler-Silacci et al. 2006), but also detailled studies of individual objects, like the borderline brown dwarf (hereafter, BD) BD2 from Merín et al. (2007) or the BD in the Taurus cloud from Bouy et al. (2008).

We present in the following, some results from the c2d Spitzer Legacy Program "From Molecular Clouds to Planets" (Evans et al. 2003). This work is the continuation of a series of papers, studying the grains, PAHs and the gas in the inner disk regions around young stellar objects. In Sec. 2, we first present general results on the apparition of crystalline features, then in Sec.3, we study the relations between the different crystalline features and finally, in Sec.4 we address the question of the typical grain sizes in our sample.

[1] Laboratoire d'Astrophysique de Grenoble, CNRS/UJF UMR 5571, 414 rue de la Piscine, B.P. 53, F-38041 Grenoble

2 Cristallinity in circumstellar disks

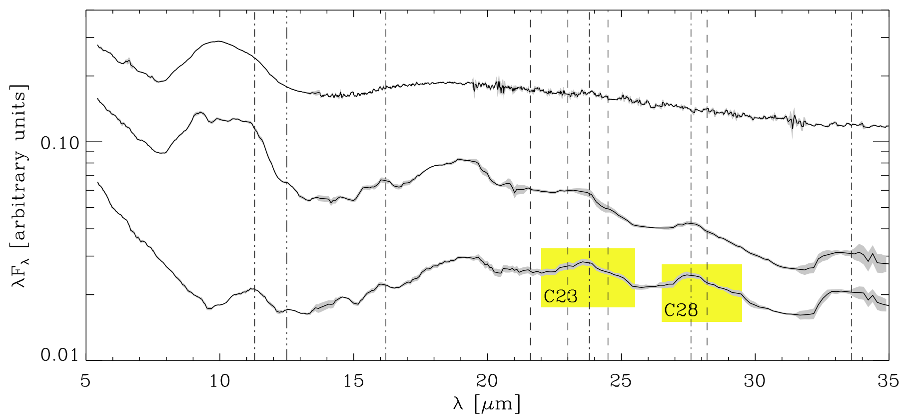

Fig. 1. From bottom to top, Spitzer/IRS spectra of ISO-ChaII 54, SSTc2d J033036.0+303024 and AS 205, in arbitrary units of λF_{λ}. The vertical lines show the peak positions of the enstatite (dashed lines) and forsterite (dot-dashed lines) crystalline features we attempt to identify in every spectrum of our 110 star sample. The two boxes correspond to the C23 and C28 crystalline complexes.

2.1 IRS observations and source sample

We present in this study the infrared spectra of disks around 110 young stellar objects, obtained as part of the c2d Legacy Program. The spectra were obtained using the InfraRed Spectrograph (IRS) instrument onboard the Spitzer Space Telescope. The sample is mainly composed of Class II objects, even if 39 of them have no classification in the literature, but show clear amorphous silicate features in emission. The source list contains 110 stars, distributed among 6 major clouds: Perseus (16 objects), Taurus (9), Chamaleon (23), Ophiuchus (26), Lupus (16), Serpens (16) plus 4 isolated stars. Out of these 110 stars, 60 are young solar analogs (TTauri stars, hereafter TTs), 9 are HAeBe and 1 is a BD. The 40 other young objects have no known classification. Fig. 1 shows the different kind of spectra we have in our sample, from amorphous to very crystalline (e.g. ISO-ChaII 54).

2.2 Crystalline species

In many spectra, broad 10 and 20 μm features can be easily identified and are attributed to amorphous silicate grains. But narrower features due to crystalline grains can also be identified. In this study we consider features arising from Mg-rich silicates, enstatite (pyroxene group) and forsterite (olivine group). The example spectrum of ISO-ChaII 54 displayed in Fig.1 shows that the 23.0, 24.5 μm enstatite and the 23.8 μm forsterite features can be blended into one single complex. The same happens to the 27.6 μm forsterite feature with the 28.2 μm enstatite feature. In the following we will treat these features as two complexes, independent of the actual crystals responsible for their emission, and will refer to them as the C23 and C28 complexes.

2.3 Fraction of disks showing silicates features

We develop an IDL routine that determines the characteristics of the crystalline features, mainly, the peak positions, peak fluxes and line fluxes. Only 6 objects out of the 110 spectra we study do not show any amorphous or crystalline silicates features. What comes out first from this analysis is that silicate crystallization is not a marginal phenomenon in Class II circumstellar disks, since both the C23 and C28 complexes are present at rates higher than 50%. The amorphous 10 μm feature on the other hand has an apparition frequency of about $\sim 65\%$, which is consistent with the analysis on HAeBe stars from Acke & van der Acker (2004). The question of the localisation of these silicates is addressed in Sec. 3.

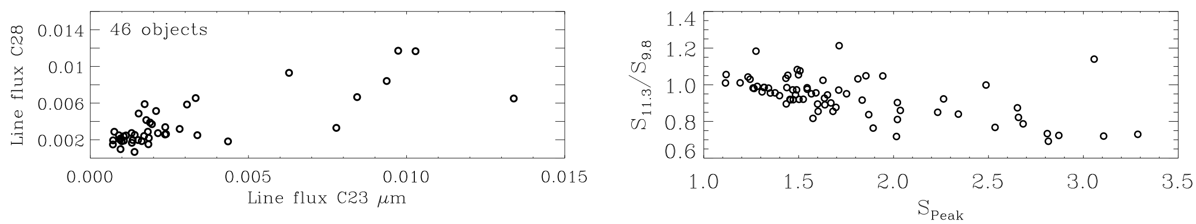

Fig. 2. *Left panel*: Normalized line fluxes correlation between the C23 and C28 complexes. *Right panel*: Correlation between shape and strength of the amorphous 10 μm feature. Large grains ($a \sim 1.0\,\mu$m) are located on the left side of the plot.

3 Localisation of silicate grains

3.1 Relationship between the 10 μm feature and the crystallinity

We evaluate in the following the relationship between the 10 μm amorphous feature and the crystallinity probed by features arising at wavelengths larger than 20 μm, mainly the two complexes C23 and C28 and the forsterite feature at 33.6 μm. To achieve this, we search for correlations between the energy contained in the various features. To get rid of possible distance and/or brightness effect, we normalise the line flux by the mean value of the estimated continuum multiplied by the central wavelength. To quantify the presence of a correlation, we compute a Kendall τ test, which returns a τ value (between -1. and +1.) and a probability P that there is no correlation. A τ =1 means that the correlation is perfect, while a τ value of -1 means that it is a perfect anti-correlation. For the 10 μm feature and the C23 complex, we find τ =0.08 and P =0.43 that the two *line fluxes* are not correlated. For the 10 μm feature and the C28 complex; we obtain τ =-0.028 and P =0.8 (no correlation). Regarding the 10 μm feature and the 33.6 μm feature we compute a τ value of 0.11 and P =0.44, that they are not correlated. To verify this first tendancy, we compute correlation coefficients on the *apparition frequency* of the corresponding features. For the 10 μm and the C23, we have τ =0.046 with P =0.49. With the C28, we obtain τ =0.094 and P =0.159. Finally, between the 10 and 33.6 μm features, we have τ =-0.021 and a probability P =0.753 that the presence of these two features are not correlated. Overall this suggests that the crystalline features observed at wavelengths larger than 20 μm and the amorphous 10 μm feature do arise from independent grain populations. In addition to this, we investigate the effect of the shape of the 10 μm feature, which is related to the grain size (see Sec. 4), as a function of the presence of one of the two complexes C23 or C28. We find that there is no relation between the grain size of grains emitting at 10 μm and the presence of the two complexes. This basically means that the growth of the grains emitting at 10 μm is not linked to the degree of crystallinity of the grains emitting at wavelengths larger than 20 μm.

3.2 Relationship between crystalline features

Grains probed by emission at 10 μm and emission at $\lambda > 20\,\mu$m do come from independant dust population, but is it the same for crystalline grains that emit at large wavelengths? We compute correlation coefficients, the same way as explained above (Sec. 2), for C23, C28 and the 33.6 μm feature. Regarding the line fluxes emitted by the two complexes, C23 and C28, we obtain τ =0.53 and $P = 2.4 \times 10^{-7}$ (see left panel of Fig. 2), for the C23 complex and the 33.6 μm feature, we have τ =0.54 and $P = 1.5 \times 10^{-4}$ showing that there is correlation. For the C28 complex and the 33.6 μm feature, we obtain τ =0.58 and $P = 1.8 \times 10^{-4}$, confirming the fact that crystalline features emitting at wavelengths larger than 20 μm are correlated to each others, and thus are probably probing the same dust population.

4 Deriving typical grain sizes

4.1 The amorphous 10 μm feature

The amorphous 10 μm feature is present at a rate higher than 65% in our sample. Bouwman et al. (2001), van Boekel et al. (2003) or Kessler-Silacci et al. (2006) have shown that detailled study of this feature can provide a lot of information on the dust characteristics and in particular on the typical size of the emitting grains. To perform this analysis, we use the same computation method as the one described in Kessler-Silacci et al. (2006), i.e. building two indexes at 9.8 and 11.3 μm from a normalized spectrum, and plotting their ratio as a function of the strength of the feature. We find that there is an anti-correlation, with τ =-0.44 and a probability $P = 5.96 \times 10^{-8}$ that there is no correlation, as shown in the right panel of Fig. 2. This correlation can be interpreted as larger grains producing flatter features. Using theoretical opacities, we show that the bulk of the points is located in the place where the typical grain size is micronic. This means that for grains emitting the 10 μm feature, grain growth has taken place.

4.2 The C23 complex

In the following we attempt to find a similar correlation for the C23 complex. We use the same computation method as before and build two indexes, at 23 and 24 μm. The correlation coefficient between the ratio of these two indexes and the strength of the C23 complex is τ =-0.56 with a probability below the IDL simple precision that there is no correlation. Also, using theoretical opacities, we find that grain growth has occured for grains that produce the C23 complex.

5 Conclusion

Compared to the silicate mineralogy in the ISM, we show that strong modifications occured inside a majority of circumstellar disks. Mainly, grain growth has taken place, for all grains that are probed by Spitzer/IRS spectra. Secondly, crystallinity is not a marginal phenomenon in disks compared to the ISM, the apparition frequency of crystalline silicates is about $\sim 50\%$ in young circumstellar disks. This means that dust is subject to a strong and efficient process that modify its lattice structure.

The study of the shape versus the strength of different features not only showed that grain growth has occured, we also learned something about the hydrodynamical state of the disk. In a simple case where turbulence is not present in the disk, we can expect to see a strong settling of intermediate-sized grains ($\sim 1.0\,\mu$m) toward the midplane. The fact that we can see large grains in the optically thin layers of the disk means that turbulence is still very active and sufficient to vertically mix the grains.

Finally, we find that grains emitting at 10 μm and grains emitting at wavelengths larger than 20 μm are arising from independent dust populations. Considering a simple Wien's law, the first population is close to the star, and rather warm (T$\sim$ 300-600 K) while the second one is much colder (typically 100 K). The fact that this cold dust component shows many crystalline features is intriguing: we indeed expect the crystalline grains to form by thermal annealing, requiring temperatures larger than 800 K, while we see crystalline grains at T$\sim$ 100 K. This indicates that a radial transportation mechanism is very active inside the disk.

References

Acke, B. & van den Ancker, M. E. 2004, A&A, 426, 151

Bouwman, J., Meeus, G., de Koter, A., et al. 2001, A&A, 375, 950

Bouy, H., Huelamo, N., Pinte, C., et al. 2008, ArXiv e-prints, 803

Evans, II, N. J., Allen, L. E., Blake, G. A., et al. 2003,

Furlan, E., Hartmann, L., Calvet, N., et al. 2006, ApJS, 165, 568

Gail, H.-P. 2004, A&A, 413, 571

Kessler-Silacci, J., Augereau, J.-C., Dullemond, C. P., et al. 2006, ApJ, 639, 275 PASP, 115, 965

Merín, B., Augereau, J.-C., van Dishoeck, E. F., et al. 2007, ApJ, 661, 361

van Boekel, R., Waters, L. B. F. M., Dominik, C., et al. 2003, A&A, 400, L21

Wooden, D. H., Harker, D. E., Woodward, C. E., et al. 1999, ApJ, 517, 1034

SF2A 2008
C. Charbonnel, F. Combes and R. Samadi (eds)

MAGNETIC GEOMETRIES OF SUN-LIKE STARS : IMPACT OF ROTATION

Petit, P.[1], Dintrans, B.[1], Aurière, M.[1], Catala, C.[2], Donati, J.-F.[1], Fares, R.[1], Gastine, T.[1], Lignières, F.[1], Morin, J.[1], Paletou, F.[1], Ramirez, J.[2], Solanki, S.K.[3] and Théado, S.[1]

Abstract. Sun-like stars are able to continuously generate a large-scale magnetic field through the action of a dynamo. Various physical parameters of the star are able to affect the dynamo output, in particular the rotation and mass. Using new generation stellar spectropolarimeters (ESPaDOnS@CFHT, NARVAL@TBL), it is now possible to measure the large-scale magnetic field of solar analogues (i.e. stars very close to the Sun in the stellar-parameter plane, including strict solar twins). From spectropolarimetric time-series, tomographic inversion of polarized Zeeman signatures allows us to reconstruct the field geometry and its progressive distortion under the effect of surface differential rotation. We detail the first results obtained on a sample of four main-sequence dwarfs, with masses close to 1 solar mass and rotation rates between 1 and 3 solar rotation rate.

1 Introduction

All rotating Sun-like stars show spectral features indicating the presence of magnetic fields in their atmosphere. Chromospheric emission (as measured in the cores of CaII H & K lines) is often taken as a good magnetic tracer, following the correlation observed in the Sun (Schrijver et al. 1989). For a few tens of stars, time-series covering several decades are now available and provide information about the existence and length of magnetic cycles that different types of stars can exhibit (Baliunas et al. 1995, Hall et al. 2007a). From this long-term monitoring, several trends can be derived. First, the chromospheric flux increases with the rotation rate. Also, all active stars do not undergo smooth activity cycles, as the Sun does today. The activity of the most active dwarfs has a tendency to fluctuate erratically, while regular cycles are rather observed in less active (older) dwarfs, like the Sun. It seems as well that the magnetic activity of Sun-like stars is very sensitive to fundamental parameters, so that stars very similar to the Sun can obey to a different magnetic behaviour. While being often considered as the brightest solar twin, 18 Sco was recently reported to follow an activity cycle shorter than solar, with a period of ≈7 years (Hall et al. 2007b).

Knowing that many stars go through a series of activity maxima and minima as the Sun does, and bearing in mind that many stars do not, a very natural question is then to determine whether such oscillations are associated to a global polarity reversal of the large-scale magnetic field, as observed on the Sun between two successive solar minima. On the Sun, this global magnetic field component displays a strength limited to a few Gauss only (e.g. Sanderson et al. 2003). If present on a Sun-like star, the detection of this magnetic component requires highly sensitive spectropolarimetry to capture Zeeman signatures that should not exceed 10^{-4} of the continuum in circularly polarized light.

We achieve this detection with the help of spectropolarimetric data sets collected with the NARVAL spectropolarimeter. From a set of observations of a sample of four Sun-like stars covering a range of rotation periods, we reconstruct their large-scale photospheric magnetic geometry and discuss the impact of rotation on their magnetic properties. We then briefly present the extention of this observing project to a larger sample of stars.

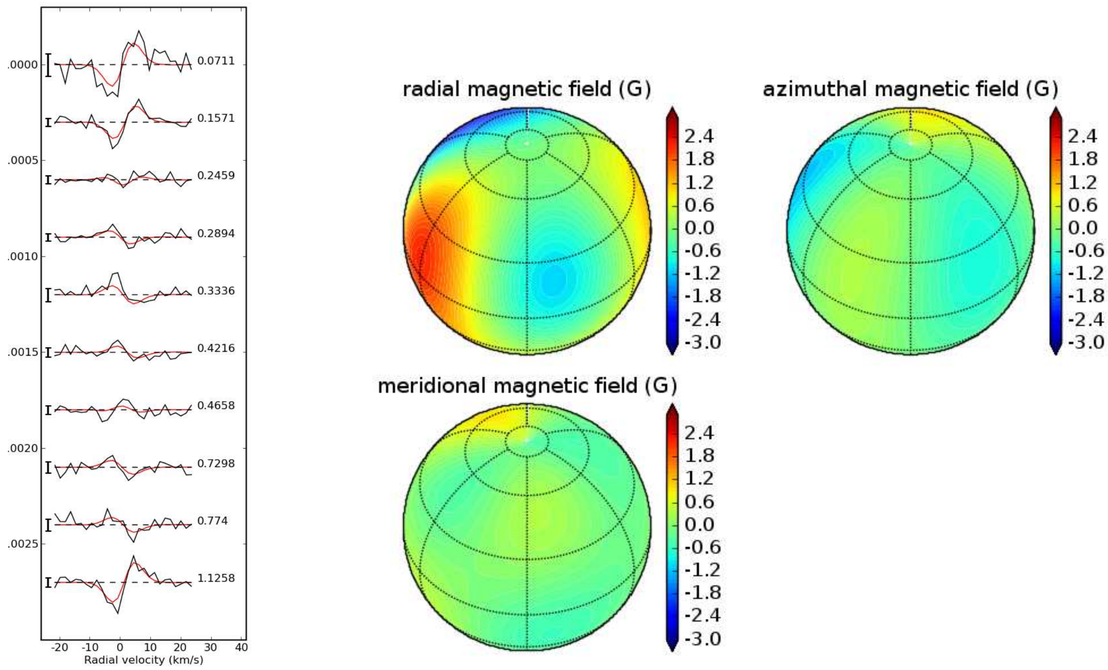

Fig. 1. Left panel: Stokes V profiles of 18 Sco, after correction of the mean radial velocity of the star. Black lines represent the data and red lines correspond to synthetic profiles of our magnetic model. Successive profiles are shifted vertically for display clarity. Rotational phases of observations are indicated in the right part of the plot and error bars are illustrated on the left of each profile. **Right panel:** magnetic map of 18 Sco (here with observer facing the rotational phase 0.5). Each chart illustrates the field projection onto one axis of the spherical coordinate frame. The magnetic field strength is expressed in Gauss.

2 Observations

Our stellar sample is constituted of four nearby dwarfs (18 Sco, HD 76151, HD 73350 and HD 190771). Their fundamental parameters are chosen to be as close as possible to the Sun's (Valenti & Fischer 2005). The observational material consists of high-resolution spectra obtained simultaneously in classical spectroscopy (Stokes I) and circularly polarized light (Stokes V) in 2007 winter and summer, using the newly installed NARVAL stellar spectropolarimeter at Télescope Bernard Lyot (Observatoire du Pic du Midi, France). The data reduction is performed by Libre-Esprit, a dedicated, fully automated software described by Donati et al. (1997) and implementing the optimal spectral extraction principle of Horne (1986) and Marsh (1989).

A single, average photospheric line profile was extracted from each spectrum using the LSD technique (Donati et al. 1997), according to a line-list matching a solar photospheric model. Using this cross-correlation method, the noise level of the mean Stokes V profiles is reduced by a factor of about 40 with respect to the initial spectrum. The resulting noise level are in the range $2 \times 10^{-5} - 8 \times 10^{-5}$ I_c (where I_c denotes the continuum level), enabling us to detect the Zeeman signatures of 18 Sco's large-scale photospheric field (Fig. 1, after Petit et al. 2008).

Assuming that the rotation alone is responsible for the variability observed throughout the time-series, we

[1] Laboratoire d'Astrophysique de Toulouse-Tarbes, Université de Toulouse, CNRS, France
[2] LESIA, Observatoire de Paris-Meudon, 92195 Meudon, France
[3] Max-Planck Institut fuer Sonnensystemforschung, Katlenburg-Lindau, Germany

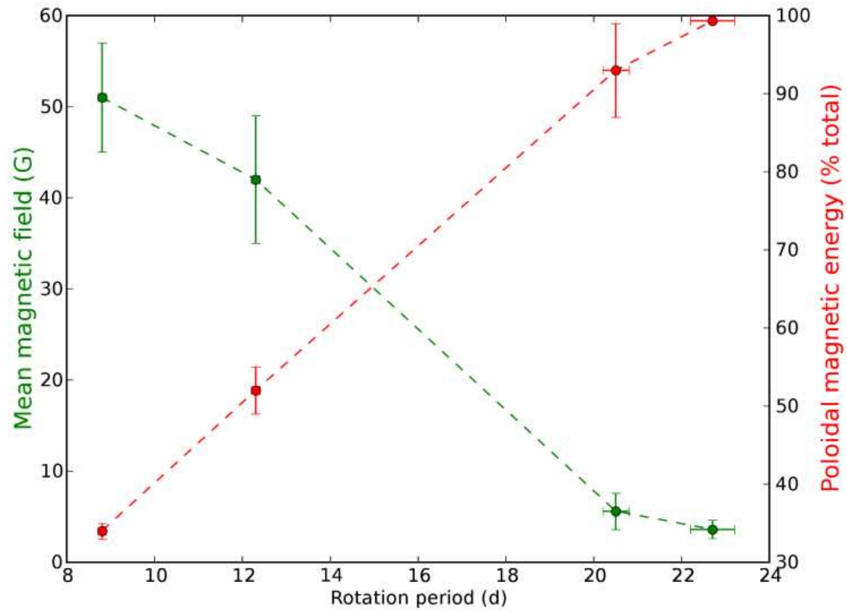

Fig. 2. Rotational dependence of the mean (unsigned) magnetic field (green line) and of the fraction of magnetic energy stored in the poloidal field component (red curve).

derive the rotation period of the targets, with measured values between 8.8 d (for HD 190771) to 22.7 d (for 18 Sco). For HD 190771, the data set cannot be modelled down to the noise level without further including some latitudinal shear in our magnetic model. By doing so, we obtain a difference of rotation rate between polar and equatorial regions of 0.12 ± 0.03 rad.d^{-1}.

The magnetic map of 18 Sco is shown in the right panel of Fig. 1. The large-scale magnetic field can be modelled under the assumption of a purely poloidal field geometry. The mean strength over the stellar surface is about 4 Gauss, with $34 \pm 6\%$ of the magnetic energy showing up as a dipole, $56 \pm 6\%$ in the quadrupole and no detectable magnetic energy above the octopolar expansion.

We illustrate in Fig. 2 the results obtained for the full sample and observe two clear tendencies. First, the unsigned magnetic field of the reconstructed maps increases with the rotation rate (green line). The second noticeable effect of rotation is to increase the fraction of the magnetic energy stored into a large-scale toroidal component of the surface magnetic field (red curve). From our observations, we infer that a rotation period lower than ≈12 days is necessary for the toroidal magnetic energy to dominate over the poloidal component.

3 Exploring the mass-rotation plane

This first stellar sample has been enlarged to offer a sampling of the mass-rotation plane, from 0.7 to 1.3 $M_{\odot}$. The full sample is now constituted of about 20 main-sequence dwarfs. We plan to monitor the selected targets over 5 to 10 years to estimate the long-term variability of their magnetic topologies. The temporal evolution of the total magnetic energy, the poloidal/toroidal distribution of the surface field or the distribution of the magnetic energy between the axisymmetric and non-axisymmetric components will then provide us with a new set of surface observables that will help to constrain numerical models of stellar dynamos.

References

Baliunas, S.L., Donahue, R.A., Soon, W.H., el al. 1995, ApJ 438, 269

Donati, J.F., Semel, M., Carter, B.D., Rees, D.E. & Collier Cameron A. 1997 MNRAS 291, 658

Hall, J.C., Lockwood, G.W. & Skiff, B.A. 2007a, AJ 133, 862

Hall, J.C., Henry, G.W. & Lockwood, G.W. 2007b, AJ 133, 2206
Horne, K. 1986, PASP 98, 609
Marsh, T.R. 1989, PASP 101, 1032
Petit, P., Dintrans. B., Solanki, et al. 2008, MNRAS 388, 80
Sanderson, T.R., Appourchaux, T., Hoeksema, J.T. & Harvey, K.L. 2003, JGR, Vol. 108, Issue A1, SSH 7-1
Schrijver, C.J., Cote, J., Zwaan, C. & Saar, S.H. 1989, ApJ 337, 964
Valenti, J.F. & Fischer, D.A. 2005, ApJS 159, 141

MULTI-TECHNIQUE OBSERVATIONS AND MODELING OF PROTOPLANETARY DISKS

Pinte, C.[1], Ménard, F.[2], Duchêne, G.[2] and Augereau, J.C.[2]

Abstract. Most of the studies on circumstellar disks are based on models that put an emphasis on fitting either SEDs or scattered light images or molecular emission maps. In this contribution, we present a more general approach which aims at interpreting the increasing amount of observational data in the framework of a single model, in order to obtain a more global picture and to better characterize both the dust population and the gas disk properties. The main objective of this general method is to couple the constraints from the gas- and dust-oriented studies to shed light on aspects of the disk structure that are cannot otherwise be studied in a coherent manner.

1 Numerical modeling

1.1 Radiative transfer code

Synthetic images, spectral energy distributions and molecular emission maps are computed using MCFOST, a 3D continuum radiative transfer code based on the Monte-Carlo method (Pinte et al. 2006). It includes multiple scattering with a complete treatment of polarization, dust heating and continuum thermal re-emission. Dust properties may vary with location within the disk, allowing us to model vertical dust settling (e.g. IM Lupi) or increase of ice mantles from the inner, hot regions to the outer, cold edge of the disk (e.g. IRAS 04158+2805). NLTE radiative transfer in molecular lines has recently been implemented in MCFOST. Calculations are performed using a long-characteristic Monte Carlo method similar to the one presented in Hogerheijde & van der Tak (2000).

1.2 Model definition

We assume a simple disk geometry, with a gaussian vertical profile: $\rho(r,z) = \rho_0(r)\,\exp(-z^2/2\,h(r)^2)$ valid for a vertically isothermal, hydrostatic, non self-gravitating disk. We use power-law distributions for the surface density $\Sigma(r) = \Sigma_0\,(r/r_0)^p$ and the scale height $h(r) = h_0\,(r/r_0)^\beta$, where r is the radial coordinate in the equatorial plane, h_0 the scale height at the radius $r_0 = 100\,\mathrm{AU}$. We consider homogeneous spherical grains and calculate optical properties with the Mie theory. The grain sizes are distributed according to the power-law $\mathrm{d}n(a) \propto a^{-3.5}\,\mathrm{d}a$, with $a_{\min}$ and $a_{\max}$ the minimum and maximum sizes of grains.

2 IM Lupi

IM Lupi (Schwartz 82) is an M0 T Tauri star, with a modest emission-line activity but surrounded by a large amount of dust. We have performed a simultaneous modeling of the various observations (SED, infrared spectroscopy, multi-wavelength scattered light images and millimeter visibilities) and analyzed a grid of models over a large fraction of the parameter space via Bayesian inference. The best model can reproduce all of the observations of the disk (Fig 1). Our analysis illustrates the importance of combining a wide range of observations in order to fully constrain the disk model, with each observation providing a strong constraint

[1] School of Physics, University of Exeter, Stocker Road, Exeter EX4 4QL, United Kingdom
[2] Laboratoire d'Astrophysique de Grenoble, CNRS/UJF UMR 5571, 414 rue de la Piscine, B.P. 53, F-38041 Grenoble Cedex 9, France

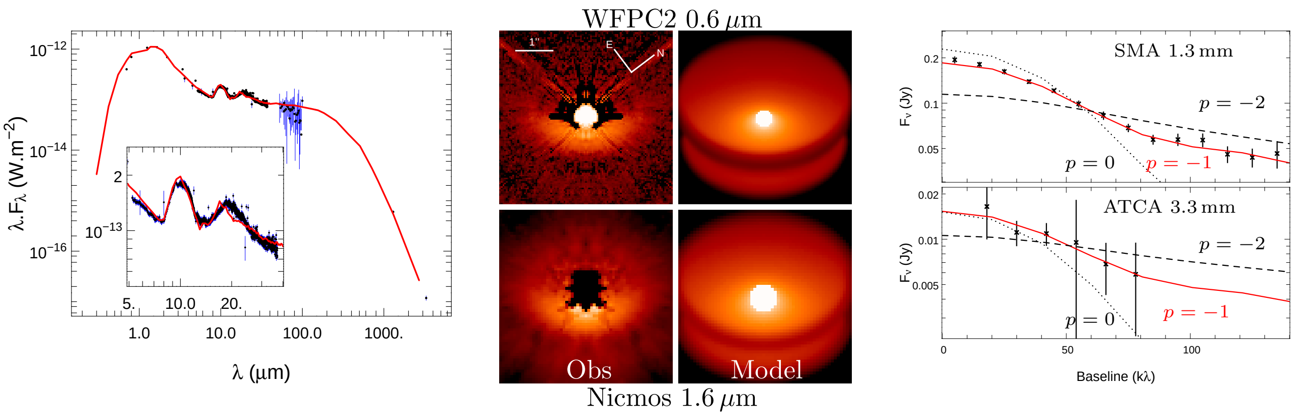

Fig. 1. Comparison of the best model with observations (Pinte et al. 2008). *Left:* SED and *Spitzer/IRS* spectroscopy. *Center: HST/WFPC2 and Nicmos* scattered light images. *Right:* millimeter visibilities. Only the model with a surface density $p = -1$ can reproduce the visibilities.

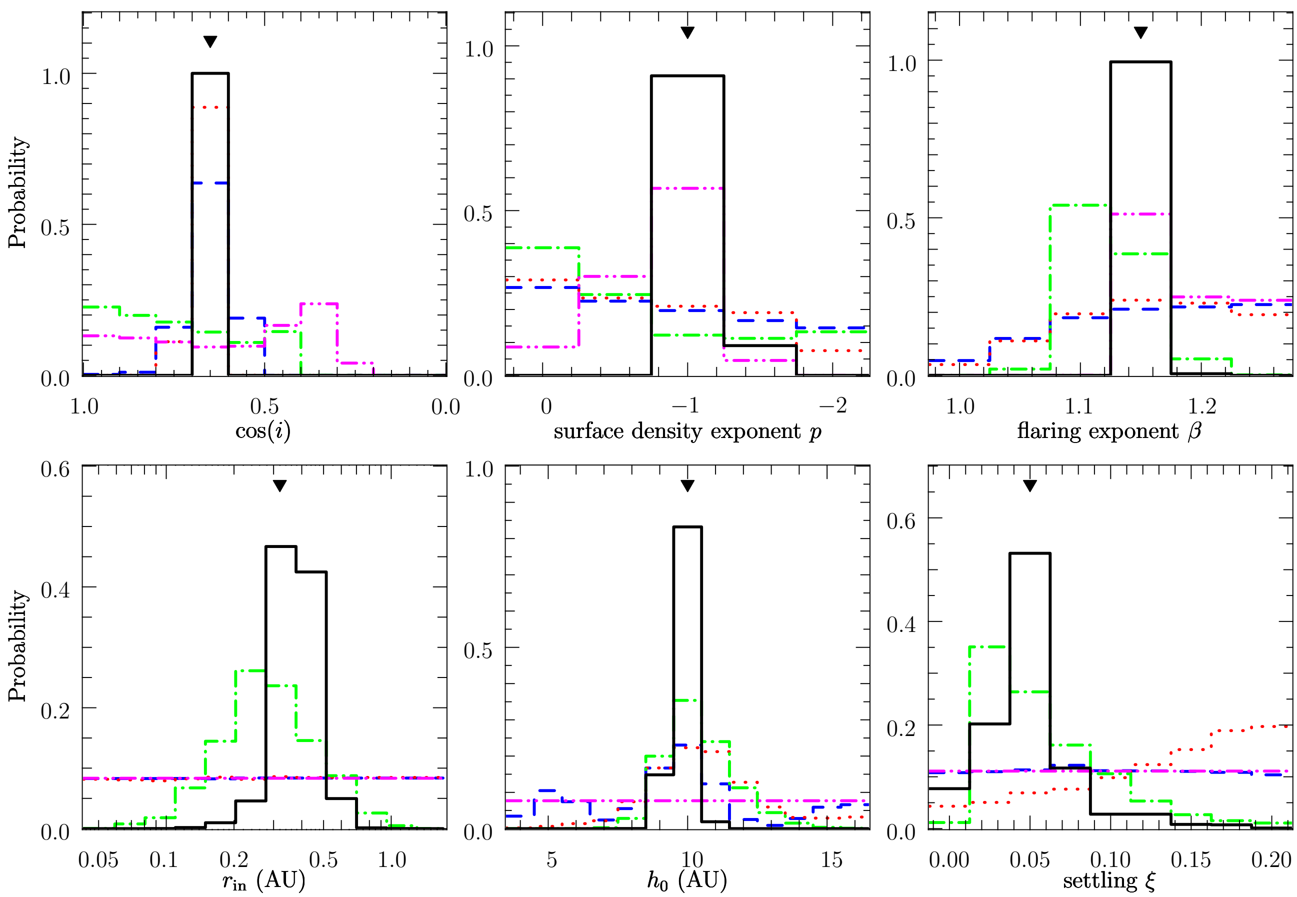

Fig. 2. Bayesian probabilities of the various parameters for the scattered light images at 0.6 μm (dashed blue) and 1.6 μm (dotted red), the SED (dot-dash green), the millimeter visibilities (dot-dot-dash pink) and for the images, SED and mm visibilities simultaneously (full black line). The triangles represent the parameters of the best model (Pinte et al. 2008).

only on some aspects of the disk structure and dust content (Fig 2). Quantitative evidence of dust evolution in the disk is obtained: grain growth up to millimeter-sized particles, vertical stratification of dust grains with micrometric grains close to the disk surface and larger grains which have settled towards the disk midplane, and possibly the formation of fluffy aggregates and/or ice mantles around grains (Pinte et al. 2008).

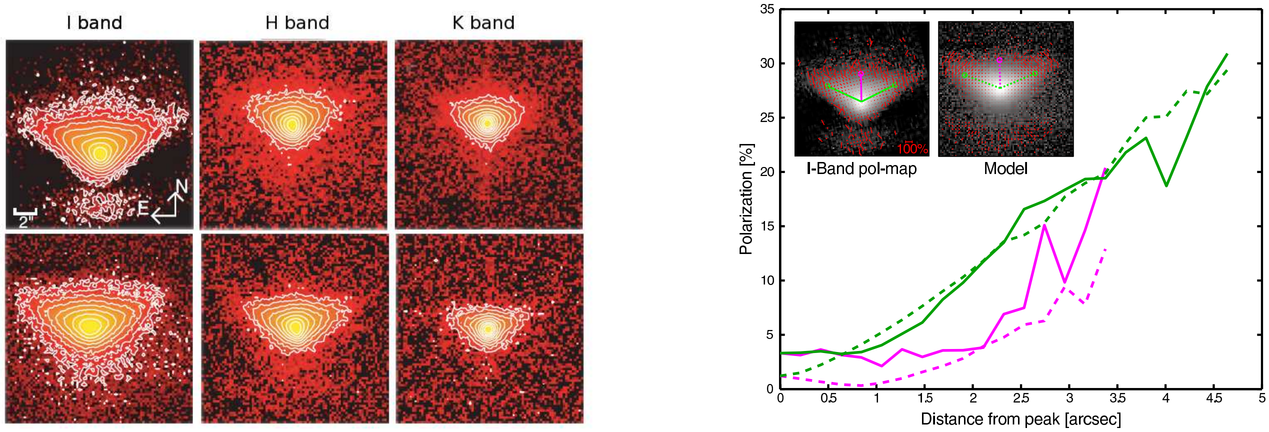

Fig. 3. *Left panel:* comparison of observed (top) and synthetic (bottom) images in I band (left), H band (center), and K band (right) of IRAS 04158+2805. Contour levels are $I = I_{\max} 2^{-n}$ with $n = 1 \ldots 8$. *Right panel:* comparison of the polarization level as a function of the position in the observed (solid) and modeled (dashed) nebula. Polarization (red vectors in insets) is compared along the ridge (green) and symetry axis (pink) of the nebula (Glauser et al. 2008).

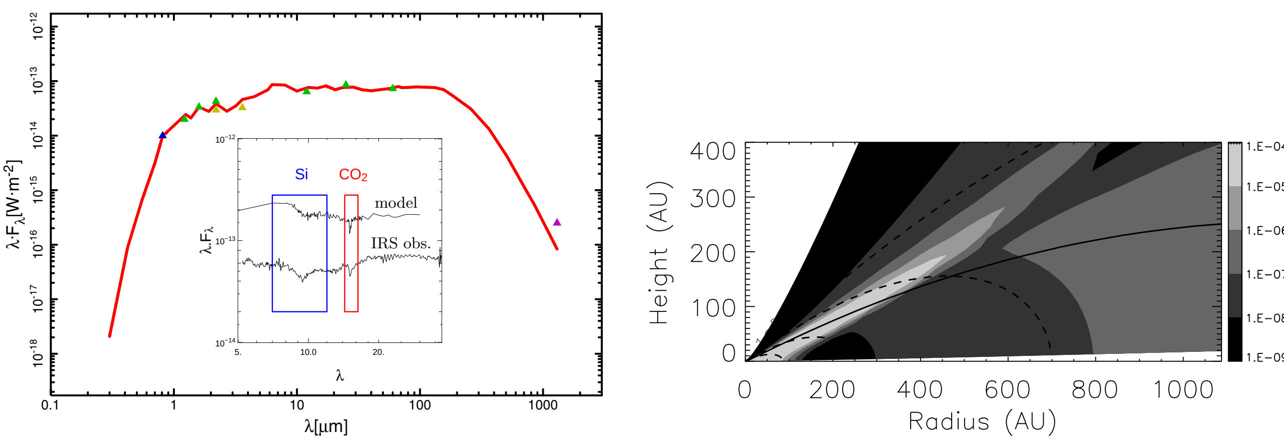

Fig. 4. *Left panel:* comparison of the observed (triangles) and modeled (red line) SEDs (Glauser et al. 2008). The SED, reminiscent of a class I is reproduced by a close to edge-on disk around a class II source. The IRS spectrum (inset) presents silicate and CO_2 absorption features (flux level is arbitrarily shifted), also seen in the model (CO_2 was added in disk regions where $T_{\rm dust} < 50$ K). *Right panel:* Calculated CO abundance as a function of the position within the disk.

3 IRAS 04158+2805

3.1 Modeling of the dust phase

IRAS 04158+2805 is an M5 star, near the substellar boundary. It presents evidence of circumstellar dust up to a large radius ($\approx$ 1 100 AU). We interpret optical and near-IR images, (VLT-FORS1, CFHT-IR), I band polarization map (VLT-FORS1), mid-infrared spectrum (SPITZER-IRS) and the SED in terms of a central star surrounded by an axisymmetric circumstellar disk, but without an envelope, to test the validity of this simple geometry. All the observations can be succefully reproduced with such a disk model observed at a grazing incidence. This allows us to establish strong constraints on the geometry of the disk and on its dust content (Fig. 3 and 4, Glauser et al. 2008).

3.2 Modeling of the gas phase

The density, temperature profiles and UV flux density derived from dust modeling are used to calculate the CO abundance throughout the disk (Fig. 4, right panel), by considering that CO molecules freeze-out onto the dust

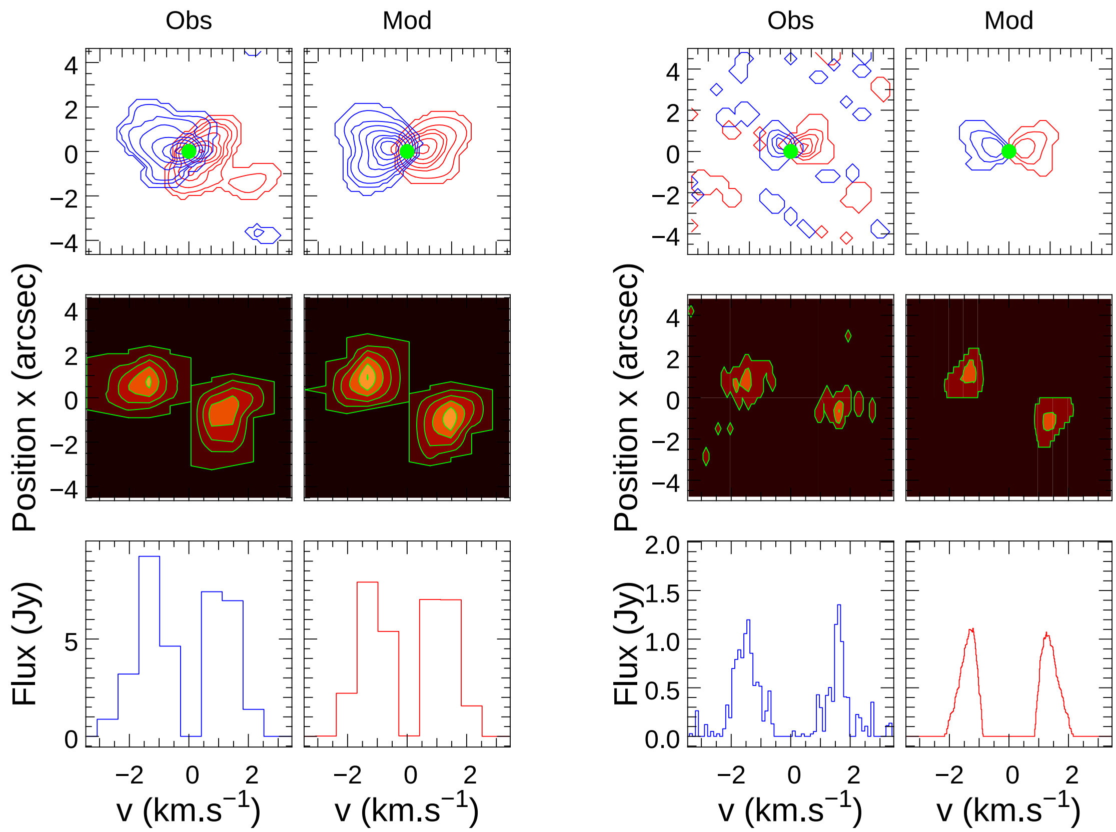

Fig. 5. Comparison of the observed and synthetic emission maps (top), position-velocity diagrams (middle) and integrated spectra (bottom). Left panel is for the J=3-2 SMA observations and right panel is for the J=2-1 IRAM/PdB observations.

grains in the midplane and are photo-dissociated by the FUV in the upper layers (Ceccarelli & Dominik 2005). From these abundances, the level populations of the CO molecules and corresponding emission maps are calculated with MCFOST (Fig. 5, Pinte et al, in prep.). Both the dust and gas observations of the disk can be reproduced consistently within the framework of this single model. The modeling allows us to constrain further the thermal and cinematic structures at large scale in the disk and additional information on the mass of the central object (in the range 0.3-0.5 $M_\odot$) and on the turbulence velocity (≈ 0.3 km.s^{-1}) is obtained.

4 Conclusion

The interest of the approach we present here is to combine coherently the disk density and temperature structure calculated using the dust disk geometry, as provided by continuum tracers to the different pieces of information provided by gas line tracers. The bulk of the disk mass is in the gas phase, but because most of the heating is provided by absorption of energy by dust, it is important (although difficult) to combine both approaches to improve curent modeling efforts of complex data sets. Such a global approach is needed to fully exploit present observational data sets and to prepare observations with future instruments like Herschel and ALMA.

References

Ceccarelli, C. & Dominik, C. 2005, A&A 440, 583–593

Glauser, A. M., Ménard, F., Pinte, C., Duchêne, G., Güdel, M., Monin, J.-L., & Padgett, D. L. 2008, A&A 485, 531–540

Hogerheijde,M. R. , & van der Tak, F. F. S. 2000, A&A 362, 697–710

Pinte, C. , Ménard, F. , Duchêne,G. , & Bastien, P. 2006, A&A 459, 797–804

Pinte, C. , Padgett, D.L. , Ménard, F. et al. 2008, A&A accepted, astro-ph/0808.0619

SF2A 2008
C. Charbonnel, F. Combes and R. Samadi (eds)

PULSATIONS OF RAPIDLY ROTATING STELLAR MODELS BASED ON THE SELF-CONSISTENT-FIELD METHOD: NUMERICAL ASPECTS AND ACCURACY

Reese, D.[1], MacGregor, K. B.[2], Jackson, S.[2], Skumanich, A.[2] and Metcalfe, T. S.[2]

Abstract. We use the numerical method developed in Lignières et al. (2006) and Reese et al. (2006) to calculate pulsation modes in stellar models generated by the Self-Consistent-Field method described in Jackson et al. (2005) and MacGregor et al. (2007). A discussion on the numerical method and its accuracy is given, followed by a very brief description of some of the results.

1 Introduction

Rapid stellar rotation introduces a number of phenomena which complicate stellar modelling. These include centrifugal deformation, gravity darkening, baroclinic flows and various forms of turbulence and transport phenomena (e.g. Rieutord 2006). As a result, the structure and evolution of these stars remain poorly understood and require observational constraints. Asteroseismology provides a promising way to probe the internal structure and dynamics of these stars, and thus to constrain stellar models.

Recent efforts to calculate stellar pulsations in rapidly rotating stars include Espinosa et al. (2004), Lignières et al. (2006), Reese et al. (2006), and Lovekin & Deupree (2008). These works either included a number of approximations, used a low resolution, or made use of simplified stellar models which limited the applicability of the results to actual observations. In the present paper, we use the numerical methods developed in Lignières et al. (2006) and Reese et al. (2006) to calculate the pulsation modes of stellar models based on the SCF method described in Jackson et al. (2005) and MacGregor et al. (2007), in an attempt to overcome these limitations.

2 The stellar models

The Self-Consistent-Field (SCF) method was first developed 40 years ago (Ostriker & Mark 1968). The basic idea in this method is to alternate between solving Poisson's equation, which gives the 2D shapes of the equipotentials, and solving the hydrostatic equation, which gives the 1D profile of thermodynamic quantities along a radial cut. This iterative procedure produces a series of models which converges to a rotating model which satisfies both equations. At the time, the method was restricted to massive stars due to what appeared to be numerical limitations. Since then these issues have been solved in a recent series of paper, and more realistic micro-physics have been included, thus allowing 1 or 2 $M_\odot$ models (Jackson et al. 2004, 2005; MacGregor et al. 2007).

Currently, models based on the SCF method are chemically homogeneous ZAMS models. The rotation profile is given by one of the following two equations:

$$\Omega(s) = \frac{\eta\Omega_{\mathrm{cr}}}{1+\left(\frac{\alpha s}{R_{\mathrm{eq}}}\right)^2} \qquad \text{or} \qquad \Omega(s) = \eta\Omega_{\mathrm{cr}}\left\{1+\left(\frac{\alpha s}{R_{\mathrm{eq}}}\right)^2\right\} \tag{2.1}$$

where s is the distance to the rotation axis, R_{eq} the equatorial radius, Ω_{cr} the equatorial break-up rotation rate, and α and η two parameters which control the rotation profile. This type of rotation profile is conservative,

[1] Department of Applied Mathematics, University of Sheffield, Hicks Building, Hounsfield Road, Sheffield S3 7RH, UK
[2] High Altitude Observatory, National Center for Atmospheric Research, Boulder, CO 80307, USA

i.e. the centrifugal force derives from a potential. As a result, the stellar structure is barotropic: different thermodynamic quantities remain constant on surfaces of constant total potential, the sum of the centrifugal and gravitational potentials. Furthermore, the angular momentum $s^2\Omega$ increases with s, thus satisfying the dynamical part of the Solberg-Høiland stability criterion.

In the first type of rotation profile, the rotation rate decreases with increasing distance from the rotation axis. As a result, it is possible to construct configurations in which the central part rotates at an angular velocity which is several times $\Omega_{\rm cr}$. Such configurations can take on very distorted shapes and can be used to try to explain Achernar's oblateness (Jackson et al. 2004), as revealed by interferometric observations (Domiciano de Souza et al. 2003). In the second case, the rotation rate increases with distance to the rotation axis, thus partially resembling the solar rotation profile.

3 The stellar pulsations

Acoustic pulsation modes in the adiabatic approximation are governed by the following set of equations in an inertial frame:

$$\left[\lambda + im\Omega\right]\rho = -\vec{v}\cdot\vec{\nabla}\rho_0 - \rho_0\vec{\nabla}\cdot\vec{v}, \tag{3.1}$$

$$\left[\lambda + im\Omega\right]\rho_0\vec{v} = -\vec{\nabla}p + \frac{\vec{\nabla}P_0}{\rho_0}\rho - \rho_0\vec{\nabla}\Psi - 2\Omega\vec{e}_z\times\rho_0\vec{v} - \rho_0 s\frac{\partial\Omega}{\partial s}v_s\vec{e}_\phi \tag{3.2}$$

$$\left[\lambda + im\Omega\right]\left(p - c_0^2\rho\right) = \left[-\vec{\nabla}p_0 + c_0^2\vec{\nabla}\rho_0\right]\cdot\vec{v} \tag{3.3}$$

$$0 = \Delta\Psi - \Lambda\rho. \tag{3.4}$$

where $\vec{v}$ is the velocity perturbation, ρ the Eulerian density perturbation, p the Eulerian pressure perturbation, Ψ the Eulerian perturbation to the gravitational perturbation, $\lambda = i\omega$ the eigenvalue (where ω is the eigenfrequency) and quantities with the subscript "0" equilibrium quantities. These equations are supplemented with boundary and regularity conditions which ensure that the pulsation modes are regular in the centre, the Lagrangian pressure perturbation vanishes on the stellar surface and the perturbation to the gravitational potential goes to zero towards infinity. The resultant system constitutes a 2D eigenvalue problem.

These equations are solved using the numerical method described in Lignières et al. (2006) and Reese et al. (2006). Firstly, an adapted coordinate system which follows the shape of the star is used. Rather than working with the equipotentials from the models, the same coordinate system is used as in Reese et al. (2006). This increases the accuracy of the geometrical terms which intervene in the equations, because the radial derivatives of r are calculated analytically. An example of a coordinate system is shown in Fig. 1.

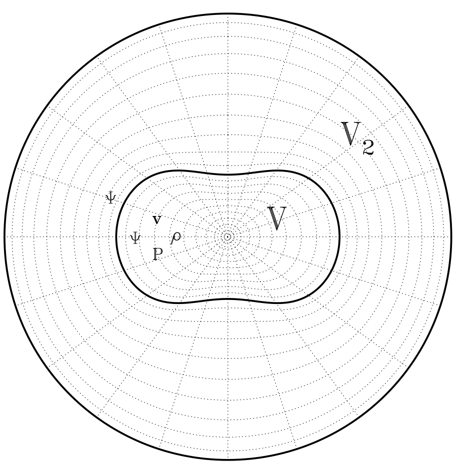

Fig. 1. An example of a coordinate system used when calculating pulsation modes. The inner domain, V, corresponds to the star. Equations (3.1)-(3.4) are solved on this domain, as represented by the symbols ρ, P, Ψ and $\mathbf{v}$. In the second domain, V_2, only eq. (3.4) is solved, as represented by Ψ. This second domain is added in order to facilitate imposing the appropriate boundary conditions on the perturbation to the gravitational potential.

Secondly, the unknowns and the equations are projected onto the spherical harmonic basis. This is done by expressing the unknowns as a sum of spherical harmonics multiplied by unknown radial functions. The equations are multiplied by the complex conjugate of spherical harmonics and integrated over 4π steradians. The resultant system is an infinite set of coupled ordinary differential equations, the solution of which yields the unknown radial functions. For numerical applications, this system is truncated at a maximal harmonic degree $L_{\max}$.

Finally, this system is discretised in the radial direction using N_r grid points thus yielding an algebraic system which can be solved using the Arnoldi-Chebyshev algorithm. This discretisation can be done using a spectral method based on Chebyshev polynomials as is done in Lignières et al. (2006) and Reese et al. (2006) or using finite differences as is the case here.

4 Accuracy of the results

Various tests can be used to assess the accuracy of the calculations. In Fig. 2, we follow the evolution of the error as a function of $L_{\max}$ and N_r. The error was calculated by using the frequency calculated at highest resolution as a reference. The first two panels apply to a star rotating at 60% of the break-up rotation rate. As can be seen in the figure the accuracy is pretty good, and depends especially on the radial resolution. The other two panels apply to a star rotating at 90% of the break-up rotation rate. Here the results are not as good. Evaluating the error in this case was not entirely straightforward due to difficulties in identifying the correct mode at different resolutions. The most likely cause for this decrease in accuracy is the presence of a cusp-like region at the equator which increases the resolution needed for calculating pulsation modes accurately.

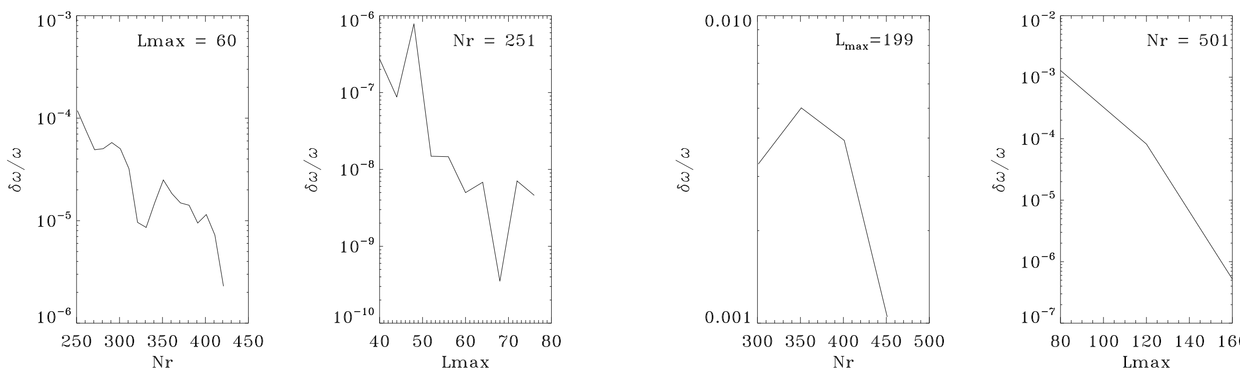

Fig. 2. Evolution of the error with $L_{\max}$ and N_r for a pulsation mode in a star at 60% of the break-up velocity (left two panels) and at 90% of the break-up velocity (right two panels).

Another test consists in applying a variational formula on the eigenmodes to yield an independent value for the frequency. According to the variational principle, the error on this frequency is proportional to the square of the error on the eigenmode, thus minimising its effect (Christensen-Dalsgaard & Mullan 1994). By comparing this value to the original frequency, it is possible to estimate the accuracy of the calculation. So far, we have only applied this test to pulsation modes in uniformly rotating models. For the pulsation mode which corresponds to the two left panels of Fig. 2, the relative error $\delta\omega/\omega$ is 2.5×10^{-3} which corresponds to 0.7 μHz. Unfortunately, the variational formula did not yield consistent values for the mode which corresponds to the two right panels.

Finally, another test consists in applying different numerical techniques to calculate the eigenmodes and seeing if they give similar results. Figure 3 shows such a comparison. The mode on the left is calculated using finite differences in the radial direction whereas the mode on the right uses Chebyshev polynomials. This second calculation required interpolating the stellar model onto the Chebyshev collocation grid using cubic splines in the same way as is done in Dintrans & Rieutord (2000) for a 1.5 $M_\odot$ CESAM model. At a given $L_{\max}$, the two calculations yield very similar results, as can be seen from the figure. The corresponding frequencies are less than 0.1 μHz apart.

5 The results

Based on this method, we investigated pulsation modes in models with masses ranging from 1.7 to 25 $M_\odot$. The rotation profile for the models went from uniform to highly differential. The pulsation modes in uniformly or

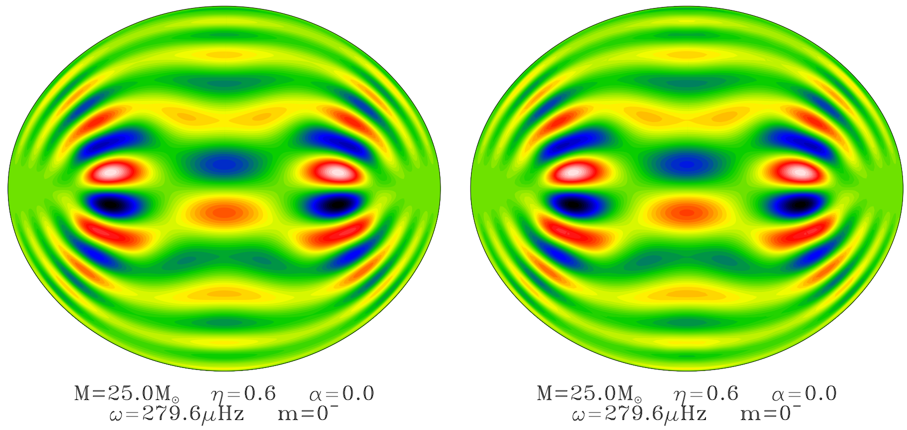

Fig. 3. Comparison of a pulsation mode calculated using finite differences (*left*) and using Chebyshev polynomial (*right*). The difference on the frequencies is less than 0.1 μHz.

nearly uniformly rotating models followed the same qualitative behaviour as was found for polytropic models (Lignières et al. 2006; Reese et al. 2008a; Lignières & Georgeot 2008) in terms of mode geometry, mode classification and frequency organisation. Pulsation modes in the models with highly differential rotation turned out to be rather chaotic and difficult to classify. A more detailed discussion of these results is given in Reese et al. (2008b).

Many of the numerical calculations were carried out on the Altix 3700 of CALMIP ("CALcul en MIdi-Pyrénées") and on Iceberg (University of Sheffield), both of which are gratefully acknowledged. DR gratefully acknowledges support from the UK Science and Technology Facilities Council through grant ST/F501796/1, and from the European Helio- and Asteroseismology Network (HELAS), a major international collaboration funded by the European Commission's Sixth Framework Programme. The National Center for Atmospheric Research is sponsored by the National Science Foundation.

References

Christensen-Dalsgaard, J. & Mullan, D. J. 1994, MNRAS, 270, 921

Dintrans, B. & Rieutord, M. 2000, A&A, 354, 86

Domiciano de Souza, A., Kervella, P., Jankov, S., et al. 2003, A&A, 407, L47

Espinosa, F., Pérez Hernández, F., & Roca Cortés, T. 2004, in ESA SP-559: SOHO 14 Helio- and Asteroseismology: Towards a Golden Future, 424–427

Jackson, S., MacGregor, K. B., & Skumanich, A. 2004, ApJ, 606, 1196

Jackson, S., MacGregor, K. B., & Skumanich, A. 2005, ApJS, 156, 245

Lignières, F. & Georgeot, B. 2008, Phys. Rev. E, 78, 016215

Lignières, F., Rieutord, M., & Reese, D. 2006, A&A, 455, 607

Lovekin, C. C. & Deupree, R. G. 2008, ApJ, 679, 1499

MacGregor, K. B., Jackson, S., Skumanich, A., & Metcalfe, T. S. 2007, ApJ, 663, 560

Ostriker, J. P. & Mark, J. W.-K. 1968, ApJ, 151, 1075

Reese, D., Lignières, F., & Rieutord, M. 2006, A&A, 455, 621

Reese, D., Lignières, F., & Rieutord, M. 2008a, A&A, 481, 449

Reese, D., MacGregor, K. B., Jackson, S., Skumanich, A., & Metcalfe, T. S. 2008b, in 38th Liège International Astrophysical Colloquium, in preparation

Rieutord, M. 2006, A&A, 451, 1025

SF2A 2008
C. Charbonnel, F. Combes and R. Samadi (eds)

MASSIVE STAR FORMATION IN NGC6334-NGC6357 PRELIMINARY RESULTS

Russeil, D.[1], Zavagno, A.[1], Motte, F.[2], Bontemps, S.[3] and Schneider, N.[2]

Abstract. On the basis of the extinction map a survey of NGC6334-6357 at 1.3 mm continuum has been done in order to find high density cores. 163 dense cores (volume-averaged density $<n_{H_2}>\sim 2.4\ 10^4$ cm^{-3}) have been detected among which 34 are massive (M $\geq$100 M$_\odot$).

1 Introduction

We are looking for the earliest phases of the high-mass stars in the star-forming complex NGC6334-6357. These are supposed to be cold, high-density and IR-quiet objects. On the basis of the extinction map (Bontemps, private communication) a survey of NGC6334-6357 at 1.3 mm continuum has been done (fig. 1) in order to find high density cores following a multiresolution analysis developed by Motte et al. (2007). 163 dense cores have been detected, for which we looked for IR counterpart using Spitzer IRAC/GLIMPSE and MIPSGAL 24μm data.

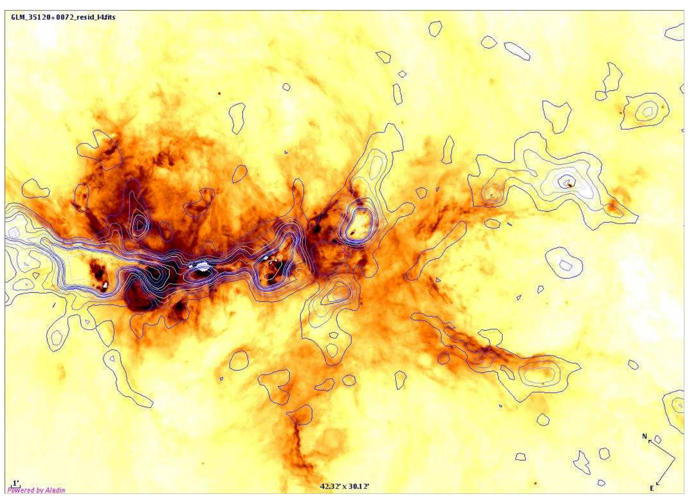

Fig. 1. Spitzer-IRAC (8μm) image of NGC6334 superimposed with SIMBA 1.3mm isocontours (Muñoz et al. 2007).

2 The results

The majority of the cores (120 on 163 detected) show no IR counterpart up to 24μm (fig. 2). The most massive infrared-quiet cores (M $\geq$100 M$_\odot$) are good candidates for either massive pre-stellar cores or the equivalent to classical "class 0" objects.

[1] LAM, Université de Provence, 38, rue Frédéric Joliot-Curie 13388 Marseille cedex 13 France
[2] AIM/SAp, CEA-Saclay, 91191 Gif Sur Yvette Cedex, France
[3] OASU, Site de Floirac, 2 rue de l'Observatoire, 33270 Floirac, France

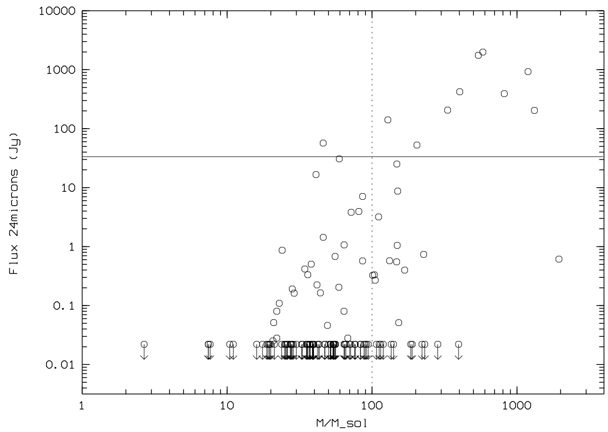

Fig. 2. Flux 24μm (aperture photometry on MIPS images) versus mass (determined from 1.3mm data and corrected from free-free emission). The line is the flux limit to have a B3 stellar core embedded in the dense core. This line separate the infrared-quiet (below the line) from the infrared-loud cores. The dashed line displays the mass limit we have assumed necessary for a core of 0.3 pc size to be able to form a massive star.

For cores with IR counterpart a trend is seen (fig. 2) in agreement with the fact that the more massive the proto-star, the more intense the warm dust emission in the core.

The slope of the core mass distribution (fig. 3) of NGC 6334 seems to be slightly different from that of NGC 6357. One can note that NGC 6334 exhibits more massive cores than NGC6357. This will be compared (in future works) with the different internal kinematics observed in both HII regions.

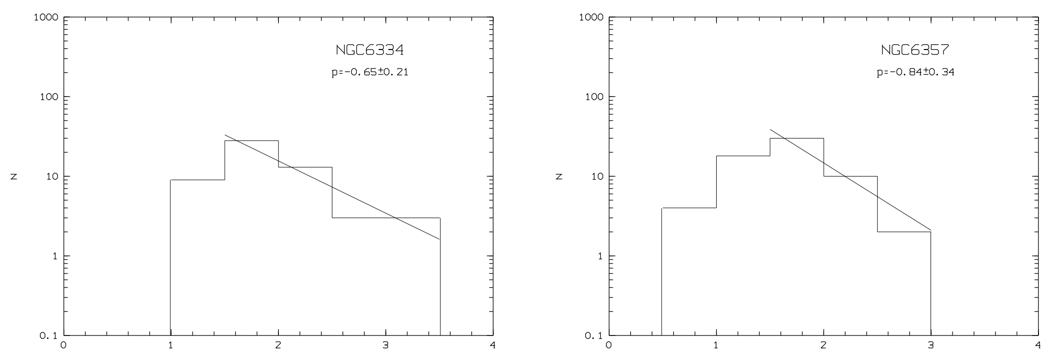

Fig. 3. Mass histogram of the cores in NGC6334 (left) and NGC6357 (right). The bin size has a constant value of $0.5M_{\odot}$. The low mass completeness limit is estimated to be $\sim 30M_{\odot}$.

Finally, the 24 massive and infrared-quiet objects are either infrared-quiet proto-star or pre-stellar cores without star. The search for associated classical tracers of stellar activity (maser emission, centimeter free-free emission, SiO, mid-infrared) is in progress. These are also excellent targets to observe with Herschel (HOBYS GT program, PIs: F. Motte, A. Zavagno, S. Bontemps) and ALMA in order to precise their nature.

References

Motte F., Bontemps S.,Schilke P., et al. 2007, A&A, 476, 1243

Munoz D., Mardones D., Garray G., et al. 2007, ApJ, 668, 906

SF2A 2008
C. Charbonnel, F. Combes and R. Samadi (eds)

PROBING THE HOT GAS IN YOUNG STELLAR OBJECTS WITH VLTI/AMBER

Tatulli, E.[1]

Abstract. In this paper, I give a summary of the recent results obtained with AMBER on spectro-interferometric observations of Herbig Ae/Be stars. This summary is not exhaustive but representative of the unique capabilities of AMBER to probe the hot circumstellar gas, in addition to the usually observed dust near-infrared thermal emission.

1 Introduction

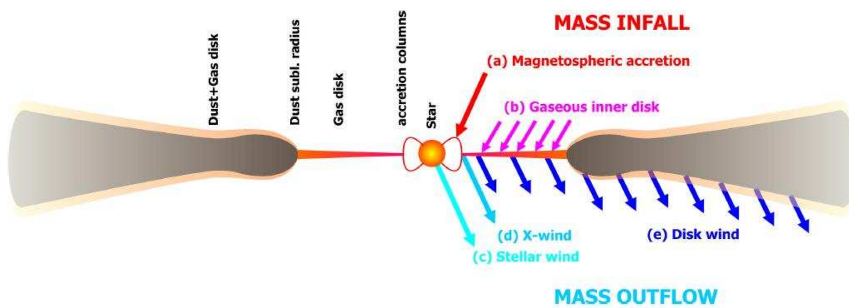

Fig. 1. Sketch of the inner environment around young stellar objects, from Kraus et al. (2008). See text for detailed description.

Observing the protoplanetary disks around young stars is a key issue to understand the first steps of planet formation mechanisms. Such processes are occurring in the very inner environment of the central star, at distances of a few Astronomical Units. The representation that we have today of this environment is sketched in Fig. 1, which is basically composed of i) magnetically-driven columns of gas accreting on the central star, ii) a gaseous dust-free rotating disk, iii) a dusty disk which inner rim is located at the dust sublimation radius; and iv) potentially outflowing winds.
Observational clues that we can obtain of the inner part of the protoplanetary disks are twofold:
- from their continuum infrared excess of the SED, that arises from the thermal emission of the circumstellar dust. It will give informations about the structure/geometry of the disk as well as about its dust grain composition (grain growth, radial/vertical distribution, mineralogy).
- from their infrared emission (/absorption) lines, in particular the hydrogen lines, that can originate from mainly three different mechanisms: i) magnetospheric accretion along the accreting columns of gas (Hartmann et al. 1994); ii) magnetically-driven outflows (Shu et al. 1994; Casse & Ferreira 2000); and/or from the rotating gaseous disk itself (Tambovtseva et al. 1999).

In order to characterize these mechanisms unambiguously, one needs both spatial and spectral resolution to localize and separate the continuum and line emission regions. At distances of the first stellar formation regions ($\sim$ 150pc), 1AU corresponds to a angular distance of $\sim$ 6mas, a resolution that only interferometric techniques

[1] etatulli@obs.ujf-grenoble.fr

can achieve. Furthermore, at such distances from the star, the temperature at the inner region of young stars is roughly between a few 100K and a few 1000K, that is radiating at near infrared wavelengths. As a result, near infrared spectro-interferometry which provides both the spatial and spectral resolution required at the desired wavelengths appears to be a technique perfectly suited to observe the inner environment of protoplanetary disks. In this instrumental context, we will focus here on the VLTI/AMBER recombiner which is so far the unique instrument that can simultaneously offer a proper spatial resolution (up to 2mas @ 2.2μm $\equiv$ 0.3AU @ 150pc), spectral coverage (K and H bands) together with a spectral resolution allowing to resolve the emission lines (R=1500).
In the following, we will illustrate how AMBER enables to probe the gas in YSOs giving two examples: in Section 2 by investigating the accretion/ejection phenomena in Herbig Ae/Be stars, and in Section 3 by probing the hot circumstellar gas around young stars.

2 The Origin of the Brγ emission in Herbig Ae/Be stars

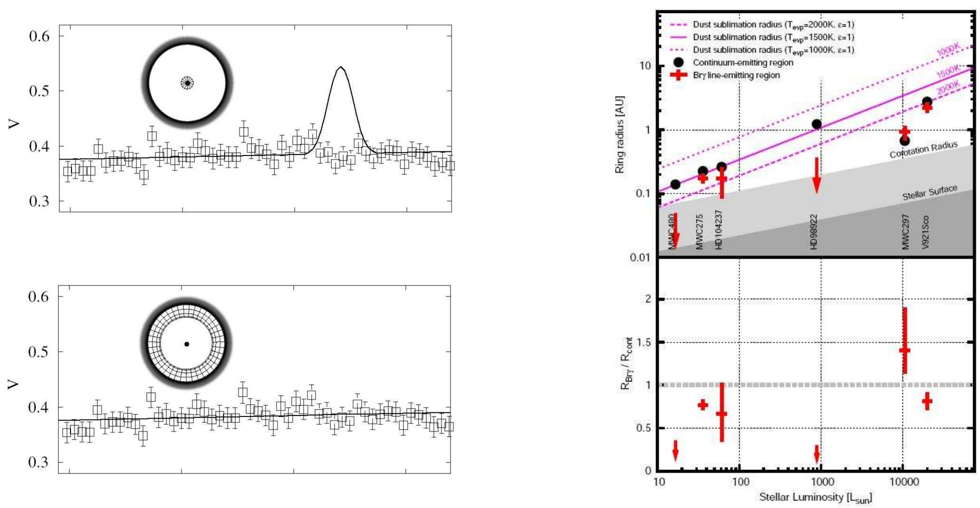

Fig. 2. Left: visibility around the Brγ line of HD104237 and superimposed magnetospheric-accretion (up) and wind (down) models, from Tatulli et al. (2007). Size of the Brγ region for 6 Herbig Ae/Be stars as a function of the star's luminosity, from Kraus et al. (2008).

From the first observation...: As summarized in previous Section, the origin of hydrogen emission lines in protoplanetary disks is still subject to debate. In order to disentangle between the possible scenarios, Tatulli et al. (2007) have used the VLTI/AMBER instrument to spatially and spectrally resolve for the first time the inner region of the Herbig Ae star HD104237 around its strong Brγ emission line. They have thus obtained visibility measurements in the Brγ line and in the adjacent continuum. The continuum was classically interpreted as arising from the inner rim of the dusty disk located at the sublimation radius. In the Brγ line however the visibility was same than in the continuum, leading them to conclude that the Brγ emission region presented, within the error bars, dimensions similar to that of the continuum one. This strong dimensional constraint enabled to unambiguously rule out the magnetospheric accretion (as well as the gaseous disk) scenario as responsible from the Brγ emission since it would have come from a much smaller region, located typically between the star and the corotation radius, and would have led to a significant increase of the visibility (see Fig. 2 (left, up)). Conversely, the behaviour of the visibility was compatible with the wind scenario, seen face-on as a ring of inner rim $R \sim 0.2$ to 0.5AU (see Fig. 2 (left, down)).

... to a systematic study: Since then, the increase in sensibility and precision of the instrument has recently allowed Kraus et al. (2008) to reproduce that type of analysis of a larger sample of 6 stars, as summarized in Fig. 2 (right). They hence shown that, if for two stars (HD98922, MWC480) the interferometric measurements were compatible with the magnetospheric-accretion for the origin of their Brγ emission, the wind scenario was favored for three of them (MWC275, MWC297, V921Sco) and also confirmed for HD104237. Taken statistically, these results are also interesting to analyze: first, the correlation suggested earlier by Eisner et al. (2007) between the origin of the Brγ emission and the star's luminosity is not observed; and most of all, at the contrary of TTauri stars for which the direct correlation between accretion and Brγ emission is well established, in Herbig Ae/Be stars we are mostly probing outflows phenomena from Brγ emission, this latter being probably in this case an indirect tracer of accretion through accretion-driven mass loss.

3 Probing the inner disk of gas

Whereas Brγ is a good tracer of whether magnetospheric accretion or outflowing winds, AMBER, by exploring other lines or by performing a two (H,K)-wavelengths analysis of the continuum, is also suited to directly probe the gas in the disk itself, as it is illustrated in the two following examples.

3.1 The hot molecular gas in 51 Oph

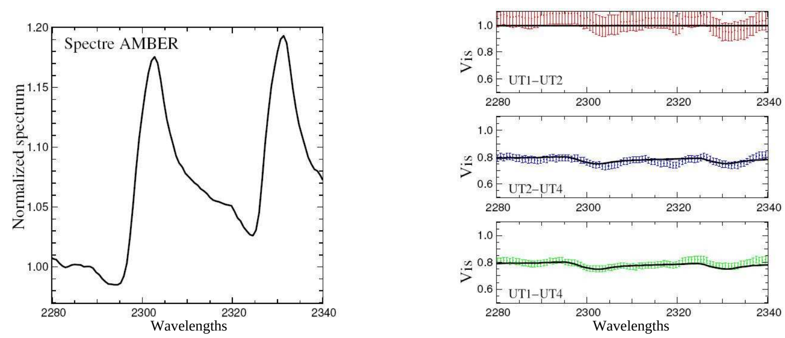

Fig. 3. AMBER spectrum of CO bandheads in 51 Oph (left) and measured visibilities (right), from Tatulli et al. (2008)

Tatulli et al. (2008) has recently presented the first interferometric observations at the 2.3μm CO overtone emission in the (B9) Be star 51 Oph, using the AMBER instrument (see Fig. 3). 51 Oph is indeed one of the very few young stars where this emission is strong enough to be observed with infrared spectro-interferometry (Thi el al. 2005; Berthoud 2008). Obtaining visibility on three baselines around the CO bandheads, they have shown for the first time that:
- the hot CO emission was resolved, located at a distance of 0.15AU from the star, thus in perfect agreement with the scenario in which the CO is emitted from the first AU of a rotating gaseous disk (Thi et al. 2005)
- the adjacent continuum is located at a distance of 0.25AU, that is too close to the star compared to the location of the sublimation radius, suggesting that i) the stellar light is shielded by the optically thick gas hence moving the sublimation radius closer to the star, and/or that ii) the hot gas inside the dust sublimation radius significantly contributes to the observed 2 μm emission (free-free emission).

3.2 Gas and dust in the inner disk of MWC 758

In this study, Isella et al. (2008) have emphasized the interest of simultaneously observed protoplanetary disks in both H and K band, showing that low spectral resolution (R=35) observations are also of interest to probe not only the dust but the gas in such objects. Indeed, if the K band will be mainly sensitive to the dust thermal emission at $\sim$ 1500K, H band will probe an hotter and closer region in which the dust is likely to have sublimated, leaving a gaseous dust-free disk. They have demonstrated this point by observing the Herbig Ae star MWC758 with AMBER, obtaining visibilities and closure phases in H and K bands, as shown in Fig. 4 (left).

If the K band observations alone are well interpreted by the classical dusty puffed-up inner rim (T_{sub} = 1400K, R_{in} = 0.34AU), it fails to reproduce the H band observations for which the emission is less resolved than expected by this model. Furthermore, with this model, the SED can be not fitted successfully, showing a lack of energy in the H band. Conversely, by adding to the model the presence of an unresolved hotter component (of T_g = 2500K), they managed to reproduce both the H and K bands measurements jointly. Note that this

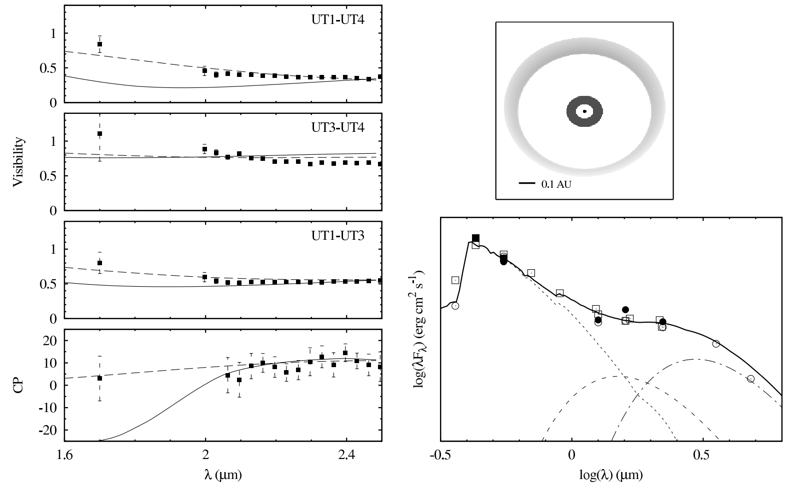

Fig. 4. Left: H and K band visibilities and closure phases of MWC758, from Isella et al. (2008). The solid line represents the model of dust inner rim only, the dashed one being the unresolved point + dust model as shown in the right top corner. Below is shown the SED, well reproduced by the star (dotted line) + unresolved point (dashed line) + dust (dashdotted line) model.

changes slightly the parameters of the dusty rim (T_{sub} = 1300K, R_{in} = 0.40AU). What is then the physical interpretation for this unresolved component? Given the temperature and the size ($\leq$ 0.1AU) of the emission region, it is likely that AMBER is directly probing the hot gas accreting close to to the star. And indeed, models of accreting gas developed by Muzerolle et al. (2004) (assuming an accretion rate of $\sim 2.10^{-7} M_{\odot}/yr$ from the star's Brγ luminosity), allow as well to satisfactory fit the shape of the SED by filling the lack of energy in the H band (see Fig. 4), hence reinforcing this interpretation.

4 Conclusion and perspectives

In summary, AMBER is so far a unique tool – in terms of spectral bands (H,K), together with spectral resolution (R=35,1500,12000) – to probe the internal region of YSO, not only for the dust but also for the gas emissions. Note that from this semester of observation, the FINITO fringe tracker is now available with the 8m telescopes of the VLTI, hence allowing to drastically increase the precision of the measurements, as well as its sensibility that enable to probe fainter emission lines (CO, Fe?,...) and to use the high spectral resolution mode of R=12000 to access the kinematics (velocity maps) of the gas along the lines.

References

Berthoud, M. G. 2008, Ph.D. Thesis
Casse, F., & Ferreira, J. 2000, A&A, 353, 1115
Eisner, J. A., Chiang, E. I., Lane, B. F., & Akeson, R. L. 2007, ApJ, 657, 347
Hartmann, L., Hewett, R., & Calvet, N. 1994, ApJ, 426, 669
Isella, A., Tatulli, E., Natta, A., & Testi, L. 2008, A&A, 483, L13
Kraus, S., Hofmann, K.-H., Benisty, M., et al. 2008, A&A, 489, 1157
Muzerolle, J., D'Alessio, P., Calvet, N., & Hartmann, L. 2004, ApJ, 617, 406
Shu, F., Najita, J., Ostriker, E., et al. 1994, ApJ, 429, 781
Tambovtseva, L. V., Grinin, V. P., & Kozlova, O. V. 1999, Astrophysics, 42, 54
Tannirkulam, A., Monnier, J. D., Millan-Gabet, R., et al. 2008, ApJ, 677, L51
Tatulli, E., Isella, A., Natta, A., et al. 2007, A&A, 464, 55
Tatulli, E., Malbet, F., Mnard, F., et al. 2008, A&A , 489, 1151
Thi, W.-F., van Dalen, B., Bik, A., & Waters, L. B. F. M. 2005, A&A, 430, L61

PNST

Sun and Earth

MAGNETIC HELICITY AND SOLAR PROMINENCE FORMATION

Aulanier, G. and Schmieder, B.[1]

Abstract. Simple laws have long-since been put forward from the chirality of observed features to derive the direction of the axial magnetic field inside solar filaments. These are the so-called "filament chirality rules". Here, we report on two uses of these rules applied to THEMIS and SVST observations and to MHD simulations. Being the first to apply these rules to the 180° disambiguation of the direction of the photospheric transverse magnetic field around filaments, we found the unprecedented evidence of magnetic support in filament feet, as predicted by former magnetostatic and recent MHD models. By combining these rules with 3D weakly twisted flux tube models, we identified the sign of the magnetic helicity in several filaments. Following their interactions with one another over a few days, we found that the observational condition for two filaments to merge is that their flux tubes must have the same helicity sign. We theoretically recovered these results, by conducting a parametric study of 3D numerical MHD simulations of sheared bipoles. This study also provided new conditions for filament merging, in yet-unobserved configurations in which sheared bipoles are oppositely oriented.

1 Introduction

Solar filaments and prominences are key-phenomena for the study of high-stressed current-carrying magnetic fields in the solar corona. They can be used to understand how magnetic helicity slowly accumulates in the Sun's corona, and is then later ejected in the heliosphere in the form of coronal mass ejections, which are known to be the main drivers of extreme space weather. In spite of impressive progress with ASP for the 2D measurement of the internal magnetic field in prominences (Casini et al. 2003), building a 3D picture still requires to combine multi-wavelength observations and magnetic models (e.g. Dudik et al. 2008).

In this context, observational laws have been put forward from the chirality of observed features to derive the direction of the axial magnetic field inside solar filaments. These are the so-called "filament chirality rules". They state that a dominant fraction of filaments located in the northern (resp. southern) solar hemisphere have right- (resp. left-) bearing feet and fibrils, left (resp. right) skewed arcades, and dextral (resp. sinistral) internal axial fields, which point rightward (resp. leftward) as the filaments are viewed from the main positive polarity field on the side of the photospheric inversion line above which they are located (Martin 1998).

The most successful filament magnetic models make use of a 3D differentially sheared arcade or a weakly twisted flux tube topology. The good applicability of these models to observations has first been proven through the comparison of plasma-supporting magnetic dips calculated in a linear force-free field model with observed filament material (Aulanier & Démoulin, 1998). Since then, this "magnetic dip filling" procedure has been applied by various groups to to analyze real observations with linear magnetohydrostatic, non-linear magnetofrictional and fully MHD models (Aulanier & Schmieder 2002, Lionello et al. 2002, van Ballegooijen 2004, Bobra et al. 2008). These topologies have also recently been found to be consistent with the evolution of the photospheric vector magnetic field during a filament formation resulting from flux emergence, as observed by Hinode/SOT (Okamoto et al. 2008). When combined with the chirality rules, these models predict that dextral (resp. sinistral) filaments correspond to left- (resp. right) hand magnetic twists, hence to negative (resp. positive) magnetic helicities.

[1] LESIA, Observatoire de Paris, CNRS, UPMC, Université Denis Diderot, 5 place Jules Janssen, 92195 Meudon Cedex

2 Disambiguation of THEMIS magnetograms and discovery of magnetic dips in a filament foot

A debate is raging in the solar physics community about the magnetic nature of filament feet, which are common underlaying and lateral extensions observed in absorption on the solar disc in Hα and in the EUV. Are these feet formed by continuously injected plasma condensation in magnetic arcades, as hinted by some observations and conceptual models (Martin 1998), or do they consist of quasi-static condensations that are maintained against free-fall by the Lorentz force in a low-lying continuous distribution of magnetic hammocks, from the feet ends to up to the filament bodies, as first predicted by linear force-free field and magnetohydrostatic models (Aulanier & Démoulin 1998, Aulanier & Schmieder 2002, Dudik et al. 2008) ? This issue is important since the former interpretation, if it were true, could put in jeopardy the family of models mentioned in Sec. 1. This debate had been lacking of new discriminators for about ten years, until this issue was recently addressed through new direct measurements of the photospheric magnetic field vector $\vec{B}$ in a filament channel located far from the center of the solar disc, resulting from the PCA-based inversion of high-precision spectropolarimetric observations with the MTR instrument of the THEMIS telescope (López Ariste et al. 2006).

A major problem with these measurements is that they still give the direction of the component of the magnetic field vector on the plane of the sky at $\pm 180°$. This fundamental ambiguity does not allow the observations, taken alone, to state whether an arcade or a dip is measured at a given place. So as to solve this paradigm, chirality rules can be applied to the disambiguation of the measured transverse magnetic fields, before deprojecting them to obtain the three components of the magnetic field vector in the reference frame of the solar surface. This procedure was proposed and applied in López Ariste et al. (2006), and rephrased by Martin et al. (2008). The studied filament was identified to be sinistral, hence with a magnetic field vector globally pointing toward the left, as viewed from the dominant positive magnetic polarity in the photosphere (Fig. 1, top). Interestingly, it was found that, for almost every area analyzed in details within the observed filament channel (indicated by rectangles in Fig. 1), only the sinistral solution that matched the chirality rule on the plane of the sky remained sinistral in the reference frame of the solar surface. Using the chirality-consistent solution to calculate the curvature $B^2/(\vec{B}\cdot\vec{\nabla})\vec{B}$ of the magnetic field at various places within the channel, the first-ever 3D magnetic dip topology was found in the photosphere below a filament foot from observations (Fig. 1, bottom). This is consistent with early linear force-free models for filament feet (Aulanier & Démoulin 1998) and with recently recovered in MHD simulations of prominence formation by twisted magnetic flux tube emergence through the photosphere (Magara 2007).

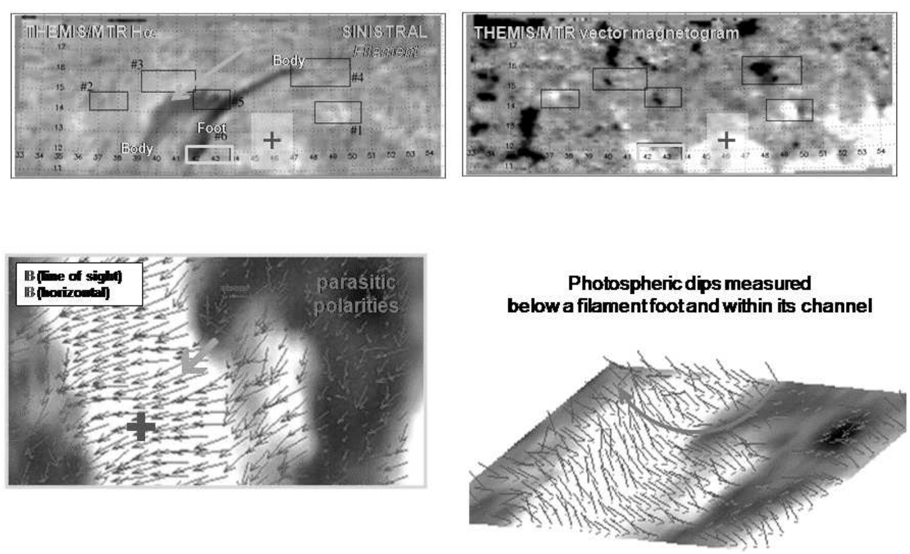

Fig. 1. First-ever dentification of a magnetic dip at the footpointof a filament foot. The vector magnetic field was measured with THEMIS/MTR and the 180° ambiguity was solved using usually observed filament chirality rules. The transverse fields which have an inverse orientation from a − toward a + polarity indicate the presence of magnetic dips above the associated inversion line. (adapted from López Ariste et al. 2006).

3 Hα/EUV observations and MHD simulations of merging/flaring filament sections

Even though a careful reader can hint from previous papers that filaments can only merge if their chirality is the same (see e.g. Malherbe 1989, Martin 1998, Rust 2001, van Ballegooijen 2004), this condition had never been tested with dedicated observational and theoretical studies until recently.

The recent multi-wavelength analyzis of three interacting filament sections F1, F2 and F3 (Fig. 2) observed during a "Joint Observing Programme" between ground-based instruments in the Canary Islands (the SVST and the MSDP on the VTT) the TRACE satellite, was the first dedicated observational study of this issue. Following their evolution over several days, it was shown that F1 and F2 gently merged into a single structure, as observed by a gradual filling in Hα of the gap R1 between both of them. This merging was associated with mild EUV brightenings and with slow Hα Dopplershifts at the merging point (Schmieder et al. 2004). While EUV brightenings are a good indicator of magnetic reconnection, the flows revealed that the merging first took place by dynamic exchanges between the two progenitors, until they formed a single long quiet filament. Two days later F2 and F3 produced a confined flare, as seen with EUV post-flare loops, as they got into contact at the point R2 (Deng et al. 2002). So as to adress the role of helicity in these two events, Schmieder et al. (2004) used the chirality laws for chromospheric fibrils and magnetic field polarity, overlaying coronal arcades and handedness of sunspots. The direction of the axial fields in the three filaments was then identified (see the arrows in the upper-middle panel of Fig. 2). It was then confirmed that when two filaments interact, magnetic reconnection takes place and leads to a merging (resp. a flare) when their helicity signs are of the same (resp. opposite) sign. It was also shown that magnetic helicity must slowly accumulate prior to filament merging, as seen by the rotation of a small twisted sunspot close to the merging point. Finally, it was suggested that magnetic reconnection first accelerates plasma between both progenitor filaments, and that it may later result in a change of topology which can sustain stable plasma all along the new filament.

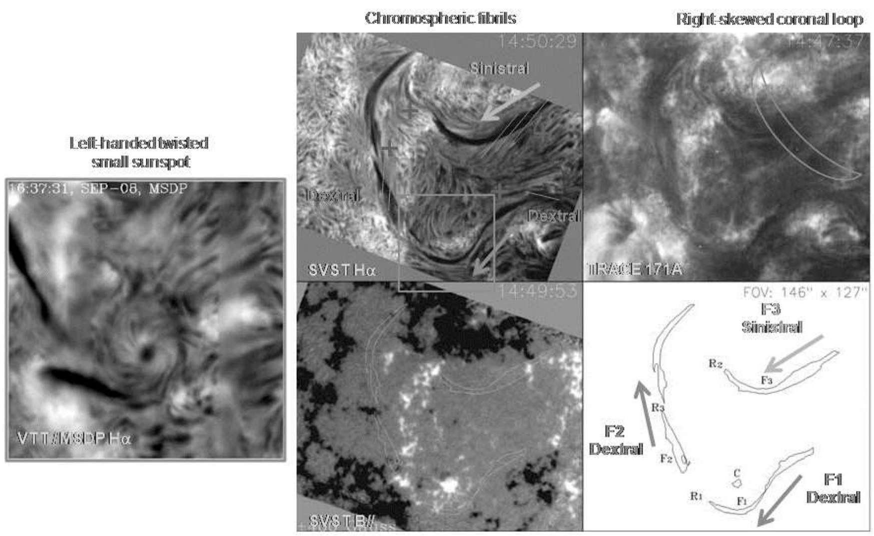

Fig. 2. Identification of the chiralities of three interacting filaments F1,2,3, using various observed features. F1 and F2 were observed to merge in the R1 area, whereas a flare took place between F2 and F3 one day later, as they interacted but did not merge (adapted from Deng et al. 2002 and Schmieder et al. 2004).

Numerical MHD simulations of the formation and interaction between pairs of solar filaments have then been conducted. Line-tied sub-Alfvénic shearing boundary motions were applied to adjacent and initially current-free magnetic dipoles. The simulations were performed in a low-β adiabatic regime, using $500\times190\times190$ mesh points in a non-uniformed grid. Four possible combinations of chiralities (identical or opposite) and axial magnetic fields (aligned or opposed) between the participating filaments were considered (DeVore et al. 2005). It was found that, when the topology of the global flux system comprising the prominences and arcades is bipolar, so that a single polarity inversion line is shared by the two structures, then identical chiralities necessarily imply identical magnetic helicity signs and aligned axial fields. In this case, finite-B slipping magnetic reconnection formed new field lines linking the two initial prominences (see Fig. 3, left). At early times, shear Alfvén waves

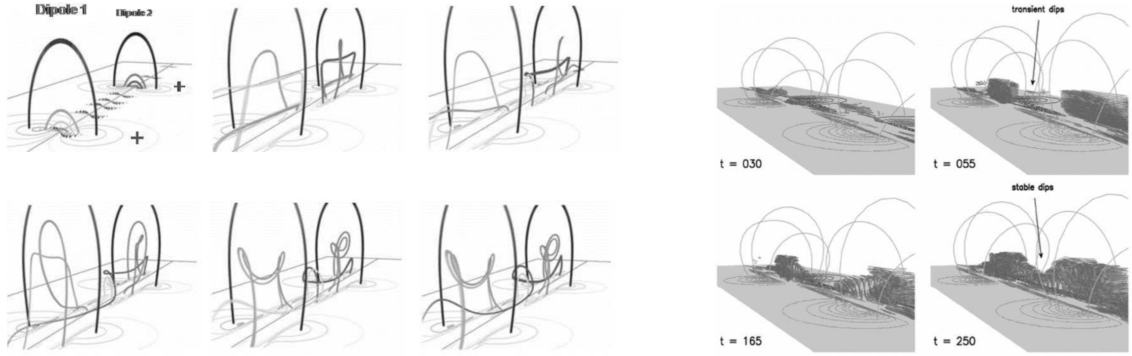

Fig. 3. 3D MHD simulation of prominence merging, resulting from finite-B magnetic reconnection between two dipoles that share a common photospheric inversion line, and whose shear result in the same magnetic helicity sign. *(Left:)* Reconnecting field lines. *(Right:)* Resulting distribution of plasma-supporting magnetic dips, simulating the prominence material (adapted from DeVore et al. 2005 and Aulanier et al. 2006).

propagated through these newly reconnected field lines, which can accelerate plasma condensations from one progenitor to another. As the shear increases, a new distribution of magnetic dips formed and increasingly filled the volume between both progenitors, so that they gradually merged into a single filament. We identified the multistep mechanism, consisting of a complex coupling between photospheric shear, slipping magnetic reconnection in the corona, and formation of quasi bald patches, that is responsible for stable filament merging through dip creation (Aulanier et al. 2006). This first model successfully reproduced the observations of filament merging by Schmieder et al. (2004). The second model, which also made use of a large-scale bipolar field, but which induced opposite helicities and axial fields between the two prominences, hardly resulted in any magnetic reconnection. The resulting lack of merging is consistent with the observations of Deng et al. (2002), although no flare reconnection occured in the model. When the topology instead is quadrupolar, so that a second polarity inversion line crossing the first lies between the prominences, then the converse relation holds between chirality and axial-field alignment. Reconnections that form new linking field lines now occur between prominences with opposite chiralities. They also occur, but only result in footpoint exchanges, between prominences with identical chiralities. These findings do not conflict with the observational rules, since the latter have yet to be derived for non-bipolar filament interactions; they provide new predictions to be tested against future observational campaigns.

References

Aulanier, G., & Démoulin, P. 1998, A&A, 329, 1125
Aulanier, G., & Schmieder, B. 2002, A&A, 386, 1106
Aulanier, G., DeVore, C.R., & Antiochos, S.K. 2006, ApJ, 646, 1349
Bobra, M., van Ballegooijen, A.A., & DeLuca, E.E. 2008, ApJ, 672, 1209
Casini, R., López Ariste, A., Tomczyk, S., & Lites, B.W. 2003, ApJ, 589, L67
Deng, Y., Schmieder, B., & Engvold, O. 2002, Sol. Phys., 209, 153
DeVore, C.R., Antiochos, S.K., & Aulanier, G. 2005, ApJ, 629, 1122
Dudik, J., Aulanier, G., Schmieder, B., Bommier, V., & Roudier, T. 2008, Sol. Phys., 248, 29
López Ariste, A., Aulanier, G., Schmieder, B., & Sainz Dalda, A. 2006, A&A, 456, 725
Lionello, R., Mikic, Z., Linker, J., & Amari, T. 2002, ApJ, 581, 718
Malherbe, J.-M. 1989, in Dynamics and Structure of Quiescent Solar Prominences, Kluwer Ac. Pub., 115
Magara, T. 2007, PASJ, 59, L51
Martin, S.F. 1998, Sol. Phys., 182, 107
Martin, S.F., Lin, Y., & Engvlod, O. 2008, Sol. Phys., 250, 31
Okamoto, T.J., Tsuneta, S., Lites, B., et al. 2008, ApJ, 673, L215
Rust, D.M., 2001, in Encyclopedia of Astronomy and Astrophysics, http://eaa.iop.org
Schmieder, B., Mein, N., Deng, Y., et al. 2004, Sol. Phys., 223, 119
van Ballegooijen, A.A. 2004, ApJ, 615, 519

SF2A 2008
C. Charbonnel, F. Combes and R. Samadi (eds)

TURBULENCE IN ANISOTROPIC HELIOSPHERIC PLASMAS

Buchlin, E.[1], Verdini, A.[2], Cargill, P.J.[3] and Velli, M.[4]

Abstract.
An alternative approach to Direct Numerical Simulations (DNS) of Magnetohydrodynamics (MHD) is presented, providing insight into the statistical properties of highly-turbulent, intermittent, anisotropic MHD turbulence: a set of shell-models coupled by Alfvén waves travelling along the axial magnetic field and which interact non-linearly, producing perpendicular fluctuations of the fields at small scales. This model can be applied to different physical situations; we present the cases of heating in solar coronal loops, and of turbulence in open coronal regions at the base of the solar wind.

1 Introduction

Because of the complexity of the nonlinear physics of MHD, and the very wide range of scales involved in MHD turbulence at the large Reynolds numbers found in space plasmas, direct numerical simulations meet strong limitations due to their computational cost: they have a low resolution (unable to describe the full range of scales) and they are very slow. For this reason, alternative approaches of numerical modelling must be sought, such as cellular automata (e.g., Lu & Hamilton 1991; see Buchlin et al. 2003 for an application to solar coronal loops) and shell-models. In shell-models (Gledzer 1973; Giuliani & Carbone 1998), the nonlinear terms of MHD are simplified by assuming local triad interactions between modes, which are scalar values for the velocity and magnetic fields in concentric shells in Fourier space. They allow to simulate MHD at high Reynolds numbers ($> 10^6$) while retaining the full dynamics of the evolution of the turbulent spectra. Using shell-models, we have developed a model of MHD turbulence that can be applied to different anisotropic plasmas, such as coronal loops and the solar wind.

2 Case of a coronal loop

In this model which is fully described in Buchlin & Velli (2007), shell-models for MHD in two dimensions are piled up along the axial magnetic field of a coronal loop. The boundary conditions are given as a velocity field imposed at the photosphere, and Alfvén waves travel along the loop. The turbulent cascade transports the energy (which is injected at large scales) towards the small scales, where it is dissipated intermittently (Fig. 1); the average power of dissipation is of the order of 10^2 to $10^3\ \mathrm{W \cdot m^{-2}}$, which is enough to heat a loop, and it is concentrated near the footpoints if the expansion of the loop with altitude is considered.

3 Case of a coronal hole and the solar wind

In order to model magnetically open regions such as coronal holes and the solar wind, several modifications of the coronal loop model have been performed: one of the boundaries is now open, the incoming waves are only produced by a reflection of the outgoing waves by Alfvén speed gradients, a wind (imposed) advects the waves, and the computing grid is non-uniform (allowing to extend the computation to 50 solar radii). We get the amplitudes of Alfvén waves, the power of heating (Fig. 2), and the spectra of turbulent fluctuations, as a function of position.

[1] Institut d'astrophysique spatiale, CNRS and Université Paris Sud, Orsay, France
[2] Royal Observatory of Belgium, Brussels, Belgium
[3] Imperial College, London, UK
[4] Jet Propulsion Laboratory, Pasadena, California, and University of Florence, Italy

4 Conclusion

These models, which provide results unattainable by direct numerical simulations, show that heating following a MHD turbulent cascade is a viable mechanism for heating coronal loops. In coronal holes, this heating could provide a contribution to the acceleration of solar wind.

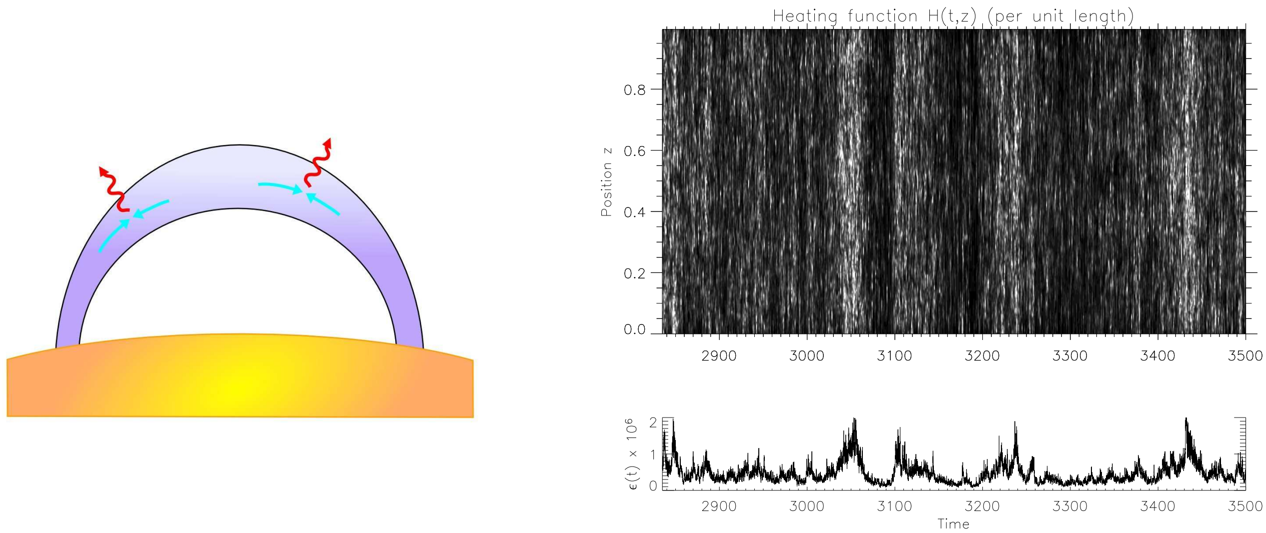

Fig. 1. Left: geometry of a coronal loop. Right: heating in a as a function of time (in seconds) and position along the loop (with the loop length of 10 Mm as unit).

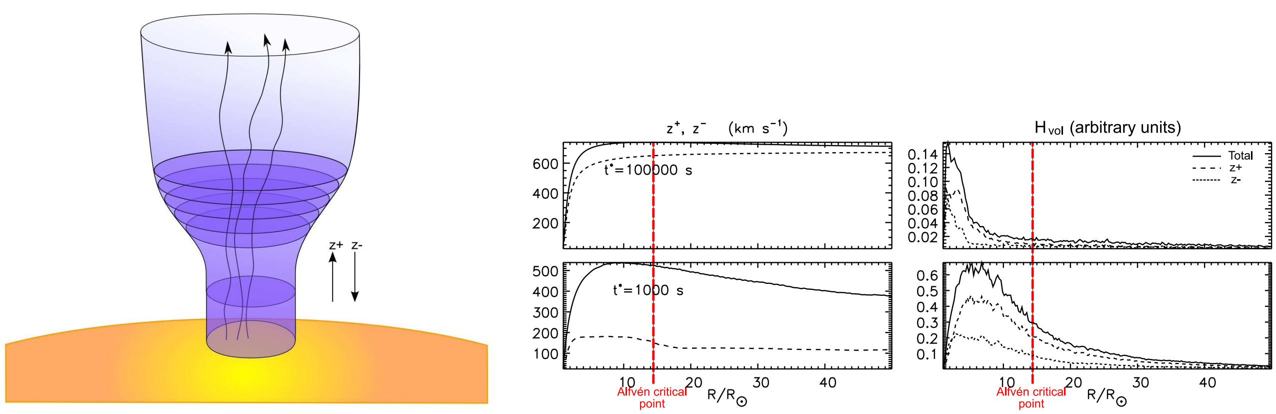

Fig. 2. Left: geometry of a coronal hole. Right: average amplitude of the waves and power of heating as a function of position.

References

Buchlin, E., Aletti, V., Galtier, S., et al. 2003, Astron. Astrophys., 406, 1061

Buchlin, E. & Velli, M. 2007, Astrophys. J., 662, 701

Giuliani, P. & Carbone, V. 1998, Europhys. Lett., 43, 527

Gledzer, E. B. 1973, Sov. Phys. Dokl., 18, 216

Lu, E. T. & Hamilton, R. J. 1991, Astrophys. J., 380, L89

SF2A 2008
C. Charbonnel, F. Combes and R. Samadi (eds)

EXTENSION OF THE KOLMOGOROV 4/5'S THEOREM TO HALL-MHD WITH AN APPLICATION TO THE SOLAR WIND

Galtier, S.[1]

Abstract. I present an extension of the Kolmogorov 4/5's theorem to 3D Hall-MHD in the case of an homogeneous and isotropic turbulence. The multi-scale law found provides a relevant tool to investigate the non-linear nature of the high frequency magnetic field fluctuations in the solar wind or, more generally, in any plasma where the Hall effect is important.

1 Introduction

Turbulence remains one of the last great unsolved problem in classical physics which has evaded physical understanding and systematic description for many decades. For that reason, any exact results appear almost as a miracle. In his third 1941 turbulence paper, Kolmogorov found that an exact and nontrivial relation may be derived from Navier-Stokes equations – which can be seen as the archetype equations for describing turbulence – for the third-order longitudinal structure function (Kolmogorov, 1941). Because of the rarity of such results, the Kolmogorov's four-fifths law is considered as one of the most important results in turbulence (Frisch, 1995).

Very few extensions of such a result to other fluids have been made; it concerns scalar passively advected, such as the temperature or a pollutant in the atmosphere, and astrophysical magnetized fluid described in the framework of MHD (Chandrasekhar, 1951; Politano & Pouquet, 1998). The addition in the analysis of the magnetic field and its coupling with the velocity field renders the problem more difficult and, in practice, we are dealing with a couple of equations. In this paper, I present the extension of the Kolmogorov 4/5's theorem to 3D Hall-MHD (Galtier, 2008).

2 Hall MHD equations

We start our analysis with the following 3D incompressible Hall MHD equations

$$(\partial_t + \mathbf{v} \cdot \nabla)\mathbf{v} = -\nabla P_* + \mathbf{b} \cdot \nabla \, \mathbf{b} + \nu \Delta \mathbf{v} \,, \tag{2.1}$$

$$(\partial_t + \mathbf{v} \cdot \nabla)\mathbf{b} = \mathbf{b} \cdot \nabla \, \mathbf{v} - d_I \nabla \times [\mathbf{J} \times \mathbf{b}] + \eta \Delta \mathbf{b}, \tag{2.2}$$

with $\nabla \cdot \mathbf{v} = 0$, $\nabla \cdot \mathbf{b} = 0$. The magnetic field $\mathbf{b}$ is normalized to a velocity ($\mathbf{b} \to \sqrt{\mu_0 n m_i}\, \mathbf{b}$, with m_i the ion mass and n the electron density), $\mathbf{v}$ is the plasma flow velocity, P_* is the total (magnetic plus kinetic) pressure, ν is the viscosity, η is the magnetic diffusivity and d_I is the ion inertial length ($d_I = c/\omega_{pi}$, where c is the speed of light and ω_{pi} is the ion plasma frequency); $\mathbf{J} = \nabla \times \mathbf{b}$ is the normalized current density.

3 Result

The extension of the Kolmogorov 4/5's theorem to 3D Hall-MHD is (Galtier, 2008):

$$-\frac{4}{3}\varepsilon^T r = B^{vvv}_{\|ii} + B^{vbb}_{\|ii} - 2B^{bvb}_{\|ii} + 4d_I \langle [(\mathbf{J} \times \mathbf{b}) \times \mathbf{b}']_\| \rangle \,,$$

[1] Institut d'Astrophysique Spatiale, Bât. 121, Université Paris-Sud XI, 91405 Orsay, France; Institut Universitaire de France

where ε^T is the mean (total) energy dissipation rate per unit mass, $B_{ijk}^{\alpha\beta\gamma} = \langle(\alpha'_i - \alpha_i)(\beta'_j - \beta_j)(\gamma'_k - \gamma_k)\rangle$ is the third-order structure function combining the (i,j,k) components of the vector fields α, β and γ measured at two different points (M and M') separated by a distance $\mathbf{r}$ which defines the parallel direction. Note the use of the Einstein's notation.

To find this exact result, we assume homogeneity and isotropy (Batchelor, 1953). Furthemore, we consider the long time limit for which a stationary state is reached with a finite ε^T; we take the infinite (magnetic) Reynolds number limit ($\nu \to 0$ and $\eta \to 0$) for which the mean energy dissipation rate per unit mass tends to a finite positive limit. This result is thus valid at first order in the inertial range.

4 Discussion

The most remarkable aspect of this exact law is that it does not only provide a linear scaling for the third-order correlation tensors within the inertial range of length scales, but it also fixes the value of the numerical factor appearing in front of the scaling relations. Another important remark is about the fields used to build the third-order correlation tensors. Indeed, the convenient variables are not only the velocity and magnetic field components but also the current density components.

The exact result presented here provides a better theoretical understanding of Hall MHD flows. It shows that the scaling relation does not change its power dependence in the separation r at small-scales if the statistical correlation tensor used is modified. The interesting point to note is the compatibility with previous heuristic and numerical results (Biskamp et al., 1996). Indeed, a simple dimensional analysis gives the relations $r \sim b^3$ for large-scales, and $r^2 \sim b^3$ for small-scales (since $J \sim b/r$), which give respectively the magnetic energy spectrum $E \sim k^{-5/3}$ and $E \sim k^{-7/3}$. Therefore and contrary to the appearance, the exact result found may provide a double scaling relation.

These multi-scale law provides a relevant tool to investigate the non-linear nature of the high frequency magnetic field fluctuations in the solar wind whose (dissipative *vs* dispersive) origin is still controversial (Goldstein et al., 1994; Galtier, 2006). The use of multi-point data may give information about both the magnetic field and the current density which can be used to check the theoretical scaling relations. The observation of such a scaling law would be an additional evidence for the presence of a dispersive inertial range and therefore for the turbulent nature of the high frequency magnetic field fluctuations. The recent observation of the Yaglom MHD scaling law (Sorriso-Valvo et al., 2007) at low frequency provides a direct evidence for the presence of an inertial energy cascade in the solar wind. The theoretical results given here allows now to extend this type of analysis to the high frequency magnetic field fluctuations and, more generally speaking, to better understand the role of the Hall effect in astrophysics.

Aknowledgments

This work was supported by the ANR project no. 06-BLAN-0363-01 “HiSpeedPIV”.

References

Batchelor, G.K. 1953, The theory of homogeneous turbulence, Cambridge Univ. Press

Biskamp, D., Schwarz, E., & Drake, J.F., 1996, Phys. Rev. Lett., 76, 1264

Chandrasekhar, S., 1951, Proc. Roy. Soc. A, 204, 435

Frisch, U. 1995, Turbulence: the legacy of A.N. Kolmogorov, Cambridge Univ. Press

Galtier, S., 2006, J. Low Temp. Phys., 145, 59

Galtier, S., 2008, Phys. Rev. E, 77, 015302(R)

Goldstein, M.L., Roberts, D.A., & Fitch, C.A., 1994, J. Geophys. Res., 99, 11519

Kolmogorov, A.N., 1941, Dokl. Akad. Nauk SSSR, 32, 16

Politano, H., & Pouquet, A., 1998, Phys. Rev. E, 57, R21

Sorriso-Valvo, L., Marino, R., Carbone, V., Noullez, A., Lepreti, L., Veltri, P., Bruno, R., Bavassano, B., & Pietropaolo, E., 2007, Phys. Rev. Lett., 99, 115001

SF2A 2008
C. Charbonnel, F. Combes and R. Samadi (eds)

ULYSSES MISSION: THE END OF AN ODYSSEY

Issautier, K.[1], Hoang, S.[1], Le Chat, G.[1], Meyer-Vernet, N.[1] and Moncuquet, M.[1]

Abstract. After almost 18 years in space, the Ulysses mission explored the entire heliophere out-of-the ecliptic plane over the solar activity cycle. The end of this unique mission is planned before the end of December 2008 due to the decline in power produced by its on-board generators. We enlighten some major impacts of the scientific results of the mission to the heliospheric community.

1 Introduction

The Ulysses mission is a cooperative programme between ESA and NASA, launched on 6 October 1990. The goal of the mission was to study in four dimensions (space and time) the heliosphere, the magnetic bubble created by the solar wind, which carries the solar magnetic field well beyond the outer reaches of the solar system. Ulysses was also designed to study the solar wind, a constant stream of charged particles expelled by the Sun at a speed up to 800 km/s. Ulysses provided the first-ever map of the heliosphere from equator to the poles thanks to its special out-of-ecliptic orbit over the Sun. Ulysses is in a six-year orbit around the Sun. Its long path through space carries it out of Jupiter's orbit and back again. Ulysses explored the uncharted high latitude regions of the heliosphere from 80^o south to 80^o north, within 5 AU of the Sun over a wide range of solar activities. About the orbit of Ulysses over the Sun, the most interesting periods are the fast latitudinal scans from 80^o S to 80^o N, lasting ten months, and occuring near solar minimum of activity in 1994-1995 and near solar maximum in 2001. Since February 2007 Ulysses undertook a third pole-to-pole fast transit near the minimum of cycle 23 when the solar magnetic dipole reversed with respect to the previous minimum (Smith et al., 2003). The spacecraft carried 10 instruments to diagnosing the heliosphere through the solar activity. French space laboratories, mainly supported by CNES, were fully associated to some of the main discoveries so far. Ulysses, which is studied the Sun and its effect on the surrounding space for almost four times its expected lifespan, will ceased to function because of the decline in power. We highlight below some major impacts on the heliospheric physics.

2 Legacy of Ulysses

Ulysses was the first mission to survey the environment in space above and below the poles of the Sun in the four dimensions of space and time. It showed that the sun's magnetic field is carried into the solar system in a more complicated manner than previously believed. Particles expelled by the sun from low latitudes can climb up to high latitudes and vice versa, even unexpectedly finding the way down to planets. Before Ulysses, the magnetic field was though to follows generally an archimedean spiral at all latitudes. Ulysses revealed it is more complex. It spreads in latitude much more than was though (Fisk et al. 1996). Ulysses fast latitude scans reveals that the radial field does not vary with latitude. The magnetic field is also more simple since it simply rotates to 180^o to achieve the polarity reversal. Indeed, the Sun does not emit solar wind steadily, but the emission varies through a cycle of magnetic activity lasting approximately 11 years. The cycle culminates in the reversal of the direction of the Sun's magnetic field. Ulysses saw that on a large scale, the complexity of the magnetic field near the solar surface simplifies into a field created by a bar magnet inside the Sun. When the solar activity is at minimum, this bar magnet is aligned with the rotation poles. Six years later, at maximum, the bar magnet has moved to lie at 90^o to the rotation poles. It then continues moving so that by the time of

[1] Observatoire de Paris, LESIA, CNRS UMR 8109, Université Paris Diderot, UPMC, 92195 Meudon, France

the next minimum, it is aligned with the rotational pole again, but in the opposite orientation (Smith et al., 2003).

The fast solar wind is coming from polar coronal holes of the Sun, and is blowing at 800 km/s. This kind of wind was sporadically observed in the ecliptic plane before the Ulysses mission in contrast to the slow wind, of 400 km/s, predominantly present. Thanks to Ulysses unique trajectory, it was shown on the opposite that the fast wind is the common wind, present all over the solar cycle, "disappearing" at solar maximum when coronal holes are not anymore present on the solar surface. Ulysses thus demonstrated the bimodal nature of the wind: it discovered that a steady fast wind is present throughout most of the solar cycle. The average speed at high latitudes is 750 km/s at all phases. The slow wind emerges on another hand from the sun's equatorial zone.The transition from slow to fast wind is showed to be relatively abrupt (see review of Neugebauer, 2001)

Energetic particles were studies in great detail near equator in the past. Could particles accelerated at low latitudes near the sun or in interplanetary space reach high latitudes? At solar minimum, although acceleration sites are restricted to low latitudes, energetic electrons and ions can reach into the polar caps. At solar maximum, particles are present at all latitudes and are confined to the inner heliosphere in reservoirs from which they slowly escape. Energetic particles are present at all phases of the solar cycle, also at quiet times. Their fast transport to high latitude has revealed large scale restructuring of the coronal magnetic field, during solar events (Pick et al., 1995). Acceleration mechanism that operates is still under question.

Ulysses detected and studied dust flowing into our solar system from deep space and showed that it was 30 times more abundant than astronomers suspected. Ulysses also detected heavy atomic nuclei racing into the solar system. Known as cosmic rays, these are thought to have been accelerated by the explosion of high-mass stars. Ulysses estimated that the average of a cosmic ray entering the solar system is 10-20 million years and they have spent their lives streaming through the galaxy's outer regions before finding their way into the solar system. Galactic cosmic rays observed near the equator before Ulysses were known to be affected by changes in solar activity. At both minimum and maximum, the distribution of cosmic rays is essentially spherically symmetric: the flux is the same at the equator and in the polar regions. Do they have easy access to polar regions of the heliosphere where the magnetic field is radial and weak? They don't because their access is opposed by large-amplitude waves on the magnetic field in the fast wind from the poles (Heber & Potgieter, 2008) .

During Ulysses pole-to-pole exploration around the Sun, the Unified Radio And Plasma (URAP) instrument acquired in routine the electron density and temperature versus the heliolatitude using the QTN method. It is based on in situ measurement of the electric field using wire antennas connected to a sensitive receiver. The QTN method has been successfully applied to various environments encountered by Ulysses. For specific plasma conditions, the radio technique is the only way to measure the density. The QTN method on Ulysses gave in routine the electron density and temperature of the solar wind, and produced unique measurements of the Io plasma torus aboard Ulysses, which led to a new understanding of the Io torus structure and stability. Because of its reliability and accuracy, this technique is also used to calibrate and crosscheck other plasmas sensors (Issautier et al., 2001; Maksimovic et al., 1995; Zouganelis, 2008). The accurate electron diagnostics give the unique opportunity to understand the 3D structure of the solar wind over a full solar cycle. Especially, for the first time the radial profiles of the electron density and temperature in the steady state fast solar wind were obtained with accuracy during both solar minimum (in 1994-95 and in 2007) and maximum (2001) (Issautier et al., 1998; Maksimovic et al., 2000; Issautier et al., 2004; Issautier et al., 2008). A north/south asymmetry was found and studied over the full solar cycle (Issautier et al., 2003), thus extending our understanding of the origin of the fast solar wind and its properties (Meyer-Vernet & Issautier, 1998; Zouganelis et al., 2004; Maksimovic et al., 2005)

As a beautiful by-product from the URAP experiment, a result regarding the plasma populating the inner magnetosphere of Jupiter, known as the Io plasma torus (IPT), was obtained by the Ulysses radio spectra acquired in 1992. In contrast to the Voyager 1 or Galileo spacecraft, Ulysses passed through the IPT on a north-to-south trajectory (of course because of Ulysses' primal aim of going out of the Ecliptic) and nearly tangentially to a magnetic shell ($L \cong 8\ R_J$), which allowed us, for the first time, the determination of the electron density and temperature along the magnetic field (Meyer-Vernet et al., 1993; Moncuquet et al, 1995). The principal and most unexpected result was that the electron temperature increased substantially with magnetic latitude (doubling over 7^o of latitude) and was anticorrelated with the electron density, obeying a polytropic law $T \propto n^{\gamma-1}$, with an index γ of 0.48 (Meyer-Vernet et al., 1995). The need for a new plasma torus model, especially its latitudinal structure, was driven by this result (Moncuquet et al., 2002; and references therein).

In radioastronomy, combined observations derived from the HISCALE, URAP instruments, VIIM and FCM magnetometers and Nançay radio heliograph, discovered the existence of magnetic channels, anchored in active regions of the sun corona, which can survive over very large distances in the interplanetary medium, beyond 4 AU. Triggered by these beams, Langmuir waves were observed in these channels, being sources of solar Type III bursts (Buttighoffer et al., 1995). In addition, radio observations combined with the Artemis radio spectrograph provided for the first time measurements of their directivity. Ulysses also allowed tracking type II bursts over long distances, a day before the shock hits the spacecraft, and unambiguously identifies the source region of electrons, upstream of the shock. Finally, the URAP receivers monitored the Saturn kilometric radiations, which are used to derive the rotation period of the planet. Observations have shown a striking difference in this rotation, up to 1% from Voyager (Galopeau & Lecacheux, 2000). This problem is now extensively studied from Cassini observations around Saturn.

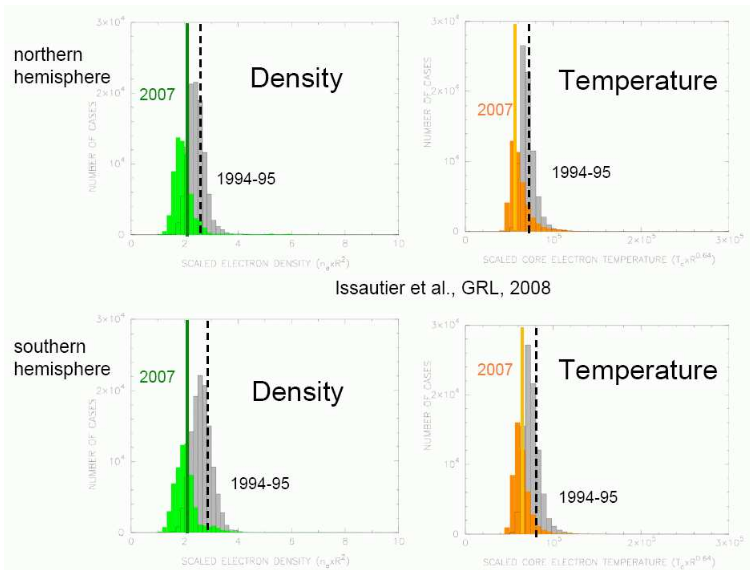

Fig. 1. Histograms of the electron density and temperature measured in 2007 and 1994-95 during Ulysses fast polar pass at high latitudes for northern and southern hemispheres. Adapted from Issautier et al., 2008.

3 Latest solar wind results from Ulysses' third orbit

In 2007, Ulysses undertook its third polar pass over the Sun. The fast solar wind coming from polar coronal regions on the Sun surface is now not so dense, not so hot compared to measurements previously obtained near solar minimum in 1994-95 during Ulysses first orbit, a solar cycle ago.

Electron properties of this fast wind have been investigated using the onboard URAP radio experiment. We observe a significant drop of 20 % of the electron density as well as a drop of 13% of the electron temperature of the solar wind (Issautier et al., 2008). During that period, the solar wind is still blowing fast at 750 km/s. Fig. 1 illustrates these results. It shows histograms of the electron density and temperature respectively of the fast solar wind. We compared theses numbers for both solar hemispheres (north and south) during Ulysses fast polar scans near minimum of activity in 1994-95 and 2007. Vertical lines represent averaged values showing the drop on each hemisphere.

These results are based on wave measurements using electric antennas and a sensitive receiver. It gives an accurate plasmas diagnostics of a few percent. It is important to point out that the weaker solar wind observed in 2007 is also confirmed by other plasmas properties as discussed by McComas et al. (2008) and Smith et al. (2008) from other instruments on Ulysses, thus avoiding any instrumental effects due to the aging of Ulysses and its 18 years in space.

The fast solar wind is significantly less dense and cooler suggesting the present solar cycle minimum is unusual. Indeed, sunspots number is dramatically low during this minimum. However, the structure of the magnetic configuration of the Sun's corona does not show a classical minimum structure: During the third Ulysses polar pass at high latitudes, polar coronal holes are not as well developed as in 1994-95. One more thing to note is that as seen for example on STEREO coronal images, a mid-latitude coronal hole is present at the surface of the Sun, which is unusual during this stage of the cycle. These results call in question our knowledge on the solar cycle and enlighten that the variations observed in the solar wind properties might be related to the 22-year solar cycle or longer periods, due to fluctuations of the solar dynamo.

4 The end of Ulysses

Ulysses uses a small Radioisotope Thermoelectric Generator (RTG). The amount of power available gradually decreases with time. Since 2002, due to lack of power, not all of the instruments and systems could remain switched on. Thus, they were alternatingly switched off. But one has to be careful not to switch anything off for too long to avoid creating cold spots within the spacecraft body, otherwise its thruster fuel will freeze when it reaches the critical level of temperature of 2^o C . Once this appends, as it inevitably will, there is no way to control the spacecraft.

Last year, the power drop became too serious. Ulysses no longer has enough power to run all of its communications, heating and scientific equipment simultaneously. It was thus decided to test a new power-saving strategy: the main transmitter was switching off for a while. Unfortunately, it was impossible to switch it on again and it has left in addition a cold spot critically near a fuel line. This has a consequence of reducing the data transmission rate, and using a less powerful transmitter on board and large ground antennas (70 m) on Earth. Now Ulysses is slowly cooling as it is going away from the Sun. Once the temperature falls below 2^o C, its hydrazine fuel will freeze, and it will be impossible to manoeuvre because it will be impossible to point the high gain antenna towards Earth. Ulysses will however continue unrelentingly its journey around the Sun.

Be that as it may, the rich treasure of unprecedented observations will keep the mission alive long after the actual spacecraft has died.

References

Buttighoffer, A. et al., 1995, J. Geophys. Res., 100, 3369
Fisk, J., 1996, J. Geophys. Res., 101, 15547
Heber, B. & M.S.Potgieter, 2008, Galactic and anomalius cosmic rays through the solar cycle: new insights from Ulysses, *The heliosphere through the solar activity cycle, Springer-Praxis books in Astrophysics and astronomy*, ed. A. Balogh, L. Lanzerotti, S. Suess, pp. 195-250
Galopeau P. and A. Lecacheux., 2000, J. Geophys. Res, 105, 13089
Issautier, K. et al., 1998, J. Geophys. Res., 103, 1969
Issautier, K. et al., 2001, J. Geophys. Res., 106, 15, 665
Issautier, K. et al., 2003, AIP, 679,59
Issautier, K. et al., 2004, Sol. Phys., 221, 351
Issautier, K., et al., 2008, Geophys. Res. Lett., 35, L19101, doi:10.1029/2008GL034912
Maksimovic, M. et al., 1995, J. Geophys. Res., 100, 19, 881
Maksimovic, M. et al., 2000, J. Geophys. Res. 105, 18337
Maksimovic, M. et al., 2005, J. Geohys. Res., 110, A09104, doi:1029/2005JA011119
Meyer-Vernet, N. & K. Issautier, 1998, J. Geophys. Res., 103, 29,705-29,718
McComas, D.J., et al., 2008, Geophys. Res. Lett., 35, L18103, doi:10.1029/2008GL034896
Meyer-Vernet, N. et al., 1993, J. Geophys. Res., 98, 21163
Moncuquet, M. N. Meyer-Vernet, S. Hoang, 1995, J. Geophys. Res., 100, 21697
Moncuquet, M., F. Bagenal, and N. Meyer-Vernet, 2002, J. Geophys. Res., 107(A9),1260, doi:10.1029/2001JA900124
Neugebauer, M., 2001, The solar wind and heliospheric magnetic field in three dimensions, *The heliosphere near solar minimum: the Ulysses perspective, Springer-Praxis books in Astrophysics and astronomy*, ed. A. Balogh, R. Marsden & E.J. Smith, pp. 43-99
Pick, M. et al., 1995, Geophys. Res. Let., 23, 3377
Smith, E.J. & A. Balogh, 2008, Geophys. Res. Lett., in press.
Zouganelis, I. et al., 2004, Astrophys. J., 606, 542-554
Zouganelis, I. 2008, J. Geophys. Res., 113, doi:10.1029/2007JA012979

SF2A 2008
C. Charbonnel, F. Combes and R. Samadi (eds)

MAGNETIC RECONNECTION AND PARTICLE ACCELERATION INITIATED BY FLUX EMERGENCE

Masson, S.[1], Aulanier, G.[1], Pariat, E.[2,3,4], Klein, K.-L.[1] and Schrijver, C. J.[5]

Abstract. So as to perform an MHD simulation of the evolution of the corona driven by the evolution of the photosphere, a key aspect is the definition of the boundary conditions for reaching a good compromise between physical conditions and numerical constraints. In this work, we focused on the simulation of a confined flare observed on Nov 16, 2002. As initial configuration, we considered a uniform temperature corona, with a magnetic field resulting from a 3D potential field extrapolation from a SOHO/MDI magnetogram. We prescribed a velocity field at the photospheric boundary of the domain, so as to mimic the observed flow pattern associated to a flux emergence. This resulted in a combination of "slipping reconnection" in a halo of QSLs surrounding a 3D null point, through which a "fan reconnection" regime took place. This simplified approach of flux emergence has successfully reproduced the main characteristics of the observed flare: the flare ribbons observed in the EUV with TRACE being due to the chromospheric impact of particles accelerated along reconnecting field lines, this bimodal regime could explain both the shapes and dynamics of these ribbons. We foresee that this kind of modeling should be able to simulate the evolution of slipping magnetic flux tubes in open configurations, allowing to predict the spatio-temporal evolution of particle beams injected into the heliosphere.

1 Introduction

The emergence of magnetic flux at the photospheric level is partly responsible of the solar activity. Indeed, this process injects magnetic flux and energy in active regions, and it can eventually destabilize the magnetic configuration, resulting in the acceleration of energetic particles through magnetic reconnection. Modeling this process can be done in the framework of MHD. But the photosphere-chromosphere layer displays strong gradients in temperature and density, which involve sharp numerical gradients during any MHD simulation. So the treatement of flux emergence at this interface is not easy to perform, especially when dealing with complex overlaying coronal fields. Coronal simulations, however, in which one simply introduces boundary conditions to reproduce the flux emergence at the photosphere, can be used to simulate the temporal evolution of observed active regions. Here we present the results of a such 3D MHD simulation, directly applied to the interpretation of a solar flare which was driven by flux emergence.

2 Magnetic flux emergence, flare ribbons and coronal magnetic field of the C-class flare

We study a C-class flare which occured in AR 10191 on Nov 16, 2002. In order to understand its magnetic context, we used SOHO/MDI line-of-sight magnetograms. Figure 1 shows that this region was formed by a negative leading-sunspot, and a positive trailing-sunspot. Within the trailing region, a nearly circular area of negative polarity is enclosed within the dominant positive flux. The flux of this enclosed polarity increased during three days preceding the flare. Between Nov 15 at 12:30 UT and Nov 16 at 06:27 UT, an important flux emergence also occurred in the central region of the AR, between the main polarities (Figure 1, right column).

[1] LESIA, Observatoire de Paris, CNRS, UPMC, Université Denis Diderot, 5 place Jules Janssen, 92190 Meudon Cedex
[2] Space Weather Laboratory, NASA Goddard Space Flight Center Greenbelt, MD 20771, USA
[3] Space Science Division, Naval Research Laboratory, Washington, DC 20375, USA
[4] CEOSR, George Mason University, Fairfax, VA 22030, USA
[5] Lockheed Martin Solar and Astrophysics Laboratory, 3251 Hanover Street, Palo Alto, CA 93304-1191, USA

The evolution of the magnetic field essentially produced a diverging migration of opposite polarities, as well as the formation of small bipolar fields, typical of emerging flux events. Since this emergence occured prior to the flare, one can state that it probably triggered it, according to the standard 2D model (Heyvaerts et al. 1977).

The ribbons of this C-class flare were observed with the TRACE spacecraft in the 1600 Å EUV continuum. Their brigthenings are known to be partly produced by the impact in the chromosphere of accelerated particles, travelling along magnetic field lines and originating from the region where they reconnect in the corona (e.g. Mandrini et al. 1991). In the left-bottom panel of Figure 1, the three ribbons of the flare are overlaid upon a co-aligned MDI magnetogram. A circular-ellipsoidal ribbon RC enclosed an elongated ribbon RA, while another elongated ribbon (RB) was located outside of the circular ribbon RC. During the temporal evolution of the flare, these ribbons were progressively formed throughout the extension of the brightenings, which eventually formed a final circular and elongated shape.

The presence of an ellipsoidal ribbon may be a good indicator of the presence of a null point. But only a topological study, using an extrapolation of the magnetic field above the photosphere, could confirm or infirm the existence of such a 3D null point. To perform the extrapolation, as bottom boundary conditions, we used the MDI magnetogram taken on Nov 16 at 06h27 UT, a few hours before the flare took place. We calculated a potential magnetic field (Alissandrakis 1981), since it allowed to obtain a reference field with no free magnetic energy to start with, and preserving the correct magnetic topology. The extrapolation confirmed that a 3D null point was present. It was then shown that it divides the coronal domain in two connectivity domains, separated by a so-called “fan” surface enclosing the included negative polarity. In each domain, a singular spine field line which passes through the null point is also present (see e.g. the Fig. 1 of Pariat et al. 2008). Comparing the positions of the ribbon RC and the magnetic topology, we found that RC is almost perfectly co-spatial with the intersection of the fan surface with the photosphere: they both assumed exactly the same circular-like shape. This perfectly agrees with the flare models which stipulate that ribbons are to be found at the footpoints of the separatrices (e.g. Priest & Forbes 2002). By extension, the ribbons RA and RB respectively correspond to the inner and the outer spines. A key issue is that they are not point-like, as one would assume from the fact that the spine is a single field line.

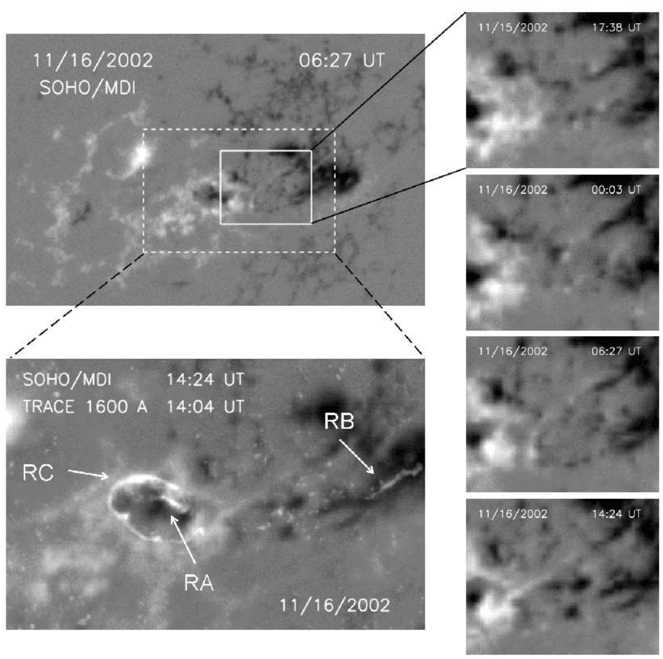

Fig. 1. SoHO/MDI observations of the evolution of AR 10191, begining 24 hours prior to the flare. Flux emergence is manifested in the white rectangle (right column). The left bottom panel shows the flare ribbon observed by TRACE at 1600 Åcoaligned and overlaid upon the photospheric magnetic field.

3 3D MHD simulation of slipping and fan reconnection & interpratation of the EUV ribbons

To perform an MHD simulation, we used a 3D visco-resistive code which has been developed by Aulanier et al. (2005). This code solves the MHD equations in a cartesian box with a fixed but non-uniform mesh. At the top and side boundaries of the domain, we assumed open conditions. At the bottom boundary, in order to account for the photospheric driving of the corona, we assume line-tied reflective and kinematic conditions. So as to reproduce as reliably as possible the observed evolution of the AR and the flare, we used the output of the potential field extrapolation as an initial condition for the magnetic field. Initially, an uniform density $\rho_{min} = b^2_{max}/\mu\ c^2_{A,max} \simeq 5.10^{12}$ cm^{-3} was prescribed, and we fixed $c_{A,max} = 1000$ km.s^{-1} as the initial maximum the Alfvén speed. The initial temperature was set to be uniform $T = 3.10^5$ K, so that the initial pressure allowed $\beta << 1$ everywhere in the domain but close to the null point. The resulting averaged value of $\beta \simeq 10^{-2}$, while $\beta \geq 1$ only within a radius of 1 Mm around the null point. In order to simulate the evolution of the active region, we devised a new method for modeling the observed flux emergence and its coronal consequence in a complex magnetic environment by prescribing a simple analytical diverging velocity field at the bottom boundary (for more details, see Masson et al. 2009). This velocity field was built so as to respect the shape of the emergence region and the velocity ratios and orientations of the flows in this area. But it did not result in the increase of magnetic flux.

Firstly, a thin current sheet developed around the null point, associated with a tearing of the spine, which both induced a fan reconnection regime (according to the terminology of Priest & Titov 1996). Figure 2 shows two snapshots of the reconnecting field lines above the included negative polarity. It appears there clearly that the field lines reconnect at the null point. But before they reconnected at the null point, we found that field lines slipped along the photosphere toward the inner spine, with increasing speed, along a current sheet located inside the included polarity, different from that of the null point. After field lines jumped to the outer spine, they also slipped away from it, with decreasing speed. We found that observed chromospheric ribbons RA and RB did match with the trajectories of the footpoints of these slipping field lines. Also, the temporal evolution of reconnection was consistent with the propagation of brightenings of the ellipsoidal ribbon RC. More details will be given in Masson et al. (2009).

The slipping motion of the field lines before and after the null point reconnection can be explained by the presence of a halo of so-called "Quasi-Separatrix Layers" (QSLs) which surrounds the separatrices, a property that has never been reported before. The presence of QSLs induces slipping and slip-running reconnection (Aulanier et al. 2006) : when field lines reconnect at QSLs, there is not a jump of connectivity, but rather a continuous reconnection pattern along the QSL footprints (Démoulin et al. 1997). This explains why we obtained a slow sub-Alfvénic slipping reconnection regime away from the spine, and a fast super -Alfvénic slip-running reconnection regime close to the spine. Classicaly,at the null, the field lines jump from one place to another. This bimodal regime naturally explains why the spine-associated flare ribbons are sheet-like instead of point-like.

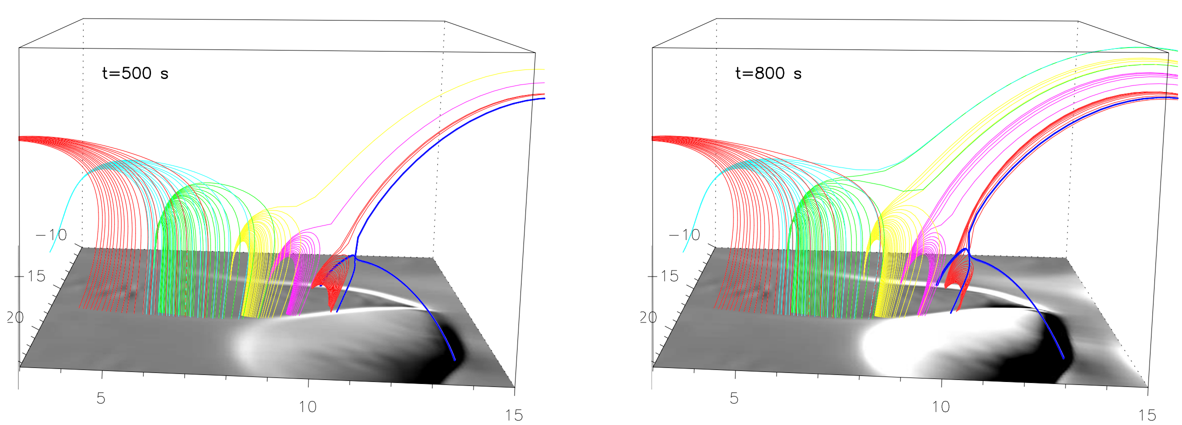

Fig. 2. Evolution of reconnecting magnetic field lines around the null point. The grey scale color coding the electric current density $j_z(z=0)$. Left panel at t=500s s and right panel at t=800 s

4 Extension to open field configurations and SEP beams

The flare-accelerated particles detected at the Earth, are generally coming from active regions that are well-connected to the Interplanetary Magnetic Field (IMF) tube reaching the Earth. Nevertheless, Klein et al. (2008), showed recently that flare-accelerated particles can be detected even if the active region is far from the interplanetary flux tube connecting the Earth, i.e. behind the limb or near the center of the solar disk. They have shown indeed that the open flux tube rooted in the active region can strongly expand in the corona. This magnetic configuration is such that some magnetic field lines of this open flux tube can be connected to the IMF connecting the Earth.

Traditionnaly, if one considers that the reconnection sites are very localized in the active region, and that according to null point reconnection theory, the accelerated particles should mostly propagate along the open outer spine (a single field line). It seems then difficult for flare-accelerated particles to be injected in the part of the extended flux tube connected to the Interplanetary flux tube reaching the Earth. But with the results of the present study, if one considers a magnetic configuration where a null point is included in an halo of QSLs, with an outer spine opened in the corona, one could argue that a slipping motion of the reconnected field lines may take place, exactly like in our closed field configuration of the C-class flare. This type of reconnection regime could successively inject particles in a more or less wide bundle of field lines around the open spine, much like a whip rooted in the low corona swinging in the heliosphere. These effects may explain the injection of particles along the IMF field line connected to earth, even though the latter was not connected to the reconnection point early on. It could also allow particles to be injected in interplanetary flux tubes of different topologies at different times while they slip, thus leading to complex spatio-temporal patterns for particles detected at 1 AU. In the future we plan to conduct this type of analysis, coupling MHD simulations, radio and in-situ observations of particle beams.

5 Conclusion

The analytical diverging velocity field obtained from MDI observations was used as an input in the initial conditions of our MHD simulation. Although this velocity field did not include the increase the magnetic flux, it did reproduce the observed photospheric flows and it allowed for magnetic energy to be stored quasi-statically in the corona. We found a good agreement between the temporal evolution of the magnetic field lines obtained by the simulation and the evolution of the flare ribbons observed by TRACE. Using observational data as initial conditions, our simulation therefore allowed us to interpret the dynamical evolution and the physics of the flare. Our findings, implying the existence of slipping field lines before and after null point reconnection, offer new perspectives for the study of the injection of accelerated particles in the IMF.

References

Alissandrakis, C. E., 1981, A&A, 100, 197
Aulanier, G., Démoulin, P., Grappin, R., 2005, A&A, 430, 1067
Aulanier, G., Pariat E., Démoulin, P., DeVore, C. R., 2006, Sol. Phys., 238, 347
Démoulin, P., Bagala, L. G., Mandrini, C. H., Hénoux, M. G., 1997, A&A, 325,305
Heyvaerts, J., Priest, E. R., Rust, D. M., 1977, ApJ, 216, 123
Klein K.-L., Krucker, S., Lointier, G., Kerdraon, A., 2008, A&A, 486, 589
Mandrini, C. H., Demoulin, P., Henoux, J. C., Machado, M. E., 1991, A&A, 250,541
Masson S., Pariat E., Aulanier G., Schrijver C. J., 2009, ApJ, in preparation
Pariat, E., Antiochos, S. K., DeVore, R. C., 2008, ApJ, in press
Priest,E. R., Titov, V. S., 1996, ApJ, 472, 840
Priest, E. R., Forbes, T. G., 2002, A&A Rev, 10, 313

SF2A 2008
C. Charbonnel, F. Combes and R. Samadi (eds)

THE MAGNETIC FIELD OF SOLAR PROMINENCES.

Paletou, F.[1]

Abstract. In his famous monographs, Einar Tandberg-Hanssen writes that "the single, physically most important parameter to study in prominences may be the magnetic field. Shapes, motions, and in fact the very existence of prominences depend on the nature of the magnetic field threading the prominence plasma". Hereafter we sumarize recent contributions and advances in our knowledge about the magnetic field of solar prominences. It mostly relies on high resolution and high sensitivity spectropolarimetry made both in the visible and in the near infrared.

1 Introduction

Solar prominences (filaments) are made-up of dense and cool chromospheric plasma hanging in the hot and low density corona (Tandberg-Hanssen 1995). Besides its intrinsic interest, as a natural laboratory for plasma physics, the study of these structures is also of a more general interest in the frame of space weather studies. Indeed, among other closed magnetic regions such as active regions, eruptive prominences are often associated with coronal mass ejections, or CMEs, that is huge plasma "bubbles" ejected from the solar corona and able to strongly affect Sun-Earth relationships, by their interactions with the terrestrial magnetosphere (see e.g., Gopalswamy et al. 2006, for a recent review upon the various precursors of CMEs).

Despite systematic observations made since the nineteenth century and decades of study, prominence formation mechanisms are still not well understood. In particular, yet no theory can fully explain their remarkable stability in a hotter and less dense medium. However, since the plasma β is low in prominences, the magnetic field is very likely to play a major role in the physical scenarios which could explain prominences formation, stability and, finally, the triggering of these instabilities leading to CMEs (see Fig. 1).

However, the 3D magnetic field topology of solar prominences is not *directly* measureable in the corona. Even though indirect methods are available, the best possible determination of prominences magnetic fields comes from the inversion of spectropolarimetric data, which collection still remains a difficult task. He I multiplets such as $\lambda 10830$ Å in the near-infrared, and the Fraunhofer "yellow line" D_3 at $\lambda 5876$ Å are the best tools, so far, to study prominence magnetic fields. Indeed, only a few spectral lines are intense enough for ground-based observations in the optical spectrum of solar prominences i.e., at these wavelength at which spectropolarimetry is usually done. These helium multiplets provide, even if they are fainter than Hα for instance, the most suitable information necessary for the purpose of determining the magnetic field pervading the prominence plasma. Indeed, Hα is generally optically thick in prominences which, together with its hyperfine atomic structure, makes this spectral line still much more difficult to deal with, as compared to the above-mentioned helium multiplets. First spectropolarimetric observations of prominences and associated results about the magnetic field properties have been recently reviewed by Paletou & Aulanier (2003).

2 Recent advances

After very fruitful years of observations made mostly in the 80's, mainly at the *Pic du Midi* in France and at Sacramento Peak by NSO and HAO groups in the USA, spectropolarimetry of prominences seems to resume after the pionnering work of Lin et al. (1998) and the full-Stokes observations of a filament (i.e., a prominence as seen on the disk) in the $\lambda 10830$ Å multiplet.

[1] Laboratoire d'Astrophysique de Toulouse-Tarbes, Université de Toulouse, CNRS, 14 ave. E. Belin, 31400 Toulouse

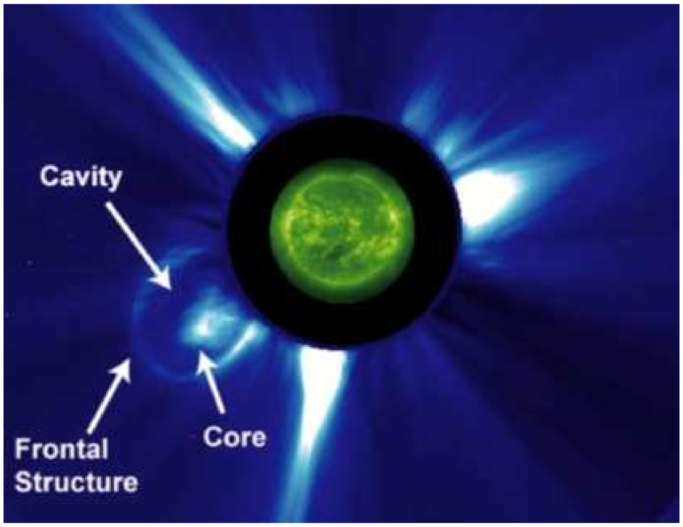

Fig. 1. A view of the standard three-part structure of a coronal mass ejection, as observed on December 20, 2001 with the LASCO coronagraph on-board SoHO. The so-called bright core is the remains of an eruptive prominence (from Gopalswamy et al. 2006).

A few years after, the first *full-Stokes* and high spectral resolution observation of a prominence in the He I D_3 multiplet is made at THéMIS (Paletou et al. 2001). These observations revealed a mixture of Hanle and Zeeman effects signatures. And the direct analysis, under the weak-field approximation, of the measured Stokes V signals pointed at a longitudinal magnetic field value of the order of 40 G, i.e. quite larger than what was usually measured in quiescent prominences (Leroy 1989, Leroy et al. 1984). Magnetic field strengths of the order of 50 G were also reported by Wiehr & Bianda (2003).

The new THéMIS observations have also led to a revision of magnetic field inversion tools (López Ariste & Casini 2002). In particular, these authors demonstrated how taking into account *all* Stokes parameters, and not only linear polarization signals, can increase the reliability of the inversion process.

Shortly after, Casini et al. (2003) published the first *maps* of the vector magnetic field i.e., its modulus, azimuth and inclination, as inferred from *Advanced Stokes Polarimeter* observations made at D_3 of He I, at the Dunn Solar Tower (DST, NSO/SP, USA). Even stronger field measurements were confirmed, up to 70 G, and variations of the orientation of the magnetic field across the prominence body were revealed.

2.1 Indirect methods

Long sequences of observations, more likely provided by spaceborne observatories, offer the possibility, to a certain extent, for an indirect diagnosis of the mean magnetic field in a filament/prominence. Using a 7h30 observing sequence made with the CDS EUV spectrometer on-board SoHO, and from the identification of certain oscillation modes associated to Alfvén and magnetoacoustic waves, Régnier et al. (2001) could infer the angle between the mean magnetic field and the filament long axis, and the magnetic field strength vs. the electronic density (although the latter remained undetermined).

Some important properties of the magnetic field of prominences can also be deduced from vector magnetic maps made at the *photospheric* level, in association with Hα imagery of the area below were stands the prominence. The latter images have to be used *simultaneously* with the photospheric vector magnetograms, and analysed taking into account the so-called *chirality rules* which were established by Martin (1998).

Taking advantage of the multi-line capabilities of THéMIS, and after a delicate analysis of several sets of data, López Ariste et al. (2006) could indeed identify the presence of photospheric magnetic field dips, also known as *bald patches* (see Fig. 2). According to these authors, this observed magnetic field topology in the photosphere tends to support MHD models of prominences based on magnetic dips located within weakly twisted flux tubes.

2.2 Near-infrared observations

The λ10830 Å multiplet of He I is routinely observed at the German VTT with the TIP polarimeter developed at the IAC (Mártinez Pillet et al. 1999, Collados et al. 2007). Filaments and prominences observations made with such instruments have recently conducted to very interesting results.

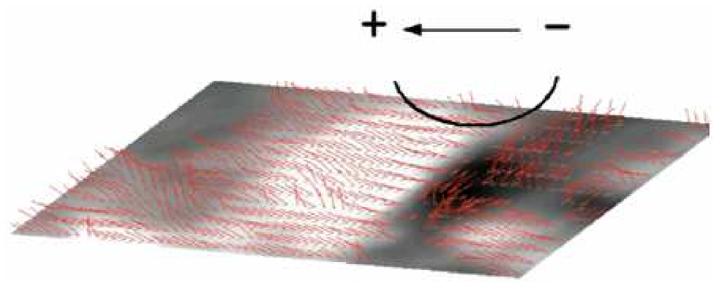

Fig. 2. The presence of magnetic dips supporting the prominence plasma against gravity can be inferred from a careful analysis of both (photospheric) vector magnetic field maps and simultaneous Hα images of the filament and its environment (from López Ariste et al. 2006, using THéMIS multi-wavelength observations).

From observations of a filament at disk center, Trujillo Bueno et al. (2002) could show, from the analysis of linear polarization signals observed in the two well-separated components of the λ10830 Å multiplet, and taking advantage of the forward-scattering geometry of this observation, that the effect of selective absorption from the ground-level of the triplet system of He I is at work. This implies the presence of magnetic fields of the order of a few gauss that are highly inclined with respect to the solar radius vector.

More recently, Merenda et al. (2006) published a quite surprising result concerning the orientation of the magnetic field deduced from the observation of a *polar crown* prominence. A magnetic field of 30 G strength inclined by about 25° with respect to the local solar vertical direction was inferred. These authors could also deduce from their analysis that, this nearly vertical magnetic field appeared to be slightly rotating around a fixed direction in space as one proceeds along the direction of the spectrograph's slit (which was, in that case, parallel to the local limb).

3 THéMIS on the front line

Nowadays, the 1-m aperture class THéMIS solar telescope installed at the *Observatorio del Teide* in Izaña (Tenerife, Spain) is the tool of choice for observing programmes dedicated to the spectropolarimetry of solar prominences. Since 2006, and the rejuvenation of the pool of detectors for the MTR observing mode (see e.g., Paletou & Molodij 2001), it provides indeed a *unique* capability of high spectral resolution, multi-line spectropolarimetric observations *simultaneously* in the visible and in the near-infrared spectral domains.

On Fig. 3, we display Stokes profiles extracted from data taken on June 2007. With our MTR setup, observations of D_3, Hα and λ10830 Å spectral domains are made simultaneously. For these observations, a polarimetric sensitivity better than 10^{-4} was reached. Such a combination of measurements with high spectral resolution and polarimetric sensitivity is, so far, a unique capability which is fully relevant for the deeper study of prominences magnetic fields in the coming years.

In the frame of our programme of spectropolarimetric observation of prominences, we could also put in evidence "enigmatic" circular polarization signals in Hα, both symmetric and having amplitudes which can be comparable to linear polarization signals, unlike what is predicted by the theory of the Hanle effect (see e.g., Landi Degl'Innocenti 1982). This was confirmed by observations made at the DST with the ASP spectropolarimeter (López Ariste et al. 2005). Even though other groups, such as Stenflo's (ETH, Zürich) using the 45-cm aperture Gregory-Coudé telescope at Locarno with the ZImPol spectropolarimeter could not yet confirm our findings (Ramelli et al. 2006), the analysis of data collected during our 2007 and 2008 observing campaigns do confirm the existence of such V signals. Our present study of this set of data aims at understanding under which conditions such circular polarization signals appear and, which are the physical implications of their presence or absence.

There are several physical processes capable of generating the observed net circular polarization (hereafter NCP) at Hα and, it is still unclear which one, or which combination of effects, is indeed at work in prominences. This may result from the presence of *electric* fields in the prominence plasma (see e.g., Casini & Manso Sainz 2006). However, some authors have also shown that collisional effects, either anisotropic (Derouich 2007) or isotropic (Štěpán & Sahal-Bréchot, these proceedings), can also generate NCP.

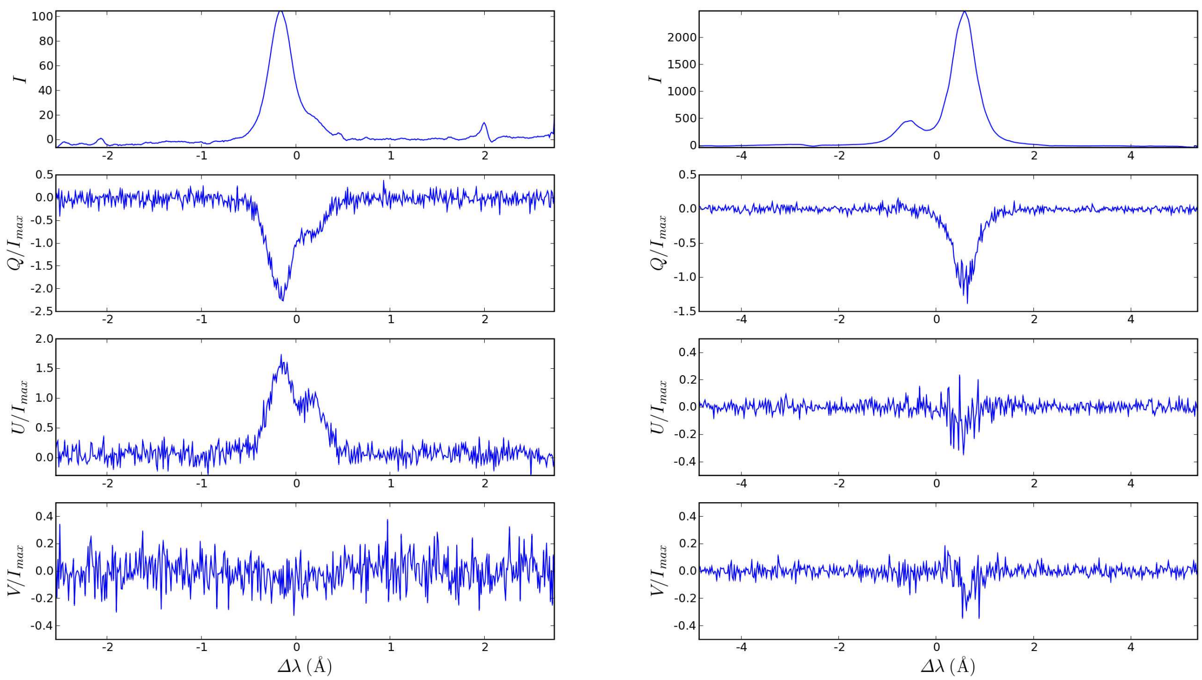

Fig. 3. Full-Stokes measurements of polarized signals formed in a solar prominence observed simultaneously with THéMIS on June 2007, at 5876 Å (left) and at 10830 Å (right). The Stokes profiles Q, U and V are normalized to the maximum of I after removal of the scattered light. Hα was also observed simultaneously with our MTR set-up. Polarization signals displayed here have been obtained with a sensitivity better than 10^{-3}.

4 The need for complex radiative modelling

It happens that measurements of the ratio between the amplitude of the two components of Stokes I, resulting from the atomic fine structure, for the He I λ10830 Å and D_3 multiplets (see e.g., Fig. 11 in López Ariste & Casini 2002) are often in contradiction with the commonly used hypothesis of *optically thin* multiplets (see e.g., Bommier 1977).

Besides, up to now the most recent radiative models (Labrosse & Gouttebroze 2001, 2004) still assume mono-dimensional (1D) static slabs and *no* atomic fine structure for the He I model-atom, which lead to the synthesis of unrealistic Gaussian profiles. Given the high spectral resolution of actual observations, it is therefore important to use the best numerical radiative modelling tools in 2D geometry, as a first step, and a more detailed He I atomic model in order to improve our spectral diagnosis capability.

As a first application of the new 2D radiative transfer code developed by us (Paletou & Léger 2007, Léger et al. 2007), we have shown how *multi-thread* models, for which one considers the emission resulting from a bunch of cool small-scale structures distributed along the line of sight, could explain the measured intensity ratios (Léger & Paletou 2008).

Such a forward complex radiative modelling now have to be exploited and developed further. It should also be used for the generation of synthetic polarization signals, possibly combined with recently developed numerical tools such as HAZEL (Asensio Ramos et al. 2008).

5 Conclusions

The spectropolarimetry of solar prominences have been renewed during the last decade with the advent of both new telescopes, new spectropolarimeters and detectors. Even though the data collection has not been huge so far, most of the measurements of quality have led to new and surprising results.

In that field, the solar telescope THéMIS with its unique multi-line spectropolarimetric capability is definitely, at the present time, the instrument of choice for such studies. In a near-future, only the dedicated ProMag spectropolarimeter currently developed at HAO/NCAR, and to be deployed at the Evans Solar Facility (NSO/SP, USA), will provide almost comparable sets of data.

It is finally expected that the future 4-m aperture solar telescope EST will allow too, at the 2020 horizon, for the collection of the most suitable combination of spectropolarimetric data necessary for ever more precise determinations of the magnetic fields of solar prominences.

Arturo López Ariste (THéMIS, CNRS), Roberto Casini (HAO, NCAR, Boulder), Reza Rezai (KIS, Freiburg) and Ludovick Léger (LATT, U. Toulouse, CNRS) are the main collaborators of our observing programme related to the spectropolarimetry of solar prominences. THéMIS is operated on the Island of Tenerife by CNRS-CNR in the Spanish *Observatorio del Teide* of the *Instituto de Astrofísica de Canarias*.

References

Asensio Ramos, A., Trujillo Bueno, J., & Landi Degl'Innocenti, E. 2008, ApJ, 683, 542

Bommier, V. 1977, Thèse de Doctorat de 3ème cycle, Univ. de Paris VI

Casini, R., & Manso Sainz, R. 2006, J. Phys. B: At. Mol. Opt. Phys., 39, 3241

Casini, R., López Ariste, A., Tomczyk, S., & Lites, B.W. 2003, ApJ, 598, 67

Collados, M., Lagg, A., Díaz García, J.J. et al. 2007, in ASP Conf. Ser. 368, The Physics of Chromospheric Plasmas, eds. P. Heinzel, I. Dorotovič & R.J. Rutten (San Francisco: Astronomical Society of the Pacific), 611

Derouich, M. 2007, A&A, 466, 687

Gopalswamy, N., Mikić, Z., Maia, D. et al. 2006, Space Science Reviews, 123, 303

Labrosse, N., & Gouttebroze, P. 2001, A&A, 380, 323

Labrosse, N., & Gouttebroze, P. 2004, ApJ, 617, 614

Landi Degl'Innocenti, E. 1982, Solar Phys., 79, 291

Léger, L., & Paletou, F. 2008, A&A (in press)

Léger, L., Chevallier, L., & Paletou, F. 2007, A&A, 470, 1

Leroy, J.-L. 1989, in Dynamics and Structure of Quiescent Solar Prominences, ed. E.R. Priest (Dordrecht: Kluwer)

Leroy, J.-L., Bommier, V., & Sahal-Bréchot, S. 1984, A&A, 131, 33

Lin, H., Penn, M.J., & Kuhn, J.R. 1998, ApJ, 493, 978

López Ariste, A., & Casini, R. 2002, ApJ, 575, 529

López Ariste, A., Aulanier, G., Schmieder, B., & Sainz Dalda, A. 2006, A&A, 456, 725

López Ariste, A., Casini, R., Paletou, F. et al. 2005, ApJ, 621, L145

Martin, S.F. 1998, Solar Phys., 182, 107

Mártinez Pillet, V., Collados, M., Sánchez Almeida, J. et al. 1999, in ASP Conf. Ser. 183, High Resolution Solar Physics: Theory, Observations, and Techniques, eds. T.R. Rimmele, K.S. Balasubramaniam & R.R. Radick (San Francisco: Astronomical Society of the Pacific), 264

Merenda, L., Trujillo Bueno, J., Landi Degl'Innocenti, E., & Collados, M. 2006, ApJ, 642, 544

Paletou, F., & Aulanier, G. 2003, in ASP Conf. Ser. 307, Solar Polarization Workshop 3, eds. J.Trujillo Bueno & J. Sánchez Almeida (San Francisco: Astronomical Society of the Pacific), 458

Paletou, F., & Léger, L. 2007, JQSRT, 103, 57

Paletou, F., & Molodij, G. 2001, in ASP Conf. Ser. 236, Advanced Solar Polarimetry – Theory, Observation, and Instrumentation, ed. M. Sigwarth (San Francisco: Astronomical Society of the Pacific), 9

Paletou, F., López Ariste, A., Bommier, V., & Semel, M. 2001, A&A, 375, L39

Ramelli, R., Bianda, M., Trujillo Bueno, J. et al. 2006, in ASP Conf. Ser. 358, Solar Polarization 4, eds. R. Casini & B.W. Lites (San Francisco: Astronomical Society of the Pacific), 471

Régnier, S., Solomon, J., & Vial, J.-C. 2001, A&A, 376, 292

Tandberg-Hanssen, E. 1995, The Nature of Solar Prominences (Dordrecht: Kluwer)

Trujillo Bueno, J., Landi Degl'Innocenti, E., Collados, M., Merenda, L., & Manso Sainz, R. 2002, Nature, 415, 403

Wiehr, E., & Bianda, M. 2003, A&A, 404, L25

SF2A 2008
C. Charbonnel, F. Combes and R. Samadi (eds)

HYDRODYNAMICAL SIMULATIONS OF SLOW CORONAL WIND, CORONAL INFLOWS AND POLAR PLUMES

Pinto, R.[1], Grappin, R.[1], Wang, Y.-M.[2] and Léorat, J.[1]

Abstract. We use a hydrodynamical time-dependent coronal flux tube model extending from $\sim 1\ R_\odot$, where nonreflecting boundary conditions are applied, to $30\ R_\odot$, which includes a transition region sustained by the equilibrium between thermal conduction, radiative losses and a prescribed mechanical heating flux. We recover the observed inverse relationship between asymptotic wind speed and expansion factor if the coronal heating rate is a function of the local magnetic field strength. We show that inflows can be generated by suddenly increasing the rate of flux-tube expansion, and suggest that this process may be involved in the closing-down of flux at coronal hole boundaries. We also simulate the formation and decay of a polar plume, by including an additional, time-dependent heating source near the base of the flux tube.

1 Introduction

The slow solar wind comprehends a wide variety of flows with different measured velocities, composition, as well as spatial and temporal variability. It is often considered the slow wind originates from within closed field regions. We adopt here the opposite view in which both high- and low-speed wind come from coronal holes (open field regions), and that it is the rate of flux-tube expansion and/or the location of the coronal heating which control the measurable characteristics of the slow wind. Considering flux tubes which cross the vicinities of active regions and/or boundaries between neighbour coronal holes may account for the high variability of the slow wind flow. Swarms of overdense small-scale inflows are observed around the heliospheric current/plasma sheet between $2-5\ R_\odot$ (Sheely & Wang 2002), which seem to be connected to the the closing-down of magnetic flux at coronal hole boundaries. Coronal plumes are filamentary structures aligned along open field lines with densities ∼2–5 times higher than the interplume regions. Plumes are found to overlie EUV bright points, these having a shorter lifetime (Wang 1994).

We use the 1D time-dependent hydrodynamical numerical model of a coronal flux tube described in Grappin et al. (*in preparation*) and Pinto et al. (*submitted*) to study the effects of varying the expansion factor near the coronal base and the coronal heating function on the solar wind flow. We set the computational domain from near the photosphere to $30\ R_\odot$. Non-reflecting boundary conditions are imposed both at the bottom and the top of the domain. The momentum, mass and energy (with $\gamma = 5/3$) conservation equations read

$$\partial_t \mathrm{u} + (\mathrm{u}\cdot\nabla)\,\mathrm{u} = -\frac{\nabla P}{\rho} - \frac{GM}{r^2}\hat{\mathrm{r}}, \qquad \partial_t \rho + \nabla\cdot(\rho \mathrm{u}) = 0 \tag{1.1}$$

$$\partial_t T + \mathrm{u}\cdot\nabla T + (\gamma-1)\,T\nabla\cdot\mathrm{u} = -\frac{\gamma-1}{\rho}\left[\nabla\cdot F_h + \nabla\cdot F_c + \rho^2\Lambda\,(T)\right] \tag{1.2}$$

where $F_h,\ F_c$ are respectively the mechanical heating and conductive fluxes, and $\Lambda\,(T)$ is a fit to the radiative loss function in Athay (1986). In the above, the divergence operator is defined in terms of the tube's expansion factor The magnetic field is $B \propto r^{-2}$ for $r \geq 2.5\ R_\odot$ and $B \propto r^{-\nu}$ below.

The background heating function is either a standart phenomenological form (Eq. 1.3, left) or proportional to $B^{1/2}$ (Eq. 1.3, centre). Heating perturbations are achieved through variations of the expansion factor ν, a

[1] Observatoire de Paris, LUTH, CNRS, 92195 Meudon, France
[2] Space Science Division, Naval Research Laboratory,Washington, DC 20375-5352

time-dependant combination of two heating sources (the two expressions in Eq. 1.3, left and centre) and the addition of a heating source concentrated just above the coronal base (Eq. 1.3, right; $\delta r \sim 10^{-3}\ R_\odot$)

$$F_h^1 = F_{p0}\left(\frac{B}{B_0}\right)\exp\left[-\frac{r-R_\odot}{H_p}\right], \quad F_h^2 = F_{b0}\left(\frac{A_0}{A}\right)\left(\frac{B}{B_0}\right)^{1/2} = F_{b0}\left(\frac{B}{B_0}\right)^{3/2}, \quad \nabla\cdot F_r \propto e^{-\frac{(r-r_0)^2}{\delta r^2}} \qquad (1.3)$$

2 Results

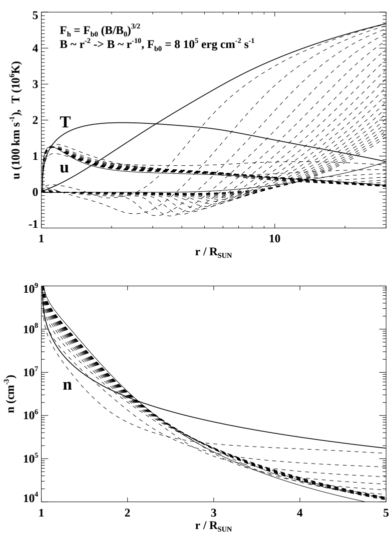

Fig. 1. Here, the magnetic falloff index is suddenly increased from 2 to 10 while keeping F_{h0} fixed. The radial profiles of u, T, and n are shown at $t/\tau = 0$ (thick lines), 1, 2, ..., 20 (dashed lines) and 40 (thin lines). Strong transient inflows are generated below the sonic point.

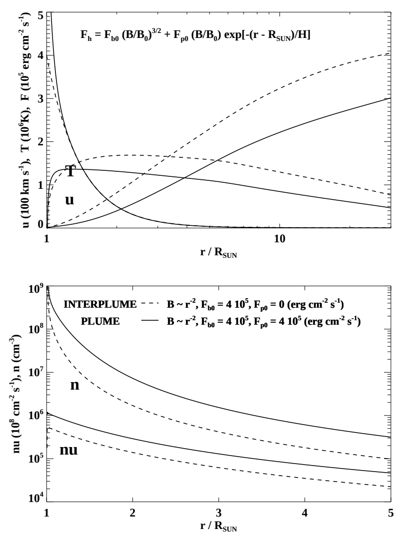

Fig. 2. Effect of an additional heating term near the coronal base. *Solid curves:* steady-state "plume" solution. *Dashed curves:* steady-state "interplume" solution. In both cases, the global heating term is given by $F_{b0}(B/B_0)^{3/2}$, with $F_{b0} = 4\times10^5$ erg cm^{-2} s^{-1} and $\nu = 2$.

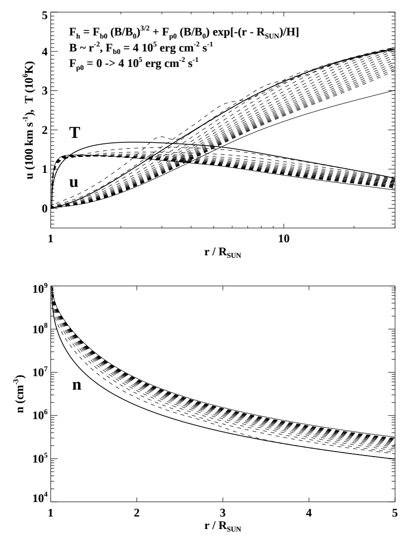

Fig. 3. Formation of a plume. The initial state is the interplume solution ($F_{p0} = 0$); F_{p0} is suddenly increased to $F_{p0} = F_{b0}$. The radial profiles of u, T, and n are shown at $t/\tau = 0$ (thick lines), 1, 2, ..., 20 (dashed lines) and 40 (thin line)

3 Conclusions

a. Variations in the coronal heating function can produce a wide variety of solar wind flows.
b. The observed inverse correlation between wind speed and expansion factor is can be retrieved if $F_h \propto B^\mu$. A rapidly diverging field results in a large mass flux at the coronal base and a low speed far from the Sun.
c. Strong inflows can be generated in the subsonic region by decreasing the local heating rate and/or increasing the field expansion rate, as might occur when opposite-polarity field lines merge at a neutral sheet. The evacuation of the flux tubes would further accelerate the merging and reconnection process.
d. Densities comparable to those observed in polar plumes can be obtained by depositing a large amount of energy just above the coronal base. A steady-state equilibrium is reached only after ∼1 day, which may explain why coronal plumes appear to evolve more slowly than their underlying EUV bright points.

References

Athay, R. G. 1986, ApJ, 308, 975
Sheeley, Jr., N. R. & Wang, Y.-M. 2002, ApJ, 579, 874
Wang, Y.-M. 1994, ApJ, 435, L153
Withbroe, G. L. 1988, ApJ, 325, 442

SF2A 2008
C. Charbonnel, F. Combes and R. Samadi (eds)

MAGNETIC RECONNECTION BY ALFVÉN WAVES

Pinto, R.[1], Grappin, R.[1] and Léorat, J.[1]

Abstract. We investigate the effects of the injection of alfvén waves into the solar corona using an axisymmetric 2.5 MHD numerical model extending from the top of the transition region up to about 15 solar radii. Transparent boundary conditions are applied at the top and bottom of the numerical domain and waves are injected by perturbing the alfvénic characteristic at the bottom boundary. We study two kinds of magnetic configuration: a) a quadrupolar region inside an equatorial streamer and b) a small bipole within an unipolar flux polar coronal hole region. In configuration a), waves generate a pattern of convective flows ($10 - 50$ km/s) inside the streamer and simultaneously slow reconnection around the magnetic null point, which continuously rises upwards (≈ 25 km/s). In configuration b), we observe an increase in density, wind speed and mass flux along its central axis in a behaviour which resembles that of polar plumes in coronal holes. Current density accumulates around the magnetic null point.

1 Introduction

The understanding of the destabilisation of magnetised coronal structures and of the subsequent dynamical events (CMEs, plumes, jets, inflows, etc) relies on the correct assessment of the energy transport mechanisms taking place from down below the photosphere up to the corona. Numerical models need to make use of simple approximations to such transport phenomena. Most often, the coronal plasma is assumed to be "line-tied" to the photosphere, which translates into setting the horizontal velocities at the photosphere as rigid lower boundary conditions (footpoint shearing), neglecting any feedback from the coronal dynamics over the photosphere; energy flows upwards through the photosphere (e.g, Aulanier et al. 2005) but not downwards (being reflected there, instead). Grappin et al. (2008) show this approximation severely overestimates the magnetic energy and velocity shear transmitted to coronal loops, unless for rather short timescales. We search for destabilisation methods which do not rely on linetied footpoint shearing. We use an axisymmetric MHD numerical model of an isothermal ($\gamma = 1$) corona starting from just above the TR. We inject alfvén waves through the transparent lower boundary by perturbing the alfvénic characteristic there. We test two magnetic configurations: a) quasi-quadrupolar system with a magnetic null point within an equatorial streamer (Fig. 1); b) magnetic bipole in polar coronal hole ("plume-like" configuration, Fig. 2).

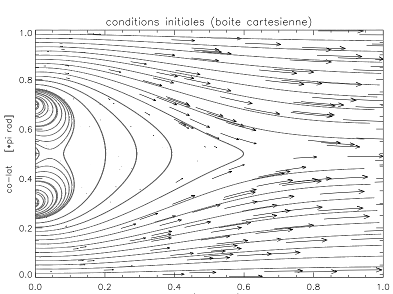

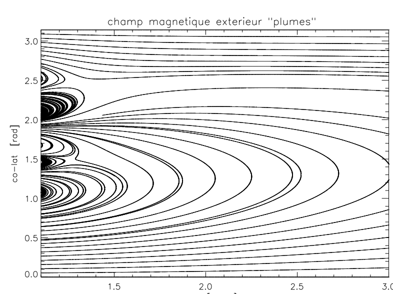

Fig. 1. Magnetic configuration a) in a cartesian representation of the numerical domain; x-axis is R from 1 to 15 $R_\odot$ in log-scale, y-axis is co-latitude from 0 to 2π.

Fig. 2. Magnetic configuration b) in a cartesian representation of the numerical domain; x-axis is R from 1 to 3 $R_\odot$, y-axis is co-latitude from 0 to 2π.

2 Results

Figure 3 shows the flow pattern which forms within the equatorial streamer shown in Fig. 1 at about 5 h after the wave injection starts. A stagnation point forms over the magnetic null point as in classical 2D reconnection, but

[1] Observatoire de Paris, LUTh, CNRS, 92195 Meudon, France

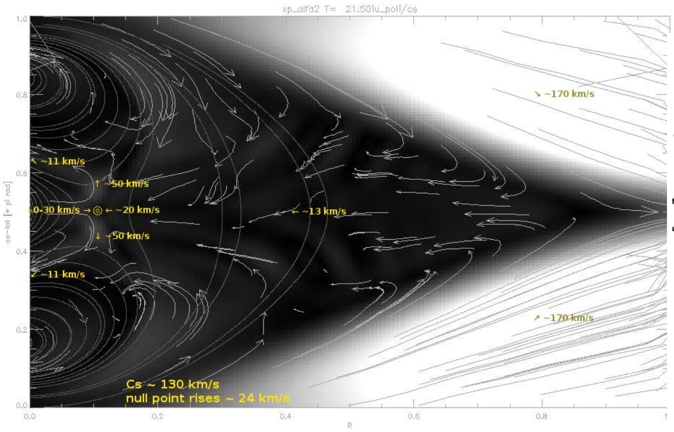

Fig. 3. The convective flow pattern inside the equatorial streamer (cf. Fig. 1) at time $\delta t \approx 5$ h ($\approx 20\ \tau_{alfven}$ for the internal loops). Only the sub-domain $1 < r/R_\odot < 2.5$, $0.17\ \pi < \theta < 0.83\ \pi$ is shown. Grayscale represents $|u|/c_s$. A stagnation point forms over the null point, its position being indicated by a yellow circle.

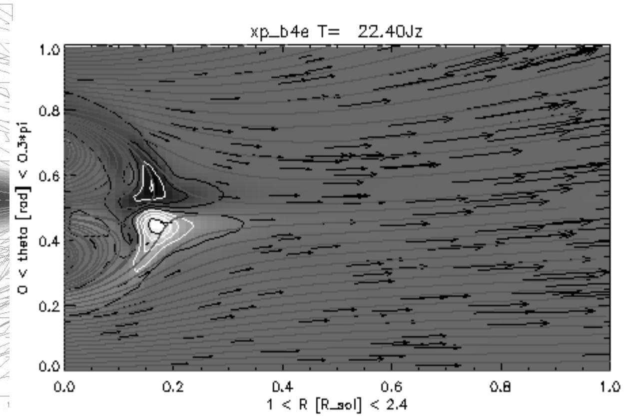

Fig. 4. Snapshot of the accumulation of current density around the null point above the dipole in the configuration in Fig. 2. Only the sub-domain $1 < r/R_\odot < 2.4$, $0 < \theta < 0.3\ \pi$ is shown. Grayscale represents J_Z, grey lines are magnetic fieldlines and black arrows show the local flow velocity. An overdense jet forms along the magnetic axis, above the null point.

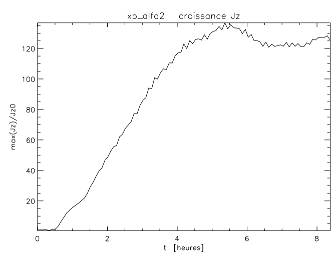

Fig. 5. Current density accumulation around the null point in figs. 1 and 3, which seems to saturate after $\approx 20\ \tau_{alfven} \approx 5$ h. The reconnection do not stop, though.

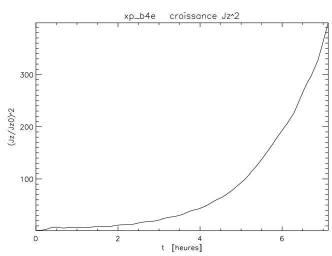

Fig. 6. Current density accumulation around the null point in figs. 2 and 4. $|J_z|$ seems to grow without bound, for at least $\approx 50\ \tau_{alfven} \approx 7$ h.

here the null point moves upwards at a nearly constant velocity 24 km/s without any signs of deceleration. Wave injection is restricted to zones not directly connected to the neighbourhood of the null point. The reconnection process is triggered by a re-arrangement of the magnetic and gas pressures after the wave propagation pattern occupies a large portion of the streamer. Figure 5 shows the accumulation of current density around the null point as a function of time. As we use transparent boundaries the accumulation of energy in the system cannot be a trivial consequence of footpoint shearing as when using linetying conditions, because here there is a well defined upper limit for the energy added (see Grappin et al. 2008).

Figure 4 shows the formation of a coronal jet along the magnetic axis of a magnetic bipole within a unipolar flux region. Unlike in the previous case, the topology is stationary. There is, however, reconnection going on around the null point. Also here, a pattern of convective flows with a stagnation point coincident with the magnetic null settles in. Density, velocity and mass flux build up in the vicinity of the bipole axis, making up a small coronal jet. Current density accumulates; its spatial distribution is shown in Fig. 4 and the peak density is shown as a function of time in Fig. 6.

References

Grappin, R., Aulanier, G., Pinto, R., 2008, A&A, *accepted for publication*

Aulanier, G., Démoulin, P., Grappin, R., 2005, A&A, 430, 1067-1087

SF2A 2008
C. Charbonnel, F. Combes and R. Samadi (eds)

,

PHOTOSPHERIC FLOWS AROUND A QUIESCENT FILAMENT AT LARGE AND SMALL SCALE AND THEIR FFECTS ON FILAMENT DESTABILIZATION

Roudier, Th.[1], Malherbe, J.M.[2], Švanda, M.[3], Molodij, G.[2], Keil, S.[4], Sütterlin, P.[5], Schmieder, B.[2], Bommier, V.[6], Aulanier, G.[2], Meunier, N.[7], Rieutord, M.[1] and Rondi, S.[1]

Abstract. We study the influence of large and small scales photospheric motions on the destabilization of an eruptive filament, observed on October 6, 7, and 8, 2004 as part of an international observing campaign (JOP 178). Large-scale horizontal flows are invetigated from a series of MDI/SOHO full-disc Dopplergrams and magnetograms from THEMIS. Small-scale horizontal flows were derived using local correlation tracking on TRACE satellite, Dutch Open Telescope (DOT) and The Dunn Solar telescope (DST) data. The topology of the flow field changed significantly during the filament eruptive phase, suggesting a possible coupling between the surface flow field and the coronal magnetic field. We measured an increase of the shear below the point where the eruption starts and a decrease in shear after the eruption. We conclude that there is probably a link between changes in surface flow and the disappearance of the eruptive filament.

1 Introduction

Filaments (prominences seen on the limb) which are common solar features always occur along lines where the underlying photospheric magnetic field changes sign. They represent regions where magnetic fields are interacting with the plasma in a subtle way in the different parts of the solar atmosphere. The filament's existence in the corona is mainly due to magnetic fields that support dense material against gravity inside dipped arcade loops or flux tubes (Kuperus & Raadu 1974). The filaments are structures of the solar corona which are anchored at footpoints in the solar photosphere. Knowledge of photospheric motions over long periods is needed to understand the action of the plasma on the filament. In particular, barbs, footpoints of prominences when observed on the disk, are always associated with parasitic polarities implying a reversal of the transverse horizontal magnetic field. The mechanism generating such magnetic configurations must take into account photospheric motions. Most observational studies of filaments have been carried out to describe their properties and structures in the corona and chromosphere. However, the magnetic field contributing to the formation of the filaments can transfer photospheric perturbations into the corona. Very few papers exist on the determination of photospheric motions beneath and in the vicinity of filaments. Such measurements require multi wavelength observations In this paper we investigate a filament observed over a large field of view with high spatial resolution.

2 High spatial and temporal horizontal flows

Our data come from a combination of ground and space based telescopes on October 6, 7 and 8, 2004 during a JOP 178 campaign (http://bass2000.bagn.obs-mip.fr/jop178/index.html).

[1] Laboratoire d'Astrophysique de l'Observatoire Midi-Pyrénées, Université de Toulouse, CNRS, 57 Avenue d'Azeirex, 65000 Tarbes, France
[2] LESIA, Observatoire de Paris,Section de Meudon, 92195 Meudon, France
[3] Astronomical Institute, Academy of Sciences of the Czech Republic, Fričova 298, 25165 Ondřejov, Czech Republic
[4] National Solar Observatory, Sacramento Peak, Sunspot, NM 88349, United States
[5] Sterrekundig Instituut Utrecht, Postbus 80 000, 3508 TA Utrecht, T he Netherlands
[6] LERMA, Observatoire de Paris,Section de Meudon, 92195 Meudon, France
[7] Laboratoire d'Astrophysique de l'Observatoire de Grenoble, CNRS, Univ. J Fourier, BP43,39041 Grenoble cedex France

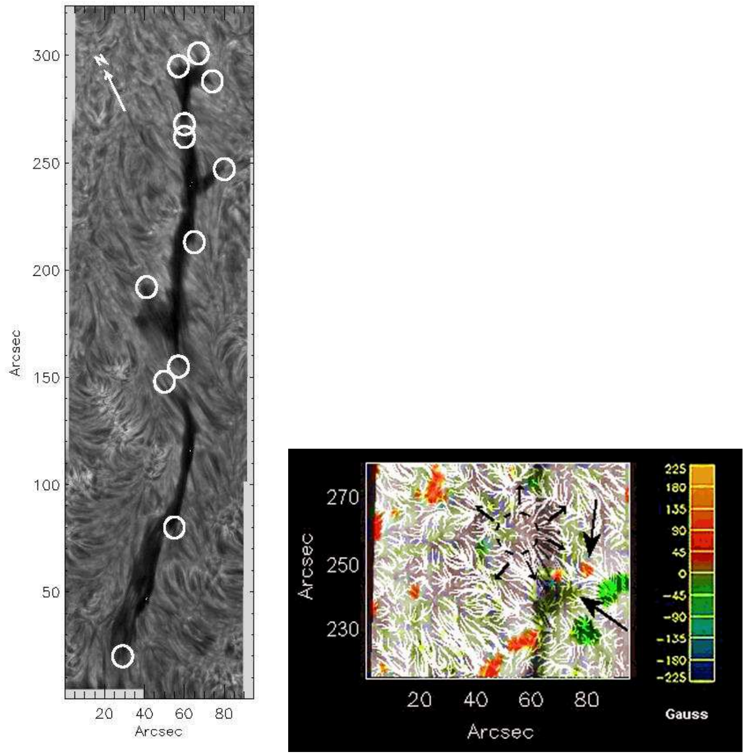

Fig. 1. (left) A mosaic of the filament in $H\alpha$ observed with the DOT, made from 6 frames selected at about 8:50 UT on October 6, 2004. The circles indicate the footpoint locations of the filament. The arrow indicates solar north. (right) Detail of a parasitic polarity. The longitudinal magnetic field lies between ±447 Gauss. The thick arrows show two parasitic polarities and the dotted circle indicates roughly the center of the divergence (while thin arrows indicate the direction) of the horizontal flow on the scale of a supergranule.

Fig. 1 (left) shows a mosaic at 8:50 UT of the $H\alpha$ filament structure that was observed in the southern solar hemisphere (S16E11) on October 6, 2004 during the decaying phase of the solar cycle. This filament has a sinistral chirality which is a normal configuration in that hemisphere. The smallest chromospheric features on the image show that the angular resolution is around 0.5 arcsec over the field of view of 95arcsec×323 arcsec. The 5 arcsec radius circles indicate the region of apparent footpoints.Fig. 1(right) shows some of the details between these parasitic polarities and the flow. The dotted circle indicates a center of divergence on the scale of a supergranule, while the small arrows show the direction of the flow field. The large arrows on the right of the figure point towards the parasitic polarity (in red) and the dominant polarity (of the weak background field) in green. The cork trajectories cross beneath the filament indicating that the flow transports corks (and thus flux tubes) across the filament channel and could in this manner create parasitic polarities. Convection could push opposite polarity fields, by the outward dispersal of magnetic flux, through the PILs. Thus supergranule cells could induce a significant flow into the polarity inversion zone thereby transferring field of opposite polarity from one side of the PIL to the other one.

In the south part of the filament Fig. 2(right), we observed the transport of parasitic and normal polarities by a continuous diverging horizontal flow, lasting at least one day, located in the filament gap where the filament starts to disappear. Such a purely horizontal motion could lead to the destabilization of the filament and to the sudden filament disappearance (Lin et al 2001). The second is the mixing of opposite polarities induced by the horizontal flows which in turn implies a reorganization of the magnetic field at the origin of the filament eruption.

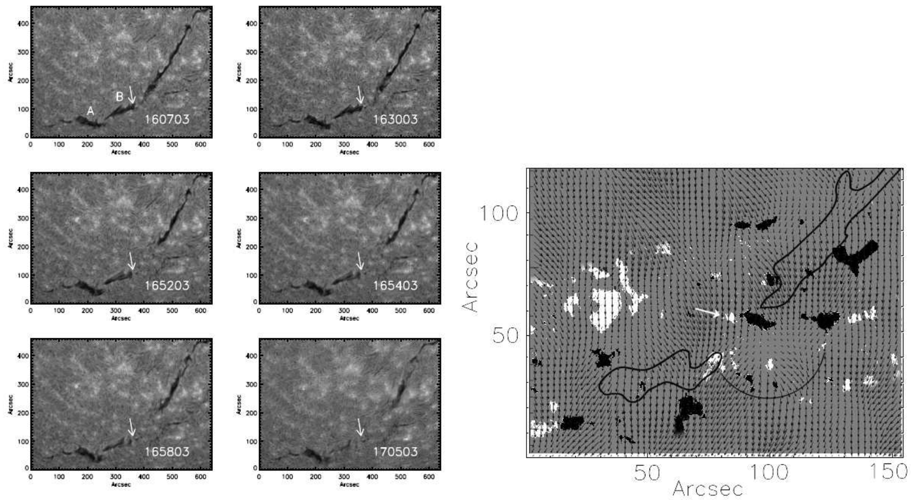

Fig. 2. Evolution of the filament during its eruption around 16:30 UT on October 7, 2004. The arrow indicates a fixed position for all the subframes. A and B denote two parts of the filament. Magnetic field measured by THEMIS on October 7, 2004 between 14:30- 15:17 UT, with the SE extremity of the contour of the filament, and with horizontal photospheric flows, measured with TRACE data, superimposed. The arrow indicates a magnetic feature which is observed to move and interfer with the close opposite polarity (on its right) in the MDI magnetograms. The highest absolute values beeing saturated on this map. North is located at the top of the figure.

3 Large-scale horizontal flows

In order to map the horizontal component of the large-scale photospheric plasma velocity fields, we applied local correlation tracking (LCT; November 1986) to a set of full-disc Dopplergrams obtained by the MDI instrument onboard SoHO. The aim of this method is to track the proper motion of supergranules that are clearly detectable on Dopplergrams everywhere except for the disk centre

The filament's evolution can be seen in Fig. 2 (left). The North–South stream flow visible in Fig. 3 (left, top) crosses over the part of the filament labeled A. The arrow on Fig. 2 (left) indicates the same fixed point (325 arcsec, 167 arcsec) in all of the subframes. We observe a general southward motion of both the A and B segments of the filament. More precisely, we measure a tilt of these two filament segments at the point of their separation. Between 16:07 UT and 16:58 UT the longaxis of segment A rotates by an angle of 12 degrees (clockwise) relatively to its western end, and the long axis of segment B of the filament rotates by an angle of 5.5 degrees (clockwise) relatively to its western end. These rotations are compatible with the surface flow shown in Fig. 3 (top, left) and in particular the North–South stream flow visible.

Before the eruption Fig. 3 (top left),we can clearly see the North–South stream parallel to and about 10 degrees East of the filament. This stream disturbs differential rotation and brings plasma and magnetic structures to the South. Although differential rotation tends to spread the magnetic lines to the East, the observed North–South stream tends to shear the magnetic lines. After the eruption, only a northern segment of the filament is visible and the North–South stream has disappeared. The evolution in the shear velocity computed as the difference between the mean flow in the two boxes as a function of time is shown in Fig. 3 (bottom). One can see that the shear velocity is increasing before the eruption and decreasing after the eruption.

4 Conclusions

We have presented multi−wavelength observation of the evolution and eruption of a filament obtained during the JOP 178 campaign on October 6 through 8, 2004. We analyzed the photospheric motions below and in the immediate neighborhood of the filament to search for systematic flows that could both sustain the filament and lead to its eruption. Our observations show that the supergranules can play a role in the transport of parasitic polarities through the filament channel and thus contribute to the formation of barbs (filament footpoints)

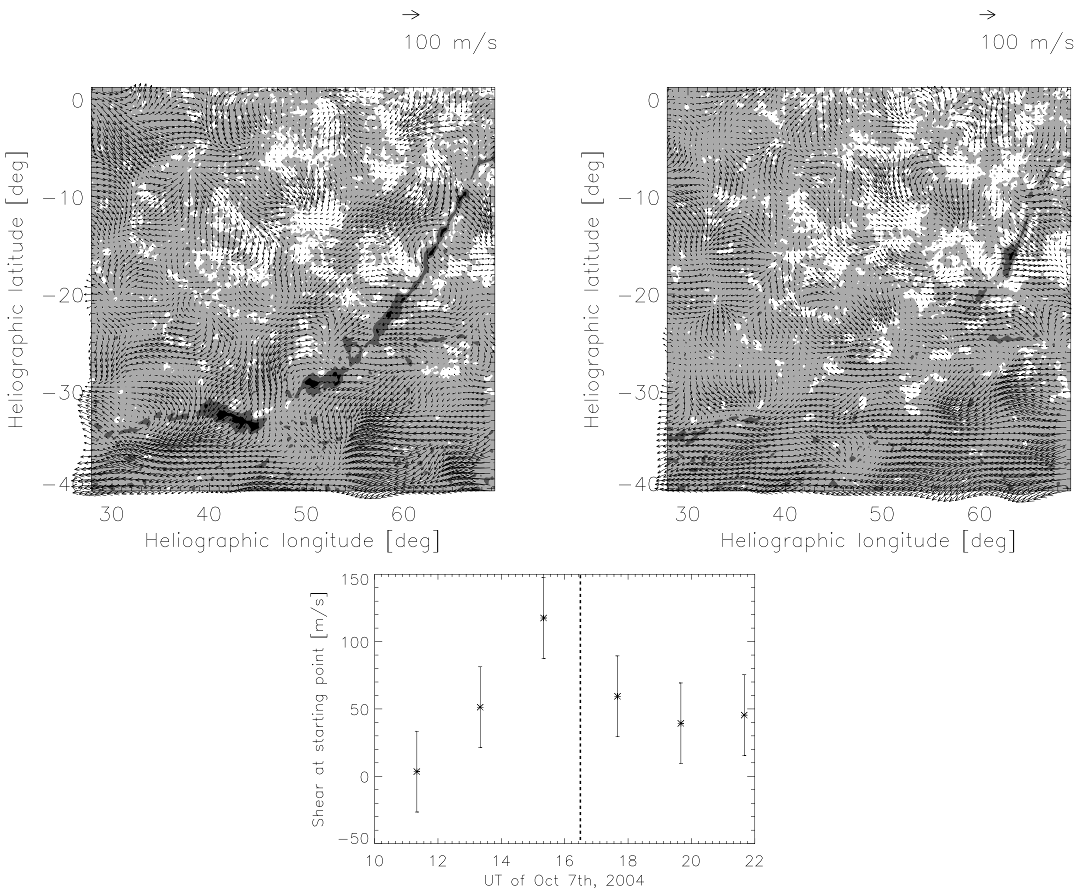

Fig. 3. Horizontal motions measured by *LCT-Doppler* before (top left) and after (top right) the eruption over a wide field of view. The filament observed by ISOON on October 7 2004 at 13:30 UT is superimposed. The evolution of the velocity shear in zonal components in time (bottom). The eruption of filament took place at 16:30 UT.

The filament eruption started at about 16:30 UT at the latitude around -25 degrees where the measurements of the horizontal flows based on Dopplergram tracking show a modification of the slope in the differential rotation of the plasma. This behavior is not observed in the curves obtained by both tracking the longitudinal magnetic field. This result seems to be a consequence of the presence of a North–South stream along the filament position, which is easily measured by tracing Doppler structures, which is only slightly visible in maps obtained by tracking of magnetic elements. The observed North–South stream has an amplitude of 30–40 $\mathrm{m\,s^{-1}}$. In the sequence of Hα image that record the filament's evolution, the part of the filament, which is in the North–South stream, is rotated in a direction compatible with the flow direction of the stream. This behavior suggests that the foot-points of the filament are carried by the surface flows. The influence of the stream is strengthened by differential rotation. We should keep in mind that the filament extends from -5 to -30 degrees in latitude and that the northern part of the filament is subjected to a larger rotation than the southern part. The North–South stream, along with contribution from differential rotation causes the stretching of the coronal magnetic field in the filament and therefore contributes to destabilizing the filament. The topology of the North–South stream changed after the filament eruption, nearly vanishing.

References

Kuperus, M., & Raadu, M. A. 1974 A&A, 31, 189

Lin, J., Forbes, T. G., & Isenberg, P. A. 2001 JGR,.106, 25

November, L.J. 1986, Appl. Opt. 25, 392

SF2A 2008
C. Charbonnel, F. Combes and R. Samadi (eds)

POSSIBLE CREATION OF NET CIRCULAR POLARIZATION AND NOT ONLY DEPOLARIZATION OF SPECTRAL LINES BY ISOTROPIC COLLISIONS

Štěpán, J.[1,2] and Sahal-Bréchot, S.[1]

Abstract. We will show that isotropic collisions of electrons and protons with neutral hydrogen can lead to creation of net orientation of the atomic levels in the presence of a magnetic field. Consequently, the emitted Stokes-V profile of the spectral lines can be almost symmetric in contrast to the typical antisymmetric signature of the Zeeman effect. Moreover, the amplitude of the symmetric lobe can be significantly higher than the amplitude of the antisymmetric components. This mechanism is caused by a $\pm M$ symmetry breaking of the collisional transitions between different Zeeman sublevels. We will show an example of our first results for the Hα line. This new mechanism could perhaps explain the net circular polarization of spectral lines observed in some solar limb observations and which are currently not understood. However, our results are very preliminary and more developments are needed for going further on.

1 Introduction

Recent spectropolarimetry measurements of the hydrogen lines in solar prominences made by López Ariste et al. (2005) at THEMIS have revealed an interesting property of the Hα circular polarization profile: it has been found to be almost symmetric in most of the observations (see Fig. 1 and Fig. 2 of that paper). Such a profile cannot be explained as a result of the Zeeman effect which leads to antisymmetric V-profiles.

Physically, emission of the line with net circular polarization (NCP) requires presence of atomic level orientation, i.e., imbalance of populations of the Zeeman sublevels M and $-M$,

$$N(\alpha JM) \neq N(\alpha J\, -M)\,. \tag{1.1}$$

Such an imbalance can be created by absorption of circularly polarized photon or by the the so-called alignment-to-orientation mechanism (Kemp et al. 1984). However, these mechanisms can hardly explain all the observations of NCP. A theoretical explanation of this enigmatic signal has been proposed by Casini & Manso Sainz (2006). Their calculations based on the quasistatic approximation of the turbulent microscopic electric field seem to give a possible explanation of the measurements.

However, the quasistatic approximation is not valid for interactions between the hydrogen atom and the protons or electrons of the medium in the physical conditions of solar prominences. In fact, the proton or electron density is so small (typically $10^{10}\mathrm{cm}^{-3}$) that the duration of the interaction is very small compared to the mean interval between two interactions, even for transitions $nljM \to n\,l \pm 1\,j'M'$ among the fine structure levels. Consequently, it is the impact approximation which is valid, and not the quasisatic one. The treatment of the interaction of hydrogen with the protons and electrons of the medium for these transitions, which play the role for modifying the atomic polarization, requires the theory of collisions (Bommier et al. 1986; Sahal-Bréchot et al. 1996). This is also the case for Stark broadening of Hα lines at astrophysical densities (Stehlé et al. 1983 and further papers) .

In this work we argue for a new mechanism leading to atomic orientation. It is based on the fact that the spherical symmetry of the thermal electron-H I and proton-H I collisions is broken by the presence of the magnetic field in the prominence. We show that this can lead to a significant modification of the $\Delta n = 0$ collisional transitions among the hydrogen Zeeman sublevels.

[1] LERMA, Observatoire de Paris – Meudon, CNRS UMR 8112, 5 place Jules Janssen, 92195 Meudon Cedex, France
[2] Astronomical Institute ASCR, Fričova 298, 25165 Ondřejov, Czech Republic

2 Collisional transitions $nljM \to n\, l \pm 1\, j'M'$ within the fine structure levels

It is a well known fact of quantum mechanics that the transition amplitude (or probability) of the system affected by the action of an external time-dependent perturbation $V(t)$, depends on the duration of the interaction (τ_c) and on the splitting of the levels (ω). If the interaction is very short with respect to the level splitting ($\omega\tau_c \ll 1$) then the collisional transition amplitude is practically independent of ω. This can be easily understood from the Heisenberg uncertainty relation between time and energy. On the other hand, if the interaction time is comparable to the splitting ($\omega\tau_c \approx 1$), the amplitude can be very sensitive to ω. As a consequence it follows that a modification of the energy splitting of the levels can be used for tuning the transition probabilities in some cases. In other respects, the duration of a collision is most often very small compared to the inverse of the Larmor frequency, and thus the magnetic field can be neglected for calculating the cross-sections. In fact, up to now, they have always been calculated in zero-magnetic field in solar polarization studies. Thus the axial symmetry of the problem is conserved and only alignment of the sublevels can be obtained. Consequently only net linear polarization can be observed.

Although, this is only an idealization of realistic problems and a more refined theory is sometimes required for explaining certain experimental situations or certain observations. Gay & Omont (1974, 1976), Gay & Schneider (1979), and other references therein, have proved that the transition rates among the Zeeman sublevels of Hg (6^3P_1) colliding with rare gases are significantly modified by the presence of a magnetic field. They have shown that the inclusion of the Zeeman splitting in the energies of the Zeeman sublevels breaks the axial symmetry and creates orientation. Their measurements of the σ and π fluorescence intensities, emitted at right angles to the excitation direction by a discharge lamp, are in a good qualitative agreement with their semiclassical calculations, obtained by using a Van der Waals interaction potential : cf. for instance Fig. 4 of Gay & Omont (1976) and Fig. 3 of Gay & Schneider (1979). The cross-sections $\sigma(\alpha J0 \to \alpha J+1)$ and $\sigma(\alpha J0 \to \alpha J-1)$ are different, creating orientation by isotropic collisions, and the resulting circular polarization is of the same order of magnitude than the linear polarization.

The situation with hydrogen in prominences is slightly different. First of all, we recall that the anisotropic excitation of the levels is due to the incident underlying photospheric radiation field. This only creates alignment, and thus linear polarization, due to the axial symmetry of the problem. The magnetic field is responsible for the Hanle effect, modifying the polarization degree and the direction of linear polarization. Collisions with electrons and protons of the medium depolarize the line. Only linear polarization can be obtained. This is the usual interpretation of the observations.

Concerning collisions, it was shown in the past by Bommier et al. (1986) that the inelastic dipolar transitions $nljM \to n\, l \pm 1\, j'M'$ among the fine structure levels due to isotropic collisions with thermal electrons and protons are the collisions which play the significant role in hydrogen line depolarization in prominences. The hydrogen fine structure is quasi-degenerated. It is due to a specific character of the nuclear electric field. The separation of the fine-structure levels due to spin-orbit interaction and to the Lamb shift is very small. For $n = 3$ it varies from approximately 10^{-7} to 10^{-5} eV, and it is well below the thermal energy of the 10 000 K particles of the prominence. The cross-sections $\sigma(nljM \to n\, l \pm 1\, j'M')$ are very high and, though of inelastic nature, can depolarize the Hα line. A typical value of the magnetic field strength in a solar prominence is of the order of 10 G. Such a field leads to a splitting of the $nljM$ sublevels (Zeeman effect) comparable to the fine-structure splitting (see Fig. 1). Considering the preceding, the question comes up in mind whether this splitting can affect the inelastic collisional rates among the Zeeman sublevels. Such a symmetry breaking could be responsible for conversion of the alignment and population of the levels into an orientation of the levels. A quantitative calculation shows that in the physical conditions of a prominence, the condition $\omega\tau_c \approx 1$ is satisfied for $\Delta n = 0$ and for a significant fraction of thermal electrons and especially protons. The problem to be solved is to calculate the appropriate collisional cross-sections.

A first attempt to take into account the modification of the ion-hydrogen cross-sections in the case of a weak and uniform magnetic field has been done by Sakimoto (1992a,b) for applications to plasma physics. For the purpose of solar prominence diagnostics, we need to calculate more detailed cross-sections. It is known that in the physical conditions of prominences the semiclassical limit for these collisions is usually well satisfied: the major role is played by distant collisions of ~ 1 eV particles for which the colliding particle can be treated classically and moves along a straight path unperturbed by the hydrogen-perturber interaction. The time-dependent electrostatic interaction potential $V(t)$ can be used and expanded to the second order. The first-order perturbation theory is valid for calculating the collisional probability amplitudes, provided that a symmetrization of the S-matrix is made (Seaton 1962). An integration over the relevant impact parameters and energies then gives the desired cross-sections. In our calculations we have used the first-order impact-parameter method (Seaton 1962; Sahal-Bréchot 1969; Sahal-Bréchot et al. 1996) which is equivalent at the high-energy limit, to the first-order plane-wave Born approximation (Taulbjerg 1977). In fact our impact parameter method is better than the Born one for line polarization studies because we have used the improvements made by Bommier (2006) who has taken into account the momentum transfer in the calculations of the cross-sections.

3 Preliminary results

Fig. 1 and Fig. 2 show our preliminary results: we find that this mechanism can lead to atomic orientation (i.e., net circular polarization) if the excited levels are radiatively pumped by a non-Planckian radiation. The statistical equilibrium of the hydrogen levels in the prominence results from radiative pumping of the Zeeman sublevels by the cylindrically symmetric radiation field of the solar surface, from the Hanle effect, from the redistribution of populations and coherences of the sublevels by thermal collisions, and by emission of radiation with thus a modified polarization signature. To keep the problem computationally simple[1], we suppose that the magnetic field is oriented vertically, i.e., is parallel to the preferential direction of the incident anisotropic radiation.

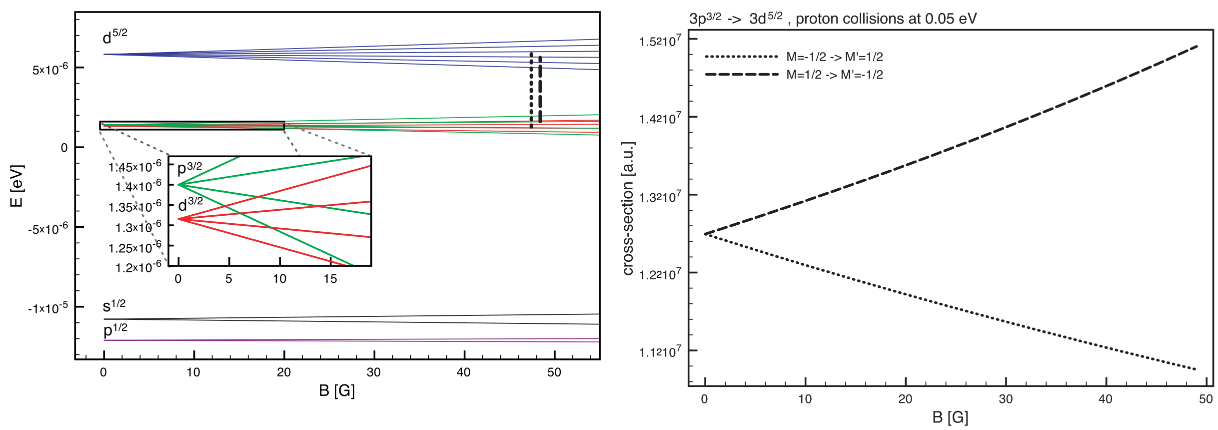

Fig. 1. Left: Zeeman splitting of the $n = 3$ fine-structure levels of hydrogen. The energy difference leads to modification of cross-sections. **Right**: Comparison of the angle-averaged proton cross-sections for $3p^{3/2}(M = -1/2) \rightarrow 3d^{5/2}(M' = +1/2)$ and $3p^{3/2}(M = +1/2) \rightarrow 3d^{5/2}(M' = -1/2)$ transitions at the collision energy 0.05 eV (close to the maximum cross-section value). The transitions are schematically illustrated in the left part of the figure using the same line patterns.

The effect of isotropic collisions on creation of atomic orientation seems to be significant, even in our simple configuration. The field of few tens of Gauss and typical thermodynamical properties of prominences lead to a significant suppression of the antisymmetric Stokes-V profile of the emitted Hα line in favor of the symmetric lobe. An interesting property of the calculations is that the effect on the *linear* polarization signal is quite negligible and all the previous calculations of collisional depolarization in solar prominences remain valid.

4 Conclusions and future prospects

We propose that this effect could be a possible explanation of the net circular polarization observed in solar prominences.

The density of the perturbers must be high enough to redistribute the radiatively unequally populated Zeeman sublevels before their radiative decay, but not too high to establish equal populations (typically $10^{10}\,\mathrm{cm}^{-3}$).

In contrast to the linear polarization degree (that is always decreased by isotropic collisions), the amplitude of circular polarization can be increased in typical prominence conditions.

[1]There are no Hanle effect and thus no quantum coherences among the Zeeman sublevels for this particular geometry.

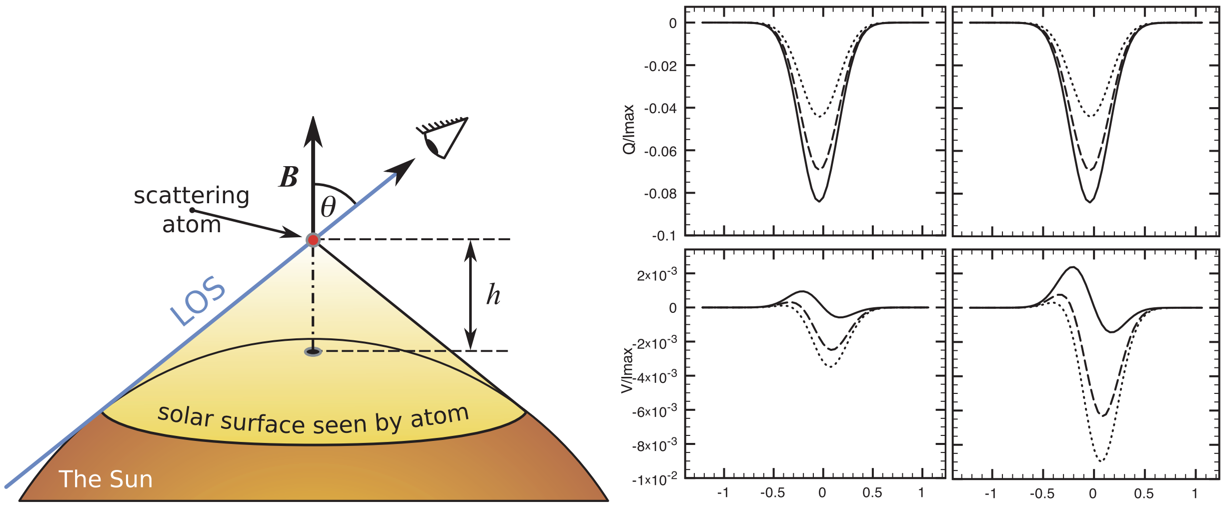

Fig. 2. Left: The geometry we consider in our example. The hydrogen atom is at the height h above the solar surface. The magnetic field vector, $\vec{B}$, is vertical. The line-of-sight (LOS) is inclined with an angle θ from the vertical. The angle θ is only determined by $h/R_{\rm sun}$. **Right**: Stokes Q and V profiles normalized to the maximum intensity $I_{\rm max}$ of the scattered Hα radiation with a radiation anisotropy $w = 0.42$ ($h = 131\,000$ km, $\theta = 57.3°$; see Fig. 2). Stokes-U identically vanishes in our configuration. Horizontal axis: distance from line center (Å). Left (right) panels show the profiles for a magnetic field of 20 G (50 G). The electron and proton densities are equal: $0\,{\rm cm}^{-3}$ (solid line), $10^{10}\,{\rm cm}^{-3}$ (dashed line), and $5\times10^{10}\,{\rm cm}^{-3}$ (dotted line). The temperature of the plasma is 8 000 K. The linear polarization signal is not affected by the magnetic field in the particular considered geometry.

This mechanism does *not* significantly alter the linear polarization.

More detailed calculations are needed: a realistic direction of the magnetic field must be introduced, and thus coherences have to be introduced in the calculations of the effects of collisions.

Our results are thus only preliminary and a deeper investigation of the conditions of validity of our approach also needs to be discussed.

References

Bommier, V. 1980, A&A, 87, 109

Bommier, V., Leroy, J.L., & Sahal-Bréchot, S. 1986, A&A, 156, 79

Bommier, V. 2006, Solar Polarization 4, ASP Conference Series, Vol. 358, Proceedings of the conference held 19-23 September, 2005, in Boulder, Colorado, USA. ed R. Casini and B. W. Lites, p.245

Gay, J.C., & Omont, A. 1974, J.Phys.Fr., 35, 9

Gay, J.C., & Omont, A. 1976, J.Phys.Fr., 37, L69

Gay, J.C., & Schneider, W.B. 1979, Phys.Rev.A, 20, 879

Kemp, J.C., Macek, J.H., & Nehring, F.W. 1984, ApJ, 278, 863

López Ariste, A., Casini, R., Paletou, F., et al. 2005, ApJ, 621, L145

Sahal-Bréchot, S. 1969, A&A,1, 91

Sahal-Bréchot, S., Vogt, E., Thoraval, S., & Diedhiou, I. 1996, A&A, 309, 317

Sakimoto, K. 1992a, J. Phys. B: At. Mol. Phys., 25, 3641-3654

Sakimoto, K. 1992b, J. Phys. B: At. Mol. Phys., 25, 5399-5411

Seaton, M.J. 1962, Proc.Phys.Soc., 79, 1105

Stehlé, C., Mazure, A., Nollez, G., & Feautrier, N. 1983, A&A, 127, 263

Taulbjerg, K. 1977, J. Phys. B: At. Mol. Phys., 10, L341-L346

SF2A 2008
C. Charbonnel, F. Combes and R. Samadi (eds)

ELECTRON ACCELERATION IN CONNECTION WITH RADIO NOISE STORM ONSETS OR ENHANCEMENTS

Vilmer, N.[1] and Trottet, G.[1]

1 Introduction

Radio noise storms are generated by suprathermal ($\simeq$ 10 keV) electrons accelerated continuously over time scales of hours or days in active region magnetic fields. They are related to emerging magnetic loops interacting with overlying loops and leading to magnetic coronal reconfiguration (e.g. Bentley et al. 2000). Noise storm onsets or enhancements have been sometimes observed in association with a flare-like sudden energy release in the active region producing a localized microwave (Raulin et al. 1991) or soft X-ray brightening (Raulin & Klein 1994). A few cases have also been reported in which 10-30 keV emission from a superhot plasma or from non-thermal electrons have been observed at the onset of noise storms (Crosby et al. 1996) confirming that a flare-like energy release in the lower corona could be a necessary condition for noise storms to start. No spatially resolved hard X-ray observations were however available in the case of the latter analysis, allowing to check that the flare-like emission and the noise storm were originating from the same active region. We present here an event for which both radio and hard X-ray (HXR) spatially resolved observations are available.

2 Observations and Results

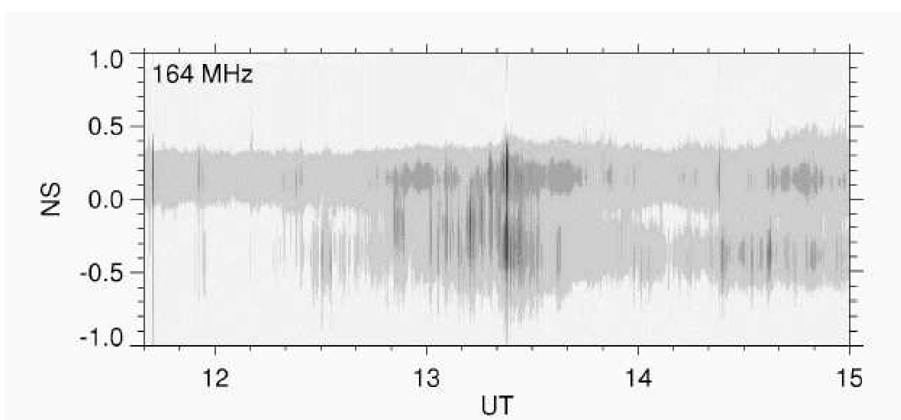

Fig. 1. Isocontours of the radio intensity at 164 MHz as a function of the north-south position on the Sun for the noise storm radio sources observed on 29 April 2005 by the Nançay Radioheliograph. Notice the appearance of a new noise storm toward the south from 12:30 UT.

Figure 1 shows the isocontours of the radio intensity at 164 MHz as a function of the north-south position observed by the Nançay Radioheliograph (NRH) on 29 April 2005. A radio noise storm is observed from 11:00 UT to 15:00 UT in the northern hemisphere at all the NRH observing frequencies. At 164 and 150 MHz, the intensity of the noise storm is observed to increase around 12:50 UT. A new radio noise storm appears in the

[1] Observatoire de Paris, LESIA, CNRS-UMR 8109, Meudon, France

southern hemisphere at these 2 frequencies (and also at 236 MHZ) after 12:30 UT. The GOES X-ray flux is observed to slowly rise after 12:00 UT. The X-ray flux observed by RHESSI in the 6-12 keV range also exhibits a rise from 12:00 ut to 13:00 UT (night time) with a succession of small peaks.

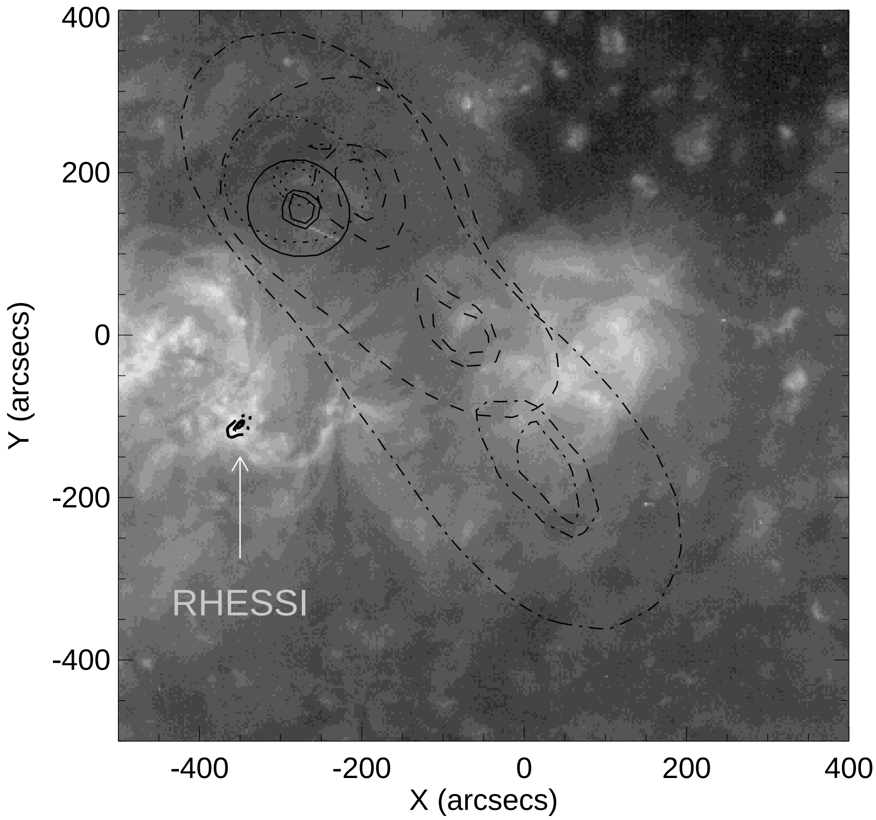

Fig. 2. Positions of the noise storm radio sources observed at 13:01 UT with the Nançay Radioheliograph: at 164 MHz (dashed-dotted contours), 236 MHz (dashed contours), 327 MHz (dotted contours) and 410 MHz(full contours) and of the X-ray emission in the 6-12 keV range observed with RHESSI between 12:47 and 12:49 UT. The radio and HXR contours are overlaid on a SOHO/EIT image taken at 13:13 UT.

Figure 2 shows the positions of the two radio noise storms observed at 13:01 UT with the NRH together with the contours of the X-ray emission observed by RHESSI in the 6-12 keV range shortly before the RHESSI night. The flare-like X-ray emissions observed by RHESSI from 12:00 UT originate from the active region which is closely linked to the radio noise storms. The PFSS extrapolation of the magnetic field in the vicinity of the active region (method from Schrijver & DeRosa (2003) available via Solar Soft) shows the magnetic connections between the location of the X-ray flare in the active region and the radio noise storm in the southern hemisphere (Vilmer and Trottet, in preparation).

References

Bentley, R.D., Klein, K.L., van Driel-Gesztelyi, L. et al. 2000, Sol Phys, 193, 227

Crosby,N., Vilmer, N., Lund, N., et al. 1996, Sol Phys, 167, 333

Raulin, J.P., Kerdraon, A., Klein, K.L., et al. 1991, A&A, 251, 298

Raulin, J.P., & Klein, K.L. 1994, A&A, 281, 536

Schrijver, C.J., & DeRosa M.L. 2003, Sol Phys, 212, 165

Author Index